10 copies
07/25/80 MM.

SEPTEMBER 10-14, 1979
MONTAUK, N.Y.

Dr: 1562

BNL 51134

CONF-790927--

MASTER

PROCEEDINGS OF THE 1979 LINEAR ACCELERATOR CONFERENCE



Edited by:
R.L. Witkover

BROOKHAVEN NATIONAL LABORATORY
ASSOCIATED UNIVERSITIES, INC.
UPTON, NEW YORK 11973

DISTRIBUTION OF THIS DOCUMENT IS UNLIMITED

DISCLAIMER

This report was prepared as an account of work sponsored by an agency of the United States Government. Neither the United States Government nor any agency Thereof, nor any of their employees, makes any warranty, express or implied, or assumes any legal liability or responsibility for the accuracy, completeness, or usefulness of any information, apparatus, product, or process disclosed, or represents that its use would not infringe privately owned rights. Reference herein to any specific commercial product, process, or service by trade name, trademark, manufacturer, or otherwise does not necessarily constitute or imply its endorsement, recommendation, or favoring by the United States Government or any agency thereof. The views and opinions of authors expressed herein do not necessarily state or reflect those of the United States Government or any agency thereof.

DISCLAIMER

Portions of this document may be illegible in electronic image products. Images are produced from the best available original document.

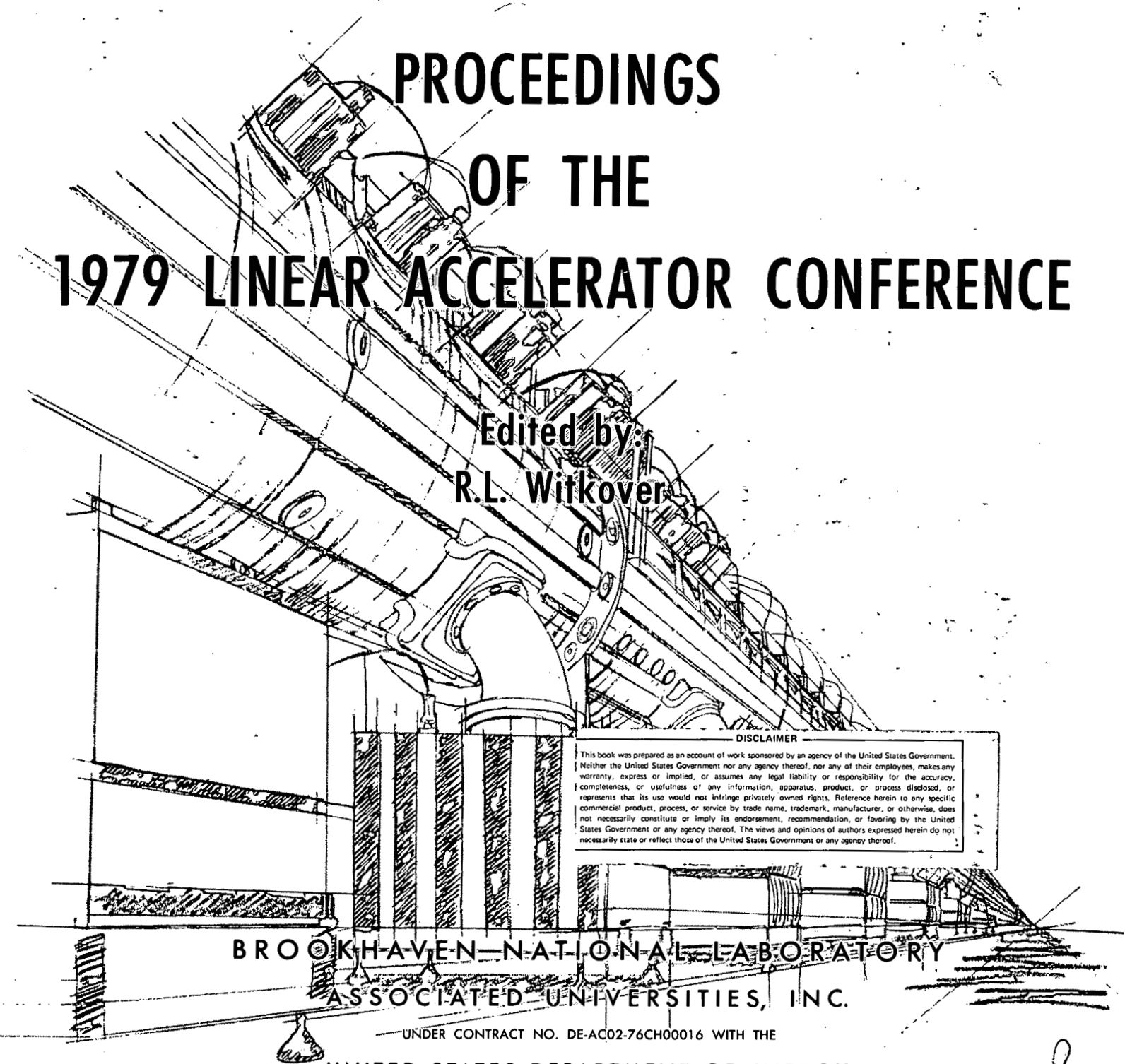

100% DUTY FACTOR

SEPTEMBER 10-14, 1979

MONTAUK, N.Y.

BNL 51134

PROCEEDINGS OF THE 1979 LINEAR ACCELERATOR CONFERENCE



Edited by:
R.L. Witkover

DISCLAIMER

This book was prepared as an account of work sponsored by an agency of the United States Government. Neither the United States Government nor any agency thereof, nor any of their employees, makes any warranty, express or implied, or assumes any legal liability or responsibility for the accuracy, completeness, or usefulness of any information, apparatus, product, or process disclosed, or represents that its use would not infringe privately owned rights. Reference herein to any specific commercial product, process, or service by trade name, trademark, manufacturer, or otherwise, does not necessarily constitute or imply its endorsement, recommendation, or favoring by the United States Government or any agency thereof. The views and opinions of authors expressed herein do not necessarily state or reflect those of the United States Government or any agency thereof.

BROOKHAVEN NATIONAL LABORATORY
ASSOCIATED UNIVERSITIES, INC.
UNDER CONTRACT NO. DE-AC02-76CH00016 WITH THE
UNITED STATES DEPARTMENT OF ENERGY

DISTRIBUTION OF THIS DOCUMENT IS UNLIMITED

DISCLAIMER

This book was prepared as an account of work sponsored by an agency of the United States Government. Neither the United States Government nor any agency thereof, nor any of their employees, makes any warranty, express or implied, or assumes any legal liability or responsibility for the accuracy, completeness, or usefulness of any information, apparatus, product, or process disclosed, or represents that its use would not infringe privately owned rights. Reference herein to any specific commercial product, process, or service by trade name, trademark, manufacturer, or otherwise, does not necessarily constitute or imply its endorsement, recommendation, or favoring by the United States Government or any agency thereof. The views and opinions of authors expressed herein do not necessarily state or reflect those of the United States Government or any agency thereof.

Printed in the United States of America
Available from
National Technical Information Service
U.S. Department of Commerce
5285 Port Royal Road
Springfield, VA 22161
Price: Printed Copy $15.00; Microfiche $3.00

TABLE OF CONTENTS

OPENING REMARKS by G. H. Vineyard xvii

OVERVIEW OF CONFERENCE by George W. Wheeler xiii

SECTION I - LINAC APPLICATIONS, NEW LINAC DESIGNS xix

APPLICATIONS OF LINEAR ACCELERATORS by J. P. Blewett 1

DESIGN STUDY OF THE BEJING 200 MeV PROTON LINAC by Shu-Hung Wang, Tzu-Hua Lo, Yi-Jin Chang and Ying-Hsong Lo 5

THE PHOTON FACTORY 2.5 GEV INJECTOR ELECTRON LINAC by J. Tanaka, I. Sato, K. Nakahara, S. Anami, S. Fukuda, K. Matsumoto, T. Shidara and A. Enomoto 8

THE LINAC FOR THE NATIONAL SYNCHROTRON LIGHT SOURCE by K. Batchelor, J. Bittner, T. Dickinson, V. Racaniello and J. Sheehan 13

THE UNILAC UPGRADING PROGRAM BY N. Angert, D. Böhne, J. Klabunde and H. Trautmann 17

THE FUSION MATERIALS IRRADIATION TEST (FMIT) ACCELERATOR by E. L. Kemp, D. J. Liska and M. D. Machalek 21

A HIGH-ENERGY BEAM TRANSPORT SYSTEM by K. E. Melson, J. A. Farrell, D. J. Liska and P. Meads 25

STATUS OF THE VARIABLE FREQUENCY HEAVY ION LINAC, RILAC by M. Odera, Y. Chiba and T. Kambara 28

ACCELERATING STRUCTURE PARAMETERS OF THE NEW ENGLAND NUCLEAR CORP. PROTON LINAC by D. Comastra 32

LINAC EFFICIENCY AND BEAM QUALITIES IN p, d, $^{3}_{2}He$ and $^{4}_{2}He$ ACCELERATION by J.-P. Auclair, P.-A. Chamouard, J.-L. Lemaire 37

LIMITATIONS AND IMPROVEMENTS OF HEAVY ION ACCELERATION WITH A 20-MEV PROTON LINAC by J.-P. Auclair, P.-A. Chamouard, J.-L. Lemaire 43

PLANS FOR H^- ACCELERATION IN THE AGS LINAC by D. S. Barton and R. L. Witkover 47

RF LINAC-PUMPED LASERS by W. E. Stein, T. R. Loree, C. A. Brau and S. D. Rockwood 53

LASL ELECTRON LINAC WORKSHOP by W. E. Stein 57

SECTION II - OPERATING MACHINES 59

HIGH-CURRENT HEAVY-ION LINACS AS IGNITERS FOR COMMERCIAL-SCALE INERTIAL-FUSION POWER PLANTS by David L. Judd 61

THE NEW CERN 50-MeV LINAC by E. Boltezar, H. Haseroth, W. Pirkl, G. Plass, T. Sherwood, U. Tallgren, P. Têtu, D. Warner and M. Weiss 66

LAMPF OPERATIONS AT 500 μA by D. C. Hagerman 78

OPERATION OF THE BROOKHAVEN 200-MeV LINAC by N. M. Fewell and V. LoDestro 83

THE RUTHERFORD LABORATORY 70-MeV LINEAR ACCELERATOR by N. D. West 88

STATUS OF THE KEK INJECTOR LINAC by S. Anami, H. Baba, S. Fukumoto, K. Ito, T. Kakuyama, C. Kubota, Y. Mori, T. Sakaue, I. Sato, A. Takagi, T. Takenaka, S. Takano and J. Tanaka 94

STATUS REPORT ON THE UNILAC by D. Böhne 98

STATUS OF THE ARGONNE SUPERCONDUCTING-LINAC HEAVY-ION BOOSTER by J. Aron, B. Benaroya, L. M. Bollinger, B. G. Clifft, W. Henning, K. W. Johnson, J. M. Nixon, P. Markovich and K. W. Shepard 104

OPERATION OF THE HEIDELBERG HEAVY-ION POSTACCELERATOR by H. Ingwersen, E. Jaeschke, R. Repnow, Th. Walcher, B. Huck and B. Kolb 109

OPERATION OF THE KARLSRUHE SUPERCONDUCTING POST ACCELERATOR TEST SECTION IN THE SACLAY TANDEM HEAVY ION BEAM by K. W. Zieher, G. Hochschild, A. Hornung and J. P. Fouan, J. Gastebois, P. Joly 114

PRECISION BEAM FORMATION IN 2 GeV LINEAR ACCELERATOR OF ELECTRONS by V. I. Artyomov, V. A. Vishnyakov, A. N. Dovbnya and N. A. Kovalenko 118

A 5-MEV ELECTRON LINAC WITH HIGH ENERGY RESOLUTION by Yu. P. Vakhrushin, V. M. Nikolaev, A. V. Rjactsov, Yu. A. Svistunov, Yu. P. Severgin and V. L. Smirnov 122

SECTION III - STRUCTURES 127

LOW-BETA LINAC STRUCTURES by D. A. Swenson 129

AN RF POWER MANIFOLD FOR THE RADIO FREQUENCY QUADRUPOLE LINEAR ACCELERATOR by James M. Potter 138

VOLTAGE BREAKDOWN TESTING FOR THE RADIO-FREQUENCY QUADRUPOLE ACCELERATOR by S. W. Williams, G. W. Rodenz, F. J. Humphry and J. M. Potter 144

WORK ON RF QUADRUPOLE FOCUSING STRUCTURES AT GSI by R. W. Müller 147

THE DESIGN OF A 12.5-MHZ WIDEROE LINAC FOR ION BEAM FUSION by A. Moretti, J. M. Watson, R. J. Stockley, J. S. Moenich, R. J. Lari, T. K. Khoe, J. A. Bywater, R. J. Burke and S. Jorna 152

A HEAVY ION POST-ACCELERATOR WITH COUPLED SPIRAL AND SPLIT-RING RESONATORS by A. Schempp, H. Klein, W. Rohrbach, W. Caspar, G. Lotterbach and E. Müller 159

HIGH-BETA LINAC STRUCTURES by S. O. Schriber 164

LIMITATIONS OF THE DISK-AND-WASHER STRUCTURE by S. O. Schriber and J. M. Potter 176

BEAM LOADING EXPERIMENTS WITH A SIDE-COUPLED STRUCTURE by G. E. McMichael, J. McKeown and J. S. Fraser 180

DETUNING EFFECT IN A TRAVELING WAVE TYPE LINAC by S. Arai, K. Kobayashi, E. Tojyo and K. Yoshida 184

PARTICLE ACCELERATION WITH TE_{011} CAVITY by Z. D. Farkas 190

C-BAND SUPERCONDUCTING CAVITY RESEARCH AT KEK by T. Furuya, K. Hosoyama, T. Kato, Y. Kojima and O. Konno 194

MODELLING OF BIPERIODIC SLOW-WAVE STRUCTURES by V. L. Bukharin, A. Y. Novozhilov, O. V. Plink, N. P. Sobenin, V. V. Stepnov, V. K. Shilov and E. J. Shkolnikov 197

SECTION IV - THEORY 203

RF QUADRUPOLE BEAM DYNAMICS DESIGN STUDIES by K. R. Crandall, R. H. Stokes and T. P. Wangler 205

INFLUENCE OF SPACE CHARGE ON AXIAL PARTICLE MOTION IN HEAVY ION LINACS by P. Junior, H. Deitinghoff, H. Klein 217

LONGITUDINAL CURRENT IN A LINAC ACCELERATING CELL by Juris G. Kalnins 223

THE SIGNIFICANCE OF BEAM OPTICS CONCEPTS AS APPLIED TO THE NEW CERN LINAC by M. Weiss 227

ON EMITTANCE GROWTH IN LINEAR ACCELERATORS by R. A. Jameson and R. S. Mills 231

A STATISTICAL APPROACH TO THE ESTIMATION OF BEAM SPILL by G. P. Boicourt and R. A. Jameson 238

GENERAL LEAST-SQUARES FITTING PROCEDURES TO MINIMIZE THE VOLUME OF A HYPERELLIPSOID by E. Alan Wadlinger 242

FOCUSING OF HIGH CURRENT BEAMS IN CONTINUOUSLY ROTATED QUADRUPOLE SYSTEMS by Robert L. Gluckstern 245

LINEAR ACCELERATORS WITH INTERTANK FOCUSING by B. Franczak, K. Blasche and B. Franzke 249

BEAM DYNAMICS IN A PROTON LINEAR ACCELERATOR FOR A NEUTRON SPALLATION SOURCE by K. Mittag 253

A PHASE ADJUSTED FOCUSING LASER ACCELERATOR by Peng Huanwu and Zhuang Jiejia 257

SIMULTANEOUS BEAMS OF DIFFERENT ENERGY FROM LAMPF by G. R. Swain and D. C. Hagerman 262

SECTION V - CONTROLS AND BEAM DIAGNOSTICS 267

A MICROCOMPUTER CONTROL SYSTEM FOR THE SUPERHILAC THIRD INJECTOR by H. D. Lancaster, S. B. Magyary, J. Glatz, F. B. Selph, M. P. Fahmie, A. L. Ritchie, S. R. Keith, G. R. Stover and L. J. Besse 269

A DISTRIBUTED LINAC CONTROL SYSTEM FEATURING SDLC LOOP COMMUNICATION by R. W. Goodwin and M. F. Shea 274

DISTRIBUTED CONTROL SYSTEM FOR THE FMIT by J. A. Johnson, D. R. Machen and R. M. Suyama 279

LAMPF FIRST-FAULT IDENTIFIER FOR FAST TRANSIENT FAULTS by Arthur R. Swanson and Robert E. Hill 283

COMPUTER CONTROLLED FORMATION OF THE 750-keV ACCELERATOR COLUMN ON THE NEW CERN 50-MeV LINAC by H. Haseroth 286

LONGITUDINAL AND TRANSVERSE BEAM OPTIMIZATION AT THE UNILAC by L. Dahl, J. Klabunde, P. Strehl and V. Schaa 291

MEASUREMENTS OF ENERGY, ENERGY SPREAD AND BUNCH WIDTH AT THE UNILAC by J. Klabunde, V. Schaa, E. Schaffner, P. Strehl, H. Vilhjalmsson and D. Wilms 297

CALIBRATION DURING INSTALLATION AND DURING INITIAL OPERATION OF THE CERN 50 MeV LINAC by D. J. Warner 304

NEW LINAC THREE PHASE PLANES PULSED EMITTANCE MEASUREMENT by P. Têtu 309

BEAM TOMOGRAPHY IN TWO AND FOUR DIMENSIONS by O. R. Sander, G. N. Minerbo, R. A. Jameson and D. D. Chamberlin 314

SINGLE BUNCH ACCELERATION AND DETECTION IN S-BAND ELECTRON LINEAR ACCELERATOR by J. Tanaka, I. Sato, S. Anami, S. Fukuda, H. Matsumoto and Y. Tabata, K. Kobayashi, S. Tagawa, M. Washio 319

SECTION VI - RADIOFREQUENCY TECHNOLOGY 325

RF SOURCES DEVELOPMENTS by Jean V. Lebacqz 327

RECENT DEVELOPMENTS IN HIGH POWER VACUUM TUBE TECHNOLOGY by J. Ross Faulkner 336

NEW ENGLAND NUCLEAR LINAC RF POWER SYSTEM by R. F. Lankshear 340

THE RF-SYSTEM OF THE CERN "NEW LINAC" by J. Cuperus, F. James and W. Pirkl 344

RECENT IMPROVEMENTS OF THE ACCELERATOR COMPONENTS AT THE UNILAC by D. Böhne, M. Emmerling and A. Gasper 348

DEVELOPMENTS OF THE RF SYSTEM FOR THE FUSION MATERIALS IRRADIATION TEST ACCELERATOR by M. V. Fazio, H. P. Johnson and Dennis M. Riggin 356

CONDITIONING EXPERIMENTS ON THE 100% DUTY FACTOR 3 MeV ALVAREZ LINAC by B. G. Chidley, J. Ungrin and J. C. Brown 360

200 MHz FAST PHASE SHIFTERS AND PHASE DETECTION FOR A RAMPING ENERGY by J.-P. Auclair, P.-A. Chamouard and J.-L. Lemaire 364

HIGH POWER ISOLATOR FOR THE KEK PROTON LINAC by S. Anami, H. Baba, Y. Mori, J. Tanaka, S. Fukumoto, T. Takenaka, C. Kubota, K. Ito , T. Sakaue and K. Shinohara. 367

SECTION VII - MECHANICAL TECHNOLOGY 371

THE DRIFT TUBE AND BEAM LINE QUADRUPOLE PERMANENT MAGNETS FOR THE NEN PROTON LINAC by R. F. Holsinger 373

TIPLESS PERMANENT MAGNET QUADRUPOLE LENSES by N. V. Lazarev and S. Skachkov 380

MECHANICAL ASPECTS OF THE NEW ENGLAND NUCLEAR LINAC by R. Damm, J. Aggus and G. Greenberg 384

CAVITY AND DRIFT TUBE TECHNOLOGY FOR THE UPGRADED UNILAC by D. Bohne, H. Gaiser and E. Malwitz 388

MECHANICAL DESIGN OF CERN NEW LINAC ACCELERATING STRUCTURE by E. Boltezar 392

MODULAR DESIGN ASPECTS OF THE FMIT DRIFT-TUBE LINAC by D. J. Liska, R. G. Schamaun, W. Fox, J. A. Frank, W. Coops, C. Potter, T. Cole, D. Greenwood, H. Norman, P. Giles, K. Creek and D. Clark 396

MECHANICAL DESIGN CONSIDERATIONS IN FMIT RFQ DEVELOPMENT by C. W. Fuller, S. W. Williams and J. M. Potter 401

SECTION VIII - ION SOURCES AND PREACCELERATORS 407

RECENT PROGRESS IN ION SOURCES AND PREACCELERATORS by David J. Clark 409

TESTS WITH A MULTIDIPOLE ION SOURCE ON THE CERN 500-keV EXPERIMENTAL PRE-ACCELERATOR by J. Grando, H. Haseroth, C. Hill and M. Hone 420

DEVELOPMENT OF A HIGH BRIGHTNESS ION SOURCE by A. J. T. Holmes and M. Inman 424

PROPERTIES OF H^- AND D^- BEAMS FROM MAGNETRON AND PENNING SOURCES by Th. Sluyters and V. Kovarik 428

THE EBIS AS AN INJECTOR FOR HEAVY-ION LINACS by R. W. Hamm 432

DEVELOPMENT OF HIGH CURRENT HEAVY ION SOURCES AT GSI by R. Keller and N. Angert 436

NEW METHOD FOR POSITRON PRODUCTION AT SLAC by B. Aune and R. H. Miller 440

THE COMPENSATION FOR BEAM LOADING ON THE PREINJECTOR OF THE NEW CERN 50 MeV LINAC by H. Haseroth, M. Hone and J. L. Vallet 444

DESIGN CRITERIA FOR HIGH VOLTAGE, HIGH CURRENT ACCELERATING COLUMNS by J. D. Hepburn, J. Ungrin, M. R. Shubaly and B. G. Chidley 448

ION SOURCE AND TRANSPORT SYSTEM FOR BNL-HIF PRE-ACCELERATOR by G. M. Gammel, E. F. Meier and R. M. Mobley 453

DEVELOPMENT OF A HIGH-CURRENT DEUTERON INJECTOR FOR THE FMIT FACILITY by J. D. Schneider, H. L. Rutkowski, E. A. Meyer, D. D. Armstrong, B. A. Sherwood and L. L. Catlin 457

PRE-ACCELERATOR FOR THE NEN LINAC by R. F. Bentley 462

INJECTOR OPERATIONS AT LAMPF by Ralph R. Stevens, Jr., John R. McConnell, E. P. Chamberlin, R. W. Hamm and R. L. York 465

CONFERENCE CHAIRMAN

John P. Blewett

CONFERENCE SECRETARY

Richard L. Witkover

ORGANIZING COMMITTEE

Kenneth Batchelor
John P. Blewett
Norman Fewell
John Keane
Pierre Grand
R. McKenzie-Wilson
Joseph Sheehan
Richard L. Witkover

PROGRAM COMMITTEE

Pierre Grand, BNL, Chairman

B. Chidley, AECL
C. Curtis, FNAL
N. Fewell, BNL
J. Fraser, AECL
R. Jameson, LASL
J. Keane, BNL
G. Loew, SLAC
E. Parker, ANL
S. Penner, NRS
F. Selph, LBL
G. Wheeler, Temple Univ.
R. Witkover, BNL

PROCEEDINGS EDITOR

Richard L. Witkover

CONFERENCE ARRANGEMENTS SECRETARY

Patricia Tuttle

BROOKHAVEN LIAISONS

Virginia Sayre, Special Programs Coordinator
Dorothy Schroeder

SESSION CHAIRMEN

P. Livdahl, FNAL
E. Knapp, LASL
D. Bohne, GSI
J. Fraser, CRNL
J. Leiss, DOE
D. Young, FNAL
K. Batchelor, BNL

SESSION SECRETARIES

N. Fewell
J. Sheehan
R. McKenzie-Wilson
R. Lockey
E. Grove
D. Barton

AUDIO/VISUAL ASSISTANTS

D. Klein
V. LoDestro
J. Talent

EDITOR'S NOTE

The 1979 Linear Accelerator Conference was held at Gurney's Inn, Montauk, New York. It was the tenth meeting in this series and was distinctive in several ways. It was the largest in number of participants (155 plus BNL visitors) and papers presented. It inaugurated the use of Poster Sessions, with more than half of the papers presented in this mode. It was the most international in scope, with accelerator scientists from the Peoples Republic of China attending for the first time.

The meetings were held over a period of five days, with a break at mid-week to allow participants to visit Brookhaven National Laboratory. Each conference day consisted of a 4-hour morning session of oral presentations, a 2-hour period after lunch during which poster papers were displayed but not manned, followed by a 2-hour period during which authors were present at the poster papers, and a post-dinner evening session for oral presentations. This format seemed to work well and allowed sufficient mid-day time for informal discussions.

These Proceedings form the record of the Conference. They consist of 91 technical papers plus the Welcoming Address and Conference Overview. Two of the papers were contributed for "publication only" because the authors were unable to attend. All of the remaining papers were given as invited papers, oral papers or poster presentations. From the large number of abstracts submitted to the Program Committee, it became clear that only a fraction could be chosen for oral presentation. The decision was made to join the growing trend toward Poster Sessions to provide an open forum for discussion, rather than accept the papers for publication only. From comments at the Conference, it seemed that the participants shared this view. An attempt was made to record the discussions at the poster presentations, by requesting attendees and authors to write a synopsis of their questions and answers; this proved to be a total failure. Although the sessions were the scene of lively discussion, not a single record was submitted for inclusion in the Proceedings. Perhaps in the future, some clever individual will develop a means of documenting the often illuminating questioning that these sessions produce.

The papers are organized into eight sections; the order is not always the same as at the Conference. This is because the poster papers were deliberately distributed among the three sessions to provide topics of interest to all at each of the sessions. For the Proceedings, these have been regrouped according to topic.

All papers were reviewed prior to printing. Changes were made to have the papers conform to the specified format and to the recommendations of the "Style Manual" of the American Institute of Physics. In cases in which an appreciable number of changes were made, or retyping was necessary, the papers were returned for the authors' approval. In no case was any attempt made to edit technical content.

ACKNOWLEDGEMENTS

The organizing and planning of a conference as large as this would be of no value without the hard work and dedication of those individuals who really made it happen. Among these, special thanks must go to Pat Tuttle and Dot Schroeder, who were the front line troops at the Conference Desk. Ginny Sayre provided the vital link between BNL and the Conference. The audio services were provided by George Walczyk and Denny Klein, who along with Jack Tallent, ran the slide projectors.

Transcription of the taped discussion was capably performed by Lillian Kouchinsky, Marion Newton and Barbara Barrett. Additional editing was provided by Harriet Fadem and Margaret Deines of the Research Library. Jackie Mooney did the bulk of the corrections and final typing. Special thanks to Marietta Gray for her assistance.

Pat Tuttle was everywhere and did everything. She was the catalyst that made the Conference a success. Working with her in editing these Proceedings was a pleasure I will not forget.

THIS PAGE

WAS INTENTIONALLY

LEFT BLANK

Review of the Conference

THIS PAGE

WAS INTENTIONALLY

LEFT BLANK

OVERVIEW OF THE CONFERENCE

George W. Wheeler
Temple University
Philadelphia, Pennsylvania

This conference is rapidly drawing to its conclusion, so I will be mercifully brief. In part for this reason, I will not attempt to summarize in a few minutes all of the things which you have been listening to for an entire week. However, for those who, later on, wish some guidance in studying the Proceedings, I recommend four invited papers which will give the flavor and essence of the conference. They are those by Blewett and by Judd for flavor, and those by Swenson and by Shreiber for much of the essence. For some years we have been talking increasingly about the applications of linacs. This year, the "applied" linacs seem to me to be more exciting and challenging than the physics machines. However, almost all of the papers were of high quality, perhaps higher on average than some of the earlier conferences.

From among the papers on operating machines, I was particularly pleased to hear that LAMPF has now met all of its design criteria and awaits only a sufficiently powerful target system to operate at full power. As I will point out a little later on, the linac meson-factory is an old dream that has, at last, come true.

From among the papers on new machines, I am particularly pleased to note the one describing the 200-MeV proton injector being proposed for Beijing, because this signals the first time that we have been joined here by our colleagues from the People's Republic of China. The first of these conferences was not in any sense international, but the succeeding ones very quickly became so. We have always had excellent attendance from Europe and from the USSR and more recently from Japan, so now it is most fitting to have our friends from China here, also.

The area of rf superconductivity has had a painfully slow development but at last seems close to being incorporated into operating machines. It is interesting that the major application may be in heavy-ion linacs rather than in electron linacs, as many people expected some years ago.

Real progress in the field comes when the users demand machines whose parameters exceed the capability of our present technology. This year, as always, the users are demanding bigger and bigger machines, but it is important to note that now it is the "applied" machines which are stretching the technology to new limits. Consider the demands placed upon us by PIGMY, FMIT, HIF and the possible use of accelerators for nuclear fuel production. In the PIGMY effort, we are being asked to take a very large, powerful and sophisticated accelerator, and to put it in a very small and inexpensive box in order that it may fit into both the budget and the space available in a hospital. This has led the people at LASL to examine a number of the old truths in an attempt to develop structures with higher gradients and greater efficiency.

The FMIT and HIF devices are simply demanding higher and higher power so that in every respect we are being forced to extend our technologies to meet these requirements. One of the results of these pressures has been the RFQ which is perhaps the most important development that we have heard about this week. Calculations and model tests which have been carried out so far, suggest that this system can solve some of the most vexing problems in the low-beta section of proton linacs. As you know, we have turned and twisted in all kinds of ways over the years in attempting to solve these problems.

The permanent magnet quadrupoles which we have been hearing about, will contribute further to the solution of the problems of the low-beta section. But those of us who are somewhat conservative will continue to worry about having to give up the ability to adjust the transverse focusing, when using devices such as the permanent magnet quadrupoles or the RFQ structures. But surely we will be able to handle these problems in due time. As with any radically new design, such as the RFQ, we are going to have some fun finding out about all of the possible modes by which the beam can interact with the structure, and how to deal with the inevitable instabilities that those interactions will produce. But in order to solve these problems we must build the devices and try them out.

As I listened to some of the papers on new projects, I was struck by the following paraphrase: "Old Linacs never die. They just pass on to somebody else's project." If you think about it, it's true, they just won't go away. I want to give you just two examples: One is the old Harwell 50-MeV PLA. One of the original proton linacs, it has now come back to life to be built into the new 70-MeV Rutherford machine. The PLA did not have to move very far but it has surely changed its purpose a number of times over the years. The other example touched me personally, and is the story of a machine which has travelled very far and wide. Joe Sheehan told us in his paper on the injector for the National Synchrotron Light Source, that there are a couple of sections of linac which were built at SLAC, then were sent to a laboratory in Holland and used there for some years, and now are back at BNL. It seems that some years ago when I was with the AEC, it was brought to my attention that the Dutch were finished with those linac sections and wished to send them back to the United States. I thought I had accomplished a great thing when I talked the AEC, with some difficulty, into abandoning the things in place. But in spite of my best efforts they are back here, anyway.

This conference more than any other has been dominated by one laboratory. By any measure that I can think of, the Los Alamos Scientific Laboratory has been the outstanding performer here this week. They have had about 30 registrants out of 170 attending the Conference. They presented, in one form or another, about 22 papers. One of their papers deserves special mention here because it represents one of several firsts at this conference. Last night you both saw and heard that paper. It is the first time that a laboratory

has brought to the Linac Conference a live demonstration of one of the principles which they are studying. In my newly created role as art critic for the conference, I must observe that Marianne's performance last night was a most convincing demonstration that art and beauty can be very tightly coupled to the acceleration business.

I am sure that you will all agree that it is perfectly clear that this has been a successful conference. But why? In the first place, the material that has been presented here is clearly significant and is relevant to a number of current programs. In other words, the conference is indeed timely. I remember with some amusement, immediately following one of these conferences several years ago, one of our distinguished colleagues assured us that the linac business was all finished and there would be no need for any more of these conferences! In addition to having significant and timely material well presented, the other important feature of a good conference is the instant feedback which occurs between the participants and the authors of the papers. If it were not for this feedback we could just as well publish all of the materials in the first journal that comes to hand. There was a lot of this feedback this week. You could see it and hear it all around you. I want to stress that the size and the ambiance of the conference must be conducive to producing it or the conference will fail. We have been very fortunate this week in that the management of the conference has treated us to a very special affair. This is the first of these conferences that has not been held on a laboratory site, and you are aware there was some trepidation about proceeding in the direction of Gurney's Inn for this conference. I need not dwell on the pleasure of Gurney's, but it is clear that the atmosphere here and the format of the conference have played an important part in our success this week. An early and lengthy morning session followed by a free afternoon worked out very well. There was adequate time during the afternoon both for excellent recreation and for viewing the poster sessions. Then the mercifully short evening session allowed the time necessary to get in a reasonable number of presentations.

Finally, I want to end on a historical note. I have here with me a modest volume which is entitled, "Minutes of A Linear Accelerator Conference, held at the Brookhaven National Laboratory in April, 1961." This was the first of this series of conferences and you won't be surprised to hear that it was organized by John Blewett. Twenty people attended that conference compared with the 170 here this week. So, there has been some growth in the size of the conference. It is interesting to note that 13 of those people are still active in some way or another in the accelerator field. One of them is dead, and six of them have moved into other areas. There are six of us here who attended that conference and, I believe, have attended every one in between. There were 17 papers presented orally at the conference in 1961. The poster sessions had not yet been invented. And for that matter Gurney's had not been invented either as far as Linac Conference was concerned. Of those 17 papers, 4 were on linac structures, 3 each on beam dynamics and engineering aspects, 2 each on performance of operating machines and on power sources and there was one on ion sources and one on a new proposal, and finally, one about cyclotrons.

This week we have managed not to talk about cyclotrons at all! However, I think you will find the distribution of the other papers not significantly different from then to now. It seems clear to me that 18 years later we are still talking about exactly the same subjects that we talked about then. That is not to imply that we have not made any progress in those 18 years, because I think we have made a great deal. There is a scale factor which is the degree of sophistication with which we deal with these same problems. There has been an enormous improvement in the quality of our techniques and the sophistication of our calculations.

The first paper in the 1961 Conference was presented by E.R. Beringer of Yale University. I am going to take the liberty of reading the first paragraph.

> "The Yale University Proposal is directed to a proton accelerator with an output energy of approximately 800 MeV and an output particle current of 0.1 milliampere to 1 milliampere of average proton current and with a high duty circle, i.e., of the order of 5%."

The paper goes on to make it clear that the accelerator under discussion is a linac.

I certainly have found it most gratifying, personally, and I suspect others here feel the same way, to hear at this Conference that that machine, which in fact is LAMPF, has now met all of its design criteria as stated in Beringer's paper.

The 1961 paper is the first printed statement in the U.S. proposing a linac meson-factory. But it is important to keep some historical perspective. This paper, written in 1961, refers to a design study done at Harwell and started in 1953 by Bill Walkinshaw and others. That design study proposes a proton linac of sufficient energy to produce mesons, and of significantly high current. In fact, the Harwell group proceeded to construct the first part of that machine, the old 50 MeV - PLA. Furthermore, they started upon the design of a 400-MHz klystron which was to be the power source for the second section of the accelerator.

So the proton linac meson-factory has been a central theme of these Conferences over the past 18 years. Now as we move ahead, we are looking at ever more powerful and exciting machines. And one of these new machines, I suspect, may similarly be woven into the fabric of future conferences.

Welcoming Address

THIS PAGE

WAS INTENTIONALLY

LEFT BLANK

OPENING REMARKS

G.H. Vineyard, Director
Brookhaven National Laboratory
Associated Universities, Inc.
Upton, L.I., N.Y. 11973

I want to welcome you all to Brookhaven National Laboratory-East. We plan to annex this exotic site as soon as we can complete the arrangements and get a bill through Congress. You owe a great deal to John Blewett who has been appropriately introduced by Phil Livdahl as the Dean of the Linac Conferences. He and Pierre Grand had a great deal to do with the choice of this site. They worried that people would think there was a boondoggle involved, and so they leaned over backwards by scheduling meetings starting at 8:30 and going throughout the day and most of the night. I think you're going to have your heads worked off. I do have to warn you, however, that this is the hurricane season.

This Conference is number ten in the series started in 1963 by Dean John Blewett at Brookhaven. Those were the days when we were planning a 300 to 1000 GeV accelerator to be built with Soviet help, an accelerator which never materialized, but which had at least one good result--it stimulated this series of conferences to come into being. I hope someday a comprehensive history of the development of accelerators is written and when it is, I hope it includes an adequate discription of machines that were conceived but never built. That would be most interesting.

I see that you have a Brookhaven tour scheduled for Wednesday. I hope as many of you as can will actually come over to the site where we do the work. We do have, as you know, two accelerators under construction: ISABELLE and the National Synchrotron Light Source. All together that involves a total of five synchrotron-type rings and one new linac.

I was reminiscing and recalled that the first linac I ever viewed was at MIT in 1945. I was at the Radiation Laboratory in those days, World War II was beginning to approach its end and people had begun turning their minds to longer range matters because they knew that a lot of the projects then in the Laboratory would never actually be completed before the end of the War. George Collins and, I believe, Ed Purcell and some others, built a curious looking device which kicked around the Laboratory for awhile and consisted of a piece of serpentine X-band waveguide about a meter in overall extent on the top of a little table. This serpentine was pierced down its axis by a circular pipe and electrons were meant to go down the axis and X-band radiation from a magnetron was sent down the waveguide; at the intersection between the serpentine and the pipe, electric fields were supposed to produce acceleration. It was a simple and elegant idea. I don't recall whether the thing ever actually worked or not, but it should have worked--it looked good.

As an outsider, really, to the accelerator field, one who looks in upon it frequently, but not day-to-day, I'm enormously impressed with the progress that has occurred from those primitive days. Back in the time I'm speaking of, accelerators were more or less like the famous dancing bear: the marvel was not how well they worked, but that they worked at all. Now, of course, we do so many tricks--those of you who are in the field day in and day out, perhaps don't quite appreciate the enormous accumulation of skill--we accelerate electrons and positrons and protons and light ions and heavy ions, and even charged dust particles if we want. We do gymnastics wonderful to behold with these particles: We collect, cool, compress, circulate, bend, wiggle, re-inject, transport, focus, transfer, fill, stack, eject, dump. We bump and stuff and hold, strip and kick, store and handle, trim and shave, scrape, polarize and deflect, all in microseconds and with high reliability--most of the time. It reminds one of a circus aerialist act, or the New York subway system. It's done in such a routine way that people in the trade think nothing of it, but one has to be enormously impressed with this virtuosity, this complete technology, which is now in our possession. Of course this has led to practical uses which are growing all the time. You're going to hear more about that from John Blewett in a little while.

I've noticed that your program includes a number of very interesting developments indicating the life that is in the field right now. Such things as rf quadrupole focusing, the production of much higher currents and new schemes for doing that; new permanent magnets which can be applied to the accelerator art and produce fields up to five times as high as we are accustomed to expecting from permanent magnets; injection at lower energies than people used to think possible (Dean John tells me that once he proved that you couldn't inject at such low energies. Well, even the Dean can be wrong). You will hear of superconductivity applied in all kinds of ways and, of course, of interactions with lasers, both in the use of accelerated beams to impinge on laser radiation for various purposes, and the use of lasers to produce acceleration and the use of accelerators to make free electron lasers. All of these things are among the many exciting developments in this very vigorous field.

I am delighted that so many of you found your way out to this remote end of Long Island and I am pleased that you will have a little time to look around and visit the beach and historic Montauk Point and the other sights. You have a busy schedule--I'll not take more of your time except again to say welcome and have a wonderful conference. Thank you.

THIS PAGE

WAS INTENTIONALLY

LEFT BLANK

Section I
Linac Applications, New Linac Designs

1979 LINEAR ACCELERATOR CONFERENCE

APPLICATIONS OF LINEAR ACCELERATORS*

J.P. Blewett
Brookhaven National Laboratory
Associated Universities, Inc.
Upton, New York 11973

Our first essays into the linear accelerator field were, by present standards, quite tentative and amateurish. Things have changed and we are now participants in an operation recognized as really advanced science and engineering.

For example, I bring to your attention a conference on "Applications of Intense Charged-Particle Beams" starting in a couple of weeks. To go to this conference you need two things: some familiarity with engineering or physics and $510. It is really not a conference, but a course designed for managers of industrial and technical projects. I mention it only to emphasize the fact that no longer are we long-haired scientists occupied exclusively with subjects primarily having only academic objectives.

Introduction

The histories of electron linear accelerators and ion linear accelerators diverged from the start,although the modern histories of both machines began immediately after the end of World War II. Both programs were based on wartime developments of high powered radio-frequency sources. But electrons are light as feathers and are easily made to fly in the electromagnetic wind inside the rf cavities of a linear accelerator. Protons are more like billiard balls and heavy ions are like bowling balls and require considerable pushing of a more specialized type to get them moving.

The result of all this was that electron linacs were much more speedily "reduced to practice" than were ion linacs and, indeed, found applications early in the 1950's in medical and engineering fields as well as in high energy physics.

At this point I digress to note that I shall pay very little attention to applications of either electron or proton linacs in the field of high energy physics. To this audience I think I can assume that this field is well known. Briefly, electron linacs from the Stanford Mark III through the machines at Orsay, SLAC and Kharkov have made major contributions to high energy physics including Nobel Prize discoveries by Bob Hofstadter. Proton linacs have served as injectors for the high energy synchrotrons at Brookhaven, Fermilab, Argonne, Berkeley, CERN, Serpukhov and elsewhere. Only now are other applications appearing for proton machines. No heavy ion linacs, to my knowledge, are important in high-energy studies.

So much for the moment for high energy physics.

*Work performed under the auspices of the U.S. Department of Energy.

It is interesting to look back forty years and to appreciate the fact that, although microwave rf sources were not available for use at high power levels, their possible uses were appreciated by many forward-looking scientists and engineers. The best known story is that of Bill Hansen and the Varian brothers who, in 1937, were exploring the possibilities of what came to be known as radar. While they were studying the potentialities of the klystron, other groups were also in the field. I mention a couple of cases with which I was personally acquainted,with the caveat that there must have been many others. At the General Electric Company in Schenectady, Chester Rice had built a primitive magnetron, had received echoes from cars in the GE parking lot and had observed Doppler effects from their velocities. In the same laboratory, Bill Hahn and Si Ramo (now the "R" in TRW) were developing a "velocity modulation" tube which was essentially the same as a klystron. My contribution to this effort was to dissuade Hahn and Ramo from using the abbreviation "VEMO" for their tube since this was already the name of a popular deodorant.

The other group , with the same appreciation of possible use of microwaves in the national defense,was at the Naval Research Laboratory. In those days--perhaps still for all I know--the Navy was by far the most imaginative and forward-looking of our military services. In any case, they were,in 1937,or so,already sponsoring experimental programs on reflection of microwaves from ships and aircraft.

So there it was, even then,--the germination process for the microwave power sources that, a decade later, made linear accelerators possible and practical.

Electron Linacs

The first sucessful operation of an electron linac came in 1947,both at Stanford and at the Telecommunications Research Establishment in England. Magnetron rf sources developed during the wartime radar effort were the first used to supply rf power, later to be supplanted by the klystrons developed at Stanford. Parenthetically, I note that I had considerable experience with klystrons during the war. These were little tubes that you could hold in the palm of your hand and were used only as local oscillators in radar receivers. It took an enormous amount of courage, again post-war at Stanford, to extrapolate these little devices from milliwatts to megawatts of output.

With the first post-war success, the Stanford group pushed toward high energy for physics research. The British, on the other hand, began

building linacs for cancer therapy. Their first machine operated in 1952 at Hammersmith Hospital in London at 8 MeV and has operated for almost three decades providing treatment for cancer patients.

The American effort on application of the electron linear accelerator to cancer therapy was, in large part,due to a collaboration between Henry Kaplan of the Stanford Medical Department and Ed Ginzton of Stanford. Patient treatment by the machine that resulted from this joint effort began in 1956. The successes of this effort inspired many developments elsewhere and now the electron linac is by far the favored machine for radiation therapy of cancer.

Medical Applications

For medical applications electron energies are required up to about 20 MeV. Very severe requirements are imposed on the machine. First of all, it must be reliable; it must perform at the push of a button day and night; treatment schedules must not be interrupted by machine failures. It must have high intensity to hold down patient exposures. It must be possible to rotate the source around the patient so that doses can be concentrated on internal tumors. This is vastly preferable to rotating the patient since internal organs move rather surprisingly when one is turned over.

Other severe restrictions are placed on a medical machine. These seem to have been met very satisfactorily by machines now industrially available. These machines are compact, easy to operate and pleasing in appearance.

Varian Associates have pioneered this development in the United States. Worthy followers include the High Voltage Engineering Corporation and other manufacturers of electrical equipment.

We note in passing that electron linacs have an enormous advantage over ion linacs in that a section of the electron machine can fail and the machine will still work. This is not generally true of ion machines. Keep this in mind when you buy your next linac.

At present, almost a thousand electron linacs are in use in hospitals for cancer therapy. Of almost a million new cancer patients per year in the United States, about half are treated with electron linear accelerators.

Radiography

Here, also, electron energies of up to 20 MeV are favored. With the X-rays generated by electrons of a few million electron-volts, one can see through almost anything of interest. This includes big castings, machinery, pipeline sections, all sorts of welds, rocket motors and what have you. Double photographs in which either the source or the object is moved a short distance can provide stereo views of the insides of engines, rotating machines or clocks and can tell you in a moment why the object malfunctioned. Stereo X-rays give a picture that cannot be described; to appreciate this technique you must yourself look at stereo X-rays of an engine or other complex mechanism.

Probably the most extensive use of linac-generated X-rays in the field of radiography is in monitoring of welding processes. Here the X-ray pictures can be used to detect cracks, incomplete fusion, slag or oxide inclusions, porosity or many of the other disasters that occur when the welder turns his back or when he is furnished with inadequate materials.

An upper limit to the penetrating power of million-volt electron generated X-rays is set by the onset of photon pair-production. This happens generally in the energy range around 20 MeV; from this energy upward the penetrating power of the X-rays goes down. This happens, for example, in steel, at a depth of about 1.3 inches which, at this energy, is the depth where the X-ray intensity has been reduced by a factor of two.

Other Uses for Electron Linacs

Recently much interest has been evinced for the possibility that the beam from an electron linac can be directed back to its input and sent through the linac again, emerging with twice its energy. This possibility has been tested at several places including Stanford and the University of Illinois. Indeed this process can be repeated to multiply the linac's energy capability by several fold.

A possiblity for using the recirculating linac idea is found in the "free electron laser" in which the beam from an electron linac passes through achromatic bends, through a magnetic wiggler (in which transverse magnetic fields alternate in polarity) and may or may not be returned to be reaccelerated by the linac. In the course of passage through the wiggler, the electron beam has interacted with a light beam, the interaction resulting in transfer of energy from the electrons to the light beam. The reasons for this laser action are beyond the scope of this lecture but are already generously documented. High-powered, easily tunable free electron lasers can have revolutionary uses in photochemistry, purification processes and isotope separation.

An electron storage ring, like the ones that we plan for the National Synchrotron Light Source here at Brookhaven, can provide the return path for a wiggler included in one of the straight sections. We plan to try a free electron laser in one of our storage rings. It has the beautiful feature that its wavelength can be shifted over a range of a factor of ten or more merely by changing the magnetic field in the wiggler, or by changing the electron energy.

So much for electrons.

Proton Linear Accelerators

Linear acceleration of protons or other ions has always been a bit of a headache because, even at energies of several million volts, proton velocities are only a fraction of the velocity of light. Slowing down the field pattern appropriately has continually been a problem. Recently, however, there have been several breakthroughs both in the Soviet Union and at Los Alamos and it seems probable that the "conventional" linear

accelerator may soon be replaced by a simpler and much less expensive machine. When that happens we shall see proton and ion linacs in many new applications. I now mention a few with the reservation that probably new ideas are appearing elsewhere in the world about which we have not yet heard. Perhaps some will emerge during this conference.

Medical Applications

Many scientists and medical researchers have speculated about the advantages of using pi mesons (pions) for radiation treatment of tumors. They have the advantage of well defined ranges over which they do not do much damage, but at the end of their ranges they experience an annihilation, a sort of explosion quite destructive to the material in which it occurs. In principle this phenomenon would seem to make pions the ideal particles for treatment of tumors. Their only real disadvantage is that they are extremely expensive to produce.

A leading pioneer in the study of pion therapy is Henry Kaplan, who was for many years Chairman of Stanford's Medical Department. Several years ago we organized a committee to recommend a pion facility to be built in the Stanford University Hospital; the committee included members from the Stanford Medical Department, from the linac group at SLAC, from Los Alamos, from Varian and from Brookhaven. We studied electron linac, proton linac and synchrotron sources and finally came out with a slightly tentative conclusion. We recommended that at that time and in that location the wisest procedure would be to use an electron linac together with the accelerator skills of SLAC, virtually next door. We submitted a proposal to the National Cancer Institute which, I believe, is still under consideration.

But we qualified our recommendation with the comment that a proton linear accelerator could have important advantages--for one thing, producing pions with an efficiency 30 or 40 times higher than is possible with electrons. We condemned the proton machine only because it appeared to be much more expensive.

This was taken as an exciting challenge by the Los Alamos group who came to the discussion with two special strengths. One was that, in LAMPF, they already had a proton linac capable of producing pions in useful quantities. The second was that a new advanced accelerator development group was in the process of organization under the guidance of Ed Knapp and Don Swenson and an assembly of talent too numerous to list here.

The Los Alamos team set about exploiting both capabilities. Under Dr. Kligerman's direction a pion beam has been extracted from LAMPF with carefully controlled dimensions and intensity. Something like a hundred patients have been treated with this beam. This is a slow and somewhat frustrating experiment; with tumor treatments you are not sure that you have succeeded for five years or so. But the medical people associated with the program are encouraged by the symptoms that they observe. I simply am ignorant in this field and observe only that the treatment includes patients with tumors of the brain, head, neck, abdomen and pelvis. For more informed information, I must refer you to the Los Alamos group which is well represented at this conference.

Simultaneous with the LAMPF experiments has been a Los Alamos program on development of less expensive proton linacs. This is a very imaginative program--so imaginative to me that I find the Los Alamos people doing projects that, for a long time, I thought were impossible. I think now that I was wrong; I hope not on absolutely all points. We shall see. This is the PIGMI project--standing for "Pion Generator for Medical Irradiations." It is supported by the National Cancer Institute. You will hear a good deal more about it this week.

I shall mention two other medical projects. The favorite particle for tumor irradiation--at least measured by the number of papers presented at nuclear medicine conferences--is the neutron. The linac injector at the Fermilab is being used on the side as a neutron source for patient irradiation. Between 300 and 400 patients have been irradiated with, as I understand, considerable success. A proton beam is extracted at an energy of about 70 MeV and is used to generate the neutron flux.

We, at Brookhaven, have mounted a program using our 200 MeV linac to try to localize the end of the range of a 200 MeV proton. Protons from the AGS injector linac are injected into animals--my understanding is that pigs have been used since they seem to be as similar to people as is possible--and the proton interaction volume is indicated by activation of such positron emitters as carbon-11 and oxygen-15.

Isotope Production and Nuclear Chemistry

At Brookhaven and elsewhere proton beams are extracted from linacs for a number of auxiliary purposes beside the medical applications just mentioned. A favorite is isotope production, mostly I believe, for medical uses. Essentially the same beam is also used to produce a copious neutron beam by stopping the 200 MeV protons in a copper target. All of this goes on at the bottom of a 30-ft. deep water tank; for many years I have lived with the fear that eventually the proton beam will bore a hole through the window through which it enters the tank. I have never had the nerve to estimate the eventual depth of water in the linac tunnel.

The first industrial linac isotope production will soon be in progress at the New England Nuclear Corporation in Massachusetts just north of Boston. They are building a 45 MeV linac for this program and are prepared also to build linacs for sale.

Far-out Schemes Using Protons

A nice idea, that so far has come to nothing, was an idea thought up by Maglich, then at Rutgers, and Macek of Los Alamos, for producing collisions between mesons, using the LAMPF facility, together with a storage ring under study there. The idea was to dump the ring as quickly as possible into

a target in a magnetic field shaped so that positive mesons would precess in one direction around the target and negative mesons in the other. It was hoped that enough mesons could be produced that interactions between them could be observed. For reasons too complicated for description here, this scheme became converted into a fusion project and the meson program was forgotten.

Another idea that was explored some years ago in Canada was the construction of a cw machine in the GeV range. Back in the '50's a similar project had been started at Livermore. The idea is now being resurrected and we have given it some study at BNL. The intense neutron beam generated in some sort of heavy metal target could be used for a variety of purposes including production of reactor fuel. It would be a mighty machine, requiring something like a thousand megawatts just to turn it on.

Deuteron Linacs

The beauty of a deuteron linac is that, by dissociation of the deuterons in a target, one can produce a more or less monoenergetic neutron beam. We shall hear a number of papers at this Conference about the FMIT, a joint Hanford-Los Alamos project for production of a 35 MeV deuteron machine to produce an intense beam of about 15 MeV neutrons to simulate the neutron flux at the wall of a fusion reactor using the D-T fusion reaction. This calls for a flux of about 10^{14} neutrons per square centimeter per second, a flux that will be produced rather easily by the proposed linac. I don't mean to intimate that the linac will be built easily--we shall hear about its problems later.

Heavy Ion Linear Accelerators

The two pioneering heavy ion linacs that resulted from the joint efforts of Yale and Berkeley had distinguished careers and produced a number of significant discoveries in the field of heavy ion physics. The present, somewhat unlikely marriage between the Hilac and the Bevatron is something I never thought we should see; but it seems to be quite successful.

Heavy ion linacs for medical applications were given thoughtful study in a joint study between LBL and the Arizona Medical Center. This study covered radiation therapy, radiography and isotope production; it lasted two years, running until the end of 1977. The conclusions were, first, that heavy ions have special advantages for radiotherapy and, second, that the linac is not the best way to accelerate them--circular machines were thought to be more desirable and economical.

Heavy ions are beginning to be regarded with favor in the pellet fusion programs at LBL, Argonne and Brookhaven. They are thought by their proponents to have notable advantages over either lasers or electron beams. A clear picture of how to generate heavy ion beams has not yet emerged--the three laboratories I just mentioned all have different schemes. But heavy ion linacs to help in the generation of the required short, intense bursts are very much part of the study. You can visit our experimental program on Wednesday.

Another possible field of use for heavy ion linacs is as "after burners" for tandem electrostatic machines and they are under study in several laboratories. Here also there is not agreement that a linac is the best choice. That picture may change as we assimilate the developments of the last few years in basic linac design.

Superconducting Linacs

Although work on superconducting linacs has been in progress for the better part of two decades, they have had a somewhat troubled career and have not yet found many applications. But they have their strong supporters. A great deal of credit must be given to the unfailing optimism of Alan Schwettman at Stanford and it was his superconducting machine that was used in the first demonstration of the free electron laser.

Work on superconducting cavities and linacs is in progress at a number of laboratories here, in Japan and in Europe.

Perhaps by the time we are using superconductivity in accelerator magnets, in ore separation magnets, in power transmission and in levitated trains, the superconducting linac will be the standard particle accelerator. It will be interesting--if we live long enough to see it.

1979 LINEAR ACCELERATOR CONFERENCE

DESIGN STUDY OF THE BEIJING 200 MeV PROTON LINAC

Shu-Hung Wang, Tzu-Hua Lo, Yi-Jin Chang and Ying-Hsong Lo
Institute of High Energy Physics, Academia Sinica
Beijing, China

Summary

In this paper a brief description of the design parameters of the Beijing 200 MeV Proton Linear Accelerator (BPL), some essential principles considered in the design and the three computer programs used are given.

Introduction

The BPL will serve as the injector of the 50 GeV Beijing Proton Synchrotron (BPS). It will be used to accelerate H^- beams mainly, and if the circumstance should arise, it could also be used to accelerate high intensity proton beams for other applications. We have designed this new machine with reference to the fundamental structure and the operating experience of the 200 MeV linacs at BNL[1] and Fermilab[2] and the new 50 MeV linac at CERN.[3] In certain aspects we have made some necessary changes, so that it may better suit our actual conditions and needs. Fundamental parameters of this machine were computed by means of the three computer programs prepared in our institute.

In order to adopt some existing rf structures and devices whose dimensions are determined by experiments, the resonant frequency of the BPL was chosen to be 201.25 MHz. All the transverse dimensions of the cavities are the same as those of BNL and Fermilab.

This machine is composed of 9 tanks with a total of 288 cells in them. Each tank contains an even number of cells. For the sake of stabilizing the accelerated fields in the tanks, we have decided to use post couplers from tank 2 to tank 9. The detailed geometry of each tank is shown in Table 1.

If a booster were to be added to the BPS, perhaps only the first four tanks would be needed in BPL.

Design Beam Performance Parameters

Type of accelerated particles	H^-, H^+
Input energy	750 KeV
Output energy	200.04 MeV
Beam intensity	30-50mA for H^- 100mA for H^+
Normalized emittance	(6-8)πmm-mrad
Output momentum spread	0.15-0.30%
Cavity resonant frequency	201.25 MHz
Beam pulse width	230μs (H^-)
Pulse repetition rate (Max.)	10 PPS

Choice of the Phase Law and the Field Law

In order to save rf power, increase the reliability of the rf system during operation and improve the characteristics of the beam, we have adopted a variational synchronous phase law, i.e., varying linearly with the number of the cells from -35° at the input of the tank 1 to -25° at the end of the tank 2 and then keeping a constant value of -25° through the remaining tanks. We think that ϕ_s of -35° at the input of the linac is necessary to provide a wider longitudinal stable region for capturing a high intensity beam with current possibly more than 100mA.

On the other hand, in order to reduce beam losses as much as possible, especially in the high energy region, the rate of decreasing $|\phi_s|$ should be slower than that of the phase damping. The value at -25° is quite safe at the end of the tank 2 and in the remaining tanks.

Emphasizing the operational reliability of our machine, we have chosen to use a comparatively low average electrical field E (see Table 1). At the entrance of tank 1, E = 1.55 MV/m was taken. The rate of rise of E with length in tank 1 was chosen to be 0.075 MV/m^2.

As shown in the calculation of the linear particle dynamical program, if the effect of errors is neglected, a 100mA beam which is accelerated according to the phase law and the field law mentioned above will have a momentum spread of about 0.1%. The exciting rf power is then 18.89 MW, which is 14% less as compared with the constant phase (-32°) linac.

Calculation of the Field Configuration

In order to calculate the field configurations, stored energy, power dissipation, shunt impedance, transit time factors and resonant conditions, g/L etc., we referred to the method used at CERN[4] and have prepared the computer program LAC, which first calculates the potential function $U = H_\phi \cdot r$ in a cell using an analytical-numerical complex method. Then those electrical parameters mentioned above are derived. For some low energy cells, in the near axis region, where the variation of the field along the longitudinal axis is relatively large, we have tried to improve the accuracy of calculation by using a more dense mesh locally.

In our design, we have computed altogether 85 cells with given dimensions and obtained the factors F = E/E' in the following, which indicate the self-consistency of the program used:

$0.9903 \leq F \leq 1.0051$	for 25 cells in tank 1
$0.9850 \leq F \leq 0.9991$	for 16 cells in tank 2
$0.9921 \leq F \leq 1.0034$	for 18 cells in tank 3-4
$0.9912 \leq F \leq 1.0037$	for 26 cells in tank 5-9

It can be seen that these factors are very close to unity. At the same time, the resonant

frequencies calculated with program LAC for several model cells agree very well with measured values. The comparisons between computations and measurements[5] are given in Table 2.

Generation of the Drift Tube Table

The length of each accelerator tank can be roughly estimated by the amount of rf power available from the source, which did not exceed 5MW for for 100mA beam current in our case. The length of the drift tubes, their positions along the tank and the exact length of each tank are worked out with program LAD, which is similar to the GENLIN program.[6] Program LAD can be used for situations in which the transit time factors T are either modified or not. Furthermore, program LAD can be used to calculate both the longitudinal dimensions for any given E and for that E which is chosen automatically so that the rate of acceleration ($dw/dz = eE \cdot T \cos\phi_s$) at the input of the downstream tank is equal to that at the output of the upstream tank, in order to reduce the discontinuity in longitudinal motion.

Choice of the Quadrupole Field Law and the Beam Matching Calculations in Transverse Motion

In the last few years, it has been found that the transverse normalized emittance blows up by a factor of 2-3 in tank 1 of most proton linacs. The main reason seems to be coupling between longitudinal and transverse motions by nonlinear space charge forces. The other reasons are the difficulty in obtaining perfect beam matching and the effect of the nonlinear external field forces. Therefore, the selection of the quadrupole field law should be a compromising consideration. That is to say, the maximum amplitude function of focusing system, β_{max}, should have a bit larger value in tank 1 so as not to make space charge effects too strong and remain almost constant along this tank to facilitate the matching adjustments). For instance, take $\beta_{max} = 4.7$. From tank 2 to tank 9, the β_{max} should be made to change continuously with acceleration so that the matching parameters between tanks can be adjusted easily. In this way, it is expected to minimize the growth in transverse emittance as much as possible. The quadrupole field law which we have chosen preliminarily is shown in Fig. 1.

The magnetic gradients and matching parameters are computed with program LAM, which includes linear space charge forces. The transverse and longitudinal dimensions of the beam are variable during the process of acceleration.

Parameters such as the transverse envelope (shown in Fig. 2) and the energy spread of the beam were also given by the program LAM.

Acknowledgments

The authors would like to thank Dr. Shu-Da Long, Bo-Fei Cheng and et al. for their assistance in preparing computer programs. A special word of thanks is due to Prof. Shou-Hsien Fang for his valuable suggestions. We also thank Prof. Chia-Lin Hsieh and Prof. Chien-Ming Hsu for their interest in this work. We also would like to thank friends of ours who work at CERN, Fermilab and BNL linacs for helpful discussions.

References

1. G.W. Wheeler; "Status of the BNL 200 MeV Injector Linac", Proceedings of the 1970 Proton Linear Accelerator Conference, p. 1-14.
2. D.E. Young; "Construction Progress and Initial Performance of the NAL 200 MeV Linear Accelerator", Proceedings of the 1970 Proton Linear Accelerator Conference, p. 15-28.
3. D.J. Warner; "Accelerating Structure of the CERN New 50 MeV Linac", Proceedings of the 1976 Proton Linear Accelerator Conference, p. 49.
4. M. Martini and D.J. Warner; "Numerical Calculations of Linear Accelerator Cavities", CERN 68-11.
5. P.F. Dahl and et al.; "Linac Cavity Field Calculations", Proceedings of the 1966 Proton Linear Accelerator Conference, p. 115-117.
6. A. Benton; "Calculation of Drift Tube Table for BNL 200 MeV Linac", AGSCD Technical Note No. 119.

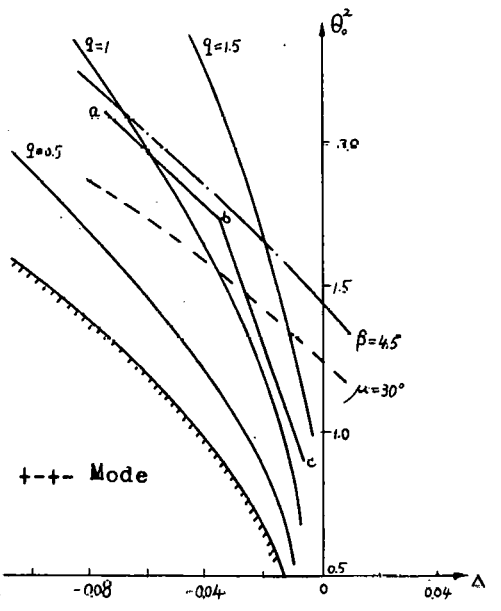


Fig. 1 - The quadrupole field law (abc) intended to be used in BPL.

Table 1: BPL 200-MeV Linac Drift Tube Table

Cavity Number	1	2	3	4	5	6	7	8	9	Total , Final
Output En.(MeV)	9.68	37.05	67.02	93.02	116.39	138.25	160.24	180.20	200.04	
Cavity Length (m)	7.272	18.675	17.016	16.170	15.595	15.524	16.561	15.858	16.545	139.220
Cavity Dia. (mm)	940	900	880	880	840	840	840	840	840	
D.T. Dia. (mm)	180	160	160	160	160	160	160	160	160	
B. H. Dia. (mm)	20-25	30	30	30	40	40	40	40	40	
B.H. Cor.Rad. (mm)	5	10	10	10	10	10	10	10	10	
D.T. Cor.Rad. (mm)	20	40	40	40	50	50	50	50	50	
Num.of Unit cells	56	60	36	28	24	22	22	20	20	288
Cell Length (mm)	60- 210	213-405	408-533	536-616	619-678	681-729	731-773	775-809	811-842	
G/L	.21-.30	.19-.31	.29-.36	.37-.41	.36-.39	.39-.42	.42-.44	.44-.45	.45-.47	
D.T. Length (mm)	47-145	173-278	288-337	339-364	392-409	410-421	422-431	432-438	439-445	
T	.67-.81	.87-.82	.83-.75	.75-.69	.73-.69	.69-.65	.65-.61	.61-.58	.58-.56	
Z (MΩ/m)	65.7-72.9	71.5-67.3	65.1-62.3	62.3-59.6	54.8-52.8	52.8-51.6	51.6-50.6	50.6-49.6	49.6-48.5	
E (MV/m)	1.55-2.08	1.93	2.45	2.46	2.31	2.31	2.31	2.31	2.31	
E_{smax} (MV/m)	8.3-9.5	11.7-9.5	12.5-12.7	12.7-13.0	12.4-12.6	12.6-12.8	12.9-13.1	13.1-13.3	13.4-13.5	
Syn. Phase	-35°-30.3°	-30.2°-25°	-25°	-25°	-25°	-25°	-25°	-25°	-25°	
C.exi.power (MW)	0.44	1.30	2.17	2.24	2.25	2.39	2.69	2.62	2.79	18.89
Space of Cav. (mm)	210	600	1200	1000	1000	1000	1000	1000		

Table 2: Comparison Between Computation and Measurement *

Cavity Number	1	2	3	4	5	6	7	8
Half Length of Cav. (cm)	3.35	4.039	4.717	5.565	6.304	3.5	11.25	26.0
f (Measurement)(MHz)	202.47	200.70	198.81	200.57	198.94	198.58	200.61	201.32
f (JESSY) (MHz)	203.07	201.64	199.59	200.24	199.23	200.48	201.36	202.56
f (MESSYMESH) (MHz)	203.06	201.16	199.24	200.19	199.20	200.38	201.09	202.40
f (LAC) (MHz)	202.47	200.79	198.89	199.90	198.96	199.70	200.96	185.91**

* Cavities 1-5 Made by MURA, Cavities 6-8 Made by BNL

** Maybe the dimensions of this cavity used in computation with LAC program are not actual ones used in measurement at BNL.

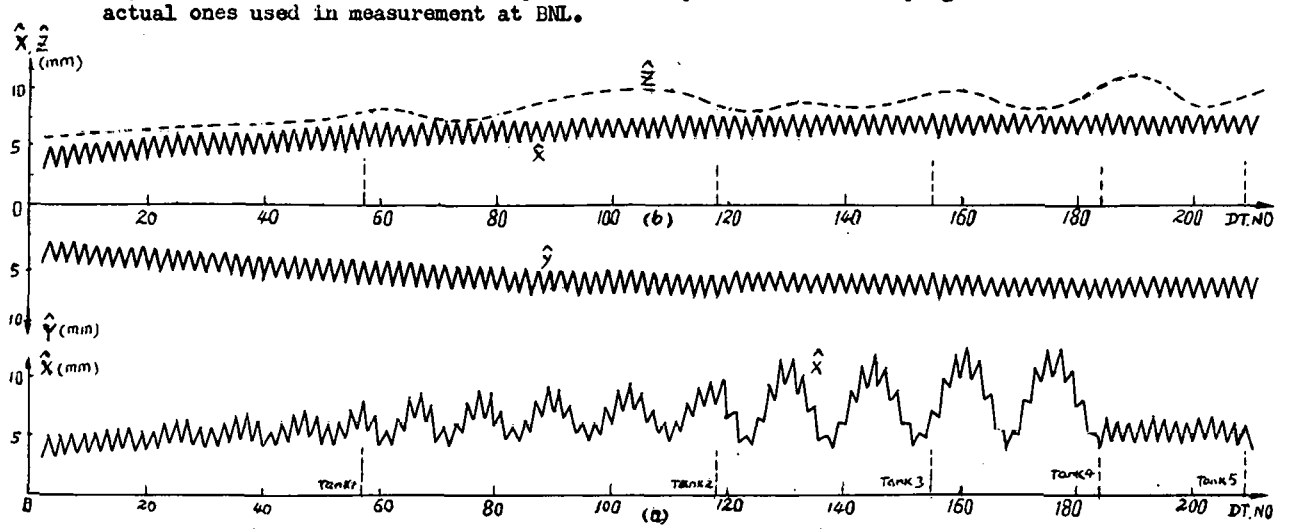


Fig.2 Linearized beam dynamics in the Linac tank 1-5, (a) unmatched beam envelopes, (b) matched beam envelopes.

1979 LINEAR ACCELERATOR CONFERENCE

THE PHOTON FACTORY 2.5 GEV INJECTOR ELECTRON LINAC

J. Tanaka, I. Sato, K. Nakahara, S. Anami, S. Fukuda, K. Matsumoto, T. Shidara and A. Enomoto
National Laboratory for High Energy Physics
Oho-machi, Tsukuba-gun, Ibaraki-ken, 300-32, Japan

Summary

The KEK Photon Factory was financed from the 1978 fiscal year, and the project will be completed at the end of the 1981 fiscal year. The accelerator of this facility consists of a 2.5 GeV injector electron linac and a 2.5 GeV storage ring. The linac will also be used as the electron and positron injector of the KEK future project "TRISTAN" and for other purposes. A prototype accelerator unit, which is composed of four 2 m long accelerator guides, a supporting girder and waveguide system, klystron modulator and other components of the linac, was completed at the end of March 1979 and is now under test.

The general picture of injector design, the status of construction and the results of tests are reported in detail.

Introduction

The Photon Factory (P.F.) is a dedicated facility at KEK for the production of Synchrotron Orbital Radiation (SOR). As an intense source of photons with wavelengths ranging from soft X-rays up to 0.1 Å hard X-rays it will be exceedingly valuable for research on various photo-induced phenomena in widely diverse scientific fields: crystal physics, molecular physics, surface physics, materials science, chemistry, biology, etc.

In 1977, preliminary planning and preparatory studies for the P.F. accelerator were begun with 40M yen taken out of KEK's own budget. The Photon Factory as a KEK facility was later officially established when in fiscal 1978 the government approved the construction of the Photon Factory. Approximatly 8000M yen was appropriated for the accelerator (injector linac and storage ring) and its experimental apparatus with an additional 8000M yen for buildings and supporting facilities. The entire construction phase is targeted for completion in 1981. These facilites are planned to be constructed on the west side of KEK's grounds. The 2.5 GeV injector linac housing is sited running south to north to allow connection in the future with project TRISTAN. The 2.5 GeV storage ring building is located at the injector-end in the northwest part of the site. The overall layout of the facility is shown in Fig. 1. Groundbreaking ceremonies for the injector tunnel were conducted in Feb. 1978.

The Photon Factory accelerator is composed of a 2.5 GeV linac and a 2.5 GeV storage ring. The ring will serve as a dedicated machine for "SOR" experiments with 6 channels including one for hard X-rays produced by a wiggler.

An electron linac was chosen for the injector not only because it can easily inject an intense beam into the storage ring, but also because it provides great flexibility; various energy beams, 400 MeV, 1 GeV etc., can be extracted for injection into lower energy storage rings dedicated for soft X-ray studies, lithography and so forth. It will also be capable of producing very short (picosecond range) single pulses of light, and, of course, eventually it can serve as the electron-positron injector for TRISTAN.

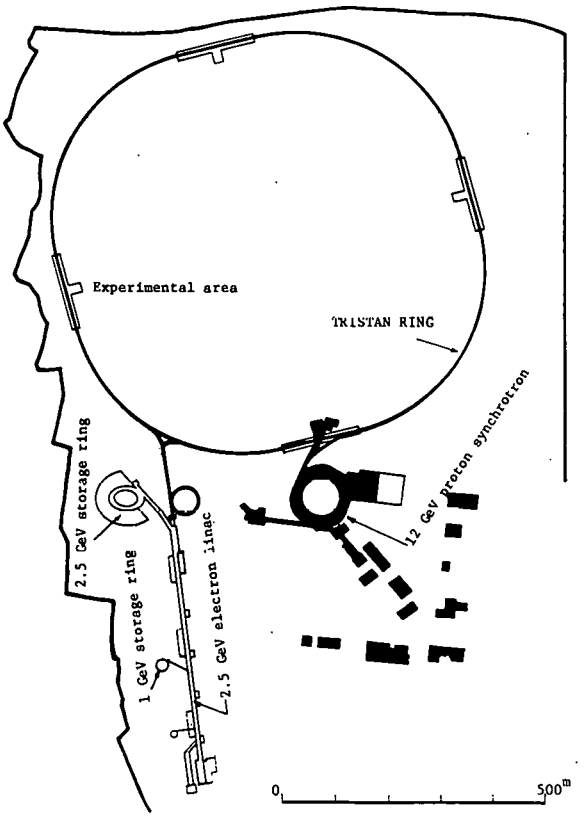


Fig.1 Overall layout of the KEK facility

General Picture of the Linac

The injector housing is a long slender two-storied building of about 500 m length, a view of the cross-section is shown in Fig. 2. The two stories are separated by a 2.5 m concrete floor for radiation shielding. The first floor is an underground tunnel housing the accelerator guides, the second floor is the klystron gallery housing the rf power supplies.

The linac was designed to be able to accelerate electron beam currents of 50 mA to energies of 2.5 GeV with the application of 840 megawatts of pulsed power from 40 klystrons fed to 160 accelerator guides. The relation between beam energy and current as a function of rf power was calculated, as shown in Fig. 3.

The general parameters of the linac and the storage ring are shown in Table 1.

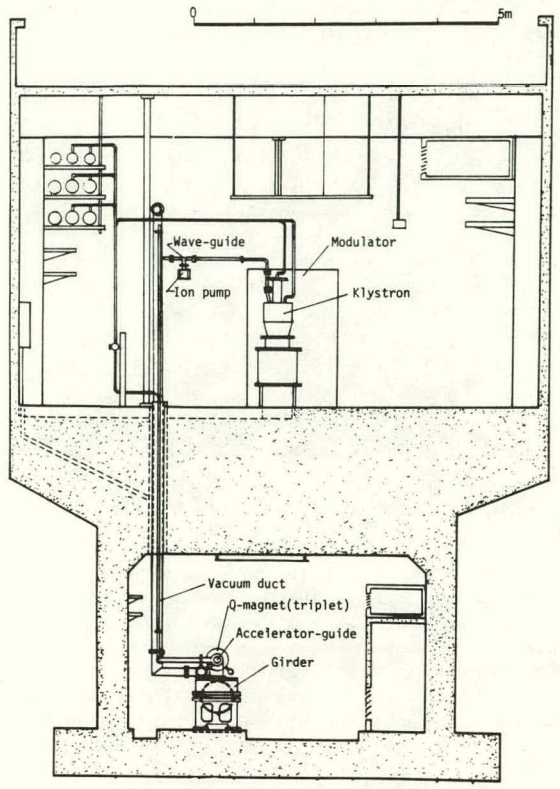


Fig.2 Cross-section of the linac building

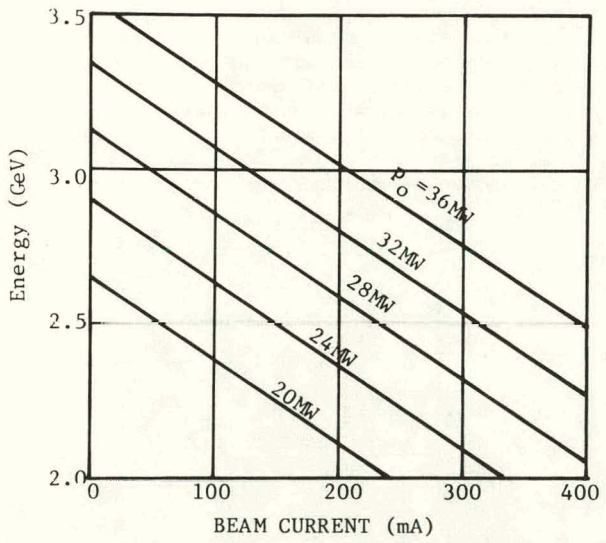


Fig.3 Relation between beam energy and current as function of rf power

A conventional disk loaded traveling wave type accelerator guide was chosen in order to facilitate manufacturing, operation and maintenance, as well as to be able to complete the linac within a limited budget, with a limited staff and short scheduled construction period. As the linac is an injector, an Energy Compression System (E.C.S.) is added downstream of the linac to improve both the stability and spread of beam energy. In addition to ordinary microsecond pulse beams, a single bunch beam can also be accelerated.

The linac is divided into five sectors and each sector is composed of eight acceleration units. One acceleration unit consists of four 2 m long accelerator guides mounted on a cylindrical supporting girder, one klystron and high power waveguide system. All the various power supplies, including the 42 klystron modulators,are installed in modular standard unit cabinets, constructed of panels.

Table 1
General Parameters of the 2.5 GeV Linac

Energy (50 mA loaded)	2.5 GeV
Peak current	50 mA
Beam pulse width	>1 μs
Repetition rate	50 pps
Eenrgy spread(without E.C.S.)	<0.5 %
Energy spread(with E.C.S.)	0.1 %
Normalized emittance	<10 cm•mrad
Short pulse operation	
peak current	<500 mA
Pulse width	2 ns, 10 ns
Single bunch operation	
Max charge	1 nc
Bunch width	16 ps
Accelerator guide (main accelerator)	
Type of structure	5 types TW Quasi-C.G.
Frequency	2856 MHz
Type of Mode	2/3π
Length of acceleration guide	1.9 m
Total number of guide	160
Attenuation parameter	0.5∿0.6
Length of acceleration unit (Composed of 4 acc. guides)	9.6 m
Number of Acc. unit	40
Number of Sector	5
RF power	
Peak power per klystron	30 MW
Number of klystrons (Including of Inj. and E.C.S.)	42
RF pulse width	3 μs
Freq. of master osc.	476 MHz
Injection system	
Gun voltage	-100 kV
Type of Gun	Triode
Gun pulse width	2 ns ∿2 μs
Out put Energy	30 MeV
Number of Acc. guides	2
E.C.S.	
Magnetic field	1.6 T
Accep. phase angle	30°
Number of Acc. guides	4

General Parameter of the Storage Ring

Energy	2.5 GeV(max 3 GeV)
Intensity	500 mA
Mean radius	29.77 m
Radius of curvature	8.66 m
Betatron number νx	6.25
νy	5.25
Bending magnet field	9.6 kG(max 12 kG)

Length of bending magnet	1.85 m
Aperture	70 x 120 mm
Length of quadrupole magnet	0.5 m
RF frequency	500 MHz
Harmonic number	312
Synchrotron radiation loss	400keV/turn (w/o wiggler)
Radiated power	208 kW
RF voltage	2.1 MV
Synchronous phase	10°
Average pressure	10^{-9} Torr
Expected storage lifetime	5 hrs

Acceleration Unit

An acceleration unit consists of 4 accelerator guides mounted on a cylindrical supporting girder, vacuum manifolds and cooling water piping. A high power klystron and waveguide feeder system is shown in Fig. 4

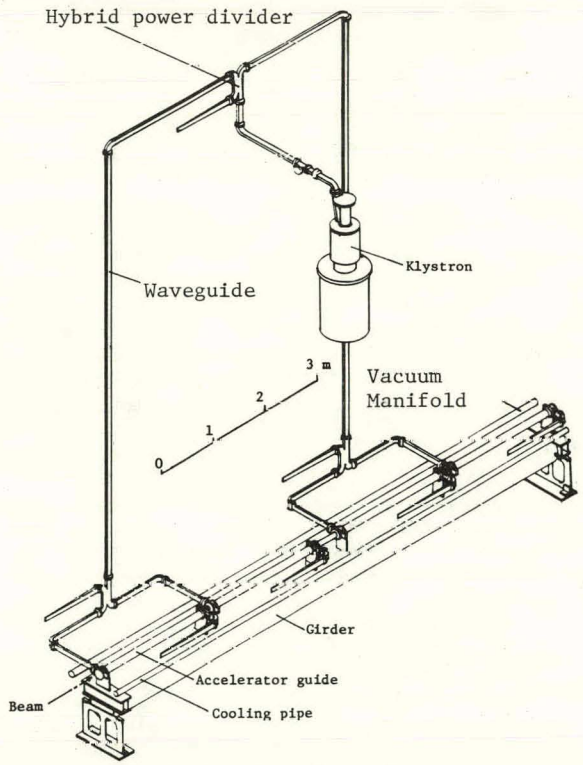


Fig.4 Acceleration unit

The accelerator guide structure was designed to have a quasi-constant gradient; the disk hole diameters decrease linearly along the length to facilitate manufacturing many accelerator guides. However, in order to reduce beam blow-up difficulties, five different structures (Types A-E) will be prepared for the accelerator guides.

A prototype acceleration unit was built in order to get basic data on both the structure and electrical characteristics of the accelerator guide and waveguide feeder system, and to check the alignment of the long supporting girder and the conductance of the vacuum duct system. The unit was completed at the end of March of this year. As a result of cold test measurements, the maximum phase shifts of respective accelerator guides were within ±2.5°. A panoramatic photograph of the prototype acceleration unit is shown in Fig. 5.

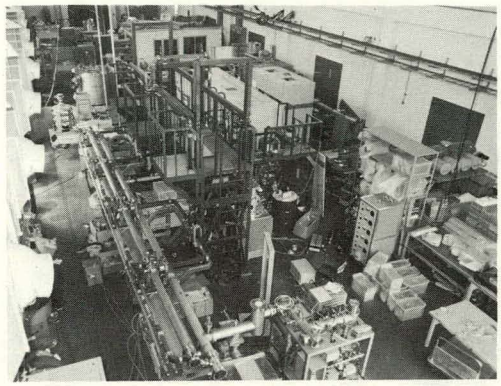


Fig.5 Prototype acceleration unit

The accelerator guides are made by means of an electro-plating method. In order to manufacture many accelerator guides in a limited period, automatic lathes, a measuring system and electroplating plant were prepared.

Recent improvements in machining were realized to automate the final precision machining of the accelerator guide parts. In this process, disks and cylinders are machined by special diamond bit lathes. The surface roughness of the finish is less than 0.1 μ and the over all dimensional accuracy of the disks and cylinders is within ±2 μ.

The precision in machining is accomplished by reducing rotational vibrations of the lathe spindle as a result of using hydraulic bearings.

The machined disks and cylinders are then stacked alternately on a stacking jig and the assembly is compressed to a specified pressure with a long mandrel put through the center holes.

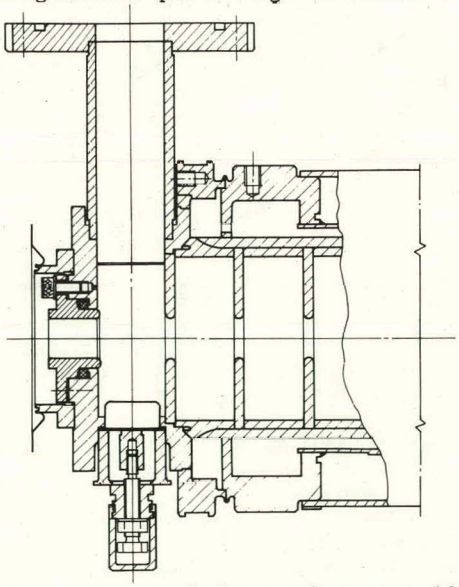


Fig.6 Cross-section of the accelerator guide waveguide coupler

The assembly is copper plated on the outside in an R-1 copper plating bath forming a solid tube of 6 mm of deposited copper. Improvements in the R-1 copper plating process enabled a uniform, smooth and high speed deposition of the copper layer.

Accelerator guide waveguide couplers are of the cavity type. The coupler has two adjusting mechanisms as shown in Fig. 6; one of them makes the coupler field symmetrical with the beam axis and the other is for tuning of the coupler cavity. The adjusting mechanisms facilitate the final tuning of the couplers connected to the accelerator guides.

In each acceleration unit, output power from the klystron is split and fed into 4 accelerator guides. The phase lengths of the 4 branch waveguide feeds from the klystron to the 4 accelerator guides are made precisely equal by precision machining and electron beam welding. Consequently, the feed system needs no high power phase shifters.

RF Power Source

The design principle for the entire power source is based not only on obtaining reliable and stable operation but also on facilitating maintenance and reducing cost.

The rf system is composed of four main stages: the master oscillator, the main booster, the sub-boosters and the main klystrons, as shown in the block diagram of Fig. 7.

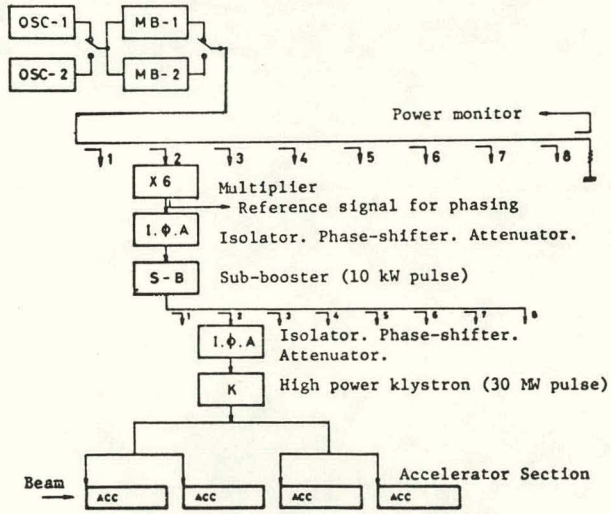


Fig.7 Block diagram of the rf power system

Almost all of the rf components have already been specified and some prototypes have been completed and are under test. The preliminary tests of the klystron modulator were successful; in particular the pulse-to-pulse amplitude variation was less than 0.1 % for a 3 % variation of the ac input voltage. Fig. 8 shows the pulse shape under those conditions.

Recently, super power klystrons with specifications similar to the SLAC XK-5 klystron have been developed commercially to operate with reasonable efficiency and costs. A prototype klystron for more than 30 MW was purchased to test with a special focusing permanent magnet. The magnetic material used is Alnico 9 which was made by the zone-melting method. This material has such a strong magnetic field that the amount of magnetic metal needed decreases by approximately one half in comparison with Alnico 8. The klystron's characteristics as an rf power source are under examination.

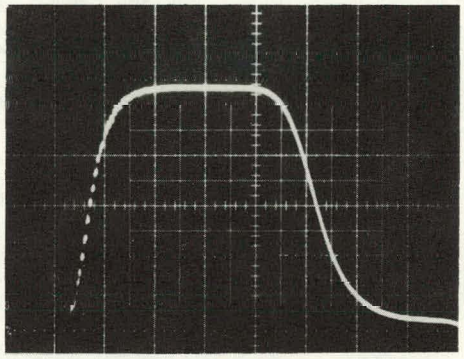


Fig.8 Output pulse shape of the klystron modulator
50 kV/div 1 μs/div

Control System

The basic design of the control system is based on local distributed processors interconnected into a network by a high speed communication loop. The entire control network is composed of a main loop for controlling the 6 accelerator subsystems, and two external loops communicating with the storage ring control center, radiation and personnel protection system, and with the environmental control plants. The accelerator subsystems control the injector, 5 regular sections, and the final energy compression section. As shown in Fig. 9, each subsystem-control station on the main loop has several subloops at the middle level, and branch loops at the lowest level. Klystron modulator controllers, vacuum equipment controllers, etc. form the nodes for the subloops.

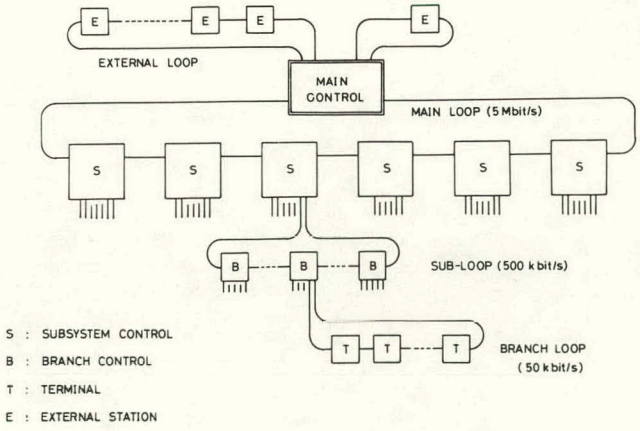


Fig.9 Block diagram of the control system

DISCUSSION

E.A. Knapp, LASL: For a given length accelerator tunnel it is possible to reduce the rf power requirements by more than a factor of two using modern standing wave accelerator cavities. Is the saving you achieve using the technology already understood by Mitshubishi Industries more important than the power saving or the length reduction possible?

Tanaka: Yes, because we have to construct the linac in a limited time.

dup

1979 LINEAR ACCELERATOR CONFERENCE

THE LINAC FOR THE NATIONAL SYNCHROTRON LIGHT SOURCE*

K. Batchelor, J. Bittner, T. Dickinson, V. Racaniello, and J. Sheehan
National Synchrotron Light Source
Brookhaven National Laboratory, Upton, NY 11973

Summary

The nominally 100-MeV electron linear accelerator to be used as an injector for the booster synchrotron of the National Synchrotron Light Source is described. The machine utilizes a combination of Varian and SLAC accelerating guides[1,2] and is interfaced by means of a microprocessor-based Intel Multibus® system, to the Data General central control computer. Provision for emittance and momentum measurement is provided in the transport line between the linac and the booster synchrotron.

Introduction

The National Synchrotron Light Source, now under construction at Brookhaven National Laboratory, (Fig. 1) will consist of two electron storage rings to provide intense sources of synchrotron light in the vacuum-ultraviolet and soft x-ray wavelengths. The electrons will be injected from a linac at about 100 MeV into a slow-cycling booster ring for acceleration to 750 MeV. A 750-MeV storage ring will be used to generate light in the ultraviolet and visible regions between 10 Å and 10^4 Å. A larger storage ring will accelerate electrons from 750 MeV to about 2.5 GeV for generation of x-rays at wavelengths between 0.2 Å and 10 Å.

Both storage rings will require multiple cycles of linac or booster injection in order to accumulate sufficient stored beam current.

The linac system is shown in schematic form in Fig. 2. It consists of a pulsed 100 kv electron gun and 3 iris-loaded cavities operating at 2856 MHz. One klystron will power the first cavity at 12 megawatts and a second klystron will provide a total of 20 KW to cavities 2 and 3 via a power splitter. The linac parameters are shown in Table 1.

The electron gun, buncher section and first cavity were formerly used as an injector at the Cornell University 10-GeV electron synchrotron. Cavities 2 and 3 were used at EVA, Amsterdam and are of SLAC design. The klystron, modulator, and waveguide systems were from BNL rf beam separator systems. All of the original hardware was manufactured in the early 1960's.

*Work supported by U.S. Department of Energy under contract No. EYU-76-02-0016.

TABLE 1.

e^- LINEAR ACCELERATOR INJECTOR

Accelerator type	S band, $2\pi/3$ mode
Frequency (at 39°C)	2855.7 MHz
Pulse repetition rate	1 pps
Number of accelerating sections	3
Rf power source	2 klystrons (21 MW/unit)
Nominal output beam parameters:	
Energy	100 MeV
Momentum spread, $\Delta p/p$	$\pm$ 0.2%
Emittance	$\frac{2}{}$ x 10^{-5} m-rad
Design beam current	20 mA
Beam modulation frequency	52.88 MHz
Chopped beam modulation frequency	10.576 MHz

The assembly of the linac has been in two distinct phases:

(1) Assembly and testing of the original components.

(2) Redesign and modification of equipment for the new facility.

The cavities were installed in a temporary shielded enclosure and powered by existing circuitry to evaluate the major components and spares. This also allowed early testing of prototype beam diagnostic equipment. Figure 3 is a schematic showing the equipment layout in the test area.

The second phase is well underway and consists of the following:

(1) Repackaging the existing Varian gun/modulator into two separate units. The repackaged gun is shown in Fig. 4.

(2) Rebuilding the modulator portion (see Fig. 5) to reduce electromagnetic noise and provide stable pulsing at low repetition rates under the control of a microprocessor system.

(3) Building or rebuilding all focusing and correction magnet systems for solid-state digital control.

(4) Rf modulator rebuilding to eliminate many vacuum tube circuits and to reduce pulsing noise.

(5) Redesign of low level rf and timing distribution system.

(6) Development of beam diagnostic equipment.

(7) Development of hardware and software for automatic operation from a central computer using many small microprocessor systems

The linac will be operated at one pps with a 20-mA, 1 μsec pulse. Because the average power is very low and the interpulse period is long, all of the gun and rf modulator circuits will be modified to resistive charging. The linac beam will be modulated via beam deflector plates in the gun-to-linac transport system, at the single bunch revolution frequency of the booster synchrotron, (10.576 MHz), in order to improve the rf capture in the booster. The linac is only required to operate for short periods of time during injection and may be dormant for many hours at a time. This will place severe demands on the stability of the system in order to avoid a warm-up and adjustment period for each injection sequence.

Controls

A microprocessor control system using Intel Multibus® hardware performs all of the local control and monitor functions as well as closing several critical servo-loops. It also allows all machine parameters that affect the beam performance to be digitally stored at the local device and free the central computer from doing real-time corrections.

A separate microprocessor will be used for: each klystron system, the gun modulator, the vacuum system, timing, beam diagnostics, and magnet systems. Each is connected by a high-speed serial asynchronous link to the central computer system. [3]

Beam Diagnostics

Beam diagnostic equipment consists of devices for measuring beam current, position and energy. All three types of measurements are digitized and may be used to servo the beam to a given condition. This requires noise-free and drift-free monitors.

These measurements are carried out in the transport system between the linac and the booster synchrotron. This line may be divided into three separate functional regions. The first section serves to transport the beam to the first dipole bending magnet. It contains a quadrupole focusing triplet; secondary emission monitors are located in this line for emittance measurement. Next, there is a momentum recombining system which is comprised of two dipole bending magnets and a center quadrupole next to which is placed a movable and variable slit for momentum selection (at the point of maximum dispersion). Tape-wound toroidal current transformers before and after the slit monitor the fractional transmission through it. The third section of line contains 5 quadrupoles for matching the linac beam to the booster. A viewing screen is provided for a final visual check of the profile before injection into the booster. Electron beam current is measured between linac tanks and at various places along the transport system by tape-wound toroidal beam current transformers.

REFERENCES

1. J. Haimson, "Electron Bunching in Travelling Wave Linear Accelerators." Nucl. Inst. Methods, 39, No. 1-13, 1966.

2. R.B. Neal, editor, "The Stanford Two-Mile Accelerator." W.A. Benjamin, Inc., publishers, 1968.

3. K. Batchelor, B. Culwick, G. Goldstick, J. Sheehan and J. Smith, "Distributed Control System for the National Synchrotron Light Source." IEEE Trans. in Nucl. Sci., NS-26, No. 3, p.3387, June 1979.

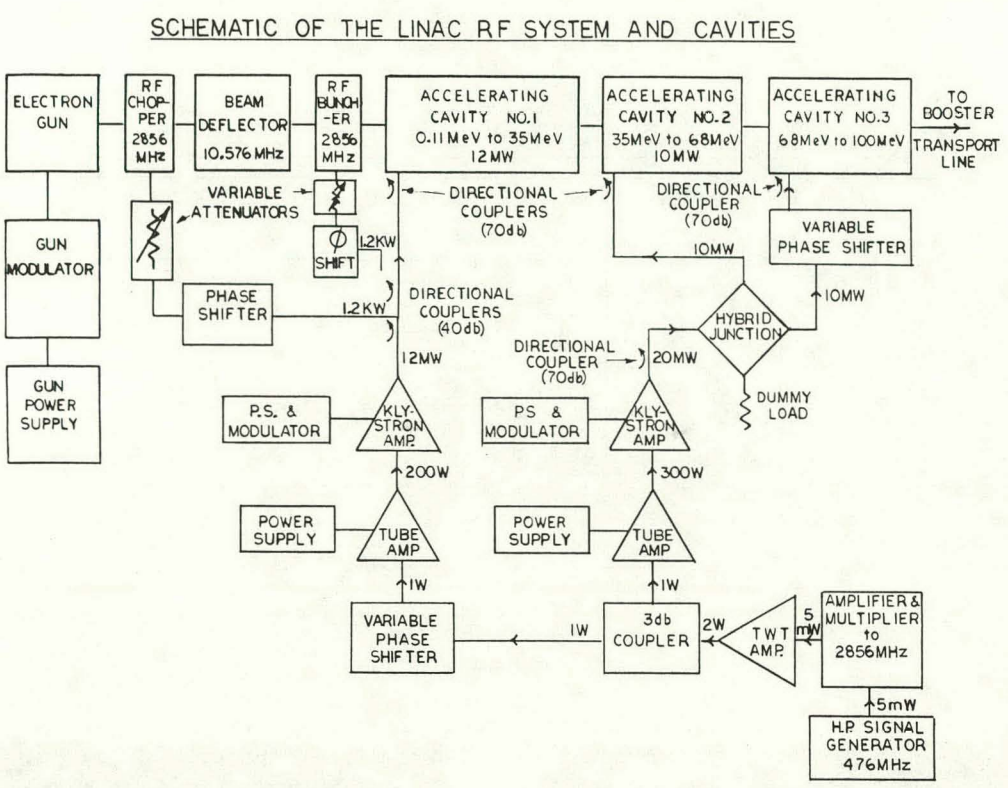


Fig. 1 National Synchrotron Light Source site layout

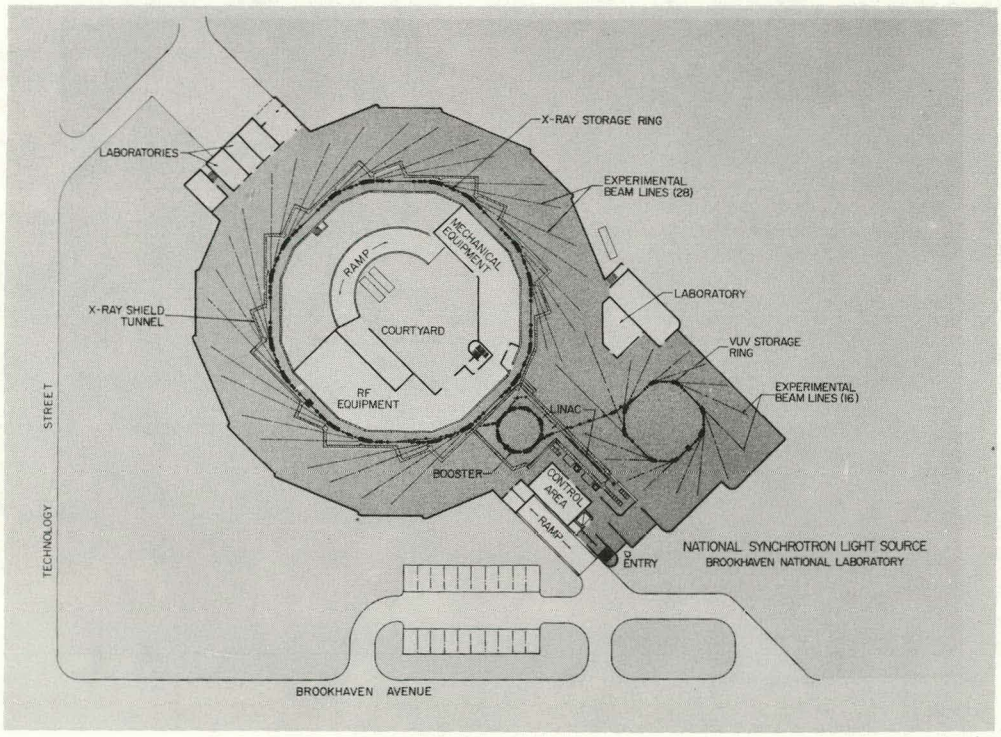


Fig. 2 Schematic of the linac rf system and cavities

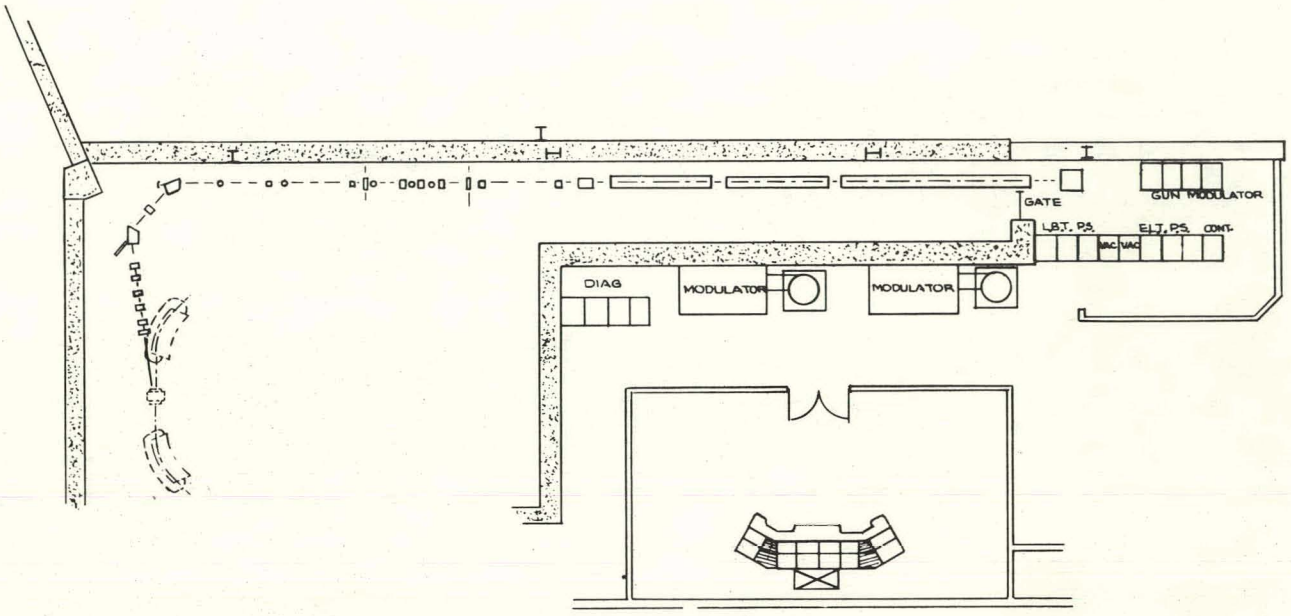


Fig. 3 Linac equipment layout

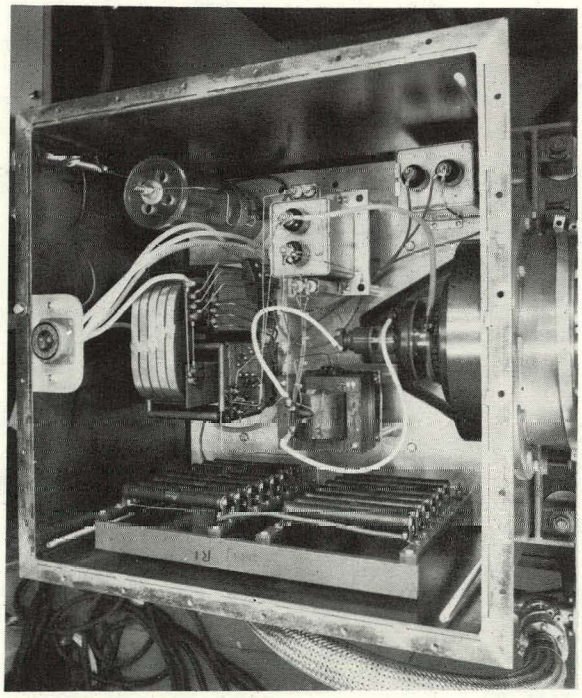


Fig. 4 Repackaged electron gun

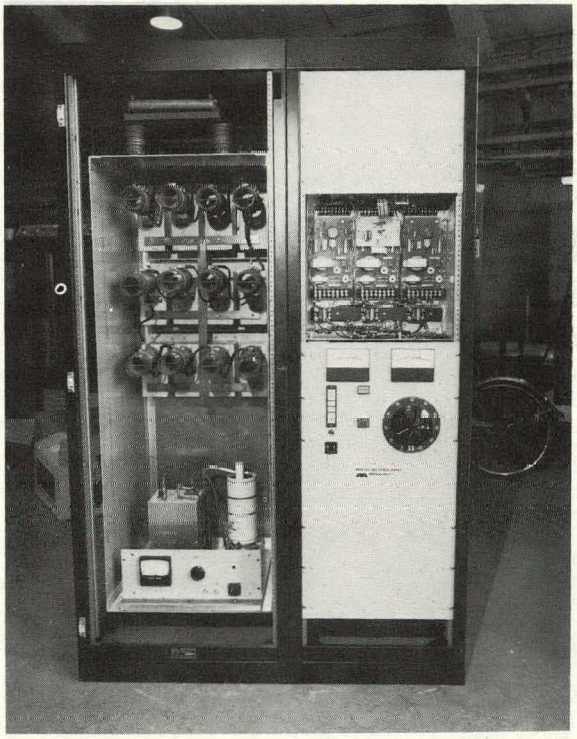


Fig. 5 Rebuilt gun modulator

1979 LINEAR ACCELERATOR CONFERENCE

THE UNILAC UPGRADING PROGRAM

N. Angert, D. Böhne, J. Klabunde, H. Trautmann
GSI, Gesellschaft für Schwerionenforschung mbH
Darmstadt, Fed. Rep. of Germany

Summary

At the present time ions of the heaviest elements can be accelerated with the Unilac up to specific energies of 8.5 MeV/u with stripping in gas and up to 10 MeV/u with a foil stripper. Using a second foil stripper in front of the single-gap cavity structure 12.5 MeV/u can be reached. By adding two Alvarez tanks, the energy will be increased for the different operation modes to 14.5, 16.0 and 20 MeV/u respectively. Details of this energy increase project are described, which is to be realized by the end of 1981. Part of the upgrading program is also the modification of the Unilac for multi-ion beam operation and the construction of a new high-current injector.

Introduction

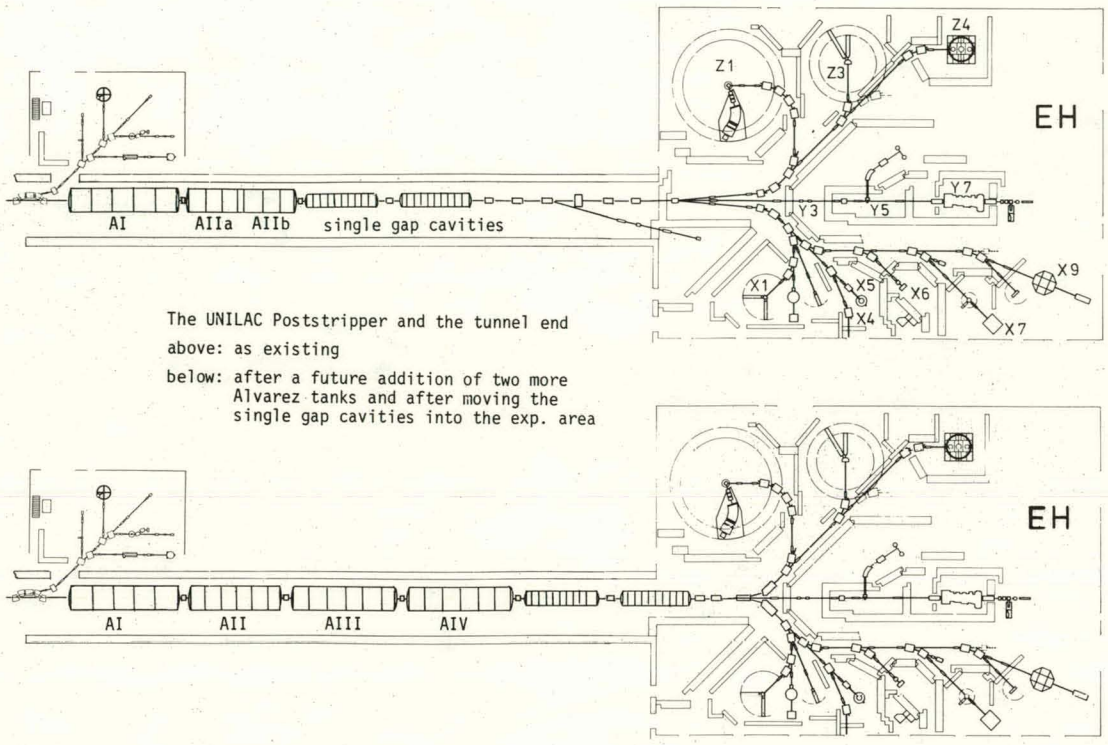
After four years of experiments with the Unilac two beam energy domains have developed which are mainly used for the experimental activities. One is the range from 4.5 to about 6 MeV/u. The other is the high energy regime from 8 MeV/u upwards, with a tendency to shift to the highest available energies. By using a second foil stripper at 5.9 MeV/u in front of the single-gap cavity structure experiments at even above the design energies have been done[1] up to 13 MeV/u with Kr. The experimental requirements for higher energies have been one reason to think about an energy increase of the Unilac. The other was that there are plans to build a synchrotron for relativistic heavy ions with the Unilac as injector. The output energy of such a synchrotron depends on the energy of the injected beam. In order to reach 10 GeV/u for uranium with the synchrotron concept which is being considered, an injection energy of 40 MeV/u will be necessary. Since this energy seems to be a very attractive extension for a lot of running research activities, a linac structure perpendicularly arranged to the existing Unilac was the favourite injector design for a long time. This linac[2] should accelerate the beam from 5.9 MeV/u to some 40 MeV/u for the synchrotron, with the possibility of transporting the beam back to the Unilac axis for further acceleration with the single-gap cavity structure for the existing experimental hall. This solution would even offer to introduce a further accelerating structure on the way back to get about 100 MeV/u beams at intensities of 10^{11} pps. Of course, other "booster"-concepts have been investigated too. All with the drawback that costs and personnel requirements are out of the running budget. When investigating the low energy capabilities of the synchrotron in connection with a new high current injector at the Unilac[3], it turned out that it can also deliver high intensities in the range between 10 and 140 MeV/u, namely 10^{11} pps for the heaviest elements, and even more for lighter ones, if an unstripped 1.4 MeV/u-beam is injected from the Unilac. On the other hand a decrease of the input energy to 20 MeV/u would lower the maximum output energy of the synchrotron to 8.8 GeV/u for uranium.

Concept of Energy Increase

In an early layout phase of the linac building, space was preserved at the end of the machine tunnel for an eventual future energy extension. At that time, a third group of single-gap cavities was envisaged, topping the maximum energy by an additional 2.5 MeV/u. The consideration of a third Alvarez tank instead was discarded at that time due to an overly complex rebunching scheme, which was felt necessary to provide the beam micro-structure restored in the whole energy span. This requirement is by far less vigorous now because the energy spread of the beam is lower by a factor of 5, in respect to the design assumptions, and the extension of the energy range by Alvarez cavities now seems to be a viable choice and a cheaper approach too.

In the meantime, however, the remaining space at the end of the tunnel is used up for different functions: a time-of-flight path for energy determination, a semiconductor counter device for the inspection of satellite energy peaks, a 13^0 beam deflection into a special beam line, a debuncher and a collimator system. Last, but not least, a good portion of the straight beam line in the tunnel is an inherent element of the beam splitting system. Those features have to be abandoned in favour of the machine extension by two more Alvarez cavities. A few features can be reinstalled in the downstream beam lines in the experimental area. This is almost certain for the time-of-flight path and the rebuncher, and it is under study concerning the beam splitting system, which tends to conflict with a kicker magnet of the synchrotron injection beam line. None of the target stations of the present experimental hall have to be moved.

Figure 1 shows the existing and the proposed future high energy end of the Unilac. The two additional Alvarez tanks number III and IV are of the same length and rf parameters as the existing ones. The stable phase was reduced to 25^0 and the g/L ratio was chosen to tune the cell frequency, keeping the diameter of each cavity cylindrical. (This was not the case in the original design.) The described extension of the machine results in an energy increase by 5.5 MeV/u. If one considers an additional foil stripper at the entrance of the single-gap cavity section, a final energy of 20 MeV should be attained for the heaviest elements. The energy graphs for different stripper options and lighter projectile mass numbers



The UNILAC Poststripper and the tunnel end

above: as existing

below: after a future addition of two more Alvarez tanks and after moving the single gap cavities into the exp. area

Fig. 1

are shown in Fig. 2. The additional intensity loss by the second stripper is only a factor of 2, when the well established multi-charge acceleration mode is used in the Alvarez section.

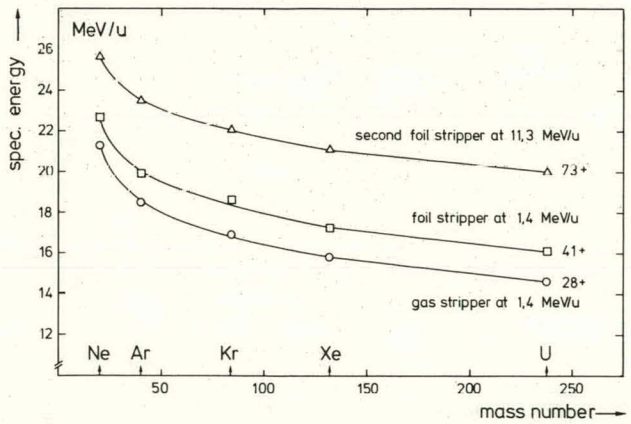


Fig. 2 Spec. energy versus mass number after extension of the Unilac by two more Alvarez tanks

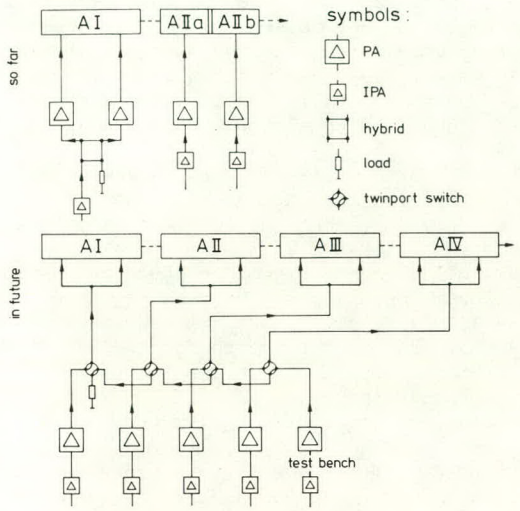
Rf System

A frequency jump by a factor of two was briefly considered for the new Alvarez tanks. However, the design of a new rf amplifier system was felt to be inhibitive. But changes have largely been applied to the mechanical engineering details of the additional tanks, which will be reported separately[4].

For the extension of the rf amplifier system, space reserves equivalent to those available in the machine tunnel could not be found. The original free space in the rf gallery is presently occupied by an indispensable test bench for the Alvarez tube testing program and for 5 additional rebuncher amplifiers. Alternate solutions in remote building areas are considered to be too inconvenient for maintenance and trouble-shooting activities. It is therefore envisaged to use the existing four final amplifier installations to power four cavities, instead of only two which is presently the case. This implies the success of the amplifier improvement program, aiming at a pulse power of 1.6 MW per amplifier unit. A reduction in duty factor from 25% to 15% is unavoidable for the heaviest ions and gas stripping, however, because the existing anode power supplies have to be reused. Figure 3 shows the existing rf system above and the proposed new configuration below. Each cavity is powered by its own amplifier chain. Two coupling loops per cavity will be maintained; they are fed via a power-dividing network. Both halves of tank two have to be unified by eliminating the rebuncher cell. The physical location of the amplifier stages and the downgoing power lines will remain unchanged; space is available in the tunnel basement for the downstream propagation of the power lines. A new feature will be the proposed installation of a rf line switch-

yard, by which the output port of the test bench amplifier can be branched to each of the 4 cavities in case of a severe amplifier breakdown.

The amplifiers of the single-gap cavity section also remain in their present location. Extended rf cables will be routed downstream in the tunnel basement.

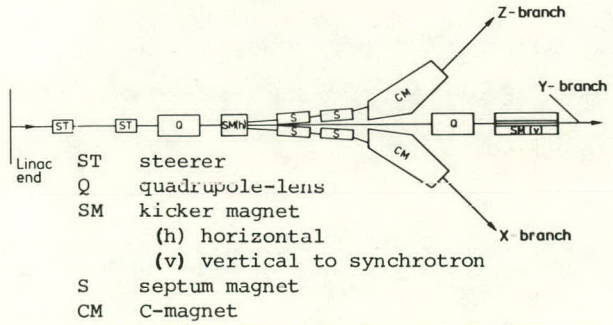


Modification of the rf system for the UNILAC Alvarez section

Fig. 3

Modifications of Beam Transport

The upgrading of the Unilac requires the change of the existing beam transfer system between accelerator and experimental area. The beam splitting system has to be reconstructed for space reasons. Figure 4 shows a schematic layout of the modified configuration. A pair of steering magnets provides for corrections of beam position followed by a quadrupole lens after which the beam is either bent to the X- or Z-yard by a switching-magnet, through two septum magnets and a C-magnet, or is transported straight to the Y-yard. The switching magnet can be operated either dc or pulsed. This allows the delivery of parasitic beams by both time -sharing and beam-splitting modes of operation of this system.



ST steerer
Q quadrupole-lens
SM kicker magnet
(h) horizontal
(v) vertical to synchrotron
S septum magnet
CM C-magnet

Fig. 4 Beam switch-yard at the end of the extended Unilac

The beam to the synchrotron is deflected downwards by an additional kicker magnet in front of the Y-yard to the beam transfer line to the synchrotron which will be installed in the basement of the experimental hall.

The existing beam transport system to and in the experimental area is designed for a maximum magnetic rigidity of 4.4 Tm. Hence it can transport beams of U^{28+} ions with an energy of up to 11.0 MeV/u. Therefore, when using a gas stripper for the heaviest masses, one cannot transport the highest energies obtainable with the upgraded Unilac. But the beam transfer line to the synchrotron will be designed for a higher magnetic rigidity in order to use the higher intensities which are possible with a gas stripper in the whole energy range.

Beam Parameters

At the exit of the accelerator the energy resolution will be $1 - 2 \times 10^{-3}$ and the bunch width 200 - 400 ps for high energies. Output energy is attainable in the range between 3.0 MeV/u and maximum. If variation is required around 3.6 MeV/u, special care must be taken in tuning the pre-bunchers and Alvarez tank I in order not to exceed an energy spread of 3×10^{-3}, which is the limit for the proper refocusing of the bunches into the single-gap cavity section. For this matching a rebuncher cell is foreseen between Alvarez tank II and III. The bunch structure of the other intermediate Alvarez energies, i.e. 5.9, 8.5 and 11.3 MeV/u can be matched to the single-gap cavities without additional rebunching provisions.

For the target stations Z3 through Z5, and X7 through X0 (see Fig. 1), the usual bunch focus of $\leq$ 300 ps can be expected. The helix cavities in the Z and X branch will be used instead of the abandoned rebuncher at the tunnel end. For maximum energies, the required rebuncher voltage of 1 MV may eventually set a limitation. For all intermediate Alvarez energies, one particularly selected single-gap cavity may serve as a rebuncher, restoring a time focus at the other target stations not mentioned above.

Multi-Ion Acceleration

If the Unilac should be simultaneously used both as an accelerator for low energy experiments (< 20 MeV/u) and as an injector for the heavy ion synchrotron, there should be as little interference between these two functions as possible. Ideally, one should be able to choose isotope and energy for these two purposes independently. For each accelerating cycle of the synchrotron it is necessary to change the operating parameters of the Unilac for the acceleration of the appropriate ion during one macro-pulse. Basic requirements for this are first, that the two injectors simultaneously deliver different ion species, second, that the accelerating rf fields can be switched from one pulse to another to accelerate different charge-to-

mass ratios, and third, that the focusing channels can be fast-adjusted.

The existing 320 kV preaccelerators allow for alternating injection of different ion species into the Unilac by just pulsing the already laminated 12.5^0-switching magnet. Provision is also made for a fast change of amplitude and phase of the rf-fields. But there are no pulsed focusing or steering elements installed at the Unilac. From this fact result severe limitations for a present multi-ion operation. Only ion species with not too different atomic numbers could be accelerated simultaneously. This is mainly due to the fact that the mass-to-charge ratio after the stripper depends on the atomic number of the ions. Table 1 shows, for ion species which are injected into the Unilac with a mass-over-charge ratio near to $A/\zeta = 22$, the corresponding values after stripping in gas at 1.4 MeV/u.

Prestripper		Poststripper	
Ion	A/ζ	Ion (Gas Stripper)	A/ζ
$^{20}Ne^{1+}$	20	$^{20}Ne^{7+}$	2,8
$^{40}Ar^{2+}$	20	$^{40}Ar^{10+}$	4
$^{46}Ti^{2+}$	23	$^{46}Ti^{13+}$	3,5
$^{65}Cu^{3+}$	21,7	$^{65}Cu^{15+}$	4,3
$^{84}Kr^{4+}$	21	$^{84}Kr^{17+}$	4,9
$^{107}Ag^{5+}$	21,4	$^{107}Ag^{19+}$	5,6
$^{132}Xe^{6+}$	22	$^{132}Xe^{21+}$	6,2
$^{154}Sm^{7+}$	22	$^{154}Sm^{23+}$	6,7
$^{208}Pb^{9+}$	23,1	$^{208}Pb^{26+}$	8,0
$^{209}Bi^{9+}$	23,2	$^{209}Bi^{26+}$	8,0
$^{238}U^{11+}$	21,6	$^{238}U^{28+}$	8,5

Table 1: Mass-to-charge ratio (A/ζ) for different ion species in the prestripper and poststripper section of the Unilac

Besides a complete redesign of the stripper section with the charge-analyzing system, about 25 focusing and steering elements must be prepared for pulsed operation. The corresponding modifications of the control systems have to be done in parallel to achieve an independent tuning for different ion beams.

This multi-ion program will be supplemented by a third injector, which will be designed for a low duty cycle and high peak currents[3]. Thus one can both preserve the very important redundancy for the existing injectors and increase the intensities for injection into a synchrotron by about three orders of magnitude for the heaviest elements.

Schedule and Cost

The aforedescribed measures leading to the desired energy increase and the outlined reconfiguration of the beam distribution system in the experimental hall are lined up in an ambitious time schedule. One reason for that is the already existing demand for beams of energies in excess of 10 MeV/u. One other substantial reason is enforced by manpower limitations. The energy increase should be completed when the multi-particle modification and the high-intensity injector project are due to start in order to meet the synchrotron commissioning schedule. Component procurement of the Alvarez tanks and rf power lines should be completed at the end of 1980. Installation in the tunnel will require a 4-month shut-down period, until beam operation can be resumed end of 1981. It is likely to occur that the new generation of rf amplifiers are not yet operational at that date, which means a slip of half a year in the time schedule for the availability of the energy increment for the heaviest elements.

The cost for the energy increase project is estimated to roughly MDM 4.7. The expenses for prototype activities for rf and hardware are already in the authorized budget for 1979 and 1980. The estimated manpower effort, mostly from internal resources, totals up to 44 man-years.

The pulsing of focusing and steering elements for the multi-ion acceleration can be partly done in the frame of an already started improvement program for the magnet power supplies. Also the changes in the beam diagnostic and control system will not cost too much so that it can be realized with the yearly budget within another two years till end of 1983. All other reconstruction, for instance, a new stripper section and a third injector, depend on funding of the synchrotron.

References

1 D. Böhne, "Status Report on the Unilac", these proceedings.

2 B. Franczak et al., "Linear Accelerator with Intertank Focusing", these proceedings.

3 R.W. Müller, "Work on Rf Quadrupole Focusing Structures at GSI", these proceedings.

4 D. Böhne et al., "Cavity and Drift Tube Technology for the Upgraded Unilac", these proceedings.

Discussion

Knapp, LASL: I didn't understand how the 140 MeV per nucleon energy range, shown in the figure, is achieved.

Angert: It is given by the tuning range of the synchrotron rf cavities.

THE FUSION MATERIALS IRRADIATION TEST (FMIT) ACCELERATOR*

E.L. Kemp, D.J. Liska and M.D. Machalek
University of California, Los Alamos Scientific Laboratory
Los Alamos, New Mexico 87545

Introduction

The Fusion Materials Irradiation Test (FMIT) Facility will be built at Hanford, Washington, and operated by the Hanford Engineering Development Laboratory (HEDL), which is managed by the Westinghouse Corporation. The function of the FMIT facility is to produce 14-MeV neutrons to develop critical materials for fusion reactors. The total estimated cost of the entire facility is $105 million.

The neutron generator consists of a linear deuteron accelerator that injects 35-MeV deuterons into a flowing lithium blanket and produces 14-MeV neutrons by a stripping process. The Los Alamos Scientific Laboratory (LASL) is responsible for the design and ultimate performance of the accelerator. The design activities will be performed by a team of LASL and HEDL engineers working at Los Alamos under the technical supervision of LASL. The accelerator components will be manufactured by U. S. industry. The HEDL will be responsible for the installation while LASL will be responsible for the final commissioning of the accelerator. This paper presents an overview of the accelerator.

Design Choices

Because of the length of the irradiation testing period, perhaps several years, the facility must operate essentially as a neutron factory with high reliability and high availability. These requirements guided the design philosophy for the accelerator.[1] Because experience has shown that the reliability of ion sources and high-voltage accelerating columns is inversely proportional to the operating voltage, a system that operates at a modest voltage is an attractive option. Often this option is not viable because of the design difficulties of the first drift tube. A recent proposal in the USSR[2] for a novel low-energy accelerating structure, which we call the Radio-Frequency Quadrupole (RFQ), allows the possibility of designing a low-voltage injector system that can be matched to a conventional drift-tube linac accelerator. The FMIT design consists of a 100-keV injector, an RFQ structure, and a conventional linac. A 5-MeV prototype accelerator is being built at LASL to develop and to certify these design concepts for the FMIT accelerator.

*Work performed under the auspices of the U. S. Department of Energy.

An 80-MHz operating frequency was chosen for FMIT to minimize the size of the components, while staying within the availability of reliable rf power components and systems. An average accelerating gradient of 1 MeV per meter was selected to stay within the Kilpatrick Criterion and to minimize the length of the linac. Certain other mechanical design features were dictated by the need for "hands on" or mechanically assisted maintenance that will be required over the 20-year life of this facility.

Table I shows the principal specifications for the accelerator.

TABLE I

ACCELERATOR SPECIFICATIONS

Particle	Deuterons
Duty Factor	100%
Frequency	80 MHz
Output Energies	20 MeV and 35 MeV
Maximum Beam Current	100 mA
Average Energy Gain	1 MeV/m
Injector Energy	100 keV
Low-β Accelerator (RFQ) Output	2 MeV
Number of Linac Tanks	2
Number of Drift Tubes	72
Inner Diameter of Linac Tanks	2.48 m and 2.40 m
Length of Linac Tanks	32 m
Total Length of Accelerator	42.7 m
Total rf Power	5.35 m
Operating Pressure	1.33×10^{-4} Pa

System Layout

Figure 1 shows the general layout of the accelerator. The injector introduces a 100-mA beam of deuterons into the RFQ that captures, bunches, and accelerates the beam to 2 MeV. The drift-tube linac consists of two rf cavities that

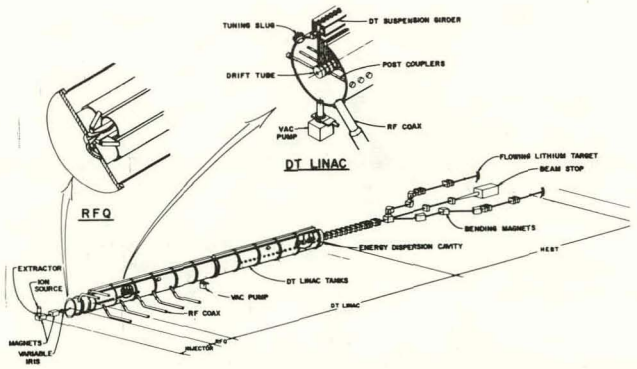


Fig. 1. The FMIT accelerator.

accelerate the beam to a maximum of 35 MeV. The second cavity can be unexcited and can be used to transport the 20-MeV beam from the first cavity to the High-Energy Beam Transport (HEBT) system Energy Dispersion Cavity (EDC). The purpose of the EDC is to spread the energy of the almost monoenergetic 35-MeV or 20-MeV beam for proper operation of the target. The straight portion of the HEBT transports the beam to a switching magnet that directs the beam to either of the two identical targets by a periodic system of bending magnets. The final magnets focus the beam to a 1-cm by 3-cm spot on the target. The system also includes a pulsed duty beam stop for tune-up of the machine.

Injector

The FMIT injector[3] being developed uses a cusp-field ion source based on a Culham Lab design.[4] The ion source is a water-cooled cylindrical anode with 30 ceramic bar magnets arranged axially around the outside of the anode wall to generate a periodic cusp magnetic field inside the anode. The filament mounting plate is installed at the top end of the chamber opposite the extractor. The cusp field prevents the electrons from moving directly to the anode and increases their lifetime in the chamber, thus significantly increasing the efficiency of the source. The 100-kV extractor is a single-gap accelerating column with molybdenum electrodes. A model of this injector has been tested with very satisfying results. The gas efficiency is over 40%. The source is very quiet and stable and the filament life is expected to be over 350 hours.

Radio-Frequency Quadrupole

The RFQ serves two functions: converts the DC beam from the injector into a bunched beam acceptable to a drift-tube linac, and then accelerates the beam to the energy required for injection into the first drift tube. A vigorous program is underway at LASL to develop an RFQ system for FMIT.[5] The RFQ consists of four periodically modulated bars in an rf cavity driven in a TE_{210} mode. This structure establishes a quadrupole focusing field so that off-axis particles experience focusing in one plane and defocusing in the other, and vice versa on alternate rf half-cycles. The result is a strong focusing system that will transport the beam without acceleration along the axis. Longitudinal acceleration occurs because of the radial modulations on the vanes, which produce longitudinal field components in the fringing field. The periodicity of the modulation is varied as the particle energy increases, to keep the particle in phase with the rf electric field.

A number of cold models have been successfully evaluated with bead-pull techniques. The Z/Q is satisfactory and methods for coupling radio frequency into the cavity have been developed. The design and the construction of a 425-MHz proof-of-principle test are underway with experiments scheduled to begin by January 1980. Simultaneously, design studies have begun for an 80-MHz RFQ prototype system that is scheduled for evaluation in 1981.

Linac

The Linac is being designed[6] for a nearly maximum shunt impedance (ZT^2) consistent with the Kilpatrick Criterion to minimize the rf power requirements. The average value of ZT^2 in both tanks is more than 37 MΩ/m. The inner diameter of each tank is about 245 cm. The 2- to 20-MeV tank is about 18 m long and the second tank is about 15 m long. The intertank spacer between the two tanks is one beta-lambda in length (54.3 cm at 20 MeV). The tanks will be fabricated of 2.5-cm-thick copper-clad steel surrounded by a continuous steel shell jacket for longitudinal counterflow flood cooling.

Although the linac will be designed for minimum beam spill, it is recognized that some spill is inevitable and it is assumed to be 3 μA/m plus some "hot spots." This will lead to activation levels that preclude anyone entering the tanks after the linac has been put into operation. A design concept used on the CERN Linac was adopted for the FMIT Linac. The FMIT system[7] uses girder strongbacks supported by the tank stiffening rings, as shown in Fig. 2. Eleven girders are required, each one about 3 m long. A girder will weigh about 3000 kg and will support from 3 to 15 drift tubes. The drift tubes will be installed and aligned on the girders in an alignment dock. After installation in the tanks the various girders will be aligned with each other.

The shape of the drift tubes was optimized using the SUPERFISH code. The drift-tube noses are tapered but still meet the Kilpatrick Criterion with a maximum surface field stress of 10.5 MV/m while minimizing the amount of rf power required. Because the FMIT is continuous duty, the drift-tube faces are water cooled by

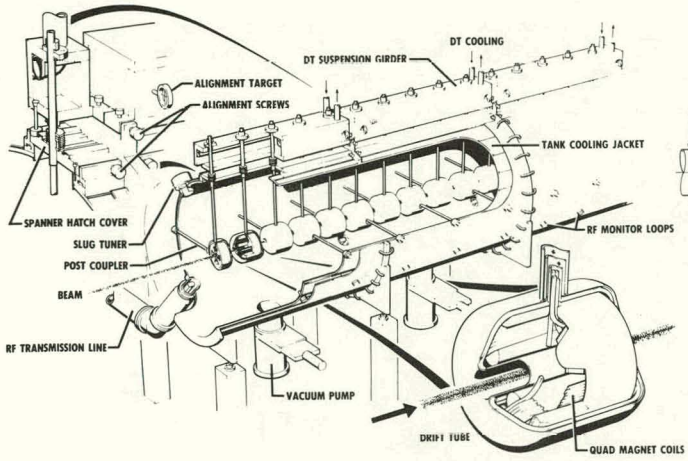


Fig. 2. The drift-tube linac.

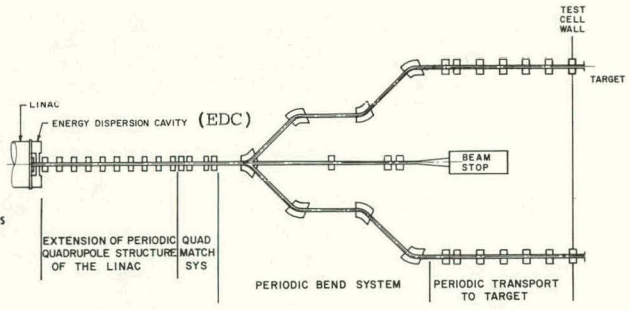


Fig. 3. The FMIT HEBT system.

an independent cooling system. Each drift tube incorporates a quadrupole magnet that is also independently cooled.

The final component in the linac is the Energy Dispersion Cavity (EDC), which is required to spread the energy of the linac by plus and minus 750 keV so that the energy will be deposited at various depths in the lithium target. The EDC is a simple capacitively loaded TM_{010} resonator that has a gap about equal to the last gap in the linac and a diameter equal to the linac tank. It is driven slightly off the 80-MHz resonance so that the resultant beat is only a few megahertz.

High-Energy Beam Transport

The HEBT system[8] is designed to transport the 3.5-MW, 100-mA continuous deuteron beam from the linac to either of two targets. The HEBT must transport a beam with a total possible geometric emittance of 68.5π cm-mrad unnormalized with a total energy spread of 1.5 MeV.

Figure 3 shows the layout of the HEBT. The first section of the HEBT is an extension of the periodic quadrupole section similar to the quadrupoles inside the linac. This section is used to install beam diagnostics instruments required for accelerator operation. The quadrupole matching section is required to match the beam to the bending system. The periodic bending system consists of four identical bending magnets with the angle of bend of the second and fourth magnets reversed. A mirror image of this system transports the beam to the second test cell. Vertical focusing is provided by the downstream edge angle of each magnet such that the phase shift of the cell is 90° in both planes with equal cell lengths in both planes. The remaining magnets in the transport system steer the beam and finally focus it to a 1-cm by 3-cm spot on the target.

The entire HEBT will be suspended from the ceiling to line up with the 10-foot beam center line in the linac. This suspension system will allow easy access to the HEBT for maintenance.

Radio-Frequency System

The FMIT rf system[9] is designed to deliver a maximum of about 9 MW of rf power. The present design requires 3.5 MW for the beam plus about 1.9 MW for copper losses. The final amplifiers will operate at about two-thirds of their maximum ratings. A block diagram of the rf system is shown in Fig. 4. The 80 MHz is generated by a crystal oscillator and flows through the low-power signal amplifiers to the high-power amplifiers. Phase and amplitude control is done at the low-power amplifier level. The high-power amplifiers, which will be designed and constructed by a commercial vendor, will each use a single EIMAC 8973 tetrode as the final amplifier tube. This tube has been evaluated at over 500 kW at 80 MHz and it appears quite satisfactory for this application. The system uses multiple drives in all tanks and it is designed so that the accelerator can operate for a limited time with one rf module out of service in each tank.

The Prototype

A prototype of the first 5-MeV section of the accelerator will be built and evaluated at LASL to confirm the design choices in this part of the FMIT accelerator. The prototype will consist of a 100-keV injector, an RFQ low-beta accelerator, the first girder of drift tubes in a short linac tank, and an EDC. All these components, with the exception of the short tank, will be exactly prototypical of the FMIT accelerator parts. Four prototypical rf modules will be used to supply the rf power for the RFQ and the Linac; a special unit will power the EDC. The control system and the vacuum system will be equivalent to those in the FMIT system. The prototype injector will begin operating in early 1980 and beam through the entire prototype system is scheduled for early 1982.

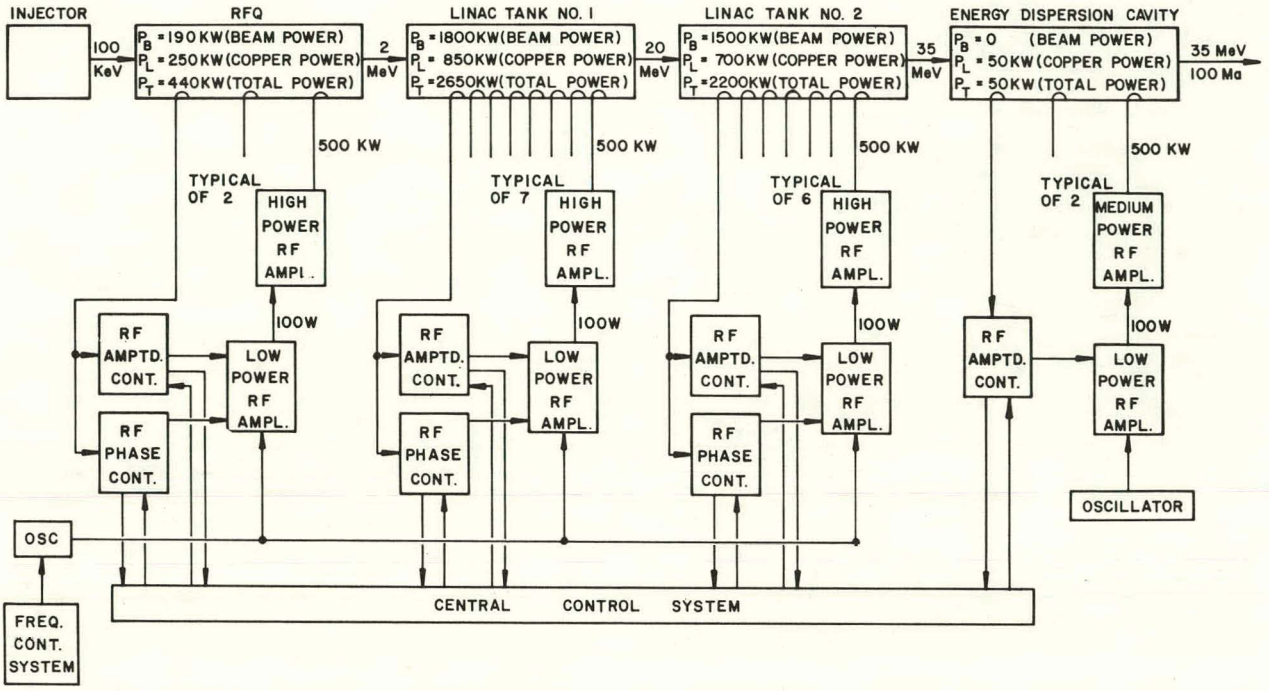


Fig. 4. A block diagram of the rf system.

Design Status and Schedule

A conceptual design of the complete FMIT accelerator has been completed and approved. Preliminary design has begun with emphasis on the design and procurement of the prototype system. Completion of the design of the entire accelerator system is scheduled for mid-1981. Accelerator installation will begin in the fall of 1982 with check-out beginning about a year later. The entire facility is scheduled to begin operating in September 1984.

References

1. R. A. Jameson, "High Intensity Deuteron Linear Accelerator (FMIT)," IEEE Trans. Nucl. Sci. NS-26, No. 3, pp. 2986-2991 (June 1979).
2. I. M. Kapchinski and V. A. Teplyakov, "Linear Ion Accelerator with Spatially Homogeneous Strong Focusing," Pribory i. Technika Eksperimenta, 119, No. 2, pp. 19-22 (March-April 1970).
3. D.D. Armstrong, E.A. Meyer, J.D. Schneider and H.L. Rutkowski, "Progress Report on Testing of a 100-kV, 125-mA Deuteron Injector," IEEE Trans. Nucl. Sci. NS-26, No. 3, pp. 3009-3011 (June 1979).
4. A. Goede, T.S. Green and B. Singh, "Particle Balance in a Picket Fence Ion Source," 8th European Conf. on Confined Fusion and Plasma Physics, Prague, Czechoslovakia, Sept. 1977, Vol. 1.
5. J.M. Potter, S.W. Williams, F.J. Humphry, and G.W. Rodenz, "Radio Frequency Quadrupole Accelerating Structure Research at Los Alamos," IEEE Trans. Nucl. Sci. NS-26, No. 3, pp. 3745-3747 (June 1979).
6. G.P. Boicourt and D.A. Swenson, "Choice of Geometry for the Alvarez Section of the FMIT Deuteron Linac," IEEE Trans. Nucl. Sci. NS-26, No. 3, pp. 3012-3014 (June 1979).
7. D.J. Liska, R.G. Schamaun, R.C. Potter, D.M. Clark, D.R. Greenwood and J.A. Frank, "Design of the Accelerating Structures for FMIT," IEEE Trans. Nucl. Sci. NS-26, No. 3, pp. 3052-3054 (June 1979).
8. K.E. Melson, J.A. Farrell, D.J. Liska, D.D. Chamberlin, M.T. Wilson, P.M. Giles, R.C. Potter, T.R. Cole and C. Caldwell, Jr., "High-Energy Beam Transport in the Hanford FMIT Linear Accelerator," IEEE Trans. Nucl. Sci. NS-26, No. 3, pp. 3050-3051 (June 1979).
9. M.V. Fazio, H.P. Johnson, W.J. Hoffert and T.J. Boyd, "A Proposed RF System for the Fusion Materials Irradiation Test Facility," IEEE Trans. Nucl. Sci. NS-26, pp. 3018-3020 (June 1979).

1979 LINEAR ACCELERATOR CONFERENCE

A HIGH-ENERGY BEAM TRANSPORT SYSTEM*

K.E. Melson,† J.A. Farrell, D.J. Liska, P. Meads††
Accelerator Technology Division
Los Alamos Scientific Laboratory
Los Alamos, New Mexico 87545

Summary

The High-Energy Beam Transport (HEBT) system for the Fusion Materials Irradiation Test (FMIT) Facility is to be installed at the Hanford Engineering Development Laboratory (HEDL) at Richland, Washington. The linear accelerator must transport a large emittance, high-current, high-power, continuous-duty deuteron beam with a large energy spread either to a lithium target or a beam stop.[1] A periodic quadrupole and bending-magnet system provides the beam transport and focusing on target with small beam aberrations. A special rf cavity will spread the energy in the beam so that the Bragg Peak is distributed within the lithium target. Operation of the rf control system, the Energy Dispersion Cavity (EDC), and the beam transport magnet will be tested on the beam stop during accelerator turn-on. Characterizing the beam will require extensions of beam diagnostic techniques and noninterceptive sensors. Provisions are being made in the facility for suspending the transport system from overhead supports using a cluster system to simplify maintenance and alignment techniques.

Introduction

The HEBT system (Fig. 1) contains four subsystems: the EDC, the beam transport optics and other beam-line components, a beam spreader (a quad doublet), a beam stop, and the HEBT support system. The EDC must create a large energy spread in the beam delivered to the target. The beam optics must transport a large emittance, 100-mA deuteron beam with large energy spread at either 20 or 35 MeV to one of the two lithium targets or to a beam stop. The lithium target requires an incident 1-cm by 3-cm FWHM Gaussian spot whereas the beam stop requires a 16-in diameter circular spot. The beam spreader and beam stop have been provided for tune-up using a pulsed beam. A minimum 2.1-m (7-ft) clearance must be maintained between the support structure and the HEBT hardware to allow component maintenance.

The Periodic Beam Transport System

The primary design consideration in the beam transport system is minimization of beam spill to prevent unacceptably high activation of components. The use of a magnetic transport system with an acceptance equal to or greater than the maximum possible output emittance of the accelerator is the best way to accomplish this minimization of beam spill; however, care must be taken so excessively large apertures do not drive the magnet costs too high. Magnet apertures are minimized with a properly matched beam in a periodic system. Although such systems often appear to be complicated at first glance, they are invariably cheaper to build because of the smaller aperture requirements, relaxed tolerances, shared power supplies, and many identical components.

The simplest method of transporting the beam the relatively short distance to the first bending magnet is to extend the periodic structure of the linac. The quadrupoles are slightly weakened to compensate for the lack of rf defocusing. A matched beam in the accelerator will, therefore, be nearly matched in this section. The periodic quad structure offers the advantage that diagnostics in this section can give the operator an indication of the beam conditions inside the machine because of the nearly identical focusing structure.

The bending magnet system is also periodic, consisting of four identical magnets with the angles of bend of the second and fourth magnets reversed. Vertical focusing is provided by the downstream edge angle of each magnet. The edge angles are adjusted so that the phase shift of a single-bend cell is 90° in both planes. The calculations were done using the computer code, TRANSPORT.[2] This arrangement is achromatic because any system composed of n identical cells of phase shift μ such that $n\mu = 360°$ is automatically achromatic and all second-order geometric aberrations are also zero. Second-order chromatic aberrations can be

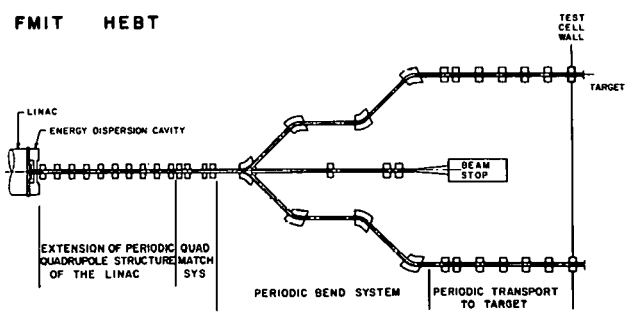


Fig. 1. The FMIT HEBT.

*Work performed under the auspices of the U. S. Department of Energy.
†Westinghouse/Hanford Engineering Development Laboratory employee working at the Los Alamos Scientific Laboratory.
†† Wm.M. Brobeck & Associates, Berkeley, CA.

corrected easily with the introduction of sextupoles[3] but this is unnecessary in the present case.

The bending magnet apertures remain quite small because there are no quadrupoles in the region of high dispersion. All four bending-magnets can be run in series on a single power supply. A mirror image of the bend system provides the transport to the second target cell.

The quadrupole array following the linac is matched to the bending-magnet system using a scheme devised by K. L. Brown.[4] The required matching conditions are determined from the transform matrix, R, of a single cell. The Courant-Snyder parameters are

$$\cos \mu_x = \frac{1}{2} (R_{11} + R_{22}) \quad ,$$

$$\alpha_x = \frac{1}{2} \frac{(R_{11} - R_{22})}{\sin_x \mu} \quad , \text{ and}$$

$$\beta_x = \frac{R_{12}}{\sin \mu_x} \quad ,$$

with similar equations for the y-plane. The matching system is constructed by placing a matching quadrupole ,Q1, midway between waists of the periodic quadrupole system (where $\beta_x = \beta_y$, $\alpha_x = -\alpha_y$) and a second quadrupole, Q2, at the corresponding location in the bending-magnet system. Two fixed-strength quadrupoles are added to complete the matching system, which has a 90° phase shift in both planes from the center of Q1 to the center of Q2. This procedure essentially decouples the two matching conditions, with Q1 controlling β (in both planes) and Q2 controlling α at the match point, which is at the center of Q2. The drifts at each end of the matching system were varied slightly to compensate for the fact that a quadrupole does not behave quite like a thin lens with $F_x = -F_y$.

Transport from the last bending magnet to the target can be accomplished in a number of ways. The last four quadrupoles are adjusted to obtain the desired spot size at the target. The large energy spread and the potentially large emittance coupled with the relatively small (1-cm vertical spot required at the target) require that chromatic and third-order geometric aberrations be considered. Calculations were made using the computer code TURTLE[5] with modifications to include the bimodal momentum distribution. The results indicated that, depending on the emittance, it may be impossible to achieve the desired spot size if the last quadrupoles are too far from the target unless the aberrations are corrected. Correction of the aberrations could be done with sextupoles and octupoles but a much simpler procedure is to place the last quadrupole close to the target (within 50 cm) in which case the aberrations are negligible.

Other Systems

Energy Dispersion Cavity

The EDC is a special rf cavity at the end of the linac that operates at a frequency slightly different from the 80 MHz of the accelerator itself, so that the energy dispersion is a "beat" of a few MHz. The cavity is a TM_{010} resonator that has a gap about equal to the last gap of the drift-tube linac. The EDC is amplitude controlled but not phase controlled. Frequency control is not critical. The current design creates a ±750-keV spread in beam energy with a dispersion profile that is a strong function of the inherent linac dispersion and a weak function of beat frequency. Positioning the cavity at the end of the linac permits its use for either beam-line branch.

Beam Stop

A beam spreader and a beam stop have been provided for initial tune-up purposes using an H_2^+ beam in a pulsed mode or a very low, steady state current of deuterons. Because the fill time of the linac tanks is under 2 ms, 10-ms pulse widths can be used to exercise adequately the operation of the rf control system, the set points of the drift-tube quads in the linac, and the HEBT up to the first bending magnet. The short pulse widths allow low duty-factor operation at full peak power, which greatly simplifies the design, construction, and expected lifetime of the beam stop. The beam stop will utilize the calorimeter principle and resembles the Lawrence Berkeley Laboratory designs, which consist of two thick and angled copper plates joined at the apex.[7]

Beam Diagnostics

Monitoring the progress of the transported beam will require noninterceptive sensors such as current transformers, magnetic position monitors, inductive pickups, and spill detectors. The information and feedback from these sensors must be processed through the control system and then returned to beam-handling elements with sufficient speed and sensitivity to correct out-of-bounds conditions with minimal spill of the deuteron beam. The feasibility of providing profiles of the density distribution within the beam by viewing (and digitizing) the light emitted from recombination processes of ionized residual gases in the beam tube is being studied. Three such optical profiles may be converted to a two-dimensional density plot and three or four such density plots from differing transport conditions may be reconstructed to give emittance information.

Further requirements for the diagnostics system include measurement of longitudinal phase, and verification of the required energy spread on target. The shape of the beam spot on target must be well defined because it is the source both of 3.5 MW of lithium target heating

and of the product neutrons. These measurements must be made reliably in the presence of quite intense neutron fields.

Beam-line Suspension System

The facility is being designed to allow the transport system to be suspended from overhead supports to facilitate mechanized maintenance of activated components. The transport support system is a grid of I-beams supported by the walls of the building. Alternate methods are being studied for attaching the beam-line components to the support system and a variety of mounts have been proposed. The mounting stand will give all degrees of freedom of movement to the element to allow for its proper alignment.

References

1. K. E. Melson, J. A. Farrell, D. J. Liska, D. D. Chamberlin, M. K. Wilson, P. Giles, C. Potter, T. Cole, and C. Caldwell, Jr., "High-Energy Beam Transport in the Hanford FMIT Linear Accelerator," IEEE Trans. Nucl. Sci. NS-26, No. 3, pp. 3050-3051 (June 1979).
2. K. L. Brown, F. Rothacker, D. C. Carey, and Ch. Iselin, "A Computer Program for Designing Charged Particle Beam Transport Systems," SLAC-91, Rev. 2 (May 1977).
3. K. L. Brown, "A Second Order Magnetic Optical Achromat," IEEE Trans. Nucl. Sci. NS-26, No. 3, pp. 3490-3492 (June 1979).
4. K. L. Brown, Stanford Linear Accelerator Center Publication 2370, to be published.
5. K. L. Brown and Ch. Iselin, "DECAY TURTLE," CERN 74-2 report (February 1974).
6. D. Liska, R. Schamaun, C. Potter, C. Fuller, D. Clark, D. Greenwood, and J. Frank, "Design of the Accelerating Structures for FMIT," IEEE Trans. Nucl. Sci. NS-26, No. 3, pp. 3052-3054 (June 1979).
7. J. M. Haughian, W. S. Cooper, and J. A. Paterson, "The Design and Development of Multi-Megawatt Beam Dumps," IEEE Trans. Nucl. Sci. NS-24, No. 3 (June 1977).

1979 LINEAR ACCELERATOR CONFERENCE

STATUS OF THE VARIABLE FREQUENCY HEAVY ION LINAC, RILAC

M. Odera, Y. Chiba and T. Kambara
Riken Institute (The Institute of Physical and Chemical Research)
Wako-shi, Saitama 351 Japan

Summary

A variable frequency heavy ion linac is under construction at the Institute of Physical and Chemical Research (IPCR). The linac operates in π-3π and π-π modes and its acceleration frequency can be set between 17 and 45 MHz. The maximum energies of ions are 4 MeV/amu for light ions and 0.8 MeV/amu for heavy ions. The characteristics of the linac and the present status of the construction are reported in this paper. A plan for an energy booster of the linac is described.

Introduction

RILAC under construction is a π-mode variable frequency heavy ion linac. It realizes efficient acceleration of a variety of ions by choosing the acceleration frequency according to the charge-to-mass ratios. Therefore the design of the resonators differs from that of fixed-frequency linacs. It consists of six quarter-wavelength resonators excited by six rf amplifiers separately[1]. The acceleration frequency can be set between 17 and 45 MHz. The construction work was started in 1975, and the installation of major equipment has been more than 90% completed.

In parallel with the installation work, several preparatory tests of individual elements of the linac, such as rf excitation of the cavity, beam acceleration by the injector, and a check of the injection beam line optics, were performed. Remaining installation work, such as the wiring of the control system, will be finished this year.

In this paper, mechanical and electrical characteristics of the linac, status and schedule of the construction work and a future project of the accelerator facility will be described.

Accelerator Outline

Figure 1 shows a layout of the facility. Figure 2 is a photograph of the accelerator taken in the linac vault in June. The cavities have unusual shapes, as illustrated in Fig. 3, to meet the requirements of frequency variability and mechanical rigidity at the same time. Each of six rf amplifiers has two long stubs for impedance matching at the output stage. Owing to the stubs, the housing of the amplifier is very tall.

The injector terminal with a volume of 4×4 ×2.5 cubic meters is shown in Fig.4. Maximum acceleration voltage of the injector is 500 kV.

An example of energies of ions are listed in Table I. Those energies can be obtained without any charge stripping procedures. If it is necessary to save rf power, a charge stripper can be inserted between the fourth and the fifth cavities. Then the charge-to-mass ratio of the ions increases by a factor of three, which cuts the rf power dissipation in the following cavities by an order of magnitude.

Ten experimental sites are provided in three shielded rooms. Research proposals submitted cover many fields --- nuclear physics, atomic physics, solid state physics, radiation chemistry and biology. Requests for particle species, beam intensity and beam quality are varied. There is no plan of simultaneous multiple beams at present. The linac can be operated in a CW mode for most beams and, if a pulsed beam is desired, it can be produced by a chopper in the injection beam line.

Table I

Ion	m/q	Accelerating RF freq. (MHz)	Voltage (MV)	Energy (MeV/n)
$^{12}C^{3+}$	4	45	16.5	4
$^{20}Ne^{4+}$	5	39	16.5	3.1
$^{40}Ar^{7+}$	5.7	39	18	3.0
$^{84}Kr^{8+}$	10.5	31	20	1.9
$^{132}Xe^{9+}$	14.7	25.5	20	1.36
$^{238}U^{10+}$	23.8	20	20	0.84

Resonators

As shown in Fig.3, the cavity is a quarter-wavelength coaxial resonator. It is made of copper-clad steel except for drift tubes. The resonant frequency of the cavities ranges from 17 to 60 MHz, but the uniformity of the acceleration voltage across each drift tube gap was found guaranteed only up to 45 MHz. Coarse frequency tuning is made by a movable shorting device, fine tuning by a large capacity compensator and very fine tuning by a small capacity compensator. The position of the shorting device is preset according to the velocity of the ions. The large compensator is used to accommodate the thermal tuning drift and the small one is coupled with a tuning error detector which automatically keeps resonance.

Figure 5 shows the frequency span and Q-values measured for some cavities. The distribution of the accelerating voltage and its frequency dependence were reported at the 1976 Linac Conference.[2] Two turbomolecular pumps (2400 ℓ/s and 5000 ℓ/s) are used in the vacuum system of each cavity and a final pressure of 3×10^{-7} Torr has been achieved. In order to keep the vacuum clean, only welded bellows are allowed to introduce mechanical motion into the cavity.

Drift Tubes

Every second drift tube is electrically connected to the outer conductor of the cavity. The drift tubes have outer diameters of 160 mm and contain quadrupole magnets. They are supported by a hollow beam of square cross-section. Electric current and coolant are fed to the quadrupole magnets through the inside of the beam. The drift tube shell is made of oxygen free copper, electron beam-welded.

Alignments of the magnetic axis of the quadrupole magnets were measured by the hot-wire method.[3,4] Accuracy of the alignment is within 0.1 mm.

Two types of coils are used for the quadrupole magnets : tape coil type and quadrant stacked type. The maximum power consumption of a quadrupole magnet is 600 W at 7 kG/cm for pole tip distance of 23 mm. The smallest beam aperture is 20 mm.

The other drift tubes attached to the inner conductor of the cavity are made of solid copper and water-cooled. The outer diameter of them is 100 - 160 mm and no quadrupole magnets are set in them. Figure 6 is the view of the drift tube array seen from a cavity window.

Radio-Frequency System

Figure 7 is a block diagram of the amplifier system. The first amplifier was constructed and tested from 17 to 40 MHz with a water-cooled resistive load and then from 20 to 30 MHz with the first cavity coupled through a feeder, in January 1979. The first rf system drove the cavity through the multipactoring region within two hours after the start-up and about 80% of designed voltage was achieved a few days later. For the amplifier test, a temporary plate power supply and cooling system were used, which were then removed and replaced by permanent units in the spring of 1979. The remaining five amplifiers and power supplies were manufactured by vendors with some modifications found necessary by the power test of the first unit. The installation of the amplifiers and related power supplies began in April and was finished in August. The power feeders are scheduled to be installed in September and will be completed in the middle of October 1979.

The rf tuning, phase and amplitude in each unit are controlled locally by hard-wired feedback circuitry. The positions of the shorting device, capacities and stubs are preset by the control system computer at the beginning of each machine time. The reference values of the phase and amplitude are given by the computer. The hardware for automatic feedback and interface to the computer system are now under fabrication.

Control System

The control system uses a minicomputer HP2171A and the IEEE-488 Interface Bus (GP-IB). As the interface between the accelerator and the computer, four data stations are installed in the linac vault and one in the control room. Those in the linac vault are connected to the computer by a serial data link and GP-IB. A control console with two CRT's is used for the man-machine interface.

The installation of the control system started in June and will end in October 1979. Figure 8 shows a block diagram of the control system.

Beam Test

At present, acceleration tests of the injector and studies of the injection beam line optics are performed using singly charged ions of H, N, and Ar. An axial extraction PIG ion source installed in the injector terminal is used for the tests. A side extraction PIG ion source to produce multiply charged ions will be usable from next spring. Beam acceleration tests with the first rf system were started in September using N^{1+} ions.

Schedule of Construction and Operation

Those remaining items of the linac to be installed and debugged before starting acceleration tests are the control system, beam buncher, beam attenuator and beam monitoring devices. At present, it is supposed that minimum conditions to begin acceleration tests will be satisfied at the end of October 1979. Acceleration tests are planned to continue until spring 1980 and then use of the facility for research will begin.

Plan for Future Extension of the Facility

Since the energies of heavier elements ($A \geq 50$) are insufficient for the study of nuclear reactions, an energy booster for RILAC is being proposed.[5] Our intention is to build a separated sector cyclotron as a post-stripper accelerator and to amplify the energy of ions by a factor of roughly twenty. Figure 9 is a layout of the proposed facility and Table II gives tentative characteristics of the cyclotron. The parameters of the RF systems of both machines can be well synchronized owing to the frequency variability of the linac. If approved, the facility will be a powerful tool for multi-disciplinary research.

Table II

Characteristics of proposed cyclotron

Maximum Energy for U^{37+}	15 MeV/n
Maximum Energy for C^{6+}, Ne^{10+}	80 MeV/n (120 MeV/n)*
Number of Sectors	4
Sector Angle	50°
Injection Beam Radius	78 cm
Extraction Beam radius	338 cm
Number of Dees	2
Peak Voltage	250 kV
RF Frequency	17-45 MHz
Number of Harmonic Acceleration	4*, 6*, 8, 12

* An AVF cyclotron used as an injector for light ions.

References

1. M. Odera and T. Tonuma, Proc. Sixth Int. Cyclotron Conf., AIP Conf. Proc., 283 (1972).
2. M. Odera, Proc. 1976 Proton Linear Accelerator Conf., 62 (1976).
3. R. M. Main, LBL-1224, Sept. (1972).
4. I. Takeshita, I. Yokoyama and T. Kambara, Reports I.P.C.R. (in Japanese) 53, 44 (1977).
5. H. Kamitsubo et al., IEEE Trans. Nucl. Sci. NS-26, 2070 (1979).

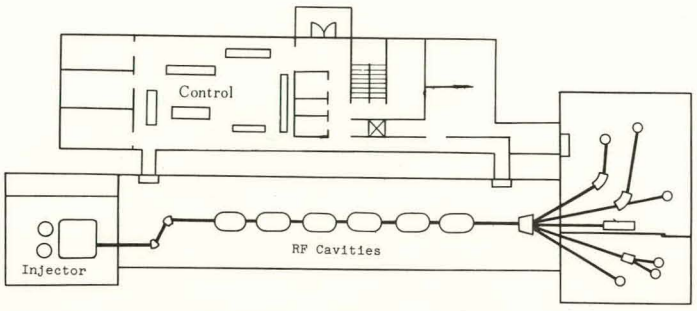


Fig.1. Layout of the RILAC facility.



Fig.2. RILAC seen from upstream side.

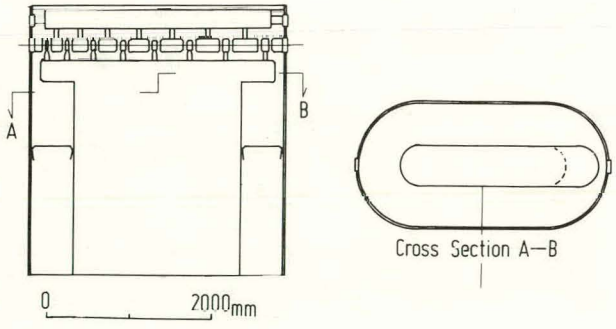


Fig.3. Resonator schematics.

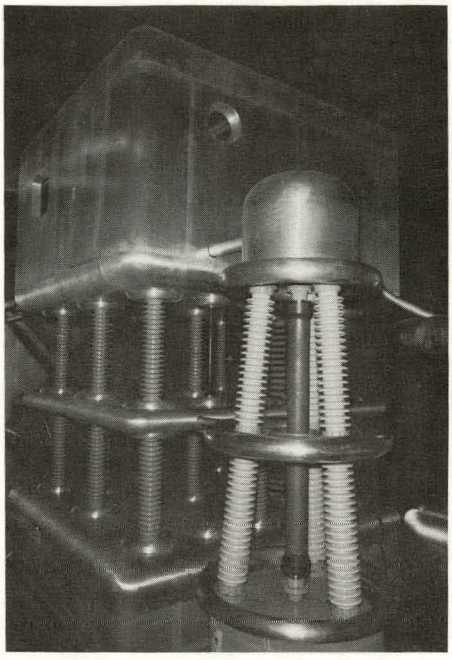


Fig.4. High-voltage terminal of the injector.

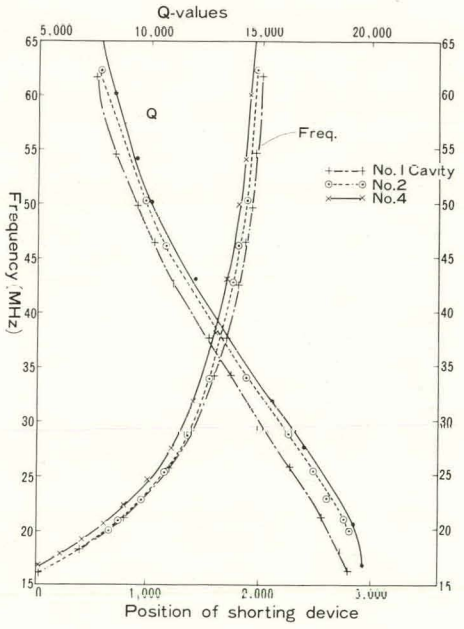


Fig.5. Characteristics of resonators.

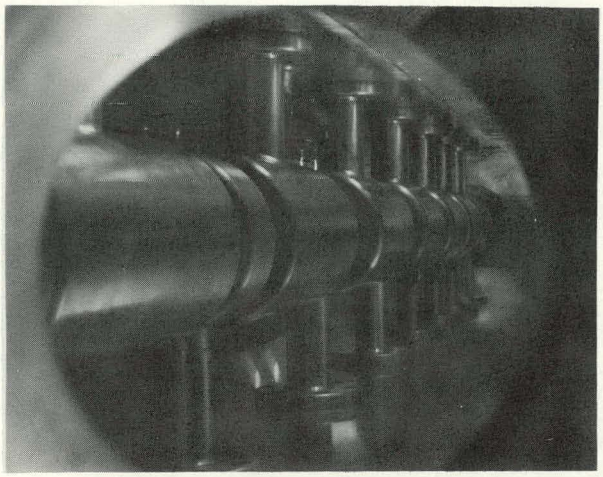


Fig.6. Drift-tube array.

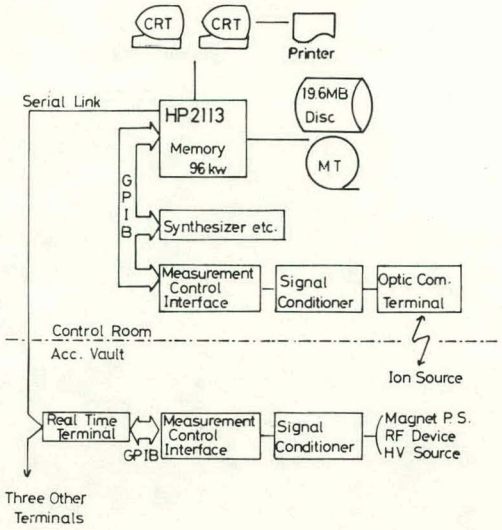


Fig.8. Control system.

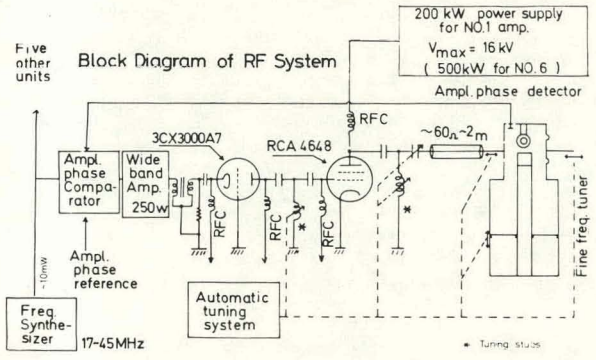


Fig.7. Block diagram of the power amplifier.

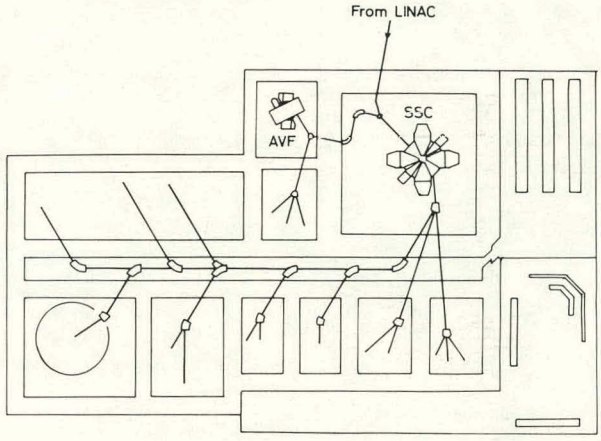


Fig.9. Proposed facility layout.

ACCELERATING STRUCTURE PARAMETERS OF THE NEW ENGLAND NUCLEAR CORP. PROTON LINAC

D. Comastra
New England Nuclear Corp.
N. Billerica, Mass. 01862

Summary

The design parameters of the New England Nuclear (NEN) 45-MeV Linac are presented. Emphasis is given to the small drift tube geometry used in conjunction with permanent magnet drift tube quadrupoles. Single cell and multi-cell rf cavity computations, as well as multiparticle dynamics results are discussed.

Linac Geometry

Preliminary design plans for a proton linac at NEN called for conventional electromagnetic quadrupoles for radial focusing at the low energy (0.75 MeV - 5 MeV) section of the accelerator. These electromagnets were to be followed by permanent magnet quads at higher energies, where gradient requirements are lower. The accelerating structure dimensions were to be similar to other facilities (BNL, CERN, LASL).[1]

In September of 1978 it became apparent that a new permanent magnet design, being developed by K. Halbach[2] of LBL and R. Holsinger[3,4] of NEN would allow the construction of magnets of sufficient strength to provide focusing for the entire linac. Since the outer diameter of magnets of this type with ∿10 Kg pole tip field is 7 cm, drift tube sizes approaching this value could conceivably be used. It was decided to investigate a geometry with a drift tube diameter of one half the conventional dimension of 18 cm. Several advantages are inherent in a design employing small permanent magnet quads. Primarily, they allow a geometry which has a shunt impedance higher than standard geometries, thereby offering the possibility of reduced power requirements. Secondly, engineering problems associated with drift tube quad power and cooling are eliminated. Also, drift tube length manufacturing tolerances are eased, since a deviation from design length has less effect on frequency than larger drift tubes.

The first step in geometry evaluation was to estimate the tank diameter required for 9 cm drift tubes and reasonable values of gap length to cell length ratios (g/L). This was done using data by Wilkins.[5] Single-cell geometries were then computer modeled using the program SUPERFISH,[6] which calculates resonant frequencies, fields, stem effects, power requirements and dynamics coefficients (T, S, etc.) for the unit cell. Gap lengths were adjusted to achieve resonance at the design value of 201.25 MHz. Given the average axial field (E_o), the synchronous phase (ϕ_s), and the dynamics coefficients from SUPERFISH, subroutine GENLIN of the program PARMILA[7] interpolates parameters of each cell in the linac and calculates exact cell dimensions, power requirements and the total number of cells. Several different geometries were evaluated in this manner.

For the linac section from injection (780 keV) to 5 MeV, a 110 cm diameter cavity was found to offer high shunt impedance, reasonably high values of the transit time factor and low drift tube surface fields. A geometry change at 5 MeV was dictated by a decreasing transit time factor (T), due to the increasing g/L values required to maintain resonance. For a design of this type which utilizes small drift tubes and larger tank diameters, g/L values have to increase more rapidly than in more familiar geometries.

At 5 MeV a cavity diameter change to 106 cm allowed g/L to be reduced to 0.216 which increased T to 0.85. This diameter is used to 22 MeV, where again low T values require a change in geometry to maintain structure efficiency.

The overall design (Fig. 1) achieves an estimated 15 - 20% savings in rf power in addition to the power savings from the use of permanent magnets.

Transition Regions

Unlike most previous linacs, where cavities of different diameter are separate, the NEN linac will have one tank of three different diameters (110, 106, and 102 cm). The changes in diameter are made rather abruptly at "transition regions" which were extensively modeled with SUPERFISH (Fig. 2). These multi-cell computations showed that the effect on the axial electric field was very small. Specifically, the diameter change at cell 28 perturbed cell 26 and cell 30 less than 1%. Average axial E-fields at cell 27 (increased) and cell 29 (decreased) were changed by ∿2.5%. When these perturbations were modeled with the dynamics program and compared with flat E-field dynamics data, no significant differences in longitudinal phase space plots were observed.

Dynamics Parameters

General Design Principles

Because the linac will be used to accelerate high average currents, basic dynamics considerations have centered around minimizing the possiblity of beam loss in the structure. A small average beam size and large transverse acceptance dictated high quadrupole gradients in a +-+- (N-1) configuration.

Also, we have attempted to match the beam longitudinally as well as transversely to minimize the emittance and beam size growth through coupling effects due to space charge forces.

Quadrupole Groups

As mentioned previously, transverse focusing will be provided by Samarium-Cobalt permanent magnets. The first of three magnet groups has the highest gradient readily achievable consistent with the drift tube geometry. Bore-size increases at 5 and 22 MeV decrease the radial space available for magnet material and therefore significantly decrease the quad gradient. To reduce the seriousness of mis-matches between sections, magnet lengths are increased (in half-inch increments) at these points. In this manner the quad focusing "strength" (effective length x gradient) is kept more nearly constant. The operating points on the

familiar stability diagram[8] (zero space charge) are shown in Fig. 3. Single particle radial and longitudinal oscillations (Fig. 4) as well as multiparticle, zero space charge, horizontal and vertical profiles (Fig. 5) were used in selecting the final quadrupole group parameters.

The central position on the stability diagram of the group I magnets suggests a high value for the transverse acceptance. PARMILA computations indicate a value of approximately 50π cm-mr for the transverse phase space (space charge forces neglected) area.

Matching

Chasman[9] and Batchelor[10] have investigated the parameters associated with matching in 6-D phase space assuming a uniformly charged ellipsoid. Using the formulation presented in that work, a computer program[11] was written to find the matched beam input parameters (average beam size and energy spread), given an initial phase spread and transverse emittance. This data was then used to estimate transverse and longitudinal beam parameters (alpha, beta, ΔW) when a more realistic beam (non-uniform charge distribution) was input into PARMILA. Emittances and beam profiles were then plotted (Fig. 6). Once we had determined the matched beam parameters in this manner with this somewhat idealized beam (ellipsoidal in longitudinal as well as radial phase space), the next step was to attempt to approximate the $\Delta\phi$-ΔW phase space ellipse with the buncher (CERN design harmonic type). Because the effective voltage required for a well matched beam is known, the dynamics program was used to find the buncher-linac distance which effectively populated a specified phase spread of 27°. With buncher voltages of 27 KV and 10.8 KV on the 200 MHz and 400 MHz bunchers, respectively, this distance was found to be 125 cm. Figures 7 and 8 show 50 mA beam profiles with a bunched beam input. Capture efficiency is calculated to be ~85%. Those particles outside the longitudinal acceptance are lost before 5 MeV and therefore should not be a significant source of induced radioactivity.

The low energy beam transport (LEBT) focusing will be provided by three quad triplets before the buncher and four quad singlets after the buncher. Program TRACE[12] has been used extensively in modeling LEBT, especially that section after the buncher which is used for transverse matching into the linac. Figure 9 shows an example of TRACE output in this beam line section.

Conclusion

Extensive computer analysis of the accelerator is nearly complete. Simulation of particle dynamics and computer modeling of the accelerating structure indicate that the small drift tube geometry and high gradient permanent magnet focusing will give NEN a linac capable of efficiently accelerating high average beam currents.

Acknowledgements

All of the above work was done in cooperation with R. Bentley, W. Jule and R. Holsinger, whose valuable contributions are gratefully acknowledged. Thanks also go to J. Stovall of LASL for his help with the dynamics program and S. Gruverman who made the numerous SUPERFISH runs necessary in geometry evaluation.

References

1. Batchelor, K., "Linac Design Considerations", LINEN/KB/3-77. Internal document.

2. Halbach, K., "Strong Rare Earth Cobalt Quadrupoles", Proc. of 1979 Particle Accelerator Conference, San Francisco, March 1979, p. 3882.

3. Holsinger, R. and Halbach, K., "A New Generation of Samarium-Cobalt Quadrupole Magnets for Particle Beam Focusing Applications", Proc. of Fourth International Workshop on Rare Earth Cobalt Permanent Magnets and their Applications, Hakone, Japan, May 1979, p. 37.

4. Holsinger, R., "The Drift Tube and Beam Line Permanent Magnets for the NEN Proton Linac", (Proc. of this conference).

5. Wilkins, J., "Design Notes on Resonators for Proton Linear Accelerators", A.E.R.E. GP/R, 1955.

6. Halbach, K., and Holsinger, R., "SUPERFISH - A Computer Program for the Evaluation of RF Cavities with Cylindrical Symmetry", Particle Accelerators, Vol. 7, 1976.

7. Swenson, D. and Stovall, J., "PARMILA" , LASL Internal Document, June 18, 1969.

8. Smith, L. and Gluckstern, R., "Focusing in Linear Ion Accelerators", Review of Scientific Instruments, Feb. 1955.

9. Chasman, R., "Numerical Calculations of the Effects of Space Charge on Six Dimensional Beam Dynamics in Proton Linear Accelerators", Proc. of 1968 Proton Linear Accelerator Conference, BNL, May 1968.

10. Batchelor, K., "Choice of Initial Operating Parameters for High Average Current Linear Accelerators", Proc. of 1976 Proton Linear Accelerator Conference, Chalk River, September 1976.

11. Jule, W., "Space Charge Matching", Internal Document.

12. Crandall, K. R., "TRACE: An Interactive Beam Transport Program", Los Alamos Scientific Lab. LA-5332, October 1973.

Parameter	Unit	Cavity Section:	1	2	3
Cavity Length	M		2.85	10.20	14.60
Cavity Diameter	M		1.10	1.06	1.02
Input Energy	MeV		0.78	4.97	21.95
Output Energy	MeV		4.97	21.95	45.34
No. of Cells			27	43	38
Cavity RF Power (Approx.)	MW		0.25	0.79	1.16
Synchronous Phase	Deg.		-30	-26	-26
Axial Transit Time Factor (T)			0.652-.745	0.850-.750	0.834-.721
Average Axial Field (E_o)	MV/M		2.30	2.30	2.30
Peak Surface Field	MV/M		11.0-9.1	13.6-12.1	14.5-14.4
Average Shunt Impedance (Z)	MV/M		78.0	88.6	86.9
Drift Tube Diameter (d)	cm		9.0	9.0	9.0
Bore Hole Diameter (HD)	cm		2.0	2.50	3.0
Upper Profile Radius (r)	cm		2.0	2.0	2.0
Lower Profile Radius (r_{hc})	cm		0.5	0.5	0.5
Stem Diameter	cm		2.86	3.18	3.18
Gap/Cell Length (g/L)			0.242-.352	0.216-.365	0.283-.376
Quadrupole Length	cm		3.81	5.08	7.62
Quadrupole Gradient	Kg/cm		8.80	6.00	3.80

Fig. 1 Geometry and Dynamics Parameters

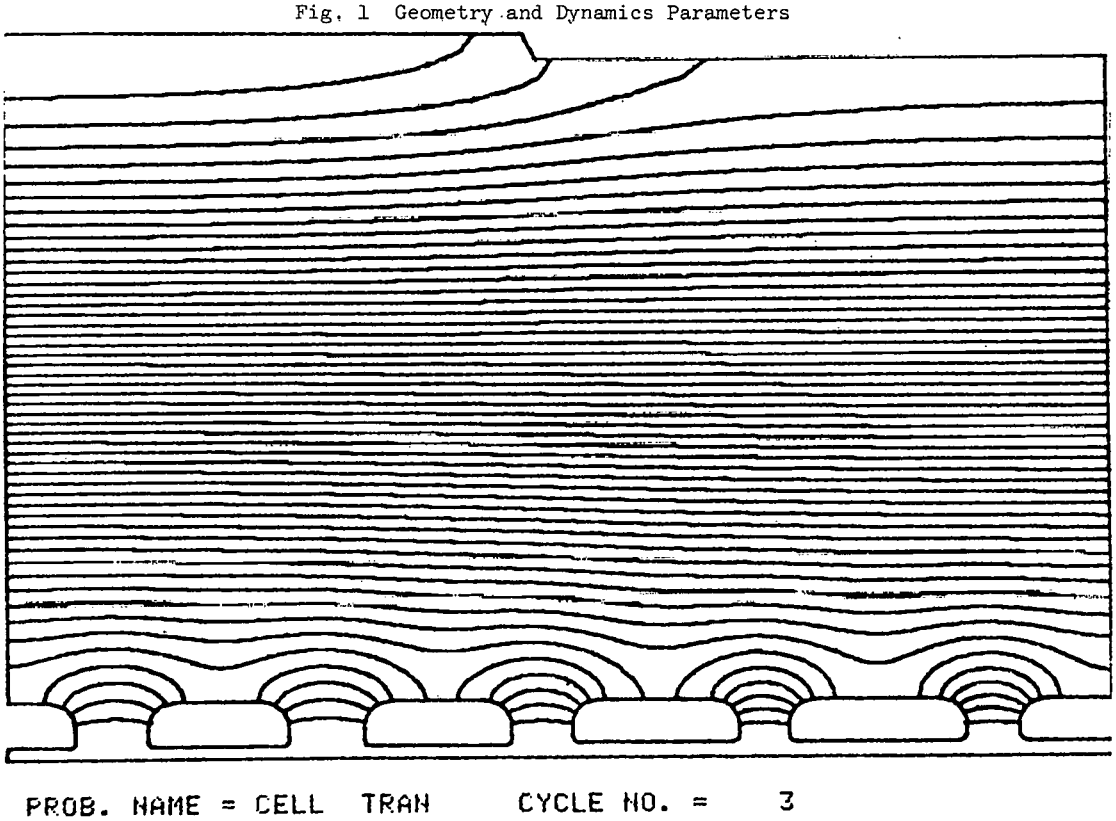
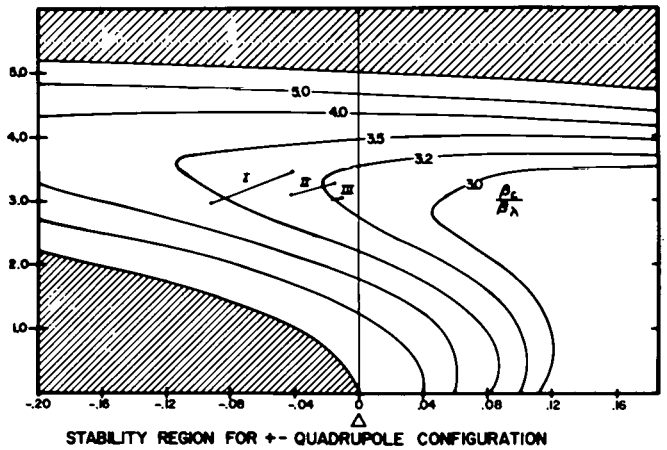


Fig. 2 Transition Region SUPERFISH Output

$$\left[\frac{\varepsilon\beta\lambda L}{B\rho}\left(6 - \frac{4L}{\beta\lambda}\right)^{1/2}\right]$$



STABILITY REGION FOR +- QUADRUPOLE CONFIGURATION

Fig. 3

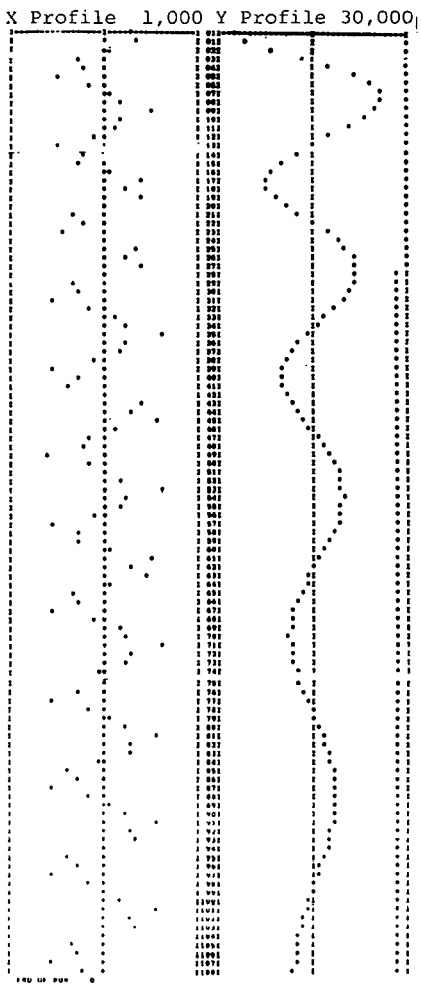


Fig. 4

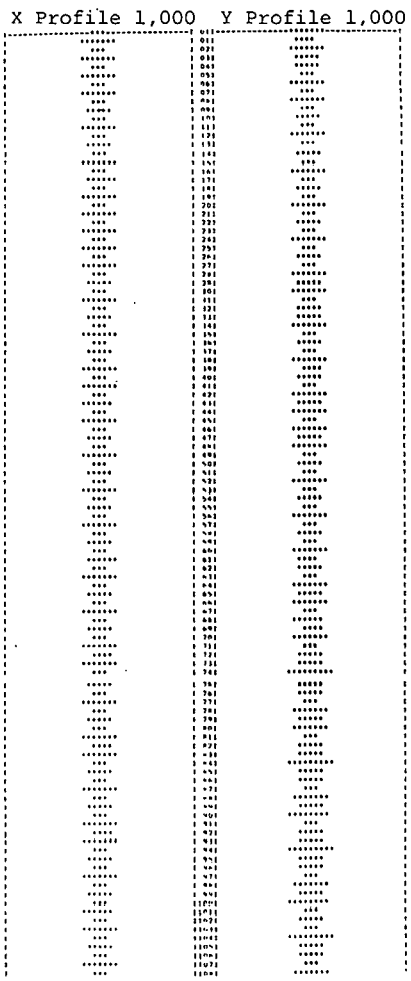


Fig. 5

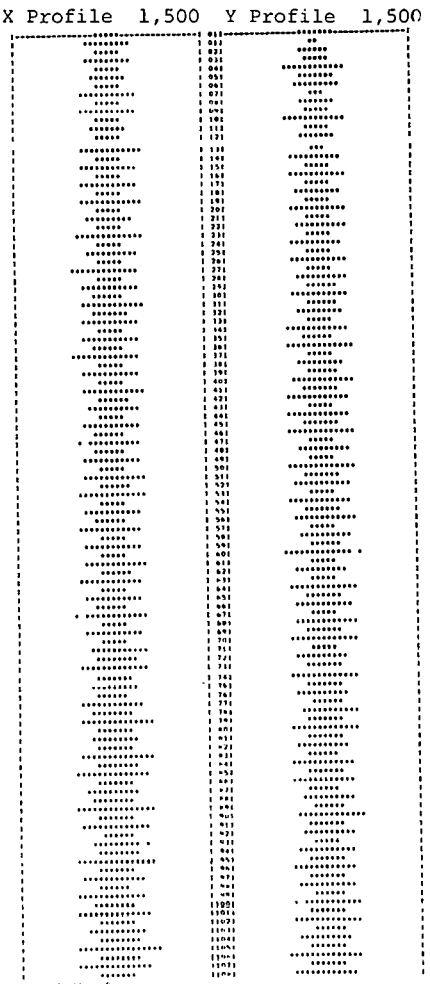


Fig. 6

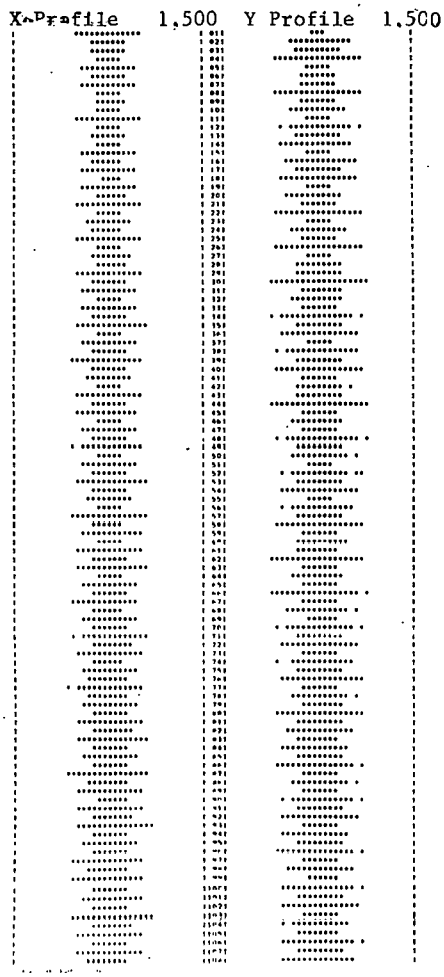


Fig. 7

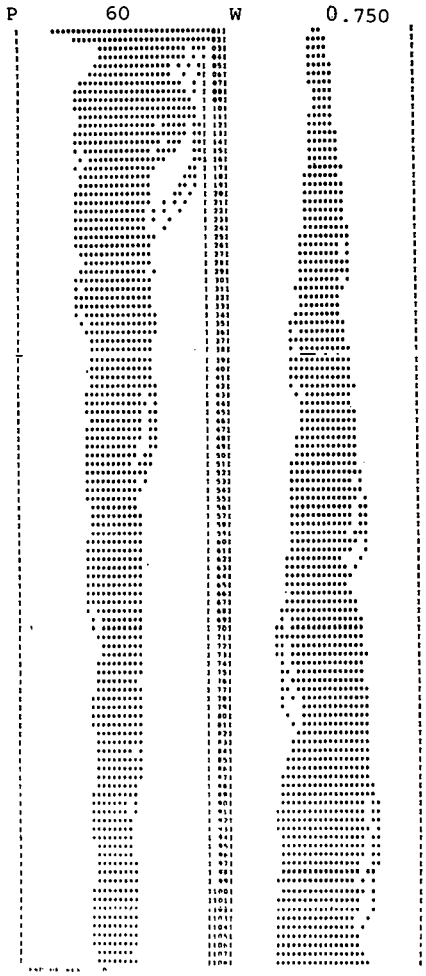


Fig. 8

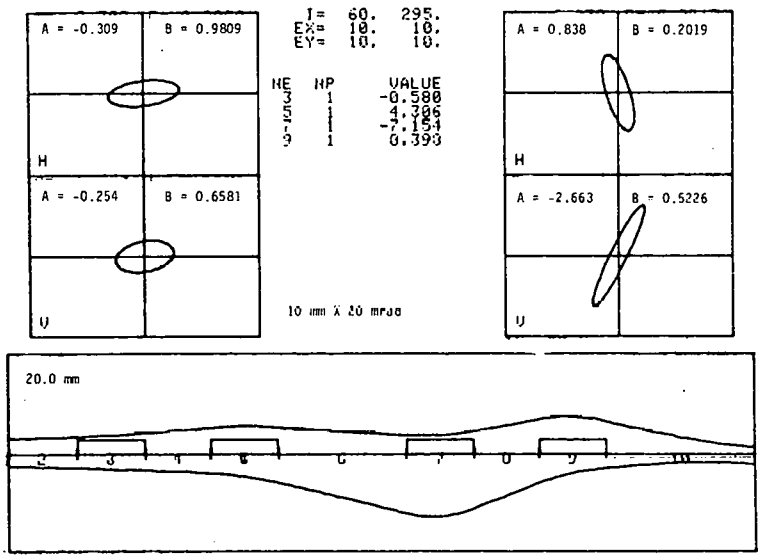


Fig. 9

LINAC EFFICIENCY and BEAM QUALITIES in p, d, $^3_2$He and $^4_2$He ACCELERATION

JP. Auclair, PA. Chamouard, JL. Lemaire,
Laboratoire National Saturne
C.E.N. Saclay, France

Summary

Results of deuteron (d) and two helium isotopes ($^3_2He^{2+}$ and $^4_2He^{2+}$) acceleration with the 20 MeV SATURNE proton linac injector, operated in the 2βλ mode are presented. Included are discussions of operation of the ion source, low energy beam transport transparency, longitudinal and transverse matching to the linac, linac efficiency, consequences for the high energy beam transport tuning and the best achievements.

Introduction

The 20-MeV Alvarez linear accelerator was designed to accelerate protons.[1] Over the years experimenters expressed interest for heavy ions such as deuterons and helium. Acceleration of these ions has been achieved with the present linac. As known, acceleration is possible for ions having a charge-to-mass ratio $\varepsilon = z/A = \frac{1}{2}$ provided they enter the linac at the right velocity and keep in synchronism with the accelerating phase. As a consequence, the linac has to be run in the 2βλ-mode.[2,3] The final kinetic energy is 5 MeV/A which is 10 MeV for deuterons, 15 MeV for $^3_2$He, 20 MeV for $^4_2$He. Good optical qualities of the accelerated ion beams were the main goal so the output current was intentionally reduced but the best performances stand respectively at 63%, 32% and 20% efficiencies for p, d, and $^3,^4_2$He.

Injector System of Saturne 2

The injector layout is shown in Fig. 1. It shall be briefly described below.

The ion source is a duoplasmatron type housed with the accelerating column inside a pressurized preaccelerator. It delivers single charge state ions accelerated up to 800 kV, during a beam pulse of 400-μs duration, at a repetition rate of 1 Hz, for normal operation.

Since the low energy beam transport has been redesigned for a better transverse matching to the linac,[4] higher beam brightness has been achieved. A single buncher at the fundamental frequency is installed for matching in the longitudinal phase space.

The design synchronous phase of the 200-MHz linear accelerator is 45° for the initial gaps, tapered to 25° for the final gaps. At the very end of the linac the mean energy of the beam is made to vary by 3% through the use of a 200-MHz ramping cavity[5] to deal with the injection method.

The high energy beam transport is an entirely new design[6] which is a strong focusing system made of triplet quadrupoles and separated achromatic sections allowing easier setup of the line. In addition to the usual beam diagnostic system a debuncher was installed which is not only sufficient for reducing energy spread but for stabilizing of the mean energy during the pulse.

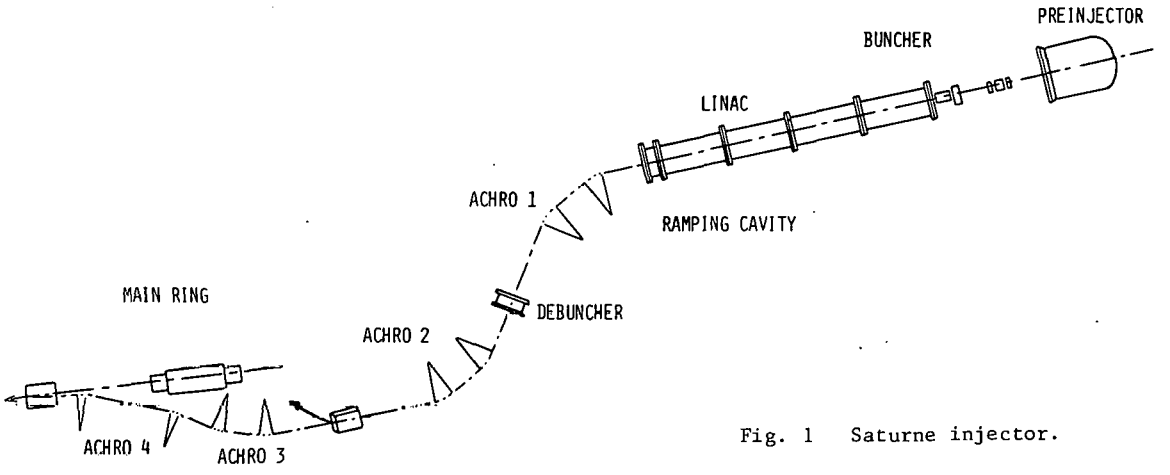


Fig. 1 Saturne injector.

Preinjector and Low Energy Beam Transport Operation

Ion Production - Intensity Limitation

The operating mode of the preaccelerator produces single charge state ions (the duoplasmatron source gives H^+, D^+, $_2^3He^+$ and $_2^4He^+$); therefore one has to use a stripper for He operation. It is made of carbon foils of 10 -µg/cm^2 thickness, mounted on a rotating frame. A set of 14 foils will allow approximately 240 hours of running. Switching between different species takes a few hours depending upon the type of ion(residual radiation,different focusing and accelerating voltages). The measured stripper efficiency for both helium isotopes is 50%.

Let W_i be the kinetic energy of an ion beam entering the linac

$$W_i = \frac{1}{2} m_o A \beta_i^2 c^2$$

β_i is the same for all heavy ions. As mentioned above,

$$\beta_i = \frac{\beta p}{h}$$ where

h is the number of rf periods needed when an ion travels from one gap of the linac to the next one (h = 2 in the $2\beta\lambda$ mode). Therefore accelerating voltages and electrostatic lenses scale as $1/\varepsilon h^2$ while magnetic fields scale as $1/\varepsilon h$. Space charge however scales as $1/\varepsilon h^3$. The preinjector and the LEBT line have been designed to deliver 100 mA of protons at 750 kV

Table 1 gives the expected values which correspond to the scaling and the operational results for protons and deuterons.

	Protons		Deuterons	
	Design	Obs.	Calc.	Obs.
Preaccelerator Voltage (kV)	1000	750	375	375
Output Current VBI (mA)	100	40	25	25

Table 1

The corresponding results for d, $_2^3He$ and $_2^4He$ are given in able 2. The accelerating voltages as far as helium isotopes are concerned are higher than the scaled values due to the energy loss through the stripper carbon foil. It is in good agreement with $\frac{dE}{dx} = 2.10^3$ MeV/g/cm^2 which is about the same for the two species.

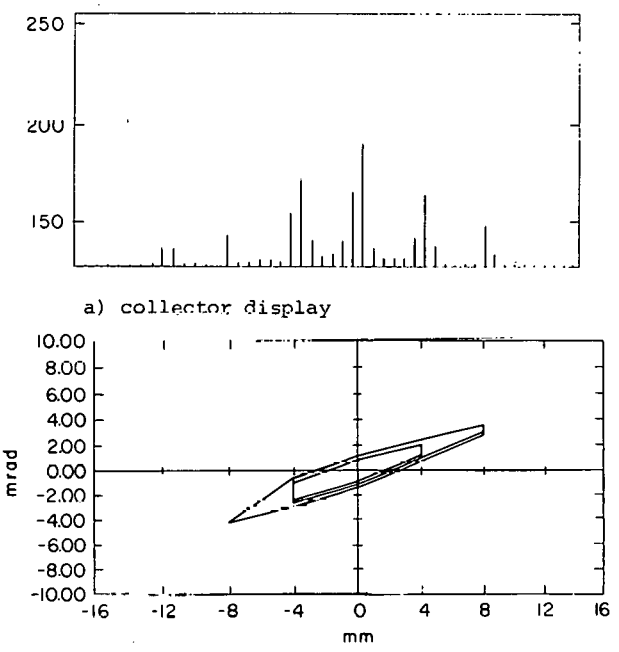
	Deuterons		$_2^3He^+$		$_2^4He^+$	
	Cal.	Obs.	Scaling	Oper.	Scaling	Opr.
Preaccel. Volt.(kV)	375	375	562.5	600	750	790
Output Cur. VBI (mA)	25	25	37.5	17	50	18

Table 2

Emittance Measurement

The beam intensity is measured with either Faraday Cup current monitors (graphite plate biased by a resistor) or current transformers. Also used are aluminum oxide flags coated with CrO_2 to observe both size and shape of the beam, the beam image being displayed on a TV monitor.

The emittance is measured in the following way : the beam is masked by a graphite plate in which cylindrical holes are horizontaly spaced, defining elementary beam pencils. The analysis of angles is made by a collector containing 48 copper strips deposited on an aluminium-oxide plate. This measurement is performed 6 times in the same pulse using an analog device[7] and the results are displayed with the aid of a microprocessor. Figure 2 shows a typical display (collector spectrum and emittance contour for different thresholds).



a) collector display

b) emittance contour for different thresholds

Fig. 2 750 keV emittance measurement

The precision of the measurements is about 20% which is rather bad for an absolute value of the emittance but good enough to control the quality of the beam coming out of the ion source and emittance growth through the linac. However it has a great advantage of being very fast and giving the shape of the emittance 6 times in any single pulse, which permits quicker investigation of ion source behavior. Experimental results are given in Table 3 for different ions.

	protons	deuterons	$^3_2He^+$	$^4_2He^+$
beam intensity (mA)	40	25	15	16
normalized emittance for 90% & 80% of the peak distribution (mm.mrad)	2.0 1.6	0.8 0.5	0.8 0.5	1.5 1.0

Table 3

Linac Operation

Theoretical Aspect

The fundamental relationship is the energy gain per cell. The following approximation was used:

$$\Delta W_h = z\, e\, \overline{E}_h\, L\, T_h \cos \phi_h$$

where $\overline{E}_h$ is the mean accelerating field, L the cell length and T_h the transit-time factor corresponding to the harmonic number h.

Along the accelerator $\Delta W_h = \frac{A}{h^2}\, \Delta W_p$, ΔW_p being the energy gain by a proton in the normal operation mode. According to this, the final energy will be

$$W_h = \frac{A}{h^2}\, W_p$$

Once the energy gain is fixed, it turns out that the following equation has to be satisfied in order to get acceleration.

$$E_h = \frac{1}{\varepsilon h^2} \frac{\overline{E}_p\, T_p \cos \phi_p}{T_h \cos \phi_h}$$

with $T_h = 1/I_o \left(\frac{h\omega a}{v}\right) \cdot \sin \left(\frac{h\pi g}{L}\right) / \left(\frac{h\pi g}{L}\right)$

Actually the calculations used the correct relation for the transit-time factor because it is a crucial parameter and errors can rapidly grow too large.

$$T_h = \frac{\int_{cell} E_z \cos (2h\pi/L) dz}{\int_{cell} E_z\, dz}$$

The most severe limitation appears to take place in the first cells where the transit-time factor is as low as 3 times that for $\beta\lambda$ operation. This leads to very high gap voltage requirements which are beyond the possibilities of the linac and sparking is most likely to occur.

Before giving the experimental results, it is worthwhile to establish the equation for the longitudinal acceptance. For the phase it is of the order of $\Delta\phi_h \sim 3\phi_h$, taking into account the former considerations about transit time factor and maximum acceptable rf field. Then the energy acceptance becomes :

$$\Delta W_h/A = \pm 2 \sqrt{\frac{\varepsilon}{h^3} \frac{m_o v^3}{\omega}\, e\, \overline{E}_h T_h\, f(\phi_h)}$$

where $f(\phi_h) = \phi_h \cos \phi_h - \sin \phi_h$

Experimental Results

The linac acceptance in energy and phase was measured first for protons using the usual flattened field in the $\beta\lambda$-mode in order to have a reference, then for deuterons and $^{3,4}_2He^{2+}$ using the maximum power available and the calculated tilted field (Fig. 3).

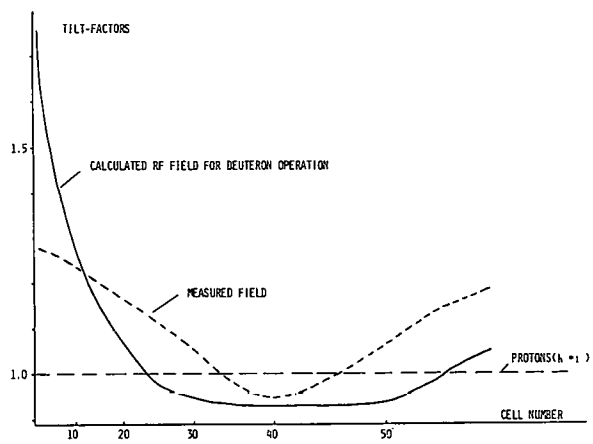


Fig. 3 Tilted rf field in $2\beta\lambda$-mode

The experiment consisted of measuring the ratio of injected and accelerated ion current of a non-bunched beam as a function of injection energy, using downstream and upstream current transformers. Different tilted fields were tried, to deal with the previous remarks and to keep the transverse stability of the beam. Consequently, the focusing quadrupole laws had to be modified, and we had to find out a compromise between the required tilt and the maximum power available for the quadrupoles. Table 4 gives the compared results.

	p	d	$^3_2He^{++}$	$^4_2He^{++}$
Input C.T. (mA)	25	15	13	17
ΔW_h (keV) measured	±90	±25	±50	±80
$\Delta\phi_h$ (°) measured	100	38	39	42
$\Delta W = \frac{K}{\Delta\phi_h}$ computed	±80	±7	±11	±15
Output C.T. (mA)	13.5	1.5	2.5	3.5
Linac efficiency	52%	30%	19%	21%
Energy spread (keV)	±125	±85	±110	±140
	±62::	±30::	†	†

Table 4

:: Measured with a pepper-pot of 10% transparency. Therefore the increasing is due to longitudinal space charge effects.

† Beam current leaving the pepper-pot was too small to measure.

Proton results are in good agreement with the expected values in normal operation but as far as heavy ions are concerned it is clear that the rather small phase acceptance ($\phi_h \sim 13°$) does not fit with the energy acceptance results. The first conclusion is in agreement with Ref. 2 but we did not observe what they pointed out about the choice of the preaccelerator voltage.::: Looking at Fig. 4 where we have drawn the stable boundary defined by the rf field and dotted line representing a possible rf field taking into account an error margin, one sees that instabilities are likely to happen for cell 1 and further downstream for cells 37 to 45. Therefore losses should occur, but unfortunately we did not pursue the theoretical computation.

::: In our case, changing the preaccelerator voltage did not increase linac efficiency for deuterons like they suggested.

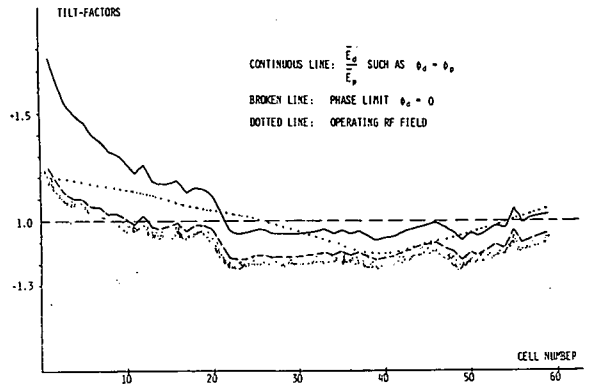


Fig. 4 Operating tilted rf field

High Energy Beam Transport Operation

Beam Optics - Beam Diagnostics

The transport line is made of 4 separated achromatic sections which can be theoretically set up independently. The elementary cell is composed of 2 bending magnets and a focusing quadrupole, the latter being movable to cope with space charge mismatching. Transverse focusing is achieved with triplet quadrupoles which bind the achromatic sections together. The last achromatic section includes an electrostatic deflector (E = 50 kV/cm) whose septum is a stainless steel foil of 0.5 mm thickness) and an additional quadrupole to perform both matching to the main ring and final achromatism. This strong focusing system is then easy to tune step-by-step and allows one to save time. Steering magnets are provided to properly center the beam through the line.[8] All magnetic elements are computer controlled and computer aided operation is essential for different particles.

The beam diagnostic elements are located all along the line. It was decided to measure beam current and position in two different ways in order to improve reliability and confidence. They are very similar to the ones described previously for the LEBT.

A 39°- bending magnet, inserted between achromatic section 2 and 3, allows momentum spread measurements with and without debuncher. This measurement has the disadvantage of being destructive. A graphite slit samples a beam of 0.5 mm width ; the resolution of the detector is 25 keV for protons.

Emittance measurements are performed at the end of the linac using a method similar to that in LEBT. The acquisition electronics are identical for all detector devices, and allow 6 measurements in the pulse duration. Both momentum spread and emittance measurements are analyzed and displayed by the central MITRA-125 computer.[9]

Momentum Spread and Emittance Experimental Results

Momentum spread is measured after a drift length of about 10 m allowing longitudinal space charge effects to occur if they are present. Usually results are taken at 80% of the peak value (Fig. 5) and are given in Table 4. There is a constant $\Delta W/A \sim 38$ keV for deuterons and helium in rather good agreement with theory which shows that linac behavior is the same for these particles.

In addition, it is clear from the measurements with the pepper-pot, that longitudinal space charge affects momentum spread even for deuterons. Unfortunately for He^{2+} ions, the net current leaving the diluter was too small. The approximate factor of 2 measurement of momentum spread increase is also in agreement with theory and can be reduced to a more acceptable value by running the debuncher (±50 keV for protons and less than ±12 keV, which is thr present resolution of the collector, for deuterons). The improvements of injected intensity and injection stability were straightforward.

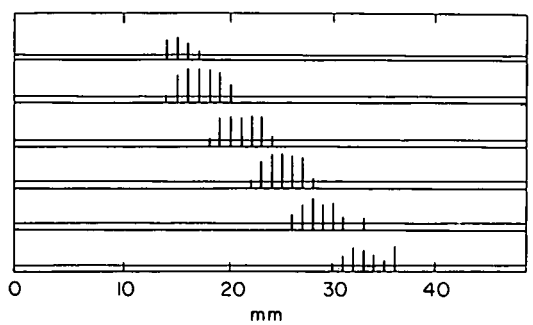


Fig. 5 Momentum spread and ramped energy display

Table 3 gave low-energy beam emittance for $^3_2He^+$ and $^4_2He^+$. Correction for multiple scattering leads to larger values for the emittance. It was evaluated using the following formula for $^3_2He^{2+}$ et $^4_2He^{2+}$.

$$\theta^{rms} = z \frac{15\ MeV}{p.v} \quad \frac{L}{L_{rad}}$$

where p is the mean momentum

L is the foil thickness

L_{rad} = 50 g/cm^2 radiation length for carbon

The corresponding results are given in Table 5 where low and high energy beam emittances are compared, while emittance values versus accelerated current are plotted in Fig. 6. The transverse emittance growth is then seen to be about a factor of 2 for protons, which is a normal result according to theory, and 3 for deuterons. For He, net emittance growth is not observed, which is certainly due to a smaller beam intensity.

		p	d	$^3_2He^{2+}$	$^4_2He^{2+}$
ε_n (LEBT)	90%	2	0.8	2.6	2.9
(mm-mrad)	80%	1.6	0.5	2.3	2.4
ε_n (HEBT)	90%	5	2.7	5	-
(mm-mrad)	80%	2.5	1.5	2.3	-

Table 5

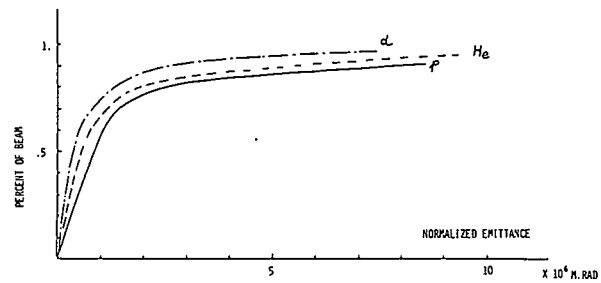


Fig. 6 Emittance versus accelerated current

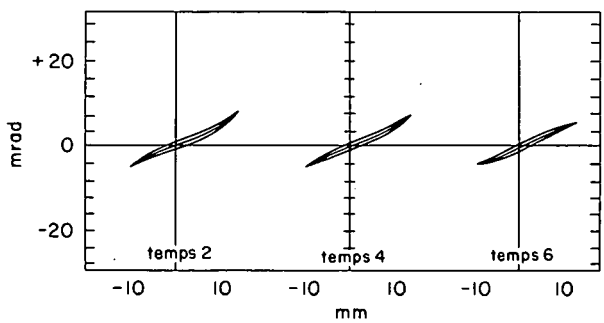


Fig. 7 HEBT emittance measurements at 3 different times in the same pulse

Conclusion

The final goal is to inject the maximum intensity of good quality beam into the main ring. Optimized proton beam led to 9.3 x 10^{12} injected particles using the debuncher. Also obtained was 2 x 10^{12} deuterons, and 1.3 x 10^{12} $^3_2He^{2+}$, without the debuncher, which was not yet running. We expect 1.6 x 10^{12} of $^4_2He^{2+}$. Making use of the debuncher, which has been recently put into operation, we should obtain a gain of 25% for these 3 species, merely by extrapolating the proton results.

References

1. JL. Lefebvre, M. Promé, "Operation report of the Saturne linac." Prof. 1970 Linac Accelerator Conference, NAL LCO-015, p.29.

2. S. Ohnuma, Th. Sluyters, "Limitations of acceleration of deuterons in Alvarez-type proton linacs." Proc. 1968 Linac Accelerator Conference, BNL 50120, p.191.

3. PA. Chamouard, JM. Lefebvre, M. Olivier, M. Prome, "Deuterons acceleration with the Saturne linac." Proc. 1972 Linac Accelerator Conference, LA-5115, p.326.

4. PA. Chamouard, M. Olivier, "Improvement in the 20-MeV beam brightness at Saturne." Proc. 1976 Linac Accelerator Conference, AECL-5677, p.372.

5. JP. Auclair, PA. Chamouard, JL. Lemaire, "200-MHz fast phase shifters and phase detection for a ramping energy." Proc. of this Conference.

6. H. Brown, J. Faure, JL. Lemaire, M. Olivier, "L'optique d'injection de Saturne II." Saclay Internal Report DSS.GERS 74-77/IE02 17/01/1974.

7. JM. Lagniel, "Rapport de stage." Saclay Internal Report DDS.985 15/06/1976.

8. D. Moro, M. Olivier, "Etude de la ligne de transport de Saturne II." Saclay Internal Report DSS.GERMA 75-50/IE 83 04/08/1975.

9. F. Mathy, "Traitement informattique des mesures par capteur à fil sur la ligne d'injection." Saclay Internal Report LNS/SD AS 11/10 DMA 05 06/08/1979.

DISCUSSION

R.W. Hamm, LASL: What are the electron beam current and energy for the results that you have given? Are these the same current and voltage for the results at the 1979 Particle Accelerator Conference?

Lemaire: Yes, 250 mA, 4 kV.

D. Bohne, GSI: The intensity figures you gave us, are they relevant for the output of the synchrotron or during the injection pulse?

Lemaire: They apply to the injection pulse.

E. Parker, ANL: What was the deuteron polarization?

Lemaire: The results have been obtained just a few days ago and I do not have the value yet.

LIMITATIONS AND IMPROVEMENTS OF HEAVY ION ACCELERATION WITH A 20-MEV PROTON LINAC

JP. Auclair, PA. Chamouard, JL. Lemaire
Laboratoire National Saturne
C.E.N. Saclay, France

Summary

CRYEBIS will be the next heavy ion source to be installed in the 20-MeV proton linac injector for the strong focusing synchrotron SATURNE II. The possibilities offered in running the linac in the $2\beta\lambda$-mode and the limitations to accelerate heavy ions characterized by $\varepsilon < 0.5$ (where $\varepsilon = z/A$) were studied. Other proposed improvements to increase the efficiency of this injector are described.

Introduction

Early in 1980 a new preinjector terminal having a heavy ion source will be put into operation. The new ion source, using cryogenic techniques and high electron-beam density is able to yield either polarized particles (protons and deuterons) or completely stripped heavy ions, up to iron. It is intended to run the 20-MeV Alvarez linac in the $2\beta\lambda$-mode, as was done for deuterium and helium,[1] but the efficiency is lower since ε is less than 0.5. Several improvements, such as increasing the linac duty factor, modifying the first cells of the existing linac, or increasing the trapping efficiency, are discussed.

The CRYEBIS Source

The ion source[2] (Fig. 1) is essentially constructed of a cryogenic solenoid and an electron gun, delivering a high-density electron beam ($j > 1000$ A/cm^2). The potential is defined by a set of cylindrical electrostatic electrodes. The potential distribution is shown in Fig. 2a during the containment time, where the ions are trapped by the radial space charge potential of the electrons, and the longitudinal potential well. They are completely stripped step-by-step. During this process the positive charge fills up the radial potential of electrons. Ions are then extracted by the potential configuration of Fig. 2b. At this time their energy is about 5 keV/A.

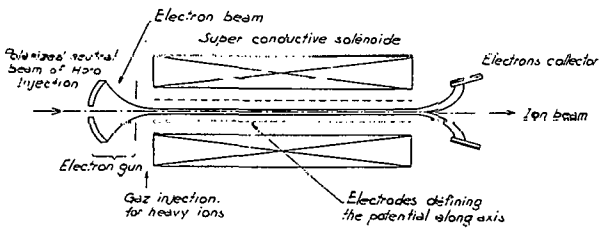
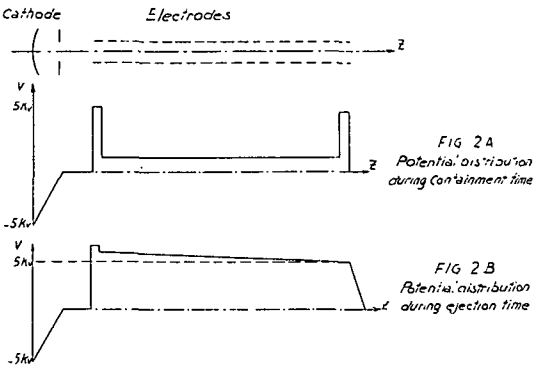


Fig. 1 CRYEBIS ion source

Ions are transported to the accelerating column through the very low-energy beam transport system (VLEBT) and accelerated to the nominal energy of 187.5 keV/A before being injected into the linac (Fig. 3)



Beam characteristics are:

Max. no. Ions:	$N_i = 10^{11}/Z$
Extraction Pulse Width:	50-300 μsec
Transverse Emittance: (normalized)	5×10^{-7} m-rad
Energy Spread:	$< \pm 50$ eV

The containment time depends upon ion species but is typically of the order of 10 ms allowing the source to operate at 10 Hz.

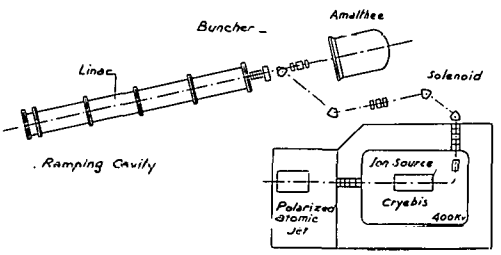


Fig. 3 New injector system

Linac Behavior for Ions with $\varepsilon < 0.5$

The linac will operate in the $2\beta\lambda$-mode, where the ion velocity is half that of protons in the normal $\beta\lambda$-mode. Thus ions travel through one unit-cell in two rf cycles, and the energy gain per gap and per nuclei is:

$$\Delta W_i/A = z\, e\, \bar{E}\, L\, T \cos \phi_i$$

where z, $\bar{E}$, L, T and ϕ_i represent the charge state, mean accelerating field, cell length, transit-time factor and synchronous phase, respectively.

The injection energy is 375 keV for deuterons having $\varepsilon = 0.5$, but for heavier ions ε may be less than 0.5 and to satisfy the velocity requirement the accelerating column must be set at a higher voltage according to the formula:

$$V_i = V_p/\varepsilon h^2 = V_d/\varepsilon \quad .$$

This is shown in Fig. 4.

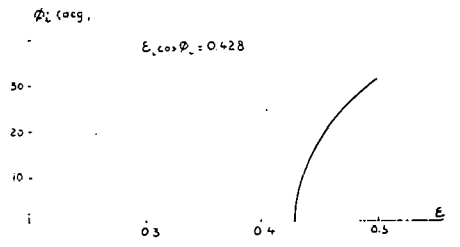


Fig. 4 Preaccelerator voltage requirements versus ε

Taking deuteron acceleration as reference, fixes the harmonic number h, accelerating field and transit-time factor, which are identical for any heavy ion. It turns out that the following relationship must be satisfied:

$$\varepsilon_i \cos \phi_i = \varepsilon_d \cos \phi_d \qquad \begin{matrix} i \rightarrow \text{any ion} \\ d \rightarrow \text{deuteron} \end{matrix}$$

This means that the phase acceptance depends upon the charge-to-mass ratio and sets a lower limit for ε_i. Thus, linac efficiencies decrease with small ε values. Specifically, with $\varepsilon_d = 0.5$ and $\phi_d = 31^o$, the experimental results give a measured energy acceptance of $\pm$ 10 keV/A. The lowest acceptable ε_i, equal to 0.428, corresponds to the smallest phase acceptance, $\phi_i = 0$, for zero longitudinal acceptance (Fig. 5).

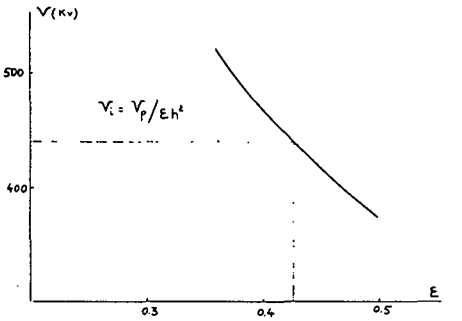


Fig. 5 Stable phase versus ε

Energy acceptances were calculated using the following formula:

$$\Delta W_i/A = \Delta W_d/A \sqrt{2c_i} \sqrt{\frac{(\phi \cos \phi - \sin \phi)_i}{(\phi \cos \phi - \sin \phi)_d}}$$

Trapping efficiences for different ε values were computed, using the existing buncher and optimizing its rf field requirement. It was found that this buncher was too far from the linac entrance and cannot completely fill the energy acceptance (Fig. 6). Table 1 gives the final efficiencies versus ε.

ε_i	ϕ_i (°)	$\Delta W_i/A$ (keV)	ρ
0.5	31	10	0.66
0.49	29	8.9	0.65
0.48	27	7.9	0.65
0.47	24	6.8	0.63
0.46	21	5.5	0.62
0.45	18	4.1	0.58
0.44	13	2.6	0.52
0.43	5	0.6	0.39
0.428	0	0	0

Table 1

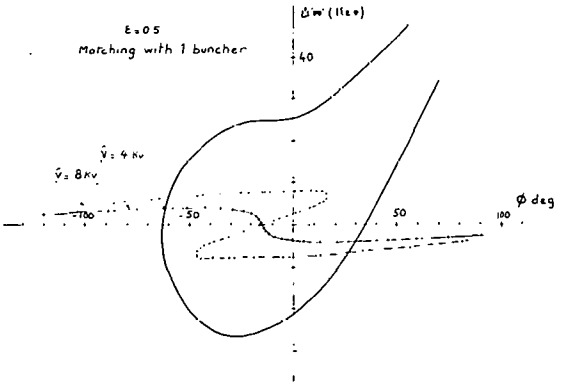


Fig. 6 Bunching schemes with the present buncher

Possible Improvements

It is clear that the linac was not designed for the purpose of accelerating heavy ions in the $2\beta\lambda$-mode. As already seen, the longitudinal acceptance is small due to the low transit-time factor in the first cells, and the buncher position is not correct for particles other than protons. It is proposed first, to put a second 200-MHz buncher operating at low rf level, which, together with the existing buncher, will provide a much better trapping efficiency; second, to install either a diaphragm inside the linac cavity to increase the longitudinal acceptance, or to operate the present linac at the higher duty cycle allowed by the 10-Hz repetition rate of the CRYEBIS source.

Trapping Efficiency

The deuteron case in which the existing buncher is used was found to lead to an underbunched beam. As shown in Fig. 6, the efficiency is only 30%. By decreasing the bore radius, one should get a better transit-time factor (0.15 instead of 0.05), but the efficiency only increases to 55%. A more flexible solution is to set up a second 200-MHz buncher located at a distance L = 4 m from the existing one and phase-locked to it. The respective voltages are optimized to give the best bunching efficiency. Figure 7 shows that such longitudinal matching leads to 80% efficiency for $\varepsilon = 0.5$. A great advantage of this system[3] is that it is easily tuned for particles having ε less than 0.5, where the efficiency decreases to 70% (Fig. 8). The solution, which would completely fill the energy acceptance, requires a buncher located much closer to the linac, and a higher rf field. The first is unfortunately not achievable due to lack of space. Figure 9 shows the bunch incompletely filling the bucket, as described above.

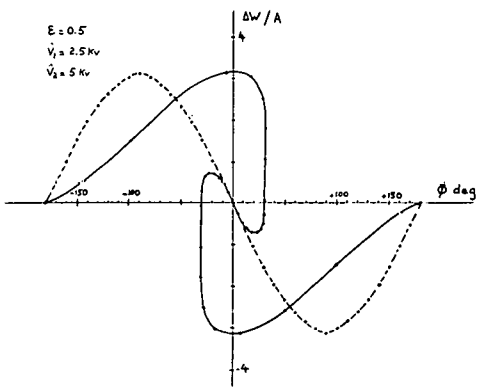


Fig. 7 Bunching scheme with two bunchers

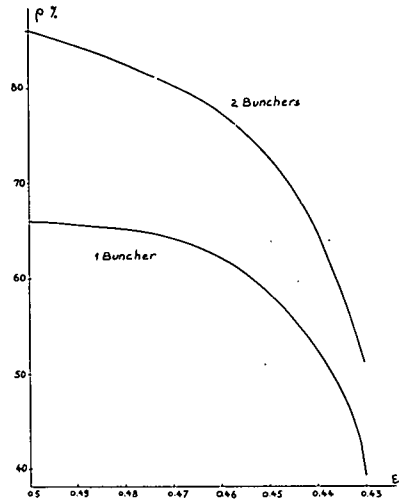


Fig. 8 Trapping efficiency versus ε

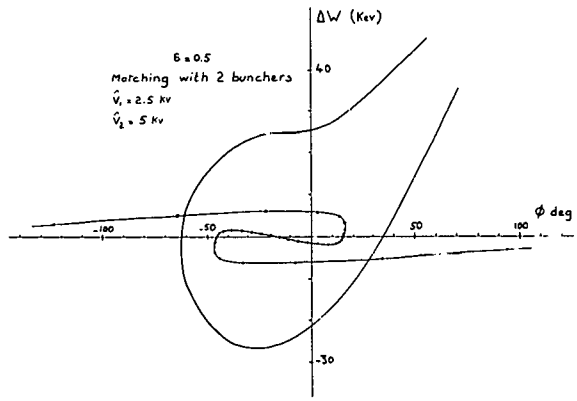


Fig. 9 Longitudinal matching with 2 bunchers

Modification of the First Cells

The solution of turning off a few accelerating gaps by installing a diaphragm in the cavity has already been investigated.[4] A serious drawback in the present case is that the preaccelerator would have to be operated at a different voltage than that for which it was designed.

An alternative is to add an accelerating cavity before entering the linac. The cavity would accelerate the ion beam to the synchronous energy corresponding to cell number 10. The most serious problem is to match the beam longitudinally between the two cavities because the drift is about 4 m and debunching will occur.

Instead of turning off the first 10 cells, it might be possible to modify them mechanically. This means that these drift tubes must be redesigned and replaced by a new optimized structure operating in either $\beta\lambda$- or $2\beta\lambda$-mode.[5] This possibility should enable the linac to accelerate ions with ε as low as 0.35.

Higher Linac Duty Cycle

A third possible means of increasing the total number of injected heavy ions to the main ring is to accumulate several linac pulses. The repetition rate of the accelerator is 1 ms. The possibility was studied of accumulating 5 pulses of 100-μs duration spaced in time by 5 ms. The improvement is a straightforward factor of 5. As mentioned previously, the CRYEBIS source is able to operate at this repetition rate.

This can be achieved without major modification of the injection system. Additional coils in the main ring magnets will provide the required $\dot{B}_i$ for stacking and usual injection process will be used for each pulse. The only hardware improvement is to increase the power of the high voltage supplies feeding the rf generator in order to maintain the same rf accelerating field on each pulse.

References

1. JP. Auclair, PA. Chamouard, JL. Lemaire, "Linac efficiency and beam qualities in p, d, $_2^3$He and $_2^4$He acceleration." Proceedings this Conference.

2. J. Arianer, A. Cabrespine, G. Deschamps, Ch. Goldstein,"Cryebis, a multi-purpose ebis for the synchrotron SATURNE II."IEEE Trans. Nucl. Sci., NS-26, No. 3, 3713 (1979).

3. JP. Auclair, JM. Lagniel, "Amélioration du groupement du faisceau d'ions lords dans le linac 20 MeV." Saclay Internal Report, LNS/SM 79/51, INJV-08 30/09/1979.

4. M. Promé, "Linac: accélération avec les premières cellules à l'arrêt." Saclay Internal Report SEFS TD 72-50 IHE 272 22/03/1972.

5. M. Olivier, "Amélioration de l'acceptance en ions lourds du linac de SATURNE II." Saclay Internal Report LNS SD IL 79-02 OEL 43 04/04/1979.

1979 LINEAR ACCELERATOR CONFERENCE

PLANS FOR H^- ACCELERATION IN THE AGS LINAC*

D.S. Barton and R.L. Witkover
Brookhaven National Laboratory
Upton, New York 11973

Introduction

Since its commissioning in 1970, the 200 MeV Linac at the Brookhaven AGS has been capable of producing peak proton beam current of greater than 100 mA with pulse lengths up to 300 μsec at a repetition rate of 10 pulses/second. The linac typically runs at 5 pulses per second, providing a 60 mA pulse of 120 μsec duration every 1.6 - 2.4 seconds for conventional multiturn injection into the AGS. The intervening pulses of length up to 300 μsec are used by the radio-isotope production, chemistry and medical facilities. Preparations are now being made to inject and accelerate H^- ions in order to implement charge exchange injection into the AGS. This paper describes the aspects of this work leading to an H^- beam at 200 MeV.

The use of an H^- beam for charge exchange injection is standard practice now at the Argonne ZGS[1] and in the Fermilab Booster.[2] In this method of injection, the H^- beam trajectory is overlapped with the proton closed orbit in the circular machine. A thin stripper foil located at the overlap point removes the electrons yielding a source of protons on the closed orbit. This irreversible process allows multiturn injection into the same phase space (with some small dilution from multiple scattering in the foil) without violation of Liouville's Theorem. The use of charge exchange injection was first suggested for the AGS in 1972,[3] in particular, as a means to higher intensities. The successful implementation of the method at the Fermilab Booster has been a principal motivation for the renewal of interest in its use at the AGS. The use of an H^- beam is expected to show advantages both for the linac operation and for the injection process. The lower beam current (20-30 mA) will give less loading of the rf cavities in the linac, which is expected to significantly increase the mean lifetime of the RCA 7835 triodes. The efficiency of charge exchange injection is very high (> 98%), in contrast to the low efficiency (20-30%) of conventional H^+ multiturn injection. Substantial reductions in radiation damage and activation of equipment are expected. Finally, improvements in injected beam quality and flexibility in the injection process are considered desirable in preparation for ISABELLE.

An H^- source assembly and its associated instrumentation is now under construction and will be installed in the existing second 750 keV terminal at the AGS linac. A second low energy transport line (LEBT2) will be built and other minor modifications will be made to permit the acceleration of the H^- beam. In the following sections, the motivation for the conversion to negative ions will be discussed in more detail and then the various development and conversion tasks will be described. Finally, a comment on the current status of the project and a summary of future plans will be given.

Motivation

The present system of H^+ injection into the AGS, which involves stacking multiple turns in transverse phase space, results in a circulating beam after injection with an emittance more than 5 times larger than the linac beam for 10^{13} protons accelerated. The use of charge exchange H^- injection will allow more flexibility in the injection process by permitting the filling from a small fraction up to the full horizontal aperture of the machine. In principle, a considerably brighter beam is possible at injection. Whether increased brightness can be preserved through capture and acceleration depends on intensity related space charge tune shifts. At intensities of 3×10^{12} required for ISABELLE injection, a brighter beam with more flexible injection control is a reasonable expectation.

The use of highly reliable carbon stripper foils like those developed at Fermilab[4] should provide better than 98% injection efficiency. In contrast, the present system of H^+ injection is limited by injection losses of 70-80%. These losses occur in the straight section between the A and B superperiods on the inflector system and during the multiturn stacking process. Figure 1 shows the output of the AGS ring radiation monitor[5] during the injection period. A major goal of the conversion to charge exchange injection is to remedy this situation. A substantial reduction in personnel radiation exposure during maintenance

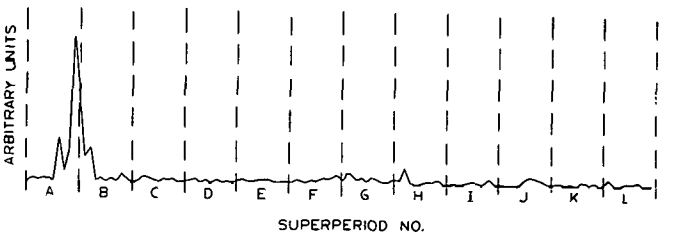


Fig. 1. Radiation monitor output during injection.

*Work done under the auspices of the U.S. Department of Energy.

and a decrease in the radiation damage to equipment in the injection area are anticipated.

While only minor adjustments to the linac rf will be required, the reduced beam loading is expected to be of significant benefit. At lower beam current it is possible to reduce the filament current of the RCA 7835 power amplifiers, which should significantly extend the tube lifetime. To obtain an estimate of this effect, tests using the H^+ beam were performed on Tank 2, a typical tank in terms of filament current. First, the filament current was adjusted to the minimum value which would sustain operation at 60 mA of beam current. Then, the current from the linac was reduced to 30 mA by adjusting the ion source and the filament current was again set at the minimum value for acceptable operation. The difference was only 2.25%, but when filament current is plotted versus emission lifetime[6] (Fig. 2), such a change is seen to correspond to a doubling of the tube life. Since lack of filament emission is the dominant mode of 7835 tube failure in the BNL linac, it is believed that the rate of tube replacement can be substantially reduced, resulting in direct cost savings and less downtime.

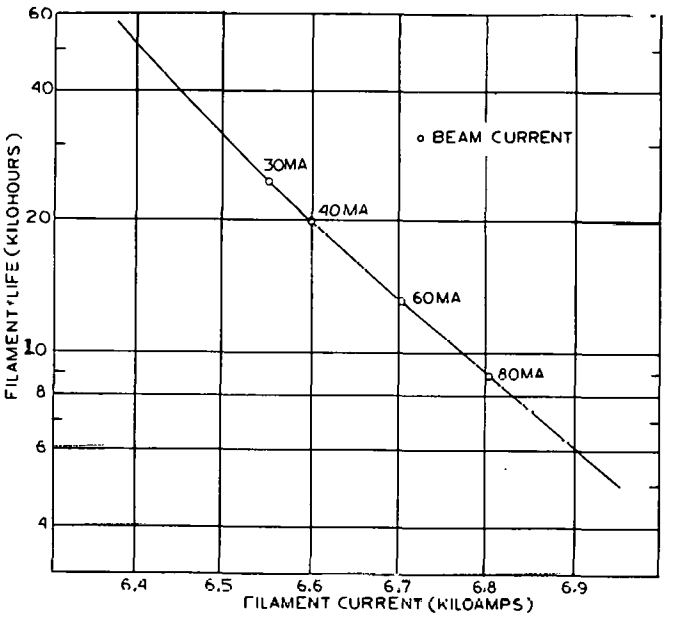


Fig. 2. RCA 7835 tube life vs filament current.

Preinjector

Extensive research and development of H^- ion sources has occurred during the last decade. Fermilab has developed and now routinely runs with a high current magnetron-type H^- source,[7] in an application essentially identical to that proposed for the AGS. The development of the Fermilab system benefited from related work at Novosibirsk,[8] Los Alamos,[9] Argonne[10] and by the Neutral Beams Group at Brookhaven.[11] Upon review of the requirements for the AGS preinjector, it was apparent that the Fermilab source design was well suited for the Brookhaven project. In addition to the advantage of commonality between the two laboratories with respect to comparisons of test and operation results, it has been possible to acquire two of several magnetron subassemblies recently fabricated at Fermilab.

The H^- source will be installed in the second preinjector pit which contains the Phillips Cockcroft-Walton generator from the original BNL 50 MeV linac. The Fermilab source design includes a 90^o bending magnet to transport the extracted H^- beam away from the source and to prevent cesium from entering the transport system. To accommodate the rather large transverse dimension of this arrangement, it has been necessary to adapt the design to the BNL high gradient column,[12] which was designed with air insulation on the outside, requiring long support cones for the electrodes. The AGS H^- source will be mounted on the rear flange of the column as shown in Fig. 3; in this arrangement the 40-50 mA beam must be transported at 18-20 keV between the bending magnet and the first electrode of the column. The Fermilab design of the 90^o combined-function bending magnet has a gradient index equal to 1.0 to focus the beam transverse to the bend plane. The BNL system includes, as shown, two pulsed quadrupole magnets which will contain the beam in the re-entrant portion of the column. The design of this system has been carried out using the program TRANSPORT, including linear space charge effects. Preliminary beam size measurements taken following the 90^o magnet at Fermilab[13] have been used to constrain the output beam conditions in a calculation using the Fermilab geometry. It has been concluded that the beam inside the bending magnet is more than 90% space-charge neutralized by positive ions during normal operation. Initial beam parameters deduced from this study have been used in the design of the BNL transport system. The gradient index of the BNL bending magnet has been increased to 1.35 to provide the proper coupling to the quadrupole characteristics. Figure 4 shows the approximate beam size assuming substantial neutralization throughout the region.

Recent work by Sherman and Allison, at Los Alamos,[14] has shown that significant aberrations occur in a similar bending magnet geometry, especially in the transverse phase plane. The authors suggest that a non-zero sextupole term can reduce these aberrations which arise because of fringe field and finite pole effects. This technique has also been used in the design of the magnets for the National Synchrotron Light Source (NSLS) at Brookhaven.[15] A sextupole coefficient chosen to minimize the Y-Y' aberrations has been included in the BNL pole tip design for the H source bend magnet.

A pulsed quadrupole doublet has been acquired from the BNL Neutral Beams Group.[16] The pole-tip diameter is 7.6 cm, with a typical maximum field of 1.5 kG. To allow the power supplies to be referenced to ground, the beam is shielded from the magnet by a quartz sleeve and inner extraction tube, as shown in Fig. 3. The extraction tube,

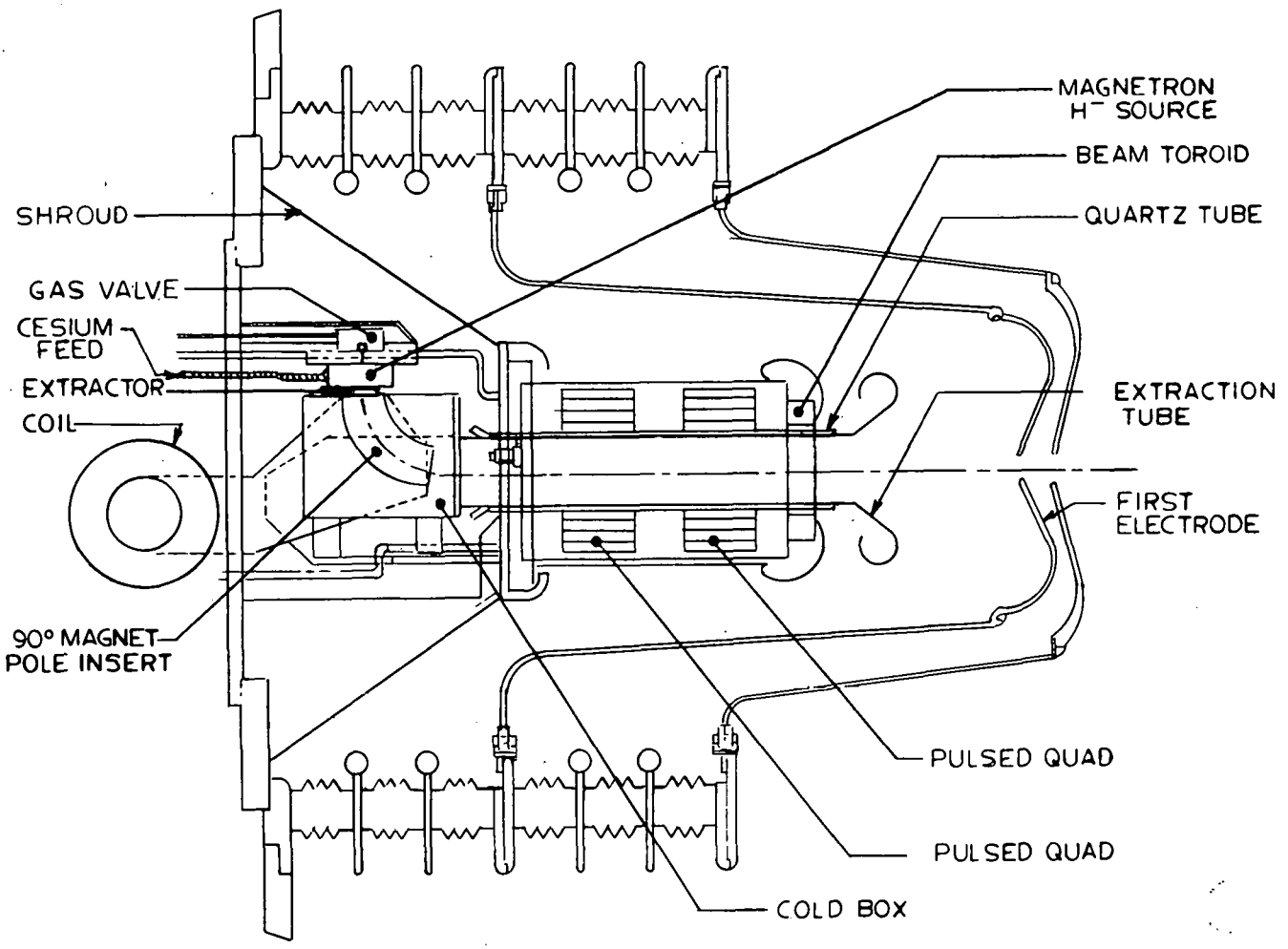


Fig. 3. Layout of H^- source in BNL high gradient column.

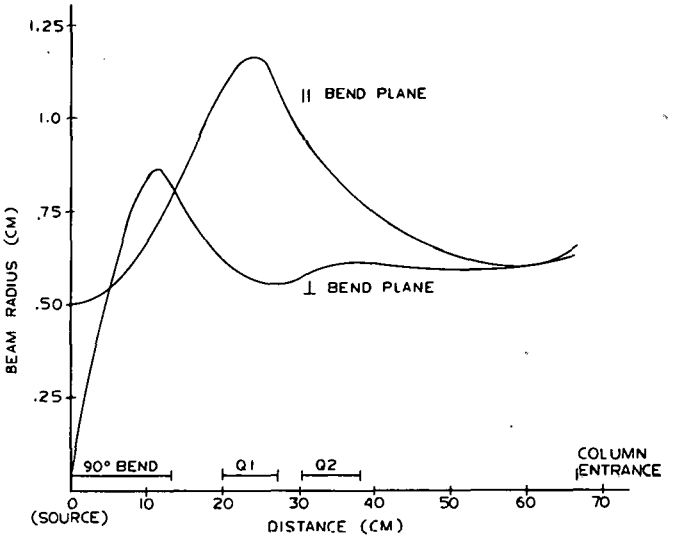


Fig. 4. 20 keV beam size profile in preinjector transport system (calculated).

along with the cold box and bend magnet pole-tips will follow the pulsed 18-20 kV extraction potential.

The Fermilab source operates with a beam pulse width of 60 μsec duration at repetition rate of 15 Hz. Since the source operation requires approximately the same duty factor, the BNL source which will run at 5 Hz needs a discharge pulse approximately 200 μsec long. The discharge pulser, with adjustable amplitude and timing characteristics, is an SCR switched pulse-forming network (PFN) of 1 Ω impedance and 300 V peak voltage. Modification of the Fermilab design has incorporated SCR's better suited to the BNL pulse width which has a maximum of 300 μsec.

A high voltage extractor electrode is used to pull the H^- ions from the magnetron plasma. Tests at Fermilab have indicated that this electrode must be pulsed to avoid breakdown below the normal 18 kV operating level. The Fermilab design has again served as a starting point for the BNL extraction pulser. In particular, a thyratron has

been added to the circuit to rapidly cut off the extraction pulse. This is triggered by the "stop" pulse and will be used in place of a chopper for fast beam turn-off. The extractor HV power supply must be remotely adjustable, as must the starting time and pulse width.

Two independently controllable pulsed power supplies are required for the quadrupole doublet. The standard linac quad pulser would have been electrically compatible with the quadrupole, but physical space requirements in the terminal made this impractical. A simple compact pulser has been built using a Darlington power transistor linearly discharging a capacitor bank of 139,200 μf. By using a feedback circuit the pulse has been kept constant to within 0.1% for more than 1 msec at 250 A. The risetime is determined by the L/R of the quad and pulser and is about 2 msec. The final unit housing two such pulsers has been built into a chassis 9 in. high which fits into a standard 19 in. relay rack. These units each have remotely adjustable amplitude and common start-trigger and pulse-width settings.

Locating the H^- source in Pit II requires a translating achromatic bend to transfer the beam into the input line to the linac. While the beam intensity is significantly lower for operation with an H^- source, it is still sufficient to cause a significant droop in dome potential during a long pulse. At the Pit II terminal a 50-mA beam experiences an 18.5-keV energy change over the course of a 200 μsec pulse. This corresponds to a momentum spread of 1.25% which would cause large beam excursions in the dispersive section of the beam line. Thus, a bouncer is required even for the relatively small extracted beam currents involved. For the recharge current required and the charging impedance available for Pit II, a bouncer of only 40-kV range will be sufficient. The extractor pulser for the H^+ duoplasmatron presently in use in Pit I can deliver the correct negative pulse with these characteristics. With this bouncer it should be possible to hold the momentum spread during the pulse to less than 0.1%.

Other required supporting subsystems include the 90° bending magnet power supply (remotely adjustable) and the -30° freon chiller for the cold box. Heaters are required for the cesium boiler, valve and transfer tube, of which only a fine adjustment of the boiler heater will be remotely controlled. In addition, there are several readbacks needed for thermocouples and vacuum gauges in the dome.

Controls

A total of 9 timing signals and 8 analog reference voltages must be sent to the dome controls from the ground station. Readback of 14 analog signals and approximately 16 digital status bits from hardware supporting the H^- source is also necessary. To handle this quantity of data it was clear that a multiplexing scheme was needed to keep the number of optical links reasonable.

Following the lead of Shea and Goodwin,[17] a control and communication system based upon a microprocessor has been developed. The hardware was chosen to be compatible with that of the National Synchrotron Light Source now under construction at BNL to make use of much of their system software.[18] This has allowed programs to be assembled on the AGS PDP-10 and directly downloaded into random access memory (RAM).

The system configuration is shown in Fig. 5. The processor is an 8080 packaged as an Intel/National 80/204 single board computer, utilizing the Multibus configuration and protocols. This board contains a UART (Universal Asynchronous Receiver/Transmitter) and 4 kilobytes of RAM. The Intel monitor, modified to permit communication through the 8080 to the PDP-10 and downloading of assembled programs, resides in 3K of the 4K Programmable Read Only Memory (PROM) on the board. The UART on this board is connected to a CRT terminal, in the case of the ground station, which serves as the normal operator interface. In the dome unit an optional terminal can be connected to this interface for local control.

An Intel/National 116 board is used to provide additional memory and the auxiliary UART. This UART may be connected to the PDP-10 for direct downloading of data or programs, or to the optical link for communication across the high voltage interface. This board is presently populated with only 4K of a possible 16K of RAM needed to store the control and display programs and data.

Analog reference voltages for control of the programmable power supplies are provided from commercial digital-to-analog (DAC) cards which are compatible with the Multibus. An 8-channel, 12-bit unit made by Data Translation Corporation is presently being used. Two such cards are required for the ground station.

The readback of analog data is also by means of a commercial multibus compatible card manufactured by Burr Brown Research Corporation. This unit handles 32 channels of 12-bit data as memory mapped I/O. Sample and hold circuits precede the inputs where needed.

A special card utilizing Intel 8253 counter/timer chips is being designed to provide the necessary triggers and pulses for both the dome and ground station hardware. Synchronization between the two stations will be provided by a separate optical link, which can also be used to reset the dome microprocessor.

Commercial receivers and transmitters are used for the optical links. These have been in service for some years on the existing ion source and will be continued for the H^- source. The units are connected via a 25-m quartz-fiber optic cable. This length allows the ground station units to be located outside the pit, providing greater safety against arcdown damage. The

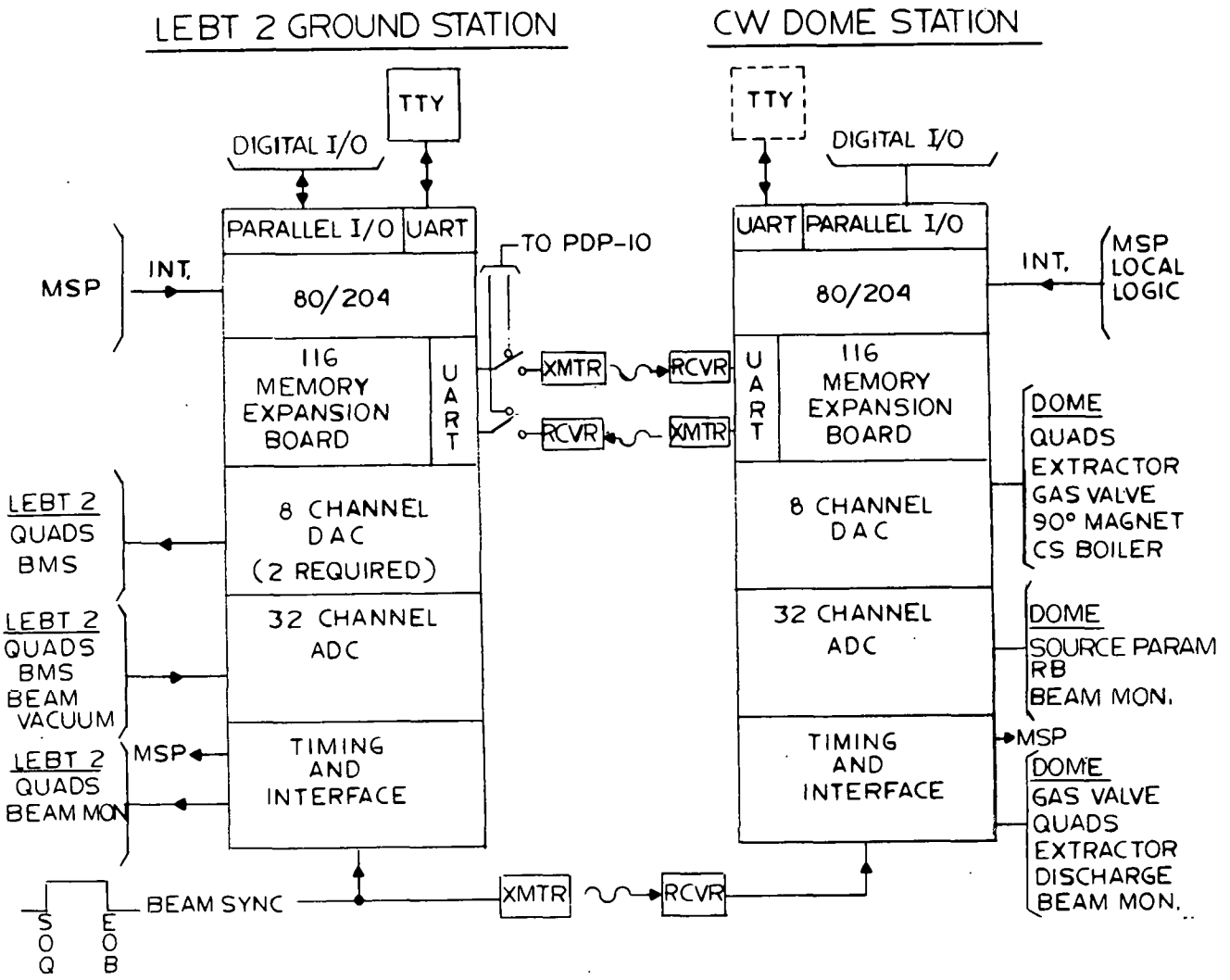


Fig. 5. Block diagram of H^- preinjector control system.

data communication between the UART's will be as 7-bit ASCII code at a rate of 19.2 kilobaud. This should allow a complete refresh of data within the 200 msec inter-pulse period; however, this is not required. Data exchange between the two microprocessors will be as a character-by-character handshake of reference data from the ground station and readbacks from the dome station.

As can be seen, the two stations are similar in configuration with the ground station having a greater number of DAC cards to control the LEBT2 quadrupoles. The software will, however, be different. It will be possible to load the ground station programs into the dome when local control is required from that location.

The ground station software presents a multipage format to the operator. Input is by keyboard cursor control and numeric keys. The operator can make as many entries as desired before transmitting the input data as a group to the controlled elements.

Readback data is averaged over 8 beam pulses for display purposes. This is done local to the data-taking processor, with the display being updated upon data transmittal.

In addition to the computer-controlled hardware, local hard-wired logic will be utilized where system protection is required. This will typically be used during turn-on or turn-off sequences or when out-of-tolerance conditions indicate a danger to the hardware.

During the development and testing stages, this control system will be operated locally at the ground station. When actual acceleration in the linac begins, the ground station microprocessor will be interfaced to the PDP-10 so that it may be controlled from the AGS Control Room as a part of the accelerator system.

Low Energy Transport and Linac

After acceleration to 750 keV the H^- beam

must be transported into conjunction with the present Low Energy Beam Transport (LEBT) line before input to the linac. Floor pads for a second beam line were provided as part of the original building design. This line crosses from Pit II at 60° to intercept the beam line from Pit I just before the dual bunchers. A design study has been made, using the version of TRANSPORT which includes linearized space charge forces, for net un-neutralized beam currents up to 50 mA with a 60% filling factor. Immediately following the high gradient column are two pulsed quadrupole triplets of the BNL LEBT design.[19] These magnets will be used to match the beam from the column to the existing LEBT1 line. The 10 m section between the two 60° dc bending magnets is designed to be achromatic. Small air-cooled dc quadrupoles will be used in this section.

A destructive emittance measuring device is located just after the intersection of LEBT2 with LEBT1 to facilitate the matching. In this procedure the horizontal emittance of the H^- beam is made similar in orientation to the vertical emittance of the present H^+ beam so that polarity reversal of all quadrupoles downstream of the intersection is not necessary. It is expected, however, that some fine-tuning of the linac quadrupoles may be needed since the present tune was designed for a beam current of 100 mA. Readjustment of filament currents will be made on the rf amplifiers to optimize tube performance at the lower beam current. In addition to the standard beam transformers and emittance monitors, LEBT2 instrumentation must include means of measuring the beam profile or position because of the dispersive nature of the beam line. The choice of monitor for this purpose has not been made. Existing instrumentation in the linac will be upgraded and interfaced to the computer system where this has not yet been done. The beam transformers and low energy emittance monitors are already capable of bipolar operation, but the SEM profile monitors and the 200 MeV emittance devices will require modification in this respect.

Looking Ahead

The fabrication of the source assembly and instrumentation necessary to begin bench tests, including emittance measurements, is nearly complete. In early October, 1979, studies of source operation characteristics over as wide a range of parameters as possible will begin. Full computer-controlled emittance measurements will be made at the output of the subsystem consisting of source and 90° bending magnet in order to accurately determine the extent and importance of the space charge neutralization of the beam. The influence of variation of the gas flow and cesium supply will be made with both Fermilab and BNL bending-magnet pole-tip designs so that direct comparisons with the results of the TRANSPORT design study can be made. These tests should be invaluable, since the quadrupole doublet system can only be meaningfully tested in the full preinjector.

The full instrumentation of Pit II is expected to be completed by the beginning of 1980, so that complete preinjector tests can be carried out during the first quarter of the year. Much of the work on the LEBT2 construction will parallel that effort, with completion expected by early spring. No substantial impediment is then anticipated to achieving a 200 MeV H^- beam shortly thereafter.

Acknowledgments

The invaluable advice and assistance of C. Curtis and C. Schmidt of Fermilab is gratefully acknowledged. The encouragement of Y.Y. Lee and the support by J. Curtiss, N. Fewell, E. Grove, E. Jablonski, V. LoDestro and E. Rodger in the design and development are greatly appreciated. The authors also wish to thank K. Prelec, Th. Sluyters and P. Allison for helpful discussions.

References

1. E. Crosbie, et al., IEEE Trans. Nucl. Sci., NS-22, 1056 (1975).
2. C. Hojvat, et al., IEEE Trans. Nucl. Sci., NS-26, 3149 (1979).
3. A. Maschke, K. Prelec, Th. Sluyters, "Proposal for H^- Injection into the AGS", Nov. 10, 1972, unpublished.
4. C. Hojvat, M. Joy, R.C. Webber, IEEE Trans. Nucl. Sci., NS-26, 4009 (1979).
5. R.L. Witkover, IEEE Trans. Nucl. Sci., NS-26, 3133 (1979).
6. J.D. Stabley, Power Devices Application Engr., Solid State Div., RCA, Lancaster, PA, private communication.
7. C.W. Schmidt, C.D. Curtis, IEEE Trans. Nucl. Sci., NS-26, 4120 (1979).
8. Yu. I. Belchenko, G.I. Dimov, V.G. Dudnikov, Proc. 2nd Symp. on Ion Sources and Formation of Ion Beams, Berkeley, CA, VIII-1, LBL-3399 (1974).
9. P. Allison, IEEE Trans. Nucl. Sci., NS-24, 1594 (1977).
10. J.A. Fasolo, G.J. Marmer, J.S. Moenich, IEEE Trans. Nucl. Sci., NS-18, 94 (1971).
11. K. Prelec and Th. Sluyters, IEEE Trans. Nucl. Sci., NS-22, 1662 (1975).
12. Th. Sluyters, et al. Particle Accelerators, I, 15 (1970).
13. C. Schmidt, private communication.
14. J.D. Sherman and P.W. Allison, IEEE Trans. Nucl. Sci., NS-26, 3916 (1979).
15. J. Galayda, private communication.
16. R. Clipperton, K. Prelec, L. Sinsabaugh, "A Small Pulsed Quadrupole", AGS Div. H^- Tech. Note No. 3, BNL, Sept. 25, 1974.
17. R.W. Goodwin, R.F. Kocanda, M.F. Shea, Proc. 1976 Linear Accel. Conf., Chalk River Nuclear Lab., Ontario, Canada, AECL 6577 (1964) 264.
18. K. Batchelor, et al., IEEE Trans. Nucl. Sci., NS-26, 3387 (1979).
19. R. Damm, A. Otis, V. LoGrasso, Proc. 1970 Linear Accel. Conf., National Accel. Lab., Batavia, IL, 561 (1970).

RF LINAC-PUMPED LASERS*

W. E. Stein, T. R. Loree, C. A. Brau, and S. D. Rockwood
Los Alamos Scientific Laboratory
Los Alamos, New Mexico 87545

Summary

Excitation of gas lasers by a small emittance beam of electrons from an rf linear accelerator has been proposed.[1] Potential advantages of pumping with a linac rather than a fast transverse discharge include higher average power, higher repetition rate and significantly improved reliability. In addition, electron beam pumping should provide improved efficiency and a lower capital cost when compared with discharge pumped lasers.

An experiment to test this concept is in progress at the Los Alamos Scientific Laboratory (LASL). A 4-MeV side-coupled, standing-wave linear accelerator is being used to provide a pulsed electron current of 2 A with a 1-μs duration. The electron beam, focused to a 5-mm dia spot, is confined in the high-pressure gas (≤10 atm) by a superconducting solenoid with a central magnetic field of 3 T (30 kG).

Experimental studies include: fluorescence of various rare-gas halide mixtures as a function of pressure; transport of the electron beam through the gas; and the optimum configuration of the electron beam, magnetic field and the laser cavity.

Introduction

Electron beams have been used in recent years to pump high-pressure rare-gas halide lasers. Although axial pumping has been used,[2] in most cases these lasers are pumped by an electron beam directed transversely to the laser axis.[3] In the latter arrangement, electrons are produced in vacuum from a cold cathode and accelerated by a pulsed potential of the order of 0.2 to 2 MV, which is formed by a Marx or L-C generator. The electrons enter the high-pressure gas through a thin metallic foil that is usually supported by a mesh or a plate containing closely spaced holes. Usual electron beam characteristics are: current density of 5 to 500 A/cm^2 over the cathode area, total current of 5 to 50 kA and a pulse duration of about 50 ns to 1 μs. Typically only a small fraction (a few percent) of the electron beam energy is deposited in the gas; the remainder of the energy is absorbed either in the walls of the laser or more importantly in the foil and support. The difficulty in cooling the large area foil and support is the principal limitation of this arrangement in attaining high average power. Reliability at high repetition rates is also seriously hampered by the capability of available spark-gap switches.

Axially pumping by a smaller diameter electron beam confined to the laser axis by a solenoidal magnetic field alleviates the limitation caused by foil and structure heating. However, axial beams produced by Marx or L-C generators generally have a kinetic energy that is too low to effectively pump the high-pressure gas, and they are still limited in reliability and repetition rate by spark gap capability.

Linac-Pumped Laser

To avoid the above limitations, we proposed to pump these excimer lasers axially with an electron-beam from a microwave linear electron accelerator. Pumping with a linac electron beam has these potential advantages over conventional methods: higher average power, higher repetition rate and improved reliability. In addition, this arrangement should provide a laser with improved efficiency and lower capital cost when compared with conventional electron beam or discharge lasers. A schematic indicating the expected efficiencies and repetition rate of such a laser is shown in Fig. 1.

Table I gives the projected ultimate performance for transverse discharge lasers compared with the desired performance of the linac pumped lasers.

Table II shows the near-term expected performance for laboratory models. In each case the linac-pumped lasers are expected to be considerably more reliable.

TABLE I
PROJECTED KrF LASER PERFORMANCE

	Transverse Discharge	Linac Electron Beam	
Average Power (kW)	16	10	100
Pulse Repetition Frequency (Hz)	4	10	100
Energy/Pulse (J)	4	1	1
Efficiency (%)	1.5	2	2
Capital Cost ($/watt)	150	250	100

TABLE II
NEAR-TERM KrF LABORATORY PERFORMANCE

	Transverse Discharge	Linac Electron Beam
Average Power (W)	40	60
Pulse Repetition Frequency (Hz)	200	300
Energy/Pulse (J)	0.2	0.2

*Work performed under the auspices of the U. S. Department of Energy.

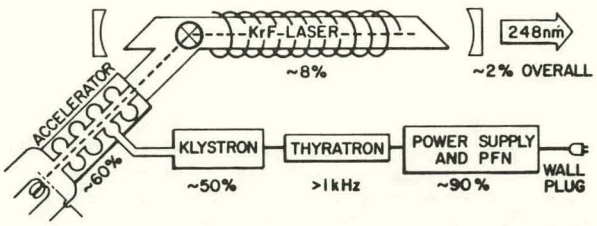


Fig. 1. Schematic of microwave-pumped laser.

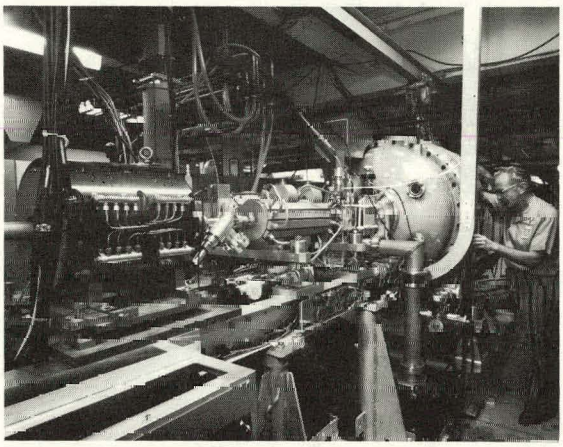


Fig. 2. The LASL 4-MeV electron linac.

Experiment

An experiment to test this excimer laser concept is in progress at LASL. An electron beam from a small microwave linear accelerator is being used to axially excite a high-pressure (≤10 atm) rare-gas halide mixture in a high-pressure cell. The accelerator, which is a side-coupled, standing-wave type, can deliver a pulsed 4-MeV electron beam with 2-A peak current for 1-μs duration at a 50-Hz repetition rate. Modifications are in progress to increase the pulse repetition rate to 300 Hz. The injector tank, prebuncher, accelerator and quadrupole steering and focusing magnet (from right to left) are shown in Fig. 2.

The electron beam, which is focused to a 5-mm dia. spot, emerges from the end of the beam pipe into the air through a 0.1-mm thick stainless steel foil. The beam then traverses about 3 mm of air and enters the high-pressure gas cell through a similar foil.

A superconducting solenoid with a central magnetic field of 3 T (30 kG) confines the beam to a region close to the axis of the gas cell. Otherwise, nuclear scattering of the electrons in the foils and gas would cause the beam to diverge and spread rapidly.

For laser application, the electron beam must be injected off axis and at a small angle with respect to the solenoid and laser axis. This is necessary to avoid the upstream optical mirror that forms part of the laser oscillator. Particle trajectory calculations, ignoring foil and gas scattering, have been performed to find a geometry in which the beam is injected into the laser cavity around the edge of a 25-mm dia. mirror that is coaxial with the magnet axis and forms one end of the optical cavity. The calculated trajectory for a promising case is shown in Figs. 3-7. In this case, the electron beam was injected 8 mm above the magnet centerline and at an angle of 12 mrad (0.7 deg). The foils and mirror are at -0.34 m with respect to the magnet center. This case has been tested experimentally. The results for an electron beam with finite size, divergence and scattering are in reasonable qualitative agreement with the calculated trajectories.

The fluorescent output of a number of xenon fluoride and krypton fluoride gas mixtures was studied prior to attempting laser action. A schematic of the apparatus is shown in Fig. 8. The electron beam entered from the left, passing through a pair of foils in the gas cell. The electrons were confined to a 1-cm dia. cylinder on the cell axis by the magnetic field of 3.0 T. The current out of the accelerator was 2 A, giving current densities in the gas of the same order. The light out of the cell was turned by a mirror to allow adequate radiation shielding of the fast photodiode, and was optically filtered to allow only the lasing wavelength (248 nm for KrF, 350 nm for XeF) to be detected. Checks for background contributions gave null results in all sensible permutations of conditions.

The resulting data are shown in Fig. 9. The fluorescence output (on an arbitrary scale) is derived from the peak voltage of the photodiode signal divided by the measured beam current for each pulse, with appropriate corrections for filter transmissions and wavelength response of the photodiode. The curves represent the best output obtained for each family of gas mixtures. As the light output was not strongly affected by small variations in the mix, the specific proportions (see caption) are not believed to be critical.

It is desirable to use a high-pressure gas, because this will increase the beam energy deposited in the laser. This criterion makes the neon diluent superior in every regard (save for the cost) for both xenon fluoride and krypton fluoride. The choice between these excimers for the best lasing candidate is not as clear, because the lasing depends on many factors. The narrower linewidth of xenon fluoride may make it competitive in spite of the greater light output of krypton.

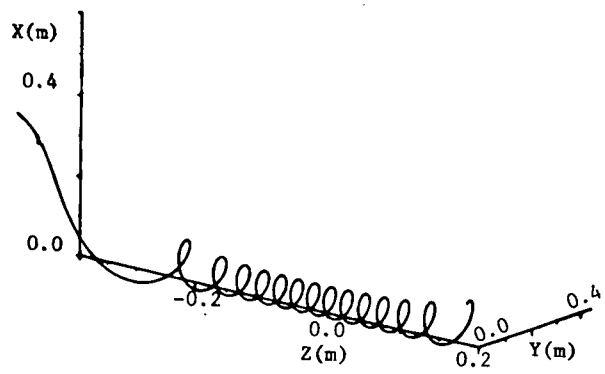


Fig. 3. Isometric view of calculated electron beam injection into superconducting magnet. Distances in meters. The magnet axis is colinear with the z-axis, and the magnet extends from -0.165 to +0.165 m .

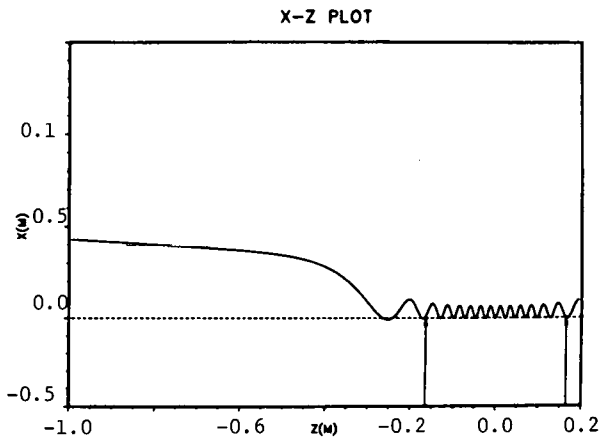


Fig. 4. The X-Z calculated electron trajectory.

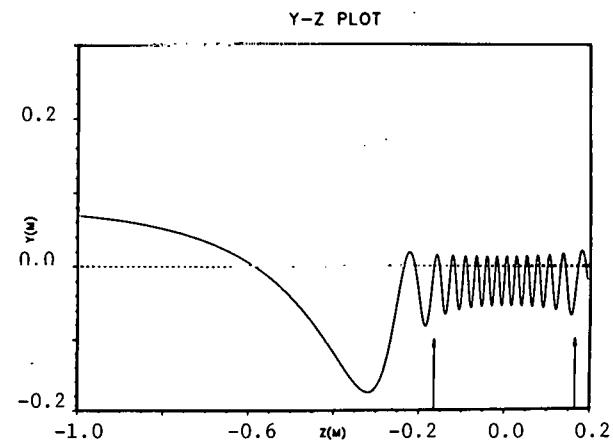


Fig. 5. The Y-Z calculated electron trajectory.

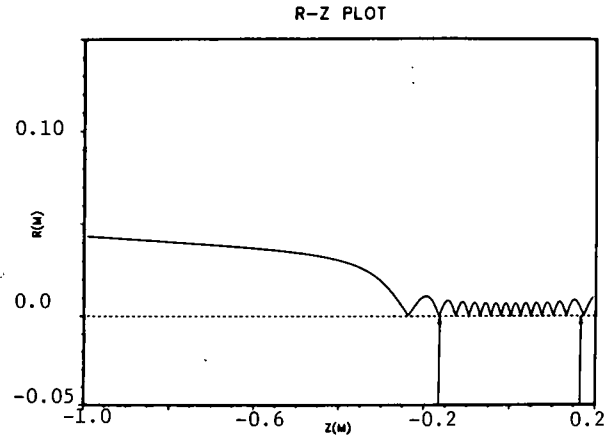


Fig. 6. The R-Z calculated electron trajectory.

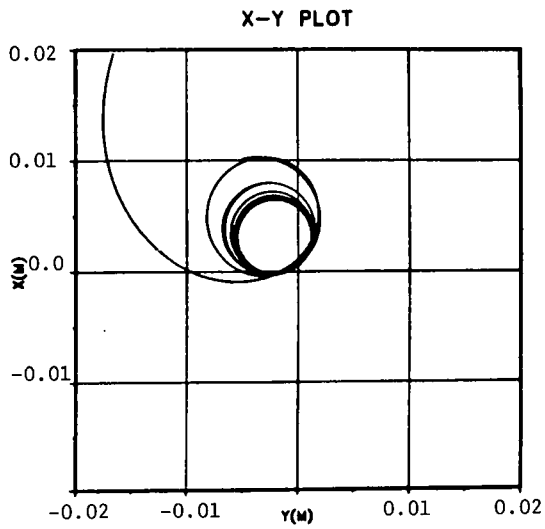


Fig. 7. The X-Y end view of calculated electron trajectory.

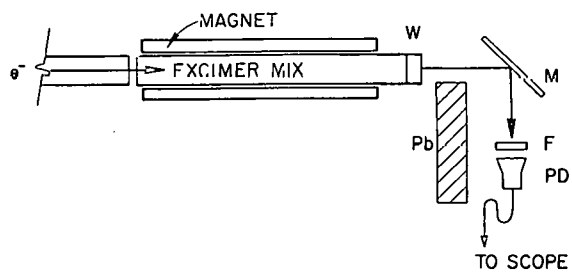


Fig. 8. Schematic of the apparatus used for fluorescence measurements. The electron beam enters the high-pressure excimer mix cell from the left, and photons exit the cell through a quartz window, W. The light is turned by mirror, M, filtered of all but the lasing wavelength by filter F, which falls on the fast photodiode PD. The photodiode is shielded from radiation by lead bricks, Pb.

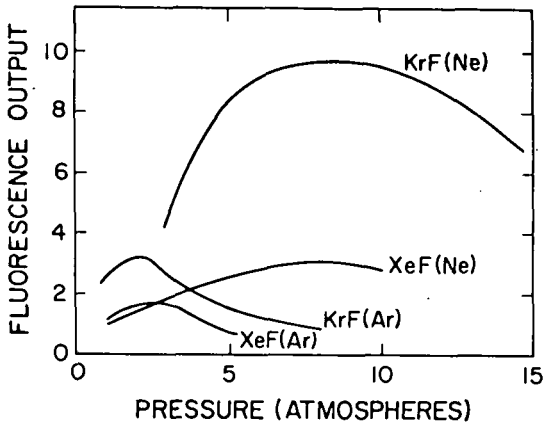


Fig. 9. Summary of fluorescence data. Gas compositions were:
KrF(Ne); 0.01% F_2/0.20% Kr/bal.Ne
XeF(Ne): 0.04% NF_3/0.12% Xe/bal.Ne
KrF(Ar); 0.04% F_2/1.0% Kr/bal.Ar
XeF(Ar); 0.2% NF_3/1.0% Xe/bal.Ar

References

1. C. A. Brau, T. R. Loree, S. D. Rockwood and W. E. Stein, "Linac Lasers," 8th Winter Colloquium on Quantum Electronics, Snowbird, Utah and 1978 IEEE International Conference, Monterey, CA.
2. J. M. Hoffman, A. K. Hays and G. C. Tisone, "High-Power UV Noble-Gas-Halide Lasers," Applied Physics Letters, Vol. 28, No. 9, 1 May 1976.
3. J. J. Ewing and C. A. Brau, "Laser Action on the $^2\Sigma^+1/2 \rightarrow {}^2\Sigma^+1/2$ Bands of KrF and XeCl," Applied Physics Letters, Vol. 27, No. 6, 15 September 1975.

dup

1979 LINEAR ACCELERATOR CONFERENCE

LASL ELECTRON LINAC WORKSHOP*

W. E. Stein
Los Alamos Scientific Laboratory
Los Alamos, New Mexico 87545

Summary

An electron linac design workshop was held at the Los Alamos Scientific Laboratory (LASL) on July 12 and 13, 1979. The primary purpose of this workshop was to address the problems of attaining high single-pulse electron currents (>200 A) and concurrently maintaining good energy dispersion (≤1%) and minimal beam emittance. Present and future applications of intense single micropulses include detector-response measurements, chemical photolysis and high-energy physics experiments. For the free electron laser application, a train of many ($\sim 10^4$) intense micropulses is required.

The workshop began with a brief review of existing accelerators capable of producing high current in a single micropulse. Next, future requirements and plans were discussed briefly. Most of the workshop covered presentations and discussions on electron injectors, space charge, energy compression and single-bunch beam loading.

Introduction

In the recent past electron accelerators have been developed that are capable of delivering an intense single micropulse with about 30-ps duration. These pulses with peak currents of about 100 A have been used in measurements of the time response of detectors of nuclear radiation and in chemical photolysis studies. Recently, new applications of intense single-electron bunches have developed. A single-pulse capability on the Stanford Linear Accelerator Center (SLAC) linac is desired for high-energy nuclear physics experiments and a long train of intense micropulses separated by a few rf cycles is required in the development of a high-power free electron laser at LASL.

An electron linac design workshop was held at LASL to study the possibility of improving the performance of present accelerators and to determine the ultimate performance to be expected from future machines. The workshop was organized as a small, informal meeting with the time divided nearly equally between presentation and discussion of the various pertinent subjects. The participants, who are actively working in this area, were: N. Norris and L. Detch, EG&G, Santa Barbara; G. Mavrogenes, Argonne National Laboratory (ANL); R. Miller and R. Koontz, SLAC; G. Saxon, Daresbury; S. Penner, National Bureau of Standards (NBS); W. Gallagher, Boller & Gallagher; J. Haimson, Haimson Research; T. Smith, High-Energy Physics Laboratory (HEPL). From LASL: R. Cooper, T. Boyd, K. Crandall, R. Hamm, E. Knapp, S. Schriber, and D. Swenson.

An abbreviated agenda indicating the topics covered is: Existing High-Current Linacs, Future High-Current Linacs, Electron Injector, Space Charge, Single-Bunch Beam Loading, Energy Compression.

A reasonably detailed report of this meeting is in preparation. At this time, I will cover what I consider to be the highlights of this workshop.

Present Performance and Future Requirements

Experimenters have recently requested shorter, more intense single micropulses for the detector response and chemical photolysis studies. Single bunches of 5×10^{10} electrons per pulse (8 nC/p) are contemplated for future high-energy physics experiments at SLAC.

A comparison between present linac performance and desired future capability for the free-electron laser application is given in Table I.

Clearly the emphasis in a new design will be on emittance and the number of micropulses while maintaining existing peak current and energy spread.

Single-Bunch Beam Loading

Beam loading in an accelerator by a single micropulse was a topic of much discussion. Electrons traversing an accelerator gap radiate rf power into the fundamental mode and a number of higher spatial modes. Even though the fields induced by this radiated power decay rapidly (a few ps), the electrons in the latter part of the micropulse experience a lower acceleration. Thus the earlier electrons have a higher energy than the latter electrons in the same bunch. A less accurate, but more transparent, approach to single-pulse loading is to consider the stored energy available to the electrons in the micropulse. Earlier electrons extract some of the stored energy from the cavities and the energy cannot be replaced in time for use by the latter electrons. This gives rise to a decreasing electron energy during the micropulse. Roger Miller described experimental work done previously at SLAC and the theoretical modal analysis by E. Keil.[1] Experimentally, the average decrease in energy for a micropulse containing 5×10^8 electrons in SLAC was about 50 MeV. Calculations by P. Wilson[2] using the modal analysis are in fair agreement with the

*Work performed under the auspices of the U. S. Department of Energy.

TABLE I

LINAC PERFORMANCE AND REQUIREMENTS

	ARGONNE LINAC PERFORMANCE	FREE ELECTRON LASER REQUIREMENTS
Electron Energy (MeV)	20	20 to 100
Electron Energy Spread (%)	~1	±1
Peak Current (A)	100 to 400	25 to 250
Charge per pulse (nC)	3 to 12	1 to 10
Micropulse Length (ps)	30	>10
Emittance (mrad-mm)	to be measured	3π to 0.2π
Intense μ-pulses	single	Train, 10 to 50 μs long or cw

experiment. For the proposed charge per micropulse of 5×10^{10} electrons at SLAC the energy spread from this effect is expected to be about 7 GeV.

Compensation for this energy spread in the lower energy accelerators (ANL and EG&G linacs) is accomplished by proper phasing of the second accelerating section with respect to the first. For proper phase closure the electron pulse is injected into the second section ahead of the peak of the rf field. Thus the earlier, higher-energy electrons in the pulse experience a smaller electric field than the latter, lower-energy electrons. The excellent energy spectrum (<1%) for a 12-nC pulse from the ANL linac demonstrates the viability of phase closure. Without proper phasing of the second accelerator section a 5% energy spread would have been expected for a 12 nC per pulse. It was noted that an adequate phase spread is required to accomplish this energy compression.

Space Charge

Both longitudinal and transverse effects of space charge were presented by S. Penner. In the latter case, the equations of motion in the transverse direction were described. These equations included the electric and magnetic forces between the particles in the beam as well as external focusing forces.

A transverse beam instability caused by nonlinear space charge forces was predicted. The considerations were based on previous work on the stability of intense beams by L. J. Laslett and Lloyd Smith[3] and numerical simulations of I. Haber.[4] Estimates of the maximum electron current that can be transported without emittance growth was given as

$$I\ (\text{Ampere}) \leq 5.2\beta\gamma\epsilon_n B_z,$$

where B_z is the axial magnetic field in kilogauss and ϵ_n is the normalized emittance in units of milliradian-centimeters. Based on this prediction, the injector for the Argonne linac (25 A at 135 keV) is at the maximum limit when the beam is bunched to about 70 degrees. At higher injection energy, larger currents would be allowed.

The subject of injecting at higher electron energies was presented by J. Haimson. The advantages of these techniques were stressed and the excellent performance of accelerators using high-energy injection was described.

I wish to thank the participants for a very interesting and lively workshop.

References

1. E. Keil, "Diffraction Radiation of Charged Rings Moving in a Corrugated Cylindrical Pipe," Nuclear Instruments and Methods, 100, 419-427 (1972).
2. P. B. Wilson, J. B. Styles, K. L. F. Bane, "Comparison of Measured and Computed Loss to Parasitic Modes in Cylindrical Cavities with Beam Ports," IEEE Trans. Nucl. Sci., NS-24, No. 3, 1496 (1975).
3. L. J. Laslett and Lloyd Smith, "Stability of Intense Transported Beams," ibid., p. 3080.
4. I. Haber, "Space Charge Limited Transport and Bunching of Non K-V Beams," ibid., p. 3090.

Section II
Operating Machines

THIS PAGE

WAS INTENTIONALLY

LEFT BLANK

HIGH-CURRENT HEAVY-ION LINACS AS IGNITERS FOR COMMERCIAL-SCALE INERTIAL-FUSION POWER PLANTS*

David L. Judd
Lawrence Berkeley Laboratory, University of California
Berkeley, California, 94720

Introduction

For over a quarter century, the hope of producing commercial electric power by magnetically confined fusion has stimulated research and development projects at an increasing scale, in this country and abroad. The size and complexity of the required reactor vessel and its equipment appear to have been increasing, as we have gained knowledge about the problems, while the goal has retreated, still seeming to be a quarter century away. There is no proof that the program will converge, but even granted convergence there remains the concern that operation and maintenance of such complicated systems may be uneconomic or impractical.

Over a decade ago it was proposed, as a part of the Plowshare Program ("beat your swords into plowshares"), that large-scale power could be produced by reducing the problem to one previously solved: the detonation of fusion bombs. Such explosions could be contained in large cavities dug deep in the earth, and their heat energy transported to the surface; a few tens of megatons (high explosive equivalent) per year could produce a thousand megawatts of electric power. This plan has a good chance of being feasible but today might displease reviewers of its environmental impact statement.

A more acceptable form of this concept was then put forward; "miniaturize it!" One ton per second, or a tenth of a ton, ten times a second, would provide heat for the same 1000 MWe plant, and such explosions could be contained in man-made "boilers" on the earth's surface. The science and technology of larger thermonuclear explosions are well understood and provide a basis for calculations of ignition requirements for such small "pellet" targets, whose inertia contains the fuel during its burn.

For several years the inertial fusion program was based on development of high power pulsed laser systems and was known as laser fusion. The search for a "brand-x laser" continues, but since 1976 some small effort has been spent on the study of high-energy heavy-ion beams as igniters. In three successive annual workshops, about a hundred experts in accelerators and related fields have examined the technical feasibility of accelerator systems to provide the needed energy, power, and density of energy deposition; the results have been encouraging. The topic is appropriate to this conference because, although initially it appeared that synchrotrons might serve best as the main drivers, it now seems that the two most promising types of accelerators for this purpose are linacs. This presentation will: (1) state the fusion pellet target requirements and the demands they place on heavy-ion linac igniter systems; (2) indicate why high-energy heavy-ion beams are suitable, and why linacs appear capable of meeting the requirements; (3) outline some of the characteristics of conceptual linac system designs now under study; and (4) describe some of the problems that are not yet solved. Pellets, reactor vessels, other components of a future power plant, or economic issues will not be discussed. The most complete and convenient sources of technical information on the "heavy-ion fusion" accelerator system studies are the reports of the workshops[1-3] mentioned above. A good general account, together with an interesting economic analysis, has been prepared by Herrmannsfeldt.[4]

* Work supported by the U.S. Department of Energy.

Pellet Target Requirements

Since 1976, the accelerator designers have been working with target parameters in the following ranges:

Energy supplied: 1-10 megajoule
Peak power: 100-600 terawatt (1 TW = 10^{12} watt)
Duration of peak-power pulse: (τ) 6-10 nanosec
Pulse shape: About 40% of the energy in a rising precursor of duration about 5 τ
Specific energy deposition: 20-30 megajoule/gram of heavy stopping material
Irradiated spots: number $\geq$ 2, each of radium $\geq$ 1 mm.

From the beginning attention has been focused on power plants (nominal 1000 MWe) rather than on "scientific break-even" or other demonstration experiments. The requirements have been taken as:

Reactor vessel radius: 5-10 m
Repetition rate: 1-10 Hz
Efficiency (mains to beam): >10%
Reliability: 80%
Lifetime: 20-30 years

The cost of 1000 MW fossil-fuel or fission power plant today is about one billion dollars, which might serve as a plausible order-of-magnitude of allowable cost.

Why High-Energy Heavy Ions?

For a relatively small number of irradiated spots, the requirements above lead to a particle range within an order of magnitude of 1 g/cm^2. From the range-energy relations, it is found that

for light ions (e.g., protons) the ion energy required is of order 10 MeV and the current of the order of 10 million amperes. Similar energies and currents are needed for electrons, which however have ill-defined range. Acceleration and reliable repetitive transport of millions of amperes over many meters to millimeter spots is far beyond present technological capability. In contrast, for heavy ions ($A \sim 200$) in a low charge state (q) the energy and current are about 10 GeV and 10 thousand amperes. The space charge repulsion in a kiloampere beam of such ions does not spoil the spot size.

The capabilities of an existing mature and versatile accelerator technology that are relevant to this new task, include experience with circulating beams having kinetic energies in the megajoule range; with long complex systems (the appropriate length unit is the kilometer); with small beam spots at ten-meter distances; with relevant repetition rates; with reliable systems having long working life; and with a variety of heavy-ion sources and accelerators. In addition, the world's accelerator builders have succeeded in constructing their machines within their budgets and schedules and in making them work.

At first sight the requirement for "current multiplication" from the 50 milliamperes one might expect from an ion source to 5 kiloamperes at the target might seem a formidable obstacle. However, many mechanisms for multiplication are available. These include acceleration at constant bunch length, multi-turn injection and single-turn extraction from accumulator (storage) rings, longitudinal bunch compression, large-aperture sources, and "funnel-loading" of rf linacs. From these, several multiplicative factors of 10 to 100 each are available.

Present Conceptual Designs

Work on such accelerator systems has proceeded, at low levels, primarily at the Argonne and Brookhaven National Laboratories and the Lawrence Berkeley Laboratory. There has been neither time, money, nor manpower to develop detailed designs. Initially, considerable effort went into the study of synchrotrons as the main drivers; because the structure is traversed so many times by each ion, there appeared to be a cost advantage over any single-pass linac structure. However, during the study the trend in final ion kinetic energy was downward and the synchrotron injection energy needed to accomodate space charge went upward, leaving a smaller energy range for synchrotron acceleration. Further, the long residence time of an ion in the system will lead to loss, even in a perfect vacuum, by ion-ion charge-state-changing interactions between beam ions. Therefore attention has been focused on rf linacs and induction linacs during the past year.

RF Linac Systems

These systems start with a multiplicity of ion sources feeding short, low-frequency, low-energy linacs in parallel, whose output beams are combined by pairs, having bunches in tandem filling alternate "buckets" of half as many second-stage linacs at twice the rf frequency. Following acceleration, the merging by pairs is repeated into linacs with redoubled rf frequency, continuing until finally all the bunches enter a single main linac in which most of the kinetic energy is gained. Use of such a "linac tree" is called funnel loading. For illustration Table I shows a few numbers for conceptual designs presented by Young et al.[5] and Maschke.[6] In these designs the ion charge state is raised by stripping at an appropriate low energy; the electric current in the desired charge state does not change importantly.

Table I

Young et al., Case 23 ($A = 200$, $q_{in} = 1$, $T_{inj} = 1.8$ MeV)

Stage	1	2	3	4	5
Current/linac (mA)	25	50	100	200	400
Freq (MHz)	5	10	20	40	80
T_{out} (MeV)	14	115	930	7000	20,000
q	1	3	3	3	3
Number of linacs	16	8	4	2	1

Manschke ($A = 238$, $q_{in} = 1$, $T_{inj} = 0.5$ MeV)

Stage	1	2	3	4	5	6
Current/linac (mA)	20	40	80	160	160	160
Freq (MHz)	2	4	8	48	96	192
T_{out} (MeV)	6	13	30	120	480	20,000
q	1	1→2	2	2	2	2
No. of linacs	8	4	2	1	1	1

After reaching full energy the linac beam is debunched and successively fills a number of storage rings by multi-turn injection. Various schemes, sometimes employing intermediate rings, are used to allow filling both transverse phase spaces in the final rings. After filling, the beam in each is collected into a single bunch (or perhaps two), starting gently but then suddenly forced by very high voltage on the rf system to start an implosive longitudinal (azimuthal) compression, during which many normally unstable resonances are crossed too quickly to lose beam. (A demonstration of this process has been conducted in the ACS at Brookhaven.) The imploding bunches from all the rings are extracted at once and carried to the reactor vessel by transport lines which also contain pulse-gap elements like those in an induction linac, but with steeply ramped pulses that produce even more powerful longitudinal bunch implosion. Just outside the reactor wall, each line ends in a final focusing quadrupole lens system, which converges the beam bunch to a small spot on the target, just at the distance at which the implosion is being checked by longitudinal space charge and kinetic pressure of the ions.

Linear accelerator designers may have interest in many features of such systems, including: (1) the need to match longitudinal phase space ellipse axis ratios at frequency jumps, to avoid phase

space dilutions; (2) consideration of the possible utilization of the newer low-velocity linac structures, as compared to the Wideröe, as elements of the "tree"; (3) the need to identify engineering and cost factors leading to optimum structures and parameters in the main rf linac; (4) the problems of beam loading, because it is desired to put a very large fraction of the rf power into the beam; and (5) the need to debunch the rf beam to dc with minimal phase space dilution.

Induction Linac Systems

This type of accelerator is less well known to workers at high energy laboratories, because thus far it has been used only for electrons up to 30 MeV. However, it is very well suited to direct acceleration of currents of many thousands of amperes in very short pulses of from a few microseconds down toward the nanosecond range, providing an obviously good match to the pellet target requirements. It consists of a linear array of singly-pulsed nonresonant structures having annular gaps across which the accelerating fields appear. The pulsing sequence is synchronized so that a field is present at a gap only when the beam bunch is passing through,such that the particles experience a sequence of essentially dc fields. The technology is relatively simple and is well understood. The energy for each module is stored in capacitors and switched by triggered spark gaps. The desired pulse duration corresponds to the time needed to saturate the magnetic material with which a module is loaded; this may be iron for pulses of 0.2 to 2 microsec and ferrite, or ferritic glass, down to about 10 nanosec, below which no loading is needed and a radial line geometry is suitable. An important property is that the efficiency of energy transfer to the beam may be very high. Practical experience covers currents to 5000 A, gap voltages to 500 kV, and path-averaged fields up to $\sim$ 1 MV/m. A machine with 550 modules has been operated at 360 Hz for several years with high quality pulse reproducibility.

Such an accelerator has the unique potential of providing a single-pass straight-through system from injector to target without need of storage rings. This simplicity is very attractive, avoiding loss and dilution in multi-turn injection, extraction, and the other beam manipulations. Because the ion residence time is so short, vacuum requirements are nominal and charge-changing interaction loss is negligible.

In adapting the induction linac to nonrelativistic ions, a new advantage appears; the pulses may be slightly ramped so as to decrease the field seen by ions at the bunch front relative to those at the rear, thereby gradually compressing the bunch during acceleration. Therefore, determining the bunch length as a function of distance along the linac becomes a part of the design problem which greatly complicates the task of finding an economic optimum. At one extreme, a very short bunch has higher current which requires a stronger quadrupole focusing for transverse containment, leaving a smaller fraction of the space for accelerating elements and resulting in a longer system. The basic parameter of an induction linac is volts-seconds per module (or per meter), in contrast with volts per gap (or per meter) in an rf linac; thus,at the other extreme,a very long bunch will experience lower fields, resulting again in a longer system. Cost factors and electrical and mechanical design features enter significantly into determination of optimum variations of several parameters along the linac. In addition, new questions regarding longitudinal dynamics, particularly space charge and other effects near bunch ends, must be studied. Longitudinal emittance requirements indicate that perhaps only a fraction of one longitudinal "phase oscillation" should take place during acceleration.

The accelerating modules become undesirably bulky for pulse durations more than a few microseconds, so the injected current must be several tens of amperes and a novel injector is required. Large-aperture surface-ionization sources, followed by a few long non-resonant pulsed drift tubes, are being built and tested and other options are being considered to meet this need. After acceleration to full energy the beam passes through a steeply-ramped pulse-gap buncher section (like that mentioned above for beams from the rings of a rf linac system) to provide the final implosive longitudinal compression, which continues to the target. The beam is then expanded transversely to bring the energy per unit area below the spallation limit on septum edges, and passes through beam-splitting elements which divide it transversely into a number of beamlets, each led to its own final focusing-lens system at the reactor vessel.

In this country, induction linacs for electrons have been built and used at both the Lawrence Berkeley and Lawrence Livermore Laboratories and at the National Bureau of Standards. The work on heavy-ion induction linacs for inertial fusion is being done at Berkeley. For illustration, some parameters of one of the preliminary (i.e., not fully optimized) conceptual designs developed by Keefe et al. for a 160 TW system using A = 238, and presented at the 1978 workshop[7] are shown in Table II.

The mean accelerating field in the main part is of order 1 MV/m and its length is of order 5 km. The design of such a system is dominated by the maximum allowable tune shift due to beam current in the quadrupole transverse focusing system along the linac. The results of extensive theoretical analysis and computer simulation are in agreement that a tune depression from 60° per period (unloaded) to 24° covers a range safe against transverse instabilities. Detailed information on the design procedure and the computer program being used in conducting it can be found in Reference 8.

Some Ongoing Research and Development Topics

It seems a general property of high current accelerators that a substantial part of the

Table II

Component	T_{out} (MeV)	Current (A)	Pulse length (μsec)	q
Surface-ionization source	2	4	40	1
Pulsed drift tube	4			1
Pulsed drift tube	6	6		1
Pulsed drift tube	13			4
Low-voltage induction modules	200	60	4	4
Iron-core induction modules	8,000	800	0.3	4
Ferritic glass induction modules	19,000	1,600	0.15	4
Buncher (± 1 MV/m ramped pulses)	19,000	8,000	0.03	4
Beam splitter (4x4 = 16 beamlets)	19,000	34,000 total	0.007	4

problems arise at the very low energy end. Work on ion sources is proceeding at all three Laboratories mentioned above; progress, both on extensions of conventional types and on large-aperture high-current sources, has been very significant. Some of this work is being reviewed at this conference by Clark.

The very low velocities of heavy ions in the megavolt range produced by typical high-voltage columns require special low-velocity accelerating sections. The Wideroe system and the long pulsed drift tubes mentioned above are not the only contenders. Some newer developments are being reviewed by Swenson[9] at this conference. Subdivision of the beam at low energy has been considered by Herrmannsfeldt,[10] Gabor lenses are being studied at Brookhaven,[11] and Maschke has put forward the MEQALAC concept,[12] a highly subdivided array of small beams focused by electrostatic quadrupoles.

The chromatic and third-order geometric aberrations of final-focusing quadrupole lens systems place serious limitations on system performance. Substantial efforts are under way to examine the degree to which correction of these aberrations is practical. A clear review of this work has been given by Garren.[13]

Further analytic work and computer simulations are needed to obtain a complete picture of longitudinal dynamics, especially near bunch ends, in the induction linac.

The necessity to satisfy the six-dimensional phase space constraint (with allowance for inevitable dilutions of phase space density) arising from Liouville's theorem has presented difficulty to all those who have constructed system design examples. This constraint turns out to be uncomfortably tight under realistic assumptions of performance of system components and on dilutions one might expect during various beam manipulations. It was shown[14] for rf linac systems that the "ideal available dilution factor" by which the 6-D phase space density may be diluted without failing to meet target requirements can be expressed as the product of factors depending on the target requirements, parameters having upper bounds in principle or for practical reasons, and a linac "figure of merit". Details must be sought in the paper, but the expected actual dilutions come close to the available factor, or exceed it, for some system designs. One must emphasize the importance of avoiding or minimizing dilutions at every stage, and also to state the strong need to maximize the linac figure of merit, which is

$$I_L/[(\varepsilon_{\perp L})^2\ \varepsilon_{11\,LB} f_{LB}],$$

in which I_L mean electric current, $\varepsilon_{\perp L}$ transverse normalized emittance, ε_{11LB} longitudinal emittance (eV-sec) per bucket, and f_{LB} the frequency with which bunches emerge from the linac. Note that in the funnel loading described earlier the ratio I_L/f_{LB} is ideally a constant if I_L is the current in a single branch at any stage; also, electric current is approximately conserved during stripping to increase the charge state. Therefore the figure of merit may be evaluated (with allowance for dilutions) at the first stage. $I/(\varepsilon_\perp)^2$ is of course a measure of source brightness.

Finally it should be mentioned that only the first approximations of the final longitudinal implosive process (which all systems require) have been studied;[15,16] possible instabilities and other details remain to be investigated.

References

1 Final Report, ERDA Summer Study of Heavy Ions for Inertial Fusion, Claremont Hotel, Berkeley (July 1976) LBL-5543.

2 Proceedings of the Heavy Ion Fusion Workshop, Brookhaven National Laboratory, Upton, New York (October 1977) BNL 50769.

3 Proceedings of the Heavy Ion Workshop, Argonne National Laboratory (September 1978) ANL-79-41.

4 W.B. Herrmannsfeldt, "The Development of Heavy Ion Accelerators as Drivers for Inertially Confined Fusion", LBL-9332, SLAC-221, UC-21.

[5] D.E. Young et al., Proceedings of the Heavy Ion Fusion Workshop, Brookhaven National Laboratory, Upton, New York (October 1977) BNL 50769, p. 17.

[6] A.W. Maschke, Proceedings of the Heavy Ion Workshop, Argonne National Laboratory (September 1978) ANL-79-41, p. 249.

[7] D. Keefe, Proceedings of the Heavy Ion Workshop, Argonne National Laboratory (September 1978) ANL-79-41, p. 31.

[8] A. Faltens et al., Proceedings of the Heavy Ion Workshop, Argonne National Laboratory (September 1978) ANL-79-41, p. 31.

[9] D. Swenson, "Low Beta Structures", this conference.

[10] W.E. Herrmannsfeldt, Proceedings of the Heavy Ion Workshop, Argonne National Laboratory (September 1978) ANL-79-41, p. 273.

[11] R. Mobley, Proceedings of the Heavy Ion Workshop, Argonne National Laboratory (September 1978) ANL-79-41, p. 299.

[12] A.W. Maschke, "MEQALAC", A New Approach to Low Beta Acceleration", BNL-51029 (June 1979).

[13] A.A. Garren, Proceedings of the Heavy Ion Workshop, Argonne National Laboratory (September 1978) ANL-79-41, p. 141.

[14] D.L. Judd, Proceedings of the Heavy Ion Workshop, Argonne National Laboratory (September 1978) ANL-79-41, p. 237.

[15] D.L. Judd, Proceedings of the Heavy Ion Fusion Workshop, Brookhaven National Laboratory, Upton, New York (October 1977) BNL 50769, p. 34.

[16] T.K. Khoe, Proceedings of the Heavy Ion Fusion Workshop, Brookhaven National Laboratory, Upton, New York (October 1977) BNL 50769, p. 131.

Discussion

R. Mobley, BNL: We have what we term strong focusing, which was magnetic perpendicular forces invented by Courant, Lewis, Synder at Brookhaven in 1950 or thereabout. The fringe field focusing that you get from electrostatic effects in the longitudinal multiple beams and the annular rings are edge focusing effects similar to that of Pierce type electrodes, but we have restricted our considerations of strong electrostatic focusing to perpendicular (radial) electric fields, either electrostatic quadrupoles or Gabor lenses. That is a distinction that we should continue to make. What do you call strong focusing? If the main field component pushes the particles towards the axis, I consider that stronger than that of a percentage of the fringe field giving it a little shove that way.

D. Judd: I agree with your desire to sort out our different kinds of focusing and give them clear labels. My reference to the work by Herrmannsfeldt, which is something rather different from what you people are doing, was to indicate that people are thinking of all kinds of methods of dealing with these very low beta systems. Not that anyone holds any particular brief for them or even for the way I characterized them.

P. Meads, Brobech Associates: I wonder if anybody has looked into the Russian proposal of Dymnikov et al., about 20 years ago, of using opposing electrostatic quadrupoles to correct the chromatic aberration which you mentioned.

D. Judd: The problem I was alluding to occurs at beta of about one half at a final energy of about 10-20 GeV for heavy ions in a charged state 2,3,4,6, perhaps, and it is my impression that nobody really wants to use electrostatic focusing under those conditions.

THE NEW CERN 50-MeV LINAC

E. Boltezar, H. Haseroth, W. Pirkl, G. Plass, T. Sherwood, U. Tallgren, P. Têtu, D. Warner, M. Weiss
CERN, Geneva, Switzerland

Summary

In this invited paper the new CERN 50-MeV linac will be described from several aspects including the general project background, a comparative treatment of services, components and phenomena along the beam, and some details of systems and techniques with emphasis on new approaches. A comprehensive list of references is included and a review of present status and performance.

Introduction

To introduce this general paper on the CERN 50-MeV linac we briefly enumerate the main sources of detailed information on the machine design. Starting with the general technical solutions proposed in the Project Study[1] (1973), several aspects of the machine design and parameters were updated and a status report[2] made at the 1976 Linac Conference, with full accounts of the RF structure design[3], the beam optics[4], the control system[5] and of measurement topics concerning the double drift harmonic buncher (DDHB)[6] and emittance[7]. At the 1979 US National Accelerator Conference (San Francisco), a summary of the linac design was presented with emphasis on experimental results at 0.75 MeV and 10 MeV, and on the first experience with 50-MeV operation for machine studies and then as the injector to the CERN accelerator complex[8].

In this conference many of the gaps can be filled, for example, by papers on the mechanical design[9], on the preinjector fast HT level control (bouncer)[10], the RF system[11] and the 50-MeV beam measurement system[12] with other papers on calibration[13], beam optics[14], HT formation[15] and a new ion source[16]. Many topics have also been treated in internal reports, often in more detail and appealing to a more specialized public.

Linacs used as injectors to large accelerator complexes must be conservatively designed and basically reliable, and these aspects do not normally lead to entirely novel solutions. In particular, at CERN the new linac was designed to replace the injector linac which had passed through several improvement programs since 1959, until its electrical and mechanical design and building limitations had been reached[17]. Nevertheless, if lacking in stability and peak current, this aging machine achieved less than 1% downtime in recent years; so the first aims for the new linac were to displace the intensity limitation to one of the subsequent synchrotrons[18] and yet keep comparable long-term reliability if possible in the changeover period as well. However there are features in the design of all systems which represent distinct advances in linac technology as will be detailed in the following sections.

The Project: History, Resources and Milestones

In May 1973, a study group was set up to make a project proposal concerning the upgrading or replacement of the 50-MeV linac injector to the CERN accelerator complex (booster synchrotron, the CERN 28-GeV PS and the Intersecting Storage Rings) which was in the process of being extended to 300 GeV by the SPS. The required improvement in intensity and quality (Table 1) was such that with experience gained on the 3-MeV experimental accelerator[19,20] on cavity calculations, low energy beam dynamics with space charge, measurements of high brilliance beams and on a thoroughly tested mechanical engineering approach, one already had the basis for an improved design. Accelerator design programs using linearized space charge forces for computing low energy beam transport (including bunching) and for defining focusing and matching in the linac proper were also available[21] and a double buncher scheme had been proposed[22]. In addition it had already been decided to develop a computer system based on PDP 11/45 computers for the linac, PS booster, and CERN PS combined control system. Thus the project proposal, presented and approved in October 1973[1], was in several important technical aspects more final and confident than one would expect after four months study (Table 2). By comparison, it was more difficult to arrive at the resources and time scale predictions.

Table 1. Beam Specification (Debunched)

Energy	50.0 MeV
Current	50 mA to 150 mA
Pulse duration	200
Repetition rate	2 pps
Normalised emittance	$<8\pi$ mm mrad (90% of beam)
Energy spread	±150 keV (90% of beam)

Table 2. Linac Parameters (as constructed)

Pre-accelerator	
Duoplasmatron ion source	I=300 mA
High gradient, two gap column	W=750 keV
750 keV (low energy) beam transport (LEBT)	
Transverse matching	18 quadrupoles (4 triplets)
Matching with bunchers	2 at 202.56 MHz
	1 at 405.12 MHz
Linear accelerator	
3 Alvarez tanks (202.56 MHz) with post couplers	
Focusing (FD) 131 quadrupoles (in drift-tubes)	
Synchronous Phase -35° to -25° (Tank 1) then -25°	
50 MeV (High energy) Beam Transport (HEBT)	
Junction with existing line after 54 m (two bends)	
Transverse matching	14 quadrupoles
Debunchers	2 at 202.56 MHz, 1 at 405.12 MHz
Beam Measurements in 3 phase planes	

The net final result was that the linac was built and achieved its specified beam within its budget (23 MSF). The amount of mechanical engineering effort available, in particular at the start of the project was, however, not enough to keep within the original four-year schedule. From

another point of view, it is evident that the extra year for tests and the installation of ancillary apparatus contributed considerably to the very short delay between first acceleration to 50 MeV and reliable operation as an injector.

In Table 3 the final material costs are quoted by accelerator system while the in-house effort was 165 my. In Table 4, some key dates of the project realization are listed.

Table 3.

	MSFr.
Preaccelerator	2.0
LEBT	0.9
Structure	3.7
RF	2.6
Controls	3.7
HEBT	2.1
Bldg and Installations	5.0
Total material	20.0
Hired labor (about 65 my)	3.0
Total expenditure	23.0

This corresponds within a small margin to the original estimate of 21.3 MSFr. in 1973 prices, up-dated by the yearly index.

Table 4

Project approved	Oct. 73
Excavation started	Dec. 73
Preinj. + Controls area ready	Mar. 75
Building complete	Dec. 75
1st 750 keV beam	Dec. 75
LEBT	Dec. 76
Tank 1 ready	Apr. 77
1st 10 MeV beam	May 77
150 mA at 10 MeV	Sep. 77
Tank 3 ready	Mar. 78
Tank 2 ready	Aug. 78
1st 50 MeV beam	6 Sept 78
Design current (150 mA) attained	5 Oct. 78
1st test with booster	7 Oct. 78
Routine Operation	Dec. 78

An Overview of the Linac

Building and Machine Layout (Fig. 1)

The new linac was sited as closely as possible to the original linac within the limitations of existing buildings and the site topology. These limitations and the decision to separate the ancillary electronics, radio-frequency power sources and focusing power supplies from the accelerator led to a building section (Fig. 1) where accelerator tunnel, equipment room, and the air-conditioning plant are sited one on top of the other. To reduce tunnel costs the minimum acceptable cross-section was chosen; for an operating machine it is comfortably large but was very restricting vertically during installation. Other implications of the building position and design concerned the shape of the Faraday Cage and length of beam transfer lines (39 m longer than for old linac). The control room and its associated data room (housing the computers) were built in the corner of the existing South Hall.

Alignment Using External Reference Axes

The CERN PS orbit level, 433.66 m (above sea level) determines the linac beam axis height. A reference axis for preinjector, LEBT and accelerating cavities is parallel to but offset 0.6 m vertically and 0.3 m horizontally relative to the beam axis and is defined by four massive steel "monuments" situated near the two ends of the accelerating structure and the intertanks (Fig. 1).

Consider the low energy beam transport (LEBT Fig. 2) where each section is provided with a pair of targets and a (spirit) level reference face prealigned in the workshop to the physical or magnetic axis. With a microalignment telescope supported by a monument (on the offset axis) one can align elements to 0.15 mm (relatively) and 0.25 mm(absolutely) by adjustable tables to which the sections are bolted. Note that the last LEBT section is aligned to and supported from the first linac tank by a large diameter buncher (energy corrector, B3); similarly the first LEBT section and the preinjector column make one mechanical unit.

For the preinjector and linac tank alignment the same concept (as for the LEBT) is followed, i.e. easy adjustment and quick positional check. The relative alignments of tanks, girders and drift tubes are dealt with in other papers at this conference[9].

To be compatible with the PS injection and ejection lines the high energy beam transport (HEBT) elements use an alignment reference line 0.5 m vertically above the beam axis.

The Vacuum System

Throughout the linac, the vacuum system is based on turbomolecular pumping stations for initial pumping (or heavy gas load) with ion pumps for permanent high vacuum operation. Metal joints are used throughout with aluminium wire joints preferred in the LEBT and structure, diamond section aluminium joints in the HEBT. Clean assembly conditions consistent with the ion pumps and all-metal system were adopted with strict avoidance of organic matter in the preinjector and LEBT regions to minimize contamination of the high gradient HT column.

The particular pumping requirements of each region (defined by sector valves) are satisfied as follows:

a) for the preinjector two 1500 ls^{-1} turbomolecular pumps cope with the continuous hydrogen load and achieve a pressure (one pump) of 5×10^{-5} Torr. The accelerating column and LEBT are connected only by the low conductance beam tube (20 ls^{-1}) through the "gun" assembly (Fig. 2). Further pumping at the entrance to the LEBT is provided by two 400 ls^{-1} diode ion pumps.

b) The LEBT has a turbomolecular pumping station (450 ls^{-1} turbopump and 10 ls^{-1} backing pump) and a 400 ls^{-1} triode ion pump for the DDHB region, supplemented recently by the 200 ls^{-1} ion pump (Fig. 2). With ion pumps alone the operating pressure is $<1 \times 10^{-6}$ Torr.

c) For the accelerating structure, Fig. 3, there are two 450 ls^{-1} turbomolecular pumping stations per tank and one 1000 ls^{-1} triode ion pump per structure section (total 10). This allows rf conditioning with turbopumps alone and pump-down to 2×10^{-6}Torr in <2 hours after being at atmospheric pressure. Ultimate pressure is 2×10^{-7}Torr.

Focusing

Throughout the linac, quadrupoles of the BNL physical design[23] are used with some modifications in manufacturing techniques and different dimensions for LEBT singlets and triplet I.

Magnetic field tests were made on individual quadrupole magnets using a long coil field integration technique[24] to find the harmonic content of the field, the magnetic centre, the angular position of field symmetry planes relative to a keyway in the magnet yoke, and the important calibration for operation, $\int$(field gradient) dz as function of exciting current. To obtain precise results when iron proximity effects are important, measurements were made on realistic assemblies of two or three triplet elements. Each of the 125 drift tube quadrupoles was calibrated just before installation of the support girders in the cavities[13] to obtain absolute and comparative results, including effects of the copper drift tube shell and stainless steel bore tube. At normal operating fields the departure from linearity is >0.5% only for Types I, II and III (i.e. up to 5 MeV) while throughout the drift tube linac and within a quadrupole type, a constant relation gives sufficient accuracy to set the quadrupole field by the supply current.

The power supplies operate on the principle of a resonance circuit (LC) producing a half sine wave (2 ms long) which is clipped by a parallel transistor bank working in a feed-back circuit to give a precisely controlled flat top of >200μs with stability $\pm 2 \times 10^{-3}$during the pulse, and pulse-to pulse[25]. As the switching elements (thyristors) are rated at 1.0 kV, any increase in pulser current near this limit is made by increasing the capacitor bank (stored energy) and adjusting the triggering delay time.

With 160 quadrupole elements to power, the pulsers represent a considerable investment and control problem, so one connects magnets in series where possible within beam optics and pulser-load limitations. Thus, in the LEBT one has two pulsers per quadrupole triplet, in Tank I the first sixteen quadrupoles are powered individually, and where possible the others are in series pairs, while in the other tanks most quadrupoles are connected three to a pulser. The HEBT system (14 Type VII quadrupoles up to BH3) is not periodic so only one pairing was practical, and finally a total of 90 power supplies was required.

Bunching, Acceleration and Debunching.

Here we compare design, operation and associated hardware of the elements which affect the longitudinal motion. One has drift tube structures throughout and for the purposes of comparison the simple (non-relativistic) formula applies to the longitudinal action of any gap :

$$\Delta W = eV_{pk} T \cos\phi$$

with V_{pk} the peak voltage on a gap, W the kinetic energy, ϕ the RF phase of proton arrival (relative to positive maximum) and T the transit time factor , which is a function of gap geometry and energy.

For acceleration one generally has $\cos\phi$=0.80 to 0.90 whereas bunchers and debunchers normally give no net energy gain to the mean proton of a bunch i.e. $\cos\phi$=0. Radial defocusing is also important both at low energies and for bunchers, but its reduction with grids was not considered justifiable.

Structure Design. For each rf structure one aims to minimize the power for the required $\Delta W_{eff} = eV_{pk} T$, but with heavy beam loading, transient level and phase problems, severe aperture requirements, need to house focusing elements and need to maintain mechanical simplicity, the final solutions are inevitably compromises. The cavity dimensions, losses and dynamics coefficients (e.g. T) were computed using the program CLASL[26] for the three bunchers and the linac (128 unit cells). Generally, to ease fabrication and surface finish problems, we could accept 25% more rf power losses than for perfect copper (representing <10% of total power including beam loading).

The bunchers have moderate requirements in ΔW_{eff} (<35 keV) so the mechanical and dynamics contraints strongly influence the design. For the 202.56 MHz bunchers the chosen asymmetric design (half a unit cell) has a gap of 13 mm, aperture diameters 20 mm and 25 mm (for B1 and B3 respectively) giving acceptable values of T (0.71, 0.60). The half drift tube can house a quadrupole or beam transformer (d=180 mm) and the cavity diameter (700 mm) leads to an efficient rf design within mechanical constraints of incorporation in the Tank I input cover (B3). For the 405.12 MHz case (B2) the symmetric design gives the specified separation between the double drift harmonic buncher (DDHB) gaps. The beam dictated an aperture diameter of 18 mm (gap=10 mm) which gives T=0.36; the variation in T with radius across a well adjusted proton beam could help longitudinal matching[27]. To first order, the energy modulation of an unbunched beam (in DDHB) causes no real or reactive beam loading. All bunchers were made from mild steel, copper-plated to 15 μ, with aluminum wire joints for vacuum and rf contact.

The 202.56 MHz accelerating cavity geometries are dictated by the size of drift tubes (containing quadrupoles), need to maintain $0.2 < g/L < 0.35$ (high value of T), acceptable shunt impedance and the computed dynamics, which determines individual cell lengths[3]. The tank (cavity) lengths are mainly determined by the rf amplifier arrangement (one amplifier and feed loop for 10 MeV acceleration). The cavity diameters 0.94 m, 0.90 m, and 0.86 m, respectively, keep T high and rf losses near their minimum. Further design details are given elsewhere[9] (also under Accelerating Structure).

For the debunchers, the peak energy changes of ∿400 keV at 202.56 MHz make a high shunt impedance desirable. The large beam apertures cause

problems due to reduction of T and penetration of the electric field into the beam tube especially at 405.12 MHz (DB14).

Field Calibration. Several methods are available:
a) Effective field as a function of input power comes from cavity calculations (normalized by measured Q).
b) Field on the axis (hence T and tilt) by perturbation methods[13].
c) Observations on longitudinal dynamics at nominal rf level and comparison with computed predictions[13].

With methods a) and c) the cavity field is measured by the monitoring loops which couple to H_ϕ at the cavity wall.

For adjustment of buncher rf levels method a) is sufficient but b) has been used to confirm symmetry of field in the asymetric bunchers while c) has been applied to the DDHB using a fast probe[6] and also by reference to the 10 MeV beam characteristics. For debunchers c) is applicable in the longitudinal measurement line (DB12) by beam energy change versus phase shift.

Multipactoring. This problem in the initial powering of all rf cavities is discussed here by reference to the linac cavities. Ideally one needs a clean vacuum ($<10^{-5}$ Torr), temperature control of cavities, correct input match, variable feeder line length and control of the rf pulse rise time. Even so ionization pumps and ionization gauges directly on the tanks had to be switched off to obtain the initial erratic acceptance of power with a glow discharge (observed near the feed loops) and much evolution of gas from copper surfaces. After some hours (<12 hours) of steady improvement, power was eventually accepted up to 20% above nominal level on all pulses with ion pumps on, quadrupoles pulsing and rf amplifiers on slowest rise time. This process only takes a significant time when first powering a cavity.

In the single-gap cavities, the conditioning was sometimes lengthy with more apparent dependence on surface cleanliness and on relative timing of adjacent cavities (supposedly producing ions or electrons). However, during scheduled operation, the number of bad pulses one ascribes to multipactoring is negligible.

Evolution of the Beam along the Linac

To complement the two comprehensive approaches to beam optics[4,14], this section describes the beam qualitatively as it passes from preinjector to booster input. In Fig. 5 we give in one transverse plane and in the longitudinal plane, beam envelopes (2 x rms size in mm and in deg.) assuming computed results (modified by measurements where possible) with time (ns) as abscissa. The virtual longitudinal aperture is half the estimated bucket width. Note that the rms envelope representation is relevant for beam transport with space charge but it can seriously underestimate the beam limits if there are long tails on the density distributions.

Generally, this plot brings out the similarities between LEBT and HEBT, both transversely (envelopes and lens separations), and longitudinally, (transition from continuous to bunched beam and vice-versa). The preinjector which represents only 20 ns of acceleration at 6 MeV m^{-1} is designed to take the dense beam rapidly through a difficult space charge region. In the first part of the LEBT, an essentially round unbunched beam is contained by 4 quadrupole triplets, limited proportionally in diameter and angle (apertures AP1 and AP2) and steered (ST1 to ST4) to the DDHB. The bunching system performs a six-dimensional matching to the linac input with 6 quadrupoles and 3 bunchers compressing 80% of the beam into an ellipsoid of mean diameter 7 mm and length 10 mm. In the linac the +- focusing system starting with $\mu=30^o$ maintains a very small beam size, even with transverse emittance growth of 2.3 due to the compensatory reduction in the space charge effect and resulting increase of μ, an effect enhanced also by the growth in longitudinal emittance (x 5 measured). In HEBT there is rapid transverse growth to match the longer period of the focusing, while longitudinally, both energy spread and space charge act to increase the bunch length. Other features of the HEBT are an achromatic section between BH2 and BH3, and the use of debunchers to shape the energy spectrum.

Users Facilities on the Control System

Users have access over two maxiconsoles, two midiconsoles and two analog consoles in the control room, plus one mobile midiconsole in the equipment gallery. The midiconsoles each have four "knobs", one "access" card reader, a numeric keyboard, a touch panel for parameter and task selections and a color TV monitor. The latter displays any four beam transformers plus any four parameters (Fig. 6), where, given access, the operator can act, either by a "knob" or by the numeric keyboard. Synoptic displays are used for groups of parameters, e.g. the LEBT (Fig. 7) or the vacuum system (Fig. 8) where a valve or pump can be selected via the touch panel and acted on, registering as a visible status change on the display. The maxiconsole has additional facilities: a 611* storage scope, a video terminal, and a touch panel for measurement tasks. The analog console allows one to select and "hook" a parameter to any of four traces on two scopes or to a waveform digitizer which can "freeze" or, if necessary, store the display.

A powerful feature is the List Processor which takes any parameter name list and sends a matching list of values from a disk file, e.g. for setting tank quadrupoles. Value files can be prepared for different conditions, and later be activated by a touch panel or by a surveyor task.

One can, using only parameter names, write application programs in BASIC-11, FORTRAN 4+ or PASCAL, e.g. CORLIN (in BASIC), corrects the offset between desired and actual currents from the quadrupole pulsers, whereas TRACE, (in FORTRAN) predicts, from user input values, LEBT beam envelopes and emittances on the 611 storage scope. BASIC has also been convenient for log programs and ad-hoc programs where on-line debugging is essential[28].

*Tektronix

Particular Design Features

Preinjector

HT Equipment. The high-voltage generator (Cockcroft-Walton) and associated electronics, electronics platform and the original beam-loading compensation were bought from Haefely, Basle. For maintenance reasons an open Cockcroft-Walton was chosen. It operates at 5 kHz with maximum output 850 kV and 4 mA DC and is connected to the electronics platform by a 5-MΩ damping resistor. A three-stage isolation transformer rated at 7 kVA (14 kVA at reduced voltage) supplies power to the electronics platform. The insulation is rated at 300 kV per stage with 2500-MΩ resistors incorporated to ensure equal potential distribution. The original beam-loading compensation (bouncer), a compact two-tube arrangement housed in an oil-filled tank, has been replaced for maintenance and reliability reasons by an open (air-insulated) structure. This new bouncer uses only one tube, has a wider band width and shows better reliability than the previous system[10].

Ion Source. The original duo-plasmatron ion source of the old linac[29] was already modified some years ago[17]. For the reduced diameter of the accelerating column anode in the new linac, this source had to be made smaller, mainly by cutting away superfluous parts and redesigning the magnet coil, with most of the inner parts inter-changeable with the old source. Armco iron parts are nickel-plated, to provide corrosion protection. Another improvement was the replacement of the old oil-cooling system by a circuit using distilled water with 30% ethanol as corrosion inhibitor with a fluid-to-air heat exchanger on the electronics platform. The oil was a potentially serious hydrocarbon contamination risk for the column and the oxide cathode during source changes, compared to the relatively volatile water-ethanol mixture. In addition, one has less flow and circuit pressure for equivalent cooling.

The arc pulser consists of a delay line (defining the maximum pulse length) with a large series resistance to supply constant current to the source. Pulse length reduction is achieved by thyristors short-circuiting the arc when triggered.

Accelerating Column. The 750 kV accelerating column (built by HVEC) is a modified version of the CERN 500 kV design[30] with 19 sections (instead of 14), of the same diameter, which necessitated a reduction in anode and source diameters and larger radii on the central inner shielding rings. Both gap and gradient have increased from 43 kV cm^{-1} across 11.7 cm to 58 kV cm^{-1} across 12.9 cm and there is an intermediate electrode (as in the old linac) to improve voltage holding and focusing. The total capacity associated with the column is 2.6 nF of which 1.5 nF is connected via a 2 kΩ damping resistor to the bouncer. The dissipation of the stored energy (during column breakdown) has not caused observable damage. The cathode requires -4-kV bias to avoid frequent breakdown and high radiation levels, although this potential only forms a barrier against back-streaming electrons at the edge of the cathode hole.

The column is a structure made of ceramic rings glued together with epoxy resin and supported like a cantilever at the cathode end. With the column fully loaded and not under vacuum, the epoxy resin bond has a safety factor of 20 proved both by tests and by calculations (epoxy resin tensile strength $\sim 10 N/mm^2$). Nevertheless, for safety reasons, at the anode end a force is added (rope and counterweight) minimizing the bending moment along the column. Inside the cathode is the "gun", a tubular vacuum-tight structure containing the first magnetic triplet (T1), beam transformer (IM2), steering magnets ST1) and an electron trap. This assembly is bolted onto the column making one mechanical unit for support, alignment and vacuum (see Fig. 2).

Performance. The source geometry was optimized experimentally by adjusting its longitudinal position and the expansion-cup shape, but the required small Gaussian-type emittances seemed unavoidably associated with rather noisy pulse shapes at normal operating beam currents > 250 mA (and vice versa). One initially adjusts the operating parameters such as hydrogen flow, arc current and cathode current by reference to output current, pulse shape and emittance (measured at EM2). Measurements made over several months show that beam characteristics are stable and can be set to values stored in the control computer. Source lifetime, determined by cathode emission and anode erosion, is > 1 year in normal operation.

After a source change the conditioning of the evacuated column to 750 kV takes $\sim$ 1 hour when done automatically[15]. In typical operation the HT breakdown rate is $\sim$ 1/day. As this sometimes disturbs the source-computer interface, the source parameters are reset automatically.

LEBT

The LEBT has been designed to transport the preinjector beam, to shape it and to match it in both transverse and longitudinal planes (6 dimensions) to the linac input. Functionally it consists of a long unbunched beam section which provides an essentially round beam about 10 mm diameter at DDHB, and a bunching section which performs the matching to the linac via six quadrupoles and three bunchers.

Mechanical Engineering and Components. The main objectives in the mechanical concept of the LEBT were an easy and rapid alignment without disturbing the vacuum, a clean vacuum and the possibility to put diagnostic equipment in any of several foreseen places.

The part of the LEBT installed in the column cathode has been described above. Between the column output and DDHB, the LEBT is a classical beam line with five independent units mounted on individual supports and connected by flexible vacuum chambers. The bunching section, the last and most important part of the LEBT, is extremely crowded and forms one mechanical unit for alignment and support via its main element, a large diameter buncher (B3) which is bolted on and aligned to the first linac tank (see Fig. 2).

The diagnostic equipment, defining apertures (AP1, AP2) and beam stoppers use tantalum plates

which have a good resistance to beam damage. Nevertheless under certain focusing conditions the proton beam could eventually burn a hole through the stopper which forms part of the radiation safety interlock chain. Thus the stoppers have a safety device, an additional plate, which, if pierced by the beam develops an air leak and switches off the linac. More details of vacuum and alignment are given under corresponding headings.

Beam Optics[27]. The figure of merit for the LEBT/Linac beam optics is the measured (as previously computed) trapping efficiency of 80% which allows the design beam current at 50 MeV, 150 mA, to be obtained with < 200 mA injected into the linac (∿ 250 mA from the source). The position of bunchers was studied for beam currents between 50 and 250 mA and the optimum distances for trapping efficiency, bunching voltages and acceptable geometry determined. The distances from B1(202.56 MHz), B2 (405.12 MHz) and B3 (202.56 MHz) to the first linac gap are 101 cm, 86 cm and 16 cm, respectively (see Fig. 2). Note that for the highest currents the computed trapping remains > 80% in spite of severe linac input conditions (e.g., mean beam diameter ≈ 7 mm), which would allow us to provide more output current if necessary. In the bunching region one has sufficient quadrupoles to keep the beam well inside the 45 mm diameter aperture and to match it to the linac input.

Practical Aspects of Beam Matching. One needs a round axial beam at the input of the DDHB, < 10 mm diameter, limited proportionally in angle and diameter so as to have equal vertical and horizontal emittances. Thus one has to adjust the four triplets, the steering magnets (ST1 to ST4) and the apertures (AP1 and AP2) with reference to beam currents (IM3, IM4 and IM5) and emittance measurements at EM2 and EM3 (Fig. 2). On-line computer programs are available to derive quadrupole settings using the measured rms values as input data and steering settings, using mean beam positions. This procedure is even more necessary for adjustment of the bunching region quadrupoles to match to the linac acceptance. As noted above (bunching, field calibration) buncher amplitudes are set to computed values. Solutions for several beam conditions can be stored on the linac computer and parameters set by pressing one or more touch buttons.

Operation and Performance. An important aspect of the LEBT operation is the reproducibility and no further fine adjustment of parameters is required after setting-up. There is good transmission through the LEBT as an unlimited beam has decreased by only 15% (probably heavier particles) at the DDHB and there are no further losses to the linac input. The performance of the LEBT has fulfilled its design predictions in handling all beam conditions without reaching limitations in element position or strength. No down-time has yet been ascribed to LEBT malfunction.

Accelerating Structure

Many of the construction techniques first tried at CERN on the 3 MeV accelerator[19,20] were suitable for the 50 MeV accelerator structure[9] e.g., copper-clad steel fabrication, aluminium wire joints for rf and vacuum, and demountable drift tube support girders. The rf and beam duty cycle are < 10^{-3} and as the proton beam takes ∿ 70% of the RF power there is less reason for fanatical attention to cavity losses. All components except bulk tuner are demountable from outside the cavity while the intertanks are combined with end half cells into a demountable unit and the three tanks form a single vacuum system (Fig. 3). Before installing the girders in the cavity one has complete accessibility for mounting the drift tubes and for adjusting their relative alignment.

Cavities. The accelerating structure (Fig. 3) is divided into three tanks accelerating from 0.75 to 10.4 MeV, then to 30.5 MeV, and 50.0 MeV, respectively. The tanks are subdivided into a total of 10 sections with lengths varying between 3.16 m and 3.54 m (average 3.29 m) and dictated by positions of rf feed-loops (at L/4 and 3L/4 in the long tanks) and gaps. Copper-clad steel (15 mm steel + 2 mm copper) was used for the fabrication, with welded inserts to extend the copper to the circular joints between tank sections and to the rectangular girder slot. The departure from circular section introduced by this slot produces a resonant frequency decrease (300 kHz) which is less than the support stem frequency perturbation (in Tanks II and III) ; normally the bulk tuners introduce as much frequency perturbation. For fabrication simplicity the smaller holes were left unlined thus slightly increasing the rf losses. To assess the copper surface quality and the circular aluminium joints, rf measurements were made on Tank I without drift tubes, giving ∿ 80% of theoretical Q.

Drift Tubes. The cylindrical part of the drift tube body is an alignment reference surface, so one ensures accurate concentricity of the quadrupole magnetic axis by a close fit of the quadrupole yoke in the drift tube. It is closed by electron beam welding of the end cap(s) to the body and to the stainless steel bore tube. Water cooling is made via the stainless steel inner support stem which fits closely in the drift tube body. In addition to the standard dimensional checks on assembly, the flatness of the Tank I drift tube front faces and the shape of the Tanks II and III radiused profiles were checked by precise and quick capacitive methods.

Rf Feed Loops (Fig. 9). Two important criteria in the design were (a) large and predictable coupling variation with minimum movement and (b) minimum field perturbation. This leads to an eccentric line (outer diameter = 127 mm) near the cavity (which reduces coupling due to cavity field penetration), then a step up to the 230 mm coaxial line in which the PTFE ("Teflon") rf to vacuum window is mounted at about $\lambda/2$ from the short circuit at the cavity. The five loops installed perform reliably and give the specified coupling variation $\beta = 1$ to $\beta = 4$, for a movement of 30 mm.

Bulk Tuner (Fig. 3). This fixed tuner corrects the gross errors in frequency and field distribution so that in particular the final cavity resonant frequency falls in the piston tuner range. It is made in "T" sections ∿ 1 m long with the top of the "T" demountable so one can selectively

place the sections to make the first-order field and frequency corrections.

Piston Tuners. Of ten tuners mounted (one per structure section) only two per tank are used for automatic tuning as less than ± 5 kHz range is necessary at the correct cooling water temperature (20 °C) compared with ± 30 kHz available. A gap ∿ 1 mm was left between the tuner and the cavity wall in preference to installing a possibly unreliable sliding RF contact.

Post Couplers. To stabilize the field one post coupler is mounted per two drift tubes in Tanks I and II and one per drift tube in Tank III. The fields were set up by perturbation measurements[13] first by using variable penetration aluminum couplers, and then the final copper post couplers to produce greatly improved field stability in all tanks. For Tank I, where the accelerating field increases linearly with distance, the post penetration can be varied (in situ) by ± 5 mm and the orientation by ± 5°. In the other tanks the couplers are made to the fixed lengths predicted by the variable aluminium ones.

Rf Monitoring Loops. There are 34 pyrex thimbles mounted along the structure, allowing access to the H_ϕ field. Half of the available locations have unshielded matched loops (∿ 15 mm^2) which are adjusted by rotation to give a signal 40 dB relative to the tank input power. This is ample for all monitoring, frequency, rf level and phase control purposes.

Operational Reliability. There have been no failures on the structure which have required significant time for repairs since it came into service. A recent check has shown that there has been no decrease in cavity Q factors since installation.

High Energy Beam Transport (HEBT)

The 50-MeV beam line joins the old linac to the booster line at the bending magnet BH3 (see Fig. 4). This layout allows injection of the new linac beam either directly into the PS or into the booster. In the latter (normal) case one can use the old emittance line to check the matching of the beam to the booster, and the spectrometer line to adjust the three debuncher cavities for the required energy spectrum.

Focusing, Steering and Debunching. In the first part of the HEBT (before BH2), there is ample focusing (8 quadrupoles) to prepare the beam for the more critical achromatic part between (and including) bending magnets BH2 and BH3 (6 quadrupoles). Initially the beam is measured at the output of the Linac in the three phase planes which gives sufficient data for input to TRANSPORT. This program which can be run interactively with the CDC computers, gives results for quadrupole settings which can be used unmodified up to BH3 and thereafter the matching is made empirically by observation in the old single pulse emittance system and adjustment of 6 DC quadrupoles.

The beam steering is also critical, with 5 pulsed steering magnets adjusted systematically by reference to 8 magnetic beam position pickups to ensure > 95% transmission.

Ideally the first debuncher, DB11, adjusts the bunch length for best conditions at DB13 and DB14 (405.12 MHz) but one can often satisfy booster energy spread requirements with one (202.56 MHz) debuncher. However, for a recently-studied hollow distribution, DB14 is essential (see below).

Phase Plane Measurements[12]. With the two new measurement lines at the linac output, one can treat (one measurement per second) the horizontal and vertical planes and the longitudinal plane respectively. The data from the battery of collectors are treated and displayed similarly in all planes except for the units (mm, mrad) transversally, and (degrees, keV) longitudinally.

The Control System Design Features[5,31]

The control system is based on two DEC PDP 11/45 computers, each having 128k of core memory, in a back-up scheme. The control room consoles are all interfaced to seven CAMAC crates on a parallel branch. Each computer has access over a "branch mixer" to each crate and to a common Data Base of 64k of core memory, which contains status and description of each parameter and which interfaces to a special CAMAC module. Two 2.5 MHz serial CAMAC loops are also driven from the parallel CAMAC. One loop crosses the high voltage of the preinjector via infrared optical links to control the ion source parameters at 750 kV. The other loop links 14 CAMAC crates in the equipment gallery.

The system solves the mapping between a parameter name list to the CAMAC addresses, and may perform several CAMAC operations to achieve the desired result. All CAMAC activity related to process parameters is synchronized to the linac cycle (500 ms minimum). All system software, and some critical programs, are, for maximum speed, in MACRO-11 assembler language.

There are 900 individual parameters in the system, and about 1700 status bits for the surveillance task to handle. When a change in status or a parameter out-of-limits is detected, an alarm message gives the name of the process synoptic on which a flashing arrow indicates the offending parameter.

Due to the proximity of the preinjector, breakdown of the EHT occasionally blocks the computer. Normally the linac continues to function due to the local buffering of all command values. However, it is planned to install a "watch-dog" which will automatically reboot the computer if a blockage occurs. The MTBF of the computers was around 1200 hrs last year and still improving. The 384 CAMAC modules have a MTBF of 370 hrs. Serial CAMAC for the process has proven successful, with easier debugging than on the parallel CAMAC.

User acceptance of the control system has been very positive and several outside laboratories have shown interest in installing similar systems.

Rf System[11]

An independent rf chain fed from a common phase stable reference line is associated with each of the three bunchers, three tanks and four debunchers. Each chain comprises fast amplitude and

phase servo-mechanisms acting at low level, and a slow-cavity tuning servo. The control elements for phase (hybrids with varicaps) and for amplitude (PIN-diode attenuators) act on the low-level side of each chain; their structure is therefore the same throughout the whole rf system, with varying output of standard power amplifiers:

- 2 buncher chains with 35 kW available rf power
- 3 debuncher chains (110 kW available)
- 3 linac cavity chains with a total of 5 output amplifiers of 2.5 MW (2.2 MW required for 150 mA beam).

  Simple and reliable PFN-circuits together with a highly efficient charging circuit based on low-loss current-limiting chokes provide the 40 kV pulsed plate supply; FTH 170 triodes, a water-cooled version of the former FTH 470 are used in the final and drive stages.
- 2 second-harmonic stages of 25 kW each at 405.12 MHz feed the harmonic buncher and debuncher(DB14).

For a bunched beam in cavities operated near to zero crossing ($\cos\phi=0$), the phase and level control have to cope with a large reactive load as well as resistive loads from the cavity and varying in-phase beam components (e.g. in the third buncher and debunchers).

Performance

As already reported[8], the new CERN linac has met, practically from start, all the specifications including the maximum ouput current of 150 mA. Usually, running conditions are set according to demands from the first downstream accelerator (booster); the present operational beam characteristics are given in the following table:

Table 5 - Beam Characteristics

Symbol	Description, Units	Value
I	Intensity [mA]	125
E_{in}	750 keV emit. { $5E_{rms}$ / 90% of I } [π mm mrad]	40 / 50
E_{out}	50 MeV emit., 90% of I [π mm mrad]	15
$E_{\ell\ out}$	50 MeV long. emit., 90% of I, [π MeV degree]	7
W	Energy spread at "old meas. lines" [keV]	on request
$\frac{\Delta I}{I}$	Beam intensity ripple at 50 MeV [%]	±4

The transverse output emittance is considerably smaller than the specified one (25π mm mrad for 100 mA), in spite of an emittance increase factor in the linac of ≈ 2.5 (see Fig. 10). No specification was given for the longitudinal emittance, hence operating conditions are optimized for other parameters, leaving E_ℓ to increase in the linac by a factor ∿ 5. On the contrary, precise requests concerning ΔW are given for the booster and the new debunching system can form a variety of energy distributions. Apart from "normal" distributions (see Fig. 11a), "hollow" distributions can be achieved by special combinations of the 3 debuncher settings[32] (see Fig. 11b).

Operation

The operation of the new CERN linac is considerably simplified by the possibilities offered on the control system. Essentially, one distinguishes between starting up and running the machine.

Start-up. The starting-up procedure is as follows:

1) Automatic formation of HT[15].
2) Setting of "groups" of parameters to reference values stored on disk; at present, touch buttons are allocated to ion source, LEBT, linac and HEBT focusing, rf (amplitudes and phases) LEBT steering and HEBT steering, respectively.
3) Control of beam intensities along the accelerator and emittance measurements at 50 MeV.
4) Log of all machine parameters.

Running. No permanent operator is needed in the linac control room. At present, the state of the machine is quickly obtained via process synoptics e.g. Fig. 7. In future, a "watch-dog" program should ease the control even more by indicating parameters which go out of the specified range.

Reliability

The reliability of all systems has been good. For the first two complete runs (each > 1000 hours) the downtime was 1.1% and 0.9%. A large fraction of this can be attributed to the inexperience of the operators and to a few "teething problems".

Acknowledgements

This project has actively involved the whole linac group with essential support in the PS Division, in particular on mechanical design, vacuum technology, magnetic measurements and mechanical and electronic fabrication. Additional help was provided within CERN on surveying and generally by SB Division. We have also profited from the traditional friendly collaboration with other labs and from the presence of many short and long term visitors. All the above have contributed significantly to the success of the project.

References

1. D. Warner (Editor), Project Study for a New 50 MeV Linear Accelerator for the CPS, CERN/MPS/LINP 73-1.
2. E. Boltezar, H. Haseroth, W. Pirkl, G. Plass, T.R. Sherwood, P. Standley, P. Têtu, U. Tallgren, D. Warner, M. Weiss, Review and Status of the CERN New 50 MeV Linac Project, Proc. of the 1976 Proton Linear Acc. Conf., p. 45, AECL-5677 (1976).
3. D. Warner, Accelerating Structure of the CERN New 50 MeV Linac, Ibid., p. 49.
4. D. Warner and M. Weiss, Beam Optics in the CERN 50 MeV Linac, Ibid, p. 245.
5. A. Cheretakis, J. Knott, P. Mead, A. van der Schueren and U. Tallgren, The Control System of the CERN New Linac, Ibd., p. 49.
6. J. Knott, D. Warner and M. Weiss, Adjustment of a Double Drift Harmonic Buncher and Bunch Shape Measurements, Ibid., p. 208.

7. J. Guyard and M. Weiss, Use of Beam Emittance Measurements in Matching Problems, Ibid., p. 254.
8. E. Boltezar, H. Haseroth, W. Pirkl, G. Plass, T. Sherwood, U. Tallgren, P. Têtu, D. Warner and M. Weiss, Performance of the New CERN 50 MeV Linac, Proc. of the 1979 Acc.Conf., IEEE Trans NS-26, No. 3 (1979), p. 3674.
9. E. Boltezar, Mechanical Design of the CERN Linac Accelerating Structure, This Conference.
10. H. Haseroth, M. Hone and J. Vallet, The Compensation for Beam Loading of the New CERN 50 MeV Linac, This Conference.
11. J. Cuperus, F. James and W. Pirkl, The RF system of the CERN "New Linac", This Conference.
12. P. Têtu, New Linac Three Phase Planes Pulsed Emittance Measurement, This Conference.
13. D. Warner, Calibration During Installation and During Initial Operation of the CERN 50 MeV Linac, This Conference.
14. M. Weiss, The Significance of Beam Optics Concepts as Applied to the New CERN Linac, This Conference.
15. H. Haseroth, Computer Controlled Formation of the 750 KeV Accelerating Column on the New CERN 50 MeV Linac, This Conference.
16. J. Grando, H. Haseroth, C. Hill and M. Hone, Tests with a Multi-Dipole Source on the CERN 500 keV Experimental Pre-accelerator, This Conference.
17. H. Haseroth and P. Têtu, Recent Operation and Modifications on the CPS 50 MeV Linac (Old Linac), Proc. 1976 Proton Linear Acc. Conf., p. 381, AECL-5677 (1976).
18. M. Weiss, Parameters of a New Linac Matched to Top PSB Performance, CERN/MPS/LINP/Note 72-1 (1972).
19. E. Boltezar, H. Malthouse and D. Warner, A 3 MeV Experimental Proton Linac, Proc. 1968 Proton Linac Acc. Conf., p. 626, BNL 50120 (1968).
20. D. Warner, Accelerator Research and Development with the CERN 3 MeV Linac, Proc. 1972 Proton Linear Acc. Conf., p. 33, LA-5115 (1972).
21. B. Bru and M. Weiss, Linac Quadrupole Gradients and Matching Parameters at Different Beam Intensities, Proc. 1970 Proton Linear Acc. Conf., p. 851, NAL (1970).
22. B. Bru and M. Weiss, Single and Double Drift Bunchers as Possible Injection Schemes for the CPS Linac. Proc. 1973 Particle Acc. Conf., IEEE Trans. Nucl. Sci., NS-20, p. 963 (1973).
23. R. Damm. A. Otis and V. Lo Grosso, Quadrupole Focusing System for the 200 MeV Linac, Proc. of the 1970 Proton Linear Acc. Conf., p. 561, NAL (1970).
24. R. Littlewood and C. Mazeline, The New Linac Quadrupole Measurement System, CERN/PS/SM/Note 78-8 (1978).
25. M. Bourgeois, Etude d'une Alimentation Pulsée et Régulée en Courant, CERN/MPS/LIN/Note 74-17 (1974).
26. M. Martini and D. Warner, Numerical Calculations of Linear Acc. Cavities, CERN 68-11(1968).
27. B. Bru and M. Weiss, Design of the Low Energy Beam Transport System for the New 50 MeV Linac, CERN/MPS/LIN 74-1 (1974).
28. P. Mead and U. Tallgren, Interfacing BASIC to the New Linac Control System, CERN/PS/LIN/Note 78-21 (1978).
29. B. Vosicki, M. Buzic and A. Cheretakis, The Duo-plasmatron Source for the CERN PS Linac, Proc. 1966 Linear Acc. Conf., p. 344, LA-3609 (1966).
30. J. Huguenin, R. Dubois, G. Visconti and R. El Bez, The New 500 keV Single Gap Preinjector Tube for the CERN Proton Synchrotron, Ibid., p. 355.
31. P. Mead, The System Software of the New Linac Control System, Proc. of the Digital Equipment Users Society, p. 93, Vol. 4, No. 1 (1977).
32. K. Schindl, Private Communication.

DISCUSSION

D.J. Liska, LASL: What was your reason for using aluminum seals throughout the machine?

Warner: They are cheap; the cavities do not need baking out and the force to deform them is small. Copper needs more (factor of 5) sealing force.

K. Mittag, Karlsruhe: How do the actual quadrupole settings used now correspond to those at the design stage - are they the same or did you change them?

Warner: We set them initially to $\mu = 30^{o}$ throughout the linac at one stage, but now μ is set slightly lower. As I pointed out, if we have an emittance growth, the μ will go up as you go along the linac because the space charge effect is decreasing. But we calculate quadrupole gradients with a program which has no emittance growth in it (normally).

K. Mittag: If you had used permanent quadrupoles to begin with, would the machine performance be as good now as it is?

Warner: We made a special attempt to bridge across the place where quadrupole sizes change and I am not sure you can do this with permanent magnet quadrupoles. I do not know whether you can design a permanent quadruple system to cover a large range of accelerated currents. In face, we lower the gradients for working at 50 mA or with a pencil beam. Even if permanent quadrupoles would have been available, I believe we still would have chosen quadrupoles which could be varied over the complete gradient range.

C. Curtis, FNAL: Starting with your design settings for the quads, have you then tried empirically various settings of the quads for the same beam current to see what happened to the quality of the beam?

Warner: We have the facility of adjusting the end quadrupoles (up or down) and the rest of the quadrupoles follow accordingly. This program is in FORTRAN. Now,the results are not very clear; there is a very broad optimum. I can give you an example. Where we varied the Tank II and III quadrupoles from 50% to 125% of normal operating level and

looked at the output beam position, it moved around, but the current only started to fall at about 60% of the normal operating level. So, you certainly could not use the beam current as a criterian for setting the quadrupoles.

Curtis: Did you measure the emittances at that time?

Warner: The emittances looked all right over a wide range, but this particular experiment was not aimed at measuring beam quality. We have not really investigated the beam quality as a function of the quadrupole law.

D. Hagerman, LASL: At LAMPF it has been essential to have the ability to reduce the quadrupole strength systematically so we can see what is going on inside a tank. It is a very tedious procedure, but I do not think we could have managed that machine without that technique being available. Therefore permanent quadrupole magnets would have been a bad choice.

S. Ohnuma, FNAL: Is the observed transverse emittance growth of 2 to 2.5 in agreement with the rms-type numerical calculation and, if so, what is the main cause of the emittance growth?

Warner: Our design predictions gave less transverse emittance growth but we made all our calculations with a larger input emittance (80π mm-mrad) compared to measured values of 50π-mm mrad. I believe we may have much less than that instantaneously because we measure the integrated emittance over 10 μsec. The longitudinal growth is also much higher than we calculate. To satisfy the booster synchrotron we are more concerned with the transverse emittance, but it is well within the acceptable level as we inject a much smaller emittance than was intended.

S. Ohnuma: Do you think you have gained a lot by having a fancy beam shaping system in the longitudinal phase space?

Warner: Yes. We insisted in the paper on the figure of merit being over 80% trapping, but the original aim was also to have the beam matched in longitudinal phase space at injection into the linac and we believe we have this also. We have not yet had much time for measurements but we will be able to do some more measurements in 1980.

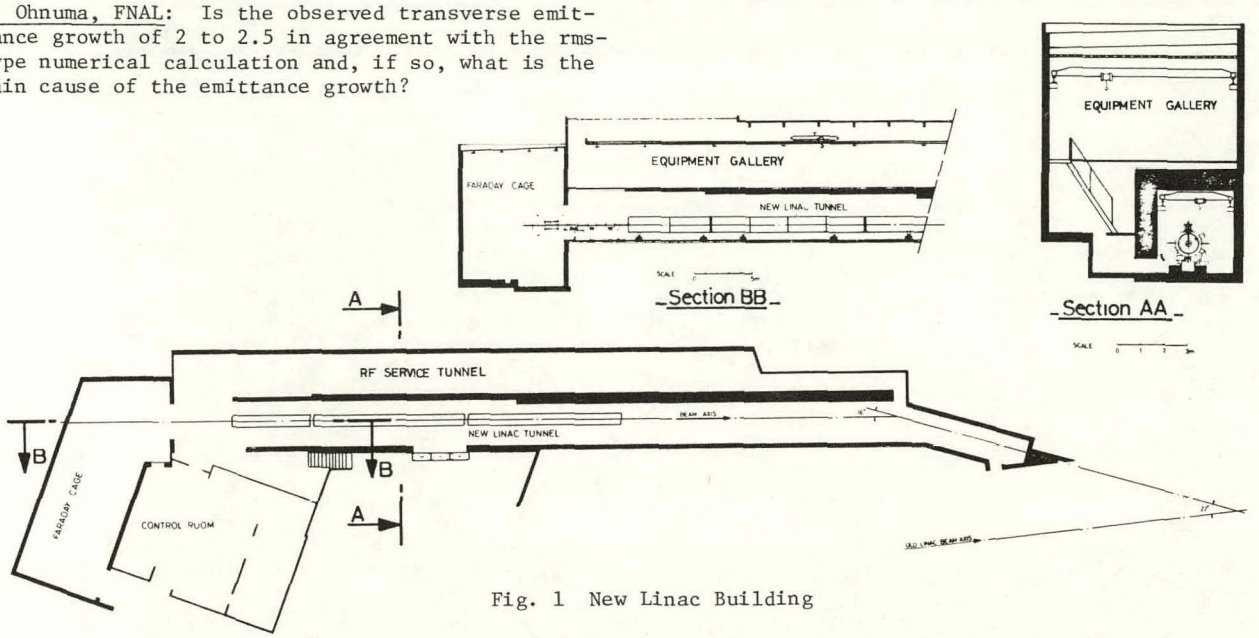


Fig. 1 New Linac Building

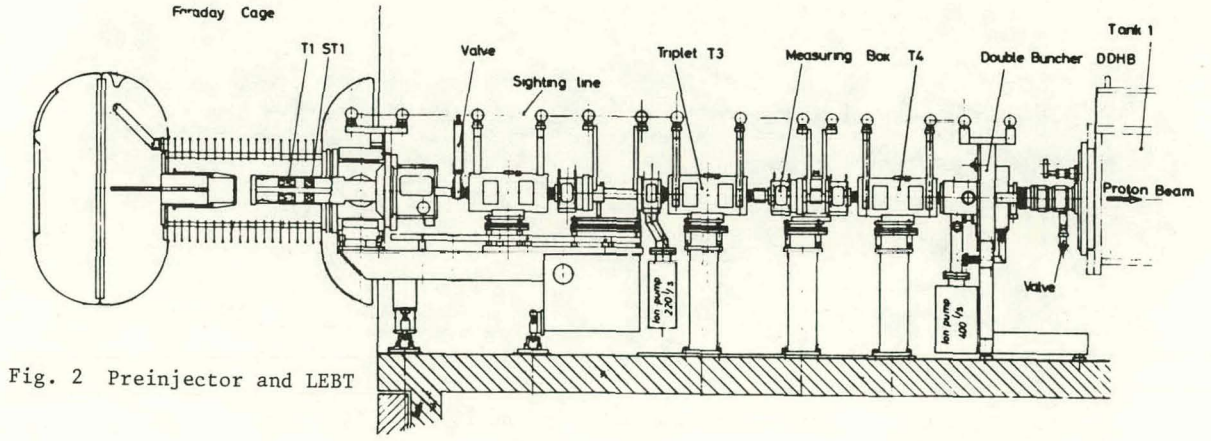


Fig. 2 Preinjector and LEBT

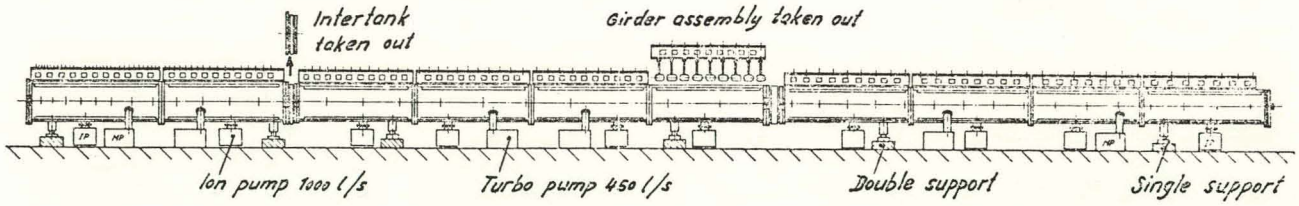


Fig. 3 Accelerating structure side view and cross-section above

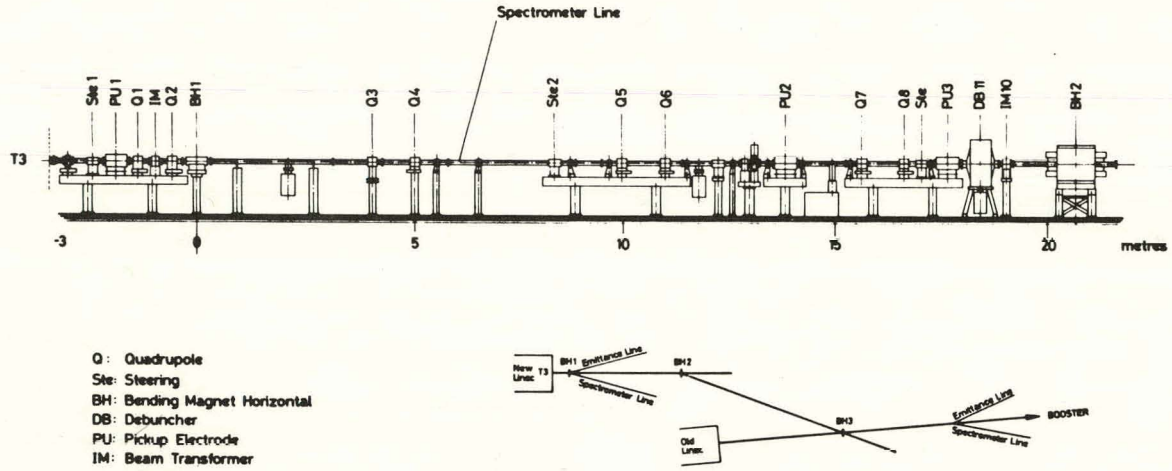


Fig. 4 HEBT side view to BH2 and schematic plan

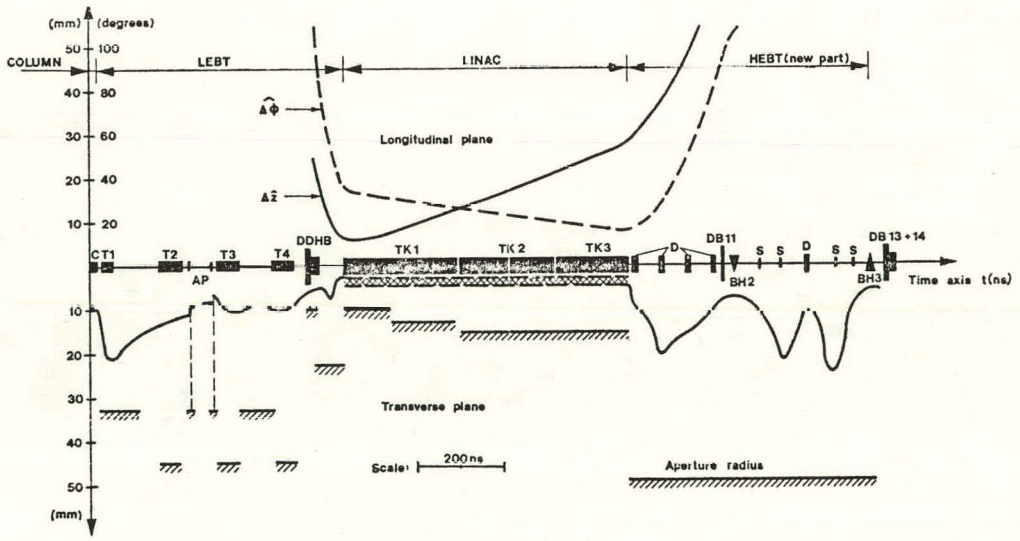


Fig. 5 Evolution of the beam from preinjector to debunchers

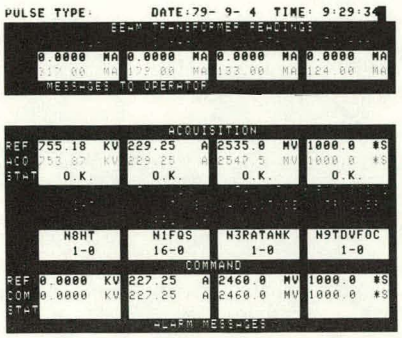


Fig. 6 Colour TV monitor on midiconsole

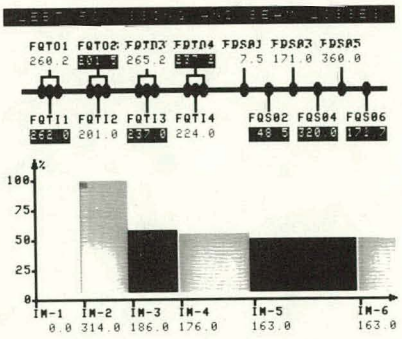


Fig. 7 Synoptic display of LEBT

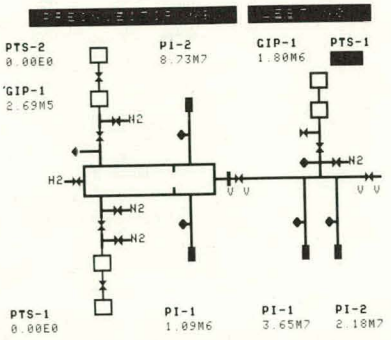


Fig. 8 Synoptic display of pre-injector and LEBT vacuum

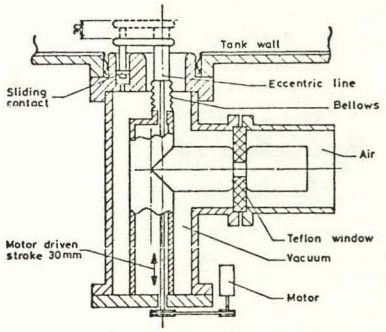
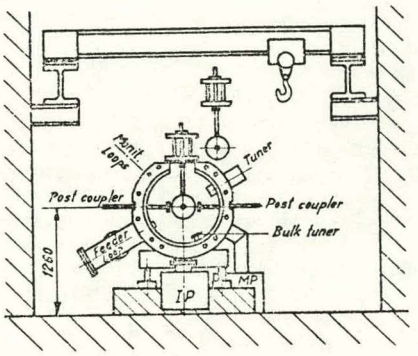


Fig. 9 RF Feed Loop (schematic)



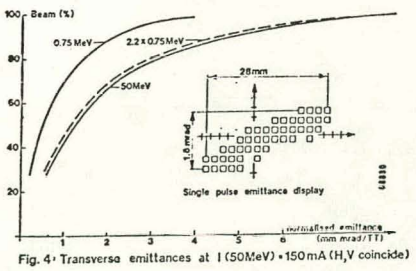


Fig. 4: Transverse emittances at I (50MeV) = 150mA (H,V coincide)

Fig. 10 Transverse emittances for I = 150 mA (H,V coincide)

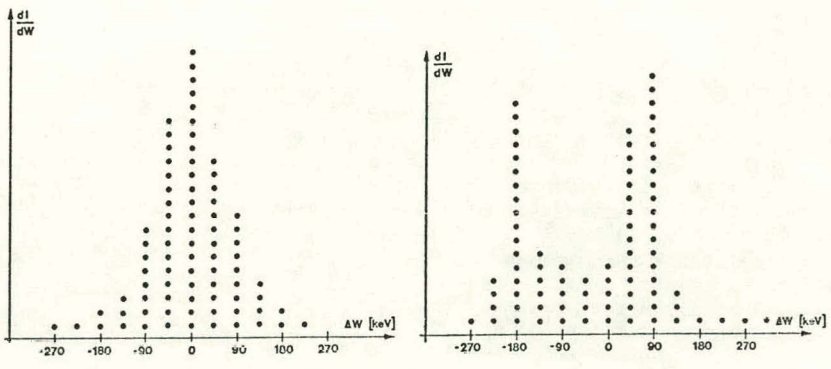


Fig. 11 Energy spectrum at "old" measuring lines
a) normal b) hollow

1979 LINEAR ACCELERATOR CONFERENCE

LAMPF OPERATIONS AT 500 μA*

D. C. Hagerman
Los Alamos Scientific Laboratory
Los Alamos, New Mexico 87544

Summary

LAMPF now operates reliably producing 500 μA of H^+ beam and a few μA of H^- beam or 10 nA of polarized H^- beam. Beam loss in the accelerator is quite acceptable at these currents. This level of performance has been achieved through solution of a wide variety of accelerator problems and a continuous evolution of the experimental areas. The future of the facility is promising both in terms of the existing experimental programs and the opportunities for significant facility improvement projects.

Introduction

The Los Alamos Meson Physics Facility** (LAMPF) accelerator has matured in the sense that it runs reliably at significant currents and apparently can fulfill all of the expectations of its designers and builders. In addition to the high-current beam a low-current H^- beam is simultaneously produced. This combined operation satisfies the needs of a very broad research program. It has taken more than seven years, after the first full-energy beam, to reach this level of performance. This rather lengthy time scale has many different causes including complexity of the accelerator, unprecedented beam currents, need for production operation pre-empting time for accelerator development, lack of adequate test dumps for high-current beams, and budgetary problems. Nonetheless, this machine has served the needs of the research program very well for several years in addition to being a major step in the art of accelerator technology.

General descriptions of this accelerator are given in several sources.[1,2,3] Briefly, the machine simultaneously produces H^+ and H^- beams at a maximum energy of 800 MeV. The H^+ ion source is duoplasmatron.[4] The H^- ions are provided from either a duoplasmatron charge-exchange source or a Lamb shift polarized source. Each source has its own Cockcroft-Walton machine to accelerate the ions to the 750 keV injection energy. Acceleration[5] from 750 keV to 100 MeV is accomplished in a drift-tube accelerator that is post coupled above 5 MeV; this operates at an rf frequency of 201.25 MHz. From 100 to 800 MeV a side-coupled accelerator is used operating at 805 MHz. The overall length of the accelerator is ∿780 m. Peak rf power required is about 50 MW. The macroscopic beam duty factor is 7.5% with 120 macroscopic pulses/s. The H^+ beam is the high-intensity beam and is used primarily for meson production. The H^- beams are low intensity and used for a variety of nucleon-nucleon or nucleon-nucleus research programs.

* Work performed under the auspices of the Department of Energy.

** The formal name is the Clinton P. Anderson Meson Physics Facility located at Los Alamos, New Mexico, U.S.A.

Progress in Beam Quality

A simple measure of our progress in beam quality is shown in Figure 1 which displays the relative beam induced activation (normalized to production current) of the high-energy portion of the accelerator as a function of H^+ production current. The beam induced activation has been averaged over many locations and long periods of time so it is a trend indicator rather than a measure of the quality of any particular beam.

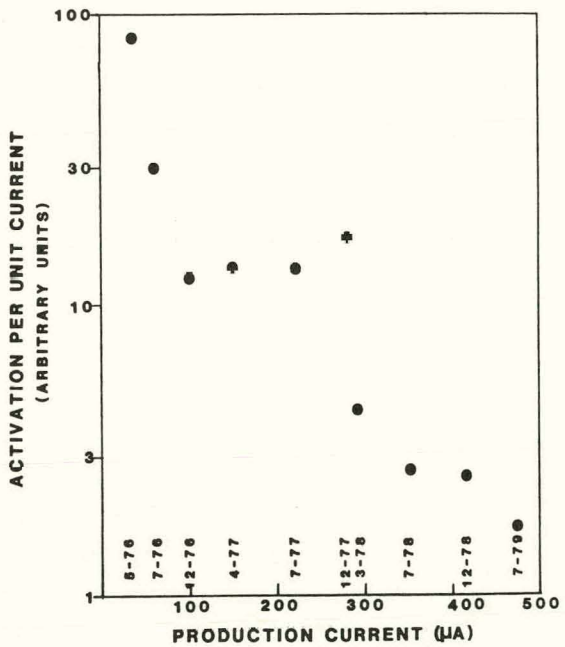


Fig. 1 A short history of accelerator activation and LAMPF average production beam current. Activation is the average of 67 separate measurements in the side-coupled linac between 240 and 800 MeV; each measurement is at a limiting aperture. The dates are a few weeks after start of production operation at that current.

If the emittance of the beam increased with current and the accelerator acceptance was unchanged during the period described by this figure, the activation would have increased faster than the current increased. Instead, this measure of beam loss dropped nearly a factor of 40 while the current was increased a factor of 13. This improved performance is the result of both reduced beam emittance at injection and improved acceptance of the accelerator.

The improvements in the emittance of the H^+ beam at injection have resulted from a variety of geometry and field changes in the source. In general, apertures are now smaller, hydrogen pressure and arc current are higher, and the extraction field has been modified from the original Pierce geometry. The result of these changes is that the emittance of an 8 mA beam is now about the same as that of a 2 mA beam a few years ago.

Improving the acceptance of the accelerator has been an iterative process since the first operation of the machine. One of the perplexing aspects of this development work has been the difficulty in determining, at any particular stage of development, the dominant cause of beam spill. This difficulty is caused in part by the very achromatic beam transport of the accelerator which can transport off-energy beam a long distance before it hits the wall of the accelerator and is detected by a spill monitor. For example, beam spill at that location in the accelerator corresponding to, for example, a beam energy of 365 MeV can be caused by any one or combination of the following: (a) improper adjustment or operation of any of the 24 rf amplifier accelerator structure subsystems upstream of this point, (b) some defect in injector operation or adjustment, (c) poor steering causing the beam to strike the wall at this location or be accelerated improperly at some upstream location, and (d) misadjustment of some quadrupole focusing element causing a large radial excursion in the beam envelope at this point. Anyone of these difficulties can be masked by some other compensating defect for that particular spill location; yet, when two things are wrong the overall machine acceptance is reduced even though some localized spill is improved. This extremely complex set of inter-relationships has been partially unraveled by many different development projects, nearly all of which required a significant effort in computer simulation of the beam in the accelerator. In addition, reliability and reproducibility of machine parameters has been greatly improved by diligent attention to the quality and performance of accelerator components. Some specific problem areas that have received attention are:

1. Comprehensive studies searching for the optimum longitudinal tune of the machine (i.e., optimum phase and amplitude values for the accelerating field) have been done. This problem has required development of very accurate techniques for measurement of beam properties since all accurate phase and amplitude setpoints are derived from observed effects of the field on the beam.

2. By using a combination of the beam as an indicator of misalignments and the best available surveying techniques, the machine has been systematically realigned.

3. The long (~12 m) 750 keV transport lines connecting the injectors to the accelerator are troublesome since the beams have varying degrees of space charge neutralization along the transport system. Much of the tuning done in these lines is still very pragmatic in nature.

4. The general problem of matching simultaneously both H^+ and H^- beams is one of the major limitations in machine performance. These beams have different emittances and intensities at injection, hence, space-charge forces are different. Further, in the 100-MeV transition region, where the beams are spatially separated, not enough degrees of freedom are available to satisfactorily match both beams into the side-coupled linac.

A more quantitative measure of the degree of perfection of our present beams is that at 500 μA H^+ production current the beam lost between 70 and 800 MeV ranges from a few parts in 5000 to 2 parts in 500 with the typical value of 1 part in 1000. The off-energy portion of this beam that is lost in the switchyard is significantly less than 1 part in 10,000. When an H^- beam of 3 to 5 μA is accelerated simultaneously with the 500 μA H^+ beam, spill is increased in a minor way at a few locations.

Accelerator Tuneup

The procedures for complete tuneup are now very well understood with only a few exceptions associated with radial beam matching and optimization of drift-tube linac performance. Assuming that all equipment is operational and no major increase in beam current is planned something like three shifts are necessary for a complete tuneup. Six to nine shifts are usually scheduled for this activity at the start of a cycle since we continue to make changes in the ion sources or current on a cycle-by-cycle basis.

The reproducibility and stability of the equipment is now good enough so that a complete retune is required only three to five times a year. This reproducibility was strengthened significantly by the development of redundant methods of measuring and systematic monitoring of the most important accelerator parameters. By using all the information available, it is practical and routine to reproduce a satisfactory beam in short order even though one or more setpoints have been lost due to equipment failures. The control computer of course is essential in any tune-up operation.*

* The main control computer can be turned off during production without losing beam or any element of beam protection. Operation of one smaller computer is required at all times to maintain integrity of beam protection devices in the experimental area.

Some idea of the complexity of the tuneup can be gained from the brief listing of the more important tuning algorithms or measurement techniques given below. Nearly all measurements are processed through the computer which transforms the data into some easily understood form.

Transverse Tuning

1. Emittance measurements[6] provide beam size, orientation, centroid position, and centroid angular information that is used as input to matching and steering programs so that the beam is properly focused and steered into the accelerator.

2. Wire scanners provide beam position and size information used for steering and check of radial match. Beam position can also be measured by a nonintercepting system.

3. Experimental area beam profile measurements are made with harps or wire scanners.[7]

4. Experimental area main beam-line magnets are set up using a computer algorithm that cycles the magnets to selected field strengths.

Longitudinal Tuning

1. Drift-tube accelerator phase and amplitude setpoints are determined from phase-scan measurements that are compared with computer simulations. These measurements also include a differential phase scan to measure phase width of the beam entering the side-coupled linac.

2. A beam energy measurement using a time-of-flight method based on rf measurement techniques in combination with a detailed simulation of the side-coupled linac is used to determine phase and amplitude setpoints between 100 and 800 MeV. This is the only fully automated closed-loop tuning algorithm presently in use.

3. Energy width and low-energy components of the beam are measured in the switchyard where the beam transports provide energy dispersion. These measurements are particularly valuable in elucidating minor errors in the longitudinal tune.

Display Programs

1. A wide variety of computer displays are in use that present accelerator and beam parameters in a variety of formats. Graphical displays are particularly valuable when evaluating machine performance.

2. All important parameters are monitored; significant changes in value are automatically called to the attention of the operator.

Protection Methods

1. The usual sort of hardwired "run-permit" system controls personnel access and requires that the necessary equipment be "on" before beam can be turned on.

2. A "fast-protect" system[8] switches off beam on a 10 μs time scale in the event of malfunction of an rf amplifier, excessive beam loss, etc.

3. Beam transmission is continuously monitored by radiation detectors and differential current-measuring devices. These turn off the machine automatically if loss exceeds a predetermined value.

Beam Availability and Machine Reliability

During FY 1979 (Oct. 1978-Sept. 1979), production beam was scheduled for nearly 4600 h and long-term average beam availability was typically in excess of 80%. Of course, beam availability has wide variations from day-to-day. Difficulties that cause extended off periods (4 to 24 h) are infrequent; during the past year this level of difficulty has been caused by ion-source problems, control computer problems, major power outages, or some vacuum or rf-system fault in the drift-tube accelerator. Off periods ranging from a few minutes to 4 h are more frequent and are caused by minor vacuum failures, tube faults, or minor failure of some sub-system.

The availability of the experimental area plays an important role in overall beam availability; some of its particular problems are discussed below. Unfortunately, when a major experimental area problem arises its repair is frequently a matter of weeks which causes a major shift in schedules. Sensible definitions of beam availability in that circumstance are lacking. During FY 1979, we had one such incident that occurred between production cycles and caused a delay of the next production cycle for about two months.

Use of the facility is scheduled in terms of production cycles that have recently ranged in length from 8 to 15 weeks. In each production cycle, maintenance days (24 h total beam interruption) are scheduled on alternate weeks. Short development periods (12 h) are also scheduled on alternate weeks. Longer development periods are scheduled at midcycle and before and after each cycle. During the cycle, each week has on the average 132 h of production beam scheduled.

During the design of LAMPF, electron tube lifetime was a major concern and it was thought that this would be a strongly limiting factor on beam availability. Happily this has not been the case. Our latest information on tube lifetime is given in Table I for some of the more important tubes. The klystron information should be statistically sound due to the large amount of operating experience. In all cases, the data clearly displays a very satisfactory range of tube life.

The Experimental Areas

Successful operation and development of the accelerator is strongly dependent on the viability of the experimental areas. In turn, success of the entire facility depends on the vitality of the experimental program. It is inappropriate in this

paper to discuss the experimental program but some description must be made of the experimental areas.

The most important features of the experimental areas[9] are those that permit simultaneous performance of 10 to 12 experiments. The H^- low-intensity beam is easily split into as many as three beams by change of charge state in thin foils; these beams are used either for direct interaction studies and/or for production of neutron beams.

The H^+ beam provides mesons in six secondary beam channels, is used for isotope production, and provides neutrinos from the beam stop. The beam passes sequentially through three targets, finally coming to rest in the beam stop. Time sharing is used to provide H^+ beam to a pulsed neutron facility. A high-resolution (50 keV) proton spectrometer and a high-resolution pion spectrometer (150 keV) are permanently installed. Two of the meson channels provide beam to multiple caves giving great freedom in scheduling use of these particular beams.

The overall utility of the H^- beams will be increased when the time-shared dual-energy operation starts next spring. Increased flexibility in the use of the polarized beams will be provided when installation of spin-rotation equipment in the switchyard is completed this winter.

The high-intensity H^+ beam (500 μA average current ≡ 400 kW beam power) must be very accurately controlled in position and size to avoid damage to targets, beam pipes or windows; this control requires accurate measurement of beam properties and continued monitoring of beam transmission. The target cells are difficult engineering problems. The level of induced activity is so high that they can only be serviced with remote handling techniques. The heat load from the targets is significant and all components in the vicinity of the targets or beam stop are subject to high levels of radiation damage. Progress to higher current will be paced by the ability of the experimental area to accept increased beam power.

Future Development Work

The preceeding paragraphs support the position that nearly all of the original expectations for the performance of LAMPF have been fulfilled. The major step yet to be made is that of routine production at the 1 mA level. This level of operation is nearly in hand from the accelerator. Duty-factor tests in late August 1979 showed that 9% duty-factor operation is practical without major retrofitting. Recent beam tests at peak currents of 13 mA show satisfactory beam quality, so an average current from the accelerator of 1 mA is within reach. However, operation at 1 mA average current may well uncover major problems in the experimental area which thus far has seen a maximum average current of only 670 μA.

Other improvements in the facility are mainly in response to the requirements of the experimental program. In the spring of 1980, a time-sharing method of providing a lower energy H^- beam will be in operation. This will provide an H^- beam of energy, as needed, between 400 and 800 while an H^+ beam of 800 MeV is produced. A more sophisticated method of dual-energy operation has been explored and is reported in a separate paper at this conference.[10]

Similarly, there is a strong demand for higher intensity polarized beams. The present source should be operating in late 1980 at the 30 nA level using known technology. If the atomic beam sources prove practical, one of these devices will be installed in a few years.

Further in the future, a 100 μA average-current proton storage ring[11] is to be filled from LAMPF. This will use a high-intensity H^- beam that will necessitate major changes in the H^- injector and transport, the transition region, and the switchyard. Changes in the transition region will be made first since they will upgrade the present dual-beam operation significantly.

TABLE I

Tube Type	Function	Total Operating Experience (Mh)	Mean Life (kh)
7835*	Triode rf amplifier	0.14	12
4CW250,000	Series modulator	0.27	10
LPT-44**	Switch tube	1.7	19
VA862A	Klystron rf amplifier	1.4	50
L-5120	Klystron rf amplifier	0.3	12

*At the time of writing, LAMPF had on line two 7835 tubes that had been in use 30 kh.

**These high-voltage switch tubes require reprocessing every 2 to 3 kh.

Acknowledgement

The LAMPF project was first discussed some 17 years ago; a proper acknowledgement of the contributions made by a large number of people is beyond the scope of this report. Lew Agnew, Andrew Browman, Joe Bergstein, Ralph Stevens, Jr., Bob Cady, Lois Rayburn, and George Tubb were very helpful in preparing this paper.

References

1 D.C. Hagerman, "Meson Factories - 1977," IEEE Trans. Nuc. Sci., Vol. NS-24, No. 3, June 1977, pp. 1605-1610.

2 E.G. Michaelis, "Review of Meson Factories," IEEE Trans. Nuc. Sci., Vol. NS-23, No. 3, June 1975, pp. 1385-1396.

3 D.C. Hagerman, "The Status of LAMPF," Proc. 1976 Linear Accelerator Conf., AECL-5677, Sept. 14-17, 1976, pp. 12-19.

[4] R.R. Stevens, Jr., J.R. McConnell, E.P. Chamberlin, R.W. Hamm, and R.L. York, "Injector Operations at LAMPF," Proc. this Conference.

[5] E.A. Knapp, "High-Energy Structures" in Linear Accelerators, P.M. Lapastolle and A.L. Septier, Eds. (North-Holland Publishing Co., Amsterdam, 1970) pp. 601-616.

[6] O.R. Sander, G.N. Minerbo, R.A. Jameson, and D.D. Chamberlin, "Tomography in Two and Four Dimensions," Proc. this Conference.

[7] E.W. Hoffman et al., "High Intensity Beam Profile Measurements for the LAMPF Primary Beam Lines," IEEE Trans. Nuc. Sci., Vol. NS-26, No. 3, June 1979, pp. 3420-3422.

[8] A.R. Swanson and R.E. Hill, "LAMPF First-Fault Identifier for Fast Transient Faults," Proc. this Conference.

[9] LAMPF Users Handbook (November 1974).

[10] G.R. Swain and D.C. Hagerman, "Simultaneous Beam of Different Energy from LAMPF," Proc. this Conference.

[11] R.K. Cooper and G.P. Lawrence, "The Design of the WNR Proton Storage Ring Lattice," IEEE Trans. on Nuc. Sci., Vol. NS-24, No. 3, June 1977, pp. 1037-1039.

1979 LINEAR ACCELERATOR CONFERENCE

OPERATION OF THE BROOKHAVEN 200-MeV LINAC*

N.M. Fewell and V. LoDestro
Brookhaven National Laboratory
Upton, New York 11973

Introduction

At the last Linear Accelerator Conference held at Chalk River, Kenneth Batchelor[1] reported on the first five years of operations of the BNL 200-MeV linac. This paper describes the recent modifications to the machine and its continued operational status.

Operational Performance

The linac continues to run in a very reliable manner; Fig. 1 shows that the reliability has risen to 95% of the scheduled operating time of approximately 6,000 hrs/year. Machine downtime has stabilized to an average of 250 hrs/year over the past three years. This low figure has been accomplished even though the linac building is manned only during normal working hours. After the normal workday period, the AGS operators, who are remote from the linac building, must diagnose and rectify the fault, or in more complex failures, call in linac personnel.

The linac continues to run at 5 pps, with short runs at 6.7 pps for the Chemistry line; the normal AGS requirement is 1 pulse/2.4 sec. The repetition rate was reduced from 10 pps at the beginning of 1976 due to a series of 60-kV power supply transformer and 12-inch transmission line failures. Running at the lower repetition rate has reduced these failures considerably and although the average current delivered to the BLIP facility was reduced, the total current/year has actually increased. The linac average monthly output current for the past three years is shown in Fig. 2; it can be seen that we now run with a peak intensity of about 60 mA. Prior to September 1978, we had run long periods in excess of 70 mA and at times, 80 mA; however, after running in this manner, we noticed a marked decrease in the life of our RCA 7835 power triodes. (This is discussed later.) The output current of the linac was, therefore, reduced to 60 mA which is sufficient for the AGS to run at 1 x 10^{13} protons/pulse.

System Performance

Rf System

A year-by-year breakdown of system failure is shown in Fig. 3. It can be seen that although the rf system accounts for 50% of the linac downtime, the actual hours of downtime have fallen to an average of 120 hrs/year. Approximately half of this time are minor faults of less than one

LINAC OPERATIONAL PERFORMANCE

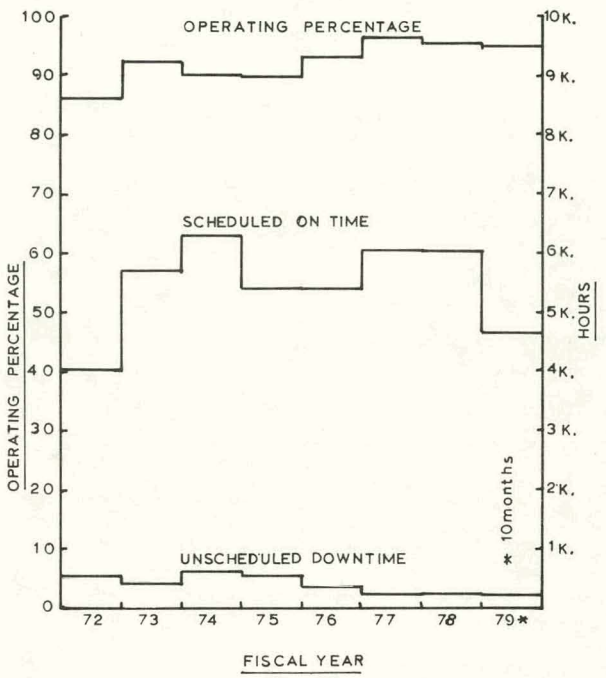


Fig. 1

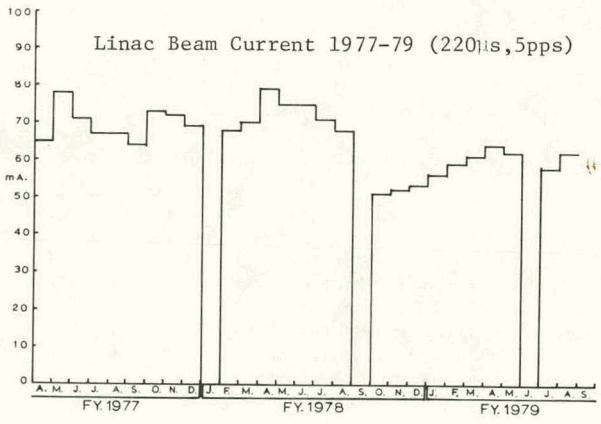


Fig. 2

*Work performed under the auspices of the U.S. Department of Energy.

hour, such as tuning, etc. On the whole, the rf systems perform very well and it is difficult to pick out an area which could significantly reduce the downtime further.

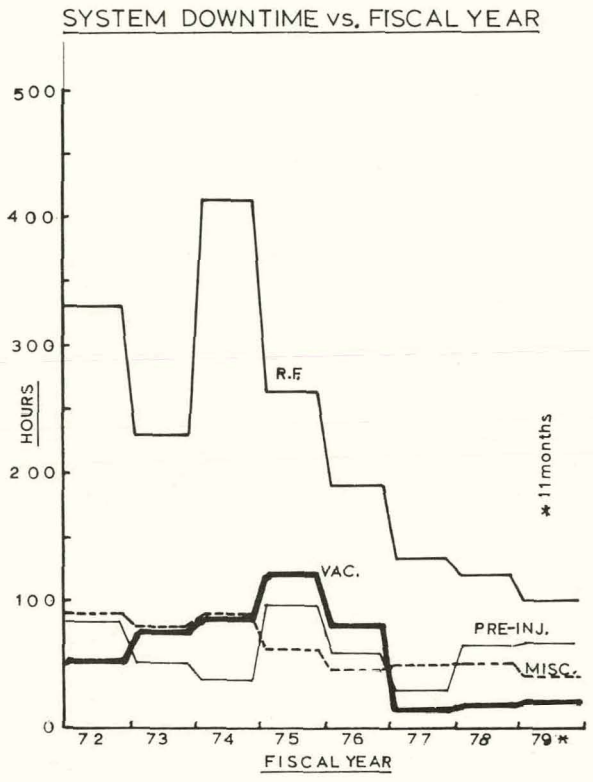


Fig. 3

Vacuum System

The vacuum system, which was the second major contributor to downtime, now only accounts for approximately 20 hrs/year. This improvement is mainly due to the changes in tank monitor probes and BLIP transport line, described by Ken Batchelor at the last Linac Conference, and also due to the long radiation monitoring system[2] that inhibits the beam, if the radiation at any point along the machine exceeds a pre-set limit, i.e., it keeps the machine honest.

Preinjector

Problems with the ion source and the bouncer account for most of the approximately 65 hrs/year of downtime attributed to the preinjector. We went through a period when the source filament life steadily declined and they had to be run at increasingly higher currents to obtain a discharge. Finally after changing the complete source, it was discovered that the source had a minute freon leak. This leak, although difficult to find (10^{-8} mmHg scale) was sufficient to poison the filament. Los Alamos has recently experienced a similar fault.

Leaking oil on the Cockcroft-Walton generator stack led to the discovery of a badly burnt capacitor, Fig. 4. This failure is thought to be due to

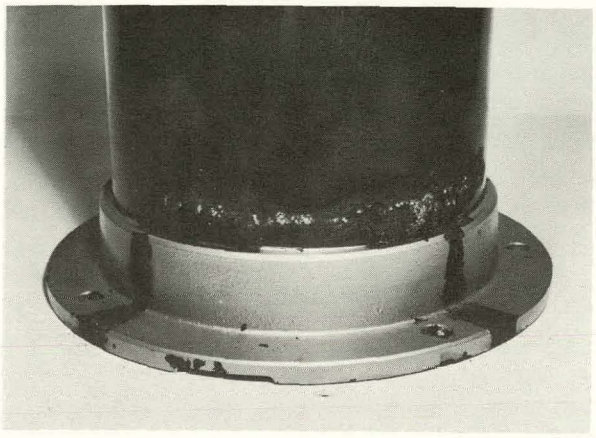


Fig. 4. Damaged Cockcroft-Walton capacitor.

the fact that these capacitors have painted mounting flanges onto which corona shields are clipped. The paint is non-conductive and arcing through the paint due to the ac component between the flange and shield has occurred. It seems that this arcing also occurred from the top of the corona shield through the glass-epoxy case to the capacitor sufficient to burn a large area of the case. Flexible connecting straps have now been connected from the mounting flanges to the corona shields to prevent this from recurring.

More recently, several small vacuum leaks were found around one of the ceramic spacer joints of the high gradient column. These were filled by an epoxy bead applied around the joint while the column was under vacuum. The high voltage was applied two days later and no difficulty was found in conditioning the column.

Miscellaneous Systems

The final 50 hrs/year of downtime is due to the remaining control, quadrupole, water systems etc.; no significant reduction in this downtime is likely.

Machine Modifications and Improvements

Radio Frequency Interference

An off-site complaint of TV reception interference initiated an investigation into the rf radiation from the linac building. The building which houses the rf system is approximately 500 ft long and is clad in aluminum. Field strength measurements outside this building confirmed two radiation lobes of sufficient strength to cause TV interference. Measurements inside the building indicated that the main rf leakage areas were

the grid-input sliding section of the 7835 power amplifier, its grid cooling hose and the RCA driver cart. These inside measurements, however, were well below the Federal limit of 2 MW/m^2. Metal braid was placed over the grid cooling hose and metal "top hats" were placed over the input sections of the 7835 cavities, Fig. 5. This resulted in a 22 db decrease in the radiation levels outside the building.

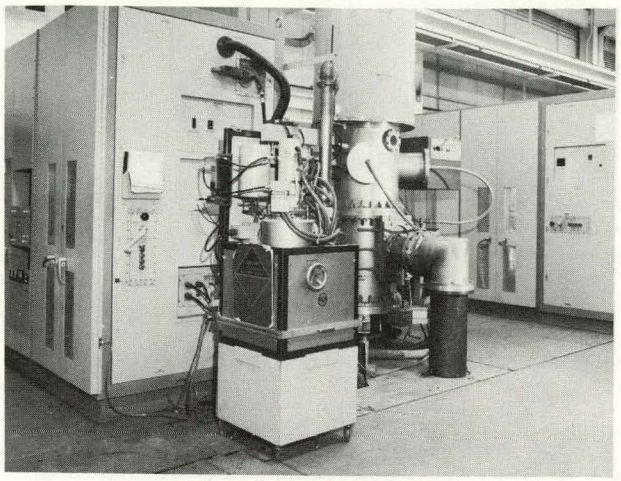


Fig. 5. 7835 power amplifier with RFI shielded input section.

The RCA driver cart is now the major source of RFI. This cart houses a 4616 driver stage with its two 7651 pre-driver stages. In its present form this is very difficult to shield. However, due to the age of the 7651 amplifier cavities and the cost of maintaining them, the first pre-driver stage will be replaced by a 350 W solid-state amplifier stage. This will free up spare units for the second stage and also allow us to remodel the driver cart to allow for RFI shielding.

7835 Tube Life

As has been stated earlier, the linac beam output has been reduced to 60 mA because of the reduction in tube life. At BNL we have accumulated in excess of 500,000 hours of 7835 tube operation. From this operational experience, together with data supplied by RCA, we are able to predict reasonably well the expected filament life of an 7835 tube at BNL. Here we run the filament current just above the emission limiting point that will give the required power output conditions. This power requirement and, therefore, filament current is determined by the accelerating tank powered and the beam accelerated. The large difference in accelerating power requirement shows up a large difference in tube life; this is shown in Fig. 6 where tube life for a number of tubes is plotted against the plate power required. The scatter on the graph is due to incomplete records of linac beam levels and some movement of tubes to

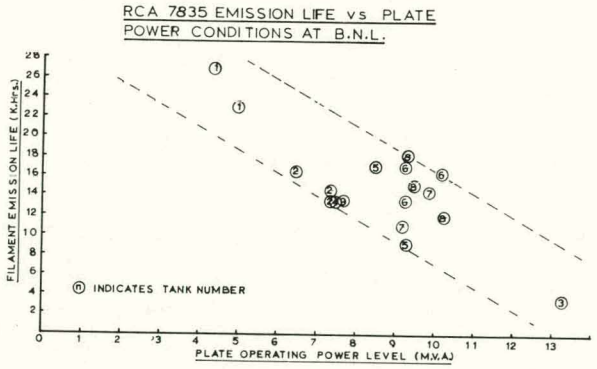


Fig. 6

different tanks; however, the trend is quite clear. Measurements of the necessary filament current for various linac beam currents were made on tank #2 which is typical of most of the linac tanks. Calculated filament temperatures for these currents are supplied by RCA[3] and using these temperatures, life expectancy was obtained from a curve by Ayer.[3] These results are plotted in Fig. 7 and are in good agreement with our actual experience.

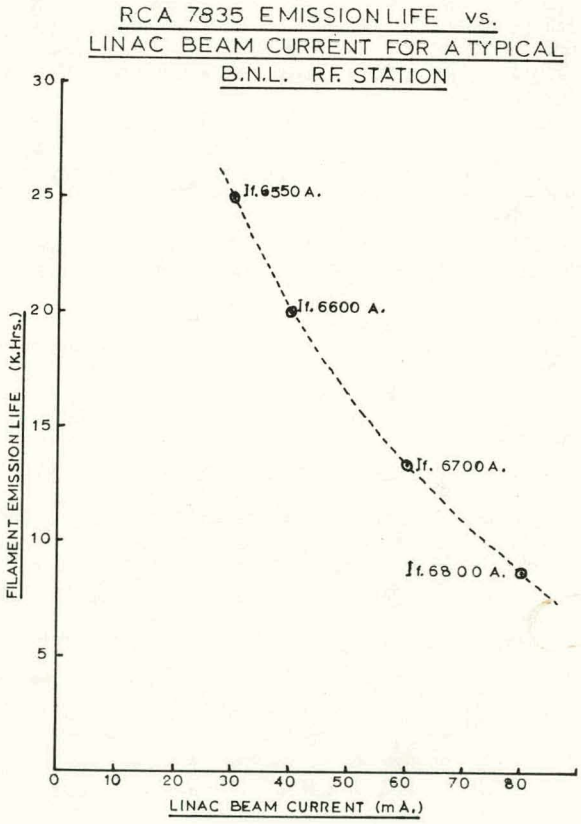


Fig. 7

Rf Phase Control System

The low level phase control system[4] utilizes a number of phase shifters to bring the phase of the rf inputs to the phase servo to within its control range of ±35°. These phase shifters are also used in the phase monitoring systems. Initially these phase shifters were mechanically adjusted with a phase range of 180°. Because of this limited phase range and also because of mechanical problems, these phase shifters were replaced by electronically controlled units having a phase range in excess of 360°. Similar 180° units are now being installed as the controlling element, together with a new control amplifier card, to replace the old phase servo control. By separating the rf signals and control, we have a more stable system with a greater phase range and faster servo time than the old system.

Rf Phase Shifter Design

These phase shifters use the same principles used at the P.L.A. at the Rutherford Laboratory.[5] However, this phase shifter uses strip-line techniques that enable a very compact unit to be made with a large phase range. The 180° units are composed of a 3 db, 90° strip-line coupler with varactor diodes on control ports 2 and 4. The phase change for this type of coupler is equal to the angular change in reflection coefficient at each of the control ports. The varactor diodes used (BB-105A) give a 90° angular change at 200 MHz for a bias change of 0 to 10 V. However, this angular change is increased to 180° at the control port by the use of an intermediate high impedance transmission line of suitable length. With the low dielectric constant strip line board used, the required strip width of this intermediate line would be impractically thin. This was overcome by spiralling the line and removing the ground plane on either side of it.

The 360° units are two 180° units in series printed on one board. The characteristics of these shifters are shown in Table I.

180° Phase Shifter - (D28-ILE-695)

Control Voltage	0 thru 10 Volts
Phase Shift	0 thru 210°
VSWR	1 thru 1.2
Insertion Loss	0.2 thru 0.6 db

TABLE I

Preinjector

As mentioned in the last conference, the old Phillips set has been installed in the second preinjector pit. It has run satisfactorily and the Heavy Ion Fusion Group[6] has accelerated both protons and Xenon using a standard BNL duoplasmatron ion source. After completion of that program, the Linac Group is now preparing the preinjector to accelerate an H^- beam.[7]

Machine Users

Brookhaven Linac Isotope Producer (BLIP)

As mentioned earlier, the average beam current to BLIP was reduced at the beginning of 1976 to increase the reliability of the linac operation. This increase in reliability has made up for the low beam current as is shown in Fig. 8. The total

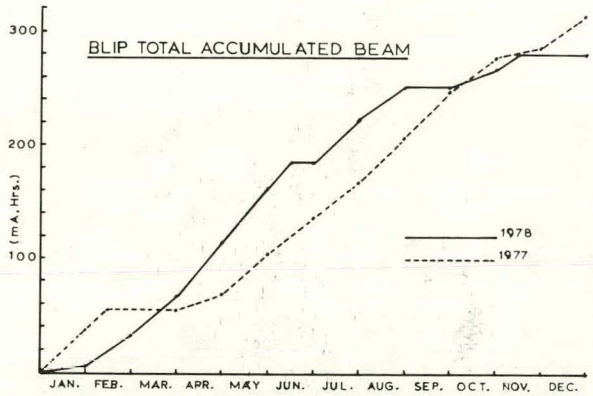


Fig. 8

intergrated beam for 1977 and 1978 was 315 mA hours and 280 mA hours compared with 133 mA hours and 177 mA hours for the previous two years. This is reflected in a production of 34,820 mCi of Xenon-127 in 1978, compared to 5,640 mCi in 1976. This production rate will, however, be somewhat less in the future due to reducing the peak current of the linac to 60 mA.

Chemistry Linac Irradiation Facility (CLIF)

Since the last conference, this beam facility has been renamed, "The Medium Energy Intense Neutron (MEIN) Facility". The MEIN facility produces an intense, energetic beam of neutrons by stopping the 200-MeV proton beam of the linac in a water-cooled copper beam stop. Yields of neutron-deficient isotopes in the product element relative to the desired neutron-rich isotopes can be suppressed by factors of 10 to 100 through the use of these energetic neutrons instead of using protons. Characterization of the decays of new neutron-rich nuclei is thus made possible in spite of their generally short half-lives. Decay scheme information and atomic mass measurements from these studies are useful when applied as checks of current theoretical models for the behavior of nuclei far from stability. It is in this manner that the discovery of ^{196}Os was reported in October 1977.[8]

Brookhaven Proton Bio-Medical Facility

Medical applications of the linac are being developed in a spur beam dedicated to this purpose ("The Brookhaven Proton Bio-Medical Facility").

Three avenues have been pursued to date.

Visualization of the proton beam interaction volume by means of in vivo activation of positron emitters, Oxygen-15 with two minute half-life and Carbon-11 with 20 minute half-life, has been demonstrated.[9] An extension of this technique offers exciting possibilities for quality control in particle beam therapy.

The second application, presently in the planning stage, is "radio-surgery", using the proton beam for ablation of intra-cranial benign tumors. This approach uses multiple beams with different entrance sites, with the Bragg peaks from each beam overlapping at the target volume. This technique produces a nearly ideal concentration of dose at the tumor, while sparing nearby critical organs.

The third application currently being developed is the study of the transport, from a locally irradiated volume, of the positron emitters produced by the beam interaction in tissue.[10] The Oxygen-15 generated is principally bound in water molecules. This labeled water is removed from the beam interaction region by means of perfusion. Information is thus available concerning regional blood flow. The carbon isotope appears to offer similar data about local metabolism. This facility is the only one with a positron camera on-line with a penetrating particle beam.

Conclusions

During the past three years the 200 MeV-linear accelerator has continued to operate at a high level of performance and reliability. The linac output beam current has been limited to 60 mA in order to obtain the maximum rf power tube life without compromising the output performance of the AGS. Despite a reduction in pulse repetition rate, total beam current to the BLIP facility has increased to an average of 300 mA hrs/year.

Acknowledgments

The authors wish to acknowledge the dedicated work of the linac maintenance technicians whose efforts play such an important part in maintaining the excellent record of this machine. The help given by J. Stabley of RCA in understanding the factors governing tube life is also acknowledged.

References

1. K. Batchelor, Linear Accelerator Development at Brookhaven National Laboratory, Proc. 1976 Proton Linear Accel. Conf., Chalk Rover, AECL-5677.
2. J. Balsamo, N.M. Fewell, J.D. Klein, R.L. Witkover, IEEE Trans. Nucl. Sci., NS-24, (3) (1977).
3. Private communication with J.D. Stabley, Power Devices Appl. Eng., Solid State Div., RCA, Lancaster, PA.
4. I. Weitman, Phase Control and Frequency Control of 200 MeV Linac for the AGS, Proc. 1970 Proton Linear Accel. Conf., NAL, Batavia, IL.
5. K. Batchelor and N.M. Fewell, Phase Shifting Using Varactors, Rutherford Laboratory Report, RHEL/R156.
6. R.M. Mobley, A.A. Irani, J-L LeMaire, A.W. Maschke, Neutralization of Positive Particle Beams by Electron Trapping, Proc. Symp. on Production and Neutralization of Negative Hydrogen Ions and Beams, (BNL 50727, Sept. 1977).
7. D.S. Barton and R.L. Witkover, Plans for H^- Acceleration in the AGS Linac (this conf.).
8. P.E. Haustein and E-M Franz, Phys. Rev., C, Vol. 16, No. 4, October 1977.
9. G.W. Bennett, J.O. Archambeau, B.E. Archambeau, J.I. Meltzer and C.L. Wingate, Visualization and Transport of Positron Emission from Proton Emission from Proton Activation in Vivo, Science, Vol. 200, June 9, 1978.
10. C. Duncan and G.W. Bennett, IX Intern'l. Conf. on Brain Metabolism, Tokyo, May 1979.

THE RUTHERFORD LABORATORY 70-MeV LINEAR ACCELERATOR

N. D. West
Rutherford Laboratory
Chilton, Oxfordshire, England

Summary

A 70-MeV proton linear accelerator, originally built as an injector for the Nimrod proton synchrotron, is described. The accelerator is now being modified to serve as the injector for a new rapid-cycling synchrotron which is being constructed for a pulsed neutron source facility.

Introduction

The linear accelerator was originally constructed in the years 1973-76. It was built as a new injector for the Nimrod 7-GeV proton synchrotron, to replace the 15-MeV injector, with the object of increasing the synchrotron beam intensity. The injector was required to provide a 500 μs pulsed proton beam of 75 mA, at a maximum repetition frequency of 1 Hz.

Shortly before the construction of the accelerator was completed, a firm date for the closure of Nimrod was announced, which made a change-over to the new injector no longer worthwhile. In view of a possible future use for the accelerator, however, work was continued to complete its construction and to commission an accelerated beam. The first 70-MeV beam was produced in May 1976, and operational tests continued until a shutdown in March 1977.

In June 1977, approval was given for the construction at the Laboratory of a pulsed spallation neutron source (SNS). The neutron source will be based on an 800 MeV, high intensity, rapid-cycling synchrotron with the 70-MeV linear accelerator used as the injector. Injection will be by stripping of H^- ions and the linear accelerator is to provide 500 μs, 20 mA pulses of H^- ions at a repetition rate of 50 Hz.

A description of the linear accelerator in its original form as an injector for Nimrod will be given, followed by an account of the modifications which are underway to convert it for use with the SNS.

The Nimrod Injector

The 70-MeV new injector for Nimrod was proposed as a way of increasing the synchrotron beam intensity at a minimum cost, by utilizing equipment taken from the Laboratory's 50-MeV proton linear accelerator (PLA) which had been closed down in 1969. With the addition of another cavity to raise the energy to 70-MeV, it was hoped to gain a factor of five in the space-charge limited intensity at injection.

A layout of the accelerator is shown in Fig.1. The accelerator is housed in a new building alongside the existing 15-MeV injector, with the 70-MeV beam taken via a short tunnel through the synchrotron earth shielding and then to a straight section in the magnet ring. The building is divided into a 200-m^2 Faraday screened room for the pre-injector, a 350-m^2 linac equipment area and a 250-m^2 shielded enclosure of concrete blocks containing the accelerating cavities. The cavities are supported on a steel framework above a basement, which provides the height necessary to accommodate the rf amplifiers and vacuum pumps.

The Pre-injector

The ion source, which has been described in detail elsewhere[1], is a compact duoplasmatron with a 20-mm diameter expansion cup. Typical performance figures are given below.

		On test rig		On Column	
Extraction gap	(mm)	21.3	18.3	12.5	12.5
Extraction volts	(kv)	30	50	18	14.5
Arc Current	(A)	35	60	34	24
Beam Current					
- at source exit	(mA)	200	600	-	-
- at 665 keV	(mA)	-	-	210	125

The accelerating column, also described elsewhere[2], was designed for an energy of 665 keV and a target value of beam current of 200 mA. It is constructed from a stack of 16 titanium electrodes, bonded to pyrex spacer rings by PVA adhesive, and enclosed in an outer glass-fibre reinforced epoxy resin vessel pressurized with SF_6. To ensure reliable operation, the column is designed for the modest value of accelerating gradient of 1.5 kV/mm. At this gradient it is possible to include a large value of reservoir capacity in the high voltage supply without the danger of voltage decondition-ing in the event of a spark-over. It is also about the lowest value at which a 200-mA beam can be satisfactorily accelerated to 665 keV and matched to the input of a practical beam transport line. The column is evacuated by turbo-molecular pump.

A view of the pre-injector high voltage equipment is shown in Fig.2. The high voltage supply is a Haefely generator, rated at 750 kV, which charges a 0.01 μF storage capacitor. The capacitor limits the voltage drop due to a beam pulse to 10 kV which in turn is compensated by a bouncer stabilizer circuit connected to the low voltage terminal of the capacitor. The bouncer employs a transformer coupled control tube which takes its error signal from a special capacitive potential divider. By suppressing the bouncer between

pulses, the operating voltage is determined by the fundamental d.c. stability of the high voltage supply. The stabilizer has a frequency response of 500 kHz and at full pulse loading provides stabilization to within 0.4 kV.

The 665-keV Beam Transport Line

A beam line containing three quadrupole magnet triplets connects the pre-injector to the first tank of the linac. The first triplet is mounted inside the vacuum system of the pre-injector column in order to capture the emerging beam before it diverges too far, while the final triplet is mounted as close as possible to the linac to achieve the short characteristic length matched beam parameters, required at the input to the first accelerating gap. The first two triplets have element lengths of 100/200/100-mm, apertures of 90 mm and provide maximum gradients of 5 T/m. Corresponding figures for the third triplet are 80/160/80-mm, 60-mm aperture and 17 T/m.

A single fundamental frequency buncher cavity is used in the beam line for longitudinal matching. The buncher drift distance is 800 mm and the peak proton energy change is 23 keV. The cavity, which is of the half wavelength coaxial line design, is fed with rf power from an adjustable coupling loop in the first linac tank.

The Linear Accelerator

The accelerator is divided into four separate cavities, the parameters of which are given below. A view of the accelerator cavities is shown in Fig.3.

Tank No.	1	2	3	4
Construction	Cu clad steel	Vac vessel & Cu liner		Cu clad steel
Length, m	7.15	11.96	11.24	12.11
Energy out, MeV	9.91	30.44	49.71	70.44
No. of cells	56	41	27	24
DT aperture, mm	20-25	38.1	38.1	30
Acc rate, MeV/m	0.84-1.55	1.72	1.71	1.77-1.66
Q-theoretical	76,100	70,900	56,800	66,000
- measured	60,900	58,600	39,700	55,100
Power for $\phi_s=30^\circ$				
-theor loss, MW	0.44	1.31	1.40	1.51
-practical incl 75 mA beam	1.24	3.12	3.45	3.36
Focusing magnets				
-period	FDFD	FFDD	FFDD	FFDD
-excitation	Pulsed	DC	DC	DC
-gradient, T/m	85-29	7.5-6.1	4.6	5.3
-length, inches	1.0-2.75	4.5-6.0	9.0	7.5

For the design value of accelerated current it was considered essential to use the FDFD focusing mode at the input end of the linac. Tank 1 of the PLA had used grid focusing and although conversion to quadrupole focusing would have been possible, because of an unfavourable drift-tube shape only the FFDD mode could have been achieved. A new tank was required therefore, and to save effort it was decided to base this on an existing design. This was made possible by the generous supply of information by Fermilab on the design of their 200-MeV linac. To adapt the design to the 70-MeV linac, a new set of unit cell lengths was interpolated to give an output energy matching the input to tank 2, and the design was extrapolated forwards to produce an acceptable input energy, arbitrarily put at less than 700 keV. With the exception of minor details the tank and drift-tube construction is identical to that at Fermilab.

Tanks 2 & 3 are taken from the PLA and used with only minor modifications. These were originally built in the late 1950's, and are constructed with separate sheet copper cavities and outer steel vacuum vessels. The drift-tubes contain d.c. powered quadrupole magnets which are limited to the FFDD operating mode. Tank 4 is another new tank built to the Fermilab design, including the use of post couplers, but with the drift-tubes fitted with d.c. powered quadrupoles. The quadrupoles have solid cores and low current windings, and by operating them in the FFDD mode the dissipation is sufficiently low to allow them to be cooled by conduction to the drift-tube body.

In order to save cost, tanks 2 & 3 are still fitted with the oil diffusion pumps used earlier on the PLA and tanks 1 & 4 are fitted with oil diffusion pumps which were surplus from elsewhere on Nimrod. An operating pressure of better than 2×10^{-6} torr can be achieved on all tanks.

The Rf System

The high power rf system[3] consists of a common low power drive-chain which feeds four separate two-stage amplifiers, one for each tank. The drive-chain provides four outputs, at a maximum level of 12 kW each, by means of four adjustable loops coupled to the anode circuit of the output stage. The two-stage amplifier comprises an RCA 4616 tetrode operating in grounded cathode followed by a Thomson-CSF TH116 triode operating in grounded grid. The circuit for each of these valves uses tunable coaxial resonators for input and output circuits, with input and output coupling via adjustable taps. The RCA 4616 operates at an output of up to 500 kW and the TH116 has been tested at a maximum output of 4.25 MW into a dummy load.

Rf power is coupled to each tank by an adjustable loop situated on the air side of a vacuum window of cross-linked polystyrene. The power is fed via a 300-mm diameter transmission line, polystyrene disk supported, which incorporates a trombone phase shifter and a calibrated reflectometer. The tank phase is set by a trombone phase shifter in the TH116 drive line.

Anode power for the TH116 valves is provided by individual pulse modulators, consisting of a pulse forming network feeding a 2½:1 step-up pulse transformer via a CX1174 deuterium thyratron. The pulse transformer also supplies the anode of the RCA 4616 via a series resistor. Stabilization of the field level in the tank is arranged by

anode modulation of the RCA 4616, by controlling an ML 8786 tetrode placed in shunt with it. This system has provided satisfactory stabilization against beam loading up to the full design value of beam current.

70-MeV Beam Transport Line

Beam transport between the linac and synchrotron is provided by a line containing two achromatic bends and an electrostatic inflector as the final element. Focusing throughout the beam line is by triplet quadrupole magnets, of which the end elements are air-cooled magnets taken from the PLA and the higher strength center element is a proprietary water-cooled magnet. The beam alignment can be adjusted by four steering magnets located at the linac exit. A debuncher cavity is installed to reduce the beam energy spread, but the cavity was also intended to be fast phase ramped to provide energy modulation of the beam during the pulse. At the time the injection project was abandoned, a 100 kW fast ferrite phase shifter was under development for this purpose, power for the debuncher being coupled from tank 4 by an adjustable loop.

Beam Monitoring

The pulsed beam current is measured by a system of 14 beam transformers which provides both analogue pulse and digital panel meter display. The other main monitoring device is a multiwire beam profile monitor, consisting of a number of 0.02-mm tungsten wires at 2-mm spacing which can be inserted into the beam. The output is available as an oscilloscope histogram display or can be stored in a transient recorder for subsequent digital readout. To prevent melting these can only be used in the 665-keV beam with short beam pulses.

The emittance of the 665-keV beam is measured using a multi-slit plate followed by a traversing slit. Data taking is semi-automatic but data analysis is carried out off-line. Other equipment available includes threshold foils to identify accelerated from unaccelerated beam, and also a momentum spread measurement system using a slit bending magnet and profile monitor.

Control System

An original plan to provide computer control had to be abandoned because of financial constraints. The system chosen, however, was one which could be later adapted to computer control and yet was no more expensive than a totally hardwired system. Communication with the machine equipment, from either the injector control center or the Nimrod control room, is via a CAMAC system operated by an autonomously cycling control unit. At either control point the operator selects the device to be controlled on a push button selector panel, which gives control of the device parameters at a central control panel. All controls are of the push button, on-off or raise-lower, type. Device selection also switches appropriate parameters for display on digital panel meters.

Operation

Operating experience with all components of the pre-injector has been generally very satisfactory, with the reliable production of a 665-keV beam over an 18-month period and the achievement of the design values of pulse current and duty cycle. As expected, 200 mA has proved to be about the maximum current obtainable at the output of the column, and even at this current there is evidence that the beam is scraping the bore of the first triplet magnet. Measurements of the 665-keV beam emittance area have yielded: 160-mA beam, 90% of current inside 38π μmr; 100-mA beam, 90% of current inside 40π μmr, 95% inside 50π μmr and 95% inside a circumscribed ellipse of 66π μmr.

Commissioning of the linac beam commenced with the first operation of tank 1 in February 1976. Although a 10-MeV beam was established fairly quickly, operation was severely troubled by a multipactor problem which caused the loss of 50% and upwards of all pulses. Following unsuccessful attempts at conditioning the tank, carbon black was applied to all the drift-tube faces. This produced an improvement, but it was not the complete success that it had been on the 15 MeV linac, and only after many weeks of running was it possible to achieve adequately reliable operation. Even then, periods of multipactor could still arise, particularly at the full 1 Hz repetition rate. A further problem has been the failure of the quadrupole inside drift-tube number 8. However, by reversing the polarity of all upstream magnets, a satisfactory beam acceptance has been achieved giving, for example, an 80-mA beam at 10 MeV for 135 mA at the tank input.

Following operation at 10 MeV, the three remaining tanks were progressively commissioned, with the first 70-MeV beam produced in May 1976, and the 75-mA design current obtained by the end of that year. Operation at the 1-Hz repetition rate and 500-μs pulse length were separately achieved, but the accelerator was always operated at less than the combined full duty cycle because of incomplete installation of the radiation shielding. Probably the greatest operating problem experienced was in setting up the tank phases, with the aid of the energy threshold foils, and in maintaining the phase from one operational period to another. The difficulty was largely due to phase variations during the rf pulse which were of a different form for each tank. It is thought that these may be caused by reactive loading due to multipactor type discharges at the operating field level. Another problem was the collapse of the buncher cavity field with long beam pulse lengths, thought to be due to thermionic emission from the grids in the gaps. This could usually be avoided by careful focusing of the 665-keV beam.

The emittance of the 70-MeV beam was determined by measurement of the beam width at a single profile monitor for a range of settings of an upstream triplet quadruple magnet. Measuring at

the 10% signal level, the emittance area for a 50-mA beam was found to be approximately 11π μmr in both planes. Assuming a gaussian density distribution this area contains 90% of the beam current.

Prior to the linac close down in March 1977, the performance of tank 1 was examined with the quadrupoles re-connected for the FFDD mode, since this was relevant to its future use. With the gradients approximately halved, except for the magnets adjacent to the faulty number 8 which were empirically optimized, the transmission factor for the tank was found to be only about 50% compared with the previous value of 60% or better. Some improvement in this figure can be expected with the faulty magnet replaced and with more careful optimization.

Conversion of the Linac to an Injector for the SNS

Following the approval given for the SNS project, work has been underway to modify the linear accelerator to act as the injector for this new machine. The main changes are concerned with the increase in repetition rate to 50 Hz and in the change of accelerator beam to H^- ions, but other necessary improvements suggested by the previous operating experience will also be carried out. A brief discription will be given of the principal changes.

The Building. Because of the anticipated increase in radiation levels, additional shielding will be installed and all electronics will be removed from the linac enclosure. Increased room for equipment will be provided by building extensions to house the water plant and a new local control center.

Ion Source. An H^- ion source of the Penning surface plasma type is now under development. This has the basic discharge chamber geometry of the Dudnikov source, described by Allison[4], and is fitted with a pulsed gas valve and external cesium boiler. Operation in the cesium mode, at an arc current of 100 A and a pulse length of 500 μs, has been maintained for over 40 hours at the reduced repetition rate of 14 Hz. A source with improved cooling and fitted with a 90° analysing magnet is about to be tested.

Pre-injector. A new bouncer circuit has been designed to accommodate the reversal in high voltage polarity.

Linac Tanks. A change to the FFDD focusing mode and the design of an improved pulsed power supply to give shorter pulse rise and decay times, will allow the quadrupole magnets in tank 1 to be operated at 50 Hz without overheating. On all tanks, the diffusion pumps are being replaced by turbo-molecular pumps and all water-cooling circuits are being modified to provide the required increased flow rates.

RF System. It is believed that the 4616 and TH116 circuits will be satisfactory at the new duty cycle with only minor modifications. Four separate low power drive systems will be built to enable fast phase and amplitude control to be carried out at low power level. New anode power supplies now under construction include a hard valve modulator for the TH116 which uses the ML8786 as the series control valve. A prototype of this modulator has been operated successfully and has enabled preliminary tests to be carried out on the rf amplifiers at the full duty cycle.

Controls. The control of the injector will be integrated into a computer control system being designed for the SNS. This uses a central GEC 4070 computer linked to three similar peripheral computers, one of which is dedicated to the injector. A new interpretive control language called GRACES is being written for the 4070. Much of the injector equipment will have to be modified to accept digital control.

70-MeV Beam Transport. A new beam line will make use of the existing design of quadrupole magnets, many of which will now be operated as singlets, and a number of ex-Nimrod beam line dipoles will be used as bending magnets. Injection into the SNS will involve the use of orbit bump magnets and a stripper foil. With a mean beam current of 500 μA from the injector, the monitoring of beam loss in both the linac and the beam line is expected to be an important function of an up-rated beam diagnostic system.

Conclusion. It is anticipated that the accelerator can be converted to a high duty cycle injector for the SNS with only minor modifications to major components such as the d.c. and rf accelerating structures and the rf system amplifiers. In other areas, far more extensive changes are required. Work on most of the areas of modifications is now in progress. It is planned to produce a 665-keV H^- beam in the second half of 1980 and work on the remainder of the linac is aimed at a target date for the completion of the SNS towards the end of 1982.

Acknowledgements

Construction of the original 70-MeV injector was the work of a number of the staff of the former Nimrod Division, under the leadership of the late Norman Venn. The author wishes to acknowledge the contribution of these individuals to the work described and also that of his colleagues in the smaller, and largely new, group who are engaged on the present modification work.

References

1. R. G. Fowler, R. Sidlow, G. Soulby, N. D. West, 'The Proton Duoplasmatron Ion Source for the Preinjector of the New Injector for Nimrod', Rutherford Laboratory Report RL-74-048.

2. R.G.Fowler, R.Sidlow, N.D.West, 'The 665-keV Preinjector for the Nimrod 70MeV Injector', Rutherford Laboratory Report RL-76-070.

3. C.W.Planner, 'The Rf System for the 70-MeV Linac Injector', Rutherford Laboratory Report RL-75-178.

4. P.W Allison, 'Experiments with a Dudnikov-Type H^- Ion Source', Proceedings of the Symposium on the Production and Neutralisation of Negative Hydrogen Ions and Beams, Brookhaven, 1977, BNL 50720,p.119.

DISCUSSION

A. Wadlinger, LASL: Why does carbon black help the multipactoring and how did that idea originate?

West: Carbon black has a secondary emission coefficient of less than unity. The mechanism of operation is like a cliff wall with lots of holes in it. If you throw a ball at the wall, there is a good chance that it will enter the nearest cave, bounce around and never come out again. So, I do not think it is the fact that it is carbon that matters; I think it is the structure of carbon black. To make it, you take carbon black, mix it with alcohol and just paint it on. You get a nice black surface just like a flame-smoked surface. It's very crude - it sounds like a terrible thing to put in a rf cavity; in fact it has no effect on the rf power, but it really stops multipactoring.

D.A. Swenson, LASL: Did you put post-couplers in the fourth tank of your new linac, and if so, were your experiences of tuning the post-couplers satisfactory?

West: We did put post-couplers in; there seems very little reason to have done so if you remember that we have three other tanks without any stabilization, but we chose to make it identical to the FNAL tank. Setting up the post-couplers was satisfactory - we have not done any tests on the tank to see how good the stabilization is, but it's only a 20-MeV tank, so perhaps the problems are very small anyway.

C. Curtis, FNAL: You mentioned the phase shift during a beam pulse. Can you speculate on what causes this - is it associated with your rf tube?

West: We do not think it is the rf tube because it varies from one tank to another and it is a function of the tank tuning. I believe it is an electron resonant discharge somewhere in the structure of the accelerator cavity at a high level, multipactor discharge essentially, but well away from the drift tubes. Tanks 2 and 3 have lots of pumping slots and there is opportunity for rf to leak out of these areas. We have the same trouble in Tank 4 and that is copper-clad steel construction. I can only assume it is some sort of multipactor discharge around the support stems. But this is speculation - I mean we haven't any direct experimental evidence as to what is causing it.

R.L. Witkover, BNL: With the high duty factor for the H^- injection that you envision, do you foresee any problems with the stripper foil?

West: So far we have not done any work on stripper foils, but the Argonne experience would suggest that a solution should not be too difficult. I think the life of stripper foils should be all right providing we can have a suitable mechanism for replacing them at perhaps fairly frequent intervals.

J.P. Blewett, BNL: It seems sort of surprising to me that this multipactoring only happens in England. Is there an explanation of this?

West: It is not that it only happens in England - it only happens to me!

E.A. Knapp, LASL: What is the schedule of operation of the SNS, and also of the injector linac?

West: The present construction schedule for the SNS is that we should have a beam to the neutron target by the end of 1982; however, that depends very much on the rate at which we receive funds and that is something that is adjusted from one year to another. I would hope to have a beam from the linac 6 to 12 months before that date.

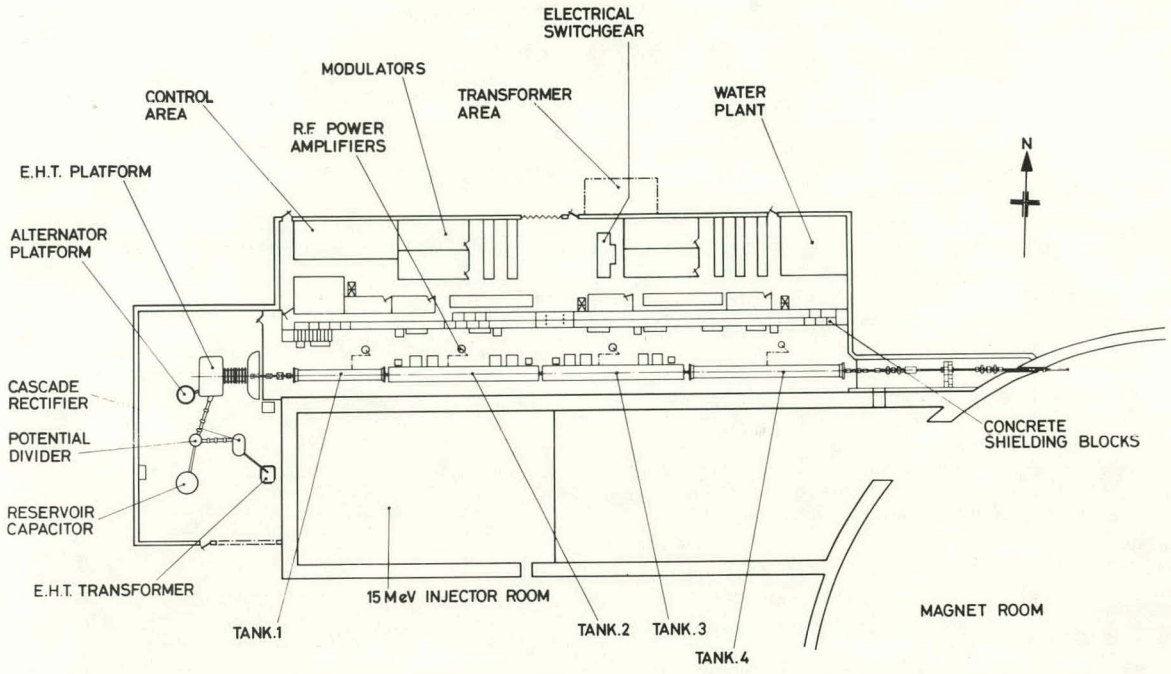


Fig. 1 Layout of the 70-MeV accelerator

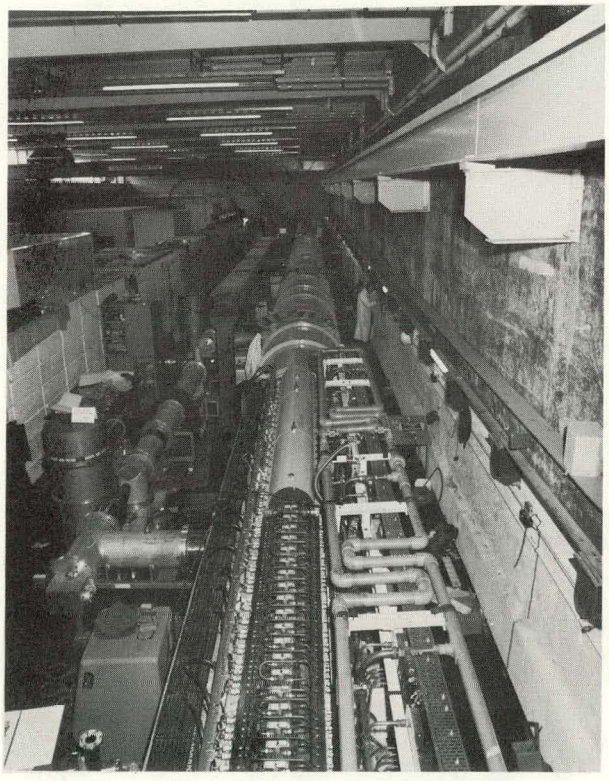


Fig. 2 The pre-injector high voltage area

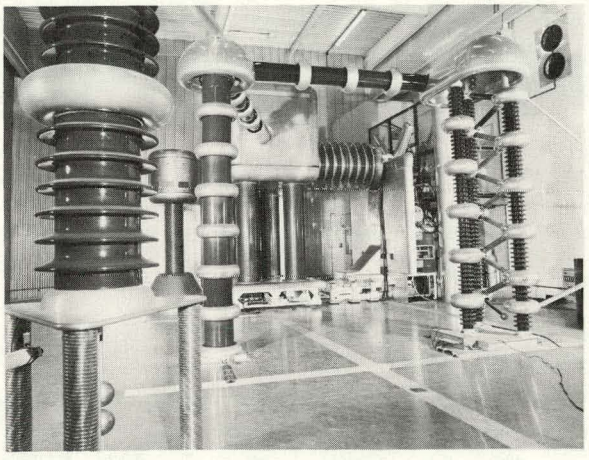


Fig. 3 View of the linac from tank 1

STATUS OF THE KEK INJECTOR LINAC

S. Anami, H. Baba, S. Fukumoto, K. Ito, T. Kakuyama, C. Kubota, Y. Mori, T. Sakaue,
I. Sato, A. Takagi, T. Takenaka, S. Takano and J. Tanaka
National Laboratory for High Energy Physics
Oho, Tsukuba, Ibaraki, 300-32, Japan

Summary

In April 1977, the KEK proton synchrotron started to run for experiments in high energy physics. Typical beam intensities of the injector are currently: 620 mA from the preinjector column 250-mA beam into the linac and 130 mA at the linac exit at 20 MeV. The rf system was modified to feed more power into the buncher and the debuncher. Rf windows, isolators, control system of the Cockcroft generator and an optical fiber data transfer system have been developed or improved. The linac beam of 200 mA has been achieved by removing grids from the buncher and lowering the column pressure of the preinjector. Although beam loading is not completely compensated in the accelerating field of the tank, the momentum spectrum of the beam is not seriously affected by the beam loading.

Introduction

The first beam was accelerated in the KEK linac to 20 MeV in August of 1974. Its design goal for intensity was 100 mA and it was achieved in the early stage of operation.[1,2] In April 1977, the KEK proton synchrotron started to run for high energy physics experiments. Typical beam intensities of the injector are presently as follows: the column current of the 750-kV preinjector is 620 mA, 250 mA is injected into the linac and 130 mA is delivered from the linac. Some modifications have been done to ensure more stable operation and efforts are being continued to get a more intense beam of high quality.

Operation and Modifications

Table 1 shows the total operation time of the KEK proton synchrotron complex with downtime due to the accelerator failure from October 1976 to July 1979. The operation time has increased steadily and the machine ran 10 or 11 days in every two weeks in the last period. It should be noticed that downtime due to the trouble in the 20-MeV beam line was included in the linac failure until March 1979, whereas it is excluded later. Troubles of the linac rf were reduced by improvements of various power supplies.

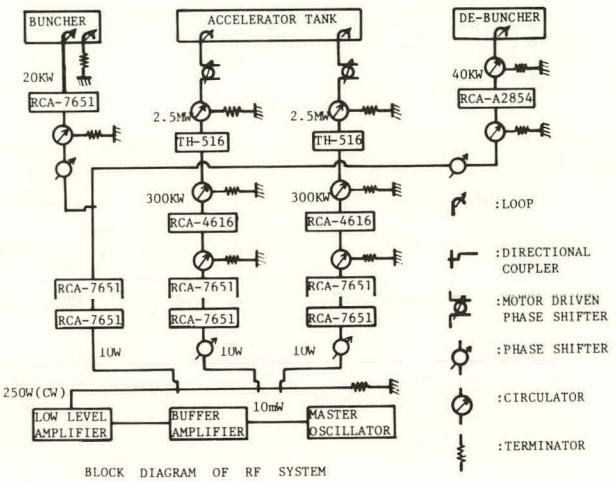


Fig.1 Block diagram of rf system.

The rf system has beem modified as shown in Fig.1. The maximum available power was raised from 6 kW to 20 kW in the buncher and from 20 kW to 40 kW in the debuncher. Medium and high power isolators were developed.[3] They are installed between an RCA-4616 tube and a TH-516 power tube, and between the power tube and the linac tank. They reduce reaction of the power tube to its driver as well as coupling between two power tubes in the two-feed system.

New rf windows were made and put into the tank. In the old window, a metal ring was brazed to periphery of a ceramic disk, and a viton O-ring was inserted between the ring and the flange for vacuum seal. Unfortunately, breakdown had sometimes occurred on the ceramic surface due to sharp edges of solder alloy. Thus, brazing is avoided in the new one, and vacuum is sealed with a metal gasket of Al Helicoflex between the ceramic disk and the flange as shown in Fig.2. They have worked well for more than a year.

The control system of the Cockcroft-Walton generator was renovated. It has two modes of operation: stabilized mode and high impedance

	OCT.'76 ∫ MAR.'76	APR.'77 ∫ SEP.'77	OCT.'77 ∫ MAR.'78	APR.'78 ∫ AUG.'78	SEP.'78 ∫ MAR.'79	APR.'79 ∫ AUG.'79
Total Operating Hours	1000.6	1595.4	1655.7	1706.4	2384.1	1760.3
Total % of Acc. Failure	7.7 %	8.9 %	5.8 %	4.5 %	5.2 %	6.5 %
Preinjector	0.73 %	0.43 %	0.14 %	0.28 %	0.24 %	0.24 %
Linac	2.34 %	1.52 %	1.46 %	1.34 %	1.02 %	0.40 %

Table 1 System down-times in % of total operating hours.

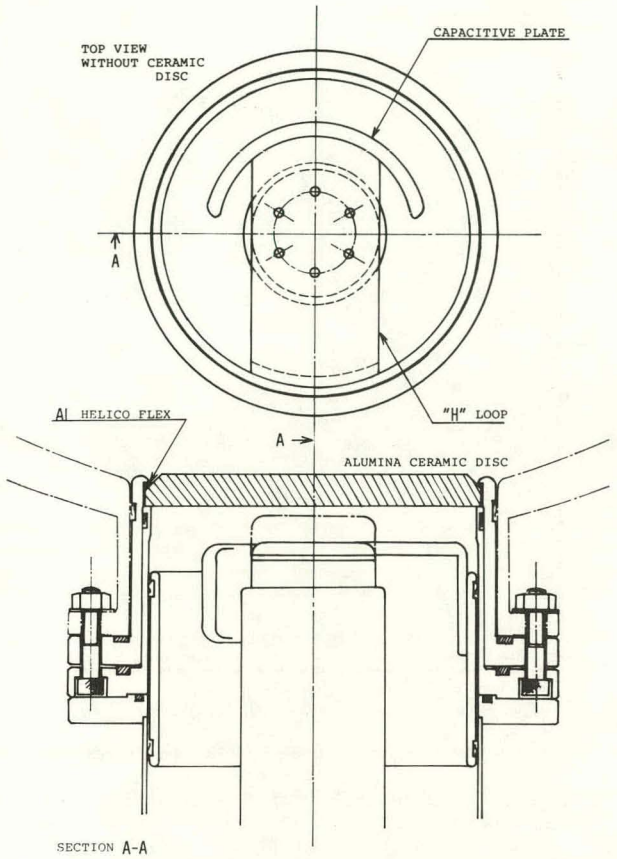


Fig.2 Rf window and coupling loop.

mode. In the stabilized mode, the generator has a feed-back loop with a feed-forward circuit. As the KEK synchrotron is a cascade machine, 9 beam pulses are injected into the 12-GeV main ring in 0.5 s, then it begins to accelerate them. Thus, the preinjector delivers 9 successive beam pulses in one main ring cycle of 2.5 s. The accelerating voltage decreases in 9 pulses by beam loading as shown in Figs.3a and 3b. It is improved by feed-forward as shown in Fig.3c. When arcing tends to occur frequently in the accelerating column, for example, after the column is exposed to the atmosphere, the high impedance mode is preferred to reduce damage to the accelerating electrodes in the column. It uses an unstabilized power supply which has an adjustable reference voltage and a comparator. If the difference between the reference voltage and the output voltage exceeds a preset limit, the output voltage is changed by 0.2 kV every 0.1 s or 1 s or according to an external program.

The high voltage terminal is equipped with a new optical fiber data transfer system.[4]

Usually, little conditioning is necessary for the preinjector as well as for the linac at the beginning of every run. So far, there are two long shutdowns a year, and the oxide cathode

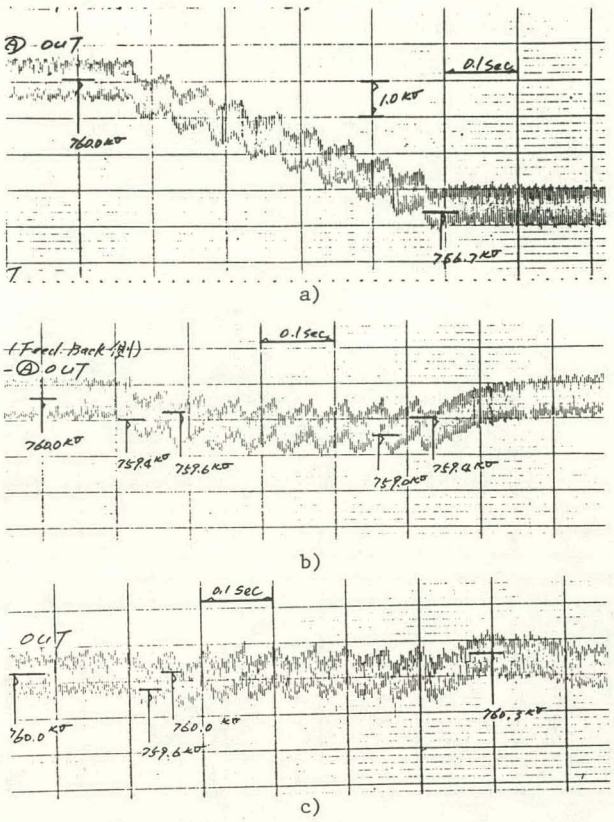


Fig.3 Output voltage of Cockcroft-Walton generator. 9 beam pulses are accelerated successively in one main ring cycle.
a) without feed-back loop and feed-forward pulse.
b) with feed-back loop, without feed-forward pulse.
c) with feed-back loop and feed-forward pulses.
Horizontal: 0.1 s/div, Vertical: 1 kV/div.

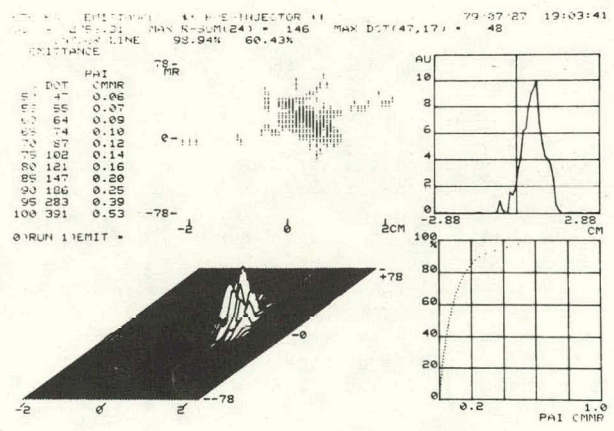


Fig.4 Horizontal emittance display at entrance of linac tank (270-mA beam).

of the duoplasmatron ion source is replaced by a new one during the long shutdown. An oxide cathode lasted more than 2300 hours without signs of deterioration.

The beam emittance is monitored at the entrance of the linac tank (Fig.4). The RMS emittance,[5] which is defined by eq.(1), is compared with the 90 % emittance for the 1-st, 3-rd, 5-th, 7-th and 9-th beam of the 9 beam pulses in Table 2.

$$E_{rms} = 4[\langle y^2\rangle\langle y'^2\rangle - \langle yy'\rangle]^{\frac{1}{2}} \qquad (1)$$

The normalized RMS emittance is denoted by ε_{rms}. If the intensity distribution is Gaussian in both directions, then 86 % of the beam is included in the RMS emittance. Twiss parameters are also shown in Table 2.

Beam Ordinal Number	$E_{90\%}$ mm·mrad	E_{rms} mm·mrad	ε_{rms} mm·mrad	α	β $\frac{mm}{mrad}$	γ $\frac{mrad}{mm}$
1	2.68	64.0	2.56	3.70	1.00	14.7
3	2.70	65.2	2.61	3.68	1.03	14.7
5	2.66	62.8	2.51	3.80	1.00	15.4
7	2.44	63.5	2.54	3.95	1.10	15.1
9	2.75	67.5	2.70	3.60	1.00	14.0

Table 2 Vertical 90 % emittance and RMS emittance for 1-st, 3-rd, 5-th, 7-th and 9-th beam in 9 beam pulses. Twiss parameters α, β and γ are shown.

New Intensity Record

When the rf field is raised in the tank, the linac beam increases rapidly at first, then it shows saturation as shown in Fig.5. Thus it seems difficult to increase the linac beam further by raising the rf level. It was noticed that some beam loss occurred from the grids of the buncher, which is a coaxial cavity with two gaps. By removing the grids, the beam which is injected into the linac is increased by about 10 %. It was already shown that higher pressure cures breakdown in the high gradient accelerating column.[6] However, this mode of operation has a drawback of poor transmission in the 750-keV beam line. This is supposed to be caused by H_2^+ or H_3^+ ions produced in the plasma cup of the ion source.[7]

By lowering the column pressure as shown in Fig.6, 420-mA beam was injected into the linac and 20-MeV beam of 200 mA was achieved. For such a high intensity beam of about 5 μs duration, it is difficult to compensate rf beam loading completely as shown in Fig.7. It affects the momentum spectrum structure in one beam pulse as shown in Fig.8. The detector has 96 segments for momentum analysis, while the first channel and the last one are devoted for the marker. Each channel corresponds

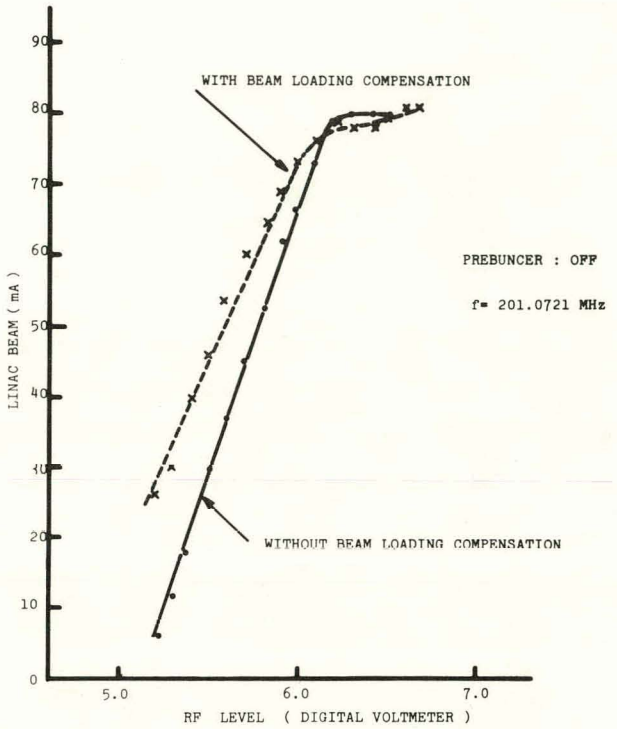


Fig.5 Tank rf level vs. linac beam intensity.

to 20 keV. The debuncher rf field was kept in routine operation level and it was very low, because the beam, with rather broad spectrum, is favorable for injection into the booster synchrotron to achieve an intense circulating beam. Thus, it seems not to be serious, that the momentum distribution changes slightly by the rf beam loading in one beam pulse. Figure 9 shows the forward rf power into the tank, and the reflected rf power from the tank. Emittance of 20-MeV beam will be measured thoroughly after completion of the device for routine operation.

References

1) J. Tanaka, Proc. 1976 Proton Linear Accelerator Conf., 27, 1976.
2) J. Tanaka, H. Baba, T. Sato, S. Inagaki, S. Anami, T. Kakuyama, T. Takenaka, Y. Terayama, H. Matsumoto, ibid., 333.
3) S. Anami, H. Baba, Y. Mori, J. Tanaka and S. Fukumoto, proceedings of this conference.
4) T. Sakaue and S. Takagi, IEEE Trans. Nucl. Sci., NS-26, 3938, 1979.
5) P.M. Lapostolle, IEEE Trans. Nucl. Sci., NS-18, 1101, 1971.
6) S. Fukumoto and S. Takano, Proc. 1976 Proton Linear Accelerator Conf., 189, 1976.
7) S. Fukumoto, H. Ishimaru, K. Ito, C. Kubota, T. Sakaue, A. Takagi and S. Takano, IEEE Trans. Nucl. Sci., NS-24, 1121, 1977.

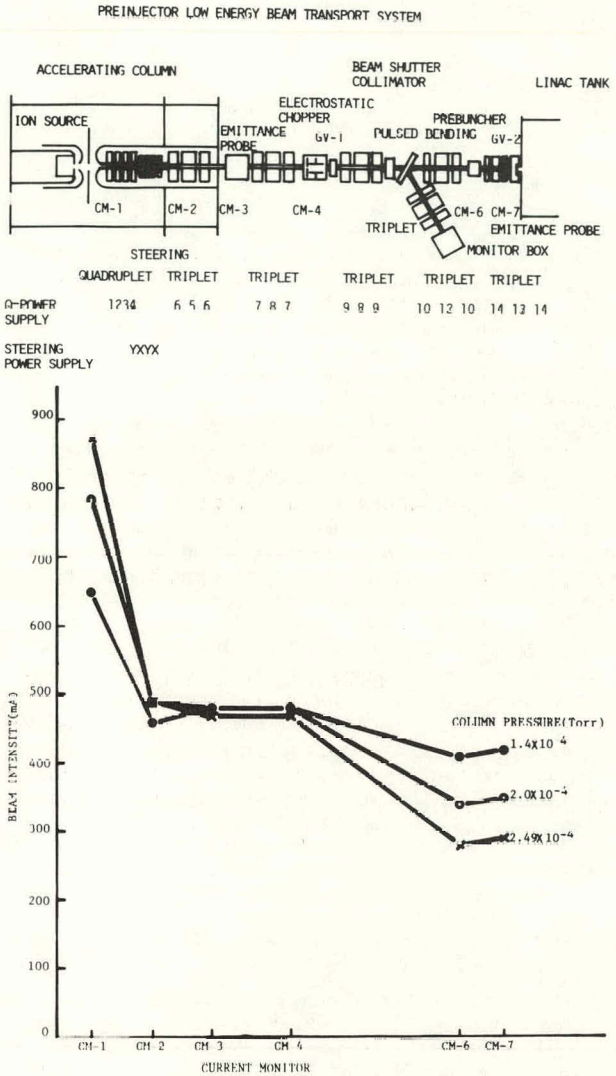


Fig.6 Beam intensities along 750-keV line.

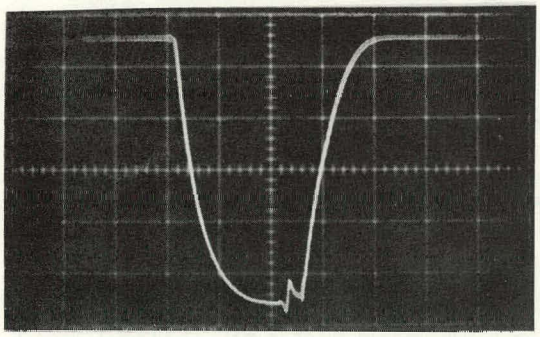


Fig.7 Rf power level in tank (180 mA beam).
Time seale: 100 μs/div.

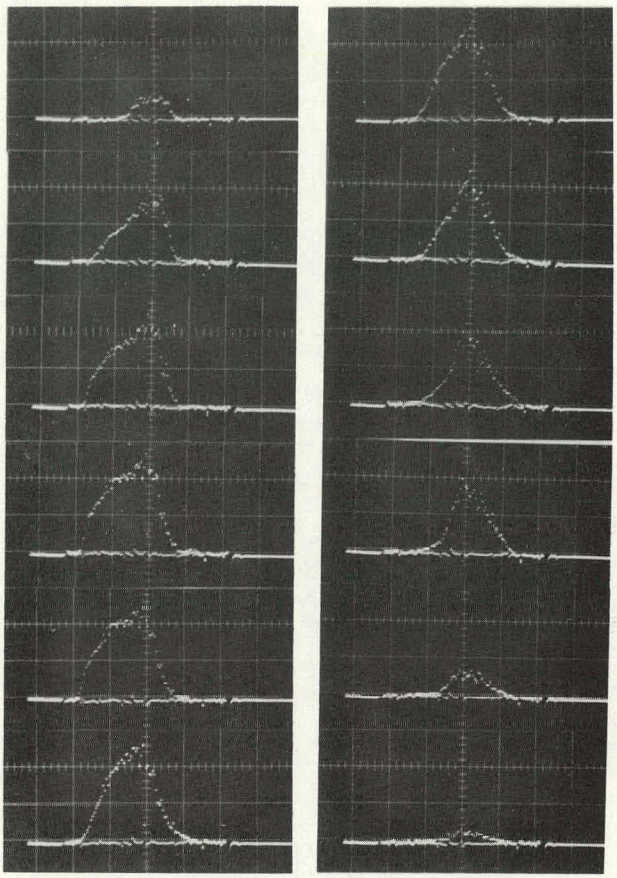


Fig.8 Momentum spectra of 5 μs beam measured every 0.5 μs.
Horizontal scale: 0.4 MeV/div.

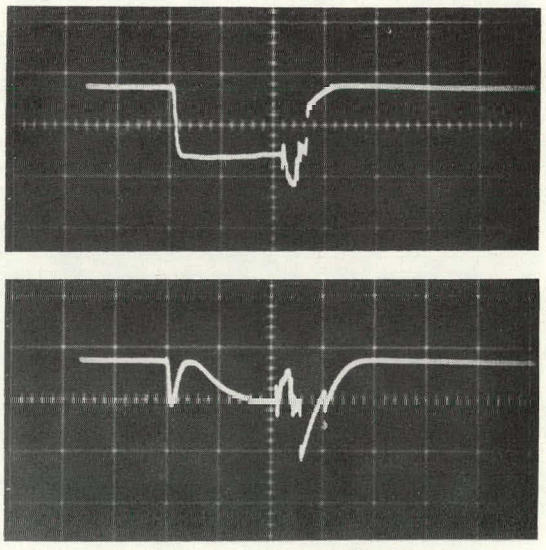


Fig.9 Rf power to tank (upper) and from tank (lower)
Time scale: 100 μs/div.

1979 LINEAR ACCELERATOR CONFERENCE

STATUS REPORT ON THE UNILAC

D. Böhne
GSI, Gesellschaft für Schwerionenforschung mbH
Darmstadt, Fed. Rep. of Germany

Summary

This paper outlines the present operation mode of the Unilac, including records of beam availability. The beam quality is described in terms of intensity, energy and microstructure. A review of component performance concentrates on problems with the injection and rf system. Comments on the status of the control system are also given.

Introduction

A status report on the start-off[1] and the early operation period of the Unilac[2] was presented in 1976 and 1977. In those papers references are given for a machine description. This paper continues the before mentioned reports, however, the following subjects are left out here and are reported in separate articles in these proceedings: Energy and bunch measurements[3] , the Unilac upgrading[4], component improvement[5], beam optimization[6]. In this paper the operational aspects, how they appear after nearly four years of routine service, are described. It is evident, however, that the most significant progress was made in the first year. Imperfections, which were left as problems at that date, still tend to be problems today.

Machine Operation

The Unilac continues to deliver heavy ion beams for fundamental research in nuclear physics, nuclear chemistry, atomic physics and, on a small scale, for practical applications, too. All 20 target stations in the experimental hall are now complete and about 56 proposals for experiments are presently scheduled for obtaining beam. An equal number of experiments already were completed.

The machine is in continuous operation 21 shifts per week. Every fourth week is scheduled for maintenance, minor modifications and accelerator development. This schedule was introduced in January 1979, subsidizing an earlier schedule with one maintenance and one development shift per week and two 6-weeks shut-down periods per year. Those long shut-downs for machine alterations are no longer necessary. For the large number of minor improvements a long shut-down proved to be less efficient and regularly raised coordinative problems. The maintenance weeks now are planned well ahead and each week is exclusively devoted to one particular activity. Due to increased maintenance efficiency, part of this week became available for machine developments jointly with computer program improvements. Interlaced with the research shifts, a few shifts for accelerator experiments are available.

In Fig. 1 a breakdown of the total operation time in the first half year of 1979 is shown and a brief comment on the individual columns should be given In general, the pattern has not changed significantly during the last two years, contrary to what one would have expected. The high fraction of the tune-up time was influenced favorably by the fact that the individual runs on the average last three times longer compared to the early survey experiments. On the other hand the beam quality requirements from the users went up considerably. Tuning the injection to maximum intensities and to perfect isotope separation became laborious. The phasing of bunchers and cavities is much more critical, if a sharp and stable time focus of the bunch structure is essential on the target. A refined adjustment of the beam center in respect to the machine axis is required if the beam splitter is used. Some experiments depend on an extremely clean energy spectrum, which is not a natural feature of a rf linac. The success in attaining those requirements depends on refined diagnostics, human judgement and interaction, which is correlated to the actual status of the hardware. The specific tune-up procedure can hardly be automated.

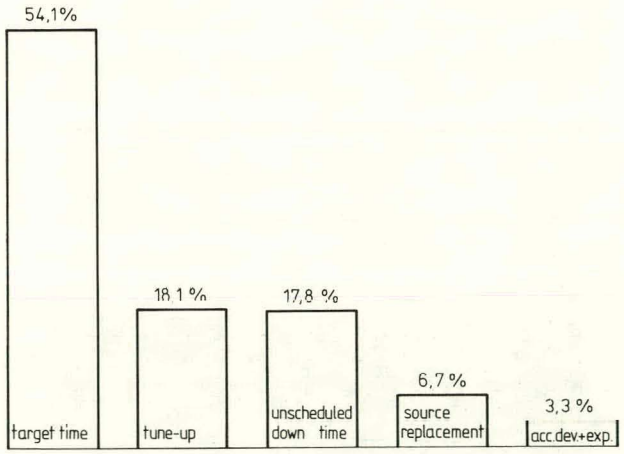


Fig. 1 - Breakdown of Operation Time in the First Half Year of 1979

The fraction of the unscheduled downtime equally is of serious concern. Compared to a proton machine, a heavy ion linac is much more complex and the frequent parameter changes contribute significantly to the amount of fault events. Reviewing the last two years, the weak points in the hardware could not yet be eliminated and every gain in

component reliability was spent by increased performance stress. A histogram of the fault sources is given in Fig. 2, the individual deficiencies will be described later.

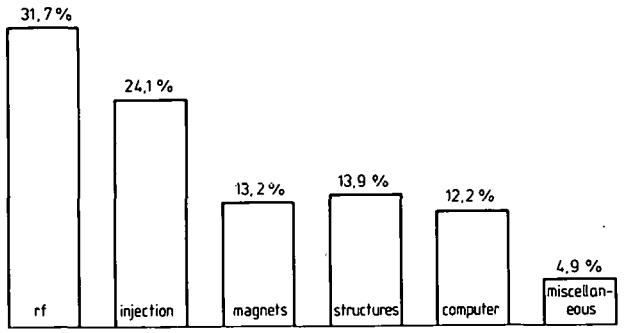


Fig. 2 - Breakdown of Unscheduled Downtime in the First Half Year of 1979

The column "source replacement" only accounts for normal and trouble-free source replacement. If a source turns out to be weak or of unusually short lifetime, this time loss is included under "unscheduled downtime".

The share of accelerator experiments in Fig. 1 seems to be small, but it is actually not unduly low, taking into consideration the limited manpower available for performing and interpretation of those studies.

Not included in Fig. 1 , is the additionally available target time provided by the parasitic beam. This supplementary research time amounts to about one-third of the main beam time.

If one desires to derive conclusions on the beam availability following the data of Fig. 1, only downtime and source replacement are quoted as missing time. Hence the availability, the ratio between obtained and attributed beam time amounts to about 71 %. Bringing up this figure to above 80 % still is a vigorous goal of the Unilac staff.

Beam Properties

The beam intensity remains to be a marginal parameter for all heavy ion accelerators operated so far. Table I lists the optimum values obtained at the Unilac for a variety of ion and isotope species. Compared to the data published in 1977[2], intensities of the very heavy ions went up by about one order of magnitude. This increase could also have been attained for light ions, but was not required. There is no hope for further intensity improvements, except for a factor of 2 or 3

Table I

ISOTOPE	POSTSTRIPPER CHARGE STATE	AVERAGE INTENSITY (PARTICLES/S)	ENERGY (MEV/U)
^{40}Ar	10+	$9.4 \cdot 10^{12}$	10
^{46}Ti	13+	$1.4 \cdot 10^{11}$	
^{48}Ti	13+	$1.2 \cdot 10^{12}$	
^{50}Ti	13+	$9.6 \cdot 10^{10}$	
^{56}Fe	14+	$2.8 \cdot 10^{12}$	
^{58}Ni	14+	$4.0 \cdot 10^{11}$	
^{65}Cu	15+	$2.5 \cdot 10^{11}$	
^{84}Kr	17+	$7.0 \cdot 10^{11}$	
^{86}Kr	17+	$2.0 \cdot 10^{11}$	
^{86}Kr	17+/30+	$1.0 \cdot 10^{10}$	13.1 (2.STRIPPER)
^{107}Ag	19+	$3.3 \cdot 10^{11}$	
^{129}Xe	21+	$7.0 \cdot 10^{11}$	
^{132}Xe	21+	$7.0 \cdot 10^{11}$	
^{136}Xe	21+	$2.4 \cdot 10^{11}$	
^{136}Xe	29+/41+	$6 \cdot 10^{10}$	12.0 (2.STRIPPER)
^{154}Sm	32+	$6.0 \cdot 10^{10}$	
^{184}W	34+	$2.0 \cdot 10^{10}$	
^{208}Pb	36+	$4.4 \cdot 10^{10}$	
^{208}Pb	36+/MC	$1.2 \cdot 10^{11}$	10.5 (2.STRIPPER)
^{209}Bi	37+	$8.0 \cdot 10^{10}$	
^{238}U	40+	$9.4 \cdot 10^{10}$	9.0
^{238}U	MC	$4.0 \cdot 10^{11}$	8.8

MC (MULTI CHARGE STATE OPERATION)

by increasing the injection beam line aperture. The present situation is characterized as follows: The optimum intensity values obtained by the source - although at the expense of source lifetime - just coincides with the intensity limitations of the stripping foil and of the target as well.

Figure 3 shows a histogram of the ion species accelerated in the first half year of 1979 in percent of the obtained target time. During the past years, the peak shifted continuously from the light to the very heavy ions, e.g. from Ar to Pb, W and U, which now are accelerated nearly 60 % of the time. This trend, which still goes on steadily, imposes a high degree of stress on the ion source and most of the accelerator components, which sometimes have to be operated beyond their design ratings. The trend for higher mass numbers, higher intensities and higher energies continues to enforce an exhausting effort in attaining a decent reliability increase on low bid machine components.

Practically all runs require isotopically pure beams, which are regularly provided by the isotope separation feature of the low energy beam transport system. The tune up of a pure ^{208}Pb beam sometimes is laborious and time consuming if impaired by unstable source performance. The use of isotopically pure primary material in the ion source so far has been restricted to very few runs, which were dependent on the ultimate beam intensity. The availability of those enriched elements has become increasingly

limited on the market.

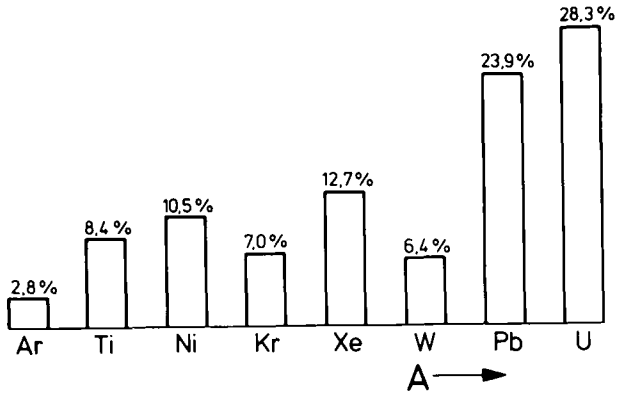


Fig. 3 - Ion Species Accelerated by the UNILAC in the First Half Year of 1979

The duty factor of the machine is set to 25% for all ions. In principle it could be increased to 50 % for medium heavy ions and to 100 % for light ions. But this was not done for a number of minor reasons, which could easily be eliminated, if a higher duty factor would be in heavy demand from the users.

In the past, the required beam energies were concentrated in the range between 4.5 and 5.9 MeV/u. Half of the runs required many energy changes in sometimes very close increments, which now can be quickly adjusted.[6] However, there is a firm trend to higher energies, and the original design aims have been surpassed by inserting a second foil stripper at the entrance of the single-gap cavities. If the charge analysis system in the first stripper section is bypassed , and if the multi-charge state mode is chosen in the Alvarez section, an intensity loss of a factor of only two is encountered by the second stripper. The figures for the maximum energies obtained so far are also listed in Table I. The demand for still higher energies led to an upgrading program[4], which is currently underway on a high priority level.

The excellent energy stability and the small energy spread of 0.1 % was already reported[2] as a result of an improvement effort on rf amplitude control loops. Four helix resonators are in service in the experimental area to refocus the well confined bunch structure of the Unilac to even the most remote target stations, about 80 m away from the machine end. Best values of time focus are about 0.18 ns, and the tune-up[6] is largely computer aided. The occasionally encountered difficulties in obtaining a satisfactory energy spread and time structure could be attributed to ion source instabilities; the interaction mechanism, however, is not yet understood.

Experiments, investigating steep exitation functions near the coulomb barrier, are sometimes fooled by small amounts of satellite energies of the beam. If this occurred, it was hard to eliminate these impurities, the sources of which seem to be numerous, fluctuating and hard to analyze. As a matter of fact, the generally used semiconductor counters tend to read more satellite peaks than the beam actually contains.

The beam splitting system at the end of the Unilac, described in 1977 as a future development[2], has been in use for two years. It provides a continuously variable share of the primary beam into two or three main beam lines of the experimental area. The second beam initially was considered to be a "parasitic beam" for check-out of the experimental set-up. The user of this beam did not have influence on ion species, energy and quality of the beam. As a matter of fact, this parasitic beam was even due to be canceled, if the intensity of the main beam was unsatisfactory. From the standpoint of the users community, the beam splitter is declared as an important success, and the above mentioned understanding of "parasitic" vanished in practice since the second beam really is used for experiments with nearly equivalent priority. On the average, 30 % more target hours have been recorded. The operating crew, however, suggests that this success is not quite real. The cut-down in tune-up time for the machine by a factor of two, as a result of increasing experience and computer based parameter preset, was totally spent by the extremely refined beam centering procedure, which is mandatory for avoiding excessive beam loss on the septum blades. During the run, the operators must keep track of ion source wear-out and must continuously rematch the beam in order to satisfy the extreme beam centering requirement, imposed by the splitting device. It was not entirely clear so far, which particular optical elements should be included in the correcting procedure, therefore a computer-based control loop was not closed at this time.

The design of a micro-bunch suppressor also mentioned as a further improvement[2] in 1977, was completed. The specifications are briefly as follows: Travelling wave deflector, at a phase velocity v/c = 0.005, to be inserted into the injection beam line. Total length: 0.7 m, deflection at ± 600 V and 2 cm spacing of the deflection electrodes: 30 mrad; switching time: 6 ns. Investigations of commercially available wide band amplifiers and measurements of delay line samples confirmed the feasibility of the system. This universal beam chopper, which equally would have served as a convenient tool in particle dynamics studies , was never built. Because of the increasingly broad application of the beam splitting system in the last two years, it was felt unreasonable to shape the time structure of the beam for the main experiment and make it less useful at the same time for the parasitic experiment. Instead of an universal beam chopper in front of the accelerator, it is now stated as a general rule that the users should provide dedicated deflectors

in the high energy beam line, leading to their individual target set-up. In one case, so far, where such a deflector was built, it turned out to be simple and highly successful.

Hardware Performance

Since a separate report[5] is given on achieved improvements of a few components, this paragraph will concentrate on operation experiences of most critical subsystems and will equally outline proposed measures for further reduction of still existing deficiencies. According to Fig. 3, mostly the rf and injection system deserve further comments.

A few general remarks: The continuing high fraction of downtime as marked in Fig. 2 seems to compare unfavorably with other linacs, even with heavy ion linacs. But since there is no unified accounting scheme among all accelerators, the figures do not entirely bear evidence. Technically it is clear that amplifiers and power supplies can be trimmed to operate safely and stably at one particular set value, as in proton accelerators. However, it is technically non-comprehensive that amplifiers from a supplier X behave much more reliably than those procured from company Y under essentially identical operating circumstances. Therefore an assessment on the state of the art is readily available. The operations budget of the Unilac in the last years would have allowed for elimination of faulty equipment to some extent, but in most cases it was not clear whether the equipment was inherently underdesigned, or whether it could be made to give satisfactory service. For this analysis, available maintenance time never sufficed. As a result of an excellent collaboration with the users' representative, runs of various degrees of difficulty for the linac performance could mostly be scheduled according to the operational status of the machine or its particular subsystems. This situation however, will change in the future. Plans for a heavy ion synchrotron facility, for which the Unilac is included as an injector, clearly imply the need for a vigorous reconsideration of the reliability aspect. This is mandatory since fewer maintenance people will be available then for the linac.

Injection

The ion source and electronic equipment contribute nearly equally to the problems in the injection system. The duoplasmatron, earlier reported as an alternate source, was abandoned completely in favor of the Penning source. The latter shows much better beam currents for metal ions and equal properties for gaseous elements. No drastic progress can be reported for the source lifetime and there is no meaningful figure on an average value. Instead, there is a broad distribution almost from zero to 8 hours, if it was pushed hard, or to 40 hours, if it was run decently. The output intensity runs up slightly during the first two hours, then drops steadily, until the intensity becomes intolerably low for the particular experiment or until a short develops between anode and sputter electrode. A continuous monitoring and retuning of the source and beam matching elements is necessary on a trial and error basis. Spurious plasma oscillations, apparently giving rise to considerable energy oscillation of the beam, sometimes prevent an acceptable beam quality in terms of time structure and energy spread. Eliminating this behavior is by trial and error adjustment of source and extractor parameters, rather than a rationally substantiated operation. There are good and bad sources, differing by a factor of 5 in beam intensity, though they are fabricated or refurbished from precisely identical pieces and assembled with well controlled clearance settings. This inconvenient operation behavior was not previously experienced during the long years of test bench investigations, because more fundamental questions had to be pursued. Recent emittance measurements, performed on the high voltage terminal of the injector, revealed an incredibly erratic reaction of the emittance shape on incremental variations of the magnetic field and the extractor position. An emittance break-up by a factor of five can easily occur, accounting probably for the above mentioned intensity discrepancies from source to source. Taking into account the already laborious operation of charge state optimization and isotope selection, it is deemed unreasonable to implement a sophisticated emittance shaping effort into the routine procedure for beam tune-up. Instead, an ECR source is under development and is expected to replace the PIG source in a few years. This new source is not supposed to yield much higher brilliance figures, but it is a promising candidate for a stable and a long life device.

In principle, two completely identical injectors are available. It is still the aim to have a pretuned source on stand-by in the second injector, if the source in the first one expires. This might not be advisable, if simple beam quality without isotope separation is sufficient. In this case a source change in the same injector may be effected in half an hour and easily coordinated with a target change. But those easy runs are becoming rare. In the case of an ion change, a pretuned stand-by source certainly will save 3 - 5 hours of tune-up time. After a completed pretune, with the optimized beam stopped in front of the switching magnet, filament and discharge current are run down. The source then comes right on with the same beam parameters if turned on again. Thus far, frequent breakdowns in electronic equipment on the source platform or in the high voltage supply prevented the success of the envisaged twin injector concept. Semiconductor circuitry, in the sophisticated data transmission chanels and power supply control units, are highly susceptible to nearly unavoidable high voltage transients and discharges. Two injectors present nearly twice the probability for break downs and present also the need for nearly twice the maintenance effort.

A rigorous reconstruction of the injection beam lines, extending from the DC gap to the switching magnet is under consideration, eliminating in the future inconvenient acceptance constraints imposed by the isotope separator optics. In the original design the actual source emittance has been underestimated and adequate reserves for a a less ideal beam centering were not included. Thus,

an increase of magnet and lens aperture from the present 4 to about 8 cm is planned. This will alleviate the presently encountered beam loss of a factor of 3 and will considerably simplify the tune-up of the beam through the injection lines. In addition, this alteration is indispensable for the application of a multi mA source for singly charged Ne ions, which is a substantial tool in future investigations of the longitudinal and transverse space charge limits of the Wideröe structure.

Rf-System

The Wideröe rf amplifiers, built by a commercial company specializing in industrial heat application, continue to operate as reliably as communication equipment. Anode and grid voltages have been increased in order to obtain the excess power, especially in module No. IV, for the acceleration of U^{9+} instead of the design charge state U^{11+}.

Irrespective of an elaborate test bench program, the situation of the Alvarez amplifier system remains unchanged: The tetrodes in the final amplifiers become unstable beyond one quarter of their design power ratings. The implementation of sophisticated protection circuitry did not inhibit tube damage but seems to shut off the system too often. If a tube becomes defective, crowbar firing becomes more frequent even at decreased power levels. Inspection of the interior structure of a broken tube does not reveal the fault causes. It is still believed that parastitic oscillations inside the tube initiate the damage. Sensing circuits, tuned to 0.76 and 1.2 GHz indicate a coincidence of microwave signals with an over-current trip-off. A large variety of attenuating measures have been applied without conclusive success. This activity will be continued until alternate approaches, which are pursued in parallel, result in an ultimate solution. The design aim still remains to obtain 1.6 MW pulse power at 25 % duty out of one single amplifier. The achievement of this goal is crucial for the Unilac upgrading program[4], for which the space for two amplifiers per Alvarez cavity will not be available. In the meantime nearly two tubes per stage have to be replaced in one year, and the useful tubes have to be selected properly.

As a consequence of the rf power shortage in the Alvarez section, foil stripping has to be used for ions heavier than Xe. In case of a high current run, for instance with a few µA Uranium beam, foils of 40 µg/cm^2 are damaged in less than one hour. This damage is not visible, nor does it result in a drastic drop of charge state abundance. It is mostly a pile up of energy straggling, which inhibits a proper phase space matching after the flight path between stripper and Alvarez tank I.

The amplifiers for the single-gap cavities and the re- and debunchers, altogether 30 identical units, perform nearly acceptably. After the elimination of several systematic failure sources, the required maintenance effort is still high: two technicians just manage to have on the average 28 out of the 30 units operational.

The replacement of the rf power lines for the Alvarez and for the single-gap cavity section was delayed, since a complete rearrangement of the line routing has to be effected anyway for the upgraded machine. A satisfactory design for the supporting insulators[5] has been found. Meanwhile, the fault rate drastically decreased, as a result of a yearly line inspection and replacement of deficient parts.

The suppression of rf leakage is a lengthy story of only a partly technical nature. The choice of the Unilac frequencies, 27.12 MHz for the prestripper and 108.48 MHz for the poststripper, was based on a recommendation of the German communication authority. They only lately discovered that the upper frequency falls into the air navigation band and drew the attention of the air control authority to this fact. An avalanche of bureaucratic reactions was the result, though this particular channel is not occupied by the near-by Frankfurt Airport.

GSI finally was assigned to suppress the radiation of the 27.12 MHz harmonics "only" to below the legally admitted level. This turned out to be an extremely tedious and laborious undertaking, which took almost three years. About 20 leaks had to be fixed on the 34 amplifier chains, each of them having additionally very special leakage sources. A series of mechanical parts had to be redesigned and remade. The problem was not so much the fixing of the leaks, as their detection.

Magnetic and electric probes, when used for scanning the metal surfaces and leads, are unable to discriminate irrelevant leaks from relevant leaks. This determination can only be made by a test antenna in the remote field, scanning the radiation pattern and polarisation. Leaks tend to be quite frequency selective, and leakage generally is much more intense for higher harmonics than for the fundamental, for which chokes and traps already had been designed in the circuit. This subject gives rise to the question about the frequency selection for future accelerators. So far, there is no optimum choice. Any fundamental below a few 100 MHz will imply harmonics, which fall into broadcasting bands, for which the restrictions are more severe than for the communication bands. In the far future, multiples of 27.12 MHz will be a perfect selection, because the association of industrial rf heat equipment manufacturers argue strongly on international frequency allocation committees in favor of a cancellation of limitations for the 27.12 MHz harmonics out of channels.

Computer Control

The Sigma 6 computer facility was upgraded to its ultimate configuration and capacity and it no longer is shared with the users taking data. It is extremely useful for off-line programs supporting accelerator operation and optimization[3,6]. It provides convenient and highly instructive information on the machine status via display screens in the main control room. The following data are presently available: all faraday cup and profile harp signals along the machine, all magnet currents referenced to the optimized set values, a pattern of the beam current along the machine, derived by nondestructive probes, a read out of interlock events, charge and isotope spectra of the injection beam line, charge spectrum after the stripper, display of source parameters, printout of energy measurements. On-line programs, which really are meant by the word "computer control", are limited to a few examples: The run-up of the source until striking the arc is automated, all magnet currents can be set as computed values or as stored data from earlier runs, the beam can automatically be centered in the injection and at the high energy end of the machine.

The envisaged superiority of the computer facility, namely a drastic saving in tune-up time, can not yet be reported. The use of the computer as an intelligent switchboard and as a convenient display processor are not considered to be control functions. Mainly two reasons prevented the envisaged saving in set-up time: first, the steadily changing hardware imperfections of the machine (disabled elements, misalignments, current offsets, non linear reactions of magnet power supplies etc.) are not registered or updated in the data base. The second reason is the lack of a reproducible emittance pattern as a start-off basis for lens current determination. It is possible in fact, to measure the emittance and to let the computer evaluate the particle dynamics and set the beam optical parameters, but this procedure does not save much in tune-up time.

A general short coming of the existing computer facility with the highly centralized scheme of one powerful computer and a few small non-self-sustaining satellites is the slow reaction time, especially for automated optimization loops. An improvement of the system software and an increased assignement of control functions to decentralized microcomputers is under consideration, along with a continuous stabilization effort of hardware components and a more thorough understanding of the accelerator behavior.

References

[1] D. Böhne, "The Unilac, Development and Present Status". 1976 Proton Linear Accelerator Conference, Chalk River. AECL-5677, Chalk River Nuclear Laboratories, Chalk River, Ontario (November 1976)

[2] D. Böhne, "Status Report on the Unilac", 1977 Particle Accelerator Conference. IEEE Transactions on Nuclear Science, Volume NS-24, Number 3, (June 1977)

[3] J. Klabunde et al., "Measurement of Energy, Energy Spread and Bunch Width on the Unilac", this proceedings

[4] N. Angert et al., "The Unilac Upgrading Program", this proceedings

[5] D. Böhne, "Recent Improvements of Accelerator Components at the Unilac", this proceedings

[6] L. Dahl et al., "Longitudinal and Transverse Beam Optimization", this proceedings

Discussion

L. Teng, FNAL: Could you tell us something about your future development program especially in connection with heavy ion fusion? I understand you have a project actually funded for heavy ion fusion.

Böhne: Compared to the plans here in the States, ours is a very limited and preliminary undertaking. We are looking at very particular developments which we feel we can easily do because they are on the line which we have to follow for the synchrotron project anyway. We have a high intensity ion source under development, presently delivering about 60 mA Xenon. We will make accelerator experiments on the Unilac when the acceptance of the injection beam line is increased, so we can do space charge experiments on the Wideröe, a so-called low beta structure, to evaluate emittance growth and space charge thresholds if they exist with our beam intensities of about 10 mA. A high intensity low beta structure is under consideration and R.W. Müller will report on this study. We don't have activities in storage rings or in final beam transport or anything else.

STATUS OF THE ARGONNE SUPERCONDUCTING-LINAC HEAVY-ION BOOSTER*

J. Aron, B. Benaroya, L. M. Bollinger, B. G. Clifft, W. Henning,
K. W. Johnson, J. M. Nixon, P. Markovich and K. W. Shepard
Argonne National Laboratory
Argonne, Illinois 60439

Summary

A superconducting linac is being constructed to provide an energy booster for heavy ions from an FN tandem. By late 1980,the linac will consist of 24 independently-phased superconducting resonators, and will provide an effective accelerating potential of more than 25 MV. While the linac is under construction, completed sections are being used to provide useful beam for nuclear physics experiments. In the most recent run with beam (June 1979), an eight resonator array provided an effective accelerating potential of 9.3 MV. Operation of a 12 - resonator array is scheduled to begin in October 1979.

Introduction

This paper reports the status of the Argonne superconducting heavy-ion linac, which has been developed to boost the energy of heavy-ion beams from an FN tandem accelerator.[1,2,3] The intent of the project has been both to develop superconducting rf technology for the acceleration of heavy ions, and to provide a useful accelerator for use with the Argonne FN tandem. At this time all significant development tasks have been completed. Current funding provides for a linac of four modular sections, of which two have been completed.

The physical layout of the accelerator system is shown in Fig. 1. The pre-tandem beam-bunching system and a post-tandem superconducting buncher are housed in the tandem vault. The linac and most of the helium refrigeration system are located in a previously existing target room, with the linac output going into a small new target area.

Preserving the good quality of the tandem beam requires an exceedingly narrow beam pulse injecting the linac. This has been accomplished with little loss in the tandem beam intensity by a two-stage bunching system.[4] The pre-tandem buncher is a gridded-gap (room temperature) driven by a sawtooth-like voltage generated by

*Work performed under the auspices of the Office of Basic Energy Sciences of the U. S. Department of Energy.

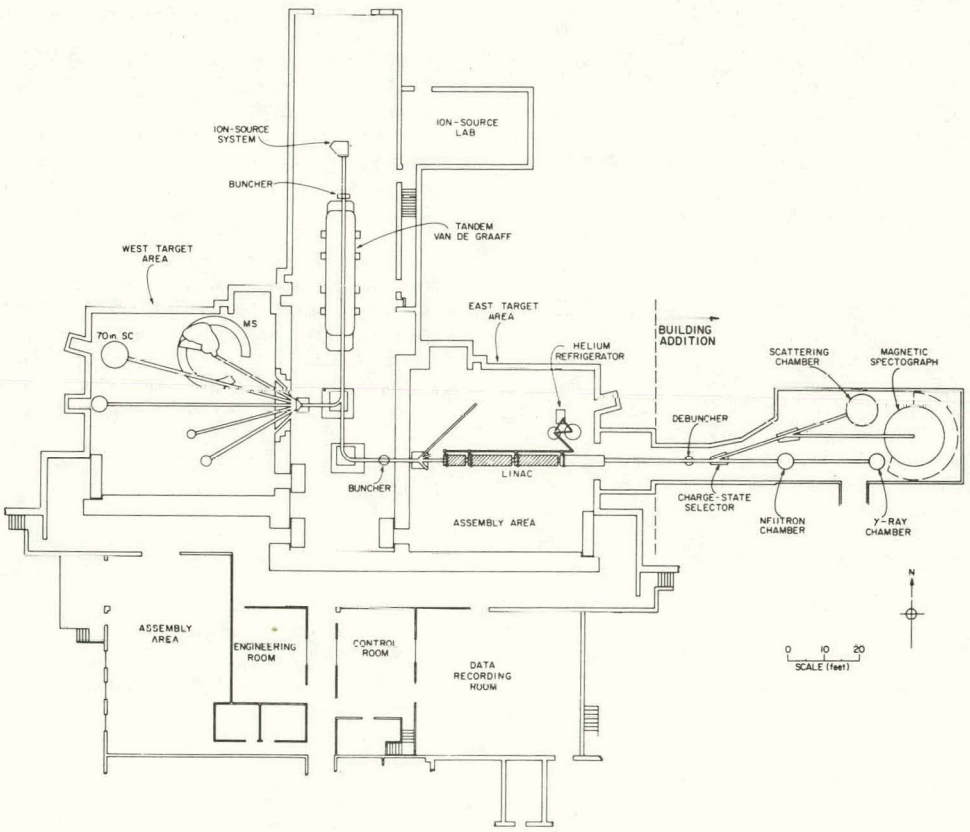


Fig. 1. Overall layout of the accelerator system.

superposing four rf harmonic components. This system compresses about 80% of the dc tandem beam into 1 nsec pulses at the tandem output. The post-tandem buncher is a single superconducting split-ring resonator which linearly compresses these pulses to a width of less than 100 psec at the linac entrance.

The linac is formed of modular cryostat sections any one of which can be taken off-line without disturbing operation of adjacent sections.[1] Figure 2 shows a cross section of a typical cryostat. Thus the linac consists of an independently-phased array of superconducting split-ring resonators, each of which can provide more than 1 MV of effective accelerating potential over a range of a factor of two in particle velocity.[5,6,7] Independent phasing allows the velocity profile of the linac to be varied over a wide range, and provides a high degree of operational flexibility. Focusing within the linac is accomplished with a superconducting solenoid following every pair of resonators.[8] Beam diameter within the linac is typically kept smaller than 6 mm both to prevent beam impinging on the superconducting surfaces of the resonators and to limit radial variation of the energy gain within the resonators.

The linac target area was constructed in 1977, and installation of the experimental equipment shown in Fig. 1 will be completed in 1979-80. For initial operation, experiments are being performed on the zero-degree beam line. Later, with the installation of the superconducting debuncher-rebuncher and the charge selector magnet, the location of the various experimental stations will be changed to that shown in Fig. 1.

The modular nature and variable velocity profile of the linac have permitted useful operation with completed sections while construction continues. Beam acceleration tests began in June 1978,with two resonators in a six-foot cryostat module, and have continued to the present array of twelve resonators in two twelve-foot cryostats, scheduled to run with beam in October of this year.

Table I outlines the several runs with beam. Initial operation revealed a number of system flaws, and the first three runs were focused primarily on system development, as has been discussed elsewhere.[3] As is discussed below, in the last two runs with beam the remaining significant development tasks have been completed, and the emphasis has shifted to providing beam for users.

Linac Systems

The fourth run, in March 1979,was the first in which beam was provided for users over an extended period of time. However three significant problems remained with linac performance. Firstly, the resonators provided on-line an effective accelerating potential of 0.9 MV/resonator, substantially less than the 1.4 MV/resonator obtained in off-line tests. Secondly, mechanical vibration of the resonators caused occasional excursions of rf eigenfrequency beyond the range of the fast tuning system. The consequent loss

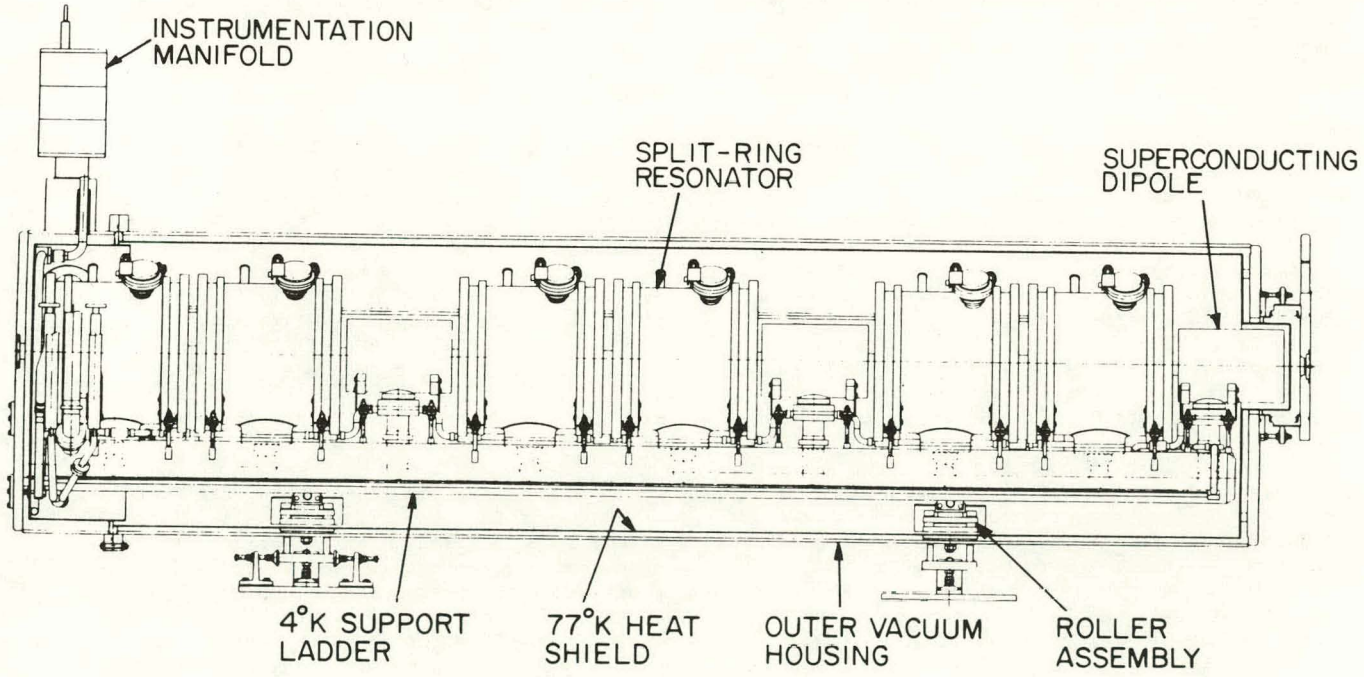


Fig. 2. Cross-section of a linac cryostat module. The cryostat disassembles by rolling the resonator array, together with all cryostat plumbing and electrical leads, out of the vacuum housing.

TABLE I

Outline of Linac Beam Tests

Date	Duration	Number of Resonators	Max. Acc. Potential	Ion Species
June 1978	3 days	2	1.6 MV	O_{16}^{6+}, F_{19}^{6+}
Sept. 1978	5 days	5	4.0 MV	O_{16}^{6+}
Dec. 1978	8 days	6	5.2 MV	S_{32}^{14+}
March 1979	31 days	8	7.6 MV	S_{32}^{14+}
June 1979	30 days	8	9.3 MV	S_{32}^{14+}, Si_{28}^{12+}, O_{16}^{8+}

of phase control caused output energy variations which required blanking of either the beam or data taking for 10-20% of the time, i.e., the effective duty factor of the linac was 0.8 - 0.9. Thirdly, the linac output energy was found to vary by a few parts in 10^3 over a time period of several hours.

The resonator field level was limited by thermal instability at an rf input power less than the design level of 4 watts. Following the fourth run, it was found by radiography that plastic tubes used to vent helium gas from the resonator interior were out of position in a way that would cause a gas bubble to accumulate and prevent cooling of a critical portion of each resonator. The tubing was modified with the result that in the fifth run with beam, the effective accelerating potential was increased to 1.2 MV/resonator.

The rf control system was modified to provide rf damping of mechanical vibration in each resonator. This was achieved at the cost of varying the rf amplitude in each resonator at the frequency of the mechanical motion. In the system used, an amplitude variation of 2 parts in 10^4, which has a negligable effect on beam quality, reduced the vibration by 40%. The system also provides temporarily increased damping for any resonator that loses phase-lock. In this condition, the output beam is useless, so that an increased rf amplitude variation is tolerable. The result is that vibration resulting from any large mechanical perturbation is quickly damped out. In the fifth run with beam, the rf damping system reduced the vibration-induced loss of phase control to less than 1% of the time for the eight-resonator array.

Finally, it was found that the slow drift in linac output energy was correlated with a change in the liquid nitrogen level in a portion of the cryostats through which the rf cabling is run to the resonators. Apparently, the liquid nitrogen permeates the rf cabling and causes a slight change in electrical length. Thus variations in the liquid nitrogen level induce a slight shift in the resonator rf phase and amplitude, and in the beam energy gain. Modification of the control system to maintain a constant liquid level eliminated the drift in output energy.

Linac Operation

More than 1800 hours of beam time have been logged. The most outstanding operating feature has been the general reliability of the linac.[3,9] While accelerating beam, the linac systems generally require little or no operator intervention for periods of many hours. Linac downtime has been small, typically an hour per day.

Beam quality is essentially as expected,[1] although three factors limit presently available performance. (1)-The second stripper is temporarily located upstream of the tandem beam-analyzing magnet, rather than at the time focus at the linac entrance; thus energy straggling in the stripper dominates the output time-energy spread. (2)-In the temporary linac configuration used thus far, a six-foot gap exists between two cryostat modules which produces a significant time spread of the particle bunch prior to acceleration through the final cryostat module. (3)-Also, absence of a debuncher-rebuncher downstream of the linac prevents obtaining the full time or energy resolution capability of the linac in the experimental areas.

Linac tuning has proven straightforward. At present this is accomplished by calibrating the rf phase of each resonator by varying the phase and observing the output beam energy. In this procedure, the first resonator is tuned, with all others off, and then one successively turns on and tunes each resonator in the chain. At present tuning is done manually, and requires several hours. Eventually, the operation will be fully computer-controlled, and should go very much more rapidly.

Future Plans

Planned hardware additions in 1980 include modifying a six-foot cryostat and constructing a fourth, twelve-foot cryostat which together will add twelve resonators to the linac array. Also a superconducting debuncher-rebuncher is to be installed downline of the linac.

Acknowledgments

Of the many people at Argonne who have contributed to the linac project, the linac staff would particularly like to acknowledge the contributions of R. P. Breuss, A. J. Rogers and E. K. Gutowski in resonator construction, F. J. Lynch and R. N. Lewis in development of the pre-tandem bunching system, and R. T. Daly and J. E. Kulaga in implementing the computer-control system.

References

1. L. M. Bollinger, et al., Proc. of the 1976 Proton Linear Accelerator Conf., AECL-5677, 95 (1976).

2. L. M. Bollinger, IEEE Trans. Nucl. Sci. NS-24, 1076 (1977).

3. K. W. Shepard, IEEE Trans. Nucl. Sci. NS-26, 3659 (1979).

4. F. J. Lynch, R. N. Lewis, L. M. Bollinger, W. Henning, and O. D. Despe, Nucl. Instr. and Meth. 159, 245 (1979).

5. R. Benaroya, et al., IEEE Trans. Mag. MAG-13, 516 (1977).

6. K. W. Shepard, et al., IEEE Trans. Nucl. Sci. NS-24, 1147 (1977).

7. K. W. Shepard, C. H. Scheibelhut, P. Markovich, R. Benaroya, and L. M. Bollinger, IEEE Trans. Mag. MAG-15, 666 (1979).

8. A. H. Jaffey, R. Benaroya, and T. K. Khoe, Proc. of the 1976 Proton Linear Accelerator Conf., AECL-5677, 102 (1976).

9. J. M. Nixon and L. M. Bollinger, to be published in Advances in Cryogenic Engineering.

DISCUSSION

J. Dick, Cal Tech: Could you describe the changes you made to increase the performance of the cavities in the accelerator cryostats and could you quantify the phase and amplitude jitter of the cavities in the actual accelerator configuration?

Shepard: We initially had some design problems in the cooling system; these have been cleared up - it has mostly been implementation. We have had some epoxy seals which gave us leak trouble. We had some plastic tubing which cracked early on but minor design changes seemed to have cured these problems. With respect to phase and amplitude jitter, the residual phase jitter is less than a degree peak-to-peak on the resonators. The amplitude control is good to a few parts in 10^4 at the present time.

D. Young, FNAL: Could you say a few words about the stability of the Niobium coating on the structures, especially with regard to repeated opening to atmospheric pressure?

Shepard: The thinnest Niobium in the system is a 16-tension Niobium sheet. Last summer we had a catastrophic vacuum accident which caused considerable degradation of 4 of the resonators. Other than that, we've not experienced degradation of the resonators in operation, either by re-cycling or by operation of the beam in 1800 hours of beam time.

J.P. Blewett, BNL: This technique for supressing vibrations I regard as a very considerable achievment, but it was not clear to me how you use the information from the rf to apply mechanical force to stop the vibration.

Shepard: The rf itself is coupled to the system. If you turn up the rf amplitude in one of these resonators, radiation pressure effects shift the eigen-frequency typically by several kilohertz, so that the rf mode and the acoustic modes are coupled. If you wiggle the rf amplitude at the resonant frequency of one of the acoustic modes, you can, for example, stimulate a vibration of the system. By sensing the vibration by watching the eigen-frequency of the resonator, you can detect the presence of a vibration and vary the rf amplitude in such a way as to damp the vibration itself. It is very weakly coupled, but the mechanical Q's are extemely high at these temperatures so the small damping has an appreciable effect. An electromagnet force is used to damp.

E. Jaeschke, Heidelberg: You mentioned some helium conditioning you had done in the June runs. How frequently did you have to do this and were these special cavities somehow nearer to the normal conducting outside world?

Shepard: Of the 8 resonators on-line, I think two of them would require conditioning perhaps every 48 hours and another one somewhat less frequently. The conditioning process itself requires about an hour to implement and so far we have found that we are required to do this periodically in order to maintain the full accelerating potential of the machine. It is our dominant source of downtime, but at the moment it does not seem to be a serious operating problem. It is less troublesome, let's say, than sparking in the tandem seems to be during operation.

L. Teng,FNAL: Were you able to observe any beam

loading effect on the phase stability or phase lagging?

Shepard: No, we do not see that, but I should say that beam loading is a very small term in the rf losses of the system because of the very low beam current; it is a fraction of a watt and the dominant rf loss of 100 watts in the tuning system, I think, just completely blanks that out.

A. Citron, Karlsruhe: With respect to the question on beam loading; in our superconducting proton linear accelerator with helical structures, we went up to something like 200 μA and at that level the rf system feels the beam loading, but it can still manage.

OPERATION OF THE HEIDELBERG HEAVY-ION POSTACCELERATOR

H. Ingwersen, E. Jaeschke, R. Repnow, Th. Walcher, B. Huck and B. Kolb
Max-Planck-Institut für Kernphysik
Heidelberg, Germany

Summary

The 3MV-stage of the Heidelberg Heavy-Ion Postaccelerator went into operation in December 1977, and is in the state of full user availability since May of 1978. The machine uses spiral resonators at room temperature. Ten such resonators with design velocity $\beta_o = 0.10$ at 108.48 MHz are operated either CW at 20 kW or in a pulsed mode (DF = 0.25) at 80 kW. Due to the flexibility of the independent phasing of the 10 resonators presently in operation, a wide variety of ions between ^{12}C and ^{79}Br have been accelerated for user experiments. Acceleration voltages as high as 3.3 MV (CW) and 5.5 MV (Pulsed Mode) could be demonstrated.

An energy resolution of $\Delta E/E < 4 \times 10^{-4}$ allowing rebunched pulse widths of $\Delta t_{FWHM} < 70$ ps could be measured, showing the tandem-like beam quality. The machine is exclusively computer-controlled, a prerequisite for the operation of the many parameters of a tandem-postaccelerator-combination. The overall availability of the postaccelerator together with the MP Tandem was above 80% of the scheduled user beam time. The operation of the 3-MV stage is now interrupted for a 4-month shutdown till the end of 1979, to allow for the extension of the machine to its full 10 MV (CW) acceleration voltage by the addition of 20 more spiral resonators.

The Spiral Resonator - Postaccelerator

Development, construction and prototype tests of the normal conducting spiral resonator of the Heidelberg-type have been described in Refs. 1 and 2. Figure 1 shows a cut drawing of the structure to summarize the main features of this type of resonator. The dominant element in the figure,

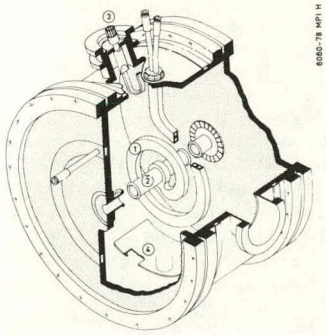


Fig. 1
Cut drawing of the Heidelberg spiral resonator. Tank inner diameter is 35 cm.

labeled (1), is a $\lambda/4$ line resonator wound as a spiral. The leg of the spiral is screwed to the outer shell of the resonator, while the free end, the location of the voltage maximum, holds the drift tube (2) between the two grounded tubes forming the accelerating gaps. Gap width and drift tube bore are 2 cm each; gap-to-gap distance is $\ell = \beta_o \lambda/2$. Thus the structure has a very wideband transit time factor necessary for the desired high flexibility to accelerate ions of very different initial velocities and charge-to-mass ratios from the MP-Tandem. The rf power is coupled to the resonators by a turnable inductive loop (3) extending into the resonator near the leg of the spiral. The resonance frequency is maintained by a servo loop controlled capacitive tuning plate (4). Characteristic parameters of the resonators are listed in Table I.

Table I. Parameters of the spiral resonators used in the 3 MV-stage of the Heidelberg Postaccelerator

Operating frequency (MHz)	108.48
Quality factor Q	3500
Design velocity β_o	0.10
Shuntimpedance Z (MΩ/m)	30
Input power N_{cw} (kW)	20
N_p (kW (25% duty cycle)	80
Effective voltage ($\phi_s = -20^0$)	
U_{cw} (MV)	0.33
U_p (MV)	0.60

Figure 2 is a drawing of a postaccelerator module stacking four spiral resonators. Two resonators always share one common flange carrying the grounded drift tubes. One operational module yields a total effective voltage of 1.3 MV (CW) at a synchronous phase $\phi_s = 20^0$. Each set of four spiral resonators has an external quadrupole doublet with a maximum field gradient of 3 kG/cm, 45 mm aperture and 15 cm length per singlet. A

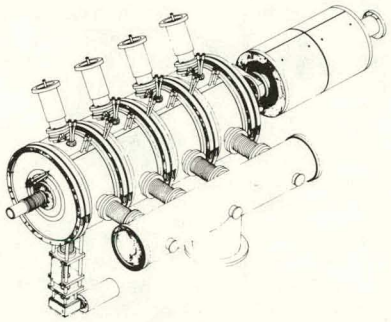


Fig.2 Accelerator module consisting of four spiral resonators, quadrupole doublet and pumping line.

vacuum better than 1×10^{-7} mbar is maintained by a cryopump (2 W, 20 K closed-cycle refrigerator) with an external pumping line arrangement. The characteristic beam dynamics parameters of such a setup have been discussed in[1,3].

For the first 3 MV-stage of the Heidelberg booster three accelerator modules were manufactured in the Institute's main workshop in 1977.

The accelerator layout and beam transport system have been designed to fit the postaccelerator into the present MP-Tandem accelerator building and to bring the postaccelerated beam back to the existing experimental area. Details can be found in Ref.3. Figure 3 shows a photograph of the linac and the beam transport system.

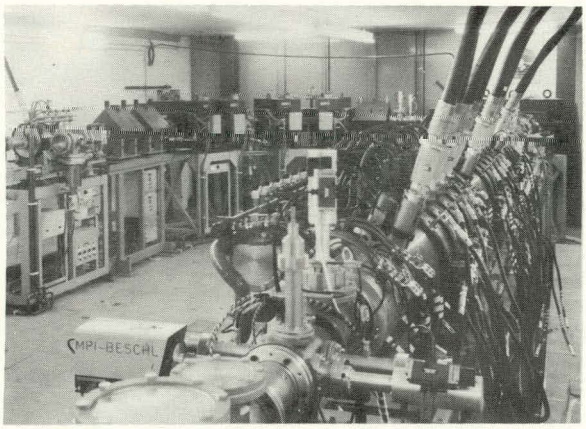


Fig.3 View of the 3-MV-stage of the Heidelberg Postaccelerator. Three modules with β_o=0.10 - spiral resonators are seen at the right side, followed by part of the beam transport system and debuncher (to the left). See Ref. 3.

Rf Generators and Control Electronics.

In the first 3-MV-stage of the booster, 12 commercially available FM broadcast transmitters with an output power of 20 kW CW are used to feed the cavities. They are of the same type operated in the power and beam test in the years 1975-76, and have proven to be reliable and rugged. For use as the rf supply of the linac they had, however, to be modified considerably to meet the requirements of the computer-control as well as to operate them from one common anode power supply and to run them in pulsed mode. Figure 4 shows a view into one row of the transmitter gallery. The generators are set up in groups of four, one group belonging to one accelerator module. The 19" racks in the background house the driver amplifiers, the reference signal distribution, the regulation units for phase, amplitude and resonance frequency and the phase shifters necessary for each individual cavity as well as a CAMAC crate of the computer-control. All the regulation units have been designed and manufactured in-house.

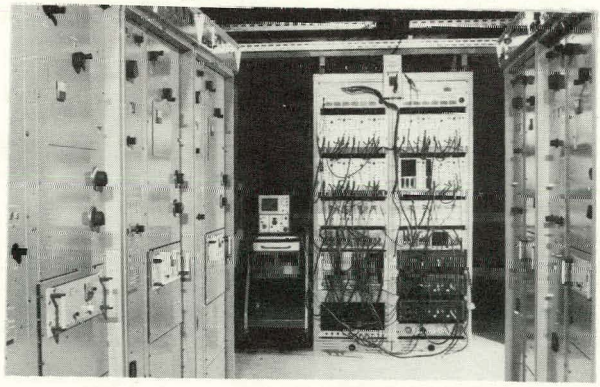


Fig. 4 View of the rf gallery showing transmitters and regulation and control systems.

The Computer-Control System

The use of independently phased resonators for acceleration of a large variety of different ion species delivered by the electrostatic tandem injector, demands efficient computer assistance of the operator. A computer program to calculate all settings for rf amplitudes, phases, quadrupole gradients and dipole fields which depend strongly on the injection parameters, was mandatory. Control of all parameters directly by a computer maintaining the accessability for manual interaction was highly desirable.

The concept of the computer-control (see Ref.4) was based on the following general guidelines in order to limit the complexity of the overall system:

a) all remote control of the postaccelerator should be performed only via the computer. As no hardwired back-up system for control was to be installed, this decision enormously simplified the wiring as well as the logic of the programming, but demanded a reliable and comfortable interface between the operator and the accelerator hardware.

b) The computer-control system should not be used for closed-loop regulation of parameters or for operating safety interlocks. Every critical device should have its own hardware regulation system keeping track of the values set by the computer and should be protected by its own hardware interlocks which should react even in the case of a computer failure. Similarly, the computer should not have to synchronize with the accelerator to acquire time-dependent parameters. All rapidly varying parameters, e.g., in the pulsed operation mode, have to be latched to be read at any time. By these provisions, timing problems were greatly alleviated.

c) The control system should reflect the modularity and expandability, which are the key features of the accelerator itself. Thus, the inclusion of additional parameters, controls or functions as well as the expansion of the overall system by a factor of three, should be easily possible without major modifications to the existing system.

d) As most of the rf regulation electronics had to be designed and built in-house, the control system had to be based on standard, commercially available products to the widest possible extent. Thus, the CAMAC standard was adopted for the control system of the Heidelberg postaccelerator.

The Control Hardware

The accelerator control hardware is schematically indicated in Fig.5. The system is controlled by a dedicated PDP 11/34 minicomputer equipped with 128k of memory, a floating point processor and standard peripherals facilitating the development of the software.

All accelerator components and the operator's console are accessed via a single JY 411-CAMAC interface, which can directly drive a parallel CAMAC branch as well as a serial high-

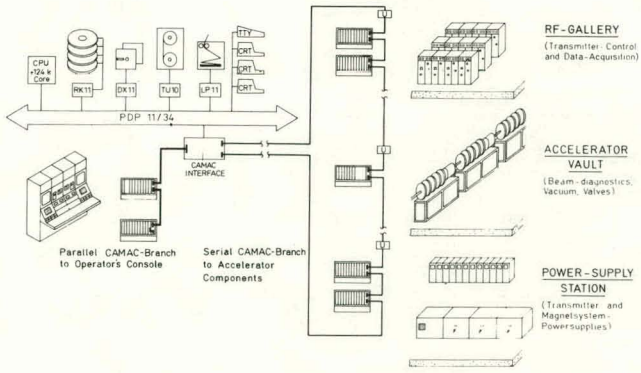


Fig.5 Schematic diagram of the Heidelberg postaccelerator control system.

way. Both branches are completely compatible with respect to software as they use the same control registers, and all features like direct memory access from CAMAC into the memory, or vice versa, are implemented for both branches. The high speed parallel branch is used for servicing the operator's console where various display units need to be updated rapidly. Though refresh rates between 1 Hz and 10 Hz depending on the type of unit, have proven to be sufficient, much care was taken to minimize the response to an operator's intervention. The serial highway runs as a large loop of about 300 m total length from the computer through three floors of a remote part of the building. Only one cable, consisting of 9 twisted pairs necessary for a byte-parallel serial highway, interconnects the different hardware components of the accelerator and essentially is the only link for communication between the operator and the postaccelerator. Basically, four standard types of highly integrated CAMAC modules are used throughout the accelerator, keeping the number of crates down to a minimum. Readout of analog values is achieved by an ADC module with 32 independent differential input channels. Setting of analogue values by the computer is performed by 12-channel DAC modules. A specially designed transmitter-control module combines 24 relay contacts and 24 status flags for a completely remote operation of one 20-kW rf station. A fourth type of module is used for the control of one magnet power supply each. In addition to these four basic modules there are relay multiplexers, which are used to select analog signals for inspection at the console for diagnostic purposes.

Though these modules are quite different in function they all meet one common criterion which has proven to be essential for easy software development: to perform a specific operation the computer needs to know and execute only one single CAMAC command and not a series of consecutive steps. Thus, formally, all units can be handled identically and no special device drivers are necessary.

Software Organization

The PDP 11/34 is operated fully under control of the multitasking operating system RSX-11M. The control software is largely subdivided into different smaller programs which are responsible for specific operations and can be run independently from each other in parallel. By this scheme the software development and maintainance was greatly facilitated. Tasks which have to perform larger numerical calculations are written in FORTRAN, whereas the control software is written in assembler language.

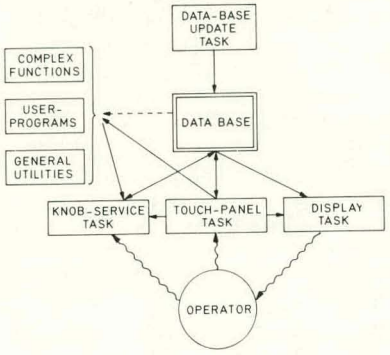


Fig. 6

Structure of the control software

Figure 6 shows the structure of the main software. The main effort was invested into the scheme of a data base which contains all information on the accelerator components, e.g. CAMAC addresses and commands, actual values, calibration factors and the names of the parameters. This data base is stored in the memory. Using a memory-resident data base guarantees fast access and fast response.

All tasks can access the CAMAC hardware only by using the information stored in the central data base. After changes or additions to the hardware, in most cases, just the data base needs to be updated. Without further programming the basic control routines will then have access to the newly installed components.

Three primary control routines are provided which together with their related hardware components at the console are completely equivalent to a conventional operator's console and enable the operator to perform all necessary operations manually. These are
i) a display routine, to inspect all required parameters on a TV-screen; ii) a knob service routine to change or optimize settings of parameters manually; and iii) a touch panel service routine as the central program.

By touch panel interaction, the operator has full access to the data base. At maximum, four logically consecutive steps are required to uniquely specify a parameter, which afterwards, by touch panel command, can be included in the display table or connected to one of four control knobs. Simple functions, like switching operations, are directly performed via the touch panel. For convenience, there are preformatted pages of parameter sets which can be called for display.

Without appreciable difference the operator can perform more complex operations like the startup sequence for one rf generator or even the whole accelerator. For such purposes there now exist a large number of different tasks which can be started via the touch-panel and which communicate with each other under control of the operating system.

Initial setting of the postaccelerator components is achieved by an interactive optimization routine which from basic information on the injected beam parameters optimizes the linac parameters for a requested output energy with respect to the beam acceptance. All focusing and beam handling elements as well as the rf amplitudes and phases are set to the calculated values directly by that program. Only minor manual fine tuning and optimization with respect to beam transmission for the injection and extraction region is required afterwards, whereas the linac settings can remain unchanged.

The control console of the postaccelerator consisting of two equivalent stations is shown in Fig. 7. The center part is the touch panel, a CRT display just above, and four control knobs below. The control knobs are simple, two-speed pulse-generators which feed a presetable up-down counter. For each knob the actual assignment and the current value of the parameter can be read on a small alphanumeric display. Other beam diagnostic elements like beam profile monitors, fluorescent screens or slits are operated similarly, a normal TV-monitor and a small oscilloscope being used for display purposes. For diagnostics the rf signals from resonators or transmitters can be selected for display on the larger oscilloscope.

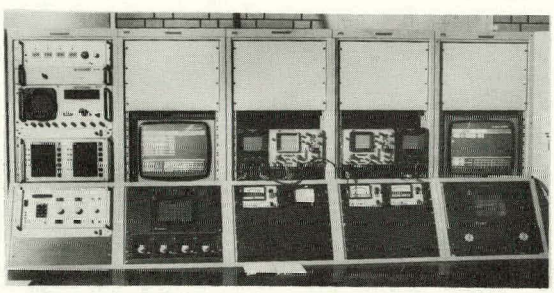


Fig. 7 Operator's console

This scheme of control system has been readily accepted by the operators, as it does not require any knowledge of computer hardware or software. The use of typical computer peripherals like keyboards for control purposes has been almost completely avoided.

As all parameters have their names in plain language with minimal use of abbreviations the operation of the touch panel has become transparent and straightforward even for untrained personnel.

IV. Operation Experience with the Postaccelerator

The Heidelberg postaccelerator started test operation in December 1977, and is in the state of full user available operation since May of 1978. By the end of July 1979, 17 user beamtimes could be operated. Altogether 1498 hours of user time had been scheduled from which for 1223 hours of useful beam were provided for the experiment. These figures correspond to an overall availability of the combination MP-Tandem postaccelerator of 82%. Table II summarizes characteristic data of selected postaccelerated heavy-ion beams as typical examples of the machine performace. The table shows

Table II

Ion	q_{NB}	E_{MP} (MeV)	E_{PA} (MeV)	U_{eff} (MV)	I_{el} (nA)	$\Delta E/E$ (10^{-3})	ε_r (π mm, mrad)
^{12}C	6+	72	90	3.03	100	<4.3	--
^{32}S	14+	132	178	3.30	85	<5	3.1
	15+	132	181	3.28	30	--	4.2
	14+	108	152	3.15	50	~0.4	2.9[1]
	12+	140	178	3.13	40	<1	2.8[2]
	13+	150	190	3.11	15	-	
^{32}S	12+	140	206	5.52	30	-	- [3]
^{58}Ni	16+	177	225	3.01	30	-	3.22[2]
^{79}Br	16+	177	246	4.31	10	-	- [3]

1) (140 ps→300 ps), 2) User Run, 3) 65 kW)

that ions between ^{12}C and ^{79}Br can be accelerated by the present 10 resonators with almost equal effective voltage, (column 5), which is in all cases above 3 MV. The measured energy resolution of less than 5×10^{-3} (column 7), in some cases well below 1×10^{-3}, will be improved by one order of magnitude with the debuncher. The radial emittance ε_r is smaller than the projected value of 5π mm - mrad indicating that the postaccelerator is longitudinally and transversally properly matched to the tandem beam. Row 7 shows an example of the machine performance in pulsed mode. Running the cavities with a peak power input of 65 kW (1:4) resulted in an effective voltage gain of 5.52 MV. In the setting shown in row 4 a ^{32}S beam was gas stripped in the MP to a charge state of 8+ and further foil stripped before the booster to 14+. The final energy was 152.1 MV. Measured at the linac exit and 50 m downstream, the time halfwidth of the micropulse had only increased from 140 ps to 300 ps. From this an energy spread of $\Delta E/E \sim 4 \times 10^{-4}$ can be deduced. Beams of this quality have been rebunched in user runs to pulse widths of less than 70 ps[2].

V. Status of the Further Extension

The status of the extension of the machine to its final 10 MV acceleration voltage in early September 1979, is as follows: The fabrication of the additional five modules (3 modules $\beta_0 = 0.06$, 2 modules $\beta_0 = 0.08$) already started in August 1978, in the Institute's workshop. Since July 1979, this new part of the Linac is assembled, vacuum tested and prealigned, ready to be moved to its final location. Rf generators, regulation electronics and the additional CAMAC modules are in-house. The extension of the computer control system has been completed. A four-month shutdown of the post-

accelerator began in early September 1979; operation is scheduled to start again at the end of this year. Normal MP-Tandem operation will not be affected.

Acknowledgement

The authors want to thank Professor P. Brix for his continuous support and encouragement, and Professor U. Schmidt-Rohr for valuable help in the realization of the project. The skillful and enthusiastic work of many technicians of the Max-Planck-Institut made fast construction and successful operation of the postaccelerator possible. The work has been supported by the Bundesministerium für Forschung und Technologie.

References

1. E. Jaeschke, R. Repnow, Th. Walcher, H. Ingwersen, G. Ihmels, B. Kolb and H. Schwarz, IEEE Trans. Nucl. Sci NS24 No.3 (1977) 1136
2. E. Jaeschke, H. Ingwersen, R. Repnow, Th. Walcher, B. Huck and B. Kolb, Nucl. Instr. Methods 157, (1978)
3. E. Jaeschke, H. Ingwersen, R. Repnow, Th. Walcher, B. Huck and B. Kolb, IEEE Trans. Nucl. Sci NS26 No.3 (1979) 3667
4. R. Repnow, H. Ingwersen, E. Jaeschke, H. Kandler and Th. Walcher, IEEE Trans. Nucl. Sci NS26 No.3 (1979) 3398

1979 LINEAR ACCELERATOR CONFERENCE

OPERATION OF THE KARLSRUHE SUPERCONDUCTING POST ACCELERATOR TEST SECTION IN THE SACLAY TANDEM HEAVY ION BEAM

K. W. Zieher, G. Hochschild, A. Hornung
Kernforschungszentrum Karlsruhe, Institut für Kernphysik
Karlsruhe, Federal Republic of Germany

and

J. P. Fouan, J. Gastebois, P. Joly
Centre d'Études Nucléaires de Saclay, Service de Physique Nucléaire à Basse Énergie
Gif-sur-Yvette, Republic of France

Summary

The test section of a superconducting heavy-ion post accelerator (SNB-Karlsruhe) was set up at the C.E.N.-Saclay Tandem Lab. It was operated with beam in order to demonstrate the feasibility of a superconducting booster accelerator for heavy ions behind a tandem accelerator. In addition, the cavities were used as a beam rebuncher. The energy modulation due to the test section was measured and reproduced the original calibration. In bunch experiments beam pulses were generated and measured.

Introduction

The ion energy of an existing tandem accelerator can be increased appreciably only by a post-accelerator. One possible approach, a linear accelerator of independently phased cavities, has many advantages as a booster: the transmission of the prebunched and stripped ion beam can be 100%. The good tandem beam qualities can be maintained (small transverse emittance, energy resolution of a few 10^{-4}), and, simple energy variation is possible. In addition very narrow beam bunches can be obtained on the experimental target. The use of superconducting cavities is quite cost saving both in investment and running expenses.[1,2] Also the radiated rf power can easily be kept at a low level, which is valuable for the sensitive detection devices used in nuclear physics experiments. Two such boosters are already under construction.[3,4]

Reliability and handling is best demonstrated by an experiment. This was the first reason for repeating some of the Heidelberg experiments[5] at the CEN Saclay Tandem Lab, using the SNB test section. The second purpose of this installation is to use the velocity modulation given by a cavity in order to compress a prebunched beam down to the 100 ps range. Such short beam pulses allow mass identification on flight distances below 50 cm for the tandem mass-energy ranges. This is intended to be used in the fusion-evaporation cross-section measurements presently in progress with a less effective setup at the Saclay tandem. This time structure will also be used in the search and measurement of medium life-time isomeric states expected among the high spin levels populated by heavy-ion reactions.

The cavities were originally optimized for accelerating bromine ions with charge q=23 from 1.67 to 6 Mev/n. Figure 1 shows a cross-section of the cavity. At design field the maximum electric field is $\sim$ 16 MV/m, the effective accelerating travelling wave amplitude is E_{acc} = 1.05 MV/m ($\cos\phi$ = 1, flange-to-flange) and the stored energy is 0.172 J.

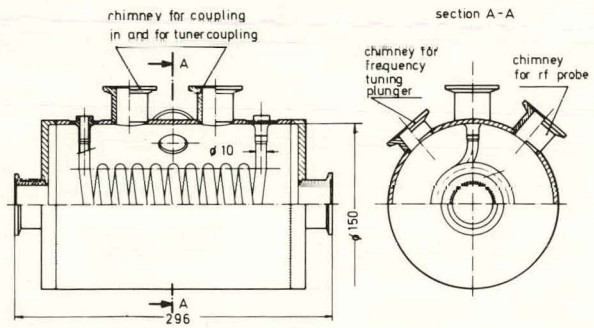


Fig. 1: Cross-section of the rf resonator.[2]

Treatment of the Cavities and rf Measurements

The cavities had been operated at MPI-Heidelberg up to January 1977.[2] Thereafter the test cryostat was moved to KfK-Karlsruhe, where it was standing idle without any pumps installed. In August 1978, the cryostat was opened and the two cavities HD1,2 were removed for laboratory measurements. By oxipolishing HD 1 two cycles, and HD 2 three cycles, $E_{acc} \geq 1.2$ MV/m was achieved in laboratory experiments in both cavities. The two cavities were then mounted into the test cryostat and cooled down. The first cool-down was accompanied by oscillations due to a modification in the helium-gas-fluid system, not allowing rf measurements. There were also indications that an uncontrolled burst of gas might have entered the cavities. Rinsing with methanol in the mounted position after warm-up was not sufficient to achieve the old performance of the cavities due to high field electron emission. After oxipolishing two cycles, HD 1 was limited at $E_{acc} \sim 1.4$ MV/m by thermal breakdown, while HD 2 showed a sharp limitation at E_{acc} = 1.2 MV/m (local breakdown).

At the end of November 1978, the cryostat was moved to CEN-Saclay and cooled down to 4.2°K. The performance of the cavities was unchanged. Later warm-up and cool down cycles did not degrade the resonators either.

The zero field frequency of HD 1 was 108.452 kHz

and the one of HD 2 could be adjusted with the slow tuner[6] between 108.429 kHz and 108.493 kHz. The frequency shifts due to radiation pressure are 44 kHz (HD 1) and 26 kHz (HD 2) at E_{acc} = 1.05MV/m.

Figure 2 shows the principle of the rf control system as it had been designed for the experiment at MPI Heidelberg.[7,8]

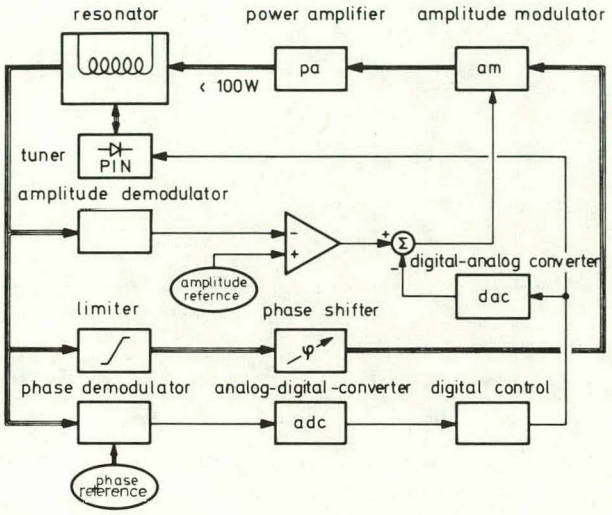


Fig. 2: Principle of the rf system.[2]

After being set up at Saclay, the amplitude stability was $\Delta U/U \simeq 3\times10^{-3}$ peak-to-peak. The eigenfrequency changes of the resonators which had to be corrected by the tuner were ∿ 700 Hz peak-to-peak while the ponderomotive feedback loop reduced it to ∿ 220 to 450 Hz. The tuning range was 1.4 kHz peak-to-peak. The cavities were phase locked to a frequency synthesizer for several hours. An experiment with a different tuner has been reported elsewhere.[9]

The two phase cooling[10] worked without problems. Figure 3 shows the cooling principle. The cool-down time was between 18 and 12 h depending on the pressure in the dewar. For constant level operation 1.15 bar was sufficient. The heat flow into the LHe was measured as 0.6 ± 0.1 W due to cavity losses and 0.6 ± 0.1 W due to rf power losses of the tuner for each cavity at E_{acc} = 1.05 MV/m, while heat conduction in the 500 l LHe dewar contributed 0.17 ± 0.02 W.

The losses of two cavities at E_{acc} = 1.05 MV/m, with the tuners plus one dewar connected by the transfer line to the cryostat maintaining a constant level, was 6.6 W.

Beam Experiments

The experimental arrangement is shown in Fig. 4. The beam optics system is designed to deliver an intermediate image at the center of the cryostat and a final one at the center of the scattering chamber with an overall magnification of 1 (from the analyzing magnet image slits). The drift lengths are ∿ 24 m from tandem to cryostat and 5.5m from cryostat to target.

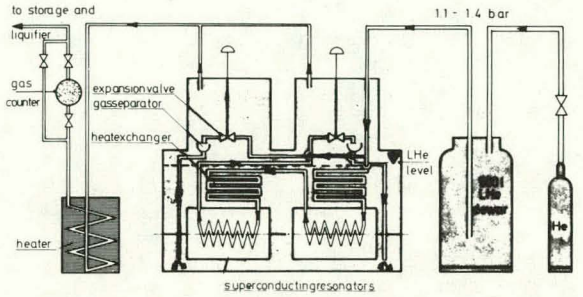


Fig. 3: Cooling principle in the test cryostat

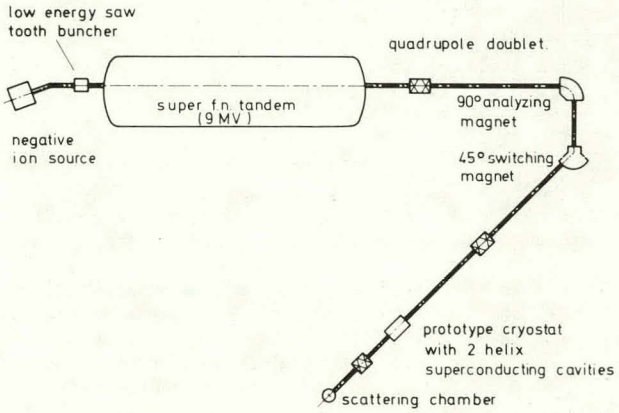


Fig. 4: Experimental arrangement

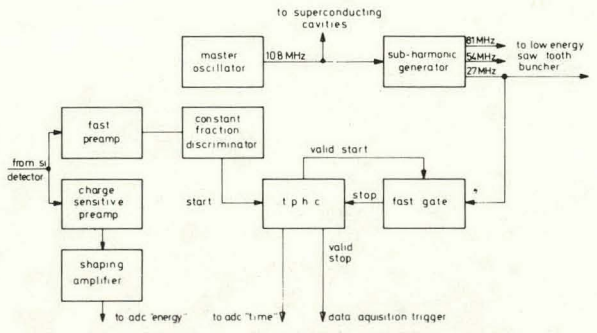


Fig. 5: Block diagram of the time-energy measurement

In order to measure the longitudinal emittance of the beam, particles elastically scattered by a 100 µg/cm^2-thick gold foil were detected at various forward angles. Figure 5 shows the electronic setup used. A Si surface barrier detector 120 µm

thick at 120 V delivered ∿ 3 ns rise time pulses. Both a fast and a charge integrating preamplifier[11,12] were connected to the detector. For each scattered particle the total energy and time difference with the master oscillator phase were digitally encoded and sent to the on-line data acquisition computer. Live displays of the energy and time distributions (spectra) were thereby obtained. The raw data (event-by-event) could also be written on tape and a 256 × 256 array of a limited portion of the time-energy space was also integrated on line. The intrinsic resolution of this detection setup is ∿ 200 keV for the energy measurement (mostly due to target thickness and angular opening of the detector). The intrinsic time resolution could not be measured but can be estimated to be ∿ 100 ps coming mostly from the Si detector rise time.

The first two experiments were performed with a d.c. ^{16}O beam (q=7+, U_{Tandem}=8.5 MV, T = 68 MeV). The very first run took place as early as December 22, 1978, and lasted only for a limited time. The energy modulation given by cavity HD 1 close-to-nominal field could be measured. In addition, operating the same cavity at reduced field delivered a slightly overbunched beam. A width of 230 psec was observed without any fine adjustment of the electronics and rf field.

During the second run (January - February 1979), the same beam at 64 MeV was energy-modulated by both cavities. The relative phase of the modulation amplitude due to each cavity could be determined after two energy modulation measurements from a simple vector addition. The maximum energy modulation obtained with the two cavities phase-locked at nominal field is shown in Fig. 6. Using a single cavity, the appropriate setting for optimum bunching on target could be determined fast by comparison between the time distribution obtained in the overbunched case with the calculated one.

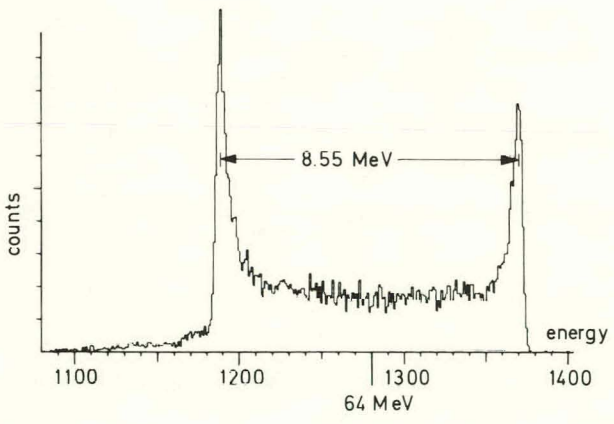


Fig. 6: Energy distribution of a $^{16}O^{+7}$ (T=64 MeV) beam energy modulated by both cavities close to design field at optimum relative phase

A fluctuation of the pulse timing was then observed to be correlated with terminal voltage variations of the tandem (ΔU ∿± 5 kV). This could be partially compensated by adding the generating voltmeter differential signal to the time-to-pulse height converter information. Thereafter a width of 120 psec could be observed over several minutes as shown in Fig. 7.

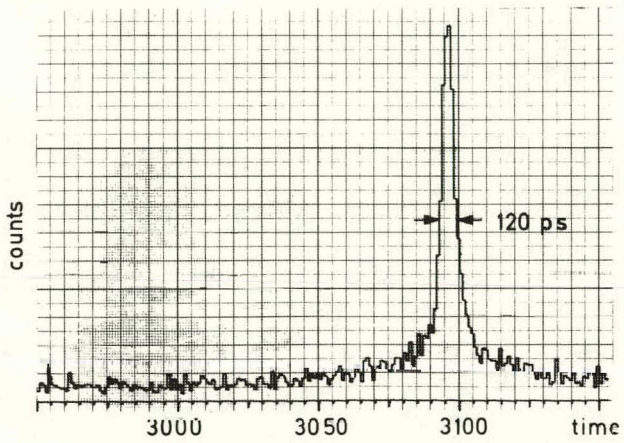


Fig. 7: Time distribution of a $^{16}O^{+7}$ (T=54.6 MeV) beam bunched by the high energy buncher

The following set of beam measurements (March and June 79) used the newly-constructed low energy buncher in connection with the superconducting cavity. This low energy buncher is similar to the ANL buncher [13] and consists of a gridded 1.5 mm long modulation gap which is fed with three frequencies (27, 54, 81 MHz) from two coaxial resonators. It provided a linear energy modulation for 70% of the beam. The distance of about 37 ns between bunches is quite suitable for most experiments. Details on the construction and performances of this device will be published elsewhere. The 100 kV injector under construction was not operational for these measurements and the bunching system could only be tested with a $^{16}O^{-}$ beam at 70 keV from a duoplasmatron exchange source and a $^{12}C^{-}$ beam at 20 keV from a standard sputter source. The bunches observed on target were 6 and 3 ns FWHM, respectively. About 70% of the intensity were in the peak for ^{16}O accelerated to 55 MeV and ^{12}C to 48 MeV.

The low energy buncher was then phased with the superconducting cavity at required field. One measurement was performed with the master oscillator replaced by a self-oscillating loop consisting of the superconducting cavity with a simple amplitude regulation; a typical time distribution observed is shown in Fig. 8. Bunching performance was identical to the previous case.

Conclusion

The tests showed that the superconducting helix cavities can be considered as reliable components for technical applications, if the maximum surface electric design field stays below some value around 16 MV/m. Most of the failures were related to con-

ventional technique and not to superconductivity nor to the vacuum seals at low temperature nor to thermal expansion and contraction during the thermal cycling between 4.2°K and 300°K.

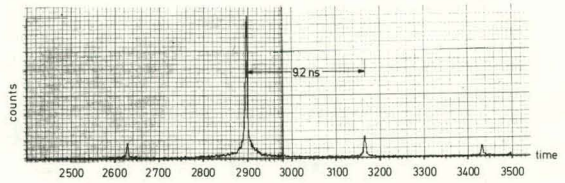


Fig. 8: Time distribution of a prebunched (27, 54, 81 MHz) and rebunched (108 MHz) beam of $^{16}O^{+7}$ (T = 55 MeV)

From early December 1978 to June 1979, the cryostat was cooled down and warmed up to room temperature five times and no difficulty was encountered in reaching the maximum fields even for operators of little experience.

The beam experiments have confirmed the accelerating capabilities of such phase-locked cavities. The major components of the beam bunching are now in routine operation and with the use of the 100 kV injector and a high energy chopper presently under design, intense bunches of ∿ 100 psec with low background will be used in nuclear physics experiments.

Acknowledgement

The help of L. Schappals, P. Schlick, M. Frauenfeld, B. Messerschmidt, N. Münch as well as the helpful discussions with J. E. Vetter were essential for the successful run of the test section.

The contributions of E. Chamaux and L. Bianchi to the experimental setup and that of J. L. Gizma and the tandem crew were important for the various beam experiments.

We are also indebted to J. P. Passérieux for the electronics design (low energy buncher and detection system) and for his help during the beam runs.

References

1 H. Deitinghoff, H. Klein, M. Kuntze, J. E. Vetter, E. Jaeschke and R. Repnow, KfK-Bericht 2141 (Karlsruhe,1975)

2 G. Hochschild, H. Ingwersen, E. Jaeschke, W. Lehmann, B. Piosczyk, R. Repnow, F. Spath, J. E. Vetter and Th. Walcher, KfK-Bericht 2624 (Karlsruhe, 1978)

3 K. W. Shepard , IEEE Trans. NS-26, 3659 (1979)

4 J. R. Delayen et al., IEEE Trans. NS-26, 3664 (1979)

5 G. Hochschild, B. Piosczyk, J. E. Vetter, H. Ingwersen, E. Jaeschke, R. Repnow, H. Schwarz, Th. Walcher, IEEE Trans. NS-24, 1150 (1977)

6 B. Piosczyk, Int. Ber. 77-223-SNB (Karlsruhe, 1977) unpublished

7 G. Hochschild, Bericht 10.01.06 P 01 D (Karlsruhe,1978) unpublished

8 G. Hochschild, Bericht 10.01.06.P 01 E (Karlsruhe,1978) unpublished

9 D. Schulze, A. Hornung, P. Schlick, IEEE Trans. NS-26, 3748 (1979)

10 J.E. Vetter, Int. Ber. 77-226-SNB (Karlsruhe, 1977) unpublished

11 B. Delaitre et J. P. Passerieux Rapport Interne D. Ph. N./B.E/75/4

12 J. P. Passerieux et al., Compte rendu d' Activité du Departement de Physique Nucleaire C.E.A.-N-2070 (1979) p. 291

13 F. J. Lynch, R.N. Lewis, L. B. Bollinger, W. Henning and O. D. Despe, Nucl. Instrum. Methods, 159, 245 (1979)

PRECISION BEAM FORMATION IN 2 GeV LINEAR ACCELERATOR OF ELECTRONS

V.I. Artyomov, V.A. Vishnyakov, A.N. Dovbnya, N.A. Kovalenko
Kharkov Physico-Technical Institute

Summary

Data is presented pertaining to the phase volume increase at the linac and beam transport system exits. Also, a comparison is drawn between two achromatic beam transport systems, showing that the quinti-lense system has certain clear-cut advantages over the tri-lens one.

Introduction

Improving the parameters of charged particle beams while increasing their energy and intensity, is a characteristic goal of accelerator equipment development.

The precision of a physical experiment (and in some cases the feasibility of carrying it out) relies fundamentally on the beam emittance and energy spread. The attainment of the necessary parameters for precision beam formation (energy spread of about 0.01%, and beam emittance less than 0.01 mm-mrad) is a very complicated problem which so far has not been satisfactorily solved for electron linacs.

This paper puts under consideration some precision beam formation methods which are being currently used in Kharkov's 2 GeV electron accelerator.

The Energy Spread

In a multisection linac there exists a coupling between transverse and longitudinal motions. Transverse rf fields[1] are primarily responsible for the observed coupling. The trajectories of particles, whose initial parameters differ only in their longitudinal motion (or phase), can be seen to undergo deviations from the system axis under the influence of transverse fields. The existence of this coupling can be used to create a so-called "Narrow Phase Channel" (NPC) as well as form an energy-spread electron beam. The Kharkov accelerator-developed NPC[2] contains a number of remote-controlled collimators and quadrupole doublets. A 20-MeV acceleration section is used as an injector, where electrons are bunched along the start-up stretch, with the wave phase velocity varying in step-up stages from 0.7 to 1.0 C.

When this method of formation was employed, the energy spectrum proved to be wider than was calculated; its semi-height width being 0.13% against the theoretically expected 0.05%. The initial energy-spectrum width was 1%. The difference between the spectral experimental and theoretical widths is conceivably the result of amplitude-phase fluctuations.

Two main problems whose handling is indispensable in forming the monochromatic electron beam will be discussed. These problems are: (a) bunch formation of insignificant longitudinal dimensions, and, (b) quenching various fluctuations down to the needed level.

All the fluctuations can be roughly divided into two categories: slow ones, that go from impulse-to-impulse, and, fast fluctuations, which occur during the impulse. The very existence of the amplitude-phase fluctuation, stochastic-stabilization mechanism of the acceleration-imparting field in multisection linacs, enables us to fulfill the task of quenching the fast fluctuations.[3]

Beam Emittance

The effective beam emittance (its multipulse integrated mean-profile value) immediately prior to the exit from the linac, is substantially different from the "superinstant" one, which is measured during an infinitesimal fraction of the bunch duration. The beam transverse phase space volume increase occurs largely due to the following phenomena:

- Phased transverse particle separation;
- Fast amplitude-phase fluctuations during the acceleration impulse;
- Slow fluctuations in the connection, focusing and control systems.

Emittance stratification of numerous phases across the phase-profile, takes place in the acceleration process, thus giving rise to the beam effective emittance increase prior to the exit from the linac. This can be expressed as:

$$S = K E_o/E S_o$$

where S_o, S are entry and exit emittance values, K is the increase coefficient arising from phased particle separation, and E_o, E are the beam energy at the injector and linac exits, respectively. To suppress the effect, a supplementary beam focusing system is used which includes quadrupole doublets to zero-in the "superinstant" linac exit beam emittance on the same phase-profile center. The increase coefficient is observed to be K = 1.2, for longitudinal bunch measurement of t = 8°.

The experimental studies have demonstrated the beam emittance at the impulse median position to be less than at its extreme positions, for which K = 2.3. Clearly shown here is the role of fast amplitude-phase fluctuations.

The effective pulse train emittance exceeds a single-impulse emittance, with K = 2.1 for n = 10

(where n is the impulse number).

The ways of quenching these effects are obvious, namely: stabilizing klystron high voltage impulse peaks as well as stabilizing the power supplies of the beam focusing and control systems. Figure 1 shows the progress to date in low emittance beam formation for the 2 GeV linac.

Beam Transport System Influence on the Emittance

Up to 1976, the electron beam parallel transfer from the 2-GeV linac to the magnetic spectrometers was accomplished by employing the beam transport system (BTS) which consisted of two bending magnets ($\theta = 45^{\circ}$), three quadrupole lenses between the magnets, and a quadrupole triplet at the exit of the second magnet. This system's design and its peculiar features, are given in minute detail coverage in Ref. 4. This system is good for forming an image of several mm with 1-mrad semidivergence, that is well suited to electron beam spectrometric experiments.

However, in the case of the experiments with polarized gamma quanta generated on the goniometric device diamond monocrystal, it was necessary to reduce both the electron beam emittance and its divergence.

Figure 2 gives the schematic layout of the BTS. The system was rebuilt to include two additional quadrupole lenses: L_1 and L_5. The previously employed system was achromatic (Panofsky inversion system); however, the beam envelope reached several cm in the long drift spaces between the magnets. This in turn, led to the effective on-target beam emittance increase because of quadratic aberrations. While in the present case chromatic aberrations have the predominant influence.

Several attempts were made to decrease the effective beam emittance by determining the optimal angle cut for bending magnets in the traditional Panofsky scheme. As a result, the envelope curve maximum horizontal excursions were cut in two, while the effective emittance at the system's outlet in that same plane decreased three times. Still, as expected, the BTS under those conditions gets extremely sensitive to the vertical beam emittance. The change in beam divergence by 0.03 mrad from the precalculated data, results in doubling the beam size at the second bending magnet's exit, with the beam getting partially scraped on the chamber walls. Those conditions, therefore, cannot be operational for a prolonged experiment.

The next step was an attempt at reducing the chromatic aberrations by introducing non-linearity field quadratic into the central lens. The field non-linearity was accomplished by changing the magnetic potentials of two poles by way of a manganin shunt. The quadratic non-linearity of approximately 1%, resulted in decreasing the effective emittance on the horizontal plane by half. Nonetheless, the trial run of this system displayed the same difficiencies as with the original design, i.e., superhigh sensitivity both to the emittance shape and current fluctuations in magnetic elements. Finally, it was only in the quinti-lensed BTS that any further emittance reduction could be achieved. According to calculations, the BTS-5 has certain advantages over the BTS-3, namely:

(a) particle trajectories on both planes agree irrespective of the entry beam parameters;
(b) Chromatic aberration contributions to the effective emittance increase is insignificant (one-eighth that of the BTS-3).

The absolute requirements for the BTS-5, though, put restrictions on the bending magnets' input power stability and the L_3 adjustment. To this end, there has been developed a system for the bending magnet current supply from a single generator whose permissible fluctuation level, though, should not exceed 0.05%. The difference of the magnetic parameters (less than 1%) was eliminated by exciting the second magnet's auxiliary winding from a high stability source. This mode of operation for the magnet ensured the equivalent stabilization to be less than 0.001% and helped reduce the beam on-target fluctuations to $\Delta = 1.2$. This accomplished, it was possible to determine each magnetic element's contribution to the beam on-target fluctuations. With this in mind, the derivatives of beam on-target current induced deviations in each magnetic element were measured and the correlation analysis carried out. The results were used to ascertain each element's contribution to the beam median position fluctuations. The adjusting was done by a combined method. First, the derivatives of beam on-target deviations were employed to determine the quadrupole deviations from the optical axis. Then the adjusting proper was carried out, involving the use of a "local system" of calculations and some geodetic surveying technique. The lowest possible reading of beam on-target deviation derivatives served as the criterion. The lenses adjusted, the mean quadratic value of on-target charge center fluctuations equaled $\Delta = 0.72$ mm. The top contributions to this parameter were made by the current fluctuations in the lens L_3. Its power stabilization improvement to 0.05% decreased the on-target charge center fluctuations down to 0.2 mm, which met the requirements of the experiment. The experimental research conducted over a wide energy range, as well as the BTS-5's two-year operation service, both prove its superiority to the BTS-3.

References

1 I.A. Grishayev et al., Zh. Tech. Fiz. Vol. 41, N 4, pp. 783-788, 1971.

2 V.I. Artyomov et al., ibid. 43, 1, 178, 1973.

3 G.P. Averyanov et al., ibid. 43, 12, 2617, 1973.

4 I.A. Grishayev et al., ibid. 39, 1, 197, 1969.

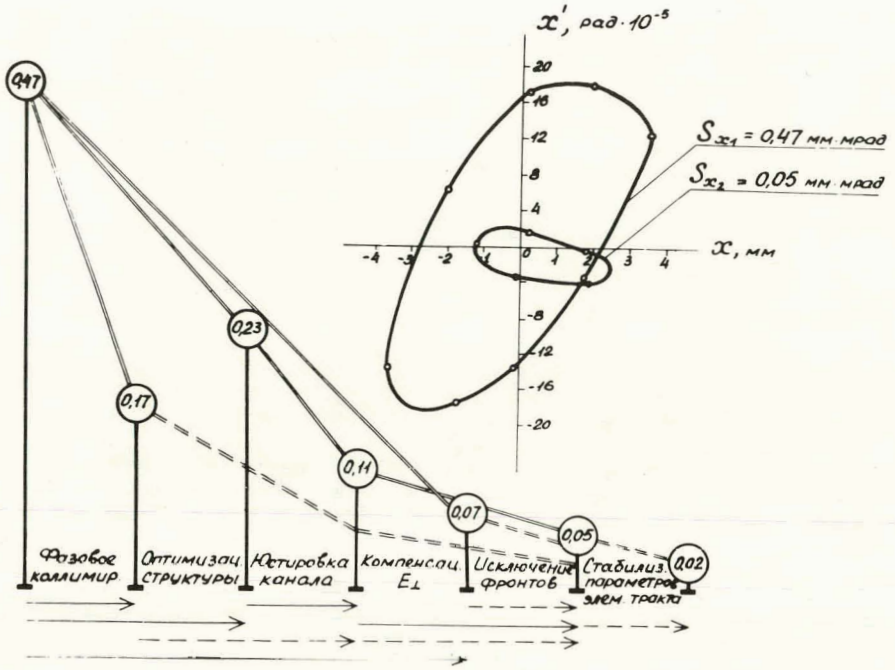


Fig. 1 2-GeV linac beam emittance decrease (the completion of the experiment in question is schematically staged from left to right in the following order):
- NPC
- Focusing system structural optimization
- Channel adjustment
- Compensation $E_\perp$
- Impulse rise time elimination
- Stabilization of power supply system

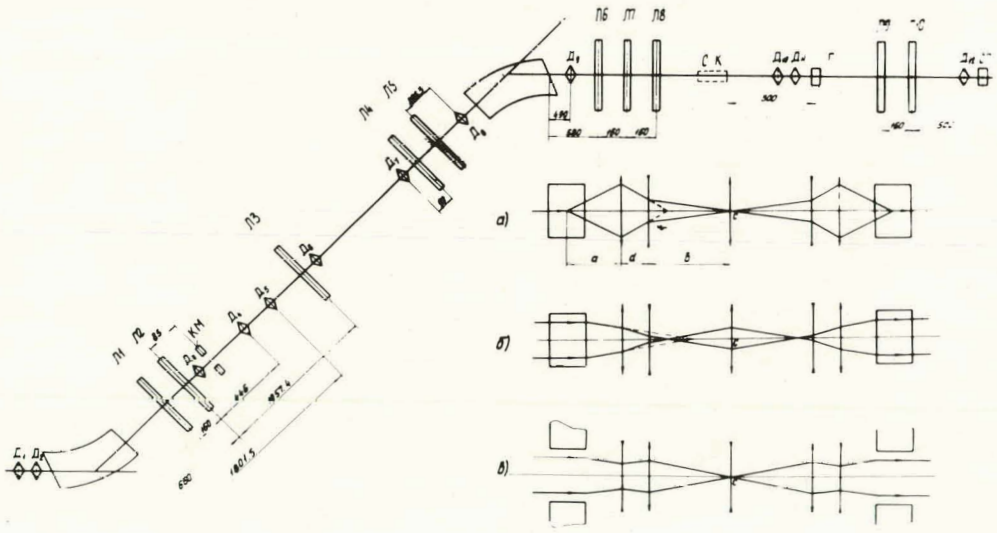


Fig. 2 2-GeV linac BTS layout

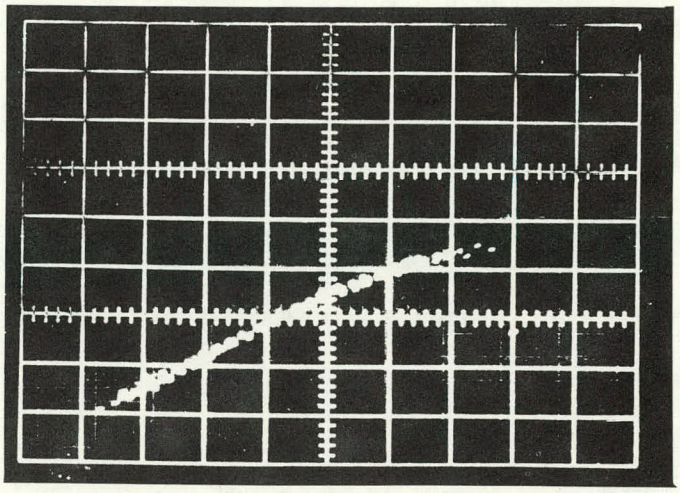
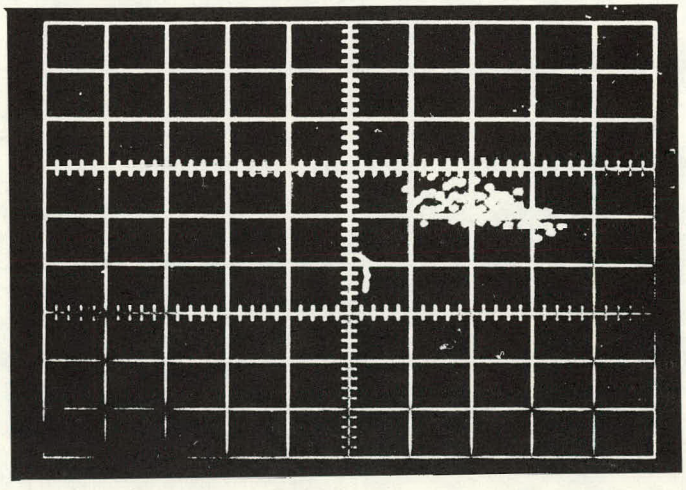


Fig. 3 A comparison of the BTS-3 and BTS-5 exit beam emittance on the horizontal plane (see BTS-3 above: horizontally - 1mm/div; vertically - 1 mrad/div; BTS-5 below: horizontally - 1mm/div; vertically - 0.08 mrad/div)



A 5-MEV ELECTRON LINAC WITH HIGH ENERGY RESOLUTION

Yu.P. Vakhrushin, V.M. Nikolaev, A.V. Rjactsov,
Yu.A. Svistunov, Yu.P. Severgin, and V.L. Smirnov
D.V.Efremov Scientific Research Institute of
Electrophysical Apparatus, Leningrad, USSR

Summary

The design parameters of a 5-MeV electron linac with low energy spectrum and beam emittance are presented. The accelerator includes the following main components:

(a) an injection system comprising an electron gun, rf chopper, and prebunching cavities,
(b) a traveling-wave accelerating structure operating at room temperature, and
(c) an active monochromatization system with variable longitudinal dispersion.

Three-dimensional numerical studies of beam dynamics were performed taking into account space-charge forces. With the peak current of 3 mA, it is possible to obtain an energy spread less than $\pm 5\times10^{-5}$ and a transverse emittance less than 1 mm-mrad.

Introduction

Electron linear accelerators with high energy resolution are of considerable interest for research in nuclear and high energy physics and for electron microscopy. To date, accelerated beams with the best parameters have been obtained with superconducting linacs;[1] but, the construction of a superconducting linac requires the solution of many technical problems and cannot be considered routine. However, not all the possible ways of improving the beam characteristics in conventional machines have been exhausted. For example; use of an active monochromatization system allowed reduction of the beam energy spread by an order of magnitude for the machines in Mainz[2] and Tokyo.[3]

In this paper, the basic design characteristics are given for a 5-MeV conventional electron linac with a beam energy spread within $\pm 5\times10^{-5}$ and an average accelerated beam current of 15 μA. To meet these specifications, the accelerator has chopper and prebuncher cavities and an active monochromatization system; provision is made for strong stabilization of the basic operating parameters. It is expected that such a machine will be usable in electron microscopy.

Figure 1 shows a schematic layout of the main accelerator components, and a detailed description of the scheme is given below.

Electron Source

A Pierce diode gun with a 2-mm-diameter thermo-emission cathode is chosen as the electron source. The peak current of a continuous beam at the anode plane is 70 mA at the 80-kV cathode-anode voltage. The gun electrode configuration allows the beam diameter to be decreased to 1 and 0.5 mm at the anode and cross-over planes, respectively. In the rest of the accelerator, the beam diameter is maintained at this level by means of the uniform axial magnetic field of ∿ kG produced by the focusing coils.

To reduce the electron transverse momentum gain in the cathode-anode region, it is desirable that the electron trajectories coincide with the magnetic field lines. The required magnetic field distribution is provided by a magnetic shield and bucking coils. The electron flow structure is assumed to be laminar in this region. The coincidence of the magnetic field lines and the electron trajectories is distorted by the electrostatic lens in the anode hole; therefore, the electrons are moving from the anode along spiral trajectories.

The electron dynamics were studied by using a three-dimensional beam model, with the beam represented by a number of small "balls" each of charge q and diameter d. This model was chosen because (1) the rf field in the chopper has no axial symmetry, and (2) the finite beam diameter causes the initial rotational symmetry in charge distribution to be disturbed when electrons cross the slit in the chopper clipping collimator. However; the initial charge distribution at the anode plane is considered to be axially symmetric, both longitudinal $\varepsilon_{\parallel}$ and the transverse $\varepsilon_{\perp}$ emittances being zero (Figs. 2a and 3a).

Chopper and Prebuncher

A well-known system including rf chopper and prebuncher cavities will be used to provide a well-defined electron bunch at the accelerator input. The two-cavity chopper structure suggested by J.P. Mangin[4] was chosen. Its advantages are:

(1) capability of producing short bunches at a relatively low electron energy (up to 100 keV),
(2) restoration of the transverse beam geometry at the chopper output, and
(3) density of heat dissipation in the clipping collimator than with the linear chopping technique.[5]

The 1.5-mm-wide clipping collimator slit transmits an electron bunch with well-defined boundaries and a total phase spread of about 27°. Because the beam diameter is finite, the charge distribution along the bunch is of a trapezium

type with 3-mA peak beam current or 15-μA average at a duty factor of 0.5%.

One of the essential features of the particle dynamics in the chopper is the sharp change in the space-charge forces influencing the particle when it crosses the collimator plane. This change affects mostly the axial motion. In a continuous beam the axial Coulomb field is zero, but in a chopped beam it plays a significant role resulting in essential increase of the longitudinal emittance. Computations show that the limiting value of $\varepsilon_{\parallel}$ is closely approached when the bunch leaves the chopper (Fig. 2b). Additional bunch compression in the prebuncher influences only the shape of the phase-space region occupied by the particles and changes $\varepsilon_{\parallel}$ very little. Thus, the main function of the prebuncher is to transform the longitudinal beam emittance in a manner that allows minimization of high-order aberrations of the accelerator sections. In this case, a prebuncher providing a bunch phase width of 10° and an energy spread of ± 2 keV at the accelerator entry (Fig. 2c) was found to be close to optimum. Note that the multi-cavity prebuncher concept shows no essential advantages compared with the single-cavity one.

The transverse (x, x') emittances ε_x at the chopper exit and at the accelerator entry are shown in Figs. 3b and 3c. The ε_x value is changed slightly while the bunch phase width is decreased by a factor of 3.

Accelerating System

The 5-MeV linear accelerator comprises two traveling waveguide sections of identical length (0.9 m). A Klystron providing 5-MW rf peak power and 25-kW average at 2450-MHz frequency is chosen as the rf power source. In waveguide W_1, fed at 3.5 MW, the electrons are accelerated to a nominal energy of 5 MeV. Waveguide W_2, fed at 1 MW maximum, serves to change the energy gain from 3 to 5 MeV. It can also be used to reduce the energy spread if a bunch has any phase-energy correlation, or to provide modulation on particle energies, which is necessary in bunch phase-length measurements.

The rf field in the input coupler cavity and adjacent cells decelerates and defocuses electrons. To reduce this effect, the accelerating field gradient must be comparatively low. Various sets of E(a) and $\beta_w(z)$ curves have been analyzed, where E is accelerating field gradient and β_w is normalized phase velocity. To find the optimum set of these curves, a gradient method[6] was applied which had as a criterion the minimum value of the function

$$F(E,\beta_w) = A \cdot \sum_{i=1}^{N} (\phi_i - \bar{\phi})^2 + \sum_{i=1}^{N} (u_i - \bar{u})^2 \qquad (1)$$

where A is a weight constant; N is the number of particles;

$$\bar{\phi} = \frac{1}{N} \sum_{i=1}^{N} \phi_i ; \quad \bar{u} = \frac{1}{N} \sum_{i=1}^{N} u_i ; \text{ and } \phi_i \text{ and } u_i = \frac{W_i}{m_o C^2}$$

are the phase and the normalized energy of the i^{th} particle at the W_1 exit.

As a result of this analysis, the version was chosen in which the E(z) and $\beta_w(z)$ curves vary smoothly over the ranges 16 to 75 kV/cm and 0.42 to 1, respectively, over the initial part of a W_1 that is 2λ in length (where λ is the rf field wavelength).

The longitudinal and transverse emittances at the accelerator exit are shown in Figs. 2d and 3e. The former remains unchanged during the acceleration time. The latter is reduced, but at a rate slower than the rate predicted by a simple theory, which would be inversely proportional to the longitudinal momentum, because the transverse momentum imparted to the electrons by the rf field in the injection part of W_1, is phase dependent and therefore increases the transverse emittance area.[7] To illustrate this, Fig. 3d shows the transverse emittance at the point $\lambda/2$ downstream from the W_1 waveguide entry, where the average particle energy after deceleration and subsequent acceleration again becomes 80 keV. At this point the ε_x value is nearly twice as large as at the accelerator entrance.

As shown in Fig. 3f, the transverse emittance ε_y in the (y,y') plane at the accelerator exit has a value slightly different from that of ε_x; consequently, the disturbance of the axial symmetry caused by the chopper is of no importance.

Thus, the above analysis confirms that under ideal stability conditions the chosen accelerator scheme allows one to obtain electron bunches with a phase width of 2° and an energy spread of $\pm 0.15\%$ About 80% of the accelerated particles are within an ellipse of area $\varepsilon_x = 0.25$ mm mrad.

Active Monochromatization System

The energy spread in a bunched beam of charged particles can easily be compensated without intensity losses by using an active monochromatization system. This idea was first proposed by K. W. Robinson[8] and has been tested on the injector for NINA.[9] The bunched beam consisting of relativistic electrons is passed through the achromatic magnet system (debuncher) with high longitudinal dispersion D_{11}. Movement of electrons of different energies along trajectories of different lengths resulted in an elongated bunch, with a linear correlation between particle energy and phase. If such a bunch passes through the rf field at the appropriate phase, the energy spread can be reduced by a large factor.

The active monochromatization system (Fig. 1) consists of a debuncher and two rf compensating cavities C_1 and C_2. The debuncher includes bending

magnets M_1-M_3 and quadrupole lenses Q_3, Q_4. The debuncher magnet system is symmetrical relative to plane AA', and half of it is symmetrical relative to 00'. The optical properties of this system have been studied in a linear approximation by Basargin.[10] The longitudinal dispersion of the debuncher can be regulated by the current variation in lenses Q_3, Q_4, and thus the optimum compensating regime can be chosen for a given energy spread at the accelerator exit. The dispersion D_{11} is determined by

$$D_{11} = R\left[\frac{16.2}{u^2} + 70\left(\frac{\omega_L^2}{\ell} R - 0.795\right)\right], \text{cm} \cdot \left(\frac{\Delta W}{W}\right)^{-1} \quad (2)$$

where R is the trajectory radius in the magnets; u is the normalized particle energy; ℓ is the effective quadrupole lens length; and ω_L is a dimensionless lens parameter.

The magnet field is inhomogeneous in the radial direction with a field index of n = 0.8317 and R = 30 cm. The bending angles are 135° for magnets M_1 and M_3, and 270° for magnet M_2. The quadrupole pair Q_1, Q_2 matches the beam emittance to the debuncher acceptance.

The beam energy spread is eliminated in compensating cavities C_1 and C_2, excited at the frequencies f and 2f respectively, where f is 2450 MHz.

A measure of the system efficiency is the monochromatization factor k_m, defined as

$$k_m = \Delta W_{in}/\Delta W_{out} \quad (3)$$

where ΔW_{in} and ΔW_{out} are the energy spread values at the monochromatization system input and output.

The system can operate in monoharmonic (MHC) as well as biharmonic (BHC) compensation modes. In the MHC mode, only cavity C_1 is energized, and the maximum value k_{m1} is given by

$$k_{m1} = \frac{5}{3}(\Delta\phi_{in})^{-\frac{2}{3}} \quad (4)$$

where $\Delta\phi_{in}$ is the bunch halfwidth at the debuncher input.

In the BHC mode, both the C_1 and C_2 cavities are used, and the maximum value k_{m2} is

$$k_{m2} = 2(\Delta\phi_{in})^{-0.81} . \quad (5)$$

Assuming $\Delta\phi_{in} = 0.02$, in accordance with Fig. 2d, one finds $k_{m1} = 23.0$ and $k_{m2} = 47.7$. The residual energy spread value in the BHC mode is

$$\Delta W_{out} = \pm 7.5/47.7 = \pm 0.16 \text{ keV} .$$

The rf field amplitudes in cavities C_1 and C_2 are 9 kV and 1.5 kV, respectively. The longitudinal emittance of the monochromatic beam is shown in Fig. 2e.

Estimation of the beam properties in the MHC mode shows that elimination of the second-order debuncher aberrations is not required because the emittance values are small; about 80% of the accelerated particles being inside the transverse emittance area of 0.29 mm-mrad. In the BHC mode; however, the chromatic aberrations of the longitudinal motion should be eliminated because of greater bunch elongation. For this purpose, two sextupole lenses should be introduced in the debuncher near lenses Q_3 and Q_4.

Tolerances

To obtain these low values of beam emittances, many of the accelerator parameters should be strictly stabilized. It was determined, in particular, that the tolerable variations of rf power and frequency and of waveguide temperature must be within $\pm 5\times10^{-4}$, $\pm 1\times10^{-6}$, and ± 0.2°C, respectively.

In the monochromatization system, the stability of the bending magnetic field and of the rf field phase in cavity C_1 should be strictly maintained. For example, a change of ± 50 eV, in the average electron energy, results from variation either in the magnetic field by 5×10^{-6} or in the rf phase by ± 0.3°.

If these tolerances are satisfied, the residual beam energy spread in the BHC mode does not exceed $\pm 5\times10^{-5}$.

Brightness

Brightness B is one of the important parameters of the electron beam used in an electron microscope. Substitution of the average beam current $\bar{i}$ = 12 μA and $\varepsilon_x = \varepsilon_y$ = 0.29 mm-mrad into the brightness equation,

$$B = \bar{i}/\varepsilon_x\varepsilon_y \quad (6)$$

gives B = 14,300 A/cm^2-ster. An electron beam with these parameters can be effectively used in an electron microscope of the translucent type.

References

1 J.R. Calarco et al., IEEE Trans. Nucl. Sci. NS-24 (3), 1091 (1977).

2 H. Herminghaus et al., Nucl. Instrum. Methods 113, 189 (1973).

3 M. Sugawara et al., Nucl. Instrum. Methods 153, 343 (1978).

4 G. Azam et al., Onde Electr. 49, 1136 (1969).

5 J. Haimson, IEEE Trans. Nucl. Sci. NS-9 (2), 32 (1962).

6 V.N. Petrov et al., in Proc. 2nd All-Union Conf. on Charged Particle Accelerators, Moscow, Vol. 2, p. 159, 1972.

7 Linear Accelerators, P. 126, P.M. Lapostolle and A.L. Septier, Editors, North-Holland, Amsterdam, 1970.

8 Ibid., p. 512.

9 M.C. Crowley-Milling et al., IEEE Trans. Nucl. Sci. NS-18 (3), 968 (1971).

10 Yu.G. Basargin et al., JETP 42, 1727 (1972).

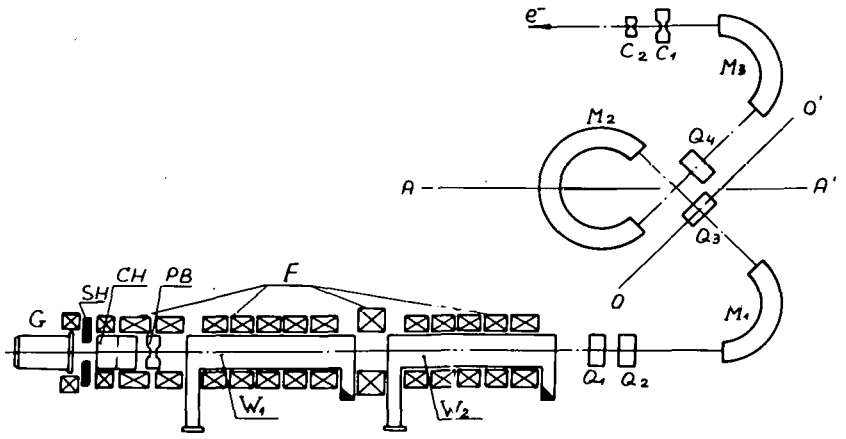


Fig. 1 Schematic layout of the accelerator

G-electron gun; W_1, W_2-accelerating waveguides;
SH-magnetic shield; Q_1, Q_4-quadrupole lenses;
CH-chopper; M_1, M_2-bending magnets;
PB-prebuncher; C_1, C_2-compensating cavities.
F-focusing coils;

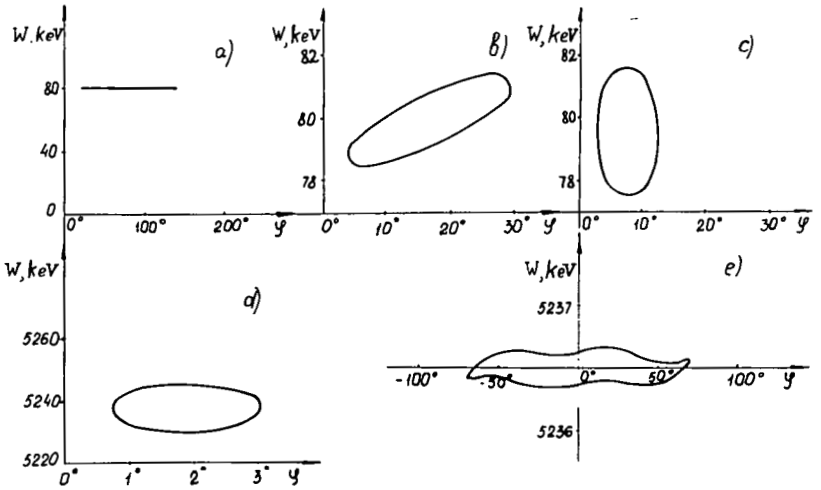


Fig. 2 Longitudinal emittances at different locations along the beam axis

a) in the anode plane;
b) at the chopper exit;
c) at the accelerator entry;
d) at the W_2 waveguide exit;
e) at the monochromatization system exit.

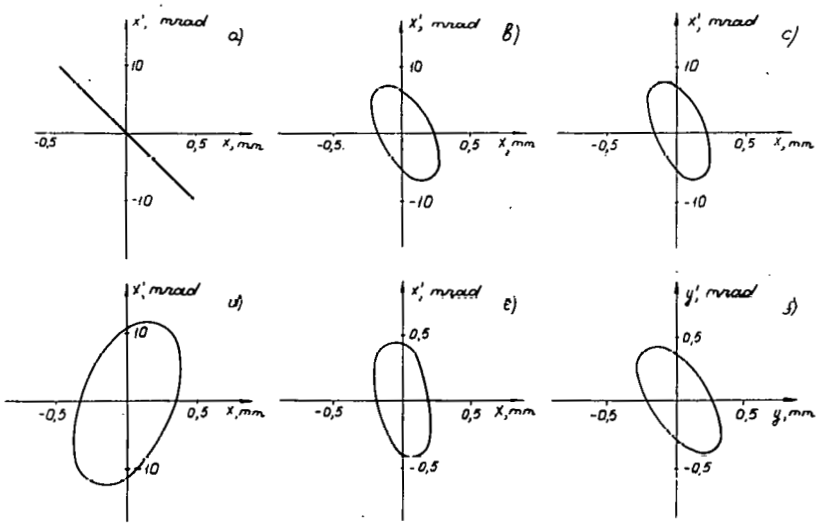


Fig. 3 Transverse emittances at different locations along the beam axis

a) in the anode plane;
b) at the chopper exit;
c) at the accelerator entry;
d) at the point 0.5 downstream of the accelerator entry;
e) at the W_2 waveguide exit, in the (x,x') plane;
f) at the W_2 waveguide exit, in the (y,y') plane.

Section III
Structures

THIS PAGE

WAS INTENTIONALLY

LEFT BLANK

LOW-BETA LINAC STRUCTURES*

D. A. Swenson
Los Alamos Scientific Laboratory
Los Alamos, New Mexico 87545

Summary

The magnetically focused, post-coupled, drift-tube linac is the standard linac structure. It offers efficient acceleration and adequate focusing over a remarkably large range of beta from $\beta = 0.04$ to $\beta = 0.50$. The term "low-beta linac structure" has come to mean those linac structures that out-perform the standard Alvarez structure in the region below $\beta = 0.04$, and the term "high-beta linac structure" has come to mean those linac structures that out-perform the standard Alvarez structure in the region above $\beta = 0.50$. A companion to this paper will be presented in this conference on the subject of high-beta linac structures.[1]

Low-beta linac structures are the bane of the existence of linac specialists. It is here that one must work hardest and achieve the least in the way of acceleration and focusing. The structures in this region are characterized by inadequate focusing, limited apertures, and poor transit-time factors. It is here that the beams are the most poorly bunched, have the largest angular divergence, are the most susceptible to space-charge effects, and are thought to be the most vulnerable to "emittance growth" driving terms. Everything that is bad in linacs is worse at the low-beta end. Nevertheless, every linac has one, and work is continuing to develop and improve these structures.

Introduction

The principal linac structures that are considered for this duty, in addition to the standard Alvarez linac, are: (1) the $2\beta\lambda$ Alvarez linac structure; (2) the π,π Wideroe linac structure; (3) the $\pi,3\pi$ Wideroe linac structure; (4) the Interdigital H-Mode structure; (5) the Parallel-Plate Transmission Line structure; (6) a variety of heavily loaded, low-frequency cavity structures with independent phasing and intercavity focusing; (7) the Alternating Phase Focused (APF) linac structure; and (8) the Radio-Frequency Quadrupole (RFQ) linac structure. The relative geometry of a number of these structures is shown in Fig. 1 from the particle's point of view.

The most serious problem at low beta is to keep the beam small compared to $\beta\lambda$. As always, focusing elements are needed to control the size of the beam. The vast majority of the efforts have been expended on magnetically-focused structures in spite of the fact that magnetic focusing is particularly ineffective at low beta because of the velocity term in the force equation. Electric focusing, on the other hand, has no such velocity term in the force equation and should be a prime candidate for the focusing role in low-beta linac structures.

Linac designers have, for a variety of practical reasons, chosen not to develop the electrostatically-focused linac structure in spite of its potential advantage at low beta. Perhaps in the renewed quest for low-beta linac structures for the heavy-ion fusion program, a fresh look will be taken at the practical problems of electrostatic focusing,[2] and some solutions will be found.

Two types of rf electric focusing are being studied at LASL. One is the APF linac structure[3], which was developed for the low-beta chore in PIGMI (Pion Generator for Medical Irradiations)[4] under the support of the National Cancer Institute. The other is the RFQ linac structure[5] which is being developed for the low-beta chore in the Fusion Materials Irradiation Test (FMIT) facility[6] under the support of the Department of Energy. An operating model of the APF structure exists, and progress is well underway towards a working model of the RFQ structure.

APF Linac Structure

The APF linac structure[7] is being developed for the acceleration and focusing role in the low-beta portion of PIGMI. In this structure, the transverse, as well as the longitudinal focusing forces are produced by the rf

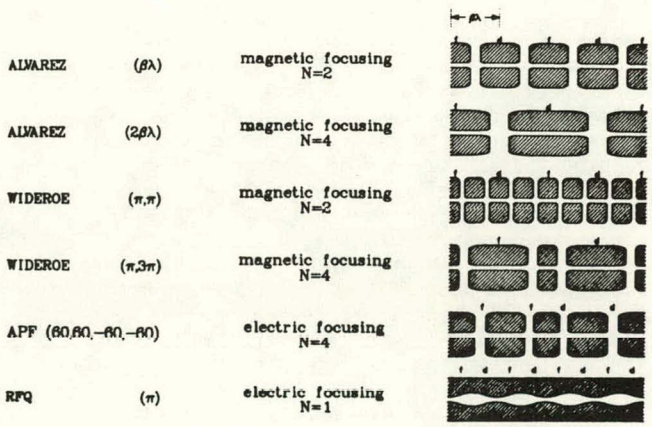


Fig. 1. Low-beta linac structures from the particles point of view.

*Work performed under the auspices of the U. S. Department of Energy and the National Cancer Institute.

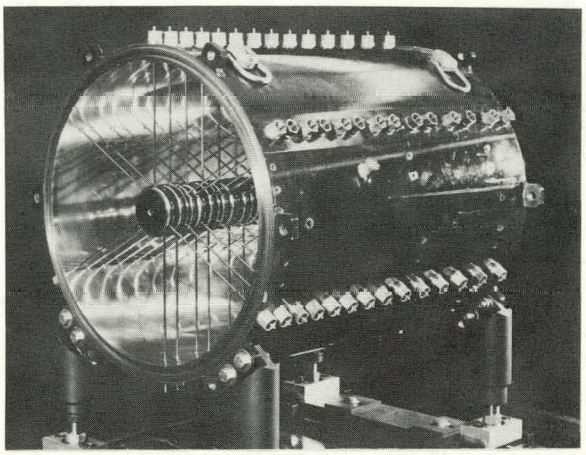


Fig. 2. The PIGMI prototype.

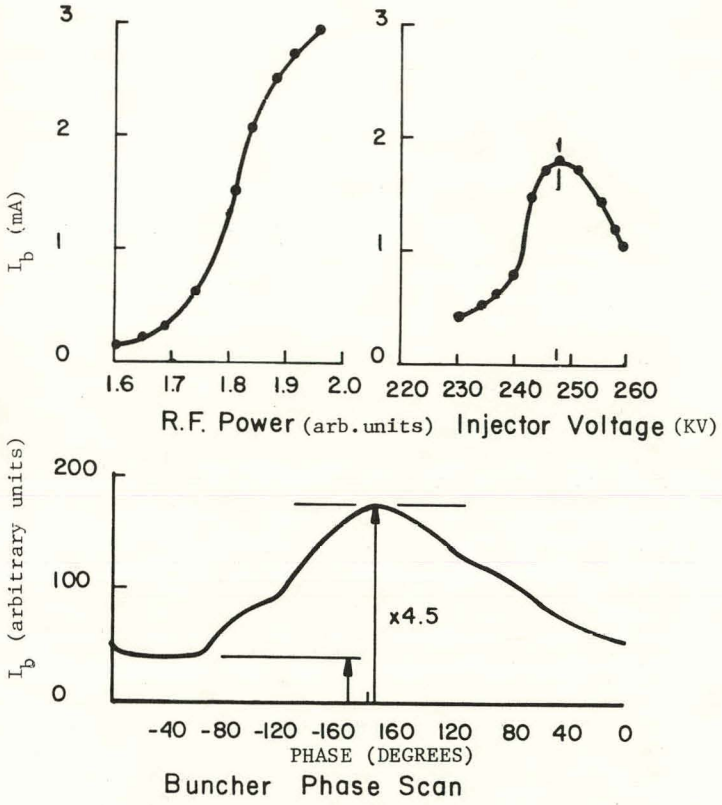


Fig. 3. The APF performance data.

electric fields. By arranging the drift-tube lengths, and hence gap positions, in an appropriate way, in an essentially conventional standing-wave drift-tube linac, the particles can be made to experience acceleration and a succession of focusing and defocusing forces which result in satisfactory containment of the beam in six-dimensional phase space without dependence on additional focusing fields.

The APF portion of the PIGMI prototype[8] is shown Fig. 2. It is 63 cm long, 46 cm in diameter, and contains 28 drift tubes, none of which contain quadrupole lenses. The drift-tube bodies vary in length from a minimum of 0.690 cm to a maximum of 3.003 cm, and are 8 cm in diameter. The bore-hole radius increases from 0.402 cm in the first drift tube to 0.487 cm in the 28th drift tube. It is designed to operate at 450 MHz and to accelerate a proton beam from 250 keV to 1.011 MeV.

Preliminary tests of the performance of the APF linac structure were made in the following way. The APF section, which has no provisions for rf excitation, was bolted to another short linac section that does have such provisions. A special drift tube, containing an energy-discrimination foil (600 keV) followed by a Faraday cup, was installed between the structures to adjust the resonant frequency of the combination and to provide a minimal beam-diagnostics capability. The combined structure requires a total rf power of about 700 kW to reach the design excitation.

The combined structure was driven to a peak power of about 850 kW, corresponding to an average axial electric field approximately 10 per cent higher than the design value of 6 MV/m. The maximum surface fields were in the vicinity of 28 MV/m.

The 250-keV proton beam from the PIGMI injector[9] was used for the preliminary beam tests. The net current signals from a Faraday cup at the entrance to the linac, the energy-discrimination foil in the special drift tube, and the Faraday cup in the special drift tube were monitored as a function of rf power, injector voltage, solenoid current, steering current, buncher excitation, buncher phase, and ion source parameters. Some of these data are presented in Fig. 3.

Protons entering the special drift tube with an energy less than 600 keV are absorbed in the foil and contribute to the signal from that element. Protons entering the special drift tube with an energy greater than 600 keV pass through the absorber and contribute to the signal from the Faraday cup within the drift tube. Stray electrons from the foil and Faraday cup are returned to their original element by a 1-kG magnetic field produced by a pair of permanent magnets. The signal from the Faraday cup is taken as a measure of the accelerated beam current.

The dependence of accelerated current, I_b, on rf power is shown in Fig. 3. The threshold for acceleration (1.75 in the arbitrary units given here) corresponds to an rf power of 750 kW, and the peak acceptance corresponds to an rf power of 850 kW. These data are in fair agreement with our expectations.

At the optimum excitation, the percentage capture of a well-collimated beam is 15.7% or $\pm$28 degrees of phase. This is in good agreement with the expected performance.

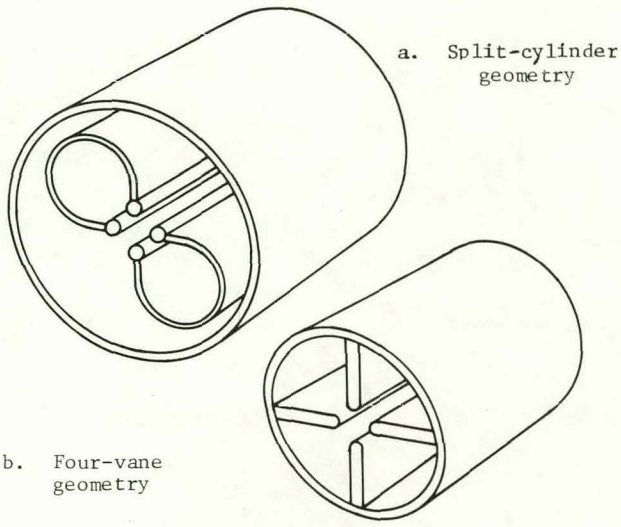


Fig. 4. Two basic configurations of the RFQ.

The dependence of accelerated beam on injector voltage is shown in Fig. 3, revealing a rather sharp peak at 248 kV. The width of the peak is in good agreement with the design calculations. The apparent deviation of the peak position from the design value of 250 kV may be real or may be due to an error in the calibration of the voltage measurement.

The dependence of accelerated beam on buncher phase is shown in Fig. 3 for the buncher excitation that produces the maximum accelerated beam at the optimum phase. The general features of this phase scan look correct, but the detailed shape has not been analyzed.

The maximum current accelerated to date is 3 mA. There are a number of hardware problems and it is hoped that this limit can be raised in the near future.

RFQ Linac Structure

A variety of schemes for producing a quadrupole focusing component in the rf accelerating fields of linac structures have been described in the literature of the last decade. Some of the most recent and promising work is that of I. M. Kapchinskii and V. A. Teplyakov[10] and of N. V. Lazarev[11] based on a four-wire configuration excited so as to produce an electric quadrupole field in the plane perpendicular to the wires.

In the case of uniform wires with no longitudinal variations, the electric fields are strictly transverse, and have no accelerating component. As such, the structure is primarily a focusing structure and not an accelerating structure. Kapchinskii and Teplyakov have introduced an accelerating component by modulating the wire geometry in a periodic way. In this form it represents a very exciting

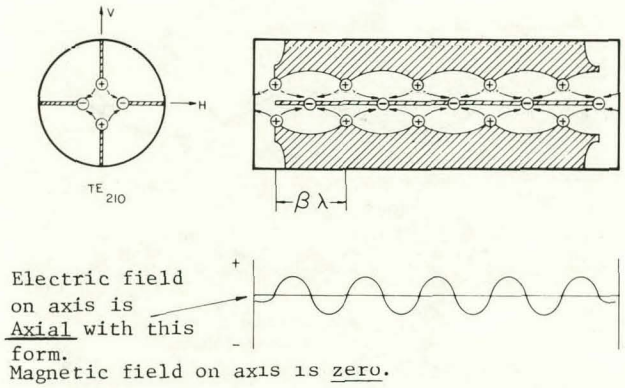


Fig. 5. Four-vane linac structure.

accelerating and focusing structure for low-velocity protons, deuterons, and heavy ions.

There are a variety of ways to connect the four wires into an rf circuit. The Russians have chosen to use the "split-cylinder" geometry shown in Fig. 4a. Our interest is based primarily on the "four-vane" geometry shown in Fig. 4b. At LASL, preference is for the four-vane configurations, based on its four-pole symmetry, and its apparent mechanical simplicity. Nevertheless, in preliminary investigations, both configurations were studied.

Figure 5 shows the four-vane configuration with a "ball and scallop" modulation on the vane geometry. The structure is excited so that the top and bottom vane tips are of one polarity, while the side vane tips are of the other polarity. The quadrupole electric field is readily apparent in the end view. These same vectors, when viewed from the side, have a longitudinal component that is due to the interlaced nature of the horizontal and vertical vane modulations. From the symmetry, it can be established that the electric fields on the axis are strictly axial, and that there are no transverse electric fields or magnetic fields on the axis. The axial electric field alternates in direction as shown in the figure.

The structure shown in Fig. 5 should be capable of both accelerating and focusing a beam of charged particles. Because the focusing forces are electric, the focal properties are velocity-independent, and the structure should be superb for low-beta applications.

In actual practice, the vanes would not be built with the "ball and scallop" geometry, but rather with a smooth scalloped geometry as shown in Fig. 6, where the modulation factor "m" is seen to be the ratio of the maximum radial dimension to the minimum radial dimension over the scallop. The longitudinal components of the electric field are zero at the two points of symmetry in the scalloped geometry, and non-zero elsewhere. The transverse components of the elctric field are spatially uniform, and independent of the longitudinal position within the scalloped geometry.

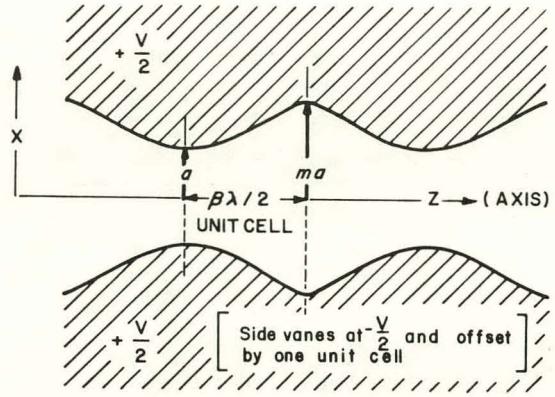


Fig. 6. The RFQ pole-tip geometry.

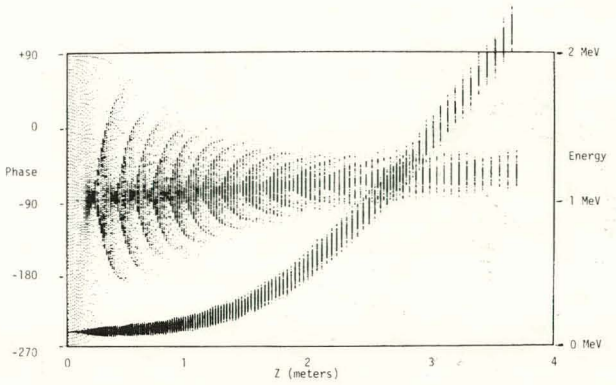


Fig. 8. Phase and energy profiles through the structure.

The structure is simple, consisting of a vane-loaded cylinder excited with rf power. In fact, the structure is so simple that, for the first time, one might consider configuring the linac for adiabatic capture of a continuous beam at low energy. This could be done by introducing the scallops gradually so that the structure acts primarily as a buncher at the beginning, transforming gradually to an accelerator at the end. A computer-generated picture of such a vane tip is shown in Fig. 7.

Simulation of the longitudinal beam dynamics without space charge in such structures demonstrates that capture efficiencies approaching 100% are feasible in reasonable lengths.[12] Figure 8 shows the phase and energy profiles of a beam in one such structure that bunches a 100-keV deuteron beam and accelerates 100% of it to 2 MeV in a total length of about 3.6 meters. Figure 9 shows the longitudinal phase space at 12 points throughout the structure. Subsequent calculations, including the transverse motion and space-charge effects, suggest capture efficiencies in excess of 90% and emittance growths of less than 50% for a 100-mA deuteron beam injected at 100 keV.[13]

The rf cavity mode employed in these structures is a TE_{210}-like mode,[14] which is a "cut-off" mode, and cannot be excited in a finite-length closed cylinder. With special terminations, however, it is possible to excite the mode in all but the immediate vicinity of the end walls. The vanes must not touch the end wall of the termination, as this would short-out the desired mode. The vanes may be cut away near the cylinder wall to provide a cross-over for the magnetic flux, and extended toward the terminating plane near the axis to provide additional capacitive loading between the vanes and to the terminating plane. These features tend to support the wanted TE_{21} modes and destroy the unwanted TE_{11} modes.

A coaxial manifold has been developed that provides a symmetrical, multi-slot driving arrangement for the RFQ cavity.[15] A coaxial cavity surrounding the RFQ cavity is excited in a coaxial TEM mode. The magnetic fields in the TEM mode are orthogonal to the magnetic fields in the RFQ mode. These fields can be coupled by diagonal slots, where the slot angle is

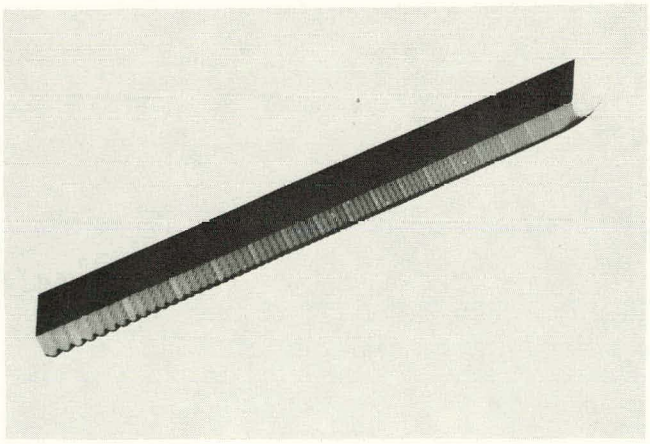


Fig. 7. An RFQ vane tip.

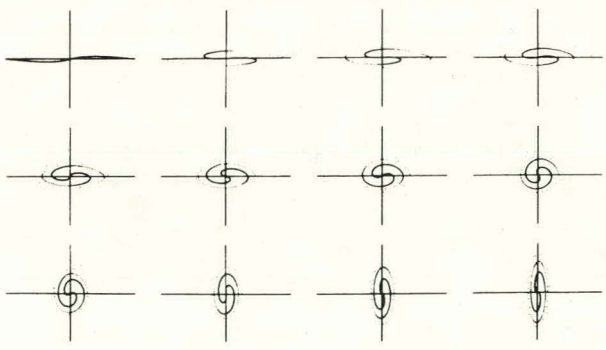


Fig. 9. Longitudinal phase space at every 10th scallop.

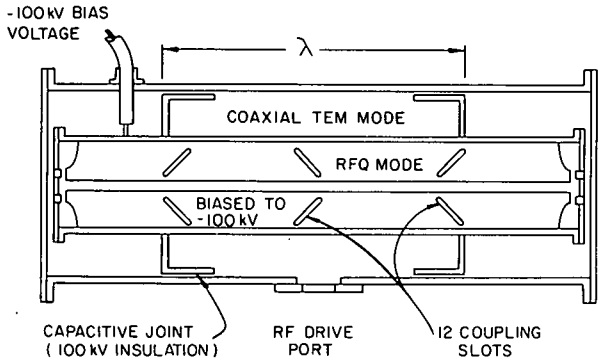


Fig. 10. Biased, manifold-driven RFQ linac structure.

determined by the magnitude and direction of the magnetic fields in the vicinity of the slot.

The first operational model of the RFQ linac structure to be tested at LASL is shown in Fig. 10. Fabrication is well underway. The structure will accelerate 100-keV protons to an energy of 640 keV in a length of 1.2 meters. It will be manifold-driven through a total of 12 symmetrically located coupling slots. For the first test, the structure will be electrically grounded, rather than biased as shown in the figure. For subsequent tests, the structure can be biased to -100 kV, making it possible for the ion source and its control and instrumentation to be at ground potential.

Comparison of Linac Focusing Properties

It is natural to extend the magnetically-focused linac structures downward in energy (and beta) to the limits of the technology. In so doing, it is necessary to pack as much magnetic focusing in the limited confines of the drift tubes as possible. The standard 200-MHz Alvarez linac has been pushed to a beta of 0.04 by this technique. To go lower in beta with these structures, it is necessary to increase the space available for focusing, or increase the field intensities that can be packed into the available space.

One way to get more room for focusing is to lower the frequency, making everything larger. At the lower frequencies, the larger size of the Alvarez structure is a distinct disadvantage, and the smaller size of the Wideroe structure becomes a significant advantage.

Another way to get more room for focusing is to eliminate some of the accelerating gaps in exchange for longer, larger drift tubes. In the Alvarez structure this is referred to as the $2\beta\lambda$ configuration, and in the Wideroe structure it is referred to as the $\pi,3\pi$ configuration.

Recent developments in permanent magnet technology by K. Halbach[16] of Lawrence Berkeley Laboratory, R. Holsinger[17] of New England Nuclear, and J. Farrell of LASL, and independently by N. V. Lazarev and V. S. Skachkov[18] of the Institute of Theoretical and Experimental Physics, Moscow, offer significant increases in the magnetic-field gradients which can be packed into small volumes. Furthermore, these quadrupoles require no power supplies, need no cooling, exhibit no ripple, and offer no control. These "superquads" should find their way into low-beta linac structures.

All of these linac structures employ a periodic alternating-gradient focusing system of either the magnetostatic, electrostatic, or rf electric type. In the static versions, the alternations occur in space, whereas in the rf version, the alternation occurs in time with a spatial uniformity in the instantaneous fields.

In either case, the general differential equation describing the particle motion is

$$\ddot{x} + [(g + h\cos(\omega t)x] = 0 \qquad (1)$$

where g accounts for constant linear forces and h cos(ωt) accounts for the alternating gradient force. By changing to the independent variable n, where $n = \omega t/2\pi = ft$, the equation can be written as a function of two parameters, namely $A = g/f^2$ and $B = h/f^2$:

$$\frac{d^2x}{dn^2} + [A + B(\cos 2\pi n)]x = 0 \quad . \qquad (2)$$

The quantity n advances by unity during each period of the focusing structure. The x, dx/dn phase space is identical to the $x,\dot{x}/f$ phase space of Smith and Gluckstern.[19]

This is Mathieu's equation,[20] the general properties of which are well known. It is stable for some combinations of A and B, and unstable for others. It is standard practice to map the A-B space, designating the stable and unstable regions, and giving some properties of the stable motion in the stable regions.

Figure 11 represents the stability chart for the first and most useful stability region of this equation. The properties of the stable motion are described in terms of the μ, α, β, and γ quantitites of Courant and Snyder,[21] where μ is the phase advance of the solution per period, and β is related to the size of the beam of a given emittance at a given moment. The quantity β_+ corresponds to the beta for the maximum beam size, and occurs at the moment of maximum focusing. The quantity β_- corresponds to the beta for the minimum beam size, and occurs at the moment of maximum defocusing. At these two moments, $\alpha = 0$ and $\gamma = -1/\beta$. The flutter factor, F, is defined equal to β_+/β_-. Contours of μ, β_+, and F are included on the stability chart.

For A = 0, the equation has a range of stability from B = 0 to B = 17.92, where $B = (dF/dx)/m(f/N)^2$, dF/dx is the electromagnetic force gradient, m is the particle mass, F is the frequency of the rf, and N is the length of focal period divided by $\beta\lambda$. For magnetic focusing, $dF/dx = q\beta c(dBy/dx)$, and for electric focusing $dF/dx = q(dEx/dx)$, where q is the particle charge and βc is the particle

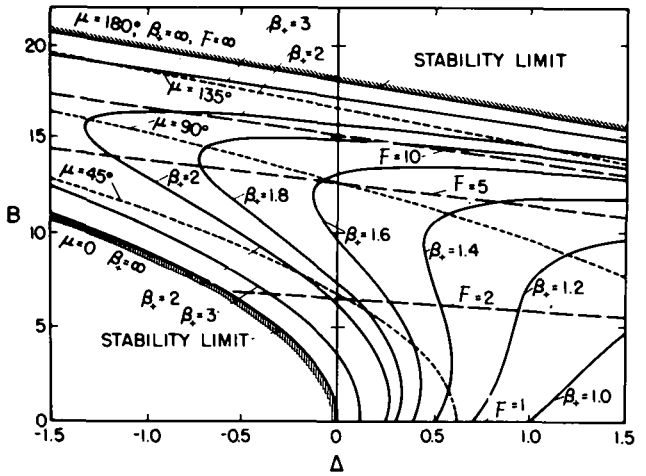


Fig. 11. The RFQ stability chart.

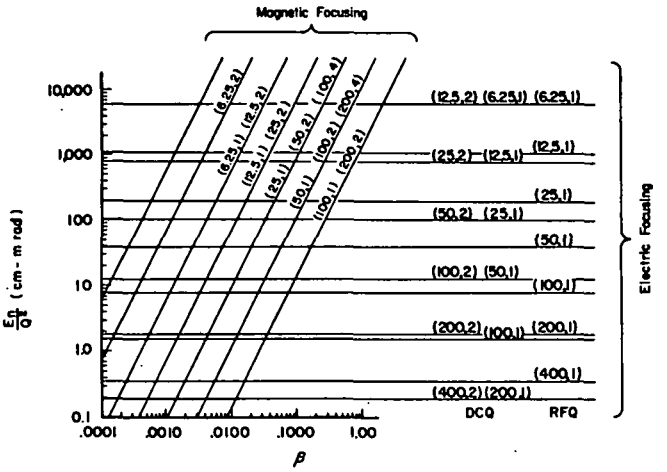


Fig. 12. Admittance of low-beta linac structures.

velocity. The maximum acceptance for A = 0 occurs at B = 11.39 where β_+ has its minimum value of 1.554.

The area in the x, dx/dn phase space that is admitted by a structure with a radial aperture of "a" is $\pi a^2/\beta_+$. Because n = z/(Nβλ), the admittance of the structure in the x,x' phase space is $\pi a^2/(\beta_+ N\beta\lambda)$, and the normalized admittance (area in xx' over π times βγ) is $a^2\gamma f/(\beta_+ Nc)$.

A convenient comparison of the relative focal properties of different linac structures can be made if one imposes a couple of reasonable constraints, namely that (1) the structures be compared at the same operating point in the stability chart (A,B); (2) the bore radius, a, be increased until the pole-tip fields reach some prescribed limit (B_s in the magnetic case, and E_s in the electric case); and (3) the average of the focusing fields over a half period is approximately consistent with the average of the sine wave over a half period. Under these constraints, the normalized admittance of the magnetically-focused structure is

$$E_n = \frac{c^3}{\beta_+ B^2}\left(\frac{ecB_s}{m_o c^2}\right)^2 \frac{\beta^2 Q^2}{\gamma}\left(\frac{N}{f}\right)^3 , \qquad (3)$$

and the normalized admittance of the electrically-focused structure is

$$E_n = \frac{c^3}{\beta_+ B^2}\left(\frac{eE_s}{m_o c^2}\right)^2 \frac{Q^2}{\gamma}\left(\frac{N}{f}\right)^3 , \qquad (4)$$

where Q is the charge-to-mass ratio of the particle as compared to a proton.

Figure 12 facilitates this comparison for the operating point A = 0 and B = 11.39, where $\beta_+ = 1.554$, a pole-tip magnetic field limit of 1 Tesla, and a pole-tip electric field limit of 10 MV/m for the static case, and 1.5 times the Kilpatrick limit[22] for the rf case. The numbers in brackets on the lines are the frequency in MHz and the N value of the focusing period. For example, the (200,2) slanted line corresponds to our standard 200 MHz, magnetically-focused, drift-tube linac structure in the + ~ + - configuration.

The lines representing the magnetically-focused structures have a slope of 2 on this log-log plot as a result of the β^2 dependence of the admittance. The admittance of the electrically-focused structures is independent of β, and hence represented by the horizontal lines. The admittance of the RFQ structure is higher than the admittance of the corresponding electrostatically-focused structure (DCQ), because of the higher surface field limits at rf frequencies.

Given the normalized emittance, E_n, of the ion beam, the charge-to-mass ratio, Q, and the N value of the first magnetically-focused structure, the following quantities are immediately obvious from Fig. 12: (1) the maximum frequency of the RFQ that will accept the beam, (2) the beta value at which the admittance of this RFQ intercepts the admittance of the magnetically-focused structure with the same frequency and given N value. The aperture, a, of the RFQ can readily be determined from the equations given above, from which the minimum suitable beta for the RFQ can be determined ($\beta_{min} \sim 2a/\lambda$).

A Uranium +11 RFQ Example

Let us consider an RFQ/Wideroe marriage for U^{+11}. This choice allows convenient comparison with the first Wideroe tank (π,3π) of the UNILAC,[23] which spans a range of beta from 0.005 to 0.0216 in a length of 5.58 meters.

TABLE I

URANIUM +11 RFQ LINAC STRUCTURE

Frequency	25 MHz
Cavity length	4 m
Number of cells	88
Radial aperture	1.3 - 0.9 cm
Injection voltage	100 kV
Beta initial	0.00315
W/q initial	0.1 MeV
Beta final	0.01580
W/q final	2.5 MeV
Normalized admittance	0.28 cm mrad
Capture efficiency	92%

Tom Wangler of LASL did a preliminary design of such a machine. The admittance of a 25-MHz RFQ is approximately equal to the admittance of a 25-MHz (π,3π) Wideroe linac at $\beta = 0.005$ corresponding to the UNILAC injection voltage of 250 kV for U^{+11}. However, this initial beta does not realize the maximum benefits from the RFQ, which for the best bunching action, prefers a lower starting value.

The design presented in Table I is based on an initial beta of 0.00315 corresponding to an injection voltage of 100 kV for U^{+11}. This RFQ intercepts the (π,π) Wideroe linac acceptance at a beta of 0.0158, corresponding to an energy of 2.5 MeV per unit charge.

General Role of RFQ

The general properties of the RFQ and some speculation on its role in the general scheme of things are:

1. It is the strongest focusing device now known for low beta.
2. Consequently, the beam sizes are shockingly small.
3. Furthermore, the aperture for a given normalized emittance is independent of β, and hence constant throughout an accelerating structure.
4. The minimum β would seem to be limited only by the relationship of $\beta\lambda$ to the beam aperture. Perhaps, for some applications, $\beta\lambda$ could be as small as twice the radial aperture.
5. The maximum β is also limited by the relationship of $\beta\lambda$ to the beam aperture. As this ratio gets too large, the acceleration efficiency drops. It appears to be a prime candidate up to the point where the Wideroes can take over.
6. It offers some of the same size advantages that the Wideroe offers in comparison to the Alvarez structure. In the four-vane configuration, it is considerably smaller than an Alvarez structure of the same frequency but somewhat larger than a Wideroe.
7. The rf efficiency is a strong function of frequency and aperture, and in general is comparable or superior to the other low-beta structures.
8. It is mechanically sound and simple, particularly in the four-vane configuration.
9. It is the best buncher ever observed, offering capture efficiencies in excess of 90%.
10. It offers the lowest injection voltages of any known structure.
11. It offers higher frequencies than other very low-beta structures.
12. In the realm of emittance growth, it seems to be no worse than, and perhaps even better than, other known structures.

In addition to this impressive list of properties, the biased version of the RFQ offers: (1) a grounded ion source with its associated equipment and control; (2) a grounded rf manifold and drive port; (3) no exposed high voltage; and (4) no beam loading on the high-voltage power supply.

Acknowledgments

We are all indebted to I. M. Kapchinskii of ITEP and V. A. Teplyakov of IHEP and their associates in the USSR for their invention of the RFQ linac structure, and their pioneering work in the design, analysis, fabrication and operation of the first prototypes.

The author credits J. J. Manca of Varian, Pierre Grand of BNL, and R. A. Jameson of LASL for triggering our current interest in the RFQ in this country. The RFQ developments reported here are the work of a strong team pulled together at LASL for this purpose consisting of R. Stokes (theoretical program coordinator), K. Crandall (beam dynamics), T. Wangler, S. Schriber (CRNL), S. Inagaki (KEK), J. Potter (rf structures), F. Humphry, A. Thomas, S. Williams (HEDL), G. Rodenz, and C. Fuller (engineering).

The APF linac structure whose initial operation is reported here was designed, fabricated, and put into operation by J. Stovall (principal responsibility for the PIGMI laboratory), L. Hansborough (chief mechanical engineer), E. Bush, V. Hart, R. Hamm (ion source), R. Sturgess, T. Boyd, P. Tallerico, D. Keffeler, J. Johnson, R. DePaula, S. Klosterbuer (control and diagnostics), and V. Martinez.

References

1. S. O. Schriber, "High-Beta Linac Structures," to be published in the Proceedings of the 1979 Linear Accelerator Conference, Montauk, NY (Sept. 1979).
2. A. W. Maschke, "MEQALAC: A New Approach to Low Beta Acceleration," Particle Accelerators and High Voltage Machines-TID 4500, Brookhaven National Laboratory report BNL-51029 (June 1979).
3. D. A. Swenson and J. E. Stovall, "Low-Energy Linac Structure for PIGMI," IEEE Trans. on Nucl. Sci. NS-24, 1127 (June 1977).

4. E. A. Knapp and D. A. Swenson, "The PIGMI Program at LASL," Proc. of the 1976 Proton Linear Acc. Conf., Chalk River, Ontario, Canada, Sept. 14-17, 1976, Atomic Energy of Canada Limited report AECL-5677 (November 1976).
5. J. M. Potter, S. W. Williams, F. J. Humphry, and G. W. Rodenz, "Radio-Frequency Quadrupole Accelerating Structure Research at Los Alamos," IEEE Trans. on Nucl. Sci. NS-26, 3745 (June 1979).
6. R. A. Jameson, "High-Intensity Deuteron Linear Accelerator (FMIT)," IEEE Trans. Nucl. Sci. NS-26, 2986 (June 1979).
7. D. A. Swenson, "Alternating Phase Focused Linacs," Particle Accelerators 7, 61-67 (1976).
8. L. Hansborough, E. Bush, and V. Hart, "Mechanical Description of PIGMI," IEEE Trans. Nucl. Sci. NS-26, 1464 (February 1979).
9. R. W. Hamm, R. R. Stevens, Jr., D. W. Mueller, J. N. Leavitt, and H. M. Lederer, "A Compact 250-kV Injector System for PIGMI," IEEE Trans. Nuclear Sci. NS-26, 1493 (February 1979).
10. M. Kapchinskii and V. A. Teplyakov, "Linear Ion Accelerator with Spatially Homogeneous Strong Focusing," Nuclear Experimental Techniques, 1970 Consultants Bureau, Plenum Publishing Corporation, report UDC 621.384.64 (1970).
11. I. M. Kapchinskii and N. V. Lazarev, "The Linear Accelerator Structures with Space-Uniform Quadrupole Focusing," IEEE Trans. Nucl. Sci. NS-26, 3462 (June 1979).
12. R. H. Stokes, K. R. Crandall, J. E. Stovall, and D. A. Swenson, "Rf Quadrupole Beam Dynamics," IEEE Trans. Nucl. Sci. NS-26, 3469 (June 1979).
13. K. R. Crandall, R. H. Stokes, and T. P. Wangler, "Rf Quadrupole Beam Dynamics Design Studies," to be published in the Proceedings of the 1979 Linear Accelerator Conference, Montauk, NY (Sept. 1979).
14. J. M. Potter, S. W. Williams, F. J. Humphry, and G. W. Rodenz, "Radio-Frequency Quadrupole Accelerating Structure Research at Los Alamos," IEEE Trans. Nucl. Sci. NS-26, 3745 (June 1979).
15. J. M. Potter, "An Rf Power Manifold for the Radio-Frequency Quadrupole Linear Accelerator," to be published in the Proceedings of the 1979 Linear Accelerator Conference, Montauk, NY (Sept. 1979).
16. K. Halbach, "Strong Rare Earth Cobalt Quadrupoles," IEEE Trans. Nucl. Sci. NS-26, 3882 (June 1979).
17. R. Holsinger, "The Drift Tube and Beam Line Permanent Magnets for the NEN Proton Linac," to be published in the Proceedings of the 1979 Linear Accelerator Conference, Montauk, NY (Sept. 1979).
18. N. V. Lazarev, "Permanent Magnet Quadrupoles without Marked Poles," to be published in the Proceedings of the 1979 Linear Accelerator Conference, Montauk, NY (Sept. 1979).
19. L. Smith and R. L. Gluckstern, "Focusing in Linear Ion Accelerators," Rev. Sci. Inst. 26, 220 (February 1955).
20. L. Jackson Laslett, Focusing of Charged Particles, "Strong Focusing in Circular Particle Accelerators, (Academic Press, New York, 1967), Vol. II, p. 355. 2.
21. E. D. Courant and H. S. Snyder, "Theory of the Alternating-Gradient Synchrotron, Ann. Phys. 3, 1-48 (January 1958).
22. S. W. Williams, G. W. Rodenz, F. J. Humphry, and J. M. Potter, "Voltage Breakdown Testing for the Radio-Frequency Quadrupole Accelerator, to be published in the Proceedings of the 1979 Linac Accelerator Conference, Montauk, NY, (Sept. 1979).
23. Klaus Kaspar, "The Prestripper Accelerator of the UNILAC," Proc. of the 1976 Proton Linear Acc. Conf., Chalk River, Ontario, Canada, Sept. 14-17, 1976, Atomic Energy of Canada Limited report AECL-5677 (November 1976).

Discussion

Ohnuma, Fermi Lab: You mentioned so many good things about RFQ that the natural reaction I have is that it can't all be true. I admit that I'm an old-fashioned man so that's kind of natural. Just one or two questions - As I understand it, one of the peculiar features of this focusing system is that it is spatially uniform, as you mentioned, and it is changing as a function of time. When the unbunched beam comes in, the matching requirement would be changing as a function of time, so that for some particles, it would be matched, but for some other particles, it will be unmatched. I would expect, depending on the aspect ratio of x and y in the throbbing matched shape, you would get some kind of dilution. I didn't quite understand the function of the tapered initial section.

Swenson: If you start out essentially with the rf quadrupole turned off, that is, with a very large aperture where you have no focusing, and then at some distance (we originally said some 20 cm later), turn it on by tapering these poles down, the beam that enters will be influenced by the gradual introduction of this rf quadrupole, such that it adjusts itself and is essentially matched.

Ohnuma: You said the beam size is shockingly small; does that require something very special in your low energy beam transport?

Swenson: Yes, I think if it's magnetically focused transport, the beam does not have to be shockingly small, it just has to be converging into the entrance of the RFQ.

Teng, Fermi Lab: Why did you choose that particular shape for the scallop of the pole? Is it because you want a spatially uniform transverse focusing?

Swenson: Yes, Dick Stokes tells me that this shape produces a perfect quadrupole field in the transverse space and a sinusoidally varying field in the longitudinal dimension which, we have approximated by some circular arcs truncated on the side, as shown.

Miller, SLAC: I have difficulty believing that the quadrupole fields are spatially uniform because the relationship between longitudinal fields and transverse fields involves the derivates of the longitudinal fields. Is that really true? It must depend on the shape, surely of the vanes. There must be space harmonics, depending on the shape you choose.

Stokes: The shape of the poles which we have chosen is really based on a lowest order of potential function given by Kapchinskii and Teplyakov, and this potential function does give the properties that have been described. The strength of the quadrupole field, in fact, is spatially constant through a unit cell and can be made constant through the whole accelerator if you wish. In addition, it produces a simple sinusoidal shape for the longitudinal field. Connected with this potential function, is a pole shape which is somewhat complex but can be realized mechanically.

Miller: I have a related question. Doesn't the longitudinal variation in the pole shape introduce some transverse magnetic field and, consequently, isn't there some component of magnetic focusing?

Stokes: We have estimated the strength of the magnetic fields and they are very low. Typically, the forces are something like 10^{-5} times the electric forces, and 0 on axis.

AN RF POWER MANIFOLD FOR THE RADIO FREQUENCY QUADRUPOLE LINEAR ACCELERATOR*

James M. Potter
Los Alamos Scientific Laboratory
Los Alamos, New Mexico 87545

Introduction

An important consideration in the design of a practical radio-frequency quadrupole (RFQ) accelerator is the electromagnetic properties of the rf power coupling circuit. Coupling rf power through an iris or coupling loop into one quadrant disturbs the symmetry of the azimuthal field distribution and the uniformity of the longitudinal field distribution, both of which are crucial for good performance of an RFQ accelerator.

Stabilizing the field distribution against perturbations with some form of resonant coupling was found to be impractical because of limitations inherent in the RFQ structure. Instead, a means was developed for coupling to the RFQ by using a resonant power manifold without perturbing the RFQ fields. This paper discusses the properties of rf power manifolds for the RFQ in the context of a coupled-circuit model.

A Circuit Model for the RFQ

The success of the coupled-circuit model of Nagle, Knapp, and Knapp[1] has led us to consider a similar concept for studying the RFQ. The coupled-circuit model has been an effective means for understanding some of the rf properties of the side-coupled, the post-coupled drift tube, and the disk-and-washer linear accelerator structures. However, these structures can all be approximated to some degree by one-dimensional chains of coupled discrete oscillators.

This approximation is not well suited for describing the RFQ because, except for the small modulations of the vanes necessary to produce an accelerating component of electric field, it is a waveguide transmission line of constant cross section. Two-port network analysis using the chain matrix notation,[2] on the other hand, provides an ideal framework for describing continuous transmission lines. This theory also accommodates discrete circuits easily, permitting them to be combined with distributed circuits in the same model.

Let us examine, briefly, a two-port model for the RFQ. The general form for a uniform transmission line of length ℓ is:

$$M = \begin{bmatrix} \cosh \gamma\ell & Z \sinh \gamma\ell \\ Z^{-1} \sinh \gamma\ell & \cosh \gamma\ell \end{bmatrix} ,$$

where γ is the propagation factor for the transmission line and Z is its characteristic impedance. For waveguide, both γ and Z are functions of the excitation frequency and the cutoff frequency. The characteristic impedance is also a function of the normalization chosen. Note that this matrix represents only one waveguide mode. A different set of parameters, γ and Z, are required for each waveguide mode being considered.

The matrix M relates the voltage and current at the output port to the voltage and current at the input port (Fig. 1). That is:

$$\begin{bmatrix} V' \\ I' \end{bmatrix} = M \begin{bmatrix} V \\ I \end{bmatrix} .$$

The variables need not actually be current and voltage. In fact, a more useful normalization uses variables related to the square root of stored energy analogous to the variables used in the original coupled-circuit model.[3]

The RFQ operating mode is an electric mode, heavily loaded, capacitively, by transverse vanes, topologically equivalent to and derived from the TE_{210} mode of a right circular cylinder. This mode is chosen because it has the necessary quadrupole component of electric field with a uniform distribution from end to end.

Existence of the TE_{210} mode requires open-circuit boundary conditions. This is achieved, in practice, by terminating each end of the RFQ with a shorting plane spaced a small distance from the end of the vanes. The effective shunt inductance of this termination is resonated with the capacitive end tuners (Fig. 2) to achieve a high impedance termination at the frequency of the TE_{210} mode.

A suitable model for this configuration is illustrated in Fig. 3. In the stored energy normalization, the shunt conductance of the parallel LC combination becomes

$$Y_o = 1 - \omega_o^2/\omega^2 .$$

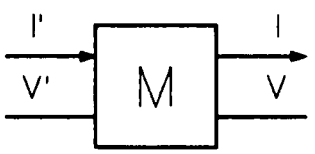


Fig. 1. Representation of a general two-port network.

*Work performed under the auspices of the U. S. Department of Energy.

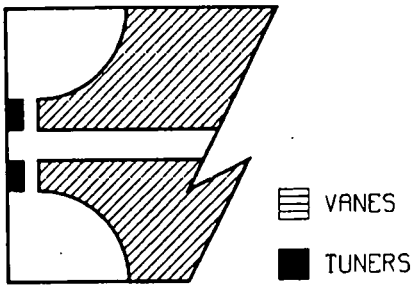


Fig. 2. The RFQ end cap and end tuners.

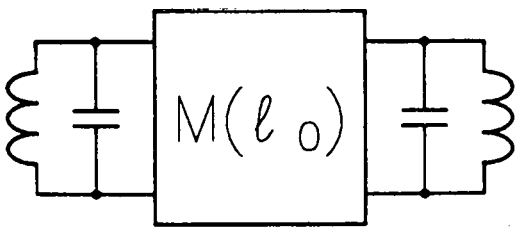


Fig. 3. Two-port model for RFQ.

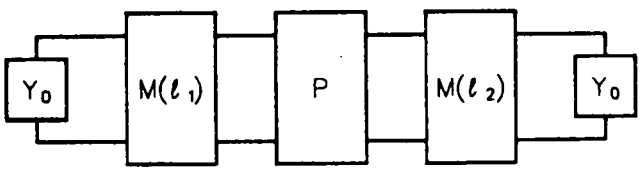


Fig. 4. Two-port model with added perturbation.

The effects of perturbations on the field distribution can be studied by breaking M into sections of length less than ℓ_0 and inserting appropriate two-port representations of the perturbing elements (Fig. 4).

The above model describes only the longitudinal field distribution of the RFQ. Because the symmetry of the vane-tip potentials is important to the quality of the beam in the transverse plane, we would like the ability to model the azimuthal distribution of fields as well. The four-fold symmetry of the RFQ cross section suggests that we could describe an arbitrary distribution of vane-tip potentials by considering the fields to result from an admixture of TE_{21}, TE_{11}, and TE_{01} waveguide modes.

Although such a model might be feasible, it is unnecessarily complex for our present purposes. Instead, we propose to ignore coupling between the azimuthal and longitudinal field distributions and to develop a separate model for the azimuthal direction.

With increasingly heavy loading, i.e., a smaller aperture, the frequencies of the TE_{110} and TE_{210} modes asymptotically approach each other. This suggests that if we ignore the higher modes, TE_{11n} and TE_{21n} for $n > 0$, we can approximate the RFQ by a ring of coupled oscillators as illustrated in Fig. 5. This amounts to ignoring the longitudinal extent of the RFQ.

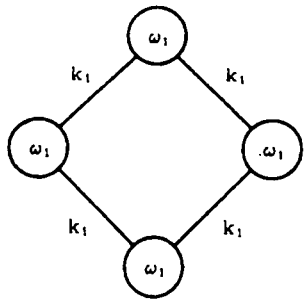


Fig. 5. Four-resonator model for RFQ.

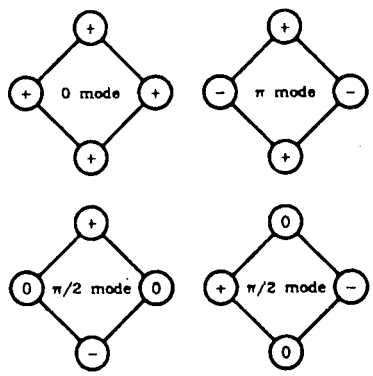


Fig. 6. Field patterns for the four-resonator model.

A ring of four oscillators is characterized by four modes of oscillation (Fig. 6). The ring will have a π mode, corresponding to the TE_{210} mode; two degenerate $\pi/2$ modes, corresponding to the two TE_{110} modes; and a zero mode. We are tempted, by simple extension, to identify the zero mode with the TE_{010} mode. However, there is a problem: experimentally there is no fourth mode in the mode spectrum near the other three modes. Furthermore, the effect of the vanes on the TE_{010} mode suggests that it would be far removed in frequency from the TE_{110} and TE_{210} modes.

This apparent problem has an interesting resolution. For an appropriate form of resonator, the zero mode frequency can be zero Hertz. Figure 7 depicts two forms, equivalent through a series-to-parallel transformation, that the unit oscillator might take to have a zero mode of zero frequency. That is, the network will pass direct current. Four of these oscillators are joined together (Fig. 8) to form a circuit model for the azimuthal direction of the RFQ.

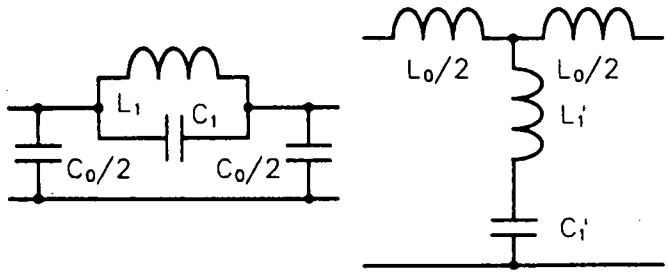


Fig. 7. Equivalent unit cells for RFQ coupled-circuit model.

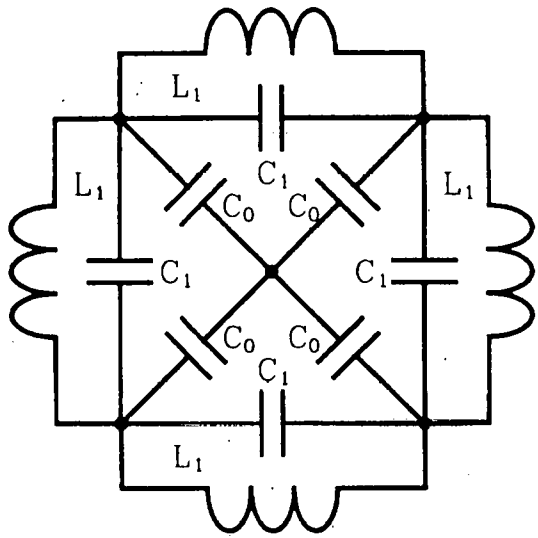


Fig. 8. Equivalent circuit for RFQ.

Resonant Coupling Techniques

At first, resonant coupling methods were considered as a means of stabilizing the azimuthal and longitudinal field distributions against perturbations. Figure 9 shows a scheme for stabilizing the azimuthal field distribution with coupling cells using the same principle as the side-coupled structure. This version suffers from a fatal defect: the $\pi/2$ mode is doubly-degenerate because of the circular symmetry. With only a slight tuning error most of the stored energy could end up in the coupling cells.

Although azimuthal resonant coupling has been rejected for now, it could probably be saved if the degeneracy were eliminated by removing one of the coupling cells.

Attempts to find internal modes suitable for longitudinal resonant coupling in the manner of the post-coupled drift tube or disk-and-washer structures have failed.

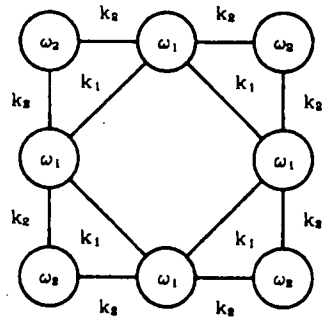


Fig. 9. Resonant coupling of four-resonator model.

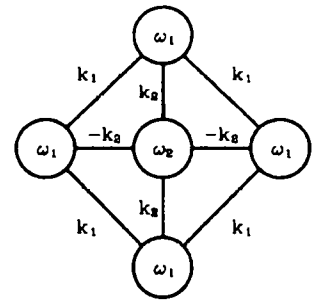


Fig. 10. Four-resonator model with nonresonantly coupled manifold.

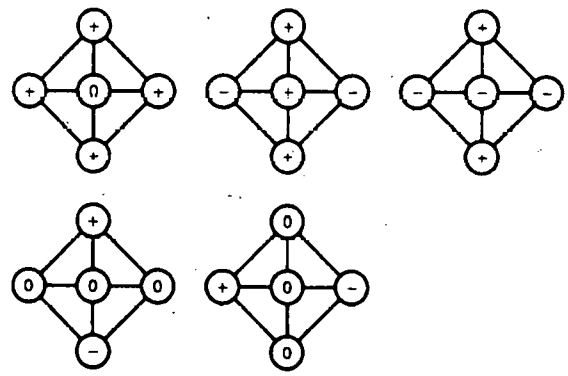


Fig. 11. Field patterns for four-resonator model with manifold.

These problems led to the investigation of an external means for stabilizing the RFQ fields using an arrangement related to the manifold of Voelker.[4]

A Nonresonantly Coupled Manifold for the RFQ

The manifold concept that subsequently evolved is not suitable, directly, for stabilizing the field distribution. However, it does

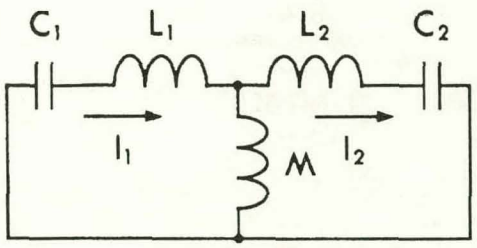


Fig. 12. Two-resonator, coupled-circuit model of RFQ with manifold.

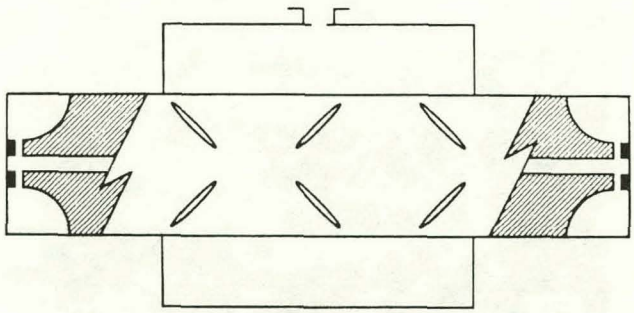


Fig. 13. Cross section of RFQ with nonresonantly coupled manifold.

provide symmetric drive points that do not, in principle, disturb the RFQ field distribution.

Figure 10 illustrates the simplicity of the nonresonantly coupled manifold. The central oscillator represents the manifold. With five oscillators there are five modes of oscillation (Fig. 11). Only two of the modes shown can be excited by driving the manifold. These two modes can be thought of as radial zero and π modes involving only the RFQ TE_{210} mode and the manifold.

By symmetry, we see that the coupling k_2, at worst, perturbs the azimuthal distribution in a way that cannot mix in the $\pi/2$ modes and introduce sextupole field components.

The situation is even better than it seems. To see this we first simplify the discussion by reducing our model to two coupled oscillators, one representing the RFQ TE_{210} mode and one representing the manifold. Figure 12 is a schematic of a discrete-circuit model of two coupled oscillators. If L_1C_1 equals L_2C_2, then I_1 equals I_2 for zero mode and I_1 equals $-I_2$ for the π mode. Furthermore, the frequency of the zero mode is $(L_1C_1)^{-1/2}$, independent of M.

How does this relate to the RFQ and manifold case? Suppose that an otherwise unperturbed RFQ is magnetically coupled to the manifold through a slot. If the frequency of the TE_{210} mode equals the manifold frequency before the coupling slot is cut, the zero mode of the combination will be at the frequency of the TE_{210} mode. The consequences of this are that the longitudinal field distribution of the RFQ is still flat because it is being excited at its cutoff frequency. In addition the current intercepted by the slot is equal and opposite on opposite sides of the wall. There is no excitation of the slot and, therefore, no perturbation of the RFQ by the slot.

This fact is not easy to illustrate using the coupled-circuit theory in the stored-energy normalization because the definition of the frequencies of the oscillators includes the effects of the coupling slots and because the wall currents are related to the stored energy in a geometry-dependent way.

A Physical Realization of the Manifold

The requirements of symmetry dictate that the manifold should couple equally to each quadrant of the RFQ. This is achieved by placing the RFQ inside the manifold that operates in a TEM coaxial resonator mode with the RFQ shell as its center conductor (Fig. 13). The length of the manifold must be a multiple of a half-wavelength at the operating frequency or tuned to the electrical equivalent by capacitive tuners at the electric field maxima. Coupling between the manifold and the RFQ takes place through slots cut in the RFQ walls at the current maxima of the manifold. Advantage is taken of the multiple maxima to increase the effective coupling.

The fields to be coupled are orthogonal to one another. The manifold magnetic field is azimuthal and the RFQ magnetic field is longitudinal. To couple them, the coupling slots must make an angle with respect to both fields to intercept wall currents on both sides. The sign of the slot angle must be alternated to compensate for the alternating signs of the RFQ fields azimuthally and the manifold fields longitudinally.

The relative stored energies of the RFQ and manifold can be controlled by adjusting the slot angle to intercept more current on one side and less on the other. The tuning considerations discussed above insure that the intercepted fractions of the wall currents are equal.

Coupling to the manifold is achieved by a loop or iris at a magnetic field maxima. If center drive is desired, the manifold should be an even number of half-wavelengths long.

Experimental Data on a Cold Model

A cold model of the RFQ with constant vanes was combined with a nonresonantly coupled manifold as described above. The model is pictured in Fig. 14. The RFQ structure operates at 313 MHz, nominally. The manifold is one-wavelength long and coupled to the RFQ through twelve 45° slots about 90 mm long by 10 mm wide.

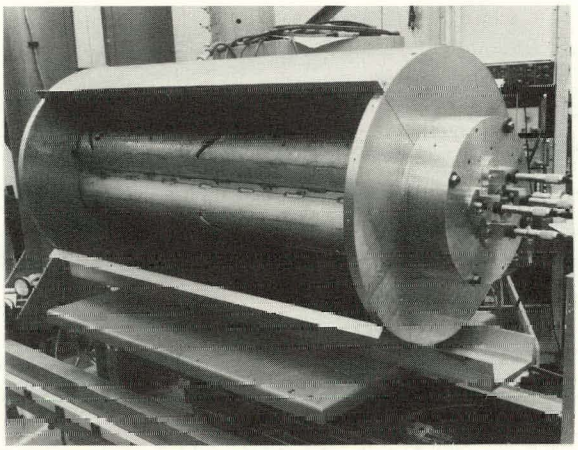


Fig. 14. The RFQ cold model with nonresonantly coupled manifold.

The frequency of the zero mode was 313.268 MHz and the frequency of the π mode was 310.618 MHz. The net coupling constant from the twelve slots was determined to be 0.0085 by measuring the change in RFQ stored energy resulting from a perturbation of the manifold frequency. According to the coupled-circuit analysis of the two oscillator model, the coupling constant is given by

$$k = \frac{\Delta f_{man}/f_{man}}{(\Delta U_{RFQ}/U_{RFQ})^{1/2}} ,$$

if the oscillators have the same frequency.

The accuracy of the coupling-constant determination was insufficient to permit calculating the individual frequencies of the two oscillators from the frequencies of the zero and π modes. Figure 15 is a graph of $(\Delta U_{RFQ}/U_{RFQ})^{1/2}$ versus manifold detuning.

The change in RFQ stored energy was measured by comparing the frequency perturbation of a needle pulled along the RFQ axis for various perturbations of the manifold to the case with no manifold detuning. The fraction of stored energy in the RFQ was similarly measured by comparing beadpulls with and without the manifold. In the zero mode 71% of the stored energy was in the RFQ and in the π mode 30% was in the RFQ. The fact that the ratio of RFQ to manifold stored energy for the π mode is the reciprocal of the same ratio for the zero mode is predicted by the coupled-circuit model.

Variations on a Manifold

It is possible to construct a resonantly coupled manifold by interposing a resonator between the RFQ and the manifold resonator

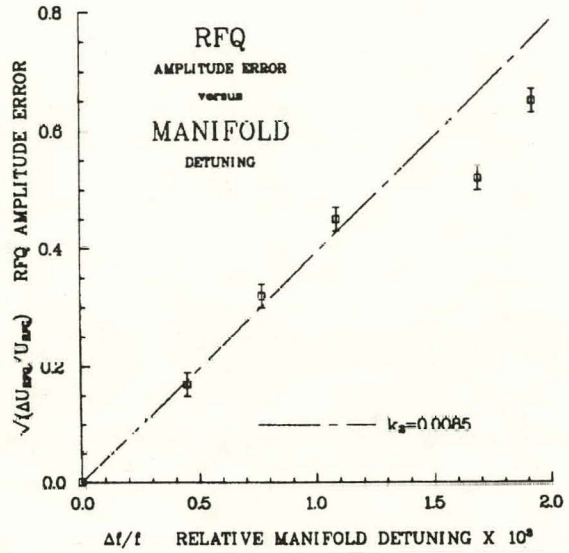


Fig. 15. The RFQ amplitude error versus manifold detuning.

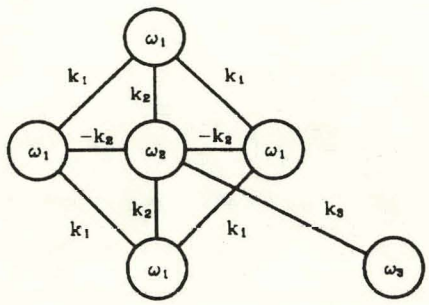


Fig. 16. Four-resonator model with resonantly coupled manifold.

(Fig. 16). The intermediate oscillator is most conveniently a TEM-mode resonator coaxial with the RFQ and manifold. Coupling between the manifold and coupling resonator is through azimuthal slots in the magnetic field region of the intermediate wall.

In principle, this "triaxial" manifold should lock the average RFQ amplitude to the outer resonator amplitude in the $\pi/2$ mode. However, it does not serve to stabilize the internal field distribution of the RFQ. In addition, there are two serious drawbacks to this scheme: fabrication and tuning are more complicated than for the relatively simple nonresonantly coupled manifold; and the RFQ slots are excited and could affect the longitudinal field distribution. The cold model was adapted to the triaxial configuration, but test results were inconclusive because of a design error in the intermediate cavity.

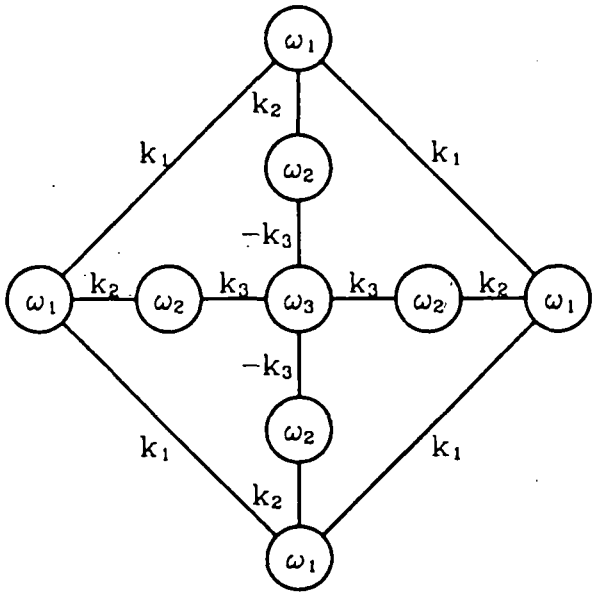


Fig. 17. Four-resonator model with individual coupling resonators.

If each of the coupling slots could be replaced by individual resonators (Fig. 17), perhaps stabilization of the RFQ internal fields could be achieved. An attempt to model this concept was made using resonant coupling loops. Insufficient coupling was obtained with these loops for proper mode separation.

Conclusions and Opinions

A simple manifold has been developed that permits coupling rf power to the RFQ without seriously perturbing the field distribution. Resonantly coupled manifolds could provide better performance at the expense of increased complexity. It is not known if the improved performance would really be useful with a practical RFQ structure.

An extension of the coupled-circuit model to include distributed circuits has proved useful in obtaining a qualitative understanding of the RFQ structure. Further understanding could be developed through computer simulations based on this model.

Acknowledgments

The author would like to express his appreciation to D. Swenson, E. Knapp, R. Jameson, S. Schriber, and S. Williams for their contributions to many useful discussions, and to F. Humphry for his invaluable assistance in testing and modifying the RFQ and manifold cold models.

References

1. D. E. Nagle, E. A. Knapp, and B. C. Knapp, "Coupled Resonator Model for Standing Wave Accelerator Tanks," Rev. Sci, Instrum. 38 , No. 11, p. 1583, 1967.
2. L. Brillouin, Wave Propagation in Periodic Structures, 2nd ed., Dover Publ., 1953.
3. B. C. Knapp, E. A. Knapp, G. J. Lucas, and J. M. Potter, "Resonantly Coupled Accelerating Structures for High-Current Proton Linacs," IEEE Trans. Nucl. Sci. NS-12, No. 3, p. 159, 1965.
4. F. Voelker, "Theory of the RF Manifold and Measurements on a Model Manifold System," Univ. of Calif., LRL, UCLR-17508, 1967.

VOLTAGE BREAKDOWN TESTING FOR THE RADIO-FREQUENCY QUADRUPOLE ACCELERATOR*

S. W. Williams,† G. W. Rodenz, F. J. Humphry, and J. M. Potter
Accelerator Technology Division
Los Alamos, New Mexico 87545

Summary

Designs of radio-frequency quadrupole (RFQ) accelerators with reasonable length require operation with surface fields above the limit imposed by Kilpatrick's Criterion. A cavity was designed using SUPERFISH to test the validitv of this criterion and to determine operating limits for the RFQ. The experimental setup and procedure are described, as are the data and results. A method of calibrating the test is presented.

Introduction

The choice of an RFQ as the low-beta accelerator in the Fusion Materials Irradiation Test (FMIT) linac depends on the successful demonstration of operational feasibility by a prototype RFQ, the Proof-of-Principle (POP) structure. In the design for this structure, questions arise concerning the field strengths that will exist in the cavity during excitation. Because of the very small beam-channel dimensions and the constraint that useful structures have reasonable length, the fields during operation must exceed those predicted by Kilpatrick[1] as breakdown levels. The question that follows, then, is a basic issue concerning RFQ design: to what field levels may RFQs be designed so that the field strengths are maximized and so that breakdown occurrences are tolerable?

Test equipment designed to determine the maximum standoff voltage in an RFQ was subject to several constraints. As in all high-voltage rf equipment, vacuum and cleanliness considerations were important. It was necessary that the resonant frequency be between 400 and 450 MHz for compatibility with the available klystron power unit and controller. Scheduling commitments were such that rapid test completion was necessary. Finally, to provide useful information, the cavity design was required to be capable of developing fields several times those predicated by Kilpatrick as the breakdown limit for 400-450 MHz with the available 1-MW power level.

Background Information

For this work, sparking is defined as the abrupt dissipation of energy stored as electric fields across a gap between electrodes. For a practical vacuum system such as that used in this study, there exists a definite threshold gradient for which electrodes of a given metal may spark. The breakdown mechanism is dependent on this gradient at the electrode surface for spark initiation.[2]

Kilpatrick's Sparking Criterion defines the frequency for which sparking may occur for a given gradient:

$$f = 1.643 \times 10^{4}\, E^{2} e^{-\frac{0.085}{E}} \qquad (1)$$

where

f = frequency in MHz,
E = field gradient in MV/cm.

Thus, at 425 MHz, sparking is predicted at 20 MV/m.

The restraints imposed on the use of this criterion are several in that it:

- deals only with single-gap sparking
- ignores effects involving the quantity of stored energy
- includes practical vacuums of 10^{-3} to 10^{-1} mm pressure
- includes metal electrodes that are not specially prepared
- does not include the presence of external magnetic fields.

The work presented here differs from these restraints in two respects. First, the RFQ configuration has not a single gap, but four, as shown in Fig. 1. Second, although it is small,

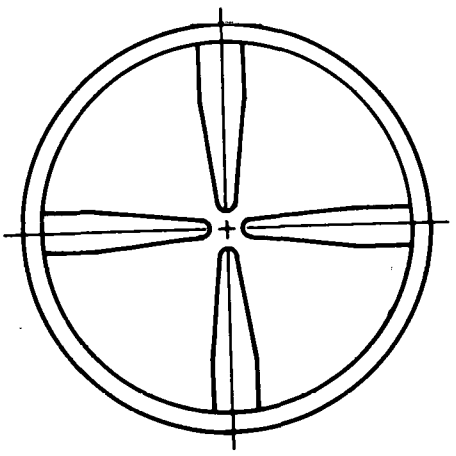


Fig. 1. Sparking cavity configuration.

*Work performed under the auspices of the U. S. Department of Energy.
† Westinghouse/Hanford Engineering Development Laboratory employee working at the Los Alamos Scientific Laboratory.

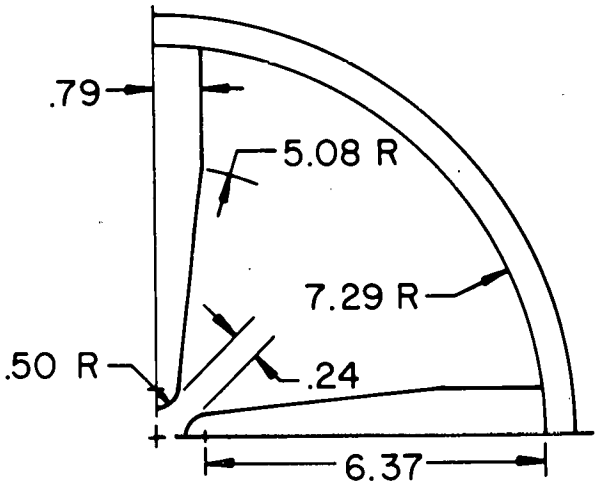


Fig. 2. Sparking cavity quadrant (cm)

the magnetic field component near the electrode tips is non-zero. To first order, however, neither of these differences has much effect on the final gradient achieved before breakdown occurs.

For gradients less than about 10 MV/cm, the electron current caused by field emission is small. Ions in the gap, however, may be accelerated to strike the cathode, causing the emission of electrons and neutral gas atoms from the cathode. A cascade process follows which may result in the formation of a spark, by which an abrupt change in the stored energy dissipation occurs. Such a breakdown mechanism is characteristic of vacuum systems having a high enough ion population for the cascade process to work.

Test Apparatus

The computer code SUPERFISH[3] was used to design the sparking cavity. The first set of runs was a frequency/power scan for a suitable cavity configuration. The goal was to determine cavity dimensions for a 425-MHz resonator that would require a substantial fraction of the klystron's 1.2-MW capacity when the surface gradients were about 50 MV/m. This study showed that the main cavity body could be constructed from an available length of 15-cm i.d. copper tubing if the vanes were sized properly.

The SUPERFISH-aided design produced the cross-section for which a single quadrant is shown in Fig. 2. In the structure that was tested, the vanes were 30.48 cm long and located in the center of the copper cavity that was 76.20 cm in length. Figure 3 is a diagram of the cavity with the vanes installed and the support feet and flanges in place. The flanges at each end were connected to ells of the same inside diameter as the cavity.

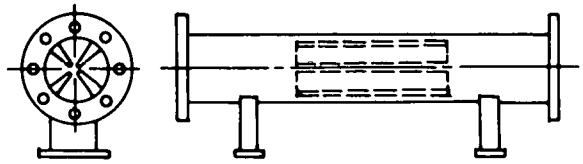


Fig. 3. Cavity with vanes in place.

A 600-ℓ/s ion pump was hung on one of the ells and the other had ports for an ion gauge and a liquid-nitrogen-trapped roughing pump. A screen-covered copper gasket was installed between each ell flange and cavity flange. This device was designed to contain the rf fields inside the test cavity but was shown to be only marginally necessary.

Power was coupled into the cavity from the klystron unit through a waveguide. This setup terminated with a vacuum window attached to a transition piece brazed onto the cavity wall. Inside the transition, a slot was bored through the cavity wall to provide inductive coupling between the waveguide and the resonator volume. After tuning the waveguide, the load presented a VSWR of 1.3:1 to the klystron, at a resonant frequency of 417 MHz.

A 450-ℓ/s turbomolecular pump was connected to a port in the sidewall of the rf vacuum window. Using this pump and the ion pump, an operating pressure of 6×10^{-7} mm was achieved. The entire test setup is diagrammed in Fig. 4.

Test Procedure

The first part of the test procedure was the assembly of the vacuum envelope. All parts that would be exposed to vacuum were cleaned using a three-step procedure, then stored in plastic bags until required for assembly. For all pieces, the procedure involved surface cleaning first with acetone, then methanol, then ethanol, each a reagent-grade solvent. Smaller parts were cleaned in an ultrasonic bath using ethanol as the solvent.

After assembly, the resonator was excited at low power with high duty to heat the rf surfaces. The cavity external wall was heated to about 150°F for two hours to drive out most of the volatiles.

The procedure for determining the RFQ breakdown gradient was to increase the power delivered to the cavity until the level was reached that produced sparking. The gradient magnitude was determined by measuring the power and using the relation:

$$E_{spark} = (P/k)^{1/2} \qquad (2)$$

where k was an experimentally-determined constant.

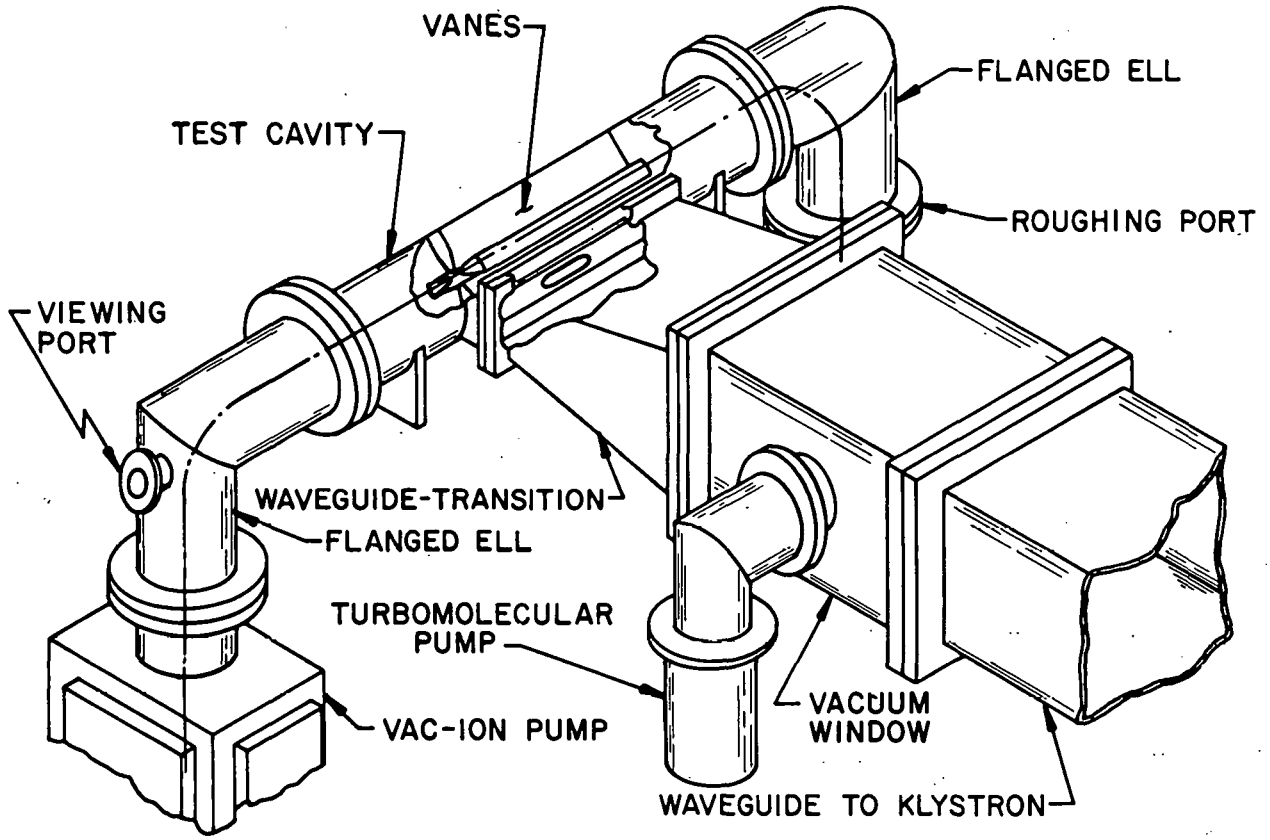


Fig. 4. The 440-MHz RFQ sparking cavity schematic.

Results and SUPERFISH Correlation

The method for evaluating k used a SUPERFISH simulation, and a measurement of the quality factor, Q, of the cavity. The simulation analysis showed the geometry had a field-enhancement factor of 1.63; that is,

$$\frac{E_{max}}{E_{pole\ tip}} = 1.63 \quad .$$

The analysis also predicted a theoretical Q of 8665, and, that a structure excitation of 39.2 W/m would produce pole-tip fields of 0.347 MV/m. The active length of the structure was 0.305 m so pole-tip fields of 0.347 MV/m theoretically required 11.96 W of drive. This power was adjusted for the actual Q of the cavity, which was measured as 5400. Therefore,

$$K_{sf} = \frac{11.96\left(\frac{8665}{5400}\right)}{(0.347 \times 1.63)^2} = 59.9\ W/(MV/m)^2 \qquad (3)$$

An observed cavity input power of 62.2 kW (duty factor = 0.2%) was required to initiate sparking. The resultant maximum electric field using Eqs. 2 and 3 was, then, 32.2 MV/m. Kilpatrick's Criterion predicted that sparking was possible at 19.7 MV/m for f = 417 MHz.

Error Analysis

Because the dimensions of the spark gaps were small (see Fig. 2) and the cavity body had a cylindricity error of $\pm$0.008 cm, the gap spacing between the four vanes varied. An analysis using the measured-gap spacing for each of the four quadrants was done using SUPERFISH. The error was assigned an rms value according to the comparison between the four quadrants. Other sources of error were the measured values for the cavity Q and the effective length of the vanes. Table I lists the sources and values for the errors as percents of the breakdown field. Thus, the total error is 19.6% and the observed breakdown field is 32.2$\pm$9.8% MV/m or 32.2$\pm$3.2 MV/m.

In the absence of any quantitative data, no corrections were made for the quadrant asymmetry introduced by the drive iris or the longitudinal field distribution. Such adjustments would increase the estimate of the voltage required to cause a spark. Inspection of the spark

TABLE I

SUPERFISH Results	RMS ERROR (% E_s)
Cavity Q	0.6
Power/length	7.7
Field intensity	7.9
Measured Results	
Cavity Q	3.2
Cavity length	0.001
Measured Power	0.16

discoloration density on the vanes showed that most sparks had indeed occurred opposite the iris, as would be expected. Also, electron loading was observed during the approach to the sparking threshold, accompanied by soft x-ray radiation of 10^3 R/hr. Correcting for this effect would lower the sparking assignment.[4]

Acknowledgments

The authors would like to thank E. A. Knapp, R. A. Jameson, E. L. Kemp, and T. J. Boyd for their participation in interesting discussions related to this work.

References

1. W. D. Kilpatrick, "Criterion for Vacuum Sparking Designed to Include Both RF and DC," UCRL-2321 (Sept. 1953).
2. W. D. Kilpatrick, "Sparking and X-Rays in a Mercury Pumped Vacuum System," UCRL-1907 (Aug. 1952).
3. K. Halbach, et al., "Properties of the Cylindrical Rf Cavity Evaluation Code SUPERFISH", Proc. 1976 Proton Linear Accel. Conf., 122, Chalk River, Canada, AECL-5677.
4. T.J. Boyd, unpublished note, Los Alamos Scientific Laboratory (July 1979).

WORK ON RF QUADRUPOLE FOCUSING STRUCTURES AT GSI

R.W. Müller
GSI Darmstadt, Fed. Rep. of Germany

Summary

Layouts have been made for a linac accelerating heavy ions ($^{238}U^{1+}$, 40 m long, or $^{238}U^{2+}$, 18 m long) from low energies up to 0.1 MeV/u, designed for high intensities and working at low duty cycle. At this energy the beam is to be stripped and transferred to the UNILAC, replacing the low brilliance ion sources for the planned synchrotron filling regime. Because of the need for very strong focusing, the linac must have rf quadrupole focusing which is similar in principle, but of different technical shape from those of Kapchinski - Teplyakov and the Los Alamos approaches. Also the rf cavity design is different. The frequency is typically low, around 10 MHz or lower. The linac will have the property of adiabatic bunching. This is a good condition for transporting beams of more than 10 mA, or even 1 ampere.

Introduction

Rf quadrupole (RFQ) linac structures have been recognized to be probably the most powerful structure for very slow ion beams ($\beta < 1$ %) of high intensity. At GSI, Darmstadt, two applications have triggered development work: (1) the high-intensity mode of the heavy ion synchrotron (SIS) demands for a bright U^{1+} or U^{2+} beam; (2) the structure is a promising candidate for the first section of a heavy ion ignited fusion (HIF) accelerator, the design of which is aided if it is able to transport and accelerate currents of 1 ampere or more of Cs^{1+} or Bi^{1+} ions. In this case the micro-bunch frequency, or the frequency of the first linac stage, must be low (2 or 4 MHz), but even this frequency is an inherent advantage to the scenario.

Electrode Structure

The merits of the RFQ structure originally described by Kapchinskij and Teplyakov can be reviewed as follows: at velocities $\beta < 1$%, electric quadrupoles are more powerful than magnetic ones. Generally, rf voltages and fields of high amplitudes can be generated and handled easier than electrostatic fields because of the absence of solid insulators, and because of higher sparking limits in the vacuum. Since the focusing period is as short as possible, ($\beta\lambda$), and the lenses are as strong as possible, RFQ channels have a high stability, a high acceptance at modest aperture, and a high current holding ability.

A homogeneous RFQ channel of aperture radius R, with a voltage U of wavelength λ applied to the electrodes, has a focusing phase σ per $\beta\lambda$ cell, or "focusing frequency" :

$$\sigma_{oo} = \frac{1}{\sqrt{8}\,\pi}\left(\frac{q}{A}\right)_{ion}\frac{U}{932\ MV}\cdot\left(\frac{\lambda}{R}\right)^2 \qquad (1)$$

By shaping the electrodes longitudinally, one can generate an accelerating field distribution with a potential distribution on the axis:

$$\Phi = \frac{U}{2}\,(1 + A_1\cos(kz) + \text{higher harmonics}) \qquad (2)$$

with $k = 2\pi/(\beta\lambda)$. The amplitude A_1 can be interpreted as the transit time factor T, of drift tube structures:

$$T = (\pi/4)\cdot A_1 \qquad (3)$$

By shaping the electrodes and keeping a clear aperture of 2 R, the quadrupole strength is weakened, so that the focusing frequency σ_r becomes smaller than the focusing frequency of the homogeneous channel, σ_{oo}. It again becomes smaller due to the well-known acceleration defocusing term, by a factor f, which depends on details of the geometry, the particle phase ϕ, and on σ_{oo}:

$$\sigma_r = \sigma_{oo}\cdot f\ (\text{geometry}, \phi, \sigma_{oo}) \qquad (4)$$

The general form of f is :

$$f = \sqrt{a + b\cdot\cos^2\phi + \sqrt{2}\pi^3(R/\beta\lambda)^2\cdot(A_1/\sigma_{oo})\cdot\sin\phi} \qquad (5)$$

where a and b are functions of only the geometry. There is an "orthodox" layout of RFQ structures which keeps the quadrupole strength constant along z, and simultaneously avoids higher harmonics than the fundamental in Φ (eq.(2)), so that b = 0, and the transverse motion has the least possible coupling with the phase motion. It would be wise to apply this orthodox shaping at least in the very first few meters of a structure, especially when adiabatic bunching is applied. But in order to design an economical structure, with appreciable transit time factors of more than a few percent, it is more pragmatic to allow for b > 0. To enhance the transit time factor T, or A_1, a "drift-tube with long quadrupoles" was designed, as shown in Fig. 1. This also has advantages for the type of rf cavities described later. The calculating procedures for finding the values of the coefficients a and b are nearly as easy as in the case of the orthodox structure[3].

Figures 2, 3, and 4 show the parameters for a U^{1+} layout, with R = 1.2 cm, U = 200 kV, f = 9 MHz, and $\sigma_{oo} = 0.765$. The structure for $\beta_i = 0.15\%$ to $\beta_e = 1.5\%$ will be 40 m long, and capable of transporting a 25 mA beam current. A similar 18 m long structure for U^{2+} at 13.5 MHz will transport 35 mA. The currents have been estimated from the formulae for transverse stability. Looking at the bunch shape (Fig. 4), there is a high level of confidence that longitudinal instabilities will play a minor role. The long "cigar" shape of the bunches is a consequence of the adiabatic bunching used in this design. The stable phase ϕ_s (Fig. 3) is shifted gradually from -75° to -30°. The growing stable area condition necessary for the adiabatic bunching procedure is fulfilled when β grows linearly with z. The capture efficiency in this design is 70 %. A few more details are available from a GSI report[4].

Frequency Considerations

Looking at the scaling laws, with the electric field strengths kept invariant at about 15 MV/m, one finds that the transportable current is a function of the wavelengths squared:

$$I \approx 8\ \text{amp}\cdot(q/A)_{ion}\cdot\beta\cdot(\lambda/m)^2 \qquad (6)$$

This means that for q/A = 1/133 (Cs^{1+}), $\beta_i = 0.3$%, the frequency must not be higher than 4 MHz if a

current of 1 ampere is required. The aperature of this structure must be large, 2 R ≈10 cm, and the system voltage U ≈ 720 kV, to avoid σ_r values greater than $\pi/2$. Typically one has to deal with very low frequencies.

Rf Cavity Design

It is obvious that in the heavy ion situation as discussed before, the cavity types used in the proton case (Los Alamos: Clover-leaf type[2], and Teplyakov: Split-ring type[1]) are not adequate. Even usual Wideröe stub-line cavities (GSI type) would become too bulky for frequencies below 10 MHz. Studies were made of ways to arrange the inductive stub-line of the Wideröe structure in the longitudinal direction, and to design a TM mode cavity. The design is quite successful, resulting in a cavity of excellent properties (see Fig. 5).

The capacitive currents caused by feeding the acceleration electrodes with a constant voltage, U, are gathered on two pairs of spear-shaped collectors. The shape of the collectors is such that the current density on their surfaces is uniform. In this way an essentially ring-shaped magnetic field is produced, and the power dissipation is minimized. The total magnetic flux around the collector assembly will induce the voltage U. The shape of the collectors has still another good effect: the net electric field flowing to the outer conductor (e.g. in a TEM cavity) is approximately eliminated; therefore, the voltage distribution along the cavity is of an excellent flatness.

The most important effect is that the size of a cavity cell is reasonable even at low frequencies. For instance, the length ℓ is 1/15 of the wave - length, if $r_a/r_i \simeq 3$ and $C' \simeq 30\ \varepsilon_o$. Nevertheless, the R_p value is high (some 100 kohms) and also the shunt impedance is high. Because quotation of shunt impedances will lead to misunderstandings for an adiabatically bunching cavity, it is more meaningful to state that the power loss in the structure is of the order of the power taken by the beam at its current limit, or even much less for the 1 ampere accelerator, because of its low frequency.

The problem of the possible energy step at the entrance of the system arising from the structure asymmetry with respect to ground potential, (while the longitudinal magnetic field structures in use so far are symmetric), can be solved by proper shaping of the first $\beta\lambda$-cell. To avoid repetition of this problem, one should tightly couple together a larger number of cavity cells into a long super-cavity fed by a common power amplifier, or a set of synchronous amplifiers. Thus a continuous bed for the drift tubes is prepared.

Planned Model Work

In cooperation with the group of H. Klein, University of Frankfurt, we plan to build a scaled model (1:4) for protons. The σ values along the accelertor will be identical with those planned for a heavy ion accelerator. The voltages, powers and currents will be moderate, but the model will allow study of all the instabilities which also would occur in a large accelerator.

References

[1] I.M. Kapchinskij, V.A. Teplyakov. Pribori i Tekh. Eksp. No. 2 (1970), 19-22.

[2] J.M. Potter et al., "RFQ Accelerating structure Research at Los Alamos", IEEE Trans. NS-26 (1979), 3745-7.

[3] R.H. Stokes et al., "RFQ Beam Dynamics", IEEE Trans. NS-26 (1979), 3469-71.

[4] R.W. Müller, "Layout of a High-Intensity Linac for Very Heavy Ions with RFQ Focusing", GSI report 79-7 (1979).

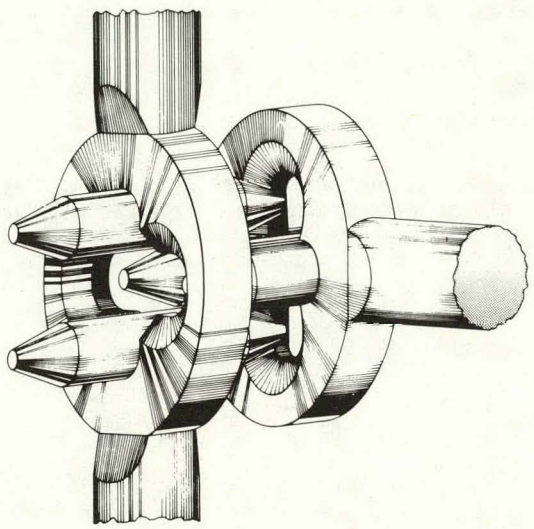


Fig. 1. Drift tube with quadrupole fingers.

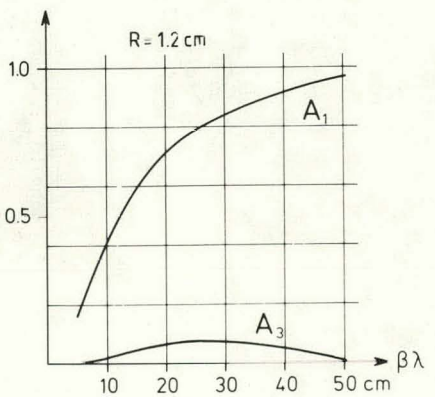


Fig. 2. Potential amplitudes vs $\beta\lambda$

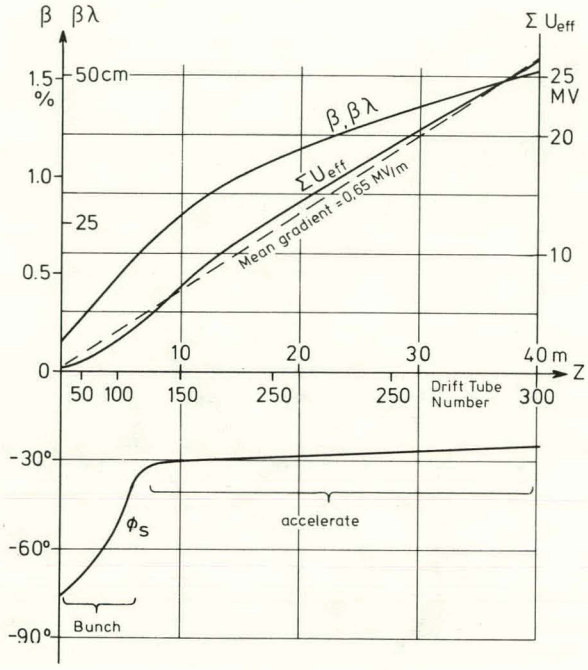


Fig. 3. Beta and phase profile of a 9-MHz layout. In the adiabatic bunching region β grows linearly with z.

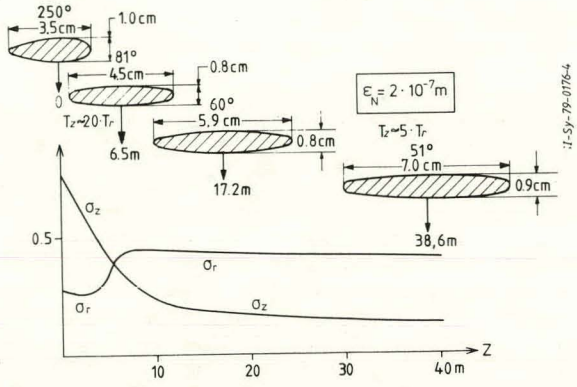


Fig. 4. Radial and longitudinal phase advances ("focusing frequencies"), and bunch shapes. T_r and T_z are the temperatures, T_z is decreasing because of adiabatic expansion.

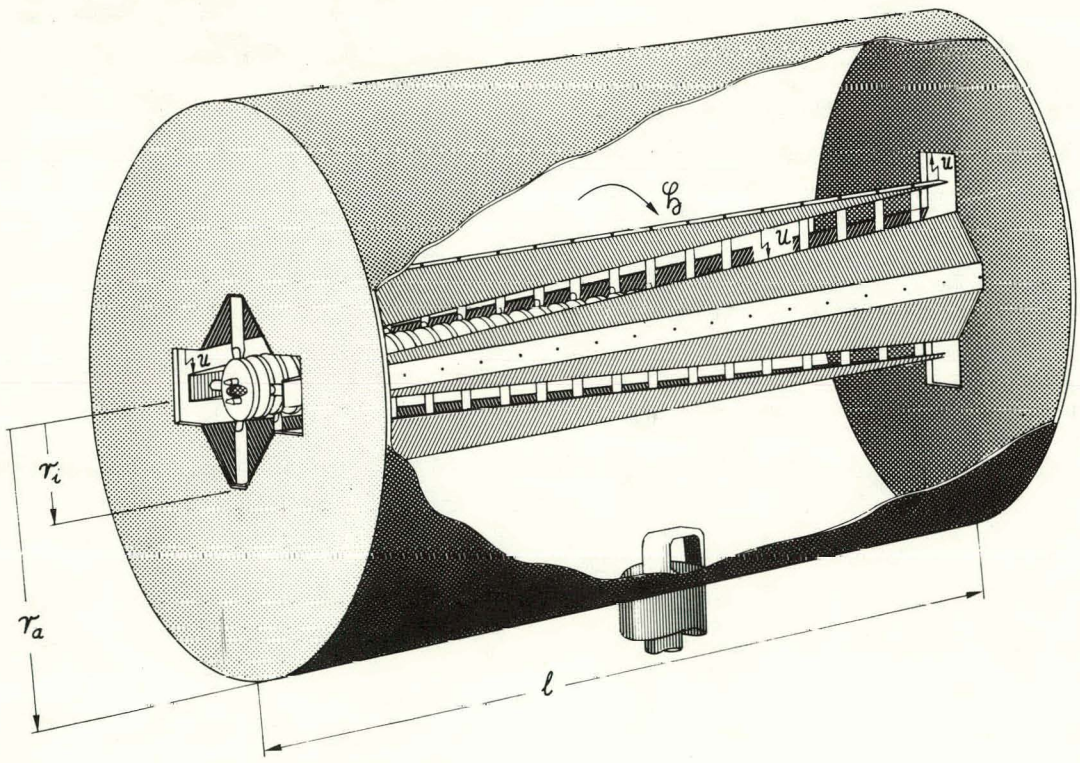


Fig. 5. Rf Cavity

Discussion

Meads, Brobeck: It looks like a very complicated structure to try to align. I wonder what you'd estimate would be the tolerances in lateral positioning of those pieces compared to the radius.

(Editor's Note: The following discussion appears to refer to Fig. 5.)

Müller: The structure is not difficult to align. Perhaps, if you could show the last slide again, I can show you how to align it. First, if you assemble one set of electrodes together with the current collectors, you will be able to align it. Now, the problem which you mentioned is how to align these parts together. Now, this one has a turning point on the other end. You can tilt it there and so you can get it well aligned.

Meads: I guess I was more concerned about the posts that are near the center, in the perpendicular plane; those extensions that come out of each piece - longitudinally, inside there.

Müller: You mean these? They are the entrance to the whole structure, which we use as a short matching region before it. But, in general, I think that adjusting this structure is no more critical than adjusting a drift tube linac.

Meads: I guess I misunderstood, I thought those pieces went all the way down through the structure, and that each of those sections had two of those.

Müller: There are two different types of shaping; that one you mentioned, and one looking more like four vanes near the axis. In both cases, since you can see each electrode, by looking through the structure, you will also be able to adjust it. I don't see any difficulties.

THE DESIGN OF A 12.5-MHZ WIDERÖE LINAC FOR ION BEAM FUSION

A. Moretti, J. M. Watson, R. J. Stockley, J. S. Moenich,
R. J. Lari, T. K. Khoe, J. A. Bywater, R. J. Burke, and S. Jorna**
Argonne National Laboratory*
Argonne, Illinois

Summary

Argonne National Laboratory (ANL) is currently developing a heavy ion beam driver for the inertial confinement fusion (ICF) program. The R&D program has as its goal to store a Xe^{+8} beam at 220 MeV by October, 1982. The preaccelerator is on station and near to meeting its design of 50 mA of Xe^{+1} at 1.5 MV. The first section of the low beta linac, which is to accelerate 20 mA of Xe^{+1} to 2.32 MeV, consists of four independently-phased short resonators. Two of the four short resonators have been tested beyond the rf linac power requirements without breakdown, or any major difficulties. The remaining two are currently being fabricated. The next section of the linac consists of three double-stub 12.5-MHz Wideröe linacs to accelerate the beam to 22.48 MeV. The first and third tank of the Wideröe array uses non-conventional FOFODODO quadrupole focusing, while the second tank uses FODO focusing. A pulsed quadrupole design has been selected for the Wideröe tanks because of the high power requirement of conventional DC quadrupoles. At 22.48 MeV, the beam is to be stripped to charge state +8, and accelerated in an array of 25 MHz triple-stub Wideröe linacs to 220 MeV, and then injected into a storage ring.

Introduction

Argonne National Laboratory is building a low beta linac and storage ring in conjunction with an on-going preaccelerator and ion source development program to demonstrate the adequacy of conventional accelerator technology as an ICF driver for a power plant. The initial phase of the program will accelerate 20 mA Xe^{+1} in an array of 12.5-MHz independently-phased linac resonators and Wideröe linacs to 22.48 MeV; strip to charge state +8, accelerate in a 25-MHz Wideröe an additional 7.7 MV to an energy of 84 MeV; inject and accumulate beam in a storage ring (using the Princeton-Penn accelerator magnets) housed in the ZGS tunnel. A later phase of this program will add: additional 25-MHz Wideröe linacs to make the final energy 220 MeV of Xe^{+8}; a storage ring and stacking ring. The extracted beam then will be transported, compressed, split into four beams and focused onto target foils. The program as planned allows upgrading of the facilities to reach a beam energy of 200-500 kJ which may be adequate to demonstrate a significant pellet burn.

Preaccelerator

The high voltage power supply is a modified Radiation Dynamics, Inc. (RDI) 4-MV Dynamitron[1] which had been obtained from Goddard Space Flight Center. It is a parallel-fed, capacitively-coupled multiplier, driven by a 110 kW oscillator at 105 kHz. Extensive modifications have been made to increase the current capability and allow pulsed operation.[2] As modified, the oscillator could ramp the terminal voltage from 0.5 MV to 1.5 MV in 7 ms with a peak stack current of 70 mA. At 1.5 MV, the voltage droop is less than 0.25% for 42 mA of associated beam current.

The low-emittance heavy-ion source for the preaccelerator was developed under contract by Hughes Research Laboratories.[3] It is a scaled-up version of their 2 mA single aperture source.[4] These utilize a Penning discharge for low plasma temperatures, and a Pierce geometry for minimal emittance dilution during acceleration. The source is capable of 100 mA Xe^{+1} at a current density of 15 mA/cm^2.

Conditioning of the accelerating column with beam had proceeded rapidly to 1.3 MV and 50 mA of Xe^{+1}. Before proceeding further with the conditioning to 1.5 MV, it was decided to examine the column. Damage of the ceramic and T-shaped rings along the outer shell was noted. The column and T-rings are being modified to reduce the electrical stress on the ceramic-metal interface and in the T-ring gaps.

12.5-MHz Wideröe Linacs

The first section of the linac is shown schematically in Fig. 1. It consists of the capacitively-loaded, single drift tube resonator, two "drum" loaded resonators with four gaps, and a π-3π double-stub Wideröe with 30 gaps. Not shown in the figure is the buncher, which is separated from the first accelerating resonator by a drift space of 4 m, containing a quadrupole triplet and beam diagnostics.

The capacitively-loaded resonator and the lumped-inductor resonator used as the buncher are described in Ref. 5. The capacitively-loaded resonator, which requires about 10 kW to reach its design value of 100 kV peak per gap, has been tested up to 25 kW without breakdown or multipactoring. Likewise, the lumped-inductor resonator, which requires 2 kW to reach its design value of 23 kV peak per gap, has been tested to 25 kW without breakdown or multipactoring. They both are installed in the beam line in preparation for acceleration measurements upon completion of the preaccelerator modifications. The "drum" resonators are currently being fabricated and should be on-line soon.

*Work supported by U. S. Department of Energy.
**Physical Dynamics, Inc; sub-contracted to ANL.

The π-3π double-stub Wideröe linac shown in Fig. 1 is followed by two more 12.5 MHz double-stub Wideröe linacs, shown schematically in Figs. 2 and 3. These in turn will be followed by a gas stripper to charge state +8, and 4 more triple-stub Wideröe linacs at 25 MHz, similar to the GSI[6] and Berkeley[7] designs, to reach 220 MeV.

The outside shell, stub lines, and inside structure of the Wideröe tanks in our design will be made of mild steel and electroplated with 0.254 mm copper, as was successfully accomplished by GSI. The drift tube, which does not contain quadrupoles ("short" drift tubes), are planned to be made of solid aluminum and electroplated with copper. It is not planned to provide direct cooling of the stems. This will greatly simplify the construction and cooling of the inner line. Since there is no outside penetration for cooling tubes, the inner line will be cooled by flooding the inside with water. At the same time, this will provide cooling of the inner stub lines. The alignment of the drift tubes containing quadrupoles("long" drift tubes) is to be accomplished with bellows. The original plan called for using a fixed shim. This approach was abandoned in favor of a simple holding and adjusting fixture. By using this adjusting fixture and bellows, there was no cost savings in using the fixed-shim approach. The "short" drift tubes are to be aligned by attaching the stems to the inner line by silver-plated C-rings. This will allow up to 0.76 mm of adjustment, while maintaining good electrical contacts to the inner line; another advantage of using the solid stem without cooling. It is planned to align the axes of the drift tubes to $\pm$ 0.1 mm.

The Wideröe tanks were designed using a Wideröe linac code developed at the Lawrence Berkeley Laboratory[8] in collaboration with GSI.[9] The program is interactive and iterative. By varying the position and length of the stubs, input/output energy, and line loading, a consistent solution is found for frequency, drift tube table, energy gain per cell and gap voltages. In order to minimize phase space dilution, the tanks were designed to achieve a constant energy gain of 1.0 MV/m throughout the whole linac.

Table I lists the design parameters of the three 12.5 MHz Wideröe linac tanks. Tank 1 takes the beam energy from 2.32 MeV to 8.84 MeV. It operates in a π-3π mode with FOFODODO focusing, and has 30 accelerating gaps with a bore of 4 cm. Tank 2 takes the energy from 8.84 MeV to 15.24 MeV, operates in the π-3π mode with FODO focusing and has 20 gaps with a bore of 4 cm. Tank 3 takes the beam from 15.24 MeV to 22.48 MeV, operates in π-π mode with FOFODODO focusing, and has 34 gaps with a bore of 4 cm.

Rf System

Each independently-phased cavity of the linac is to be driven by a 25 kW pulsed rf amplifier, which uses push-pull 4CX5000A tetrodes as the final stage. The amplifiers are being built to ANL specifications by the firm: Instruments for Industry, Inc. Two of five units ordered have been delivered thus far. The amplifier is coupled to the cavity by an adjustable loop. A standard 3-1/8" rigid 50 Ω coaxial cable gas-barrier is used to separate cavity vacuum from the air-dielectric feed line. The feed line is 1-5/8" air-dielectric Heliax® cable and is 1/2 wavelength long.

Each 12.5-MHz Wideröe linac tank will be driven by a 450-kW pulsed rf amplifier. It is planned to use feed-forward as well as fast feedback loops to control tank field amplitude to 1% and phase to 1 degree. A specification has been written for the amplifier and proposals are currently being evaluated. It is planned to couple the amplifier to the tank through an adjustable loop, and separate the feed line (5" Heliax®) from tank high vacuum by a standard 6-1/8" rigid 50 Ω line gas-barrier. The feed line will be one wavelength long.

Quadrupole Magnet Design

In addition to the quadrupole gradients shown in Table I, other parameters are as follows:

Radius of the bore	2.5 cm	
Effective length (range)	11 - 43 cm	
Field gradient uniformity	$\pm$ 1.0%	for $r \leq 2.0$
Field harmonic uniformity	$\pm$ 0.5%	

The large bore and high gradient eliminate the possibility of using rare earth cobalt permanent magnets. A conventional water-cooled conductor design was chosen because of the large ampere-turns required. The number of turns per pole was determined by matching the magnets to available pulsed power supplies.

A conformal transformation was made on a hyperbolic pole magnet with a two-layer coil. This resulted in a dipole magnet as shown in Fig. 4, with the dashed line as the pole tip. The computer program MIRT[10] was used to shim this magnet. One possible set of shims is also shown in Fig. 4. Transforming these shims back to the quadrupole results in the 1/8 magnet of Fig. 5.

The design philosophy is to use one pole contour for all laminated magnets. All magnets in a given tank are of the same length as the smallest one in that tank. The magnet ends will be chamfered to reduce the n = 6 duodecapole harmonic due to the ends. Many magnets will be pulsed in series from one power supply, using current shunts for each magnet to adjust the current. These shunts will have the same time-constant as the magnets.

Actual mechanical design of the magnets has recently started. Present plans call for stacking the cores in halves from stamped, deburred and oxide-insulated laminations. Individual laminations will be bonded together as core halves with "B" stage epoxy resin.

The coils will be insulated and wound on a separate fixture. Two coils will be assembled onto a core half, then two halves assembled using a steel ring to clamp them together. After testing the magnet electrically and checking it dimensionally, the entire unit will be vacuum impregnated to insure adequate electrical insulation and mechanical stability.

Simulation Studies

A detailed study of beam evolution and emittance growth was carried out for the first tank with a three-dimensional simulation code developed at Physical Dynamics, Inc.

The linac geometry was FOFODODO operating in a π-3π mode. Input parameters for the Xe^+ beam were: average beam current 25 mA, input energy 2.27 MeV, gap voltage gradient 5 MV/m, synchronous phase -32°, normalized transverse emittance $\beta_s\epsilon_T$ = 0.3 mm mrad, longitudinal emittance 10^{-4} cm. The quadrupole length was taken as $\beta_s\lambda$ and the gap length as 0.2 $\beta_s\lambda$. The stability limits set by magnetic, gap and electrostatic defocusing forces govern the optimum choice of the magnetic field gradient, g , and limit the phase spread. For the present parameters, g = 5.1 kG/cm and the phase spread is $\pm$ 18°. The bunch length is thus limited to 0.7 cm, which is well within the 'bucket' size.

The matched beam input parameters for a K-V distribution at the injection point midway between x- focusing magnets were x_o = 2.2 cm, x' = 2.4 x 10^{-3}, y_o = 0.78 cm, y_o' = 6.7 x 10^{-3}. The beam envelope radius for 100%, 80%, 70%, and 50% of the total particle number is shown in Fig. 5. A bore radius of 4 cm would thus be required to transmit the full 25 mA. For a lower current of about 20 mA the radius can be limited to 2 cm.

Emittance calculations indicate (Fig. 7) that most of the growth in the transverse emittance occurs in the first 10 $\beta_s\lambda$, with little increase thereafter, for at least 80% of the particles. The total growth after about 7 m is a factor of about 8 for the full beam, and a factor of about 5 for 80% of the beam. This growth results from the nonlinear coupling between longitudinal and transverse motion and the nonlinear space charge forces. Studies are underway to determine whether lowering the gap voltages, and hence reducing the defocusing forces, will provide a better match to the input emittance. Also, the sensitivity of emittance growth to the input distribution will be studied.

Table I

12.5-MHz Wideröe Linac Parameters

Parameter	Wideröe Tank #1	Wideröe Tank #2	Wideröe Tank #3
Mode	π-3π	π-3π	π-π
Focusing	FOFODODO	FODO	FOFODODO
Number of Gaps	30	20	34
Length (m)	6.49	6.63	7.09
Peak Voltage on First Gap (kV)	242.1	372.8	245.3
Peak Voltage on Last Gap (kV)	378.3	458.9	297.2
First Gap Width (cm)	3.33	6.47	4.91
Last Gap Width (cm)	6.42	8.44	5.93
First Cell Length (cm)	30.31	58.20	37.88
Last Cell Length (cm)	56.89	74.40	45.47
First Quadrupole Gradient (T/m)	48.03	29.88	56.38
Last Quadrupole Gradient (T/m)	21.16	23.36	44.26
Excitation Power on Beam Current (KW)	192	278	151
R.f Power with Beam Current (KW)	355	438	332
Shunt Impedance (MΩ/m)	43.81	28.74	61.92

References

1. M. R. Cleland and P. Farrel, "Dynamitrons of the Future," IEEE Trans. Nucl., Sci., Vol. NS-12, No. 3 p. 277 (June 1965).

2. J. M. Watson, et al., "A High Intensity 1.5 Mega Volt Heavy Ion Preaccelerator for Ion Beam Fusion," IEEE Trans. Nucl. Sci., Vol. NS-26, No. 3, Part 1, p. 3098 (June 1979).

3. R. P. Vahrenkamp and R. L. Seliger, "A 100-mA Low Emittance Ion Source for Ion Beam Fusion," IEEE Trans. Nucl. Sci., Vol. NS-26, No. 3, Part 1, p. 3101 (June 1979).

4. M. G. Mazarakis, et al., "Transport Experiments with Neutralized and Space Charge Dominated Deneutralized 2 mA 80 keV Xe^{+1} Beams," IEEE Trans. Nucl. Sci., Vol. NS-26, No. 3, Part 1, p. 3042 (June 1979).

5. A. Moretti, et al., "A 12.5-MHz Heavy Ion Linac for Ion Beam Fusion," IEEE Trans. Nucl. Sci. Vol. NS-26, No. 3, Part 1, p. 3045 (June 1979).

6. K. Kaspar, "Univac Prestripper Accelerator," Proc. of 1976 Proton Linear Acc. Conference, Chalk River, p. 73, 1976.

7. J. Staples, et al., "A Wideroe Preaccelerator for the Super Hilac," Proc. of 1976 Proton Linear Accelerator Conference, p. 81, 1976.

8. J. Staples, Private communication on Berkeley's Wideroe Program.

9. K. Kaspar, "Studies for Dimensioning a Heavy Ion Linear Accelerator of the Wideröe Type," GSI Report 73-10 and UCRL-Trans-1522 (1973).

10. "M1RT" was developed by K. Halbach, LBL, and R. Holsinger, NEN, and was kindly supplied by them.

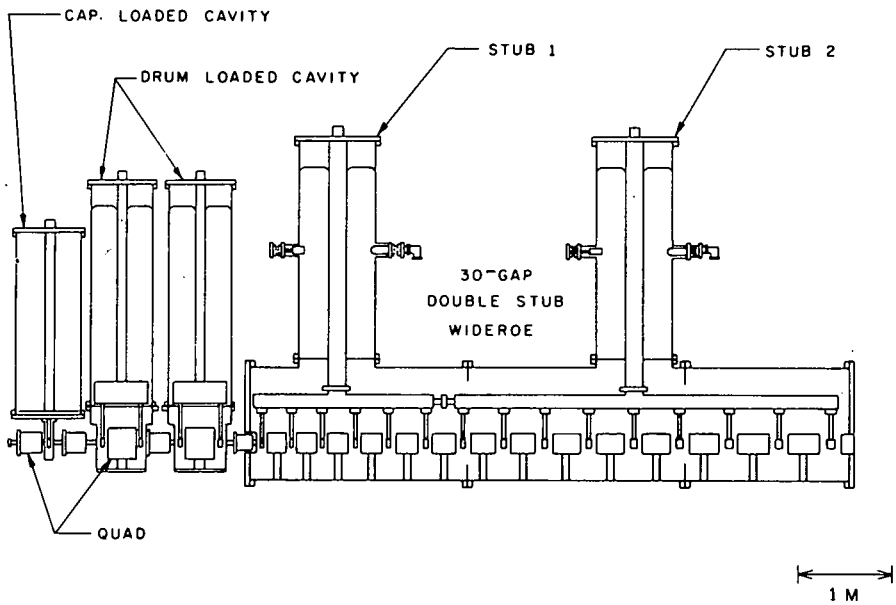


Figure 1. 30-Gap π-3π Double Stub Wideröe (Tank No. 1) and Independently-Phased Cavity Linac: 1.5 MeV to 8.84 MeV

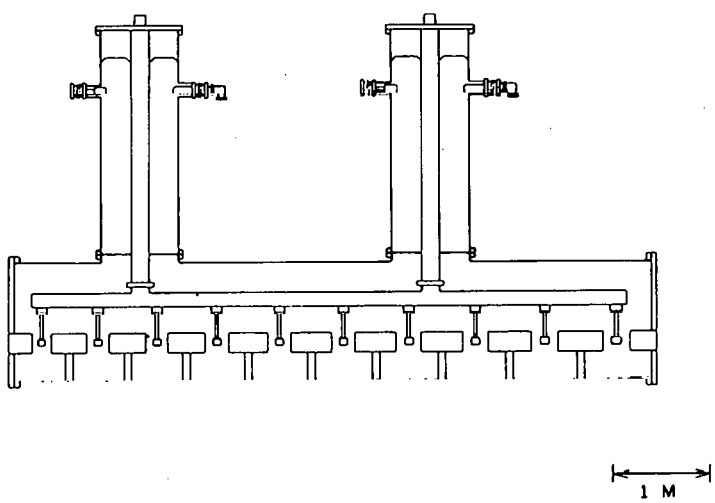


Figure 2. 20-Gap π-3π Double Stub Wideröe Linac (Tank No. 2): 8.84 MeV to 15.24 MeV

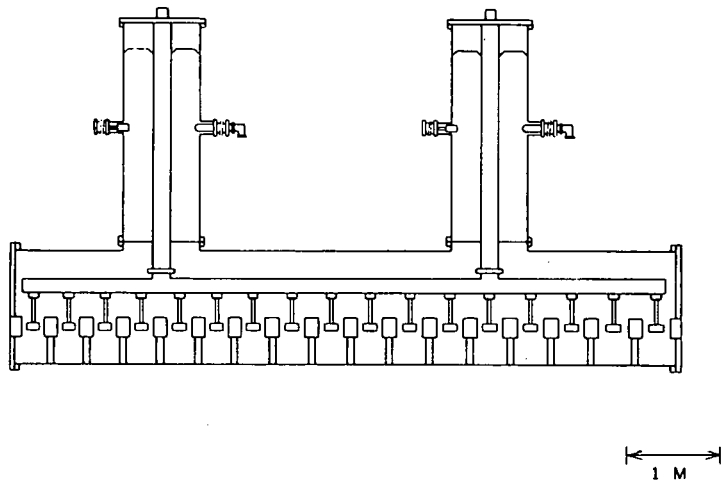


Figure 3. 34-Gap π-π Double Stub Wideröe Linac (Tank No. 3): 15.24 MeV to 22.48 MeV

Figure 4. Transformed Quadrupole Magnet

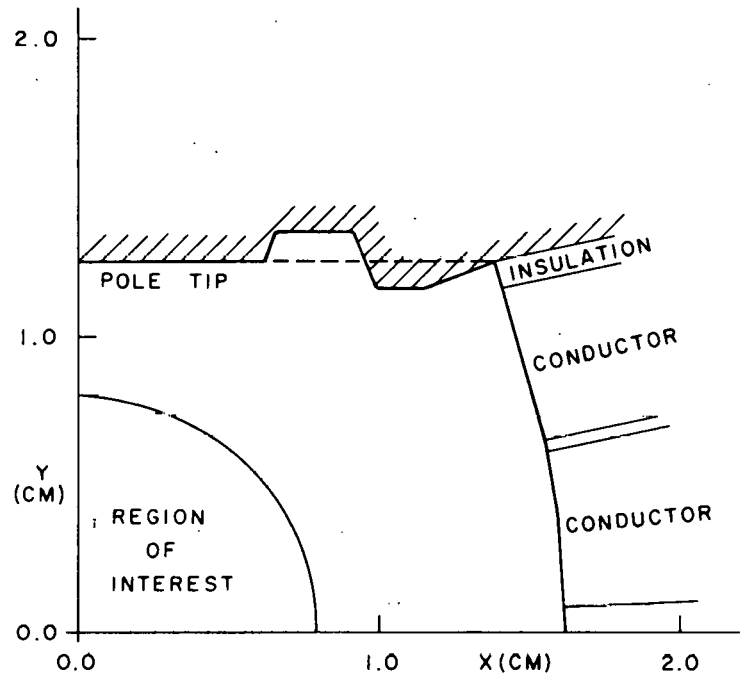
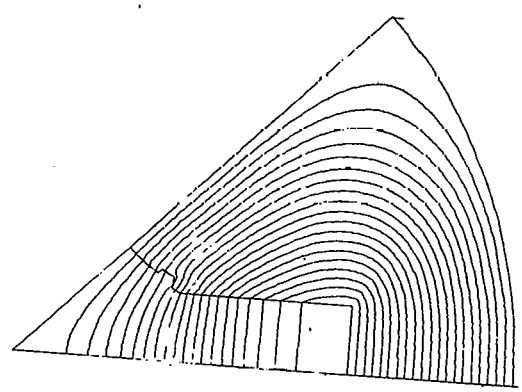


Figure 5. 1/8 Shimmed Quadrupole Magnet



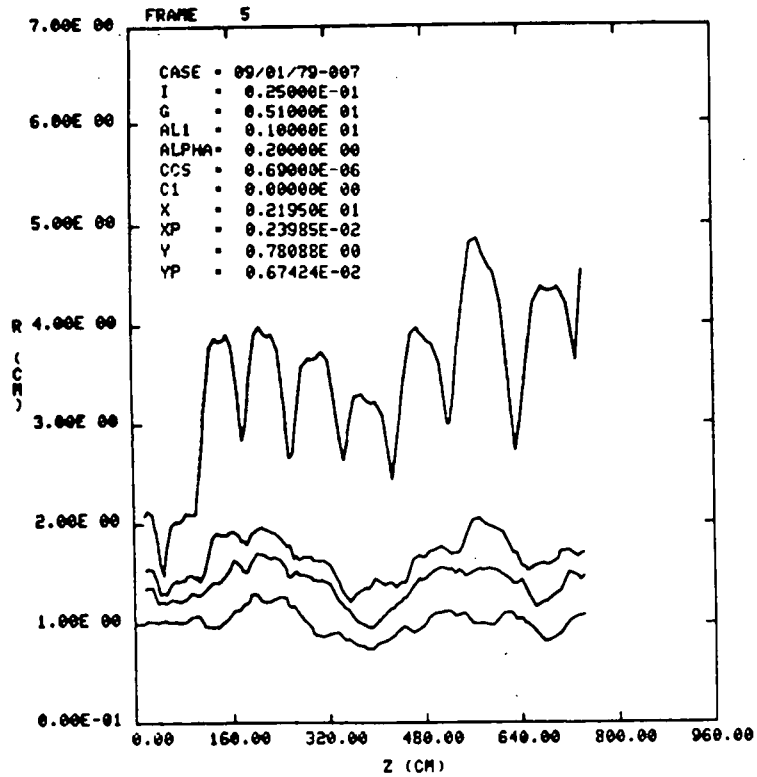


Figure 6. Beam Radial Envelope

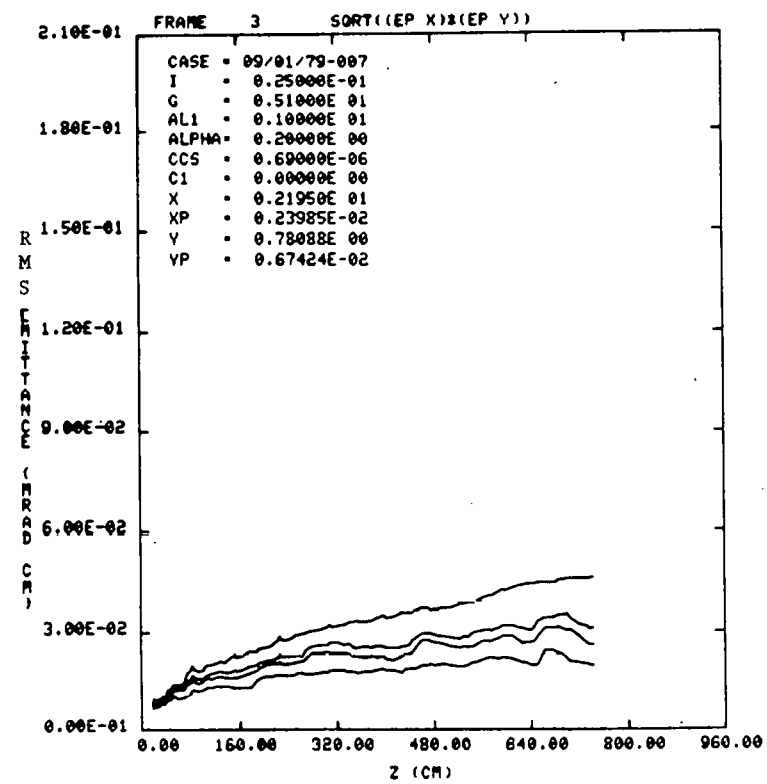


Figure 7. Transverse Emittance

Discussion

Mobley, BNL: With a 100 mA X_e^{+1} source, what did you start off with for the bore size? How many mA per square-centimeter?

Moretti: I think the diameter is about 3 cm and 15 mA/sq. cm.

Mobley: And at the first tank after one stage of rf acceleration are you getting 25 mA?

Moretti: Well, the space charge limit is 20 mA. We have not run the experiment yet.

Mobley: I see. What current are you shooting for at 22 MeV?

Moretti: 20 milliamps.

Mobley: On your quadrupoles in the rf system, what are the pole tip fields that you need?

Moretti: The gradients are 46 Tesla/m, or about 12 KG at the pole tip. That is the highest, then it goes somewhat lower, as beta increases.

Penner, NBS: Is the emittance growth at the beginning a non-linear space charge effect? If so, how was it calculated?

Moretti: Well,it is a non-linear effort due to the space charge. It was a numerical space charge simulation.

Penner: How many particles did he use? In a matched beam, the emittance should not start to grow immediately, if you carry enough particles to get the proper simulation.

Moretti: Well, I think S. Jorna has found that 160 is sort of the minimum required to get a fairly accurate distribution. He has gone to a thousand and noticed only 10-25% changes. The majority of calculations have been in the area of 160-200 particles.

Penner: I might make a comment for people who are trying to predict nonlinear space charge effects with particle simulations. We have two rather thorough independent studies by I. Haber and by A. Galejs and myself. You really don't see the effect you are looking for until you get to over one-thousand beamlets in a two-dimensional case. The problem is that when you simulate a beam with a small number of beamlets, matching isn't well defined. As a result, the entire beam is not matched and you get growth associated with that mismatch. You really must match the beam into the system properly,which requires a large number of particles and then you find that the moments of the beam will begin to grow at first, but the (rms) emittance will not start to grow for awhile. I think this is very well verified by the results, which in my case, went to 2,000 particles; in Haber's case to 16,000.

Moretti: Well, this is a three-dimensional code. Jorna has studied 1,000 particles and says it reflects accurately the beam dynamics to within 25%.

A HEAVY ION POST-ACCELERATOR WITH COUPLED SPIRAL AND SPLIT-RING RESONATORS*

A. Schempp, H. Klein, W. Rohrbach, W. Caspar, G. Lotterbach, E. Müller
Institut für Angewandte Physik, Universität Frankfurt/Main
D-6000 Frankfurt/Main, Germany

Summary

At the single-ended 7-MV Van de Graff machine in Frankfurt, a small post-accelerator is being built, which will be partly used as a test facility for new linac structures. Therefore different types of resonators will be installed, starting with coupled spiral and split-ring resonators. Properties of these resonators and the status of the project are discussed.

Introduction

Significant upgrading of static accelerators can be obtained only by post-acceleration. For this purpose independently-phased short rf cavities are well suited. Normal conducting spiral and split-ring resonators combine high-shunt impedance with flexibility over a wide range of particle energies. Modular design and ease of fabrication are other important arguments for these structures to be used in relatively small post-accelerator projects. Our work concentrated on theoretical and experimental optimization of spiral and split-ring resonators for high field levels at good mechanical and electrical stability.

This post-accelerator project was funded in late 1978 with a budget of 0.4 MDM. Two accelerator sections and a buncher-chopper system will be installed at the 7-MV Van de Graaff generator at the Institut für Kernphysik in Frankfurt.[1,2] The improvement of the Van de Graaff generator, including the development of a new Penning ion source, cooling and power supply is being done by the Institut für Kernphysik.

Layout of the Post-Accelerator

A schematic representation of the accelerator is shown in Fig. 1. The beam transport and the accelerator system have been designed to fit into the existing experimental area. The beam from the Van de Graaff passes a foil stripper, is then bent horizontally, and after bunching, chopping, and accelerating is bent back to the ground floor, where a new experimental area will be installed. Beam matching and radial focusing is obtained by two triplets and a quadrupole doublet. The design of the machine is to reach a voltage gain of 1 MV per accelerator section, which leads to the ion energies summarized in Table 1. Ions between N and Ar will be accelerated to energies between 1 and 2 MeV/N at an estimated particle current between 5 and 20 nA. A future plan is to place the stripper at 4.1 MV in the accelerator tube,[1] which will give another increase in particle energy, but presents problems with respect to service and damage of the accelerator tube.

The limiting factor in a post-accelerator project like this is the cost of the transmitters. An existing rf transmitter was rebuilt which yields up to 100-kW in pulsed as well as in cw operation. A second transmitter with 80-kW pulsed power is of the same type as used in the Heidelberg post-accelerator project and will be delivered in November.

The buncher amplifier, the transistorized preamplifiers, and the regulation and control system are developed and built by ourselves. The control system consists of three parts: a slow resonance frequency control tuning capacity, a fast amplitude control, which keeps the amplitude constant within 0.5%, and a fast phase control, which gives a phase ripple of less than 1°. First tests have shown that the design values can be obtained. In this stage of the project, no computer control

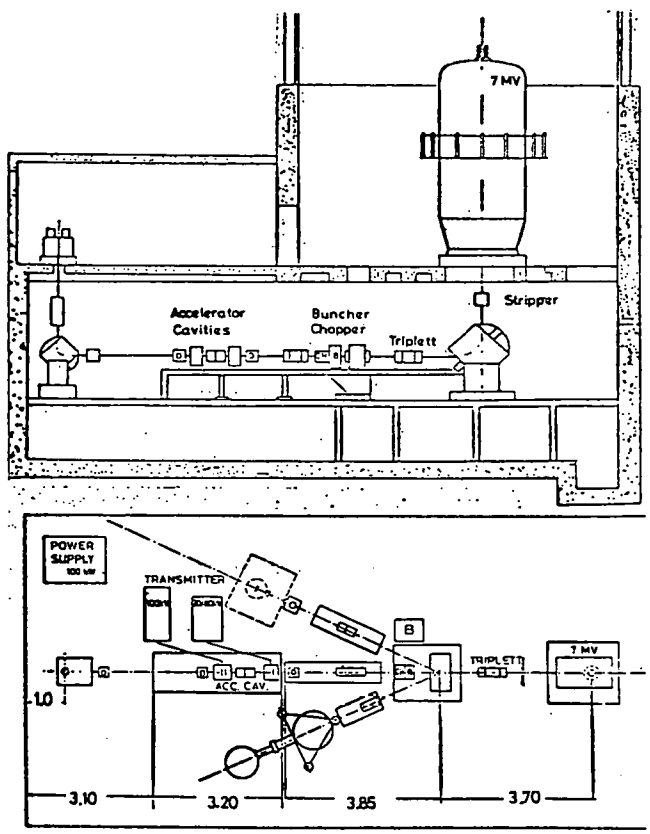


Fig. 1 Layout of the accelerator system

* Work supported by BMFT and DFG.

is planned because the system is rather simple. Later, microcomputers may support manual operation.

Projectile	z_A	z	E_0 CN-output (MeV)	E_0 CN-output (MeV/N)	E_1 (MeV/N)	E_2 (MeV/N)	E_2 (MeV)
$^{14}_{7}N$	2	6	14	1.0	1.43	1.86	26.0
$^{20}_{10}Ne$	3	8	21	1.05	1.45	1.85	37.0
$^{27}_{13}Al$	3	8	21	0.78	1.1	1.4	37.8
$^{32}_{16}S$	3	9	21	0.66	0.90	1.15	36.8
$^{40}_{18}Ar$	4	10	28	0.7	1.06	1.42	56.8

$5\ nA \leq I_{outp.} \leq 20\ nA$

Table 1 Ion energies of the accelerator system

Accelerator Structures

The post-accelerator will partly be used as a test facility for the development of new accelerator structures. So even at the first stage two different structures will be used. The spiral structure, which will be discussed first, is well developed and tested.[3-9]

For this project a further development using electromagnetically-coupled spirals was tried, to increase the efficiency. Thus, the rather high design value of 1-MV resonator was obtained with our transmitters (80 - 100 kW, 25% dc).

The spiral resonator is a two-gap structure with the spiral conductor excited to quarter wavelength oscillations (Fig. 2):

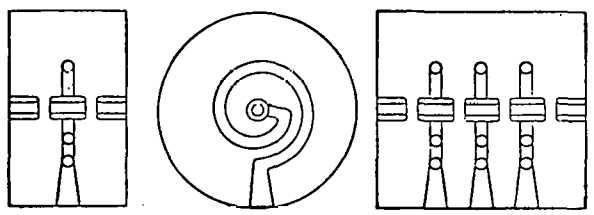


Fig. 2 Schematic drawing of the spiral resonator

Optimization shows that the efficiency, which is characterized by the shunt impedance η,

$$\eta = \frac{E_{acc}^2}{N/L} = \frac{\Delta U^2}{N \cdot L}$$

$$\Delta U = \int_0^L E(z)\cos(\omega t - \phi)\,dz$$

(ΔU voltage gain, E_{acc} average accelerating field, L cavity length, N rf power.)

decreases with increasing spiral tube diameter, caused by increased capacitive load. On the other hand, for good mechanical stability, a large tube diameter would be best. It becomes obvious that maximum efficiency and maximum stability exclude each other. With the single spiral prototypes, effective accelerating fields up to 6 MV/m and voltage gains up to 1.3 MV per resonator, have been achieved for pulse power of 200-kW, with excellent stability. An even smaller value of $\Delta f_{stat} = 0.05$ Hz/kW was obtained with a single spiral buncher cavity, which was built for the Unilac. A single spiral resonator with a tube diameter of 15 mm and an η of 42 MΩ/m, will be used as the buncher cavity. A significant increase in efficiency is obtained by combining several electro-magnetically-coupled spirals in one cavity, as shown in Fig. 2. For the case in which the properties of the individual spiral remain unchanged and the rf power per cavity is constant, the voltage gain ΔU of such a resonator increases with the square root of the number of spirals

$$\Delta U_n = \sqrt{n} \cdot E_{acc} \cdot L$$

The R_p value, defined as η times length L of the cavity,

$$R_p = \eta \cdot L = \frac{\Delta U^2}{N} = n \cdot \frac{\Delta U_0^2}{N}$$

is proportional to n, the number of spirals. This increase in efficiency; however, leads to some reduction of flexibility with increasing number of spirals per cavity. This is demonstrated in Fig. 3, which shows transit time curves for cavities with different numbers of spirals. Resonators with 3 electro-magnetically-coupled spirals were chosen as a good compromise. Resonators with coupled spirals have several modes of oscillation. The so-called π-mode, where adjacent spiral drift tubes have opposite polarity, has in all realistic cases the highest shunt impedance and the lowest resonance frequency. The frequency, the parameters of the spirals, and the distribution of the fields in the resonator depend strongly on the coupling mode and strength. A lot of work has been done to ensure equal distribution of rf power to the different spirals. This flatness is necessary to minimize static frequency shift in order to get high stability of the resonator.

At design field levels, forces cannot be neglected, and any structure may be stimulated to mechanical vibrations.[6] Forces of up to 2 kp tend to detune the spiral conductors. Mechanical displacement of the drift tube up to several mm, corresponding to a frequency shift of $\Delta\nu \approx 1$ MHz, have been observed. This has been measured with cavities specially designed to study these ponderomotive effects. High power measurements of such resonators with coupled spirals, indicated that all the axial fields should also have the same value to compensate the axial forces. This is done by using approximately a half gap-length

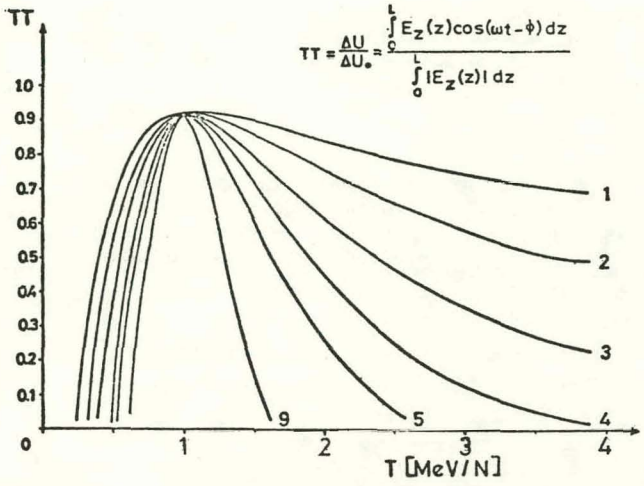


Fig. 3 Transit time factor TT as function of particle energy T.
Parameter: number of spirals per cavity

between spirals and end plates, a "flat" field distribution. Equal distribution of rf power to the individual spirals can be reached by choosing the resonance frequency of the "end spirals" lower than for the central one. The ratio of resonance frequencies depends on coupling strength between the spirals, which is usually very high. The coupling can be described in terms of the frequency separation of π-mode and 0-mode, which can be as high as 65 MHz with a π-mode of 108.5 MHz. Such strong coupling is obtained by arranging the spirals to alternate the winding direction, thus adding capacitive and inductive coupling. The frequency-tuning of the individual spirals is done by varying the length of the spiral tube, which in some cases differs up to 30%. Additionally, the coupling of the spirals leads to a further field concentration near the axis, and gives a better shunt impedance. η values of 47 MΩ/m were measured, compared with only 25 MΩ/m for single spirals with the same parameters.

The first cavity of the post-accelerator is a three spiral resonator optimized for a particle energy of 1 MeV/N (Table 2).

Tank length 32 cm,
Tank diameter 35 cm,
Spiral tube diameter 20 mm,
Drift tube diameter 40 mm,
Drift tube length 50 mm,
Aperture diameter 20 mm,
Gap length 20 mm, end plate gap 9 mm,
Resonance frequency 108.5 MHz, Q = 4200,
η_o = 55 MΩ/m, η_{eff} = 45.5 MΩ/m, $R_{p_{eff}}$ = 14.6 MΩ,
T_o = 1 MeV/N, ΔU (100 kW) = 1.2 MV,
E_{acc} (100 kW) = 3.8 MV/m

Table 2 Parameters of the 3-spiral resonator

The individual spirals have been milled out of copper plates and brazed together as indicated in Figure 4. Additionally, the spirals and the

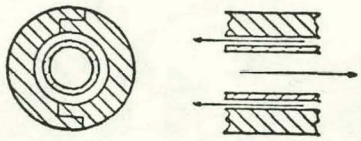


Fig. 4 Cross-section of the spiral tubing

water-cooled drift tubes had been copper-plated and placed in a copper-plated stainless steel tank (L = 32 cm, diameter 35 cm). The parameters of the spirals and the coupling strength can be calculated approximately. The final tuning is done by iteratively mapping the field and changing the resonance frequencies of the individual spirals. Figure 5 shows the final axial accelerating field of the first post-accelerator cavity, which has a shunt impedance of 45 MΩ/m.

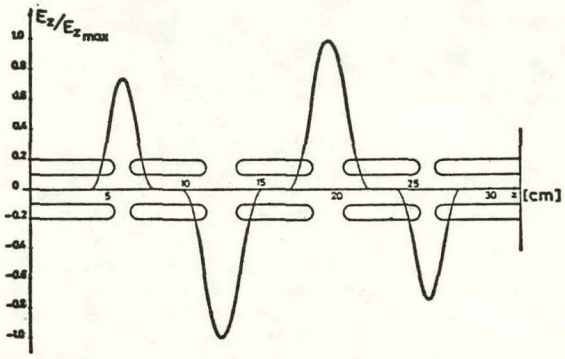


Fig. 5 Axial field distribution of the 3-spiral resonator

In Figure 6, the transit time factor is plotted versus the particle energy. Figure 7 shows a view of this first post-accelerator cavity. In high power tests with this spiral resonator, a voltage gain of ΔU = 1.2 MV was obtained for an rf power of 100 kW in pulsed operation. This corresponds to an accelerating field of 3.8 MV/m.

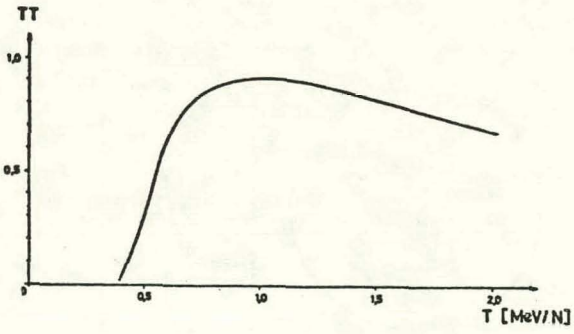


Fig. 6 Transit time factor TT as function of the particle energy T for the spiral resonator

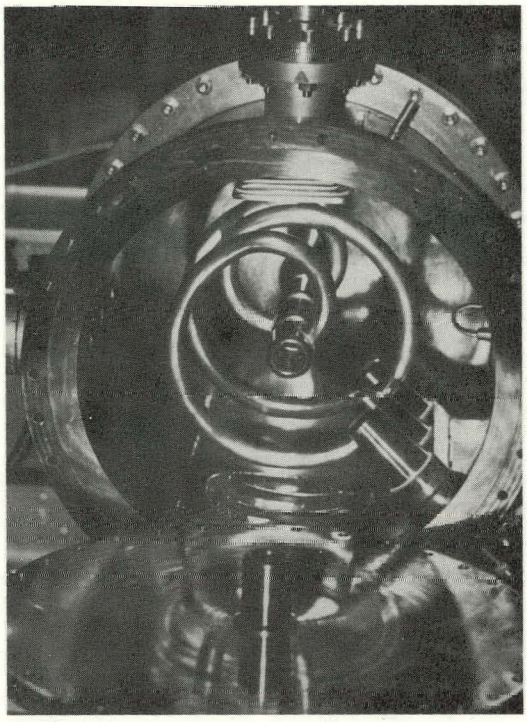


Fig. 7 View of the 3-spiral resonator

The second structure to be used in the project is the split ring. The split-ring resonator was first proposed at CIT and is used as a superconducting post-accelerator structure in the Argonne and Stony Brook tandem boosters.[10-12] We have done work on normal conducting split-ring versions since 1976. The optimization of split-ring resonators with respect to a high shunt impedance and good mechanical stability, leads to similar results for the geometrical shape as in the superconducting case.

Figure 8 shows a schematic drawing of this structure. It consists of two coupled $\lambda/4$ resonators shaped like two "semi-rings" and ending in drift tubes, which oscillate with 180° phase difference. This arrangement may be compared with two coupled spirals with rather large pitch, mounted on a common "leg". For high efficiency, in this case, a slightly larger tank is needed to reduce the capacitive load compared with separate spiral resonators. Values for the shunt impedance

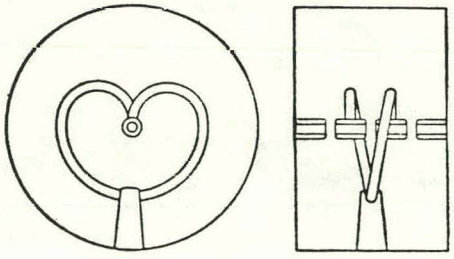


Fig. 8 Schematic drawing of the split-ring resonator

η up to 60 MΩ/m and voltage gains of 1 MV/resonator[13] have been achieved with prototype units. The detuning due to radiation pressure, which is represented by the static frequency shift, is comparable to that of a spiral resonator, ranging from 0.2 to 5 kHz/kW.

Table 3 shows the parameters of the split-ring resonators, and in the last row, the parameters of the second post-accelerator split-ring cavity, which is optimized for a particle energy of 1.3 MeV/N.

TANK LENGTH [mm]	TANK DIAM. [mm]	SPLITRING TUBE DIAM. [mm]	DRIFT TUBE DIAM. [mm]	GAP WIDTH [mm]	Q_0	η_{EFF} [MΩ/m]	$R_{P_{EFF}}$ [MΩ]	RF POWER [kW]	ΔU_{EFF} [MV]	$E_{Z_{EFF}}$ [MV/m]
181	350	18	4	15	4300	38.6	7.0	70	0.7	3.9
208	350	18	6	20	4120	29.1	7.0	100	0.84	4.0
240	350	18	4	28	5300	34.8	7.2	125	0.96	3.9
290	500	22	4	20	5400	59.6	17.3	(80)	(1.18)	(4.1)

Table 3 Parameters of split-ring resonators

The axial field distribution and the transit time factor TT are plotted in Figures 9 and 10.

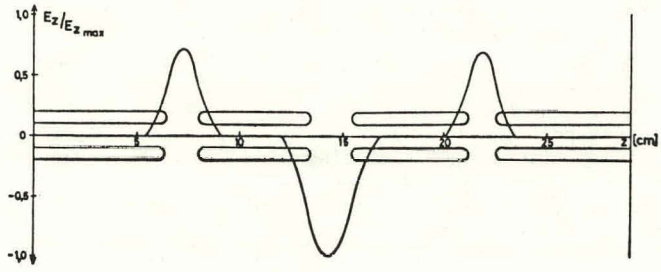


Fig. 9 Axial field distribution of the split-ring resonator

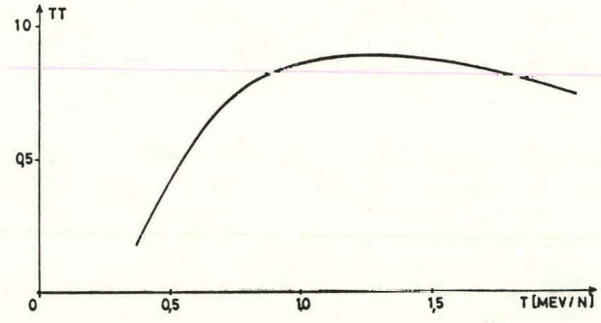


Fig. 10 Transit time factor TT as function of particle energy for the split-ring resonator

Figure 11 shows a view of this normal conducting split-ring resonator, which will undergo

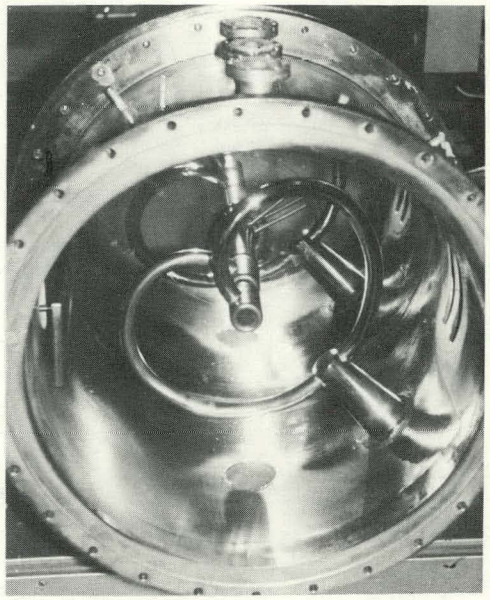


Fig. 11 View of the split-ring resonator

rf tests at the end of September.

Beam Dynamics

The post-accelerator will have a normalized acceptance of 3π cm-mrad. The calculations have been done with a code including non-linear coupling between radial and axial phase space. The emittance of the Van de Graaff will be matched with two triplets to give a circular beam envelope at the entrance of the post-accelerator, with gradients between 0.5 and 1.5 kG/cm, and 2 cm aperture diameter. Energy resolution of the heavy ion beam will be between 10^{-3} and 10^{-2}. Pulse lengths of 0.4 nsec can easily be produced depending upon tuning of the buncher-chopper system. Thus the beam emittance will be increased by a factor of about 4, which is reducable with help of a debuncher-rebuncher system.

Status

The first accelerator cavity, the 3 coupled-spirals module, together with the 100-kW transmitter, the control system, the cooling and the power supply are completed and have been tested. High power tests of the split-ring resonator will start in September. In October the sections, the first transmitter, and the buncher-chopper system will be installed at the Van de Graaff generator, and first beam tests can be done. After delivery of the second rf transmitter in November, the post-accelerator will be completed, so that an improved heavy ion beam will be available at the beginning of next year.

Future plans include the insertion of new accelerator structures, such as rf quadrupole cavities, and modified IH resonators using the post-accelerator as beam test facility.

Acknowledgements

The authors would like to express their gratitude to K. Meinel (Institut für Kernphysik), H. Stöcker, W. Blum, and K. Küllenberg (Institut für Angewandte Physik).

References

1 K. Bethge, H. Baumann, K. Meinel, H. Klein, P. Junior, A. Schempp, H. Deitinghoff, Proc. 4th Conf. Appl. Small Acc., Denton 1976.

2 A. Schempp, Int. Rep. 78-11, 1978.

3 G.J. Dick, K.W. Shephard, Appl. Phys. Lett. 24 (1974) 40.

4 D.D. Armstrong et al., LA-UR 74-211 and Part. Acc. 6 (1975) 175.

5 A. Schempp, H. Klein, Nucl. Instr. Meth. 135 (1976) 409.

6 A. Schempp, W. Rohrbach, H. Klein, Nucl. Instr. Meth. 140 (1977) 1.

7 A. Schempp, H. Klein, Proc. 1976 Proton Linear Acc. Conf., Chalk River 1976, AECL-5677 (1977) 67.

8 E. Jaeschke, H. Ingwersen, R. Repnow, Th. Walcher, B. Huck, B. Kolb, Nucl. Instr. Meth. 157 (1978) 195.

9 E. Jaeschke, H. Ingwersen, R. Repnow, Th. Walcher, B. Huck, B. Kolb, IEEE Trans. NS-26 (1979) 3667, Proc. 1979 Part. Acc. Conf., San Francisco 1979.

10 K.W. Shephard, J.E. Mercereau, G.J. Dick, IEEE Trans. Nucl. Sci. NS-22 (1975) 1979.

11 K.W. Shephard, IEEE Trans. Nucl. Sci. NS-26 (1979) 3659, Proc. 1979 Part. Acc. Conf., San Francisco 1979.

12 J.R. Delayen, G.J. Dick, J.E. Mercereau, J.W. Noe, P. Paul, G.D. Sprouse, IEEE Trans. Nucl. Sci. NS-26 (1979) 3664, Proc. 1979 Part. Acc. Conf., San Francisco 1979.

13 E. Muller, G. Lotterbach, A. Schempp, Int. Rep. 78-5, 1978.

HIGH-BETA LINAC STRUCTURES*

S. O. Schriber
Accelerator Technology Division
Los Alamos Scientific Laboratory
Los Alamos, New Mexico
USA 87545

Summary

Accelerating structures for high-beta linacs which have been, and are in use, are reviewed in terms of their performance. Particular emphasis is given to room-temperature structures, and the disk-and-washer structure. The disk-and-washer structure has many attractive features that are discussed for pulsed high-gradient linacs, for 100% duty-cycle medium-gradient linacs, and for high-current linacs that require maximal amounts of stored energy in the electric fields be available to the beam.

Introduction

The following discussion is limited to rf structures for linear accelerators that accelerate particles with betas near unity. Particular emphasis is given to room-temperature structures, not because they are superior or inferior to superconducting structures, but because a large number of institutions are involved in operating, designing and/or building structures of this type. The reader is referred to recent literature[1-5] regarding improvements and status of superconducting structures. An excellent review of the induction accelerator, not discussed here, can be found in Ref. 6.

Much development and improvement to rf accelerating structures has taken place since their introduction in the 1930's. Progress has been associated with technological advances in materials and fabrication methods; e.g., superconducting structures; and with innovative ideas and advances in rf expertise; e.g., the Stanford Linear Accelerator Center (SLAC) Energy Doubler (SLED) program;[7] standing-wave structures operating in the $\pi/2$ mode,[8] and storage cavities[9] for the Large Electron-Positron (LEP) storage ring. The incentives for these advancements were improved efficiency of converting rf power into useful beam power, improved reliability, simplified fabrication and assembly, improved overall structure performance and above all to save costs and meet the needs of experimentalists.

Topics covered in this report do not represent the full range of research and development in high-beta accelerating structures. The author apologizes to those whose work has not been referenced. Typical examples of some of the structures being used are given. Traveling-wave (TW) and standing-wave (SW) structures are compared, followed by a review of the latest structures for storage rings. Superconducting structures are referred to briefly. Most of the material in this report pertains to the disk-and-washer structure first introduced by Andreev et al.[10]

Review of Operating High-Beta Structures

Pulsed electron linacs are employed all over the world in medicine, industry and research. A description and comparison of the different facilities was made recently by Loew.[11] Output energies from 4 to 30 MeV with 0.1% duty factor are available from linacs packaged into machines that are used for radiotherapy treatment of cancer. Research linacs vary from very high-energy machines, such as the one at SLAC,[12] to high duty-cycle machines, such as the one at the Massachusetts Institute of Technology.[13] Industrial linacs generally are similar to medical linacs except for high-current short-pulse machines, such as the EG&G/DOE electron linac.[14] Most research linacs employ TW structures, whereas a large fraction of the industrial and medical linacs employ SW structures.

TW Structures

Disk-loaded waveguides are used for the majority of pulsed electron linacs in operation. The accelerating sections are either constant-gradient or constant-impedance structures, with an rf load at the end to absorb unused rf power. Design information, choices and operating performance can be found in Refs. 12 and 15. Improvements to the width of the output energy spectrum have been made on several linacs by employing energy compression systems. In a short-pulse, high-current linac, 300-A peak current in the micropulse has been accelerated.[16] Recently Loew et al.[17] have shown how properties of TW structures can be calculated using the computer program SUPERFISH.[18]

Improvements to TW sections and the consideration of TW sections in future machine studies continue. The design of a pion radiotherapy linac using TW structures based on SLAC sections or redesigned SLAC sections was described by Loew et al.[19] An innovative addition[7] to the SLAC accelerating structures, shown in Fig. 1, was associated with a desire to increase the output energy in an economical

*Visitor from Chalk River Nuclear Laboratories, Chalk River, Ontario, Canada K0J1J0

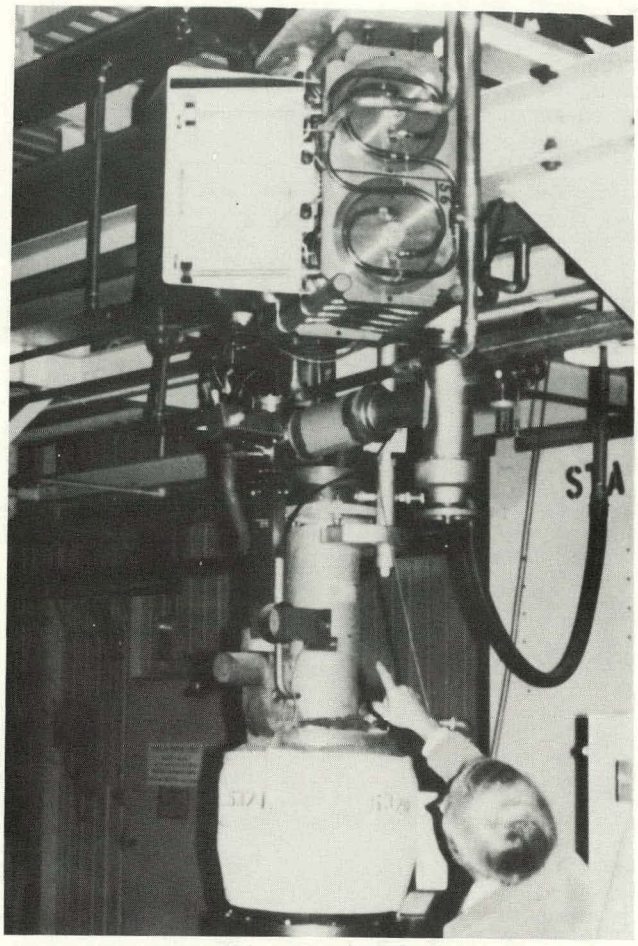


Fig. 1. View of second SLED prototype installation in klystron gallery.

manner. Peak rf fields are increased at the expense of rf pulse-length, by using resonant cavities that store rf energy during the first part of the pulse. This energy is discharged quickly to the structure at the end of the pulse.

SW Structures

Considerable development work on rf structures in the 1960s led to the optimization[20] of an SW cavity geometry. At the same time, advantages associated with operating an SW structure in the $\pi/2$ mode were explained.[8] Optimization of the geometry led to improved rf efficiency, and $\pi/2$ mode-operation led to inherently more stable structures, that could be fabricated with reduced tolerances. The degree of structure stabilization is related directly to the intercavity coupling constant; hence, the desire to increase this coupling constant, and the resultant disk-and-washer structure.[10] Recently[21] it has been shown that the disk-and-washer geometry not only has a high coupling

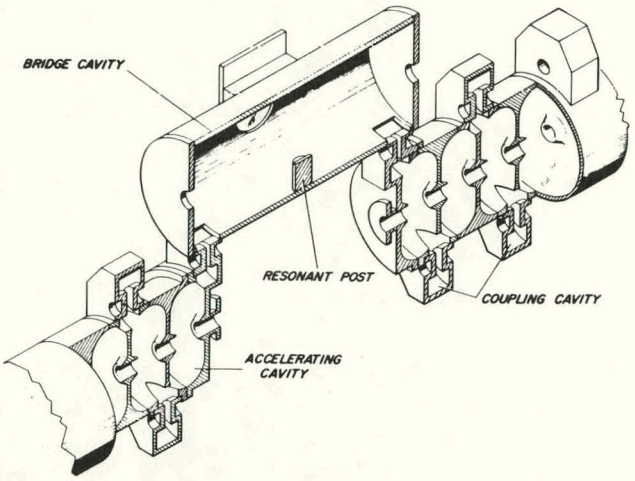


Fig. 2. Isometric view of side-coupled structure used on LAMPF.

constant, but also has a higher rf efficiency than the shaped cavities developed for the Clinton P. Anderson Meson Physics Facility (LAMPF).[22]

The LAMPF accelerator is the only pulsed proton linac operating with particle betas in excess of 0.6. A cross-sectional view of a typical side-coupled structure adapted for the higher energy portion of LAMPF is shown in Fig. 2. Similar structures are being used in medical and industrial linacs throughout the world. Work on a USSR meson facility[23] continues with studies of the disk-and-washer structure for the high-energy portion of the proton linac. Electric fields of 4 MV/m were reported[23] to have been attained at 991 MHz.

Knapp and Swenson[24] described design parameters for a pion radiotherapy machine, based on accelerating protons with an SW linac. Stovall[25] presented a recent project review covering injector status and revised parameters.

A cw, or 100% duty cycle, 4-MeV electron linac has been in operation at Chalk River Nuclear Laboratories (CRNL) since 1972. The two-section 805-MHz linac operates routinely with an average on-axis accelerating gradient of 0.9 MeV/m, the limit being imposed by available rf power. Recent progress, reported in Refs. 26 and 27, included design details for an on-axis coupled structure that will be added to the linac. An industrial proposal, based on this work, for radiation processing of bulk waste was reported by Fraser.[28] The on-axis coupled structure discussed in Refs. 27 and 28 will be used for the Mainz cw-microtron.[29]

Vaguine[30] has described a novel way of interlacing a side-coupled structure and reported accelerating gradients of 40 MeV/m for a 3-GHz, 10-cm structure. Similar accelerating gradients should be attainable with the disk-and-washer structure, but with a higher rf efficiency.

TABLE I

COMPARISON OF LAMPF SHAPED CAVITY, DISK-AND-WASHER CAVITY AND A SCALED SLAC CAVITY (β = 1.0, 1350 MHz) NORMALIZED TO 1-MV/m AVERAGE ON-AXIAL ELECTRIC FIELD

	LAMPF Shaped Cavity	Disk-and-Washer Cavity	SLAC Cavity
Operating mode	$\pi/2$	$\pi/2$	$2\pi/3$
Quality factor, Q	25,754	63,671	20,124
Z (MΩ/m)	106.7	137.1	38.8
Z_{eff} (MΩ/m)	69.3	90.6	26.4
Transit time factor, T	0.806	0.813	-
Stored energy in $\beta\lambda/2$ structure length (joules)	0.0039	0.0061	0.0068
E_{max} on surface (MV/m)	4.1	4.0	2.8
Group velocity, v_g/c	0.05	0.5	0.0122
Outer radius (cm)	8.343[a]	16.84	8.735
Beam-bore hole radius (cm)	1.1	1.1	2.391
Fill time (μs)	6.8[b]	16.9[b]	0.3 for 1 m of structure

[a]Applicable to an on-axis coupled structure, however it does not include space occupied by off-axis couplers such as for the side-coupled structure.

[b]Assuming unit coupling factor and 25% overdrive power.

TW and SW Structure Comparison

A comparison between the LAMPF shaped cavity, a disk-and-washer cavity and a scaled SLAC cavity (see p.129, Ref. 12) is given in Table I. Effective shunt impedance, Z_{eff} or ZT^2, is two-to-three times higher for the SW structures, meaning they convert rf power to useful beam power more efficiently.

The disk-and-washer structure quality factor, Q, is the largest of the three. Surface fields are higher on the SW structures, associated with the drift-tube nose, near the beam axis. Group velocities are much higher in the disk-and-washer structure, implying that energy can be propagated down the structure quickly, an important feature for heavily beam-loaded structures such as in storage rings. The TW structure's outer diameter is smaller than that of the disk-and-washer cavity, but only slightly larger than the LAMPF shaped cavity. If space is important, an on-axis coupled SW structure would be a good choice.

A distinct advantage for the TW structure accelerator is the short fill time. This can be important for pulsed systems which provide limited pulse length from the rf source, and a limited gun current. For very high duty cycles this advantage disappears, because the SW structure can be operated cw, with risetime being important only when the structure is first turned on. This is true especially when the time between rf pulses is less than several times the SW structure fill time; complex and expensive pulsed modulators can be eliminated. Another advantage of the TW structure is that an isolator or circulator is not required between the structure and the rf source.

Storage Ring Structures

The PEP, SPEAR and PETRA storage rings all employ similar accelerating structures[31-34], five-cavity SW structures shown in Fig. 3, that are coupled together by slots in the common cavity wall, and operate in the π mode. The PETRA cavities are made from copper, whereas the PEP and SPEAR cavities are made from aluminum, with a layer of titanium nitride deposited on the surface to inhibit multipactoring. Tuners in the end cavities appear adequate to compensate for detuning effects.

An improvement to these standard five-cell π-mode cavities has been under study[35] at CERN. Increases in Q and energy gain are expected to result from the addition of a spherical storage cavity to the accelerating structure. Wilson[36] has described a method to

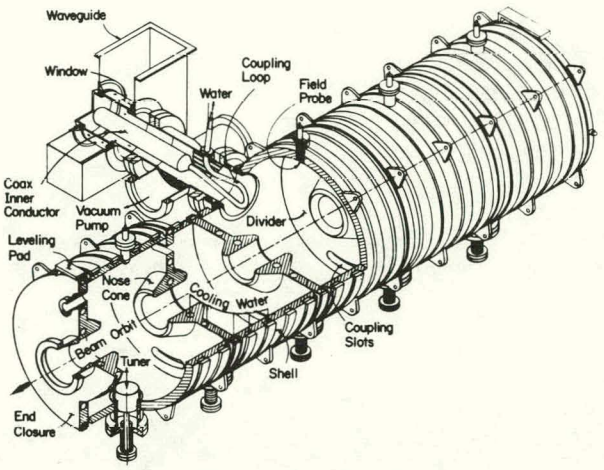


Fig. 3. Isometric drawing of five-cell accelerating cavity operated in the π-mode.

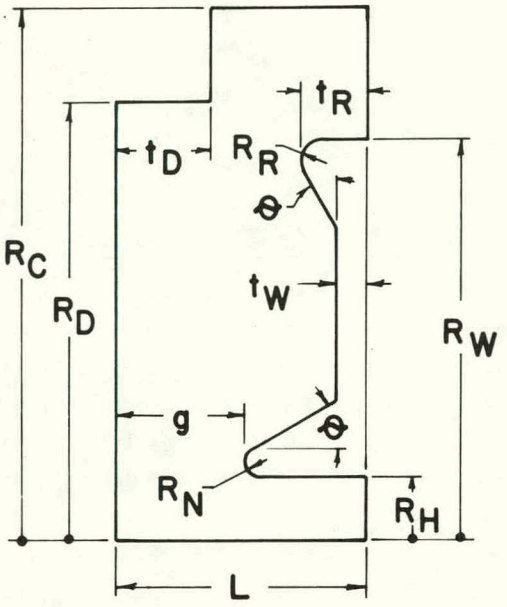


Fig. 4. Illustration of the disk-and-washer geometry showing symbols used to define the various dimensions.

reduce rf power requirements for future accelerating structures of large storage rings by introducing pulsed rf systems with TW structures.

Another structure with many interesting properties for storage rings has been described by Sundelin et al.[37] It is a parallel-coupled structure, similar to a series of manifolded resonant cavities that are coupled only to the manifold. A nine-cavity disk-and-washer structure is being considered for the proton storage ring to be added to LAMPF.

Superconducting Structures

During the past decade much has been learned about cavity profiles, materials, fabrication techniques and one-point multipactoring. Significant work[1-5] continues, and structures may be built to operate with high accelerating gradients in the future. Presently, limitations appear to be in the 3-MeV/m region. Field emission and multipactoring can drive a structure normal, if intense enough, and can drive other cavity modes and cause unwanted frequency shifts.

Multipass high-quality beams through the same accelerating structure have been routinely delivered[1,5] with duty factors up to 100%, demonstrating structure suitability.

The Disk-and-Washer Structure

Compared to the LAMPF shaped cavity, the disk-and-washer cavity has many advantages: higher coupling constant (less sensitive to assembly and fabrication errors, better power flow, longer structures can be built); more open structure (better vacuum conductance, more and varied assembly techniques); all coaxial structure (easier to assemble); higher quality factor (more stored energy available for heavily beam-loaded systems); higher effective shunt impedance (more efficient structure that is more economical to operate and to remove heat); a means to Q-spoil higher order modes. References 21, 38-40 contain recent information regarding characteristics, design data and assembly of the disk-and-washer structure. The following discussion will review some of this material and present some new information.

Geometrical Choices

The disk-and-washer cavity shown in Fig. 4 has an extra degree of freedom compared to the LAMPF shaped cavity, giving the designer more flexibility in dimensional choices. Once the optimized gap, g, and optimized disk thickness, t_D, have been determined, the choice of outer radius , R_C, can be made based on dimensions of available material. Required frequencies for the π/2 accelerating mode, π/2A, and the π/2 coupling mode, π/2C, are satisfied by adjusting the washer radius, R_W, and the disk radius, R_D. Figure 5 shows ZT^2 as a function of R_C for four particle betas, from 0.4 to 1.0, as determined by SUPERFISH. These curves apply to geometries without a bulb at the outer extremity of the washer; i.e., $t_R = t_W$. Maximum ZT^2 values are 115, 81, 59 and 34 MΩ/m for particle betas 1.0, 0.8, 0.6, and 0.4, respectively. These values should be compared to 69, 65, 57, and 39 MΩ/m for an equivalent LAMPF shaped cavity. Because coupling slot and coupling cavity rf losses are included in calculations for the disk-and-washer structure, agreement between experimental and calculated values will be much better than for LAMPF shaped cavities.

TABLE II

PARAMETERS FOR THE DISK-AND-WASHER STRUCTURE (1.35 GHz)
AS A FUNCTION OF THE OUTER RADIUS, R_C
(β = 1.0, t_D = 2.65 cm, $t_W = t_R$ = 0.35 cm, R_H = 1.1 cm,
R_N = 0.25 cm, R_R = 0, θ = 30°, L = 5.555 cm)

R_C (cm)	R_D (cm)	R_W (cm)	ZT^2 (MΩ/m)	T	Q	E_{max} on Surface (MV/m)	% Power on Metal Walls		
							Cylinder	Disk	Washer
10.84	7.50	10.06	49.83	0.812	22369	4.02	6.7	36.1	57.2
11.84	8.96	9.50	66.71	0.813	32215	3.98	2.4	32.7	64.9
12.84	10.25	9.10	74.88	0.813	40179	3.97	1.5	29.1	69.4
13.84	11.46	8.93	80.14	0.813	46962	3.97	1.3	25.9	72.8
14.84	12.63	8.84	84.25	0.813	53033	3.97	1.2	23.2	75.6
15.84	13.77	8.78	87.70	0.813	58577	3.97	1.2	20.9	77.9
16.84	14.90	8.73	90.61	0.813	63671	3.96	1.2	18.9	79.9
17.84	16.01	8.70	92.69	0.814	68355	3.94	1.2	17.3	81.5
18.84	17.10	8.67	95.06	0.813	72746	3.96	1.2	15.9	82.9
19.84	18.19	8.65	96.86	0.813	76827	3.96	1.2	14.6	84.2

A restriction (other than the obvious one associated with structure weight and size) in the outer radius, R_C, for long structures is related to preventing mode overlapping with the $\pi/2A$ mode. The mode dispersion curve begins to turn over at large R_C with many of the mode frequencies between the $\pi/2A$ and the π mode being very close to the $\pi/2A$ mode frequency. This overlap is associated with increasing second-neighbor coupling as the space between the washer and disk increases. At 1350 MHz, interference from this overlapping can be prevented by restricting R_C to less than 17 cm. This restriction also ensures that the $\pi/2A$ mode group velocity remains large.

Figure 5 shows that a constant R_C can be chosen for all beta, simplifying material procurement and some assembly and fabrication steps. Viewed externally the high-energy portion of a proton machine employing disk-and-washer cavities would be identical in outer dimensions, making supports and alignment fixtures interchangeable except for the different section lengths. Figure 6 gives dimensions for radii of the washers and disks for betas from 0.4 to 1.0 as a function of the outer radius R_C. Selecting an outer radius larger than 15.5 cm for β = 0.4 (14.5 cm for β = 0.6) at 1350 MHz permits a consideration of different assembly methods because the washer will always be smaller in diameter than the disk. Vacuum conductance is also improved for this choice.

Table II lists parameters for a β = 1.0 disk-and-washer cavity as a function of the outer radius. Optimized g and optimized t_D have been used for the calculations while R_W and R_D were altered to ensure that frequencies for the $\pi/2A$ and $\pi/2C$ modes were both 1350 MHz.

As expected, ZT^2, Q and the percent power on the washer increase as R_C increases. Although percent power on the washer increases as R_C increases, the amount of power deposited on the washer decreases slightly because ZT^2 is increasing. Obviously, heat has to be removed from the washer and the washer has to be supported in some manner. Washer supports can be

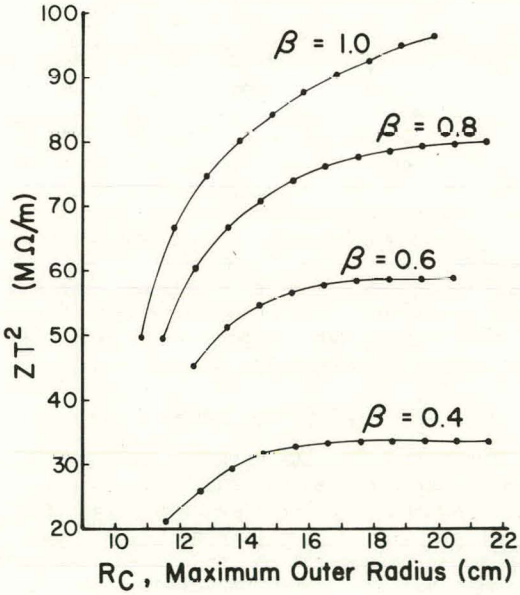


Fig. 5. Effective shunt impedance, ZT^2, of the 1.35 GHz disk-and-washer geometry as a function of the outer cylinder radius, R_C, for betas from 0.4 to 1.0.

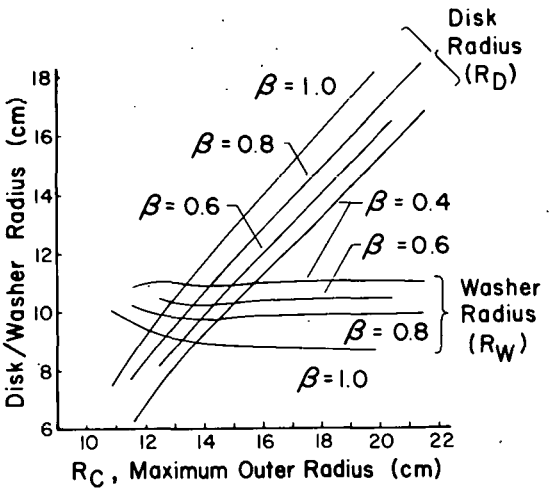


Fig. 6. Radii of the disk-and-washer associated with Fig. 5 versus the outer cylinder radius, R_C for betas from 0.4 to 1.0.

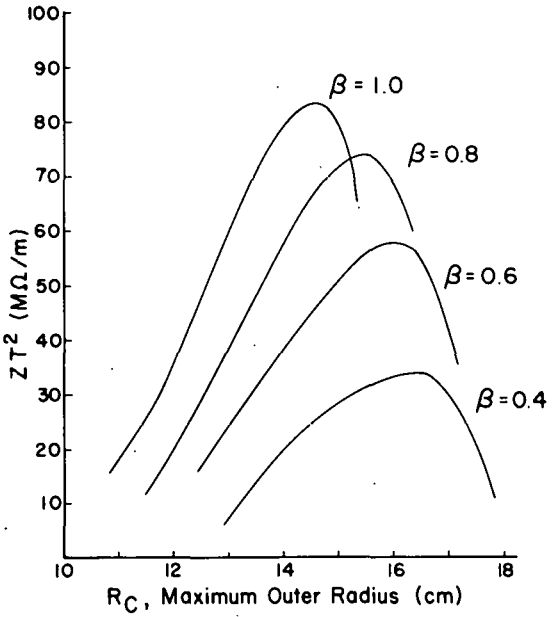


Fig. 7. Effective shunt impedance, ZT^2, of the 1.35 GHz disk-and-washer geometry as a function of the outer cylinder radius, R_C, for betas from 0.4 to 1.0; The stem length or the difference between R_C and R_W, the washer radius, is kept constant at $\lambda/4$.

of many types: several radial support stems made of hollow rod connecting the washer to the outer radius in the plane of the washer, several cylindrical hollow rods passing through the washers near the rf voltage minimum and traversing the length of the structure, or several T-shaped supports made of hollow rod connecting washers to adjacent disks, to list a few.

Recently it was determined experimentally, and by simulation calculations, that the radial support stem length should be close to $\lambda/4$. At the time of writing, measurements continue in the laboratory; preliminary results are reported[40] elsewhere in the conference proceedings. The effect this restriction has on ZT^2 is illustrated in Fig. 7. The gap, g, has to be adjusted to obtain the desired $\pi/2A$ frequency, unlike procedures described above. Maximum ZT^2 for β = 1.0, 0.8, 0.6 and 0.4 are 83, 74, 58, and 34 MΩ/m, respectively; values larger than an equivalent LAMPF shaped cavity. For PIGMI[24], Pion Generator for Medical Irradiation, which requires accelerating structures with betas from 0.5 to 0.8, a common outer radius of 15.75 cm could be selected. With this geometry, the washer radius for all beta is constant (because the outer radius is constant), further simplifying fabrication procedures.

A bulb on the washer extremity is necessary for mounting radial support stems. Figure 8 shows results of calculations associated with determining the size and shape of the washer bulb. As expected, to have the highest ZT^2, the angle θ_2 from the washer web to the bulb and the width, t_R, of the bulb should be as small as possible. ZT^2 is given as a function of the gap between the disk and the washer bulb for angles θ_2 from 20° to 75°.

Three methods to support washers that should not result in field tilts along the

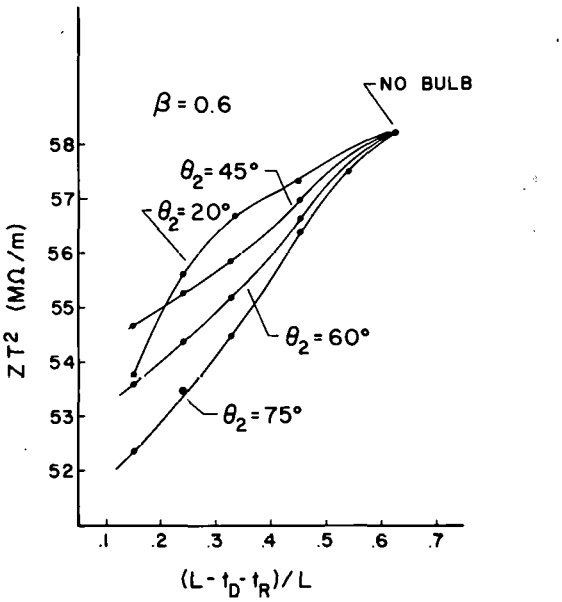
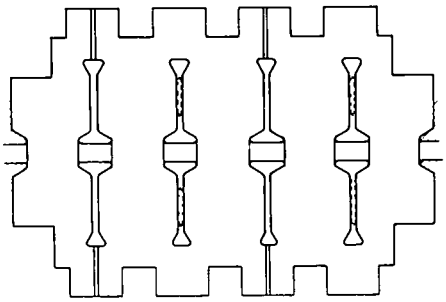
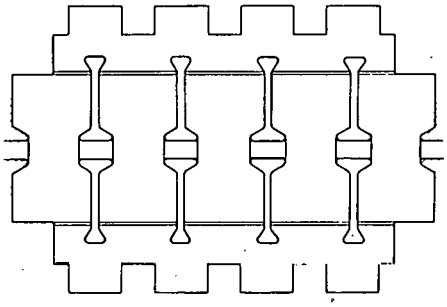


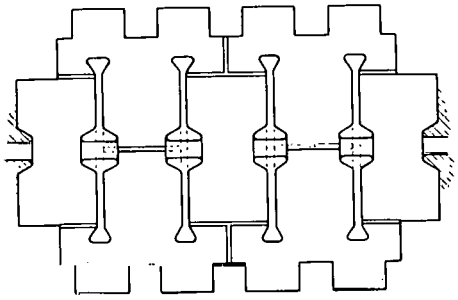
Fig. 8. Effective shunt impedance, ZT^2, of the 1.35 GHz, β = 0.6, disk-and-washer geometry as a function of the gap between the disk and the washer bulb for different bulb angles.



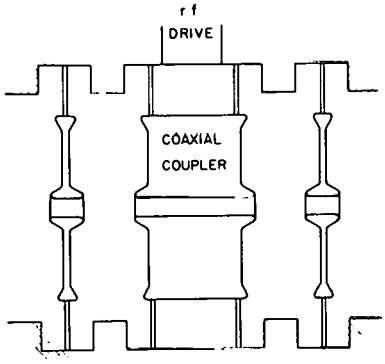
(a) Four radial supports per washer rotated by 45° from washer to washer.



(b) Four longitudinal supports running the length of the structure.



(c) Two T-shaped supports between each washer that are rotated by 90° between adjacent gaps.



(d) Coaxial coupler excited in TEM-like mode, employing radial supports and interconnecting adjacent accelerating sections.

Fig. 9. Disk-and-washer structure illustrating various support methods.

length of the structure are shown in Fig. 9. Field tilt should not occur because washer supports are symmetrical about the washer plane, keeping coupling constants similar along the length of the structure. Figures 9a, 9b and 9c show, respectively, a five-cavity structure terminated in full cells with four radial supports per washer rotated by 45° from washer to washer, with four supports running the length of the structure and with two T-supports between adjacent washers that are rotated by 90° from gap-to-gap. Coupling to an rf drive can be accomplished at the end wall, where magnetic fields are maximum. Figure 9d shows a coaxial coupler that connects adjacent sections excited in a TEM-like mode. The coaxial coupler[41] also serves as the means of coupling to an external rf drive, and provides space for beam diagnostics or handling with connections via the radial stems that support the inner cylinder.

Minimal tuning should be required for the structure. If needed, the $\pi/2$A-mode frequency can be adjusted by changing g, while the $\pi/2$C mode frequency can be adjusted by changing R_D. Frequency sensitivities for the different parts of the disk-and-washer geometry are given in Ref. 21. Reference 38 describes a method to fabricate the structure in 1-m sections rather than by the usual single or half-cavity method. Copper-plated steel disks and copper washers with copper-plated steel radial support stems are jigged and mounted in a copper-plated steel outer cylinder with brazing material located as required. Eight longitudinal cooling channels are mounted on the outer wall to match locations

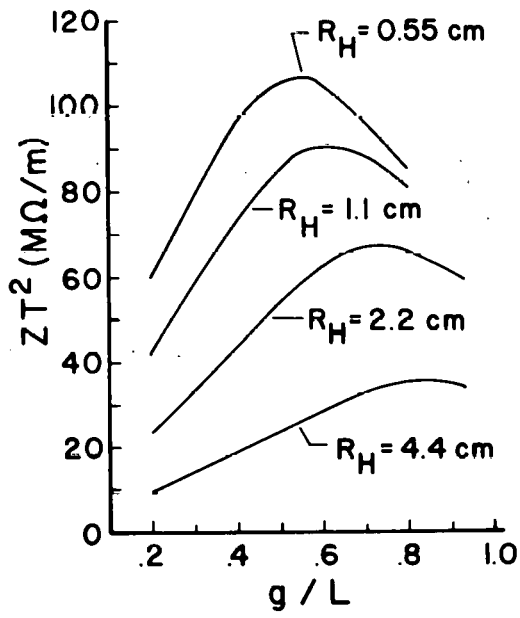


Fig. 10. Effective shunt impedance, ZT^2, of the 1.35 GHz, $\beta = 1.0$, disk-and-washer geometry as a function of the g/L ratio for different beam bore hole radii, R_H.

TABLE III

PARAMETERS FOR THE DISK-AND-WASHER STRUCTURE (1.35 GHz) AS A FUNCTION OF THE g/L RATIO
($\beta = 1.0$, $R_C = 16.84$ cm, $t_D = 2.65$ cm, $t_W = t_R = 0.35$ cm,
$R_N = 0.25$ cm, $R_R = 0$, $\theta = 30^\circ$, L = 5.555 cm)

							Full Cavity		
g/L	R_D(cm)	R_W(cm)	ZT^2(MΩ/m)	T	Q	E_{max} on Surface (MV/m)	Power to Metal Walls (Watts)	Stored Energy (Joules)	τ
					R_H = 0.55 cm				
0.2	15.05	6.37	60.97	0.971	44470	8.7	1718.1	0.009008	0.959
0.3	15.00	7.13	85.29	0.946	51372	6.4	1165.5	0.007059	0.913
0.4	14.94	7.89	96.30	0.908	52948	5.8	951.7	0.005941	0.843
0.5	14.90	8.55	104.61	0.864	60637	4.6	793.4	0.005672	0.762
0.6	14.87	9.06	105.09	0.812	68477	4.2	696.4	0.005622	0.676
0.7	14.85	9.40	96.07	0.762	74487	3.3	670.7	0.005889	0.609
0.8	14.83	9.57	85.09	0.714	77727	2.6	665.7	0.006100	0.566
					R_H = 1.1 cm				
0.2	15.11	6.25	41.82	0.953	46523	8.4	2414.2	0.013240	0.951
0.3	15.05	6.91	58.15	0.928	47804	6.3	1645.0	0.009274	0.912
0.4	14.99	7.58	72.88	0.894	51381	5.2	1218.7	0.007382	0.857
0.5	14.93	8.25	85.33	0.851	57461	4.5	943.3	0.006390	0.787
0.6	14.89	8.83	90.80	0.805	65105	3.8	791.8	0.006078	0.714
0.7	14.86	9.33	88.54	0.757	72046	3.2	719.7	0.006117	0.647
0.8	14.84	9.53	80.75	0.721	76861	2.7	715.6	0.006484	0.603
					R_H = 2.2 cm				
0.2	15.20	6.64	19.06	0.895	50450	8.2	3853.0	0.022916	0.906
0.3	15.13	7.09	33.54	0.875	51042	6.1	2536.8	0.015265	0.876
0.4	15.06	7.57	43.95	0.849	52710	5.1	1823.8	0.011333	0.835
0.5	14.99	8.12	54.12	0.820	56369	4.3	1379.1	0.009165	0.787
0.6	14.92	8.65	62.37	0.789	62142	3.9	1109.0	0.008125	0.735
0.7	14.88	9.14	66.62	0.762	69246	3.3	968.7	0.007908	0.690
0.8	14.84	9.51	65.44	0.744	75693	3.0	940.8	0.008396	0.662
0.937	14.82	9.78	58.98	0.741	80060	2.2	1035.1	0.009770	0.662
					R_H = 4.4 cm				
0.2	15.32	8.23	9.45	0.815	50953	7.3	7810.8	0.046918	0.800
0.3	15.25	8.48	14.10	0.809	53215	5.9	5154.2	0.032331	0.789
0.4	15.16	8.71	18.89	0.801	55372	4.8	3775.4	0.024646	0.775
0.5	15.06	8.98	23.76	0.793	58349	4.4	2940.4	0.020222	0.759
0.6	14.97	9.29	28.54	0.785	62645	3.9	2399.8	0.017717	0.744
0.7	14.90	9.67	32.71	0.779	68616	3.8	2059.2	0.016658	0.732
0.8	14.84	10.05	35.16	0.775	75693	3.6	1895.6	0.016914	0.725
0.937	14.80	10.47	33.99	0.774	82019	3.3	1959.8	0.018952	0.725

of the radial support stems. Brazing tests based on this fabrication procedure are underway at LASL.

Gap Optimization and Stored Energy

The effect of changing the gap, g, on structure efficiency is shown in Fig. 10 for different beam bore holes, R_H, for $\beta = 1.0$, 1350 MHz disk-and-washer cavity, with 16.84-cm outer radius. As R_H increases, the optimum value of g increases and maximum ZT^2 decreases. For an extremely large bore hole, $R_H = 4.4$ cm, the drift-tube nose on the washer is almost eliminated for maximum ZT^2. For maximum efficiency, beam bore-hole radius should be as small as possible consistent with actual particle beam size, beam spill that can be tolerated and errors in alignment or transmittal of the beam.

Table III summarizes calculated results for the $\beta = 1.0$, $R_C = 16.84$ cm, 1350 MHz disk-and-washer geometry for changes in g and R_H. The table is useful in designing cavities for

structures accelerating high-current beams, where stored energy is an important quantity. One method to design cavities is to maximize the stored energy, S, associated with the electric fields in the beam bore-hole relative to the particle energy gain, ΔE; i.e., $S\tau/(\Delta E)^2$ is maximized, where τ is a transit time factor related to the stored energy available to the beam as it traverses the cavity:

$$\tau = \frac{\int_{-L}^{L}\int_{0}^{a}\left[E(z,r)\cos\left(\frac{\pi z}{2L}\right)\right]^2 drdz}{\int_{-L}^{L}\int_{0}^{a} E(z,r)^2 drdz}$$

where

E(z,r) the electric field at position (z,r)
2L the cavity length, and
a the radius within the beam bore-hole over which stored energy is considered.

At the same time the power, P, dissipated as rf losses in the cavity walls to provide the energy gain, should be minimized; i.e., $(\Delta E)^2/P$ should be maximized. Combining the two effects gives $S\tau/P$, which when multiplied by $2\pi f$ gives a quality factor, Q_B, related to "a", the beam bore-hole size considered. Thus, $Q_B\tau$ should be maximized. Figure 11 presents the quality factor as a function of the gap for different beam bore-holes and radii (indicated in the parenthesis) within the range of R_H over which the stored energy was calculated. Values for τ reported in Table III are for pencil-beam volumes along the beam axis. Work is underway at present to determine transit time factors which consider the entire volume. Sample calculations have shown that this τ, and the one that considers the entire volume, scale linearly.

Using τ in approximate calculations to maximize $Q_B\tau$ has demonstrated that the optimum g/L ratio for $\beta = 1.0$, $R_C = 16.84$ cm, 1350-MHz disk-and-washer cavities with R_H values of 0.55, 1.1, 2.2 and 4.4 cm are 0.2, 0.4, 0.66, and 0.84, respectively. This should be compared with optimum g/L ratios of 0.55, 0.59, 0.73, and 0.84, respectively, to maximize ZT^2. Measurements by Koontz et al.[42] with intense single pulses traversing a TW accelerator demonstrated that the beam size should not be used in considering the stored energy available to the beam. The radius "a" should be close to the size of the rf structure beam's bore-hole. A 16.84-cm outer radius, 1350-MHz disk-and-washer cavity with a 2.2-cm bore-hole radius has a Q_B of 8800. This is two times larger than an equivalent scaled SLAC cavity with a 2.4-cm bore-hole radius, that has a Q_B of 4200. The Q_B's for a 1.1-cm beam bore-hole radius, 16.84-cm outer radius disk-and-washer cavity, and a

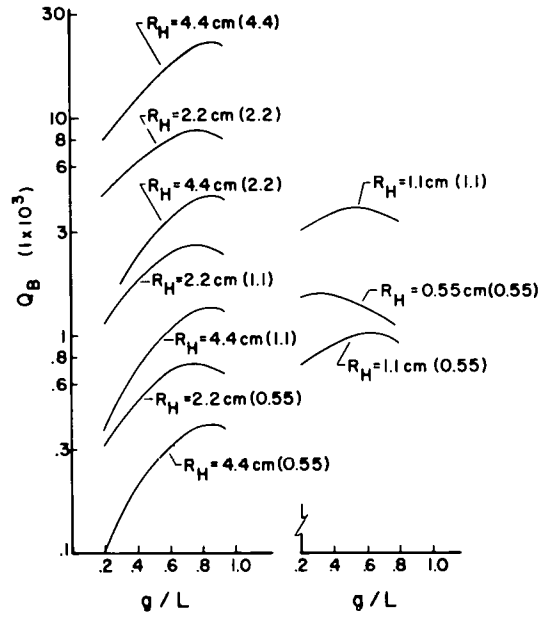


Fig. 11. Beam quality factor, Q_B, of the 1.35 GHz, $\beta = 1.0$, disk-and-washer geometry as a function of g/L for different beam bore hole radii, R_H and for different radii (in parenthesis) used to determine available stored energy.

LAMPF shaped cavity are 3800 and 2800, respectively, indicating an advantage for the disk-and-washer geometry.

Other Properties

Operation of a disk-and-washer structure as a "harmonic accelerator" is discussed in Ref. 21. Combining the fundamental frequency and its first harmonic frequency with proper relative amplitude and phase can make the rf wave during transit of the beam bunch more linear, reducing transverse beam emittance growth. Reference 21 also describes different termination methods and a means to design a graded-beta structure from disk-and-washer cavities.

Higher-order modes can be Q-spoiled by factors from 2 to 7, by fabricating the outer cylinder from 304 stainless steel; at the same time the worst case would be only a 6% loss in Q for the $\pi/2A$ mode.

Conclusions and Summary

Many TW and SW structures are accelerating charged particle beams to very high velocities. Each has properties peculiar to the application. Choices were made to optimize accelerator performance based on specific criteria. Traveling-wave accelerators offer an advantage of fast fill time but are very inefficient converters of rf power to beam power when compared

to SW structures, particularly when compared to the disk-and-washer structure. Improvements in ZT^2 of TW accelerators could be realized by shaping the cavities, in particular, by adding drift-tube noses. For this geometry the usual iris coupling scheme would have to be replaced by some other method, such as slot couplers.

It is hoped that developments in superconducting structure technology will continue to result in improved performance. Significant breakthroughs in the understanding of phenomena that limit accelerating gradients have been made. For very heavily beam-loaded systems where most of the installed rf power is associated with beam power requirements, it is not clear that superconducting linacs offer a significant advantage over room-temperature linacs, unless accelerating gradients are very high, resulting in cooling limitations for a room-temperature structure.

As an accelerating structure the disk-and-washer geometry offers many advantages: high coupling, good vacuum conductance, high rf efficiency, high quality factor and ease of fabrication. Measurements now in progress will demonstrate the performance of experimental systems. Experience in the USSR shows that experimental characteristics are very close to calculated parameters. The disk-and-washer structure also offers significant advantages for applications when the stored energy in the rf accelerating fields available to the beam has to be maximized.

Acknowledgments

The author thanks T. J. Boyd, Jr., R. A. Jameson, J. M. Potter and D. A. Swenson who participated in many aspects of the work presented here, both as "devil's advocates" and as problem presenters. Assistance from M. A. Allen, G. A. Loew and T. I. Smith is gratefully appreciated. The author is indebted to B. K. Addessio who ran many of the SUPERFISH calculations.

References

1. C. M. Lyneis, M. S. McAshan, R. E. Rand, H. A. Schwettman, T. I. Smith and J. P. Turneaure, "The Stanford Superconducting Recyclotron," IEEE Trans. Nucl. Sci. NS-26, #3, 3246 (1979).
2. C. M. Lyneis, J. Sayag, H. A. Schwettman and J. P. Turneaure, "Performance of a Superconducting Accelerator Structure with a Modified Geometry," ibid., 3755 (1979).
3. W. Bauer, A. Brandelik, A. Citron, W. Lehmann, L. Szecsi and M. Yashioka, "Superconducting Accelerating Cavities for High Energy $e^+ - e^-$ Storage Rings," ibid., 3252 (1979).
4. G. Arnolds, H. Heinrichs, R. Mayer, N. Minatti, H. Piel and W. Weingarten, "Design and Status of an Experimental Superconducting Linear Accelerator for Electrons," ibid., 3775 (1979).
5. P. Axel, L. S. Cardman, H. D. Graef, A. O. Hanson, R. A. Hoffswell, D. Jamnik, D. C. Sutton, R. H. Taylor and L. M. Young, "Operating Experience with MUSL-2," ibid., 3143 (1979).
6. J. E. Leiss, "Induction Linear Accelerators and their Applications," ibid., 3870 (1979).
7. Z. D. Farkas, H. A. Hogg, G. A. Loew and P. B. Wilson, "Recent Progress on SLED, the SLAC Energy Doubler," IEEE Trans. Nucl. Sci. NS-22, #3, 1299 (1975).
8. E. A. Knapp, B. C. Knapp and J. M. Potter, "Standing Wave High Energy Linear Accelerator Structures," Rev. Sci. Instr. 39, 979 (1968).
9. W. Schnell, "Design Study of a Large Electron-Positron Colliding Beam Machine - LEP," IEEE Trans. Nucl. Sci. NS-26, #3, 3130 (1979).
10. V. G. Andreev, V. M. Belugin, V. G. Kulman, E. A. Mirochnik and B. M. Pirozhenko, "Study of High-Energy Proton Linac Structures," Proc. of 1972 Proton Linac Conf., Los Alamos Scientific Laboratory Report No. LA-5115, 114 (1972).
11. G. A. Loew, "Electron Linacs," Proc. of 1976 Proton Linac Conf., Atomic Energy of Canada Ltd. Report No. AECL-5677, 217 (1976).
12. R. B. Neal, ed., The Stanford Two-Mile Accelerator, W. A. Benjamin Publishers, 1968.
13. J. Haimson, "Initial Operation of the MIT Electron Linear Accelerator," IEEE Trans. Nucl. Sci. NS-20, #3, 915 (1973).
14. N. J. Norris and R. K. Hanst, "Velocity Modulation System for Enhancement of 50-Picosecond Radiation Pulse," IEEE Trans. Nucl. Sci. NS-16, #3, 323 (1969).
15. P. M. Lapostolle and A. L. Septier, eds., Linear Accelerators, North Holland Publishing Co., (1970).
16. G. Mavrogenes, W. Ramler, W. Wesolowski, K. Johnson and G. Clifft, "Subnanosecond High-Intensity Beam Pulse," IEEE Trans. Nucl. Sci. NS-20, #3, 919 (1973).
17. G. A. Loew, R. H. Miller, R. A. Early, and K. L. Bane, "Computer Calculations of Traveling-Wave Periodic Structure Properties," IEEE Trans. Nucl. Sci. NS-26, #3, 3701 (1979).
18. K. Halbach, R. F. Holsinger, W. E. Jule and D. A. Swenson, "Properties of the Cylindrical Rf Cavity Evaluation Code SUPERFISH," Proc. of 1976 Proton Linac Conf., Atomic Energy of Canada Ltd. Report No. AECL-5677, 338 (1976).
19. G. A. Loew, K. L. Brown, R. H. Miller and D. R. Walz, "Electron Linac Design for Pion Radiotherapy," IEEE Trans. Nucl. Sci. NS-24, #3, 1006 (1977).
20. H. C. Hoyt, D. D. Simmonds and W. F. Rich, "Computer Designed 805-MHz Proton Linac Cavities," Rev. Sci. Instr. 37, 755 (1966).

21. S. O. Schriber, "Room-Temperature Cavities for High-Beta Accelerating Structures," Proc. of Conf. on Future Poss. for Electron Accel., Charlottesville, Virginia, January 1979, to be published.
22. A Proposal for a High-Flux Meson Facility, Los Alamos Scientific Laboratory, September (1964).
23. V. G. Andreev, I. K. Guslitskov, E. A. Mirochnik, V. M. Pirozhenko and B. I. Polyakov, "Investigation of the Accelerating Structure for the Second Part of the Meson Factory Linac," Proc. of 1976 Proton Linac Conf., Atomic Energy of Canada Ltd. Report No. AECL-5677, 269 (1976).
24. E. A. Knapp and D. A. Swenson, "The PIGMI Program at LASL," ibid., 230 (1976).
25. J. E. Stovall, "New Developments in Accelerator Technology at LASL," IEEE Trans. Nucl. Sci. NS-26, #1, 1450 (1979).
26. G. E. McMichael and J. McKeown, "Operational Experience with Coupled Cavity Structures in a High Duty Factor Accelerator," IEEE Trans. Nucl. Sci. NS-26, #3, 4108 (1979).
27. J. McKeown, "Experiences at Chalk River with a CW Electron Accelerator," Proc. of Conf. on Future Poss. for Electron Accel., Charlottesville, Virginia, January 1979, to be published.
28. J. S. Fraser, "High Power, Low Energy Linac for Radiation Processing," IEEE Trans. Nucl. Sci. NS-26, #1, 1455 (1979).
29. H. Euteneuer, "Performance and Blowup Properties of the MAMI Structure," Proc. of Conf. on Future Poss. for Electron Accel., Charlottesville, Virginia, January 1979, to be published.
30. V. A. Vaguine, "Standing Wave High Gradient Accelerator Structure," IEEE Trans. Nucl. Sci. NS-24, #3, 1084 (1977).
31. M. A. Allen and L. G. Karvonen, "High Duty Factor Structures for e^+e^- Storage Rings," Proc. of 1976 Proton Linac Conf., Atomic Energy of Canada Ltd. Report No. AECL-5677, 175 (1976).
32. M. A. Allen, L. G. Karvonen, J. L. Pellegrin and P. B. Wilson, "Rf System for the PEP Storage Ring," IEEE Trans. Nucl. Sci. NS-24, #3, 1780 (1977).
33. H. Gerke, H. P. Scholz, M. Sommerfeld and A. Zolfaghari, "The PETRA Cavity," DESY internal report, DESY PET-77/08 (1977).
34. The Doris Storage Ring Group, "Doris at 2 x 5 GeV," IEEE Trans. Nucl. Sci. NS-26, #3, 3135 (1979).
35. W. Schnell, "Design Study of a Large Electron-Positron Colliding Beam Machine - LEP," ibid. 3130 (1979).
36. P. B. Wilson," Pulsed Rf Systems for Large Storage Rings," ibid., 3255 (1979).
37. R. M. Sundelin, J. L. Kirchgessner and M. Tigner, "Parallel Coupled Cavity Structure," IEEE Trans. Nucl. Sci. NS-24, #3, 1686 (1977).
38. D. A. Swenson, "Fabrication and Excitation of the Disk-and-Washer Linac Structure," Proc. of Conf. on Future Poss. for Electron Accel., Charlottesville, Virginia, January 1979, to be published.
39. J. M. Potter, S. O. Schriber and F. J. Humphry, "Experimental and Calculated Rf Properties of the Disk-and-Washer Structure," IEEE Trans. Nucl. Sci. NS-26, #3, 3763 (1979).
40. S. O. Schriber and J. M. Potter, "Limitations of the Disk-and-Washer Linac Structure," paper presented at the 1979 Linear Accelerator Conference, Montauk, NY, September 1979.
41. J. J. Manca, "Rf Coaxial Couplers for High-Intensity Linear Accelerators," Los Alamos Scientific Laboratory report, to be published.
42. R. F. Koontz, G. A. Loew, R. H. Miller and P. B. Wilson, "Single Bunch Beam Loading on the SLAC Three-Kilometer Accelerator," IEEE Trans. Nucl. Sci. NS-24, #3, 1493 (1977).

Discussion

Miller, SLAC: First, I just would like to make a quick comment that actually the two people who are most knowledgeable about SLED are here from SLAC - David Farkas and Harry Hogg. David Farkas was actually the person who originated the idea, and Harry and Dave have both worked on the project. My question is: I presume when you said that there might be advantages in the superconducting structure where you need very high gradient, you are making an assumption that indeed one learns how to support high gradients in superconducting structures.

Schriber: That's right. You have to get higher than 3 MeV/m obviously. But it is hoped that in the future they can get higher gradients.

Hagerman, LASL: Could you summarize how much high power testing there has been on the various support schemes for the disk and washer structure?

Schriber: The only high power tests on different support schemes are high power tests at RTI with something close to "L" supports. Each washer is connected to an adjacent disk. The RTI group, Andreev and Fedotov, measured about 95% of theoretical ZT^2. At LASL we are presently doing low power measurements on $\beta = 0.6$ and $\beta = 1.0$ cavities. As I said, the $\beta = 0.6$ results look very good, but there are some things we do not understand about the results with the $\beta = 1.0$ cavities.

Farkas, SLAC: You said that the group velocity of the disk and washer structure is about fifty times greater than the others. That is not an unmixed blessing because you need very long structures or you need extremely high power sources for traveling wave structures. Also, when you compared the efficiency of the SLAC structure to the other structure, the SLAC structure was not optimized to maximum efficiency. It was optimized to give you the highest gradient at 10% loading.

Schriber: To answer your first question, I showed ways of putting rf drives in various locations and these coaxial couplers can be placed at appropriate locations all the way down the system. The structure is still one completely rf-coupled system. The structure is a standing wave structure. And with regards to the second comment, I have done quite a number of calculations on different types of geometries for traveling wave cavities and looked at different ones that have been reported by SLAC. One still observes the difference of about a factor of 2 or 3 in efficiency in favor of the disk-and-washer cavity. The reason is associated with a drift tube nose close to the axis for the standing wave structure. With a disk loaded wave guide you just have the disk thickness.

Jameson, LASL: Comment: During the next two years under the PIGMI Program at LASL, disk and washer structures will be tested at high power. A number of sections, a few cells long, will be fabricated to test construction techniques and scaling relations. A full power section of 15-20 cells will then be tested (without beam).

Schriber: There is also planned some high power measurements at 2388 MHz. That should be done in the next few years.

1979 LINEAR ACCELERATOR CONFERENCE

LIMITATIONS OF THE DISK-AND-WASHER STRUCTURE*

S. O. Schriber† and J. M. Potter
Los Alamos Scientific Laboratory
Los Alamos, New Mexico 87545

Summary

A preliminary analysis of measurements on $\beta = 0.6$ and 1.0 disk-and-washer linac cavities has indicated some limitations on washer support methods. In particular, the use of radial supports should be avoided until further testing provides a complete understanding.

Introduction

The disk-and-washer cavity geometry[1] for an accelerating structure offers many advantages including high rf conversion efficiency and high coupling factor. A detailed study was initiated which included computer calculations and experimental measurements, to determine limitations, if any, which would have to be considered in an operational system.

Other than geometrical choices that have been discussed elsewhere,[2,3] the method used to support and cool the washer must be considered carefully because of the implications it has on compensation procedures required to give acceptable on-axis electric field distributions, and on structure tuning. An earlier study[3] of support methods with aluminum cavities, shows the importance of symmetrical washer support schemes, because they either eliminate or reduce the complexity of these compensating procedures. Figure 1 shows the support methods studied (L, TO and radial). The radial support appeared to offer the most advantages, but the effects this scheme would have on quality factor, Q, and structure impedance, Z, were unknown. For this reason, computer studies were initiated and $\beta = 0.6$ and 1.0, copper structures were fabricated to investigate the effects of symmetrical support techniques on Q and Z.

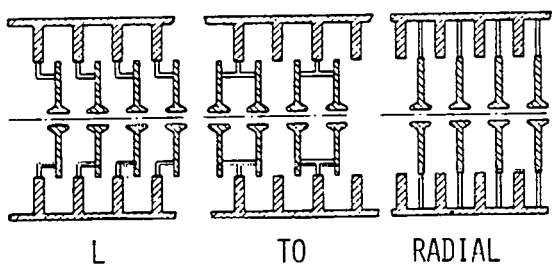


Fig. 1.
Washer support methods.

*Work performed under the auspices of the U.S. Department of Energy.
†Visitor from Chalk River Nuclear Laboratories, Chalk River, Ontario, Canada.

Calculations

Computer calculations for the different cavity geometries have been done using the code SUPERFISH.[4] Geometrical parameters for this study are shown in Fig. 2.

Radial Support Effects

The effects that radial support diameter and length have on cavity quality factor are illustrated in Fig. 3. The ratio of quality factor Q, with stems, to the quality factor Q_0, without stems, is shown as a function of stem length and diameter in dimensionless units based on the resonance wavelength. The $\beta = 0.6$ disk-and-washer cavity geometry with radial support stems was simulated by a coaxial cavity with its axis of rotation centered on the stem and washer, because SUPERFISH does not handle three-dimensional geometries. (See Fig. 4.) Size and volume of the washer, disk, outer cylinder, and stem were scaled to give a 1320-MHz coaxial mode that had a field distribution equivalent to the accelerating mode field distribution of the real cavity. Stem effects were determined by comparing calculated

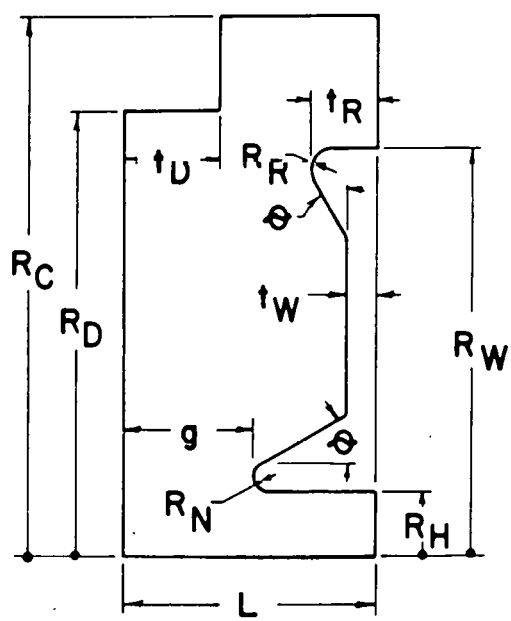
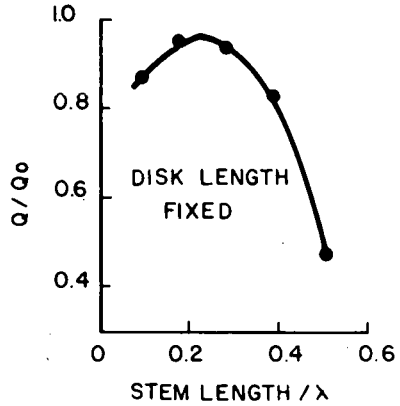
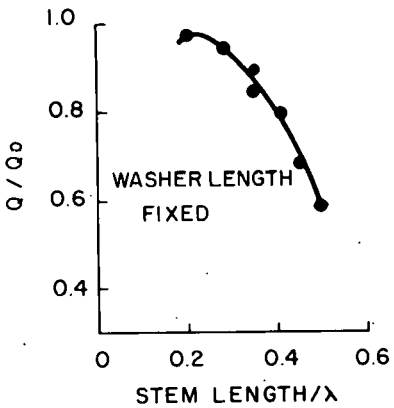


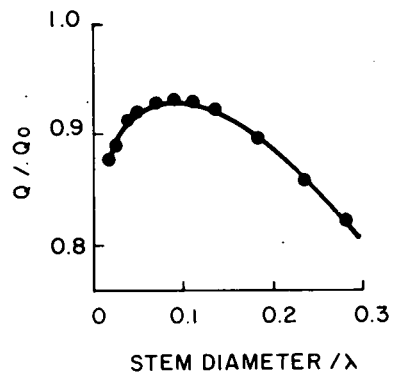
Fig. 2.
Geometrical parameters of disk-and-washer structure.



a. Q/Q_0 vs stem length for fixed disk length.



b. Q/Q_0 vs stem length for fixed washer length.



c. Q/Q_0 is stem diameter for stem length = 0.28 λ.

Fig. 3.
Study of β = 0.6 cavity quality factor using a coaxial model.

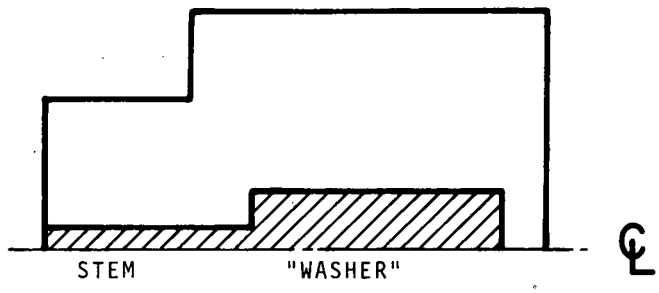


Fig. 4.
SUPERFISH simulation model with coaxial geometry used to study the β = 0.6 cavity.

results with and without a stem. Variation of stem length was accomplished in two ways, both with similar results. The first method, shown in Fig. 3a, was to change the washer length keeping the disk length or coaxial cavity length fixed. Figure 3b shows results of calculations for the washer length fixed and disk length or coaxial cavity length changing. Both methods show that the length of the radial support stem should be close to a quarter wavelength to achieve approximately 96% Q/Q_0. Results not shown in the figure demonstrated that the radial stem should be an odd multiple of λ/4 in length; the smaller the multiple, the lower the losses. Figure 3c shows the ratio Q/Q_0 as a function of stem diameter for a 0.28λ length stem. An optimum stem diameter of approximately 0.09λ is indicated for this geometry. For four support stems, this would be equivalent to approximately 0.045λ.

These results indicate that there should be a resonance between the stem and the rest of the cavity, such that the resonant frequency of the structure with a stem should cross through the resonant frequency of a stemless structure as the stem length is varied from, say, λ/8 to 3λ/8. It was thus proposed to look for this effect experimentally.

Optimum ZT^2 for λ/4 Radial Supports

Computations were also done to investigate the consequences upon effective shunt impedance, ZT^2, when radial support stems must be approximately λ/4 long. An optimum gap between noses no longer can be selected to maximize ZT^2, because the gap must be adjusted to achieve the required π/2 accelerating mode frequency, π/2A. The frequency was held at 1350 MHz, and the washer radius, R_W, set equal to the cavity radius, R_C, minus λ/4. Figure 5 shows how ZT^2 varies as a function of the outer cylinder radius, R_C, for particle betas from 0.4 to 1.0. There is an optimum R_C for each beta that maximizes ZT^2. Table I lists some of the calculated parameters for different beta geometries.

TABLE I

DISK AND WASHER PARAMETERS

(1350 MHz, $t_W = t_R = 10.35$, $\theta = 30^o$, $R_H = 1.1$ cm, $R_N = 0.25$ cm)

Beta	R_C	R_D	g/L	t_D	Q	T	ZT^2 (MΩ/m)	Max. Surface Field (MV/m)	% Power Deposited in Metal Walls		
									Outer Cyl.	Disk	Washer
0.4	13.57	8.57	0.070	0.35	14457	0.881	16.32	15.9	< 0.1	1.2	98.8
0.4	16.57	11.76	0.315	0.35	19319	0.849	33.56	5.3	< 0.1	1.0	99.0
0.4	17.89	13.12	0.842	0.35	21165	0.758	18.70	2.4	< 0.1	1.1	98.9
0.6	14.45	10.29	0.229	0.9	24109	0.909	43.94	6.5	< 0.1	3.3	96.7
0.6	16.45	12.40	0.525	0.9	31687	0.822	55.51	3.8	< 0.1	3.9	96.1
0.6	17.18	13.18	0.895	0.9	34647	0.735	35.34	1.9	< 0.1	4.2	95.8
0.8	14.50	11.17	0.387	1.68	34061	0.887	65.99	4.8	0.2	8.8	91.0
0.8	15.50	12.23	0.550	1.68	41438	0.822	73.73	3.9	0.4	10.5	89.1
0.8	16.38	13.16	0.921	1.68	49736	0.720	51.87	1.6	0.5	13.2	86.3
1.0	12.84	10.57	0.331	2.65	36046	0.918	56.55	5.9	0.9	17.4	81.7
1.0	14.45	12.17	0.588	2.65	50789	0.810	82.85	3.9	1.3	24.4	74.3
1.0	15.34	13.11	0.937	2.65	66066	0.708	65.21	1.8	1.8	33.6	64.6

For a slight overall loss in ZT^2, a common R_C can be selected for all beta. The choice obviously depends upon the particle accelerated and the final energy. For electrons, a radius would be used that is heavily weighted in favor of highest ZT^2, where $\beta = 1.0$. For the Pion Generator for Medical Irradiation, PIGMI,[5] which requires structures with beta from 0.5 to 0.8, a common outer radius of 15.75 cm could be used, because this dimension not only matches available pipe size, but makes a reasonable compromise for ZT^2. A common R_C for all beta structures leads to the same R_W for all the washers. Fabrication and material procurement should be simplified because of the common radii. Externally, the accelerator would have the same diameter for all beta, which could simplify alignment and installation fixtures.

Measurements on Radial Supports

Measurements of Z and Q have been done on $\beta = 0.6$ and $\beta = 1.0$, OFHC copper, disk-and-washer cavities that were built at 1320 MHz for tests of PIGMI geometry.[3] Only a preliminary analysis of these measurements will be presented here. The cavity Q was measured using lightly coupled loops to determine the shape of the resonance curve for the $\pi/2A$ mode. The 0 and π-mode Q's were also checked for reference, because radial supports have very little effect on these modes. In all instances, proper care was taken to insure good contact and clean surfaces. Measurements were repeated many times to insure there were no systematic errors or inconsistencies in the data. Measurements of Z/Q were done using standard beadpull techniques.

In this study, washers were supported by radial support stems of different diameters and materials (copper, aluminum, and stainless steel). Effects of metal supports were determined by comparison to measurements made with the washer supported by a low-loss, dielectric material such as Teflon. The highest quality

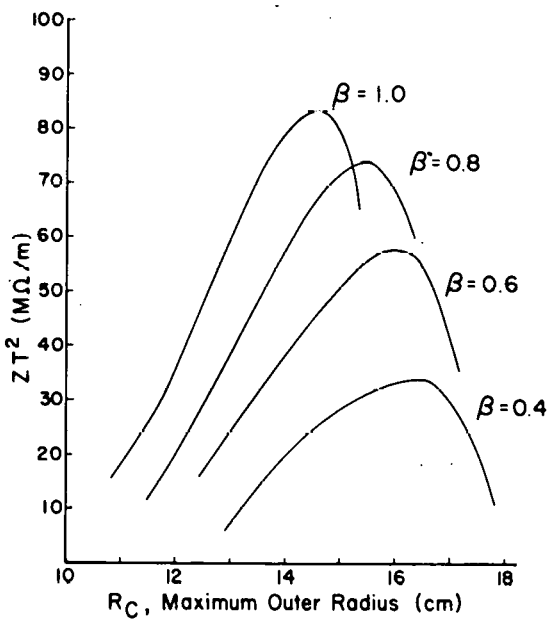


Fig. 5.
Shunt impedance versus cavity outer radius at 1350 MHz.

factor was obtained using the smallest diameter supports consistent with constraints of rigidity and supplying cooling. As expected, the lowest resistivity (copper) supports yielded the best results. A value at 91% of the theoretical Z was achieved for a cavity without supports, with a $\beta = 0.6$ PIGMI geometry with radial support stem length of approximately 0.28λ. A slight improvement in Q was obtained when the stems were soldered in place. An additional measurement was made in which one of the four radial supports was converted into a stub tuner extending beyond the outer cavity wall. The result was similar to that shown in Fig. 3a.

Measurements with the $\beta = 1.0$ PIGMI geometry gave G's less than 80% of theoretical for a geometry with a stem length of about 0.35λ. A special, copper plated-aluminum cavity was built for the $\beta = 1.0$ PIGMI washer to make the stem length $\lambda/4$, but again, less than 80% of theoretical Q was measured for the $\pi/2A$ mode. A series of measurements was then made to look for effects as predicted in Fig. 3, by using an aluminum pillbox cavity and copper washers of different diameters, thus requiring different stem lengths. The predicted trends were not observed and there was no indication of a stem resonance effect.

Conclusions

Incomplete agreement between theoretical and experimental results on radial washer supports in the disk-and-washer structure indicate that radial stems should not be used unless further measurements and calculations show better results. There appears to be some agreement for the $\beta = 0.6$ cavity, but not for the $\beta = 1.0$ structure. The reduction in Q and Z presently observed for the $\beta = 1.0$ structure, at least, appears to preclude the use of radial stems. For low-beta cavities, it appears that radial stems should be about $\lambda/4$ long and have the smallest diameter consistent with other design constraints.

Acknowledgments

The authors would like to thank R. A. Jameson and D. A. Swenson for their participation in discussions related to this work.

References

1. V. G. Andreev, V. M. Belugin, V. G. Kulman, E. A. Mirochnik, and B. M. Pirozhenko, "Study of High-Energy Proton Linac Structures," in "Proceedings of the 1972 Proton Linear Accelerator Conference, October 10-13, 1972," Los Alamos Scientific Laboratory report LA-5115, 114 (1972).

2. S. O. Schriber, "Room-Temperature Cavities for High-Beta Accelerating Structures," Proc. of Conf. on Future Poss. for Electron Accel., Charlottesville, VA, January 1979, p. L-1.

3. J. M. Potter, S. O. Schriber and F. J. Humphry, "Experimental and Calculated Rf Properties of the Disk-and-Washer Structure," IEEE Trans. Nucl. Sci. NS-26, #3, 3763 (1979).

4. E. A. Knapp and D. A. Swenson, "The PIGMI Program at LASL," Proc. of 1976 Proton Linac Conf., Atomic Energy of Canada Ltd. Report No. AECL-5677, 230 (1976).

5. K. Halbach, R. F. Holsinger, W. E. Jule and D. A. Swenson, "Properties of the Cylindrical Rf Cavity Evaluation Code SUPERFISH," Proc. of 1976 Proton Linac Conf., Atomic Energy of Canada Ltd. Report No. AECL-5677, 338 (1976).

BEAM LOADING EXPERIMENTS WITH A SIDE-COUPLED STRUCTURE

G.E. McMichael, J. McKeown and J.S. Fraser
Atomic Energy of Canada Limited, Research Company
Physics Division, Chalk River Nuclear Laboratories
Chalk River, Ontario, Canada K0J 1J0

Summary

Experiments to investigate the performance of side-coupled structures under heavy beam loading have been carried out with the Electron Test Accelerator at Chalk River. Initially, an 18-cell structure was excited at 805 MHz by a 1.4 MeV cw beam. The induced power dissipated in the structure shows a square-law dependence upon beam current (0.013 kW/mA^2) up to 12 mA. With an externally applied field to give an energy gain of 0.1 to 0.2 MeV/m, beam was accelerated under conditions designed to achieve greater than 80% beam loading, i.e. more than 80% of the klystron applied power was converted into beam power. These conditions are important in applications of accelerators to nuclear breeding.

Introduction

In electro-nuclear breeding and other applications of high duty factor linacs, heavy beam loading of the structure is anticipated. In long accelerators with high duty factors, where the cost of rf power is a dominant factor, it is important not only that the structure have a high shunt impedance, but to an even greater extent, that the power from the generator be delivered to the beam with maximum efficiency. In the general case of high reactive beam loading,[1] which occurs when the synchronous phase is not zero, maximum energy transfer is obtained when the complex generator admittance is matched to the cavity admittance, as seen by the generator.

Most theoretical studies on beam loading have been carried out for pulsed linacs[2] or cyclic machines,[3] and the representations are not directly applicable to control systems developed for a high-power cw linac. There is a considerable imbalance between theory and experiment in this field,[4] and experimental data on the behavior of standing-wave systems at very high beam loading have not been previously reported.

An approximation to the principle of maximum energy transfer is employed in the combined resonance, amplitude and phase control circuits[5] of the Chalk River Electron Test Accelerator (ETA), by minimizing the reflected power. Ultimately, a dynamic matching device might be employed to reduce the reflected power to zero. With the first of the two accelerator structures delivering an electron beam of up to 22 mA at 1.4 MeV, beam loading experiments have been carried out in the second structure, with widely varying field amplitude and phase.

Experimental Arrangement

The Chalk River Electron Test Accelerator (Fig. 1) is dedicated to the study of the various

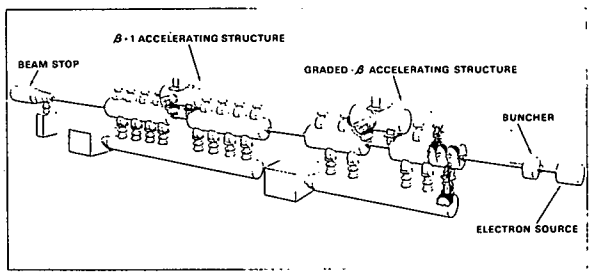


Fig. 1 Chalk River Electron Test Accelerator - 1.4 to 4 MeV, 0 to 25 mA cw.

accelerator properties which are important in the understanding of the behavior of a proton linac that might be used for breeding nuclear fuel. The ETA is comprised of an electron gun, a buncher, a graded-β structure, and a β=1 side-coupled structure modelled on the LAMPF design. Beams up to 22 mA cw have been accelerated so far. The energy is continuously variable between 1.4 MeV and 4.0 MeV.

The control system has been described previously[5,6] and differs somewhat from those of other machines. There are three separate control loops for amplitude, phase and resonance control, as shown in Fig. 2. Phase control is accomplished by varying the phase of the klystron drive. A mechanical tuner is used to keep each resonant structure at minimum reverse power. In this way reactive beam loading is not compensated by cavity detuning but rather by changing the impedance of the source.

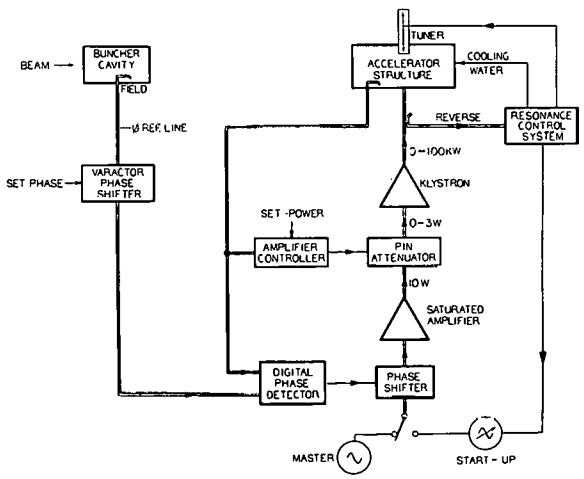


Fig. 2 Accelerator Structure Control System Block Diagram

The 18 accelerating cell, β=1 structure is powered by a 100-kW cw, 805-MHz klystron and dissipates 60 kW when a 4-MeV beam is required (accelerating gradient ≈ 0.8 MeV/m). Under these conditions, there is only sufficient power available to reach 40% beam loading. Beam loading in excess of 80% can, however, be achieved with the available rf power supply by reducing the accelerating gradient to between 0.1 MeV/m and 0.2 MeV/m.

The resonance control system is sufficiently flexible to allow the structure to run at any arbitrary power dissipation level. In the beam loading experiments, the amplitude and phase of the accelerating fields were kept constant to within 1% and 1° respectively.

Resistive Beam Loading Experiments

Effect on Impedance Match

To first order, if the centroid of a symmetrical beam bunch reaches the center of an accelerator cell gap when the field is maximum (beam phase $\phi_B = 0$), the beam acts as a purely resistive load on the cavity. The ETA accelerator structures are iris coupled to the waveguides; for the β=1 structure, the iris was machined to provide critical coupling at zero beam current. The progressive undercoupling as the beam current is increased at different accelerating gradients is shown in Fig. 3. The match changes with beam loading as follows[7]:

$$\sigma = \text{VSWR} = \frac{P_S + P_C}{P_S + P_B} \quad \text{(overcoupled)}$$

$$= \frac{P_S + P_B}{P_S + P_C} \quad \text{(undercoupled)}$$

$$P_C = P_S(\sigma_o - 1)$$

where: P_S = power dissipated in the structure, P_B = power added to the beam, P_C = power added to the beam to critically couple the structure to the transmission line, and σ_o is the VSWR with zero beam loading.

A key component in the resonance controller is a mechanical tuner in the bridge coupling cell. Because of the proximity of the tuning plunger to the iris coupler, the impedance match at zero beam current changes with tuner position such that σ_o varies from 1.0 to 1.2. A value of $\sigma_o = 1.16$ gives good agreement between theory and experiment.

Change in Q

When the structure is driven at a frequency ddiffering by Δf from the resonant frequency f_o, the admittance phase angle, ϕ_A, is given by

$$\phi_A = \tan^{-1} 2Q_L \frac{\Delta f}{f_o}$$

where Q_L ≡ loaded quality factor for the structure. For small perturbations about the tuner

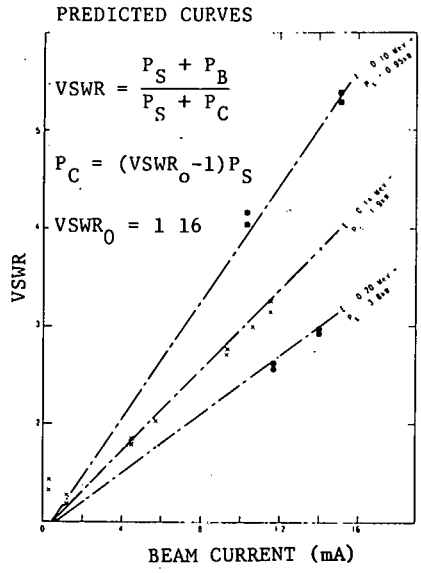


Fig. 3 Resistive Beam Loading - Impedance Match Changes

mid-position,

$$\Delta f = 80\ S\ \text{(kHz)}$$

where S is the linear tuner motion expressed as a fraction of its full range. ϕ_A was measured by connecting the inputs of a vector voltmeter to a field probe in an accelerator cell, and to a directional coupler in the waveguide. The cavity was detuned manually with the tuner and Q_L was calculated for beam loading factors up to 85% (see Fig. 4).

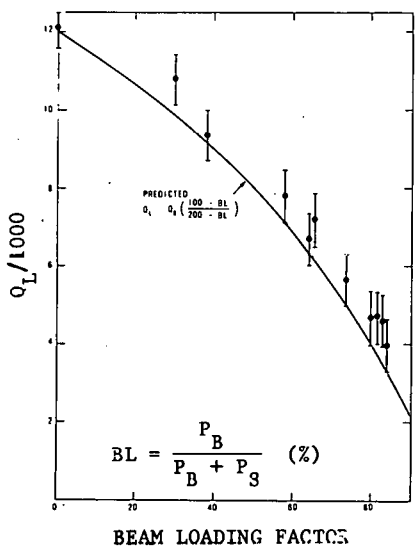


Fig. 4 Resistive Beam Loading - Q_L Changes

Beam loading affects Q_L in two ways. Let Q_o ≡ unloaded Q with no beam (for the β=1 structure, Q_o = 24000). Beam loading has no effect on the energy stored in the cavity (the amplitude controller maintains constant field), but the

internal energy loss per cycle is proportional to $P_S + P_B$. Therefore the "unloaded" Q with beam is given by

$$Q_b = Q_o \frac{P_S}{P_S + P_B}$$

However, beam loading also changes the impedance match or coupling to the transmission line so that

$$Q_L = \frac{Q_b}{1 + \frac{1}{\sigma}} = Q_o \cdot \frac{P_B}{2P_S + P_B}$$

for a structure critically coupled with zero beam. Or, in terms of the beam loading factor

$$BL \equiv \left(\frac{P_B}{P_S + P_B}\right)100 \quad \text{(percent)}$$

$$Q_L = Q_o\left(\frac{100 - BL}{200 - BL}\right).$$

In Fig. 4, this relation is shown to be in good agreement with the experimental data.

Field Tilts and Shunt Impedance

The amplitude of the field in the accelerating cells was found to tilt along the structure less than 2% (field depressed in the cells remote from the drive point at the bridge coupler) as beam loading was increased from 0 to 85%.

Calorimetric measurements of beam power delivered to the beam dump at the output of the β=1 structure and of structure dissipation power imply an effective shunt impedance of 33.6 ± 1 MΩ/m (35.4 ± 1 MΩ/m if the bridge coupler dissipation is excluded). A similar value was obtained when the beam energy was determined from neutron threshold measurements (γ,n) using a D_2O target after the beam stop. No change in shunt impedance was observed for accelerating gradients of 0.1 to 0.81 MeV/m and beam loading factors of 10 to 85%. The theoretical effective shunt impedance for this structure is 47.6 MΩ/m (excluding the bridge).

Reactive Beam Loading Experiments

For the beam phase angle $\phi_B \neq 0$, the beam admittance is complex. The admittance phase angle ϕ_A was measured while ϕ_B was varied (Fig. 5). A strong dependence on beam loading was noted. The resonance controller permits small variations of the structure resonant frequency about the accelerator frequency during an experimental run, causing a scatter in the measured values. Corrections for this effect have been made and the data shown in Fig. 5 are accurate to ± 2° for the 85%, and ± 1° for the 67% beam loading cases.

The impedance match of the accelerator to the transmission line was examined as the beam phase was varied. The complex admittance of the beam[1], $(I/V)e^{j\phi_B}$, combined with the conductance of

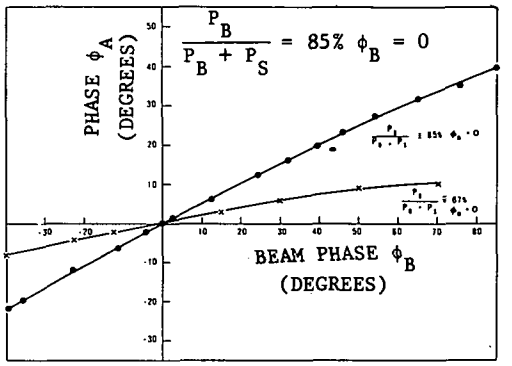


Fig. 5 Reactive Beam Loading - Transmitted Phase Angle Changes

the tuned cavity gives, to first order,

$$\sigma = \left(\frac{P_S + P_B}{P_S + P_C}\right)\left|1 + j\,\frac{P_B}{P_B + P_C}\tan\phi_B\right|.$$

In second order, $\tan\phi_B$ and P_B averaged over the beam phase distribution, should be used. The experimental data (Fig. 6) for two runs agree well with the predicted VSWR, the match varying relatively slowly while the incremental beam power changes by more than a factor of two.

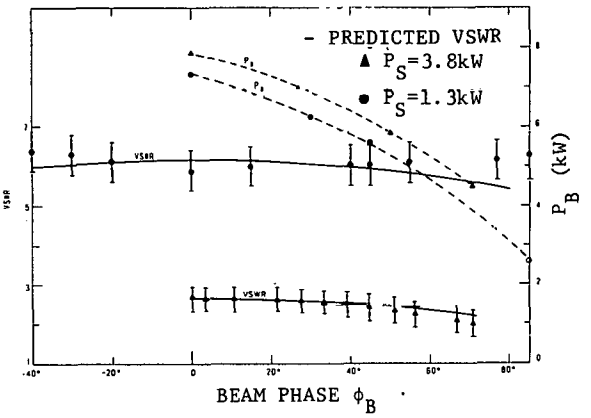


Fig. 6 Reactive Beam Loading - Impedance Match Changes

Cavity Excitation by a Bunched Beam

Under normal operation, an accelerator structure is driven by two sources: the external generator (klystron in the present work) and the bunched beam itself. To investigate the coupling between the beam and structure, the external generator for the β=1 structure was operated with zero drive. Up to 22 mA from the graded-β structure (1.4 MeV) was drifted through the β=1 structures and the mechanical tuner manually adjusted to keep the structure resonant at the accelerator frequency (tuner adjusted to maximize the induced field in the structure). The phase and amplitude of the induced field were measured. As expected, the phase was shifted 180° from the

normal accelerating case, indicating that the structure appears as a resistive load to the beam.

Field amplitude was measured using probes in the accelerating cells and a directional coupler in the waveguide. The waveguide was left connected to the klystron through a 3 dB ferrite isolator in the waveguide. The power dissipated in the structure (Fig. 7) was shown to vary as the square of the beam current for currents up to 10 mA, and approximately linearly with beam current above 12 mA. A roughly equivalent power flow was observed in the waveguide with a negligible amount reflected back from the isolator/klystron combination. Thus the power lost by the beam was roughly twice the power dissipated in the structure, a fact that was confirmed by calorimetric measurements at the beam stop after the β=1 structure.

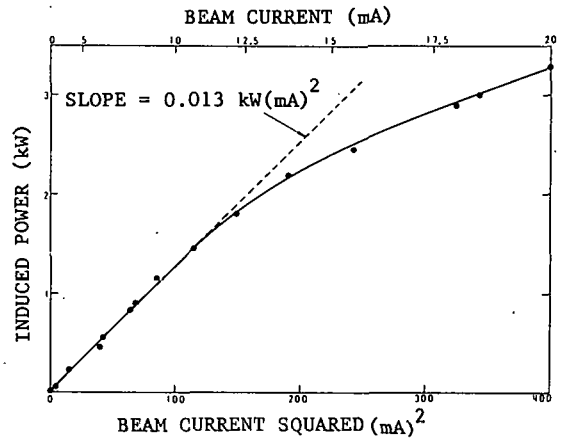


Fig. 7 Cavity Excitation by Bunched 1.4 MeV Beam - Structure Dissipated Power

Using the fact that the power lost by the beam is approximately twice the power dissipated in the structure, the fractional energy loss as a function of beam current can be plotted (solid curve in Fig. 8). Little additional deceleration occurs above 12 mA which contrasts sharply with the situation under 10 mA where the fractional energy loss is proportional to the current. Calculating shunt impedance in the same manner as for the accelerating case,

$$Z_{SH} = \frac{(\text{Energy change per meter})^2}{\text{Power in structure per meter}}$$

gives the dashed curve in Fig. 8.

The proportionality of induced power to beam current squared, and energy loss to beam current, observed here for currents up to 10 mA, has been reported by others.[9] Obviously with a finite input energy beam, these relations must fail before all the energy has been extracted from the beam. We are unable to significantly vary the energy of the input beam to the β=1 structure, so cannot confirm our suspicion that the 10 mA break-point in the curves is beam energy dependent. The shunt impedance value below 10 mA is surprisingly low; at 15.2 MΩ/m it is less than half the value (33.4 MΩ/m) measured when the structure was externally powered.

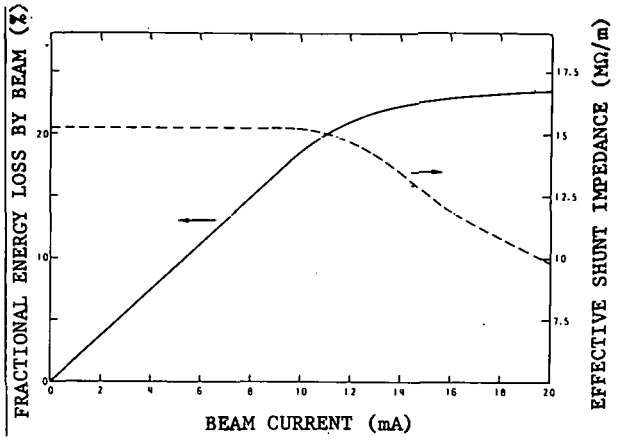


Fig. 8 Cavity Excitation by Bunched 1.4 MeV Beam - Power Lost by Beam and Structure Shunt Impedance

The excitation of spurious modes, a possible explanation for this discrepancy, is under study.

Attempts to represent beam loading with the vector model favored by many theoretical studies have so far been unsuccessful. However an equivalent circuit model is successful in predicting changes in VSWR with beam current and beam phase. Fundamental considerations are adequate to understand the observed changes in Q with beam loading. For a more complete understanding of the beam-cavity interaction further experiments are necessary.

References

1. M.J. Lee, "Steady-State Beam Loading of a Standing Wave Linac rf System", Proc. Proton Linear Accelerator Conf., BNL-50120, 114 (1968).
2. R.A. Jameson, "Automatic Control of rf Amplifier Systems", ibid., 149.
3. P.B. Wilson, "Beam Loading in High-Energy Storage Rings", Proc. IX Int. Conf. on High Energy Accelerators, CONF 740522, 57 (1974).
4. A.M. Sessler, "Beam-Surrounding Interactions and the Stability of Relativistic Particle Beams", IEEE Trans. Nucl. Sci., NS-18, No. 3, 1039 (1971).
5. J. McKeown, J.S. Fraser and G.E. McMichael, "Field Control in a Standing Wave Structure at High Average Beam Power", Proc. Proton Linear Accelerator Conf., Atomic Energy of Canada Limited, Report AECL-5677, 291 (1976).
6. G.E. McMichael and J. McKeown, "Operational Experience with Coupled-Cavity Structures in a High Duty Factor Accelerator", IEEE Trans. Nucl. Sci., NS-26, No. 3, 4108 (1979).
7. R. McConnell, "Rf Design Formulae for SPEAR", SPEAR-164 (1973).
8. H.C. Hoyt, D.D. Simmons and W.F. Rich, "Computer Designed 805-MHz Proton Linac Cavities", Rev. Sci. Inst. 37, 755 (1966).
9. M. Kuntze, K. Mittag and J.E. Vetter, "Beam Cavity Interactions in a Superconducting Proton Accelerator Structure", IEEE Trans. Nucl. Sci. NS-16, No. 3, 1023 (1969).

DETUNING EFFECT IN A TRAVELING WAVE TYPE LINAC

S. Arai, K. Kobayashi, E. Tojyo, and K. Yoshida
Institute for Nuclear Study, University of Tokyo
Tanashi, Tokyo, Japan

Summary

A 15-MeV traveling wave type electron linac is used as the injector for the 1.3-GeV electron synchrotron at the Institute for Nuclear Study, University of Tokyo. The resonant frequency of this accelerator waveguide is 2758.00 MHz at 30°C. The performance of the linac, however, is improved when it is operated with a frequency which is higher than the design value by 200-400 KHz. It is shown that the detuning due to the beam loading is serious in such an accelerator waveguide in which the buncher and regular sections are combined, and the detuning effect can approximately be compensated by changing the operating frequency. The detuning effect in the traveling wave-type accelerator waveguide was studied both from experimental and theoretical aspects by using a short test waveguide.

Introduction

The microwave amplitude reduction due to beam loading results in decreasing the energy gain, while the microwave phase variation due to the detuning effect not only reduces the beam energy, but also deteriorates the energy spectrum by upsetting the synchronism between the electron bunch and microwave. The detuning effect has been studied by many authors for proton linacs, synchrotrons and storage rings. The traveling wave (TW) electron linac, however, has had little study except for the resistive beam loading effect.[1] In a linac used as the injector for an electron synchrotron, a narrow beam energy spread is required, so that the detuning effect is serious. A 15-MeV TW type electron linac[2] is the injector for the 1.3 GeV electron synchrotron at the Institute for Nuclear Study (INS), University of Tokyo. The INS linac consists of a single accelerator waveguide, which includes a buncher section and an accelerator section. In this case, the phase shift produced by beam loading in the buncher section is carried along. The beam loading in the accelerating section becomes reactive, and the detuning effect is severe. In designing the INS linac, the effect of resistive loading was considered but that of reactive loading was not.

Operating Characteristics of the INS Linac

The specifications and microwave characteristics of INS linac are summarized in Tables I and II. It has been confirmed by low power test that the accelerator waveguide was constructed with the resonant frequency within ±100 KHz of the design value. In the actual operation, however, it is found that the capture efficiency of injected beam, the energy gain and the energy spectrum of output beam are improved by setting the operating frequency higher than the design value of 2758.00 MHz, by 200-400 KHz. The above operating characteristics measured in relation with the beam current and operation frequency are shown in Figs. 1, 2 and 3. Since the difference between the optimum and design frequencies increases in proportion to the accelerated beam intensity, these phenomena seem to be due to the detuning effect in the accelerator waveguide. To examine the phase relation between the electron bunch and the accelerating field when the operating frequency is changed, the microwave phase shift caused by the beam loading in the accelerator waveguide has been measured. The phase shift is obtained by comparing the rf phases of the input-to-output rf with and without beam loading. The experimental result is shown in Fig. 4. It is seen from the behavior of the phase shift, that the bunch surmounts the crest of the accelerating field when the operating frequency is changed to higher values. And, it is also clear that the acceleration efficiency is best for the frequency that produces a phase shift slightly greater than zero.

Table I Specification of INS Linac

Length of accelerator structure	∿2.5 cm
Type of construction	semi constant gradient
Number of cavities in buncher section	9 (3 step)
Number of cavities in regular section	51 (4 step)
Accelerating mode	2/3 π
Frequency	2758.00 MHz (at 30°C)
Unloaded Q	12000
Total voltage attenuation	0.45 neper
Filling time	0.5 μsec
Input RF power	7 MW
Injection voltage	100 KV
Beam energy	15 MeV
Beam current	250 mA
Beam pulse length	2 μsec
Energy spread	5 %
Repetition rate	21.5 pps

Table II Dimensions and Microwave Characteristics of Accelerator Waveguide

	2a (mm)	2b (mm)	d (mm)	f_0 (MHz)	v_p/C	v_g/C	r_0 (MΩ/m)
BI	29.795	88.236	28.093	2758.069	0.7753	3.09×10^{-2}	29
BII	27.111	86.364	35.314	2758.027	0.9746	2.39	49
BIII	26.522	86.140	35.900	2758.059	0.9908	2.26	50
RI	25.534	85.842	36.233		1.0000	1.86	50
RII	24.049	85.469	26.233		1.0000	1.62	53
RIII	22.255	85.056	36.233	2758.005	1.0000	1.13	55
RIV	19.893	84.587	36.233	2758.027	1.0000	0.79	58

* B and R in the first column mean the buncher and the regular sections, respectively. f_0, v_g/C, and r_0 are experimental values.

Experiment with a Test Accelerator Waveguide

In the actual linac, information about the detuning effect is obtained only from the output beam or the rf power to the dummy load, and the interaction of the bunch with the accelerating field along the waveguide cannot be directly observed.

In order to investigate the correlation between the TW accelerator waveguide and the detuning effect, a test accelerator waveguide was fabricated. As shown in Table III, the structure of the test waveguide was exactly the same as a part of the regular section of the INS linac. By passing the bunched beam from the INS linac through the test waveguide, the detuning effect was studied systematically and analytically. The measurement system is illustrated in Fig. 5. The microwave power to excite the test waveguide was distributed from the traveling wave tube amplifier in the rf system of the linac, so that the electron bunch and the microwave in the test waveguide were synchronous with each other. The phase relation between the bunch and the rf wave was determined by the line stretcher (A) which allowed various conditions of beam loading to be produced.

Table III Parameters of Test Accelerator Waveguide

Type of construction	constant impedance
Number of cavities	6
Diameter of disk hole (2a)	19.893 mm
Diameter of cylinder (2b)	84.587 mm
Distance between disks (d)	36.233 mm
Disk thickness (t)	5.000 mm
Accelerating mode	2/3 π
Frequency	2758.00 MHz (at 30°C)
Normalized group velocity v_g/c	7.97×10^{-3}
Normalized phase velocity v_p/c	1.00
Unloaded Q	11400
Peak shunt impedance	58.0 MΩ/m

The variation of the output power and the phase shift due to the beam loading were measured by letting the bunch ride on the various phase of the external driving field. In this measurement, the INS linac was operated with the resonant frequency of the test waveguide without the beam loading. The results are shown in Fig. 6. The rf power released from the exit coupler varied sinusoidally with the phase on which the bunch rode, and the phase shift of the accelerating field varied most steeply when the bunch was near the crest of the accelerating field. These results are similar to that for the standing wave accelerator.[3]

Studies were made to see if the phase shift due to the reactive beam loading could be compensated by changing the frequency of the external driving field. The phase shifter was adjusted with the beam switched off to minimize the vector summation of two microwaves to the magic-T_{cc}. When the beam was switched on, the phase of the accelerating field shift due to the reactive beam loading, and the vector summation of the two microwaves, deviated from the minimum value. To minimize the vector summation again, the frequency of the external driving field was adjusted and the degree of the frequency change was recorded.

As seen from the experimental results in Fig. 7, the frequency must be changed to lower or higher value for the phase shift compensation when the bunch is before or behind the crest of the accelerating field, respectively.

Theoretical Analysis

The detuning effect in the test accelerator waveguide is analysed here by normal mode analysis for a microwave cavity, which has been developed by J.C. Slater, T. Nishikawa and others.[4-7]

The TW accelerator waveguide can be regarded as composed of a chain of unit resonant cavities. The wave equation in the unit cavity is represented as

$$\frac{d^2}{dt^2}\int \bar{E}\bar{E}_a^* dV + \frac{\omega_a'}{Q_0}\frac{d}{dt}\int \bar{E}\bar{E}_a^* dV + \omega_a'^2 \int \bar{E}\bar{E}_a^* dV = -\frac{1}{\epsilon_0}\frac{d}{dt}\int \bar{J}\bar{E}_a^* dV \quad , \tag{1}$$

where $\bar{J}$ is the current density of the electron beam, $\bar{E}$ is the electric field in the unit cavity, $\bar{E}_a$ is the a-th normal mode field in it, ω_a' is the resonant frequency of the unit cavity without the beam loading, Q_0' is the unloaded Q of the unit cavity and ϵ_0 is the dielectric constant of vacuum. $\bar{E}_a$ can be written as $\bar{E}_a = \bar{E}_{a0}e^{-jkz}$ in terms of the propagation constant of the microwave, k, and the amplitude of the normal mode field, $\bar{E}_{a0}$. In the TW type accelerator waveguide, the stored energy of the microwave is propagated with the group velocity v_g. It can, therefore, be considered that the unit cavity, for which eq. (1) holds, moves along the waveguide with the velocity v_g.

The right hand side of eq. (1) represents the external force of the forced oscillation and can be expressed as

$$-\frac{1}{\epsilon_0}\frac{d}{dt}\int \bar{J}\bar{E}_a^* dV = -j\frac{2FI_0E_{a0}\omega}{\epsilon_0}e^{j(\omega t+\phi_b)} \quad , \tag{2}$$

where ϕ_b is the phase of the external field on which the bunch rides, F is the form factor of the bunch and I_0 is the peak beam current. F is assumed here to be unity.

The relation between the amplitude of the normal mode field E_{a0} and the peak shunt impedance r is given by the equation,

$$r = \frac{2Q_0E_{a0}^2}{\epsilon_0\omega_a'} \quad . \tag{3}$$

When the axis of the accelerator waveguide is

defined as the z-axis, the entrance of the waveguide being the origin of the coordinates, the electric field at z is obtained by substituting the relation, $t = z/v_g$, into the solution of eq. (1), as:

$$E(z) = \{E_0 e^{-\frac{\omega}{2v_g Q_0}z} - I_0 r e^{j\phi_b}(1-e^{-\frac{\omega}{2v_g Q_0}z})\} \cdot e^{j(\omega t - kz)} \quad , \tag{4}$$

where E_0 is the electric field amplitude at z = 0 and t = 0. The first and second terms of the right hand side in eq. (4) represent the attenuation of the external field and the build-up of the beam induced field, $E_b = I_0 r$, respectively.

The phase shift of the accelerating field is regarded to be the result of the detuning of the accelerator waveguide due to the beam loading. The wave equation in the unit cavity, eq. (1), is rewritten by using the relation, $\int \vec{E}\vec{E}_a^* dv = \text{constant} \cdot e^{j\omega t}$, as:

$$j(\frac{\omega}{\omega_a'} - \frac{\omega_a'}{\omega}) + \frac{1}{Q_0} = \frac{j}{\varepsilon_0 \omega \omega_a'} \frac{\frac{d}{dt}\int \vec{J}\vec{E}_a^* dV}{\int \vec{E}\vec{E}_a^* dV} \quad . \tag{5}$$

The imaginary part in the right hand side of eq. (5) represents the reactive component of the beam loading and its contribution to the resonant angular frequency shift, $\Delta\omega = \omega - \omega_a'$ is:

$$\Delta\omega_i = \frac{\omega_a'}{2Q_0} \frac{-E_0 T E_b \sin\phi_b}{E_0^2 T^2 + E_b^2 (1-T)^2 - 2E_0 T E_b (1-T)\cos\phi_b} \quad , \tag{6}$$

where T represents the attenuation of the microwave in the accelerator waveguide, $e^{-\frac{\omega}{2v_g Q_0}z}$. The real part represents the resistive component, and gives the beam quality factor, Q_b:

$$\frac{1}{Q_b} = \frac{1}{Q_0} \frac{E_0 T E_b \cos\phi_b - E_b^2(1-T)}{E_0^2 T^2 + E_b^2 (1-T)^2 - 2E_0 T E_b (1-T)\cos\phi_b} \quad . \tag{7}$$

The total Q, Q_T, is given by $Q_T = Q_0 Q_b/(Q_0+Q_b)$, and the contribution to the resonant frequency shift is :

$$\Delta\omega_r = \omega_a' (\sqrt{1 - (\frac{1}{2Q_T})^2} - 1) \quad . \tag{8}$$

The whole resonant angular frequency shift due to the beam loading is given by eqs. (6) and (8) in the following form,

$$\Delta\omega = [\{\omega_a' - \frac{\omega_a'}{2Q_0} \frac{E_0 T E_b \sin\phi_b}{E_0^2 T^2 + E_b^2 (1-T)^2 - 2E_0 T E_b (1-T)\cos\phi_b}\} \cdot \sqrt{1-(\frac{1}{2Q_T})^2} - \omega_a'] \tag{9}$$

When the resonant frequency of the accelerator waveguide changes by Δf, the phase velocity of the accelerating field is, assuming the group velocity to be constant around the resonant frequency, given in the form,

$$v_p = \frac{v_g \lambda_g f_0}{v_g - \lambda_g \Delta f} \quad , \tag{10}$$

where λ_g and f_0 are the guide wavelength of the accelerating field and the original resonant frequency.

The phase difference between the accelerating fields with and without the beam loading can be written as

$$\Delta\phi = 2\pi f_0 L(\frac{1}{v_{p0}} - \frac{1}{v_p}) \quad , \tag{11}$$

where v_p is the phase velocity without the beam loading and L is the length along the accelerator waveguide passed by the waves. The rf power at the position z is expressed in terms of the electric fields as

$$P(z) = P_0(z)[1+\{\frac{E_b(1-e^{-\frac{\omega}{2v_g Q_0}z})}{E_0 e^{-\frac{\omega}{2v_g Q_0}z}}\}^2 - 2\frac{E_b(1-e^{-\frac{\omega}{2v_g Q_0}z})}{E_0 e^{-\frac{\omega}{2v_g Q_0}z}}\cos\phi_b] \quad , \tag{12}$$

$$P_0(z) = \frac{v_g Q_0}{r\omega} E_0^2 e^{-\frac{\omega}{v_g Q}z} = P_{in} e^{-\frac{\omega}{v_g Q_0}z} \tag{13}$$

where P_{in} is the input power to the accelerator waveguide and $P_0(z)$ is the rf power at z, without the beam loading. Numerical results are shown in Fig. 6.

Finally, the subject of compensating the phase shift due to the beam loading by changing the operation frequency will be discussed. As seen in eq. (9), the resonant frequency varies with the position along the accelerator waveguide. Therefore, when the operation frequency is changed to make the phase shift zero at the exit of the waveguide, the new frequency is a certain mean of the resonant frequencies of the cells in the accelerator waveguide.

The value of frequency change for the compensation as defined above has been calculated as a function of the beam current and the phase of the external field on which the bunch initially rides. The calculated result is compared with the experiment in Fig. 7. It is seen that both results agree well with each other.

Analysis of the Operating Characteristics of INS Linac

A program for tracing the beam based on the above mentioned theory of the detuning effect, has been developed in order to analyze the operating characteristics of INS linac. In the beam trace calculations to date, the rf power loss due to the beam loading and the wall resistance of the accelerator waveguide have been taken into account, but the detuning effect due to the beam loading has not been considered.

In the calculation, the following assumptions are used: 1) the group velocity of the microwave remains constant when the resonant frequency varies due to the beam loading, or the operating frequency is changed from the resonant frequency of the accelerator waveguide; 2) since the frequency passband of the TW linac is wide, the rf reflection due to the detuning of the accelerator waveguide can be neglected; 3) the value of the phase shift due to the beam loading, when the linac is operated with the frequency different from the resonant frequency as determined from the mechanical dimensions, is obtained by the same method as for the case of operating with the resonant frequency.

Calculated results, together with the experimental results of the output beam current and the beam energy, are shown in Figs. 1 and 2, respectively. The calculation of the energy spread is shown in Fig. 8. The calculated results of the microwave phase shift due to beam loading by passing through the whole accelerator waveguide are indicated in Fig. 4, with the experimental results. Since the present program gives a good explanation of the experimental results at the exit of waveguide, it is concluded that the methods of the analysis and the calculation are both correct. The state of detuning inside the accelerator waveguide, which cannot be directly measured, has been estimated. The results of the resonant frequency shift, the phase shift due to the beam loading, and the effective loading angle of the bunch, are indicated in Fig. 9.

Conclusion

From the experimental results and the theoretical analysis, it has been confirmed that the detuning effect on the accelerating field deteriorates the acceleration performance of the linac which performs bunching as well as the beam acceleration in a single accelerator waveguide.

The detuning effect can be compensated fairly well by taking the operating frequency higher than the design value.

The disks and the cylinders of the waveguide can be machined with an accuracy of a few μm, and the accuracy of the phase advance in the accelerator waveguide is better than three degrees. This mechanical accuracy has been regarded to be of major importance in providing an electron beam with as narrow energy spread as possible. Even if the accelerator waveguide is constructed with extreme mechanical accuracy, however, it is of little use unless the detuning effect due to the beam loading, which causes the phase shift amounting to some tens of degrees, is taken into account.

The ideal design for the future accelerator waveguide including a buncher section should be as follows: when very narrow energy spread is required, as in the case of an injector for a synchrotron, each cavity of the accelerator waveguide should be designed so as to resonate at the operating frequency under the expected beam loading conditions. However, it is complicated and not practical to make an accelerator waveguide with cavities having different resonant frequencies. It is better to design the cavities of the waveguide to yield the phase advance which is correct when the beam loading exists. Although such a linac is, to be exact, for a specific amount of beam loading, the average performance will be much better than that for no beam loading. The phase advance for each cavity can easily be determined by the beam loading detuning theory presented in this work.

Reference

1 J.E. Leiss, "Beam Loading in Linear Accelerators", IEEE Trans. on Nucl. Sci. NS-12, 566 (1965).

2 T. Katayama, S. Arai, K. Yoshida and J. Tanaka, "The Construction of 15-MeV Linear Accelerator as Injector for INS Electron Synchrotron", INS-Report 240 (1975).

3 S. Arai, T. Katayama, E. Tojyo and K. Yoshida, "Beam Loading Effects in a Standing Wave Accelerator Structure", INS-TH-118 (1978).

4 J.C. Slater, "Microwave Electronics", Reviews of Modern Physics, 18 441 (1946).

5 T. Nishikawa, "Normal Mode Analysis of Standing Wave Linacs - Field Excitation and Beam Loading in Linac Cavities", BNL Accelerator Dept. Internal Report AADD-87 (1965).

6 R. Beringer and R.L. Gluckstern, "On the Normal Modes in Linac Structures", Yale Univ. Internal Report Y-9 (1964).

7 M. Bell, "Normal Mode Analysis of Standing Wave Linacs and the New Linac", CERN/MPS/DL 75-3 (1975).

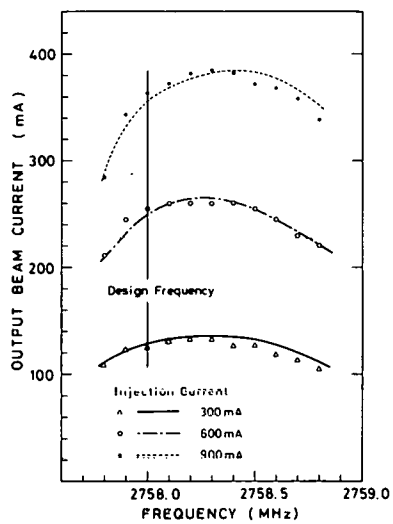


Fig. 1 Frequency dependence of the output beam current of the linac for the injection currents of 300 mA, 600 mA and 900 mA. The curves are calculations.

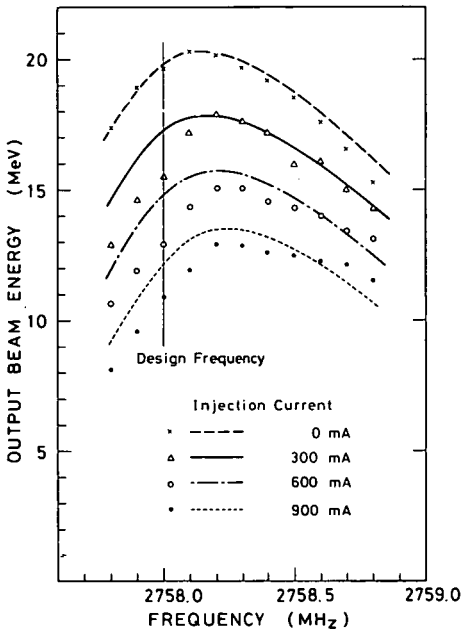


Fig. 2 Frequency dependence of the output beam energy of the linac.

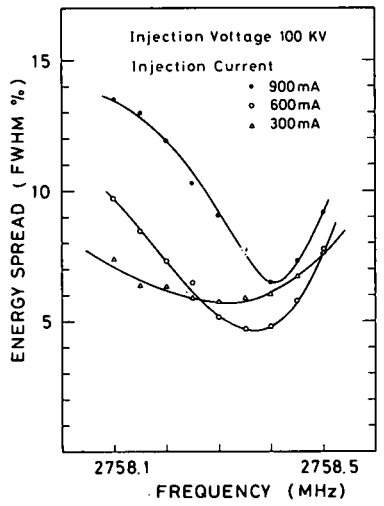


Fig. 3 Frequency dependence of the energy spread of the output beam. The solid lines are the best fit curves to the experimental values.

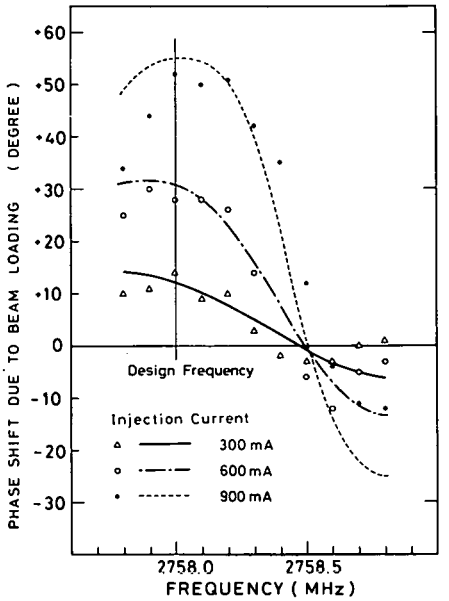


Fig. 4 Frequency dependence of the phase shift due to the beam loading.

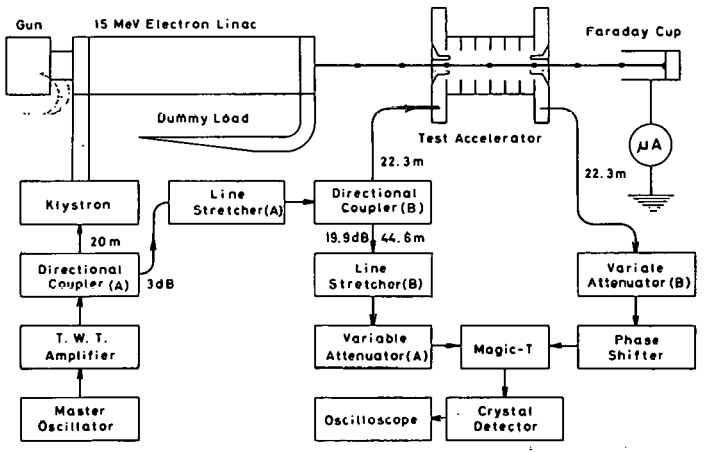


Fig. 5 Experimental setup for investigating the detuning effect in the test waveguide.

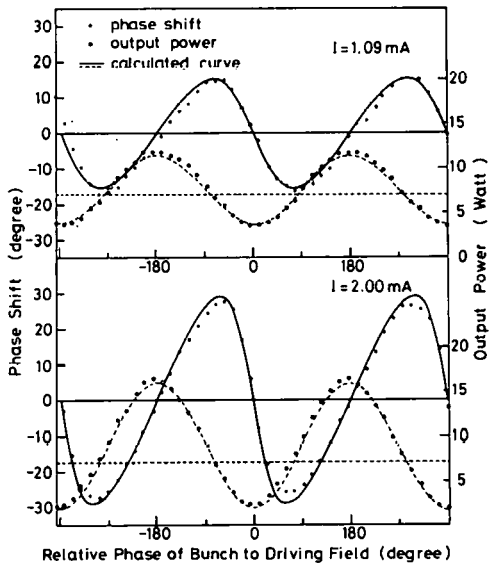


Fig. 6 Phase shift and output power of the microwave riding the bunch on the various phase. Input power is 8.2 Watt.

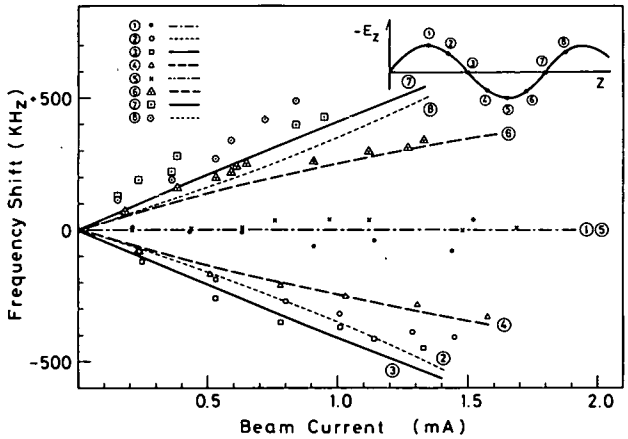


Fig. 7 Frequency change needed in compensating the phase shift due to the beam loading. Input power is 8.7 Watt.

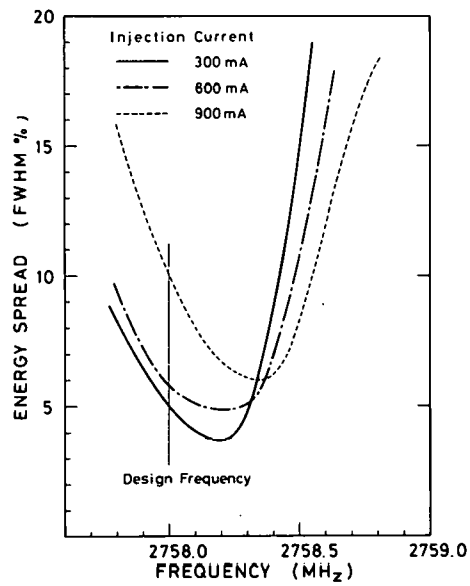


Fig. 8 The calculated result for the frequency dependence of the energy spread.

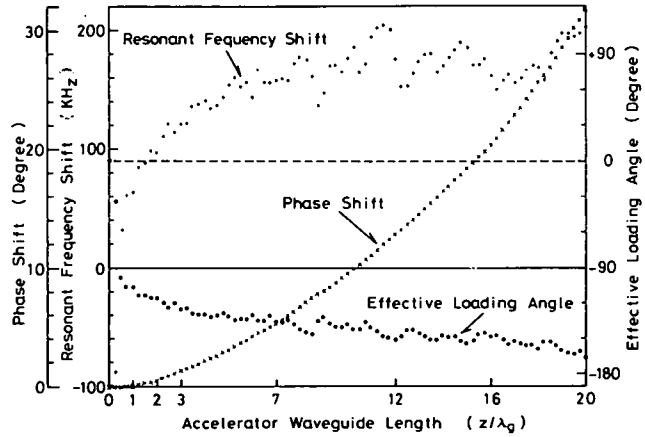


Fig. 9 Calculation of phase shift, resonant frequency shift and change of the effective loading angle along INS linac for the operation frequency of 2758.00 MHz.

Discussion

Miller, SLAC: I believe J. Haimson has worked on this same problem and many have reported on his work in one of the IEEE Particle Accelerator Proceedings, or perhaps in the linear accelerator book edited by Septier.

My question is this: since the phase detuning is dependent on beam intensity, doesn't it make sense to correct for the phase detuning by adjusting the operating frequency as you have done?

Arai: The designed beam current of the INS linac is about 200 mA.

Miller: Or can one perhaps pick an intermediate current over the range of which you want to run and then have a pretty good design over a wide range?

Leiss, DOE: Of course with a single cell machine you have, not only possible beam dc tuning, but also the bunching and stable phase angle depend on current, so it is very complicated in a one section machine.

Miller: In a multiple section machine you can always correct for this effect by appropriately phasing the downstream sections. And I think it does not have a striking effect on the bunching itself, rather on the phase with which the beam rides after it essentially reaches the velocity of light. This occurs because the bunching occurs very early in the structure.

Arai: I agree with your opinion.

PARTICLE ACCELERATION WITH TE_{011} CAVITY

Z. D. Farkas
Stanford Linear Accelerator Center
Stanford University, Stanford California 94305

Summary

Presently, the maximum effective electric field, E_a, in an accelerating structure is limited by the available peak rf power. If the structure is superconducting, the peak power requirements are reduced by several orders of magnitude, but E_a is limited by electron loading caused by surface electric fields. A right circular cylinder TE_{011} cavity has no surface electric fields and therefore, E_a is not limited by electron loading, but can reach a much higher value, which is limited by magnetic breakdown. A particle traversing the cavity along a chord of a cylinder wall circle gains a net voltage. This paper calculates the shunt resistance of a TE_{011} structure. It concludes that for the same E_a, a 4.2°K TE_{011} structure at 500 MHz requires 1/1000 the peak power and one fourth the average power of a non-superconducting TM_{010} structure, and can sustain an E_a several times greater than presently allowed by a superconducting TM_{010} structure. Acceleration by a TE_{111} right circular cavity is also considered.

Cavity Fields

The TE_{011} cavity fields are:

$$H_z = HJ_o(3.832r/a)\sin(\pi z/L)$$
$$E_\phi = H\eta(\lambda_c/\lambda)\,J_1(3.832r/a)\sin(\pi z/L)$$
$$H_r = H(\lambda_c/\lambda_g)\,J_1(3.832r/a)\cos(\pi z/L) \quad ,$$

where:
a is the radius and L is the length of the cavity. The relative field values are shown in Fig. 1. Using $PQ = \omega U$

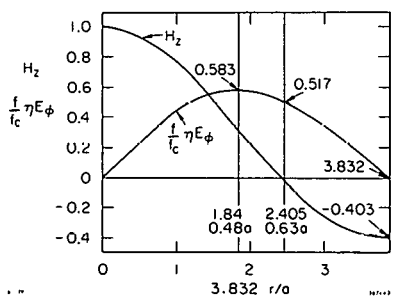


Fig. 1. Relative field values along a radius at z = L/2.

and integrating E^2 or H^2 over the volume of the cavity to obtain U, we have:

$$H = H_{zm} = 2\sqrt{2}\,(D/L)/\pi\eta\lambda\,(D/\lambda)^{5/2}(PQ)^{1/2}; \quad D = 2a$$

To obtain Q, it is necessary to integrate the square of magnetic field over the cavity surface. It is given by:

$$QR_s = 722[1+0.168(D/L)^2]^{1.5}/[1+0.168(D/L)^3]$$

For copper, $R_s = 2.61 \times 10^{-4} f^{1/2}$. R_s is the surface resistance in ohms, f is the frequency in MHz. Thus, for a given power dissipated in the cavity, the value of the maximum electric field, $E_{\phi m}$, and E_ϕ at any point in the cavity can be obtained.

TE_{011} Cavity Shunt Resistance

After traversing a path tangent to the E_ϕ circle, located at the middle of the cavity axis, as shown in Figs. 2 and 3, a charged particle gains a voltage, V, given by:

$$V = 2\int_o^{x_o} E_x\,dx \quad ,$$

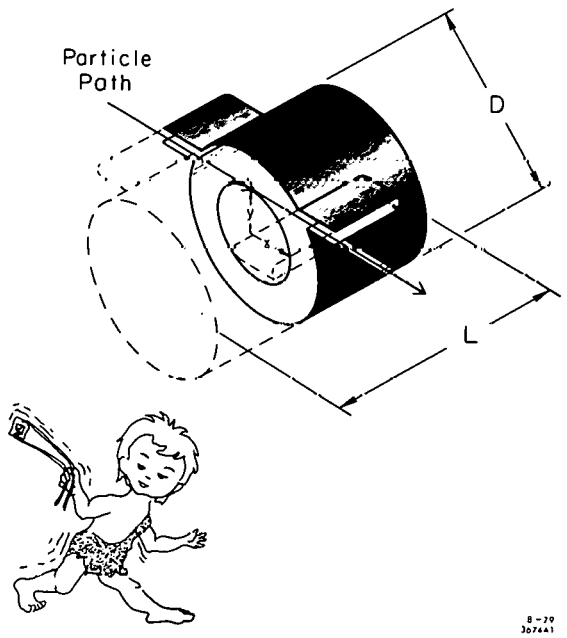


Fig. 2. Electric field circle and beam path in a TE_{011} cavity.

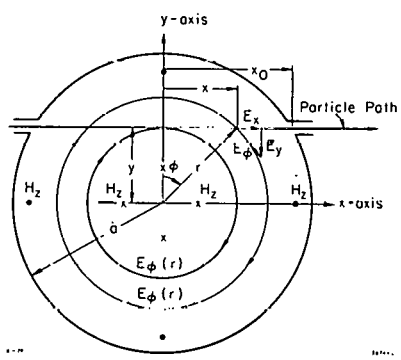


Fig. 3. Coordinate system and field lines at z = L/2.

where E_x is the amplitude of the instantaneous electric field in the x direction, as seen by a particle which arrives at the y-axis when the electric field is maximum. $E_x = E_{\phi m}$ at y = 0.48a and x = 0. E_x decreases from its maximum value due to 3 factors:

1. The space factor S_f; the amplitude of E_ϕ decreases as r deviates from r = 0.48a.
2. The direction factor D_f; the x component of E_ϕ decreases as we move away from the y-axis.

3. The time factor, T_f; E_ϕ decreases with time as we move away from the y-axis. Thus,

$$E_x = E_{\phi m} S_f D_f T_f \quad ,$$

where

$$S_f = J_1(3.832r/a)/J_1(1.84)$$
$$D_f = \cos\phi = y/r$$
$$T_f = \cos(2\pi x/\lambda)$$
$$r = (x^2 + y^2)^{\frac{1}{2}}$$

The value of E_x as a function of x/a at y = 0.48a with D/L = 1 is plotted in Fig. 4. After integrating $E_x dx$

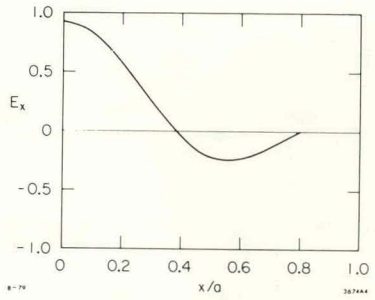


Fig. 4. Accelerating electric field, E_x, vs normalized distance, x/a.

numerically the voltage change along the particle path per Watt dissipated in the cavity is obtained, and hence its shunt resistance. The ratio of the TM_{010} shunt resistance to the TE_{011} shunt resistance for a $\lambda/2$ length cavity, which is defined as the degradation factor, D_f, of a TE_{011} cavity is 39:1. Nevertheless, a superconducting TE_{011} cavity requires less rf and line power than a copper TM_{010} cavity.

The rf and line power ratios which are defined as the rf and line power improvement factors, respectively, are:

$$I_{frf} = S_{if}/D_f, \qquad I_{f\ell p} = I_{rf}/E_{\ell rf} R_{eff}$$

where S_{if} is the superconducting (surface resistance) improvement factor, $E_{\ell rf}$ is line-to-rf power klystron efficiency, and R_{eff} is the refrigeration factor. For Niobium[1] at 4/2°K: $S_{if} = 10^9 f^{-1.5}$, $R_{eff} = 350$. Assume $E_{\ell rf} = 0.7$. The rf and line power improvement factors are shown in Fig. 5.

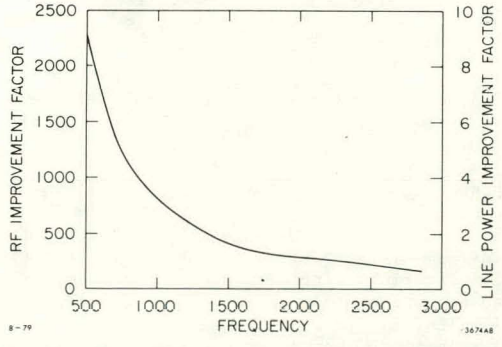


Fig. 5. Rf and line power improvement factors vs frequency.

Why not use superconducting TM_{010} cavities? One reason is that at frequencies less than 1 GHz, the effective accelerating field of a superconducting TE_{011} cavity, 14 MeV/m, is greater than can be sustained by a superconducting TM_{010} cavity. The electric field lines are generated by induction and do not end on charges. (The "hang-loose" mode.) Thus, the problem of multipactoring, which has so far resisted solution, is bypassed. True, the beam hole creates a surface electric field, but the field is localized, and is smaller than the TM_{010} surface fields. But even if not limited by the maximum effective electric field, the TE_{011} cavity might be preferable because of its following unique characteristics:

1. There are no axial currents, and no currents between cylinder wall and end plates, so it can be put together without the need for exotic methods, such as electron beam welding.
2. The simple topology facilitates chemical processing and coating the surface with exotic superconductors.
3. The surface can be protected by an oxide coating so that exposure to air will not deteriorate the cavity. In a TM_{010} cavity, the electric field lines are normal to the surface and pass through the oxide layer and cause prohibitive losses.

For an Nb cavity at 4.2°K, the maximum accelerating gradient is 13.7 MV/m, the maximum accelerating potential, at 500 MHz, is 8 MV, for an rf input of 3 kW and line power input of 1 MW. For the same 8 MV, a copper cavity requires 7 MW rf and 10 MW line power. If Nb_3Sb is used, the rf and line powers are further reduced by the improvement factor of Nb_3Sb compared to Nb. At Wuppertal,[2] an improvement factor of 50 has been achieved. It is possible that with TE_{011} cavities the theoretical value of 200 can be approached.

Accelerating Structure

Several cavities can be placed in tandem to form an accelerating structure as shown in Fig. 6. Because

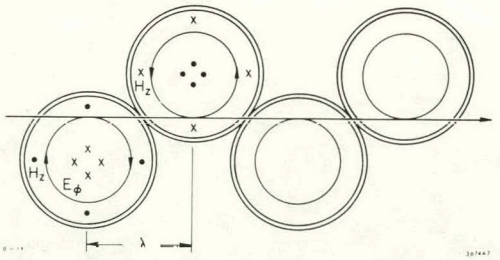


Fig. 6. Coupled TE_{011} cavities accelerating structure.

the length along the particle path of an optimized cavity is approximately λ, the degradation factor per unit length (the ratio of the per unit length shunt resistances of the TM_{010} over a TE_{011} cavity) is twice as large as D_f for a single cavity. Thus, for structures the values of the improvement factors given in Fig. 5 should be halved. The cavities can be parallel-coupled with a TEM line similarly to the CESR [3] structure.

Perturbation of Cavity Geometry

It is hoped that the holes for the beam passage and for coupling into and between cavities, will not perturb the TE_{011} mode sufficiently to negate its advantages. The geometry can be adjusted, put drift tubes inside the cavity to shield the particles from the E field near the wall, or the cavity made elliptical. Both perturbations will increase the non-superconducting shunt resistance and the maximum gradient, but will cause E-lines to terminate on the surface and negate the main justification

for using the TE_{011} mode. If these perturbations are carried to their logical extreme, a ridged cylindrical TE_{111} cavity (shown in Figs. 7 and 8), or an elliptical TE_{111} cavity results. The ratio of surface area and volume of a TE_{111} to a TM_{010} cavity, and hence their shunt resistance and R/Q are comparable. Therefore, even though a TE_{111} cavity does not have the main advantages of the TE_{011} cavity, i.e., no E field terminating on the surface, and no current between cylinder and end plates, it should still be considered for particle acceleration because it offers the following advantages over a TM_{010} cavity:

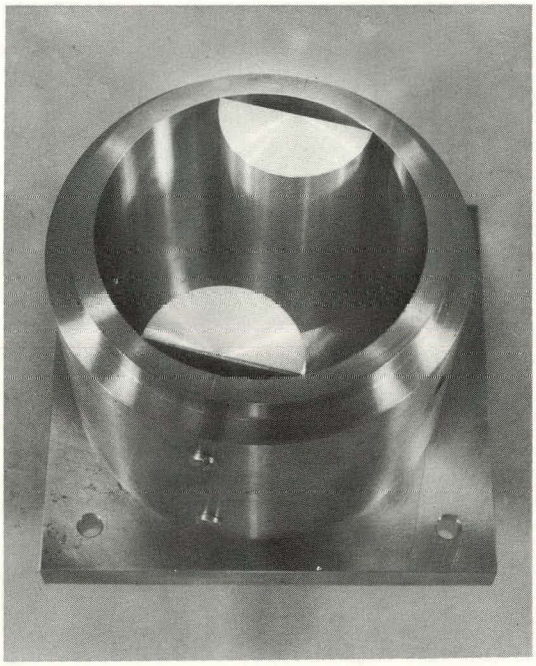


Fig. 7. TE_{111} cavity with half-cylinder ridge.

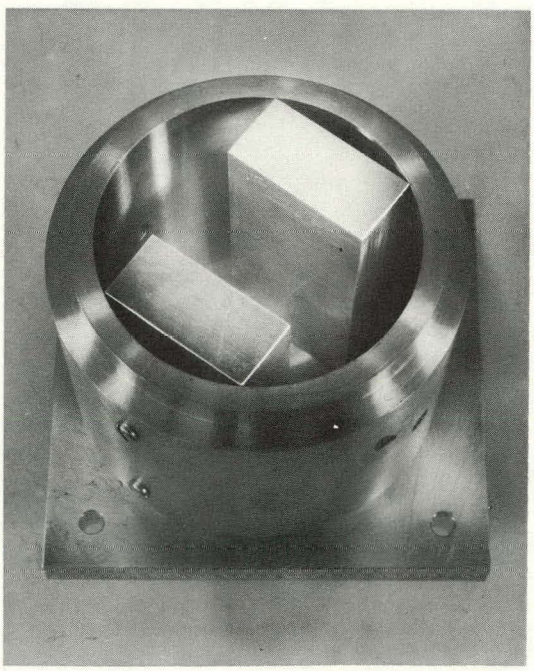


Fig. 8. TE_{111} cavity with rectangular ridge.

1. Asymmetrical transverse cross-section - the width can be made arbitrarily long (at the expense of shunt resistance).
2. As with the Muffin-Tin [4] structure, there are no cavity wall currents across the plane of the maximum E-field, and there is no current across the plane z = L/2. Therefore, blind-holes can be machined in two half-blocks, which can be linked together to form a TE_{111} structure as shown in Fig. 9.
3. No E-fields terminate on a flat surface. Generally, a TM_{010} structure cell is circular in the transverse direction and rectangular in the beam axis direction. To prevent multipactoring, Wuppertal[2] made the cell also circular in the beam axis direction, resulting in a spherical cell. The TE_{111} cell goes one step further and makes the transverse cross section rectangular. Even though there is a flat plane, there are no E-lines terminating on it because of the nature of the mode, and therefore the TE_{111} cavity should resist multipactoring, as does a spherical cavity.
4. Because of cylindrical geometry, the TE_{111} structure is easy to machine and make mechanically rigid. Also, tubes can be drilled across the cylinder wall and end plates to achieve good cooling of the cavity material near the beam aperture.
5. Easier removal of higher order modes, and lower higher order modes shunt resistance.

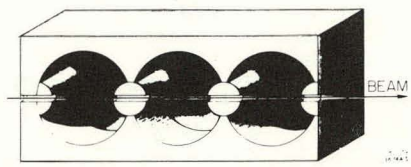


Fig. 9. Accelerating structure formed by ridged cylindrical TE_{111} cavities in tandem.

Other Types of Geometric Alterations

One reason for the low TE_{011} cavity shunt resistance and low maximum field gradient, is that only a fraction of the electric field circle is used for acceleration. One way to get around this is to place a toroidal conductor along the E-circle with a gap for the beam path. This will substitute, over a large fraction of the E-circle, conduction current for displacement current. The complete E-circle voltage will not be recovered, because the cavity will become smaller and the unloaded Q will decrease. This modification makes this cavity the same as the Argonne cavity [5] except without the twist.

A way to make use of the high Q and large energy storage capacity of a TE_{011} cavity and still have an effective high shunt resistance and field gradient, is to

place a sapphire, gas-filled tube similar to the one described by Birx and Scalapino,[6] along the E-field circle with a gap at the beam path. When the field in the cavity reaches a given value, the gas breaks down and the tube becomes a conductor. Because the magnetic field threading the tube does not change instantaneously, the full E-ring potential should appear across the gap. In effect, the storage and accelerating cavities are one and the same. If the above postulates are indeed true, then for one watt input to a copper cavity, the accelerating potential across the cavity is $(\pi D/2)\, E_{\phi m}$ = 5000 volts. The effective shunt resistance is 25 megohms, about the same as for a TM_{010} cavity. For a niobium cavity at 4.2°K, at 500 MHz, the maximum voltage limited by magnetic breakdown is 90 MV and the maximum gradient is 100 MV/m.

Conclusion

It was shown that the TE_{011} and TE_{111} cavities have possibilities for particle acceleration and merit further study.

Acknowledgment

The use of non-superconducting TE_{010} cavities for particle acceleration was suggested by W.K.H. Panofsky and linking them together as in Fig. 6 was suggested by H. Hogg. I am grateful to P. Wilson, R. Miller, and J. Weaver for valuable discussions.

References

1. P. Wilson, "Surface Resistance of Superconducting Niobium at 4.2°K," Internal Document, SLAC, November 28, 1978.
2. D. Proch, "A Proposed 130 MeV Superconducting Recyclotron for Electrons," Conference on Future Possibilities for Electron Accelerators, J-13, January 8-10, 1979, University of Virginia.
3. R. M. Sundelin et al., "Parallel Coupled Cavity Structure," IEEE Trans. Nucl. Sci. NS-24, 1686 (1977).
4. J. Kirchgessner et al., "Superconducting Cavities for Synchrotron Use," IEEE Trans. Nucl. Sci. NS-22 1141 (1975).
5. K. W. Shepard et al., "Development and Production of Superconducting Resonators for the Argonne Heavy Ion Linac," IEEE Trans. Mag. MAG-5, 666 (1979).
6. D. L. Birx and D. J. Scalapino, "A Cryogenic Microwave Switch," IEEE Trans. Mag. MAG-5, 33 (1979).

C-BAND SUPERCONDUCTING CAVITY RESEARCH AT KEK

T. Furuya, K. Hosoyama, T. Kato, Y. Kojima and O. Konno
National Laboratory for High Energy Physics
Oho-machi, Tsukuba-gun, Ibaraki-ken, 300-32, Japan

Summary

Fabrication and surface preparation techniques have been studied on C-band TM_{010} niobium single cavities. A Q_0 of 10^{10} and effective accelerating field strength of 10 MeV/m have been obtained by electro-polishing, anodizing and vacuum firing.

Electron acceleration has been tested with a nine-cell π-mode structure. A preliminary test resulted in an accelerated beam at 0.64 MeV with 70 keV injection energy, corresponding to an effective accelerating field strength of 3 MeV/m.

Introduction

Superconducting cavity research is being carried out at KEK to obtain further understanding of rf superconductivity, and explore the feasibility of applying superconducting rf structures to a future accelerator such as a large electron storage ring. Cavity geometry, cavity fabrication techniques and surface preparation methods have been investigated to obtain high quality factor Q_0 and high accelerating rf fields in a pure niobium TM_{010} single cavity.

C-band (6 GHz) has been chosen as the microwave frequency because the size of cavities are convenient to handle, and microwave equipment is commercially available, as this frequency band is being used for the satellite communication.

Electron acceleration by a nine-cell C-band structure has been demonstrated and used to study problems typical of superconducting accelerators.

In the future TRISTAN[1] project, the orbit bending radius will be at most about 250 meters, which comes from the limited area of KEK campus. If a normal conducting rf structure is applied to the electron ring of TRISTAN, the electron and positron energies will be limited to ∿20 GeV due to the huge rf power requirement. To obtain higher energy for the electron ring, the feasibility of a superconducting rf structure is now being considered at KEK, and 500-MHz niobium cavity research has been started.

This report describes the results obtained up to the present for C-band cavity research.

Single Cavity Experiments

Cavity geometry

From the viewpoint of the reduction of surface electric and magnetic fields, and concern about electron multipactoring, several kinds of cavity geometries were studied, both by LALA computation and experiment. Three typical geometries are shown in Fig. 1. Type A is round-cornered with the beam-hole edge of circular cross-section. Type B is sharp cornered[2] with the beam-hole edge of elliptical cross-section,[3] and Type C is a spherical cavity with the beam-hole edge of elliptical cross-section. Beam-hole diameter is 10 mm for Type A and 15 mm for Type B and C.

Cavity fabrication and surface treatments

Each half cavity was machined from solid niobium rod and electro-polished, removing 100-150 μm from the surface, and welded together to form complete cavities. They were electro-polished again slightly, anodized at 50 volts in NH_4OH solution and heat-treated at 1500-1600°C in 10^{-8} Torr vacuum.

For the 500 MHz, it is planned to form the half cavities by spinning or coining. C-band cavities are also under preparation by spinning.

Most of the cavities were welded by electron beam welding; argon arc welding was also tested. The welding torch and rotating jib were mounted in a vacuum vessel, which was filled with pure argon gas after first evacuating the vessel. Argon arc welded cavities showed almost similar rf test results compared to the electron beam welded cavities.

After firing in a vacuum furnace, cavities were assembled to a coaxial window. This process was done mostly in the air, after which the cavities were evacuated and pinched off.

Results of single cavity tests

Fifteen cavities were fabricated and tested. Some cavities were tested several times after reprocessing each time by anodizing and firing.

Figure 2 shows the results for these tests. Open circles are for cavities of Type A, triangles are for Type B and squares are for Type C. Black dots represent multipactoring breakdown for Type A.

Figure 3 shows Q_0 for increasing rf field at 1.5°K for the typical Type A cavity.

Several observations can be made from the present results:

Multipactoring breakdown was observed for a few cases of Type A cavities. The electrons were observed by a biased voltage collector.

The effects of various cavity shapes are not clear in this frequency band but surface

preparation effects are more dominant.

No x-ray radiation was observed.

In recent experiments, heat pulses were observed at the bottom wall of the cavities at the breakdown field level.

Electron Acceleration by a Nine-cell Structure

A C-band, π-mode, nine-cell structure as shown in Fig. 4 was fabricated by a method of preparation similar to that of the single cavity. Phase velocity was 0.85c for the injection electron energy of about 80 keV. End cavities have slightly different diameters to obtain the flat field distribution on the axis. Dimensions were determined by calculation and also from the experimental results of the three-cell structure. The irregularity of the axial field distribution measured by the bead measurements has not yet been compensated by squeezing the cavity wall.

A schematic drawing of the arrangement for the acceleration test is shown in Fig. 5. Electrons were injected from a 100-kV gun through an inner conductor pipe of a coaxial rf line, into a niobium structure.

The preliminary test showed that Q_0 for the π-mode was 5×10^8. The effective accelerating field was 3 MeV/m and accelerated electrons reached an energy of 0.64 MeV with injected energy of 70 keV. Beam intensity was a few μA and FWHM of the energy spectrum was 0.1 MeV.

Acknowledgements

We wish to express our thanks to Director T. Nishikawa for continuous encouragement, to Dr. K. Mittag for many helpful suggestions, and to the people of KEK machine shop for the design and construction of the equipment.

References

1 S. Kamada et al., KEK-79-16, Japan (1979).

2 C.M. Lyneis, H.A. Schwettman, J.P. Turneaure, Appl. Phys. Lett. 31, 541 (1977).

3 W. Bauer, K. Mittag, KEK-2194, Karlsruhe (1975).

4 U. Klein, D. Proch, WU B 78-31, Wupperpal, Germany (1978).

Discussion

R.H. Miller, SLAC: Is the 500-MHz cavity intended for use in a storage ring or a linac?

Kojima: We are now considering the feasibility of using superconducting rf cavities for the TRISTAN electron ring.

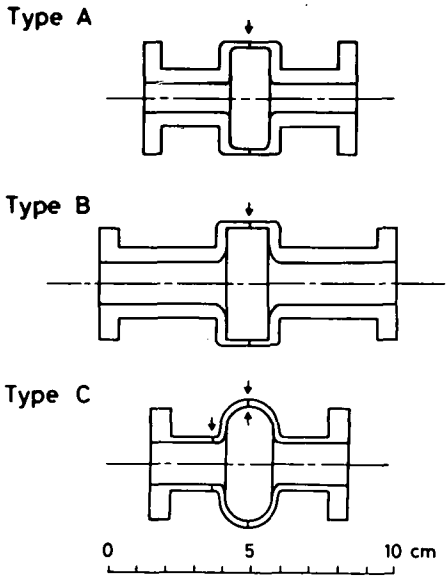


Fig. 1 Various geometry of C-band cavities, arrows indicate the welding points.

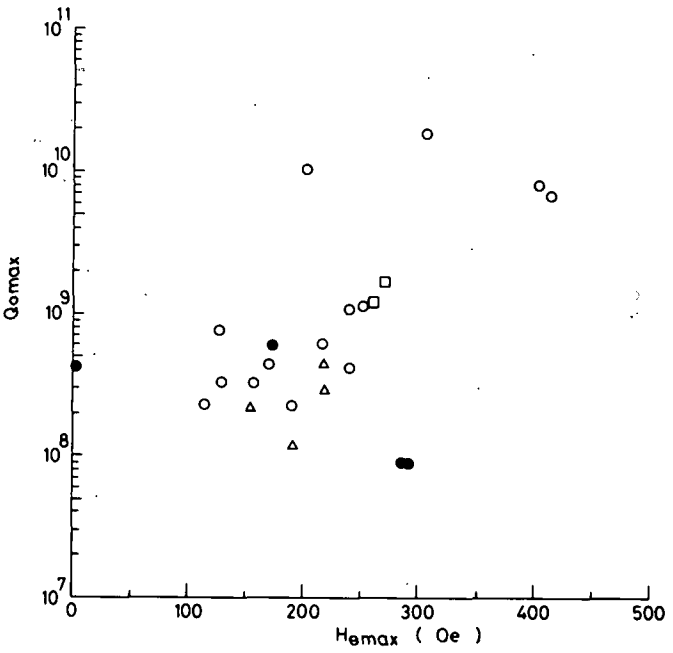


Fig. 2 Results for C-band cavities, circles are for Type A in Fig. 1, triangles are for Type B and squares are for Type C.

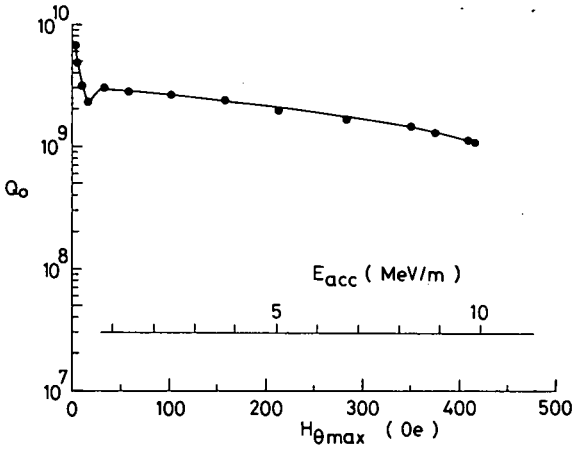


Fig. 3 Typical results for Q_0 vs rf field.

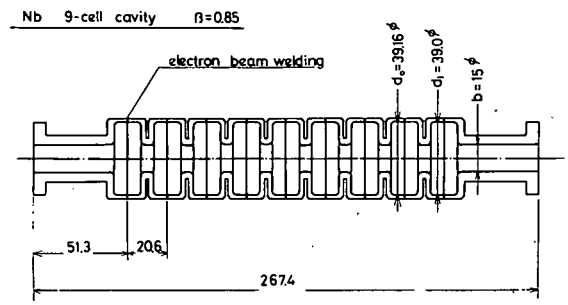
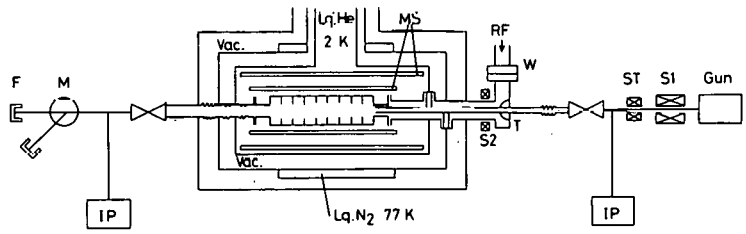


Fig. 4 A nine-cell structure.



S1 S2	Solenoid coil
ST	Steering coil
W	Ceramic window
T	Transition from waveguide to coaxial line
MS	Magnetic shield
M	Analyzer magnet
F	Faraday cup

Fig. 5 Schematic drawing for the arrangement of electron acceleration.

MODELLING OF BIPERIODIC SLOW-WAVE STRUCTURES

V.L. Bukharin, A.Y. Novozhilov, O.V. Plink, N.P. Sobenin, V.V. Stepnov, V.K. Shilov, E.J. Shkolnikov
Moscow Physics Engineering Institute
Moscow, USSR

Summary

Two models are considered for defining the electrical parameters of biperiodic slow-wave structures (BSWS) with beam loading. The first model is represented by a chain of coupled cavities and the second one by a chain of lumped-parameters circuits. The feeding waveguide is accounted for in both models. Two computing programs which use a finite difference method on a square mesh were written. Some computational results are given.

Introduction

A number of requirements in radiography and medicine, strongly demand development of compact standing-wave electron linacs. Theoretical and experimental research on the performance at low and high power levels, at biperiodic slow-wave linacs, made it possible to start commercial production of these machines.

The design of standing-wave electron linacs requires the development of computer programs. In the modelling of biperiodic slow-wave structures (BSWS), two models were considered. In the first model, the BSWS was represented by a chain of coupled cavities; in the second a chain of coupled lumped circuits was used. In both models the rectangular feed guide was taken into account, and considered to be essential for the design of a standing-wave linac with a 3 db hybrid junction rf feed scheme.

Biperiodic Slow-Wave Structures As A Chain Of Coupled Cavities

In this model all rf and accelerating systems are divided into two regions: the biperiodic slow-wave structure proper, and the feeding waveguide (Fig. 1). This separation is quite practical because it allows regular and irregular regions to be considered independent of each other. The boundary lies on the surface of the coupling iris. The thickness of the separating wall is assumed to be negligibly small. Considering the tangential component of the field at the boundary to be known, one can evaluate the electromagnetic fields in regions I and II. Indeed, to preserve continuity of magnetic field as one goes through the opening in the iris, the following equation must be valid:

$$\left[\vec{H}^{I}\left(\vec{j}^{I}_{ex},\vec{E}_{tg}\right)\vec{n}_{21}\right]+\left[\vec{H}^{II}\left(\vec{j}^{II}_{ex},\vec{E}_{tg}\right)\vec{n}_{12}\right]=0 \quad . \quad (1)$$

Here H^{I} and H^{II} are boundary magnetic field vectors in regions I and II. The fields are excited by some external sources and by a tangential electric field, E_{tg}. $\vec{n}_{21}$ and $\vec{n}_{12}$ are normals to the boundary surface directed correspondingly into regions I and II. Assume first there is no current in the BSWS. Then, according to the superposition principle, and taking into account that $j^{II}_{ex}=0$, for a linear system it is found:

$$\left[\vec{n}_{21}\vec{H}^{I}(0,\vec{E}_{tg})\right]+\left[\vec{n}_{12}\vec{H}^{II}(0,\vec{E}_{tg})\right]=\left[\vec{H}^{I}\left(\vec{j}^{I}_{ex},0\right)\vec{n}_{21}\right] \quad . \quad (2)$$

The Ritz-Galerkin method[2] can be used to solve equation (2). In this method, the field is represented as an expansion in the full system of coordinate functions :

$$\vec{E}_{tg}=\sum_{p}e_{p}\vec{\mathcal{J}}_{p} \quad . \quad (3)$$

Substituting (3) in (2), and after the usual transformations, yields a system of linear equations with respect to unknown coefficients e_p (the order of the coefficients is determined by the number of the coupling slots and the number of coordinate functions taken into account):

$$\sum_{p}e_{p}\int_{S_{slot}}\vec{\mathcal{J}}^{*}_{m}\left[\vec{n}_{21}\vec{H}^{I}(0,\vec{\mathcal{J}}_{p})\right]dS+\sum_{p}e_{p}\int_{S_{slot}}\vec{\mathcal{J}}^{*}_{m}\left[\vec{n}_{12}\vec{H}^{II}(0,\vec{\mathcal{J}}_{p})\right]dS=\int_{S_{slot}}\vec{\mathcal{J}}^{*}_{m}\left[\vec{H}^{I}\left(\vec{j}^{I}_{ex},0\right)\vec{n}_{21}\right]dS \quad , \quad (4)$$

where $\vec{\mathcal{J}}^{*}_{m}$ is the complex conjugate of $\vec{\mathcal{J}}_{m}$, S_{slot} is the surface of the coupling slot. The accuracy of solving (4) depends on the number of terms in (3). For terms of (3), take a set of coordinate functions ψ_ℓ and ψ_h which have to satisfy the wave equation and homogeneous boundary conditions on the coupling iris:

$$\nabla^{2}\psi_{\ell,h}+\varkappa^{2}_{\ell,h}\psi_{\ell,h}=0 \qquad \frac{\partial\psi_{h}}{\partial n}=0 \qquad \psi_{\ell}=0 \quad ,$$

where $\vec{n}$ is the normal to the surface. In this case

$$\vec{E}_{tg}=\sum_{h}e_{h}\vec{\mathcal{J}}_{h}+\sum_{\ell}e_{\ell}\vec{\mathcal{J}}_{\ell}=\sum_{p}e_{p}\vec{\mathcal{J}}_{p}$$

and

$$\vec{\mathcal{J}}_{h}=\left[\nabla\psi_{h}\vec{n}\right] \qquad \vec{\mathcal{J}}_{\ell}=\nabla\psi_{\ell} \quad .$$

The next step is to find H^I and H^{II} in (4). The Kysun'ko method[2] can be used for the determination of the magnetic field H^I in the feeding waveguide. According to this method, the electromagnetic field is represented by a series in eigenvector functions

$$\vec{E}=\sum_a U_a\vec{\mathcal{E}}_a \qquad \vec{H}=\sum_b I_b\vec{\mathcal{H}}_b \quad , (5)$$

where unknown coefficients U_a, I_b are derived from the so called waveguide equations. To find the first term in the left side of (4), $H^I(0,\vec{\mathcal{J}}_p)$ must be determined (the value of the magnetic field which is excited in the rectangular waveguide by the component $\vec{\mathcal{J}}_p$ at the iris). Then, in accordance with (5), and taking into account that in (4) the unknown field is a part of the vector product, it will suffice to derive only the field transverse components in region I at the coupling iris.

$$\vec{H}^I(0,\vec{\mathcal{J}}_p)=\sum_h \frac{1}{Z_h}\int_{S_{slot}}\vec{\mathcal{J}}\vec{\mathcal{E}}_h\,dS\,\vec{\mathcal{H}}_h \quad . (6)$$

For the ultimate solution of (6) it is necessary to write eigenvector functions $\vec{\mathcal{E}}_h, \vec{\mathcal{H}}_h$ and coordinate functions $\vec{\mathcal{J}}_p$ in explicit form. Eigenvector functions $\vec{\mathcal{E}}_h$ and $\vec{\mathcal{H}}_h$ are formed in a similar manner to $\vec{\mathcal{J}}_p$. $\vec{H}^z(\vec{j}^I_{ex},0)$ in the right-hand side of (6) is defined likewise, but the source here is j^I_{ex}, a microwave generator and the coupling iris is metal coated, i.e. $E_{tg}=0$. In this case

$$\vec{H}^I(\vec{j}^I_{ex},0)=\sum_h \frac{1}{Z_h}2A_h\vec{\mathcal{H}}_h \quad , (7)$$

where A_h depends on magnetic wave power (with index h) flowing into the iris:

$$P_h=\frac{1}{2}\frac{A_h^2}{Z_h}\int_S \vec{\mathcal{H}}_h^2\,dS \quad .$$

The last term in (4) must be defined. This problem is similar to the definition of fields in a BSWS with a side hole in one of its cells. The structure is excited by tangent field E_t or its component $\vec{\mathcal{J}}_p$. For the solution Slater's equation[3] will be used with the method described in Ref. 4, 5. As shown in Ref. 6, a set of equations with respect to complex amplitudes U_n and I_n for a chain of cavities coupled by slots, has the following form:

$$(\omega_{mn}^2-\omega^2)U_{mn}=\omega^2(1-j)\frac{1}{Q_{mn}}U_{mn}-\frac{\omega_{mn}}{\sqrt{\varepsilon\mu}}\int_{S_{slot}}[\vec{E}_{tgn}\vec{\mathcal{H}}_{mn}]\vec{n}\,dS; \qquad I_{mn}=j\omega\varepsilon 2\pi C\omega_{mn}U_{mn} \quad . (8)$$

It is assumed that the electric and magnetic fields to be determined in (8) can be expressed as

$$\vec{E}_n=\sum_m U_{mn}\vec{\mathcal{E}}_{mn} \; ; \; \vec{H}_n=\sum_m I_{mn}\vec{\mathcal{H}}_{mn} ,$$

where n is the cavity number, $\vec{\mathcal{E}}_{mn}$ and $\vec{\mathcal{H}}_{mn}$ are electric and magnetic field eigenvectors in cavities without slots. In (8), ω_{mn} is the frequency of the m-mode in n-cavity, Q_{mn} is the quality factor of the cavity, E_{tg} is tangent electric field on the surface of the coupling slot. In the following considerations, the fields in cavities of a BSWS will be represented by the first term of expansion in functions $\vec{\mathcal{E}}_m$ and $\vec{\mathcal{H}}_m$. In case of axially symmetric cavities, it is similar to considering the E_{010} mode (m=1). If the coupling slots are narrow enough and cut along the azimuthal coordinate near the side wall, they can be represented by a transmission line with a T-mode wave.[4,5] Then the integral over the slot between cavities n and n-1 looks like:

$$\int\limits_{(S_{slot})_{n,n-1}}[\vec{E}_{tgn}\vec{\mathcal{H}}_n]\vec{n}\,dS=j\omega L_0\left[I_n\mathcal{H}_n(r_s)-I_{n-1}\mathcal{H}_{n-1}(r_s)\right]\times\left[2\tan\frac{k\ell_s}{2}-k\ell_s\right]\cdot\frac{\mathcal{H}_n(r_s)}{K^3} \quad . (9)$$

Here r_s is the location of slot radius; ℓ_s is the slot length; $k=2\pi/\lambda$. The equation set (8) is non-homogeneous, due to the term

$$\int_{S_{slot}}[\vec{E}_{tgn}\vec{\mathcal{H}}_n]\vec{n}\,dS \quad . \qquad (10)$$

Since E_{tg} in (10) is identically equal to $\sum_p e_p\vec{\mathcal{J}}_p$ the definition of the remaining term in (4), $\vec{H}^z(0,\vec{\mathcal{J}}_p)$ is carried out in the following way. After substituting $e_p\vec{\mathcal{J}}_p$ for E_{tg} in (10) and taking the integral, (8) must be solved with the right-hand side in the form of (10). The solution is carried out separately for every component of the tangent electric field E_{tg}. From (8) amplitudes I_n, V_n of the fields in cavities of BSWS with a feeding waveguide are obtained. The value of the magnetic field at the coupling slot is substituted into (4) for the ultimate integration. When all the terms of equation (4) are finally determined, it may be solved with respect to e_p by any appropriate method. The solution allows evaluation of the dispersion relation, input impedance, reflexion coefficient and the electric field distribution in the structure. The beam loading problem for the first model of BSWS is solved by the introduction of terms containing the beam current $\vec{J}_n$ into (8)

$$\frac{1}{\mathcal{E}}\frac{d}{dt}\int_{V_n}\vec{J}_n\vec{\mathcal{E}}_n\,dV \quad . \qquad (11)$$

To express (11) in explicit form, assume that the continuous beam entering BSWS has constant density.

Divide this beam at every time interval (0,T where $T = 2\pi/\omega$) into M elementary bunches. Each bunch can be represented by the first harmonic of the Fourier series. Then (11) becomes

$$\frac{1}{6}\frac{d}{dt}\int_{V_n}\vec{j}_n\vec{E}_n dV = \frac{j\omega}{6M} I\left(\sum_{K=1}^{M}\frac{e^{-j\varphi_{1K}} - e^{-j\varphi_{2K}}}{\varphi_{1K}-\varphi_{2K}}\right)\int_0^{L_n} E_n dz e^{j\omega t} \quad (12)$$

where φ_{1K} is the field phase when the bunch appears at the cavity entrance and φ_{2K} is the field phase when it leaves the cavity. I is the peak current. With the terms like (12) present, the equations set (8) and consequently (4) become non-linear, and an iteration method is used to solve them. At each iteration, the solutions of (8) and (4) were combined with the solution of the longitudinal motion equation for the bunches in BSWS. This method allowed evaluation of the longitudinal electron dynamics in BSWS, and takes into account the beam loading influence on the parameters of BSWS.

Biperiodic Slow-Wave Structure As A Chain Of Coupled Lumped-Parameters Circuits

Figure 2 shows an equivalent circuit of a beam loaded BSWS with a feeding waveguide. To each cell in BSWS ascribe capacitance C, inductance L and resistance R. The interactions of the cells are due to the mutual inductance, which is characterized by coupling coefficient K_c . A microwave generator is simulated by a voltage source U_G with resistance W. A feeding waveguide is simulated by a transmission line with the wave impedance of the same value W. The coupling of the feeding waveguide with BSWS is simulated in the equivalent circuit by inductive coupling with transformation coefficient m. The power is fed into the g-cell at the terminals "a-a". The beam loading effect is taken into account by an ideal current source U_n . For the circuit of the type shown the Kirhgoff equations with respect to the mesh currents have the following form after some transformations:[7]

$$\begin{cases} X_0\Phi_0 + K_{c1}X_1 = J_0 \\ X_1\Phi_1 + \frac{1}{2}(K_{c1}X_0 + K_{c2}X_1) = J_1 \\ \cdots\cdots\cdots\cdots\cdots\cdots \\ X_g\Phi_g + \frac{1}{2}(K_{cg}X_{g-1} + K_{cg+1}X_{g+1}) = J_g + \frac{U_{aa}}{j\omega\sqrt{2L_g}} \\ X_N\Phi_N + K_{cN}X_{N-1} = J_n \end{cases} \quad (13)$$

Here $X_n = L_n\sqrt{2L_n}$, $\frac{1}{2}|X_n|^2$ is the stored energy in circuit n, $\Phi_n = 1-(\omega_n/\omega)^2 + \omega_n/jQ_n\omega$, Q_n is the circuit n quality factor, ω_n is the resonant frequency, U_{aa} is the voltage amplitude at "a-a" terminals. The second term in the right side of g equation (13) may be transformed to

$$\frac{U_{aa}}{j\omega\sqrt{2L_n}} = \frac{2S_{aa}X_g}{j\omega|X_g|^2} \quad . \quad (14)$$

Here $S_{aa} = \frac{1}{2}U_{aa}i_g^*$ is the complex power at the input circuit terminals. For the input voltage:

$$\frac{U_{aa}}{j\omega\sqrt{2L_n}} = \frac{Z_{aa}X_g}{j\omega 2L_g} \quad , \quad (15)$$

where Z_{aa} is the input impedance of the chain at the "a-a" terminals. Keeping in mind that the microwave generator is represented by an ideal voltage source with inner resistance W, an expression for complex power S_{aa} can be obtained in terms of the generator's power:

$$S_{aa} = \frac{4m^2 W P_G}{|m^2 W + Z_{aa}|^2} Z_{aa} \quad . \quad (16)$$

Combining (14), (15) and (16) one can get

$$\frac{8P_G}{|1+1/\beta|^2} = q\omega_g|X_g|^2 \quad . \quad (17)$$

Here $q = m^2W/\sqrt{2L_g/C_g}$. Note that $\sqrt{2L_g/C_g}$ is g circuit characteristic impedance. $\beta = m^2W/Z_{aa}$ is the coupling coefficient between BSWS and the feeding guide at the operating mode. Divide each equation of (13) by X_g and introduce new variables $\mathcal{X}_n = X_n/X_g$. These equations show that for deriving the unknown value, one has to solve two equations for the circuits adjacent to the one with the feeding guide. In case of the negligible beam loading, all J_n are equal to zero (n=0÷N) and a set of linear algebraic equations are obtained from which dispersion relation, BSWS parameters, fields distribution along the structure and their dependence on the generator power may be defined. The beam loading problem is solved similarly to the first model.

Electrical Parameters of an Axially Symmetric Cavity Excited in the Lowest Mode

For the solution of practical problems requiring the use of equations (8) and (13) one should know the electrical parameters of cells, such as frequencies, quality factors and shunt impedances. The values of these parameters were defined with the help of a computer program similar to LALA.[8] The program was written by converting the equation to finite difference forms using a square mesh. This approach uses relaxation method for the iterations.

Since there are two unknown values (magnetic field H_g and wave constant $K = 2\pi/\lambda$) the double iterative process for field and wave constant is used. To speed-up the convergence, the program provided iteration on the mesh succession, when the mesh length decreased from one iteration number to another. For the same purpose, smaller meshes were used when the field changed rapidly. For simplicity of use, the program provides automatic mesh superposition and boundary point

specification, which reduce preparation time before computing. The program described has the following features: If the EC-1040 computer and 6000 mesh nodes are used, the computation time is about five minutes. The error of the wave constant computation appeared to be less than 10^{-3}.

Some Computational Results

Two computing programs, "CAMEA" for the first model, and "LUCH" for the second model, were written and executed by the EC-1040 computers. The development of these programs was stimulated by the design of standing-wave linacs and the study of their performance.[1] The use of a 3 db hybrid junction seems to be the main difference of the linacs under investigation from standing-wave linacs operating elsewhere. The function of the hybrid junctions are to isolate the rf generator from the resonant load and to increase the frequency stability. From this point of view, parameters of interest of BSWS are input impedance and reflection coefficient, and their dependence on frequency. Some results computed by the programs are presented herewith: Figure 3 shows the experimental dependence of the VSWR in the feeding guide, on the coupling iris width.[1] The accelerating guide here has 6 on-axis coupling cells. The solid points on the curve indicate the results obtained by the "CAMEA" program. They show a good agreement of the calculated and experimental data. Figure 4 shows the dependence of β (see eq. 17) module and phase on the frequency. The dependence is computed by "LUCH" program. As can be seen from (17) β module is proportional to the input susceptance, hence Fig. 4 may be interpreted as a frequency response characteristic of the accelerating guide. The accelerating guide under consideration consists of a regular BSWS with on-axis coupling cells. The respective values for accelerating cell and coupling cell Q factors are equal to 12×10^3 and 3×10^3; the coupling coefficient is equal to 0.24. The rf power is fed into the 6th cell. Curve 1 corresponds to the negligible beam loading case and curve 2 corresponds to the peak beam current I, equal to 100 mA. It is of interest, that without a beam, the input susceptance phase at the operating frequency is equal to zero, while with the beam of 100 mA peak current, it differs from zero. This effect shows that the guide is detuned due to the reactive beam loading, i.e. shifting of the bunch synchronous phase. This leads to the feeding wave guide coupling change: overcoupling $\beta = 2.1$ when $I = 0$ and overcoupling $\beta = 0.5$ when $I = 100$ mA.

Conclusion

The investigations carried out showed good agreement between the data calculated by means of the "Camea" and "Luch" computing programs and experiments. Thus the developed computing programs may be recommended for the design and adjustment of electron standing wave linacs using BSWS.

References

1 V.F. Vikulov, A.A. Zavadsev, B.V. Zverev, V.E. Kaljuzhny, V.I. Kaminsky, N.N. Nechaev, V.V. Rusin, N.P. Sobenin, V.V. Stepnov, "A compact standing-wave electron linac with rf drive system using 3-dB hybrid junction", IEEE Trans. on Nucl. Sci., NS-26, 4292 (1979).

2 B.M. Mashkovtsev, K.N. Tsybisov, B.F. Yemelin, "Theorya volnovodov", Nauka, Moskva, 1966 (in Russian).

3 J.C. Slater, "Microwave Electronics", D. Van Nostrand, New York, 1950.

4 M.A. Allen, G.F. Kino, "On the theory of strongly coupled cavity chain", IRE Trans. on MTT, MTT-8, 362 (May 1960).

5 R. Bevensee, "Electromagnetic Slow Wave Systems", J. Wiley and Sons, New York, 1964.

6 T.A. Nishikawa, "Study of field distribution and beam loading in proton linacs at high energies", IEEE Trans. on Nucl. Sci., NS-14, 600 (1967).

7 E.A. Knapp, B.C. Knapp, J.M. Potter, "Standing wave high energy linear accelerator structure", Rev. Sci. Inst. 39, No. 7, 979 (1968).

8 H. Hoyt, D. Simmonds, W. Rich, "Computer designed 805-MHz proton linac cavities", Rev. Sci. Inst., 37, No. 6, 755 (1966).

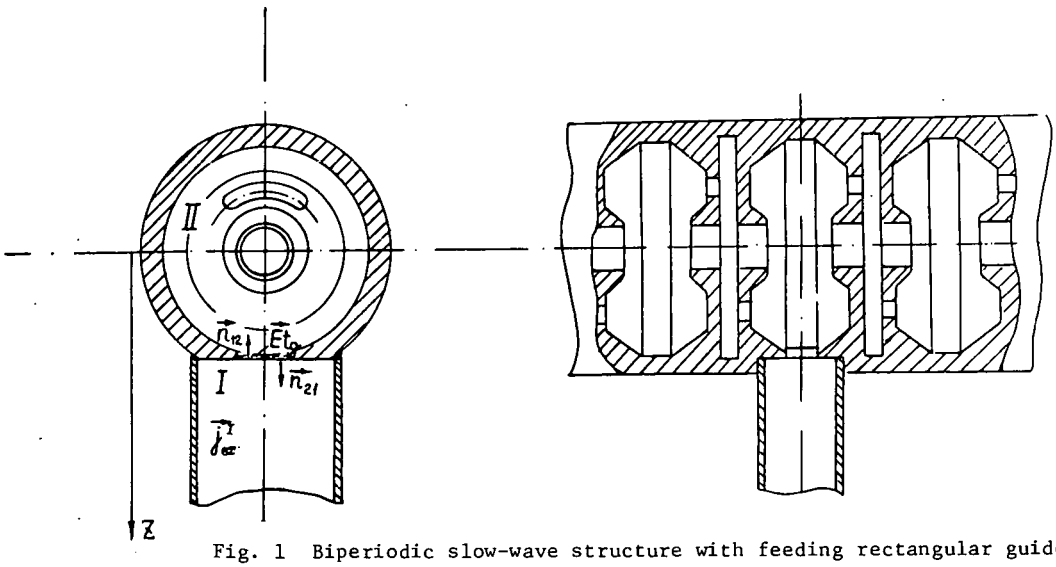


Fig. 1 Biperiodic slow-wave structure with feeding rectangular guide

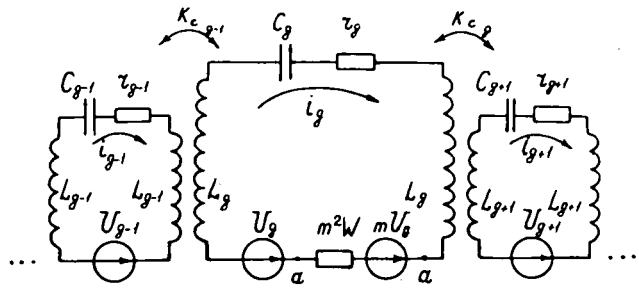


Fig. 2 Equivalent circuit of a beam loaded BSWS

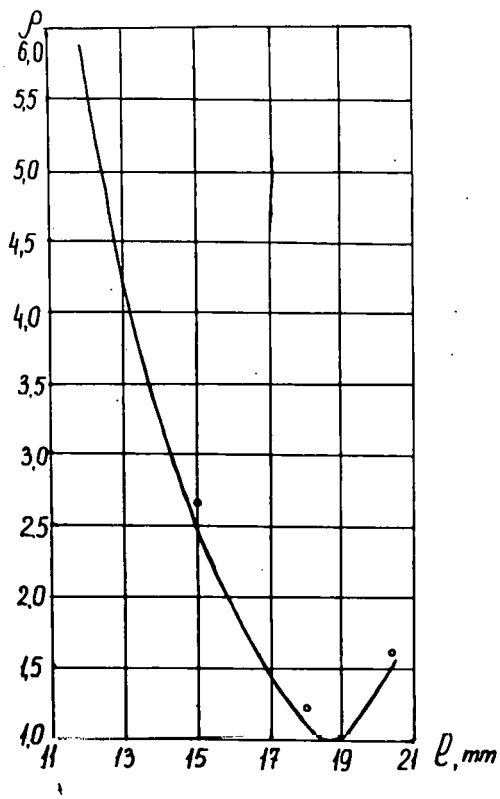


Fig. 3 Dependence of the VSWR in the feeding guide on the coupling iris width

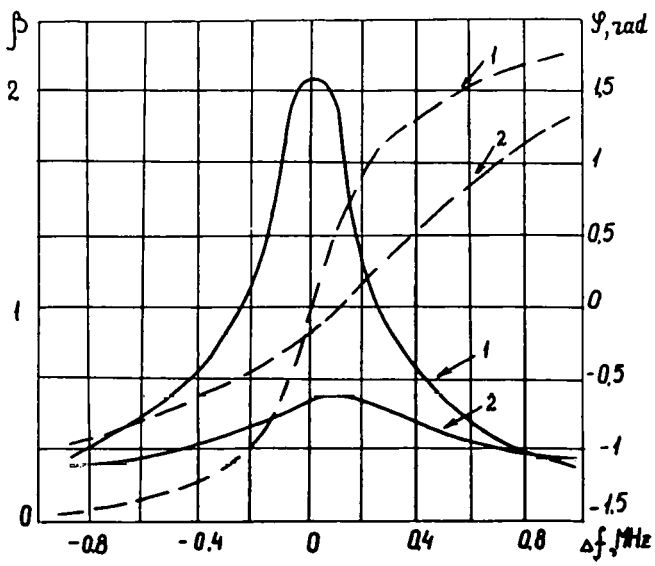


Fig. 4 Dependence of β module and phase on the frequency

THIS PAGE

WAS INTENTIONALLY

LEFT BLANK

Section IV
Theory

THIS PAGE

WAS INTENTIONALLY

LEFT BLANK

1979 LINAC ACCELERATOR CONFERENCE

RF QUADRUPOLE BEAM DYNAMICS DESIGN STUDIES*

K. R. Crandall, R. H. Stokes, and T. P. Wangler
Los Alamos Scientific Laboratory
Los Alamos, New Mexico 87545

Summary

The radio-frequency quadrupole (RFQ) linear accelerator structure is expected to permit considerable flexibility in achieving linac design objectives at low velocities. Calculational studies show that the RFQ can accept a high-current, low-velocity, dc beam, bunch it with high efficiency, and accelerate it to a velocity suitable for injection into a drift-tube linac. Although it is relatively easy to generate a satisfactory design for an RFQ linac for low beam currents, the space-charge effects produced by high currents dominate the design criteria. Methods have been developed to generate solutions that make suitable compromises between the effects of emittance growth, transmission efficiency, and overall structure length. Results are given for a test RFQ linac operating at 425 MHz.

Introduction

Soon after the linear accelerator was invented, searches began for methods to circumvent the incompatibility between longitudinal and radial stability. The use of drift-tube foils or grids, externally applied fields, and alternating phase focusing have met with success in specific areas of application. However, each of these solutions has serious disadvantages, particularly in the acceleration of low-velocity ions. Since 1956, there have been suggestions that linear accelerator electric fields could be used for radial focusing as well as for acceleration.[1-4] These proposals were based on non-cylindrically symmetric electrode shapes that would generate transverse quadrupole fields. This rf self-focusing is an important new idea especially at low velocities because the electric force is velocity independent.

In 1970, Kapchinskii and Teplyakov[5,6] (K-T) proposed a particularly attractive form of these new ideas. The previous proposals to generate quadrupole fields used specially shaped gaps between drift tubes or waveguides to generate localized focusing forces. However, the scheme proposed by K-T was a more basic and flexible idea in which the quadrupole focusing field was spatially continuous along the z-axis. This structure is called the RFQ. Figure 1 shows a schematic view of a four-vane resonator that is the form of the RFQ being developed at the Los Alamos Scientific Laboratory (LASL).

The RFQ may have important applications in the low-velocity part of many types of ion accelerators. It can provide several necessary functions in a continuous manner to produce a final beam suitable for injection into a conventional accelerator. Briefly these functions are the following: (1) acceptance of a dc beam (50-keV protons, for example) and radially matching it into the following sections of the RFQ; (2) bunching this beam adiabatically with high capture efficiency (>90%); and (3) accelerating the beam to an energy (1-MeV protons, for example) that is convenient for injection into the next acceleration stage. In this paper we will consider the next stage to be a drift-tube linac. Through proper design it is possible to control the particle distribution in the phase-stable bucket so that nonadiabatic acceleration effects are minimized. Also, the final synchronous phase can be brought to a value (say -30°) that is suitable for capture by a drift-tube linac. Because the radial focusing forces are electric and retain their full strength at low velocity, and also because the forces are spatially continuous, the above functions can be accomplished at low velocities with minimal effects from space charge. Also, as suggested by K-T, space-charge effects can be further minimized through proper control of the bunching process. This idea is an important contribution that is compatible with possible choices of RFQ design parameters.

There are several possible applications of the RFQ now under consideration at LASL. These include: (1) a high-intensity deuteron accelerator for the Hanford Fusion Materials Irradia-

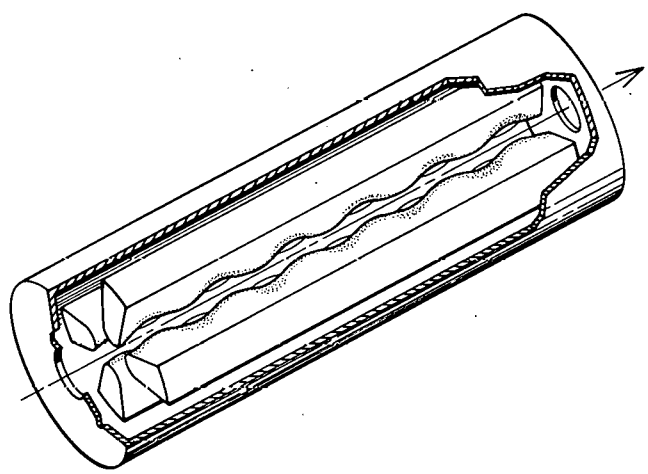


Fig. 1. Four-vane resonator.

*Work performed under the auspices of the U. S. Department of Energy.

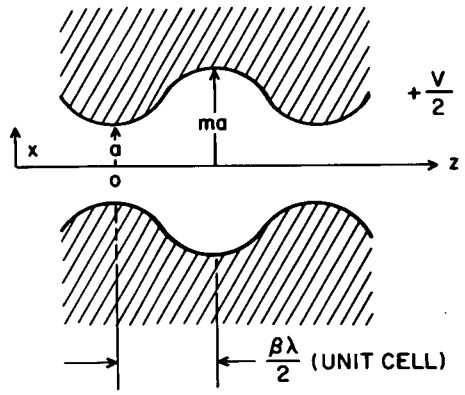


Fig. 2. RFQ pole-tip geometry.

tion Test (FMIT) Facility, (2) the Pion Generator for Medical Irradiation (PIGMI), a high-intensity proton accelerator for use in pion and neutron radiotherapy, (3) a heavy-ion accelerator for inertial fusion, and (4) a high-energy accelerator for ions such as neon. Methods which have been found useful in choosing beam-dynamics parameters for RFQ systems are presented. As a specific example, the results of these methods are applied to a proton linac designed to test the RFQ principle.

RFQ Electric Fields and Pole-Tip Geometry

In the RFQ the electric field distribution is generated by four poles arranged symmetrically around a central z-axis. The poles are excited with rf power so that at a given time, adjacent pole tips have equal voltages of opposite signs. If the pole tips have constant radius as z is varied, then only a transverse field (mainly quadrupole) is present. In the x-z plane for example, this quadrupole field is focusing for one-half of the rf period and defocusing the other half. The structure has the properties of an alternating-gradient focusing system with a strength independent of particle velocity. To generate a longitudinal accelerating field the pole tips are periodically varied in radius. The variation is such that, at a value of z where the pole tips in the x-z plane have minimum radius, the pole tips in the y-z plane have maximum radius. This is shown in Fig. 1. Figure 2 shows a cut through the x-z plane, and shows the mirror symmetry of the opposite poles. In Fig. 2 the radius parameter a, the radius modulation parameter m, and the cell length are defined. The longitudinal field is generated between the x pole tip that has minimum radius at z = 0, and the y pole tip that has minimum radius at z = $\beta\lambda/2$. The unit cell is $\beta\lambda/2$ in length and corresponds to one acceleration gap. Adjacent unit cells have oppositely direct E_z fields, so that in practice only every other cell contains a particle bunch.

In the coordinate system of Fig. 2, the lowest-order potential function given by K-T is written in cylindrical coordinates (r, ψ, z) as follows:

$$U = \frac{V}{2}\left[X\left(\frac{r}{a}\right)^2 \cos 2\psi + AI_o(kr)\cos kz\right] \cdot \sin(\omega t + \phi) \quad , \tag{1}$$

where V is the potential difference between adjacent pole tips, and $k = 2\pi/\beta\lambda$.

From this the following electric field components are obtained:

$$E_r = -\frac{XV}{a^2} r \cos 2\psi - \frac{kAV}{2} I_1(kr)\cos kz \quad , \tag{2}$$

$$E_\psi = \frac{XV}{a^2} r \sin 2\psi \quad , \tag{3}$$

$$E_z = \frac{kAV}{2} I_o(kr)\sin kz \quad , \tag{4}$$

each multiplied by sin ($\omega t + \phi$). Our method of calculating RFQ beam dynamics is based on these fields and is described in Ref. 7. The quantities A and X are given by:

$$A = \frac{m^2 - 1}{m^2 I_o(ka) + I_o(mka)} \tag{5}$$

$$X = 1 - AI_o(ka) \quad . \tag{6}$$

The quantity VA is the potential difference that exists on the axis between the beginning and the end of the unit cell. This means that the space-average longitudinal field is given by $E_o = 2AV/\beta\lambda$. The energy gain of a particle with charge q and synchronous velocity βc traversing a unit cell is approximately:

$$\Delta W = qE_o \ell T \cos\phi_s \quad , \tag{7}$$

where $\ell = \beta\lambda/2$, and $T = \pi/4$ is the value of the transit-time factor for a longitudinal field with space variation sin kz. This notation is similar to K-T except that A equals their θ divided by $T = \pi/4$.

A radial stability diagram for the RF is given in Fig. 3. The abscissa is given by:

$$\Delta = \frac{\pi^2 qVA \sin\phi}{2Mc^2\beta^2} \quad . \tag{8}$$

This is proportional to the usual "rf defocus" force that gives radial defocusing when a linac

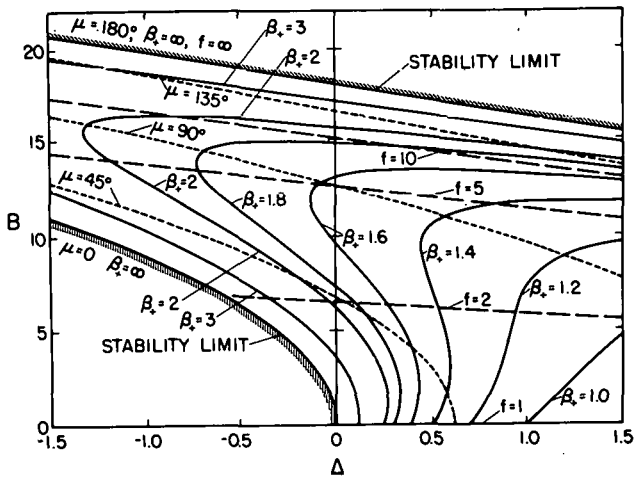


Fig. 3. RFQ radial stability diagram.

is operated with a negative phase angle in the range -90 to 0 degrees. The ordinate in Fig. 3 is:

$$B = \frac{q\lambda^2}{Mc^2} \cdot \frac{XV}{a^2} \quad . \tag{9}$$

This is proportional to the radial focusing force, and depends on the magnitude of the electric quadrupole strength XV/a^2. The electric quadrupole strength does not explicitly depend on z. This means that for given values of a, m, and β, the focusing strength is constant through a unit cell. It also means that one can maintain the same focusing strength in every unit cell by varying the parameters such that XV/a^2 is held fixed. Except for the short, initial radial matching section, the linac discussed in the section "Design of the 425-MHz RFQ Test", has been designed to have a constant radial-focusing strength. Later it will be shown that this has a geometrical consequence that may be beneficial in the design of RFQ resonators.

The pole-tip shape required to produce the above electric fields is given by:

$$x^2 - y^2 = r^2 \cos 2\psi = \frac{a^2}{X} \left[1 - AI_o(kr) \cos kz\right] . \tag{10}$$

To obtain the shape of one pole tip in the x-z plane, let $\psi = 0$. This gives:

$$\frac{x^2}{a^2} = \frac{1 - AI_o(kx) \cos kz}{1 - AI_o(ka)} \quad . \tag{11}$$

This equation was solved numerically to find values of x as a function of z. Call these values of x, which are solutions, $\alpha(z)$. To describe the geometry in the transverse plane an equation was derived for the transverse radius of curvature of the pole tip. This curvature is:

$$R(z) = \alpha(z) \frac{P + Q}{P - Q} \quad , \tag{12}$$

where

$$P = I_o(ka) + I_o(mka)$$

and

$$Q = \frac{ka^2}{2\alpha} (m^2 - 1) I_1(k\alpha) \cos kz \quad .$$

In the pole-tip geometrical design, the radius of the pole tips have been made equal to $\alpha(z)$. The pole-tip shape in the transverse plane was approximated by requiring the pole tips to have the radius of curvature R(z). The pole tips are constructed by repeated cuts in the transverse plane by a tape-controlled milling machine. This procedure is discussed more fully in Ref. 8.

At $z = \beta\lambda/4$, half way through the unit cell, the RFQ has quadrupolar symmetry. At this point both the x and y pole tips have a radius equal to $r_o = aX^{-1/2}$. Also, at this point the radius of curvature $R = r_o$. The quantity r_o can be regarded as a characteristic average radius of the RFQ pole tips. As has been stated, if V is constant, keeping the focusing strength at a fixed value requires X/a^2 to be constant, and also this is equivalent to keeping r_o fixed. In general, a fixed value of r_o can be expected to minimize variations in the vane-to-vane capacitance, and should facilitate the design of an RFQ resonator in which the pole-tip voltage distribution is required to be flat over its entire length.

RFQ Design Procedures

If the ion species and the initial and final energies are given, and if the frequency and intervane potential are specified, the RFQ design is determined when the three independent functions a(z), m(z), and $\phi_s(z)$ are given, where z is the axial distance along the accelerator. Although it may be more convenient to explicitly use other related functions such as A, X, or B, the designer must determine three independent functions that produce the desired objectives in terms of adequate radial focusing, capture efficiency, radial emittance growth overall length, or other stated criteria. Simple linear forms for the above functions can achieve these objectives for low beam currents as long as the rate of change of the variables is slow enough to approximate an adiabatic condition. However, as the magnitude of the space-charge force increases, more complex forms for these functions appear to become necessary to minimize both particle loss and radial emittance growth.

One possible solution to this problem has been proposed by K-T. In this method Ω_o, the longitudinal small oscillation angular frequency at zero current, and Z_b, the spatial length of the separatrix, are held constant. If the functional form of B is specified, then the three independent functions a, m and ϕ_s are determined. Expressions for Ω_o and Z_b are:

$$\Omega_o^2 = \frac{qVA\omega^2 |\sin \phi_s|}{4Mc^2\beta^2} \tag{13}$$

$$Z_b = \frac{\beta\lambda\Phi}{2\pi} \tag{14}$$

where Φ is the angular length of the separatrix, which is related to the synchronous phase ϕ_s by:

$$\tan \phi_s = \frac{\sin \Phi - \Phi}{1 - \cos \Phi} \tag{15}$$

In the region of small longitudinal oscillations and for adiabatic changes, constant Ω_o implies a beam envelope of constant length. For a longitudinally matched beam this also implies an invariant longitudinal charge density distribution and fixed beam length. This result holds for zero current and is also true in the presence of space-charge forces, if one assumes the beam bunch to be uniformly distributed in a three-dimensional ellipsoid of constant dimensions. Constant Z_b together with constant Ω_o, can be shown to make the charge-density distribution approximately constant for large longitudinal oscillations at zero current. As can be seen from Eqs. (14) and (15), the invariance of Z_b determines ϕ_s (β); Then equation (13) determines A(β).

This method of attempting to keep the charge density distribution approximately constant, while accelerating and bunching in phase, is expected to reduce those space-charge effects, such as radial emittance growth, that appear to be correlated with longitudinal compression of the beam bunch. However, after the resulting velocity profile $\beta(z)$ is determined, the function A(z) takes on small values, especially for large synchronous phases, and increases very slowly except near the end. This can result in an excessively long structure, particularly as the input synchronous phase approaches $\phi_s = -90^o$. To reduce the length, the initial value of ϕ_s must depart appreciably from -90^o, but this reduces the initial value of Φ, and results in reduced capture efficiency.

A generalization of the above method has been studied, in which the two constants Ω_o and Z_b are replaced by the new invariants ε and α, given as:

$$\varepsilon = \frac{-2\pi\dot{\Omega}_o}{\Omega_o^2} \tag{16}$$

and

$$\alpha = \Omega_o Z_b^2 \tag{17}$$

When $\varepsilon = 0$ this reduces to the K-T method. For positive ε, the small oscillation frequency Ω_o decreases at a constant percentage rate, and the separatrix length Z_b gradually increases. This approach is expected to yield a charge distribution that can slowly compress or expand in size depending upon the value of ε. In addition, for fixed final values of A and ϕ_s, the overall length decreases as ε increases. Generally acceptable solutions have been found with ε in the range $0 \leq \varepsilon \leq 0.2$.

The use of either the K-T approach or the generalized approach has been found to be effective in reducing radial emittance growth, while the beam is being bunched. This section of the RFQ is referred to as the Gentle Bunching Section. To obtain high capture efficiency, it is necessary to introduce a section before the Gentle Buncher in which the input variables are specified as a function of z rather than β, so that the input synchronous phase can start at $\phi_s = -90^o$ and the initial value of A can be A = 0. In order to reduce the overall length following the Gentle Buncher, a section was added that maintains a high value of A at the final synchronous phase. The remaining problem of radially matching the beam into the time-varying acceptance of the RFQ requires an initial section for matching. This leads to four stages in the overall design as shown schematically in Fig. 4.

The first stage, The Radial Matching Section, will be described. The matched ellipse parameters in the RFQ depend on the rf phase and are relatively independent of position along the linac. Therefore, the orientation of the acceptance ellipse depends on time. For proper matching into the RFQ, one must provide a transition from a beam having time-independent characteristics to one that has the proper variations with time. This means that at the input, a time-independent set of ellipse parameters is required, which will depend on the beam current. The present solution is to taper the vanes at the input of the RFQ so that the focusing strength changes from almost zero, to its full value over a distance of several (5-10) focusing periods. This procedure allows the time-independent beam to adapt itself to the time structure of the focusing system. Quadrupole symmetry is maintained throughout this section (no vane modulation).

This procedure is illustrated in Fig. 5. A display generated by the program TRACE,[9] has been modified to include rf quadrupoles,

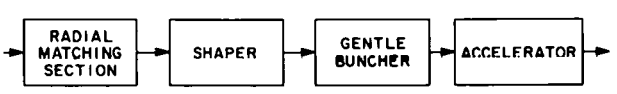


Fig. 4. Functional block diagram.

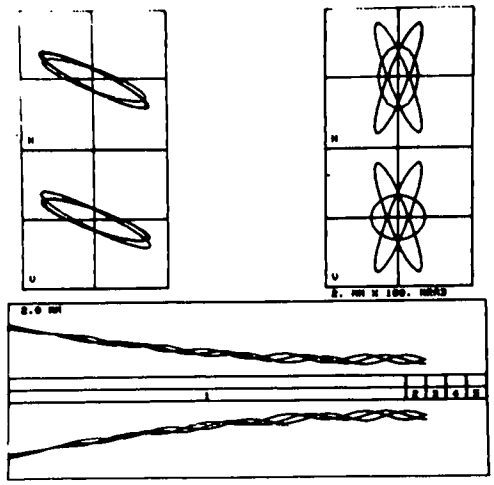


Fig. 5. Radial Matching Section.

either of constant or tapered strengths. The matched ellipse parameters are first found for various phases in the constant-strength section. Three such matched ellipses, corresponding to phases 90° apart, are shown in the upper right side of the figure for both the x-x' and y-y' planes. This graphically demonstrates how different the matched ellipses can be as a function of phase, and also shows the relatively small area of overlap that is common to all of these ellipses. The phase-space plots at the upper left are the result of following these same three ellipses backward through a tapered section of the RFQ, 5-periods long (10 cells). One can see that these ellipses are very similar and have a high degree of overlap. The bottom graph in the figure shows the horizontal and vertical profiles that result from following these three ellipses through the tapered rf quadrupole. Space-charge effects were included in this calculation, which assumed a beam current of 30 mA.

An unexpected benefit of the Radial Matching Section is that the increase in aperture at the input results in weak fringe fields and negligible fringe effects for both longitudinal and radial motions. The longitudinal field generated within the matching section is also negligible because of the fact that the change in B occurs over many rf cycles.

The second stage, called the Shaper Section, can begin at $\phi_s = -90°$. The accelerating field is increased steadily from zero, while ϕ_s is maintained at a large value, to obtain a high capture efficiency. Under the influence of the rising axial field, an input dc beam with small energy spread will rotate through many cycles of longitudinal oscillation. The filament in phase space wraps around itself to approximate a matched beam in longitudinal phase space. Some compression of the beam within the phase stable area is desirable to anticipate subsequent non-adiabatic behavior, which could lead to particle loss. At high beam currents, such compression should be limited, however, because of the large radial emittance growth that can result when the beam is tightly bunched. Even so, dramatic effects of space-charge repulsion will be especially apparent at the first phase foci for an input dc beam with small energy spread.

For the third stage, the Gentle Buncher, the generalized method is used, where Eqs. (16) and (17) are satisfied, and hold B constant. The Gentle Buncher Section completes the bunching begun in the Shaper Section and accelerates the quasi-matched beam from the Shaper until the final synchronous phase is reached. The bunch length and the charge density undergo no large change in the process.

When the final synchronous phase is reached, the Acceleration Section begins. In this section ϕ_s, m, and a are held at constant final values to apply a relatively large fraction of the intervane voltage on axis, and to bring the beam to its final energy within a short distance.

An important step in the design procedure is a choice of operating intervane potential, which normally should be as large as possible, consistent with the sparking limit. The results from program SUPERFISH[10] show that for the RFQ vanes constructed at LASL, the highest surface fields, E_s, occur in the middle of each cell at the point of pure quadrupole symmetry. The maximum field does not occur at the pole tip, but occurs at the point where the vanes have minimum separation. The field at the pole tip is V/r_o and the peak field $E_s = \kappa V/r_o$ where for this geometry $\kappa = 1.36$. Once the choice of maximum allowable surface field is made, the ratio V/r_o is determined.

After a choice of B is made, which provides a good compromise between radial stability and adequate aperture size, the quantities V and r_o can be obtained from the relations:

$$r_o = \frac{q\lambda^2 E_s}{Mc^2 B\kappa} \tag{18}$$

$$V = \frac{q\lambda^2 E_s^2}{Mc^2 B\,\kappa^2} \tag{19}$$

It is seen that higher surface field E_s and smaller B will increase both r_o and V. The average axial field then becomes:

$$E_o = \frac{2q\lambda A E_s^2}{Mc^2 B\beta\kappa^2} \tag{20}$$

Choose an initial value of m = 1. A final value of m = 2 produces a good compromise between acceleration efficiency, A, and focusing efficiency, X, at the end. If X is too small, the constraint that B is constant may make the final radius parameter too small.

Error Tolerances

After a linac has been designed, one must try to determine how sensitive the design is to all probable sources of error. The quantity and quality of the output beam can be degraded by a variety of things, such as a mismatch and a misteering of the input beam, and alignment errors and excitation errors in the linac. Tolerances can be specified for some of these errors only by running a large number of numerical simulations. For other types of errors, it is possible to make more general statements, and it is these types that we will be concerned with in this section.

The results can be specified in terms of the magnitudes of the multipoles of the focusing field relative to the quadrupole strength at the bore radius. The radial component of the nth multipole at radius, r, and angle, ψ, is defined to be:

$$E_{r,n} = A_n\left(\frac{r}{r_o}\right)^{n-1} \cos\ (n\psi - \delta_n) \quad , \tag{21}$$

where A_n is the amplitude and δ_n is the phase of the nth multipole, and r_o is the bore radius.

The values given below, as well as those given for image charge effects, (see Appendix) were obtained using a computer program that calculates the charge density induced on equipotential surfaces.[11] The unperturbed calculations were made with the vanes approximated by four circular cylinders symmetrically placed about the z-axis. The cylinder walls were a distance r_o from the z-axis and the diameter of each cylinder was $2r_o$.

Alignment errors

The vanes are displaced slightly from their proper positions. Symmetric displacements of opposite poles, inward or outward, have no significant effect other than changing the quadrupole strength slightly, which is equivalent to changing the operating voltage. Non-symmetric displacements introduce odd-order multipoles. An example of a nonsymmetric displacement is a horizontal displacement of the vertical vanes. A small displacement, d, has been calculated to produce multipoles of order 1, 3, and 5 having fractions of the quadrupole term of 0.16 d/r_o, 0.64 d/r_o, and 0.024 d/r_o, respectively. The dominant term appears to be the sextupole (n = 3), and by placing an acceptable limit on it one can specify a tolerance on d/r_o. If it is desirable to keep the sextupole term below 1%, then the tolerance on d/r_o is approximately 1.5%.

Excitation errors

The ideal excitation for the potential on each of the four vanes is oscillation between $\pm V/2$ at all points along the linac. Variations in the potential in the longitudinal direction will probably be gradual and small. Information about the longitudinal field can be obtained from beadpull measurements.

Errors in the transverse fields can be represented most generally by assuming that each vane is oscillating at a different potential. The potential on the ith-vane would oscillate between $\pm(V + \Delta V_i)/2$, and the excitation level could be adjusted so that the average potential is correct, which would make

$$\sum_{i=1}^{4} \Delta V_i = 0 \quad . \tag{22}$$

The voltage errors, ΔV_i, can be divided into symmetric and antisymmetric parts. The symmetric components correspond to errors on opposite poles having the same magnitude and the same sign; the antisymmetric components correspond to errors on opposite poles having the same magnitude and opposite signs. The symmetric components have no effect on the multipole spectrum, but the antisymmetric components will generate odd-order multipoles. Let v_x and v_y be the fractional antisymmetric components in the horizontal and vertical vanes, respectively. That is, the potential on the opposing horizontal vanes would oscillate with the magnitudes $(1 \pm v_x)V/2$. The magnitudes of the odd multipoles are found to be proportional to $v = (v_x^2 + v_y^2)^{1/2}$, and the ratio of the first four to the quadrupole strengths are given below:

$$A_1/A_2 = 0.397\ v \quad ; \tag{23}$$

$$A_3/A_2 = 0.308\ v \quad ; \tag{24}$$

$$A_5/A_2 = 0.029\ v \quad ; \tag{25}$$

$$A_7/A_2 = 0.041\ v \quad . \tag{26}$$

That is, a 10% antisymmetric component (v = 0.1) would cause a 4% dipole field and a 3% sextupole field. If it is necessary to keep the sextupole

field below 1%, then one must keep $v < 0.032$. The dipole field would simply cause a displacement of the electrical axis of the quadrupole by the same percentage.

Design of the 425-MHz RFQ Test

One of the applications of the RFQ under consideration at LASL is for the high-intensity 35-MeV deuteron accelerator being designed for the Hanford Fusion Materials Irradiation Test (FMIT) Facility to be installed at the Hanford Engineering Development Laboratory (HEDL) at Richland,Washington. An important step in evaluation of the RFQ for this linac is a full power test, which uses an existing proton injector and an existing source of rf power. As an example of the design method discussed above, the RFQ design for this test is presented, which will be called the 425-MHz Test Design. Table I shows a list of parameters. Because of limitations imposed by the existing hardware, the frequency was chosen at f = 425 MHz and the length was constrained to be equal to L = 110.8 cm.

The surface gradient, E_s, was chosen to have the conservative value 27 MV/m. After the Radial Matching Section, a constant value B = 5.85 provides a compromise between radial stability and tolerance requirements arising from the small aperture. The resulting characteristic average radius is $r_o = 0.2$ cm and the resulting intervane voltage is V = 44 kV. The objective of the test is to capture a dc beam of energy $W_i = 0.1$ MeV, bunch and accelerate it to some energy greater than about 0.5 MeV, and to study the performance as a function of input current. The exact value of the final synchronous phase is not important, as long as good bunching can be demonstrated. Two computer programs have been written to help generate parameters for the beam-dynamics program PARMTEQ (see Appendix). The first program generates the Gentle Buncher parameters as a function of axial distance z, given initial and final energies for this section and given the ε parameter. The second program takes the initial Gentle Buncher parameters as final values for the Shaper Section, generates Shaper parameters as a function of z, then traces particles through the Shaper in longitudinal phase space, thus giving an estimate of expected capture efficiency. In addition, both programs calculate several quantities as a function of z, such as the ratio of space-charge to focusing force (see Appendix), and longitudinal and radial oscillation frequencies. These results are useful as a guide to predict and interpret subsequent PARMTEQ results.

The chosen design is one with a Gentle Buncher parameter $\varepsilon = 0$, which corresponds to the K-T approach. Several designs made with $\varepsilon = 0.2$ gave comparable results. Figure 6 shows the resulting profiles from PARMTEQ for several variables. The four basic sections of the structure are indicated. The final energy after 110.8 cm and 165 cells is $W_f = 0.640$ MeV. The radial matching is done in the first ten cells or 5.2 cm, where B is linearly varied from an initial value of B = 0.20 to a final value B = 5.85, and is kept constant throughout the rest of the structure. The slow increase of m during the first half of the structure appears to be necessary in order to reduce radial space-charge effects as was discussed previously. As m increases and the acceleration efficiency A (not shown) also increases, the focusing efficiency, X, decreases. The constant value of B then implies a decrease in the radius parameter a. The transverse acceptance is determined by the final aperture and has a normalized value $A_n = 0.09\pi$ cm-mr at the nominal current of I = 15 mA. This can be compared with an expected input beam from the ion source having a normalized emittance of $E_n = 0.05\pi$ cm-mr. The input particle distribution used in the PARMTEQ calculation gave 100% of the beam within this phase-space area, and 90% within a normalized area of 0.034π cm-mr.

Table II lists the PARMTEQ results for the beam transmission efficiency, the output beam current, and the radial emittance growth. The emittance growth is the normalized emittance of the transmitted beam divided by the normalized emittance of the input beam. Both emittances are obtained from ellipses which

TABLE I

425-MHz TEST DESIGN PARAMETERS

Ion	H^+
Frequency	425 MHz
Input Energy	0.100 MeV
Output Energy	0.640 MeV
Intervane Voltage	44 kV
Minimum Radius Parameter	0.126 cm
Overall Vane Length	110.8 cm
Number of Cells	165
Nominal Current	15 mA

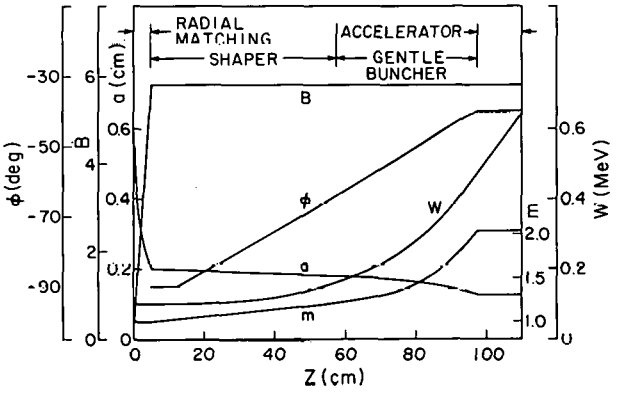


Fig. 6. Parameters for the 425-MHz test design.

TABLE II

RESULTS FROM 425-MHZ TEST DESIGN

Input Current (mA)	Transmission Efficiency (%)	Output Current (mA)	Radial Emittance Growth (90% Contour)
0	96.7	0	1.04
15	96.1	14.4	1.13
30	86.4	25.9	1.23
45	73.6	33.1	1.19
60	68.6	41.2	1.22
100	54.4	54.4	1.07

contain 90% of their respective beams. As the input current increases, a larger number of particles is lost radially to the bore, which decreases in size from the input to the output. This selective radial loss explains the decreasing emittance growth for the higher currents.

Figure 7 shows the phase, energy, and radial profiles and the transverse phase space in both planes for I=0 and for the nominal beam current of I=15 mA. The dotted lines on the x profile plot indicate the aperture size. Figure 8 shows the longitudinal phase space at several cells along the RFQ for both I=0 and I=15 mA, starting with an initial dc beam with zero energy spread. Space-charge effects, which become apparent near the first phase focus, persist throughout the remaining I=15 mA plots.

It is of interest to compare the results of the 425-MHz Test Design with those that are obtained by a more simple approach, where, after the initial matching section, ϕ_s is linearly increased from -90^o to -40^o and the modulation parameter m is linearly ramped from m = 1 to 2 over the total distance of 110.8 cm. This design is referred to as the Linear Ramp Design, and it is characterized by the lack of a Gentle Buncher Section. The Linear Ramp Design gives a larger final energy of W_f = 0.719 MeV in 150 cells, which exceeds that of the 425-MHz Test Design because of a larger average axial field. Results showing the beam transmission efficiency, output current and radial emittance growth for the Linear Ramp Design are presented in Table III.

TABLE III

RESULTS FROM LINEAR RAMP DESIGN

Input Current (mA)	Transmission Efficiency (%)	Output Current (mA)	Radial Emittance Growth (90% Contour)
0	96.9	0	1.12
15	79.2	11.9	1.48
45	41.4	18.6	1.16

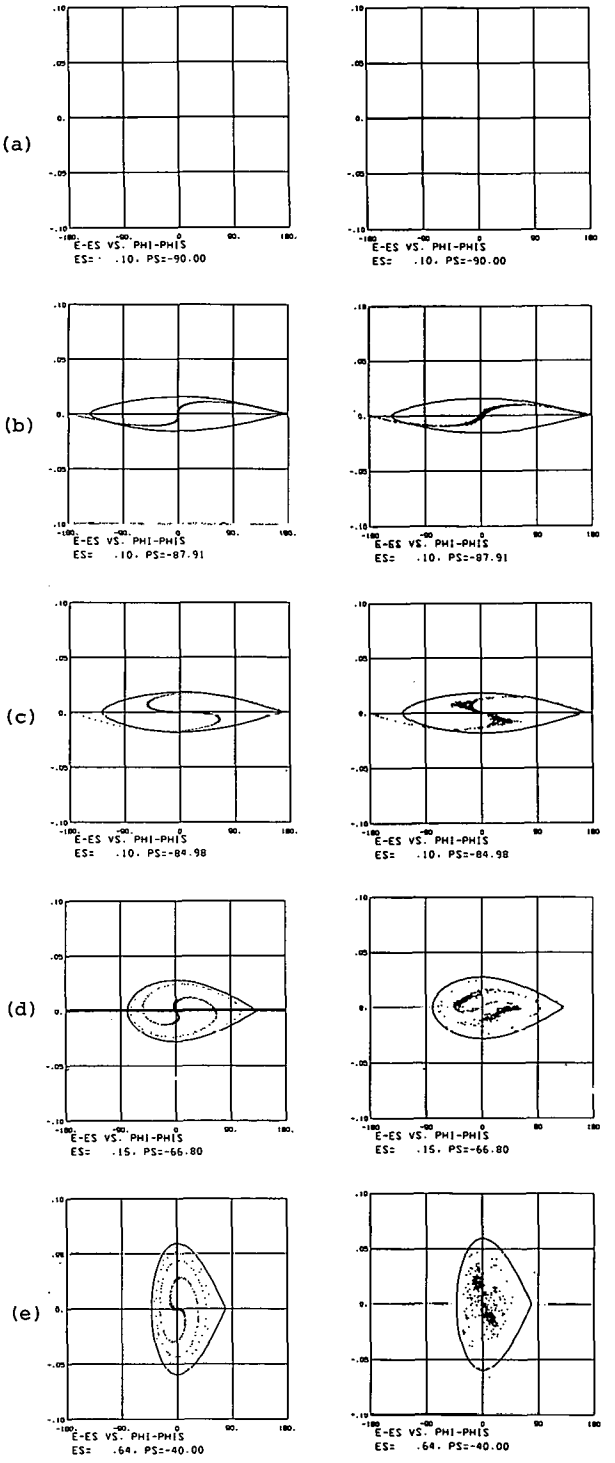
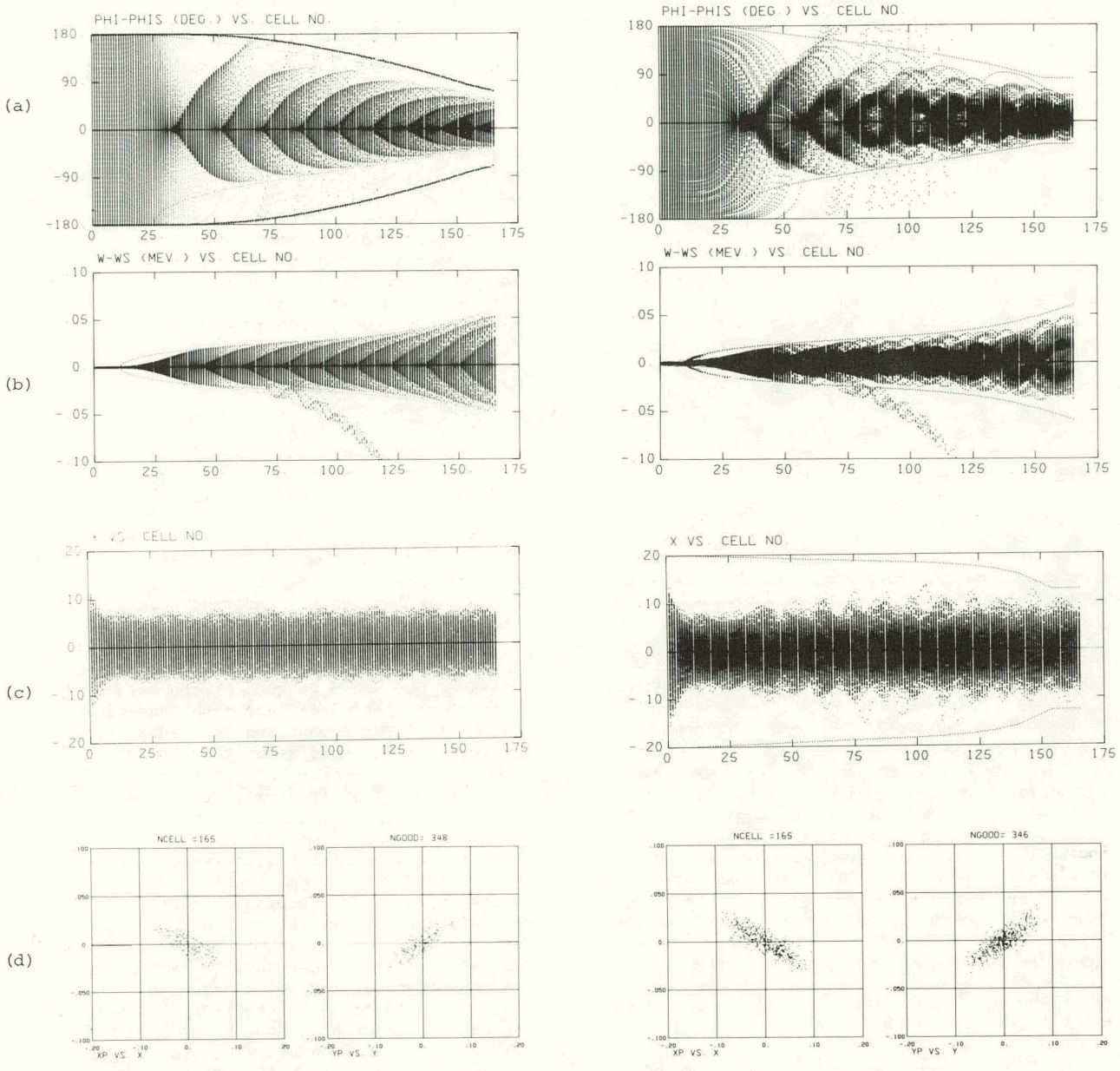


Fig. 8. Longitudinal phase space at center of cell for 425-MHz test design: (a) cell 1 (beginning), (b) cell 32 (near first phase focus), (c) cell 42 (after first phase focus), (d) cell 100 (start of Gentle Buncher), (e) cell 165 (end).



I = 0 mA

I = 15 mA

Figure 7

Results from the 425-MHz Test Design:

(a) phase profile,
(b) energy profile,
(c) x profile,
(d) final radial phase space.

If we compare the results in Table III with those presented in Table II, it is seen that the simple linear ramp approach gives good transmission efficiency when space-charge can be neglected. But, as expected, the 425-MHz Test Design is clearly superior in terms of transmission efficency at the non-zero beam currents shown. The radial emittance-growth numbers are significantly perturbed by particle loss at the larger beam currents in both designs.

Acknowledgments

We thank E. A. Knapp, R. A. Jameson, and D. A. Swenson for advice and encouragement. We acknowledge valuable discussions with R. L. Gluckstern, LASL consultant, concerning the Shaper design, and we thank G. W. Rodenz for assistance with the computer calculations.

Appendix

Image Charge Effects

We have tried to estimate the magnitude of the effects on the beam caused by the image charges induced on the vanes by the beam itself. The simplifying assumptions made in this analysis overestimate the image-charge effects.

In the high-energy end of the linac, where the beam is bunched and the vanes have a relatively large modulation, it appears that the image charges actually produce an alternating focusing and defocusing effect for both the longitudinal and radial motions. At present we have no quantitative estimate of the image forces at the high-energy end but we have calculated the effects at the low-energy end, where the main effect is radially defocusing.

The image charges produced by a continuous beam with a circular cross-section, centered on axis, will cause multipole fields of order 4, 8, . . ., proportional to the beam current. For a beam with radius r_b, the ratio of the magnitudes of the image force to the space-charge force at the edge of the beam was calculated to be:

$$\frac{\text{image force}}{\text{space-charge force}} = 0.422\left(\frac{r_b}{r_o}\right)^4 + 0.118\left(\frac{r_b}{r_o}\right)^8 + \ldots, \tag{A-1}$$

where r_o is the bore radius. If $r_b = 0.5\ r_o$, then this ratio is less than 3%.

A displacement of the beam center from the axis produces image charges that cause other multipole components, the main ones being the n = 1, 3, and 5 terms. The magnitudes of the n = 4, 8, . . . multipoles are relatively unchanged by small displacements of the beam. The strength of the dipole field is approximately 0.78 E r_c/r_o, where r_c is the displacement of the beam center from the axis, and E is the space-charge field produced by the beam at a distance r_o from its center. The magnitudes of the n = 3 and n = 5 multipole fields are each approximately half of the magnitude of the dipole field.

Based on these results, the following conclusion can be made: as long as the beam is well centered ($r_c < 0.2\ r_o$) and the beam does not fill a large fraction of the aperture ($r_b < 0.6\ r_o$) then the image forces are at least an order of magnitude lower than the space-charge forces and can be neglected without seriously affecting the results. If these conditions are violated, then the image forces might become comparable to the space-charge forces and could cause an increase in the beam loss and in the emittance growth.

Outline of PARMTEQ

The computer program used to study the beam dynamics of the RFQ linac is called PARMTEQ, (Phase and Radial Motion in Transverse Electric Quadrupoles). It is a modified version of PARMILA, and performs four basic functions. It generates an RFQ linac, generates a variety of input particle distributions, performs beam dynamics calculations, and generates a variety of outputs.

The information required for generating an RFQ linac consists of the following: the vane voltage; the linac frequency; the mass of the particles; the initial and final energies; and a table of values specifying the radial focusing strength B, the vane modulation parameter m, and the synchronous phase, all at specified distances along the structure. The linac is generated cell-by-cell, in an iterative procedure.

The beam dynamics calculations are performed as follows: each cell is divided into a number of segments (typically four, with a maximum of eight). Initial values of the dynamical quantities x, x', y, y', ϕ, and W are transformed to final values through each segment. The phase and energy coordinates are the first to be transformed. In the radial transformations, the quadrupole and the rf defocusing terms are treated separately. The quadrupole transformation is that of a standard quadrupole having a length equal to the segment length, and a strength that depends on the rf phase as the particle passes through the segment. Consequently, each particle will experience a different quadrupole force depending on its own phase. The rf defocusing term is treated as an impulse or thin lens, whose strength depends on the rf phase as well as on the location of the particle in the cell.

At the middle of each cell, the particles are given an impulse to simulate the space-charge forces. This is the most difficult transformation to make satisfactorily. In order to calculate properly the space-charge forces, one needs to know the positions of all the particles at a given instant in time. Instead,

one knows the particle coordinates as they arrive at a particular location along the linac. There is a big difference between these two situations when there is a large phase spread in the beam, as there is in the low energy portion of the RFQ. Consequently, before calculating the space-charge forces it is important to estimate the particle positions at a given instant in time, which was chosen to be the time when the rf field is zero. At this particular time, the cross-section of the beam should be very nearly circular. A series of transformation matrices is generated, considering only the quadrupole term, that transforms the radial coordinates from their values at all other phases within $\pm 180^{\circ}$ in 5° increments. For each particle the transformation matrix is found that most nearly agrees with the particle phase, and the inverse of the transformation is applied, giving an estimate of the particle's radial coordinate at the desired phase. The longitudinal position is estimated from the particle's velocity and phase. After doing this for all of the particles, the space-charge forces are calculated and the impulses are applied by changing x', y', and W for each particle. The radial coordinates are then similarly transformed back to their modified values at their original phases, and this completes the space-charge transformation for one cell.

After the space-charge transformation, the coordinates are transformed through the remainder of the segments in the cell. A variety of output subroutines can be called at the end of any cell, or at the middle of any cell, either before or after the space-charge impulse is applied.

Some RFQ Scaling Methods

Some RFQ applications may require a method of scaling an existing design to some new frequency. At fixed β a change in frequency will cause a change in the operating point on the radial stability chart, which changes the transverse beam dynamics. An exactly equivalent structure may not be obtainable when the frequency is changed. A useful guide for generating solutions at new frequencies is to impose a direct geometric scaling of dimensions in proportion to wavelength. Thus at each cell the radius parameter, a, is proportional to λ, and m is unchanged. The frequency dependence of a and E_s tends to make B, Δ, and V decrease as frequency increases and makes E_o increase somewhat with increasing frequency.

For high-current applications of the RFQ it is useful to have some means of evaluating the expected importance of space-charge effects. It is useful to compute the ratio μ of the space charge force to the average or smoothed restoring force. Assume a model where the beam bunch is represented by a uniform distribution of charge within a three-dimensional ellipsoid. For longitudinal motion it is found that:

$$\mu_\ell = \frac{90\, I(\text{amps})\lambda^3\beta^2 f(b/r_b)}{\pi^2 V(\text{volts}) b r_b^{\,2} A |\sin \phi_s|} \qquad \text{(A-2)}$$

where $r_b^2 = r_x\, r_y$ and b is the half length of the bunch. The function $f(b/r_b)$ has the approximate value $f(b/r_b) = r_b/3b$ in the range $0.8 < b/r_b < 5$.

For radial motion we use

$$\mu_r = \frac{45 q I(\text{amps})\lambda[1 - f(b/r_b)]}{Mc^2(\text{eV})\beta^2 r_b^{\,2} b k_r^{\,2}} \qquad \text{(A-3)}$$

where $k_r^{\,2} = \frac{1}{8\pi^2\beta^2\lambda^2}\left[B^2 + 8\pi^2\Delta\right]$.

Generally μ_ℓ and μ_r are kept less than about 0.5 in order to control beam losses due to a reduced stable phase space area. Since μ_ℓ and μ_r affect the frequencies of longitudinal and radial motion, the additional condition must be met, that resonance must be avoided.

Limiting current expressions can be obtained if the limits are assumed to occur when $\mu_\ell = 1$ and $\mu_r = 1$. Assume that the bunch half-length is related to the synchronous phase by:

$$b = \frac{\beta\lambda|\phi_s|}{2\pi} \qquad \text{(A-4)}$$

The approximate form for $f(b/r_b)$ is assumed and $\sin \phi_s$ is replaced by ϕ_s. For the longitudinal limit:

$$I_\ell = \frac{AV|\phi_s|^3 r_b}{120\lambda} \qquad \text{(A-5)}$$

where r_b is the beam radius. The radial limit is:

$$I_r = \frac{\beta|\phi_s| r_b^{\,2} Mc^2\left[B^2 + 8\pi^2\Delta\right]}{720\pi^3\lambda^2 q[1 - f]} \qquad \text{(A-6)}$$

The longitudinal limit decreases rapidly as the beam is bunched in phase. The radial limit increases with β, but also decreases while the beam is bunched in phase.

At the front end of the RFQ, where the beam is in transition between a dc and a bunched

beam, these formulas will not apply. The lack of separation of bunches will be expected to reduce the longitudinal space-charge repulsion, but the conditions arising at each phase focus can create localized unstable regions, where space-charge forces may exceed the focusing forces.

References

1. V. V. Vladimirskii, Prib. Tekh. Eksp. No. 3, 35 (1956).
2. G. M. Anisimov and V. A. Teplyakov, Prib. Tekh. Eksp. No. 1, 21 (1963).
3. V. A. Teplyakov, Prib. Tekh. Eksp. No. 6, 24 (1964).
4. F. Fer, P. Lapostolle, C. Beith, and A. Cabrespine, Proc. Int. Conf. on Linear Accelerators, Dubna (Aug. 1963), ed. A. A. Kolomesky, A. B. Kusnetsov, and A. N. Lebedev.
5. I. M. Kapchinskii and V. A. Teplyakov, Prib. Tekh. Eksp. No. 2, 19 (1970).
6. I. M. Kapchinskii and V. A. Teplyakov, Prib. Tekh. Eksp. No. 4, 17 (1970).
7. R. H. Stokes, K. R. Crandall, J. E. Stovall, and D. A. Swenson, IEEE Trans. on Nucl. Sci. NS-26, 3469 (1979).
8. J. M. Potter, S. W. Williams, F. J. Humphry, and G. W. Rodenz, IEEE Trans. on Nucl. Sci. NS-26, 3745 (1979).
9. K. R. Crandall, "TRACE"; An Interactive Beam-Transport Program," LA-5332, (October 1973).
10. K. Halbach, R. F. Holsinger, W. E. Jule and D. A. Swenson, "Properties of the Cylindrical Rf Cavity Evaluation Code SUPERFISH," Proc. of 1976 Proton Linac Conf., Atomic Energy of Canada Ltd. Report No. AECL-5677, 122 (1976).
11. K. R. Crandall, "Computation of Charge Distribution on or Near Equipotential Surfaces," LA-3512, (December 1966)

Discussion

(Editor's Note: The first comment refers back to Discussion following the paper by D. Swenson, "Low Beta Structures".)

Teng, Fermi Lab: I think the misunderstanding of this radial matching is just a matter of semantics. It is usually called adiabatic capture, not matching. Matching is something in which you catch the phase ellipse on-the-fly, when the shape is exactly right. In your case, you are just turning it on gently.

Wrangler: Yes, I guess we've been thinking of adiabatic capture as a longitudinal effect primarily, but this would be the transverse version.

Miller, SLAC: Could I see your first slide again with the equations of the fields. I think that I see that the quadrupole fields are indeed spatially constant but you have a solenoidal field that has a z-dependence. E_r has a z-dependence, but E_ψ does not. (Crandall: That's what we interpret as an rf de-focus term.)

Miller: You probably shouldn't call it "de-focus" because its alternating gradient and the net effect is focusing.

Wrangler: This is the rf de-focus term associated with the accelerating field.

Miller: But it has a k_z-dependence, so it's alternating and it gives a net focusing.

Wrangler: The dominant term is the quadrupole term which arises when we turn on the accelerating field. It gives us a transverse force which depends on the particle phase. When particles are being accelerated there is going to be a de-focusing force in the transverse plane. Those terms are dominating in the focusing.

Miller: Oh yes, I see.

INFLUENCE OF SPACE CHARGE ON AXIAL PARTICLE MOTION IN HEAVY ION LINACS

P. Junior, H. Deitinghoff, H. Klein
Institut für Angewandte Physik der Universität Frankfurt/Main
D-6000 Frankfurt/Main, Germany

Summary

Considerations of beam dynamics for heavy ions within the frame of linear approximation at very low velocities are carried out. Decrease of acceptance due to space-charge for axial and radial motion is estimated. The behavior of idealized axial and radial beam envelopes with respect to space-charge and linac parameters is studied.

Necessity of Linear Theory

Theories of accelerator beam dynamics have always benefitted advantageously from the establishment of linear equations of motion. However, any linear approximation involves problems as soon as space-charge effects have to be considered. Yet, under certain assumptions, linear equations may still be used. For example; special geometric shapes of a particle beam permit the application of the well-known Kapchinskij-Vladimirkskij (K-V) model[1]. Within this frame Reiser derived his formula for the maximum charge in a FODO channel[2]. Adaptation to realistic charge distributions has been performed by Sacherer[3] and Lapostolle[4] using an RMS formalism. Basically, all these theories have to be restricted to transverse motion, requiring axial dimensions of the beam to be assumed large compared to transverse ones. This postulation seems violated in many linacs, especially at initial velocities, and certainly for the case of low charge state heavy ions in a fusion linac, where the axial envelopes are comparable to or smaller than the transverse ones. This paper discusses two models, deriving linear equations for the axial motion.

Linear theory in the presence of space-charge seems effective for many reasons. The many-body problem may be treated within the convenient frame of a comprehensive envelope representation, as only linear transformations conserve the ellipse character. This formalism collapses; however, as soon as at least one of the driving forces proves non-linear. The alternative is the use of long and expensive computational efforts. Validity and applicability of these models involve problems associated with the self-consistency of the theory.

Linac Models

For the first case, consider the K-V model[1], but replace one of the transverse motion components by the axial one. In the linac, assume a uniformly charged cylindric beam with an elliptic cross-section as Fig. 1 demonstrates. Axes are a_x, a_z, respectively. The beam does not move

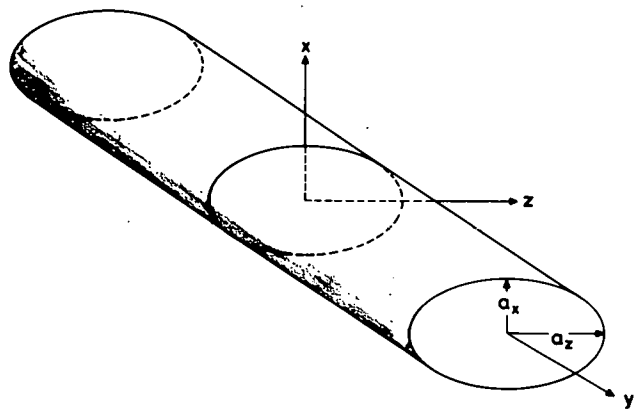


Fig. 1 Elliptic cylinder assigned to K-V model

along the y-direction but is accelerated transversely in the z-direction. Acceleration is provided by a plane wave, although it is understood that longitudinal plane electromagnetic waves do not exist. Dimensions should be regarded as infinite in the y-direction. With respect to Ref. 1, identical emittance areas in both phase space planes $x\text{-}\dot{x}$, $z\text{-}\dot{z}$ yield equations for axial and radial synchronous particles, respectively:

$$\frac{d^2z}{dt^2} + \frac{e}{m}\left(\frac{\omega}{v} E_o \sin\phi_s - \frac{3Q}{4\pi\varepsilon_o}\frac{F_z}{a_x^2 a_z}\right) z = 0 \qquad (1)$$

$$\frac{d^2x}{dt^2} - \left[\frac{e}{m}\left(\frac{\omega}{v} E_o \sin\phi_s + \frac{3Q}{4\pi\varepsilon_o}\frac{F_x}{a_x^2 a_z}\right) - D\right] x = 0 \qquad (2a)$$

There is a certain degree of freedom in the choice of a proper charge Q, which has been taken advantage of by cutting out of the beam rod a rotational ellipsoid with axes a_x, a_x, a_z, which fully contains Q, giving a relation for the uniform charge density ρ:

$$\rho = \frac{Q}{4/3\pi a_x^2 a_z}$$

Focusing is formally expressed by an elastic force Dx, where the elastic constant may be produced by an extended uniform axial magnetic field:

$$D = \frac{1}{4}\left(\frac{e}{m}\right)^2 B^2$$

An essential difference from Reference 1 must be pointed out. References 1 and 2 employ identical forces, disregarding the phase in the case of

quadrupole lenses. Consequently, a restriction to identical emittance areas certainly proves to be unimportant in the K-V case, whereas, this means a severe restriction in the present case, as axial and radial emittance areas usually are not equal.

In Eqns. 1 and 2a form factors F_x and F_z were introduced, which are expressed as:

$$F_z = \frac{a_x}{a_x + a_z} \quad , \; F_x = 1 - F_z \tag{3a}$$

for the charge distribution of Fig. 1.

As a second model consider a uniformly charged ellipsoid with axes a_x, a_y, a_z as shown in Fig. 2. As with model 1, this form yields linear equations.

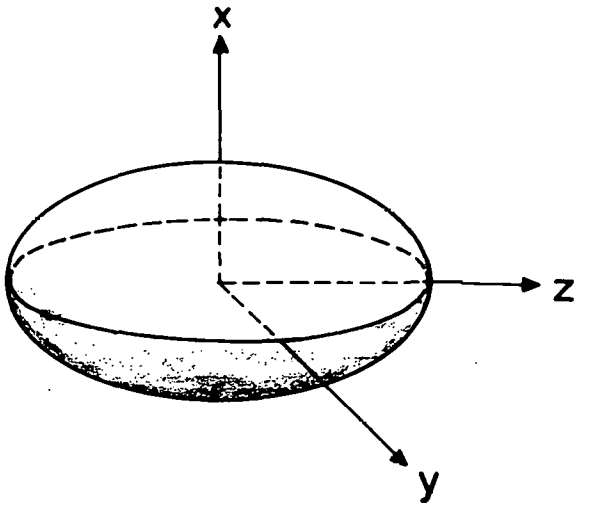


Fig. 2 Rotational ellipsoid as 3-dimensional beam model

Specifically, consider the case of rotational symmetry, $a_x = a_y$, admitting an identical axial equation (1), but a formally different radial equation[5,6,7]:

$$\frac{d^2x}{dt^2} - \left[\frac{e}{m}\left(\frac{1}{2}\frac{\omega}{v}E_o\sin\phi_s + \frac{3Q}{4\pi\varepsilon_o}\frac{F_x}{a_x^2 a_z}\right) - D\right]x = 0 \tag{2b}$$

and form factors

$$F_z = \frac{v^2}{\sqrt{1-v^2}^3}\left(\frac{1}{2}\ln\frac{1+\sqrt{1-v^2}}{1-\sqrt{1-v^2}} - \sqrt{1-v^2}\right), v = \frac{a_x}{a_z} \leq 1$$

$$F_z = \frac{v^2}{\sqrt{v^2-1}^3}\left(\sqrt{v^2-1} - \arctan\sqrt{v^2-1}\right), v = \frac{a_x}{a_z} \geq 1$$

$$F_x = \frac{1 - F_z}{2} \tag{3b}$$

In the general case of $a_x \neq a_y$ the equations are still linear, but the form factors have to be calculated numerically with elliptic integrals.

Self-Consistency

Beyond doubt the first model seems self-consistent, but an explanation should be inserted here. The space-charge field is assumed to be generated by the proper K-V particle distribution, covering the surface of a 4-dimensional ellipsoid, as will be shown later. Synchronous particles ($z = 0$, $\dot{z} = 0$) with respect to equations (2a), (2b) do not belong to these in general, but to some extent do not cause any disturbance of the external K-V field. This K-V distribution actually corresponds to the general equation:

$$\frac{d^2x}{dt^2} - \left[\frac{e}{m}\left(\frac{\omega}{v}E_o\sin\phi_s + \frac{\omega^2}{v^2}E_o z\cos\phi_s + \frac{3Q}{4\pi\varepsilon_o} \cdot \frac{F_x}{a_x^2 a_z}\right) - D\right]x = 0 \;,$$

where a coupling term, $\omega^2 E_o z\cos\phi_s/v^2$, is added for the non-synchronous K-V particles. In this interpretation equations (1) and (2a) together with (3a) are still valid.

In Table 1, the course of analysis in Ref. 1 is extended to the cases of one and three dimensions. After comparing all columns of Table 1, it is seen that the uniformity of charge distribution in real space remains intact only when two dimensions are considered. Both of the other cases are not consistent with uniform charge distribution in real space; consequently, equations (1), (2b) in combination with (3b) describing Model 2, turn out non-realistic.

The following one-dimensional example shall illustrate this: for reasons of simplicity, take the emittance ellipse in the two-dimensional phase space to be on its principal axes. Additionally, units are chosen such that this ellipse becomes the unit circle. Electrical charge is distributed uniformly on the circle arc and according to Fig. 3a, the charge density projected on the x-axis appears non-uniform. This suggests a non-uniform charge distribution on the arc such that its projection becomes uniform, as Fig. 3b indicates. Now, taking this as a synchrotron ellipse, and transporting it through the corresponding optical system, all points in phase space, including those carrying charge, are rotated by an angle μ, where μ stands for the Flocquet exponent of the optical system[8,9]. Obviously the initially uniform charge density has turned out inhomogeneous after transport, as Fig. 3c illustrates. Thus, it appears as illogical in the case of 3-dimensions as it does for 1-dimension, to enforce uniformity of the charge distribution in real space, by laying on the surface of the corresponding 6-dimensional hyperellipsoid, an inhomogeneous charge distribution according to

$$(F_o - x^2/\delta_x^2 - y^2/\delta_y^2 - z^2/\delta_z^2)^{-\frac{1}{2}}$$

Table 1

	1	2	3
Real space dimensions	1	2	3
Phase space dimensions	2	4	6
Ellipsoid equation in phase space	$(\delta_x\dot{x} - \dot{\delta}_x x)^2 + \frac{x^2}{\delta_x^2} = F$	$(\delta_x\dot{x} - \dot{\delta}_x x)^2 + \frac{x^2}{\delta_x^2}$ $+ (\delta_z\dot{z} - \dot{\delta}_z z)^2 + \frac{z^2}{\delta_z^2} = F$	$(\delta_x\dot{x} - \dot{\delta}_x x)^2 + \frac{x^2}{\delta_x^2}$ $+ (\delta_y\dot{y} - \dot{\delta}_y y)^2 + \frac{y^2}{\delta_y^2}$ $+ (\delta_z\dot{z} - \dot{\delta}_z z)^2 + \frac{z^2}{\delta_z^2} = F$
Charge density in phase space $n = n_o\delta(F - F_o)$	Uniform charge per arc unit length on plain 2-dimensional ellipse periphery F_o	Uniform charge per unit area on 4-dimensional ellipsoid surface F_o	Uniform charge per unit area on 6-dimensional ellipsoid surface F_o
Charge density in real space	$\rho(x) = \int n(x,\dot{x})\,\dot{dx}$	$\rho(x,z) = \int n(x,\dot{x},z,\dot{z})\,\dot{dx}\dot{dz}$	$\rho(x,y,z) = \int n(x,\dot{x},y,\dot{y},z,\dot{z})\,\dot{dx}\dot{dy}\dot{dz}$
Substitution polar coordinates	$\delta_x\dot{x} - \dot{\delta}_x x = \alpha$ $\dot{dx} = \frac{d\alpha}{\delta x}$	$\delta_x\dot{x} - \dot{\delta}_x x = \alpha\cos\phi$ $\delta_z\dot{z} - \dot{\delta}_z z = \alpha\sin\phi$ $\dot{dx}\dot{dz} = \frac{2\pi\alpha d\alpha}{\delta_x\delta_z}$	$\delta_x\dot{x} - \dot{\delta}_x x = \alpha\cos\phi\cos\theta$ $\delta_y\dot{y} - \dot{\delta}_y y = \alpha\sin\phi\cos\theta$ $\delta_z\dot{z} - \dot{\delta}_z z = \alpha\sin\theta$ $\dot{dx}\dot{dy}\dot{dz} = \frac{4\pi\alpha^2 d\alpha}{\delta_x\delta_y\delta_z}$
Charge density in real space	$\rho(x) = \frac{en_o}{2\delta_x}\int_o^\infty \delta(\alpha^2 - F_o + \frac{x^2}{\delta_x^2})\frac{d\alpha^2}{\alpha}$ $= \frac{en_o}{2\delta_x}\frac{1}{\sqrt{F_o - \frac{x^2}{\delta_x^2}}}$	$\rho(x,z) = \frac{\pi en_o}{\delta_x\delta_z}\int_o^\infty \delta(\alpha^2 - F_o + \frac{x^2}{\delta_x^2} + \frac{z^2}{\delta_z^2})\,d\alpha^2$ $= \frac{\pi en_o}{\delta_x\delta_z}$	$\rho(x,y,z) = \frac{2\pi n_o}{\delta_x\delta_y\delta_z}\int_o^\infty \delta(\alpha^2 - F_o + \frac{x^2}{\delta_x^2} + \frac{y^2}{\delta_y^2} + \frac{z^2}{\delta_z^2})\,\alpha d\alpha^2$ $= \frac{2\pi n_o}{\delta_x\delta_y\delta_z}\sqrt{F_o - \frac{x^2}{\delta_x^2} - \frac{y^2}{\delta_y^2} - \frac{z^2}{\delta_z^2}}$
Integral formula	$\int_o^\infty \frac{\delta(x - a)}{\sqrt{x}}\,dx = \frac{1}{\sqrt{a}}$	$\int_o^\infty \delta(x - a)\,dx = 1$	$\int_o^\infty \delta(x - a)\sqrt{x}dx = \sqrt{a}$
Uniform?	no!	yes!	no!

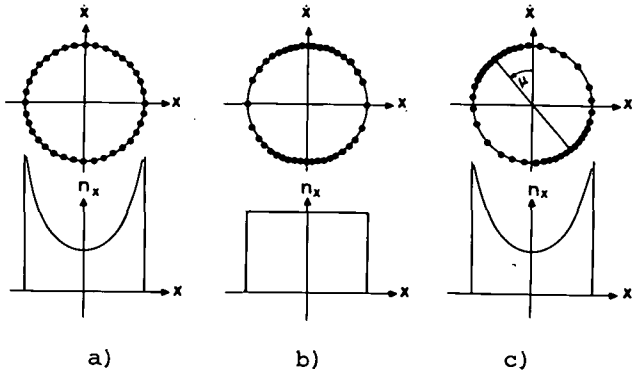


Fig. 3 a) Uniform surface charge density on phase space ellipse. Inhomogeneous charge distribution in real space

$$n_x \sim \frac{1}{\sqrt{1 - x^2}}$$

b) Inhomogeneous surface charge density on phase space ellipse. Uniform charge distribution in real space.

c) Rotated phase space ellipse after transfer over optical period, angle μ. Phase space and real space distributions both inhomogeneous.

Thus the 6-dimensional hyperellipsoid of Table 1 is not capable of producing a 3-dimensional uniform charge distribution. Both models prove non-physical. In one case, one trades conservation of uniformity for the sacrifice of a dimension, while in the other, uniformity must be abandoned because of the requirement for 3-dimensions.

Computational Results

The computations presented in this paper took into account mainly model 2, in spite of the lack of self-consistency mentioned, because of the considerable deviations associated with the extraordinary factor 2 in (2a) due to the plane wave assumption. Effects of different form factors, (3a) and (3b) cause less severe deviations. Fig. 4 shows a maximum decline at $a_x = a_z$ with 0.5 (3a) compared to 0.33 (3b), whereas both form factors merge at $a_x << a_z$ and $a_x >> a_z$.

As a linac (neglecting any practical realization at the moment) a chain of rf-resonators (helix, spiral, splitring, etc.) is favored. The scheme is shown in Fig. 5. Focusing should be provided by superconducting coils wound on the resonator tanks.

Data are summarized in Table 2.

For the calculations, a computer program has been developed, which gives the axial and radial synchrotron acceptances of the first section, using equations (1), (2b), (3b). Envelope radii required for the solutions of (1), (2b) are computed iteratively, where the chargeless case Q = 0 is taken as a zero approximation. Elements

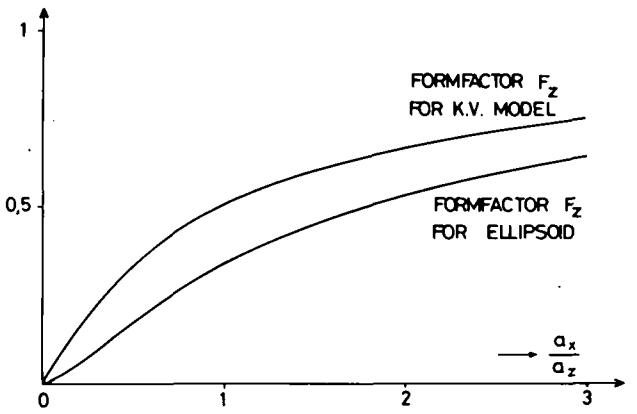


Fig. 4 Form factors for K-V model and ellipsoid

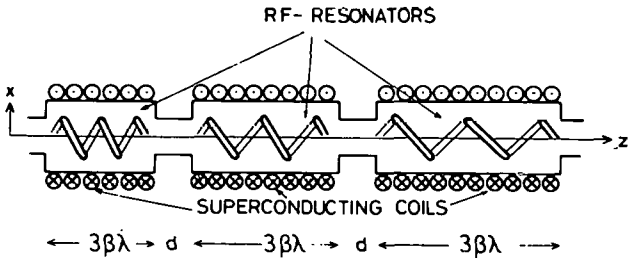


Fig. 5 Scheme of the linac considered

Table 2

Particle: $^{2}_{130}Xe$
Initial energy: 1 MeV
Final energy: 23,4 MeV
Constant voltage gain per section: 0.28 MV
Linac frequency: 13.5 MHz
Number of sections: 40
Synchronous phase: 30° (45°)
Initial axial envelope: 30°
Section length: 3βλ
Drift length: 10 cm

of all beam transports form WKB transfer matrices[10]. A more detailed report on this computer program will soon be published. It should additionally be noted that the basic implied postulate of identical emittance areas[1] with respect to both motion components is not included in this paper. For that, a further iteration procedure is required, for which work has started.

The program obviously admits similar computations of Wideroe (βλ/2) and Alvarez (βλ) structures.

Figure 6 shows a typical slope of acceptances with bunch charge, where $Q = 10^{-10}$ C corresponds to a particle current of $4.22 \cdot 10^{15}$ particles per second (duty factor 1).

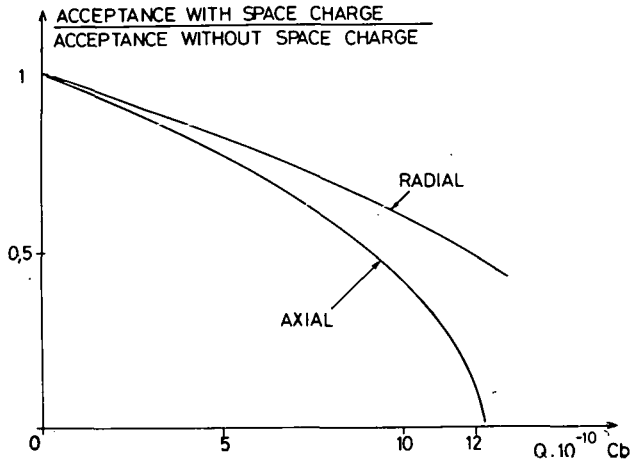


Fig. 6 Decrease of acceptances with space charge. 10^{-10} C $\hat{=}$ $4.22 \cdot 10^{15}$ particles/s. Radial envelope radius 1 cm.

Defining "maximum" charge as the one which reduces the smaller of the two acceptances to 50% with respect to the chargeless case, Fig. 7 indicates an extraordinary behavior, caused by the aperture dependence in the form factor (3b) of Fig. 4. Here this maximum charge is shown versus the radial aperture indicating that restriction of maximum charge is due to axial losses at large apertures, independent of the focusing field. Improvement with a stronger magnetic field is only seen at smaller apertures. This coupling effect of both motions, where coupling is exclusively caused by space charge effects, is more obvious in the next figure. As Fig. 8 indicates, charge and magnetic pressure, when sufficiently high, give rise to a squeezing effect to such an extent that the beam moves axially, where the pressure is less. Thus a tendency to incompressible behavior is observed, causing instabilities especially due to envelope coupling effects, as the magnetic field does not show up explicitly in the axial equation (1). With regard to the case with zero space-charge, Flocquet exponents range from $\mu_o = 30^o$ at 11 Tesla up to $\mu_o = 80^o$ at 22 Tesla.

Figure 9 shows an example of beam envelope in a long linac, data being given in Table 2. Here axial and radial beam envelopes are traced through 40 sections. Due to a rather moderate acceleration field, the phase oscillation amplitudes are increasing in the first sections, damping being delayed due to space-charge. Several pairs of envelopes which were considered, give an explanation of the beam behavior, namely: a strong envelope coupling between axial and radial motions after starting together with a rather unfavorable development of the axial Flocquet exponent. Axial and radial amplitudes turn out similar. The electrical field together with a more advantageous synchronous phase is increased, but still damping of phase oscillations is essentially prevented by

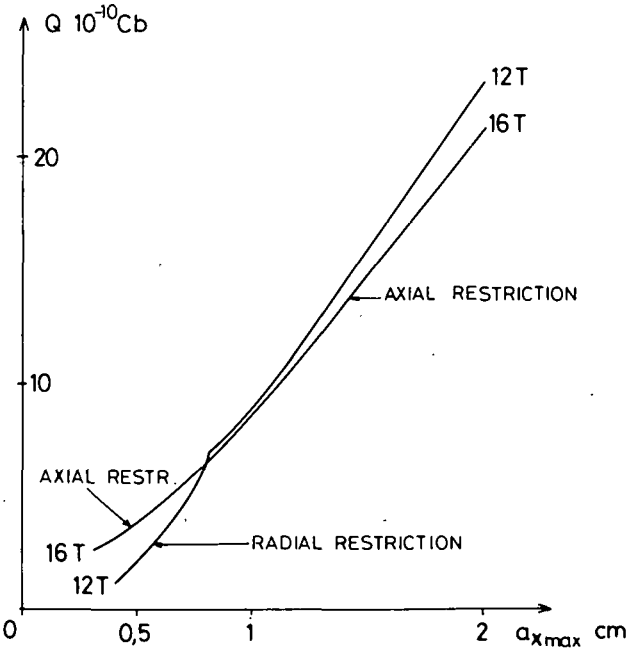


Fig. 7 Typical aperture dependence of maximum charges at two magnetic focusing fields.

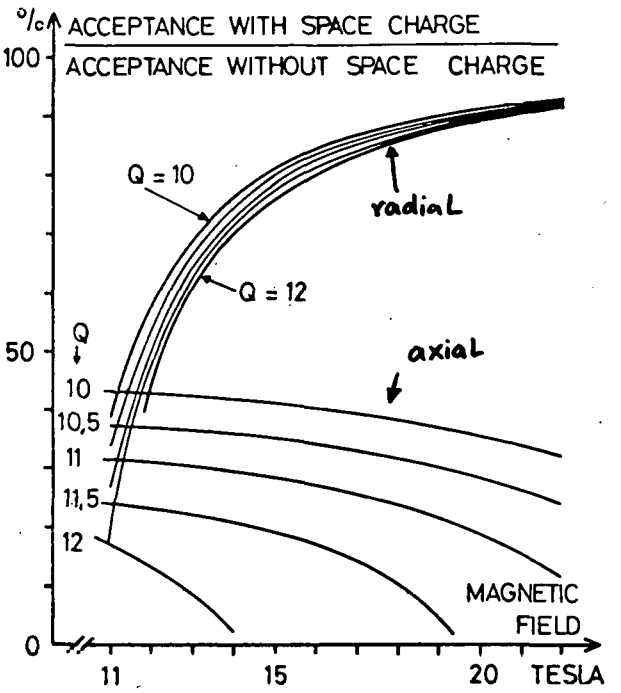


Fig. 8 Squeezing effect of strong magnetic field on axial acceptance. Radial envelope radius 1 cm.

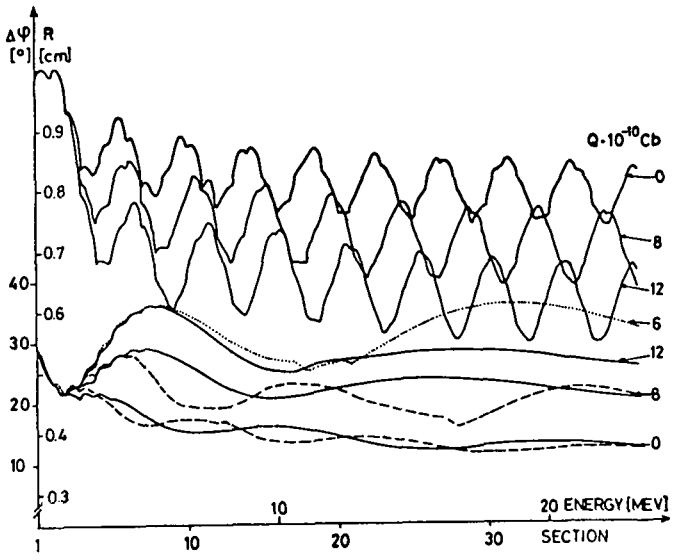


Fig. 9 Radial (above) and axial (below) envelope behavior at several bunch charges

space-charge, as the dashed curves indicate. For a comparison of the two models, the dotted curve illustrates even a more unfavorable beam behavior in case of Model 1. Doubling of rf at high space-charge should be handled with utmost care, since extrapolation of zero space-charge situations seems dangerous.

Conclusion

In the future, an iteration routine for identical emittances will be included, as dictated by the K-V formalism. The extension to 3-dimensions will be pushed forward, and a fast subroutine for numerical calculation of elliptic integrals will be installed. Investigations shall be extended to periodic linacs like Wideroe and Alvarez. Finally the model will be tested using data of existing proton linacs as well as other multiparticle programs. This might support an rms formalism for axial motion with regard to the model discussed in this paper.

Acknowledgements

We want to thank Mr. K.-D. Halfmann for his valuable help in computer programming. Work was supported by the Bundesministerium fur Forschung und Technologie. Computations have been carried out at HRZ at the University of Frankfurt/Main.

References

1 J.M. Kapchinskij, V.V. Vladimirskij, Limitations of proton beam current in a strong focusing linear accelerator associated with the beam space charge, Proc. Intern. Conf. on High Energy Acc., CERN, Geneva, p. 274 (1959).

2 M. Reiser, Periodic focusing of intense beams, Part. Acc., Vol. 8, p. 167 (1978).

3 F.J. Sacherer, rms envelope equations with space-charge, CERN/SI/Int. DL/70-12, 1970.

4 P.M. Lapostolle, Quelques proprietes essentielles des effets de la charge d'espace dans les faisceaux continus, CERN-ISR/DI-70-36, 1970.

5 G. Wendt, Statische Felder und stationäre Ströme, in: S. Flügge, Handbuch der Physik, Springer, Berlin-Göttingen-Heidelberg 1958, p. 148.

6 K. Mittag, On parameter optimization for a linear accelerator, KFK 2555, Karlsruhe, January 1978.

7 R.W. Muller, Space-charge current limits in linacs, Internal paper, GSI Darmstadt, autumn 1978.

8 E.D. Courant, H.S. Snyder, Ann. Phys., 3 (1958) p. 1.

9 P. Junior, Ein Theorem zur radialen Fokussierung von Strahlfuhrungssytemen mit wenigen Wiederholungen, Z. f. angew. Phys., 28 (1970) pp. 353 - 357.

10 P. Junior, Die Optimierung der Fokussierung unperiodischer Linearbeschleuniger, Hab.-Schrift, Inst. f. Angew. Physik, Universitat Frankfurt/M., 1969, unpublished.

LONGITUDINAL CURRENT LIMIT IN A LINAC ACCELERATING CELL

Juris G. Kalnins
Lawrence Berkeley Laboratory
Berkeley, CA

Summary

A simple analytical expression is derived for the maximum number of particles, and the corresponding average current, that can be transported in the longitudinal potential well of a linac cell. The calculation includes only the linear part of the self-fields, with the beam taken to be matched in the transverse phase space.

Introduction

The proposed use of intense beams of heavy ions for inertial fusion has generated new interest in space-charge current limits in linacs. A number of analytical studies have been made to evaluate the longitudinal current limit.[1-10] Most have evaluated the linear static limit for a variety of charge distributions. These have consisted of a uniform charge-density longitudinal acceptance area,[2,3,4] axial cylinder[8,10] and ellipsoid,[5,6,7] as well as a particular form of the (r,z)-distribution function.[9] As has been pointed out by a number of authors,[2,3,4,6] the current limit depends on the model used. In this paper, the space-charge limit will be re-examined by separating the analysis into two parts. First, the matched longitudinal acceptance area parameters as functions of the linear space charge parameter, will be calculated. Then in the last section, a general expression for the current limit, will be obtained which will be evaluated for a specific constant charge density ellipsoid model.

The Longitudinal Equations of Motion

For an ion of charge state Q and atomic mass number A, the longitudinal phase equation over one linac cell is given by

$$\frac{\Delta^2\delta\theta}{\Delta Z^2} + K_\theta{}^2 H'(\theta,\theta_s) = 0 \quad , \qquad (1)$$

where

$$H'(\theta,\theta_s) = (\cos\theta - \cos\theta_s) - (M_\ell(\theta) - M_\ell(\theta_s)) \qquad (2)$$

with $\Delta Z = L_c$ = accelerating cell length

θ = phase of the ion relative to the accelerating field

θ_s = synchronous phase angle

$$K_\theta{}^2 = \left(\frac{2\pi}{\lambda_c}\right)\left(\frac{1}{L_c\gamma_s{}^3\beta_s{}^3}\right)\left(\frac{W_{cs}}{W_A}\right)$$

$M_A = W_A/c^2$ = mass of 1 amu

λ_c = wavelength of the accelerating field with rf frequency $f_c = c/\lambda_c$

$c\beta_s$ = synchronous velocity

$W_{cs} = (Q/A)(eE_cL_cT_s)$ = peak energy gain/amu

E_c = accelerating field amplitude

T_s = transit time factor

Transverse coupling is neglected, except through the space charge term $M_\ell(\theta)$, which can be expanded as follows:

$$M_\ell(\theta) \equiv \left(\frac{1}{E_cT_sL_c}\right)\int_{cell} dz E_z(z)$$

$$= \mu_\theta(\theta-\bar{\theta}) + M_n(\theta) \quad , \qquad (3)$$

where $E_z(z)$ is the space-charge longitudinal electric field, which integrates to zero for phase angle $\bar{\theta}$. The linear space-charge parameter[6,7]

$$\mu_\ell = \frac{\mu}{\mu_0}$$

$$\mu_s \equiv -\sin\theta_s$$

is taken to be constant - the same for all ions in the beam bunch. Its value will depend primarily on the rms coordinates,[11] and so should be relatively independent of the particular particle distribution. The remaining non-linear terms $M_n(\theta)$, if not too large, could be included self-consistantly by an iterative procedure.

Integrating Eq. (1) once, keeping only the linear space-charge term, gives the energy equation

$$\left(\frac{\delta W}{\delta W_{cs}}\right)^2 = H_o - H(\theta,\theta_s) \quad , \qquad (4)$$

where H_o is the integration constant

$$H(\theta,\theta_s) = [\sin\theta - \theta\cos\theta_s] - \frac{1}{2}\mu_\theta[(\theta-\theta_s)^2 - \theta_s{}^2] \quad , \qquad (5)$$

* This work was supported by the High Energy & Nuclear Physics Division of the U.S. Department of Energy under contract No. W-7405-ENG-48.

and

$$(\delta W_{cs})^2 = \left(\frac{\lambda_c \gamma_s^3 \beta_s^3}{\pi L_c}\right)(W_{cs} W_A) \quad .$$

This equation allows the changes in the phase-stable acceptance area to be calculated as a function of the space charge parameter μ_ℓ.

The Longitudinal Acceptance Area

The ions move in the potential well given by the function $H(\theta, \theta_s)$, whose form is shown in Fig. 1 for $\theta_s = -30^o$ and $\mu_\ell = 1/3$. The shaded area, $H_0 \leq H_c$, is the longitudinal bucket where particles are trapped.

The two envelope phases $\theta_1 < \theta_s$ and $\theta_2 > \theta_s$, the maximum energy spread δW_s (half-width), and the phase-space acceptance area $A_s = \iint \delta W \delta\theta$, as functions of θ_s and μ_ℓ. They are shown in Fig. 2, and generally agree with results obtained using an analytic approximation to the accelerating potential.[6,7]

Figure 3 shows the results for the acceptance-area weighted average phase $\bar{\theta}$ and rms half-width $\delta\theta$ rms. As has been noted previously,[1-7] it is possible to make the approximation

$$\frac{\delta\theta_{rms}}{\delta\theta_o} \simeq 1 - \mu_\ell \qquad 0 \leq \mu_\ell \leq 1 \quad , \qquad (6)$$

where $\delta\theta_o$ is its value for $\mu_\ell = 0$, with the acceptance area vanishing at $\mu_\ell = 1$.

Though the acceptance area is independent of $\bar{\theta}$, it does produce a shift in the synchronous phase,[2,6] which would require a small decrease

$$\delta E_c / E_c = \mu_\ell (\bar{\theta} - \theta_s) \tan \theta_s$$

in the accelerating field to keep the bunch synchronized.

The Longitudinal Particle and Current Limits

To evaluate the space-charge parameter μ_ℓ, the self-fields of a uniform charge-density 3-D spatial ellipsoid can be used. The potential has the general form:

$$\Phi(x,y,z) = -\frac{1}{2}\left(\frac{3eQN_c}{4\pi\varepsilon_o a_x a_y a_z}\right)[f_x x^2 + f_y y^2 + f_z z^2] \quad , \qquad (7)$$

with longitudinal field

$$E_z = \left(\frac{3eQN_c}{4\pi\varepsilon_o a_x a_y a_z}\right) f_z z \quad , \qquad (8)$$

where N_c is the number of ions in the ellipsoid and a_x, a_y, a_z are the matched semi-axes.

Poisson's equation requires that

$$f_x + f_y + f_z = 1 \quad , \qquad (9)$$

and the remaining parameter is fixed by the boundary conditions.

Evaluating the space-charge parameter in the impulse approximation, that is, $M_\ell \simeq E_z / E_c T_s$, the number of ions in the bunch yields:

$$QN_c \simeq N_s a_x a_y a_o \mu_\ell (1-\mu_\ell) f_z^{-1}(\xi) \quad ,$$

where $\qquad (10)$

$$N_s = \left(\frac{4\pi\varepsilon_o}{3e}\right)\left(\frac{2\pi}{\lambda_c \beta_s}\right) E_c T_s \mu_s$$

and we have expressed f_z in terms of

$$\xi \equiv \frac{a_z}{(a_x a_y)^{\frac{1}{2}}} \simeq \xi_o (1-\mu_\ell) \qquad (11)$$

where $a_z = a_o$ is the semi-axis with no space charge. For $a_z/a_o \simeq \delta\theta_{rms}/\delta\theta_o$ the approximation of Eq. (6) was used to express QN_c as a function of μ_ℓ. The explicit relation between a_z and $\delta\theta_{rms}$ can be estimated for a particular distribution by matching the rms values; that is, $a_z \simeq \sqrt{5}\, a_{rms}$.

For example, for a matched uniform density 6-D phase space ellipsoid: $a_z = \sqrt{5/2}(\lambda_c \beta_s / 2\pi)\delta\theta_{rms}$.

The maximum number of ions, $N_c = N_M$, that can be trapped is determined by $d(QN_c)/d\mu_\ell = 0$, which gives an equation for $\mu_\ell = \mu_M$

$$(1 - 2\mu_M) f_z^{-1} \simeq \xi_o \mu_M (1-\mu_M) \frac{d}{d\xi} f_z^{-1} \quad . \qquad (12)$$

Since the actual linac boundary conditions are difficult to evaluate analytically, three cases of interest will be studied:

(i) The vacuum field as given by Lapostolle[5,7]

$$f_z^{-1} = \begin{cases} (1-\xi^2)^{\frac{1}{2}}\left[(1-\xi^2)^{\frac{1}{2}} - \xi \cos^{-1}\xi\right]^{-1} & \xi < 1 \\ (\xi^2-1)^{\frac{3}{2}}\left[\xi \cosh^{-1}\xi - (\xi^2-1)^{\frac{1}{2}}\right]^{-1} & \xi > 1 \end{cases} \qquad (13)$$

(ii) A field with E^2 = const. on the ellipsoid surface

$$f_z^{-1} = 1 + \frac{(a_x + a_y)}{(a_x a_y)^{\frac{1}{2}}}\,\xi \quad , \qquad (14)$$

which reduces in the limit $a_z \to \infty$ to the usual transverse envelope equation for an elliptic cylinder.[10,11]

(iii) A field with Φ = const. on the ellipsoid surface:

$$f_z^{-1} = 1 + \left(\frac{a_x^2 + a_y^2}{a_x a_y}\right)\xi^2 \quad . \qquad (15)$$

The ξ-dependence of f_z^{-1} is shown in Fig. 4.

All three potentials give the same result for a spherical bunch ($a_x = a_y = a_z \equiv a$), the particle number being

$$QN_c = 3N_s \mu_\ell a^3 \qquad (16)$$

This agrees with the result obtained in previous calculations [6,7] for $\xi \propto 1$, which give $\mu_M \simeq 1/3$.

In general it is not possible to evaluate μ_M in Eq. (12) for an arbitrary ξ_0. In Table I therefore, μ_M has been evaluated along with the maximum particle number QN_M in the limits $\xi_0 << 1$ and $\xi_0 >> 1$.

The maximum average current in all cases is given by

$$\bar{I}_M = ef_c QN_M \qquad (17)$$

From Table I it is seen that the range of μ_M is quite restricted, in agreement with $\mu_M \simeq 0.3 \rightarrow 0.4$ given by a number of authors.[4,6,7] The space-charge limit also appears to be relatively independent of boundary conditions for $\xi_0 << 1$.

Conclusions

Expressions have been obtained for maximum particle number and average current for a general class of linear ellipsoid fields. These have been evaluated for a number of different boundary conditions to illustrate their dependence on the specific boundary conditions. These linear static space-charge limits could be used not only to set upper current limits, but also for scaling purposes. It would be useful to evaluate the space-charge potential for more realistic linac boundary conditions, as well as to include the non-linear terms in some self-consistent manner.

Acknowledgements

I wish to thank H. Kim for helpful discussion of some aspects of this problem.

References

1. A.D. Vlasov, Trans. of RAIAN, II, issue 4, 1960, p. 27.
2. I.M. Kapchinsky and A.S. Kronrod, Proc. of Int. Conf. on High Energy Acc., Dubna, 1963, p. 1241.
3. P.L. Morton, Rev. Sci. Instr. 36, 1826 (1965).
4. B.I. Bondrev and A.D. Vlasov, Proc. of 5th Int. Conf. on High Energy Acc., Frascati, 1965, p. 621.
5. P. Lapostolle, CERN Report AR/Int., SG-65-15, 1965.
6. T. Nishikawa and S. Okumura, Proc. 6th Int. Conf. on High Energy Acc., Cambridge, 1967, p. 162.
7. R.L. Gluckstern, Proc. 1966 Linear Acc. Conf., Los Alamos, 1966, p. 237.
8. L. Smith, ERDA Summer Study of Heavy Ions for Inertial Fusion, Berkeley, LBL-5543, Dec. 1976, p. 77.
9. W.P. Lysenko, Los Alamos Report, LA-7010-MS, Oct. 1977.
10. T.K. Khoe and R.L. Martin, IEEE Trans. Nucl. Sci., NS-24, 1025 (1977).
11. F.J. Sacherer, IEEE Trans. Nucl. Sci., NS-18, 1105 (1971).
12. G.R. Lambertson, L.J. Laslett and L. Smith, IEEE Trans. Nucl. Sci., NS-24, 993 (1977).

Discussion

Ohnuma, FNAL: What would be the maximum current, in your estimate, for the Fermilab linac? At Fermilab we used to have sort of a game, and the game was played this way: somebody would predict the linac current limit and the linac people would try very hard to exceed it. And then the theory guys would try very hard to put larger limits on the current. I was wondering, taking, for example the Fermilab linac, what would be your prediction on the maximum current we can accelerate?

Kalnins: I haven't done the calculations for the Fermilab linac. The cases I have looked at were for the linacs that we have at LBL, as a reference for example, for numerical simulations. I agree this is more space charge for pedestrians; it is more to get an idea of where you might be in the ballpark. It is obvious that you have to look at it in much finer detail to get more realistic values of what to expect.

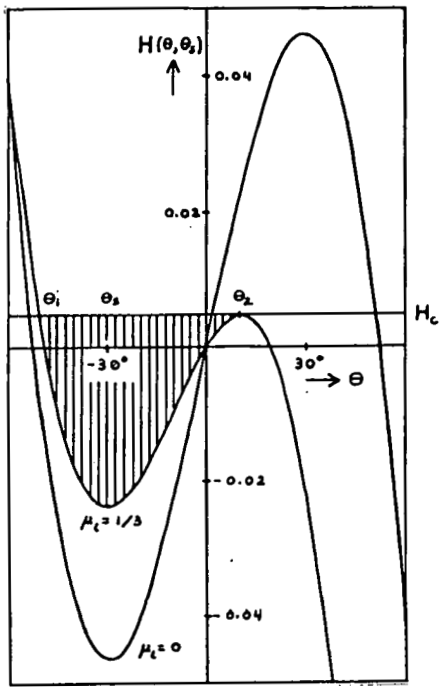


Fig. 1: The longitudinal potential $H(\theta,\theta_s)$ for $\theta_s = -30^0$ and $\mu_\ell = 1/3$.

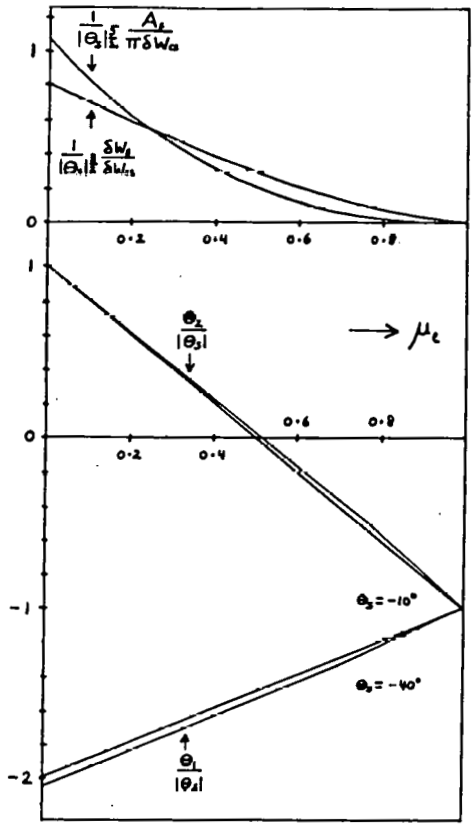


Fig. 3: The acceptance-area weighted average phase $\bar{\theta}$ and RMS half-width $\delta\theta_{RMS}$.

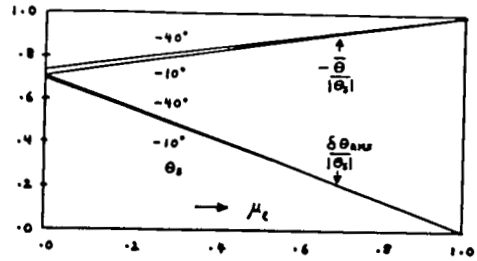


Fig. 2: The acceptance-area phase limits θ_1 and θ_2, the maximum energy half-width δW_s, and area A_s for synchronous phase θ_s and space charge parameter μ_ℓ.

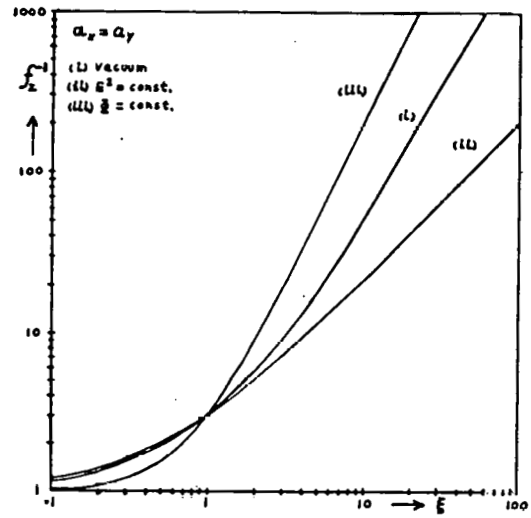


Fig. 4: The geometric form function $f_z^{-1}(\xi)$.

TABLE 1

Longitudinal Space Charge Limits

		ϕ = const.	Lapostolle vacuum	E' = const.
$\zeta_0 \ll 1$	ν_M	1/2	1/2	1/2
	f_s^{-1} $a_x=a_y$	$1+2\zeta^2$	$1+\frac{\pi}{2}\zeta$	$1+2\zeta$
	$\frac{QN_M}{N_S}$	$\frac{1}{4}a_x a_y a_0$	$\frac{1}{4}a_x a_y a_0$	$\frac{1}{4}a_x a_y a_0$
$\zeta_0 \gg 1$	ν_M	1/4	1/4	1/3
	f_x^{-1} $a_x=a_y$	$2\zeta^2$	$\frac{\zeta^2}{(\zeta \ln 2\zeta - 1)}$	2ζ
	$\frac{QN_M}{N_S}$	$\frac{1}{4}(\frac{3}{4})^3 (\frac{a_x^2+a_y^2}{a_x a_y}) a_0^3$	$\frac{1}{4}(\frac{3}{4})^3 \frac{a_0^3}{(\zeta \ln \frac{3}{2}\zeta_0 - 1)}$	$\frac{1}{2}(\frac{2}{3})^3 (a_x+a_y) a_0^2$

THE SIGNIFICANCE OF BEAM OPTICS CONCEPTS AS APPLIED TO THE NEW CERN LINAC

M. Weiss
CERN, Geneva, Switzerland

Summary

The beam dynamics equations are in general valid only for ideal situations, i.e. ideal machines and ideal beams. To deal with reality, certain assumptions and procedures have to complement the theory so as to form with it a logical or "reasonably" logical entity. The beam dynamics approach used for the new CERN linac is reviewed and important points are underlined. Computer calculations justified the procedure at the start of construction; comparison with measurements and machine performance should now evaluate the true "figure of merit" of the whole approach.

Design Methods

Beam optics problems can be approached in various ways, each approach being usually a combination of analytic and computer treatment. The analytic treatment gives an insight into the importance and interdependence of various machine and beam parameters, but to solve the equations, several simplifications have to be made. The computer treatment is more precise and is usually divided in two parts; one where linearized optimization programs are used to determine the machine and matched beam parameters, the other where beam simulation programs are applied to check the validity of the established settings.

The CERN beam optics treatment consisted of the following steps:

1) beam model
2) analytic considerations
3) optimization programs
4) simulation programs.

These topics will be treated in some detail; in particular the analytic considerations, which are the basis for the subsequent computer treatments.

Beam Model

The beam is represented by a hyperellipsoid in either a four-dimensional phase space (unbunched beam), or a six-dimensional one (bunched beam). The space-charge forces are computed from the projection of the beam density distribution in the two- or three-dimensional real space. It has been shown that for distributions with ellipsoidal symmetry, the evolution of the rms beam envelope depends almost exclusively on the linearized part (least square method) of the self-forces[1]. This important fact is extensively used in analytic calculations and linearized optimization programs, where the real beam is replaced by an "equivalent" one, having the same rms values of coordinates but being of uniform distribution.

Via rms coordinates, one can compute the matching parameters for beams with different density distributions; the results will be the more significant the more the density distribution approaches an ellipsoidal one ("well-behaved beams"). It should be noted that no direct indication is obtained about the evolution of the marginal beam envelope, which is only estimated from the rms envelope and the real beam density distribution.

Analytic Considerations

Analytic considerations are essential for choosing the basic parameters of the accelerator under space-charge conditions. It is convenient to analyse the betatron and synchrotron motion separately.

Transverse Beam Dynamics

The most useful equation to start with is the envelope equation, and it is sufficient for our purpose to analyse only the mean "smooth" envelope. Assuming that this envelope is essentially the same, over a period, for both the transverse directions x and y, one can write

$$\bar{x}'' + \bar{K}\bar{x} - \frac{E^2}{\bar{x}^3} - \frac{kI}{\bar{x}} = 0 \ ,$$

where $\bar{x}$, $\bar{K}$, E, I, k represent the smooth beam envelope, the mean outer focusing, the equivalent beam emittance, the beam current, and the space-charge factor, respectively. The condition for a matched beam is $\bar{x}'' = 0$ and the mean focusing per period must satisfy the expression

$$\bar{K} = \frac{E^2}{\bar{x}^4}\left(1 + k\frac{\bar{x}^2}{E}\frac{I}{E}\right) = \bar{\Omega}_\beta^2\,(1 + \sigma_t) \ ; \quad \sigma_t = k\bar{\beta}\frac{I}{E} \ ,$$

where σ_t is the transverse space-charge parameter, and $\bar{\Omega}_\beta$ and $\bar{\beta}$ are the smooth betatron frequency and amplitude function, respectively. If $\sigma_t \gg 1$, the mean focusing is mainly "space charge determined":

$$\bar{K} \cong k\frac{I}{\bar{x}^2} \ .$$

Some typical values of σ_t in the new CERN linac are:

	σ_t
LEBT	∿ 20 (unbunched beam) > 10 (bunched beam)
LINAC	3-5
HEBT	2.5-5

The reliability of computed settings usually drops with σ_t; in the LEBT, for example, it is essential that the beam is "very well behaved" in order to apply the computed settings.

To keep σ_t small (for a given I) becomes increasingly difficult for beams with a small emittance; one ends up with very narrow beams, requiring more focusing strength and possibly creating longitudinal space-charge problems.

The situation in the linac can be analysed a bit further: the constants of all linearized forces in the smooth approximation satisfy the expression

$$\bar{\Omega}_\beta^2 = \bar{\Omega}_Q^2 - \bar{\Omega}_{RF}^2 - \bar{\Omega}_{SC}^2 \ ,$$

with $\bar{\Omega}_Q^2$, $\bar{\Omega}_{RF}^2$, $\bar{\Omega}_{SC}^2$ being the mean force constants of

the quadrupole focusing, rf defocusing, and space-charge defocusing. Taking into account that the FD focusing in the linac is in fact a sequence of quadrupole doublets[2], one can write for the quadrupole gradient

$$G \propto \bar{\Omega}_Q = \bar{\Omega}_\beta \left(1 + \bar{\Omega}_{RF}^2/\bar{\Omega}_\beta^2 + \sigma_t\right)^{1/2} .$$

Inserting in this expression figures of a "nominal" acceleration with the new linac (I = 150 mA), one obtains roughly

$$G \tilde{\propto} \bar{\Omega}_\beta \left(1 + 1 + 3\right)^{1/2} .$$

The increase of quadrupole gradients in the linac due to space-charge is

$$\frac{G}{G_0} = \left(\frac{\bar{\Omega}_Q^2}{\bar{\Omega}_Q^2 - \bar{\Omega}_{SC}^2}\right)^{1/2} = \left(\frac{5}{2}\right)^{1/2} \cong 1.6 ,$$

a figure confirmed also by more detailed computations (optimization programs). It is interesting to note that the ratio of betatron frequencies of the beam center and an average particle is

$$\frac{\bar{\Omega}_{\beta_0}}{\bar{\Omega}_\beta} \cong \left(\frac{\bar{\Omega}_Q^2 - \bar{\Omega}_{RF}^2}{\bar{\Omega}_Q^2 - \bar{\Omega}_{RF}^2 - \bar{\Omega}_{SC}^2}\right)^{1/2} = 2 .$$

Longitudinal Beam Dynamics

The basic set of equations governing the phase and energy differences relative to the synchronous particle is

$$\frac{d}{dt}\Delta\phi = -\frac{\omega}{mc^2\beta_r^2\gamma^3}\Delta W$$

$$\frac{d}{dt}\Delta W = e\bar{E}T\beta_r c\left[\cos(\phi_s + \Delta\phi) - \cos\phi_s - \sigma_\ell|\sin\phi_s|\Delta\phi\right] .$$

The meaning of the symbols is the usual one, σ_ℓ being the longitudinal space charge parameter for the equivalent beam:

$$\sigma_\ell \cong \frac{I}{2\bar{r}\varepsilon_0\beta_r c\bar{E}T|\sin\phi_s|\overline{\Delta\phi}^2} ,$$

with $\overline{\Delta\phi}$: smooth phase amplitude, and $\bar{r}$: smooth beam radius. It is assumed that ΔW is small compared to the energy of the synchronous particle.

To solve the set of differential equations some assumptions are necessary, depending on the question one wishes to answer.

Linearized equation (analysis of the evolution of small synchrotron oscillations with time): for $\Delta\phi \ll 1$, one can linearize with respect to $\Delta\phi$ and get the set of equations in the form:

$$\frac{d}{dt}\Delta\phi = -b^2(t)\,\Delta W$$

$$\frac{d}{dt}\Delta W = a^2(t)\,\Delta\phi ,$$

a(t) and b(t) being slowly varying functions of t. At a given moment t_0, the motion (smooth) in the phase plane is given approximately by an ellipse with the axis ratio:

$$\frac{a_0}{b_0} = \left(-\frac{\Delta W}{\Delta\phi}\frac{d\,\Delta W}{d\,\Delta\phi}\right)^{1/2} = \frac{\overline{\Delta W}}{\overline{\Delta\phi}} .$$

This ratio varies during the acceleration as

$$\frac{\overline{\Delta W}}{\overline{\Delta\phi}} \tilde{\propto} (\beta_r\gamma)^{3/2}\left(1 - \sigma_\ell\right)^{1/2} .$$

The set of linearized first-order equations can be transformed into a second-order equation:

$$\frac{d}{dt}\left[\beta_r^2\gamma^3\frac{d}{dt}\Delta\phi\right] + \frac{2\pi e\bar{E}T\beta_r|\sin\phi_s|}{m\lambda}\left(1 - \sigma_\ell\right)\Delta\phi = 0 .$$

Assuming σ_ℓ = const and multiplying by $\beta_r^2\gamma^3$ and substituting,

$$\beta_r^2\gamma^3\frac{d}{dt} = \frac{d}{du} ,$$

this equation can be solved for the independent variable u by the BKW method; returning to the variable t, the solution is written as:

$$\Delta\phi(t) = C\left[\beta_r^2\gamma^3\,\bar{K}(t)\right]^{-1/4}\sin\left[\int_0^t\left(\frac{\bar{K}(t')}{\beta_r^2\gamma^3}\right)^{1/2}dt' + \phi_0\right] ,$$

where C is an integration constant and

$$\bar{K}(t) = \frac{2\pi e\bar{E}T\beta_r|\sin\phi_s|}{m\lambda}\left(1 - \sigma_\ell\right) .$$

One sees from the solution that the smooth synchrotron frequency is given by

$$\bar{\Omega}_s = \left[\frac{2\pi e\bar{E}T|\sin\phi_s|}{m\beta_r\lambda\gamma^3}\left(1 - \sigma_\ell\right)\right]^{1/2} = \bar{\Omega}_{s_0}\left(1 - \sigma_\ell\right)^{1/2} .$$

$\bar{\Omega}_{s_0}$ is the frequency in the absence of the space-charge. During acceleration $\bar{\Omega}_s$ varies as

$$\bar{\Omega}_s \propto \beta_r^{-1/2}\,\gamma^{-3/2}\left(1 - \sigma_\ell\right)^{1/2} .$$

The amplitude of small phase oscillations is damped in the course of acceleration; for $\bar{E}T|\sin\phi_s|$ = const one has

$$\overline{\Delta\phi} \propto (\beta_r\gamma)^{-1/4}\left(1 - \sigma_\ell\right)^{1/4} .$$

The parameter σ_ℓ is, in fact, not constant during acceleration, but varies (see its formula):

$$\sigma_\ell \propto \beta_r^{-1}\,\mu^{+1/2} \quad \text{for } \overline{\Delta\phi} = \text{const}$$

$$\sigma_\ell \propto \beta_r^{1/2}\,\mu^{+1/2} \quad \text{for } \overline{\Delta\phi} \propto (\beta_r\gamma)^{-3/4} .$$

In most cases, σ_ℓ increases along the linac.

The described analysis, valid for $\Delta\phi \ll 1$, is usually also applied in optimization programs for bigger $\Delta\phi$. Several precautions are, however, necessary when a parabolic potential function (linear motion) replaces the true one.

Non-linearized adiabatic equation (analysis of synchrotron oscillations with large amplitudes): to solve the non-linear equations, one must assume adiabaticity ($\beta_r\gamma$ = const); the second-order adiabatic equation is

$$\frac{d^2}{dt^2}\Delta\phi + \bar{\Omega}_{s_0}^2\left[\frac{\cos(\phi_s + \Delta\phi) - \cos\phi_s}{|\sin\phi_s|} - \sigma_\ell\Delta\phi\right] = 0 ,$$

and due to the assumption $(d/dt)\bar{\Omega}_{s_0}^2 = 0$, one can obtain the energy integral as:

$$\frac{d}{dt}\left[\frac{1}{2}\Delta\dot{\phi}^2 + \bar{\Omega}_{s_0}^2\,V(\Delta\phi)\right] = 0 ,$$

with the potential function

$$V(\Delta\phi) = \frac{\sin(\phi_s + \Delta\phi) - \Delta\phi \cos\phi_s - \sin\phi_s}{|\sin\phi_s|} - \sigma_\ell \frac{\Delta\phi^2}{2} .$$

From $V'(\Delta\phi) = [dV(\Delta\phi)/d\Delta\phi] = 0$, one gets one stability limit (unstable point) as

$$\Delta\phi_1 \cong 2|\phi_s| (1 - \sigma_\ell) \quad \text{(see Fig. 1)} .$$

The other stability limit can be obtained from $V(\Delta\phi) - V(\Delta\phi_1) = 0$ (in the easiest way by expanding this expression in a Taylor series):

$$\Delta\phi_2 \cong - |\phi_s| (1 - \sigma_\ell) .$$

The stability limits are not symmetric around the synchronous phase. To place more beam in the stable region, one injects off the synchronous phase, $\phi_s + \phi_0$, see Fig. 1. There are several points of view according to which ϕ_0 can be chosen. If one decides to inject in the middle of the stable region, then the stability limits are a function of σ_ℓ and ϕ_0:

$$\Delta\phi_1 = f_1(\sigma_\ell, \phi_0) , \quad \Delta\phi_2 = f_2(\sigma_\ell, \phi_0) ,$$

satisfying

$$\phi_0 = \frac{f_1 + f_2}{2} .$$

The maximum allowable phase amplitude is

$$\overline{\Delta\phi} = \Delta\phi_1 - \phi_0 .$$

The potential function $V(\Delta\phi)$ now has the form:

$$V(\Delta\phi) = \frac{\sin(\phi_s + \Delta\phi) - \Delta\phi \cos\phi_s}{|\sin\phi_s|} - \frac{\sigma_\ell}{2}(\Delta\phi - \phi_0) + C ,$$

and the integration constant C can be chosen so as to make the minimum of the potential function equal zero. The condition $V'(\Delta\phi) = 0$ gives $\Delta\phi_1$ [maximum, $V''(\Delta\phi) < 0$] and $\Delta\phi_0$ [minimum, $V''(\Delta\phi) > 0$], see Fig. 1. Proceeding as before, one computes $\Delta\phi_2$ and ϕ_0.

The space-charge parameter σ_ℓ has not yet been fixed; it can be chosen in such a way as to maximize the trapped beam:

$$I_{max} \cong 2\bar{r}\epsilon_0\beta_r c\bar{E}T \cos\phi_s |tg\,\phi_s| \sigma_{\ell\,opt} \overline{\Delta\phi}^2 .$$

To obtain $\sigma_{\ell\,opt}$ it suffices to differentiate

$$\frac{d}{d\sigma_\ell}(\sigma_\ell \overline{\Delta\phi}^2) = f(\sigma_\ell) = 0 \rightarrow \sigma_{\ell\,opt} = 0.425 .$$

Taking this $\sigma_{\ell\,opt}$ and the typical settings of the new CERN linac, one would get

$$I_{max} \cong 75 \text{ mA} ,$$

which is the optimum filling of the stationary bucket. In fact, at injection into the CERN linac one has

$$\sigma_\ell \cong 0.9 ,$$

and this means that the stable region is drastically reduced and that a good part of the beam lies initially outside of it. The beam starts to grow longitudinally, but the bucket length (in mm, not degrees) increases $\propto \beta_r$, and quicker than the beam; after $\sim$(10-15) cells, the σ_ℓ has dropped sufficiently for the beam to be now fully in the new bucket. Figures 2 and 3 show the initial potential $V(\Delta\phi)$ and bucket of the CERN linac for two values of σ_ℓ. Figure 4 (simulation program result) shows the phase damping of beams with I = 0 and I = 150 mA, respectively. In both cases, no particles are lost. The matching and machine parameters correspond to computed settings (optimization program results), and no attempt was made to annul the residual phase oscillations. The initially unstable beam gives rise to a large increase in the longitudinal emittance ($\sim$ 2 computed, > 5 measured), but this does not adversely affect the accelerator (booster) downstream of the linac.

Linear Optimization Programs

All parts of the linear accelerator complex have been designed by using linearized optimization programs. Programs treating the LEBT and linac have been entirely developed and written at CERN[3] and subsequently improved. They apply matrix formalism, linearized Lapostolle-Schnizer gap equations[4], and have the following special features:

1. Space-charge forces are computed for uniformly filled, infinitely long cylinders (unbunched beam) or ellipsoids (bunched beam). In the bunching region, both models are used to account for the action of the subsequently trapped as well as non-trapped particles[3].

2. The longitudinal beam emittance is formed by the non-linear energy modulation of the beam in the bunching system. This is the only "non-linearity" contained in the optimization programs; it is also responsible for the transverse beam emittance growth in rf gaps.

3. The linac (quasi-periodic structure) is treated as a periodic structure, when computing matching parameters; space-charge forces are included.

4. The gap forces are linearized around an "average" beam radius r_{eff} (effective beam radius), which is related to the envelope of the equivalent beam as

$$\frac{r_{eff}}{\hat{r}} = \sqrt{\frac{2}{5}} .$$

The divergence theorem holds.

5. The synchronous particle is abandoned as the representative particle and replaced with particles lying on r_{eff} in the transverse median plane of the beam bunch. These particles have to get the nominal acceleration.

6. Emittance increase (non-linear effect) can be artificially introduced in all phase planes.

Linear programs having the above features also proved satisfactory for setting the running machine parameters; in particular the linac. Some corrections were necessary in the LEBT (quadrupole focusing, not bunching), where the high σ_t value, intensity oscillations during the beam pulse ("grass"), and the presence of non-protons, made the situation more difficult to handle.

Beam Simulation and Experiments

In the linac, important questions concerning the design[5] and operation[6] were settled by multiparticle

programs. In particular, conditions minimizing the transverse emittance growth were analysed and a strong preference for rather narrow beams found.

However, some experiments have recently been performed confirming the importance of initial σ_ℓ values: a beam of 65 mA has been accelerated and, contrary to previous runs, a smaller μ value ($\sim 30°$) has been chosen, so as to have the beam longitudinally stable at injection. As expected, the longitudinal output emittance decreased (by a factor of 0.57), but surprisingly the transverse one was also improved (factors of 0.7 and 0.9 for 90% and 63% of beam, respectively). Perhaps this allows one to conclude that in each case an optimum combination of σ_ℓ and μ can be found.

Conclusion

The following may be said concerning the CERN beam optics approach:

1. It is complete in the sense that it contains procedures for determining all the parameters of the design;

2. All design options were subsequently proved correct;

3. Computed settings of accelerator parameters (focusing) are in general satisfactory, but corrections are necessary in areas of high σ_t values;

4. Phenomena such as emittance growth, in particular in the longitudinal plane, were underestimated by beam simulation programs, which, however, did not include steering errors. The qualitative dependence of these phenomena on machine and beam parameters was rightly foreseen.

Finally it should be noted that the CERN approach was developed for "classical" proton linacs, where variations in beam losses of the order of a percent are neglected.

References

1) F. Sacherer," RMS envelope equation with space-charge",CERN/SI/Int. 70-12

2) B. Bru and M. Weiss,"Tolerances for quadrupole focusing in the linac",CERN/MPS/LINP/Note 73-7.

3) B. Bru and M. Weiss,"Computational methods and computer programs for linearized analysis", CERN/MPS/LIN 72-4.

4) M. Promé,"Effets de la charge d'espace dans les accélérateurs linéaires à protons",thesis, Orsay, No. 761/1971.

5) D. Warner,"Accelerating structure of the CERN new 50-MeV linac",Proc. 1976 Proton Acc. Conf., Chalk River.

6) D. Warner and M. Weiss,"Beam optics in the CERN 50-MeV linac",same proceedings.

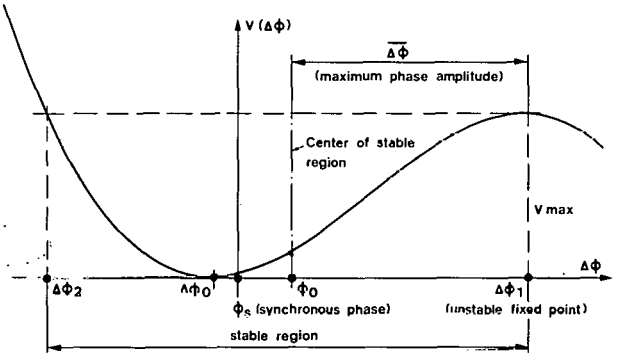


Fig. 1 Potential function for synchrotron motion with space charge.

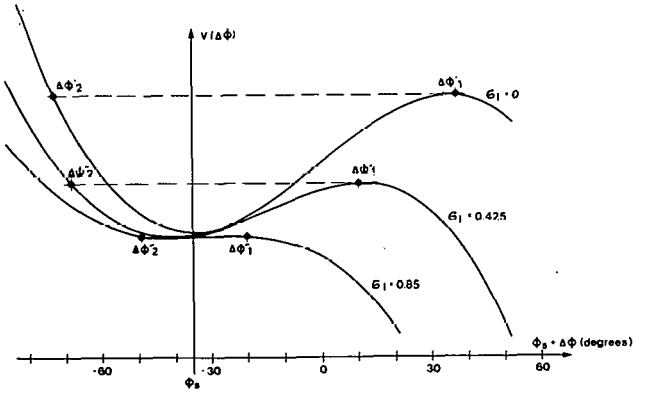


Fig. 2 Potential function with σ_ℓ as parameter.

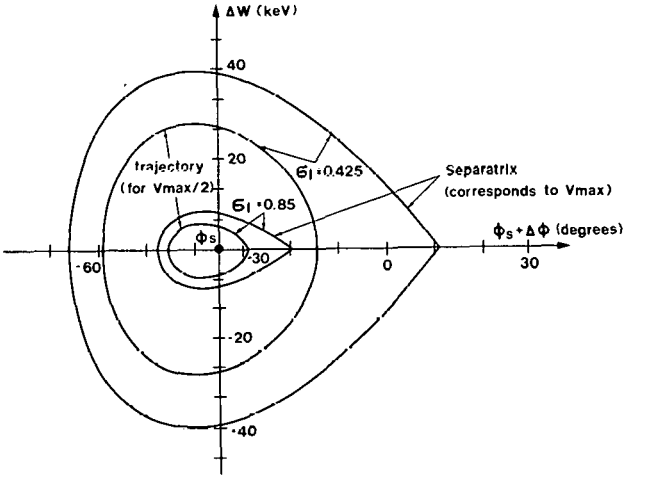


Fig. 3 Separatrix and trajectory in the $\Delta\phi$, ΔW plane with σ_ℓ as parameter.

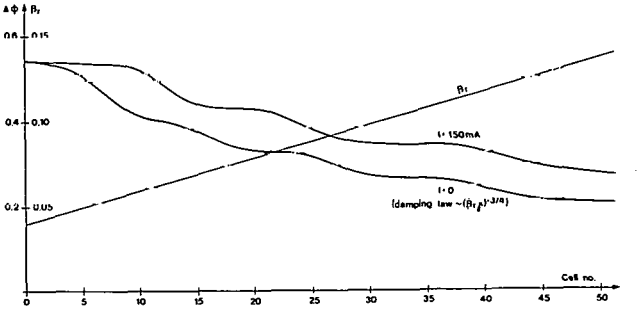


Fig. 4 Phase damping in tank 1 of the new linac.

1979 LINEAR ACCELERATOR CONFERENCE

ON EMITTANCE GROWTH IN LINEAR ACCELERATORS*

R. A. Jameson and R. S. Mills
Accelerator Technology Division
Los Alamos Scientific Laboratory
Los Alamos, NM 87545

Summary

Factors affecting emittance growth in linear accelerator applications requiring high beam quality and low in-machine beam losses are explored. A generalized method is developed for matching the average properties of an arbitrary particle distribution to an accelerator structure in the presence of space-charge and other perturbations. The effects of the particle distribution and the accelerator parameters on the preservation of input emittance and other measures of beam behavior are investigated, to study optimum performance under carefully matched conditions, and to show the degradation of performance in the presence of mismatch, steering and other errors. The concept of detailed matching invoking desirable correlations is discussed briefly.

Introduction

Growth in the effective emittance of linear accelerator beams has been observed in all operating machines, and has been the subject of much study. Gluckstern[1] pioneered in the analytical treatment of K-V distributions. R. Chasman[2] did numerical simulation experiments that demonstrated lower limits to output emittance as input emittance was reduced, which identified the importance of longitudinal-transverse coupling. P. Lapostolle[3] and coworkers at CERN did numerical and analytical work with cylindrically symmetric, continuous beams that demonstrated the presence of violent growth modes under certain parameter conditions, leading to severe filamentation of phase space.

Recent work with continuous beams has clarified a number of points. Laslett, Smith and Hofmann[4,5] have catalogued the characteristics of parametric oscillations in K-V distributions and have discussed unstable modes in terms of hydrodynamic models. Numerical calculations[6,7] agree with the theory and have addressed some questions concerning numerical effects in the codes.

The general scalability of the problem over the parameter range is beginning to be better understood;[6,8] Reiser's important work in this area demonstrates that the scaling laws do not have a single simple form, but depend on the constraints imposed on the problem by the designer, and on the zero-intensity phase advances. In the examples below, all detailed variables were deliberately submerged and are described only in terms of phased advances. These are widely scalable, and are a very useful simplification.

Adding bunching and acceleration complicates the problem substantially. Lysenko[9] extended the equilibrium distribution work to 2-D, and is presently working on 3-D. Crandall[10] elaborated on the effect of rf gaps on emittance growth. Another example of the impact of the constraints on the design problem was shown in the somewhat surprising result[9,11,12] that, for given current, input emittance is best preserved by raising the frequency of the machine. Development of the radio-frequency quadrupole structure[13] has required that attention be paid to the optimum rate of change from a continuous beam to a bunched, accelerated beam, to minimize transverse emittance growth.

Comparison of code models to actual machine performance has also progressed, with detailed analysis of measurement techniques,[14] and several examples of exacting modeling studies[15,16,17] that resulted in agreement with experimental results to a few per cent or better.

All of this work lends confidence to the further use of numerical simulation models for more detailed exploration of the causes and effects of emittance growth. The PARMILA code was used in the work below; it is a full 6-D simulation including nonlinear effects. The space-charge subroutine uses a ring model on an r-z area-weighted mesh. Five hundred macroparticles were used for most runs; salient points were checked with 5000. The random number generator was restarted for each run, except for specific checks of the effect of randomness.

Generation of A Matched Linac

It was desired to generate linacs that would be well matched under various conditions, and with arbitrary particle distributions, eventually including measured ones.[18] For the initial studies, the phase advances along the linac were specified. First, an adequate measure was needed, over each structure period, of the phase advance, σ, and the ellipse parameters, α and β, that characterize the nearly periodic system. A least-squares solution in each plane using all particles gives values that work well for matching. The space-charge parameter, $\mu = 1 - (\sigma/\sigma_0)^2$, also is available. Using the desired particle distribution, a linac can be generated with a given prescription for the phase advances, using an iterative, least-squares procedure. The quadrupole strengths are adjusted to get the proper transverse phase advance. A constant longitudinal phase advance, for example, requires the quantity $E_0T \sin \phi_s/\beta$ to

*Work performed under the auspices of the U. S. Department of Energy.

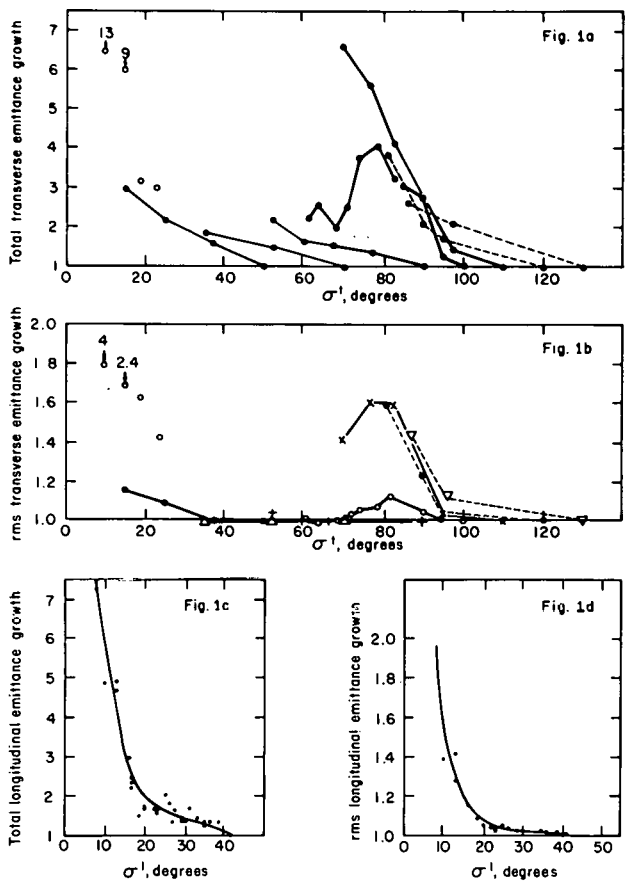


Fig. 1. Emittance growth after 20 cells, as a function of tune shift from various initial zero-intensity phase advance per transverse focusing period.

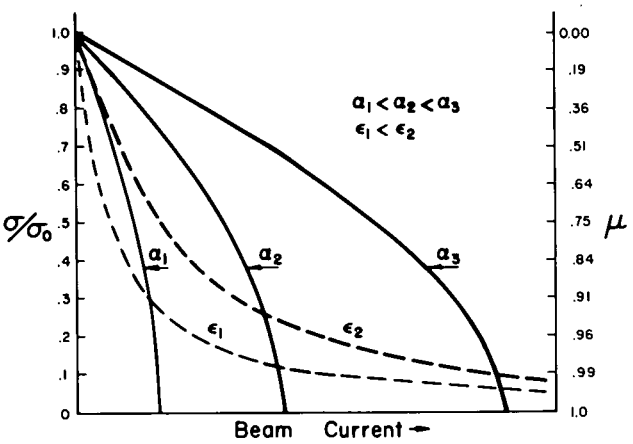


Fig. 2. Behavior of matched solutions from envelope equation, for fixed emittance, ε, or fixed average beam radius, a. For example, for a given radius and current, a certain emittance is required for a matched beam. A fixed accelerator and no emittance growth are assumed.

remain constant. The procedure converges more slowly as the tune is depressed, but is quite effective. Starting values are obtained from the envelope equations.

Emittance Growth with Matched Beams

The parameter space was explored by selecting a range of zero intensity, transverse-phase advances and depressing the tune of each by increasing the current in steps. As stated above, the detailed parameters are submerged, they are in fact quite ordinary and well within the scaling range of the proposed Fusion Materials Irradiation Test (FMIT) linac to the Clinton P. Anderson Meson Physics Facility (LAMPF), and CERN class of machine. Figure 1 shows the growth in the rms emittances and in the effective emittance for 100% of the beam at the end of 20 cells,* for a set of runs where the initial transverse emittance and longitudinal beam size are the same. An input distribution approximately uniform in real space was used. The quads were set to give constant transverse phase advance, $\sigma_0{}^t$, at zero current; this resulted in σ^t remaining approximately constant also. The synchronous phase was held constant. The accelerating gradient started from the same value, but was raised linearly with β, along with adjustment of the initial energy spread to keep the longitudinal phase advance nearly constant for each case.

There appears to be an underlying growth pattern, plus an anomolous feature[3,11] in the transverse growth, which will be discussed later. Much of this "underlying" growth is attributable to the immediate shearing effect of the rf longitudinal-transverse coupling[12], and to the steadily accumulating effect of the series of rf gaps.[10] For each $\sigma_0{}^t$, the current was increased until it became quite difficult to find a solution because of the loss of adequate longitudinal focusing in the initial few cells. For tune depressions, $\sigma^\ell/\sigma_0{}^\ell < 0.4$, the longitudinal growth increased rapidly. For the $\sigma_0{}^t = 50°$ case, the electric field was raised to keep some longitudinal focusing, and the current was increased to depress the transverse tune further. The transverse growth also increased rapidly for $\sigma^t/\sigma_0{}^t < 0.4$ (open circles, Fig. 1). The envelope equations indicate that for a fixed accelerator and fixed emittance, a matched solution should be attainable at any current by choosing the proper beam size, as indicated in Fig. 2. The emittance and space

*Total effective emittance is found by fitting ellipses with the rms emittance ellipse parameters through each particle and taking the largest.

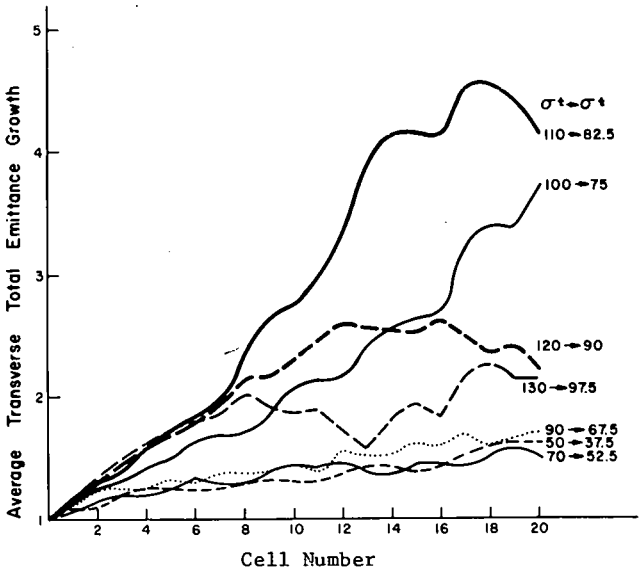


Fig. 3. Growth in average transverse total emittance vs cell number for $\sigma^t/\sigma_o{}^t = 0.75$.

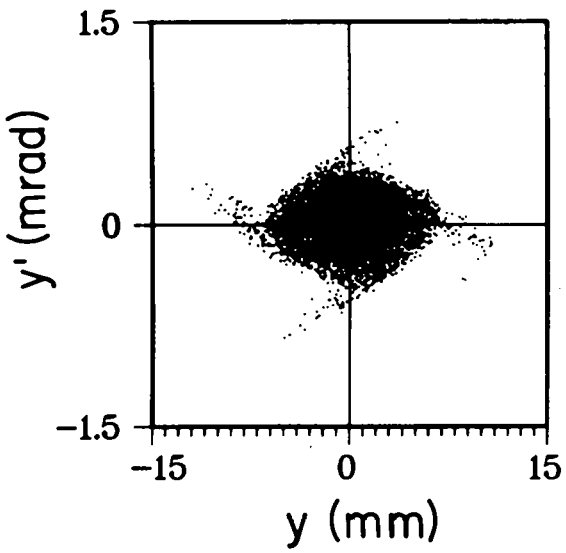


Fig. 4. The y-y' phase-space at Cell 20 for the $\sigma^t/\sigma_o{}^t = 78^o/100^o$ case. 5000 particles were computed and plotted.

charge contribute quadratically to the required size, and at $\sigma/\sigma_0 = 0.4$ (0.25), the emittance term has 0.8 (0.5) the weight of the space charge term. In those cases where the tune is depressed in the first few cells to less than 0.4, there is an immediate growth that tends to push the tune back up until a balance is achieved. The beam has not yet been followed

	1	x	x^2	x^3	x^4
1			1.4	.9	2.2
y			3.6	8.1	7.9
y^2	1.3	4.1	1.3	.8	1.7
y^3	16.4	2.3	140.9	2.6	6.2
y^4	2.6	14.9	1.9	7.0	1.8

	1	x	x^2	x^3	x^4
1			1.4	.9	2.2
x'			.9	2.2	8.4
x'^2	.7	.8	1.5	2.2	3.4
x'^3	2.7	1.6	3.4	1.5	20.7
x'^4	.6	1.9	1.7	7.6	5.6

Fig. 5. Absolute ratio of average cross-correlation products at Cell 20 to those at Cell 2 for $\sigma^t/\sigma_o{}^t = 78^o/100^o$ case.

enough to determine the asymptotic behavior, although it would be unrealistic to sustain the ramped accelerating gradient indefinitely.

This series of cases was repeated with the accelerating field held constant at the value used above in the initial cell. The results are very similar to Fig. 1, except there is less longitudinal growth (see Fig. 8). This observation, plus the fact that the longitudinal growth in Fig. 1 is a smooth curve, indicates that the anomalous transverse growth for the tunes with $\sigma_0{}^t$ in the range 100° - 120° is essentially a transverse phenomenon.

This drastic growth behavior appears similar to an unstable mode reported in Refs. 4-7 for the K-V distribution. Figure 3 shows the growth in average transverse total emittance for the $\sigma^t/\sigma_0{}^t = 0.75$ tune depression for each $\sigma_0{}^t$ case. Some evidence of beat frequencies is apparent, and the growth rate is extremely fast. Figure 4 shows a y-y' scatterplot for $\sigma^t/\sigma_0{}^t = 78^o/100^o$ at Cell 20, with the four arms characteristic of this instability mode. Figure 5 shows the ratio of average cross-correlation products at Cell 20 to those at Cell 2, out to fourth order in each axis. If the size of terms is compared as the tune is depressed, a pronounced peak is found in the vicinity of the instability, in y^2x, y^3, y^4x and a number of the x'-x terms, particularly $x'x^4$, x'^2x^4, x'^3x^4, x'^4x^3 and x'^4x^4. Other terms show a steady increase (or both ramp and peak), especially y^2x^2, y^2x^4, y^3x^4, y^4x^2, y^4x^4, x'^2x^4, x'^4x^3, and x'^4x^4. This mode may be, in fact, the Rayleigh-Taylor instability[19] arising from the alternating-gradient focusing system; the x-y nature, and the fast growth would fit this hypothesis. Theoretical development of this approach is in progress.

Figure 6 shows a histogram of the phase advance of particles in the bunch, in the frame of the least-squares parameters derived for the Cell 17-18 period. The second peak indicates that a group of particles is persistently rotating at a separate rate. This group appears to be a result of the "underlying" mechanisms and not of the instability mode. It consists of particles originating at transverse radii out to

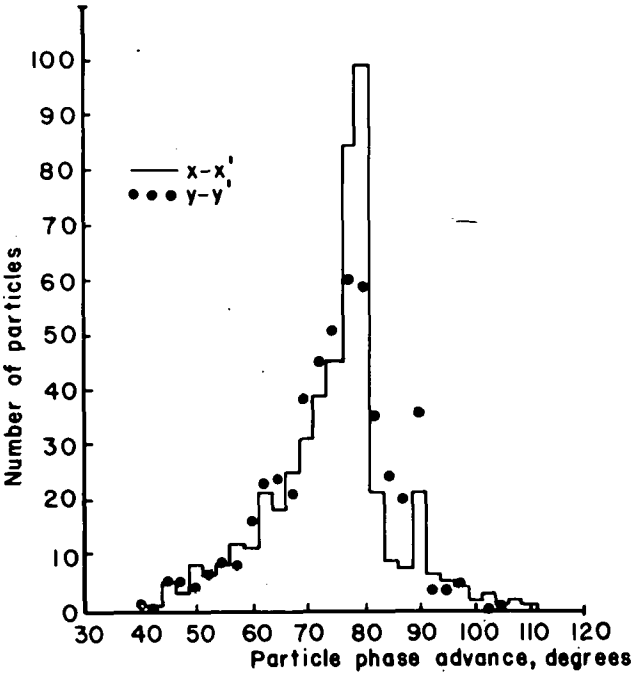


Fig.6. Phase advance histogram for $\sigma^t/\sigma_0{}^t = 78^o/100^o$ case, showing double peak. (Period from Cell 17-18).

0.4 r_{max}, is uncorrelated with particle phase at injection, and is within the 90% core of the beam in the transverse emittance projections.

Practical parameter choices for applications commonly result in $\sigma^\ell < \sigma^t$. A preliminary search was made for resonances of the $2\sigma^t = n\sigma^\ell$ type. Keeping $\sigma^t = 50^o$, E_0/β was adjusted for constant σ^ℓ with n from 2 to 8. No difference in emittance growth was seen out to 60 cells, which is beyond the point to which the E_o ramp could practically be sustained. Other possibilities should be studied.

In another slice of the parameter space, starting with the $\sigma^t/\sigma_0{}^t = 51.5^o/70^o$ case, and, keeping the current constant, reduced the input transverse emittance by factors of 2 and 4. The transverse emittance growth increased, and the longitudinal growth decreased for this example. Such transfers among the projections are commonly observed, including transfers between x-x' and y-y' if the initial emittances differ or during oscillations. This indicates that ratios of emittances are also important parameters, and suggests multi-dimensional matching with equal emittance areas, especially if the parameters change along the machine. It has been found, however, that full 6-D matching is not necessarily advantageous in all applications--another example of the influence of designer constraints on the scalings. Other sets of parameters typical

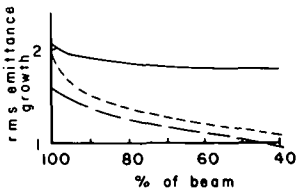


Fig. 7 Typical variation in rms transverse emittance growth with input distribution.
--- Uniform in 3-D real space
--- Uniform in 4-D transverse space, separate 2-D longitudinal
--- Gaussian in real space, truncated at 3σ

of various applications will be explored, in an effort to sort out some of the basic calculations.

Influence of Particle Distribution

The $\sigma_0{}^t = 100^o$ cases were rerun for input distributions uniform in 6-D, and Gaussian in 6-D (truncated at 3σ), keeping the rms emittances constant. The quadrupole strengths were those used to achieve a constant phase advance for the original distribution, approximately uniform in real space. The 6-D distributions grew more rapidly in the first two-to-three cells. From Cells 3-20, the growth in total emittance was very similar, but the rms growth for the 6-D cases was about double that of the 3-D case. The 6-D cases became somewhat mismatched as the beam progressed through the cells. The quads could be reset using the above procedure, for each particular distribution; it is expected that this would smooth but not necessarily reduce the growth--it may in fact increase (see below). Similar general influences of the distribution have also been observed for other choices of parameters. Figure 7 shows a typical redistribution of emittance.[17] It is concluded that the shape of the distribution does influence emittance growth, with greater effect as the beam brightness is increased, and with greater growth as the central density is increased. The unstable mode evidenced in Fig. 1 is not the result of a particular particle distribution.

Influence of Matching

Mismatched beams will be smeared by the action of nonlinear space-charge forces and eventually will assume an emittance congruent with the machine acceptance. Figure 8 demonstrates how emittance growth is affected by mismatching the input beam size up to a factor of $\sqrt{2}$ at injection, for the range of linac parameters under discussion. At a given $\sigma_0{}^t$, the sensitivity to matching becomes more pronounced as the tune is depressed.

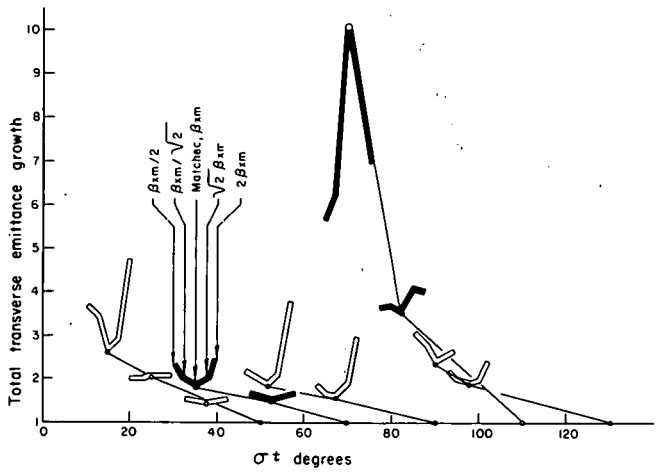


Fig. 8. Sensitivity of transverse emittance growth to input matching. Linac has constant accelerating gradient E_o. At each tune, the smaller dimension of the input beam is varied by changing the input matching-ellipse parameter β by $\pm\sqrt{2}$ and ± 2. The y and z inputs are matched. Growth is shown after 20 cells.

As $\sigma_0{}^t$ increases, the sensitivity for a given tune depression increases, an effect of the alternating gradient. The smaller absolute size of the beam (in one dimension) also becomes more important in terms of the required measurement resolution. For K-V beams, a "mismatching" instability mode has been identified[4] for $\sigma_0{}^t > 90^o$; its analog for these distributions may be a factor here.

In the vicinity of the unstable mode, the behavior becomes somewhat unpredictable. For the parameters in Fig. 8, the betatron oscillations generally subjected the beam to a lower average μ_t (higher σ^t) over the 20 cells, sometimes resulting in less growth. The $\sigma^t/\sigma_0{}^t = 70^o/110^o$ case is particularly dramatic in this respect. The changes in transverse emittance growth from mismatching are generally rather uniform with respect to the shape of the distribution function, as shown in Fig. 9, or sometimes show more growth for higher percentages.[17]

Influence of Off-Axis Trajectories

For a single gap without space-charge, Crandall[10] showed that the increase in total emittance is proportional to $(a^2 + d^2)$ if $|d| \leq a$, and $2ad$ if $|d| \geq a$, where a is the half-width of the beam and d is the displacement of the beam center from the axis. The increase in rms emittance is proportional to $(1 + d^2/\overline{a^2})$, where $\overline{a^2}$ denotes the rms half-width of the beam. It is seen that the rms emittance grows

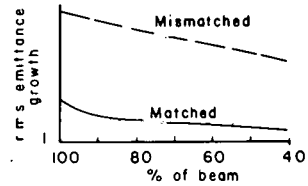
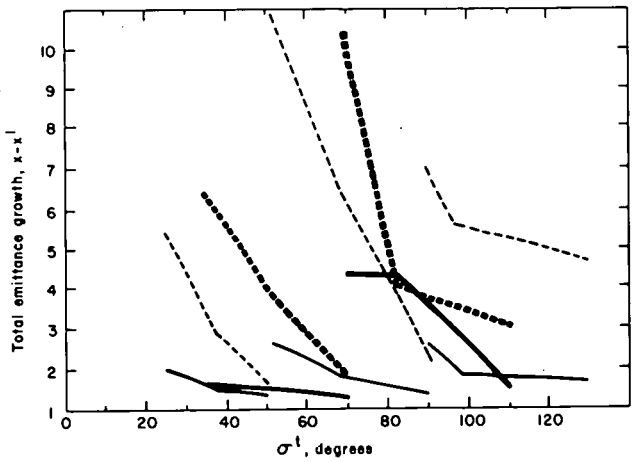


Fig. 9. Typical redistribution of transverse emittance growth for mismatched beams.



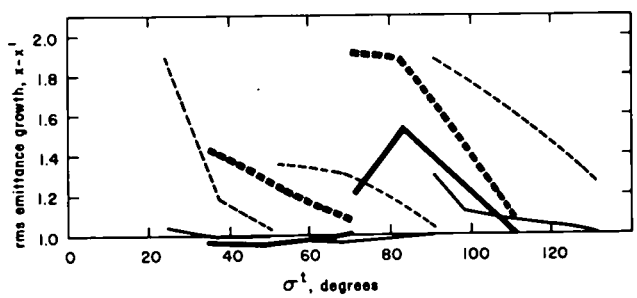


Fig. 10. Sensitivity of transverse emittance growth, after 20 cells for 100% of beam, to horizontal offsets equal to the average input beam radius. Solid -no offset; Dashed - offset.

relatively faster than the total emittance. The growth over n gaps will depend on what happens to the relative sizes of a and d. Figure 10 shows the emittance growths for (x-offset/average input-beam radius) = 1.0 for the cases of Fig. 1. Again the sensitivity increases for larger tune depressions and for higher $\sigma_0{}^t$, with a diminishing of the unstable mode's effect. The longitudinal emittance growth also is increased by the transverse oscillation. Figure 11 shows the typical redistribution that occurs in the transverse-phase space. This feature,

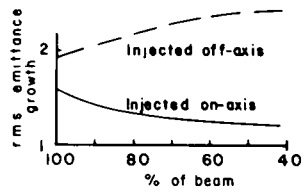


Fig. 11. Typical[17] redistribution of transverse emittance growth for mis-steered beams.

and the contrasting signature of the mismatched beam, Fig. 9, can be valuable aids in machine tuning for detecting the presence of a centroid oscillation or mismatch.

Detailed Matching

It has been hypothesized[9,12] that detailed matching procedures, which prepare the input distribution in ways more specific than just the average properties, might result in reduced emittance growth. This idea finds a general form in the theory of equilibrium distributions,[1,9] and also can be expressed in terms of introducing certain desirable correlations in the particle distribution.[20] A simple example concerns the smearing of the transverse emittance caused by the finite phase spread of the bunch, illustrated in Ref. 12. It would seem reasonable that a first-order improvement, which might be practical using an rf focusing system, would result from adjusting the transverse focusing depending on the phase of the particle. Starting with a Gaussian 6-D uniform distribution, the particles were sorted into five bins according to their initial phase. The average phase advance and matched ellipse parameters for the first two cells of the $\sigma_0{}^t = 70^o$ case were computed for each bin. A new input distribution was then prepared in which each particle was matched to the transverse parameters appropriate to the bin containing its phase. Over the 20 cells a 5-7% reduction in emittance growth resulted for both the transverse and longitudinal planes. Other cases, or other recipes, have not yet been explored. More general systems, which "adiabatically" introduce the desired correlations, are being studied. In particular, the development of the RFQ low-beta structure to accomplish capture, bunching, and preacceleration is a complete embodiment of this concept. Preparations are being made to do combined RFQ/drift-tube-linac studies in this context.

Conclusion

Some new tools useful for generating and observing matched linacs in simulation studies have been forged, and used to study some aspects of emittance growth. Some general guidance on acceptable tune ranges and the effects of some types of errors is apparent. However, the parameter space is large, and further study is needed. For example, there is interest in how far the particular parameters, such as voltages, fields, frequency, and particle type, can be condensed into relatively general parameters such as phase advance or tune depression. The concept of detailed matching appears worthy of further consideration. A better theoretical foundation would be most helpful.

Acknowledgements

We would like to thank K. Crandall, W. Lysenko, and R. Gluckstern for many helpful discussions, and C. Watson for her diligent and enthusiastic help in making the computer runs.

References

1 R. Gluckstern, R. Chasman, K. Crandall, Proc. 1970 Linac Conference, Batavia, pp. 823-849.

2 R. Chasman, Proc. 1968 Proton Linac Conf., BNL, p. 372, IEEE Trans. Nucl. Sci., NS-17, 202 (1969).

3 P. Lapostolle, IEEE Trans. Nucl. Sci., NS-18, 1101 (1971), various CERN reports, summarized in CERN-ISR/78-13.

4 L.J. Laslett, L. Smith, IEEE Trans. Nucl. Sci., NS-25, 3080 (1979).

5 I. Hofmann, Proc., op. cit. p. 3083.

6 S. Penner, A. Galejs, Proc., op. cit. p. 3086.

7 I. Haber, Proc., op. cit. p. 3090.

8 M. Reiser, Particle Accelerators, 1978, Vol. 8, pp. 167-182.

9 W.P. Lysenko, LASL Report LA-7010-MS, Oct. 1977, and Proc. 1979 PAC op. cit. p. 3508.

10 K.R. Crandall, "Transverse Emittance Increase in an rF Gap". LASL Priv. Comm. MP-9, Jan. 12, 1978, and "Transverse Emittance Growth Due to a Sequence of Rf Gaps", with R.S. Mills, LASL Priv. Comm. MP-9, Feb. 28, 1978.

11 R.A. Jameson, R.S. Mills, "Factors Affecting High-Current, Bright Linac Beams", April 8, 1977, LASL Priv. Comm.

12 J.W. Staples, R.A. Jameson, op. cit. p. 3698.

13 K.R. Crandall, R.H. Stokes and T.P. Wangler, "Rf Quadrupole Beam Dynamics Design Studies", to be presented at 1979 Linear Accelerator Conference.

14 O.R. Sander, R.A. Jameson, R.D. Patton, op. cit. p. 3417.

15 K.R. Crandall, "Summary of 805-MHz Linac Length Corrections", LASL Priv. Comm., March 26, 1975.

16 R.A. Jameson, W.E. Jule, "Longitudinal Tuning of the LAMPF 201.25 MHz Linac Without Space-Charge", LA-6863, March 1978, LASL.

17 R.A. Jameson, "Emittance Growth in the New CERN Linac - Transverse Plane, Comparison Between Experimental Results and Computer Simulation", LASL Priv. Comm. AT-DO-377(U), Jan. 15, 1979.

18 O.R. Sander, G.N. Minerbo, R.A. Jameson, D.D. Chamberlin, "Beam Tomography in Two and Four Dimensions", Proc. this conference.

19 P. Channell, LASL, Priv. Comm.

20 A. Chabert et al., op. cit. p. 3612.

Discussion

Ohnuma, FNAL: If somebody is building a high intensity linac right now, from your data or from your experience, what would be your recommendation regarding the most important thing they have to do to suppress the emittance growth?

Jameson: I have not tried to write down what all the rules are, because I don't think we are at the end of the study yet. I think if you study these pictures, it would suggest that one should probably have a tune around 70° for no current. These results so far, would suggest that in an accelerating system we can stand a somewhat higher tune than Lloyd Smith and someone found for transport systems. They suggested that you should limit the zero intensity tune to 60° and not de-tune it with current down to less than 24°, which is the .4 constant of nature again. It looks like in an accelerator, you can probably stand a somewhat higher phase advance, but 70° seems to be a good number to minimize the growth.

Penner, NBS: I think you're cutting it a little fine there, Bob. I don't think there is any difference between what you would recommend at 70° or so, and the 60° that Smith and Laslett recommend. I think their point is, and I think it is true in our numerical simulations and yours and everybody elses, that you must not be at 90° or above or there are these barometric resonances. They will always be there because you always have part of the beam that is at lower current than the main part. So the real rule is below 90°.

Curtis, FNAL: Just a small point. You said when you sliced up the beam you got a somewhat smaller emittance growth. Did you end up with the same density of particles or did you throw some of them away?

Jameson: No, I didn't throw any of them away. The paper that John Staples and I had in March showed that if you slice up the beam and plot the phase space of each slice, you will find that at the end of the beam which has the least rf focusing you will see the thing rotate so that the projection gets turned into kind of a cross and basically that was what I was doing. I was just matching to that, and it went through; no particles were lost.

1979 LINEAR ACCELERATOR CONFERENCE

A STATISTICAL APPROACH TO THE ESTIMATION OF BEAM SPILL*

G. P. Boicourt and R. A. Jameson
Los Alamos Scientific Laboratory
Los Alamos, NM 87545

Summary

Computer codes, which transform a number of pseudo-particles through a simulated machine, form the backbone of accelerator design techniques. When minimization of beam loss within the machine is a primary design objective, it becomes necessary to consider beam behavior in detail, and questions of both the physics and computational aspects of the simulation are raised. Within the constraints of the former, the effectiveness of the latter can be increased for a given amount of computer resources by the use of statistical techniques. A statistical approach to determining the maximum beam size and hence required aperture of a machine is described and illustrated. The method draws upon statistical theory to treat the maximum radius attained by a finite group of particles passing through an accelerator as a statistical variable. Once the distribution of this variable is obtained, radius values can be found inside which a given percentage of the particles can be expected. Confidence bounds can be placed on these radii, and the results used to estimate the suitability of the accelerator apertures.

Introduction

The estimation of beam spill has taken on greater importance in recent years with the call for higher currents in accelerators. LASL interest in the problem arose from the need to estimate beam spill in the Fusion Materials Irradiation Test (FMIT) linac. Here three factors combine to make an accurate estimate necessary. These are the relatively high average current (100 mA cw), the acceleration of a deuteron beam with consequent higher radiation produced per lost particle, and the requirement for no remote handling during maintenance.

At Los Alamos, the PARMILA code is used to transform particles through the six-dimensional phase space of a simulated machine. Because practical computing considerations limit the number of particles that can be followed to a few hundred or a few thousand, compared to 10^8-10^9 in the real beam, the code cannot be expected to give good answers concerning the absolute outer boundary of the beam even if the mathematical formulation of particle movement were exactly correct.

The accuracy of the mathematical formulation is a problem in physics and code design. With any given model, however, the problems caused by following only a small sample can be alleviated by using statistical methods[1,2] to assess the position of the outer boundary.

The Statistical Approach

The parameter that determines beam spill is, in the final analysis, the maximum radius (r_{max}) assumed by any particle in the bunch. The maximum radius is dependent on the focusing strength, the rf defocusing in the gaps, space-charge (hence the beam current), the degree of mismatch, and the alignment and quality of the quadrupole magnets and drift tubes. All these factors are included in the PARMILA code model.

Figure 1 shows the probability density function (pdf) for the physical radius of a beam of particles randomly selected from a uniform distribution in the four-dimensional transverse phase space. An actual pdf histogram for a typical sample of 500 particles is superimposed. Such groups of particles are transported through the accelerator code, and the maximum radius is observed at suitable intervals. (In the strong-focusing system used as the example here, the beam is observed at the center of each quadrupole.) Although the

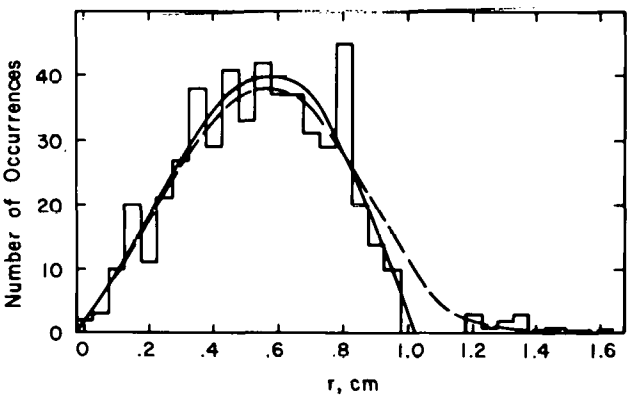


Fig. 1. The pdf for the radius of a typical input particle distribution is shown by the solid curve, along with the histogram resulting from an actual sample of 500 particles. The dashed curve is a hypothetical pdf observed in accordance with the output criterion. A particular r_{max} for the sample will occur.

*Work performed under the auspices of the U. S. Department of Energy.

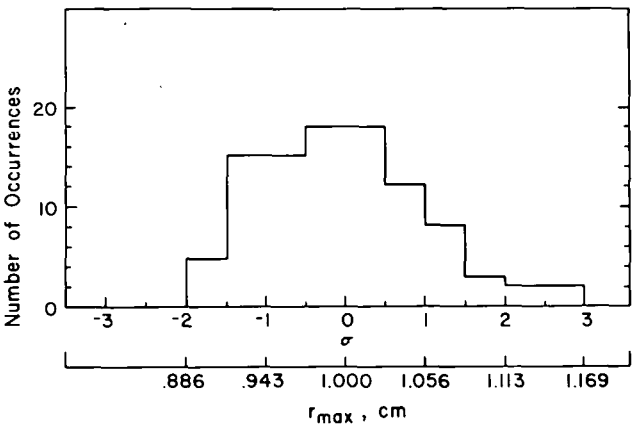


Fig. 2. Histogram of the maximum radius observed anywhere in a section of linear accelerator in 100 runs of 500 particles each. Scales unrelated to Fig. 1.

initial distribution is usually bounded, particles that are not properly accelerated or transported may reach arbitrarily large radii, except that they would strike some limiting physical surface in a real machine. The r_{max}, observed at any particular point, or over a suitable length of machine that integrates over the various oscillation effects, also may be considered a random variable. A series of simulations, starting with different particle samples from the initial distribution, will yield a set of maximum radii with a probability distribution of their own, indicated in Fig. 2.

Let $f(r) = F'(r)$ be the pdf of the distribution of radii in the region of interest, then $F(r)$ is the probability that an observed radius is less than a certain r. The probability that n independent observations all fall short of r is then $F^n(r)$; i.e, this is the probability that r is the largest among n independent observations. Let $\Phi_n(r_n)$ be the probability that the largest value falls short of r_n:

$$\Phi_n(r_n) = F^n(r_n) \quad .$$

Then the derivative,

$$\phi_n(r_n) = nF^{n-1}(r_n)f(r_n) \quad ,$$

is the distribution of the largest among n independent observations. These equations form the basis for an exact theory of extreme values, which proceeds to explore whether asymptotic distributions valid for large samples exist, their nature, how quickly they are approached, and how to estimate their parameters from sample data.

The parameters used to characterize the pdf of the extremes, $\phi(r)$, are the expected value of the extremes, u_n, and the parameters $\alpha_n = nf(u_n)$. It can be shown that:

$$\frac{du_n}{d(\log n)} = \frac{1}{\alpha_n} \quad ,$$

which indicates that $1/\alpha_n$ measures the increase of the expected largest value with the logarithm of the sample size. Distributions fall into three classes, depending on whether α_n increases, remains constant, or decreases with n. This characteristic indicates that the exponential function underlies the theory. Distributions of extremes may also be placed another way into three categories: those that are unlimited (in one or both directions) where all moments exist, unlimited distributions with only a finite number of moments, and limited distributions.

The distributions of the extremes share properties with their underlying population distribution: limited (or not) to left or right, possession of moments, and asymptotic behavior dependent on the behavior of the parent distribution. It is erroneous, however, to assume that the distribution of extremes is normal or tends to normal; most distributions of extreme values are skewed and remain that way in the asymptote. The few symmetric distributions to be found are not normal. It is seen that the empirical pdf in Fig. 2 is bounded to the left, skewed, and could be unlimited to the right.

As with other types of probability distributions, rules are derived for estimating the parameters, for estimates of extrapolated values, and for confidence bounds on the estimates. The appropriate probability paper can be derived; probability paper provides the simplest way to evaluate whether an observed distribution fits the theory (the data would plot on a straight line), and to make estimates. The fitted distribution provides a best guess as to how an infinite number of particles would behave. The effect of the finiteness of the original data is now apparent only in the confidence bounds on the fitted distribution. The fitted distribution can now be used to provide estimates of the maximum radius inside which a given percentage of maximum radii will be found.

Application

The linac data fit an extreme value distribution used by Weibull, which also finds wide use in reliability theory. The cumulative Weibull distribution is described by

$$F(r) = 1 - e^{\frac{-(r-\gamma)^{\beta}}{\alpha}} \quad ,$$

where α is called the scale parameter, β is the shape parameter, and γ is the location parameter.[3] Figure 3 shows the data of Fig. 2 plotted on Weibull probability paper. The variable $x = r - \gamma$ is plotted versus F. The points are seen to very closely approximate a

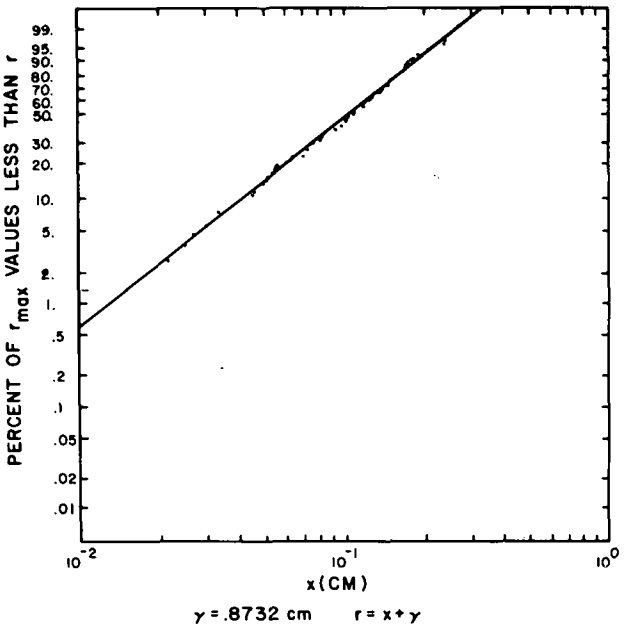


Fig. 3. One hundred values of r_{max} (from 100 PARMILA runs using independent input distributions of 500 particles each) plotted on Weibull coordinates. The straight line is the fitted Weibull distribution.

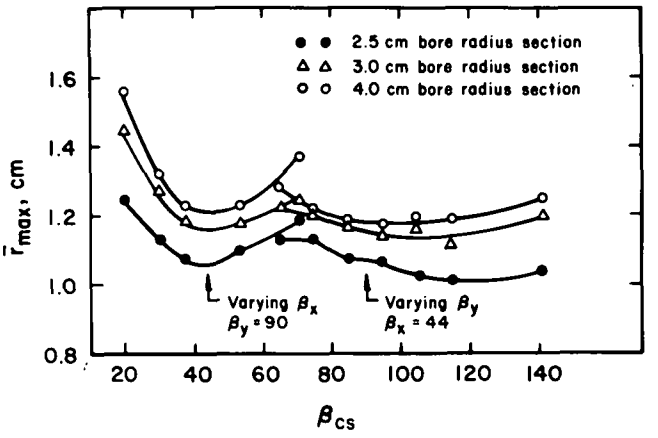


Fig. 4. Average r_{max} observed in 10 runs at each condition, in a study of the maximum beam size in lengths of the FMIT drift-tube linac having a certain bore size, as the match of the input beam is changed by varying the input beam size. β_x and β_y were varied independently.

straight line. Chi-square goodness-of-fit tests were made and show that the Weibull distribution provides a suitable description.

When good confidence bounds are required, the number of runs needed to determine the distribution will be fairly large. For parameter searches, however, as few as 10 runs can suffice. Estimates of the parameters of the distribution can be obtained from the plot; a computer program was written which accomplishes this by direct fitting of the data. Computer codes are being developed to produce maximum likelihood estimates of the parameters and to find the confidence bounds on the parameters and the distribution.

In the accelerator cases studies, the average value of the observed extremes is very close to the Weibull median value. Thus the mean $\bar{r}_{max}$ derived from a small number of runs, say 10, can be used as a quick measure to plot the effects of changes in the accelerating conditions. Figure 4 shows an example of the variation in $\bar{r}_{max}$ in sections of particular bore size of the FMIT linac as a function of how well the input beam is matched.

Another way of obtaining a quick estimate of the radius containing a given percentage of the maxima that would ever be observed, without fitting the distribution, is provided by median rank order statistics.[4] For example, with a sample of size 25, the largest of the 25 values corresponds to 97.3% of all maxima that would be observed. These points are shown on Fig. 5; each point corresponds to the largest of 25 runs. The effect of 0.25-mm random misalignment error is also shown. There is much more uncertainty in Fig. 5 than in Fig. 4, because the 97.3% estimate is based on less data than is the mean.

Conclusion

The observed extreme values from linear accelerator computer programs fit the statistical theory for extreme values very well. This theory should be used to develop estimates for beam spill in these machines. Although better models of the particle physics may also be needed, many of the effects of finite sample sizes are avoided by using the statistical approach. Work is progressing on identifying more precisely the characteristics of the particular distributions involved in the linac problem, programs for fitting data and calculating confidence bounds, and application of the results to judgments concerning the appropriate safety factors in accelerator design.

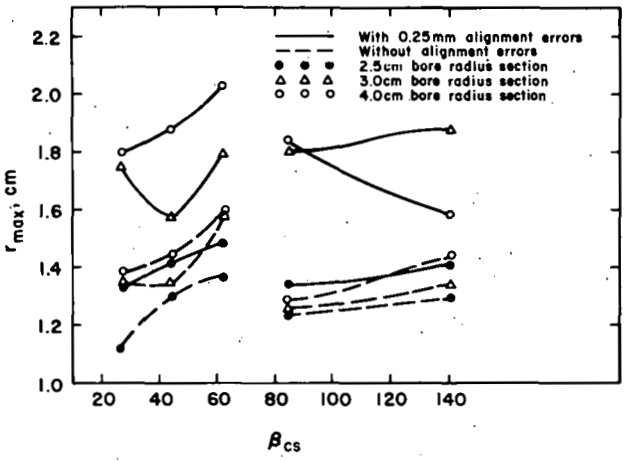


Fig. 5. For the matching experiment shown in Fig. 4, the maximum r_{max} in each series of 25 runs for each condition is plotted. These values, within a known uncertainty, should be greater than or equal to 97.3% of all maximum radii that would be observed as the number of runs increased.

References

1. E. J. Gumbel, "Statistical Theory of Extreme Values and Some Practical Applications," NBS Applied Mathematics Series, #33, Feb. 12, 1954.

2. N. R. Mann, R. E. Schafer and N. D. Singpurwalla, Methods for Statistical Analysis of Reliability and Life Data, (John Wiley & Sons, New York, 1974).

3. J. H. K. Kao, "A Graphical Estimation of Mixed Weibull Parameters in Life-Testing of Electron Tubes," Technometrics, Vol. 1, No. 4, (Nov. 1959).

4. L. G. Johnson, The Statistical Treatment of Fatigue Experiments, (Elsevier Publ. Co., New York, 1964).

1979 LINEAR ACCELERATOR CONFERENCE

GENERAL LEAST-SQUARES FITTING PROCEDURES TO MINIMIZE THE VOLUME OF A HYPERELLIPSOID*

E. Alan Wadlinger
Los Alamos Scientific Laboratory
Los Alamos, NM 87545

Summary

Several methods are presented for determining the shape parameters, which in two dimensions are the Courant-Snyder parameters, and the volume of an ellipse or hyperellipse that represent a set of phase-space points in a two or more dimensional hyperspace. The ellipse parameters are useful for matching a beam to an accelerating or transport system, and in studies of emittance growth. The fitting procedure minimizes the total volume of a hyperellipse by adjusting the ellipse shape parameters. The total volume is the sum of the individual particle volumes defined by the hyperellipse that passes through a particle's phase-space point. A two-dimensional space is treated first, then generalized to higher dimensions. Computer programs using these techniques have been written.

Two-Dimensional Case

The equation for an ellipse may be written

$$\gamma x^2 + 2\alpha xy + \beta y^2 = E/\pi = A \quad , \tag{1}$$

$$\gamma\beta - \alpha^2 - 1 = 0 \quad , \tag{2}$$

where α, β, and γ are the Courant and Snyder parameters[1] and E is the area of the ellipse. The emittance required for an ellipse centered at the origin to encompass a particle with phase-space coordinates x_i, y_i is

$$A_i = \gamma x_i^2 + 2\alpha x_i y_i + \beta y_i^2 \quad . \tag{3}$$

If there are N particles and each particle has an emittance, A_i $(i = 1,N)$, a total summed emittance can be defined as:

$$I = \sum_{i=1}^{N} A_i \quad . \tag{4a}$$

The rms ellipse parameters minimize I. These parameters are found most easily by multiplying Eq. (2) by a Lagrange multiplier λ; adding the product to Eq. (4a), giving J [Eq. (4b)]; differentiating J by α, β, γ, and λ, respectively; and setting the result to zero. The Lagrange multiplier allows α, β, and γ to be treated as independent variables. It is found that with

$$J = I + \lambda(\gamma\beta - \alpha^2 - 1) \quad , \tag{4b}$$

the results are

$$\left.\begin{aligned} \gamma &= \frac{\sum y_i^2}{D} \quad , \quad \beta = \frac{\sum x_i^2}{D} \quad , \quad \alpha = -\frac{\sum x_i y_i}{D} \quad , \\ \text{and} \quad D &= \sqrt{\sum x_i^2 \sum y_i^2 - \left(\sum x_i y_i\right)^2} \quad , \end{aligned}\right\} \tag{5}$$

which is a standard method for fitting an rms ellipse to a distribution.

If the emittance is defined to be the ellipse area that encompasses all of the beam, then to determine the ellipse parameters that minimize this area, requires use of a fitting procedure that most heavily weights those beam particles that lie farthest from the centroid of the distribution. This is done by using A_i^2 instead of A_i in Eq. (4a),

$$J = \sum A_i^2 + \lambda(\gamma\beta - \alpha^2 - 1) \quad . \tag{6}$$

Minimizing J with respect to α, β, γ, and λ then eliminating λ gives [see Eq. (3)],

$$\gamma\beta - \alpha^2 - 1 = 0 \quad , \tag{2}$$

$$\alpha \sum A_i y_i^2 + \gamma \sum A_i x_i y_i = 0 \quad , \tag{7}$$

and

$$\alpha \sum A_i x_i^2 + \beta \sum A_i x_i y_i = 0 \quad . \tag{8}$$

Equations (2), (3), (7), and (8) define α, β, and γ. An iteration procedure issued to solve these equations.[2] The starting values for the procedure may be obtained from Eq. (5).

Figure 1 compares the results of fitting an ellipse to the given set of points using both methods described above. For this distribution the weighted fitting method (dashed line) gives an ellipse with a smaller area.

Finally, it was assumed that the particle distribution is centered about the origin. This deficiency can be corrected by substituting $(x_i - x_o)$ for x_i and $(y_i - y_o)$ for y_i in Eq. (3) then minimizing Eq. (4b) or Eq. (6) with respect to x_o and y_o, where (x_o, y_o) is the origin of the ellipse.

*Work performed under the auspices of the U.S. Department of Energy.

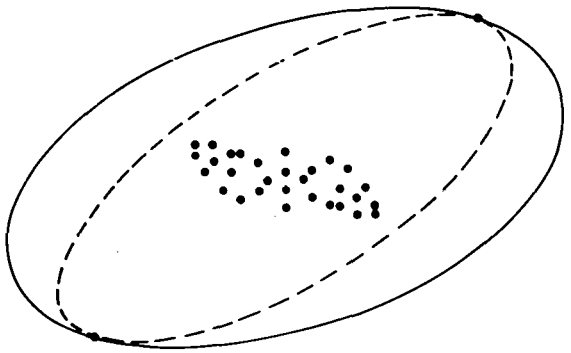


Fig. 1 Weighted and rms ellipses that encompass all particles. The inner ellipse (dashed line) resulted from the "weighted" fit.

Higher Dimensional Hyperellipsoid

The equation of a hyperellipse in an n-dimensional hyper-space is:

$$X^T \underline{A} X = 1 \quad , \tag{9}$$

where $\underline{A}$ is an n x n -dimensional symmetric matrix and X is an n-dimensional column vector. Given a set of k points (particles) represented by X_i (i = 1,k) in this hyper-space, the hyperellipse defining matrix $\underline{A}$ that best represents this set of points is found. The fit is by minimizing the volume enclosed by the hyperellipse characterized by the data. The technique[3] of minimizing the function,

$$I = \sum_{i=1}^{k} (X_i^T \underline{A} X_i - 1)^2 \quad ,$$

with respect to the elements of the symmetric matrix $\underline{A}$ was not considered. This technique minimizes the distances between the data points and the surface of the hyperellipsoid defined by $\underline{A}$.

An explicit relationship between the volume of the hyperellipsoid and the shape-defining parameters of the ellipse was first obtained. The volume of an n-dimensional upright ellipsoid,

$$\sum_{i=1}^{n} \frac{X_i^2}{d_i^2} = 1 \quad , \tag{10}$$

with semiaxes of length d_i is

$$V_n = K(n) \prod_{i=1}^{n} d_i \; ; \quad K(n) = \frac{\pi^{n/2}}{\Gamma\left(\frac{n}{2} + 1\right)} \quad . \tag{11}$$

Note that the sum in Eq. (10) and the product in Eq. (11) are over the n-dimensional vector space, not over the particle coordinates. Now let $\underline{U}$ be an orthogonal matrix that diagonalizes $\underline{A}$, Eq. (9), let $\underline{D}$ be the resulting diagonal matrix, ($\underline{D} = \underline{U}\underline{A}\underline{U}^T$), and let Y be the transformed vector, ($Y = \underline{U}X$). Then,

$$Y^T \underline{D} Y = 1 \quad . \tag{12}$$

Equation (12) is in the form of Eq. (10) with components of $\underline{D}$,

$$\underline{D}_{ij} = \frac{\delta_{ij}}{d_j^2} \quad , \tag{13}$$

where δ_{ij} is the Kronecker delta function. Using the determinant of $\underline{D}$, symbolized by $|\underline{D}|$, it is found that:

$$|\underline{D}| = \left[\prod_{i=1}^{n} d_i^2 \right]^{-1} = \left(\frac{K(n)}{V_n} \right)^2 = |\underline{A}| \quad . \tag{14}$$

The determinant value is invariant under an orthogonal transformation. Define a new matrix $\underline{B}$ whose elements are

$$\underline{B}_{ij} = \left(\frac{V_n}{K(n)} \right)^{2/n} \underline{A}_{ij} \quad ; \tag{15}$$

then,

$$|\underline{B}| = \left[\left(\frac{V_n}{K(n)} \right)^{2/n} \right]^n |\underline{A}| = 1 \quad . \tag{16}$$

From Eq. (9), it is found that:

$$X^T \underline{B} X = \left(\frac{V_n}{K(n)} \right)^{2/n} \quad , \tag{17}$$

with

$$|\underline{B}| = 1 \quad . \tag{18}$$

Note that with n = 2, Eq. (1) is obtained.

The hyperellipse volume, determined from Eq. (17), is

$$V_n = K(n) \left[X^T \underline{B} X \right]^{n/2} \quad . \tag{19}$$

The hyperellipse volume (or some power of the volume) is minimized for k particles in an n-dimensional hyper-space. Define

$$I = \sum_{i=1}^{k} V_{n_i}^{\,m} + \lambda \left(|\underline{B}| - 1 \right) \quad , \tag{20}$$

where i is the sum over k particles, m is an exponent, n is the hyper-space dimension, and λ is a Lagrange multiplier. Let $\underline{B}$ be

symmetric. Substituting Eq. (19) into Eq. (20) and absorbing the K(n) term into the Lagrange multiplier, yields

$$I = \sum_{i=1}^{k} \left(X_i^T \underline{B} X_i \right)^{nm/2} + \lambda \left(|\underline{B}| - 1 \right) \quad . \tag{21}$$

The matrix $\underline{B}$ is determined by minimizing I with respect to each element $\underline{B}_{ij}$ and λ, giving the series of equations

$$\begin{aligned} &\partial I/\partial \underline{B}_{ij} = 0 \ (i \leq j = 1, \ldots, n) \quad , \\ &\partial I/\partial \lambda = 0 \quad . \end{aligned} \tag{22}$$

The restriction ($i \leq j = 1, \ldots, n$) accounts for $\underline{B}$ being symmetric ($\underline{B}_{ij} = \underline{B}_{ji}$). Equation (22) is used to solve for $\underline{B}$. In all but the simplest cases, Eq. (22) will be nonlinear and will have to be solved by an iterative approximation scheme. If the distribution has a non-zero centroid, $(X_i - X_o)$ can be substituted for X_i in Eq. (21) which can be minimized with respect to X_o.

Given the ellipse in Eq. (17), the projected area in the two-dimensional plane defined by $\hat{\ell}$ $\hat{m}$ can be found. The gradient of Eq. (17) can be used to obtain

$$\nabla(X^T \underline{B} X) = 2 \sum_i \hat{i} \sum_j \underline{B}_{ij} X_j \quad , \tag{23}$$

where i and j are vector, not particle, indices.

The maximum projection of Eq. (17) occurs where the coefficients of $\hat{i}$ ($\hat{i} \neq \ell, m$) are zero. This gives (n - 2) relations of the form

$$\sum_j \underline{B}_{ij} X_j = 0 \quad (i \neq \ell, m) \quad , \tag{24}$$

which can be used to solve for X_j ($j \neq \ell, m$) in terms of X_ℓ and X_m. Substitute these relations in Eq. (17) to get

$$\left(X_\ell, X_m \right) \underline{R} \begin{pmatrix} X_\ell \\ X_m \end{pmatrix} = \left(\frac{V_n}{K(n)} \right)^{2/n} \quad . \tag{25}$$

The area of this ellipse is

$$A = \pi \left(\frac{V_n}{K(n)} \right)^{2/n} |R|^{1/2} \quad . \tag{26}$$

Acknowledgments

I thank K. Crandall, R. Jameson, and R. Mills for their useful suggestions and criticisms.

References

1. E. D. Courant and H. S. Snyder, "Theory of the Alternating-Gradient Synchrotron," Ann. Phys. 3, 1-49 (1958).

2. E. A. Wadlinger, "General Least-Squares Fitting Procedures to Minimize the Volume of a Hyperellipsoid," Los Alamos Scientific Laboratory report to be published.

3. A. Law, "A General Hyperellipsoid Least-Squares Fitting Routine," Los Alamos Scientific Laboratory, internal memorandum, June 1977.

FOCUSING OF HIGH CURRENT BEAMS IN CONTINUOUSLY ROTATED QUADRUPOLE SYSTEMS

Robert L. Gluckstern
University of Maryland
College Park, MD

The recent development of high field permanent magnetic quadrupoles by Halbach, opens up their potential use in drift tube linacs, beam transport lines, etc. In order to retain some ability to adjust the focusing strength of a permanent quadrupole beam line, modification is proposed of the standard + - + - system to a system where adjacent quadrupoles are rotated (axially) with respect to one another by a constant angle, which can be adjusted to yield different focal strengths. The resulting motion in the two transverse directions is coupled, and requires a 4×4 matrix analysis to solve. However, a "smoothed" system consisting of continuously rotated quadrupoles can be solved analytically without invoking the usual alternating gradient matrix analysis. This has been done in this paper, which also extends the analysis to include properly matched, self-consistent, K-V space-charge distributions.

Introduction

The recent development of high field permanent magnetic quadrupoles[1] makes possible their use in transverse focusing applications such as transport lines, drift tube linacs, etc., without costly systems to supply magnet power and cooling. The simple means of adjusting focusing by changing the magnet excitation, however, is no longer available and must be replaced by some other mechanism which will permit changes for beam matching, space-charge defocusing, etc. The possibility explored in this paper, is the rotation of the quadrupoles about the beam axis. Although this couples the two transverse directions, the degree of rotation between successive magnets in a periodic system provides an adjustment of the focal strength in the transverse directions. The general features of a rotated quadrupole focusing system will first be discussed, and then a continuously rotated system analyzed in detail, including the presence of space-charge in a two-dimensional uniform beam of elliptical cross-section.

General Analysis

In a system of quadrupoles periodically spaced, and rotated with respect to one another by a fixed angle, the 4×4 matrices corresponding to the action of the quadrupole, to a drift, and to an rf defocusing impulse, are given by:

$$M_{quad} = \begin{pmatrix} \cos\theta & \frac{\sin\theta}{k} & 0 & 0 \\ -k\sin\theta & \cos\theta & 0 & 0 \\ 0 & 0 & \cosh\theta & \frac{\sinh\theta}{k} \\ 0 & 0 & k\sinh\theta & \cosh\theta \end{pmatrix} \quad (1)$$

$$M_{drift} = \begin{pmatrix} 1 & L & 0 & 0 \\ 0 & 1 & 0 & 0 \\ 0 & 0 & 1 & L \\ 0 & 0 & 0 & 1 \end{pmatrix} \quad (2)$$

$$M_{rf} = \begin{pmatrix} 1 & 0 & 0 & 0 \\ \hat{\Delta} & 1 & 0 & 0 \\ 0 & 0 & 1 & 0 \\ 0 & 0 & \hat{\Delta} & 1 \end{pmatrix} \quad (3)$$

where the transverse vector has components x, x', y, y' along the principal axes of the quadrupole. Here the equations of motion are given by:

$$\frac{d^2x}{ds^2} = -k^2x, \quad \frac{d^2y}{ds^2} = k^2y, \quad (4)$$

and $\theta = k\ell$, where ℓ is the magnet length. The drift length is L and the rf impulse is given by:

$$\frac{x'}{x} = \frac{y'}{y} = \hat{\Delta}. \quad (5)$$

The matrix appropriate to the traversal from a given axial location to the corresponding location one magnet period later, consists of the product of matrices of the form in (1), (2), (3) followed (or preceded) by the matrix

$$M_{rot} = \begin{pmatrix} \cos\alpha & 0 & \sin\alpha & 0 \\ 0 & \cos\alpha & 0 & \sin\alpha \\ -\sin\alpha & 0 & \cos\alpha & 0 \\ 0 & -\sin\alpha & 0 & \cos\alpha \end{pmatrix} \quad (6)$$

representing rotation by an angle α. Obviously, the vector now corresponds to the rotated coordinate system.

The transverse dynamics are now controlled by repeated multiplication by the one-cell matrix M, a process which is most easily accomplished by diagonalization of M. For example, if

$$SMS^{-1} = D \quad (7)$$

is a diagonal matrix, then

$$M^n = S^{-1} D^n S. \quad (8)$$

The motion will then be stable if the diagonalized matrix is of the form:

$$D = \begin{pmatrix} e^{i\sigma_1} & 0 & 0 & 0 \\ 0 & e^{-i\sigma_1} & 0 & 0 \\ 0 & 0 & e^{i\sigma_2} & 0 \\ 0 & 0 & 0 & e^{-i\sigma_2} \end{pmatrix} \quad (9)$$

with σ_1 and σ_2 being real. If $\xi_i = (u,u',v,v')$ are components of the rotated vector, then one eventually can write

$$(\xi_i)^{(n)} = A_{1i}\cos n\sigma_1 + A_{2i}\sin n\sigma_1 + A_{3i}\cos n\sigma_2 + A_{4i}\sin n\sigma_2 \quad (10)$$

where A_{ji} are (real) parameters determined by the focusing configuration. Clearly (10) can be solved for $\cos n\sigma_1$, $\sin n\sigma_1$, $\cos n\sigma_2$, $\sin n\sigma_2$ as linear combinations of the ξ_1. Forming $\cos^2 n\sigma_1 + \sin^2 n\sigma_1 = 1$ and $\cos^2 n\sigma_2 + \sin^2 n\sigma_2 = 1$ leads to two separate quadratic invariants involving the transverse displacements and angles. These invariants can then be used to evaluate maximum displacements and angles in terms of the

initial displacements and angles. Needless to say, the algebra is straightforward but tedious. Some simplification may occur because the matrix M is symplectic and has a unit determinant. In any event, computer calculations are feasible.

Continuously Rotated Quadrupoles

As a special model, a continuously rotated quadrupole system will be considered for which the analytic calculation becomes tractable.[2] Although the details may differ from the cell-by-cell calculation outlined in the previous section, patterns of stability, variation of amplitude functions, matching requirements, and the effect of space would be expected to exhibit the same general features. For this reason, the calculations for the continuously rotated system will serve as a guide to the organization and interpretation of the computations for the cell-by-cell case which must ultimately be carried out.

Consider a quadrupole magnet system whose transverse axes rotate at an angular rate β per unit length along the axis. Since the free-space focusing force must be derivable from a potential satisfying Laplace's equation, the general form of this potential will be

$$\phi = \text{const } I_2(\beta r) \cos 2(\theta - \beta s). \tag{11}$$

Near the axis, only the lowest power of r^2 will contribute, and the equations for the transverse motion will be

$$\begin{aligned} x'' &= -Kx \cos 2\beta s - Ky \sin 2\beta s - x\Delta \\ y'' &= -Kx \sin 2\beta s + Ky \cos 2\beta s - y\Delta \end{aligned} \tag{12}$$

where K is related to the quadrupole strength, and Δ represents the (smoothed) rf defocusing gradient.

Let the transverse displacements to the rotating system be transformed in such a way that

$$\begin{aligned} u &= x \cos \beta s + y \sin \beta s \\ v &= -x \sin \beta s + y \cos \beta s . \end{aligned} \tag{13}$$

Differentiating (13), yields:

$$\begin{aligned} u' &= x' \cos \beta s + y' \sin \beta s + \beta v \\ v' &= -x' \sin \beta s + y' \cos \beta s - \beta u . \end{aligned} \tag{14}$$

Differentiating (14), gives:

$$\begin{aligned} u'' &= 2\beta v' + \beta^2 u + x'' \cos \beta s + y'' \sin \beta s \\ v'' &= -2\beta u' + \beta^2 u - x'' \sin \beta s + y'' \cos \beta s . \end{aligned} \tag{15}$$

Using (12) in Eq. (15) produces:

$$\begin{aligned} u'' &= 2\beta v' + \beta^2 u - Ku - u\Delta \\ v'' &= -2\beta u' + \beta^2 v + Kv - v\Delta , \end{aligned} \tag{16}$$

in which the βs dependence has remarkably disappeared from the coefficients. What started out in (12) as two coupled Mathieu equations, have simplified to two coupled linear differential equations with constant coefficients in (16).

The solutions of (16) are obviously of the form $\exp(\pm ips)$, $\exp(\pm iqs)$, where $z = p^2, q^2$ are the two solutions of

$$(z + \beta^2 - K - \Delta)(z + \beta^2 + K - \Delta) = 4\beta^2 z, \tag{17}$$

namely

$$\begin{aligned} z_1 &\equiv p^2 = \beta^2 + \Delta + \omega \\ z_2 &\equiv q^2 = \beta^2 + \Delta - \omega , \end{aligned} \tag{18}$$

where

$$\omega = (K^2 + 4\beta^2\Delta)^{1/2}. \tag{19}$$

Clearly, stability requires that p^2 and q^2 each be real and positive. This translates into a condition on K given by

$$2\beta\sqrt{-\Delta} < K < \beta^2 - \Delta \tag{20}$$

which is represented by the shaded region in Fig. 1, a familiar shape in strong focusing systems.

In order to explore amplitude considerations, the general solutions of (16), will now be constructed. These can be written in the form

$$\begin{aligned} u &= A \cos P + \lambda B \sin Q \\ v &= -\sigma A \sin P + B \cos Q \end{aligned} \tag{21}$$

where $P = ps + a$, $Q = qs + b$ and

$$\lambda = \frac{2\beta^2 + K - \omega}{2\beta q} = \frac{2\beta q}{2\beta^2 - K - \omega} \tag{22}$$

$$\sigma = \frac{2\beta^2 - K + \omega}{2\beta p} = \frac{2\beta p}{2\beta^2 + K + \omega} . \tag{23}$$

From (21),

$$u' = -pA \sin P + \lambda qB \cos Q \tag{24}$$

$$v' = -\sigma pA \cos - qB \sin Q. \tag{25}$$

Elimination of the terms in P,Q leads to the two quadratic invariants

$$\frac{(u' - \lambda q v)^2}{\mu^2} + \frac{(\lambda v' + qu)^2}{\nu^2} = A^2 \tag{26}$$

$$\frac{(\sigma u' - pv)^2}{\mu^2} + \frac{(v' + \sigma p u)^2}{\nu^2} = B^2 \tag{27}$$

where $\mu = p - \lambda q\sigma$, $\nu = \lambda\sigma p - q$. The maximum radial excursion

$$R^2 = (x^2 + y^2)_{max} = (u^2 + v^2)_{max} \tag{28}$$

is then determined from (26) and (27) in terms of the focusing parameters and the initial conditions. It can be shown, after some algebra, that R is the larger of

$$\lambda A + B \text{ or } A + \sigma B.$$

Self-Consistent Phase Space Distribution/Space-Charge

It is well known that any function of the constants of the motion yields a stationary distribution in phase space. In this case, the constants of the motion are given in (26) and (27).

In order to apply this principle to the present case with space-charge, phase space distribution must be restricted to one like the Kapchinsky-Vladimirsky (K-V) distribution for which

charge distribution is uniform and the space-charge force is linear. In the present case this suggests a phase space distribution of the form:

$$f(u,u',v,v') = \text{const}\ \delta[M A^2(26) + N B^2(27) - 1] \quad (29)$$

where $A^2(26)$ and $B^2(27)$ are written in terms of u, u', v, v' as in (26) and (27). The space-charge distribution can be obtained directly by integrating over u' and v', by appropriately completing squares in $MA^2 + NB^2$. The result is the uniform elliptical distribution

$$\rho(u,v) = \rho_o\{{}^{1}_{0}\}, \text{ for } \frac{MNu^2}{M\lambda^2+N} + \frac{MNv^2}{M+N\sigma^2}\{{}^{<}_{>}\}1, \quad (30)$$

where the axes of the ellipse remain clearly oriented along the principal axes of the quadrupole.

It must be verified that the forces appropriate to an elliptical space-charge distribution have been used in calculating the equations of motion. The semi-major and semi-minor axes are given from (30) by

$$a^2 = \frac{(M\lambda^2+N)}{MN}\ ,\ b^2 = \frac{(M+N\sigma^2)}{MN}\ . \quad (31)$$

Since the fields within a uniform elliptical distribution with charge per unit length τ are given by

$$E_x = \frac{4\tau}{4\pi\varepsilon_o}\ \frac{x}{a(a+b)}\ ,\ E_y = \frac{4\tau}{4\pi\varepsilon_o}\ \frac{y}{b(a+b)} \quad (32)$$

Equation (16) can be rewritten as

$$\begin{aligned} u'' &= 2\beta v' + \beta^2 u - K_m u - u\Delta_{rf} + u\Delta_a \\ v'' &= -2\beta u' + \beta^2 u + K_m u - u\Delta_{rf} + u\Delta_b \end{aligned} \quad (33)$$

where K_m is now identified only with the actual magnetic gradient, Δ_{rf} is the rf component of Δ, and Δ_a, Δ_b are the space-charge terms, derived from (32), given by

$$a\Delta_a = b\Delta_b = \frac{120\ \text{ohms}\ eIc}{Mv^3(a+b)}\ . \quad (34)$$

Equation (33) returns to the original form (16) if one makes the identification

$$K = K_m + \left(\frac{\Delta_b - \Delta_a}{2}\right) \quad (35)$$

$$\Delta = \Delta_{r-f} - \left(\frac{\Delta_b + \Delta_a}{2}\right). \quad (36)$$

These expressions are easy to understand. Equation (36) represents the enhancement of the rf defocusing by the (average) space-charge defocusing. Equation (35) represents the contribution to the magnetic quadrupole gradient from the eccentricity of the elliptical space-charge.

Phase Space Projections, Transverse Emittance

The appropriate momenta to use for the x and y phase space projections, are the canonical momenta derived from the Hamiltonian representation of (16), namely

$$\xi = u' - \beta v,\ \eta = v' + \beta u. \quad (37)$$

In terms of ξ and η, the invariants (26) and (27) can be written as

$$\begin{aligned} \frac{(\xi+\beta\varepsilon v)^2}{\mu^2} + \frac{\lambda^2(\eta-\beta\delta u)^2}{\nu^2} &= A^2 \\ \frac{\sigma^2(\xi-\beta\delta v)^2}{\mu^2} + \frac{(\eta+\beta\varepsilon u)^2}{\nu^2} &= B^2 \end{aligned} \quad (38)$$

where

$$\varepsilon = \frac{\omega - K}{2\beta^2}\ ,\ \delta = \frac{\omega + K}{2\beta^2}\ . \quad (39)$$

Integration of (29) over v and η yields the u, ξ phase space projection (the x, x' projection at s = 0) as an ellipse with boundary

$$\frac{MNx^2}{M\lambda^2+N} + \frac{MNx'^2}{(\delta^2\sigma^2N+\varepsilon^2M)\beta^2} = 1. \quad (40)$$

Similarly, the v, η projection (the y, y' projection at s = 0) is

$$\frac{MNy^2}{M+N\sigma^2} + \frac{MNy'^2}{(\delta^2\lambda^2M+\varepsilon^2N)\beta^2} = 1. \quad (41)$$

The emittances corresponding to (40) and (41) are

$$\frac{W_x}{\pi} = \frac{(M\lambda^2+N)^{1/2}(\varepsilon^2M+\delta^2\sigma^2N)^{1/2}\beta}{MN} \quad (42)$$

$$\frac{W_y}{\pi} = \frac{(M+N\sigma^2)^{1/2}(\delta^2\lambda^2M+\varepsilon^2N)^{1/2}\beta}{MN}\ . \quad (43)$$

In the special case $W_x = W_y$, one finds

$$M\lambda = N\sigma \quad (44)$$

and

$$\frac{a}{b} = \left(\frac{\lambda}{\sigma}\right)^{1/2} = \left(\frac{\beta^2 + K - \Delta}{\beta^2 - K - \Delta}\right)^{1/4}. \quad (45)$$

In this case, lines of constant a/b are straight lines in Fig. 1, given by

$$\frac{K}{\beta^2} = \left(1 - \frac{\Delta}{\beta^2}\right)\left(\frac{a^4 - b^4}{a^4 + b^4}\right). \quad (46)$$

Selection of Parameters

A sequence by which the parameters can be selected is as follows:

1) The parameters Δ/β^2 and K/β^2 are selected so that the "operating point" will lie comfortably within the region of stability in Fig. 1. The known extremes of Δ_{rf} then suggest a desirable value for β, from which the value of K follows.

2) The parameters λ, σ, ε, δ are functions only of Δ/β^2 and K/β^2, and are therefore determined. From the predetermined emittances W_x and W_y, one finds the necessary values of M and N, using (42) and (43).

3) The matched beam parameters a, b and the corresponding angles can now be found from (31), (40) and (41).

4) Equation (36) can now be used to determine the movement of the operating point in the presence of space-charge, and (35) will give the necessary magnetic quadrupole strength.

5) Equation (29) describes the matched four-dimensional phase space, which, in effect, requires some restrictive correlations between the two-dimensional projections in (42) and (43).

Summary

It is possible to design a periodic transport system, consisting of quadrupoles rotated by a fixed angle relative to their nearest neighbors, which will provide for focusing in the two transverse directions. The general analysis can be carried out by means of 4×4 matrices, and the focal strength of the configuration can be adjusted by increasing or decreasing the angle of rotation between adjacent quadrupoles.

The analysis has been carried out in detail for a simplified model consisting of a continuously rotated quadrupole system, including space-charge, in the form of a matched K-V beam. Simple formulas have been derived for the stability region, the amplitude variations, and the transverse matching requirement necessary to maintain a self-consistent equilibrium distribution. These results should serve as a useful guide in the design of a periodic transport system consisting of rotated quadrupoles.

Acknowledgment

I would like to thank Klaus Halbach and Ron Holsinger for useful discussions about applications of high field permanent magnets and mechanisms to adjust their focal strength; Ernest Courant and Alex Dragt for helpful discussions about the general features of 4×4 matrix analysis for transverse beam optics in periodic systems, and Shoroku Ohnuma for alerting me to the earlier literature on magnetic helical quadrupole channels.

References

1. K. Halbach, LBL-8906 (1979); also private communication.
2. This calculation has been carried out earlier for low space charge. See, for example, L. Teng, Argonne Rpt. ANLAD-55 (Feb. 1959); G. Salardi, et al., Nucl. Instr. & Meth. 59, 152 (1968); S. Ohnuma, TRIUMF Rpt. TRI-69-10 (1969); R. M. Pearce, Nucl. Inst. & Meth. 83, 101 (1970).

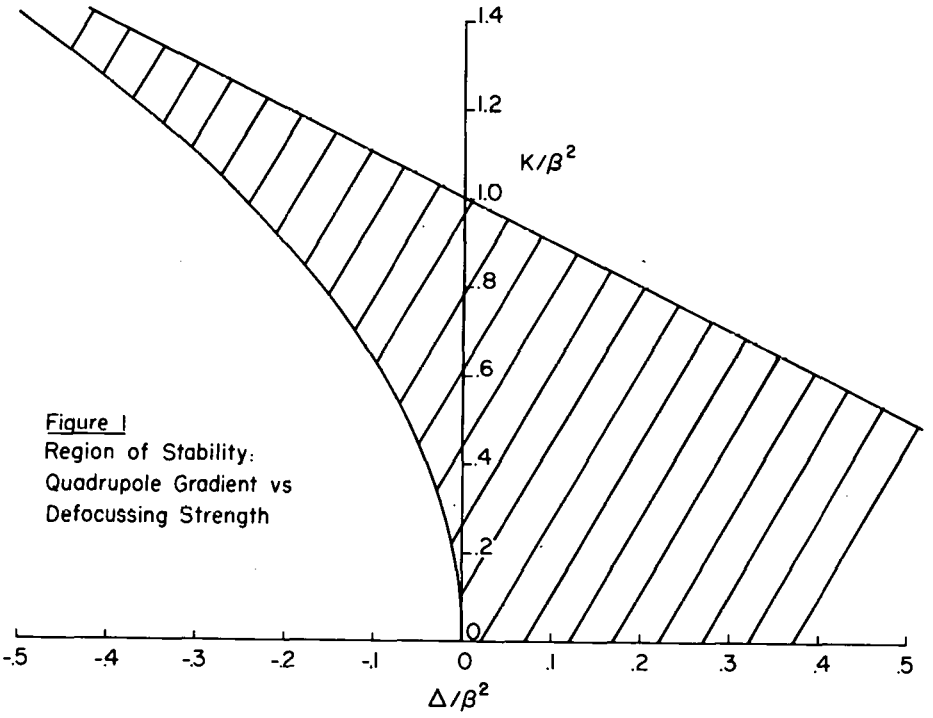


Figure 1
Region of Stability:
Quadrupole Gradient vs
Defocussing Strength

LINEAR ACCELERATORS WITH INTERTANK FOCUSING

B. Franczak, K. Blasche, B. Franzke
Gesellschaft für Schwerionenforschung mbH
Darmstadt, W.Germany

Introduction

In 1978 different concepts for an extension of the UNILAC energy range beyond the present limit of about 10 MeV/u were discussed at GSI. For energies up to 100 MeV/u linear accelerator structures as well as sector field cyclotrons were reconsidered. The straight-forward approach is the extension of the present Alvarez structure operating at 108 MHz. There are, however, good reasons to study linear accelerator structures that operate at higher frequencies, e.g. 216 or 351 MHz. In this high frequency range the well-known focusing scheme of magnetic quadrupole lenses, which are mounted inside the drift tubes, has the following disadvantages:

a. The capacitive loading of the rf-cavities due to drift tubes with a large diameter (20 cm or more) is rather high (216 MHz) or even not tolerable (351 MHz).
b. A large number of drift tubes (N) with magnetic quadrupole lenses is quite expensive (N ~ frequency).
c. Furthermore, an alignment system for the drift tubes, which is only required with drift tube quadrupoles, is quite expensive, too.

Permanent magnetic quadrupole lenses with a rather small outer diameter could reduce the capacitive loading. However, they do not fit the needs of a heavy ion linear accelerator, where a large aperture and variable field gradients for a broad range of ions are required. Therefore a different approach was studied, which does not make use of drift tube quadrupole focusing: short accelerator cavities without quadrupole focusing and intersections between cavities, which provide radial focusing with magnetic quadrupole lenses and, eventually, even phase focusing by means of rebuncher cavities.

Phase Focusing

In linear accelerator structures that make use of intertank quadrupole focusing instead of drift tube quadrupole focusing, rather short cavities and quite long intertank sections are used in order to provide the necessary radial focusing. It has to be proven that the phase motion is stable in accelerating structures with intertank sections which are long in terms of the rf cell length $\beta\lambda$, and that the phase acceptance is adequate.

For periodic structures the phase motion can be described in the same matrix formalism that is well-known for the radial motion. This linear approximation was used to study the stability criteria. In canonical coordinates $\delta\varphi$ and δW, the transport through an accelerating gap is given in the thin lens approximation by the matrix M_G with $k = -\zeta eU \sin\varphi_s$ and through a drift space of length L by M_D, with $\ell = -(2\pi/W_o\beta^3\gamma^3)*(L/\beta\lambda)$

$$M_G = \begin{pmatrix} 1 & 0 \\ k & 1 \end{pmatrix} \qquad M_D = \begin{pmatrix} 1 & \ell \\ 0 & 1 \end{pmatrix}$$

The resulting transfer matrix M_S for the coordinates $\delta\varphi$ and δW through one section can be written as

$$M_S = \begin{pmatrix} \cos N\mu_1 + \frac{d}{2\beta_1}\sin N\mu & -\beta_1(\sin N\mu_1 - \frac{d}{\beta_1}\cos^2\frac{N}{2}\mu_1) \\ \frac{1}{\beta_1}(\sin N\mu_1 + \frac{d}{\beta_1}\sin^2\frac{N}{2}\mu_1) & \cos N\mu_1 + \frac{d}{2\beta_1}\sin N\mu_1 \end{pmatrix}$$

where
N is the number of cells per cavity
$\mu_1 \approx \sqrt{-k\ell}$ is the phase advance per cell
d is the matrix element for the intertank space
$\beta_1 = (1/w)\sqrt{-1/k}$
$w = \sqrt{(1 + k1/4)} \approx 1$

The stability criterion for the phase motion is

$$\frac{1}{2}\,TR\,(M_S) = \left|\cos N\mu_1 + \frac{d}{2\beta_1}\sin N\mu_1\right| < 1$$

For accelerating structures that have no intertank sections at all (d=0), the phase motion is stable for all phase angles with $\sin\varphi_s < 0$ and all values of N. The insertion of drift spaces between cavities will result in an unstable phase motion for some ranges of N, even with phase angles in the well-known stability region $-90^o < \varphi_s < 0^o$ (Fig. 1).

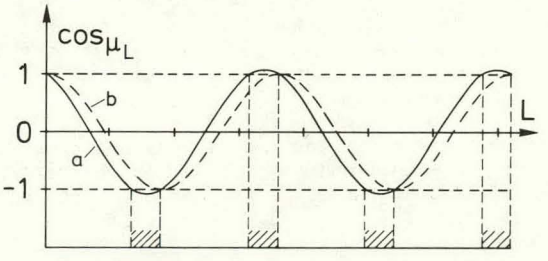


Fig. 1: Instability regions of a linear accelerator structure with intertank sections (a). The phase motion for a continuous accelerating structure is always stable with $\sin\varphi_s < 0$ (b).

In Fig. 2 the limitation of the cavity length is shown as a function of the normalized particle velocity β. It is well-known for the radial motion, and it will be shown for the phase motion, that the optimum acceptance is achieved for the phase advance per section $\mu_L = \pi/2$. Therefore the cavity lengths for $\mu_L = \pi/2$ are also plotted versus β. In the velocity range from 0.1 to 0.2 (5 MeV/u to 20 MeV/u), which has to be passed immediately behind

the UNILAC, the optimum cavity length lies in the range from 1 m to 3 m.

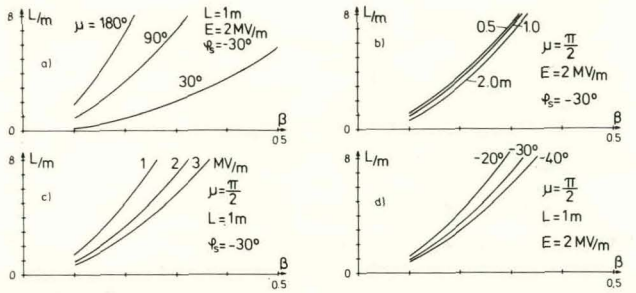


Fig. 2: Limitation of the cavity length L at $\mu_L = \pi$ versus normalized velocity ß and optimum cavity lengths at $\mu_L = \pi/2$ for some values of the mean accelerating field E_S, the phase angle φ_s and the intertank distance L

The linear treatment for the phase motion has only approximate answers for the following questions:

a. What is the phase acceptance in the non-linear theory?
b. How many sections will be required to develop the effects of unstable phase motion (Fig. 3)?

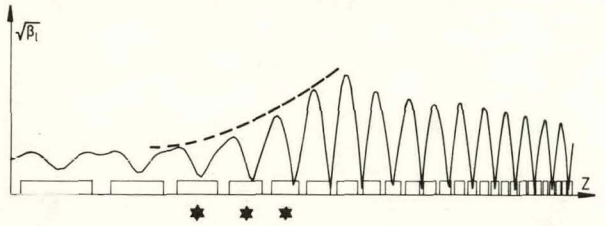


Fig. 3: Phase amplitudes for a particle bunch that is accelerated from ß = 0.1 through a linac structure with 3.4 m long cavities and 1 m long intersections. The three sections marked with an asterisk are operated in the instability region (Fig.1) causing an exponential growth of the phase amplitudes.

In order to study the non-linear phase motion, first iso-Hamiltonians of the phase motion in periodic structures were derived numerically (Fig. 4). These iso-Hamiltonians can be transformed in a second step through the real semi-periodic accelerating structure in order to display the development of instabilities (Fig. 5). From these studies the following conclusions were derived:

a. The optimum acceptance is achieved at $\mu_L = \pi/2$. At an intertank distance of 1 m the acceptance is comparable in size to the acceptance for the continuous accelerating structure.
b. A phase advance much above $\mu_L = \pi/2$ is not advisable. Even at $\mu_L = 2\pi/3$ the acceptance is remarkably reduced.
c. In accelerating structures that are operated in the instability region the phase acceptance shrinks drastically.

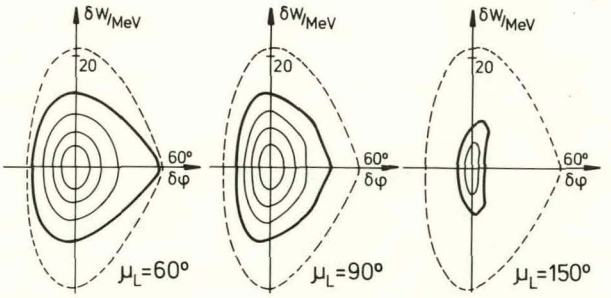


Fig. 4: Iso-Hamiltonians at ß = 0.1 for three different values of phase advance μ_L in linac structures with 1 m intertank distance and, for comparison, the separatrix (dashed) for a continuous accelerator structure.

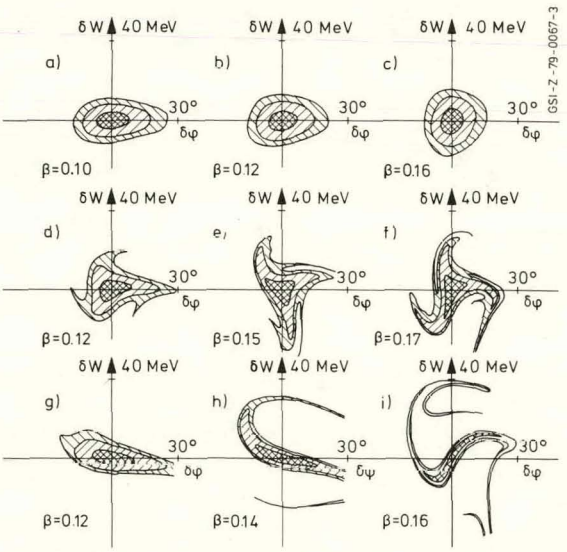


Fig. 5: Transformation of the iso-Hamiltonians (a) through structures with $\mu_L = 90^\circ$ (b,c), $\mu_L = 120^\circ$ (d,e,f) and through a structure with 3.5 m cavities (g,h,i) all with 1 m intertank distance.

If for technical or economical reasons linac sections longer than about 1 m are desired, rebunchers can be introduced in order to restore phase stability. Two schemes for the insertion of rebunchers were considered: either one rebuncher cavity in the center of the intertank sections (I), or two rebunchers before and behind the section, which can be integrated in the neighboring accelerator cavities (II). The rebuncher focusing strengths required for perfect matching are respectively:

$$b_R = -\frac{d}{ß_I^2 + \frac{d^2}{4}} \qquad (I)$$

$$b_R = -\frac{1}{2d}\left(1 - \sqrt{1 - \left(\frac{2d}{ß_I}\right)^2}\right) \qquad (II)$$

Figure 6 shows the amplitude functions β_1, for both configurations. The rebuncher amplitudes for $\beta = 0.1$ and $\beta = 0.25$ are given in Table I.

	double	single
$\beta = 0.1$	undefined	0.75
$\beta = 0.25$	1.25	0.96

Table I Rebuncher amplitudes (in MV) for two schemes of insertion

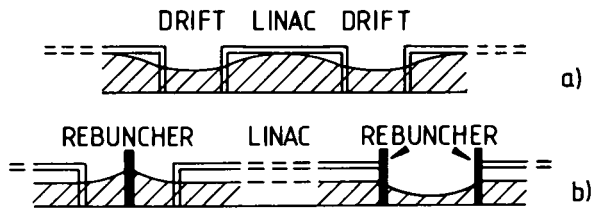


Fig. 6: Amplitude functions β_1 for linear accelerator structures with intertank sections (a). The intertank sections can be matched to the accelarator by means of rebunchers.

It can be seen that for the double rebuncher system (II), the maximum intertank space is restricted while for the single rebuncher system the only limitation is the linearity range of the rebuncher voltage, which does not appear in the linear approximation. If rebuncher focusing is provided, it is also possible to operate the cavities at a phase angle of $\varphi_s = 0^\circ$. This means that neither phase focusing nor radial defocusing occur in linear approximation; the cavity can be treated as a drift space. Phase stability has to be maintained by appropriate settings of the rebunchers, giving about 90° phase advance per period . Numerical calculations have shown, however, that the acceptance decreases rapidly with increasing length of the cavity. Sufficient phase acceptance at a length of about 3.5 m cannot be achieved. For the use of rebuncher matching it may be concluded:

a. With rebuncher matching there is no limitation for the lengths of the accelerator sections.
b. In the velocity range from $\beta = 0.1$ to $\beta = 0.2$ with the parameters considered here, rather high rebuncher voltages are required for perfect matching (Table I).
c. Although phase matching can be achieved for longer accelerator sections, radial focusing and radial acceptances will be reduced with increasing cavity length as shown below.

Radial Focusing

In linear accelerator structures that have no drift tube focusing, magnetic quadrupole lenses are installed in the intertank sections. The maximum radial acceptance is again achieved for a betatron phase advance $\mu_R = \pi/2$. In Fig. 7 the radial amplitude functions are plotted for two different structures, one with short cavities, which are matched in length to 1 m intertank sections, and the other with long cavities and rebuncher matching. The focusing strengths, quadrupole parameters and radial acceptances for an aperture of $2R = 4$ cm are listed in Table II.

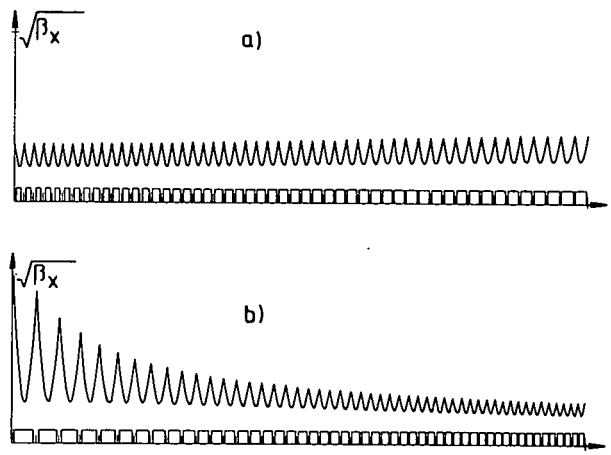


Fig. 7: Radial amplitude functions for structures with $\mu_L = 90^\circ$ (a) and with 3.5 m cavities (b), all with 1 m intertank distance. The intertank quadrupole triplets are tuned to the radial phase advance $\mu_R = 90^\circ$.

β	short cavities B' (T/m)	short cavities A_n (mm*mrad)	long cavities (3.5 m) B' (T/m)	long cavities (3.5 m) A_n (mm*mrad)
0.1	15.0	9.39	14.0	1.05
0.25	25.3	12.67	25.3	12.67

Table II Focusing parameters for two accelerator structures with intertank focusing.

Alternate Phase Focusing

A structure with 3.5 m long cavities and 1 m intertank distance has a very poor radial acceptance due to the strong radial defocusing in the first part of the linac. There are two ways to reduce radial defocusing and to improve radial acceptance. One can either shift the equilibrium phase angle φ_s towards 0°, or one can introduce sections with positive equilibrium phase angle and hence, with inherent radial focusing (APF structures). Both schemes improve radial acceptance at the expense of phase acceptance.

For APF structures, alternate sections with $\pi/4$ phase advance per period produce minimum excursions of the amplitude function and thus the best phase acceptance. Nevertheless, the phase acceptance is reduced by a factor of 4 compared to the continuously focusing structure in the linear approximation and even more, by a factor of 10 taking into account the strong non-linear phase motion. Thus the perfect APF structure designed

for heavy ion beam parameters at ß = 0.1 has an adequate radial acceptance but only a poor phase acceptance. A compromise with moderate acceptances for both the phase and the radial motion can be found, if one reduces the length of the radially focusing sections with positive phase angles in the APF structure (Fig. 8).

For a heavy ion accelerator behind the UNILAC, a frequency jump from 108 MHz to 351 MHz was proposed. Therefore any reduction of phase acceptance is unwelcome and as a consequence has to be ruled out.

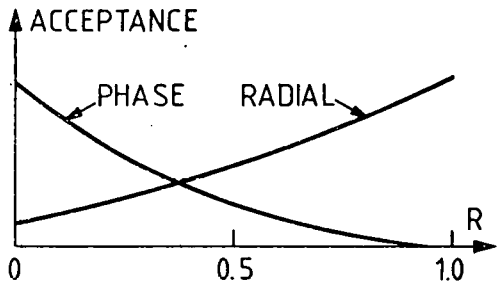


Fig. 8: Phase and radial acceptance for APF structures versus the ratio R of phase defocusing to phase focusing sections at ß = 0.1

Parameter Discussion for a 100 MeV/u Linear Heavy Ion Accelerator

For an extension of the UNILAC energy range beyond the present limit of 10 MeV/u, a 351-MHz Alvarez structure with intertank focusing was studied. In order to provide adequate phase and radial focusing short sections starting with 1 m length are required in the first part of the accelerator. Figure 9 presents a scheme for an 100-MeV/u accelerator with intertank focusing. The machine parameters are listed in Table III. Even for the acceleration to an energy of 30 MeV/u, about 36 cavities are required, which have, with intertank sections, a total length of 120 m. The great accelerator length is due to the assumption of the acceleration of U^{41+} at a mean accelerating field of 2 MV/m. With a second stripper at 5.9 MeV/u and with an increased field of 4 MV/m, which is still low compared to PIGMI prototype results, the total length could be reduced to about 35 m for 30 MeV/u and 120 m for 100 MeV/u. For comparison with an 108-MHz Alvarez accelerator with drift tube focusing the following arguments have to be evaluated:

a. Accelerating structure and quadrupole focusing are inexpensive at 351 MHz.
b. Rf power amplifiers operating at 351 MHz are not yet commercially available.
c. Accelerator cavities of 1 m length are too small units for the 351-MHz Rf power amplifiers. Therefore methods of coupling several cavities should be studied.

Since it was finally proposed to extend the UNILAC energy range only to maximum energies of about 20 MeV/u, the 108-MHz Alvarez accelerator was preferred as the most appropriate solution in order to avoid the lengthy development of new power amplifiers.

ß	0.1	0.25	0.42
W (MeV/u)	5	30	100
ΔU (MV)		151	403
Number of cavities		36	66
L (m)		122	299
$A_{x,y}$ (mm*mrad)	13 (normalized)		
A_φ	27 MeV * 60°		

Table III Parameter list for a 351-MHz Alvarez accelerator. At an average field of E = 2 MV/m U^{41+} ions are accelerated from 5 to 100 MeV/u.

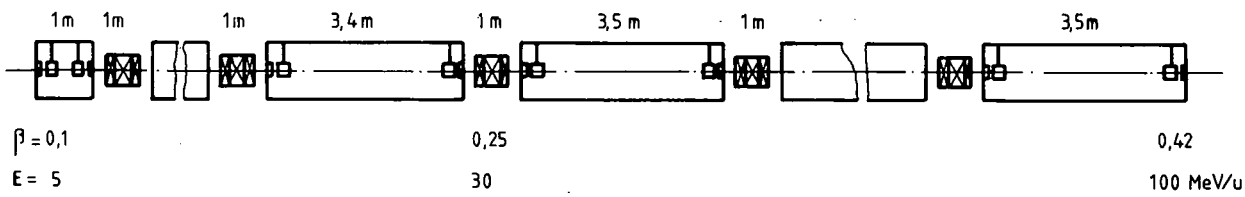


Fig. 9: Heavy ion linear accelerator with intertank quadrupole focusing for the acceleration of U^{41+} from 5 to 100 MeV/u

1979 LINEAR ACCELERATOR CONFERENCE

BEAM DYNAMICS IN A PROTON LINEAR ACCELERATOR FOR A NEUTRON SPALLATION SOURCE

K. Mittag
Kernforschungszentrum Karlsruhe, Institut für Kernphysik
7500 Karlsruhe, Federal Republik of Germany

Abstract

The frequency choice for a 600 MeV - 100 mA pulse - 10 mA average proton linac is discussed. A 108-MHz Alvarez accelerates the protons from 500 keV to 100 MeV; a 324-MHz high energy structure follows. Space charge effects play a dominant role in the beam dynamics. This choice of frequencies insures large longitudinal and transverse acceptances at injection, small longitudinal emittance blow-up in the Alvarez, and a large enough longitudinal acceptance of the high energy structure. The transverse emittance at injection must not be too small in order to alleviate transverse matching, and to avoid longitudinal emittance blow-up, which would lead to particle loss after transition.

Introduction

For a neutron spallation source,[1] a proton linear accelerator[2] with about 600-MeV final energy,[2] and 10-mA average current has been proposed. The current in the beam pulse has been limited to 100 mA, since otherwise the installment cost for the rf power sources gets high, and the space charge problems in the accelerator severe. Lowering the pulse current increases the power bill. The dc injector voltage should not be larger than 500 kV in order to insure a reliable operation with the relatively high average beam current. From experience with existing machines, the Alvarez frequency ought to be in the 100 to 200 MHz range, and the frequency of the high energy part between 300 and 800 MHz. The availability of large rf power sources for a high duty factor strongly favors frequency choices around 108 MHz and 350 MHz, for which similar demands exist presently at GSI - Darmstadt and CERN (LEP). The total investment cost for the rf power sources is smaller for a 108 MHz - 324 MHz frequency choice compared to 200 MHz - 600 MHz. This more than compensates for the higher construction cost of the accelerator structures at a lower frequency.

In the following the frequency choice will be studied from the beam dynamics point of view. A major concern is to minimize particle loss in order to keep the activation of the machine low. To this end, the transverse emittances will have to be tailored at definite locations along the linac, at which a higher activation will have to be tolerated. At transition between the Alvarez and the high energy structure, the longitudinal phase acceptance is reduced by the frequency ratio (space charge effects neglected). Hence, special emphasis has to be given to insure a large enough phase damping in the Alvarez, and to have a well-defined longitudinal emittance without tails at transition.

Bunching

The space charge influence will be estimated during bunching for a single buncher. The analysis can be carried through analytically for two limiting cases. First, neglecting space charge forces, one can estimate the longitudinal focal length d, and the bunching efficiency. Second, in the highly space charge limited case, one can calculate the distance L, after which a small longitudinal velocity modulation produced by the buncher becomes zero in the beam center.[3] Comparing d and L one gets an idea of the importance of space charge effects during bunching. d << L is required. It is seen that:

$$\frac{d}{L} \approx 5\times10^{-4}\,\frac{W}{\Delta W}\sqrt{\frac{I/\mathrm{Amps}}{\beta^3}} \qquad (1)$$

W is the injection energy, β the corresponding relative velocity, I the beam current, and ΔW half the maximum energy spread imparted to the particles by the buncher. In order to achieve longitudinal matching in the phase-energy phase space at the linac input, ΔW is set equal to the energy acceptance of the Alvarez (space charge included). Note that ΔW is larger at the lower frequency. Taking this as a criterion, the result is that bunching for a 400 keV - 108 MHz system is comparable with respect to space charge problems to a 750 keV - 202 MHz one, and for a given injection energy the lower frequency is more advantageous (Fig. 1). Neglecting space charge, the bunching efficiency is independent of frequency. Also, the option of using the rf quadrupole structure[4] as an accelerating buncher looks more promising the lower the Alvarez frequency is chosen.

Acceptances at Injection

The acceptances at injection have been studied analytically as a function of injection energy and Alvarez frequency.[2,5] Linear transverse quadrupole focusing (FODO), rf defocusing, and space charge forces (the bunch is a uniformly-charged ellipsoid) are assumed. The non-linearity of the longitudinal motion is kept to second order terms. The rapid increase of the acceptances due to acceleration is neglected. The result is that all of the basic beam dynamic parameters are the more favorable the higher the injection energy. Further, the acceptances of a 750 keV - 202 MHz linac are similar to those of a 400 to 500 keV - 108 MHz one.

In Fig. 2,3, and 4 the acceptances and the required quadrupole field at 500 keV injection energy are shown as a function of the normalized transverse input emittance βγE (100% of beam). Having fixed the transverse focusing strength (betatron phase advance per focusing period, $\mu = 40^0$, at a 0.1 A beam current) the average beam radius[6] is $\sqrt{E2\beta\lambda/\pi\mu}$

In order to stay well inside the region of transverse stability, μ is kept constant when varying the emittance. This means that a smaller transverse emittance leads to a smaller average beam radius, hence to larger space charge forces, which in turn have to be compensated by larger focusing forces. For normalized emittances smaller than 1 π mm-mrad, the longitudinal acceptance gets extremely small and the required quadrupole fields can no longer be obtained for a 202-MHz Alvarez.

A too small transverse emittance is undesirable especially for a multi-stage linac system operating close to the longitudinal space charge limit. After injection the bunch would rapidly expand until the longitudinal rf focusing force and the defocusing space charge force are equal. The phase damping would be reduced, and at transition to the next higher frequency section the phase emittance might be larger than the phase acceptance. On the other hand, a too large transverse emittance results in a too large beam radius, and, because of that, in a too large dependence of the transit time factor on a particle's radial position. The influence of the transverse motion on the longitudinal one would get too large. The maximum beam radius that can be tolerated from this point of view is set to $0.75\ \beta\lambda/2\pi$ or 3/4 of the drift tube aperture at injection. At this radius a particle would already get a 15% higher energy gain than an on-axis one. The transverse acceptance in Fig. 3 is calculated accordingly. For a given transverse emittance, Fig. 3 shows a larger transverse acceptance for the lower frequency. Also, a relatively smaller fraction of the drift tube aperture is filled by the beam. It follows that the radial dependence of the longitudinal motion and the resulting longitudinal emittance blow-up is less at the lower frequency for a given transverse emittance. The transverse emittance blow-up is affected similarly by the radial non-linearities.

It is concluded that 108 MHz is favored over 202 MHz from the beam dynamics aspects at injection: the acceptances are larger, longitudinal space charge problems are less severe, there exists a range of transverse input emittances, for which both longitudinal and transverse motion are stable (between 4 and 7 π mm-rad), and the required quadrupole fields can more easily be realized.

Phase Damping

The phase damping along the linac can be calculated analytically using the above-mentioned approximations, and in addition, linearizing the longitudinal motion.[5,7] The transverse motion is coupled to the longitudinal via the space charge forces. It can be expressed by a single parameter, the ratio $a_{xo}a_{yo}/a_{x1}a_{y1}$ of beam cross-sections at the entrance and exit of the linac. Then the result is

$$\frac{\Delta\phi_1}{\Delta\phi_o} = \frac{\Delta W_o}{\Delta W_1} = \left[\frac{E_o T_o \sin\phi_{so}\,\beta_o^3\gamma_o^3(1-\mu_{\ell o})}{E_1 T_1 \sin\phi_{s1}\,\beta_1^3\gamma_1^3(1-\mu_{\ell 1})}\right]^{1/4} \qquad (2)$$

$$\mu_\ell = \frac{-15\Omega\ (I\lambda)\ \beta\lambda}{\pi\sqrt{a_x a_y}\ b^2 ET \sin\phi_s} \qquad (3)$$

$$\frac{1-\mu_{\ell o}}{1-\mu_{\ell_1}} = \left[\frac{\mu_{\ell o} D}{2} + \sqrt{1-\mu_{\ell o}+\left(\frac{\mu_{\ell o} D}{2}\right)^2}\right]^2 \qquad (4)$$

$$D = \left[\frac{E_o T_o \sin\phi_{so}\,\beta_1\gamma_1^3 a_{xo} a_{yo}}{E_1 T_1 \sin\phi_{s1}\,\beta_o\gamma_o^3 a_{x1} a_{y1}}\right]^{1/2} \qquad (5)$$

$$\Delta\phi_{max} = \frac{3}{2}\,\phi_s\,(1-\mu_\ell) \qquad (6)$$

$$\Delta W_{max} = q\left[-\frac{2\lambda}{3\pi}\frac{mc^2}{q} ET\,(\beta\gamma\phi_s(1-\mu_\ell))^3\right]^{1/2} \qquad (7)$$

Where: $\Delta\phi$ = half phase width, ΔW = half energy spread, E = average axial electric field, T = transit time factor, ϕ_s = synchronous phase, λ = wavelength, b = half bunch length, $\pi\Delta\phi_{max}\Delta W_{max}$ = longitudinal acceptance, mc^2/q = mass/charge.

Evaluating these formulae for typical parameters[2,5] allows the following conclusions: 1. In linear theory, the phase width at the Alvarez exit depends only weakly on the parameters of the Alvarez. 2. The influence of the longitudinal space charge force along the linac is the larger the higher the frequency and the lower the injection energy is. 3. The phase acceptance at the Alvarez exit is reduced appreciably compared to the zero space charge phase acceptance. This reduction is less pronounced at the lower frequency and higher injection energy. 4. The longitudinal acceptance reserve gets extremely small at the Alvarez end if the average beam radius is not allowed to grow along the linac. These results have to be modified if the non-linear parts of the phase focusing force are considered. They yield, together with the space charge force, a strong asymmetric depression of the potential well for particles with positive phases (that is, trailing particles). For these the phase damping will be smaller than for particles sitting close to the bottom of the well, and the effect will be the larger the larger the ratio of space charge to rf force (μ_ℓ). As μ_ℓ is smaller for a lower frequency, the linear phase focusing region is larger at a lower frequency. A too small beam diameter (e.g. caused by a too small transverse emittance) would cause a larger than necessary longitudinal space charge force, and hence a too small phase damping in the non-linear phase focusing region.

Emittance Growth

Transverse emittance growth is mainly caused by a combination of the phase dependence of the rf plus space charge defocusing, and the fact that consequently the transverse matching can never be perfect for all parts of the bunch.[8] A single slice of the bunch will experience the phase dependence of the rf defocusing at the synchrotron oscillation frequency, the space charge forces then will change at twice the synchrotron frequency, and both together cause the beam radius to oscillate about its matched value at twice the betatron frequency. The combined effect will be a rapid transverse emittance increase after injection, settling down in the early sections of the linac, because the amplitudes of the oscillations about the matched solution depend only on the initial mismatches.[9] This effect can only be neglected

if [2,10]

$$\frac{k_\ell^2|\sin\phi-\sin\phi_s|}{k_{t\rho}^2|\sin\phi_s|} = \frac{q}{mc^2}\,\frac{4\pi\lambda\ ET|\sin\phi-\sin\phi_s|}{\beta\gamma^3\mu^2} << 1 \quad (8)$$

k_ℓ is the longitudinal wave number for zero current, and $k_{t\rho} \approx \mu/2\beta\lambda$ the radial one including the space charge effect. At injection, for parameters as in Fig. 2, the ratio (8) = 1.9; thus a large transverse emittance increase must be expected, being less severe at a higher frequency. The effect is more pronounced the smaller the emittance as reducing the emittance towards zero without changing the quadrupole gradients [11] means also $\mu \to 0$. On the other hand, if one keeps μ constant when scaling the emittance to zero, the beam radius will go down making the space charge forces and the tune shift with respect to zero current very large. As a real bunch is not a uniformly-charged ellipsoid, the radial space charge force depends on the longitudinal position being smaller at the ends of the bunch. This again causes a phase dependence of the transverse motion, and hence a larger transverse emittance blow-up the smaller the emittance is. Also this effect is more troublesome at a lower frequency, as the ratio of transverse space charge to focusing force and the tune shift is larger. [2]

Transverse emittance growth could also be caused by transverse bunch instabilities [12] or by temperature exchange between longitudinal and transverse directions, both being more probable at a lower frequency. [2] However, at a lower frequency the transverse acceptance is larger, and a larger emittance blow-up can be tolerated. The current carrying capability is larger at the lower frequency; if on the other hand a high brightness is the major design goal, a higher frequency choice looks more promising.

To study emittance growth in more detail, multi-particle beam dynamic simulations were performed for a 108-MHz Alvarez with parameters as at injection. Note that $\mu = 40^\circ$ at I = 0.1 A is kept constant along the linac for all runs. The computer programs [6,13] used are of CERN origin. A total of 4 x 2000 macro particles were traced. The cut-off distance for the space charge force was set equal to the average particle distance resulting in about 3 close collisions per particle per cell of length $\beta\lambda$. The mesh of the "space charge cage" was 60 × 60 × 60 fitted closely around the bunch. Typical rms values change by 10% when varying any of these program parameters by a factor of 2.

In Fig. 5 and 6 the emittance increase and phase damping along the Alvarez is shown for matched beams. The emittance at 100% of beam is defined e.g. as $E_{rms} \cdot \max(x) \cdot \max(x') / (\mathrm{rms}(x) \cdot \mathrm{rms}(x'))$. Although these emittances scatter a lot, it is clearly shown that they increase much more than the rms ones. (Comparing measurements and calculations one has to refer to the same percentage of beam!) This corresponds to the formation of tails, being especially dangerous in a high average current linac. Most of the growth has happened after one synchrotron oscillation (at about 2.3MeV), which fits into the picture given above. The growth rate is larger for a smaller initial emittance. [11] The phase damping is nearly the same for rms and maximum phase widths, and is only slightly less at the lower transverse emittance, as has been expected for our parameter choice. Figure 7 shows the rms emittances and the phase width at 100% of beam at the Alvarez exit (100 MeV). For these runs the input matching conditions and the quadrupole gradients are kept constant, equal to the matched values for a 4.65 π mm-mrad input emittance; hence all other runs were mismatched at injection. A large transverse emittance increase is noticed for small input emittances (for which good matching will be very difficult in a real linac). Due to this the longitudinal motion is not affected much, although a decrease of the phase damping at small input emittances is observed.

At 100 MeV, a transition to a 324-MHz high energy structure is proposed, [5] which has about a ± 27° phase acceptance, safely larger than the phase emittance of about 3 × 7°.

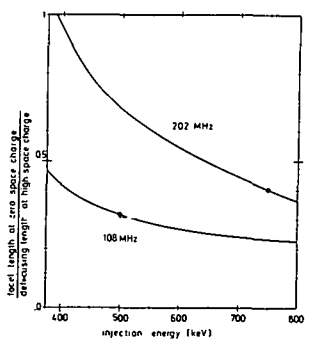
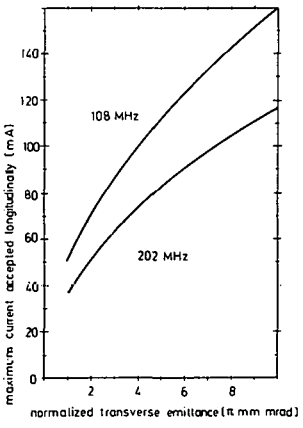


Fig. 1:

Influence of space charge effects during bunching for 0.1 A proton beam



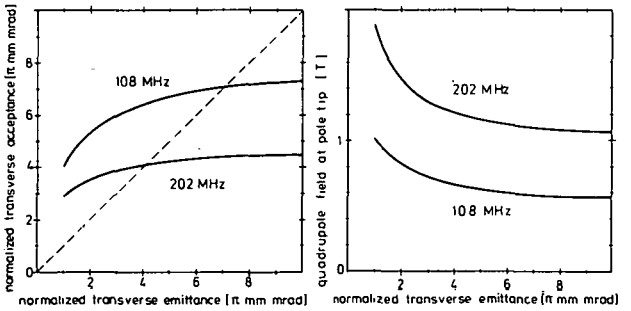


Fig. 2, 3, 4:

Acceptances and required quadrupole field at 500 keV injection energy as a function of the input emittance for I = 0.1 A, $\phi_s = -35^\circ$, $\Delta\phi = 35^\circ$, E = 2 MV/m, ET = 1.45 MV/m, E_{peak} = 11.7 MV/m, FODO focusing, μ(I = 0.1 A) = 40°

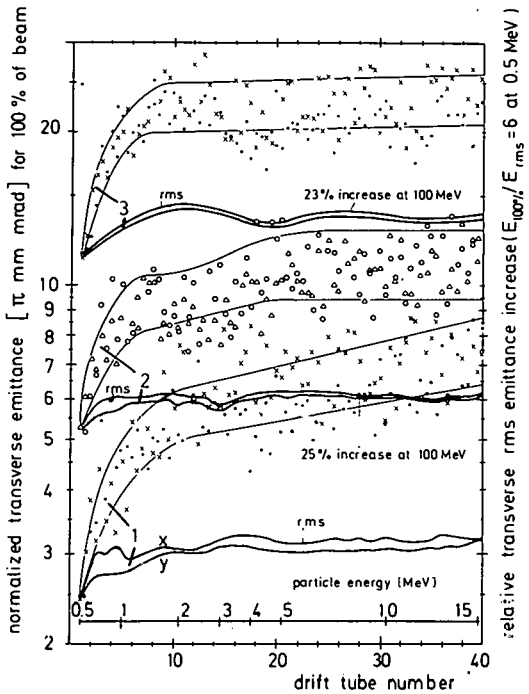


Fig. 5: Transverse emittance increase along the Alvarez for matched beams

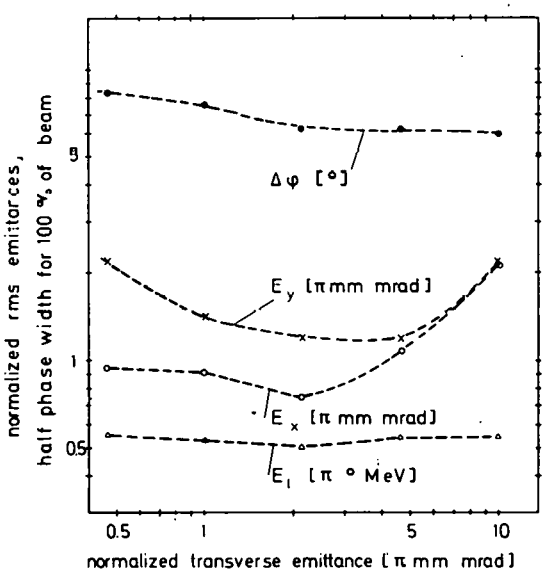


Fig. 7: Emittances and phase width at the Alvarez exit (100 MeV) as a function of the input emittance. Matching and quadrupole gradients for 4.6 π mm-mrad input emittance. Ratio of maximum to rms emittance assumed to be 5 at injection.

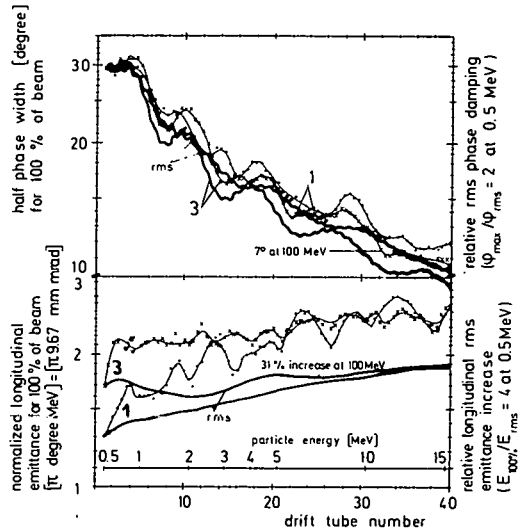


Fig. 6: Longitudinal emittance increase and phase damping along the Alvarez for matched beams

References

1 Bericht des ad-hoc-Ausschusses "Mittelflußreaktor" des BMFT, Teil II, Spallationsneutronenquelle, Bonn (1979)

2 K. Mittag, G. Dammertz, G. Hochschild, R. Lehmann, B. Piosczyk, J.E. Vetter, Primärbericht 10.01.06P02B, Kernforschungszentrum Karlsruhe (1979)

3 P.N. Lapostolle, IEEE Trans. NS-14, No. 3, 572 (1967)

4 R. H. Stokes, K.R. Crandall, J.E. Stovall, D. A. Swenson, IEEE Trans. NS-26, No. 3, 3469 (1979)

5 K. Mittag, Primärbericht 10.01.06P02A, Kernforschungszentrum Karlsruhe (1979)

6 D.J. Warner, M. Weiss, Proc. of the 1976 Prot. Lin. Acc. Conf., Chalk River, Ontario, AECL 5677, 245 (1976)

7 K. Mittag, KfK 2555, Kernforschungszentrum Karlsruhe (1978)

8 J.W. Staples, R. A. Jameson, IEEE Trans. NS-26, No. 3, 3698 (1979)

9 H.G. Hereward, private communication

10 R.L. Gluckstern, in "Linear Accelerators" by P.N. Lapostolle, A.L. Septier, North Holland Publ. Co., Amsterdam (1969)

11 G.W. Wheeler, K. Batchelor, R. Chasman, P. Grand, J. Sheehan, Part. Acc. 9, No. 1, 1 (1979)

12 I. Haber, A.W. Maschke, Phys. Rev. Let. 42, 1479 (1979)

13 D.J. Warner, AECL-5677, 49 (1976)

Acknowledgement

This work has profited by discussions with G. Dammertz, H.G. Hereward, G. Hochschild, R. Lehmann, B. Piosczyk, P.J. Tallerico, D.J. Warner, M. Weiss, J.E. Vetter. My special thanks go to my CERN colleagues for helping me understand their beam dynamic codes.

A PHASE ADJUSTED FOCUSING LASER ACCELERATOR

Peng Huanwu* and Zhuang Jiejia
Institute of High Energy Physics, Academia Sinica
Beijing, China

Abstract

In this paper a proposal is discussed to accelerate charged particles by an axially symmetrical electromagnetic field of a focusing laser. The axis of the field is the equilibrium orbit of the charged particles. It is shown that the charged particles can be focused transversally and longitudinally in the field. For continual acceleration of the charged particles, the phase of the incident laser has to be suitably adjusted. It is estimated that with an incident power density of 5×10^{10} W/cm^2, the effective energy gain for such an accelerator may be as high as 90 GeV/m, so the size and the cost of a Phase Adjusted Focusing Laser Accelerator (PAFLA) may be drastically reduced. This seems to offer an economical way to a super high energy accelerator.

Introduction

The progress of high energy physics has always been associated with the development of accelerators of higher and higher energy. The size and cost of a machine accelerating particles to such high energy as 10 Tev, for example, would be formidable if it were built in the usual way. In order to reduce this, it is most important to increase the energy gain per unit length of the accelerator. High frequency power sources are used in the usual accelerators and the accelerating field obtained is limited by the power density. Stronger electromagnetic fields are available with a high power pulsed laser and even stronger fields can be made available by focusing. For example, in connection with the pulsed laser fusion program, the power density at the focus is as high as 10^{17} - 10^{18} W/cm which corresponds to an electric field of 10^{10} V/cm. As the focus is far away from the material and lies in vacuum, the power density there can be made to exceed by orders of magnitude the limit which materials can tolerate. Hence, if particles can be accelerated with the electric field of a pulsed focusing laser, the size, and with it the cost, of a super high energy accelerator will be drastically reduced.

Many proposals for laser accelerators have appeared in recent years,[1-11] mostly working on a slow wave pattern of the field. The accelerating field strength is limited by the breakdown strength of the material or the medium. It seems so far as super high energy is concerned, that laser accelerators working with a slow wave field pattern will compete somewhat unfavorably.

*Now at the Institute of Theoretical Physics, Academia Sinica.

In the present paper it is proposed to accelerate the charged particles along the axis of an axially symmetrical electromagnetic field of a focusing laser. The phase velocity along the axis of the focusing field is, quite the contrary to what is usually the case, larger than that of light in vacuum. It is easily shown, by studying the dynamics of the charged particles, that conditions for the focusing of the orbits transversally and longitudinally agree with one another under very wide conditions without additional lenses. In this way, it is possible to obtain an accelerating field, higher by many orders of magnitude than that limited by materials. But the phase velocity of the accelerating field is also larger than the velocity or the particles, so it is necessary to adjust the initial phase of the initial phase of the incident laser by a certain amount after a certain short distance along the axis. It appears at first sight that the sooner the phase adjustment the better the acceleration, but we must remember that the phase adjustment is done on the wall of the accelerating tube and what we needed is the change of phase for the field on the axis. Boundary value problem calculations based on Maxwell's equations show that, for an accelerating tube of a radius of ten thousand wavelengths, the distance for phase adjustment cannot be chosen smaller than a wavelength or the change of phase will be completely blurred on the axis. Taking this into account, it is estimated that with an incident power density of the laser of 5×10^{10} W/cm, which can be tolerated by the material of the wall of the accelerating tube, the effective energy gain may be as high as 90 GeV/m. Thus, PAFLA seems to offer a new way to super high energy accelerators with drastically reduced size and cost. Such an accelerator can be used for protons, electrons and, more favorably, for short-lived particles.

Acceleration by a Focusing Laser Field

Take, for simplicity, a laser accelerating tube of an inner radius larger than the laser wavelength by many orders of magnitude. Consider the axially symmetrical TM wave and use cylindrical coordinates z, r and θ. The non-vanishing components E_z, E_r and B_θ, as functions of z, r and the time t, are of the general form

$$E_z = \mathrm{Re} \sum_h E_h J_o(k_{\perp h} r) \exp (ihz - i\omega t - i\alpha_h)$$

$$E_r = \mathrm{Re} \sum_h E_h (-ih/k_{\perp h}) J1(k_{\perp h} r) \exp (ihz - i\omega t - i\alpha_h)$$

$$cB_\theta = \mathrm{Re}\ E_h(-ik/k_{\perp h})J_1(k_{\perp h}r)\exp(ihz - i\omega t - i\alpha_h) \quad (1)$$

with

$$h^2 + k_\perp^2 = k^2 = \omega^2/c^2 = (2\pi/\lambda)^2$$

and

$$\epsilon = \mu = 1$$

Here c is the velocity of light in vacuum and with the Bessel functions $J_0(x)$ and $J_1(x)$ satisfying

$$J_0' = -J_1,\ (xJ_1)' = xJ_0$$

Maxwell's equations have been satisfied. The laser wavelength in vacuum is denoted by λ and the longitudinal and transversal components of the laser wave vector, by h and $k_{\perp h}$, the suffix h referring to the partial wave. Thus, E_h and α_h denote the magnitude and phase of the z-component of the electric field on the axis of the partial waves. In the summation only those partial waves with $h < k$ contribute to the focusing field on the axis, the other partial waves with $h > k$, being evanescent surface waves, decay exponentially away from the wall of the accelerating tube. From the properties of the Bessel function $J_0(x)$, namely

$$J_0(0) = 1 \text{ and } J_0(x) = (2\pi x)^{-\frac{1}{2}}\{\exp i(x - \pi/4) + \exp -i(x - \pi/4)\}$$

as $x \gg 1$, introduce a focusing factor F as an estimate of the ratio between the peak value of the z-component of the electric field on the axis and that of the incident wave on the wall, namely

$$F = E_z(0)/\bar{E}_z(r)_{inc} = (2\pi k_\perp R)^{\frac{1}{2}} \quad .$$

Where R is the radius of the accelerating tube and $E_z(r)_{inc}$ is the incident field on the wall.

Intuitively, the above focusing field can be realized by an axially symmetrical converging wave with its electric field polarized in the plane of incidence. A cross-section of the focusing field is shown in Fig. 1. Thus, it is found $k_\perp = k\sin\theta$, $h = k\cos\theta$ and $h < k$ is satisfied. The focusing factor can be written as

$$F = 2\pi(R\sin\theta/\lambda)^{\frac{1}{2}} \quad . \quad (2)$$

Denoting the peak value of the incident electric field at the wall by E_W so that the incident power density is

$$P = cE_W^2/8\pi \quad (3)$$

(ϵ,μ of the incident region also taken as unity) and noting from Fig. 1 that $E_z(R) = E_W\sin\theta$, it is found, approximately, that:

$$E_h = E_W F\sin\theta = E_W 2\pi(R/\lambda)^{\frac{1}{2}}(\sin\theta)^{3/2} \quad (4)$$

Now consider the motion of the charged particles in the field of the focusing laser. Although their energy gain may be very large (say 100 GeV/m), the energy gain per laser wavelength λ is very small (say, 0.1 MeV per $\lambda = 1\mu$) compared to the rest energy of the charged particle. Neglecting many body effects, one may treat the motion of the charged particles by perturbation methods and in the first approximation consider each partial wave separately. The partial wave which is referred to above as the principal propagating mode, contributes most to the acceleration and it alone will be discussed below.

For the particles moving along the equilibrium orbit, r = 0, i.e., the z-axis, to the zeroth approximation the equation of path: $t = t_o - z/(c\beta)$, corresponding to the free motion. So, the force acting on the particles is, to the first approximation, given by:

$$eE_z = eE_h \cos\Delta$$

where

$$\Delta = \{a_h + t_o + (K^{-1} - h)Z\} \quad (5)$$

is the phase of the accelerating field as seen from the moving particle. The condition for acceleration is simply

$$e\cos\Delta > 0 \quad . \quad (6)$$

Since t_o denotes the instant when the particle passes $z = 0$ with velocity $c\beta$, the condition for longitudinal focusing demands a greater acceleration for the late-coming particles, or a smaller acceleration for the faster particles. That is, either $\partial(\cos\Delta)/\partial t_o < 0$ or $\partial(\cos\Delta)/\partial\beta < 0$, gives the condition

$$e\sin\Delta < 0 \quad . \quad (7)$$

For particles moving in the neighborhood of the equilibrium orbit, the transverse force is, to the first approximation, given by

$$f_\perp = -(r/2)(h - k\beta)cE_h\sin\Delta \quad .$$

Since for the propagating mode of the focusing accelerating field we have $h < k$, it is possible to choose h and β to satisfy the rather wide condition

$$(h - k\beta) < 0 \quad , \quad (8)$$

in which case the condition for the transverse focusing coincides with that for the longitudinal focusing, namely Eq. 7. No additional magnetic lenses are needed. This is so, as may be seen from the two terms on the left hand side of Eq. 8, because the transversal force due to the magnetic field overcomes that due to the electric field.

From Eqs. 5 to 8 it may be seen that it is possible to accelerate charged particles with simultaneous focusing by properly adjusting the phase of the accelerating field as seen from the moving particles. For protons, it is limited to within the fourth quadrant, for electrons to within the second quadrant. Owing to the dependence of Δ on z, to continually accelerating the charged particles along the axis, it is necessary to change the phase α_h of the incident laser for the above conditions to be continually satisfied.

Phase Adjustments

From Eq. 5 it follows that the phase of the accelerating field, as seen from the moving particles, will change by $\pi/2$ after the particles have travelled a distance ℓ along the axis, where

$$\ell = (\lambda/4)\ (\beta^{-1} - \cos\theta)^{-1} \quad . \tag{9}$$

This will be referred to as the distance for phase adjustment. To compensate for the increase of Δ by $\pi/2$ we may change the phase α_h of the incident wave by lengthening the optical path by a quarter wavelength for every distance. For phase adjustment, as shown in Fig. 2, the wall of the accelerating tube works then as a cylindrical grating, with grating constant $D = 4\ell$, ruled in four steps. According to Eq. 9, for small θ, the distance for phase adjustment can be made very much larger than the wavelength of the laser, so the change of phase along the axis is guaranteed by elementary optics, but the accelerating field is then reduced in accordance with the factor $(\sin\theta)^{3/2}$ of Eq. 4. For a higher accleration we prefer to choose a bigger $\sin\theta$ and hence a shorter ℓ/λ. It becomes then vitally important to see that diffraction effects do not cause the change of phase on the axis to become completely blurred.

Some numerical calculations were made with Maxwell's equations, solving the appropriate boundary value problem.[12-13] Primary calculations for the case of normal incidence show, taking $R/\lambda = 10^4$ for example, that the change of phase on the axis varies linearly with the change of optical path on the wall, as shown in Fig. 3, provided that $\ell/\lambda \geq 1$ is satisfied. The fraction η of the region on the axis where the change of phase is blurred increases rapidly as ℓ/λ becomes smaller than unity, as indicated in Fig. 4.

The distance for phase adjustment depends also on the velocity of the charged particles. For particles of high energy, the variation in β is slight. For simplicity, choose the grating constant fixed but introduce some leap steps as leap days are introduced in the calendar, the distance from one leap step to the next may change in a long accelerating tube. In view of the fact that allowance, however strict, will accumulate in the long run, it is suggested that the accelerating tube be made by fitting together a large number of sections after testing and additional proper measures taken during fitting.

A Conceptual Design

Among the many possibilities of building up an axially symmetrical focusing laser field, one will be described here in more detail. In Fig. 5a, the ring-shaped laser output from a confocal resonator, after going through a special polarizer, is largely reflected at the 45 degree cone-shaped beam splitter and is made incident almost perpendicularly onto the accelerating tube. The outer surface of the tube is ruled for phase adjustment, as discussed above, and the inner surface is ruled as a diffraction grating, such that a large proportion (say η_θ) of the incident energy will go into the diffracted beam of a definite direction with the longitudinal component of the wave vector as required (i.e., with $h = k\sin\theta$, see Fig. 5b). In order to make the best use of the laser power, as indicated in the block diagram Fig. 6, the successive laser amplifiers are properly delayed in time so that the radiation of the laser and passage of charged particles along the axis may synchronize. The coherent length of the laser should be longer than the distance between the successive amplifiers.

Energy Gain

From the above discussion one can estimate the energy gain K per unit length of the accelerating tube from the component of the electric field on the axis, as given by Eq. 4, by multiplying it with the utilization factors for the blurring $(1 - \eta)$ and for phase averaging

$$\eta_\Delta = \int \cos\Delta\, d\Delta/(\Delta_2 - \Delta_1) \quad , \tag{10}$$

the phase Δ varying uniformly from Δ_1 to Δ_2. Then for the energy gain per unit length of the accelerating tube, it is found that:

$$K = eE_W 2\pi(\eta_\theta\ R/\lambda)^{\frac{1}{2}}\ (\sin\theta)^{3/2}\eta_\Delta\ (1 - \eta) \quad , \tag{11}$$

where η_θ denotes the utilization factor for energy diffraction. Let τ denote the pulse width of the laser and take 20 joules per square centimeter for the pulsed energy tolerated by the material of the wall. Then:

$$\tau p = cE_W^2/8\pi < 2.10^8 \text{erg/cm}^2 = 20 \text{ joules/cm}^2. \tag{12}$$

Evidently K varies as the square root of P. For high acceleration, short pulse is preferred, but the pulse must be long enough to guarantee the required coherent length.

$R/\lambda \sim 10^4$ $\quad \ell/\lambda \sim 1$ $\quad \sin\theta = .66 (\cos\theta = .75)$

$\tau = 3 \times 10^2 \text{sec}$ $\quad P = 5 \times 10^{10}\ \text{W/cm}^2$

$E_W + 6 \times 10^6\ \text{v/cm}$ $\quad \eta_\theta = .9$

$\eta_\Delta \sim .75$ $\quad (1 - \eta) \sim .65$

and get $K \sim 90$ GeV/m. To accelerate charged particles to an energy of W = 1 Tev with laser wavelength $\lambda = 1\mu$ requires at least the total laser

energy Q ∿ 105 x 10^3 joules and the total length of the accelerating tube L ∿ 11 meters with R = 1 cm radius.

To conclude, it is seen that for the realization of the PAFLA a number of new problems will be involved which, however, it seems, are just suitable to be solved by optical means. If the process of photo replica can be adopted in the manufacture of the accelerating tube, then PAFLA for 10 Tev energy becomes conceivable.

The authors are grateful to have benefited from discussions on various occasions with a large number of persons working here on the usual accelerators and elsewhere on lasers and it is a pleasure to thank them all collectively. Specifically we express our thanks to Professor Chu Chi-ho for his suggesting the special polarizer, and to Mr. Wu Jianwu for his writing the early version of the computer program.

References

1. K. Shimoda, Appl. Opt. 1-1, (1962), pg. 33.
2. V. Daneu, Bull. Amer. Phys. Soc., Series 2, 12-5 (1967), pg. 668.
3. Y. Takeda and I. Matsui, Nucl. Instr. Meth. 62 (1968), pg. 306.
4. K. Mizuno, S. One, O. Shimoe, Nature 253 (1975), pg. 184.
5. P.L. Csonka, Particle Acc., 5 (1973), pg. 129.
6. A. Kanofsky, Rev. Sci. Instr. (USA), 48-1 (1977), pg. 34.
7. R. Rossmanith, Nucl. Instr. Meth., 154-1 (1978), pg. 29.
8. J.D. Lawson, Rutherford Lab., lecutre notes, RL-75-043, March 1975.
9. M.A. Piestrup, et al., J. Appl. Phys. 46-1 (1975), pg. 132.
10. M.V. Fangol'd, Journal of Technical Physics, 48-7 (1978), pg. 1533.
11. G.A. Nagorskii, EFI-320 (45)-78.
12. R. Petit, Nouv. Rev. Optique t^6 π^03 (1975), pg. 129.
13. Peng Huanwu and Zhuang Tie-Jia, A New Way to super High Energy With a Phase Adjusted Focusing Laser Accelerator, unpublished.

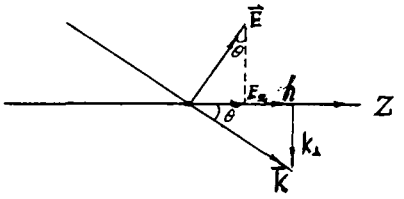


Fig. 1 - Pattern of the accelerating field E_z of the focusing laser, the wave vector k revolving around the Z-axis.

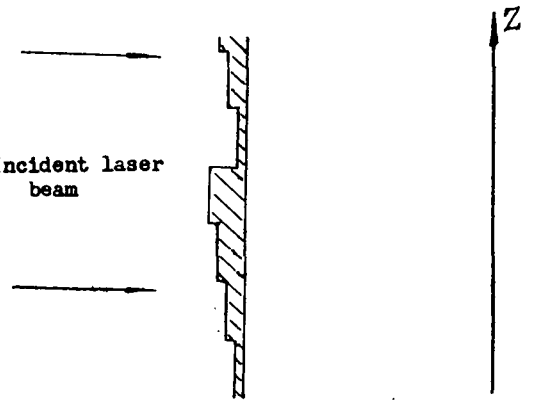


Fig. 2 - Stepwise grating (schematic) for phase adjustment, the grating and the incident laser revolving together around the Z-axis. For a four-step grating the optical path is increased by a quarter wavelength for each step.

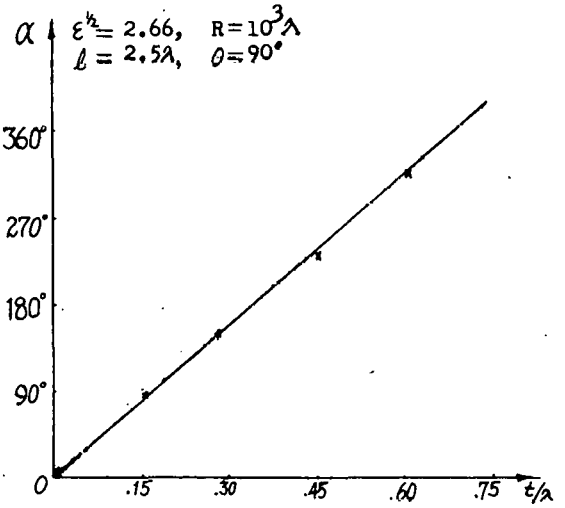


Fig. 3 - Variation of the phase delay α of E_z on the axis for various of the thickness t of step.

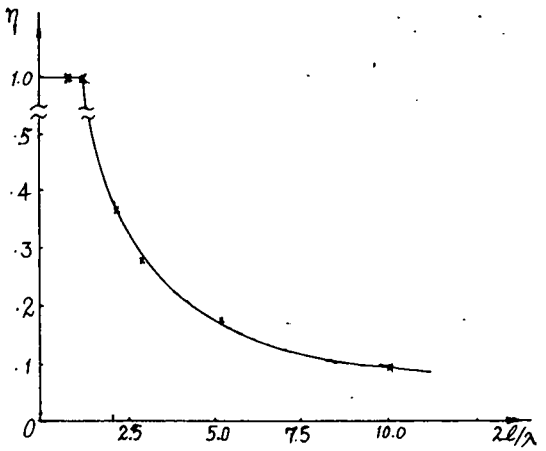


Fig. 4 - Variation of the fraction η of the region on the axis where the change of phase is blurred for various values of grating constant D = 2.

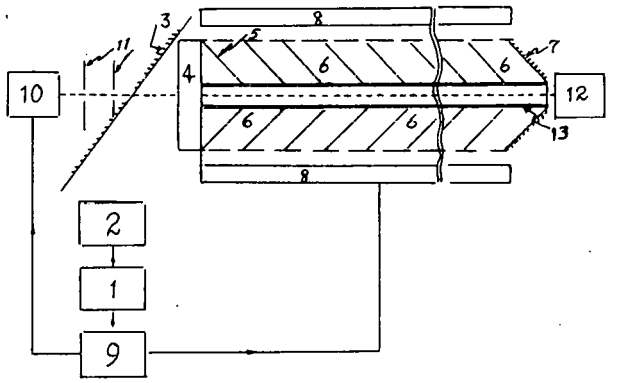


Fig. 6 - A PAFLA block diagram
1. Laser oscillator, 2. Laser amplifier, 3. Reflector, 4. Special polarizer, 5. 45° cone-shaped beam splitter, 6. Laser amplifier, 7. 45° cone-shaped reflector, 8. Pumping source, 9. Time-delayed trigger, 10. Injector of charged particles, 11. Collimating slit, 12. Detectors of charged particles, 13. Accelerating tube.

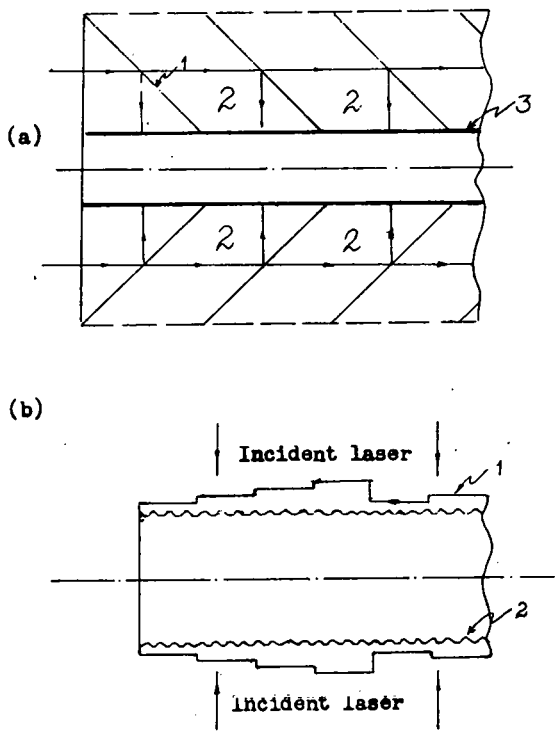


Fig. 5 - The accelerating tube
(a) Arrangement: 1. Beam splitter, 2. Laser amplifier, 3. Accelerating tube.
(b) Structure: 1. Grating for phase adjustment, 2. Grating for diffraction.

Discussion

Teng, Fermilab: I did not quite follow the details of your scheme. But generally speaking there are two difficulties with laser accelerators: (1) because of the very small wavelength, the acceptance of the field is too small; (2) the fabrication precision and operating stability required are very high. Can you comment on these in relation to your scheme?

Zhuang: Yes, we have not gotten into the required accuracy and detail, but it is expected to be very high. However, it seems to us, the problem can be suitably solved by optical means.

Blewett, BNL: Do you plan experimental tests of these ideas?

Zhuang: We want to explore the theoretical before we start on the experimental program.

1979 LINEAR ACCELERATOR CONFERENCE

SIMULTANEOUS BEAMS OF DIFFERENT ENERGY FROM LAMPF*

G. R. Swain and D. C. Hagerman
Los Alamos Scientific Laboratory
Los Alamos, NM 87545

Summary

The linac of the Clinton P. Anderson Meson Physics Facility (LAMPF) was designed to simultaneously accelerate H^+ and H^- beams to energies up to a maximum of 800 MeV. To allow more flexibility in the experimental program, it is desirable to find an operating mode such that the H^- beam may be accelerated to a lower output energy than the H^+ beam. There are two possible approaches for doing this. In one approach, the beams could time-share the rf pulses, with the radio frequency adjusted to provide the desired energy for each beam separately. In the other approach, which will be the one discussed in this paper, both beams use all of the rf pulses, and the H^- beam is kicked out of the accelerating bucket when the desired lower energy is reached. This paper discusses a possible method of separating the H^- and H^+ beams in longitudinal phase space (energy -phase), and summarizes dynamics calculations for various proposed schemes for kicking the H^- beam out of the bucket.

Introduction

The LAMPF accelerator provides an intense H^+ beam, used primarily for meson production, and an H^- beam used for nucleon-nucleon and nucleon-nucleus studies. Users of the mesons coming from the H^+ beam generally prefer as high an energy proton beam as possible, because the meson flux in most cases increases with energy. This variation in meson flux with energy is very strong if mesons near the kinematic energy limit are in use; conversely, the variation is relatively weak if low-energy mesons are desired. Typically, for intermediate energies, the flux will drop by a factor of two if the proton energy is reduced from 800 to 650 MeV. The users of the H^- beam prefer a variable energy beam permitting their measurements to be carried out as a function of energy. For most experiments, energy variation in 50-MeV steps is adequate. The energy range of most interest is from 400 to 800 MeV, giving an adequate overlap with the energies available from other accelerators.

The work reported in this paper is a preliminary feasiblity study of one possible way of modifying and operating the LAMPF accelerator to obtain an H^+ beam of 800 MeV and a simultaneous H^- beam of lower energy. The method discussed here involves separating the H+ bunches in the longitudinal (energy-phase) plane and then dumping the H^- bunch from the accelerating bucket. Both beams would be produced at the full duty factor of the accelerator.

The LAMPF accelerator has three types of components: 750-kV dc injectors, drift-tube linac tanks operated at 201.25 MHz and side-coupled linac modules operated at 805 MHz. The simultaneous beams of different energy would be produced in the 805-MHz linac portion, which accelerates the beam from 100 MeV. The method discussed here involves a separator region in the early part of the 805-MHz linac, and a dumper region (in longitudinal space) further downstream in the linac.

The purpose of the separator region is to introduce, or amplify, a deliberate oscillation of the H^- bunch in longitudinal space, yet maintain a normal H^+ bunch. This would be done by inserting special rf cavities at appropriate points between the 805-MHz linac modules. These special cavities would be operated at a subharmonic of the module frequency, and phased such that the H^+ bunch passes through them at or near a zero-crossing of the rf. When 201.25 MHz is used for the special cavities, the H^- beam arrives at the special cavities 135 degrees away from the H^+, and thus receives an energy kick from these cavities. Assuming that 20-kW peak drive power to a cavity can produce an effective gap voltage of 350 kV, one sees that each special cavity could shift the H^- energy by 0.25 MeV.

The purpose of the dumper region is to evict the H^- bunch from the accelerating bucket while retaining the H^+ bunch. This might be done by reducing the rf amplitude for a series of tanks, reducing the stable region (or fish) to fit snugly around the H^+ bunch, or by moving the rf phase of a series of tanks thus shifting the fish to leave the H^+ inside but leave the H^- bunch outside., or by some combination of these strategies.

There are four aspects of the problem:

(1) effect of separator region on H^- bunch,
(2) effect of separator region on H^+ bunch,
(3) effect of dumper region on H^- bunch and
(4) effect of dumper region on H^+ bunch.

Aspect (2) has not yet been studied. Because the extent in phase of the H^+ beam is about ± 10 degrees at 805 MHz, it would be only ± 2.5 degrees at 201.25 MHz, and the degradation of the H^+ beam by the special cavities should be very small. The other aspects are discussed below.

Separator Strategies

With any separation strategy, one attempts to get a large enough H^- oscillation to permit a choice of points downstream along the linac

*Work performed under the auspices of the U.S. Department of Energy.

where the H^- can be dumped. But it is not desirable to make the H^- oscillation so large that the H^- bunch is badly distorted, producing a long tail in energy-phase space. The more the H^- bunch is drawn out, the more difficult it becomes to dump all the H^- particles without dumping any of the H^+ particles.

Special Cavities Alone

The special cavities of the separator region may be used both to initiate an oscillation of the H^- bunch in energy-phase and to amplify that oscillation. The calculation reported here assumes that special cavities may be placed only between modules, because of space limitations. For any special cavity, one has the choice between having it add or subtract from the energy of the H^- beam. Because the longitudinal wavelength is only approximately equal to four modules, the spacing of the special cavities along the linac is irregular to achieve the most H^- to H^+ separation per cavity. Unfortunately, it appears that a large number of special cavities (over 12) would be required to both initiate and amplify an H^- oscillation. The capital cost of installing the scheme varies directly with the number of special cavities, and of course it is desirable to keep this number small.

Initial Oscillation Plus Special Cavities

The H^+ and H^- beams take separate paths through the transition region between the 201.25-MHz and 805-MHz linacs, and it is possible to start the H^- beam into the 805-MHz linac with an offset in phase. If such an offset is used, the H^- beam will oscillate in energy-phase space, and the special cavities might be used to amplify this oscillation. Fewer special cavities are needed this way to achieve a given amplitude of oscillation. Calculations indicate that eight special cavities are sufficient to fully separate the H^+ and H^- bunches.

Dumper Strategies

In contrast to the separator region, which has special cavities and occupies a fixed region of the linac, the dumper region has no special equipment and varies in position along the linac according to the energy at which the H^- beam is to be dumped.

Reduced Amplitude

One way of evicting the H^- bunch from the accelerating bucket after the H^- particles have achieved a desired energy, is to shrink the fish such that the H^+ particles are still inside but the H^- ones are not. This may be done by reducing the rf amplitude. One adjusts the design phase ϕ, such that although the field E is smaller, E cos ϕ is the same. Some exploratory calculations were made for the dumper region using this strategy. Small changes in the dumper entrance energy or phase produced large changes in output energy for the dumped particles. For example, a change in entrance phase of two degrees might produce a change of over 15 MeV in output energy.

After about five modules from the start of the dumper region, the H^- particles are far behind in energy from the H^+ particles, and it makes little difference to the H^- bunch whether or not the amplitude for subsequent modules is increased.

Shifted Phase

Another way of dumping the H^- bunch is to pick a position along the linac where the H^- bunch lies to the left (at reduced phase) of the H^+ bunch, and then to shift rf phase so that the left side of the fish is between the bunches (Fig. 1). For the next few modules, this will leave the H^- bunch outside and the H^+ bunch off center but inside. The H^- bunch will soon be left behind in energy (Fig. 2). After the H^+ bunch has made one oscillation, the rf phase may again be shifted to stop or at least reduce the oscillation (Fig. 3). This process introduces an additional but tolerable energy spread into the H^+ beam.

Because the dumper region must begin where the H^- bunch is to the left of the H^+ bunch, there are only certain points where the dumper region may be placed. The peaks in the oscillations of the H^- bunch are about 80 MeV apart. However, by starting the H^- oscillation with a phase offset of the opposite sign and operating the special cavities with the phase shifted 180 degrees, one obtains an oscillation with peaks midway between those obtained before, and dumper regions may begin there. Thus the available H^- output beam energies are roughly 40 MeV apart.

Exploratory calculations for the dumper region alone suggested that there may be regions

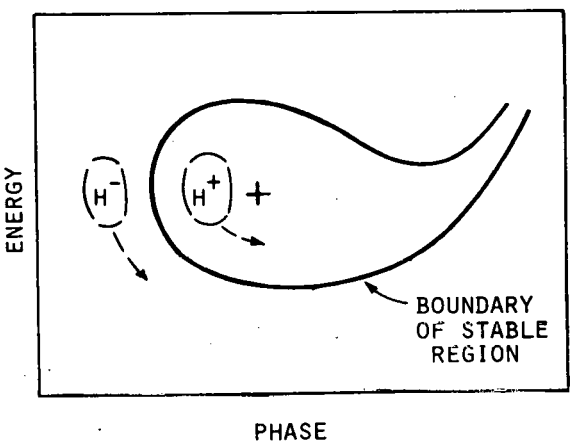


Fig. 1. Stable region (fish), shifted to the right, leaving the H^- bunch outside.

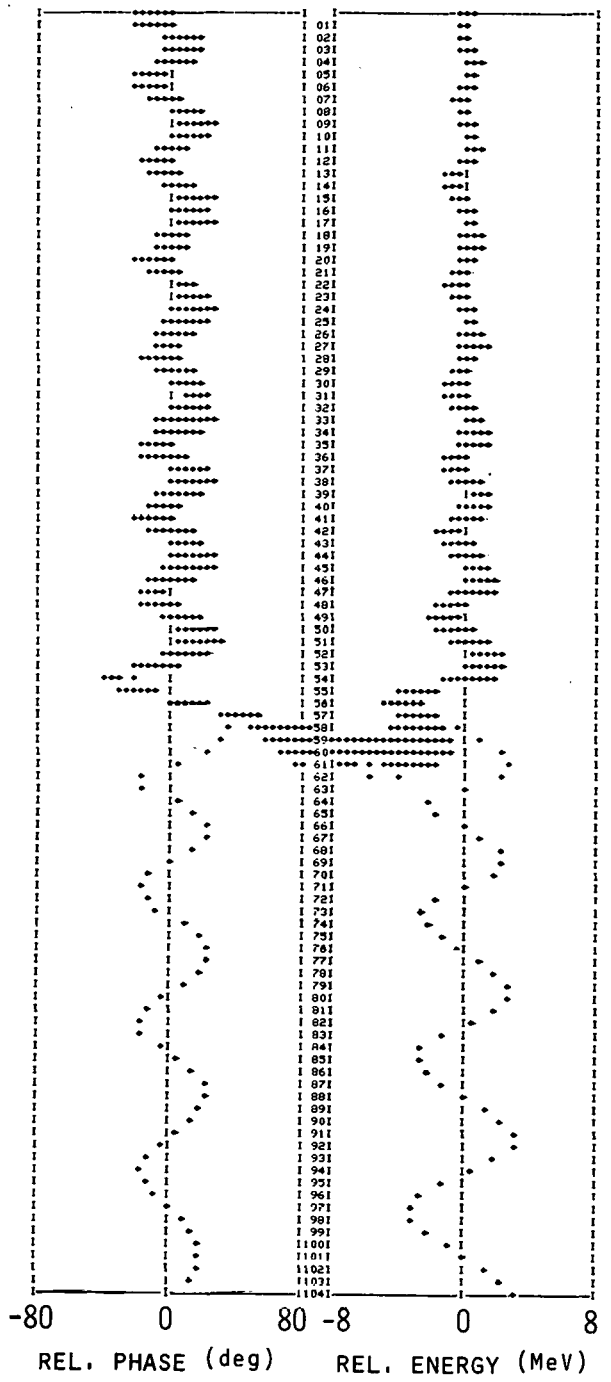


Fig. 2. Phase and energy profiles (relative to a design particle) for the 805-MHz linac for the H^- beam. The particle continuing past the dumper region was a reference particle not affected by the separator region.

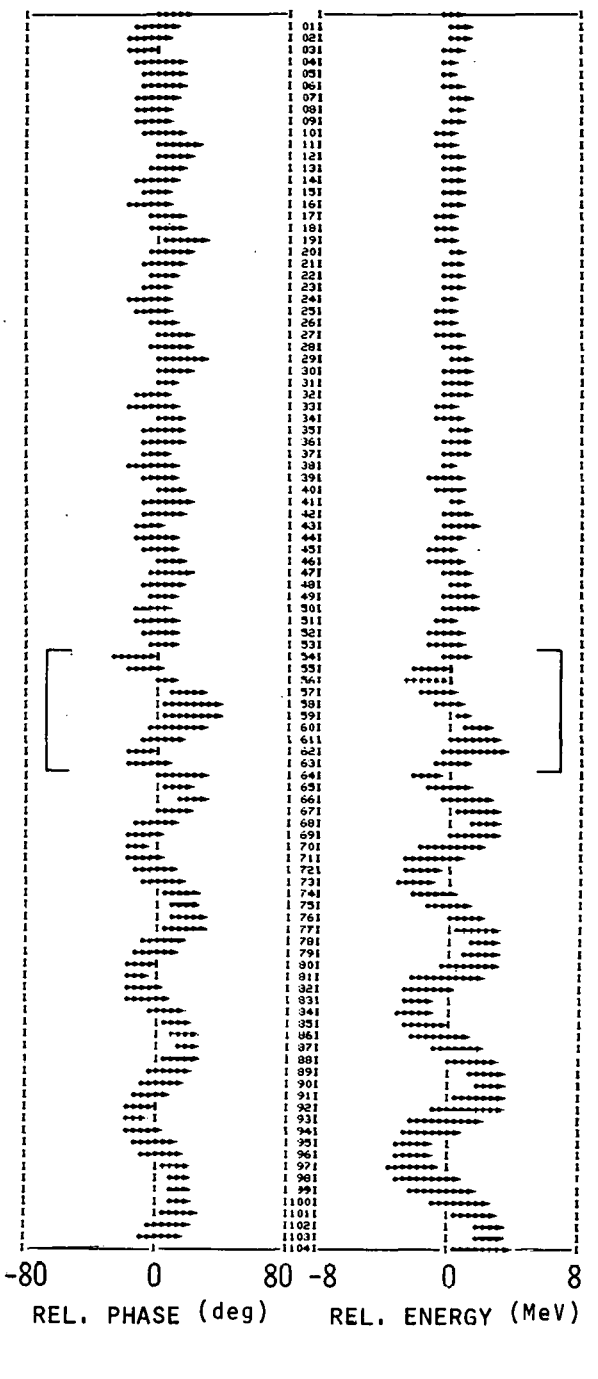


Fig. 3. Phase and energy profiles (relative to a design particle) for the 805-MHz linac for the H^+ beam. The dumper region is indicated by brackets.

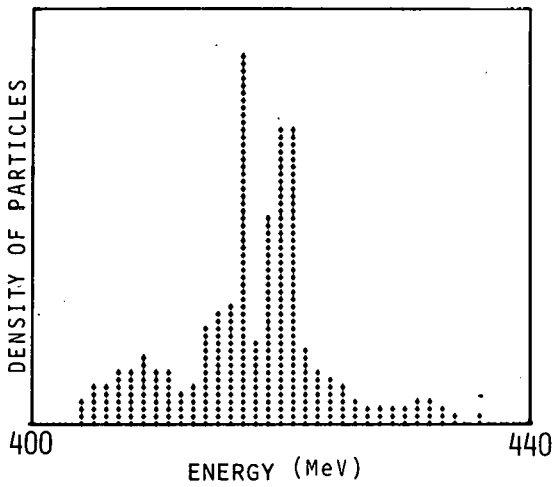


Fig. 4. Energy distribution for H^- beam at exit of linac.

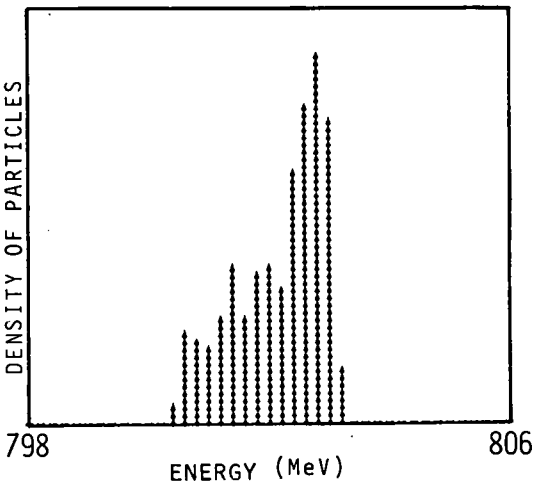


Fig. 5. Energy distribution for H^+ beam at exit of linac.

in entrance energy-phase space that give lower spread in output energy for the shifted-phase scheme than for the reduced-amplitude scheme. It is not clear if one scheme is better than the other for the limited separations of H^- from H^+ that appear plausible with eight, or fewer, special cavities in the separator region.

Whole-linac calculations, as in Figs. 2 and 3, give distributions of H^- or H^+ particles versus energy as shown in Figs. 4 and 5. The case shown in Figs. 2 and 4 produced an H^- beam with an output energy near 420 MeV. By placing the dumper region at other places, and using adjustments discussed below under Additional Refinements, it was possible to calculate cases with H^- beam output energies near 450, 490, 525, and 585 MeV. It is not certain whether H^- beam energies higher than this could be obtained, because it becomes increasingly difficult to maintain H^+ - H^- separation as the distance between separator and dumper regions is increased.

Other Strategies

Other dumper strategies are possible. One might begin as in the shifted-phase scheme, but after the H^+ beam has made half an oscillation (bringing the bunch back near design energy), reduce the rf amplitude to shrink the fish.

Additional Refinements

As one takes the H^- beam further down the linac, it becomes more and more difficult to dump all the H^- particles without dumping any of the H^+. The following schemes permit one to make small gains in H^+ - H^- separation.

Initial H^+ Oscillation. One may introduce a longitudinal oscillation of the H^+ bunch by starting the H^+ bunch in the 805-MHz linac with a phase offset. If the H^+ phase offset is opposite in sign from the initial H^- phase offset, the separation is improved. Because longitudinal oscillations are significantly damped in the early part of the linac, the maximum change in phase in the dumper regions is only about one-quarter of the initial phase offset. Thus the improvement in separation with this scheme is limited to a few degrees in phase.

Adjustment of Longitudinal Wavelength. It may be advantageous to slightly change the longitudinal wavelength so that the peak of an oscillation of the H^- bunch falls exactly at the start of a dumper region. This may be done by adjusting the rf amplitude along the linac (maintaining $E \cos \phi$ constant) between the separator and dumper regions; increasing the rf amplitude shortens the wavelength.

Conclusions

The preliminary studies suggest that by adding a series of eight low-frequency cavities, it would be possible to accelerate simultaneous H^+ and H^- beams to different energies at LAMPF. The H^- beams thus obtained are likely to have a broad energy spread; the utility of an H^- beam with this large an energy spread is still under evaluation. However, it appears that it may be difficult to achieve enough separation of the H^+ and H^- bunches along the linac such that all the H^- particles can be dumped from the accelerating bucket without dumping any of the H^+ particles.

THIS PAGE

WAS INTENTIONALLY

LEFT BLANK

Section V
Controls and Beam Diagnostics

THIS PAGE

WAS INTENTIONALLY

LEFT BLANK

A MICROCOMPUTER CONTROL SYSTEM FOR THE SUPERHILAC THIRD INJECTOR*

H.D. Lancaster, S.B. Magyary, J. Clatz, F.B. Selph, M.P. Fahmie,
A.L. Ritchie, S.R. Keith, G.R. Stover, and L.J. Besse
Lawrence Berkeley Laboratory
Berkeley, California

Summary

A new control system using the latest technology in microcomputers, will be used on the third injector at the SuperHILAC.[1] This design incorporates some new and progressive ideas in both hardware and software design inspired by the revolution in microprocessors.

The third-injector project consists of a high voltage pre-injector, a Wideroe-type linear accelerator, and connecting beam lines, requiring control of 80 analog and 300 boolean devices. To solve this problem, emphasizing inexpensive, commercially available hardware, a control system was designed consisting of 20 microcomputer boards, with a total of 700 kilobytes of memory. Each computer board, using a 16-bit microprocessor, has the computing power of a typical minicomputer.

These microcomputers operating in parallel greatly simplify the programming, literally replacing software with hardware. This improves system response speed and cuts costs dramatically.

An easy to use interpretive language, similar to BASIC, will allow operations personnel to write special purpose programs in addition to the compiled procedures.

Design Concepts

In most accelerator control systems, software costs have been several times hardware costs, because the software had to be developed for each particular job. This has usually involved substantial changes in the computer's operating system, or the invention of new networks, message services, etc., trying to solve the control problem particular to that accelerator. Besides being expensive, the systems software is generally so complicated that only a few highly specialized programmers can understand its function. This makes it almost impossible for the accelerator engineers and scientists to interact with the control system when new instrumentation or control applications are needed. Whereas hardware has increased in performance and decreased in cost, software has not kept pace. Therefore, it follows that one should buy more hardware if it reduces or simplifies the software task, at least until the two costs are equal.

* This work was supported by the High Energy & Nuclear Physics Division of the U.S. Department of Energy under contract No. W-7405-ENG-48.

In the last two years a number of very powerful, inexpensive 16-bit microprocessors have become available. The commercial board-level implementation of these products rival minicomputers in speed and memory, but are much more oriented toward control than general calculations.

The present implementation makes use of the Multibus,[2] which makes it easy to link these new computers when needed. These computer boards must have local busses, so that the Multibus is used only for intercommunication, allowing true parallel processing. (In standard single bus systems the bus becomes the bottleneck.) It was found that this approach opens up an entirely new way to implement control systems which is cheaper, more versatile and faster. Since the only software is for applications programs, they can be implemented by accelerator engineers and scientists.

A new avenue for software implementation is thus made available and one can now attack the dominant cost in a computer control system, the software. In this system the computer hardware and software were tailored to the existing control problem, rather than trying to modify the control problem so it will fit some existing computer architecture.

Each computer board performs only one permanently assigned task, in a continuous loop or on a hardware-interrupt basis. The programs are stored on-board in read-only-memory (ROM). This eliminates the need for program loading, scheduling, and synchronization. Thus, there is no need for an operating system! All programs are applications programs. Because the program on each board is self-contained, programming interference is virtually eliminated. Individual styles of programming (even languages) are acceptable.

The logical link between the various computers and processes is the database, which is available to all computers. This allows:

- fast, direct access to accelerator data without message exchanges,
- programs that are entirely unaffected by additions to the accelerator hardware, because these are only reflected in the database information, which is interpreted by the programs,
- adding processing power or new procedures by simply plugging a programmed board into the Multibus.

Through parallel processing of sections of a particular task, very fast performance can be

achieved. This allows the writing of all programs in a high level language, PL/M-86 (in spite of its slower execution), resulting in drastically shortened programming and testing times as compared to assembly language. Also, most accidental programming errors are eliminated by this compiler's elaborate syntactical checks.

This accelerator control system design, by using the latest microcomputer technology, offers a way to both lower costs and implement a system which can be understood by accelerator engineers and scientists. Experience has shown that a person with both hardware and software experience is best suited to apply this new technology.

Timing Considerations

The SuperHILAC (Fig. 1) is a relatively fast pulsed machine, running at 36 Hz. It accelerates ions from three injectors on a pulse-to-pulse basis. This means, at the hardware level, tasks are completed in at most 27.7 ms, with a new machine state or mode, e.g., linac tank gradients and magnet currents, being transmitted each pulse if needed.

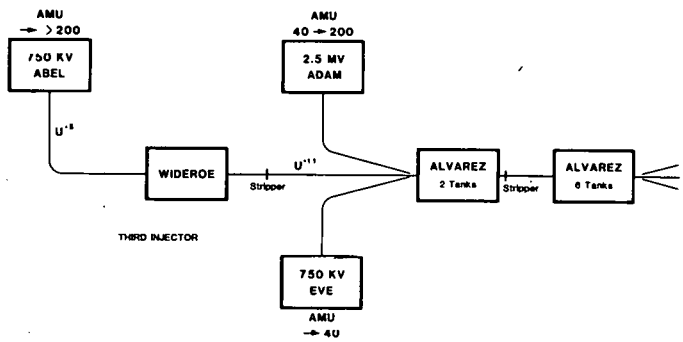


Fig. 1 Schematic layout of SuperHILAC. The control system described in this paper is needed for the third injector, comprising the 750 kv Cockcroft-Walton, the Wideroe, and associated transport systems.

Acceptable response to operator requests should be on the order of 100 ms. Interactive graphics at this rate impose a severe computational burden. The least severe requirement is for storage and retrieval of accelerator parameters, which occurs at the beginning and end of an experiment and can take several seconds. With parallel processing this range of timing and execution requirements can be covered.

Architecture

The system architecture (Fig. 2) is of the star type, which lends itself nicely to the SuperHILAC because of its clustered equipment. Each "module" in the system is an Intel SBC 660-card cage with a Multibus backplane, containing up to eight boards.

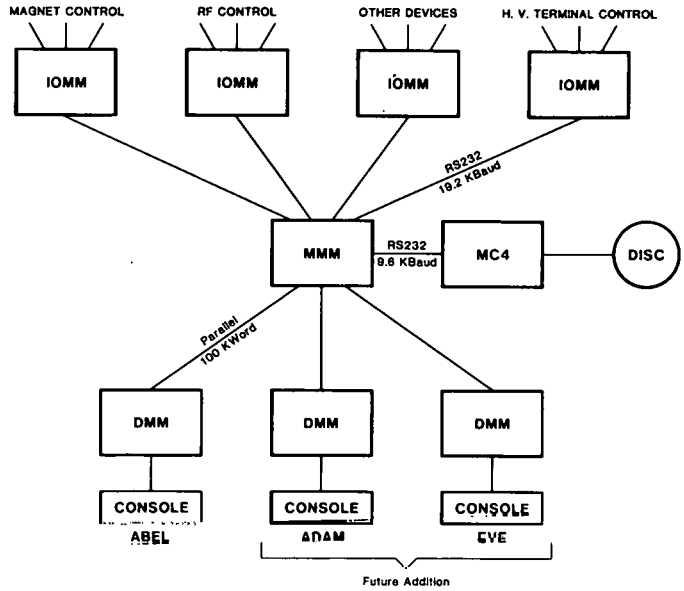


Fig. 2 The third injector control system utilizes the star concept, in which a central processor, the MMM, acts to link several hardware interfaces, the IOMMs, with several operator stations, the DMMs. The great advantage of this system over previous systems is that it employs distributed intelligence so that the MMM is not overworked, which could cause it to be a bottleneck.

There are several distributed input-output modules (IOMM) which interface to the accelerator equipment. The modules control the accelerator parameters in synchronism with accelerator timing. Data from the IOMMs is collected by a multiplexer (MMM) which then disseminates it to the display module (DMM) for data display and operator interaction. The MMM and DMMs are not synchronized with the accelerator but must respond in 100ms for adequate interaction between operator and machine. These modules are described in detail later.

To bridge the long distances between the IOMMs and the MMM, serial transmission (RS 232) over fiber-optics at 19.2 kbaud is used. This limited rate is acceptable since data is exchanged primarily on demand.

The full data flow from the MMM to the DMM is handled by a 16-bit parallel bus over a few meters. This communications system is set up to provide access to continuously updated copies of the complete database (total of all the primary databases residing in the IOMMs) for every computer in the MMM and the DMM.

Database

Each IOMM has its own database describing the connected devices completely. After initialization, the MMM and DMM contain and have control of

the sum of all IOMM databases. This gives immediate parameters and their descriptors for operator analysis.

The IOMM database is composed of three major parts: common passive, particular passive, and active. The passive parts are stored in ROM.

The common passive part contains descriptors required for every element, for example: element name, element type, and pointers to the other two parts.

The particular passive part contains the data that is unique to that element and does not change, for example, conversion constants and hardware channel numbers.

The active part located in random-access-memory (RAM) contains those element parameters which change with time; for example, set points and monitored values.

The database has two element types, the hardware and the pseudo. The hardware type element refers to parameters associated with actual hardware signals. These are: analog control, analog monitor, boolean (single bit) control, boolean monitor, digital (byte) control and digital monitor. These elements can be coupled to allow closed loops, interlocks, and complex devices.

The pseudo-type elements are system or special function elements that are required to fulfill special software constructs. For example, examining pseudo element "Link-Error" allows monitoring transmission errors between the IOMM and MMM.

Input-Output Microcomputer Module (IOMM)

Each IOMM has a common set of external interrupts and accelerator mode data supplied by a high speed serial fiber-optic link. This synchronizes the IOMM's with the SuperHILAC pulsing sequence. To satisfy timing requirements and simplify the software, it is required that all I/O programs be completed in one pulse.

The IOMM (Fig. 3) is a card cage with two SBC 86/12 computers and additional boards with 16 analog channels, 72 I/O lines, and provision for 8-bit data exchange to external devices. The 16 DAC's and 16 ADC's are 12-bit converters. The 72 I/O lines are interfaced with the real world using optically-coupled, Opto 22 modules. The database and message computer (CPU1) transmits the active data to the MMM in order of priority, which is determined by operator demand and changing parameters. Five records can be sent between machine pulses. One of these five is non-prioritized and steps through the database so that a minimum trickle rate of two seconds is assured for low priority devices. CPU1 constantly evaluates and tailors the priority based on information received from the standard I/O computer (CPU2). The MMM sends new set points to CPU1 which stores them in the active database, then echoes them back to the operator for confirmation

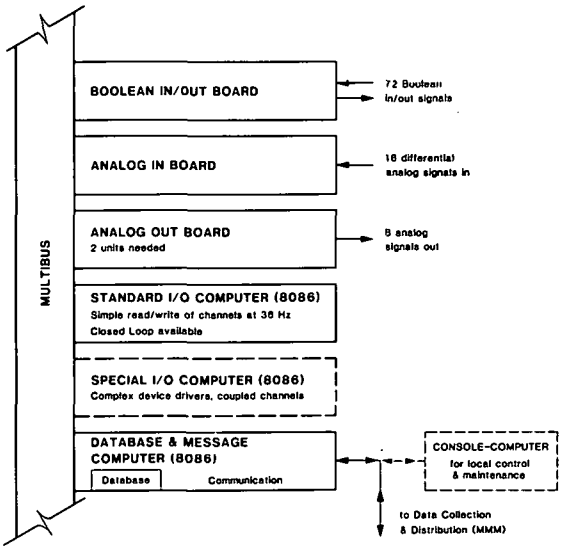


Fig. 3 Input/Output Microcomputer Module. It provides the hardware interface to the accelerator and holds the primary database. The three computer boards (shown in the lower boxes) work in parallel and have access to every board on the Multibus.

of data transfer. CPU1 contains the IOMM's database. CPU2 handles the interface to the accelerator parameters; it observes monitored data for fast and slow drift, and ability to follow the set point. Data failing these tests are flagged with an appropriate priority and sent to CPU1. Closed or open loop operation is provided. I/O channels can be treated independently or in groups for special tasks.

A portable console-computer can be connected to the IOMM in place of the MMM for local control and debugging of the IOMM and all devices connected to it. After check-out, the IOMM can be reconnected to the MMM without disturbing the rest of the system.

Multiplexer Microcomputer Module (MMM)

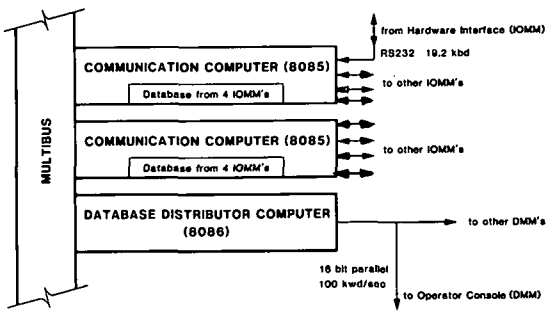


Fig. 4 Multiplexer Microcomputer Module. Database information is exchanged between eight IOMMs and one of the display microcomputer modules through this unit, using both serial and parallel transmission. Shared access to any of the IOMM databases is essential.

The MMM (Fig. 4) simultaneously collects database information from all the IOMMs via the RS 232 links and forwards it asynchronously to the DMM. Likewise, tuning data generated in the DMM is sent through the MMM to the IOMMs. Since the MMM concentrates all the IOMM data, it is a potential bottleneck. This problem was solved by parallel processing.

The data from the IOMMs comes into Intel SBC 544 communication boards via four on-board USARTs. It is mapped into the dual-ported memory, with each IOMM allotted a 4K-byte block of RAM. Each memory block contains the full database of the respective IOMM. The computer on these boards, an 8085, is fully occupied servicing the USARTs and managing the data. Each board handles four IOMMs.

A 16-bit computer, Intel SBC 86/12, then reads the databases from the dual-ported SBC 544 memory via the Multibus and transmits it to the DMM over the fast parallel link.

The MMM may also house an additional computer which operates the link to a disc used for storage and retrieval of injector parameter sets.

Display Microcomputer Module (DMM)

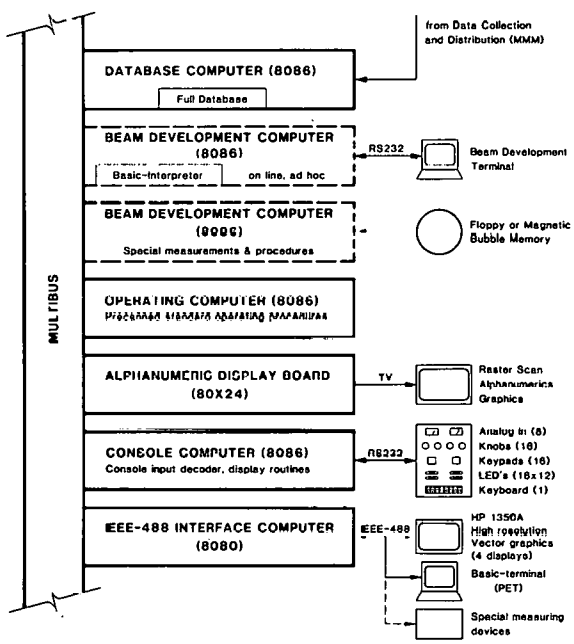


Fig. 5 Display Microcomputer Module. Up to three independent computers (boxes 2 to 4 from top) are planned to perform the operating tasks. They have access to the accelerator by writing into or reading from the database. They control the console devices by exchanging messages with the console computer over the Multibus.

The DMM (Fig. 5) displays accelerator data and generates control data from operator inputs and built-in procedures. To the DMM, the accelerator is fully represented by a database copy allowing the reading of parameter values independent of machine timing and actual access procedures. The database copy in the DMM database computer is updated through a fast link from the MMM at a rate of at least 10/sec. The operating computer is the actual master of the whole control system. It processes requests, sends these or computed set points to the database, monitors all error conditions and generates various formats for displaying the accelerator data to the operator.

The operating computer does not see the actual hardware of the console. Console devices and displays are handled by three additional boards which share the Multibus: the console computer, an alphanumeric display board, and an IEEE-488 interface computer. The console computer generates alphanumeric and graphic displays and evaluates the messages from such control units as knobs, keypads and touch buttons. For alphanumerics, the memory-mapped display board converts an 80 x 24 character pattern into a video signal.

Generation of fast, high resolution live graphics is more elaborate, using an HP-1350A graphics translator that is addressed through the IEEE-488 interface board. We plan to mix graphics with real-time analog signals. For both types of displays, the hardware choices assure a display frame update of at least 10/second. This IEEE-488 board is also used for other compatible devices as they are needed, such as a commercially available BASIC-terminal.

The operator console holds up to forty input devices and sixteen 12-character LED-displays. They are controlled by a local microprocessor (8085) in order to reduce cabling. Information is exchanged with the console computer in the DMM through an RS 232 link.

The beam development computers perform special beam measurements, such as emittance or bunch structure, and allow on-line generation and execution of one-time or prototype programs, using a BASIC interpreter. They may utilize any of the console input devices and display units by writing appropriate messages into the console computer. The interpretive language approach has proved its usefulness at a number of accelerators, particularly at the CERN SPS where the NODAL language was implemented.

Schedule

At present, we have completed and tested the software and hardware for the IOMMs, the serial communication links, and a preliminary version of the DMM. We plan to have the software for an operational control system and the operator console hardware finished by January 1980. The other hardware, which is mostly purchased, will be installed in October 1980. The third injector project is scheduled to be finished in June 1981.

References

1 J. Staples etl al., A Wideroe-Based Heavy Ion Preaccelerator for the SuperHILAC, IEEE Transactions on Nuclear Science, Vol. NS-26, No. 3, June 1979.

2 Multibus is a trademark of Intel Corporation.

A DISTRIBUTED LINAC CONTROL SYSTEM FEATURING SDLC LOOP COMMUNICATION

R.W. Goodwin and M.F. Shea
Fermi National Accelerator Laboratory†
Batavia, Illinois

Summary

A distributed control system has been designed as a possible replacement for the existing analog and digital interface equipment in use at the Fermilab 200-MeV linear accelerator. In addition to replacing the present interface equipment that is no longer supported by the manufacturer, the goals for a new system include improved reliability, easier maintenance and faster monitoring of accelerator parameters. About 15 local microcomputers, one for each major linac system, would be fabricated from commercially available Multibus-compatible hardware. These local stations can operate as stand-alone systems, providing control and readout of parameters to facilitate maintenance of the accelerator components. Values of all critical devices can be monitored at the accelerator repetition rate (15 Hz), so that beam may be inhibited by any out-of-tolerance reading on a pulse-to-pulse basis, to prevent unnecessary and damaging beam loss.

One of our design criteria is to maintain the fast response and interactive nature of the existing system. The operation of a group of individual processors as a single integrated control system depends on the type of communication link used to interconnect the local stations with the operator's console computer. For this link, the Synchronous Data Link control (SDLC) in the loop configuration was chosen. Using SDLC interface circuits with direct memory access controllers, arbitrary length blocks of binary data can be transmitted and received at bit rates of 1 MHz. Details of the hardware and software organization of this control system design will be discussed.

Introduction

The original Fermilab linac control system has been in operation for about 10 years.[1] Although the system still operates well, the interface equipment and the X530 control computer are no longer supported by the manufacturer. A change of computer would necessitate a change in the interface equipment because this equipment is structured as an extension of X530 I/O bus. However, because the linac I/O is integrated into the console computer itself, it is a very fast system. The four linac digitizers are run simultaneously by the 530's I/O processor, placing data in memory under DMA control. Because of this capability, all the linac analog data (∿ 800 channels) are collected for each accelerator cycle (15 Hz) so that current correlated data are always available to the application and monitor programs. Although binary data are not collected for each cycle, the status can be read as a single 6μs instruction by the program that needs the status information.

†Operated by Universities Research Association, Inc. under contract with the U. S. Department of Energy.

It is this type of high performance system that we are attempting to replace.

System Overview

A new control system that is being designed today should almost certainly be built with small, modular, intelligent local stations, each controlling a part of the accelerator. Experience with such systems in the Fermilab Cancer Therapy Facility and Preaccelerator areas, has shown them to be extremely flexible and reliable additions to the control system.[2,3] The new design has a microprocessor controlled station for each system of the linac. The local stations are relatively straightforward. They include the processor, a small console, and the analog and digital interface equipment. Each system is assembled from a collection of commercially available cards that are compatible with an industry standard bus structure, such as Multibus§. The more difficult part of the design, and the part that will determine the performance of the entire system, is the communication link that connects the local processors to the console computer. The response of the console (or consoles) will depend in detail upon the transmission speed, the message handling overhead and the turnaround time for receiving data requested from local systems.

It was decided to use a serial bit-oriented protocol, such as HDLC (High Level Data Link Control), to provide the communication to and from the local stations because it is fast; it is an industry standard[4]; it is supported by large-scale integrated transmitter-receiver circuits supplied by semiconductor manufacturers. The link overhead when using a DMA controller is low to allow the high performance required of the communication channel.

HDLC is a superset of the original IBM bit-oriented specification SDLC (Synchronous Data Link Control) protocol.[5] Both use the same message format, but SDLC contains some simplifications and includes a loop mode that is particularly useful for control systems.

The SDLC Protocol

Data is transmitted on a SDLC link in a format called a frame. All frames begin and end with a flag. Between the opening and closing flag, a frame contains an address field, control field, information field, and a frame check sequence as shown in Fig. 1.

OPENING FLAG	ADDRESS (1 BYTE)	CONTROL (1 BYTE)	INFORMATION FIELD (ANY NUMBER OF BYTES)	16 BIT CRC FRAME CHECK SEQUENCE	CLOSING FLAG

Fig. 1 SDLC Message Format

§Multibus is a trademark of the Intel Corporation.

The flag character is the binary pattern 01111110. It provides the frame boundary and reference for the position of other fields within a frame. The address and control fields are each one byte long. The address byte is used by the primary station to direct a message to a particular secondary. When a secondary transmits a response, it includes its own address in the address field. The control byte identifies the type of message. The information field may be any length (including zero)--it contains only data. The frame check sequence field is a two byte cyclic redundancy check (CRC) to test the integrity of the transmission. In this protocol, the link overhead is the same 6 bytes for any length message so that long blocks of data may be sent very efficiently. Only three special bit patterns are used: flag, abort (8 "ones") and inactive idle (15"ones"). All three are handled by the hardware.

In the loop mode of operation, a link controller or primary manages the message traffic on the loop. Data flow is always in the same direction around the loop and each station re-transmits the data it receives, so that messages sent from the controller are returned to the controller.

Two characteristics of the loop mode are extremely useful for the present system: 1) a controller can send data to all stations on the loop with a single transmission; and 2) with one poll sequence the controller can poll all the secondaries and receive a message from each secondary in turn. This drastically reduces the link controller overhead for most of the communication with secondaries.

In the quiescent state, the loop contains a continuous stream of flag bytes. If a secondary receives no flag bytes for a period of time, it transmits a special message, called a beacon, to the primary. This flag timeout will occur if a problem developed in the link, or in a station on the link. When the beacon is received by the primary, the address contained in the beacon message is the location of the last station that is operating normally. This feature is useful for locating malfunctions on the loop.

The SDLC protocol would be difficult to implement if it were not for the LSI circuits that have been made available by several semiconductor suppliers. For this application the Motorola MC6854 data link controller was selected, operating in conjunction with the MC6844 DMA controller. Together they allow a processor to transmit and receive messages at a 1-MHz baud rate under direct memory access. The processor need only set up pointers and byte counts and the rest of the work is done by the controllers. An interrupt is received when the message transfer is complete. The link controller also performs the functions of flag detection, CRC generation and detection, and zero insertion-deletion--a technique that causes flags to be unique while allowing binary data to be transmitted. The transmitter inserts a zero after any succession of five 1's within a frame and the receiver deletes any zero that follows 5 successive 1's. Only when a flag, abort or inactive idle is being sent will the controller permit more than 5 consecutive 1's. This operation is handled entirely by the controller--the processor is unaware that the zero insertion and deletion is taking place.

Hardware

The individual microcomputers will be fabricated from commercially available Multibus modules and card cages. Necessary cards that are not available will be designed and fabricated to comply with the Multibus specifications.

One card that will be fabricated is the CPU-Link card. This will be an MC6809-based single board computer that will include the MC6854 link controller and the MC6844 DMA controller. The card will also contain RAM, ROM, a programmable timer (MC6840) an asynchronous interface (MC6850) and a parallel I/O (2-MC6821). This computer card is expected to become a general purpose building block. Because of the bus arbitration logic, an additional CPU can be inserted in a system where more capability is needed. For example, a second CPU card in the preaccelerator ground station will provide an SDLC link to the 750-kV dome to operate the ion source electronics.

The processor's programs and fixed data are programmed into UV erasable PROM memories. In this way the local stations can restart in an operating state following a power outage. Descriptor information and nominal and tolerance values for accelerator parameters need to be updated only occasionally. These data will be placed in nonvolatile magnetic core memory.

Local Systems

Each major linac system will be controlled by a small local microcomputer as shown in Fig. 2.

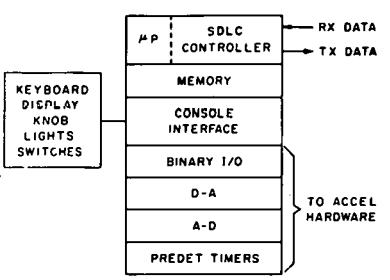


Fig. 2 Local Control Station

These will include a small console, loop interface, A-D, D-A and binary I/O.

A single Multibus card provides the operator's console interface. It contains a 16-line x 32-character video display generator, a keyboard input, an incremental shaft encoder input with up-down counter, and three bytes of binary I/O

for miscellaneous sense switches and indicators.

Loop Primary

The primary station will control no hardware except for a small console that is used to monitor the operation of the communication system. The link controller can display the number and length of messages being transmitted and received each cycle, the time spent polling secondaries, link error rates, and link malfunction locations.

Connection to Consoles

The primary also connects to other computers that service consoles in the control room. To make the system separate from the console computers, that communication occurs through the use of shared memory as shown in Fig. 3A. In a Multibus system, multiple processors automatically share memory because of the bus arbitration logic included on the processor boards. A second method of sharing memory is possible through the use of a pair of commercially available Multibus-compatible two-port memory modules that connect two independent Multibus systems (Fig. 3B).

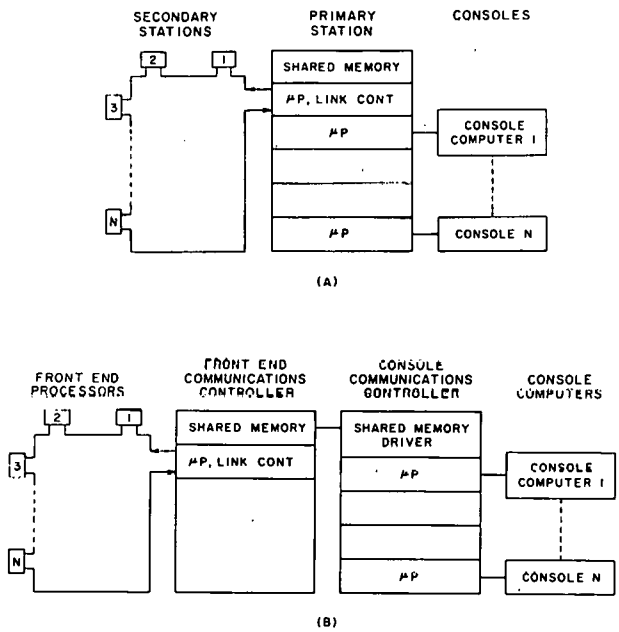


Fig. 3 Interconnection of Primary, Secondaries and Consoles

With this method, the system can be expanded to include additional Front End Communication Controllers each connected to the Console Communications Controller via separate shared memory. All consoles can then request data from any front-end communications controller in the network.

In Fig. 3, the block labeled "Console" is usually some computer that executes application programs, operates console hardware and requests and receives data from the linac through the shared memory. The connection to the console computer may be SDLC, byte serial DMA or some other communication link. A small console could be driven directly by the microprocessor--that is, no processor in the box labeled console. These various options are indistinguishable to the link primary. Each is simply a console, requesting data.

The Physical Link

Because the link is synchronous, a clock must accompany the data stream. This clock will be generated in the primary, transmitted around the loop and returned to the primary. The clock and data will be encoded and transmitted as a single, self-clocking signal using either biphase or Manchester format. Connection between chasses can be RS422, transformer coupled or fiber optic. The link driver-receiver electronics may be built as a separate chassis to allow loop bypass for an off-line station that is powered down.

System Operation

Functions of the Primary

The primary station is, in a very real sense, the loop controller. No data are placed on the link unless the primary initiates or solicits the transmission. Secondaries transmit only when polled, transmit only the data requested in the poll, and only one message per poll. In this way the primary can maintain a synchronous character to the link traffic. When a response is received, it is the answer to a specific question, not an arbitrary message initiated asynchronously from an autonomous secondary. This tight control exercised by the primary implies that a poll sequence must be sent to solicit all of the possible responses from the secondaries. This is feasible because programs for the secondaries are static; that is, it is not intended that code will be sent to a secondary for execution. This possibility is not excluded by the design and could be incorporated for some other application if needed.

Functions of the Secondaries

Secondary stations perform the task of data acquisition and monitoring for the local hardware. Each cycle, the secondary digitizes all the analog data and reads the digital status from the hardware so that a current data pool is available in the secondary. Then the secondary prepares groups of data to return to the primary. When this work is completed, the processor executes the application program to service the local console and update the video display.

Link Messages

This section describes the organization of the messages transmitted on the link to show how the individual stations and the link controller operate to collect the data required by the consoles. Three separate types of message traffic occur on the link.

Single-Terminal-Address Messages

When the primary station has an individual message to be sent to a controller, that message will contain the address of the target secondary station. This type of message is used to transmit settings to selected local hardware or to ask for data that is located only in that station, such as a memory dump. As in all other transmissions, the response from the secondary station must await the poll sequence from the primary.

All-Parties-Address Transmission

The all-parties address is used when the primary intends to send data to all secondaries simultaneously. Through the use of this transmission, the primary can assemble a group of readings collected from the present beam pulse and, with a single transmission, place these data in the memory of all stations on the loop. A nominal list of data will be sent each cycle so that each secondary will contain a "remote data pool" of selected readings from other stations. Then, for example, the Tank 4 system can display a summary of the linac operation without requesting data from the primary.

Poll Sequences

The poll command instructs stations to prepare to send data to the primary. The poll command will include an information field to allow the primary to select the type data to be sent. This is normally just the list ID number that had been sent at some earlier time. Many of the poll commands will be directed to the all-parties address (addr FF) and each station then prepares to send its contribution, if any, to the requested data list. Single-terminal-address poll commands can also be used to solicit response from a single secondary.

Several poll sequences will be done each cycle to request a variety of information: A-D data, out-of-tolerance parameters, secondary station status, etc.

List Organization

The primary communicates with the console and with the secondaries in terms of "lists". Data needed by the console, called a "request" list, is presented to the primary as a random list of channel numbers. When the data are acquired,a parallel "answer" list is assembled to return the data to the console in the order it was requested. Each channel in the request list has an index number that is simply the location of that channel within the list. In the course of retrieving the data, secondary lists are generated, containing the index numbers, requested channel numbers and the answers grouped according to the linac station where the data originate.

A console request is serviced as follows: the primary receives the request list, gives it a list ID number and sends it to the secondaries using the all-parties address. All secondaries search the list for channel numbers they recognize and construct their own secondary request list and a secondary index list. Each machine cycle the secondary station goes through its request list and builds an answer list from readings in its data pool. The primary will poll once for the secondary index lists and poll each cycle for the secondary answer lists. When the primary performs the index poll,it will receive all of the secondary index lists grouped by secondary stations in the order the secondaries are connected to the loop. When the primary polls for the answer list (which it does at 15 Hz),the secondary answer list will be in exactly the same order as the index list. The primary can then use the entries in the index list as pointers to the console answer list for returning the data to the console.

Using the technique described here, neither the console nor the primary needs to know which secondary is responsible for measuring each data channel; the secondary itself can recognize its own channels and respond accordingly. Also the primary does not know (or need to know) how many stations will respond or how long their response will be. The primary simply receives messages till the poll is finished. Secondary stations may be added to or taken from the loop without changing the primary's software. New data channels would become active automatically; data channels that are not recognized by any secondary would simply not be updated. This sequence is repeated for other consoles or requestors. Note that a requestor may be a secondary station on the loop. By this mechanism a local station can request data from any other station on the loop, so that the operator at any secondary could select a display that would show, for example, the gradient of all nine linac tanks along with the preaccelerator high voltage and source pressure. By keeping the lists separate for each requestor, the primary can cancel a given list with a single short transmission to the secondaries. The addition or cancellation of one list has no effect on other lists.

In normal operation the lists are relatively static, changing on the order of seconds or longer. When the operator calls up a new display, that act will usually result in the cancellation of an old list and the generation of a new one. The new list will remain active as long as the console display is selected. It makes little difference to the secondary if a given list is polled on a given cycle or not. The primary can choose to poll certain lists less frequently, such as only on beam cycles. Answer lists in the secondaries would be overwritten with new data each cycle in any case. Servicing the poll sequences is done at an interrupt level so that monitoring of the data can proceed at the background level.

Timing Considerations

To achieve the interactive feel of the control room consoles, careful attention must be given to servicing the console requests immediately. With the system described here, it is felt that

a console request list presented to the primary during one cycle will be transmitted to the secondaries during the same cycle and data will be polled from the secondaries on the next and all succeeding cycles. Settings sent to the primary will be passed on to the secondary on the same cycle, and changes in the hardware will reflect the changed settings on the next cycle.

Detailed timing is calculated assuming the instruction set of the MC6809 CPU. This processor is now available and is particularly adept at handling lists of data and addresses. The primary station can service one message and be ready for the next message in about 100 μs. To this one must add 50 μs for the transmission time of the six bytes of SDLC protocol, so the message overhead is about 150 μs per responding secondary. For a poll that results in 10 secondaries returning 50 bytes of data, the total time of the poll is less than 2 ms. Even if 10 such polls were conducted each cycle, only 20 ms of the 67 ms cycle would be needed for collection. The time to sort the data for return to the console in the order requested is 20 μs per channel.

An application program that plots all the linac quadrupole currents at 15 Hz, results in a request for 171 words (342 bytes) of data. This request takes 4.3 ms to collect and 3.4 ms to sort, for a total of only 7.7 ms. These times indicate that the system is fast enough to service several consoles at 15 Hz.

Present Status

Although no decision has been made regarding a replacement for the linac control system, we are implementing this system to the point that a link controller will communicate with several secondaries and with a separate processor that supports an operator's console. At this stage we can confirm the timing calculations and study the integrity of the SDLC loop communications.

A local console described here has been fabricated using Multibus card cages and commercially available A-D, D-A, memory and binary I/O cards. The console controller card, including the Video RAM display, keyboard, shaft encoder interface and two bytes of sense switches and status indicators, has been prototyped. This console is now being used to control the negative ion source in the terminal of the second Fermilab preaccelerator.

The SDLC-DMA link has been operated at 1 MHz and has shown that messages can be sent error free from one processor to another. A Multibus single board computer card that includes the MC6809-SDLC-DMA combination is being fabricated.

The distributed control system described here is a reasonable replacement for the existing linac control system. The 1-MHz SDLC loop is fast enough to collect all the data in a single cycle, although we expect to transmit only the data requested by the consoles. Limit checking and software closed loops will be done in the local stations. Because of the modularity and local console facilities, the system should be much easier to maintain than the existing system.

References

1. E. W. Anderson, H. C. Lau and F. L. Mehring, "The Computer Monitoring and Control System for the NAL 200-MeV Linac", Proc. of the 1970 Proton Linear Accelerator Conf., Natl. Accel. Lab., pp. 451-469.

2. R. W. Goodwin, R. F. Kocanda and M. F. Shea, "A Microprocessor-Based Preaccelerator Control System", Proc. of the 1976 Proton Linear Accelerator Conference, Chalk River, Ontario, AECL-5677, pp. 264-268.

3. R. W. Goodwin and M. F. Shea, "The Microprocessor-Based Control System for the Fermilab Cancer Therapy Facility", Trans. Nucl. Sci., NS-25, 496(1978).

4. American National Standards Institute, ANSI Pub. No. BSR X3.66.

5. International Business Machines Publication Nos. GA27-3093-1 and GA27-3098-0.

1979 LINEAR ACCELERATOR CONFERENCE

DISTRIBUTED CONTROL SYSTEM FOR THE FMIT*

J. A. Johnson, D. R. Machen and R. M. Suyama†
Los Alamos Scientific Laboratory
Los Alamos, NM 87545

Summary

The control system for the Fusion Materials Irradiation Test (FMIT) Facility will provide the primary data acquisition, control and interface components that integrate all of the individual FMIT systems into a functional facility. The control system consists of a distributed computer network, control consoles and instrumentation subsystems.

The FMIT Facility will be started, operated and secured from a Central Control Room. All FMIT systems and experimental functions will be monitored from the Central Control Room. The data acquisition and control signals will be handled by a data communications network, which connects dual computers in the Central Control Room to the microcomputers in CAMAC crates near the various subsystems of the facility.

Introduction

The FMIT Facility will contain a 100-mA continuous-beam deuteron accelerator and lithium target that will be used to produce 14-MeV neutrons for materials research,[1,2] and will be directed toward the development of containment materials for use in a controlled thermonuclear fusion reactor. The facility will be built at Richland, Washington, and will be operated by the Hanford Engineering Development Laboratory (HEDL). In addition to doing the FMIT accelerator design, the Accelerator Technology Division of the Los Alamos Scientific Laboratory (LASL) will build a prototype of the front end of the accelerator at LASL. The primary purpose of the prototype construction is to permit the development of a suitable injector and appropriate beam-diagnostics devices and to prove the radio-frequency quadrupole (RFQ) concept for this application.[3,4,5]

System Design

A layout of the proposed accelerator showing where the control system will connect to the various facility subsystems is depicted in Fig. 1. The control system consists of a distributed computer network, control consoles and several Instrumentation Subsystems (ISS). The FMIT facility will be started, operated and secured from a Central Control Room (CCR). All system functions will be monitored from the CCR; all data acquisition and control signals will be transmitted over a communications network that connects the main computer system in the CCR to microcomputers that are located in CAMAC[6] crates near the various subsystems of the accelerator. A block diagram of the distributed control system is contained in Fig. 2.

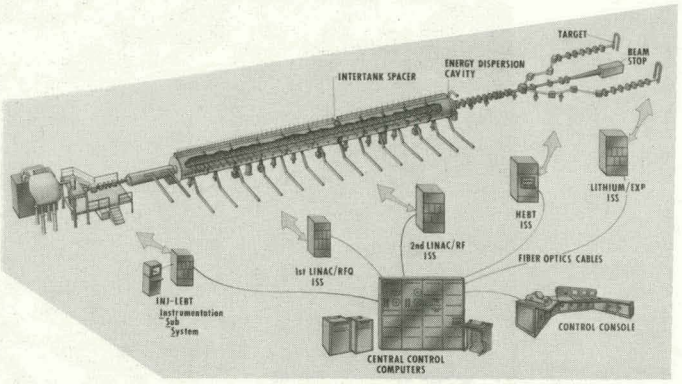


Fig. 1 The FMIT Accelerator showing facility control system connections

The main computer system consists of dual mid-to-large capacity minicomputers (PDP-11/60s for the prototype, PDP-11/70s for the FMIT facility). Two large, dual-ported disks, with a 176-million byte (67 million byte, for the prototype) storage capacity will be connected to the main computers. The operator will interact with the facility through the control consoles, the primary control computer and (via a communications network) to LSI-11 computers with CAMAC hardware at the local level.

The FMIT facility will have two system consoles, each consisting of a 19-inch raster-scan, color-graphics display scope, with touch-panel, track ball and keyboard. Two control knobs with plasma and touch panels, and a small black/white "menu" touch-panel/CRT complete the console. The knob, touch-panel and display will be used to connect control variables to the knobs and input variables to the application codes. The color scope will be used primarily to display summary or detailed system diagrams with current status of data channels associated with that system. Plots of the results of emittance calculations or of other data-reduction codes can also be displayed on the color scope. Finally, a high-resolution storage CRT will be

*Work performed under the auspices of the U. S. Department of Energy.
†Westinghouse-Hanford Company, Hanford Engineering Development Laboratory employee working at the Los Alamos Scientific Laboratory.

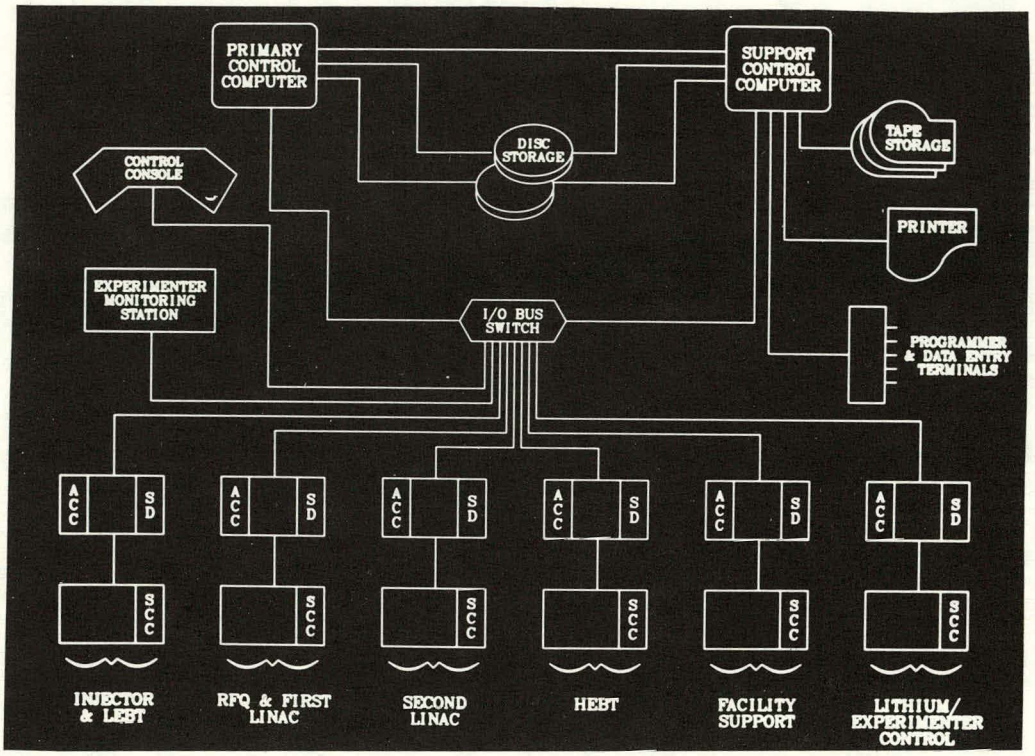


Fig. 2 Block diagram of the FMIT Facility Control System.

included for display of information requiring 10-bit by 10-bit resolution.

The support computer will be used for software development, data-base maintenance, operator training, data analysis and as a back-up for the primary computer.

The concept of a support computer has the advantage of making significant computer time available for software development without conflicting with facility operation. In a develop mental or experimental environment, software development is not permitted on a process control computer for several reasons: a system crash caused by an error in a program under development is probably the main reason for this restriction; overloading of the control computer can be another significant factor. Functions that do not fit well within real-time control constraints can easily be accomplished on the support computer. These include updating data-base files (which requires manual input); retrieving data from the data base (which requires a large number of disk accesses); and generating reports and operational logs. Large data-analysis codes, requiring significant computer time to run, would be included in these functions; the support computer has the peripheral equipment required to accomplish these tasks. These peripherals include program and data entry terminals, line printer, magnetic tape drives and access to the dual-ported disks. The primary computer is linked to the console, the dual-ported disks and through the data communications network to the Instrumentation Subsystem microcomputer nodes.

Interfaces Hardware

There will be at least six Instrumentation Subsystems, each of which will consist of one or more CAMAC crates and modules to interface FMIT Systems to the Control System. In each ISS, the node, or primary crate will contain an LSI-11 based Auxiliary Controller[7] (ACC) to serve as a communications controller for the Digital Equipment Corporation Network Software (DECNET). This ACC will also control a number of interface modules in the node crate. When the required number of CAMAC modules for a subsystem exceeds the number of slots available in the node CAMAC crate, a CAMAC Serial Highway[8] driver will be added to connect additional crates via the Serial Highway and Serial Crate Controller. It will also be possible to install additional ACCs in these added crates to provide dedicated processing capabilities at a specific area.

Software Design

The software is designed to be structured, modular and data-base driven.[9] The software requirements indicate the need for a layered structure that consists of a set of modules that interact with the console to interpret the operator instructions and to control the displays. There will be a number of modules

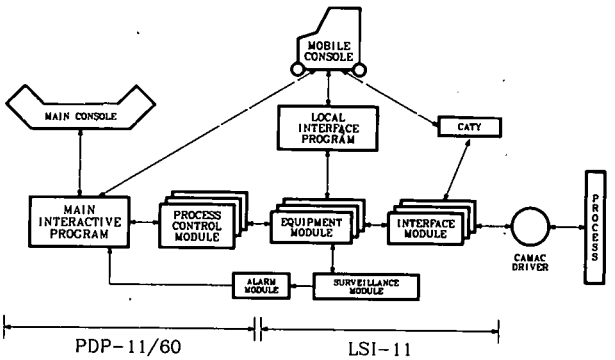


Fig. 3 Simplified software organization.

that will do the process control. A set of Equipment Modules (EM) will interact with the different equipment types. The lowest layer will contain hardware Interface Modules (IM), one for each type of CAMAC module used in the system. A block diagram of the software structure for the FMIT Control System is shown in Fig. 3.

There will be an executive task that is running at all times. This task is data driven and checks, interprets and calls the required Operator Interaction Module (OIM). The OIM will complete the interpretation of an operator command and call the proper display module (if one is required). After the required Process Control Module (PCM) is called, the OIM will transfer the commands to the PCM. The PCM contains the intelligence to progress through a sequence of EM commands to perform the required task. There will be no "wait" in the EM so that the system will not be required to wait until the response to the given command is received. Thus, commands to various EMs can be given in sequence, and other tasks can be performed before returning to insure that the proper responses have been obtained. The EM has access to a data base that contains, for example, the information to convert command settings to raw units; i.e., volts, milliamps, etc.; and to convert data from raw units to engineering units. The CAMAC addresses of the appropriate channels will also be contained in the data base.

Finally, the commands to the hardware are delivered to the Interface Module (IM) that interacts with the CAMAC hardware to complete the required functions.

The OIM and the Interactive Display Modules (IDM) must reside in the primary control computer so that operator response is acceptable. In addition, the primary control computer will make use of the disk for storing the large number of Process Control Modules that will be required, and the large files required to drive the color-graphics scope. The EMs will be located in the LSI-11 microcomputers if memory constraints permit. Certainly the IMs will reside in the LSI-11 memory. The LSI-11 must also have a Surveillance Module (SM) that will check selected data channels in each subsystem and notify the operator if any channel drifts out of preset limits.

The SM will be table-driven with scan rates set according to the response time of the process being monitored. A requirement to support a local terminal for equipment check-out and stand-alone operation can be satisfied by a Local Interface Module (LIM). This module will convert commands from the local operator into appropriate commands to the EM. In addition, the interpretative language, CATY,[10] will be available to test, or to exercise, the hardware and requires only a knowledge of the various CAMAC addresses.

Network Communications

Communication with the various Instrumentation Subsystems will be accomplished through the utilization of DECNET or a subset of DECNET. The DECNET software will be used between the main computers (primary and support) and between the primary computer and the LSI-11s located in the CAMAC crates. Any other LSI-11s that are needed, other than the node computers, will be used to perform a specific task and will communicate with the node computers over the CAMAC Serial Highway.

Conclusions

The control system for the FMIT Facility is a distributed, modular system in both the hardware and software. The computer hardware will be purchased from a single computer manufacturer. The primary and support computers will be identically configured, will use the same operating system, and the microcomputers will be of the same computer family. The microcomputer operating system will be a memory-resident subset of the operating system used in the main computers. The software will be structured and modular, and the same high-level language will be used for all of the application software. The software will be distributed, with the portion supporting the operator located in the primary computer and the portion interacting with the hardware located in the LSI-11 Auxiliary Controller. The data base will be distributed in the same way.

This approach should provide a control system for the FMIT that will be flexible, easy to maintain, and one that can easily be extended.

Acknowledgments

The authors would like to acknowledge the hard work and dedicated efforts of the joint LASL-HEDL team presently developing the details of the FMIT Control System, and to thank Dr. Axel Daneels of the CERN PS Controls team for his contribution to the software system design.

References

1. R. A. Jameson, "High Intensity Deuteron Accelerator (FMIT)," IEEE Transactions on Nuclear Science, Vol. NS-26, No. 3, Part 1, 2986 (1979).
2. E. L. Kemp, D. J. Liska, M. D. Machalek, "The Fusion Materials Irradiation Test (FMIT) Accelerator," to be published in the Proceedings of the 1979 Linac Conference.
3. J. D. Schneider, D. D. Armstrong, H. L. Rutkowski, B. S. Sherwood, E. A. Meyer, L. L. Catlin, "Development of a High-Current Deuteron Injector for the FMIT Facility," to be published in the Proceedings of the 1979 Linac Conference.
4. C. W. Fuller, S. W. Williams, J. M. Potter, "Mechanical Design Considerations in FMIT RFQ Developments," to be published in the Proceedings of the 1979 Linac Conference.
5. O. R. Sander, G. N. Minerbo, D. D. Chamberlin, R. A. Jameson," Beam Tomography in Two and Four Dimensions," to be published in the Proceeding of the 1979 Linac Conference.
6. "CAMAC - "A Modular Instrumentaion System for Data Handling," ANSI/IEEE Standard 583-1976 and EURATOM Report EUR-4100e (1972).
7. "Multiple Controllers in a CAMAC Crate," ANSI IEEE Standard 675-1979 and EURATOM Report LUR-6500e (1978).
8. "IEEE Standard Serial Highway Interface System (CAMAC)," IEEE Standard 595-1976, and EURATOM Report LUR-6100e (1977).
9. A. Daneels, "FMIT Control System Software - Proposed Layout," Accelerator Technology Division internal report, July 1979.
10. F. Golding, "CATY - or Let's Keep Things Simple," Proceedings of the Real-Time Data 79 Conference,21-26 October 1979, Berlin (West), Germany.

1979 LINEAR ACCELERATOR CONFERENCE

LAMPF FIRST-FAULT IDENTIFIER FOR FAST TRANSIENT FAULTS*

Arthur R. Swanson and Robert E. Hill
Los Alamos Scientific Laboratory
Los Alamos, New Mexico

Summary

The LAMPF accelerator is presently producing 800-MeV proton beams at 0.5 mA average current. Machine protection for such a high-intensity accelerator requires a fast shutdown mechanism, which can turn off the beam within a few microseconds of the occurrence of a machine fault. The resulting beam unloading transients cause the rf systems to exceed control loop tolerances and consequently generate multiple fault indications for identification by the control computer. The problem is to isolate the primary fault or cause of beam shutdown while disregarding as many as 50 secondary fault indications that occur as a result of beam shutdown. The LAMPF First-Fault Identifier (FFI) for fast transient faults is operational and has proven capable of first-fault identification. The FFI design utilized features of the Fast Protection System that were previously implemented for beam chopping and rf power conservation. No software changes were required.

Introduction to LAMPF Fast Protect System

During production runs of 500-μA average proton beam current, LAMPF typically has a 640-μs beam gate at 120 Hz and 8% duty factor. With a 120-Hz repetition rate a machine cycle has a 8.33-ms period. Within each machine cycle the beam gate controls the proton beam by turning the injector arc current on or off to follow the beam gate.

The LAMPF Fast Protect System (FPS) receives various timing gates and monitors beam-spill detection systems, personnel safety, machine run permit, rf stands, and injector parameters for fault conditions to ensure beam gates are allowed only when beam-on conditions are satisfied. If a fault occurs during a prescribed gated period when beam gate is allowed, the FPS will inhibit beam gate or a fraction thereof and thereby turn off beam. If beam gate is inhibited by FPS, a computer interrupt is generated. Within the interrupted machine cycle the computer interrogates each device that inputs the FPS for fault detection and displays the results. The FPS and any latched faults are reset each machine cycle. The beam gate following an inhibited beam gate will be allowed provided the fault has cleared. Latching circuits also prevent a beam-on condition during a machine cycle once a fault has occurred just in case a fault clears or is intermittent during a beam gate. This prevents fault modulation of the beam which is considered an undesirable injector operating mode.

*Work performed under the auspices of the Department of Energy.

FPS Timing

The FPS dynamic characteristics are controlled by gates produced by the LAMPF Master Timer. Master Timer gates are manipulated according to accelerator modes and conditions for power savings and to blank rf beam loading transients. The FPS uses the variable gates to generate internal gates and logic. Figure 1 represents a typical set of gates generated during a machine cycle for a 640-μs beam gate.

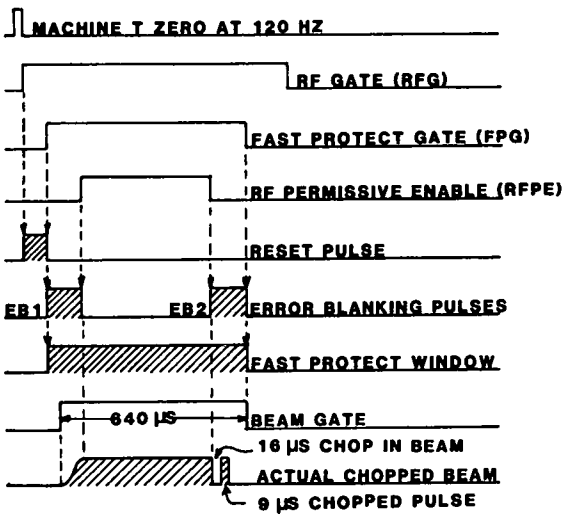


Fig. 1. Fast Protect System Timing

The machine T-zero pulse marks the start of a machine cycle and is used as a fault reset pulse by numerous modules having inputs to the FPS. The rf gate (RFG) defines when rf power is on. The leading edge of RFG and FP gate (FPG) starts and ends the FPS reset pulse. RFG "ANDed" with FPG defines the FPS window during which beam gate is allowed. Error blanking pulses (EB1 and EB2) are formed by the "exclusive OR" of FPG and RF Permissive Enable (RFPE) gate. The actual beam formed by the 640-μs beam gate has been chopped for 16 μs to allow for a fast kicker magnet turn-on to deflect the trailing portion of the beam into a secondary beam line.

FPS Transmission Line

As shown in Fig. 2, a 15-Vdc FPS transmission line (FPXL) is routed in and out of FPS chassis located throughout the accelerator and terminates in a voltage level detector located in the injector FPS chassis. If the FPXL is less than 8.2 Vdc, arc current is turned off by inhibiting the permissive pulses formed by beam gate. All FPS chassis pull the FPXL down to 5 Vdc outside of the FPS window described in Fig. 1, thereby preventing beam outside the FPS window. If any FPS chassis senses an input fault condition during the FPS window, it will pull down the FPXL to 5 Vdc, thus turning off beam. It takes approximately 2 to 4 μs for a detected fault to inhibit the beam gate permissive signal. About 6 μs after a fault, injected beam intensity starts to decline. It takes another 6 μs for the beam intensity decrease to translate to the end of the beam line. The LAMPF First-Fault Identifier for Fast Transient Faults (FFI) utilizes the 6- to 12-μs time delay between fault detection and beam decrease for blanking fault messages resulting from rf beam unloading.

First-Fault Identifier (FFI)

The FFI system mechanization was a spinoff from FPS design changes incorporated to solve problems caused by an accelerator requirement to chop beam. When a hole is chopped into a high-intensity proton beam, the rf servo system responds to a rapid beam unloading transient condition that can cause rf stands to exceed phase and amplitude error fault limits and go out of lock. The FPS which monitors rf stands would detect faults at the chopping point, turn off beam, and leave no trailing pulse to kick into the secondary beam line. When the FPS turns beam off, the FPS computer interrupt would cause the computer to register fault messages for all out-of-lock rf stands and overload the display scope. This turned out to be true, not only for chopped beam, but also anytime the FPS happened to turn off the high-intensity beam for any fault condition. The need for a first-out fault identification system became self-evident.

RF Permissive Enable Gate (RFPE)

In order to prevent rf stands from setting faults during chopped beam unloading transients, it was necessary to gain additional control over rf stands. RFPE gate (see Fig. 1) was added to all rf stand control modules to define the window when rf faults could be set. The window also defines when rf module inputs to the FPS must be in a "go" state. Figure 3 shows a simplified rf stand module. RFPE and rf gates must be present in order to set the rf fault bit flip-flop for the computer. RFPE is also gated through the rf stand module to the sector FPS chassis provided rf servo phase error is < 1°, amplitude error is < 1%, and cavity field is > 50%. In the sector FPS chassis the inputs of all respective sector rf stand modules are "ANDed" together and then "ORed" with error blanking pulses.

Error Blanking Pulses (EB1 and EB2)

The error blanking pulses (see Fig. 1, EB1 and EB2) are "ORed" with the rf stand module inputs in order to complete the "Fast Protect (FP) Window." As stated before, the FP window defines when beam gate is allowed. Error blanking pulses make it possible to run beam during EB1 and EB2, even though rf stands may be out-of-lock. By chopping beam under EB2, rf beam unloading transients can be ignored.

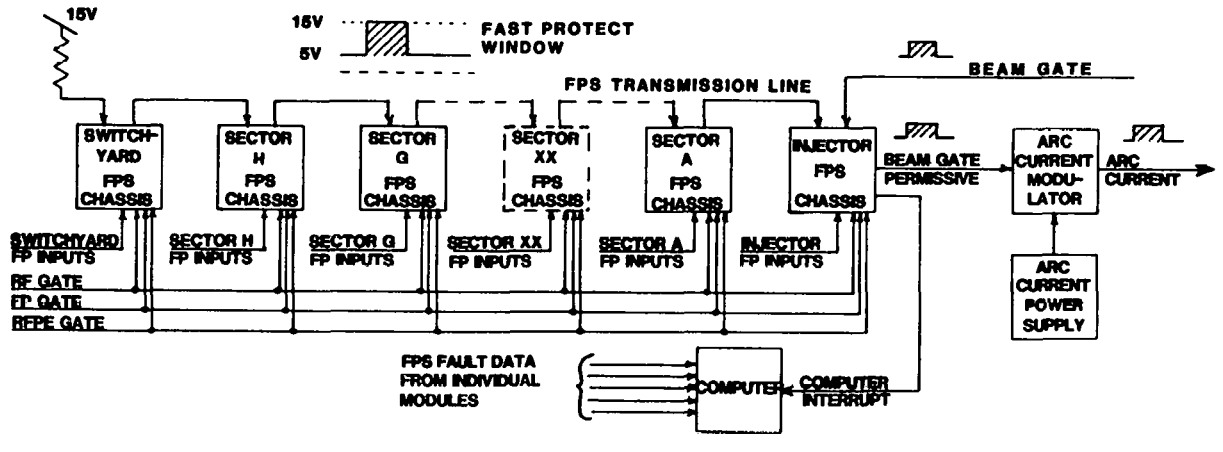


Fig. 2. Simplified Fast Protect System

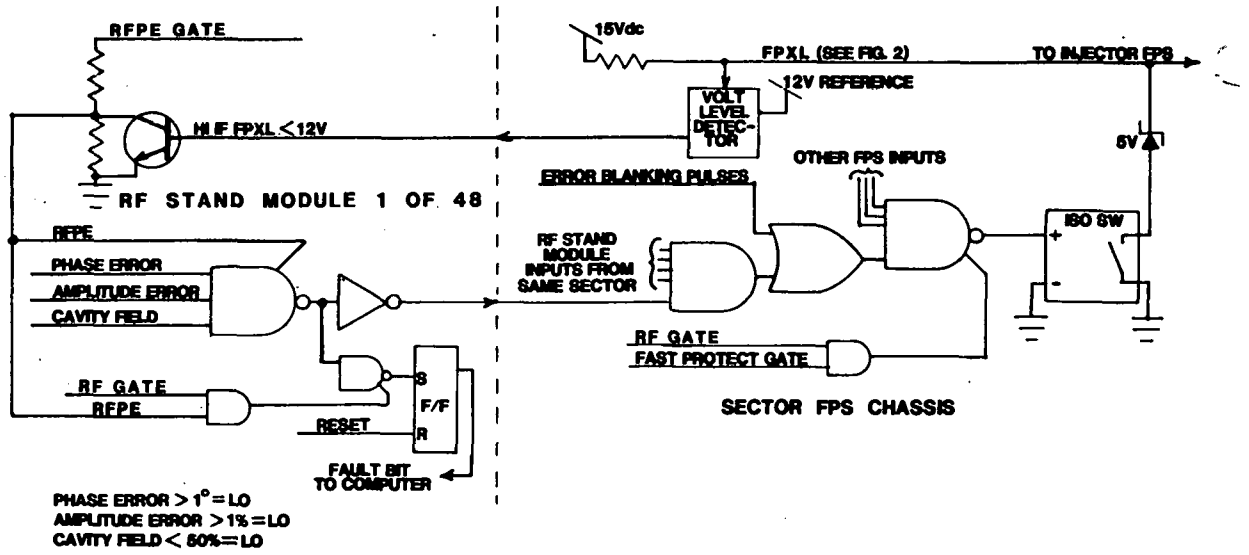


Fig. 3. Simplified First-Fault Identifier Logic

EB1 was originally incorporated to save rf power. The injector arc current could be turned on under EB1 prior to having all rf servo systems in lock. This allowed the injector to build up beam intensity early, while rf servos were coming into lock rather than wasting power waiting for in-lock conditions before turning on arc current. Recent improvements in the rf feed-forward system and reduced Klystron voltage have limited the usefulness of EB1. EB1 is still used to block rf turn-on transients as an aid while tuning beam after a shutdown. When future higher beam currents are employed, the usefulness of EB1 may increase.

The variable error blanking pulses are minimized and used with discretion, because masked rf problems can cause serious beam spills. Beam-spill detection systems are always active and offer some protection. As a precaution the FPS limits EB1 and EB2 pulse widths to 70 μs.

The most important feature of EB1 and EB2 is that in combination with RFPE they are extremely useful and flexible tools for handling unforeseen machine requirements and conditions.

First-Fault Identifier Implementation

As stated before, anytime the FPS turns off high-intensity beam, secondary faults due to the beam unloading transient can occur. Figure 3 shows how the secondary fault messages from rf stands are blocked. A voltage level detector in each FPS chassis monitors the 15-Vdc FPXL. Whenever any FPS chassis detects a fault, the entire FPXL is pulled down to 5 Vdc to turn off beam. The voltage level detector in all the FPS chassis sense when the FPXL drops below 12 Vdc and responds by turning on a transistor, which grounds RFPE gate to the rf stands. By grounding RFPE gate before the beam unloading transient occurs, secondary rf fault messages are avoided.

Conclusions

The LAMPF First-Fault Identifier for Fast Transient Faults system has proven to be a very effective and flexible tool. Being able to adapt the FPS and FFI to new and different machine requirements and conditions through variable Master Timer gates has many advantages. In any case, where beam unloading transients are anticipated, one should consider implementing some flexible mechanism for coping with potential problems.

COMPUTER CONTROLLED FORMATION OF THE 750-keV ACCELERATING COLUMN ON THE NEW CERN 50-MeV LINAC

H. Haseroth
CERN, Geneva, Switzerland

Summary

The advantages of the simple design and construction of the CERN high gradient double gap accelerating column are partially counter-balanced by a sometimes (depending on vacuum conditions) lengthy and manpower wasting formation procedure. After the introduction of a radiation measuring facility, rather than the usual cathode current monitoring, as criterion for increasing the HV, a strategy has been worked out for automatic formation. This strategy has been implemented in a computer program to run on the Linac Control Computer (PDP 11/45). The advantages are : faster formation, smaller number of breakdowns and no operator needed. This paper describes the hard and software necessary and the "teething problems".

Introduction

The 750-keV preinjector of the new 50-MeV CERN linac has a double gap short column (Fig. 1) based on the design of the 500-keV unit of the old CERN linac.[1,2] The gap sizes are 61 and 68 mm, respectively, giving a total gap, excluding the thickness of the intermediate electrode, of 129 mm, which gives an average gradient of 58 kV/cm. The electrodes are made of titanium. The outside of the column, surrounded by normal air, consists of 19 sections of 65 mm thick porcelain rings interlaced with thin metal discs and bonded with epoxy (Araldite). This construction is fairly simple but requires very clean vacuum conditions, i.e., hydrocarbon partial pressure of $\leq 10^{-10}$ mbar, otherwise breakdown of the column occurs frequently and radiation levels can be extremely high.

Process of formation

The high sensitivity to pollution also makes the formation of the column up to 750 kV a lengthy and time consuming process. The total time needed to reach the operating voltage and the total number of breakdowns occurring during this process are very much dependent on the operator. There are several "theories" about formation. Some people believe that there is a minimum number of breakdowns which one cannot avoid, in order to reach, under given conditions, the operating voltage. Others believe the number of breakdowns to be inversely proportional to the formation time. Additionally there are several ways of increasing the HV when watching, for example the column cathode current ; namely :

- keeping the cathode current at a constant a) low level ; b) high level.
- increase the HV only when the cathode current has decayed to less than say 1μA.
- increasing the HV in large steps ;
- increasing the HV in small steps ;
- reduce the HV if the cathode current keeps increasing ;
- reduce the HV only if the cathode current jumps up ;
- never reduce the HV and tolerate the breakdown(s).

It is very difficult to decide which of these assumptions are correct, because the operator, as a human being, does not apply his ideas consistently over (sometimes) several hours. In addition, the ease of formation depends very much on different boundary conditions such as vacuum (total and partial pressures), previous treatment of the column, total amount of recent time during which no HV was applied, number of breakdowns and surface layers on the electrodes. It is clear that only control by a computer can guarantee the application of a certain strategy for a sufficiently large number of times, so that a conclusion as to which technique is the most successful can be drawn. An examination of old statistics (Fig. 2)[3] seems to confirm this.

Thus there is a certain academic reason to get the computer to do the formation. There are also three very practical reasons :

- the operator's time can be used for something else ;
- the computer is reacting faster than an operator, i.e.,
  a) the formation time could be shortened;
  b) possible breakdowns can be avoided by lowering the HV before a breakdown might occur.
- a reduced number of breakdowns (by applying the proper strategy) gives a longer life to the different HV components.

Hardware

There is a computer control (command) for the HV with acquisition of the HV the radiation level, the cathode current and the vacuum (total) pressure from a Penning gauge. The cathode current is read from a resistance connecting the cathode to ground using the appropriate protections against voltage transients in case of breakdown.

It should be mentioned here that the system is able to send out one set of command values, and to acquire one set of parameters, per machine cycle which is normally about 1 sec.[4] This implies that it is not necessary to make complicated calculations as to what moment to read or to set a parameter ; for example, if the program asks twice to read a parameter, the second reading will be taken automatically on the next linac pulse. This simplifies the programming but limits, on the other hand, the response time of the program if it decides, for example, to lower the HV after having looked at the radiation. Nevertheless experience has shown that the response time seems to be adequate, and is certainly much better than the response of an operator who has stood in front of the control panel for some hours.

The radiation is measured with a conventional Geiger Muller tube (Philips ZP1220 for sensitivity reasons), which needs only one coaxial cable to feed power to its associated electronics and to transmit the signal. Thus it is possible to move

the counter easily in order to find its optimum position.

The reason for measuring the radiation is partially the fact that it is easy to get a clean signal that does not carry any transients to sensitive equipment in case the column breaks down. In addition, the monitoring of the cathode current does not necessarily measure all the current that flows to ground, but only the current flowing via the cathode. However, if there is cathode current it will also produce radiation. So the radiation is the more complete measurement of what is going on inside the column.

Program

The program is written in FORTRAN to run on the PDP 11/45 Linac Control Computer. It would have been equally possible (and much easier for debugging and modifications) to have written it in BASIC, but then linking it to a touch panel to call the program would have been impossible. Therefore, FORTRAN was used, profiting from available subroutines for controlling and acquiring parameters. Provisions have been made to store all the relevant data of a formation on two files so that some statistical analysis can be made later on, or to produce plots of different formations.

Ceneral outline of the program

The first part of the program consists of the usual housekeeping, reading and preparing files for storing the data. It asks the user also for two radiation levels which will influence the speed of the formation.

The second part contains essentially all of the logic for running the formation except for that contained in three subroutines:

- WATCH (Fig. 3)

This subroutine is called everytime a change has been made to the level of the HV. It looks at the radiation level and compares it to the reference values given by the user. It sets the corresponding logical variables to "true" if the radiation exceeds those values and returns control to the main program. If the radiation exceeds only the lower level, there is no immediate action except for setting the first logical variable to "true". The radiation will then be read again and will be compared to the previous value. If the radiation is going down, the program will read again and again until the radiation is below the lower level. The low level variable will then be set to "false" and control is returned to the main program. If the radiation on the other hand is going up, control will be returned immediately with the corresponding variable set to "true".

This method had been adopted because low levels of radiation normally tend to drop down, whereas high levels of radiation or increasing low levels, will frequently be followed by a breakdown.

- BREAK (Fig. 4)

This subroutine is called to decide in case of doubt whether there was a breakdown on the column that could have falsified the command or the acquired values. As a result of values read incorrectly, the program may decide that the formation is finished, or increase the HV further, even if in reality the radiation is already too high, thus causing another breakdown, or simply stay in a loop. As the idea of feeding the output of a special breakdown detector in the form of a status signal to the computer has been abandoned, a signal that may itself suffer from the breakdown, this subroutine looks at the acquired values and checks if they seem reasonable.

After having read the parameters, the latest acquisition value of the HV is compared to the previous one, as well as to the command value. If either of those differences is too large, a breakdown is assumed and the logical variable (as well as the two variables assigned to the radiation) are set to "true". If the result of the comparisons is normal, the cycle is repeated five times to verify that there is a stable HV situation.

- FORMFI (Fig. 5)

This subroutine is used to check if a formation can be regarded as finished and that the situation is not degrading after the desired voltage level has been reached. To check this, the subroutine BREAK and WATCH are called successively, and the message of passing both successfully is handed back to the main program via a logical variable.

The formation is going on in a loop of the main program. According to the level of the HV, an increment is chosen for increasing (or decreasing) the HV. After the program has sent a command to change the HV value, the next request will be issued only if the previous increment was set to at least 80%. This is again done by going through a loop. After three unsuccessful iterations, the subroutine BREAK is called to check for breakdown. If there is breakdown, the program will reduce the HV command value by five times the incremental value and the cycle will start again. If there is no breakdown, there are two more trials to wait for the desired result. If even this is negative, the program will switch off the HV when the hardware for the status commands is installed. At present the program just ignores this instruction, but until now there was no formation where the program arrived at this situation.

At the next step, after having asked for an incremental change in the HV, the subroutine WATCH will be called to check that the radiation is sufficiently low before the next increase of the HV level. Otherwise the HV will be slightly or drastically reduced, depending on the level of radiation.

Before every increase of the HV, the acquisition is compared with the nominal formation voltage. If this is reached or exceeded, subroutine FORMFI will be called and the validity of the formation will be checked. If the result is positive, a small correction will be calculated and the HV set exactly to the nominal value. After this, the last data are written onto the data files, some messages are displayed on the terminal and the program finishes.

Operational Experience with the Program

The first tests with the program were done by increasing the voltage only, because it was believed that with sufficiently small incremental values it would just be necessary to watch the radiation, and perhaps to stop increasing the HV, in order to avoid breakdown. It turned out that frequently it seemed much better to actually reduce the HV in order to avoid a subsequent breakdown. Another simple fault was that originally the program finished when one had reached the operating voltage. Sometimes only a few seconds later there were successive breakdowns and a drastic increase in radiation. This was the reason for introducing the subroutine FORMFI.

Less trivial problems occurred when having breakdowns in the course of formation. Sometimes the program would stop and claim that the formation was finished, sometimes it would simply stop. In order to discover the cause of this problem, command and acquired values were frequently displayed on the terminal together with information as to what point the program was at. It turned out that in the case of a breakdown there is not only "noise" coming to the computer, but more specifically the acquired values may be wrong. This was one reason for introducing the subroutine BREAK, and also to check in the main program if the previous command sent out was already successfully executed. In critical parts of the program values are read several times, to make certain that the situation was stable before drawing conclusions on how to continue.

Conclusions

With the computer controlled formation program, there is now a very quick and reproducible method of forming the accelerating column. A considerable amount of manpower has been gained and the formation is done without stressing unnecessarily the HV components. It is interesting to note that a typical formation after an ion source change used to take about three hours and cause about 20 HV breakdowns. With the help of the computer, the formation takes about one hour and causes only about ten breakdowns. By building up the statistics it is now possible to decide which are the best parameter settings for an optimum formation.

Acknowledgements

I would like to thank different people within the Linac Group who helped with the hardware and with the software, and last but not least, Th. Aarup, summer student in 1978 at CERN, working on the first version of this program.

References

1) E. Boltezar, H. Haseroth, W. Pirkl, G. Plass, T.R. Sherwood, U. Tallgren, P. Têtu, D. Warner and M. Weiss, The New 50-MeV Linac, this conference.

2) M. Hone, The Accelerating Column for the Preinjector of the New Linac, CERN Internal Report, in preparation.

3) F. Chiari and J. Knott, Le Fonctionnement du pre-injecteur du Linac en 1970, MPS/LIN/Note 71-4.

4) A. Cheretakis, J. Knott, P. Mead, A. v.d. Schueren and U. Tallgren, The Control System of the CERN New Linac, PS/LIN/Note 76-20.

Discussion

Bentley, NEN: Can you give an equivalent radiation level for your upper and lower thresholds?

Weiss: These lower and upper radiation levels depend on where you place your counter. I have shown that the counter has been placed a few meters away from the Faraday cage or the column. Placing it closer or further away would change the signal, so absolute radiation thresholds are meaningless. However, as I remember, the lower level is 0.2 rem and the higher is 1.4 rem.

Bentley: But that is not calibrated in terms of a radiation level at the column or at any particular distance?

Weiss: No, this is just something which has been found from experience.

Bentley: What is the time scale of your command steps?

Weiss: All the commands which are sent to our linac are synchronized to the linac pulse which is about once per second. So nothing will happen until the next linac pulse. Then, we first perform the data acquisition to see how the command has been executed and if the conditions for another command are satisfied. After that we can send out the next command. We have found this procedure to be extremely useful because one has just to press a button and go out of the room and come back in an hour and the column is formed.

Curtis, FNAL: When sparks or breakdowns occur during voltage conditioning of the column, is the high voltage power supply turned off or left on and just turned down in voltage?

Weiss: This program contains a subroutine which checks for breakdowns. If something unusual has been observed, for example, the command of the high voltage and the required valves are too far apart, the program checks to see if a breakdown has occurred. If so, it drastically drops the high voltage (I think it drops it 5 steps) and continues in the loop to check if it is enough or must go further.

Curtis: The power supply is not turned off then?

Weiss: No, it is not turned off.

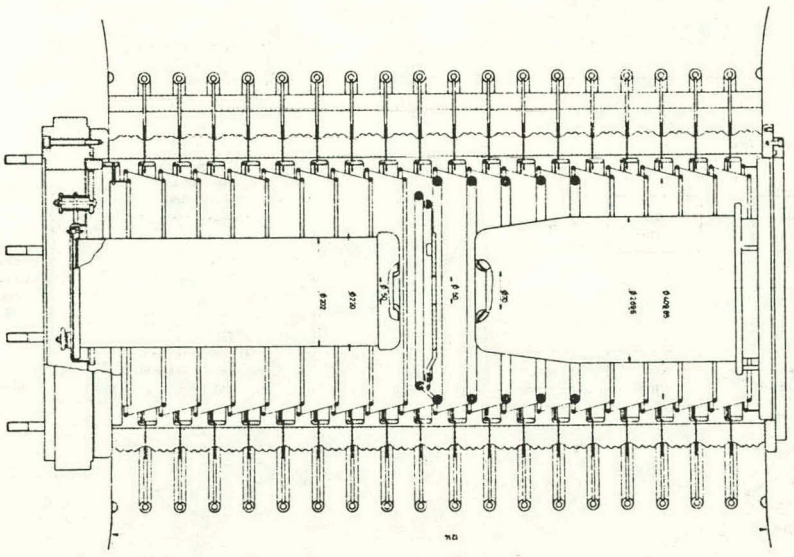


Fig. 1 Accelerating column

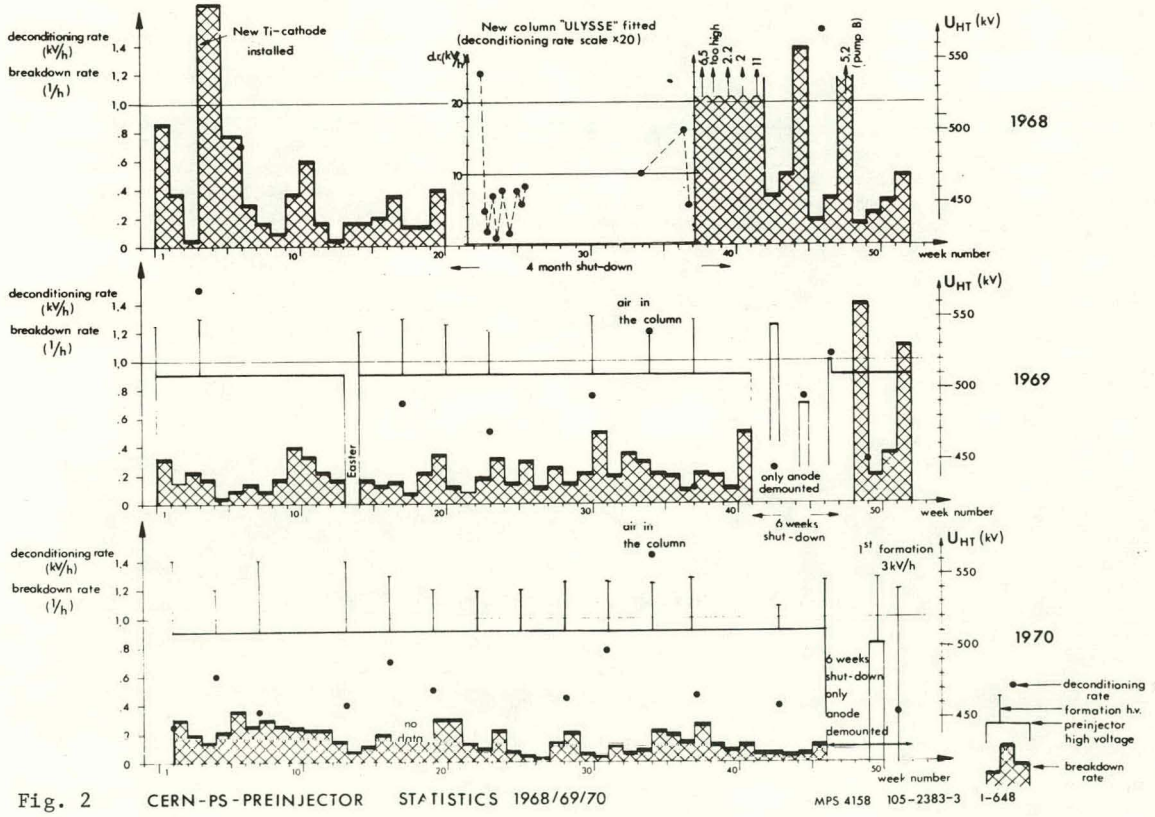


Fig. 2 CERN-PS-PREINJECTOR STATISTICS 1968/69/70

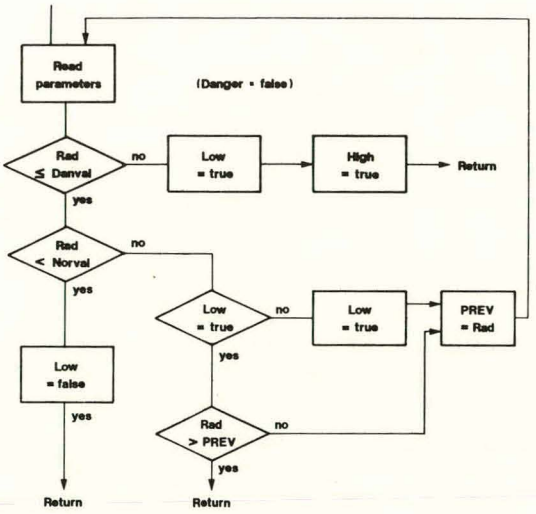


Fig. 3 Flow diagram for subroutine WATCH

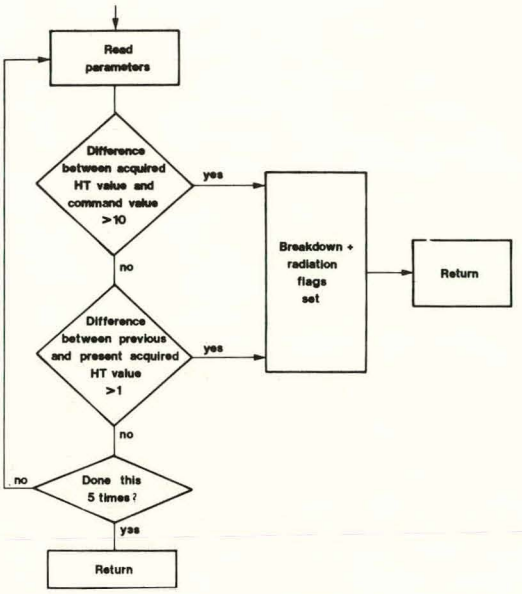


Fig. 4 Flow diagram for subroutine BREAK

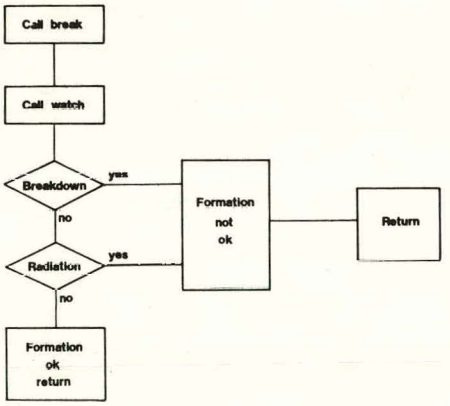


Fig. 5 Flow diagram for subroutine FORMFI

LONGITUDINAL AND TRANSVERSE BEAM OPTIMIZATION AT THE UNILAC

L. Dahl, J. Klabunde, P. Strehl, V. Schaa
GSI, Gesellschaft für Schwerionenforschung mbH
Darmstadt, Fed. Rep. of Germany

Summary

The different categories of beam optimization procedures are described, including both longitudinal and transverse phase planes. The description of the transverse computer-aided procedures concentrates on the low energy beam transport system, but these methods are applicable to the whole machine. In case of the longitudinal adjustment, typical procedures for the accelerator subsystems are presented. Present status, operating experiences and future development of the programs are reported.

Introduction

The frequent changes of accelerating conditions typical of a multi-particle, variable energy machine, tend to decrease the overall operational efficiency of the facility. Therefore efficient computer-aided operating procedures become essential.

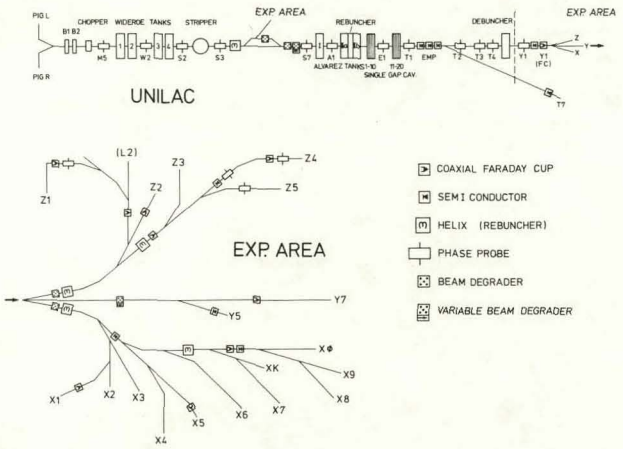


Fig. 1 Schematic diagram of the Unilac

Figure 1 shows a schematic diagram of the Unilac. From operating experience gained during the start-up phase and the subsequent routine operation, the major effort in the development of optimization procedures was focused on the following subjects:

low energy transport system from the ion source to the Wideröe preaccelerator; adjustment of the multi-stage rf accelerating system and its associated pre- and rebunching elements; energy variation by the single-gap resonator chain; high energy beam transport to the experimental areas and matching to the experimental setup; tune-up of time structure for the remote target stations with the rebuncher-debuncher system.

In the final stage, most of the procedures will be effective on-line programs which should contribute much to the accelerator performance. But the development of control programs featuring such advanced control functions requires a thorough understanding of the accelerator behavior. All hardware components have to be stabilized. Shortcomings of the computer system can have a considerable effect upon success. The present status of the Unilac is reported in a companion paper.[1] Discussion of the development of optimization routines will follow.

The extensive beam diagnostic system[2,3] at the Unilac proved to be extremely valuable for the development of operating procedures. In case of the longitudinal beam optimization, the signals of the phase probes, coaxial Faraday cups and semiconductors are mainly used. For the transverse optimization, the emittance measuring apparatus, profile grids and Faraday cups are required. The optimization procedures are based on combined use of these beam measuring devices and different transport computer codes. In the following sections the procedures will be described.

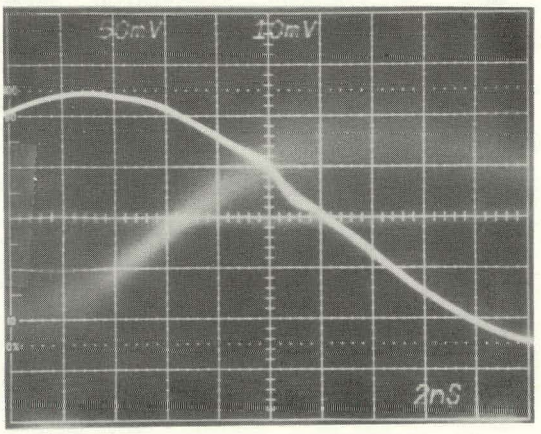
Longitudinal Matching Procedures

Many capacitative phase probes are positioned along the Unilac (Fig. 1) for use in energy measurements, correct setting of the rf amplitude and phase and matching of the different rf substructures. The time-of-flight method for energy measurements was described in detail in 1976[2] and in a separate contributed paper.[3] The advantages of the method are high accuracy and simple handling. The operations crew can quickly adjust and recheck the output energy of each accelerating substructure. The signals of phase probes T1, T2, T3, T4 (see Fig. 1) are now used for a computerized on-line measurement of the energy. The energy is displayed on the main control room console with a high refresh rate. Electronic devices and data processing are also described in Ref. 3.

Longitudinal matching procedures of rf substructures will be described in the following two sections: adjustment of the prebuncher system and matching of the pre- and poststripper accelerator. Up to now these procedures were under manual control; computer control was envisaged but with a low level of priority.

Two buncher cavities at 27 MHz are installed in front of the Wideröe prestripper accelerator.

The beam pulses from the dc preaccelerator have to be matched to the phase acceptance of the Wideröe linac. For correct setting of the rf amplitude and phase of both cavities, the following adjustments must be made: The unbunched beam must be injected in the first Wideröe tank at the injection energy of 11 keV/u. The bunch structure can be measured by the phase probes behind the first tank. Each bunching cavity is powered separately. The rf phase is adjusted to the value at which no displacement of the bunch signal occurs. An indication of the correct phase is the increase of intensity and an improvement of the bunch structure. Now with the correct setting of buncher phases, corresponding to a reference phase of -90°, the amplitudes are optimized for a maximum beam intensity. The structure of the prebunched beam can be measured by the phase probe (M5) in front of the Wideröe tank. Figure 2a shows the time relation between the bunch signal and the rf signal of the first Wideröe tank at the correct settings of the buncher cavities.



M5

Fig. 2a Time relation between the signals from phase probe behind the prebuncher and the rf amplitude of the first Wideröe tank

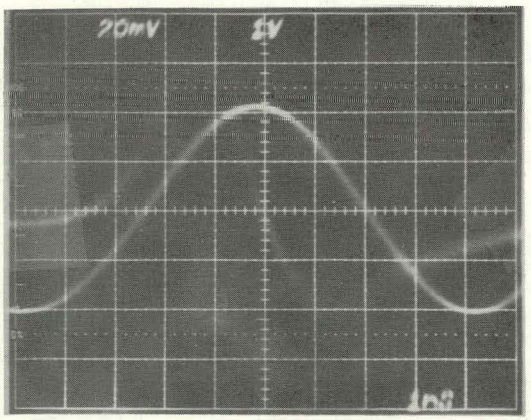


Fig. 2b Bunch position with respect to the rf signal of the first Alvarez cavity

The operators use this display for the adjustment of the injection energy. The sensitivity is quite high; a change of the dc accelerating voltage by 10^{-3} results in a bunch displacement of 1 nsec.

The output energy of the prestripper accelerator can be changed in a range of ±2% without deterioration of the time structure of bunches. In this way it is possible to adjust the design injection energy of the poststripper accelerator. The energy can be measured very accurately by phase probes S7 and A1 (distance 14.4 m, sensitivity for deviation from the design input energy of Alvarez $1\ \Delta W/W\ (\%) \sim 0.23 \cdot (6.6 - \Delta t\ (\text{nsec}))$). Taking the fixed relation between the rf tank and S7 phase probe signals, the precise rf phase of the first Alvarez tank, determined experimentally, can be adjusted and checked during routine accelerator operation (Fig. 2b).

The change of energy due to the damage of stripping foils at high beam intensities, results in a noticable displacement of the bunch signal. This change influences the beam quality considerably. Measurements are presented in Ref. 3.

With intensities of few μA U^{9+} at the stripping foil, for instance, an energy change occurs after only 1 hour of operation. At present the operator has to check and readjust for correct operation. Mainly for experiments, the efficiency of the machine drops drastically. A project exists for automatic control by a microcomputer based system. The proposed procedure is shown in a program flow-chart (Fig. 3).

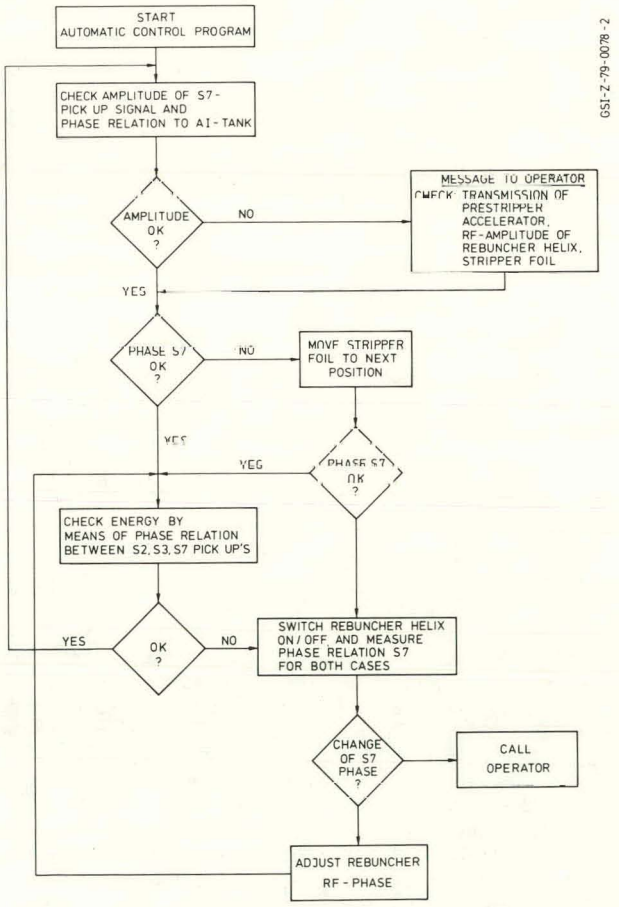


Fig. 3 Schematic diagram of on-line control in stripper section

In the following paragraphs two procedures are described which are largely computer-aided. Since the rf system has not been under computer control, the optimized settings of rf amplitude and phase are manually controlled. The design of a microcomputer based control system for the rf system was started in parallel with changes of the rf hardware and should be ready at the end of 1980.

The final energy of the Unilac can be varied in a broad range by the 20 single-gap cavities; a maximum effective accelerating voltage of about 24 MV can be generated. Energy changes are required often, sometimes 4 - 8 times during an 8-hour shift. Therefore quick adjustment of the cavities to save set-up time is the goal of computerization of the procedure.

The input parameters for the resulting optimization procedure are as follows: mass number and charge state, energy in front of the single-gap cavity chain, rf phase of the last Alvarez tank in operation in relation to the 108-MHz reference line, and the requested final energy. The energy gain of the i-th cavity is given by

$$\Delta W_i = \zeta/A \cdot U^i_{Cal} \cdot U^i_T \cdot T \cdot \cos \phi_s$$

(T Transit-time factor, U^i_T rf probe signal)

The factor U^i_{Cal} is a measure of the peak accelerating voltage (T=1, ϕ_s=0) for the i-th cavity at a probe signal of 1V. These values were experimentally found by measuring the maximum energy gain; they differ among the 20 cavities. All the 20 values are stored in a database. For the computation of power levels and the rf phases, the procedure takes into account the range of possible power levels which are also kept in a database. The agreement between requested and measured energy after setting the calculated values is quite good (1 - 2%). Only manual (or later automatic) fine tuning of the rf amplitude of the last cavity is required afterwards.

Some experiments require a sharp time focus of the bunch on the target, or an improvement of the energy spread. Then a single-gap resonator at the end of the linac and 4 helix resonators are used. At the linac output, the pulse width is 0.6 - 1.5 nsec, depending on the energy and the adjustment of the linac rf structures. Corresponding to an energy spread of 0.1 - 0.3%, the pulse width increases over a drift length of about 80 m to 2 - 5 nsec. The tune-up procedure for an improved time structure is as follows. First, energy spread and bunch width are measured;[3] from that the longitudinal phase ellipse at the end of linac can be calculated. This phase ellipse is transported to the position of the helix resonator (the debuncher is switched off). If the pulse width is within the limit of 70° (at 108 MHz), the bunch structure is optimized only by the second rebuncher. The rf amplitude is now adjusted for a minimum pulse width on the target position. Depending on the energy spread of the beam after acceleration, the phase width sometimes exceeds the limit of 70°. In order to avoid non-linear effects of the rf field, a combined action of two resonators provides the optimum transformation. The first is adjusted as a debuncher; the energy spread is now reduced and the pulse width at the rebuncher is small enough for a linear transformation.

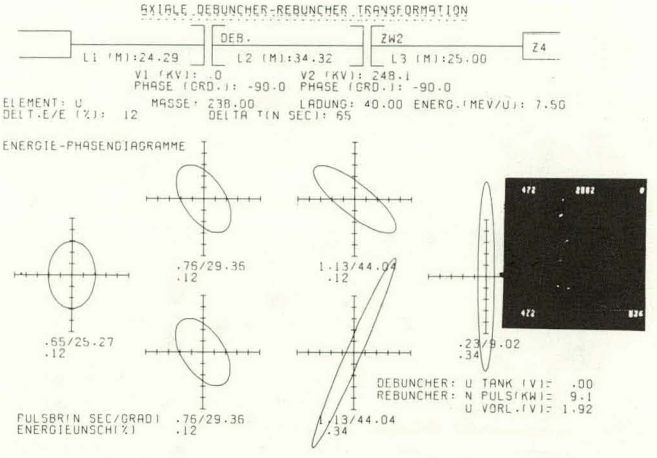


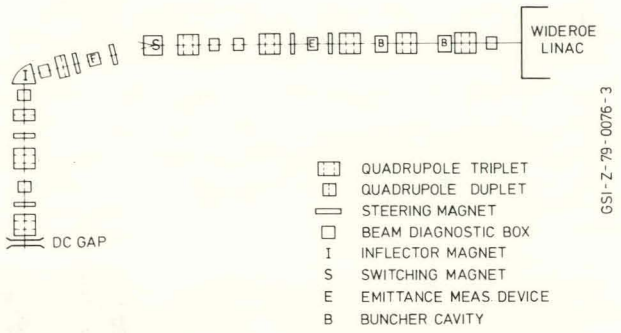
Fig. 4 Output of the program for the rebuncher-debuncher system
(right: measured bunch width on the target)

The output of this optimization program includes mainly the following information: Automatic selection of the cavities to be switched on, the rf parameters, and pulse width at target position. After setting of the calculated values, normally fine tuning immediately leads to an optimum width. The measured pulse width is in good agreement with the calculation by the computer program. An example is given in Fig. 4.

Transverse Beam Optimization of the Injection Beam Transport System

Compared to a proton machine, the low energy beam transport system of a multiparticle accelerator is much more complex. The Unilac injector was described in detail in Ref. 4. Figure 5 shows a schematic diagram of the beam line.

The most important properties are summarized. With the two dc-preaccelerators symmetrically arranged with the axis of the Unilac, ions of all stable elements from a Penning source are accelerated to 11.7 keV/u. One single charge state can be selected; the momentum dispersion of the transport line allows for a maximum mass resolution $\Delta m/m \sim 250$. Alternatively, a non-dispersive mode is used if isotope separation is not necessary. The aperture of the beam line and the magnetic lenses is 4 cm. The radial acceptance of the section from gap to the switching magnet allows transport of a beam with the maximum emittance of 32 π mm-mrad. The acceptance from the switching magnet to the input end of the Wideröe accelerator is 130 π mm-mrad. The operating experiences are described in Ref. 1.



LAYOUT OF THE UNILAC LOW ENERGY TRANSPORT SYSTEM

Fig. 5

The computer-aided optimization procedure consists of the following steps. The magnet currents are set from calculated data or data stored from earlier runs. These settings hardly ever result in a sufficient beam transmission and mass separation. The reasons are manifold: non-reproducible emittance for different ion sources, different parameter settings of the ion source for optimum intensities, tolerances of geometrical dimensions, disabled elements, misalignments, etc. If the beam intensity is not sufficient at the position of the emittance measuring device, an improvement has to be reached by retuning of the ion source and the beam matching elements. The measured emittance is transformed to the input of the transport channel with the actual settings of the magnets. Now an optimizing program calculates new settings for an optimum transport.

An important postulate of the described procedure is that the transport system is computable. Therefore time-consuming activities were started to bring all the components to their design values. The effort has mainly included verification of the calibration curves of all magnets, the precise and reproducible reaction of the magnet power supplies to the command signals, the physical locations of magnets and beam diagnostic elements. The success of this work is demonstrated in Fig. 6. The emittances were measured at two positions of the injection beam line (see Fig. 5) and in each case the envelopes were calculated; both envelopes agree very well. For a further check, the profile widths were measured along the beam line; the measurements confirm the calculated envelopes, too. The transformation excludes the section from the ion source to the gap. There were many changes of hardware, focusing elements were replaced, and the gap was reconstructed. This section will be included later into the optimization procedure.

For a successful optimization of beam transport lines, the measurement of the emittance at several positions is advantageous. The installation of more emittance measurement boxes is costly

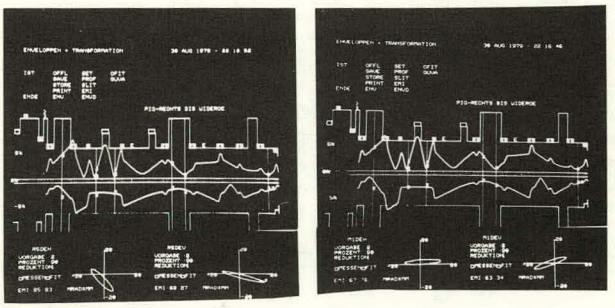


Fig. 6 Calculated envelopes on the basis of emittance measurements (+ measured profile width)

and is excluded by space limitations. Therefore an algorithm was developed using the profile data. There are about 50 profile harps available along the Unilac and in the experimental area. The basic idea is described in Ref. 5; the modified algorithm and the program structure are explained in Ref. 6. The ellipse parameters $\alpha,\beta,\gamma,\varepsilon$ are calculated by measuring the beam width (horizontal and vertical) at 3 different quadrupole settings from the equations

$$a_\nu^2\,\beta - 2a_\nu b_\nu \alpha + b_\nu^2\,\gamma = \frac{W_\nu^2}{4\varepsilon} \qquad \nu = 1,\ 2,\ 3,$$

where a, b, c, d are elements of the 2 x 2 transfer matrix from the quadrupole to the profile grid. Afterwards the emittance ellipse can be transported from the input of the quadrupole to different places on the transport line. Tests of the algorithm have shown that in many cases the measured emittance is determined correctly. Sometimes differences occur in the size of the area, but the inclination is correct. In few cases a solution of the equations does not exist. Stabilization of the routine may be expected with more sophisticated evaluation methods, on which work is underway. The first improvement was achieved by taking the profile parameters at 16 different quadrupole settings. The half widths and full widths are fitted by spline functions. An example is given in Fig. 7. For the evaluation three settings can be selected.

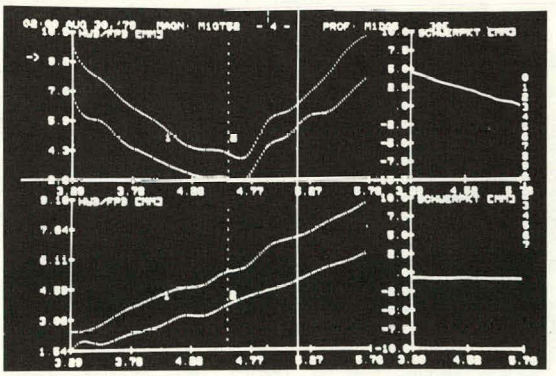
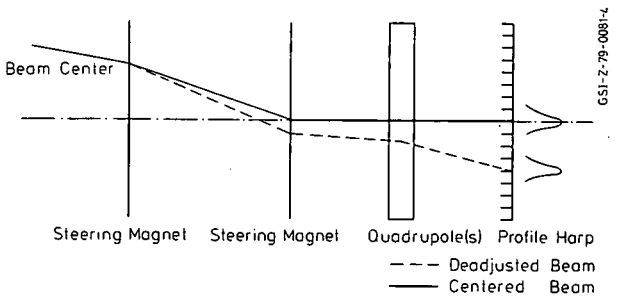


Fig. 7 Display of fitted profile data for the horizontal and vertical plane

In Fig. 7, on the right hand side, the displacement of the beam center at different quadrupole settings is displayed. Since a shifted beam influences the effectiveness of all the transverse optimization procedures, an automatic beam steering program is available. It can be activated at many places in the transport system. A schematic of the steering section is shown in Fig. 8. First, the displacement and slope of the beam center in front of the first steering magnet are determined by measuring the displacement on the profile grid at two quadrupole settings, then, the computer code calculates the set values for the steering magnets.



Layout of the Steering Section

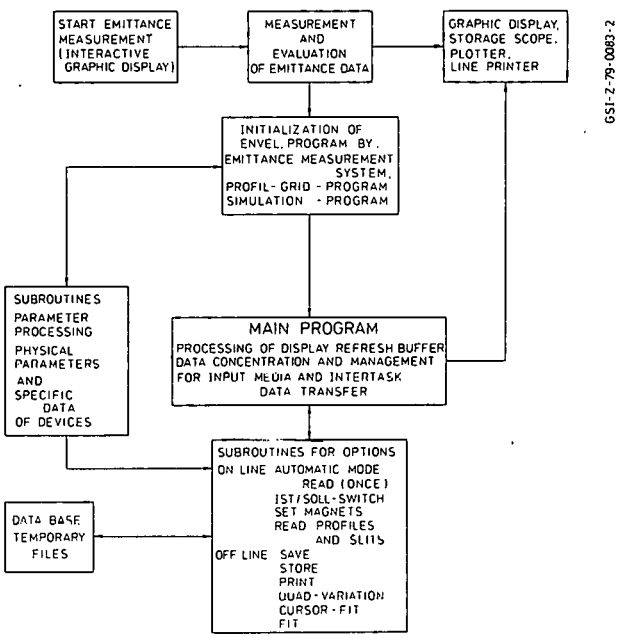
Fig. 8

Organization of the Optimizing Procedures

The optimization procedures are controlled through means of an interactive graphic display. Single routines can be selected. The main routine for transverse optimization starts with an emittance measurement. The program structure is shown in Fig. 9.

The basic idea of the optimization procedure has been described in this paper. The program also contains options which were originally provided for machine development, but they are also a valuable tool for adjustment of the machine during normal operation. One of these options is as follows: After an emittance measurement the envelopes are calculated and displayed. Then, the settings of the quadrupoles can be varied (on- or off-line) and the resulting envelope will be displayed. Furthermore, after selecting beam size constraints, new quadrupole settings are calculated. Both procedures were successfully used for the matching to the target position.

The development of a fully automatic optimization routine is in progress. The fit procedures applied up to now are not always successful. The different emittances at the input of the beam line cannot be matched to the defined reference envelope. The limited acceptance (see Ref. 1) requires tight tolerances for the fit conditions. Therefore, an upgrading program for the injection beam line was started. There is no doubt that in the future the optimization procedure will bring about better results and that the efficiency of the Unilac will increase.



SCHEMATIC DIAGRAM OF THE PROGRAM STRUCTURE FOR TRANSVERSE BEAM OPTIMIZATION

Fig. 9

References

1 D. Böhne, "Status Report on the Unilac", these proceedings.

2 J. Glatz et al., "Some Aspects of the Unilac Beam Diagnostic System". 1976 Proton Linear Accelerator Conference, Chalk River, AECL-5677.

3 J. Klabunde et al., "Measurement of Energy, Energy Spread and Bunch Width on the Unilac", these proceedings.

4 N. Angert et al., "The Unilac-Injector", 1976 Proton Linear Accelerator Conference, Chalk River, AECL-5677.

5 P. Brummer, "The Method of Measurement of the Emittance and the Betatron Phase Space Parameters in the Beam Transfer System of the I.S.R.", CERN-ISR-OP/72-6.

6 V. Schaa, Diploma-Thesis, Technische Hochschule Darmstadt, 1978.

Discussion

Jaeschke, Heidelberg: What is the energy resolution that you can get with your phase probe detecting device?

Klabunde: In the region of 5×10^{-3}.

Jaeschke: How many of these computerized steering sections that you describe are you now running?

Klabunde: Two in the injection line and two in operation at the high energy end. But, we have many places of this kind of arrangement, but these are the only ones used so far.

Ohnuma, FNAL: What kind of device do you use for your energy emittance measurements?

Klabunde: Just a simple slit-collector system.

MEASUREMENTS OF ENERGY, ENERGY SPREAD AND BUNCH WIDTH AT THE UNILAC

J. Klabunde, V. Schaa, E. Schaffner, P. Strehl, H. Vilhjalmsson, D. Wilms
GSI, Gesellschaft für Schwerionenforschung mbH
Darmstadt, Fed. Rep. of Germany

Summary

Characteristics of various beam diagnostic elements, including computation of signal shapes and signal processing, will be discussed. Some procedures for determination of beam parameters in longitudinal phase space are presented. Instrumentation and the computer program of a self-contained on-line energy measurement will be described.

Introduction

At the UNILAC, frequent changes of accelerating conditions (various ions, various energies between 3.6 - 10 MeV/u, use of foil or gas stripper) and demands for perfect beam quality (required micro-structure of bunches and pure energy spectrum on target) are standard. For efficient tuning of all rf substructures involved in accelerating processes, a rather elaborated diagnostic system for measurement of beam parameters in longitudinal phase space is essential.

A short description of fast pick-up probes and a survey of a temporary signal processing system used in commissioning of the UNILAC is given in Ref. 1. Experience from routine operation in recent years, and study periods for accelerator development, led to improvement of signal processing and utilization of measurements of longitudinal phase space.

In the present paper, various methods of measurement and signal evaluation are described in more detail. On the basis of some typical examples, the capability of procedures for efficient tuning of a multiparticle, variable-energy machine will a multi-stage rf accelerating system will be demonstrated.

Characteristics of Diagnostic Elements and Measurement Procedures

To measure beam parameters in longitudinal phase space, the following types of probes are in use at the UNILAC:

- broad band coaxial Faraday cups
- semiconductor detectors
- broad band capacitive pick-ups.

Figure 1 gives a schematic layout of the UNILAC and the experimental areas. The various elements produce signals with different characteristics, which will be described below.

Coaxial Faraday cup

Design details (without pneumatic actuator for positioning the device into beam) are shown in Fig. 2. The cup was designed to have a 50-ohm geometry. The reflection coefficient measured by a TDR (25-ps rise time test pulse) is less than 5%. A grid in front of the collector plate (not shown in Fig. 2) repels secondary electrons and shields against the longitudinal electrical field moving in front of the bunch. Both effects would result in a broadening of the fast current signals, as illustrated in Fig. 3.

The influence of longitudinal electrical fields on signal shape can be estimated for simple bunch geometries. The true induced current is given by:

$$i = \frac{d}{dt} \int_0^R \varepsilon_0 E_z 2\pi r dr \qquad (1)$$

where R = radius of collector plate placed at Z=0 and E_z = longitudinal electrical field of the moving bunch. Assuming a bunch of length Δt, with uniform charge distribution over time t, and neglecting field distortions by the cup itself, the result is (NR-approximation):

$$\frac{i}{N\zeta} = \frac{e}{2\Delta t}\left(\frac{\beta c(t+\Delta t/2)}{\sqrt{(\beta c(t+\Delta t/2))^2+R^2}} - \frac{\beta c(t-\Delta t/2)}{\sqrt{(\beta c(t-\Delta t/2))^2+R^2}}\right), \qquad (2)$$

where N = number of ions within the bunch and ζ = charge state of ions. The sum of the induced current according to (2) and pure charge current leads to a signal shape as shown in Fig. 4.

Coaxial Faraday cups are used for bunch length measurements, bunch shape observation and optimization, determination of correct rf phase settings, and calculation of proper rf amplitudes for generating a good micro-structure.

Semiconductor detectors

Due to increased demands in the quality of the energy spectra at the end of UNILAC, and the frequently desired well-defined structure of bunches on target, semiconductor detectors (ORTEC: TF-40-400-60-S; SCHLUMBERGER: BTC-50-150-859) were installed. Detectors are mounted on compressed air actuated feed-throughs, and can be moved rapidly into the beam. A system of beam degraders for fixed and variable attenuation of beam intensity, protects the semiconductors. Movement of the degraders is controlled by an interlock system.

One of the detectors at the end of the UNILAC is placed in an approximately 1200-mm long diagnostic chamber, and can be moved 1000 mm along the beam axis with better than 1-mm precision. Therefore, time-of-flight measurements for energy determination are possible using this detector.

Depending on beam parameters to be measured, different preamplifiers were developed at GSI:

- charge sensitive preamplifiers (slow output) for measurement of energy spectra, with a gain of 1 - 20 mV/MeV and a bandwidth of about 70 MHz;
- voltage sensitive amplifiers (fast output) with a gain of 44 - 2200 mV/MeV and a bandwidth of about 450 MHz ($t_r \leq 1$ ns).

Signal processing following the preamplifiers utilized procedures common to nuclear and high energy physics.

At the UNILAC, semiconductor detectors are preferred for the measurement of energy spectra. Bunch length and energy determination are performed much more efficiently by using capacitive pick-ups. Figure 5 illustrates the capability of semiconductors for optimization of energy spectra.

The energy resolution of semiconductor detectors depends mainly on the energy and mass of the ions to be detected. For $^{84}Kr^{12+}$-ions, the resolution could be determined at W = 1.4 MeV/u to $\Delta W/W$ = (0.7 ± 0.1)%, taking advantage of the small energy spread of the Wideröe prestripper accelerator, which was measured to $\Delta W_o/W_o$ = (0.08 ± 0.02)% with capacitive pick-ups.

For observation of time spectra, semiconductor signals, amplified by voltage sensitive preamplifiers, are processed in the well-known start-stop mode, using fast time-to-amplitude converters and a 4096-channel analyzer. Figure 6 shows a typical time spectrum of the bunches, where time calibration was made by subdividing the rf reference stop-signal. Using more advanced techniques, time resolution can be improved to 50 - 80 ps/channel, as shown for example, in Ref. 2.

Capacitive pick-ups

Probe Optimization and Signal Computation

Most efficient measurements in longitudinal phase space (see Ref. 2 for details) are done by using a system of capacitive pick-ups. Taking advantage of an elaborate program for computation of pick-up signals including probe and bunch parameters, the geometric shape of pick-ups could be optimized. Some insights into signal processing and signal interpretation could be gained. Relevant design parameters are shown in Fig. 7. Impedance was approximately calculated taking advantage of analogies between coaxial structure, as shown in Fig. 7, and a planar microstrip. Final matching to exactly 50 ohm is done by the bending of segmented diaphragms in front and behind the pick-up cylinder. In the case of precise matching, the reflection coefficient will be less than 5% for a test pulse with 25-ps rise time.

Shape and amplitudes of pick-up signals can be calculated to a good approximation under the following assumptions: A bunch with homogeneous charge distribution is moving with $v = \beta c$. The bunch has no dimensions in transverse directions Y and X. At time t, the center of charge is at a distance of $Z = \beta ct$ from the origin of the coordinate system at Z=0. For such a bunch, with $\Delta Z = \beta c \Delta t$, the charge distribution can be described by:

$$\rho(X,Y,Z) = \delta(X)\delta(Y)\frac{N\zeta e}{\beta c \Delta t}\,(\Theta(t+\Delta t/2)-\Theta(t-\Delta t/2)), \quad (3)$$

where $\delta(X)$ and $\delta(Y)$ are the well-known Dirac delta-functions and $\Theta(t)$ is the step function of Heaviside. Neglecting again distortions of potentials by the beam pipe and pick-up probe itself, the extracted signal current can be written (NR-approximation):

$$i(t) = \frac{N\zeta e}{2\Delta t}\left(\frac{L-\beta c(t+\Delta t/2)}{\sqrt{(L-\beta c(t+\Delta t/2))^2+R^2}} + \frac{\beta c(t+\Delta t/2)}{\sqrt{(\beta c(t+\Delta t/2))^2+R^2}}\right.$$

$$\left. - \frac{L-\beta c(t-\Delta t/2)}{\sqrt{(L-\beta c(t-\Delta t/2))^2+R^2}} - \frac{\beta c(t-\Delta t/2)}{\sqrt{(\beta c(t-\Delta t/2))^2+R^2}}\right), \quad (4)$$

where L, R and probe lengths and radius, respectively. In the chosen coordinate system, the probe is positioned from Z=0 to Z=L. Figure 8 shows some computed signals, assuming typical UNILAC β and Δt-values. For comparison in Fig. 8, one plot was calculated for a more realistic triangular shape charge distribution over the bunch, defining Δt by full-width half-maximum points.

Measured signal shapes agree very well with computation. Due to some uncertainties in signal amplification factors, cable dispersion, and plasma oscillations in the Penning source, it is very difficult, even within a 10% margin, to compare measured signal amplitudes with computed values. If strong plasma oscillations occur, as shown in Fig. 9, a comparison is impossible.

At the UNILAC, measurements of micro-structure with capacitive pick-ups, however, are the only possibility to detect such plasma oscillations. Experience has shown that optimization of a ion source by observing only the pick-up signals can be very efficient in terms of beam intensities. In some accelerator experiments, there was also observed an influence of plasma oscillations on beam quality at the end of UNILAC. This effect will be studied in more detail.

Signal Processing

Taking advantage of experience with the old temporary system as described in Ref. 1, some improvements and modifications on the signal processing system were implemented in recent years. As shown in Fig. 10, this results in a micro-

processor controlled pick-up signal selection, including some fixed programmed options (for example, automatic signal selection for energy measurements). The electronic system has been extended to also enable an on-line computed energy measurement. The capability of a new electronic system for fast determination of rf phases (also shown in Fig. 10) will be discussed in Ref. 2.

For signal amplification, a special broad-band amplifier with the following characteristics was developed at GSI:

Type	: Avantek UTO 1511, UTO 1521
Input impedance	: 50 ohm
Output impedance	: 50 ohm
Bandwith	: 5 - 1500 MHz
Gain	: 44 dB
Required input voltage for S:N=1:1	: $\sim$ 40 μV

Determination of Bunch Length

Measurements in the time domain

Due to convolution of the moving electrical bunchfield with the probe geometry, it is impossible to extract the bunch length directly from the observed probe signal. However, using Eq. 4, a relation between measured time, distance from positive-signal-maximum to negative-signal-minimum, Δk and bunch length Δt, can be derived. This relation is shown in Fig. 11. The procedure is mainly limited by the finite bandwidth of the 500-MHz oscilloscope used. For UNILAC beam parameters and capacitive pick-ups with L = 1 cm and R = 1.75 cm, the relation $\Delta k(\lim \Delta t \to 0) \sim 2L/\beta c$ also holds.

Measurement in the frequency domain

For values of Δt smaller than $\sim$ 0.8 ns, determination of bunch length, Δt, from an analysis of probe signal Fourier spectra is more effective. Using the program FAST FOURIER TRANSFORM (FFT), computation of such spectra for i(t) according to Eq. 4 and also for triangular shaped charge distribution of the bunches is straightforward. Approximating a typical pick-up signal by a polynominal relates the first minimum in the Fourier spectrum (harmonic number n), the period of accelerating rf (T) and bunch length Δt:

$$n_o = \frac{T}{\Delta t} \qquad (5)$$

This simple relation was confirmed also by FFT. Accuracy of this procedure gets better for small Δt, because from Eq. 5 it follows that

$$\delta(\Delta t) = -\left(\frac{T}{n_o^2}\right) \cdot \Delta n_o \qquad (6)$$

To estimate the bunch lengths Δt and compare different bunches with respect to signal rise time, observations in the frequency domain are very sensitive. Figure 12 demonstrates this clearly.

On-line energy measurement

A description of operator-aided procedure was given in Ref. 1. The new self-contained on-line procedure is illustrated in Fig. 13. For a single-valued plain determination of particle energy, the signals of probes T1, T2, T3, T4 (see Fig. 1) are used. Probe signals are sequentially switched by a computer controlled device to a selective rf amplifier, and tuned to the third harmonic of the bunch repetition frequency ($\hat{=}$ 81 MHz). This harmonic was chosen because SN ratio is up to a factor of 40 better than with 27 or even 54 MHz. Bunch uncertainty can be eliminated by analyzing the phase relation of all 4 probe signals.

The 81-MHz signal is fed to a sampler. A 27-MHz reference signal of the phase axis is tripled in frequency and fed to a second sampler. Both samplers are controlled by a modified Hp-Vectrovoltmeter, which is synchronized by a 108-MHz reference signal from the poststripper accelerator phase axis. This procedure results in two 15-kHz sine wave signals on the sampler outputs, which are controlled in amplitude by a standard operational amplifier. Both sine wave signals are digitized by two synchronized fast CAMAC-ADC's (conversion rate 5 MHz, memory size 1000 points, corresponding to three 15-kHz periods). Digital data from all 4 probes and 27-MHz phase axis are evaluated in a PDP 11/34 by determination of the function

$$f_k(t) = A_k \sin(\omega t + \Psi_k) \qquad (7)$$

using a simple least squares fit. In Eq. 7, index k represents signal number (T1 - T4, phase axis), and A_k, Ψ_k are amplitude and phase of the fitted sine wave, respectively. Since the 27-MHz phase axis serves as time reference, Ψ_k=0 holds for this signal. From computed differences between Ψ_k-values corresponding to the probe signals, time-of-flight, and therefore also particle energy can be determined very precisely. Beam parameters available by evaluating A_k are not interpreted at present.

Based on good experiences with this on-line measurement, some more sophisticated, microprocessor-aided procedures of beam parameter control in longitudinal phase space will be implemented in the near future (see Ref. 2).

References

1 J. Glatz et al., Some Aspects of the Unilac Beam Diagnostic System, 1976 Proton Linear Accelerator Conference, Chalk River, AECC-5677.

2 L. Dahl et al., Longitudinal and Transverse Beam Optimization, these proceedings.

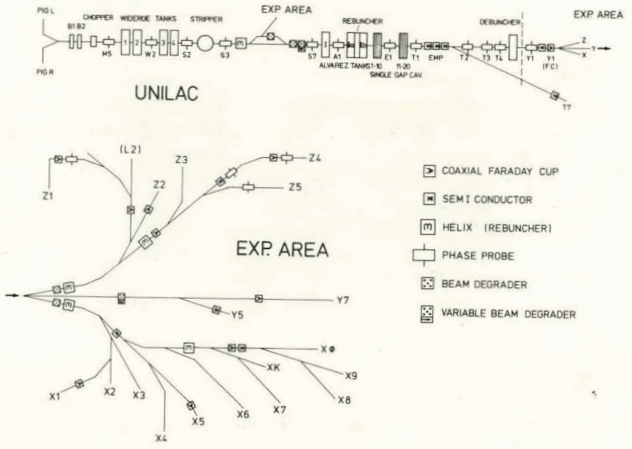


Fig. 1 Arrangement of beam diagnostic elements for measurements in longitudinal phase space along the UNILAC facility.

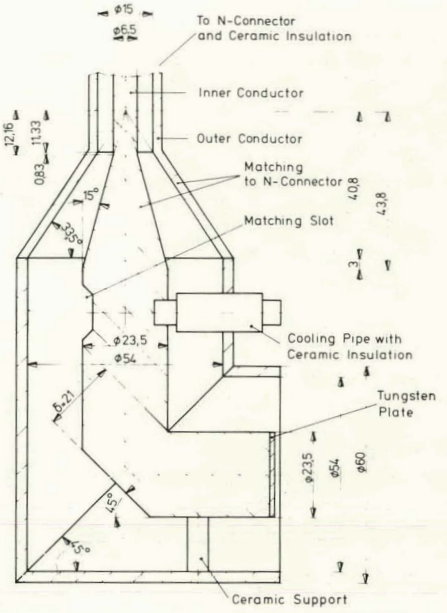


Fig. 2 Design of coaxial Faraday cup (dimensions in mm)

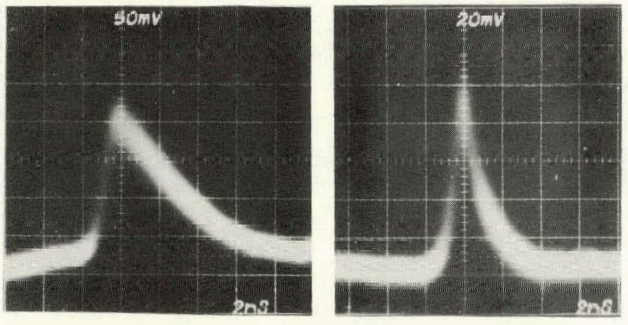


Fig. 3 Effect of secondary electrons and subsequent signal suppression by means of a grid in front of the collector plate. Left: without voltage on grid, Right: - 800 volts on grid, (mean beam current about 15 nA).

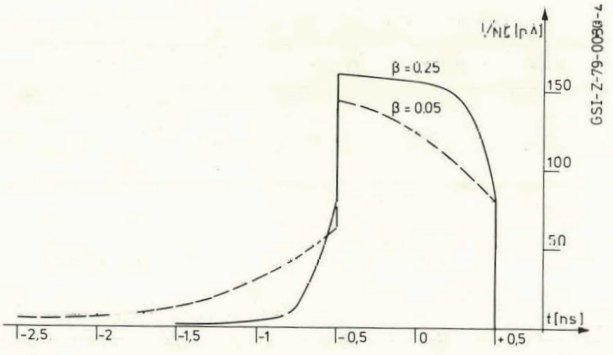
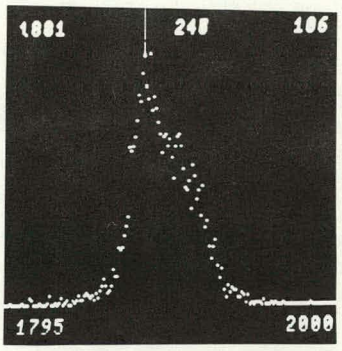
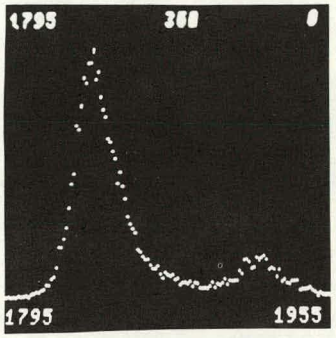


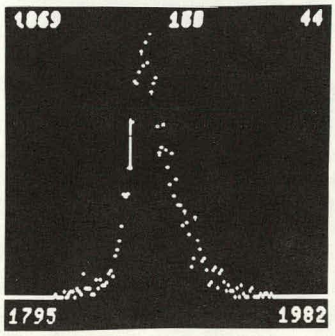
Fig. 4 Approximation of the effect of precursor longitudinal electrical field on signal shape observed by a coaxial Faraday cup.



Incorrect setting of AI - Tank amplitude (FWHM ≈ 1.8 %).



Incorrect bunch input phase (error about 500 ps, FWHM main peak on left: 1.2 %. Distance of satellite peak to main peak: ≈ 132 keV/u).



Correct settings (FWHM ≈ 1.1 %).

Fig. 5 Optimization of bunch input phase, rf amplitude setting for Alvarez I and rebuncher helix rf settings by observation of semiconductor energy spectra. Particle energy about 3.6 MeV/u, resolution (2 keV/u)/channel.

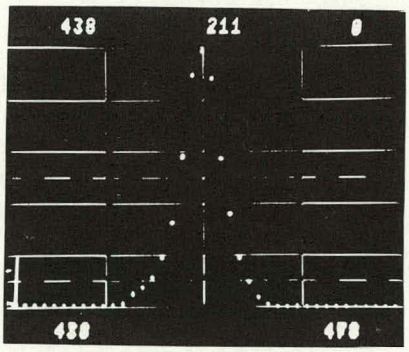


Fig. 6 Time spectra of bunches observed with a semiconductor detector behind a drift space.

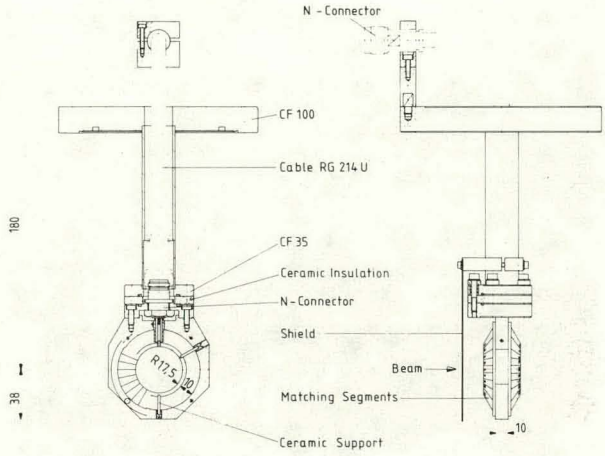


Fig. 7 Design of capacitive pick-up probes (dimensions in mm).

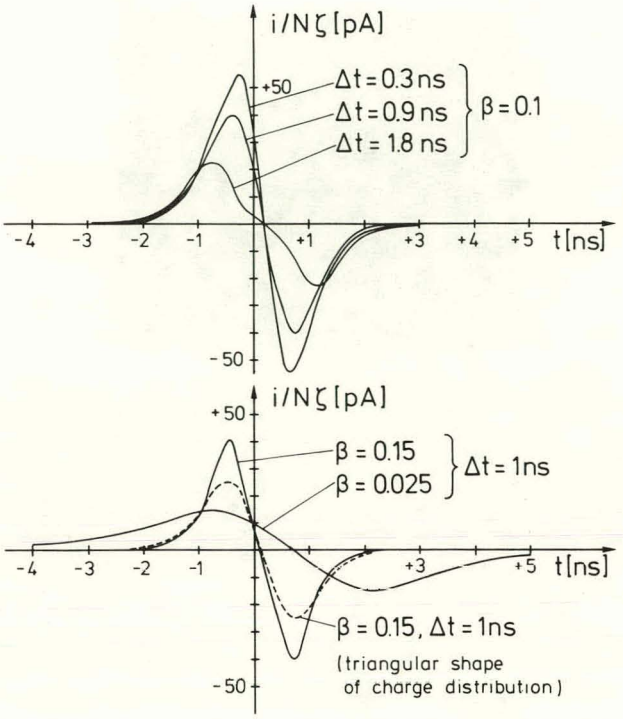


Fig. 8 Computed signal shapes for capacitive pick-ups using Eq. 4 and dimensions given in Fig. 7.

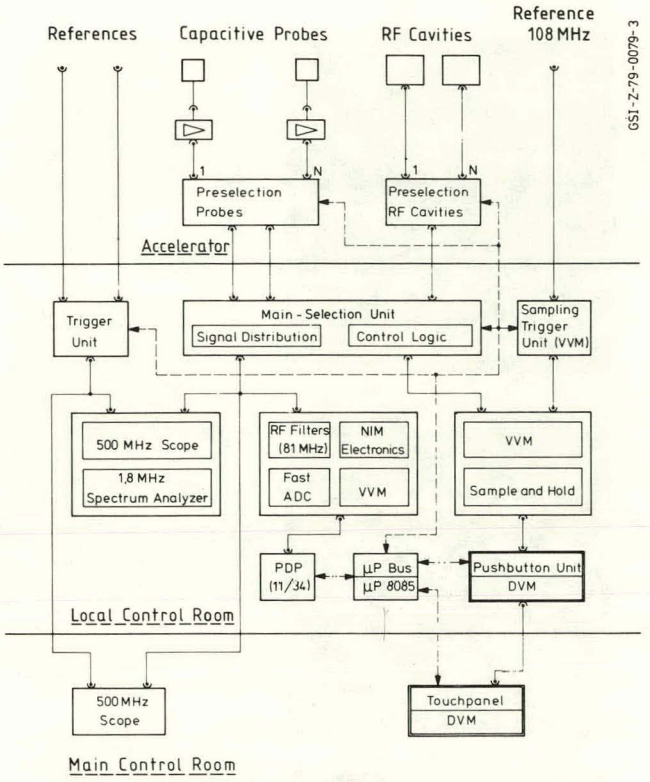


Fig. 10 Improved signal processing system for capacitive pick-ups and fast rf phase measurements.

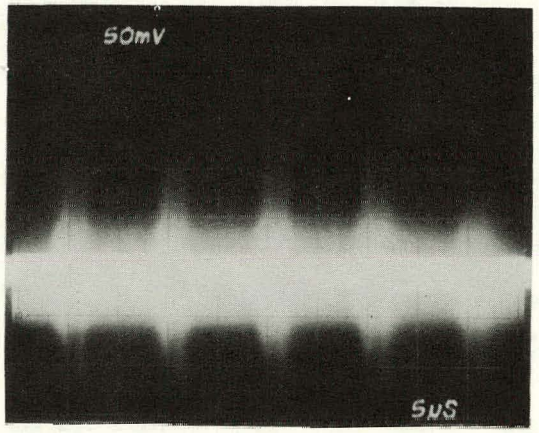


Fig. 9 Detection of ion-source plasma oscillations by means of capacitive pick-ups. In the time scale chosen, single beam bunches ($\Delta t \simeq 1.5$ ns) are not resolved. The lengths of the corresponding macropulse was 5 ms.

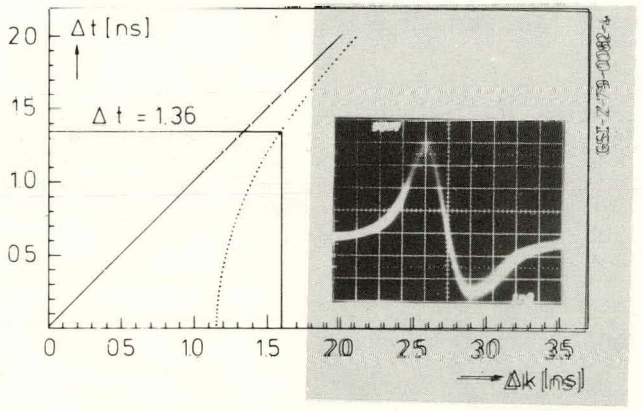


Fig. 11 Computed relation between bunch length Δt and measured time (Δk). Due to cable dispersion-effects, Δk should be determined as two times distance between maximum and zero crossing. Insert on right side shows the corresponding oscilloscope signal.

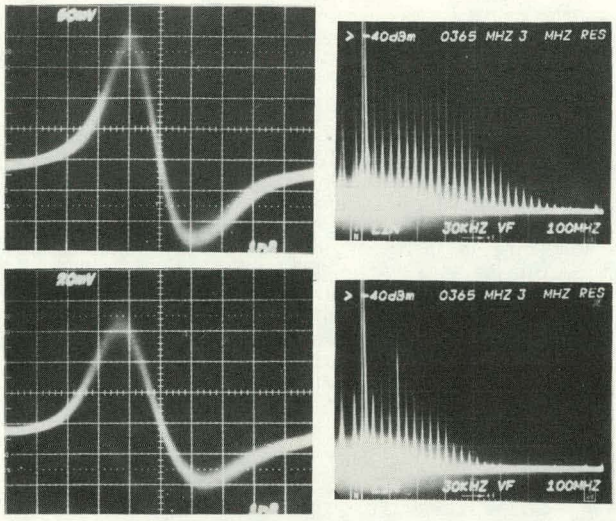


Fig. 12 Comparison of bunch signal observation in time and frequency domain, respectively ($\beta \simeq 0.055$).
Top left: $\Delta k = 1.6$ ns, $\Delta t \simeq 1.36$ ns (see Fig. 11)
top right: $n_o \simeq 26$, $\Delta t \simeq 1.42$ ns (see eq. (5))
bottom left: $\Delta k = 2.0$ ns, $\Delta t \simeq 1.88$ ns
bottom right: $n_o \simeq 19$, $\Delta t \simeq 1.95$ ns.

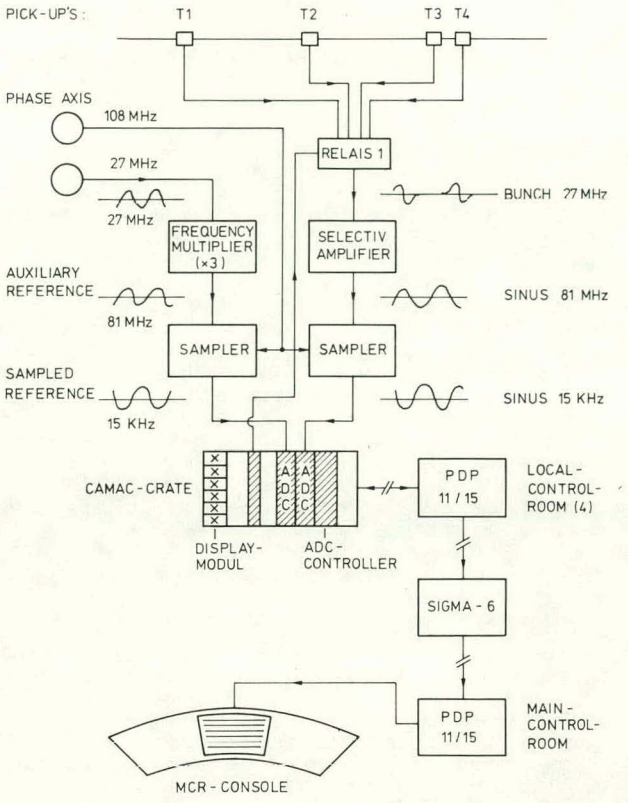


Fig. 13 Schematic block diagram of on-line energy measurement at UNILAC.

CALIBRATION DURING INSTALLATION AND DURING INITIAL OPERATION OF THE CERN 50 MeV LINAC

D.J. Warner
CERN, Geneva, Switzerland

Summary

This paper describes the connection between the design and performance of the CERN 50-MeV linac.[1] made by the calibration aspects of the commissioning and of first operation with beam. Essentially, one aims to set the accelerator working points for transverse and longitudinal motion. Both planes are treated under three main headings: alignment, calibration on installation, and calibration with beam. Results of perturbation measurements give detailed but relative fields, needing beam measurements in the longitudinal plane to fix the rf level and phase. The quadrupole calibrations are sensitive and absolute, but, apart from determining the input beam steering, the transverse beam measurements so far add little to the initial calibration.

Longitudinal Plane

Alignment: Gap Lengths and Positions

The girder support[2] essentially dictates the methods and sequences of alignment. Given an overall tolerance of ±1 mm on the length of a cavity (6.7 m for Tank 1) and drift tubes with length tolerances ±0.05 mm, the aim is to install them so that the gaps are correctly positioned. This sets the accelerating field phase relative to the proton position; the effective field magnitude can be set during perturbation measurements. Cell lengths vary between 60 mm and 465 mm (0.75 MeV to 50 MeV), so ±1° corresponds to gap position errors of 0.16 mm to 1.3 mm. Note that one wrongly positioned drift tube leads to two nearly cancelling errors.

Ideally, before drift tubes are mounted, the girders have been fitted on the cavities (in particular to set the aluminium joint compression), so that the final relative positions of tank ends and girders are known. Thus, the drift tubes can be mounted with correct gap positions, even for adjacent tubes on different girders, although these gaps and the end gaps are checked when the girders are definitively installed. In practice, the placing of the drift tubes could be done entirely via precise gap length measurements.

Calibration of the Electric Field

Bulk Tuning. The cavity is made slightly oversize, and for the first frequency tests, only drift tubes and the bulk tuner bases are installed. The copper bulk tuner has a "T" section and is made in lengths of ∿ 1 m (three per tank section) with a base and a detachable top piece. The approximate field law is determined by perturbation through the post-coupler holes. By introducing large field perturbations through the tuner holes, one can deduce the position and amount of bulk tuning to set the field roughly to the correct tilt (Tank 1), or to be approximately flat (Tanks 2 & 3). One has to allow for other components, e.g. feed loops, post couplers, frequency tuners, and "vacuum" (also ambient temperature), but with these first bulk tuner modifications the resonant frequency was within ±10 kHz of 202.56 MHz.

Perturbation Measurement and Field Stabilization. Post couplers are mounted horizontally from alternate sides of the cavity with periodicity 1 per two drift tubes for Tanks 1 and 2, and 1 per drift tube for Tank 3.[3] Using adjustable aluminium posts (25 mm diameter with eccentric tabs initially pointing downwards), one can find the TM_{01n} modes with a well-defined set of post modes near confluence on the low-frequency side, with all posts at the same penetration. To make finer adjustments, one studies the axial electric field by perturbation (bead pull) measurements (Fig. 1). Using a synthesized frequency generator and a network analyzer, one can obtain the required measurement speed by the phase-shift method for measuring frequency perturbation. With constant input frequency, one measures phase shift between the cavity signal and the forward wave to the main loops, or to a small auxiliary loop:

$$\delta\phi = \tan^{-1}\left(\frac{2\ \delta f\ Q_L}{f}\right).$$

This has good linearity for $\delta\phi < 5°$. A dielectric sphere with $\epsilon = 9$ and diameter 6 mm or 8 mm (Tanks 2 and 3) was supported along the axis of the cavity by a fine nylon thread tensioned to > 20 N. The bead was pulled with a computer-controlled stepping motor and measurements were taken at ∿ 4000 points, i.e. at ∿ 2 mm intervals in Tank 1 (gap 1 = 13.5 mm). To make the data collection at 50 points/s, the program was written in machine code (DEC-PDP-11/20, 11/40, or 11/45 computers). The sensitivity was 10 mV/°, and after amplification and A/D conversion, these data were immediately stored in a temporary file for preliminary analysis before transfer to a disk file.

The analysis of the perturbation data is made by programs in BASIC, where the interactive nature of debugging is very useful. There are simple programs for listing results on the video terminal (VT 50) or plotting experimental points on a 611 storage scope. These raw analyses are essential for debugging more sophisticated programs or assessing the measurement noise and stability. For comparisons with the theoretical fields, the center gap field E_{cg}, is found by identifying the maxima (or local minima for Tank 3) and making a least squares fitting of a parabola through five or more points near the turning point. Measurements inside the drift tube can be fitted to line segments, which define the base line while the bead is in the gap. Thus, one finds $\delta\phi \propto \delta f \propto E_z^2$ at all points, and hence E_{cg}. In Tank 1 there is a linear increase of the mean axial field $\bar{E}$ (by 21% from 0.75 to 10 MeV); $\bar{E}$ is constant in Tanks 2 and 3. The center gap fields E_{cg}, have a different variation (e.g. $E_{cg} \simeq \bar{E}L/g$) but CLASL[4] results give E_{cg} corresponding to $\bar{E} = 1$ MV m^{-1}. For Tank 1 (see Fig. 2a), there is a discontinuity in E_{cg} versus z where the aperture increases from 20 mm to 25 mm.

A complete analysis to obtain E involves the integral of the field across the cell, $\int E_z\, dz$. If $E_z < 0.1\ E_{cg}$, then $\delta\phi_z < 0.01\ \delta\phi_{cg}$ giving poor precision, so a theoretical exponential decay is fitted to measurements at $\delta\phi_z \approx 0.05\ \delta\phi_{cg}$. If larger statistical spreads are obtained in $\bar{E}$ than in E_{cg}, the constancy of bead speed becomes suspect. Transit time factors (less dependent on speed constancy) agree well with computations. For immediate appraisal of field stability, the peak method is faster, more reliable, and less dependent on bead speed.

One checks the field stability via three measurements corresponding to normal conditions and to detuning at tank input and output, respectively, analysing the results by an E_{cg} versus z plot on the 611 storage scope. Initially, all posts were set too far in, and

they were withdrawn systematically to obtain field stability.

On all tanks a large improvement was quickly obtained followed by a slow convergence to acceptable stability. For Tanks 2 and 3, final posts are machined to lengths predicted by the measurements (with a tolerance ±0.1 mm), and after installation one determines the best orientation before making the vacuum seal. In Tank 1 the post couplers rotate on a vertical axis to make the asymmetric coupling (for the field tilt) and their insertion can be varied by ±5 mm *in situ*. The required tilt and stability were obtained for Tanks 2 and 3, but in Tank 1 the wide range of cell lengths (60 mm to 220 mm) made the adjustment less straightforward and lack of time led to accepting a field tilt of 23% (cf. 21% specified) and a discontinuity in mid-Tank. Results are shown in Fig. 2.

Calibration of Input Loops and Monitoring Loops

The input loop coupling can be varied to cope with any beam current, i.e. β = 1 to 4 (Tank 1) or β = 0.5 to 2 (Tanks 2 or 3 individual loops). Coupling varies linearly with position over the 30 mm range.

The monitoring loops, set initially to -40 dB relative to input power, provide the precise measurement of the accelerating field after beam calibration.

Calibration of Field Levels and Phases on Initial Operation

In theory one could use the monitoring loop calibration and cavity Q to set the rf, but for ±1% precision in level and ±1° in relative phase, the beam behavior is a better indicator. Several methods can be used; namely: threshold of acceleration, the "$3\phi_s$" method, accelerated current, and variation of output beam energy with input phase. The computed acceptance of Tank 1 is given in Fig. 3 and the output energy as function of rf level and phase for Tanks 2 and 3 in Fig. 4. The notions of acceptance and threshold are less clear for Tank 3, owing to the relatively smaller change in energy (30 MeV to 50 MeV).

Calibration at 10 MeV. For all beam 'probe' experiments, a limited beam (I < 50 mA) gives better discrimination (less space-charge and radial effects). In Tank 1, ϕ_s decreases from -35° to -25° along the tank, and the threshold occurs when ϕ_s (output) ≈ 0, i.e. ϕ_s (input) ≈ -25°. Thus, to determine this threshold, one needs energy discrimination. A 53° spectrometer was available during early 10-MeV tests and now one can use the longitudinal acceptance of Tanks 2 and 3. From single-particle and MAPRO1 [3] computations, this threshold is 89% of normal operating rf level.

In the "$3\phi_s$" method, one identifies the separatrix by varying the bunched beam (i.e. buncher) phase relative to Tank 1 and noting when the 50-MeV (or analysed 10-MeV) beam current falls to half its maximum value. This and other methods for setting the DDHB (double buncher) phase, depend critically on preinjector energy (±1 keV ≡ ±4°). Another useful indicator is the high current trapping as a function of rf level, which levels off at ∿ 80% for a bunched beam.

Calibration at 30 MeV and 50 MeV. For these tanks the notion of threshold is much less useful and the rf level is calibrated by measuring output energy as function of input phase, with the longitudinal emittance measurement system.[5] To minimize errors due to finite bunch size, space-charge, and non-linearity near the separatrix, the beam is limited (I < 50 mA) and results with excessive emittance distortion are rejected, making comparisons with single particle dynamics well inside the acceptance. Qualitatively, one seeks distinctive features, e.g. where output energy varies slowly with phase, the synchronous energy is defined, and the rf level is easily identified from the computations. Hence, one deduces the required rf level, and the synchronous phase is where $W = W_s$ on the corresponding W-versus-ϕ characteristic. Further confirmation of levels can be found by other distinctive features, e.g. threshold and maximum energies. Theory and experiment are compared for 30-MeV and 50-MeV cases in Fig. 5 (30-MeV beam is transported through the unpowered Tank 3). With care, these methods can meet the required Phase and level tolerances.

Transverse Planes

Alignment: Drift Tube Transverse Positions

The difficult tolerance for transverse motion concerns the alignment of the quadrupole magnetic axes. The quadrupole is fitted into the drift-tube body so that the magnetic axis is concentric with the cylindrical surface of the drift tube, and one neutral plane is in line with the support stem inner. When first mounted on a support girder, the drift tubes are positioned relative to the straight reference surfaces with a precise jig and clock gauges.[2] Thus the relative alignment, drift tube-to-drift tube, can be set with sensitivity ±0.02 mm. It can be demonstrated that the short distance alignment is important, by comparing the errors in output beam trajectory when quadrupoles lie on a smooth curve or when the quadrupoles have random errors relative to a straight line. In practice, mechanical methods are also used on the cavities to check girder-to-girder alignment and the girder geometry (twist and sag) before mounting drift tubes. An axis is defined which minimizes the required offset of drift tubes relative to the girder reference surfaces; thus each drift tube is correctly positioned using the jig and calculated offsets. This method requires the usual mechanic's skills, there is little measurement fatigue, atmospheric turbulence does not affect the measurement, and it is easy to recheck (1 min/drift tube). After six weeks' operation, Tank 1 alignment was checked and the same pattern of small errors found. As a result, this linac has been aligned and operated without looking along the beam axis.

Quadrupole Magnet Calibration

Before Installation in Drift Tubes. Upon delivery, each quadrupole was tested at nominal current with a long coil and integrator[6] (controlled by an HP-9831 computer) measuring harmonic content of field, position of magnetic center relative to the yoke, and angular position of neutral planes relative to a keyway. The above measurements were repeated as a function of excitation current for at least one quadrupole per type. One could thus assign quadrupoles to drift tubes, e.g. for Types I and II (beginning of Tank 1) they were mounted in descending order of efficiency. The rms deviation in Tank 1 between magnetic and yoke centers is < 0.03 mm. This deviation is larger for Tanks 2 and 3 quadrupoles, so the mounting criterion was that there should be minimum drift tube-to-drift tube deviation in magnetic center position.

Thus accurate concentricity of magnet yoke and drift tube outer cylinder (simple machining) can be relied on to give a smooth line of magnetic axes.

With Drift Tubes Mounted on Girders. This calibration uses a precise long coil to quickly confirm the excitation curves, $\int B'dz$ versus I, with drift tubes in their final configuration. The coil has a preferential response for the quadrupolar field so that, in particular, accurate centering is unnecessary.[6] In practice it was rotated slowly while pulsing the quadrupole, and maxima and minima outputs were noted. Typically these calibrations, repeated for 3 or 4 currents, took 5 min per drift tube (and checked connection polarity also). For ease of control of the quadrupoles, they should have the same excitation characteristics within a type (and within allowable field tolerances). The calibration extends into the saturation region so the results are fitted to

$$B'/I = a + b(I - I_C)^2 \quad \text{for} \quad I > I_C$$
$$= a \quad \text{for} \quad I \leq I_C .$$

Table I gives average results for a and b and the standard deviation of a for Types I to V.

In contrast to the electric field calibration, the precision obtainable here is ±0.3% absolute, depending on the accuracy of the coil, of the integration, and of the current measurement.

Table I - Quadrupole characteristics

Quad. type	I_C (A)	a ($Tm^{-1}\ A^{-1}$)	s.d. of a (%)	b × 10^{-6} ($Tm^{-1}\ A^{-3}$)	Nominal current (A)
I	120	0.4318	0.62	-2.14	230
II	100	0.4534	0.41	-1.14	175
III	125	0.2335	0.32	-0.36	230
IV	100	0.2347	0.21	-0.42	150
V	150	0.1066	0.22	-0.01	225

Calibration of the Focusing with the Beam

Transversely, the analog of input phase is the input beam average trajectory, which at present cannot be directly determined in the LEBT.[1] However, the beam output coordinates will depend both on alignment of drift tubes and on beam input trajectory, so the way the LEBT beam steering (ST3 and ST4) is adjusted, is to observe the mean beam position on the 50-MeV measurement line[5] as a function of the focusing level in Tanks 2 and 3, or in the complete linac. The strategy adopted is to minimize the size of the resultant closed figure in the phase plane with ST3 and ST4 (Fig. 6), which takes ∿ 45 min for each plane but leads to a unique solution and improves the transport adjustment at 50 MeV. The smaller emittance traced on Fig. 6 (0.9 π mm-mrad), corresponds to a peak radial beam excursion (in the linac) of < 1.2 mm. This process would be quicker with position (profile) monitors in intertank spaces and at 50 MeV.

When one varies the Tanks 2 and 3 focusing over a wide range (e.g. 50% to 125% of nominal level), the results show a somewhat distorted periodicity, but it is certainly not feasible to interpret them in terms of a global quadrupole calibration. A better experiment would involve passing the beam through an unpowered cavity (no rf defocusing), with accurate position (profile) measurements at input and output, and focusing adjustment directly from a keyboard, but one cannot expect to deduce the average magnetic gradient to within ±1%.

Thus one must accept the direct calibration, unless very large discrepancies are found.

Conclusions

The calibrations described here concerning the transverse and longitudinal working points of the 50-MeV linac, provide a firm basis for the present operation. As the beam quality fully satisfies the following accelerators, there has been no serious study yet of the effect of these settings on beam envelopes and emittances.

Acknowledgements

The author was able to rely on willing help from many people, particularly from the linac workshop, the linac controls section and the operations team. Particular thanks are due to A. Bellanger for his thorough work on low power rf and magnetic measurements. There was useful collaboration with E. Boltezar (Mechanical engineering), P. Lienard (Assembler programming) and P. Têtu (Beam measurements).

References

1 E. Boltezar, W. Pirkl, G. Plass, T. Sherwood, U. Tallgren, P. Têtu, D. Warner and M. Weiss, "The new CERN 50-MeV Linac", proceedings this conference.

2 E. Boltezar, "Mechanical Design of the CERN Linac Accelerating Structure", proceedings this conference.

3 D. Warner, "Accelerating Structure of the CERN New 50-MeV Linac", Proc. of the 1976 Linac Conference, AECL-5677 (1976), p. 49.

4 M. Martini and D. Warner, "Numerical Calculations of Linear Accelerator Cavities", CERN 68-11 (1968).

5 P. Têtu, "New Linac Three-Phase Planes Pulsed Emittance Measurement", proceedings this conference.

6 R. Littlewood and C. Mazeline, "The New Linac Quadrupole Measurement System", CERN/PS/SM/ Note 78-8 (1978).

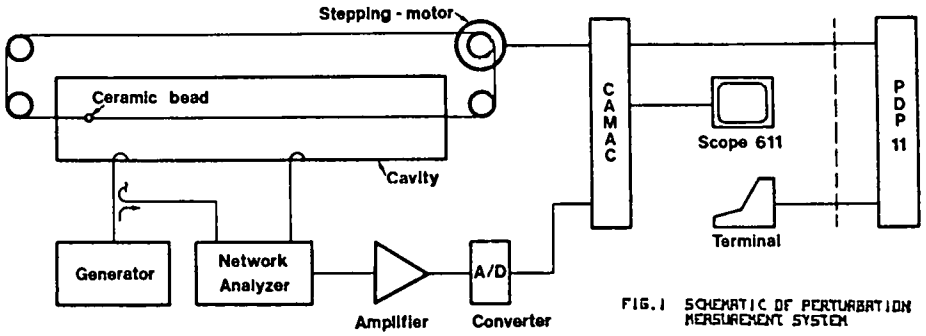


FIG. 1 SCHEMATIC OF PERTURBATION MEASUREMENT SYSTEM

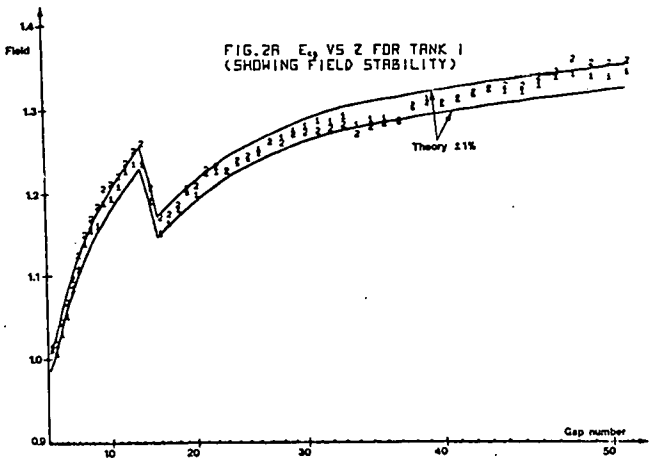


FIG.2A E_0 VS Z FOR TANK 1 (SHOWING FIELD STABILITY)

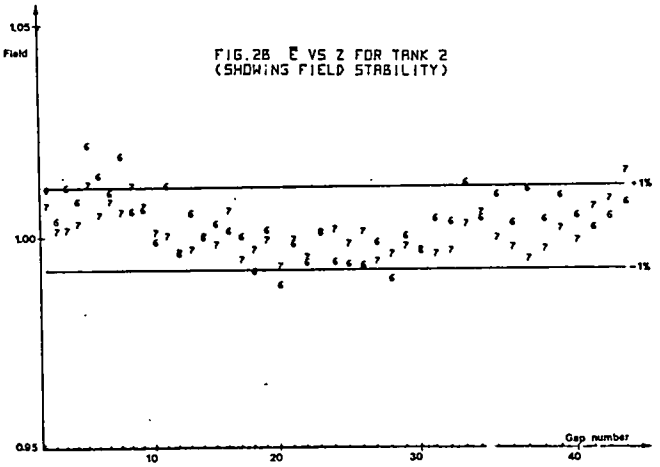


FIG.2B $\bar{E}$ VS Z FOR TANK 2 (SHOWING FIELD STABILITY)

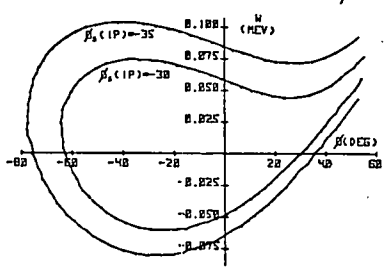


FIG.3 TANK 1, ACCEPTANCE IN W, β.

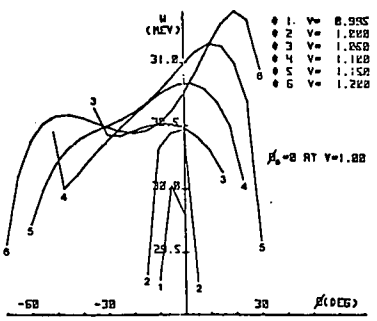


FIG.4A TANK 2, W VS INPUT PHASE OF BUNCH

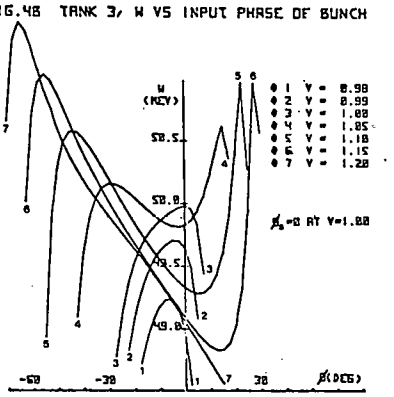


FIG.4B TANK 3, W VS INPUT PHASE OF BUNCH

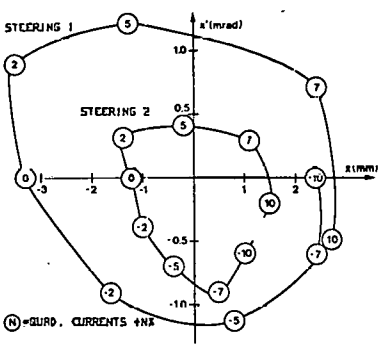


FIG.5 LOCUS OF BEAM CENTRE IN X, X'

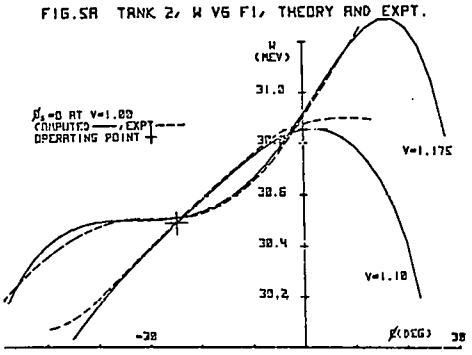


FIG.5A TANK 2, W VS Fi, THEORY AND EXPT.

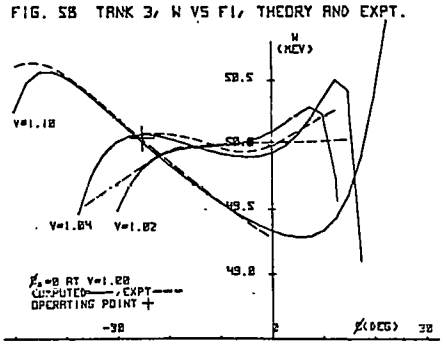


FIG. 5B TANK 3, W VS Fi, THEORY AND EXPT.

Discussion

Miller, SLAC: In the case where you went up in quadrupole current and the beam seemed to be disappearing; do you think it may have been due to getting close to a stop band in the periodic focusing array?

Warner: It could well be. If we have about a mu of 30^{o} for the envelop oscillation, then for the central motion we will have perhaps 70^{o} at the normal operating level, perhaps getting to 90^{o} or 100^{o}. Things get more stable as you go lower, which again is natural. We can go a long way down before the coherent motion is out of the region. I think that is an appropriate explanation.

Hagerman, LASL: How did you make the beam energy measurements when you were studying phase and amplitude set points?

Warner: This is done with longitudinal emittance measurement system and we assumed that where we have the correct behavior we have the synchronous energy. We do have calibrated magnets for this, but .....

Hagerman: It has a momentum analysis system in it?

Warner: Oh yes, a two magnet momentum analysis system.

Swenson, LASL: Is it your experience that the magnetic center of the quadrupoles in the drift tubes coincides with the geometrical center of the pole tips? Do you make use of the measured discrepancies between these two quantities or do you simply confirm that they coincide?

Warner: The measurements were not done relative to the pole tips but the machining of the yoke, I presume, was done with respect to the pole tips - that's the first point; it's the yoke that matters in this case. Now in the case of the quadrupoles in the first tank, we had a very small deviation, less than .03 millimeters (rms). In the outer tanks this was worse, but the way we got around this was to select the order of mounting of quadrupoles so that the variation of magnetic center from one quadrupole to the next was the minimum. So in fact, we did not adjustment in mounting, we just selected where we put them.

NEW LINAC THREE PHASE PLANES PULSED EMITTANCE MEASUREMENT

P. Têtu
CERN
Geneva, Switzerland

Summary

To measure the new linac beam, a single pulse emittance system was developed which measures the beam pulse-to-pulse in the 3 planes.

Introduction

Within the framework of the building of the CERN new linac, it has been decided that the 50-MeV beam would join the old linac-booster beam line in BH3 allowing for the use of the old measurement lines to verify the matching to the booster (emittance line) and to adjust the debunchers (spectrometer line),(Fig. 1).

To test the new linac without involving the operation of the other machines, a complete 3-phase plane measurement system (H-horizontal, V-vertical and L-longitudinal) has been developed. The L plane measurement, handled in the same way as the H and V measurements, allows us to study specially the beam transfer to the booster by using the program TRANSPORT.

The single pulse measurement principle has been kept. The old lines can be used with the new system via a simple switch. This system can be matched by an interaction process to any characteristics of the linac beam.

Phase Planes Measurement Principle

Transverse plane (H horizontal, V vertical)

Upstream of a variable slit (0.5 to 2 mm), two pulsed magnets of the window-frame type, are powered in series and in opposite phase by a sine shaped pulse (T=72 μs). The part of the sine wave between $5\pi/6$ and $7\pi/6$ is used to sweep the beam. See Fig. 2.

In this way, a linear time-beam position relation is obtained. Changing the kicker current changes the diameter unit U_d. Between the slit and a set of 24 collectors, two pulsed quadrupoles maintain two conditions:

1. that each collector represents a given angular unit U_a at the diameter slit;
2. that no particles are lost in the measurement line before the collector.

Figure 3 shows the curves of the quadrupole current versus the desired angular unit U_a.

Finally, during the sweeping of the beam, the 24 collectors measure the beam density distribution as a function of the diameter.

Measurement of the longitudinal L plane (phase versus energy)

In order to have the same handling of the 3 phase planes, it is necessary that the information given by the 24 collectors for the L plane be identical to that coming from the H and V planes. Each collector covers an extension $\Delta\phi_1$ in rf phase and receives a current as function of the various energies contained in the beam, during the sweeping of the first kicker magnet, K1V (Fig. 4).

The first spectrometer magnet works in a classical way (Fig. 4). At the A_1 exit a kicker magnet identical to those of the H-V lines sweeps the beam to be analyzed across the Z_2 slit, which thus accepts the various energies ΔE_1, ΔE_2, ΔE_n sequentially. Z_2 is the object-slit of a second spectrometer magnet with the 24 collectors at the image point. An rf cavity tuned to the linac frequency works as a rotating lens in the $\Delta\phi\Delta E$-plane transforming the phase dispersion $\Delta\phi$ into an energy dispersion $\Delta E_\phi = C\cdot\Delta\phi$, analysed by the second spectrometer magnet.

The final transverse position Z_3 of a particle is a function of its energy at the output of the rf cavity :

$$Z_3 = f(E_o+\Delta E+\Delta E_\phi),$$

E_o is the mean energy of the beam which defines the central trajectory in the spectrometers, $\Delta E=f(t)$ is the linac beam energy dispersion, which becomes a function of time after the Z_2 slit. In order that Z_3 be only a function of ΔE_ϕ (and hence of $\Delta\phi$), a second kicker magnet (K2V) powered in series with the first one cancels the effect of the function $\Delta E=f(t)$.

When varying the kicker intensity, a variable energy axis unit U_E is obtained. In varying the effective voltage in the rf cavity, one can vary the phase unit U_ϕ.

A_1 and A_2 have a deflection angle of 54,3°, the length of the mean trajectory being 1.2 m.

Collectors

Secondary emission collectors are used, transparent to the 50-MeV beam. There are 24 nickel ribbons, 1.5-mm wide, with a thickness of about 4 μ; each ribbon is separated from the other by 0.3 mm. The front and back sides are screened by a 4 μ aluminium sheet, biased to + 200 V and placed at 5 mm distance. In order to avoid mechanical movements, two such collectors (for H and V phase planes) are placed one after the other, in a sandwich arrangement (screen - H collector - screen-V collector - screen).

Analog Signals Treatment

After having been amplified on the spot, the analog signal of the 24 collectors is transferred to the equipment gallery where a single set of electronics treat the information (Fig. 5).

Figure 6 gives the general layout of the system with the old and new lines. Each signal enters a comparator (IM319). At the output, the unit signal enters a shift register, with a series input and a parallel output triggered by a 2-MHz clock. Each signal is cut into 24 parts (measurement duration 12 μs). In due course, the shift register is read and the information is transferred in series via CAMAC to the computer which puts into its memory a matrix of 24x24 bits representative of the phase plane. The parameters of an ellipse, "the nearest to the measured surface", which, at 50 MeV, is almost elliptical, is calculated by the program.

In parallel with the comparator, each collector is linked to two circuits which are unlocked by a square pulse. One of these circuits gives an output signal proportional to the input signal and is gated on during the 12 μs measurement, while the other one gives a signal proportional to the current contained in the measured emittance and is gated by the output signal of the comparator. After integration of the 24 channels, two signals are obtained : one V_t, proportional to the total current and the other V_p, proportional to the current contained in the emittance delimited by a chosen equi-density line.

Operation of the Lines

Starting the operation

The lines are controlled via the consoles of the new linac, which allow access directly to either one of the three phase planes, or the 3 synoptics of these planes, which display the technological state of the lines (see Fig. 7 for the L plane synoptic). Calling one of the lines directly, one obtains, pulse-to-pulse, on a color TV display, the shape of the emittance and in addition calculated values as I_o - total current of the beam ; E - measured emittance ; PMAX - maximum abscissa of the measured ellipse ; WMAX - maximum ordinate of the measured ellipse ; E_o - emittance containing 63% of the beam (from calculated V_p, V_t and E); I_o/E_o - quality factor of the beam ; PMEAN and WMEAN - position of the ellipse center (Fig. 8).

The touch button "Change Unit" gives access to a new page, which allows the settings of the various parameters of the line to be changed.

Settings of the line

These settings have two aims :

1. that the whole measured beam arrives on the collector set
2. that one achieves the best measurement accuracy.

Five parameters are adjustable with acquisitions pulse-to-pulse on the display unit (Fig. 8):

1) U_d. The diameter unit can be varied from 1 to 3 mm for the H, V planes and from 7.5 to 15° for the L plane.
2) U_a or U_E. Variation from 0.15 to 0.5 mrad for U_a (H and V planes) and from 30 to 90 keV for U_E (L plane).
3) Threshold. Variable from 1% to 100% of beam density.
4) Delay. From 0 to 200 μs to vary the measurement momentum within the linac pulse.
5) Gains. From 0 to 7 as function of the total current to be measured (from 10 to 200 mA).

A program written by J. Stovall and modified by P. Mead raises the threshold voltage from 0 to 100% in steps of 5%, reads the numerical results for each pulse and allows in 20 pulses to get the repartition of current densities. One example of this program (Ref. Autostep) is shown in Fig. 9.

Calibration

Before putting the lines in operation it was necessary to check the accuracy of the different measurement parameters.

Transverse planes H and V

A given change of current in BH1 produces a certain change of the mean angle of the beam, and therefore a specific change of position at the measurement slit. In this way it was possible to calibrate the U_D and U_A.

Some measurements were done with a defined beam as a function of the slit width to know the space-charge effect in the line between slit and collectors. These tests confirmed the calculations that for the range of slit widths used, the global effect is smaller than 5% in the beam angular distribution.

Longitudinal plane

- Setting of the rf cavity :

The setting of the rf cavity phase must be such that with and without rf the center of the beam on the display does not change.

To check the calibration of the U_ϕ the rf phase in the cavity was changed by 30°, which moved the mean position of the beam on the display ; knowing the sensitivity of the second spectrometer it was possible to measure the exact U_ϕ.

A Typical Measurement

Figures 10a, b, c, show a typical result in the three phase planes for $E=2E_o$. By variation of the threshold the curves of Fig. 11 were obtained and by integration the exact value of E_o was found.

CONCLUSIONS

This system has now been used for one year. The final aim is to collect, in one pulse, the values of the densities for the 24x24 matrix by using a fast A/D converter and to have, what the "Autostep REF program" gives us now in 15 pulses, in a pulse-to-pulse way.

Acknowledgements

I wish to acknowledge our indebtedness to my colleagues in the PS and visitors for their essential contributions to this measurement system.

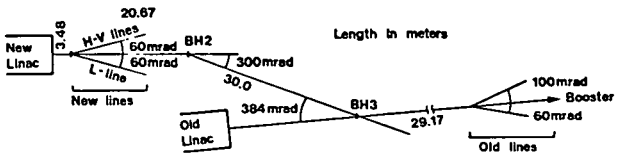


Fig. 1 Layout of the High Energy Beam Transport (HEBT) line

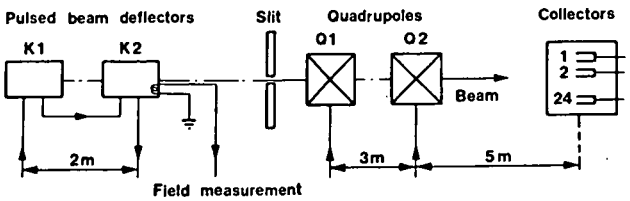


Fig. 2 Layout of the apparatus for the transverse phase planes measurement

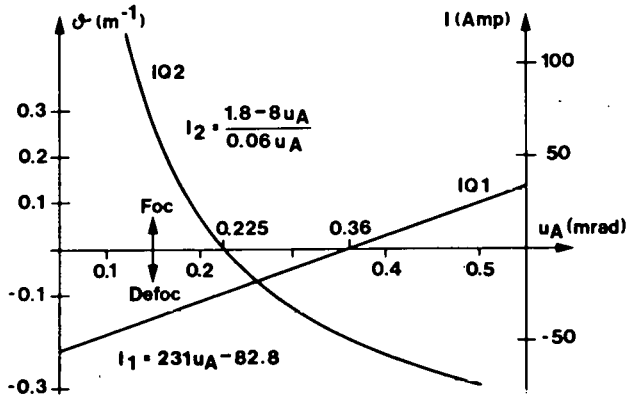


Fig. 3 Beam focusing of the transverse emittance line (measured plane)

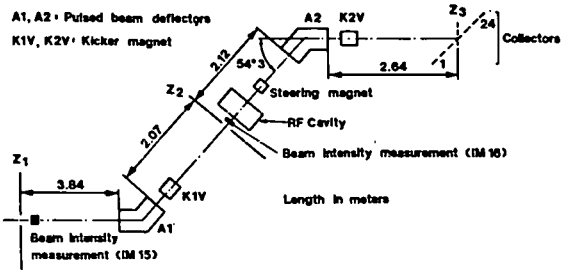


Fig. 4 Layout of the apparatus for longitudinal phase plane measurement

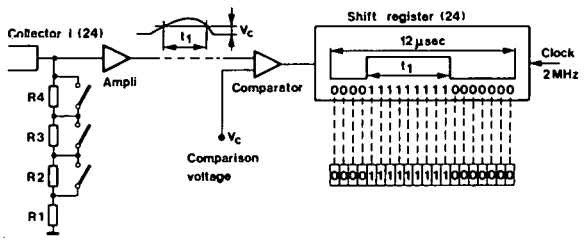


Fig. 5

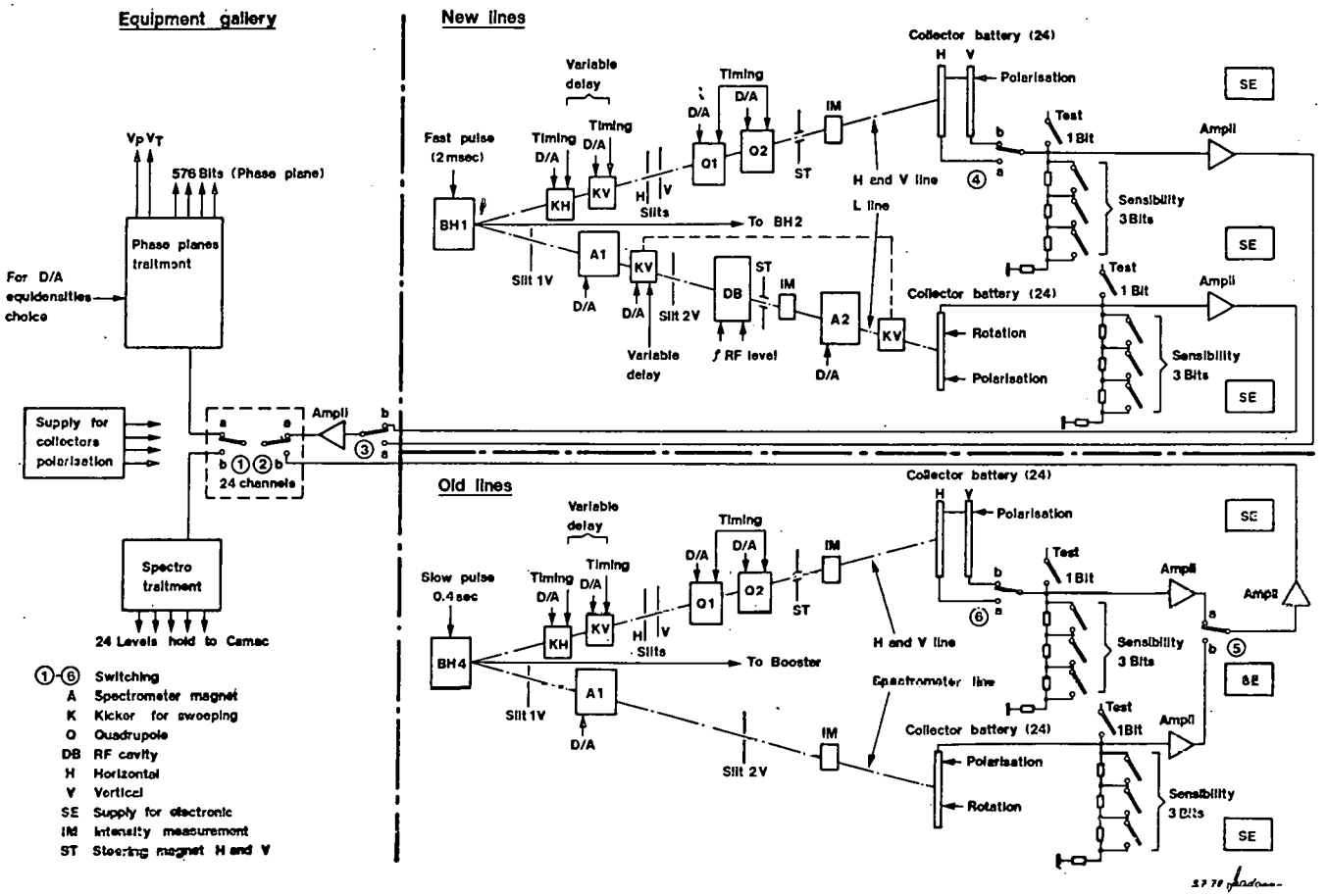


Fig. 6 General layout of the measurement lines (at 50 MeV)

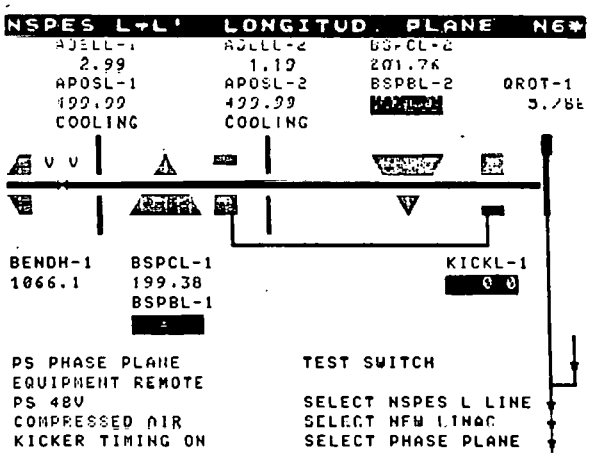


Fig. 7 Longitudinal Plane Synoptic

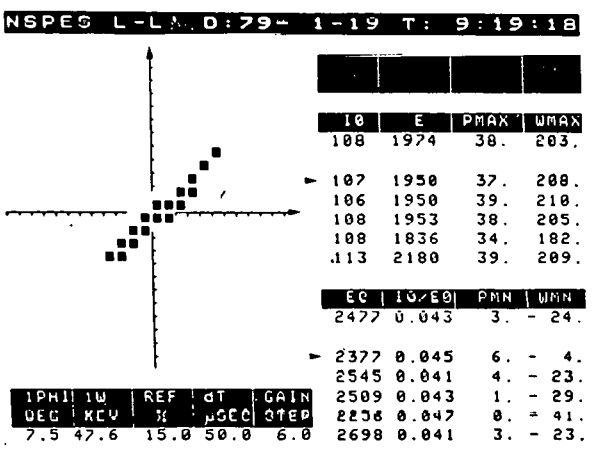


Fig. 8

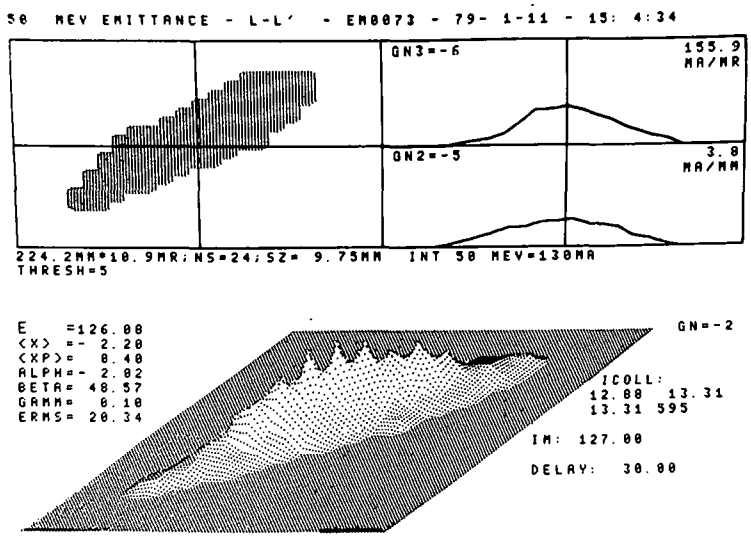


Fig. 9 Example of AUTO-STEP PROGRAM

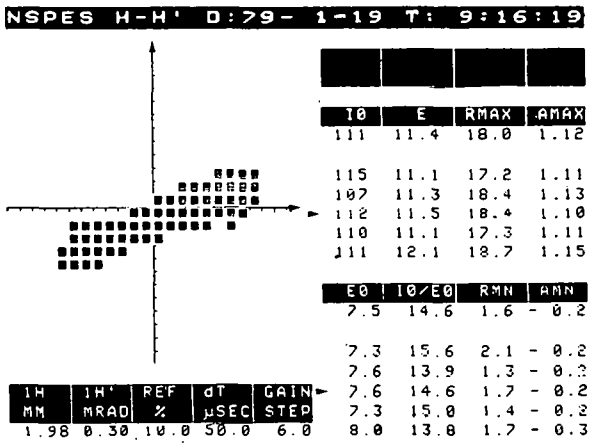


Fig. 10a

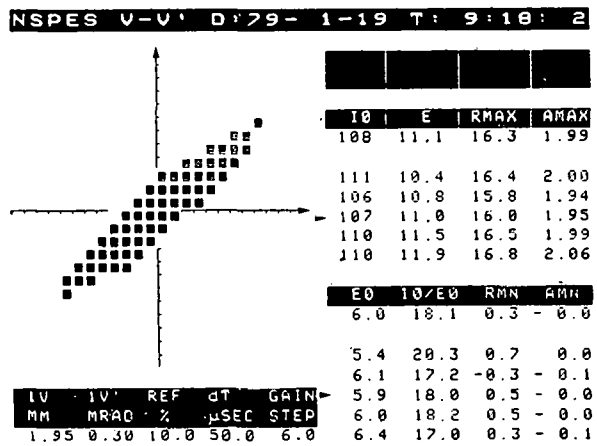


Fig. 10b

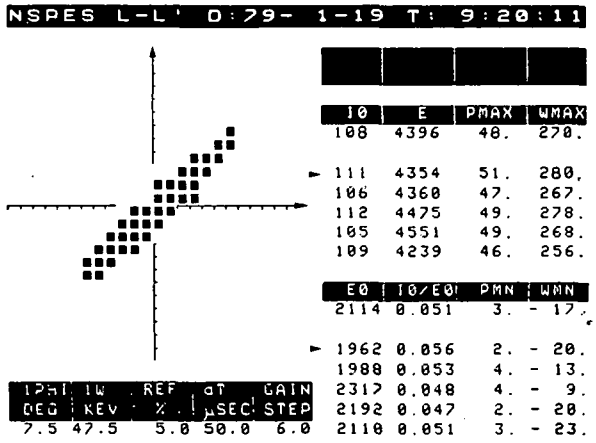


Fig. 10c

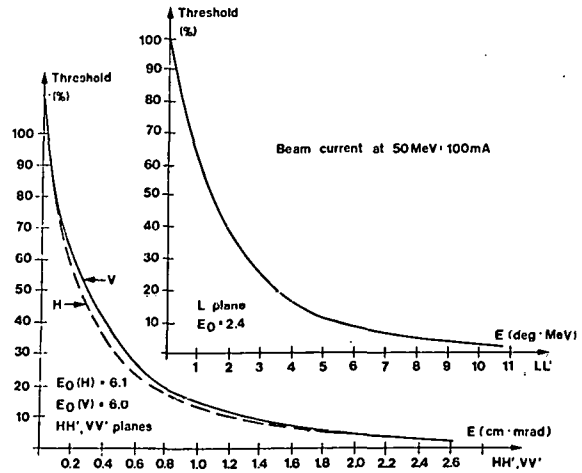


Fig. 11 Emittances as a function of threshold in the three phase planes

BEAM TOMOGRAPHY IN TWO AND FOUR DIMENSIONS*

O. R. Sander, G. N. Minerbo, R. A. Jameson,
and D. D. Chamberlin
Los Alamos Scientific Laboratory
Los Alamos, New Mexico 87545

Summary

The coming generations of high beam-power accelerators require new techniques to monitor the emittance and the shape of the beam; in particular, measurements that do not interfere with the beam itself are necessary. A new computational algorithm, MENT (Maximum ENTropy), will be presented that combines nondestructive profile measurements taken from a number of stations along the beam line, with beam-dynamics calculations to compute a four-dimensional phase-space distribution. A version of MENT has been used on experimental data to reconstruct the two-dimensional transverse emittance of the Clinton P. Anderson Meson Physics Facility (LAMPF) proton beam at 100 MeV and the H^- beam at 750 KeV. Wire scanners at three stations were used to get the one-dimensional profiles. Results will be compared with those gained using the destructive slit and collector method and with those gained using MART (Multiplicative Algebraic Reconstruction Technique) on the same three profiles.

Maximum Entropy Reconstruction Techniques

Two algorithms were used, MART[1] (Multiplicative Algebraic Reconstruction Technique), and MENT,[2] to reconstruct the emittance of LAMPF beams at 100-MeV and 750-KeV energies. Both algorithms were used to reconstruct a source from the same sets of projections or profiles. Both MENT and MART are designed to converge to a maximum entropy solution, or yield an image with the lowest information content consistent with available data; extraneous information or artificial structure is thereby avoided. Because a description of MENT and MART for two dimensional reconstruction has been given elsewhere,[1,2] only comments on these methods will be given. Theoretically both algorithms, when applied to distributions of Gaussian shape, should produce essentially exact reconstruction. MART and MENT are well suited for applications where the number of measured profiles is small and where the source distribution is somewhat Gaussian in shape. These attributes made the algorithms attractive for accelerator application because particle-beam distributions are usually smooth, unimodal, possess only moderate amounts of asymmetry and are often available for measurement at only a few stations. MENT has been used for cross-section reconstruction of fuel rod-bundles[3] and laser-imploded pellets.[4] MART has been used to reconstruct transverse emittances of particle beams.[5] In principle, MENT is simpler to implement because it only requires the use of one-dimensional measured profiles and one-dimensional back projections; MART requires not only the same one-dimensional measured profiles but also an array representation of the source. The array size can become considerable as one goes to three, four, or n dimensions. The amount of computer storage for the array is M^n, where M is the number of samples in a projection and typically varies between 50 and 100. This storage requirement eliminates the use of small and medium-size computers. The array must be transformed from one station to another by a complicated mapping of the M^n pixel-volume elements. This mapping has not been attempted for any n greater than two, and appears quite formidable for any greater n. However, the extension of MENT to four or six dimensions is straightforward. For these reasons, MENT was adopted to reconstruct transverse emittance distributions and its performance investigated in comparison to MART.

Method

Three wire scanners in the 100-MeV and in the 750-KeV transport regions of LAMPF were used to measure the beam profiles. The wire scanners were separated by nearly equal drift sections located near standard emittance measuring stations consisting of slits and collectors. At 100 MeV, the H^+ beam transmitted through the slit was observed on a wire scanner. These data were reported earlier.[5] When compared to the data collected with the standard slit method, the MART reconstruction had small differences in the ellipse parameters α and β, which could not be attributed to statistics. In the comparison of the emittance area versus percentage of total beam enclosed, both MART and the standard method results were in excellent agreement. These same profiles now have been analyzed with the MENT algorithm.

Similar measurements were made of the LAMPF low-intensity H^- beam at 750 KeV. In this case the standard emittance station used a collector consisting of a plate with conducting strips attached to it. At both energies, it was assumed that no space-charge effects were present and that the transfer matrices connecting the viewing stations were simple drifts, which they are in the zero current limit.

*Work performed under the auspices of the U. S. Department of Energy.

Results

Figures 1 and 2 show plots of emittance area versus percentage of total beam for beams of 100-MeV and 750-KeV energy. In both cases, MENT and MART are in good agreement with the data gained with the slit and collector method, which is assumed to yield a density distribution closest to the true beam distribution.

The shape parameters α and β have been compared by displaying the residual betatron oscillation[6] $\Delta R/R$ for MENT and MART. The true ellipse parameters are assumed equal to those gained with the slit and collector method. In Fig. 3 $\Delta R/R$ for the 750-KeV data is shown. Both algorithms give excellent reconstructions of the emittance distribution. Similar plots for the 100-MeV data are also shown in Fig. 3 Both methods give values of $\Delta R/R$ approximately equal to 0.1. In this case the MENT results more closely match the slit and collector results. Contour plots of the reconstructed density distribution are shown in Fig. 4 for the slit and collector method, in Fig. 5 for the MART algorithm and in Fig. 6 for the MENT algorithm.

Because situations could exist where the matching of a beam emittance to a linac acceptance should result in a value of $\Delta R/R$ as small as 0.1, an emittance-measuring method whose accuracy can be characterized by a value of $\Delta R/R$ smaller than 0.1 is desired. Therefore, corrections that will reduce the value of $\Delta R/R$ in Fig. 3 are sought. It has been determined that this small but significant value cannot be attributed to errors caused by non-ideal viewing

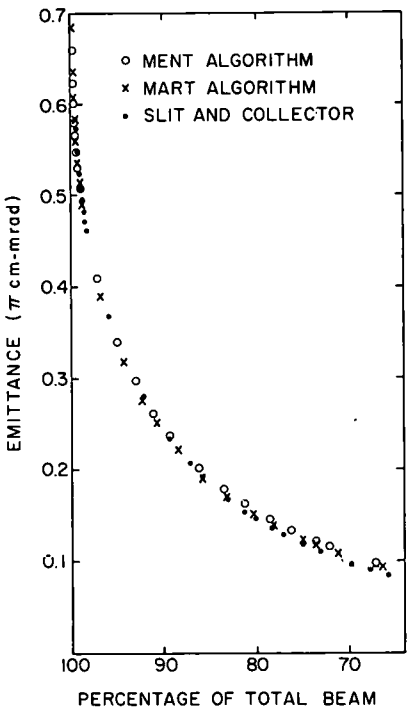


Fig. 1. Total emittances versus percentage of the 100-MeV H^+ beam.

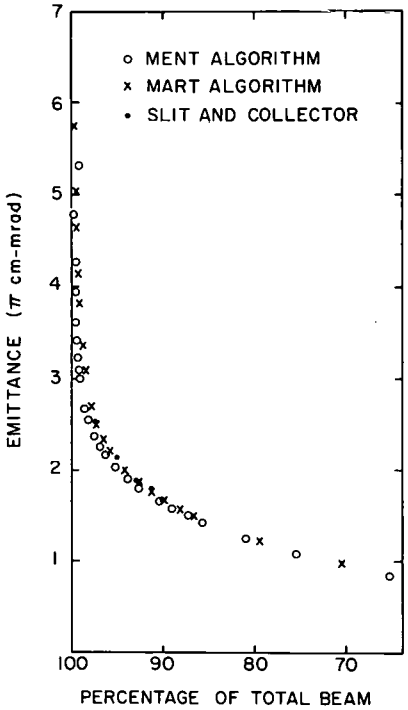


Fig. 2. Total emittance versus percentage of the 750-keV H^- beam.

angles or any artificial asymmetric emittance growth caused by the pixel mapping in MART.

An additional test of the algorithms was made using generated asymmetric Gaussian distributions. Both MART and MENT gave nearly exact reconstructions. In this case our version of MART is superior to earlier versions that gave reconstructions with jagged peaks and fluctuations. The improvement is apparently the result of reconstructing profiles from column sums of transformed pixels. Profiles were previously calculated from rays intercepting pixels.

Four-Dimensional Reconstruction Method

The MENT algorithm was chosen to reconstruct four-dimensional emittance distributions because it gives equally good, or slightly better, two-dimensional reconstruction and because it is relatively easy to expand MENT to four dimensions. For the present reconstruction only in linac sections where no energy change takes place, where first-order optics is valid, and where space-charge effects can be expressed by a linear transfer matrix, will be considered.

The phase-space density function of the beam in a reference plane z = 0 can be denoted by

$$f\left(\begin{bmatrix} x \\ x' \\ y \\ y' \end{bmatrix}\right), \qquad (1)$$

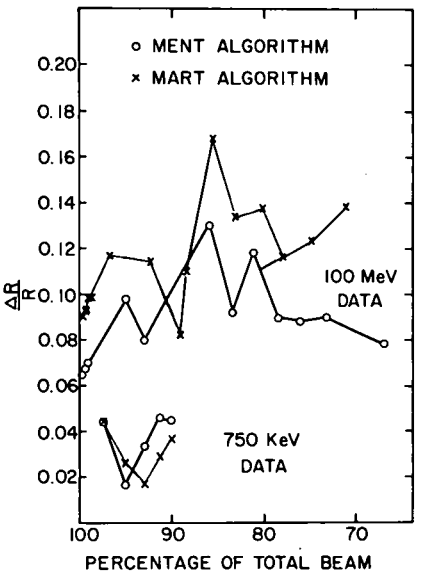


Fig. 3. Comparison of the reconstructed ellipses.

where x and y are the coordinates of the particle, and where the direction unit vector $\Omega = p/p$, (p is the particle momentum) has components x',y'. At station j (in the plane $z = z_j$) the particle will have coordinates given by:

$$\begin{pmatrix} x_j \\ x'_j \\ y_j \\ y'_j \end{pmatrix} = T_j \begin{pmatrix} x \\ x' \\ y \\ y' \end{pmatrix} , \qquad (2)$$

where T_j is a 4 x 4 transfer matrix. Computer codes, e.g., TRACE[7] and TRANSPORT,[8] are available to compute transfer matrices for different accelerator components. The density distribution at plane $z = z_j$ is, from Eqs. (1) and (2),

$$f\left(\begin{bmatrix} x_j \\ x'_j \\ y_j \\ y'_j \end{bmatrix}\right) = f\left(T_j^{-1} \begin{bmatrix} x \\ x' \\ y \\ y' \end{bmatrix}\right) . \qquad (3)$$

Consider now a scan measurement at station j that produces a projection of the beam density along a line making an angle θ_k with the positive x-axis. These one-dimensional profiles can be obtained, for example, with the wire scanner technique, or by observing light quanta emitted by suitable tracer materials or

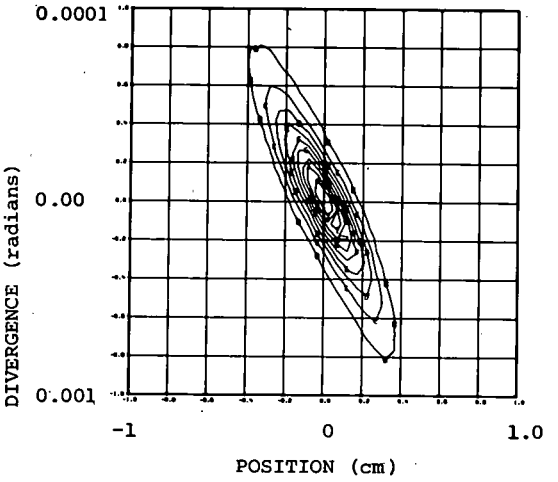


Fig. 4. Beam contours from the slit and collector method.

background gas ionization. To express the measured profile in terms of f, introduce a matrix R that produces a rotation of axes through an angle θ_k about the z-axis:

$$\begin{pmatrix} u_{kj} \\ u'_{kj} \\ v_{kj} \\ v'_{kj} \end{pmatrix} = R(\theta_k) \begin{pmatrix} x_j \\ x'_j \\ y_j \\ y'_j \end{pmatrix} , \qquad (4)$$

where

$$R(\theta) = \begin{pmatrix} \cos\theta & 0 & \sin\theta & 0 \\ 0 & \cos\theta & 0 & \sin\theta \\ -\sin\theta & 0 & \cos\theta & 0 \\ 0 & -\sin\theta & 0 & \cos\theta \end{pmatrix} . \qquad (5)$$

The measured projection profile for the angle θ_k at station z_j is :

$$g_{kj}(u) = \int dv \int du' \int dv' \; f\left(T_j^{-1} R_k^{-1} \begin{bmatrix} u \\ u' \\ v \\ v' \end{bmatrix}\right)$$

$$j = 1,\ldots,J, \quad k = 1,\ldots,K \qquad . \qquad (6)$$

Now consider the entropy associated with the distribution f. Assume that f satisfies the conditions:

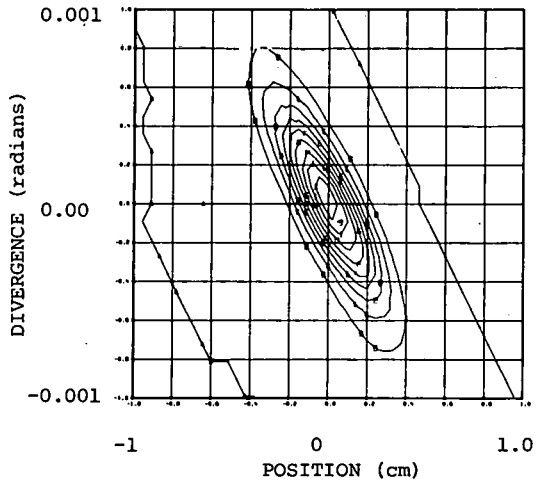


Fig. 5. Beam contours from the MART algorithm.

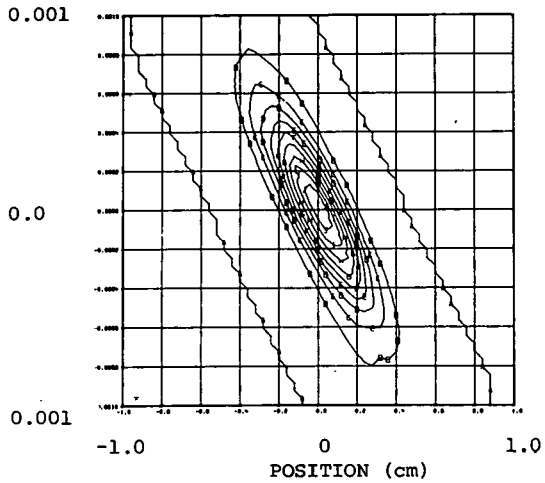


Fig. 6. Beam contours from the MENT algorithm.

$$f\left(\begin{bmatrix} x \\ x' \\ y \\ y' \end{bmatrix}\right) \geq 0 \qquad (7)$$

$$\int dx \int dx' \int dy \int dy' \; f\left(\begin{bmatrix} x \\ x' \\ y \\ y' \end{bmatrix}\right) = 1,$$

so that f can be regarded as a probability distribution function. These conditions imply that:

$$g_{kj}(u) \geq 0 \qquad j = 1,\ldots,J \quad k = 1,\ldots,K,$$

$$\int du \; g_{kj}(u) = 1. \qquad (8)$$

The entropy associated with f is:[1]

$$H = -\int dx \int_D dx' \int dy \int dy' \; f\left(\begin{bmatrix} x \\ x' \\ y \\ y' \end{bmatrix}\right) \ln\left\{f\left(\begin{bmatrix} x \\ x' \\ y \\ y' \end{bmatrix}\right) V\right\}, \qquad (9)$$

where V is the 4-dimensional volume of the set D where f is positive. Now maximize H with Eqs. (6) treated as constraints. This prescription produces the solution that is the "most probable" consistent with the measured data for g. The Lagrange multiplier method is used to solve this optimization problem.

Introduce a Lagrange multiplier $\lambda_{kj}(u)$, for each condition in Eq. (6) and perform a variation of the functional:

$$\eta(f) = H - \sum_{kj} \int du \; \lambda_{kj}(u) \left\{ g_{kj}(u) - \int du' \int dv \int dv' \cdot f(T_j^{-1} R_k^{-1} \begin{bmatrix} u \\ u' \\ v \\ v' \end{bmatrix}) \right\}. \qquad (10)$$

By changing variables of integration the second integral in Eq. (10) can be rewritten as;

$$\sum_{kj} \int dx \int dx' \int dy \int dy' \; \lambda_{kj} \left(S_k T_j \begin{bmatrix} x \\ x' \\ y \\ y' \end{bmatrix}\right) f\left(\begin{bmatrix} x \\ x' \\ y \\ y' \end{bmatrix}\right), \qquad (11)$$

where S_k is a 1 x 4 submatrix of the matrix R_k:

$$S_k = [\, \cos\theta_n \quad 0 \quad \sin\theta_n \quad 0 \,]. \qquad (12)$$

The functional derivative of η with respect to f is set equal to zero, giving;

$$-\ln\{f(\zeta)V\} - 1 + \sum \lambda_{kj} \left(S_k T_j \zeta\right) = 0. \qquad (13)$$

Thus f must have the form:

$$f(\zeta) = \frac{1}{V} \prod_{kj} h_{kj} \left(S_k T_j \zeta\right), \qquad (14)$$

where

$$h_{jk}(u) = \exp\left[\lambda_{kj}(u) - \frac{1}{KJ} \right] . \qquad (15)$$

To find the unknown functions h_{kj}, solve the KJ equations obtained by substituting Eq. (14) into the constraint equations (6):

$$g_{kj}(u) = \frac{1}{V} h_{kj}(u) \int du' \int dv \int dv' \prod_{m,\ell \neq k,j} h_{m\ell} \cdot$$

$$(S_m T_\ell T_j^{-1} R_k^{-1} \begin{bmatrix} u \\ u' \\ v \\ v' \end{bmatrix}) . \qquad (16)$$

The iteration scheme described in Ref. 1 must be modified as follows. Initially one sets

$$h_{kj}^0(u) = \begin{cases} 1 \text{ if } g_{kj}(u) \neq 0 \\ 0 \text{ if } g_{kj}(u) = 0 \end{cases} , \qquad (17)$$

and one then applies cyclic updates:

$$h_{kj}^{i+1}(u) = h_{kj}^i / R_j^i(u),$$

$$\text{if } g_{kj}(u) \neq 0 \text{ and } k + (j-1)K = \text{imod}(JK) + 1$$

$$h_{kj}^{i+1} = h_{kj}^i(u) \quad \text{otherwise,} \qquad (18)$$

where

$$R_{kj}^i(u) = [g_{kj}(u)V]^{-1} h_{kj}^i(u) \int du' \int dv \int dv' \cdot$$

$$\prod_{m,\ell \neq k,j} h_{kj}^i (S_m T T_j^{-1} R_k^{-1} \begin{bmatrix} u \\ u' \\ v \\ v' \end{bmatrix}) . \qquad (19)$$

This iteration scheme has been found to converge very fast numerically in two and three dimensions.

Future Studies

We plan to use MENT to reconstruct emittance distributions for the Hanford FMIT Accelerator where the 3.5-MW beam power precludes standard interceptive sensors. Light emitted from ionized or excited residual gases in the beam region will be collected by low-level TV cameras and digitized. Beam profiles from four views at each of three stations will be used to reconstruct the 4-dimensional distribution.

At LAMPF we are adding additional wires at our 750-KeV wire scanner stations. These wires will give us additional views with which to reconstruct the 4-dimensional emittance. We are also conducting studies to determine how space-charge effects must be incorporated into our transfer matrices connecting viewing stations, and we plan to develop a method for assigning coordinates from the reconstructed distribution to a macroparticle distribution for use in computer simulation codes.

References

1. J. S. Fraser, "Beam Tomography or ART in Accelerator Physics," Los Alamos Scientific Laboratory report LA-7498-MS (Nov. 1978).

2. G. Minerbo, "MENT: A Maximum Entropy Algorithm for Reconstructing a Source from Projection Data," Computer Graphics and Image Processing 10, 48 (1979).

3. T. G. Sanderson, "Reconstruction of Fuel Pin Bundles by a Maximum Entropy Method," IEEE Transactions on Nuclear Science, Vol. NS 26, 2685 (1979).

4. D. B. van Hulsteyn, P. Lee, J. G. Sanderson, G. N. Minerbo, "Three-Dimensional Reconstruction of X-Ray Emission in Laser Imploded Targets," Los Alamos Scientific Laboratory report LA-UR-78-3033, to be published in Applied Optics.

5. O. R. Sander, R. A. Jameson, R. D. Patton, "Recent Improvements in Beam Diagnostic Equipment," IEEE Transaction on Nuclear Science, Vol. NS 26, 3417 (1979).

6. J. Guyard, M. Weiss, "Use of Beam Emittance Measurements in Matching Problems," Proc. 19th Proton Linear Accelerator Conference, Chalk River, Canada, AECA 5677, Nov. 1974.

7. K. R. Crandall, "TRACE - An Interactive Beam Transport Program," Los Alamos Scientific Laboratory Report LA-5532, Oct. 1973.

8. K. L. Brown, B. K. Lear and S. K. Howry, "TRANSPORT/360," Stanford Linear Accelerator Center Report SLAC-91, 1977.

SINGLE BUNCH ACCELERATION AND DETECTION IN S-BAND ELECTRON LINEAR ACCELERATOR

J. Tanaka, I. Sato, S. Anami, S. Fukuda, H. Matsumoto
KEK Tsukuba Japan
Y. Tabata, H. Kobayashi, S. Tagawa, M. Washio
Nuclear Engineering Research Lab. Univ. of Tokyo.

Summary

Single bunches have been accelerated and directly monitored for pulse radiolysis studies since June 1977, at the 35-MeV S-band electron linac of the Nuclear Research Laboratory of the Univ. of Tokyo.

An extremely short, picosecond-range single electron pulse was attained by means of a beam compressing injector and an ordinary TW type accelerator guide system. The measured maximum charge density of the single bunches was 1 nanocoulomb and the detected pulse duration was 16 picoseconds which is the limit of the monitoring detector. This report also describes the low jitter (less than 20 ps) triggering system for the detectors and the injector, and a few of the monitors to detect such a short pulse.

Introduction

Picosecond-range single bunches accelerated by an S-band electron linear accelerator provide a powerful means not only for the study of pulse radiolysis in radio chemistry and of other transient phenomena but also for the study of the performance of the accelerator itself.

Sub-nanosecond range single bunches accelerator by an L-band electron linear accelerator have been reported previously.[1,2,3] The short pulse beams produced by an electron gun (with duration corresponding to one cycle of a sub-harmonic frequency) were compressed by means of a sub-harmonic buncher, a prebuncher and an ordinary accelerator guide, and were detected by a coaxial type Faraday cup and a Bi-planer photodiode. However, the detected pulse durations were in the 50-picosecond range.

In order to study picosecond-range transient phenomena a 35-MeV S-band (2856 MHz) electron linear accelerator capable of accelerating picosecond-range single bunches, nanosecond and microsecond range pulse beams was constructed at the Nuclear Engineering Research Laboratory at the University of Tokyo.[4] In addition to ordinary physical, chemical and engineering research, the linac has two main special research purposes. The first is to produce intense neutron pulses by link operation with the fast neutron reactor "Yayoi", for studies in reactor physics and engineering. The second is to get extremely short electron pulse beams to study transient phenomena including picosecond-range pulse radiolysis.

General Description of the Linac

The NERL linac is composed of an injector which consists of an electron gun, a sub-harmonic frequency buncher(476 MHz), a traveling wave type prebuncher (2856 Mhz) and focusing magnetic lenses, two 2/3π mode TW type accelerator guides(1.7 m and 2 m in length) and three beam channels including a beam transport line extending to the reactor "Yayoi".

To be as flexible as possible for research purposes, especially for pulse radiolysis using picosecond range single bunches, careful attention was paid to the design and construction of the very short pulse, high current electron injector and the triggering system which synchronize the injector and detectors with the accelerator wave.

The general parameters of the machine are shown in Table I and the schematic layout is shown in Fig. 1.

Table I General parameters of the linac

1.	Ordinary pulse mode operation	
	Energy	38 MeV(no load)
		26.8 MeV(at 200 mA)
	Beam current	230 mA(at 25 MeV)
	Pulse duration	0.1, 0.6, 1.1, 4.5 μs
	Repetition rate	single shot∿ 200 pps
	Size of beam spot	2∿3 mm
2.	Nanosecond pulse mode operation	
	Energy	37 MeV
	Beam current	2 A
	Pulse duration	2.0, 10, ns
	Beam current stability	1.5%/5min., 3%/60min.
3.	Picosecond pulse mode operation	
3.1	2,100 ps interval pulses (with S.H.B.)	
	Charge per bunch	1 nc
3.2	Single bunch	
	Bunch width	16 ps
	Charge	1 nc

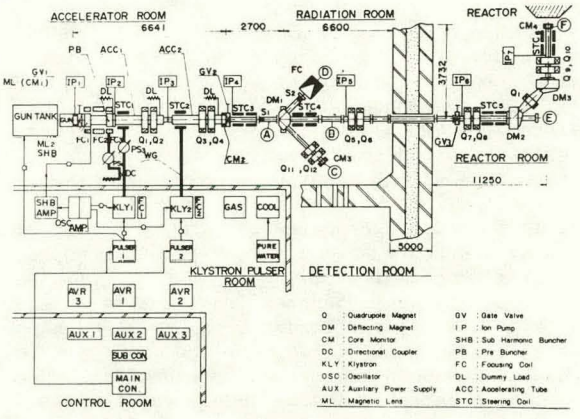


Fig. 1 Layout of the NERL facility

Injector

The injector is composed of an electron gun and a dc biased grid-cathode pulse generator placed on a -90kV, 5μs pulse transformer high potential deck, a 476-MHz (1/6·2856 MHz) sub-harmonic buncher, a 2856-MHz TW type 6-cell prebuncher and focusing system. The schematic diagram of the injector is shown in Fig.2.

In order to attain an intense single bunch isolated from the fine-structure of the 2856-MHz

accelerating frequency (350 ps interval satellites), a very short pulse electron gun is required capable of 2.1 ns pulses corresponding to one cycle of the sub-harmonic frequency (476 MHz). The electron gun is of the triode type and the grid-cathode structure is similar to that of a planer triode tube. The grid and cathode connections are coaxial and have matched coaxial ceramic seals. The impedance is 25 ohms and the VSWR is less than 1:1.5 over the frequency range from 500 MHz to 1,300 MHz. As the output of the grid-cathode

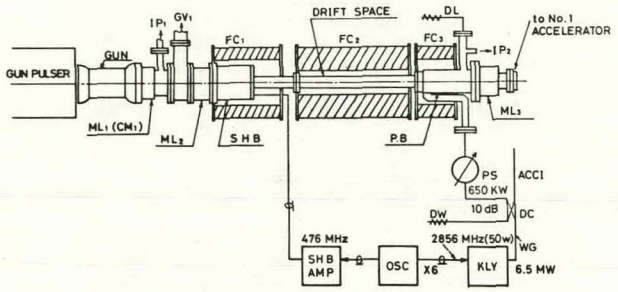


Fig. 2 Schematic diagram of the injector

pulse generator is designed for 50-ohm cable, a tapered coaxial transient adapter is inserted between the pulse generator and grid-cathode connections.

The present cathode of the electron gun is an impregnated cathode, and the duration of the electron beam pulse is 1.6 ns at a peak current of 2.5 A. However, development of a new grid-cathode assembly is proceeding, which uses a grid-cathode assembly of a commercial planer tube and will be able to attain higher currents.

To obtain a clean single bunch without satellites, a triangular electron pulse form is preferable over a rectangular pulse beam.

The grid-cathode pulse amplifier, which consists of 6 UHF planer triodes coupled together in series by broad-band coupling transformers is placed on the -90-kV high potential deck. The trigger pulse for the fast pulse amplifier is supplied from a synchronized trigger system working at ground potential via an isolation choke wound of semirigid coaxial line.

The sub-harmonic buncher is a tunable re-entrant type cavity; the loaded Q value is 700 at a coupling coefficient of 1.4. Due to the operation of the sub-harmonic buncher and prebuncher, a 2-nanosecond electron pulse is compressed to less than 100 picoseconds prior to injection into the accelerator guide. Consequently, to reduce the strong space-charge effects it is necessary to accelerate the beam to higher velocity. The prebuncher is a $2/3\pi$ mode TW type 6-cell accelerator guide and the phase velocities of the first 3 cells and the last 3 cells are $0.7c$ and $0.75c$ respectively.

The output beam is accelerated to 540 keV with 600 kW of rf power and is compressed into the acceptance angle of the first accelerator guide, which has a short bunching section.

The focusing system of the injector is composed of three magnetic lenses and three solenoids, surrounding the sub-harmonic buncher, the first drift space and the prebuncher.

Synchronized Triggering System

In a single bunch electron linac, one of the important requirements is to generate fast rise-time, low jitter trigger pulses synchronized with the accelerating rf waves in order to accelerate an intense and clean single bunch and to be able to observe the details of the picosecond-range short pulses.

A new simple, stable and low jitter synchronized trigger system was developed.[5] (Fig.3)

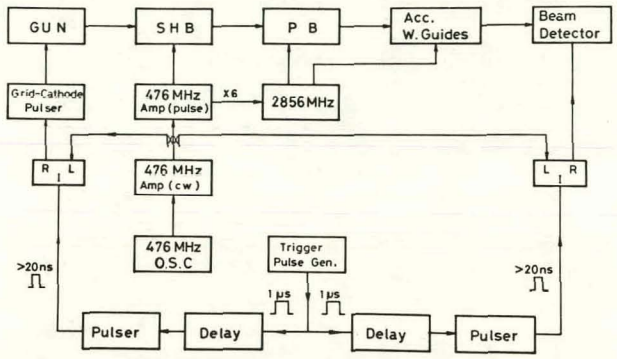


Fig. 3 Schematic diagram of synchronized trigger system

In this system, a 476-MHz sub-harmonic frequency wave, delivered from the cw preamplifier of the modulated signal, is used directly for the trigger signals. A double balanced mixer (HP 10514A) is available to slice the UHF continuous wave into wave trains of more than 20 nanoseconds duration, where the leading wave crest is used as the trigger pulse. The rise-time of the modulation pulse should be as fast as possible; however, a risetime of 10 nanoseconds was sufficient, because, even if the amplitude of the first crest was too low to trigger the gun pulse generator or the detectors, the succeeding wave crests would have an amplitude exceeding the trigger levels.

This triggering scheme enabled successful acceleration and stable measurements of single bunches with a Cerenkov-light and streak camera system and other detectors using a sampling scope with jitter of less than 20 picoseconds. This scheme is also applicable for observation of successive bunches or the fine structure in ordinary beam pulses by adjusting the trigger delay time.

When the NERL linac was first operated, trigger pulses shaped from a 119 MHz signal (the 4th sub-harmonic of 476 MHz) were used because of restrictions due to the electronic circuitry. However, the trigger system had a time-jitter of about 50 pico seconds.

The new system made the triggering not only stable and reliable for the single bunch operation and detection, but is also simple and low cost.

Performance of Single Bunch Operation

In single bunch operation of the machine, in order to obtain the optimum conditions, it is

important to be able to monitor the details of the bunches with sufficiently rapid response time to allow tuning the machine.

There are several methods to observe sub-nanosecond pulses. They are roughly classified into three groups. The first is the optical method, that is a light-photodetector combination. Cerenkov, synchrotron and transition light serve as the light sources, bi-planer photo-diodes and streak cameras are used for the photodetectors. The second is the electro-magnetic method in which fast coaxial Faraday cups, wall current monitors, etc. are used. These sensors are usually connected to a fast oscilloscope or sampling scope.

The third is an indirect method. It is based on measurements of the energy spread, higher frequency components and phase detection of the bunches.

However, at present, the most intuitively appealing, rapid and exact method for the above mentioned radio-chemical purposes is the Cerenkov-

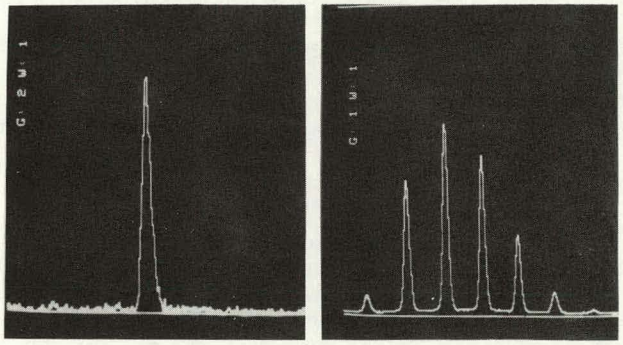


Fig. 4 (a) 16 ps single bunch by streak camera with S.H.B.
(b) Fine structure of 2 ns beam without S.H.B.

light-streak camera scheme. With this detection system, intense and clean single bunches or bunch trains are easily and rapidly obtained by adjusting machine parameters, for example the phase and power level of the sub-harmonic buncher, pre-buncher or the grid-cathode bias voltage of the electron gun. Figure 4(a) shows an example of a single bunch detected with the Cerenkov light-streak camera system; the pulse width is 16 pico-seconds, which is the limit of the detector system. Figure 4(b) shows the case of a 1.8 ns gun pulse and no sub-hamonic bunching which shows 350 ps interval bunches. Figure 5(a) shows small satellites around the main bunch. Figure 5(b) shows a picture averaging 100 single bunches. The half width is about 40 ps which shows that the time jitter of the system is less than 20 ps.

The charge per bunch measured by averaging current into a coaxial type Faraday cup was 1 nC, under optimum conditions.

At the NERL, the bunch monitoring system is used as a simple and powerful means for the tuning of the machine.

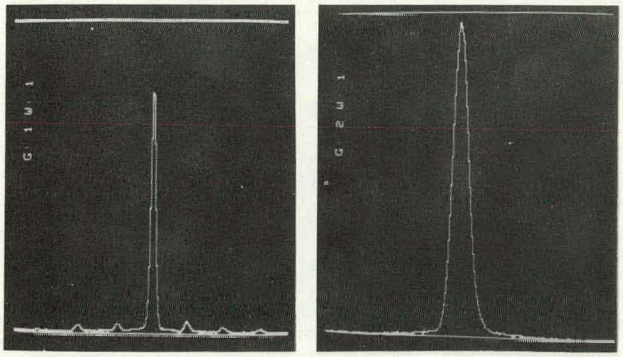


Fig. 5 (a) Single bunch with small satellites with S.H.B.
(b) 100 shots of single bunches

Development of Bunch Monitors

In order to study sub-nanosecond or nano-second range short pulse beams accelerated by an electron linac and to operate the machine as a single bunch accelerator at the optimum conditions, it is important to nondestructively monitor the fine-structure of the beams at the appropriate positions of the machine. To monitor the fine structure bunches of the S-band linac routinely, the nondestructive sensors are required to have a time resolution of less than 100 ps and are desired to be of simple structure, small size and low cost. To meet the requirements, new bunch sensors were developed jointly by KEK and NERL.

One sensor is a "One turn core monitor" which originated from an ordinary "Ferrite core beam current monitor". However, to increase the resolution down to the 100-ps range, the secondary coil is one turn and is formed like a re-entrant-type cavity as shown in Fig. 6.

The gap is closed by a low resistance ring-shaped solid resistor. In the prototype sensor, the gap resistance was 1 ohm and the inside space of the secondary coil was filled with a high frequency ferrite core ring. The gap signal voltage induced by a bunched beam was extracted by a loop and was transmitted to a sampling scope via

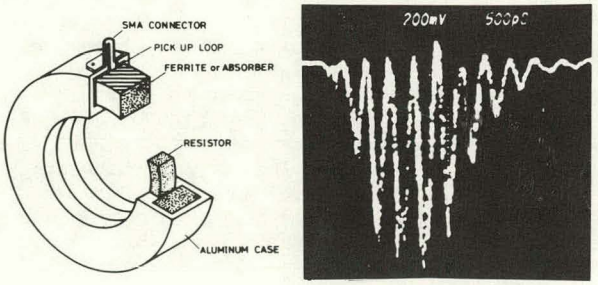


Fig. 6 One turn ferrite core monitor
Fig. 7 Fine structure by Fig. 6 monitor

a semi-rigid coaxial cable 9 m in length. The sensor was able to resolve the fine structure of the bunched beam with a resolution of better than 200 ps. (Fig.7).

The experiments showed that the ferrite core acts more as an absorber than as a magnetic material for such a high frequency range, and the gap should be made as small as possible to increase the resolution.

Consequently, three different size sensors were tested, and the ferrite cores were replaced by materials which absorb the waves from 1 GHz to 10 GHz, and a tap length of 3 mm was chosen because the bunch length is about 3 mm and that length is at the manufacturing limit for the resister ring thickness. The monitors and the measured single bunches are shown in Fig.8.

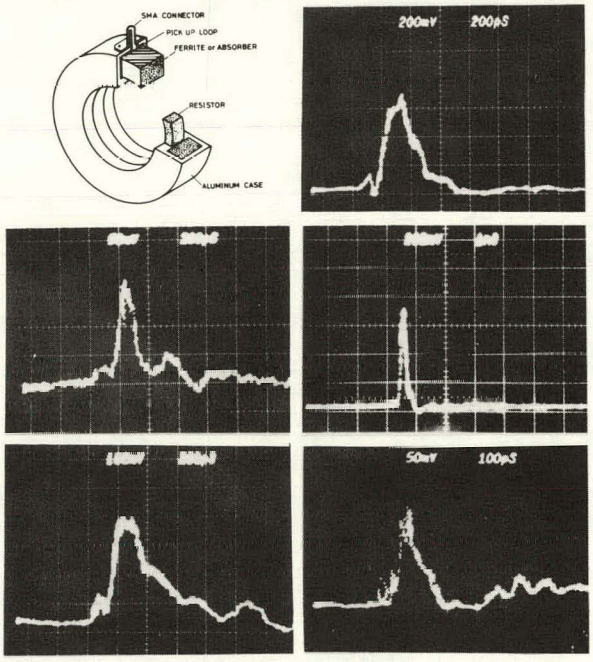


Fig. 8 (a) (b) (c) (d) (e) (f)
(a) One turn absorber loaded monitor
(b) ID 40 mm, gap 5 mm, 1Ω, 500 mv/div, 200 ps/div
(c) ID 18 mm, gap 3 mm, 1Ω, 1 V/Div, 200 ps/div
(d) ID 8 mm, gap 3 mm, 1Ω, 2 V/div, 200 ps/div
(e) ID 8 mm, gap 3 mm, 1Ω, 2 V/div, 1 ns/div
(f) ID 8 mm, gap 3 mm, 0.1Ω, 500 mV/div, 100 ps/div

The second type of sensor is a "Micro-stripline monitor", placed perpendicularly to the beam line. The sensor is made on a glass epoxy board (printed circuit) etched as shown in Fig.9.

Type A has a risetime of 60 ps and a half width of 80 ps. However, as shown in Fig. 10, ghost signals appear behind the real signal which are caused by multiply reflected waves from the borders of the strip line, and the first ghost is delayed 600 ps (600 ps corresponds to the path difference of 9 cm inside the line).

In Type B, the width of the line around the beam hole is rather small compared with Type A. Although the ghost signal levels were reduced, the half width of the real signal is wider than Type A due to the close approach of the first ghost to the real signal (Fig.11).

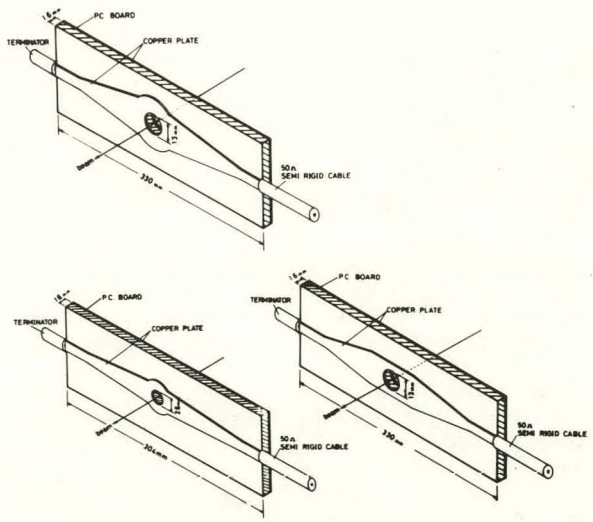


Fig. 9 Micro-stripline monitor, above (A), middle (B), bottom (C)

Type C has a reduced width and beam hole. It was placed behind a collimator with a 2-mm hole diameter; consequently the signal voltage was reduced to about half. As shown in Fig.12 the rise time and half width are 50 ps and 70 ps, respectively and the ghost signals were fairly reduced.

Both kinds of sensors as described above seem to be kinds of wall current monitors having very narrow longitudinal dimensions at the limit of the very high frequencies involved in the bunches.

The resolution depends roughly on the longitudinal size but does not depend on the vertical size of the sensors. However, to remove the reflections of the concentrically propagating signal wave, it is necessary to place good absorbers around the gap for the one-turn monitors and on the outer borders for the micro-strip line monitors.

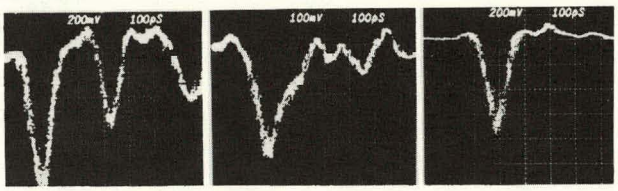


Fig. 10 Fig. 11 Fig. 12

Discussion

Penner, NBS: The last monitor you showed, the version C, had practically no reflection. I'd like to ask, how small is the beam hole to get it to behave like that?

Tanaka: This has a very small hole - the beam size is about 2 or 3 mm and the hole is 2.8 mm.

Penner: What is the sensitivity; how many volts per ampere do you use?

Tanaka: About 4 volts.

Penner: For how much current?

Tanaka: One or two amperes.

Stein, LASL: Have you measured the emittance or the energy spread of the beam from that machine?

Tanaka: We did not measure the emittance. The usual energy spread is very small as can be seen from the narrow width of the single bunch beam.

Witkover, BNL: The figures that you showed indicated a 16 pico-second width. What did you use for the monitor?

Tanaka: Cerenkov light and a streak camera.

Miller, SLAC: You said the input impedence to your gun was 25 ohms and was a good match over a wide frequency range. Is that a resistive matching and is the resistor internal to the gun or external?

Tanaka: This is measured to be resistive. It's the actual beam due to beam interception of the grid, or cathode current.

References

1 N.J. Norris and R.K. Hanst, IEEE Trans. Nucl. Sci., NS-16, 323 (1969).

2 W. Gallagher, K. Johnson, G. Mavrogens and W. Ramler, IEEE Trans. Nucl. Sci., NS-18, 584 (1971).

3 G. Mavrogens, W. Ramler, W. Wesolowski, K. Johnson and G. Clifft, IEEE Trans. Nucl. Sci., NS-20, 830 (1973).

4 Y. Tabata, J. Tanaka, S. Tagawa, K. Katsumura, T. Ueda and K. Hasegawa, J. of the Faculty of Eng., The Univ. of Tokyo, Vol. XXXIV, No. 4.

5 S. Fukuda, H. Matsumoto, I. Sato and J. Tanaka, Proc. of the 2nd Symposium of Acc. Sci. and Tech, INS. Univ. of Tokyo, March 23-25, 45 (1978).

THIS PAGE

WAS INTENTIONALLY

LEFT BLANK

Section VI
Radiofrequency Technology

THIS PAGE

WAS INTENTIONALLY

LEFT BLANK

1979 LINEAR ACCELERATOR CONFERENCE

RF SOURCES DEVELOPMENTS*

Jean V. Lebacqz
Stanford Linear Accelerator Center
Stanford University, Stanford, California 94305

Summary

The continuing need for accelerators of increasingly sophisticated characteristics, requires a great variety of rf sources to provide the energy used by these accelerators. The present status of gridded tubes will be reviewed briefly. Klystrons, which are used in many large accelerators, will be considered in some detail. Their limitations in power and frequency will be reviewed and a study of their reliability will be presented. Improvements in their efficiency will be discussed, and trends for the future will be considered. Some limitations caused by material problems will become evident and a review of some of the potential improvements in that area will be considered. Finally, new types of rf sources based on rotating electron beams which are now in the development stage will be described and compared to existing tube types.

Introduction

The present status of rf sources for accelerators has been discussed extensively by Tallerico at the San Francisco Particle Accelerator Conference in March of this year,[1] and those interested are referred to that paper. It should be stated that the present power limitation of gridded tubes (triodes and tetrodes), used at frequencies up to 200-250 MHz, is approximately 1/2 MW average at 200 MHz. Gains of 10 to 20 dB are typical. Plate efficiencies up to 90% can be achieved, although commercially the overall efficiency is only slightly over 65%. Technological developments, particularly the introduction of pyrolytic graphite grids, show promise to almost double the power available at a given frequency from a single tube in the next few years.

Probably because of a tendency to moding and oscillations when feeding a non-matched load, crossed-field amplifiers have never successfully been used in large linear accelerators in spite of the obvious advantages of high efficiency at frequencies up to 10 GHz. However, magnetrons are used extensively in commercial accelerators.

The remainder of this paper will consider the status of klystrons which are most widely used in high power accelerators. The SLAC experience with klystron reliability will be reviewed, and the physical basis for electron tube efficiency will be discussed, pointing out why klystron efficiency has been generally lower than that of other tube types, and what is being done to improve it. Finally, a promising development in field emission cathodes,[2] and the possible advantages of new tube types such as gyrocons[3] and trirotrons,[4] which operate on the principle of beam deflection modulation, will be discussed.

Klystron Reliability and Operating Cost Considerations

The bottom line on feasibility of new accelerator development or total operating time of existing machines, depends to a great extent on the cost per operating hour of the rf sources. This cost consists of three main components: capital or replacement costs, energy cost, and maintenance costs. Hourly replacement costs can be expressed as individual source initial cost, divided by Mean Time Between Failures (MTBF). Energy cost is the cost per kW-hr, at the mains divided by rf system efficiency. Klystron MTBF observed at SLAC should be a good indicator of attainable reliability.

Good statistics have been gathered since 1965 from a line of approximately 250 pulsed klystrons operating at 2856 MHz. Their power output has been gradually upgraded from 21 to 40 MW peak and from 20 to 40 kW average. Since the beginning of operations, SLAC has operated a total of slightly more than 1,000 tubes, and the operating hours have reached nearly 16,000,000. For energy conservation reasons the repetition rate of the tubes, which was mostly 360 pps during the first years of operation, has now been dropped to 180 pps or less for the majority of the runs. Hence, the statistics available on tube life may be skewed by the changes in operating conditions. One would expect an increase in life due to the reduced repetition rate; on the other hand, one would expect a decrease in life due to the gradual increase in both peak and average power of the tubes on the line, since part of the increase was achieved by increasing operating voltage. With these caveats, Fig. 1 presents three curves showing the overall tube life expectancy, including the Mean Time Between Failure

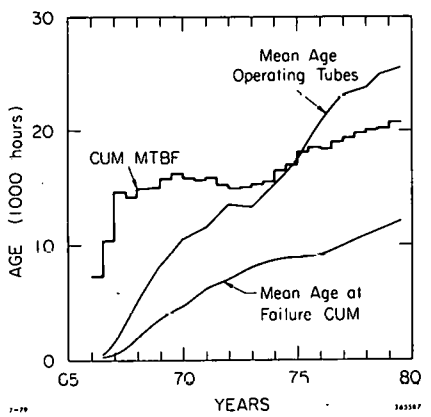


Fig. 1. Klystron operating experience at SLAC.

* Work supported by the Department of Energy under contract number DE-AC03-76SF00515.

since initial operation, mean age at failure, and mean operating age of all tubes on the line. It is worth mentioning at this time that 18 tubes (over 7% of the total complement) have operated for 60,000 hours or more without noticeable degradation in performance. Figure 2 gives the age distribution of all operating and failed tubes since the beginning of operation, and Fig. 3 gives the failure probability for all tubes and for SLAC - built tubes.

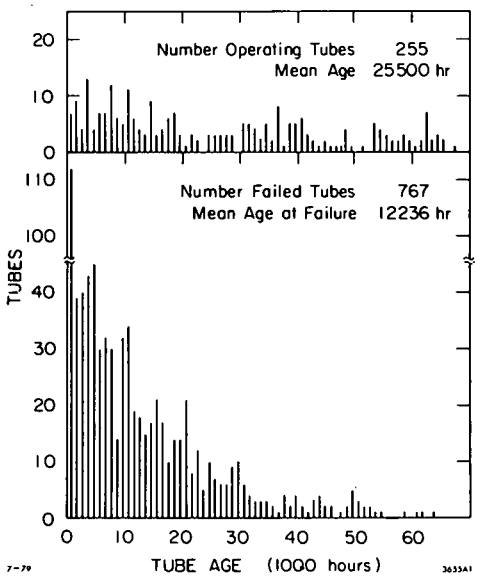


Fig. 2. Klystron age distribution at SLAC (9/1/79).

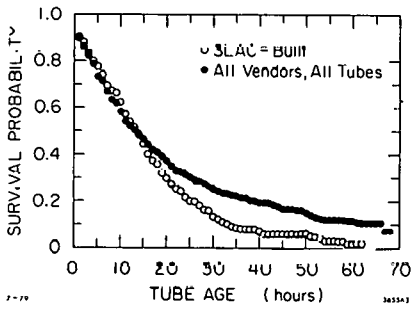


Fig. 3. Klystron survival probability.

The failures must also be analyzed for causes, if one hopes to gradually improve the tube reliability. Results of this analysis are shown in the table below, which gives the percentage of tubes which failed by the major failure causes since the beginning of operation.

As can be seen from Table I, the overall percentage of failures is approximately 25% for emission problems, 25% for cathode anode arcing problems, 25% for output window problems; 1/6 of all failures were caused by loss of vacuum, 5% by instabilities in the rf output, and only 2% by HV seal failure. In addition, a few tubes were damaged mechanically by mishandling, and they are not counted in Table I.

Table I: Percentage of Failures by Causes

Vendor	Vacuum	Emiss.	Arcing	Window	Output	HV Seal
A	13	9	19	51	5	3
B	49	6	21	16	8	0
C	18	34	26	17	4	1
D	7	38	32	13	6	4
All	16	26	26	25	5	2

Although the overall failure distribution is reasonably uniform, it is interesting to note that 50% of the failures of one of the vendor's tubes were caused by window failures, whereas another vendor had 50% vacuum failures.

Obviously, no conclusions can be drawn from the table without knowing the age of failure by the different mechanisms, but the indications are that the existing technology is not uniformly known or applied by the various vendors, otherwise there should not be this great discrepancy in the percentage of failures caused by different mechanisms.

Other types of klystrons are also used at SLAC, which has lately built all the tubes needed for its operation. The total usage to date of these types does not warrant definitive statements about their reliability. However, the 125-kW cw 353-MHz tubes used at SPEAR have now accumulated 80,000 hours of operation in 4 sockets, and the indications are that their MTBF will be as high as that of our pulsed tubes. At PEP a dozen tubes designed to operate at 353 MHz and to produce 500 kW of cw rf are being installed. It is believed that the life of these tubes will be similar to that of our pulsed tubes, and that assumption will be used to demonstrate the effect of MTBF on rf hourly costs.

As an example of the total tube cost per hour, let us consider the PEP 500-kW cw klystrons, which cost about $100,000, or $200/kW. Assuming 20,000 hours MTBF, the capital cost per rf kW hour is 1¢. At SLAC, the cost per kW hour is about 0.5¢. With a tube efficiency of 63%, the energy cost per rf kW hour is thus about 0.8¢. Increasing the tube efficiency to 70% reduces the power cost to 0.7¢. It is interesting to note, that for the above assumptions, a 10% increase in MTBF will reduce the overall cost per hour as much as a 10% increase in efficiency.

Efficiency Considerations

The electronic efficiency of a microwave amplifier can be defined as the ratio of the power extracted from the beam in the output system to the beam power. To maximize efficiency, as much energy as possible must be extracted from every electron in the bunch. If a bunch of electrons in the beam enter the output with exactly the same velocity and the same rf phase, then the energy extracted from that bunch will be the same for all its electrons, except for space-charge effects. In principle, 100% efficiency can be obtained if

all electrons are exactly stopped as they pass through the rf output system.

The work towards improving klystron efficiency has thus been directed at first decreasing the bunch size so that as many electrons as possible will be decelerated by the same potential. The addition of second harmonic cavities and changes in the accelerating structure length have been used to minimize the velocity differences of the electrons as they enter the output gap.

An overall view of the present status of klystron efficiency is given in Fig. 4.

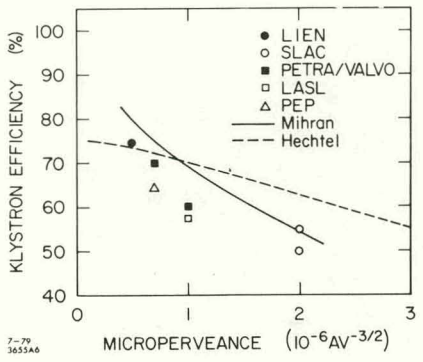


Fig. 4. Klystron efficiency vs. perveance.

The two curves labeled Mihran[5] and Hechtel[6] were obtained by analysis of the references given. Mihran's work has dealt mostly with computer simulation of the beam bunching by disc models, whereas Hechtel considered mostly the effect of the potential depression in a solid beam. The points shown represent measured data from actual tubes. For SLAC, the best efficiency achieved under special test conditions as well as the best normal efficiency is given. LASL represents the operating efficiency of the Varian klystrons used on the LAMPF linear accelerator. The PEP efficiency is that obtained for the PEP storage ring klystrons. Lien[7] gives the results of a tube built at Varian Associates to confirm theoretical predictions made by Lien on the effect of second harmonic cavities, and finally the two points PETRA/VALVO show the normal operating point of a VALVO-built klystron in the PETRA ring at microperveance 1, and the best efficiency obtained in special studies of the same tube after decreasing the perveance by modulating anode voltage adjustment and readjusting the focusing conditions and the output load.

The general trend shows a decrease in efficiency with increase in microperveance, which can be understood from general space-charge force considerations. The increases in efficiency resulting from the use of second harmonic cavities and careful detuning of penultimate and prepenultimate cavities of multi-cavity klystrons enables the formation of a bunch of optimum size in which all electrons have substantially the same velocity as they enter the output gap.

One of the main reasons why rotating beam tubes such as the gyrocon and the trirotron can have much higher inherent efficiency than klystrons, is because in those tubes, all electrons in the beam can be made to enter the output resonator at a substantially constant phase with respect to a traveling wave in that resonator. This is because basically the velocity spread is very much smaller, and the beam area entering the output is much larger than for a klystron of similar frequency range and power, resulting in lower space-charge problems in the output cavity.

From the above considerations, one can deduct that further improvements in klystron efficiency should result from the use of hollow beams to minimize the potential depression. Also, in all tube designs, engineering compromises have to be made. For instance, higher cathode current density might result in a higher efficiency, but the life expectancy could be seriously reduced. Similarly, higher beam current density might increase the magnetic field requirements. In most cases, the final choices are dictated by the availability of materials, and new or better materials and techniques could well result in higher efficiency without reducing the probable tube life.

Further Klystron Work

Although SLAC has no specific plans for new klystron types at this time, it is always useful to speculate on the next improvements of existing tubes, or on the next generation. At the present time, the improvements to the pulsed tubes consist mostly of material studies, particularly in the cathode region. Based on experience to date, there is a potential improvement in MTBF by a factor of 2, approximately, by simply preventing failures by temperature limited cathodes. Unfortunately, this is a very slow, tedious engineering work requiring extreme patience, since the result of today's changes will not be known for approximately ¼ years.

On the other hand, the PEP cw tubes have never yet demonstrated the efficiencies which had been predicted by our computer results. Here, work is proceeding on parallel approaches - one, a further study of the assumptions used in the computer code and their modifications; second, an experimental approach where the present PEP gun will be replaced by a hollow beam gun. The improvement in beam coupling coefficient and the fact that all the electrons in the hollow beam are decelerated by a more uniform field in the output gap than those of a solid beam lead us to expect a substantial efficiency improvement.

For the future, SLAC is looking at klystrons with two completely different applications. One to be used in very high energy storage rings, would operate in the 500 to 1000-MHz region, with peak and average powers up to 20 MW and 1 MW, respectively, at 500 MHz; and one half that at 1000 MHz. In order to conserve power, the tubes would be designed to operate pulsed, with a pulse length of approximately one microsecond, and a repetition rate of between 20 and 60 KHz. The main development needed to make such tubes practical is a gridded gun with a low cut-off voltage. Some useful development work is being done at Varian. It is felt that a

hollow beam gun could be another approach resulting in a satisfactory design; and finally, that the field emission gun to be discussed later may have all the desirable characteristics.

The feasibility of pulsed klystrons operating at 2856 MHz, with peak and average powers of approximately 100 MW and 50 kW, respectively, is being investigated. Some thought has been given to the design optimization, looking first at the choice of perveance. Taking a conservative average through the data of Fig. 4, one can draw a single efficiency curve, as in Fig. 5.

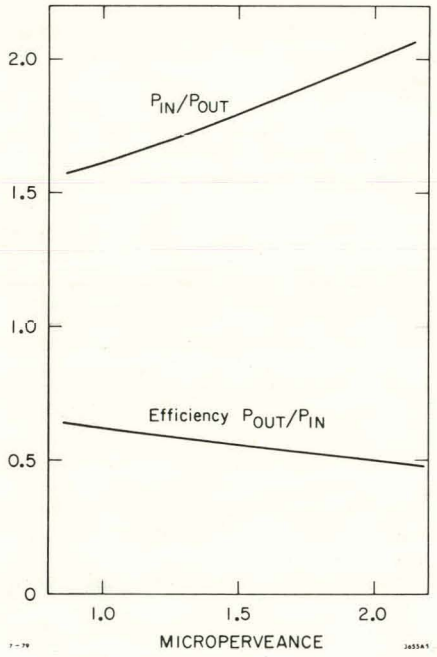


Fig. 5. Effect of efficiency on line power requirements.

The reciprocal of efficiency is also plotted, and shows the savings to be achieved in electrical capacity by decreasing perveance. Figure 6 then computes the beam voltages and beam currents needed to achieve a given power output at a given perveance. The final choice, which has not been made yet, will be determined by the best compromise between magnetic field requirements, breakdown voltages, and cathode loading.

New Cathodes

A technical advance, which has been waiting many years but seems to be on the verge of successful application to electron tubes, is that of field emission cathodes. Work has been carried out at SRI International for many years to develop field emission cathodes which are fabricated using thin film technology and microlithography.[2,8] Called thin film field emission cathodes (or SPINDT cathodes), they consist of a series of micro-cones as illustrated in Fig. 7. These cones are capable of cw emissions of between 20 and 25 microamps each and they have been stacked in densities of up to

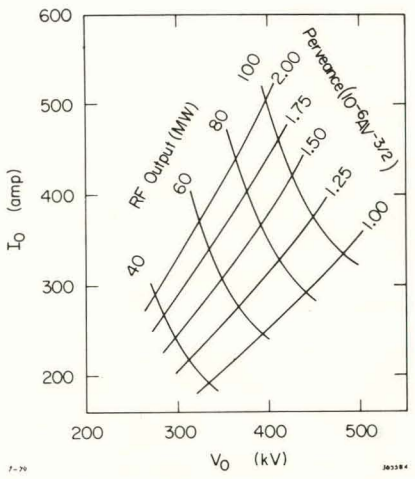
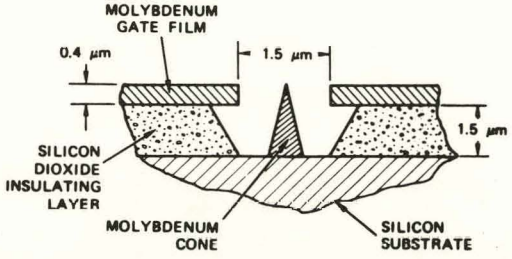
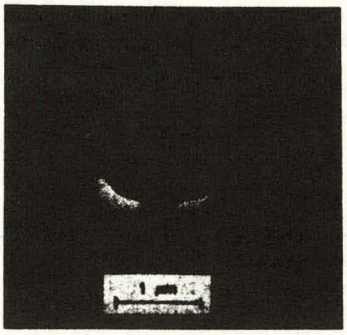


Fig. 6. Voltage-current design characteristics of high peak power klystrons.





7-79 3655A8

Fig. 7. Schematic diagram and scanning electron micrograph of thin-film field emission cathode (TFFEC).

22,000 per square millimeter. The evidence indicates that the emission is stable with time, is a function of the residual pressure but regains its initial value after the vacuum is re-established to its original operating level (Fig. 8), and that even after 38,000 hours of operation at a level of

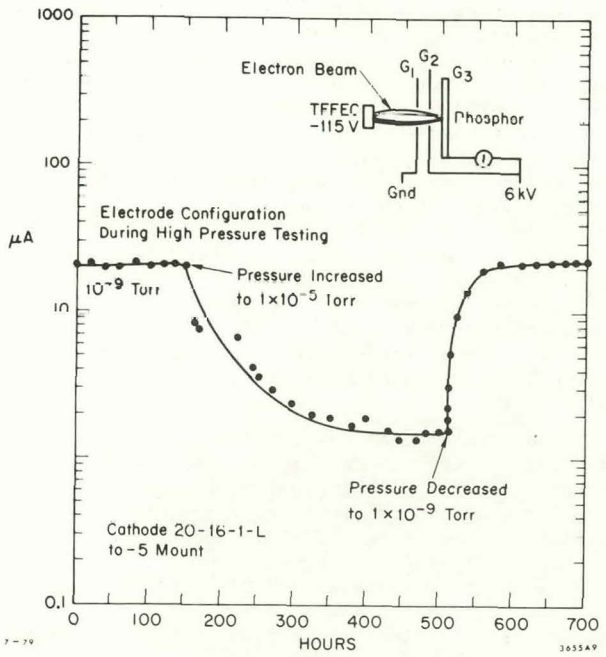


Fig. 8. Effect of ambient pressure on emission.

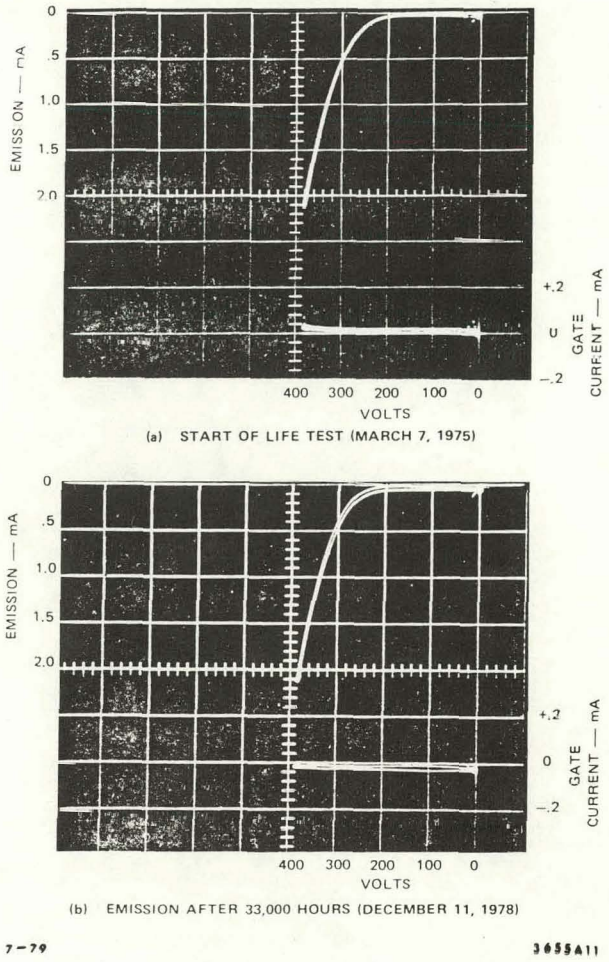


Fig. 9. Current-voltage oscillographs for 100-cone array driven by a 60-Hz half-wave voltage to a peak current of 2-mA for 33,000 hours.

20 microamps per cone, the characteristics of these thin film field emission cathodes do not alter appreciably (Fig. 9).

If these cathodes can really be proven to be a reliable source of electrons for high powered vacuum tubes one must rethink the basic design of many tubes. For instance, the PEP tube is now operating at a beam voltage of 63 kV and a current of about 12 amps; with a standard oxide cathode of approximately 12 cm diameter, the cathode current density is approximately 100 ma/cm^2. Using a SPINDT cathode, at a current density of 12 amps/cm^2 an emitting area of only one cm^2 is needed. This in turn means that one could consider an annular cathode of approximately 5 cm outer diameter and 4.9 cm inner diameter, producing a beam of equal dimensions. Controlling such a beam may impose difficult magnetic field requirements, but also means that all electrons reach the gaps at the same value of electric field and should result in a substantial efficiency improvement. Similarly, a high power pulsed cathode could be operated at current densities well in excess of 100 amps/sq cm which in principle would allow us to reduce the beam and drift tube diameters or to use annular beams. Finally, these cathodes should be of great value in the design of easily controllable beam current tubes, since a control potential swing of less than 200 volts results in a current swing of at least 5 orders of magnitude (Fig. 10).

Deflection Modulation or Rotating Beam Tubes

Work on different types of electron tubes has lately shown promise of successful development. Although the original concept was first proposed in 1946 by J. W. McRae,[9] and suggested again in 1966 by Preist,[10] it is not until Budker[11] demonstrated efficiencies of better than 75% on pulsed gyrocons at Novosibirsk that work began in this country on the study and further development of these devices.

Basically, the deflection modulation or rotating beam tubes are capable of extremely high efficiency because of the special output circuit design. The output circuit is a resonant waveguide ring sustaining a traveling wave. The beam is made to rotate at the resonant frequency of the ring. Hence, an electron beam without any velocity modulation can be made to enter the output resonator at always the same phase with respect to the traveling wave. Referring back to the efficiency considerations, this gives what is probably an ideal solution, since the beam always sees the exact same fields in the output circuit, and all electrons enter with the same velocity except for the variations caused by space-charge.

The gyrocon, which is being studied at Los Alamos by Tallerico,[12] depends on deflection modulation of a cylindrical beam to produce the rotating beam. Figure 11 shows the basic concept of the gyrocon deflection and focusing. A solid beam,

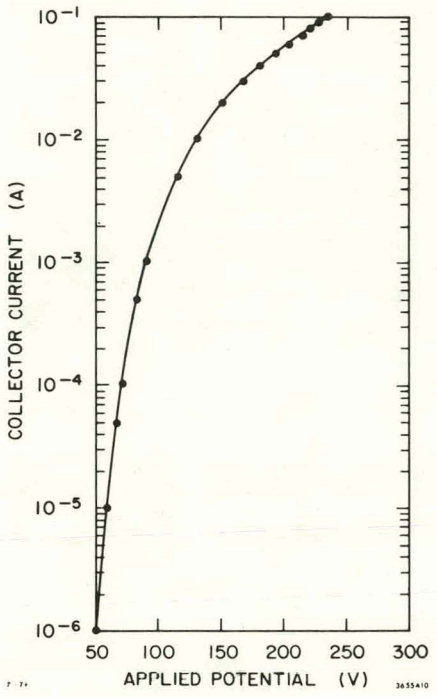


Fig. 10. Collector current vs. cathode voltage (5000 cone array).

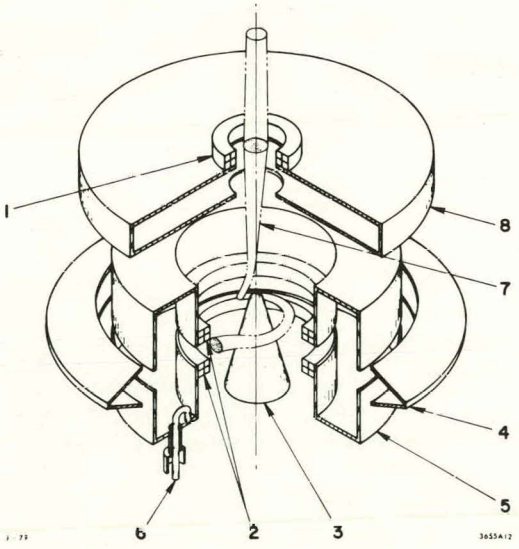


Fig. 11. The radial gyrocon: (1) gun focus coil, (2) output focal coils, (3) bender, (4) collector, (5) output cavity, (6) rf output, (7) electron beam, and (8) deflection cavity.

starting at the top of the figure from a standard electron gun, is focused by gun focus coil. The deflection cavity can support two space-orthogonal modes at the same frequency. If the two modes are fed 90° apart in phase, a rotating electric field normal to the axis of the cavity results. This field deflects the beam by a constant angle, generating a cone. The beam then enters the dc magnetic field of the bender magnet, increasing the deflection angle until the beam direction is normal to the axis. At that point, the beam is refocused in the vertical plane by coils before entering the output waveguide cavity. The spent beam energy is dissipated in the collector, and the power extracted from the beam in the output resonator is transferred to the load by two or more couplers, usually orthogonal in space.

A computer code has been developed to follow the beam through the complete deflection and output system of a gyrocon being built at Los Alamos. The computer model, which includes space-charge effects, indicates an electronic efficiency in excess of 90% and an overall efficiency of about 85%. The tube is designed to operate at 450 MHz. With a modulating anode gun operating at 86 kV and 9 amps, the power output should be in excess of 650 kW with a gain of approximately 20 dB. As can be gathered from the description above, the overall drive-deflection system of the gyrocon is extremely critical. Any asymmetry in the drive cavity will result in an elliptical cone, since the deflection angle will be different for different rf phases. Hence, the beam will no longer be deflected uniformly by the dc magnetic field. Also, any variations in beam voltage or deflection magnet current will result in improper deflection. The result is need for very careful monitoring and feedback. With the use of micro-computers, it should be possible to solve these problems.

Planar type gyrocons, in which electrons travel radially from an rf driven cathode through an accelerating gap and into the output resonator, could alleviate some of these problems. The trirotron[4] work being done at SLAC is an attempt to develop a possible solution. The trirotron's drive system is a circulating waveguide resonant at the drive frequency, and is concentric to the output resonator. By adjustment of the phase propagation constant of the two resonant waveguide rings, the input resonator guide has a smaller diameter than the output, allowing for the application of dc accelerating field between them. The cathode, insulated from the remainder of the waveguide, replaces the central portion of the inner wall (Fig. 12) and is opposite a series of grids on the outer wall to allow the electron beam formed in the drive resonator to reach the dc accelerating fields.

By adjusting the relative values of E_0 and E_{bias}, it is possible to control the beam spread from 0 to 180° and to vary the total emission, although not necessarily independently. Some of the current emitted from the cathode never exits the input waveguide because of the reversal of the rf field during the transit time. Those electrons are then returned to the cathode, and absorb more than half of the total rf power supplied to the

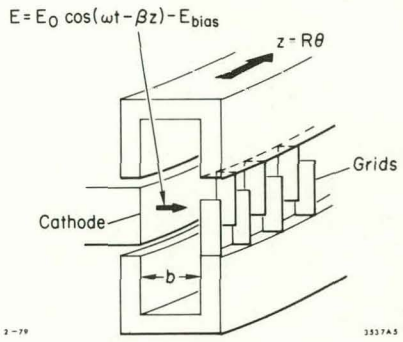


Fig. 12. The input resonator: beam formation region.

input circuit. Better choices of rf fields, dc bias, and waveguide height "b" should improve the situation, and the optimization process will continue before final design.

The production of a pure traveling wave in the input circuit is essential if good performance is to be achieved. Since a backward wave can result from relatively small reflections in the traveling wave resonator and input couplers, great care should be taken to locate two identical input coupling loops exactly 90° apart, each fed by the same power phased TC/2 apart. Also, two sets of tuners will be required to match out any residual reflections in the input circuit.

The output efficiency has been analyzed using a modified version of the computer program developed by Tallerico for the gyrocon. The results are shown in Fig. 13 for a beam assumed to extend approximately ±9% from center of the axial output resonator length. Indicated efficiencies of 85% at 1 radian beam spread and 80% at 1.5 radians are very encouraging. It appears reasonably easy to produce a 1.5 radian beam; at 1 radian, the total current available might be too low to be of value

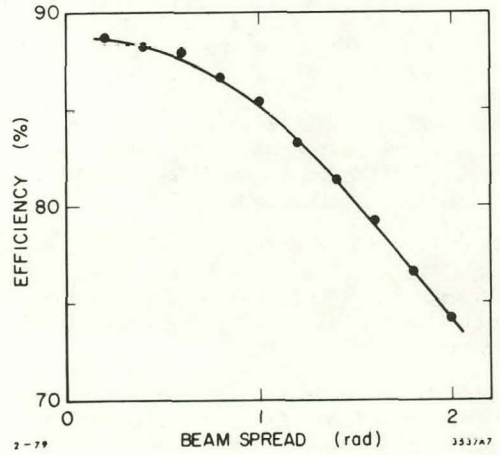


Fig. 13. Output efficiency vs. beam spread angle.

for very high power tubes. An improvement of a few efficiency points can be made by adding a very small axial magnetic field, which counteracts the beam deflection caused by the rf magnetic field.

The results of the studies carried out has led us to design a trirotron to operate at 353.2 MHz, at beam voltages of 56 to 64 kV and currents of 8 to 12 amps. The conceptual drawing is shown in Fig. 14. The following dimensions have been used:

Cathode diameter	27.65 cm
Axial cathode length	9.00 cm
Input resonator OD	29.65 cm
Input grid fins	1 × 9 × .07 cm
Output resonator ID	37.65 cm
Output resonator OD	57.65 cm
Axial output resonator length	51.50 cm
Collector OD	80.00 cm
Axial Collector length	20.00 cm

Efficiencies listed in Table II were computed assuming a uniform density beam, spread over 80° (produced by a drive power of ≃ 10 kW), with an axial length of 10 cm and no magnetic field efficiency enhancement.

Table II: KV / Amps	56	60	64
8	81.1	80.4	81.0
10	81.4	81.4	81.3
12	80.7	81.6	81.4

The trirotron shows promise of being a highly efficient device at frequencies of 200 to 500 MHz, and power outputs of one-half to several MW cw. The efficiency is not a critical function of beam voltage, drive power, or bias voltage. Hence it appears possible to control the power output over a wide range by adjusting the dc bias or the drive power without loss of efficiency and with minimal phase variation between input and output. Some possible disadvantages include the drive system dc isolation, the need for accurate tuning of the input resonator and its coupler, the cathode heating by electron back-bombardment, and the low gain computed at approximately 15-18 dB.

Conclusions

At frequencies of 200 MHz or less, the gridded tubes will apparently remain the dominant type; and one should expect to see their power capabilities double during the next few years. At frequencies of between 300 and 1000 MHz, there should be within a few years a choice between klystrons and rotating beam devices. The maximum obtainable power output should be the same for both devices, since it will almost certainly be determined by output window design considerations. One can expect 20 MW peak and 1 MW average at 500 MHz, varying in inverse ratio to the frequency. It is also likely that this limit could be increased by additional window development.

The rotating beam tubes will probably have efficiencies of 80 to 85%, with gains of 15 to 25 dB. The possibility of rf leakage from the

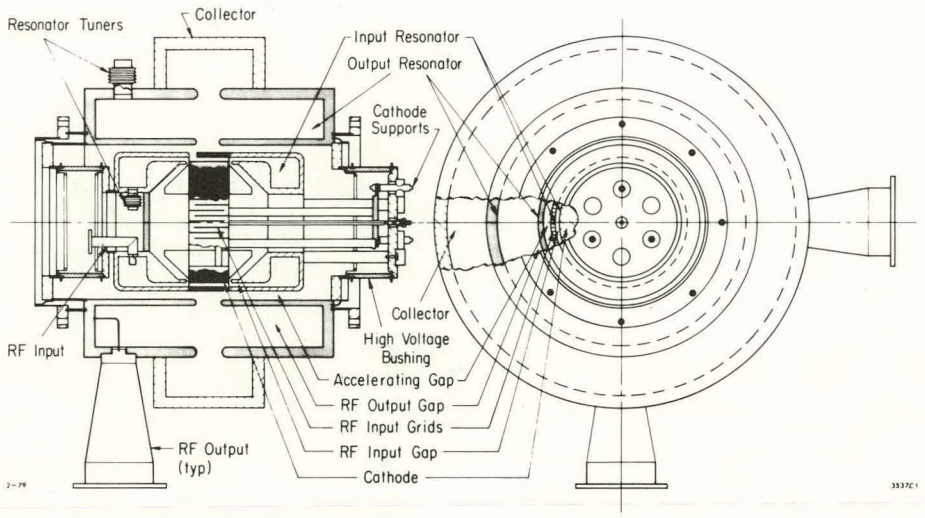


Fig. 14. Conceptual design of a 600 kW, 353 MHz trirotron.

output resonator through the beam entrance slot may produce unknown challenges and unpredictable oscillations. Finally, nothing is known about their probable life of operation, since the only experience at Novosibirsk has not been too favorable. The klystron efficiency in that frequency range is now between 65 and 70%, and computer studies indicate that the next generation will show efficiencies around 75%, with a gain of between 40 and 50 dB. The choice between the two candidates will revolve around the merits of the slightly better efficiency of one compared to overall system simplicity and reliability of the other.

From 1 to 10 GHz, the klystron is still probably the only candidate for large machines. Peak powers of 100 MW should not be difficult to attain at low repetition rates and short pulses, keeping the average power to 50 kW, at frequencies around 3 GHz. The tube life is excellent and the efficiency should gradually increase to about 55 to 60% with good gain.

Above 10 GHz new tube developments are taking place, but they have not been dealt with in this paper, since they are probably of limited interest to this audience.

Acknowledgements

The author wishes to thank the various people in the tube industry who have given of their time while he was researching the status of tube types not in his own immediate field. He wishes to express particular appreciation to Tallerico and Spindt who have kindly agreed to let him use in this paper some of the figures they had published elsewhere. He is grateful for the help he received from his co-workers at SLAC, and particularly to Alice Kalthoff who did the ground work for the klystron failure analysis.

References

1. P. J. Tallerico, "Advances in High-Power Rf Amplifiers," IEEE Trans. on Nucl. Sci., Vol. NS-26, No. 3, 3877 (June 1979).

2. C. A. Spindt et al., "Physical Properties of Thin-Film Field Emission Cathodes with Molybdenum Cones," J. Appl. Phys., Vol. 47, No. 12, 5248 (December 1976).

3. G. I. Budker et al., "The Gyrocon, A Highly Efficient Converter of Energy from Powerful Relativistic Electron Beams for Microwave Supplies in Charged-Particle Accelerators," Atomic Energy, Vol. 45, 459 (May 1978).

4. J. V. Lebacqz et al., "The Trirotron, " IEEE Trans. on Nucl. Sci., Vol. NS-26, No. 3, 3891 (June 1979).

5. T. G. Mirhran et al., "Electron Bunching and Output Gap Interaction in Broad-Band Klystrons," IEEE Trans. on Electron Devices, Vol. ED-19, 1011 (September 1972).

6. J. R. Hechtel, "The Effect of Potential Beam Energy on the performance of Linear Beam Devices," IEEE Trans. on Electron Devices, Vol. ED-17, 999 (November 1970).

7. E. L. Lien, "High Efficiency Klystron Amplifiers," Proc. of the 8th International Conf. on Microwave and Optical Generation and Amplification, Amsterdam, The Netherlands (September 1970).

8. I. Brodie and C. A. Spindt, "The Application of Thin-Film Field-Emission Cathodes to Electronic Tubes," Applications of Surface Science 2, 149 (1979).

9. J. W. McRae, "Harmonic Generation System," U. S. Patent No. 2 408 437, October 1946.

10. D. H. Preist, "Prospects for Very High Power High Efficiency Rf Generator," 6th International Conf. on Microwave and Optical Generation and Amplification," Cambridge, England (September 1966).

11. G. I. Budker et al., "Microwave Electron Discharge Device," U.S. Patent No. 3,885,193, May 20, 1975, and U.S. Patent No. 4,019,088, April 1977.

12. P. J. Tallerico et al., "Computer Modeling of the Gyrocon," IEEE Trans. on Nucl. Sci., Vol. NS-26, No. 3, 4015 (June 1979).

Discussion

Grand, BNL: There has been talk of utilizing third harmonic super position on the primary of gridded tubes, the Taylor efficiency approach. Would you say a few words on that.

Lebacqz: No, it is outside of my field of expertise. I believe that, in principle, what they're trying to do is to obtain a flat-top voltage. The gridded tube efficiency is based on the same principle as any of these devices. You want to stop the electrons that come over a certain time interval in which the voltage normally varies in a sinusoidal fashion. If you superimpose a third armonic on that to make a flat-top, then in principle, you are going to get high efficiency. But I don't know the details so I would rather not comment.

Mittag, Karlsruhe: Could you please say a few words about the frequency range over which the gyrocon or your planar gyrocon could be used for a high rf power source?

Lebacqz: My personal feeling is that the optimum frequency range for those tubes is from 200 to 500 MHz and maybe up to a thousand MHz. If you go below 200 MHz, the size of the waveguide you need gets impractical. I think that's about as low as you can go. If you go over a 1000 MHz, then the last one I talked about, the Trirotron, is not going to give you enough beam current unless you can combine it with a field emission cathode.

Fraser, Chalk River: One of the criticisms I have heard of the field emission cathode is the relatively large transverse velocities that one gets from the side of the point. What effect might this have, say, on the efficiency of a klystron?

Lebacqz: We have not used those things on the klystrons. These cathodes are being studied by SRI under the sponsorship of NASA Lewis and, at the present time, NASA is ordering or has gotten some of those to build into millimeter traveling wave tubes. If they can use them in millimeter traveling wave tubes, we can use them in klystrons. We are talking about accelerating potentials of several tens of kV and probably 100 to 500 kV, in which case the transverse velocity is not that critical.

Miller, SLAC: With respect to the last question, isn't it true that in the high power klystrons that are used as rf sources for accelerators, emittance isn't very significant, that really space charge so dominates the optics that large transverse velocities wouldn't have much effect?

Lebacqz: I think that's correct; but since it comes from you, I don't know.

1979 LINEAR ACCELERATOR CONFERENCE

RECENT DEVELOPMENTS IN HIGH POWER VACUUM TUBE TECHNOLOGY

J. Ross Faulkner
EIMAC Division of Varian Assoc.
San Carlos, CA

Summary

There have been several recent developments in vacuum tube technology which will benefit the next generation of particle accelerators now being proposed. These improvements involve devices covering the frequency spectrum from HF through millimeter wavelengths. Significant developments involving klystrons, gyrocons, or gyratrons, at frequencies above 200 MHz are being reported elsewhere in these proceedings.

The developments in the EIMAC line of conventional gridded tubes for use at frequencies below 200 MHz will be of particular benefit to those machines which will be used to accelerate heavy particles for neutron production, heavy ion fusion, and other similar applications. While some of these developments are aimed at improving tube reliability, the main thrust of these efforts is to develop high gain gridded vacuum tubes which can deliver higher powers at better efficiencies than those available today.

This paper will describe how the use of pyrolytic graphite grid construction makes it possible to achieve the tight tolerances, close inter-element spacing, and dimensional stability necessary to produce high gain tubes capable of handling higher power per unit volume. Other new construction techniques and improved cooling methods which contribute further towards improvement in vacuum tube technology will also be discussed.

Introduction

The next generation of linear particle accelerators all appear to have one common parameter which is of keen interest to those in the business of making vacuum tubes. These proposed machines will require rf power of a scale heretofore unheard of. For example, the accelerator breeder concept would require 300-500 MW of cw rf and proposed heavy ion machines talk of thousands of megawatts. While the peak power requirements for some of these proposed machines are not dissimilar to that required by existing accelerators or large radar arrays, the combination of high peak power and high average power place new constraints on the design of amplifier tubes for these applications. The trend toward higher average power is somewhat in contradiction to the trend toward use of higher frequencies. While the use of higher rf frequencies allows for significant reduction in the size of the various accelerator components, it likewise produces a similar reduction in permissible size of the rf amplifier devices to be used. Such a reduction in size makes it necessary to handle more power per unit volume and/or unit area, in both the accelerator and in the rf amplifier device. If smaller devices can be produced which can handle high average power, then materials must be used which are capable of operating at much higher temperatures, and more efficient cooling methods must be developed. Of utmost importance, however, devices must be developed which are basically more efficient, require less cooling, and hence make better use of the available energy.

Good efficiency has always been an operational goal for accelerators if only to keep the power bill to a minimum. However, some proposed machines, such as the Accelerator Breeder or the Heavy Ion Fusion machines, depend upon this improved efficiency to achieve a break-even condition and prove their feasibility. New devices for rf amplification which address this requirement are required if these machines are indeed to be feasible.

Old Technology

In considering where the EIMAC line of gridded vacuum tubes will fit into these new particle accelerators, it would seem appropriate to draw the line between the use of these devices and those applications requiring klystrons, gyratrons, or gyrocons, at about 200 MHz. Below this frequency the last three devices become rather large and expensive to build. Above 200 MHz, it would be difficult to construct a conventional gridded device large enough to handle the required power and small enough to operate efficiently at the desired frequency.

Examination of the data on tubes currently in production and availalbe for these applications reveals that the largest gridded vacuum

tube is the EIMAC X2159/8974 rated at 1.25 MW plate dissipation. However, at the present time these ratings apply only up to a frequency of 30 MHz and a de-rating factor is then applied for operation above this point. Most of this de-rating is necessary to account for the heating of the screen grid wires due to the rf current flowing in the output circuit between the screen grid and the anode. Likewise, the X2170/8973 made by EIMAC is rated for 650-kW anode dissipation to 50 MHz above which the same de-rating phenomenon occurs. In fact, for the higher frequencies in the range of 30-200 MHz, the grid dissipation will almost always be the limiting factor in the power handling capability of super-power gridded vacuum tubes. To illustrate how severely the dissipation capability of the screen grid limits the power handling capability of the tube, consider the case of the EIMAC X2170/8973 operating at 50 MHz where more than 1100 kilowatts output are obtainable while still staying under the 7.5 Kw screen dissipation rating. However, if the same tube is operated at 100 MHz only about 620 kW output is projected before the 7.5 kW screen dissipation rating is exceeded. Under the latter conditions the anode dissipation is only 300 kW. If the screen grid were more robust and able to handle more power, then the full anode dissipation of the tube could be utilized and a power output of over 1200 kW would be available from a single tube at the higher frequency.

Grids in vacuum tubes of this type are usually constructed from wires of molybdenum or tungsten which have been welded together in a "birdcage" type structure. These materials are necessary because the grid is located only a few millimeters away from a hot cathode which is operating at about 1650°C. The use of these refactory materials still permit operation of the grid wires at a maximum temperature of only about 1000°C. Both tungsten and molybdenum are fairly good emitters of both primary and secondary electrons in this type of service and measures must be taken to minimize both these phenomena. If left unchecked, the primary and secondary emissions of electrons from the grid wires will make the current division within the tube very unpredictable and somewhat uncontrolled. To reduce both these emissions, the grid wires are usually coated with a substance which helps make the wire behave as a black body radiator, lowering the temperature and reducing the primary electron emission. At the same time this coating roughens the surface of the wire to help cut down the emission of secondary electrons. The coating layer, made from platinum, carbon, zirconium, etc., is applied to the wire in a plating-sintering process which is very difficult to control and usually accounts for the sometimes wide variations in the grid currents seen between tubes of the same type. These wide variations are particularly noticeable in operating regions where the anode voltage is very near the screen grid voltage. This of course is the operating region where the highest screen grid dissipation is encountered, and if these variations are on the high side of the range the screen grid dissipation could be in a runaway condition. Clearly then, it would be desirable to use a material for grid construction which is capable of operation at nearly the same temperature as the cathode and which has a very low primary and secondary emission ratio without the need for any extra surface coating.

New Technology

An ideal material, pyrolytic graphite, is available and is being used very successfully in construction of gridded vacuum tubes. This material, a graphite formed by vapor deposition, was developed for use in spacecraft heat shields and as brake pads for large aircraft. In addition to high temperature tolerance and low secondary emission ratio, pyrolytic graphite offers several other rather significant advantages over a structure made from welded tungsten or molybdenum wires. Pyrolytic graphite has essentially a zero coefficient of expansion in the directions of interest up to 2000°C. This means that closer inter-element spacing can be achieved without concern over element movements from cold to hot conditions causing inter-element shorts. Further, since the pyrolytic graphite grids are of single plane construction rather than two plane construction made of crossed and welded wires, it is possible to close the inter-element spacing down even farther. This close spacing compensates for the higher grid currents which would normally result from the lack of primary and secondary electrons from the pyrolytic graphite. It also can result in higher gain. Another advantage of pyrolytic graphite is that the grids are cut from a precision-machined graphite cup by either sandblasting or laser cutting, resulting in a much more precise repeatable geometry than is attainable by either hand or machine winding and welding of wires into a grid. One can readily see how the use of pyrolytic graphite for a grid material enables a tube to be utilized more efficiently and pushed to its maximum ratings at the higher frequencies. In addition, it is obvious that the use of such material will enable the tube maker to produce a product with much more uniform and repeatable characteristics. To this end EIMAC has committed much of its resources to the introduction of pyrolytic graphite into its product line. Over the last 5 years, products with pyrolytic graphite have been introduced into several tube designs by EIMAC and more tubes of this type will be available in the near future. Up to the present time EIMAC has purchased the pyrolytic graphite cups from an outside source and then machined them into grids, but shortly after January 1, 1980, we will have our own operational facility for the manufacture of this unique material.

The next area to be examined is the one of basic electronic efficiency in rf amplifiers and how pyrolytic graphite can contribute to this

important parameter. As in the case of grid heating due to the flow of high rf currents in the output circuits at higher frequencies, severe screen grid heating similarly occurs with the higher screen currents which flow when the anode voltage is allowed to swing very low during the rf cycle. Since the electronic efficiency of the device is dependent upon the minimum anode voltage swing, or Eb min, a big improvement can be made if the Eb min is allowed to go down near or below the screen voltage. This will result in high screen current and high screen dissipation, but a grid made of pyrolytic graphite is able to accommodate this vigorous service and thus contribute to the overall device efficiency.

There are other areas which are being investigated which should help to improve the "state of the art" in gridded vacuum tubes. As previously mentioned, the largest gridded tube in production at this time is the EIMAC X2159-/8974 rated at 1.25 MW anode dissipation. It should be possible to further extrapolate the usual "birdcage" construction used in this tube to larger structures using pyrolytic graphite instead of the welded wire construction. Pyrolytic graphite grids should have a power dissipation capability of three times that of conventional grids of the same size. However, it is felt that the limit for extrapolation would probably only yield a 1.5 to 2.0 increase in overall tube capability. If improvements of the order of 5 to 10 are to be realized in the basic power handling capability, then some alternate method of construction must be devised which will permit better dimensional control of the basic electronic package of cathode, control grid, and screen grid. Since the tube characteristics are relatively independent of the screen grid to anode spacing, the relative geometry between cathode, control grid, and screen grid controls the quality and uniformity of the electron beam, and in very large devices, such control is essential to insure uniform loading of electron bombardment on the various elements within the device. For these new applications where rf power output of 2-5 MW per device are desirable, small differences in power density can be catastrophic. Tubes are now in development at EIMAC which should achieve the required power handling capability.

New anode designs are being used which feature high velocity water cooling, utilizing swirl tubes in the water passages to achieve the necessary turbulent flow. These are very similar to the water-cooled beam stops used at ORNL for neutral beam dumps and produce anodes which are capable of handling 1000 watts per square cm or more.

Considerable effort has gone into investigation of the so-called "Tyler" technique, for efficiency enhancement. This technique which is used very successfully at low frequencies and produces final amplifier efficiencies of 90% or more in the broadcast frequency band, begins to produce diminishing returns as the frequency of operation is raised. At the higher frequencies the size of the output capacitance in the amplifier tube becomes larger and larger when compared to the capacitance in both the fundamental and third harmonic resonator circuits and acts much like an integrator, limiting the "squareness" of the anode voltage waveform, and thus the improvement in efficiency which is achieveable. Tests run at EIMAC on typical devices produced increases in amplifier efficiency of over 10% at 1 MHz, but these improvements decreased to only 2-3% at 50 MHz. It would appear that for large devices with their attendant large output capacitances the practical frequency limit for employment of such techniques would be in the range 10-20 MHz.

Other devices are being developed which feature high efficiency techniques similar to the depressed collector used for efficiency enhancement of klystrons.

Conclusion

For many years now there have been those who have forecast the demise of the low frequency gridded vacuum tube, but with the further passage of time it is apparent that the "state of the art" of such devices can keep up with the demands and a new generation of such devices is being born to meet the stringent needs of the future.

Jaeschke, Heidelberg: How do the prolytic graphite grids behave at arc-overs? Are they more delicate mechanically and do you have any experience with that?

Faulkner: Yes, the grids are as robust, perhaps, even a little more so, than a tungsten or a molybdenum grid. They do have one disadvantage, which of course, I wasn't going to mention, and that's due to the way they're made. There is an increased chance of particulate matter, or a roughness of the surface, which might be more conducive to producing arcs. However, if an arc occurred, they're quite capable of withstanding it. Techniques are being developed now for sealing this roughness without destroying its secondary emission inhibiting capabilities to cut down on the change for these particles.

Allen, SLAC: Are there any other significant developments by other tube companies besides Eimac?

Faulkner: I'm sure that there are quite a few. A great deal of this pyrolytic graphite technique was done in France. The French government put a million dollars a year for ten years into working with pyrolytic graphite for tube developments and also Siemen's is doing quite a bit with similar material.

Stabley, RCA: The question was asked: What are other tube companies doing in other areas? Some of you might know that we at RCA have made a regulator tube for Princeton University. It's a 200,000 volt device to be used with neutral beam sources. We think we might be coming up with an rf version of this tube which might be capable of about 7 megawatts of power under cw conditions at about 50 to 100 MHz.

NEW ENGLAND NULCEAR LINAC RF POWER SYSTEM

R. F. Lankshear
New England Nuclear Corp.
N. Billerica, Mass. 01862

Summary

The proton linear accelerator,being constructed by the New England Nuclear Corporation,will have a design energy of 45 MeV and an average current of 5 mA. The machine will be energized by a pulsed rf power system with a 12% duty factor,providing 600-kW average and 5-MW peak power at 201.25 MHz.

Introduction

The rf system design requirements are to provide adequate peak and average power levels for anticipated operational demands, with precise control of the output phase and amplitude and at the same time provide test and conditioning facilities without interruption of the machine operation.

To satisfy these requirements, the rf system will comprise three semi-independent rf amplifier chains, each with a 200-kW/5-MW capability. A power combiner/splitter system with high power coaxial switches will sum the rf amplifier outputs and feed the four accelerator feed loops.

Design Considerations

The choice of operating frequency has been extensively covered in the literature. In the present design, a practical consideration was the requirement that the machine use existing technology and proven design as an insurance of its successful operation. This led to the adoption of 200 MHz as the operating frequency, in common with Fermilab, Brookhaven, and Los Alamos Linacs. Similarly,the choice of high power rf amplifiers centered around the RCA 7835 triode,with a Continental Electronics cavity.

Klystron and other tube types were considered as possible alternatives; however the availability of power supplies having reasonable perveance and efficiencies, together with possible early life difficulties and lack of firm delivery and performance guarantees, reinforced our decision to use the 7835 tube arrangement.

Facilities to test tubes and high power components are not generally available, so an important consideration is the ability to take an amplifier chain off-line for tube and component testing, with the minimum interruption of the machine operation. Similarly, in case of rf system failures, the operation may be continued with only one of the three amplifier chains. The relatively low peak power operation of the 7835 triode is expected to provide an extended tube life when the three amplifier configuration is used for driving the accelerator. A graph showing the expected beam current yields versus one, two, or three tube operation is given in Fig. 1.

Facilities

The linac building has been designed to provide the power and cooling facilities required by the accelerator, together with the necessary lifting and handling arrangements. The layout of the rf gallery is shown in Fig. 2.

The building is fed with ac power at 13200 V. Two transformers provide 480 V, 1.5 MVA, and 575 V, 2.0 MVA. The smaller unit provides power for the building and services, the 2.0 MVA unit supplies the rf power system.

An electrical room houses the switch gear, and distribution transformers, together with silicon controlled rectifiers used to control the ac inputs to the externally located plate power supply transformers. The 32000-volt, 3-ϕ output of these transformers is rectified and charges the capacitor banks, forming part of the 7835 triode anode power supply.

Three water cooling systems are combined to provide the rf system cooling, each system is rated at 300 gpm at 100 psi, a total of 900 gpm. The rf gallery air handling equipment is rated to handle approximately 60 kW. Large penetrations through the shielding wall separating the gallery from the accelerator tunnel are provided for the 12"-diameter coaxial lines connecting the power amplifiers to the accelerator. A 3-ton overhead electric crane with 13' 6" clearance under the hook covers the gallery area.

Control racks housing vacuum pump power supplies, the preaccelerator and beam transport line controls, are also located in the gallery area.

Description of the Equipment

Three rf amplifier chains with combined outputs are arranged to feed the four accelerator feed loops. Each amplifier is capable of providing 5-MW peak and 200-kW average power. A transmission line system with high power switches and power combiners/splitters, enable one, two, or three amplifier operational modes to be selected. One selected "Off-Line" amplifier may be used to drive the test load necessary for fault finding and tube conditioning.

Two buncher cavities, one operating at 201.25 MHz, and the other at 402.25 MHz,are used to bunch the beam before injection into the linac at 750 keV.

A low level rf distribution and control system provides phase and amplitude control of the two bunchers and the accelerator, together with input signals to the accelerator and buncher frequency controllers needed to maintain resonance conditions.

Each of the three main amplifier chains is essentially operationally independent. The arrangement of equipment in the rf gallery is shown in Fig. 2. The power amplifier stages are anode modulated RCA 7835 triodes, controlled by hard-tube modulators using Eimac 8973 tetrodes (Fig. 3). The 186 μfd capacitor banks are charged from a 35 kV, 15 A dc power supply, with silicon controlled rectifiers in the transformer primary circuits, providing charging current control, voltage regulation, phase-loss sensing, fault protection, and fast turn-off of the plate power supply. The plate power supply transformer steps up the 575 V primary voltage to 32,000, 29,000,

or 26,000 volts line to line selected by taps.

A 2 MVA 13.2 kV/575 V 3-phase transformer provides ac power to the three outdoor, pad-mounted power supply transformers via the switch gear and SCR controllers located in the electrical control room (Fig. 3).

A hard-tube modulator using an Eimac 8973 tetrode (x 2170) as a series tube will provide primary fault protection for the power amplifier. In the event that the modulator current exceeds a preset value, (power amplifier arc), drive will be removed from the modulator, causing an interruption of the power amplifier current in less than five microseconds. A capacitor bank crowbar will provide secondary protection if the fault persists for more than five microseconds, or if the fault current exceeds a second threshold level indicating a modulator arc. The crowbar uses an ignitron as a fast switch, and is provided with a trigger tester and shorting device for system testing.

Modulator analog control signals from ground level are transmitted across the high voltage interface with photon coupled isolators, which in turn drive a solid state amplifier and the non-inverting common cathode 4C350A, and 4CX5000A stages, which drive the 8973 tetrode. The tetrode will be used in a quasi high-mu triode arrangement, where the screen grid is the driven element, with resistance coupling to the control grid.

The frequency response of the modulator is such that the output voltages and currents will have rise and fall times of less than 2 microseconds (10 - 90%) into a resistive load at 36 kV, 300 A.

Rf drive power of 200-kW peak, is applied to the power amplifier input from the drive amplifiers, where an rf drive saturated pulsed screen grid 4616 tetrode is used. Power supplies, capacitor bank, and controls are provided, which make the drive amplifier an operationally independent unit for test purposes.

Power amplifier cavities for the 7835 triodes will be similar to those used at the Brookhaven and Los Alamos Linacs. Turbines and air/water heat exchangers housed in their own pressure vessel will provide recirculated air at 45 psi for the cavity pressurization and cooling system. A water-cooled power supply with an inductrol voltage regulator will control the filament run-up sequence and provide regulated dc current for the 7835 filament.

The 201.25-MIz and 402.5-MHz buncher cavities are driven by the two buncher amplifiers, which are identical, but for their operating frequency. Both use RCA 7651 ceramic tetrode stages with a nominal 5-kW peak output. Each of the amplifier chains is provided with 20 Watts of rf drive power from the rf distribution system (Fig. 5). The frequency source is a crystal controlled stable oscillator having a pulsed 201.25-MHz output of 40 mW into the amplifier/power splitter combination feeding the phase control units. A frequency doubler following the phase controller provide 402.5 MHz for the second buncher amplifier.

The phase controllers (Fig. 5A) are designed to set and maintain the correct phase relationships between the two bunchers and the accelerator. Frequency controls (Fig. 5B) will maintain the buncher and accelerator cavities at resonance. Additional phase control units in each of the three amplifier chains will maintain the 12"-hybrid input phase relationships necessary for their proper operation.

The three power amplifier outputs are coupled to the four accelerator feed loops with 12"-diameter, air-cooled, 50-ohm transmission line. A combiner/splitter switching system will allow seven modes of operation. Figure 6 shows a high power phase shifter, providing continuous phase adjustment between the accelerator and power amplifiers. Directional couplers are provided for monitoring the measurement of forward and reverse powers throughout the transmission line systems. A test load capable of handling 200 kW/5 MW is available at all times for system testing.

Conclusion

The construction of the equipment is proceeding according to schedule. The high power rf components, modulators, power supplies, power amplifiers, etc., are being provided by Continental Electronics of Dallas, Texas, the 12"-transmission line components by Microwave Techniques, Inc. of Raymond, Maine, and the low level rf components by NEN. Delivery of the major components will occur during mid 1980, with high power testing starting August-September of 1980.

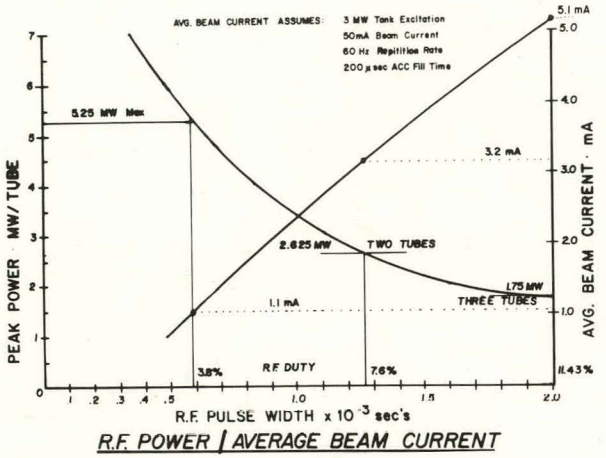
Acknowledgements

Acknowledgements are due to our colleagues at the various national laboratories and industry, who have contributed ideas and design details of components and systems, and sometimes acting as consultants.

References

1. C. S. Taylor, "Linear Accelerators", La postolle Septier, p. 925, North Holland Publishing Co., Amsterdam, 1970.

2. A. Carne, K. Batchelor, "Design of a High Current 200-MeV Linear Accelerator", NIRL/R/55.



R.F. POWER / AVERAGE BEAM CURRENT

Fig. 1

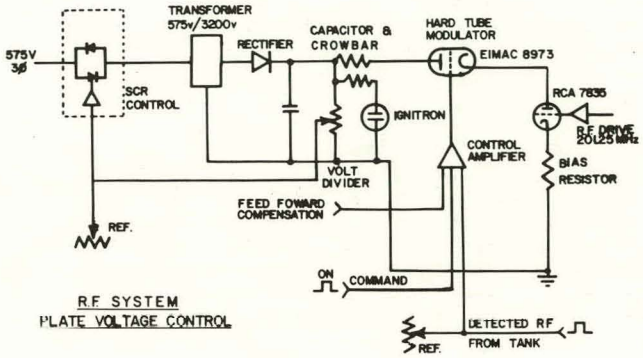
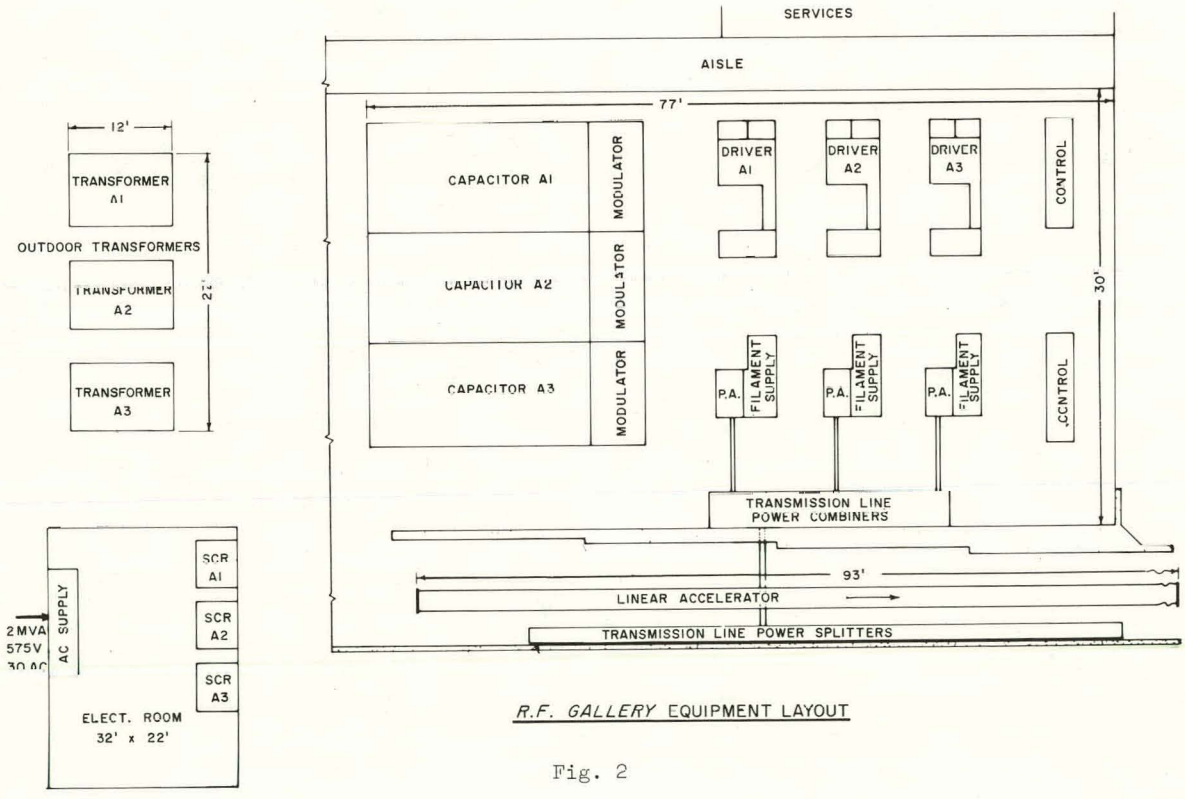


Fig. 3



R.F. GALLERY EQUIPMENT LAYOUT

Fig. 2

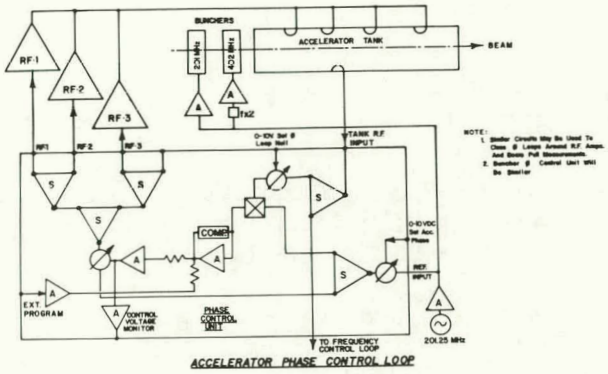


Fig. 4A

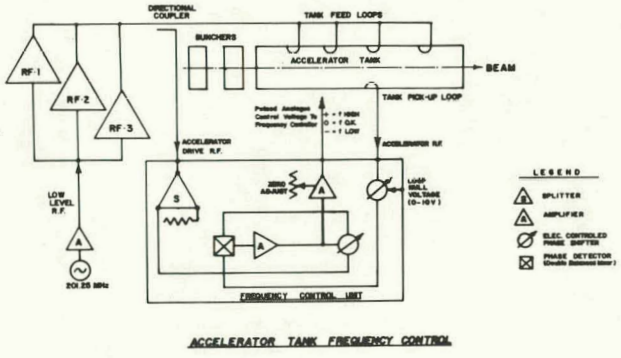


Fig. 4B

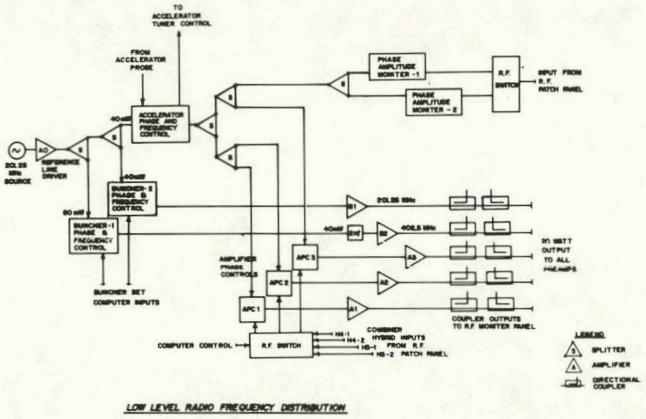


Fig. 5

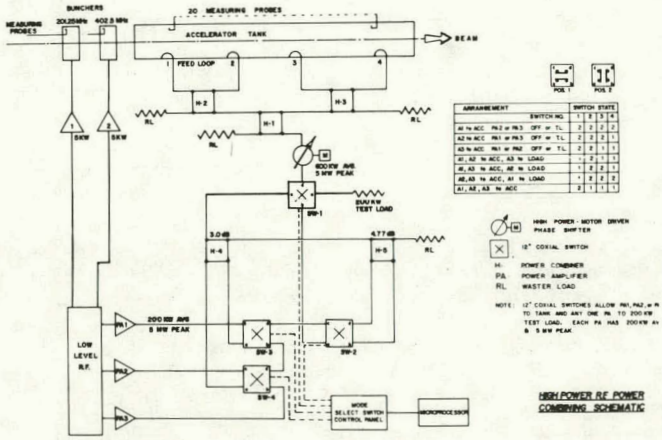


Fig. 6

THE RF-SYSTEM OF THE CERN "NEW LINAC"

J. Cuperus, F. James, W. Pirkl
CERN, Geneva, Switzerland

Summary

The rf-system of the CERN "new linac"[1] consists of ten separate amplifier chains of modular construction, with individual fast amplitude and phase regulation systems, together with a slow tuning servo. All the servomechanisms act on the low-level part of each chain, without any high-power modulators.

Constructional details of the rf hardware are given and performance figures presented.

Structure of the Rf-system

The basic design decision was to assign a separate amplifier chain to each of the ten resonators and to start at an rf-level of 2 Watts. The feedback circuitry can thus be built around high-speed, low power components, such as varactors or PIN-diodes driven by operational amplifiers.

The "semiconductor part" comprising servomechanisms and rf amplifiers up to 400 W, is essentially the same in each chain, and only the "tube part" is specifically tailored to the power requirements. Table I gives a summary of the latter.

A common master oscillator generates a quartz-controlled reference signal of 202.56 MHz, which is amplified in a pulsed 300-W-amplifier and distributed via the phase-stable reference line running along the resonators in the accelerator tunnel. Directional couplers derive the input signals for each of the 8 fundamental frequency chains with near-to-ideal decoupling. The second-harmonic chains 2 and 10, receive their input signal from doublers in the corresponding 202-MHz chains 1 and 9; this arrangement simplifies the phase setting of the double resonators.

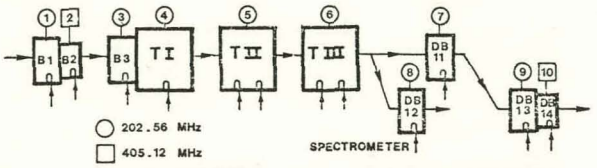
The Anatomy of a Chain

The feedback loop

The block diagram is shown on Fig. 2. The rf modulators work below 100 mW but are well shielded. Stray rf from the high power components interfered however, with the video circuits causing oscillations. With some additional filtering in these circuits, the problem disappeared.

Cross-coupling between the amplitude and the phase loop is small, except in the cavity when this is detuned for beam load compensation. In practice, the cross-coupling remains tolerable and the feedback loop is well behaved.

Bandwidth is limited by the phase shifts due to delays in the loop (total length about 50 m for the linac tank loops) and additional phase shifts in the components. It was found that an adequate safety margin was achieved at a bandwidth of about 150 kHz.



Chain	Designation	Amplifier configuration (Tube type, output power)				
1	BUNCHER 1	RS 2024 30 kW				
2	BUNCHER 2 Second harm. (405 MHz)	RCA 7651 3 kW	RCA 4665 22 kW			
3	BUNCHER 3 Energy Corrector	RS 2024 30 kW				
4	TANK I	RS 2024 30 kW	TH 170 0.5MW	TH 170 2.5MW		
5	TANK II	RCA 7651 5 kW	RS 2024 90 kW	TH 170 0.9MW	TH 170 2.5MW	TH 170 2.5MW
6	TANK III	RCA 7651 5 kW	RS 2024 90 kW	TH 170 0.9MW	TH 170 2.5MW	TH 170 2.5MW
7	DEBUNCHER 11	RCA 7651 5kW	RS 2024 90 kW			
8	DEBUNCHER 12	RCA 7651 5kW	RS 2024 90 kW			
9	DEBUNCHER 13 Bunch Rotator	RCA 7651 5 kW	RS 2024 90 kW			
10	DEBUNCHER 14 Second harm. (405 MHz)	RCA 7651 3 kW	RCA 4665 22 kW			

Table I General layout of the rf system

Other limitations to the bandwidth are resonances, one of which is shown in Fig. 3. If this resonance crosses the unity gain line, the loop oscillates at the frequency of the resonance. One cause of the resonances is higher modes in the linac cavities but, in this case, the next higher mode was more than 1 MHz away and caused no difficulties.

More troublesome are the standing waves between the final amplifier and the cavity, which can be considered a short circuit, some 50 kHz from the nominal frequency. This short circuit, transformed by the feeder line, combines with the amplifier load impedance and builds up parasitic resonances. The line length can be set between two extremes, $\lambda/4$ apart :

(a) "Maximum-Q" : resonances are at maximal distance from the nominal frequency ; highest safety

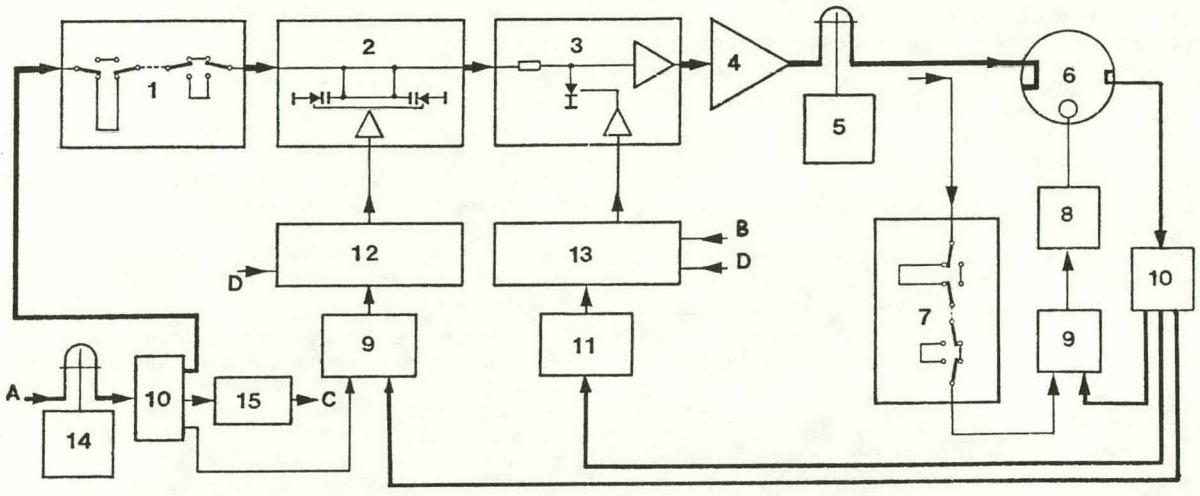


Fig. 2 Block diagram of the Feedback System
(1) 6-bit variable delay line for adjusting loop phase; (2) fast phase modulator with varicaps; (3) fast amplitude modulator with PIN diodes; (4) rf power amplifiers; (5) trombone; (6) cavity; (7) variable delay line for setting the cavity tuning; (8) control of the slow tuning loop; (9) phase detector; (10) 3-way divider; (11) amplitude detector; (12) phase feedback control; (13) amplitude feedback control; (14) trombone for setting cavity phase; (15) frequency doubler; Signals (A) rf reference; (B) amplitude reference; (C) rf reference for 2nd harmonic cavity (chain 1 or 9); (D) feedforward signals to improve the transient response when the beam comes in.

margin against overvoltages ; however, the tank rise-time is slowest and self-compensation of beam loading is poor.
(b) "Minimum-Q" : resonances are minimal distance, with the other effects at the opposite extreme.

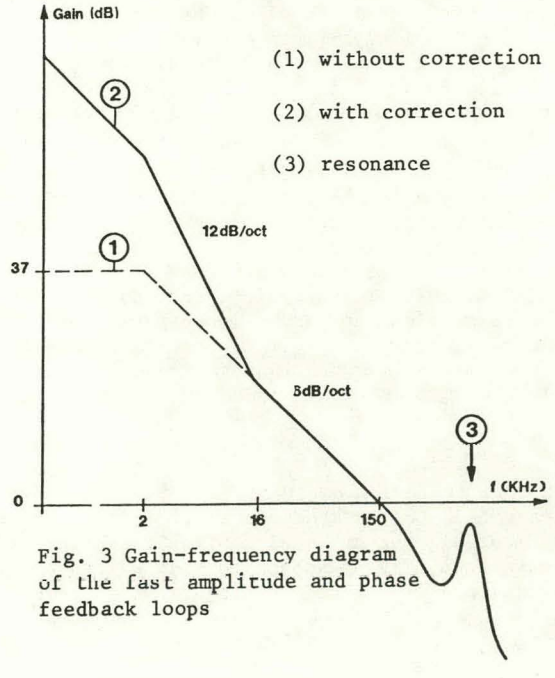


Fig. 3 Gain-frequency diagram of the fast amplitude and phase feedback loops

In practice, one starts with the safe "maxi-Q" setting and works towards the "mini-Q" until the best compromise is achieved.

In the case of DB 13, which needs high power at the end of a very long cable, the safest solution was to include a circulator in the feeder line.

Amplifier

The 400-MHz power amplifiers are commercial units using the RCA tetrodes 7651 and 4665. These are the only amplifiers that were bought ready-made. The other amplifiers have been developed here at CERN.

The transistor amplifiers are 4-stage linear amplifiers with a wide dynamic range. The final stages consist of 4-module units each delivering 100 W. Thanks to the low duty cycle, the transistors operate without cooling fins.

Three other amplifiers were developed. One started as a grounded cathode stage of 40-kW output for 300 W of drive. The Siemens RS 2024 CL was selected as the best tube for the job. By tuning-out the cathode inductance and using screen-grid inductor neutralization, the design goal was achieved. A production model suffered from a parasitic oscillation at 2.3 GHz, which took some time to cure. Although one amplifier of this type was used operationally for about a year, on the grounds of increased simplicity and higher output power, this configuration was aborted to a grounded-grid, grounded-screen design. With this change, only 36 kW with a drive of 400 W was obtained.

To ensure an ample reserve of power as drive for the high power stages, an additional amplifier known as the "pre-driver" was designed and built. Using more drive power, the RS 2024 was driven up to an output power of 100 kW. A particular feature of the RS 2024 stage is the re-entrant plate cavity with an

integral "POLYFLON" plate blocker. This is a Teflon cylinder with electroformed copper on both sides, making a distributed capacitance with high dielectric strength. The 14-kV plate supply is obtained from a capacitor bank.

The "pre-driver" also used an RCA 7651 in a grounded-grid, grounded-screen circuit. An output power of 8 kW for a drive power of 400 W has been achieved. The plate supply is 5 kV, derived from a capacitor bank.

Both amplifiers use identical screen-grid supplies; these are 1 kV, 1 A units with built-in protection against overcurrent. Fast acting protection is provided for both amplifiers by means of ignitron crowbars triggered by plate overcurrent pulses.

Eight identical 2.5-MW amplifiers are used in the final and drive stages of all tank chains. They are equipped with the TH 170 triode, a water-cooled version of the well-proven vapor-cooled TH 470 triode. It was found that this type is the most economical solution for this low duty cycle machine. The amplifier can, however, also accept the TH 116 triode, the water-cooled equivalent of the TH 516, to deliver > 50% more power.

The amplifier is a re-development of the original CERN linac amplifiers ; modifications include larger resonator diameters (up to the very limit of the first circumferential mode), improved RFI shielding, different tube cooling, completely redesigned input circuit, easily adjustable output coupling loop, and grid neutralization. The latter cured instabilities at the leading edge of the pulse that were initially attributed to tank-multipactoring due to very similar symptoms. As in the earlier version, the amplifier is two floors in height. The upper part extends into the equipment gallery with a removable cover that is part of the output resonator ; from here a tube may be changed in about 20 minutes. The lower part is based in a service tunnel and comprises the infra-structure such as blowers, filament transformer, drive mechanisms, etc., as well as rf-input and output ports imbedded in their respective resonators. A thyristor-controlled filament supply and associated electronics with an analog multiplier keeps the filament power constant despite mains fluctuations and resistance drop of the thoriated tungsten cathode. In addition, it provides smooth turn-on and turn-off during a 3-minute ramp.

HV-modulator and charging supply

Each of the tank-chains is equipped with a 40-kV plate supply, consisting of an LC pulse-forming network (PFN), an ignitron as high-power switch, a pulse transformer to provide voltage step-up and ground separation, and a crowbar system with ignitron and resistive termination.

All the (two in Tank I or three in Tank II, Tank III) amplifiers of a chain are connected in parallel to their respective pulse transformer. The modulator is designed for a pulse length of up to 1.1 msec (H⁻-operation), but is at present only equipped with condensors for 250 μsec (proton-operation) ; therefore, many special features of the circuit such as the resetting of the pulse-transformer core by the capacitor charging current, or the mere size of the transformer or the capacitor cabinet, may seem much overdesigned at first sight.

The three PFNs are charged by a common 25-kV supply via decoupling diodes. When the preset voltage is reached on the capacitors, the charging is interrupted by firing a set of parallel thyristors across the 200-V mains side of the HV transformer 50 Hz chokes limit the current in this mode as well as during the charging cycle, thus providing very high efficiency together with a minumum of mains disturbance. The modulator was designed by A. Faltens of LBL.

Due to the internal resistance of the PFN arrangement, the output voltage depends on the load current which would normally change with the rf drive. A stabilization circuit is therefore included, which consists of cathode resistances in the tubes together with a Zener-diode bank for polarization at 1200 V. This reduces the variation of the plate currents to less than 10% between full output power and quiescent state. Severe overdrive of the output tubes however, results in excessive plate currents, low plate voltage and reduced rf output. To avoid a latch-up condition with the amplitude-servo loop closed, the maximum drive power has to be limited by an adjustable threshold in the feedback circuit.

Rf plumbing

All cavities are fed by means of low-loss feeders. Air dielectric semi-rigid Flexwell cable is used in the buncher and debuncher chains, with 1"7/8 or 3"1/8 diameter. The three tanks are fed by stub-supported rigid lines of 230/100 mm diameter, supplied by Spinner, via dust-proof trombones having a range of 360° at 202 MHz. The feeder lines can be relatively easily opened for test purposes and short circuits or dummy loads inserted. While there are trombones in the feeds to all tanks and in the inputs to the final amplifiers for Tanks II and III (these for phase equalization), it was found possible to operate with fixed lengths of feeder for the other resonators, having first determined the optimum electrical length.

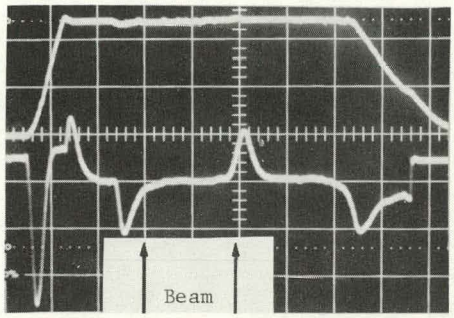
Couplers supplied by Spinner are placed at strategic points in the feeders. Detector heads are connected directly at the couplers and their video output is taken back to the monitoring system. The heads are of special design in order to achieve reliable power level indication. Each has two diodes, a balanced output, and a low-pass 225 or 450 MHz microstrip-filter incorporated. Low-pass filters are also inserted in signal paths from the tanks to attenuate higher harmonics passed by the tanks.

Control interface

Normal operation of the rf system is through the general control system of the linac. In addition, there is a full set of local controls, centralized for each chain, giving access to test points and all mechanical and electrical settings. Each power amplifier chain and the HV modulators are protected by independent, hardwired interlocks.

Performance

This is best described by the following photos taken for Tank III, while operating with a beam current of 100 mA, i.e., 2/3 of the maximum value.

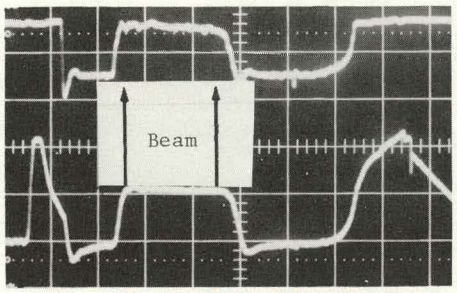


tank amplitude

tank phase
1.6°/div.

time base
50 μsec/div.

The amplitude shows a transient of 1.3%. This has negligible effect for the tanks downstream. To improve the transient response of the feedback loops, feedforward signals can be supplied when the beam comes in. This facility is not used at present as the system works satisfactorily without it.

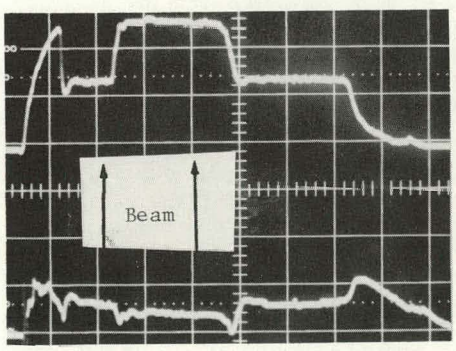


amplitude
control
7dB/div.

phase control
20°/div.

time base
as before

The second photo shows the control signals operating on the loops. During operation, it is essential that enough power is available during the beam time. Also, due to the fact that the phase modulator has only a limited range of 80°, one has to make sure that the loop delay is properly adjusted (by item 1 in Fig. 2). Note the large amount of correction required due to the heavy beam loading of 100 mA. This can also be seen on the next photo.

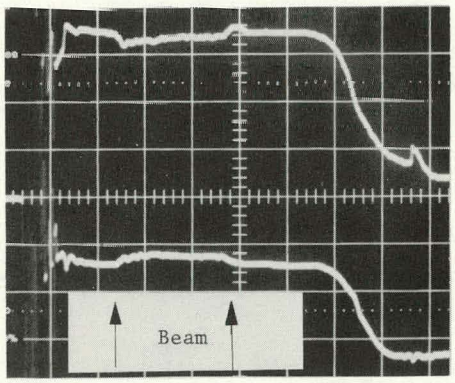


Time base
as before

forward power

reverse power

This shows signals from the directional coupler at the output of the upstream final amplifier, after rectification by the detector head. 2.7 divisions correspond to 2 MW.



time base
as before

plate volte
10 kV/div.

plate current
50 A/div.

The plate voltage and current for the final upstream amplifier are shown above. Due to the constant-current configuration of the 2.5-MW stages, the load current and hence the plate voltage show only moderate variations.

Conclusion

The system described gives adequate performance over the full range of beam current, up to 150 mA, without any resetting of parameters ; if this were applied (e.g. for feedforward, adjustment of tank loops and tank tuning for minimum reflection, etc.), there would be potential for improvement at the expense of a more complicated operation.

The system was not designed with low cost as primary goal. However, we feel that the low expenditure of 3.5 MSfr. (including all temporary labor) deserves mentioning.

Reference

1 E. Boltezar et al., "The New CERN 50-MeV Linac", proceedings of this conference.

1979 LINEAR ACCELERATOR CONFERENCE

RECENT IMPROVEMENTS OF THE ACCELERATOR COMPONENTS AT THE UNILAC

D. Böhne, M. Emmerling, A. Gasper
GSI, Gesellschaft für Schwerionenforschung mbH
Darmstadt, Fed. Rep. of Germany

Summary

Experience with coupling devices of various designs for the Wideröe, Alvarez and single-gap cavity structures are reported. Dome windows suffer from pin holes in the ceramic if not properly coated. Large domes tend to implode. Coaxial feed throughs, if used in an unbakable design, develop copper deposits on the vacuum side.

Improvements of the reliability of rf power lines by the suppression of transients and a redesigned ceramic support for the center conductor are described.

For the single-gap cavities, with their inherently high frequency detuning under rf power, a capacitive tuner was conceived to replace the usual magnetic tuning slugs.

Introduction

In high duty factor linacs (the Unilac runs at about 25% duty), electrical discharges on rf power devices are an inherent problem. This has been attributed to the buildup of high ionization rates in air and insulators due to soft x-rays, and charge accumulation which can develop on ceramic surfaces. The increased thermal stress and the higher net on-to-off ratio, enhancing time dependent effects, are different from the situation in injector linacs. The large zoology of electrical discharge phenomena is not understood to such an extent that scaling laws in power, frequency and geometrical properties can be formulated. Coupling components, operating successfully in one accelerator, frequently fail if adopted for a different situation. Thus for every machine, individual solutions have to be found. Since most of the detrimental effects are time dependent, prototype programs do not necessarily reveal the problems. Instead, alternate solutions have to be allowed for in the design phase and have to be developed and examined in the first years of routine operation.

Rf Coupling Windows at the Unilac

The rf power transmission by coaxial drive lines into the resonant load of a high vacuum accelerating cavity requires an interface element between the atmospheric pressure side and the high vacuum regime. A variety of possible discharge phenomena, which are inherently different on both sides, impose considerable constraints on the geometrical and technogical design of the coupling window. For this interface element there are two basic approaches: a) a ceramic window of disc shape or dome shape, allowing for magnetic field penetration into the cavity from a coupling loop, terminating the coaxial line on the atmospheric side; b) a classical coaxial line feed-through by a vacuum tight insulating disc, associated with a coupling loop inside the vacuum cavity. Both solutions are in use in the accelerator field; the second one, however, is more frequently used.

The window type approach presents a simpler and more elegant solution. No vacuum seal for inner and outer conductor is required, and the matching of load impedance to the line impedance can be effected without breaking the vacuum seal or providing an expensive bellows feed-through for the loop assembly. The latter feature associated with a servo drive might become important for accelerators operating in a high beam loading regime. The BNL and the KEK injector linac, the Unilac and several Russian machines are using this coupling scheme. Its application is favored for higher frequencies and higher Q-values of the cavity, and evidently in case of waveguide feeders. For high duty factor machines like the Unilac and LAMPF, this solution presents the so far unresolved phenomena of pin-hole leaks in the ceramic wall and even disastrous implosions of the whole window assembly.

The coaxial line vacuum feed-through, in general, includes a flat disc, made from organic or ceramic material, with an elastomer or a brazed metal seal at the inner and outer conductors. Temperature and temperature gradient must be kept low, in order to avoid excessive mechanical stress and cooling provisions for loop and disc are somewhat difficult to incorporate. This difficulty is aggravated by the fact that the disc should be considered to be a limited lifetime unit; thus the whole assembly must be dismountable. For high duty factor machines, the decision on coaxial line dimensions is governed by the considerably reduced break-down threshold on the atmospheric side due to the strong radiation flux of soft x-rays. This flux equally destroys organic insulators and makes it impossible to use Teflon, apart from its unfavorable mechanical strength. An oversized line, however, if continued by the same dimensions on the vacuum side, gives rise to multipactor phenomena in the 100 - 200 MHz and 0.2 - 2 MW regime. A coaxial line geometry under vacuum presents ideal boundary conditions for the buildup of a high current flow of oscillating electrons, which are slowly driven into the cavity by the magnetic rf field lines. Even if this discharge occurs only for a short time during the buildup of the cavity field, it releases enough gas from the line surfaces to sustain a minor glow discharge, and metal sputtering results in copper deposition on the insulating disc. If a linac could be made as a clean and bakable system, like electron storage ring cavities, this effect

would vanish quickly. In practice, the sputtered particles stick more to the ceramic window surface compared to organic insulators and, as a consequence, tend to develop detrimental arcing on the vacuum side more quickly. Therefore, the insulating discs may have to be replaced as a preventive measure more frequently, depending on the particular circumstances of the accelerator. In most machines, this discharge problem of a vacuum feed-through was only a start-up problem; in a few cases it tended to be persistent.

In the early design phase of the Unilac there was not much access to the state of the art in accelerator engineering. Experience was limited to the operation of a coaxial line cavity designed for sparking experiments. This cavity had to be opened frequently and the ceramic disc feed-through failed repeatedly. It was replaced by a ceramic dome window which lasted indefinitely, probably because of the low duty factor of a few percent and the typically low electric field at the short circuit plane of the coaxial line cavity. It was straightforward then, to adopt the dome window approach in a prototype of the single-gap cavity structure resonating in the TM_{010} mode.

This ceramic dome, shown in Fig. 1, item b, was made from alumina and brazed to a Vacon ring, which then was welded to a 150-mm diameter Con Flat flange. It was easy to procure from commercial sources and allowed for a simple loop design (Fig.2). After 10 to 100 hours of high power operation, the ceramic tended to become leaky and small pin holes were detected on the bottom surface. This effect was highly reproducible and did not depend on the alumina quality. It was concluded that electrical charges had built up on the vacuum surface, which in time became clean and highly resistive under high vacuum, whereas a higher resistivity always remained on the atmospheric side. A high voltage breakdown through the insulator was the result of this charge-up. Domes with a deeper penetration into the electric field of the cavity, like the example c in Fig. 1, showed a much more pronounced tendency to develop pin holes. The latter dome was conceived to keep the cavity tuner out of the vacuum; it thus could be of an extremely simple design. A tentative explanation of the breakdown effect was based on the observation that a) it occured only after a considerable clean-up time and b) seemed to depend on the strengths of the rf electric field at the ceramic surface. Hence, it was concluded that electrons were removed by soft x-rays from the surface and sucked away during the positive cycle of the rf potential. A controlled conductivity of the surface would therefore eliminate the problem.

It was not easy to find a highly resistive coating, which was specified to contribute only a factor of two to the already existent dielectric losses of the ceramic, the temperature of which should stay below 150^0 C during operation. As a safe value, a surface resistivity of 10^9 Ω/□ was determined. If this figure was lower by one or two orders of magnitude, the dome window imploded immediately. A titanium coating, as applied to klystron windows, was tried at first. The conductivity was unstable, had to be controlled under vacuum and could not be brought to the desired specifications. A microwave tube manufacturer recommended a coating of a semiconductor material, lithium-polymolybdate, for example. It turned out to be simple to achieve the conductivity according to the above mentioned specifications and to obtain a homogeneous surface distribution of the deposit and reproducible data. Pin hole leaks were not observed again during 1000 hours of prototype operation. The problem was considered to be solved. It should be added, that the above mentioned figure for the surface resistivity applies only to the particular situation and domes treated to this specifications imploded at LAMPF. For an application differing in geometry and frequency, the admissible coating thickness must be redetermined by temperature measurements of the ceramic window. For merely commercial reasons, a different manufacturer got the order for the large quantity delivery for the Unilac. This manufacturer proposed a different coating (tin oxide) and demonstrated the fulfillment of the conductivity specifications at the time of delivery. After half a year of machine operation, the problem reoccured at the single-gap cavity section; the coating was found to have disappeared completely. The original source of resistant coating could not be revived and damaged domes had to be replaced every week. Curiously, the pin hole effect did not occur with equally distributed probability over the 22 cavities; in a few cavities it never reoccurred. Dentists cement turned out to provide a safe and reliable cure for sealing the leaks. After two years, the threaded holes in the cavity wall were mostly worn out by the frequent opening of the window flange and restrictions in particle energy due to failed cavities ultimately substantiated the demand for a reliable window design. The decision on a completely different approach, which will be described later, was impaired by the satisfactory experience with dome windows on the other structure types of the Unilac.

In the Wideröe section dome windows of type c, as shown in Fig. 1, have been in use for four years without any indication of the before-mentioned pin hole problem. The position of the domes is near the shorting plane of the coaxial stub line, as shown in Fig. 1 and 5 in an earlier report.[1] As the rf power was raised in cavity IV, from 0.36 to 0.54 MW, in order to accelerate U^{9+} ions instead of the design particle U^{11+}, heavy arcing in the coupling loop occurred occasionally, which could not be eliminated by pressurizing the coaxial line. In the case of such an incident, the dome window imploded. In cavities III and IV, the rf power was divided and distributed over two coupling loops, which then had Rexolite disc windows instead of domes. Figure 3 shows the Wideroe loop assembly, however, with a much smaller loop geometry, matched for the single-gap cavity structure. This Wideröe loop assembly, which is highly flexible and adjustable, was conceived as a universal unit which could be used with or without dome windows and which easily fits into every structure type of the Unilac.

The coupling loop for the Alvarez cavities is

shown in Fig. 4; it can be installed with or without dome window, type d in Fig. 1. Initially a ceramic piece of this size (350-mm diameter) was not easy to procure. Therefore, a Rexolite disc window was used. It failed on several occasions at medium power levels, due to heavy arc discharges on the vacuum side, which eroded the disc and spoiled the cavity surface. After those repeatedly encountered incidents, a dome window was installed and the Rexolite disc remained as a support unit on the atmospheric side. The before-mentioned pin hole problem never occurred at the four Alvarez domes, however they suffer from an unexplained lifetime problem. After about one year, the dome windows tended to implode at normal power levels. Fortunately, no drift tube was damaged on the four occasions of a window implosion. The ceramic material, which in time loses its white color due to sputtered metal and radiation damage, was examined for its dielectric properties. No degradation was found, the reason for the implosions remains unexplained. In the meantime, due to a shortage in spare domes, a Rexolite window is back in service in one Alvarez cavity. It works perfectly well. Regular inspections reveal a coloring and the development of cracks and visible deposits of copper material on the surface. It is believed that these Rexolite windows have to be replaced yearly to prevent this type of damage.

About 50 small probe windows (of type a in Fig. 1) are in service at the Unilac. Initially they suffered from the pin hole problem, though they did not penetrate deeply into the cavity field. After receiving a conductive titanium coating pattern, the pin hole problem never reoccurred. About once in a year, on the average, a probe window becomes leaky due to a crack in the ceramic or a braze failure.

After this review of the coupling ports on the Wideröe and Alvarez cavities, the development of alternate solutions for the single-gap cavity section will be continued. From DESY at Hamburg a loop assembly, as shown in Fig. 5, was obtained. It is in service in the DORIS and PETRA storage rings[2] and was tested up to 190 kW cw power at 500 MHz. This design is easily adopted for the output port of the 600 kW PETRA klystron. With major modifications, the same loop assembly is in use at the SIN cyclotron cavities at 250 kW and 50 MHz. It was tested for one and a half years in the Unilac single-gap cavity section; no damage and no metallization of the ceramic disc was observed. However, this design was considered to be too expensive to be used in all 22 cavities and Wideröe type loops, as shown in Fig. 3, were installed instead. They have been in service one year and it is not yet clear whether this will be the final solution. The overly long coaxial section on the vacuum side is often subject to multipactoring phenomena at medium power levels at 108 MHz. Except for one particular cavity, this effect can be conditioned away. However, the loops need a yearly inspection and the Rexolite discs have to be replaced eventually.

A coated dome window is now under test in one single-gap cavity on a low priority basis. The coating consists of Cr_2O_3 and was supplied by a commercial ceramic manufacturer.[+] Domes with a titanium oxide coating and domes with grooves ground in the flat bottom surface, will also be tested to answer the question of whether one-side multipactoring or photo-emission is the reason for the charge-up of the ceramic surface.

An alternate solution for the Alvarez loop has been sought also. At first, an upscaled version of the DORIS design was tried. It was impossible to obtain a satisfactory braze on the ceramic disc of 320-mm diameter; therefore this approach was abandoned. At present, a redesign with a cylindric ceramic insulator is in progress (Fig. 6). Inexpensive ceramic cylinders of various dimensions are available from rf power tube manufacturers and are easy to braze.

In conclusion, for small loop units, adequate for 0.25 MW, the DORIS design is recommended. Dome windows work too, but the controlled technology of a mechanically resistent coating seems to be beyond the state of the art. For large coupling devices in the 1 - 2 MW region at high duty factors, no satisfactory solution can be reported so far from the Unilac experience. Large dome windows cannot be recommended.

Rf Power Lines

High power coaxial transmission lines and accessory components are commercially available for communication systems in a large variety of power ratings and standards. In the accelerator field those products are occasionally considered to be too expensive. This was especially the case at the Unilac, for which about 500 m of power lines had to be procured. As an in-house effort, a 100-mm and a 320-mm diameter line system were developed for the single-gap cavities running at 0.2 MW and the Alvarez cavities running at 2 x 0.4 MW, respectively. Inner and outer conductor were procured as ordinary copper tubing in sections of 3 m in length, and joined together by clamping fixtures, which contain the support insulators. This design proved to be convenient and flexible for temporary installations, but tended to be unreliable for a large scale application in a permanent system. No pressurizing provisions were included. The Wideröe cavities are powered at up to 0.58 MW by a commercially available cable, which never presented a problem. The last few meters near the cavity, however, were made from flanged copper tubing which failed on several occasions.

In about 15 events in which rf power lines were heavily damaged, the failure occurred just near the cavity and never at the remote end near the amplifier. Insulating supports of the center conductor were found to be burned away giving rise to disastrous arcing in the whole line section. No particular reason could be associated with the breakdown, from either the actual operation circumstances, or from the mechanical status of the lines. In rare

[+]Anderman & Ryder Ltd., England

cases an assembly mistake might have been at fault. It is concluded, however, that the x-ray level near the cavity and in the tunnel environment strongly reduces the break-down threshold in air and on organic insulator surfaces. Pressurizing the line sections near the cavity (Wideröe) or, if the line design did not permit this modification (Alvarez), a modest flow of dry nitrogen helped a little but did not alleviate the problem. The power level had to be reduced by providing a power splitter and two feeder lines per cavity.

For the 22 lines of the single-gap cavity structure, the approach was different. It was realized that the leading edge of the drive pulse was overly sharp and that ringing in the amplitude control loop when the cavity was not properly tuned during the run-up, overstressed the lines by too much reflected power. The drive pulse was preshaped and the run-up was closely controlled in such a way that the tracking of the tuner was locked-in first before raising the amplifier power. This improved the situation to a large extent, but not entirely. An appreciable reduction of line failures was obtained as the result of a yearly disassembly and inspection of all line components. Support insulators with spark marks and overheated center conductor joints have been discovered every time, however, at a slowly decreasing rate.

Several types of line protection devices have been discussed but were never installed or considered as a desirable interlock source. Instead, sparking of the line has to be prevented by design measures as far as possible. If this cannot be fully assured for an rf breakdown due to vacuum sparking in the cavity, the line must be rated to safely sustain an occasional arc-over. This means that organic supports should be eliminated in the line, ceramic shafts being considerably less susceptible to damage caused by sporadic arc events.

Figure 7 shows the front end of a $\lambda/4$ test cavity, assembled from 150/345-mm diameter line components. As a result of a broad testing program, ceramic shafts have been found to be a satisfactory choice and even more desirable than the commercially available triangular ceramic plate. The rods are not damaged when continuous arcing is maintained. Organic materials, like Mycalex, Rexolite and Teflon, are found to be damaged permanently when subjected to an arc-over for a short time. The forward power on a matched line, which corresponds to the observed breakdown voltage, would be about 80 MW in an unpressurized line. The breakdown voltage did not rise when the supports were eliminated; thus $\lambda/4$ stub lines instead of insulating supports would not be a better choice in this respect. For a duty factor of 30% at 108 MHz, dielectric losses in the insulators limited the forward power to about 10 MW, which still left a reasonable safety factor against voltage breakdown across the insulators, enhanced by a totally reflected wave during the early build-up of the cavity field.

The above-cited values appear to be in disagreement with practical figures experienced in operating systems. However, a rational derating recommendation cannot easily be established. The reflected power is of a transient nature and does not contribute much to ohmic and dielectric heating and was already mentioned to be tolerable from the voltage consideration. Harmonics can be suppressed such that they contribute less than 10% to the line voltage. Imperfections of line components and assembly mistakes cannot be excluded completely, but should be subject to repair and improvement. Thus, a derating of the above-mentioned 10-MW figure by a tentative factor of 2 is really an arbitrary statement. Though the test cavity, when placed into the radiation environment of the linac tunnel, did not reveal a substantial change of breakdown voltage, nor is the degradation of electrical properties of ceramics generally known, accumulated experience at the Unilac substantiate a further derating of the admissible line capacity in the tunnel area. An additional safety factor of two, or even more, is recommended here.

The above-outlined results of a test line section apply to a commercially available line standard (150/345), which is in use at the CERN SPS cavity supply at 0.6 MW and about 50% duty factor. This line will be installed at the Unilac in the future as part of the upgrading program.[3] The present homemade 137/320-mm line was tested also. It broke down in the test situation at 4-MW pulse power at 30% duty factor. The limitation was set by the burnout of the Mycalex center conductor supports. In the practical application at the Unilac, this line was felt to be marginal even at 0.8-MW pulse power. From this experience the above-cited safety factors were suggested. The present 43/100-mm lines for the single-gap cavity section will be replaced by a 4 1/8" cable, which has been in service reliably for three years as the rf power transmission to the four rebuncher resonators in the experimental hall and for the test cavity facility.

Cavity Tuners

In an early design phase of the single-gap cavity structure in 1968, an overly large frequency detuning under rf power was observed for a prototype cavity. The detuning at full power, at about 50-kW average power, was 120 kHz. The slug tuner, limited in size by the flange standards, only could compensate for 72 kHz. Since a 10^0 C rise of the cooling water temperature only resulted in a detuning of 13 kHz, as one would expect, the large frequency excursion was unexplained. The waterflow in the individual water circuits of the half drift tubes, the end walls and the cylinder wall was tentatively changed by a factor of 5 without any significant influence of the detuning range. Temperature measurements on various spots of the cavity did not reveal local overheating. A measurement of the most sensitive geometrical dimensions, namely the gap width, showed the existence of different thermal time constants of cavity components, but did not result in the detection of gap shrinkage in thermal equilibrium; thus the action of ponderomotive forces could be excluded too. The investi-

gation of the transient behavior of the frequency run-away revealed three nearly equal contributions: one of instantaneous nature and two of a different but typical thermal time constant regime. Lacking an evident and satisfactory explanation, an entire redesign of the cavity components[1] was decided upon, which should result in a much stiffer end-wall concept and intensified cooling of all components. As a fall-back position, if the frequency excursion should still persist after the mechanical alterations, sophisticated adjustment gear was incorporated, allowing for retuning the gap width from outside the cavity.

As the 21 single-gap cavities of the modified design were assembled and finally installed in the accelerator tunnel, almost the same detuning range under rf power was observed as was in the earlier prototype phase. The provided gap adjustment mechanism proved to be inadequate for continuous adjustment of the tuning device due to wear-out and scuffing tendencies of the gear. The single-gap cavity structure had to be run at half the thermal design power level, which limited either the maximum final energy or the admissible duty factor of the Unilac.

A test program on an off-line cavity was resumed, aiming at the final resolution of the detuning problem. Most of the before-mentioned measurements were carefully repeated, yielding no new evidence. It was observed on the linac that the detuning range of the individual cavities differs by nearly a factor of 2 and that the range in one cavity is reduced by about 10% if the two neighboring cavities are turned on. This stimulated the suspicion that the stiff rf end walls, which differ from one-to-another by flatness and hence by stress load, execute bending forces on the support spiders. One pair of end walls was modified in favor of much reduced stiffness, by cutting in grooves near the half drift tube and near the outer seal area. A completely different wall of only 1.5-mm thick copper sheet metal with soft soldered cooling channels was examined too. In both approaches the effect was found to be unchanged or even worse.

Since no idea was left of how to suppress the detuning, concepts for a new tuning device have been reconsidered. Resonant loop tuners were excluded due to their high rf losses encountered in earlier prototypes. An additional flange for a second slug tuner was not available. Doubling the 150-mm stroke was found difficult for bellow and ball spindle procurement and space for an extended tuning device outside the cavity was not available either. The net gain of tuning range would have been inadequate too, because the increasing effect of counteracting capacitive tuning became significant.

This led to the investigation of capacitive tuning devices. Those tuners are widely in use on spiral type resonators but are unusual for TM_{010} cavities because of a long movable stem required to extend into the gap area. Problems of sliding rf contacts at the stem base were expected due to non-ideally symmetric positioning in respect to the gap center. An insulating stem, supporting equally a metal plate or bar for shorting the electric field lines near the gap, was ruled out due to excessive dielectric losses.

After cold probe measurements with bars of different lengths and diameters oriented parallel to the cavity axis and moved radially inward, a standard slug tuner was modified, as seen on the left in Fig. 8, in order to support a longer stem topped by a bar, shown on the right in Fig. 8, instead of the magnetic displacement body. The bar is 270-mm long and its closest position to the 10-cm wide acceleration gap is also 270 mm. The tuning range, maintaining the 150-mm travel of the original drive mechanism, is about 200 kHz. The frequency versus position law, of course, is non-linear, however, in a favorable sense. At the highest power levels the bar moves near to its outer position where the frequency response is less steep and the large clearance from the gap prevents sparking risk. Q measurements revealed no increase of rf losses in comparison to the magnetic tuner. If the tuning range would have been tripled by an extended stem length, then the TE mode resonance would come close to the desired TM mode, resulting in a drastic drop of the Q value. The tuner was subjected to high power tests and the suspected contact problem on the stem base, marked by f in Fig. 8, was found to be non-existent. One cavity of the Unilac has been equipped with this new tuner for half a year and due to the satisfactory service of this prototype, mass production of stem and bar components will be initiated. The modifications are scheduled to be complete in mid 1980.

Acknowledgement

The authors would like to acknowledge the stimulating contributions of G. Schaffer during the line testing program.

References

1 T. Niewodniczansky et al.,"The Mechanical Design Features of the Unilac",1972 Proton Linear Accelerator Conference, Los Alamos (1972).

2 H. Gerke,"The PETRA Cavities",DESY Report Nr. PET-77/08, DESY Hamburg.

3 N. Angert et al.,"The Unilac Upgrading Program", proceedings of this conference.

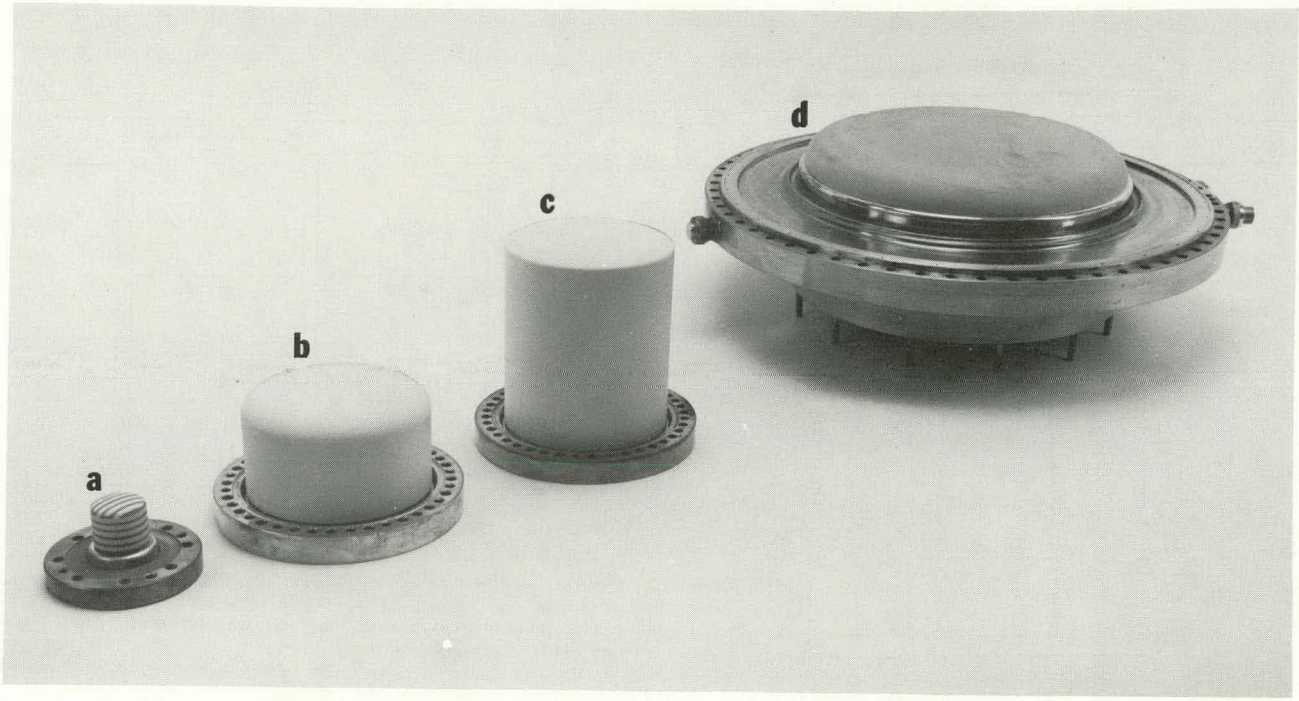


Fig. 1
Ceramic dome windows as used at the Unilac: a) rf probe window with meander-shaped titanium coating; b) dome of the original coupling loop of the single-gap cavities; c) dome of the coupling loops in Wideröe cavity I and II; d) shallow dome window of the Alvarez section, which was in service for about one year. Metal sputtering and radiation damage changed the color of the ceramic from white into grey and yellow.

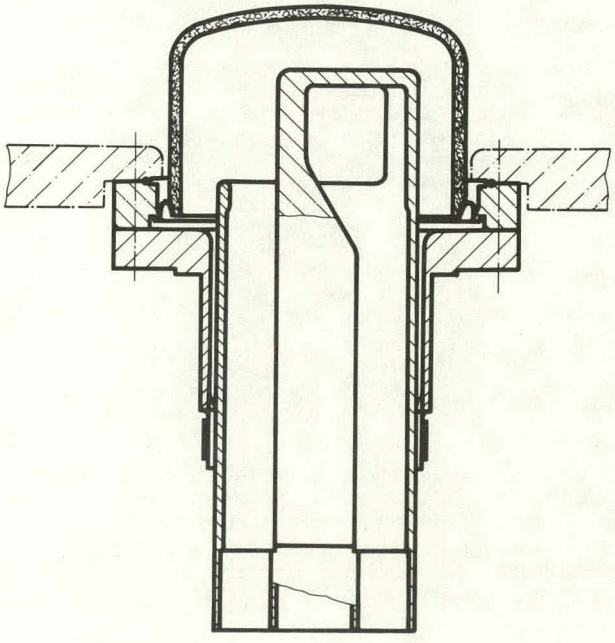


Fig. 2
Original coupling loop of the single-gap cavity structure with dome window. The center conductor is supported by the loop strap. Cooling was not necessary at 50-kW average power at 108 MHz.

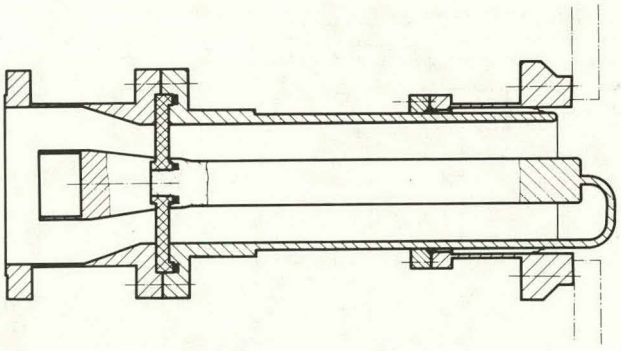


Fig. 3
Loop assembly of the Wideröe structure. Cooling channels and adjustment mechanism are omitted on the sketch. The Rexolite disc can be used as a vacuum seal or, if a dome window is used, is perforated in order to allow for pressurization of the loop area. When applied without dome to the single-gap cavities, the overly long coaxial section on the vacuum side tend to build up multipactor discharges.

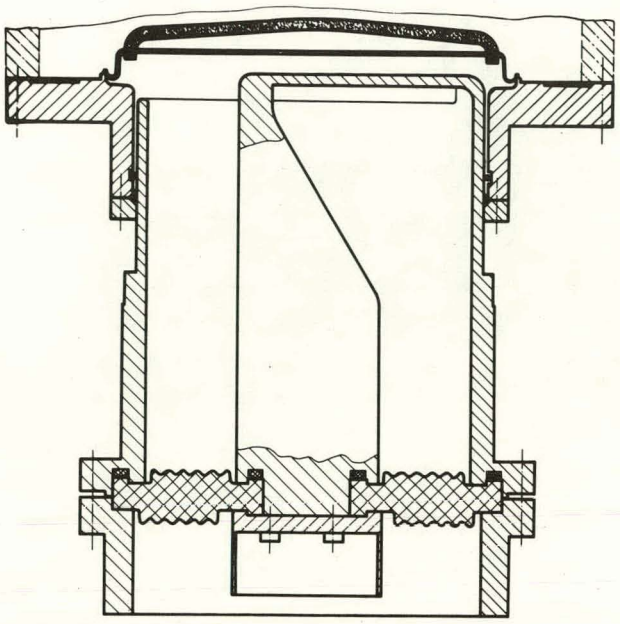


Fig. 4
Loop assembly of the Alvarez structure. Cooling channels and adjustment gear are omitted on the sketch. Line diameter is 320 mm. When used with a dome window, the Rexolite disc is perforated and dry nitrogen flushing removes ionized air compounds from the loop area.

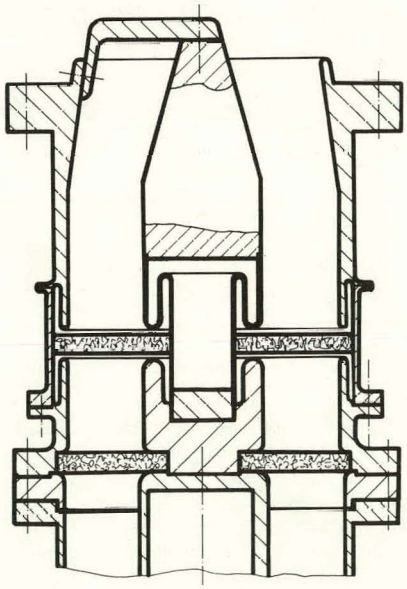


Fig. 5
Loop assembly of the DORIS storage ring cavities. The two separate water circuits and air flushing nozzles for cooling the ceramic disc are omitted on the sketch. It is essential to screen the brazed ceramic joints from the electric field.

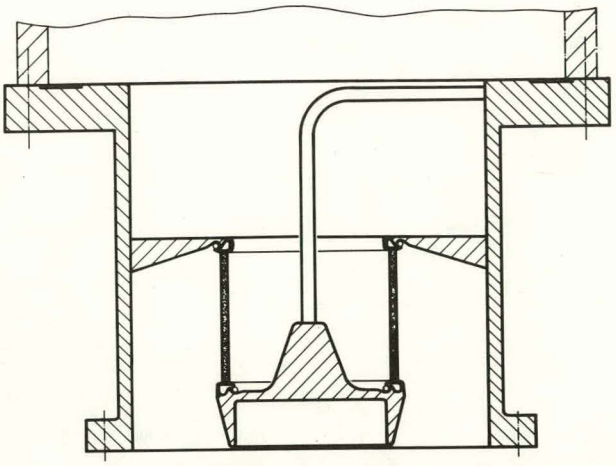


Fig. 6
Redesigned loop assembly for the Alvarez structure. Cooling channels are not shown. The vacuum window is formed by a ceramic cylinder. The cooled loop strap has a width of 90 mm. No adjustment mechanism is provided.

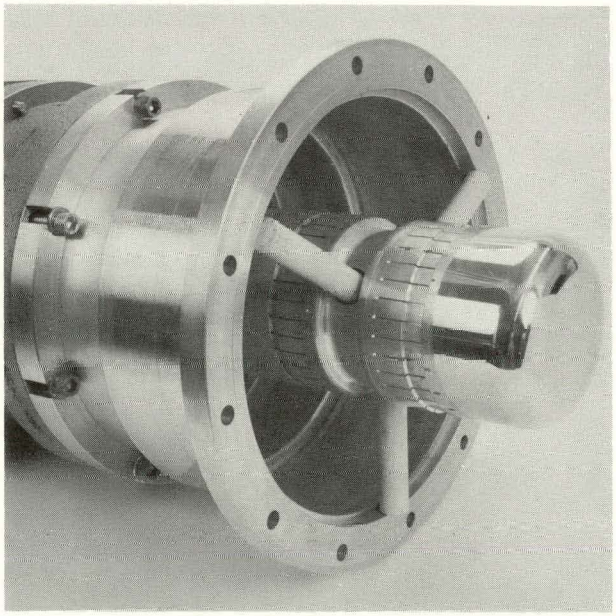


Fig. 7
Test resonator assembled from 150/345-mm line components. Part of the outer conductor, which extends to the right from the flange plane, was removed. In simulated high power tests ceramic shafts were found to be the optimum choice for the center conductor support structure.

a cavity wall
b stepping motor with magnetic break
c ball spindle with preloaded nut unit
d bellow
e linear potentiometer
f sliding contact
g magnetic displacement piston
h capacitive gap bridge

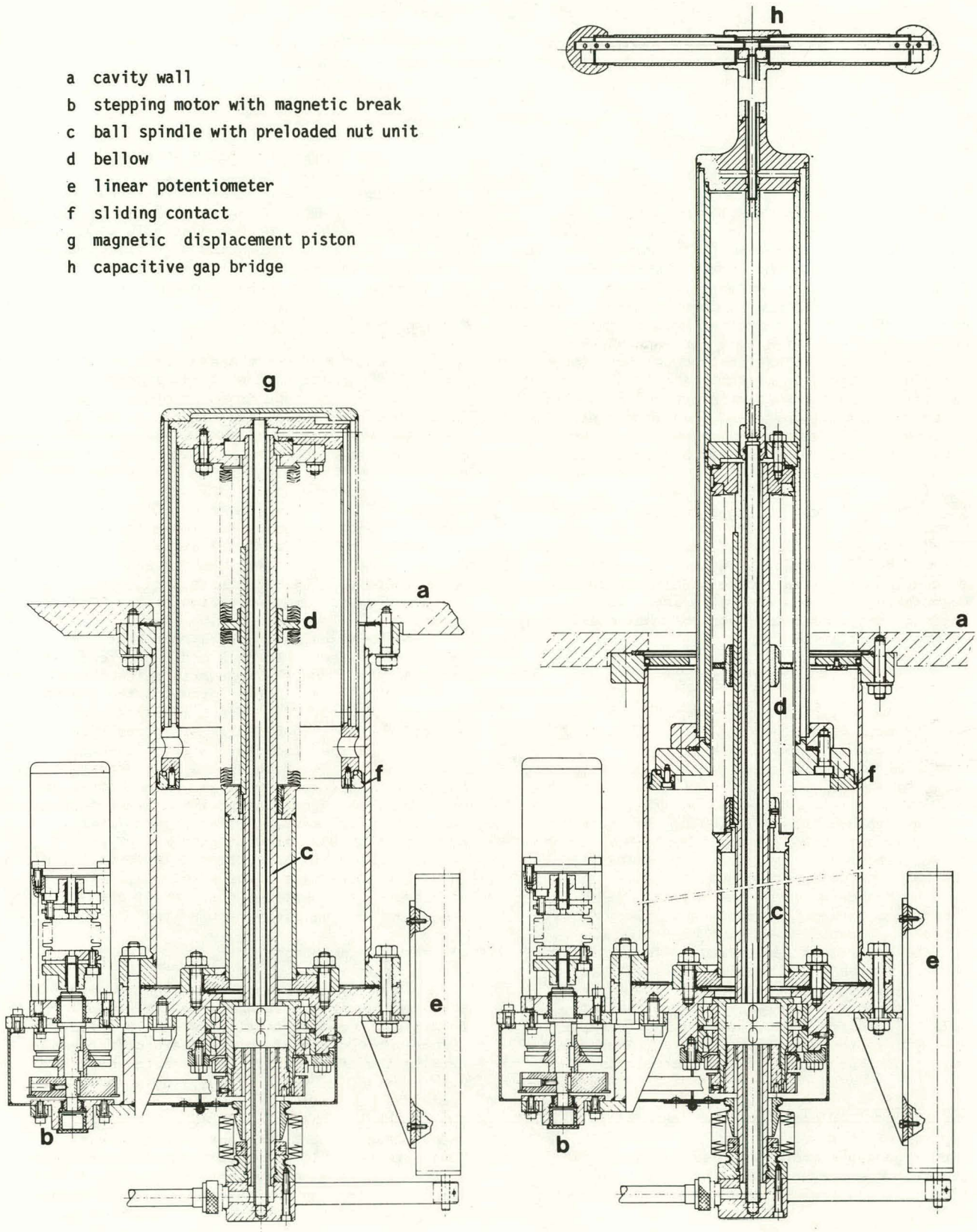


FIG. 8 MAGNETIC (LEFT) AND CAPACITIVE (RIGHT) CAVITY TUNER

DEVELOPMENTS OF THE RF SYSTEM FOR THE FUSION MATERIALS IRRADIATION TEST ACCELERATOR*

M. V. Fazio, H. P. Johnson† and Dennis M. Riggin††
Los Alamos Scientific Laboratory
Los Alamos, New Mexico 87545

Summary

The rf system for the Fusion Materials Irradiation Test (FMIT) accelerator is currently in the design phase at the Los Alamos Scientific Laboratory (LASL). The 35-MeV, 100-mA deuteron beam will require approximately 6 MW of rf power at 80 MHz. The EIMAC 8973 power tetrode, capable of a 600-kW cw output, has been chosen as the final amplifier tube for each of 15 amplifier chains. The final power stage of each chain is designed to perform as a linear Class B amplifier. Each low-power rf system (≤100W) is to be phase, amplitude, and frequency controlled to provide a drive signal for each high-power amplifier. Beam dynamics for particle acceleration and for minimal beam spill require each rf amplifier output to be phase controlled to ±1°. The amplitude of the accelerating field must be held to ±1%. A varactor-tuned electronic phase shifter and a linear phase detector are under development for use in this system. To complement hardware development, analog computer simulations are being performed to optimize the closed-loop control characteristics of the system.

General Description

Preliminary rf system design for the linear accelerator (linac) portion of the FMIT facility is in progress.[1] The 35-MeV accelerating structure will consist of a low-beta radio-frequency quadrupole (RFQ) accelerator and buncher[2] up to 2 MeV followed by two post-coupled Alvarez tanks in series, with an intertank spacer at the 20-MeV point. The 35-MeV, 100-mA cw deuteron beam will require approximately 6.0 MW of rf power at 80 MHz.

The basic layout of the FMIT rf system includes a total of 15 power amplifiers driving three linac tanks.[3] Each rf amplifier chain will be capable of generating at least 600 kW of power. The RFQ will require two amplifier chains and each linac tank will need at least six or seven. A multiplicity of drive loops will be used for inductively coupling the rf energy into the accelerator tanks. Each power amplifier (PA) will have its own coupling loop.

*Work supported under the auspices of the U. S. Department of Energy.
†Westinghouse/Hanford Engineering Development Laboratory employee working at LASL.
††Cornell University, employed at LASL Summer 1979.

Phase Control System

The output of each rf amplifier must be controlled to ±1° in phase. A diagram of the amplitude and phase control system is shown in Fig. 1. The major components of this system are a 400° electronic phase shifter, a linear rf phase detector, and a phase controller.

Electronic phase shifter

A schematic of the phase shifter is shown in Fig. 2. The phase shifter is a varactor-tuned, circulator-type device, similar in principle to those used at the Clinton P. Anderson Meson Physics Facility (LAMPF). Because of the non-existence of ferrite components (circulators) at 80 MHz, it was decided to build the phase shifter to operate at 400 MHz. This makes it possible to utilize strip-line techniques. A double-balanced mixer on the input is used to heterodyne the 80-MHz signal with a 320-MHz signal to produce the 400 MHz required by the phase shifter. The 320 MHz is derived by frequency quadrupling a portion of the 80-MHz input.

The 400-MHz signal enters Port 1 of the 4-port circulator. Ports 2 and 3 are terminated with varactors and the appropriate lengths of transmission line. Port 4 provides the 400-MHz, phase-shifted output. This signal then is heterodyned back to 80 MHz. All phase information is preserved because the same 320-MHz signal is used for both up and down conversion. An experimental model of this phase shifter has been operated successfully with 400-MHz inputs from 0.1 to 1.0 watt.[4] This phase shifter exhibits a linear response with a 400° range, as the dc bias is varied from 0-40 volts. The insertion loss varies from 2 to 5 dB. Figure 3 illustrates the measured phase shift and insertion loss versus varactor bias.

Linear phase detector

A linear phase detector is under development for use in the feedback control loop. The output will be a dc level between ±10 volts, linearly proportional to the phase difference between the two inputs. The detector must have 0.5° resolution, a 360° range, and a 100-kHz bandwidth.

Basically, the phase detector generates, then integrates the waveforms shown in Fig. 4. These are variable duty-cycle square waves whose signs are determined by whether the signal is leading or lagging the reference. The waveform is then integrated to produce a dc level

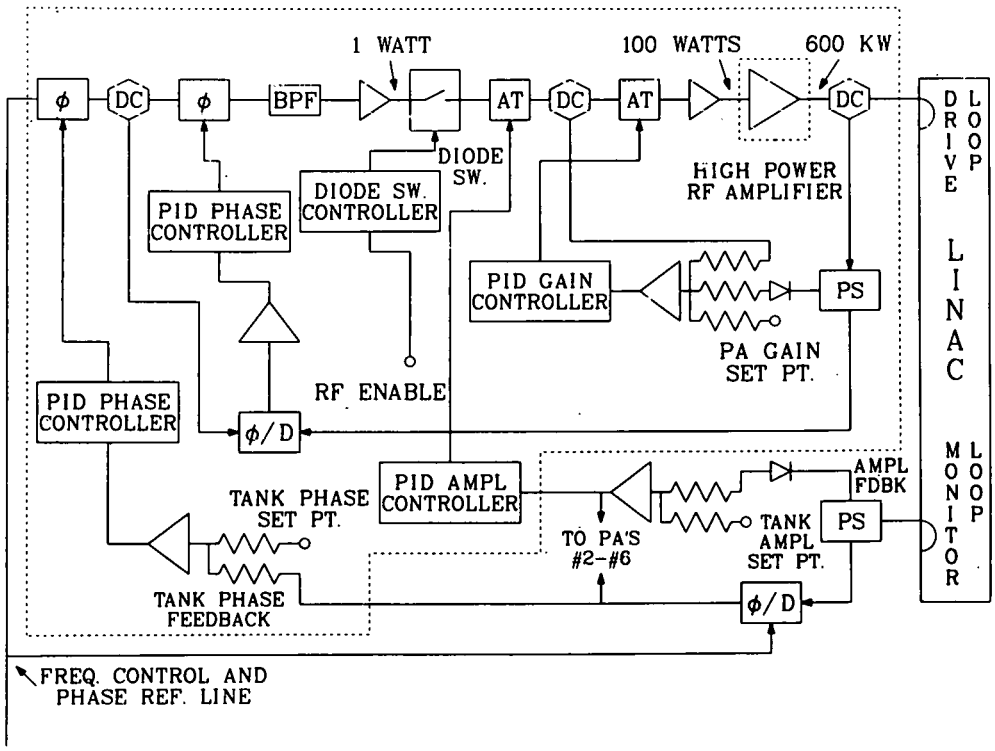


Fig. 1. A single rf amplifier chain.

proportional to the duty-cycle. For example, when the signal (SIG) and reference (REF) are in phase, a symmetrical square wave is produced that integrates to zero. When SIG leads REF, the square wave becomes asymmetrical with an increasing positive pulse width proportional to the phase difference between the two inputs. This will integrate to a positive dc level.

Figure 5 is a simplified schematic of the phase detector. Both the 80-MHz REF and SIG are mixed with a 79-MHz local oscillator signal to produce two 1-MHz signals that retain the same phase information as the 80-MHz inputs. Each 1-MHz signal passes through a voltage comparator to generate a 1-MHz square wave. A D-flipflop is used to provide a logic level that specifies whether SIG is leading or lagging. The SIG line goes to the D input of the flipflop and the REF line goes to the clock input. The flipflop changes output on the leading edge of the clock pulse, so, if the SIG is leading, the flipflop will output a high logic level and if lagging, a low. This bit addresses the multiplexer.

The waveforms of Fig. 4 can be realized by using SIG OR REF logic when SIG is leading and by using SIG AND REF when SIG is lagging. Only two multiplexer inputs need to be selected: x_0, which has the AND input, and x_1, which has the OR input.

The variable duty-cycle square-wave output of the multiplexer is then integrated, to produce a dc level proportional to the phase difference of the inputs. An alternate approach is being pursued in the event it is not possible to meet the ripple (<10 mV P-P) and bandwidth (100 kHz) specifications with an op amp integrator. This scheme would involve counting the time duration of the multiplexer output and using D-to-A conversion to generate a dc level from the counter output.

Phase control loops

Referring to Fig. 1, the phase control loop behaves in the following manner. The innermost phase control loop has a 50-kHz bandwidth and maintains a constant phase across the amplifier chain regardless of amplifier output power or other system fluctuations.

The outer phase loop is used to maintain the rf input to the accelerator at the proper phase for particle acceleration. A phase detector (ϕ/D) is used to compare the phase from an rf monitor loop in the tank, with the phase of a phase reference line. This dc output of the phase detector is sent to each PA driving that particular tank. This output signal is subtracted from a Facility Control System (FCS) computer-generated set point to produce an error

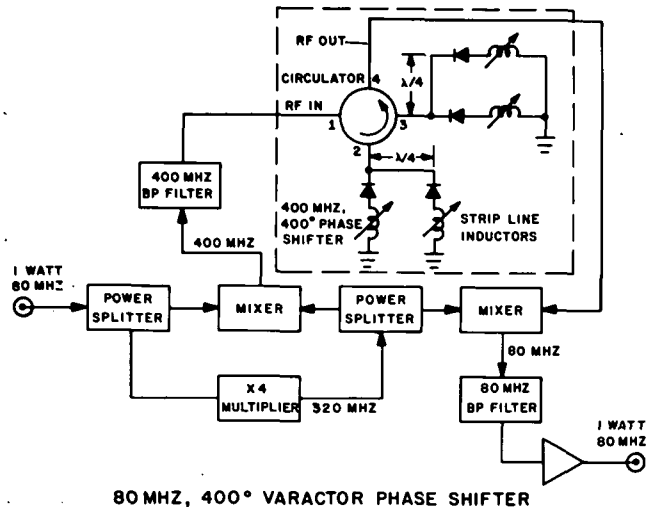


Fig. 2. An 80-MHz, 400° varactor phase shifter.

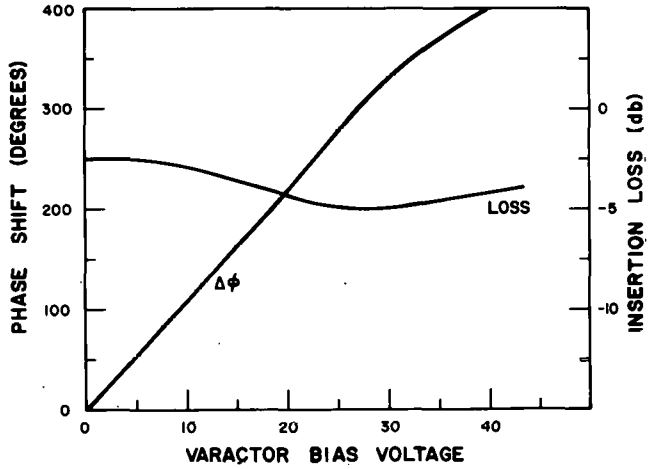


Fig. 3. Measured phase shifter characteristics.

signal. Proportional, integral, and derivative (PID) compensation is used in a controller to transform the error signal into the proper voltage to drive the varactors in the phase shifters (ϕ), thereby forcing the error signal to zero. Analog computer simulation of the phase and amplitude control system is being done to determine the proper amount of compensation required for fast, stable, feedback loops. The bandwidth of this outer loop is about 10 kHz and it is determined primarily by the linac tank characteristics.

Amplitude Control System

The amplitude control system must maintain the accelerating field in each linac tank to within a ±1% tolerance. Two levels of control are required to do this. First, the overall gain of each rf chain must be maintained at a

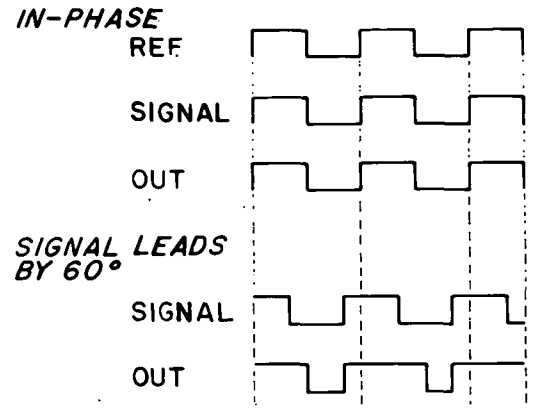


Fig. 4. Desired phase detector outputs before integration.

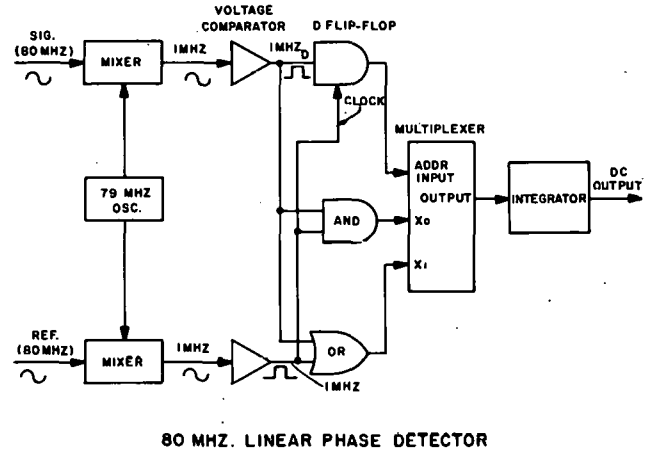


Fig. 5. An 80-MHz linear phase detector.

constant value regardless of the operating conditions (e.g., power output) of that chain. This is accomplished with an automatic gain-control feedback loop around each PA. Secondly, the power output of each PA must be adjusted to produce the required tank fields. Because each PA is a linear Class B amplifier, the output is strictly a function of the input drive level. An amplitude control system that monitors the field in the tank will control the output level of each PA.

Referring to Fig. 1, the amplifier preceding the diode switch is a leveling amplifier that provides one watt at 80 MHz under all operating conditions. This amplifier is necessary because the insertion loss of each phase shifter is not constant. With this arrangement, the rf signal into the diode switch has a constant amplitude and a variable phase. The diode switch is "open" except when the rf enable signal is applied. The output from the diode switch is passed through the voltage variable attenuators (AT), which are the control elements for the

amplitude and gain control circuits; the output signal from the last attenuator drives the constant-gain solid-state amplifier. The output from this amplifier (1 to 100 watts) drives the high-power rf system.

Because FMIT has up to seven amplifier chains per linac tank, each amplifier chain must have the same gain. This gain also should be independent of output power level. To accomplish this for each PA, the forward power from the PA is measured and is compared with a power sample taken from a directional coupler (DC) between the two attenuators. The ratio of the former to the latter is the gain of the system between those two points. This value for the actual gain is compared with an FCS computer-generated gain set point. If the actual gain is not equal to the desired gain, an error signal is produced that is acted upon by the PID gain controller. The controller adjusts the attenuator nearest the PA to drive the error signal to zero, thereby producing the desired overall gain through the power amplifier system. This automatic gain control system is being designed for a 50-kHz bandwidth.

To control the field level in the accelerator, a monitor loop in the tank samples the rf field. This rf signal (tank amplitude feedback) is detected to produce a dc level proportional to the tank field amplitude. This dc level is compared with an FCS generated tank amplitude set point that corresponds to the desired field amplitude (Fig. 1). The difference between the tank amplitude set point and the feedback signal is the error. This error signal is sent to the PID amplitude controller of each PA driving that tank. The controller will change the attenuator setting of each amplifier chain such that the error signal goes to zero. At this time, each PA will be providing the required amount of power to the linac. This amplitude control loop will have a 10-kHz bandwidth.

High-Power Amplifier

Amplification from 100 W to 600 kW will be accomplished by several stages of vacuum tube amplifiers. A preliminary design study[5] has been done to determine the configuration for the high-power system.

The tube line-up is shown in Fig. 6. The final amplifier will be the EIMAC 8973 (formerly X2170) power tetrode. Preliminary design has been done for a 600-kW cw system at 80 MHz. The system will have a 3-dB bandwidth of 200 kHz. Linearity should be better than 0.37%.



Fig. 6. Power amplifier tube line-up.

Prototype

A prototype FMIT accelerator capable of producing 5-MeV H_2^+ particles is under development now at LASL. This accelerator will require four rf amplifier chains to supply the necessary energy for beam acceleration.

The rf system for the FMIT accelerator at Hanford must be designed for 85% availability. To achieve this, each accelerator tank will use one more than the minimum number of power amplifiers necessary to drive it. This means that if one amplifier chain fails, the output of the remaining amplifiers can be increased to compensate for the loss without having to shut down the accelerator.

Acknowledgement

The authors gratefully acknowledge the technical support of R. D. Patton and S. L. Davies.

References

1. R. A. Jameson, "High-Intensity Deuteron Linear Accelerator (FMIT)," IEEE Trans. Nucl. Sci. NS-26, No. 3, 2986 (June 1979).
2. J. M. Potter, S. W. Williams, F. J. Humphry, and G. W. Rodenz, "Radio-Frequency Quadrupole Accelerating Structure Research at Los Alamos," IEEE Trans. Nucl. Sci. NS-26, No. 3., 3745 (June 1979).
3. E. L. Kemp, D. J. Liska and M. D. Machalak, "The Fusion Materials Irradiation Test (FMIT) Accelerator," proceedings this conference.
4. W. J. Hoffert, Los Alamos Scientific Laboratory consultant, private communication (1979).
5. "Design Study, 80-MHz, 600-kW Rf Amplifier," Continental Electronics Manufacturing Company, Dallas, Texas (July 1979).

CONDITIONING EXPERIMENTS ON THE 100% DUTY FACTOR 3 MeV ALVAREZ LINAC

B.G. Chidley, J. Ungrin and J.C. Brown
Atomic Energy of Canada Limited, Research Company
Physics Division, Chalk River Nuclear Laboratories
Chalk River, Ontario, Canada K0J 1J0

Summary

A number of difficulties have developed in the course of rf conditioning the 3-MeV Alvarez linac of the Chalk River Nuclear Laboratories High Current Test Facility. The tank had been designed with the drift tube stems avoiding contact with the tank wall except via external vacuum bellows. This technique had been investigated in a prototype and although it gave satisfactory rf performance, overheating of the bellows limited operation to 25% of operating power. An internal rf shield has been developed which has allowed tank excitation up to the design field level.

Introduction

The 3-MeV Alvarez linac of the Chalk River Nuclear Laboratories High Current Test Facility is a 1.605 m long, 25 cell structure, designed to operate at 100% duty factor. The linac is part of an ongoing CRNL program for the development of high current accelerators which could be used for electro-nuclear breeding of fissile fuel.[1]

A number of problems have arisen related to the high average power dissipated in the linac tank walls. The most serious one has been rf heating of bellows on the drift tube stems of the linac. An improved stem-to-tank joint has been developed to solve this problem.

Description of Linac Tank

The linac tank is a 1.605 m long, by 0.711 m diameter, 25 cell structure, designed to operate at 268.3 MHz with an input energy of 750 keV. The design gradient is 2.0 MV/m. The calculated rf drive required is 112 kW with a Q ∿ 56,000. A detailed description of the tank has been presented at a previous conference.[2]

The tank design was based partly on experience gained on a 3-cell test model that was operated successfully up to 50 kW at 100% duty factor. One problem area on the 3-cell tank was the drift tube stem to tank wall joint. Originally copper skirts were welded from the stem to the tank. These skirts, however, were partially destroyed at ∿ 30 kW and the design shown in Fig. 1 was finally used. With fan cooling on the bellows, this design was able to operate up to 50 kW.

Computer calculations indicate that currents along the drift tube stems are not necessary for normal tank excitation and that wall currents can flow around the hole. Low power field measurements on a test tank showed no difference whether the stems were grounded to the tank or insulated from it.

The stem-to-tank joint first tried on the present tank is shown in Fig. 2. Because of the possible need to replace drift tubes, the vacuum seal to the tank was changed to an O-ring seal from the weld used in the test tank. One other significant feature is the size of the drift tube holes, which are 36-mm diameter in the present case as opposed to 76-mm in the test tank.

Low Power Tank Characteristics

Measurements on the tank with a network analyzer gave a Q ∿ 42,300, which is ∿ 75% of the calculated value for pure copper. The required rf power to produce the 2.0 MV/m accelerating field for this Q is ∿ 148 kW.

Multipactor levels in the cavity were encountered at tank power levels of 150 and 400 Watts and prevented direct cw turn-on of the rf power. A pulse technique developed for a cyclotron resonating cavity at CRNL[3] has been successful in breaking through the multipactor levels. In this technique rf pulses with a turn-on time much shorter than the tank fill-time and greater than 5 kW in amplitude are fed to the tank. The power level in the tank is monitored and if after a time of 200 μs a level greater than 1 kW is reached, the rf is kept on. If the pulse fails to puncture through the multipactor levels, the rf is turned off for ∿ 100 ms before the power is reapplied. It seems to be necessary to turn the rf level completely to zero for a comparatively long period between pulses to ensure that all stray ions from the previous discharge have been neutralized. It was found accidently that puncture through the multipactor levels often will occur only if the vacuum ion pump has been switched off. A sufficient number of ions can be scattered into the linac tank from the pump to trigger the multipactor process. After exposure to atmosphere, cw operation is normally possible at levels up to 20 kW within 30 minutes.

High rf Power Operation

Heating problems on the drift tube stem bellows were encountered at ∿ 15% of the required tank power level. At ∿ 25 kW the bellows, which could not be easily cooled because of water cooling connections and current leads to the drift tube quadrupoles, reached temperatures up to 100°C. The temperature distribution on the bellows suggested that wall currents were in fact flowing through the bellows in spite of the fact that this was a much higher resistance path than the detour around the stem hole. Therefore rf fields must exist in the bellows. The effects are as though wall currents are being driven by a "constant current" driver.

Bench tests on a spare drift tube bellows indicated that a current of ∿ 50 A was necessary to produce the observed bellows heating. This is about a factor of two higher than the current estimated to be intercepted by the stem hole on simple average power considerations. Calculations by Lee-Whiting[4] on rf cavities, however, indicate that any protrusion into a cylindrical cavity is likely to increase the current density on the protrusion and will increase local heating.

An initial attempt was made to reduce the bellows heating by using finger stock in the gap between the drift tube stem and the tank copper layer. This proved to be unsuccessful. The finger stock disintegrated completely at 30 kW. Tight fitting Cu-Be coil springs were tried next but resulted in a similar failure to produce the required shunting of the rf currents. In both cases the failure appeared to have occurred because the low total mass of the materials, which had small thermal contact areas, was unable to dissipate the heat produced by the current flowing into the stems through ohmic contacts to the tank.

A copper shorting collar design was tried next. This collar, which was more massive than the springs or finger stock, could be clamped onto the drift tubes and could be cooled by them. Indium wire was used to provide electrical contact to the tank surface and the stem. This design was successful up to 60 kW of rf power into the tank, but at higher powers melting of the indium occurred.

The final design developed is shown in cross-section in Fig. 3. Figure 4 shows the collar, which is made in two parts to allow installation in situ over the drift tube stem. The two halves are held together by screws and two set screws are used to fasten the collar tightly to the stem to prevent vertical motion because of thermal expansion. The cut in the collars was oriented along the tank axis so as not to interfere with the current flow. Finger stock with very short projections was brazed both on the inside and outside collar surfaces to provide good heat transfer and electrical contact. Figures 5 and 6 show photographs of the collars mounted in the linac tank.

With this collar design the required tank rf power level of 148 kW has been attained. The long term performance of the collars at this power level has not yet been determined because of a failure of the teflon window in the rf drive line to the tank. This failure, which occurred because of a blockage in the air-cooling circuit, resulted in a large amount of window material being deposited on the drift tube and on the tank walls and has required a complete cleaning of the tank.

On inspection of the collars during clean-up two drift tube collars showed slight burn marks on the finger stock and are being replaced. No problems, however, were seen in the operation of the tank at full design fields because of local rf heating.

References

1. P.R. Tunnicliffe, B.G. Chidley and J.S. Fraser, "High Current Proton Linear Accelerators and Nuclear Power", Proc. 1976 Proton Linear Accelerator Conf., Chalk River Nuclear Laboratories, Atomic Energy of Canada Limited, Report AECL-5677, 36 (1976).

2. B.G. Chidley, S.B. Hodge, J.C. Brown, J.H. Ormrod and J. Ungrin, "The Chalk River High Current Test Facility", Proc. 1972 Proton Linear Accelerator Conf., Los Alamos Scientific Laboratory, LASL-5115, 218 (1972).

3. C.B. Bigham, private communication.

4. G.E. Lee-Whiting, private communication.

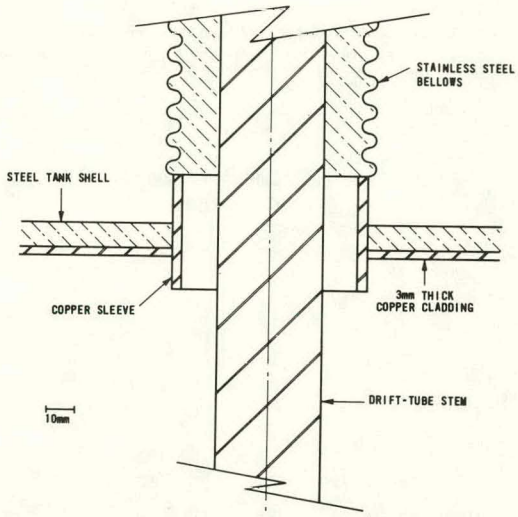


Fig. 1 Cross-sectional view of drift tube stem and bellows on test tank.

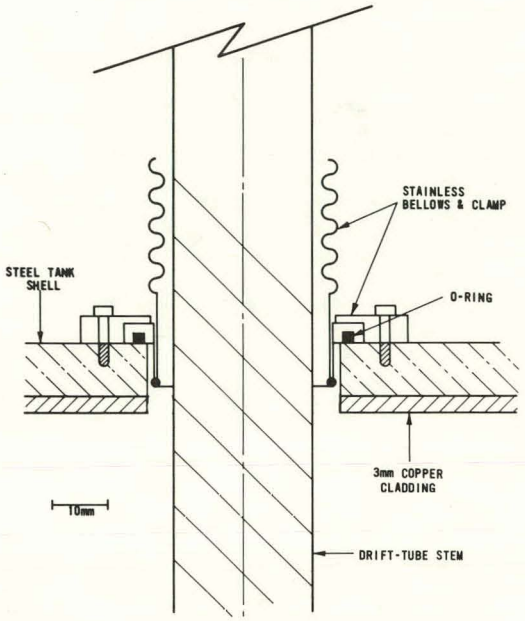


Fig. 2 Cross-sectional view of initial design of drift tube stem and bellows assembly for 3-MeV tank.

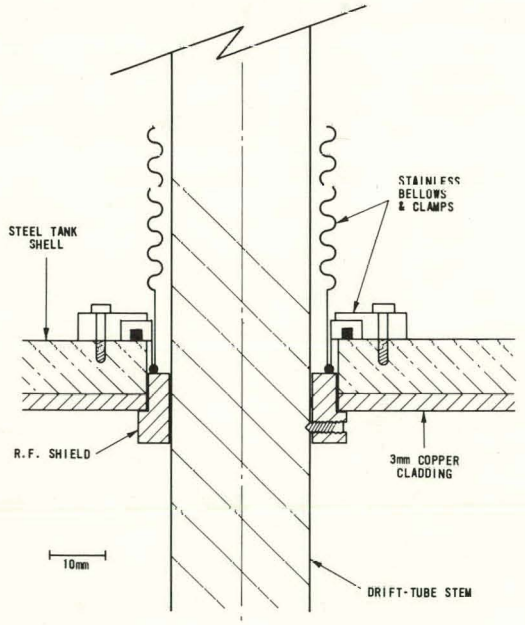


Fig. 3 Cross-sectional view of final design of drift tube stem and bellows assembly for 3-MeV tank.



Fig. 4 Bellows rf shield.

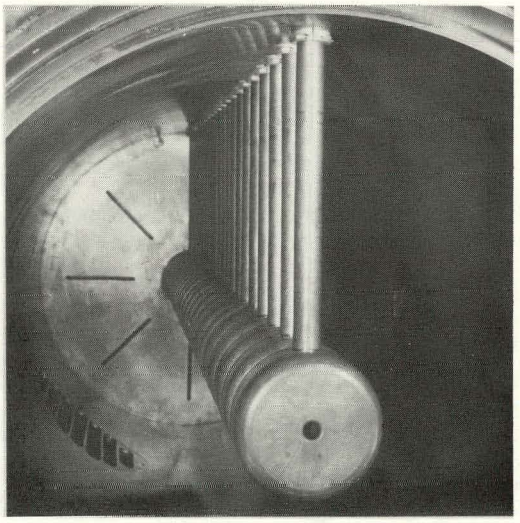


Fig. 5 Collars installed on drift tube stem.

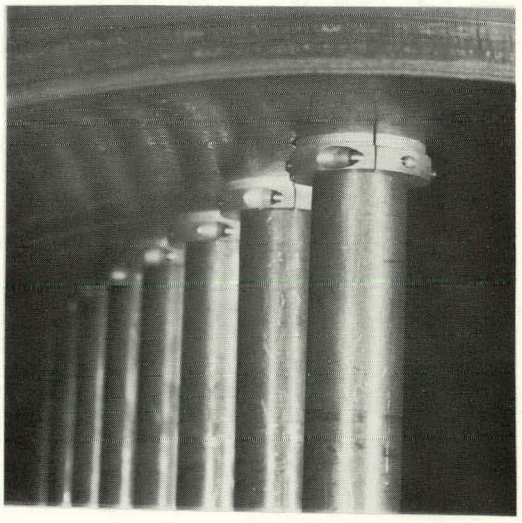


Fig. 6 Close-up view of installed collars.

Discussion

Böhne, GSI: How do you align those drift tubes with the very tight fit of this conical collar?

Ungrin: We did the alignment as carefully and as closely as we could, prior to putting the collars on. We clamped them very tightly up above. In some cases, as we put the collars in, we did get a very slight motion. It turns out that our drift tube has enough "give" that we just mechanically pushed it into place afterwards and it holds.

Boltezar, CERN: Why didn't you use aluminum joints as rf contacts between the drift tube stem and the tank wall?

Ungrin: On the drift-tube stem to the tank? We didn't envisage this problem as existing from the experiments that we did on the short tank. We thought that the problem wasn't going to come about, but were very much surprised at about 15 to 20 kilowatts. If we were doing it again, I think we would use something that would be able to take more heat than the rubber o-rings. Whether it would be aluminum or not, I don't know.

200 MHz FAST PHASE SHIFTERS and PHASE DETECTION for a RAMPING ENERGY

JP. Auclair, PA. Chamouard, JL. Lemaire,
Laboratoire National Saturne
C.E.N. Saclay, France.

Summary

Injection using a ramped energy is required at Saturne. The mean energy is linearly increased during the 400 μs of injection by means of two rf cavities (ramping cavity and debuncher). The phase of each cavity is shifted relative to the linac phase. A set of fast phase shifters using strip-line techniques have been developed, which are presently in operation.

Introduction

The multiturn injection at Saturne is performed by a linear increase of the mean energy of the beam, to follow the linear increase of the electromagnetic field ($\dot{B}$ = 4.2 T/s) in the main ring. This is obtained by means of a ramping cavity, which is located just at the end of the linac. As a consequence, the phase of the debuncher must be shifted to deal with the variation of the mean energy. The phase-shifting of these two cavities is achieved using two ferrite phase shifters, which operate between the rf linac feeder and each cavity (Fig. 1).

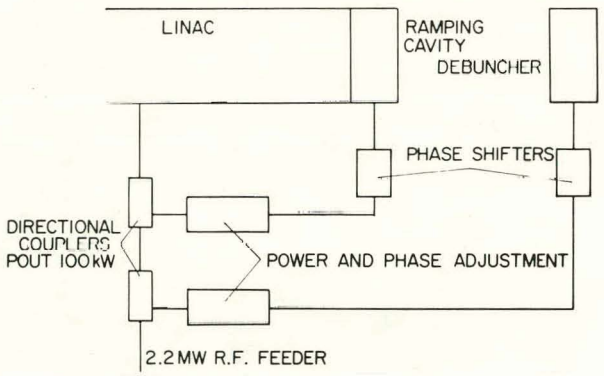


Fig. 1 Block diagram of rf power system

Description of a Phase Shifter

The phase shifter consists of an rf transmission line whose dielectric material is an rf ferrite having a dielectric constant $\varepsilon=\varepsilon'-j\varepsilon''$ and magnetic permeability $\mu=\mu'-j\mu''$. The propagation vector is then given by

$$\gamma = j \cdot \frac{2\pi \ell}{\lambda} \sqrt{\varepsilon\mu} \quad ,$$

where ℓ is the length of the transmission line and λ is the wave length.

When a magnetic field is applied to the ferrite, the phase shift decreases due to the variation of the magnetic permeability, reaching a minimum value when the ferrite is saturated.

The transmission line is strip-line, in which the inner conductor has a notched shape. The line operates like a delay line to avoid prohibitive length of the device and to limit losses in the dielectric material. The driving magnetic field is provided by 19 coiled ferrite toroids of rectangular cross-section. Additional permanent magnets are placed on each side of the strip-line (Fig. 2) and are used,

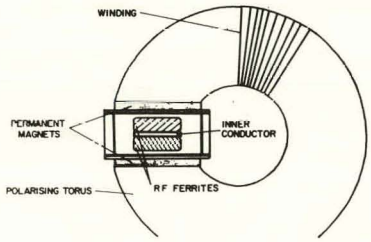


Fig. 2 Cross section of the phase-shifter

along with a steady current in the coils, to minimize the attenuation when no driving current is applied. The strip-line is 1-m long, 6-cm wide and 2-cm thick.[1] The overall load connected to the current generator is: L = 1.7 mH, R = .3Ω, and the permanent magnets give a 330 Oe magnetic field.

The line is made of printed circuit materials in order to reduce eddy-currents. As the transmitted power may reach 100 kW, the whole apparatus is housed inside a pressurized tank filled with SF_6 at a pressure of 2 bars, to avoid sparking.

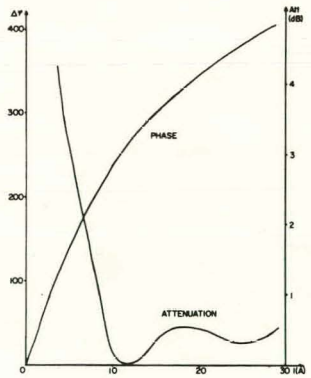


Fig. 3 Static response

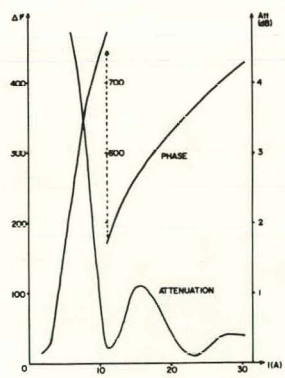


Fig. 4 Static response

Figures 3 and 4 show power attenuation and phase shift versus a dc applied current for two different types of rf ferrite. Figure 5 shows the driving current and phase shapes versus the duration of an applied rectangular voltage.[2]

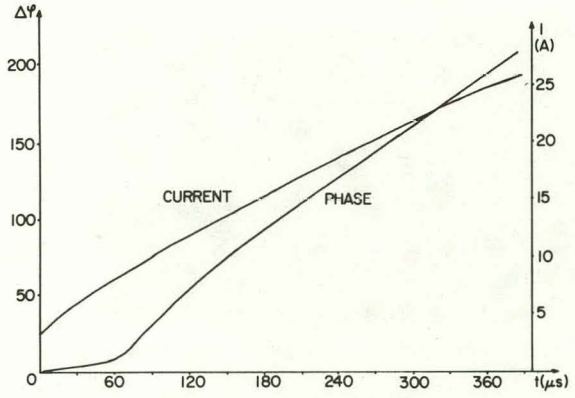


Fig. 5 Dynamic response vs duration of the excitation

Calculation of the Phase Laws

Theoretical considerations

a) Ramping cavity

Let W be the mean kinetic energy of an ion having a charge-to-mass ratio $\varepsilon = z/A$. The duration of injection is then $T_{inj} = \frac{X}{Rg} \frac{(B\rho)}{\dot{\rho B}}$.

X is the useful aperture in the main ring and g the local chromatic function.

Since the rigidity $(B\rho)$ is the same for all particles, one has for the kinetic energy ramp:

$$\dot{W} = \frac{e^2}{m_o} A \varepsilon^2 B \rho^2 \dot{B}$$

Therefore, the maximum variation given by the ramping cavity has to be:

$$\Delta W = \frac{e^2}{m_o} \frac{A \varepsilon^2}{Rg} (B\rho)^2 X$$

Because the energy ramp must be as linear as possible, the phase shift of the ramping cavity must be from -45^o to $+45^o$.

b) Debuncher

The shifting rate is going to be larger for the debuncher due to the time-of-flight between the two cavities.[3] Let D be the distance, then:

$$\Delta\phi = -\frac{2\pi D}{\lambda} \left(\frac{m_o c}{e}\right) \frac{X}{Rg} \frac{1}{\varepsilon (B\rho)}$$

$$\dot{\phi} = -\frac{2\pi D}{\lambda} \frac{m_o c}{e} \frac{1}{\varepsilon} \frac{\dot{\rho B}}{(B\rho)^2}$$

c) Numerical Results

The main parameters are the following :
$\dot{B}$ = 4.2 T/s Rg = 6.5 ρ = 6.34 m D = 8.4 m

The results are given in Table I:

Table I

	p (20 MeV)	ions (5MeV/A)	$\vec{\rho}$
T_{inj} (μs)	400	400	200
$\dot{W}_{rc}$ (keV/μs)	1.65	0.825	0.825
$\dot{\Phi}_{rc}$ (°/μs)	0.22	0.22	0.22
$\Delta\phi_d$ (°)	166	332	332
$\dot{\phi}_d$ (°/μs)	0.42	0.84	1.68

Driving Generators

To get good working conditions, the attenuations of the phase shifters must be smaller than 2 db and 0.8 db during the phase shifting time. Therefore, the biasing current is greater than 7 A or 9 A, respectively (see Figs. 3 and 4). A dc power supply provides the bias current needed to operate the transmission line at close to 1 db attenuation and a pulsed generator, which is schematically represented in Fig. 6, provides a rectangular voltage shape delivering a sawtooth-like current. The tune is then easily obtained by properly adjusting the level of the voltage.

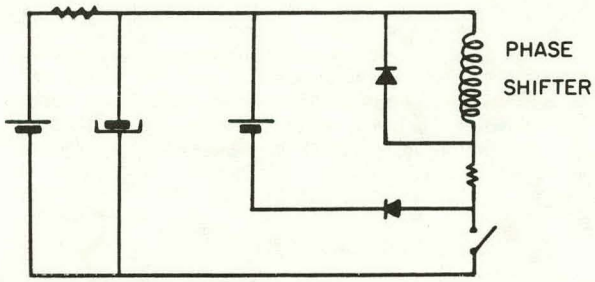


Fig. 6 Schematic of the ramping cavity driving generator

As far as the debuncher phase shifter is concerned, the problem is a bit more complicated because of the larger spread of the phase variation. Non-linear regions occur requiring an additional inductance in series with the transmission line. Consequently the linearity of the current sawtooth can be adjusted by shortcircuiting this inductance at a given time in the pulse (Figs. 7 and 8).

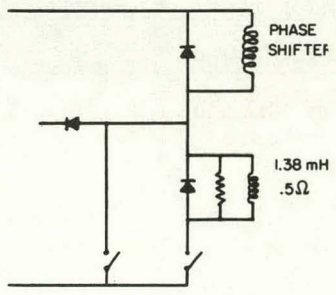


Fig. 7 Schematic of the debuncher driving generator

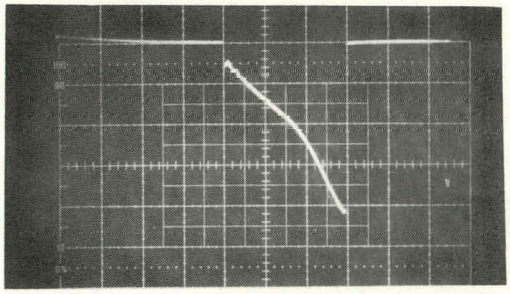


Fig. 8 Driving current shape using the additional inductance

100 μs/cm 20 A/cm

Phase Detection

The phase shifting is measured with a phase comparator. This device detects both sine and cosine of any phase between two rf inputs. Let X and Y be the output voltages, then $X = A \sin \phi$ and $Y = B \cos \phi$. The two coefficients are amplitude dependant on the input signals. Fortunately, they show a good linearity if the amplitude of the input voltages varies within a range of 5 db. The phase shifting is then given by: $\phi = \text{Arctg } c \frac{X}{Y}$, with $c = \frac{B}{A}$, obtained by calibration of the phase comparator.

The dynamic phase shifting can be observed on both computer display and X-Y scope display. The former is done using a JCAM 10 microprocessor, which gives the phase shifting versus time (30 measurements spaced by 15 μs) while the later directly shows ϕ using polar coordinates.[4]

The dotted line is obtained by chopping the electron beam. This method gives an idea of the linearity of the phase shifting (Figs. 9 and 10).

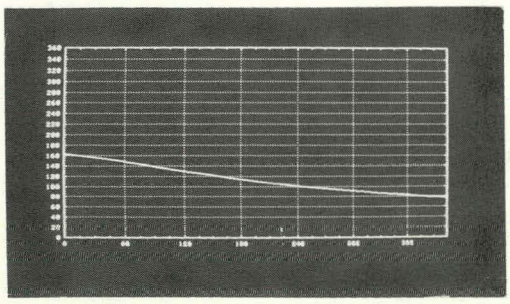


Fig. 9 Computer display of the phase shifting

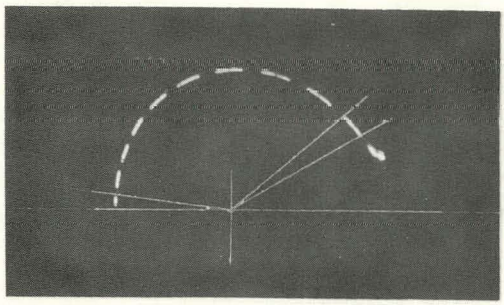


Fig. 10 X-Y scope display of the phase shifting

Conclusion

The 200-MHz phase shifters have been used for 7 years at Saturne 1 with operating $\dot{\phi}$ values from 0.15°/μs to 0.5°/μs, using n° 6311 ferrites. Due to the $\dot{B}$ increasing from 1.8 T/s to 4.2 T/s, the Saturne 2 injection method required $\dot{\phi}$ be raised to 0.84°/μs, which exceeds the range of the old phase shifters. So new devices were developed using a new type of ferrite (n° 6912) from L.T.T. Company. These are able to reach a $\dot{\phi}$-value up to 1.1°/μs. This is good enough even for heavy ion acceleration but is still under the required performances as far as polarized protons are concerned (1.68°/μs). For this use it was decided to run two-phase shifters in series, which are presently under construction.

Acknowledgments

The authors would like to thank JM. Lagniel who contributed to the first measurements of dynamic phase shifting.

References

1 - Etude et réalisation de déphaseurs à ferrite, LTT Report

2 - Mesures sur le déphaseur à ferrite, JP. Crenn, Internal Report

3 - Caractéristiques de l'injecteur pour diverses particules, PA. Chamouard, Internal Report

4 - Mesure de phase dynamique, JP. Auclair, PA. Chamouard, Internal Report.

1979 LINEAR ACCELERATOR CONFERENCE

HIGH POWER ISOLATOR FOR THE KEK PROTON LINAC

S. Anami, H. Baba, Y. Mori, J. Tanaka, S. Fukumoto, T. Takenaka, C. Kubota, K. Ito and T. Sakaue
KEK, Tsukuba, Japan

K. Shinohara
Nihonkoshuha Co., Yokohama, Japan

Summary

A high power 200-MHz isolator was developed at the KEK proton linac in order to reduce coupling interaction between the linac tank and the amplifier and to ease the operational tuning of the linac. The isolator consists of a ferrite-loaded circulator with three coaxial ports and a high power rf dummy load. The operational rf peak power is more than 2 MW and the VSWR, the isolation and the insertion loss are 1.2:1, 20 dB and 0.5 dB, respectively. The operational performance of the linac using the isolator is also described.

Introduction

As pulsed rf power is fed into a high-Q accelerator cavity, some rf power is always reflected back towards the generator during the transient phase while the rf field is building up in the tank. Also, when accelerating a high intensity beam, a considerable reflection occurs due to the resistive and reactive loading effect of the beam on the cavity matching and tuning. In order to compensate for beam loading effects, the cavity is usually detuned and over-coupled, which then results in further reflection after the buildup time until the beam is injected.

Such reflected power is returned to the generator where it is dissipated, but because the generator voltage-current relation is disturbed, the output power is reduced, as may be seen in the Rieke diagram. Not only is the output power reduced, but the wave shape is also distorted.

At the KEK proton linac, the single accelerator tank is excited by two rf amplifiers (TH516-I,II) which affect each other, since they are closely coupled through the tank. For example, if the output power from the first amplifier is changed, the reflected power to the second amplifier is also changed, and just as though its own load impedance had changed, the second amplifier accordingly also changes its output power. Therefore, operating adjustments become complicated since this kind of phenomenon frequently occurs and straightforward non-interactive adjustment is impossible.

For a long time, a means was sought that would isolate the amplifiers from the load. Figure 1 shows the amplifier (TH516-II) and tank rf field before the introduction of such an isolator. Due to the influence of the reflected power, the rising edge of the output power is rounded, lengthening the buildup time for the tank field.

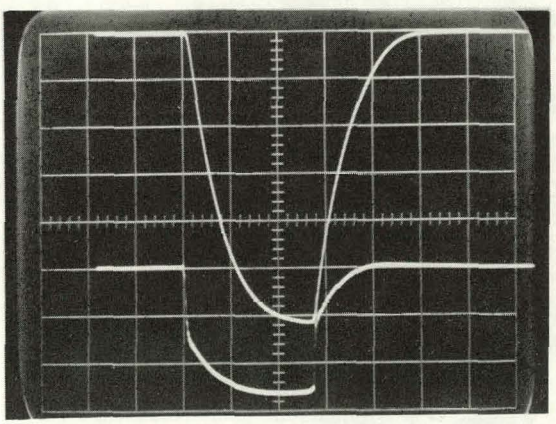


Fig. 1 Upper: rf level in the tank
Lower: TH516-II rf output power
Horizontal: 100 μsec/div

Isolator Structure and Characteristics

The design parameters for the isolator are shown in Table I. Basically, it is a Y-junction type circulator (see Fig. 2,3); the inner conductor is sandwiched top and bottom by five ferrite disks and a permanent magnet for the external magnetic field. The coaxial ports are of 203 mm diameter. A tube for cooling water is soldered around the circumference of the inner conductor and both ends of the tube are brought out at the $\lambda/4$ position, where they are electrically shorted.

In order to raise the breakdown voltage, the entire assembly is immersed in oil. In the original design, the inside was filled with SF_6 for better high voltage performance. However, after about one month of operation, discharges occurred at the circumference of the ferrite disks breaking them. After that the design was changed to oil immersion. This necessitated the insertion of compensating rings on each of the inner conductors of the three coaxial ports to allow matching. It was feared that the insertion loss would become larger because the oil used was not a special type for high frequency use, but tests at low power levels could detect no increase in loss.

Table I

Summary of isolator specifications

Frequency	201 MHz
Power rating (peak)	2 MW
(average)	10 kW
Isolation	20 dB
Insertion loss	0.5 dB
VSWR	1.2:1
Insulation	oil immersion
Cooling	water
Connector	WX-203D

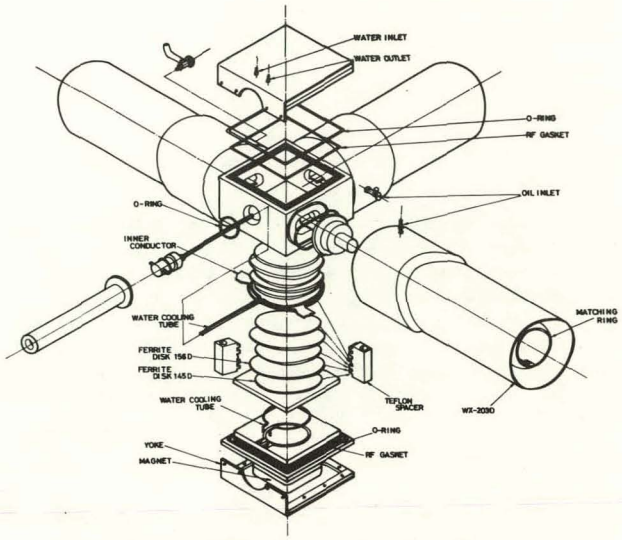


Fig.2 Circulator assembly drawing

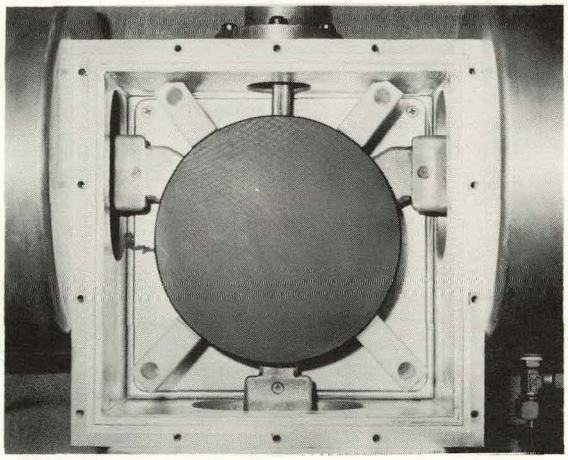


Fig.3 Circulator inside view

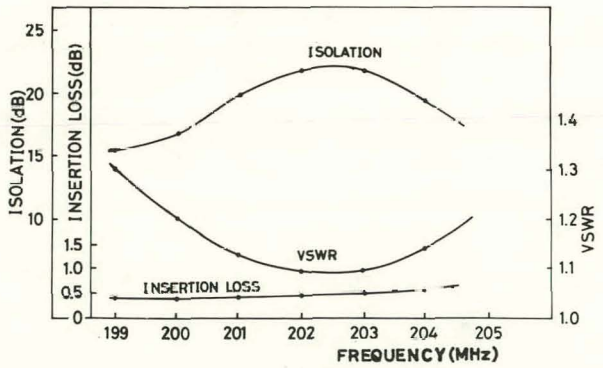


Fig.4 Isolator characteristics

The results of measurements are shown in Fig. 4. At 201 MHz, a VSWR of 1.2:1, insertion loss of 0.5 dB and isolation of 20 dB were obtained. These values measured, with oil immersion, were degraded from the 1.1:1 VSWR, < 0.5 dB insertion loss and > 25 dB isolation obtained with SF_6.

High Power Test

High power measurements were performed with the setup shown in Fig. 5. Since a testbench was still under construction, the measurements were made on the actual proton linac. Since this had to be done during the brief periods when the accelerator was shut down, there was no time to make corrections or to calibrate the rf monitor system.

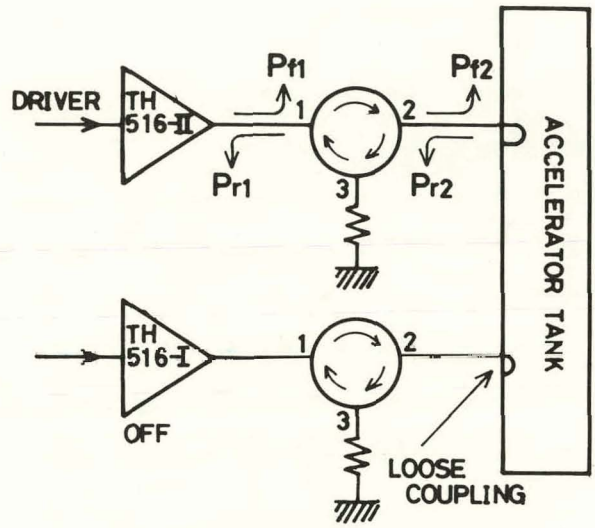
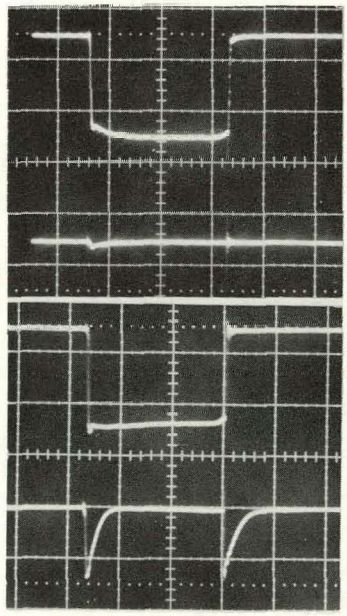


Fig. 5 High power test setup

In Fig. 5, Pf1/Pr1 and Pf2/Pr2 stand for the forward and reflected power of the respective circulator ports. The reflections at each port and from the dummy load also enter into it, but Pf2/Pf1 is related to the insertion loss and Pr1/Pr2 is related to the isolation. During the measurements, Pf1 was approximately 1 MW; the other amplifier (TH516-I) had only the heater on and its tank coupling was made as loose as possible.



Power amplifier output

← Pf1:forward power

← Pr1:reflected power

Isolator output

← Pf2:forward power

← Pr2:reflected power

Fig.6 Forward and reflected power wave forms

Figure 6 shows the Pf1/Pr1 and Pf2/Pr2 wave shapes. Without correction, their respective scalings may be in error by as much as 10%. Since only relative measurements were made, insertion loss could not be calculated. However, from the circulator surface temperature rise of about 1°C, with an average power of 6 kW, it is clear that insertion loss will not be a problem in normal operation. Also, it is thought that the isolation should be the same as in the low level tests.

Operational Performance

The most important result of installing the isolators between the amplifiers and the tank (see Fig. 7), is that it is easy to tune and adjust each component. Even when using dual feed, each amplifier can be tuned to optimum performance by simply tuning to increase the output power to its maximum value. Likewise for the tuning of the load side. Because the output power of each amplifier is stable and the wave shape is square, no matter what the load condition is, the various tuning adjustments are no longer interactive and each one has a clear and independent effect. For example, before using the isolators, the rf frequency of minimum reflected power did not coincide with the frequency of maximum rf level in the tank. With the isolator, the frequency of minimum reflected power and the frequency of maximum tank rf level are the same.

The only case in which interaction is still observed is when adjusting the tank coupling. Because of the dual feed, it is necessary to bring the output power of each amplifier to an appropriate level, otherwise the reflected power into each amplifier will be different and this will affect the coupling.

The result of this improvement is seen in Fig. 8, which shows the detected waveforms after tuning. Since the forward power from each amplifier is almost square, the tank rf level buildup time is shortened considerably compared with Fig. 1. Furthermore, improved amplifier tuning increased the maximum power out of each amplifier by about 20%.

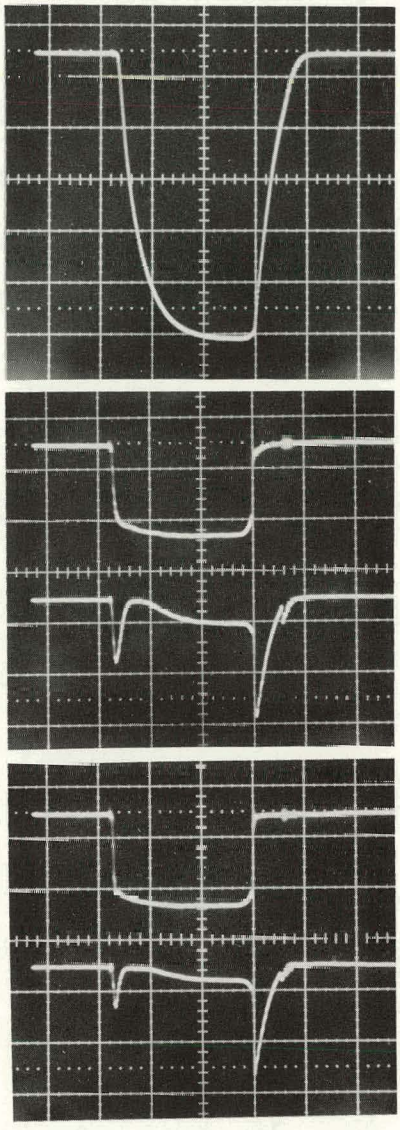


Fig. 8 Waveforms using isolators

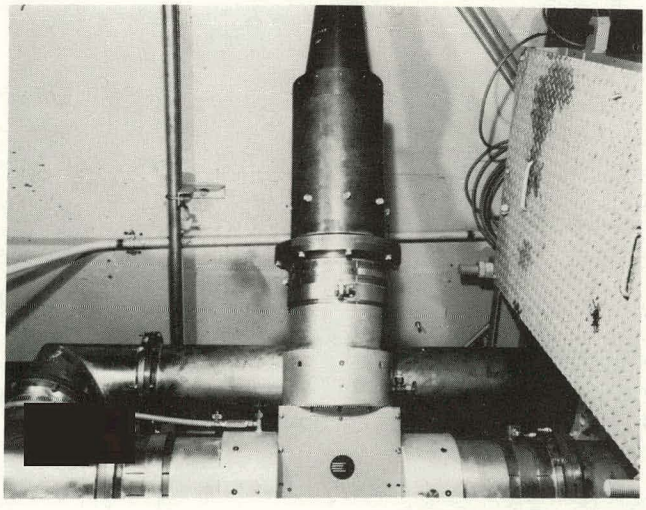


Fig.7 Isolator installation

THIS PAGE

WAS INTENTIONALLY

LEFT BLANK

Section VII
Mechanical Technology

THIS PAGE

WAS INTENTIONALLY

LEFT BLANK

THE DRIFT TUBE AND BEAM LINE QUADRUPOLE PERMANENT MAGNETS FOR THE NEN PROTON LINAC

R. F. Holsinger
New England Nuclear Corp.
N. Billerica, Mass. 01862

Summary

One hundred and nine permanent magnet quadrupoles of the new "Halbach type" will be installed in the drift tubes of the 45-MeV NEN proton linac. This new design concept utilizes, in a unique way, the anisotropy and other magnetic properties of oriented samarium-cobalt magnets to achieve high pole-tip fields and efficient use of the material. All of the drift tube quadrupoles have been designed, and the first group of 35 have been fabricated and measured. Prototype design work and computer modeling studies of similar large aperture permanent magnet quadrupoles, for the high energy beam transport system of the NEN linac, have been completed. These beam line quadrupoles will incorporate mechanisms by which their focusing strength may be adjusted.

Design Principles

Previous designs

The author and others[1,2] have been developing, for the past several years, permanent magnet quadrupoles for replacing electromagnets in applications such as the drift tubes in proton linacs. These previous designs were primarily based on replacing the coils in an electromagnet quadrupole with four suitably oriented pieces of samarium cobalt. The magnet on the right of Fig. 1 is a New England Nuclear prototype of such a "coil replacement" quadrupole. This square yoke quadrupole has an aperture radius of 1.3 cm and a pole-tip field of approximately 3.0 kilo-Gauss. These previous types of permanent magnet quadrupoles are limited to about 6 kilo-Gauss pole-tip fields using the best commercially available Rare Earth-Cobalt (REC) materials. The NEN linac requires quadrupoles with nearly 10 kilo-Gauss pole-tip fields in the low energy end of the Alvarez tank.

In the section below a new design principle will be briefly outlined, on which principle quadrupoles may be easily designed to provide pole tip fields of above 15 kilo-Gauss. This new design also makes very efficient use of the REC materials to produce medium and high strength gradient magnets.

Segmented ring quadrupoles

Recently, several papers by K. Halbach[3,4] and the author[5] have described the complete theory and some practical results of the new design principle. Selected results of this previous work will be reviewed here. It should be noted that a key spark for this new idea came from discovering the work of W. Neugebauer[6] on the clever use of the anisotropy of REC materials to minimize leakage flux in various permanent magnet assemblies.

J. P. Blewett[7] several years ago described a permanent magnet quadrupole created inside of a 4-pole symmetrically magnetized ring. He derived the relation for the pole-tip field strength of such a quadrupole:

$$B_o = 2\,\mu_o\,H_c\,(1 - \frac{r_i}{r_o}) \quad , \qquad (1)$$

where r_i and r_o are the inside and outside radii of the ring, H_c^o is the H-coercive of the material, and it is assumed that the slope of the B-H curve is unity. With the H_c values of newer REC materials approaching 10 kilo-Oersted, such a quadrupole would lead to very strong pole-tip fields. The "missing link" in Blewett's work was provided by K. Halbach in his derivation of the required easy axis variation in anisotropic, oriented, permanent magnet material. The result is, referring to Fig. 2, that the easy axis direction in a magnetized ring must be varied as:

$$\alpha = 3\theta \qquad (2)$$

Then, when the B-H function and the anisotropy are completely described by the relations:

$$\mu_o H_c = B_r \qquad (3)$$

$$\frac{dB_{//}}{\mu_o dH_{//}} = 1,\ \mu_\perp = 1 \quad , \qquad (4)$$

where B_r is the residual induction, $\mu_{//}$ and $\mu_\perp$ are the parallel and perpendicular permeabilities relative to the easy axis, a magnet made with this "perfect" material produces an error-free quadrupole field. The strength of the pole-tip field in such a magnet is given by Eq. (1). Figure 2 is the flux plot of 1/8 of this type of quadrupole, calculated with the computer program PANDIRA.[8]

The practical solution to building a ring quadrupole with the easy axis directions prescribed by Eq. (2), is to divide the ring into a number of segments. The curved segments may be further approximated by trapezoids, and the resulting configuration for sixteen segments is shown schematically in Fig. 3. In this figure, the arrows inside of the trapezoids represent the easy axis directions, and the arrows on the dashed lines represent the directions of the quadrupole field. This sixteen-piece design has magnets with three different easy axis angles and five different easy axis orientations, counting polarity.

Number and shape of segments

The two most important theoretical parameters to consider when designing a segmented ring quadrupole are: 1) the decrease in the quadrupole strength due to the non-continuous easy axis orientation, and 2) the order and magnitude of the harmonic multipole field errors introduced by the geometrical shape effects of the pieces. For a segmented ring quadrupole with M trapezoidal pieces made of "perfect" REC material, the pole-tip field is given by:

$$B_o = 2\mu_o H_c \cos^2\frac{\pi}{M}\,\frac{\sin\frac{2\pi}{M}}{\frac{2\pi}{M}}\,(1 - \frac{r_i}{r_o}) \qquad (5)$$

For M = 16, Eq. (5) gives the result that the pole-tip field is reduced by only 6.3% compared to the continuous easy axis orientation.

The nth-order harmonic multipole error fields which are excited in a symmetrical array of M identically shaped (not necessarily trapezoidal) and rotationally symmetric pieces are:

$$n = 2 + kM;\ k = 1, 2, 3 \quad , \qquad (6)$$

i.e., for M = 16 the first multipole error is n = 18, the 36-pole. The magnitude of the 36-pole for the specific case of 16 trapezoidal pieces with r_i/r_o = 1.1/3.0 is 6.8% of the quadrupole field at 100% aperture, or 0.2% at 80% aperture. It has been pointed out by Halbach, that this error may be eliminated by a suitable thickness shim between the trapezoidal pieces, in which case the first theoretical error would be of order 34: the 68-pole.

Efficient use of the REC material

The ring quadrupole with the continuous easy axis orientation given by Eq. (2), obviously produces the strongest possible pole-tip field, as given by Eq. (1), for a specific r_i, H_c, and volume of material. Such an arrangement makes very efficient use of the REC material. This can be understood qualitatively by examining the flux plot of 1/8 of an eight-piece segmented ring quadrupole, such as shown in Fig. 4. One can observe how the flux is guided into and concentrated in the aperture region. This is in contrast to the large amount of leakage flux lost into the sides of the poles of a conventional electromagnet quadrupole or permanent magnet quadrupole based on the "coil replacement" design principle. A way to appreciate quantitatively the efficient use of the REC material in the new design, is to note the fact that the material close to the aperture contributes a large fraction of the field strength. By comparison, quadrupoles based on the "coil replacement" design make inefficient use of the REC material placed at a significant distance from the aperture. For example, using Eq. (1) one finds that, in the new design, the material inside of the average radius $r_a = (r_i + r_o)/2$ contributes 80% of the strength when $r_i/r_o = 4$, whereas this material comprises only 35% of the volume.

NEN Drift Tube Quadrupoles

Specifications and characteristics

The specifications of the 109 drift tube quadrupoles for the NEN linac are summarized in Table I. The quadrupoles are divided into three groups, each group with a different pole-tip field, aperture radius, and length, but all magnets have the same outside diameter.

Two characteristics of these new quadrupoles have important consequences for the NEN linac design. Since no space is required for a coil or cooling, the quadrupole can fill nearly the entire length of the drift tube. This fact was used to advantage to achieve the required focusing strength, $\int B'dz = B'_o l_{eff}$, in the early drift tubes of the Alvarez tank.[8] A unique property of the ring quadrupoles, which was derived by K. Halbach using symmetry arguments, is that the effective length, l_{eff}, is equal to the physical axial length of the permanent magnet assembly. The second characteristic of this new design, that was used to advantage, is that since the required focusing power could be achieved with quadrupoles of only 7 cm outside diameter, it was possible to design the linac focusing structure with drift tubes of 9 cm outside diameter rather than the conventional 18 cm diameter. This leads to significant savings in rf power, as well as having other advantages.[9]

Computer modeling and design

The mathematical modeling of REC magnet assemblies is greatly simplified if one assumes "perfect" material and no other saturable magnetic materials are present in the problem. In this case, an REC piece with a uniform and parallel easy axis orientation can be replaced by current sheets, or charge sheets, on each surface of the piece. The fields and multipole components produced by an array of charge sheets may then be calculated analytically, since the fields superimpose linearly. Reference 4, for example, gives a derivation of this computational method. Much of the original development of the segmented ring quadrupole was done using this computational model.

For analyzing problems with "non-perfect" permanent magnet materials and other saturable materials, the program PANDIRA has been used. PANDIRA solves anisotropic 2-D field problems with or without normal saturable magnetic materials and allows for very general boundary conditions and symmetries. Figure 5 shows the flux plot of 1/8 of a group I drift tube quadrupole, calculated with PANDIRA. The shape of the individual magnet pieces is a "modified trapezoid", where the sides of the pieces have been cut parallel towards the outside. This shape was designed to reduce the width of the pieces and accommodate a retainer spline which positions the pieces.

The computer analysis with PANDIRA gives the field quality in terms of harmonic multipole errors for a specified geometry and material characteristics. To investigate the accuracy of the program for these types of calculations and to determine the effects of "non-perfect" REC materials, a series of problems was solved; Table II gives the results of those calculations. In Table II, the "perfect" material has $B_r = \mu_o H_c$ = 8 kilo-Gauss, and the "real" material has B_r = 8.7 kilo-Gauss H_c = 8.2 kilo-Oersted and $\mu_\perp$ = 1.03.

The geometry of the magnet analyzed has r_i = 1.1 cm, r_o = 3.0 cm and the pieces are trapezoids in the first three columns and modified trapezoids in the last two columns, designated by "parallel". The "parallel" geometry is that of the group I drift

tube quadrupoles. The analysis shows that PANDIRA has an accuracy of about 0.2% for high order multipoles and that the "allowed" harmonic errors due to non-"perfect" material are less than about 0.5%.

Production and measurement of the $SmCo_5$ pieces

All of the magnet pieces for the NEN linac drift tube quadrupoles have been manufactured by Hitachi Magnetics Corp., Edmore, Michigan. The material designation is Hicorex 90B, a $SmCo_5$ compound which has nominal properties of B_r = 8.7 kilo-Gauss, H_c = 8.2 kilo-Oersteds, H_{ci} > 15 kilo-Oersteds, where H_{ci} is the intrinsic coercivity, and a recoil permeability of 1.05.

The magnet pieces for the group I and group II drift tube quadrupoles were manufactured in the following steps. First, a block of the $SmCo_5$ material was magnetically aligned and pressed, and then sintered. This block, with approximate dimensions of 2 by 2 by 1/2 inches, has the easy axis angle aligned parallel to a 2-inch dimension, and the pressing direction is parallel to the 1/2-inch dimension. At present, this block is the largest piece of $SmCo_5$ being manufactured in large quantity. Modified trapezoidal shaped pieces are then cut out of this block, with the cutting directions parallel, perpendicular and at 45° to the easy axis orientation, so as to provide the three easy axis angles. Next, the pieces are finish ground to the required dimensions and then given a further heat treatment to enhance the coercivity. Finally, the pieces are magnetized in an external field of the specified polarity. The manufacture of the group III magnet pieces differs from the above procedure in that individual blocks are made for each piece in the pressing, easy axis alignment, and sintering stage. In this case, the three easy axis angles are provided by rotating the die relative to the alignment magnetic field.

The final stage of manufacture is to measure the effective magnetic dipole moment per unit volume of each piece and record this along with the serial number. To verify the manufacturer's data, this measurement is made at NEN with an apparatus, as shown in Fig. 6, consisting of a Helmholtz coil pair with a mechanism for positioning and rotating the pieces in the center of the coil pair, and an integrating voltmeter connected to the coils. A magnet piece is inserted in the positioning mechanism with its easy axes parallel to the axis of the coil system, the integrator is zeroed, and then the piece is quickly rotated by 180°. The integrated induced voltage in the coil pair is proportional to the dipole strength of the piece.

This measurement also includes the effect of misalignment of the easy axis angle, since the integrated signal is also proportional to the alignment of the dipole axis with the coil axis. It would be possible to measure the easy axis angle alignment relative to the axis of the piece with this apparatus, using a modified procedure.

The significance of this data is that it provides a measure of the variation of the "strength" of the pieces due to manufacturing variables. This information gives essentially one point (open magnetic circuit) on the B-H curve, averaged over the piece. Figure 7 shows a typical distribution of magnet piece "strength" for one particular easy axis orientation.

Assembly procedure

The critical practical aspect of building permanent magnet quadrupoles is to minimize the low order harmonic errors, especially the n = 3 sextupole error. In contrast to electromagnet quadrupoles, where it is simple to provide equal excitation of each pole, the permanent magnet material variables are difficult to control and somewhat tedious to measure. Fortunately, two characteristics of the new design make it possible to reduce the n = 3 multipole error to a very small value.

The first step in the assembly procedure, aimed at producing high precision quadrupoles, is to select well matched pieces in terms of "strength" for each magnet assembly. This will help assure the equal "excitation" of each pole. The dipole strength per unit volume data for all the approximately 1800 pieces for the group I drift tube quadrupoles is entered into a data base on a digital computer system. A program was written which examines this data base and makes the selection of the 48 pieces which are the best matched in strength for a particular magnet assembly.

The actual putting together of 48 magnetized $SmCo_5$ pieces into a nearly zero-clearance close-packed assembly presents a real challenge. The minimum clearance between the pieces themselves and the pieces and the aluminum retainer spline is achieved by determining the maximum thickness of brass shim strips to fit between the outer end of the pieces and the slots in the spline. The photograph in Fig. 8 shows the assembly fixture which is used to clamp and position the pieces during assembly.

Since each group I quadrupole assembly consists of three layers and the multipole fields from each layer superimpose almost exactly linearly, it is possible to rotate two layers by 180° with respect to one fixed layer and in this way minimize the axially integrated n = 3 error in the quadrupole. To this end, each quadrupole is measured after one layer is in place, and then again after two layers, and finally the complete assembly. From these three measurements, the phase and amplitude of the n = 3 error in each layer may be inferred. If the n = 3 error in the complete magnet assembly is larger than acceptable, one or two layers are rotated by 180° so that the superimposed sextupole fields approximately cancel each other. With this procedure, it has been possible to set the allowable limit of the n = 3 error at 0.3% of the quadrupole field at 100% aperture radius.

Harmonic multipole measurement

Usually the field quality in a multipole magnet is described in terms of the strength and phase of the harmonic multipole errors relative to the fundamental desired field distribution at the

magnet aperture. An elegant and simple mathematical description of superimposed multipole fields in two dimensions can be made using the concept of the complex potential. These ideas and formulae will be briefly reviewed here. The complex potential inside the aperture of a multipole magnet is written as

$$F(z) = \Sigma\, C_n(\frac{z}{r_i})^n = A(x,y) + iV(x,y) \quad , \quad (7)$$

where z is the complex space variable x + iy, and the distances are normalized by r_i, the aperture radius of the magnet.

The C_n's in this equation are the complex coefficients for the potential of the superimposed multipoles (n = 2 is the quadrupole component), and A and V are the real (vector) and imaginary (scalar) parts of the complex potential. It can be shown that the magnetic field is related to the complex potential through the following equation:

$$B_x - iB_y = iF'(z) = i\Sigma n \frac{C_n}{r_1} (\frac{z}{r_i})^{n-1} \quad . \quad (8)$$

The strength and phase of each multipole field component is given by the coefficient $nC_n/r_i = B_n$ in this equation.

Equipment for measuring the multipole field components in small aperture quadrupoles was designed and built at NEN. Reference 5 gives a detailed description of this equipment. Precision measurements of the multipole errors in the quadrupole are made by slowly rotating a coil coaxial with the magnet and recording the induced voltage at 128 steps in one revolution. The coil is long compared to the axial length of the magnet and, therefore, measures the axial integral of flux distribution, including the fringe fields, which is equivalent to the vector potential $A(\phi)$ in the 2-D case. This integrated signal is Fourier analyzed to yield the phase and amplitude of each harmonic multipole, i.e., the B_n's, up to n = 18, the 36-pole.

The right hand column of Table II gives the results of the harmonic multipole measurements of the group I drift tube quadrupoles. The values in this table are averages for the approximately 35 magnets that have been assembled. The "allowed" harmonic errors n = 6, 10 and 14 are primarily due to "non-perfect" material properties plus imperfect matching between magnet types, and the n = 18 is inherent in this segmented ring quadrupole design. The small remaining "non-allowed" harmonic errors are attributed to a combination of three factors: 1) mechanical tolerances, 2) errors in easy axis orientation, and 3) variation in the B-H properties from the ideal straight line, which is particularly probable in the third quadrant of the B-H curve.

Large Aperture Beam Line Quadrupoles

Design study

If the obvious advantages of permanent magnet quadrupoles can be utilized in large aperture beam line magnets, significant economies and simplifications of such systems would result. The two main problems to be solved are 1) making the quadrupole focusing strength adjustable, and 2) controlling the total cost of the quadrupole assembly to keep it comparable to that of an electromagnet, including the power supply.

Towards controlling the cost of the REC pieces, it is important to simplify the shape of the pieces and relax the tolerances to reduce the machining costs. Only a small fraction of the cost of the magnet pieces for the drift tube quadrupoles is due to raw material expense. Probably the least expensive shape to produce is one with a rectangular cross section.

Figure 9 shows the flux plot of 1/8 of the prototype design for a NEN beamline quadrupole. The aperture diameter of this quadrupole is 3.1 inches and the REC pieces have a cross-section of 1 by ½ inches. The PANDIRA analysis of this configuration with Hicorex 90B material, gives a pole-tip field of 4.3 kilo-Gauss. The REC pieces in this design are separated by small gaps at the aperture, which will allow the use of an external spline to position the pieces, rather than the combination internal spline and modified trapezoidal shaped pieces as in the drift tube quadrupole design. This will significantly reduce the tolerances on the pieces and still allow for the positioning accuracy required to produce precision quadrupole fields. Although the gaps between the pieces create a larger n = 18 harmonic error than in the close-packed drift tube quadrupole design, the error is only 0.1% of the quadrupole field at 75% aperture, which is quite acceptable for our beamline magnets.

Several different schemes have been proposed for adjusting the focusing strength of permanent magnet quadrupoles.[4,5] The most obvious way is to add or subtract layers, which is quite feasible due to the modular construction. For continuous adjustment, the most practical arrangement is one that consists of several axial layers which are rotated with respect to each other to provide the adjustability. Figure 10 illustrates a four-layer assembly in which successive layers have been rotated alternately by $\pm 22\frac{1}{2}^\circ$. Since each layer produces a quadrupole field and the fields from each layer superimpose linearly, the axial integral is a quadrupole field with a reduced strength proportional to the cosine of twice the rotation angle. The mechanical design of such a quadrupole requires that the magnet pieces in each layer be clamped independently and that bearings be provided for precise radial and

axial alignment during the rotation. The axial force between the layers must also be supported. This force changes from maximum repulsion to maximum attraction during a $\pm 45^{o}$ rotation of two layers.

Beam dynamics considerations

The multilayer adjustable quadrupole may be analyzed, from the beam dynamics point of view, as a series of short adjacent quadrupoles, rotated from the principle x and y focusing planes. Such a configuration leads to x-y coupling terms in the transfer matrices and some preliminary work has been done to investigate the significance of these effects. One promising configuration that has been analyzed consists of four 1/2"-long layers, where the first and last layers are rotated by a positive angle and the middle two layers are rotated by the same angle in the opposite direction. For example, consider the case where this rotation angle is chosen to be 20^{o}, which gives a 23% reduction in the integrated quadrupole strength. For this quadrupole, the emittance growth has been evaluated for a typical beam and found to be less than 1%. An investigation is underway[10] which may allow the elimination of x-y coupling in a multilayer adjustable quadrupole. This scheme would use the ratios and values of the rotation angles of some number of layers as free parameters with which to minimize or eliminate the coupling terms.

Multilayer adjustable quadrupoles will be incorporated in the high energy beam transport system of the NEN proton linac. These quadrupoles will have the following approximate specifications: an aperture diameter of 4 inches, a pole-tip field of 3 kilo-Gauss, an effective length of 2 to 8 inches. These elements will be arranged in triplet configurations.

Acknowledgements

K. Halbach provided inspiration and guidance in most aspects of the work described here. R. L. Gluckstern has contributed significantly to the multilayer adjustable quadrupole ideas and D. Comastra has helped in discussions and analysis on this problem. The work of N. E. Webber in computer programming and analysis and W. Polewarczyk in skillfully assembling and measuring the drift tube quadrupoles is greatly appreciated. Thanks also goes to W. E. Jule and I. Gruverman for their enthusiastic support of this work.

References

1. B. P. Murin, V. I. Rogachev, and A. P. Fedotov, "Concerning the Possibility of using Quadrupoles with Permanent Magnets in Linear High-Energy Proton Accelerators", Inst. Exp. Tech., 19(2), (1976).
2. N. Saito, E. D. Bush, and D. A. Swenson, "Development of Samarium-Cobalt Quadrupole Lenses for Particle Accelerator Applications", Proceedings of the Third International Workshop on Rare Earth-Cobalt Permanent Magnets and their Applications, (1978).
3. K. Halbach, "Strong Rare Earth Cobalt Quadrupoles", IEEE Trans. Nucl. Sci., NS-26, 3882 (1979).
4. K. Halbach, "Design of Permanent Multipole Magnets with Oriented Rare Earth Cobalt Material", Nuclear Instruments and Methods, to be published.
5. R. F. Holsinger and K. Halbach, "A New Generation of Samarium-Cobalt Quadrupole Magnets for Particle Beam Focusing Applications", Proceedings of the Fourth International Workshop on Rare Earth Cobalt Permanent Magnets and their Application, (1979).
6. W. Neugebauer, "Low Flux Leakage Magnet Construction", U. S. Patent No. 3,768,054, Oct. 23, 1973.
7. J. P. Blewett, BNL Internal Report AADD-89, unpublished, (1965).
8. K. Halbach, R. F. Holsinger, to be published.
9. D. Comastra, "Accelerating Structure Parameters of the New England Nuclear Corp. Proton Linac", (Proceedings of this conference).
10. R. L. Gluckstern, private communication.

NEN LINAC DRIFT TUBE QUADRUPOLE PARAMETERS

Table I

	APERTURE RADIUS (CM)	POLE-TIP FIELD (K Gauss)	GRADIENT (K Gauss/CM)	MAGNET LENGTH = L_{EFF} (CM)	OUTSIDE DIA (CM)
GROUP I D.T. 0 to 27	1.10	9.6	8.7	3.81	6.95
GROUP II D.T. 28 to 70	1.35	8.1	6.0	5.08	6.95
GROUP III D.T. 71 to 108	1.60	5.7	3.6	7.62	6.95

n	Charge Sheet "Perfect"	PANDIRA "Perfect"	PANDIRA "Real"	PANDIRA "Real" Parallel	Measured H-90B Parallel
2 gauss	9500.	9500.	10020.	9550.	9609.
3(% of 2)					0.24%
4					0.33
5					0.30
6	-	0.0	0.5	0.4	0.25
7					0.20
8					0.26
9					0.23
10	-	0.0	0.0	0.0	0.56
11					0.14
12					0.13
13					0.10
14	-	0.2	0.5	0.5	0.15
15					0.21
16					0.09
17					0.31
18	6.8	6.8	6.8	6.9	6.20

Calculated and Measured Multipoles at 100% Aperture Radius

Table II

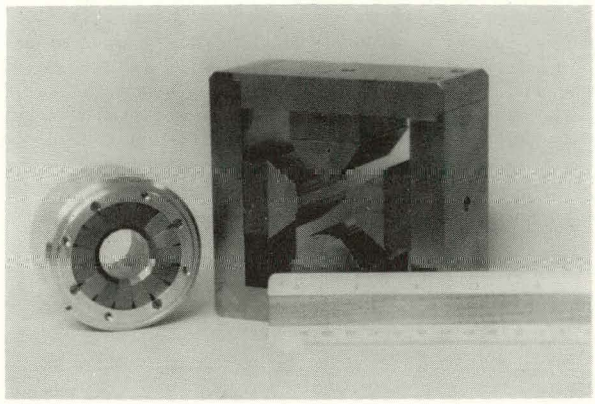
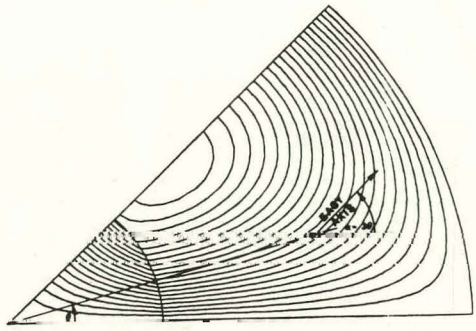
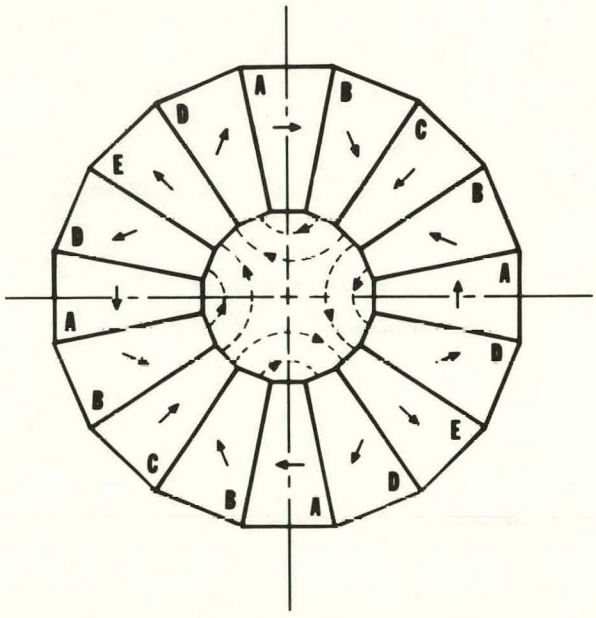


Fig. 1



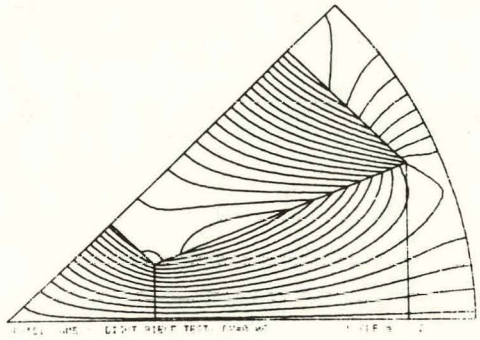
Flux Plot of "Perfect" REC Quadrupole

Fig. 2



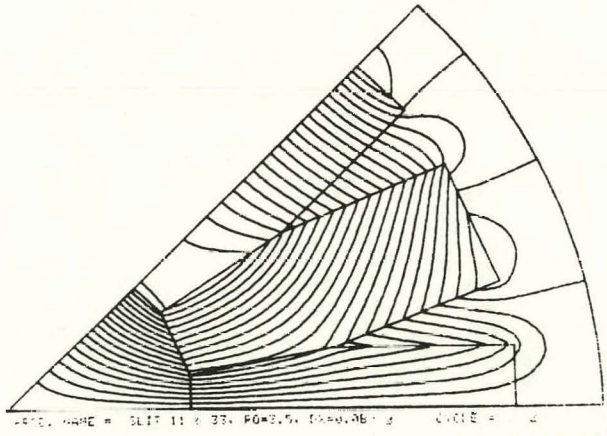
Schematic of 16 Piece Segmented REC Quadrupole With 5 Easy Axis Orientations

Fig. 3



Flux Plot of 8 Piece Segmented REC Quadrupole

Fig. 4



Flux Plot of 16 Piece Segmented REC Quadrupole With 5 Easy Axis Orientations

Fig. 5

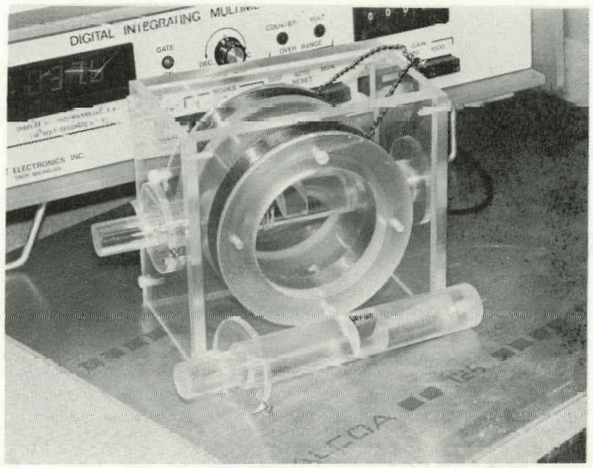
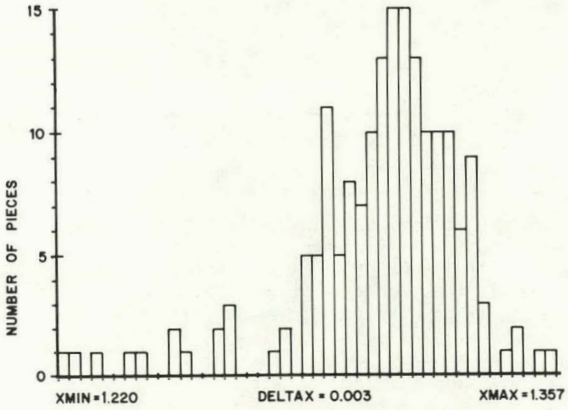


Fig. 6

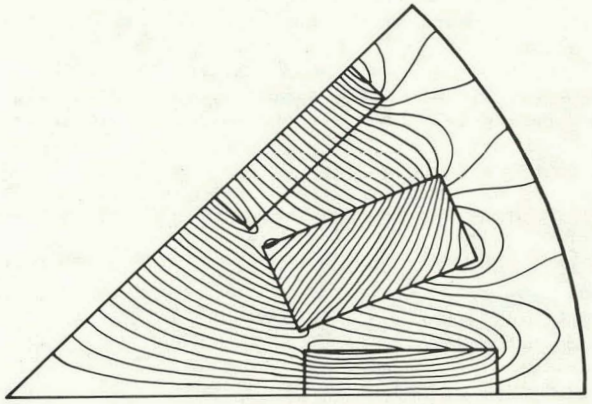


Fig. 8



TYPICAL DISTRIBUTION OF MAGNET PIECE DIPOLE STRENGTH

Fig. 7



FLUX PLOT OF PROTOTYPE ADJUSTABLE STRENGTH QUADRUPOLE

Fig. 9

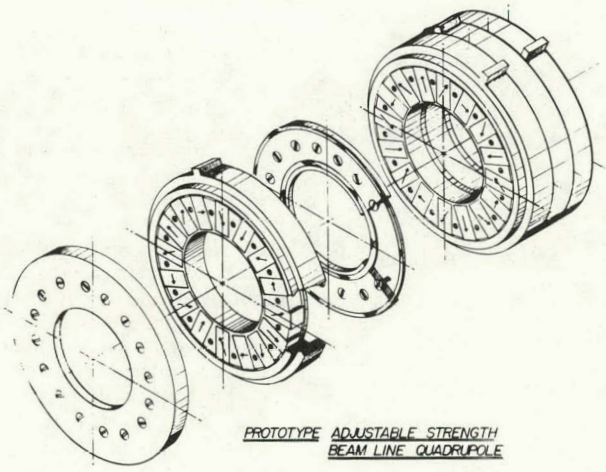


Fig. 10

1979 LINEAR ACCELERATOR CONFERENCE

TIPLESS PERMANENT MAGNET QUADRUPOLE LENSES

N. V. Lazarev and V. S. Skachkov
Institute for Theoretical and Experimental Physics
Moscow, USSR

Summary

Tipless quadrupole lenses of the rod type are proposed. Lenses with samarium-cobalt rods and < 2-cm aperture ensure a magnetic field gradient up to 6 kG/cm and allow regulation of the operating field over a wide range. The advantages of these lenses in comparison with conventional ones are shown.

Introduction

The availability of rare-earth magnetic alloys opens new possibilities for designing magnetic optics elements with formerly unattainable parameters. For example, small high-gradient quadrupole lenses assembled from $Sm\text{-}Co_5$ cylinders for the PIGMI accelerator at Los Alamos.[1] Two new types of quadrupole lenses without pole tips were suggested in 1975-1977 in the USSR. They have some advantages in comparison with the lenses now used. In a sector-type lens (Fig. 1) suggested by J. D. Rabinovich[2] and investigated at the ITEP,[3] a gradient of 6.2 kG/cm in a 2.3-cm aperture was achieved with a lens of 5.2 cm o.d. and 5.0 cm length. The rod-type lens[3] designed at ITEP can ensure a gradient of $\sim$ 6 kG/cm, is simpler to manufacture, and, although its size is the same as that of its competitors, it can produce a lower gradient. Some properties of the sector-type lens and the possibility of manufacturing the rod-type lens were discussed by K. Halbach.[4] This paper deals with analysis of the rod-type lens and the results of measurements on the first prototype.

Analysis of the Lens

The rods of this lens (Fig. 2) are mounted in cells in a non-magnetic holder (1) at a distance R_o from the axis of the lens. The angle between the intensity of the magnetization vector $\vec{I}$ and the radius vector $\vec{R}_p(R_o,\psi_p)$ of rod p is twice as large as ψ_p. The radii of rods generally are unequal. The field of a multilayer rod-type quadrupole lens can be determined by superposition of the fields of all the rods. The operating field for the closest filling of the lens can be easily calculated when the neighboring rods in the same layer and in the adjacent layers touch each other.

If the numbers of rods and of layers increase to infinity, then the field of the lens approaches an ideal quadrupole:

$$\vec{B}(r,\phi) = G\vec{r}\vec{a} \quad ,$$

where

$G = 2\pi^2 I\left(\frac{1}{r_o} - \frac{2}{d}\right)$ = gradient,

$\vec{a} \equiv \vec{n}\cos 2\phi - \vec{\tau}\sin 2\phi$,

r_o is the aperture radius,

d is the outer diameter, and

$\vec{n}$, $\vec{\tau}$ are unit vectors of the polar system r,ϕ.

In a lens with a finite number of rods, N in a layer and a finite number of layers J, the base (quadrupole) harmonic of the field

$$\vec{B}_f = \frac{N}{\pi}\sin\frac{\pi}{N}\cos^2\frac{\pi}{N}\vec{B}$$

is less than $\vec{B}$ with the same o.d., $d = d_J$ (where d_J is the o.d. of a J-layer lens), but the difference becomes negligible with increasing number of rods. The base harmonic is distorted by the influence of higher harmonics. The contribution of the higher harmonics, $\Delta\vec{B}$, can be defined in terms of the ratio of this contribution to the quadrupole harmonic modulus at the corresponding point of the field in the aperture limits $r = r^*$, $\phi = 0$:

$$\delta \equiv \frac{|\Delta\vec{B}(r^*,0)|}{|\Delta\vec{B}_f(r^*,0)|} \quad .$$

The values of δ and of the ratio $2r_o/d_J$ depend on the numbers of rods and layers, N and J, as shown in Fig. 3, where the points corresponding to the same value of J, calculated with $r^* = 0.75\ r_o$, are connected by smooth curves. Clearly, there is no need to use more than three layers to decrease the nonlinearity, and the most effective number of rods is between 10 and 16. For practical realization, it is simpler to keep the ratio $2\ r_o/d_J$ close to 0.5.

The discreteness of the distribution of the magnetization intensity leads to the appearance of a dispersion field. As N and J approach infinity, the dispersion field vanishes; at finite N and J, it decreases almost to zero with increasing distance from the surface of the lens. The dependence of the dispersion field on the ratio $2\ r/d_J$ for different values of N from 10 to 30 is shown in Fig. 4. The number of layers in the lenses with different N was chosen to satisfy the inequalities $d_{J-1} < 0.5 < d_J$. The graphs show that in a lens with $N = 20$ $(J - 3)$, for example, at a distance $d_J/10$ from the surface, the field B is $< 10^{-2}\ B_r$ (i.e., $\leq$ 100 G).

Adjusting the Gradient

Because the layers are independent of each other in a rod-type lens, it is easy to regulate the gradient. This can be done by allowing for the azimuthal displacement of one group of layers relative to another. If $\vec{B}_1 = G_1 r\vec{a}$ and $\vec{B}_2 = G_2 r\vec{a}$ are the fundamental harmonics of the fields of an inner and an outer group respectively, then, with the angle ϕ_o of relative turning of the base planes, the fundamental harmonic $\vec{B}$ of the resulting field is

$$\vec{B} = \vec{B}_1 + \vec{B}_2 = Gr\left[\vec{n} \cos 2(\phi-0) - \vec{\tau} \sin 2(\phi-\theta)\right], \quad (1)$$

where

$$G = \sqrt{G_1^2 + G_2^2 + 2G_1G_2 \cos 2\phi_o},$$

$$\theta = \tfrac{1}{2} \arccos \frac{G_1 + G_2 \cos 2\phi_o}{G}. \quad (2)$$

Equation (1) indicates that the quadrupole field $\vec{B}$ is shifted in phase relative to the field of an immovable (inner) group. The gradient of the resulting field, as seen from Eq. (2), depends on the angle ϕ_o. As this angle changes from zero to $\pi/2$, the gradient changes from a maximum value of $G_{max} = G_1 + G_2$, to minimum, $G_{min} = |G_1 - G_2|$. As a rule, the appearance of the angle θ in the phase of the resulting harmonic $\vec{B}$ is undesirable, and it must be compensated for by turning the lens as a whole, through the angle θ. The turning arrangement is simplest when $G_1 = G_2$; in this case $\theta = \phi_o/2$ and $G = 2G_1|\cos \phi_o|$, i.e., to fix the coordinate axes of the resulting field, it is enough to rotate the movable groups of layers in opposite directions by equal angles.

It is important in manufacturing the lens, to select identical rods. The higher harmonics of the rods' fields can be compensated for in the lens when their magnetic moments are equal. If the rods are not identical, the effect of demagnetization of the rod material can be compensated for outside the lens. This can be accomplished by lapping the rods to decrease the radii R_i in order to obtain satisfactory equality of the products $I_i R_i^2$. In this case the field of the lens with equalized rods corresponds to minimum magnetic moment in the primary group selected for rod lapping.

It is also important to tune the lens, i.e., to install the rods in accordance with the law of vector $\vec{I}$ rotation in a quadrupole lens. A convenient way to accomplish this is to measure the direction of the field generated at the axis of the lens by the rod being tuned. The effectiveness of such measurement is ensured by use of a Hall pickup. Every rod field at the axis of the quadrupole lens forms an angle ψ_p with the base plane. For tuning, the plane of the Hall pickup should be put at the angle $\pi/2 - \psi_p$ and the rod should be rotated around its axis to the position where the Hall emf is maximum. For final tuning it is convenient to use the zero reading of the Hall pickup by turning its plane 90^o.

The Prototype Lens

The prototype of a rod-type quadrupole lens manufactured at ITEP consists of two layers of $Sm\text{-}Co_5$ alloy rods (Fig. 5). Each layer is mounted in a separate cylindrical drum made of brass. The rods have brazed centers (Fig. 5) and are fixed in the drum cells by a stop screw, which presses them to the bottom of the cells. The length of the magnetic rod, ℓ_r, is 2 cm, and its diameter is 0.6 cm.

Each drum with its tuned rods, comprises a separate lens. The inner drum contains 12 rods and the outer one, 20. The diameter of the hole in the inner drum is 2 cm; the outer diameter of the compound lens is 4.8 cm and of the inner lens, 3.4 cm. The gradient at the axes of the inner and outer lenses (average for the lens without a yoke) are 2.6 and $\sim$ 1 kG/cm, respectively. These are not high values considering the overall sizes of the lenses. They result from the relatively low magnetization of the rods (in the inner lens, for example, $I \underline{\sim} 550$ G), from the low packing density, and from the fringing effects, since rods had a diameter $2 r_o \tilde{\sim} \ell_r$ in these lenses. This relationship between diameter and length has a strong influence on the harmonic structure of the operating field, if the dependence G(z) in such a short lens does not have a flat part. For example, the measurements showed that the inner lens with rods equalized according to their magnetic moments (with accuracy $\pm$ 2%) has an operating field with the amplitudes of the 6th, 10th, and 14th harmonics equal to 2.7%, 0.7%, and 0.6% that of the quadrupole field, with $r^* = 0.75$ cm. The other harmonics have lower amplitudes.

Designs For A Linac

The rod-type construction allows tighter packing of a lens with rods than was used in the prototype, and the length of the lens in the focusing channel of an ion linear accelerator would normally be several times that of the experimental model. Therefore, much higher gradient and linearity of the field could be obtained for the same size lens. Calculations show that a gradient of up to 7 kG/cm could be obtained for a bore diameter of 2 cm and a lens o.d. of 8 cm if a $Sm\text{-}Co_5$ alloy with higher magnetization ($4\pi I \underline{\sim} 9$ kG attainable at present) is used.[5]

The proposed rod-type quadrupole lens, which encompasses the whole range of gradients needed in the focusing channel of a linear accelerator, reduces the variety of required designs. It also simplifies the manufacturing technology and the tuning procedure in comparison with a sector-type lens or a lens with pole tips. Its linearity and dispersion are as good as those of the sector-type quadrupole lens and are much better than those of a salient pole lens. One of the major merits of the rod-type lens as an example of a tipless lens, is that it allows smooth regulation of the gradient over a wide range. This, and the other

advantages mentioned above, simplify the design and manufacture of focusing channels with a large number of lenses.

Acknowledgement

The authors would like to thank Prof. I. M. Kapchinskii for formulating the problem and for other help, Dr. V. V. Sergeev for consultation and assistance, and Drs. V. S. Rasstegaev and E. D. Shalyaev, who manufactured the magnetic rods in their laboratory.

References

1 D.A. Swensen et al.,"Accelerating and Focusing Structures for PIGMI",Proc. 10th Int. Conf. on High Energy Accelerators, Vol. 1, 295, Serpukhov (1977).

2 J.D. Rabinovich, USSR Patent No. 662979, Bulletin of Inventions 18, 216 (1979) (with priority from 23.12.1975).

3 V.S. Skachkov, "Permanent Magnet Multipole Lenses Without Pole Tips", ITEP-76, Moscow (1979).

4 K. Halbach, "Strong Rare-Earth Cobalt Quadrupoles", IEEE Trans. Nucl. Sci., NS-26(3), 3882 (1979).

5 A.A. Preobgragenskii, "Magnetic Materials and Elements", 178, Moscow (1976).

Discussion

Bentley, NEN: Can you give us an idea of how much the material costs and what the cost of the lines you showed us might be?

Lazarev: Yes, of course. The cost of this Samaerium cobalt material is high but with such lenses there is no consumption of energy. For the most part, the cost of lenses within drift tubes is in their manufacturing and not the cost of a piece of iron, so the difference is not so much as it may seem.

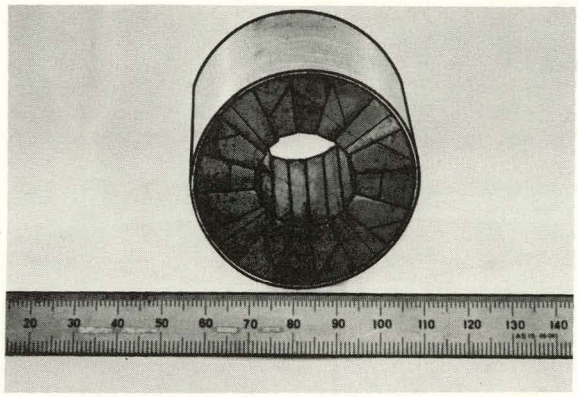


Fig. 1 Sectoral samarium-cobalt quadrupole lens with a gradient of 6.2 kG/cm in an aperture of 2.3-cm diameter

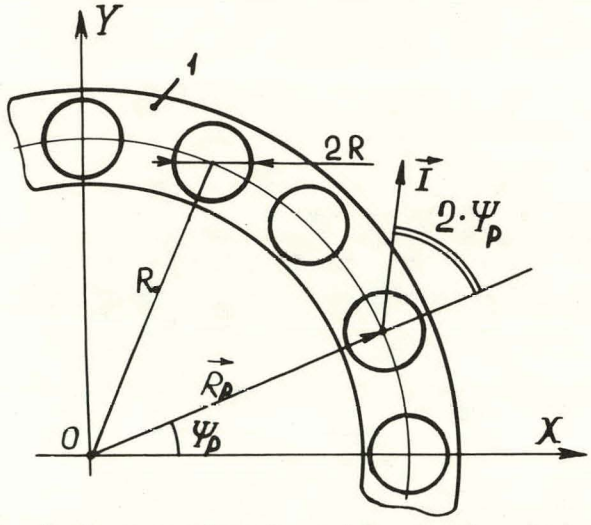


Fig. 2 Cross-section of a rod-type quadrupole lens

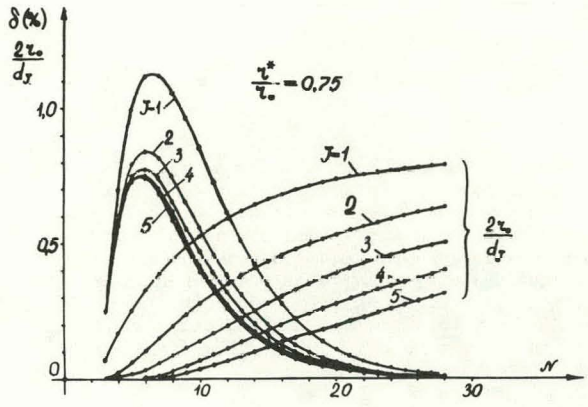


Fig. 3 Dependence of the field nonlinearity δ and the ratio $2\,r_0/d_J$ on number of rods N in each layer of a quadrupole lens with J layers



Fig. 5 Rod-type, two-layer, samarium-cobalt quadrupole lens

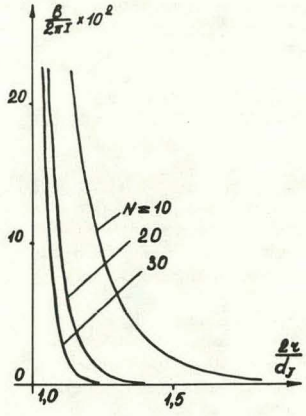


Fig. 4 Dependence of the dispersion field on distance from the lens surface and on the number of rods in each layer

1979 LINEAR ACCELERATOR CONFERENCE

MECHANICAL ASPECTS OF THE NEW ENGLAND NULCEAR LINAC

R. Damm, J. Aggus, G. Greenberg
New England Nuclear Corp.
N. Billerica, Mass. 01862

Summary

New England Nuclear Corporation (NEN) is building a 45-MeV proton linear accelerator, to be used for the commercial production of radiopharmaceuticals. The design goal of 5-mA average current at 60 pps and the use of permanent magnet drift tube quadrupoles will make this machine unique. In order to minimize risk, reduce costs and speed fabrication, this machine is being modeled after existing proton linacs in the U.S. and Europe.

This paper reviews some of the mechanical designs that are being used. Single stem drift tubes with a choke joint connection to the tank wall are discussed. Tank design and cooling are reviewed along with rf problems, such as loop design and transmission line cooling. Beam transport in the dome and the LEBT, along with the machine vacuum systems are discussed.

The column design and its support are presented. Conventional alignment techniques are planned and reviewed. The linac building and the schedule is presented.

Beam Transport Lines

A small beam transport system in the dome is being constructed for the 45 MeV linac. A 90° bending magnet, solenoid magnet, steering magnet and instrumentation box will be incorporated into the beam transport line. A 2000 l/sec turbo pump will operate in the dome for this beamline, with a water-cooled aperture (1/2" dia.) isolating the dome transport system vacuum from the column vacuum. A pressure of 10^{-4} Torr will be maintained in the beam transport line with the turbo in the dome, while 10^{-6} Torr will be maintained in the column. Column pumping will be provided by two 1000 l/sec ion pumps at the ground end. The insulator stack will be made with glass insulators. A 4" aperture through the insulator stack will allow for easy alignment and give adequate vacuum pumping conductance. The insulator stack and its SF_6 jacket assembly, is designed such that the insulator stack is always under compression, regardless of its orientation. The dome transport system will mount directly to the column support system to help reduce misalignment problems. (Fig. 1).

The low energy beam transport line is about 15 ft. long. Three triplets and four singlets with viewing boxes are being used in this line. A double-gap, 2-frequency buncher is being used to improve capture efficiency.

Tank

The linac tank is made from 6 flanged cylindrical sections that are aligned and bolted together at the time of installation. The overall tank length is 27.6 meters; the inner diameters vary from 1.1 to 1.02 meters and the tanks are fabricated from copper clad steel (.160" OFHC copper on .750" - 516 grade 70 steel). The clad material was 100% ultrasonically checked for voids in the copper-steel bond. Only two small voids were detected in one plate and will be repaired during tank fabrication. A short one-foot long tank section has been rolled and welded to aid in determining the amount of initial edge forming necessary for proper rolling, and the effect of the longitudinal weld shrinkage on the final section size (circumference). No copper cover weld is used to cover the longitudinal seam weld. All tanks are capable of being rolled from single sheets of clad material, so circumferential welds are not required.

The clad plates were polished at the rolling mill, but only a 50 micro-inch finish could be achieved without smearing the surface. The tank fabricator will polish the tanks after rolling and welding. "Q" measurements will be taken during this time to measure the effect of the polishing.

After welding and polishing, the tank sections will be stress relieved at 1100°F, with a reducing atmosphere maintained in them.

Copper inserts will be shrunk into the tank walls at the drift tube, post coupler and tuner locations.

Rf surface-current continuity across the bolted tank sections is provided by an oversize copper ring that is inserted between the flanges as they are drawn together (Fig. 2). Each tank section has two vacuum ports machined in it.

Tank vacuum will be provided by:

9 ion pumps - 1000 l/sec each,
2 turbomolecular pumps - 2000 l/sec, and
1 roots blower - 1000 CFH

The tank is cooled via a cooling jacket that encompasses the entire outer surface of the tank. A flow pattern through the jacket is created by welding bars that form flow channels in the jacket. Water is supplied to the tank at its mid-point (flanged connection between Sections III & IV) and is split to flow through single pass hair-pin loops. 600 gpm of temperature controlled water is available for tank cooling. 150 gpm of this water is tapped off the supply to the tank, passed through a pump to increase the pressure and is used for drift tube cooling. Post couplers, tuners and vacuum grids all having cooling capabilities and will be water cooled using tank water (Fig. 4).

The temperature control system uses a 3-way mixing valve, heater, heat exchanger and appropriate control units. The heater is used to maintain the tank at its normal operating temperature, when no rf power is being supplied to the tank.

Drift Tubes

The linac will contain 107 drift tubes, with a half drift tube in each end cover. All drift tubes contain a permanent magnet quadrupole. The use of these compact, high efficiency quadrupole magnets reduces the physical size, and thus, the cooling requirements for the drift tubes. All drift tubes are 9-cm OD. Drift tubes are supported

with a single vertical stem of heavy wall (.25") OFHC copper. Tank I stems are 1-1/8" OD and tanks II through VI are 1-1/4" OD. Water-cooling and a vacuum pump-out are provided through the single stem. Tank I bodies are cooled via a copper tube that is brazed into the body. Bodies in Tanks II through VI are cooled using a series of holes and manifolds that are integral with the drift tube body.

The drift tube bodies are being fabricated from hot-forged cross-grain certified OFHC copper. Two basic body designs are used: Tank I bodies are a closed end cup with cover; Tank II through VI use a heavy wall cylinder with separate end caps.

A connector plug is brazed to the body using a silver-copper eutectic alloy. The plug allows the stem to be attached to the body by electron beam welding and at the same time it forms a part of the water manifold system in the body. Bellows are not used in the drift tube support system. The copper stem passes through the tank wall through a "choke" joint. The "choke" joints are copper inserts that are shrunk into the tank wall. The inside diameter of these inserts contain a spring-finger ring which makes contact with the drift tube stem. The contact fingers are located about one stem diameter back from the tank surface. They are positioned so as to reduce their current carrying requirements. The design allows for the necessary alignment movements without the inherent problems normally associated with the use of bellows. The vacuum seal between the tank outer surface and the stem is made with "O" rings. The containment for these "O" rings is allowed to track the stem until the drift tube is aligned and then it is fastened to the tank. This technique allows drift tubes to be aligned with no external force applied to them. (Fig. 3).

Rf and Transmission Lines

Rf power is supplied to the tank through four fixed loops located at the 1/8, 3/8, 5/8 and 7/8 points along the tank. The loops will be matched to the tank at low power, and will be water-cooled. Three power amplifiers will drive the loops through a rather complex transmission line system. 12" line is being used with an aluminum outer conductor and a copper inner conductor. Transmission line losses, estimated at 1% loss per 100 feet of line, require that cooling be provided. Air cooling manifolds are located at the tank vacuum windows and at the power amplifier pressure windows. These manifolds allow cooling air to enter at the tank window and pass through the entire transmission line system. Cooling air will be dried, cooled in an air/water heat exchanger and recirculated. The transmission line system is designed to be pressurizable to 45 psi if necessary.

Deionized water (5 MΩ-cm), 1050 gpm at 120 psi) is to be used for cooling the rf system. A 3 gpm deionizer is incorporated in the system to continually polish the water. This deionizer contains two mixed resin cartridges, an oxygen removal cartridge, 5 μ and 0.2 μ filters and an UV light for sterilization. Fiberglass piping is used for the rf water system.

The linac tank sections are fabricated oversize and will be tuned with mechanical slug tuners (fixed and adjustable) and an angle type tuner bar attached to the cavity wall. Post couplers will be used in this machine. End covers are not adjustable, but the half drift tubes mounted in them are located using shims, so that end gaps can be accurately adjusted.

Alignment & Schedule

Standard optical tooling instruments will be used for the linac machine alignment. Bore-sighting is planned for the initial equipment installation, with reference offset lines for future equipment realignment. A building stability check has just begun, but it is too early to draw any conclusions. The effect of the construction of the target complex, backfilling of earth shielding and a New England winter will be checked this coming year.

The status of the program today is as follows:

1. The building construction is 75% complete. Partial occupancy (rf gallery, linac tunnel and injector pit) is promised by October 1, 1979. The building is to be completed by December 1, 1979. The target complex with its support areas has not been designed as of this date. Selection of an A/E firm is in process.

2. Most major machine components - Cockcroft-Walton and dome, linac tanks, rf systems and transmission lines have been specified, designed and ordered.

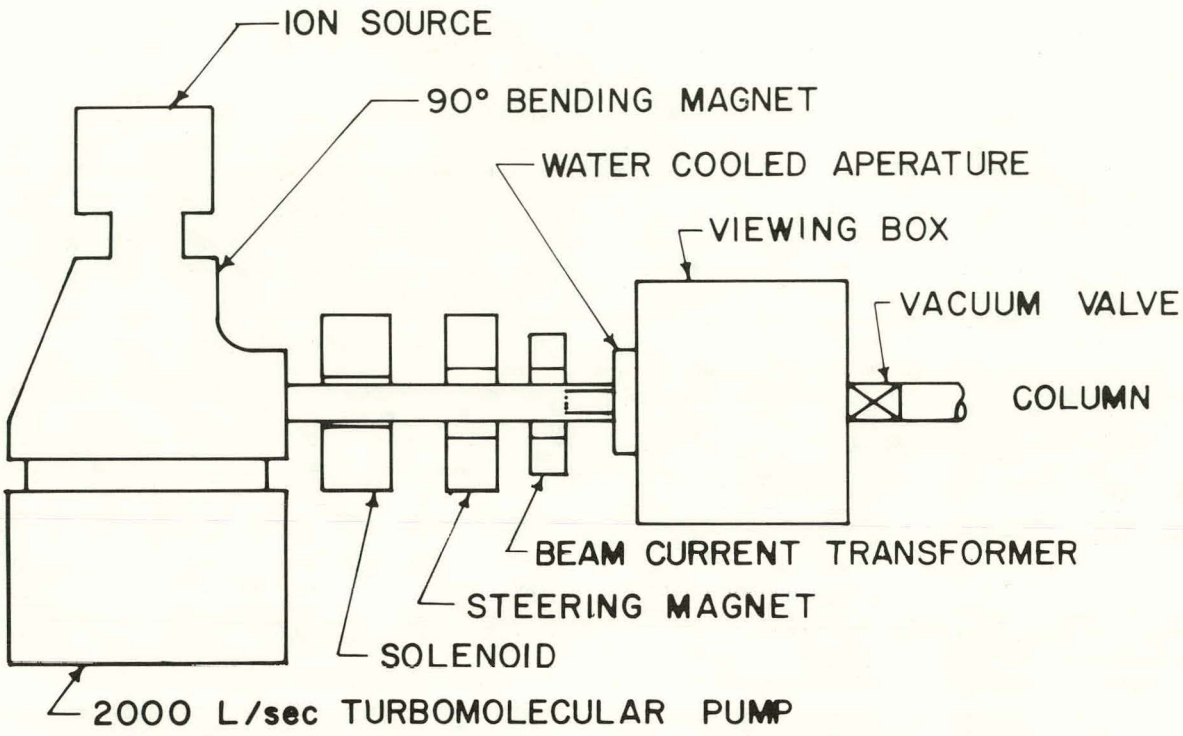
Machine turn on is scheduled for mid 1981.

Acknowledgements

The program at NEN relies very heavily on the technical support from the National Laboratories in both the United States and Europe.

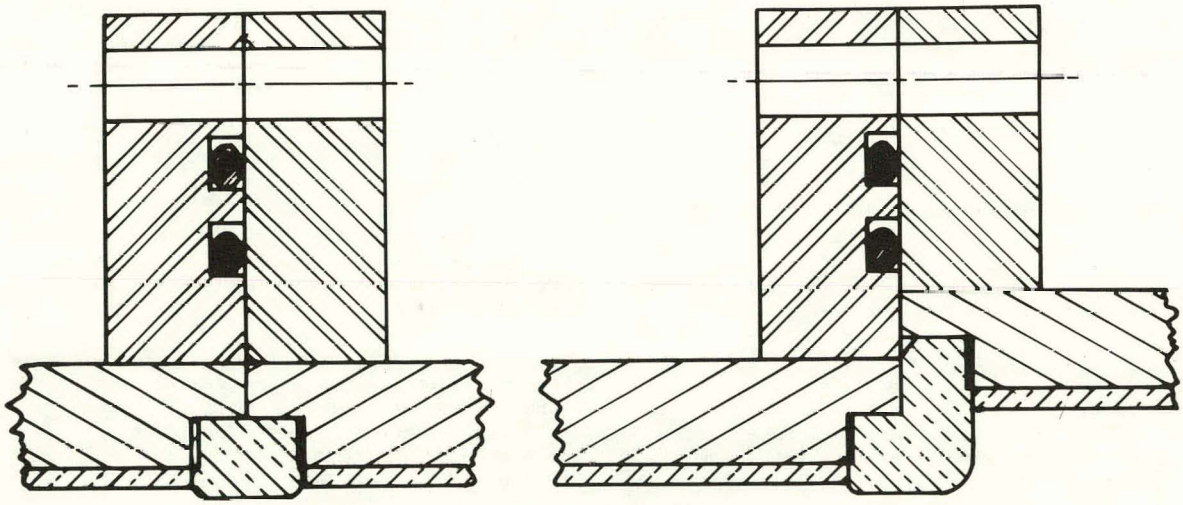
Many designs used in this machine are either a direct copy of existing designs, or are only slightly modified to meet the special needs of the NEN machine.

The program at NEN could not have proceeded to this point, and cannot be successfully completed without this technical support. The linac group at NEN is extremely grateful for this unselfish assistance and hopes to be able to someday repay its debt to the accelerator community.



BEAM TRANSPORT LINE IN DOME

Figure 1



TANK FLANGE

Figure 2

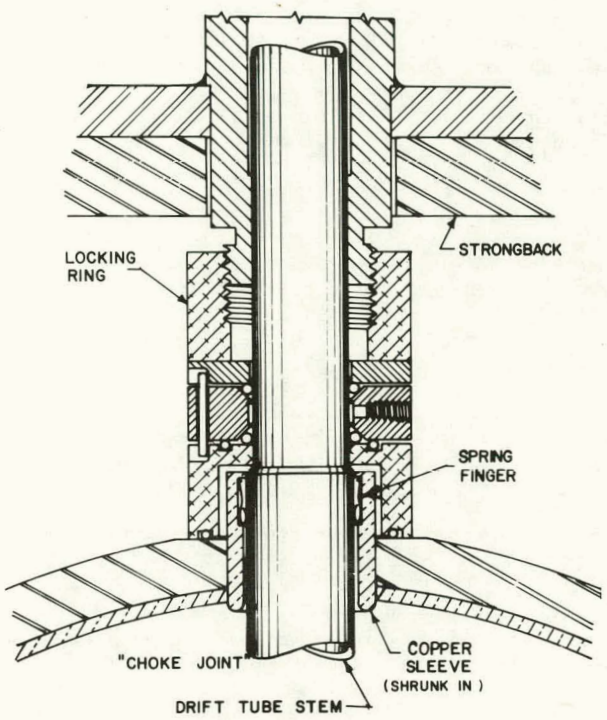
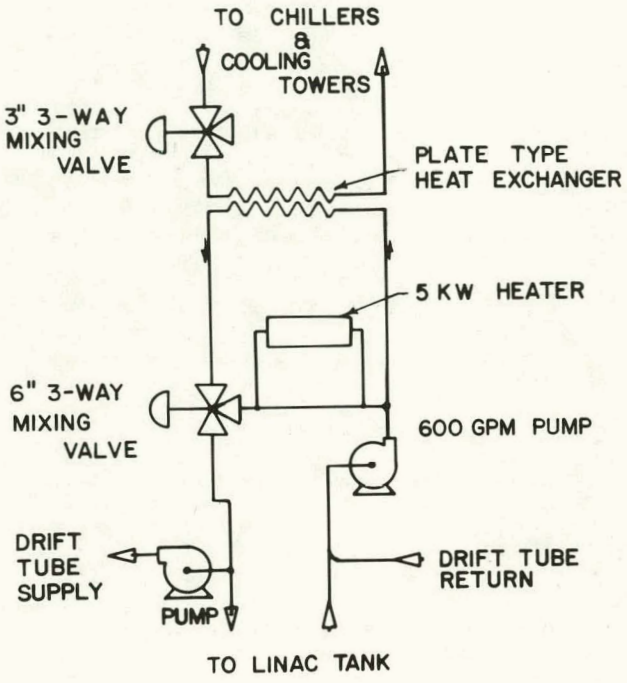


Figure 3



TANK COOLING

Figure 4

1979 LINEAR ACCELERATOR CONFERENCE

CAVITY AND DRIFT TUBE TECHNOLOGY FOR THE UPGRADED UNILAC

D. Böhne, H. Gaiser, E. Malwitz
GSI, Gesellschaft für Schwerionenforschung mbH
Darmstadt, Fed. Rep. of Germany

Summary

The extension of the Unilac poststripper section from the present 2 to 4 Alvarez cavities should be completed as early as possible. There was, however, concern whether the old drawings should be used with the appropriate changes in the drift tube table, or a redesign of essential mechanical details (simplifications) would be possible in the tight time schedule. As a result, the saving in fabrication time seems to compare favorably with the effort spent in redesigning the cavity and drift tubes. The net gain would be a cost saving of a factor of two.

This paper describes an in-place plating method for welded tank sections and a fabrication scheme for the drift tubes out of inexpensive sheet metal components.

Introduction

The design decisions on various mechanical components of the Unilac, which have been evaluated in prototype activities, were outlined in 1972.[1] A review of the actual performance of most components was given in a 1976 Status Report.[2] A strongly recommended redesign of a few mechanical components, which are exposed to high power rf fields, is described elsewhere.[3]

The Unilac upgrading program[4] includes the extension of the poststripper section by two more Alvarez cavities for the energy range of 5.9 to 11.3 MeV/u. The cavity length and the rf parameters are chosen to be identical to the existing cavities, which accelerate the stripped ions from 1.4 to 5.9 MeV/u.

The cavity and drift tube design is reconsidered here, this is not meant as an improvement over the original design, but rather as an allowable simplification. The associated cost saving was not a primary concern here.

While many of the ideas presented here were conceived earlier, it seemed to be too risky to incorporate them in the original Unilac construction. Experience with the operating machine and results of prototype studies substantiate the practicability of the proposed alternate designs.

Cavity and Endwalls

In the existing machine, copper plating technique has been used for all rf surfaces. It proved to be highly reliable and resilient. In two cases of severe burn-out of the goldwire rf contact rings, due to inadequate stress load, the copper surface remained intact. Depth limitations of plating bath containers restricted the sectional length of cavity units to 2.6 m. The assembly of one 13 m long tank required five bolted joints and hence expensive flange machining. These joints, which were not expected to be reopened, developed small leaks from an accidental heating-up of the tank as a consequence of a cooling fault.

Dispensable joints should be eliminated as much as possible in the redesign. The well established copper clad steel approach was reconsidered and bids obtained revealed that this material is available in adequate quality and quantities (this was not the case 12 years ago). As the result of detailed conceptual design studies, this approach was discarded for the following reasons: the copper is too soft to allow for all-metal seals and rf contact rings; nozzles had to be fitted with copper skirts and inserts; the many leak-tight welding operations and the finish of the rf surfaces seem to be laborious and expensive.

It was decided then, to reuse the plating technique, applied to rolled mild steel cylinder sections. The previous plating facility was restored at modest expense. After plating the individual sections, the ends of which are left copper free for a few cm, they will be welded together. The welding area will be plated over by a locally attached bath reservoir, which covers a segment of about one-fifth of the circumference. For the five sequential plating steps per seam, the tank must be turned in order to keep the reservoir perpendicularly positioned at the inner side of the cylinder. Gas bubbles and dust particles are thus kept away from the plating surface. Figure 1 shows a sectional view of the joint area. In order to avoid longitudinal shrinkage, a light welding seam is applied on the inside. The heavy weld will be applied to the stiffening ring at the outside, which also serves a centering fixture for both cylinder ends. The groove left by the shaped ends of the mating tank sections is used as a fore-vacuum channel for leak checking the welding seam. In general, a weld does not have to be leak checked if plated over subsequently.

The rolled sections are sanded on the inner surface. The final plating will reduce the roughness from about 15 µm to 0.5 to 1 µm. In the original tank design, the inner surface was machined on a vertical lathe, since the end flanges had to be machined anyway. The applied conical shape of the section was used for cell tuning, keeping the g/L ratio constant along the whole cavity. In the new design, the sections are kept cylindrical and of a constant diameter. For cell tuning, the g/L ratio is tapered. Cell dimensions

are derived from LALA computations and corrected for a systematic frequency error of + 0.03 %. This error was determined by recalculations of the existing cavities.

Postcouplers were not considered in the redesign because the cavity length, normalized to the wavelength, is relatively short and field flatness is not a relevant problem, rather than the attainment of the correct frequency.

It is believed that tolerances of the average inner diameter as close as $\pm \frac{1}{0}$ mm can be obtained. The length of the steel slab is cut to the length of the neutral line of the circumference. After tag welding of the longitudinal seam, the average diameter is derived from eight diameter measurements equally distributed over the inner circumference. If the result is found to be off tolerance, the tag weldings will be opened and the mating edges will be ground, or sheet metal spacers will be inserted, when the diameter turned out to be larger or smaller respectively. No further shrinkage during the final weld will occur if only a light welding seam is applied. As in the existing cavities, no tuning bar is necessary if the above-mentioned tolerances are observed. Fixed tuning bodies of 15 cm diameter can be inserted via flanges, four of which are provided on each section for fixed and movable tuners.

As a standard at the Unilac, the Con Flat seal will be used on all usual flanges for tuners, vacuum pumps, pick-up probes and drift tube stem heads. On the existing cavities, those joints have been machined directly into the cavity wall. At the delicate knife-edge, none of the nearly 300 flanges has ever been damaged or worn out from frequent openings. In order to avoid the requirement of large and expensive milling machines for cavity manufacturing, the Con Flat profile will not be cut into an oversized wall thickness. Instead, flat blocks of adequate thickness and size will be machined on small automated milling machines and welded into a flame-cut hole on the 20 mm thick cavity wall. Figure 2 shows an example.

Wall cooling will be provided by cooling jackets, welded on the cavity in four segments; the clearance is set by pressed-in dimples. The earlier concept of counter flow channels was never applied and no thought will be given to temperature control of the coolant circuit.

Figure 3 shows the stem head. The adjustment fixture is kept identical to the first design. The adjustment base is now a plate, levelled by three threaded studs, instead of a machined nozzle. The stainless steel bellow is placed outside the cavity field as before.

All accessory components, monitoring probes, tuners, tank supports and the vacuum system will be as in the first design. The drive loop concept, however, was changed.[3]

The end walls of the original design consisted of a thin rf wall, supported by a heavy spider, and a cast bulkhead exposed to atmospheric pressure. The volume in between, containing water joints and quadrupole leads, was pumped by an auxiliary vacuum system. Though the pressure interlock and the safety valve connecting the high vacuum and the auxiliary vacuum volume never failed in case of an accidental pressure rise in either system, this concept is felt to be overly sophisticated. A 90-mm thick endplate is planned as a rf and pressure wall, which eventually has to be reinforced by stiffening ribs. The resulting inward bend of 0.3 mm is tolerable from the field flatness consideration. Cooling channels will be cut into the plate on the rf side and covered by a welded strip. The piece will be copper plated on the machined inside surface.

The above mentioned endplate design, requiring machined surfaces and a vacuum joint, seems to present an inconsistency in the concept of a simplified design. Therefore it was at first envisaged, to weld a deep pressed bulkhead with a cylindrical collar to the end sections of the tank. Copper plating of the seam could have been performed as described before. Considerations on the rf field pattern in the end cell with a slightly spherical end wall (bulk head) did not result in a consistent cell geometry, which meets the boundary conditions of the field pattern in the neighboring cylindrical cell, and probably would have presented a flatness perturbation. This bulkhead approach, which really would reduce an Alvarez cavity to an oil-tank item, could unfortunately not be brought to a viable solution under the time constraints of the upgrading project. A bolted end joint had to be used instead, because the rectangular corner area of a welded flat end-plate could not be copper plated reliably.

At the Unilac the standard approach for making a large diameter cavity joint is to use a 1.5 mm diameter gold wire squeezed to 50% of its original thickness between properly machined and copper plated flange surfaces. Wire gages ranging from 1.2 to 1.8 mm are stocked in case of tolerance excursions of flange dimensions. For the purpose of leak checking without pumping the whole cavity, an elastomer-sealed fore-vacuum groove is provided behind the gold wire gasket. In the few cases where the metal seal became leaky, the flange rings were found to be too weak. A considerably heavier flange geometry was selected for the new design, as in Fig. 4; the machining will be done before welding the flange to the cylinder wall.

The question of whether gold wire is really superior to aluminum wire, was not reconsidered. Earlier experience on models and on one-scale cavities indicated a Q loss of several percent. Techniques for plating gold and silver on aluminum wires were developed, but no convincing cost savings over a reprocessible pure metal wire can be expected. Alternative contact schemes, like an O-ring surrounded partly by a copper strip as used in the KEK linac, have also been considered, but finally were discarded because of the lack of experience in a

high duty factor machine.

The above-outlined design changes have been applied to a prototype, made up of two short tank sections of full scale diameter. Tolerance expectations and plating technology were derived from this experience.

Drift Tubes

The original drift tube design was mostly a copy of the NAL and BNL concept, equipped with a dc quadrupole equal to the LAMPF design. The components were machined from OFHC copper to close tolerances and assembled by furnace brazing and electron beam welding. Those sophisticated technologies are probably mandatory for microwave tubes, but are unnecessary for Alvarez drift tubes of usual size. None of the nearly 200 units in the Unilac ever developed a leak or a quadrupole failure; however, this design would be overly expensive to fabricate today.

When reconstructing the HILAC in 1971[5] LBL engineers demonstrated a much cheaper solution, based on tape-wound quadrupoles and flood-cooling of coil and outer shell by a single coolant circuit. No commercial manufacturing sources for the tape-wound technique could be found in Europe and therefore the LBL design could not easily be adopted.

The solution presented here was stimulated by the following facts: a) dimensional tolerances of ± 0.2 mm, as used in the first design, can be relaxed to ± 0.5 mm if they are of random nature; b) plating techniques can avoid the expensive solid copper approach; c) subcontracting mechanical pieces and inhouse assembly and testing avoids the overhead charges of the microwave tube industry.

Figure 5 presents a longitudinal section of the assembly. The quadrupole, with classical hollow conductor coils, is assembled on the machined stainless steel bore-tube, which supports the magnet inside the drift-tube can and provides a close target fit for the optical alignment of the magnetic axis.

In the earlier drift tube procurement, not a single one was found with the magnetic axis being off the mechanical axis. Therefore, the measurement of the magnetic axis and eventual correction of the bore-centering was not considered; the dimensional inspection of yoke and pole pieces was deemed to be sufficient. Coils will be checked for shorted windings prior to assembly. The dimensions of the quadrupole are all the same throughout the 69 tubes and identical to the last drift tube of the existing Alvarez Tank II. From the particle dynamics standpoint, one could consider leaving out every second quadrupole, or even more, but this would impair eventual future multi-particle acceleration. All lenses in a tank are connected in series. No flow switches will be used for coil protection, as is also the case on the existing machine. Instead, thermal switches are soldered to the current leads leaving the stem heads.

The rf power dissipation on the drift tube surface is in the order of 2 kW and perfect shell cooling is necessary. It is provided by a double wall design for caps and cylinder body, made from stainless steel for welding considerations. The caps are simply roll-pressed over a mandril on a lathe, starting from a disc-shaped sheet metal piece, 2 mm thick. The cylindrical body is rolled from a sheet metal slab and longitudinally seam welded. Caps and cylinders obtain a shoulder fit, cut on a lathe, in order to ease assembly and centering prior to welding the joint.

Stems are welded to extruded nozzles on the cylindrical parts. An eventual tilt of the stems will be corrected for by hand bending during the final alignment in the tank. Two stems per drift tube will be used as in the existing machine, which has demonstrated perfect beam stability. On several occasions of alignment check-out, not a single drift tube was found to be displaced from the original specifications.

No particular care is taken in protecting the drift tube surface, nor in removing the welded beads. Scratches on the cap surfaces, originating from the roll-pressing, are not considered to be detrimental for reliable high gradient operation. The completely assembled drift tube will be electropolished briefly, to remove oxides and grease. During the plating process, the drift tube is just hung between two anode plates. No auxiliary anodes, screening or fluid steering fixtures are used. After receiving a thin nickel strike, copper plating takes four hours for the specified thickness of 0.2 mm to be obtained. In the area between the stems and at the entrance of the bore-tube, the plating is only about 0.07 mm, but still thick enough.

In addition to one plating sample, a complete drift tube assembly was manufactured and plated. The dimensional tolerances seem to be easily kept below ± 0.2 mm, which is less than necessary. This prototype is installed in the existing Alvarez tank, Tank II, for long term examination of the surface properties.

The author acknowledges the enthusiastic effort of W. Bleuel during the drift tube design and fabrication.

References

[1] T. Niewodniczanski, E. Malwitz, "Mechanical Design Features of the Unilac", 1972 Proton Linear Accelerator Conference, 103 (1972) Los Alamos.

[2] D. Böhne, "The Unilac, Development and Present Status", 1976 Proton Linear Accelerator Conference Chalk River, 2 (November 1976).

[3] D. Böhne, "Recent Improvements of Accelerator Components at the Unilac", proceedings this conference.

[4] N. Angert et al., "The Unilac Upgrading Program", proceedings this conference.

[5] R.M. Main, "Modifications of the Berkeley Hilac", Proceedings of the 1970 Proton Linear Accelerator Conference, 949, NAL, Batavia, Ill. (1970).

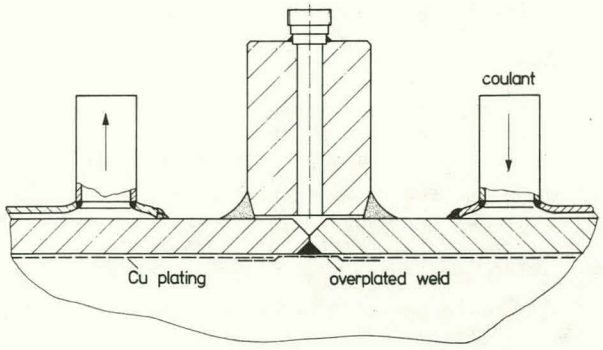


Fig. 1 Welded joint of copper plated cavity sections. The welding seam is plated over by a locally attached bath reservoir.

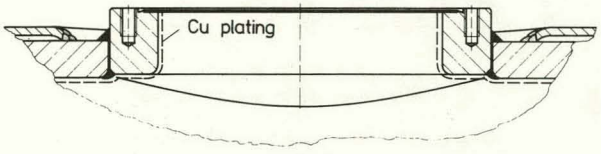


Fig. 2 Con Flat flange welded into the cavity wall. The copper deposit smoothly covers the flange surface and the knife-edge area on the outside.

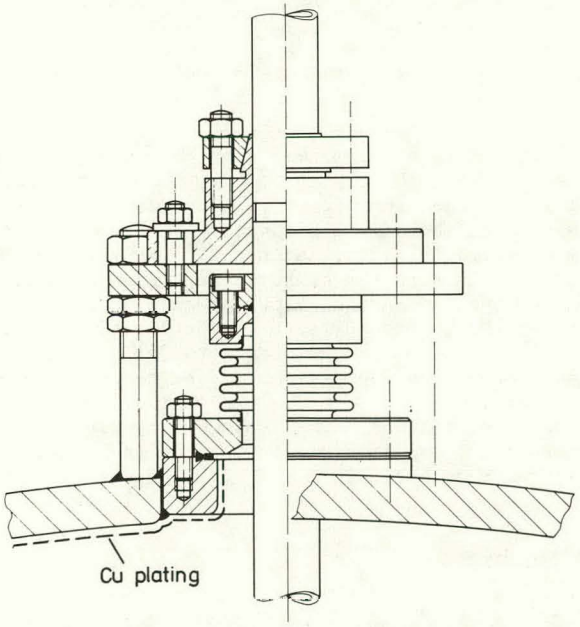


Fig. 3 Stem head supported by a levelled plate. The stem can be adjusted in three dimensions and is sealed to the cavity by the bellow assembly clamped to the stem and bolted to the welded-in Con Flat flange.

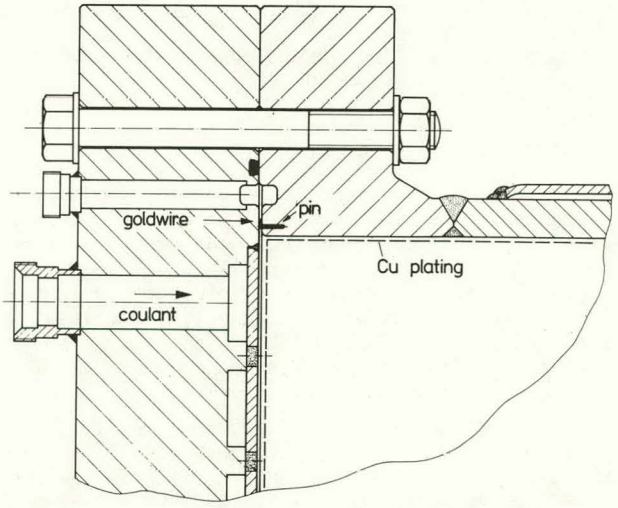


Fig. 4 End wall sealed by a gold wire to the cavity flange. The gold wire is held in place by small pins. A backing vacuum groove allows leak checking individual seals.

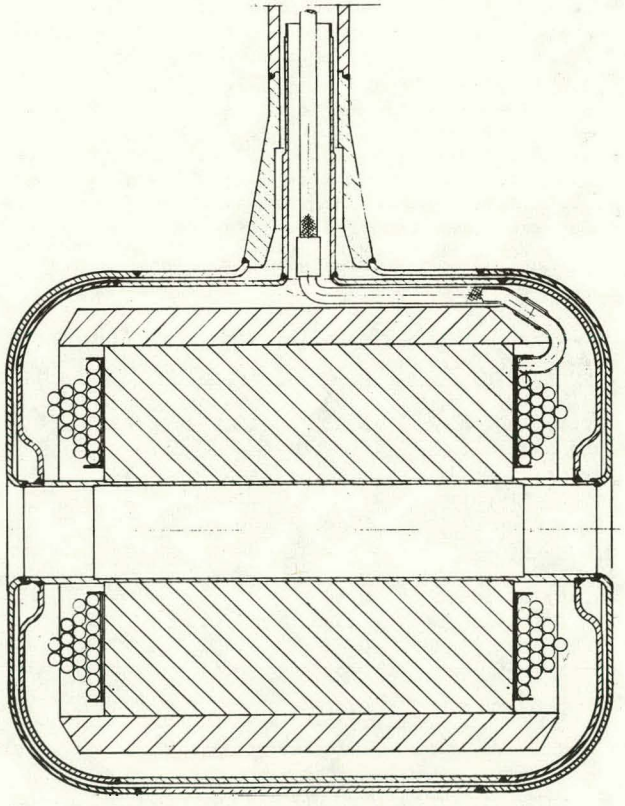


Fig. 5 Drift tube assembly. The quadrupole is supported by the bore-tube and held in place by a positioning screw in the second stem base. Joints of caps, bore tube, cylindrical body and stems are welded to plating.

MECHANICAL DESIGN OF CERN NEW LINAC ACCELERATING STRUCTURE

E. Boltezar
CERN, Geneva, Switzerland

Summary

This paper outlines the mechanical engineering design philosophy and gives a short description of major components, assembly methods and performance of the Alvarez structure for CERN's new 50-MeV proton linear accelerator now in operation as the injector for a complex of high energy machines. It replaced the old linac which could no longer satisfy the demands for a proton beam of higher peak current and better quality.

Some of the design details mentioned in this paper, such as drift tube demountable girders and the alignment method, were first tried on the 3-MeV experimental linac built at CERN.[1] Some production technologies, like copper clad steel, have been used on existing linacs. However, there are several new features incorporated in this Alvarez structure which are novel in the field of linac design.

Basic Parameters

The accelerating structure of this linac (Fig. 1) is composed of three cavities with two intertank sections for beam diagnostics at 10 MeV and 30 MeV. All cavities are rf stabilized using post couplers. The full drift tubes are suspended on a single stem, the half drift tubes are incorporated in the tank covers. All drift-tubes, including the half drift tubes, house pulsed quadrupole magnets. The nominal frequency is 202.56 MHz, the peak current is 150 mA, the pulse duration is of 70-200 μs with a maximum repetition rate of 2 pps.

The following table[4] gives some basic parameters.

	Tank 1	Tank 2	Tank 3	
Input energy	0.75	10.35	30.48	MeV
Cavity ID	0.94	0.90	0.86	m
Cavity length	6.939	12.958	13.359	m
Intertank length	0.15	0.20		m
Number of cells	52	44	32	
Number of posts	25	21	31	
Drift tube OD	0.18	0.16	0.16	m
Bore hole ID	20.25	30	30	mm
Stem OD	28	40	40	mm
Cavity rf power	0.60	1.12	1.17	MW
Rf power (150 mA)	1.44	3.02	2.93	MW
Total heat loss	0.83	1.02	0.95	kW
Drift tube loss	0.59	0.64	0.59	kW

The average heat losses are given for a 0.6×10^{-3} duty cycle, although the cooling capacity was designed for a maximum duty cycle of 2.2×10^{-3}.

For fine frequency tuning, there are ten piston tuners of 10-cm diameter. Five rf feed loops are used, one for the first tank and two for each of the following tanks. All loops are motor driven.

The tanks are also provided with a number of glass thimbles for monitoring loops and five observation windows opposite the feed loops.

The components are positioned around the circumference at different angles (Fig. 2) to avoid unwanted rf field couplings and to provide good accessibility.

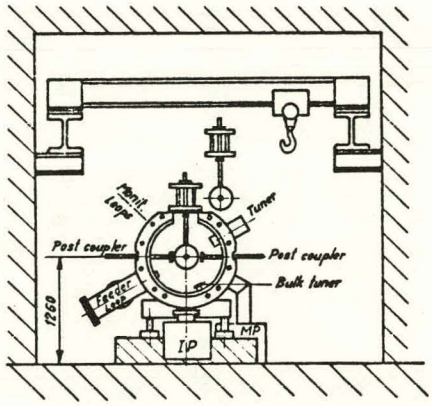


Fig. 2 Cross-section of tank in tunnel (schematic)

Design Philosophy

With more severe demands on both the performance and the reliability of linear accelerators, it is of great importance that the design concept concerning mechanical hardware fulfills as closely as possible the specified needs. The main reason for this is that the criteria for high reliability, on the one hand, and high performance on the other, may easily be in conflict. In such a situation, it is a good design philosophy to follow the rule that the proven "sufficient" is better than the unspecified "best", for both technical and economical reasons. This rule was applied wherever it was possible in the design of all major components.

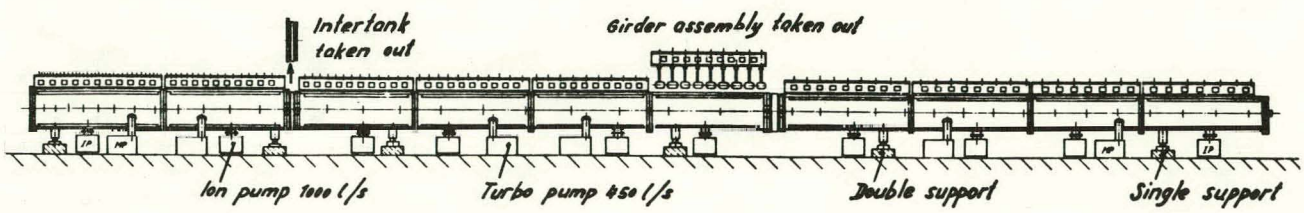


Fig. 1 Side view of the accelerating structure (simplified)

The tanks are made of copper-laminated steel, allowing relatively large tolerances for the inner diameter; the errors in frequency are to be corrected with bulk tuners. This production technique is safer and simpler than the copper plating technique, where the inner diameter has to be machined and polished after welding. The tanks are water cooled via tubes glued on the outside walls, which is quite sufficient for the small heat losses; welding channels for water-cooling on the tank walls would only cause more stresses and make the repair of leaks more difficult.

The drift tubes are of the sealed type with the quadrupoles open to air. This type has been successfully used on many linacs because the degassing rate in the critical region for sparking is relatively small. The low heat dissipation rate makes it possible to cool the drift tubes via the demountable water-cooled stem, thus excluding water leaks inside the tanks.

The vacuum seals made of aluminium wire provide, with few exceptions, the rf contacts. Compared with standard spring contacts, an aluminium vacuum joint, with correct inside flange geometry, makes a more reliable and better rf contact.

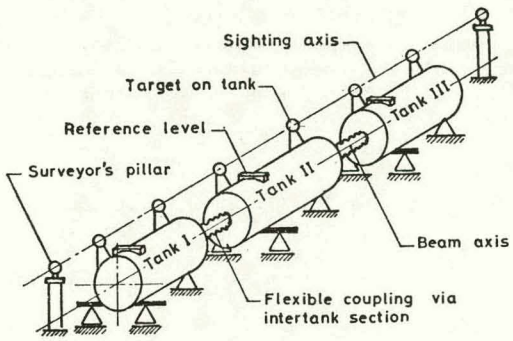


Fig. 3 Support and alignment system for structure

The support system for the tanks is shown in Fig. 3. The main reason this system was chosen is that a tank supported in a statically determinate manner, will not deform or receive additional stresses if the foundation moves. For this support system, flexible intertank sections are essential. These sections being axially compressible allow the tanks to be inserted (or removed for repair) independently into the structure.

For good operational reliability, it was assumed that an easy exchangeability of structural parts, and above all a possibility to measure and quickly correct the alignment of the drift tubes, is more important than trying to achieve long term geometrical stability. This concept resulted in :

a) The girder drift tube concept permitting the introduction of the drift tubes into the tank from the outside, contrary to the present practice on existing linacs, where the drift tubes are installed from the inside. The girder drift tube system offers a quicker, cleaner and safer (irradiation) alignment and maintenance procedure.

b) The drift tube suspension design (Fig. 5) allows the quadrupole positions to be measured directly on the drift tube body and/or on the stem at the top of the girder; it consequently allows the realignment of the drift tubes from the outside, without disturbing the vacuum in the cavities.

c) The external alignment system, which uses the girders to align the drift tubes to the tank and optical targets on the tanks (Fig. 3) to align them to a reference axis parallel to the proton beam. The reference (sighting) axis is defined by surveyor's pillars (monuments) mounted on the tunnel floor.

Tanks and Girders

For production and handling reasons, a tank is divided into several sections of varying lengths. Each section carries a girder.

The tank's section is a cylinder rolled from a copper clad steel sheet(15 mm steel + 2 mm copper), with heavy flanges welded at both ends and several flat steel profiles welded all along the cylinder, providing flat surfaces both at the top and at the bottom of the tank. On top of the tank there is a long slot which is partially cut into the end flanges. The section is sufficiently rigid torsionally and in bending with the slot open. With the girders bolted and dowel-pinned over the slots, the tank will only deform negligibly due to atmospheric pressure load.

Aluminium wire seals are used throughout the structure. The wire is backed by spacers (sheets or plates). These spacers, and not the wire, determine the distance between the sealing surfaces.

The tank manufacturing procedure included heat treatment for stress relief after welding and prior to machining. The final operation was welding the copper inserts to the copper cladding in order to extend the copper surface to the wire seals. Smaller holes for post couplers, piston tuners, etc., were left unlined; the small amount of steel exposed to rf fields increases the losses only slightly. The copper surfaces were neither machined nor ground after welding.

The specified tolerances for the tank diameters were +0.5 mm/-0.0 mm, with roundness tolerances ±2.0 mm in any plane along the length, and ±0.5 mm in planes inside the flanges. The tolerances for perpendicularities were 0.25 mm, for surface flatness 0.1 mm. The surface roughness for copper is 5 μm (R_a). The copper was specified as oxygen free with 99.95% Cu and 0.03% P.

The tank sections are water-cooled via tubes glued on the outside cylinder wall. The gluing compound is an epoxy resin mixture filled with 200% aluminium powder and has a heat conductivity of $\sim$ 0.8 kcal/m-h-^{0}C.

The girder is a closed profile, made of mild steel, with a copper plate bonded to the bottom flange by epoxy resin. This plate completes the copper lining of the cavity. The girder has several functions: it closes the cavity, carries the drift tubes with their adjustment mechanism and acts as a straight edge for the alignment.

The machining tolerances were: straightness <0.2 mm, parallelisms between reference faces 0.1 mm, perpendicularities 0.1 mm, drift tube hole centers ± 0.1 mm, cumulative over the whole length ± 0.25 mm.

The inter-tank section (Fig. 4), comprises two tank covers and cavity with ports for beam diagnostic equipment. Figure 4 does not show the ring used to center and compress the inter-tank section prior to introduction between tanks. The possible movements are: radially ±3 mm, torsionally ±10 mrad, longitudinally ± 4 mm.

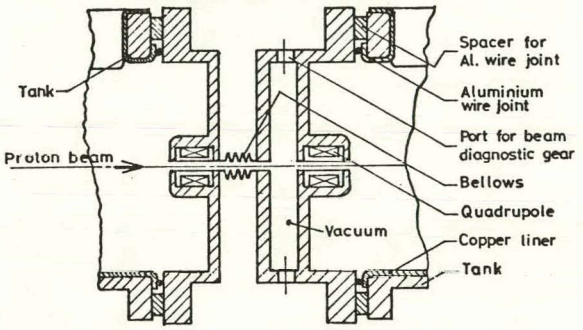


Fig. 4 Inter-tank section

Tank assembly procedure

The first assembly of the tank sections and girders is to determine the thickness of the spacers needed to correctly deform the aluminum wire seals. The second assembly is to measure and possibly correct the alignment of the girders. This finished, and everything reassembled, the relative positions of the girders (empty) concerning alignment, spacing and tilt.

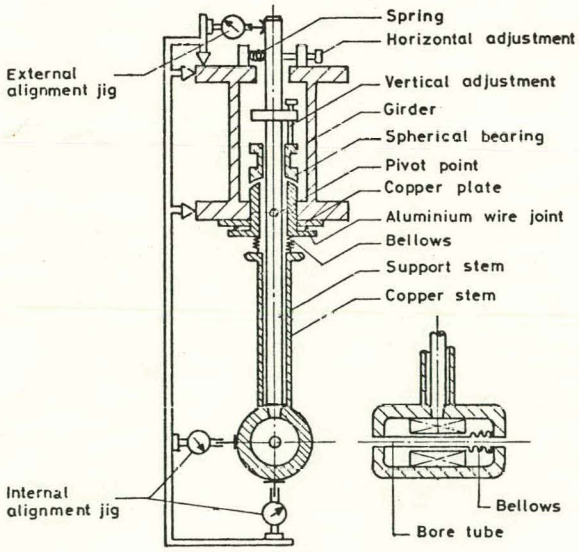


Fig. 5 Drift tube suspension (schematic)

The excessive errors for tilt and alignment are corrected by repositioning the tank sections. The alignment error of the girders on the first tank was negligible. For the two other tanks the errors were up to ± 0.2 mm and 0.25 mrad. These errors were taken into account when the drift tubes were aligned.

Some tank sections showed local indentations of up to 0.25 mm deep on the machined steel surfaces near the welds and unfortunately under the copper inserts in the region of the seal. This was probably caused by insufficient thermal treatment after welding. The problem was solved by placing shims underneath the copper liner. Some sections developed small air leaks (up to 10^{-4} Torr-l/s) on the copper liner welds, which were acceptable.

Drift Tubes

The drift tube body with the stem and bore-tube is a vacuum tight structure, with the inside open to air (Fig. 5). The materials used are: forged oxygen free copper for the body, stainless steel for the bore-tube, standard grade copper for outer stem. The bellows on top of the stem is of special brass. The manufacture of the drift tubes included diamond machining of the copper body (outside surfaces), vacuum furnace brazing, electron beam welding and induction brazing in vacuum. There have been some problems with electron beam welding the stainless steel bore-tube to the copper body of drift tubes for Tank 1. The production errors were up to 0.20 mm on the length of the drift tubes.

Heat generated in the drift tube body is transferred by conduction to the support stem which is closely fitted into the drift tube body. With this cooling method, a typical drift tube in a 2.2×10^{-3} duty cycle operation (about 40 W heat dissipation) would have an average body temperature of 4.3^{0}C above the cooling water temperature, which results in a frequency change of ~15 kHz.

With the suspension method schematically shown in Fig. 5, it is possible to make all movements needed for the positioning of drift tubes except the rotation around the stem axis, which is fixed once the vacuum seal between the drift tube stem and the girder is made. The precision achieved is 0.04 mm in horizontal plane (measured on the drift tube body) and ± 0.01 vertically. In case the drift tube is accidentally knocked, the support stem would jump out of the spherical bearing and automatically fall back in its original position with the precision given above; this protects the stem from damage during assembly. This suspension system has good damping characteristics against unwanted vibrations.

Rf Feed Loop

As shown in Fig. 6, the loop is inside the tank exposed to vacuum. The teflon rf window is placed at a distance $\lambda/2$ from the short circuit end of the loop. The vacuum sealing is made directly on the teflon window by means of lip seals. A hydro-formed bronze bellows on one side and a sliding contact made of a silver plated

helical spring on the other side of the loop, allow the displacement. The unit is cooled by heat conduction into the tank walls. No water cooling is provided.

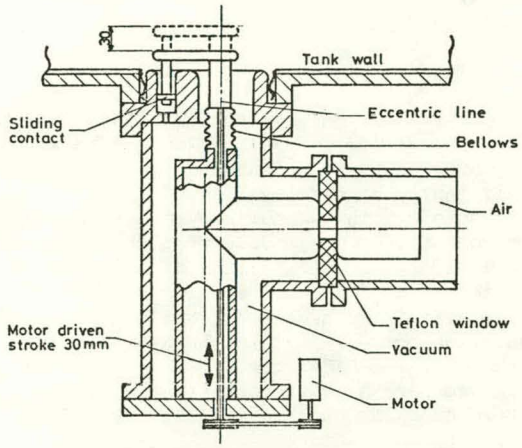


Fig. 6 Rf feed loop (schematic)

The massive 230 mm rf coaxial line is flexibly connected to the unit in order to minimize external forces on the tank.

Water-Cooling System

The closed circuit cooling system for tanks and drift tubes uses ordinary water. This circuit is cooled via a heat exchanger by town water. The total flow rate in the closed circuit is 16 m^3/h with 4.5 bar head loss for a maximum heat load of $\sim$10.3 kW. The nominal water temperature is 20^0C, matching the air temperature in the linac tunnel. The water temperature is controlled to $\pm$ 0.25^0C by a commercial thermostat unit.

Vacuum System

The three cavities form a common vacuum system with a volume of 21 m^3 and 140 m^2 of copper surface. The system includes ten 1000 l/s triode ionization pumps; for roughing, six sets of 450 l/s turbo-molecular pumps backed by 30 m^3/h rotary pumps. The final pressure in the system is $2x10^{-7}$ Torr. It is not significantly affected by the rf or proton beam. Dry nitrogen is used when the cavities are opened to atmospheric pressure. The pump-down time with conditioned tanks is $\sim$90 min to reach a pressure of $2x10^{-6}$ Torr. In a few hours the final pressure is established.

Assembly and Alignment

Each tank was completely assembled, tuned, low energy rf tested, aligned and leak tested in the assembly hall near the linac tunnel. This finished, the tanks were split in the middle (except Tank 1) for transport to the tunnel. There the tanks were reassembled, placed on supports and aligned to the proton beam. Inserting the inter-tank sections was the final operation.

A simplified version of the assembly procedure in the hall is as follows :

a) The bare girders were fitted to the tank and aligned as already described. Straight edges, spirit levels and micrometers are used.

b) The girders were removed from the tank and placed on stands for the drift-tubes to be installed, correctly spaced and aligned to the reference faces on the girders. Special jigs were used for the alignment (Fig. 5) and micrometers for the drift tube spacings.

c) The complete girder assemblies were bolted on the tanks. Then the half drift tubes (on the end covers) were aligned to the drift tubes, and the covers keyed and bolted to the tank. For this alignment an outside caliper jig was used.

d) Finally the optical targets were installed at both ends of the tank. For this, the reference faces on the girders were used once again.

Note that the alignment of a tank has been carried out without optical instruments. The precision that can be achieved using this method is better than 0.1 mm between the drift tubes and about 0.2 mm over the whole length of the tank. This is valid both for the alignment and the spacing of the drift tubes. The final alignment of the structure in the tunnel, where optical methods must be used, reduces the overall alignment precision to $\pm$ 0.25 mm all errors included.

Performance in Operation

The linac became operational at the beginning of September 1978. Since then, there have been no mechanical failures except for some trip-outs caused by the flow switches for the water cooling circuits. These were quickly repaired.

The rf conditioning of the cavities took about one day. Now the cavities can run 20% above nominal field levels without spark breakdowns.

The initial drift tube alignment was sufficiently accurate for a 150 mA beam. However, recent alignment checks show that movements have occurred between the tanks and building as well as between drift tubes and the tanks, none of which warrant realignment at the moment.

References

1) E. Boltezar, H. Malthouse and D. Warner. "A 3-MeV Experimental Proton Linac", Proceedings of the 1968 Proton Linear Accelerator Conference, p. 626, BNL 50120 (1968).

2) New Linac Working Group "Project Study for a 50-MeV Linear Accelerator", CERN/MPS/LINP 73-1 (1973).

3) E. Boltezar, G. Plass, "Specification for Sections for a Linear Accelerator", MPS/LIN/SPEC 75-5 CERN (1975).

4) D.J. Warner, "Accelerating Structure of the CERN New 50-MeV Linac", CERN/PS/LIN 76-5, Chalk River Conference, Canada 1976.

MODULAR DESIGN ASPECTS OF THE FMIT DRIFT TUBE LINAC*

D. J. Liska, R. G. Schamaun, W. Fox, J. A. Frank,† W. Coops,† C. Potter,†
T. Cole, D. Greenwood, H. Norman,† P. Giles, K. Creek,† and D. Clark
Los Alamos Scientific Laboratory
Los Alamos, New Mexico 87545

Summary

The Fusion Materials Irradiation Test (FMIT) Facility drift tube linac may be subject to high levels of activation because of distributed spill of the deuteron beam. The drift tube suspension system will use a modular design to allow repairs and alignment to be made without manned entry into the tanks. Design details are presented that show the resulting high degree of flexibility. Because the accelerator will be installed at the Hanford Engineering Development Laboratory (HEDL) at Richland, Washington, it is desirable that large prefabricated tank assemblies (15 m and 18 m long by 2.5 m diameter) be delivered to the construction site. Stress studies and vacuum sealing tests have influenced the design and these results are given. The rf power dissipation in the tank walls is 1.5 MW and requires a high-capacity cooling system. Finally, rf tuning of the tanks is complicated by the presence of girder slots and open vacuum ports.

Introduction

The FMIT Facility includes one of the world's most powerful linacs, under design by the Accelerator Technology Division of the Los Alamos Scientific Laboratory (LASL). This machine is required to deliver a 3.5-MW continuous-duty deuteron beam onto a lithium target. Neither the machine energy (35 MeV) nor the 100-mA current is unique; however, the combination of the two at continuous duty and with a deuteron beam, represents a major step forward in high-powered, low energy linacs. Other papers in this conference[1,2] deal with special systems requirements and critical beam dynamics considerations involved in working with a potentially activating beam at this power level. Some of the mechanical design aspects of the linac itself that make it especially adaptable to the project needs of high availability and reliability over an operational lifetime of 20 years, will be discussed.

Modular Design Features of FMIT

A major lesson that was learned from the Clinton P. Anderson Meson Physics Facility, (LAMPF) is the advantage of a modular design. This permits not only effective maintenance to be undertaken because of smaller and more manageable units to be handled, but also a significantly higher level of duplication of components. With a modular system an attempt is made to isolate each module from the others in a functional sense even though the operational relationship between all modules is maintained. The net result is higher reliability and less disastrous consequences in the event of major breakdowns. In LAMPF the 805-MHz linac and the rf systems are highly modularized and are classic examples of high reliability and trouble-free operation.

The FMIT is a relatively small facility and its modular design makes it very manageable through the organization of the rf system, the drift tube linac, and the beam transport line. The rf power system consists of 15 identical high-power amplifiers, each of which is broken down into several components that, using air pallets, can be quickly removed for maintenance. Spare units can be moved into position as quickly.[3] The linac drift tubes are supported on 11 separate strongback girders that can be quickly disconnected from the electrical and water services and lifted out of the linac tanks.[4] A similar technique is utilized in the High-Energy Beam Transport (HEBT) lines to the target cells. Here the magnets and associated equipment are mounted on modular carriages that can be unhooked from the overhead supporting structure and can be transported to a maintenance area.[5]

The entire linac girder system and the HEBT clusters form a very suitable arrangement for precision alignment of components. Each module can be aligned in a tooling dock with optical and magnetic-center surveying methods. When installed in the system, each module must then be aligned relative to all others by using the facility alignment monument system. Calibrated positioning guides are used to support the drift tubes on the girders. This feature will allow in situ alignment of the drift tubes, a feature that may prove crucial if precision steering of the deuteron beam becomes necessary.

The final feature of mechanical modular design that is critical to FMIT is the manner in which it provides an option to hands-on maintenance. Modular design certainly makes the system more easily serviced than other construction techniques; however, if the activation levels are as high as some sources predict, no person will be allowed to enter the tanks to service the drift tubes.[6] The modular design is adaptable to remote maintenance procedures, a

*Work performed under the auspices of the U. S. Department of Energy.
†Westinghouse/Hanford Engineering Development Laboratory employee working at the Los Alamos Scientific Laboratory.

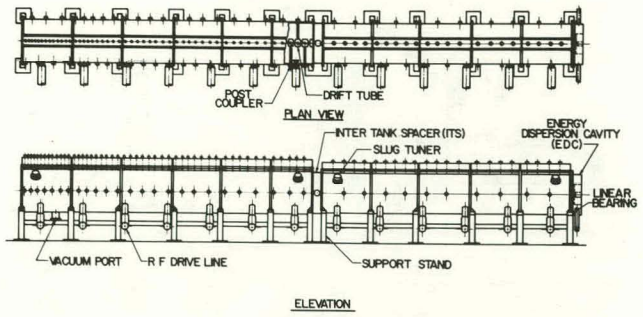


Fig. 1 The FMIT drift-tube linac.

factor that will become more crucial if the allowable limits on personnel radiation exposure are dropped from 5 R/yr to 500 mR/yr.

Mechanical Design Details

Linac tanks

The drift tube linac shown in Fig. 1 consists of two tanks that will be installed as prefabricated assemblies. Tank 1 is 248 cm in diameter and 18 m long; it raises the beam energy from 2 to 20 MeV. Tank 2 is 240 cm in diameter and 15 m long and raises the beam energy to 35 MeV. Drift tube loading of these shells results in an operating frequency of 80 MHz. A cutaway section of a typical tank is shown in Fig. 2. The tank is provided with girder slots that are strengthened by means of forgings that encircle the slots. The drift tube girder assembly is lowered through the slot and the spanner hatch overspans the gap, adds strength, and completes the vacuum seal. Heavy stiffening rings, located every three meters, support the weight of the girders. The tank material is 2.5-cm-thick copper-clad steel and it is important that the stiffening rings do not deflect excessively when the tanks are evacuated. Calculations show that the maximum compressive stresses are under 3000 psi and that the deflection of the stiffening rings is less than 0.1 mm. This assures accurate alignment support for the girder kinematic mounts.

The vacuum ports are open pipes 46 cm in diameter and 46 cm deep. As waveguides-beyond-cutoff, attenuation of the TE_{11} mode at 46 cm is about -31 dB, so only the lightest duty rf grills are provided at the base of the ports to protect the ion pumps against stray fields. Other tank openings are required for the multiple rf drive loops, the post couplers that provide rf stability, and the tuning slugs.

The welded and proof-tested tanks will be installed at HEDL. Transport from the fabricator and installation of tank sections up to 18 m in length is feasible, allowing a significant reduction in on-site assembly work. The tanks, mounted on their supporting structure, will be slipped into the injector end of the building and rolled into position. To prevent damage from overhead work, this installation will be done after the facility roof is in place.

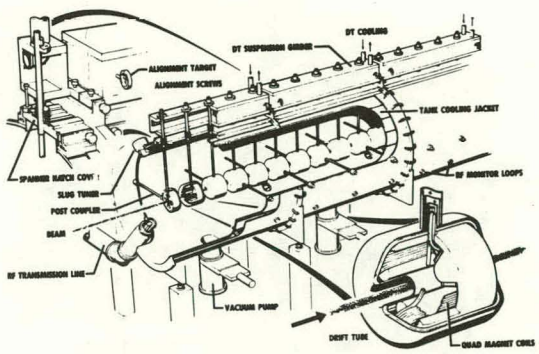


Fig. 2 Modular drift-tube suspension.

Drift tube girders

The use of modules is developed to a high degree in the girder concept for supporting the drift tubes. This technique has been applied by CERN but differs in one major respect from FMIT. The drift tube stems have been isolated from the linac tank by the bellows seen in Fig. 2. Protection of the bellows from the rf fields is by a choke joint and a rf seal, which are presently under development. Use of the bellows prevents distortions of the tanks from disturbing drift tube alignment and this further eliminates the need for precision machining of drift tube mounting sockets in the tank. The girders are supported on kinematic mounts that allow relocation to precise positions following removal for maintenance. All services for the girder are connected to a convenient panel and distributed through the girder by electrical and water manifolds.

An important feature of the alignment system is the provision of calibrated positioning guides on each drift tube stem, which can be accurately postioned with lead screws. Reproducible alignment adjustments can be made to the drift tubes under conditions of operating vacuum and temperature in direct response to beam position error measurements. Of the six degrees of freedom, x, y, z and yaw can be controlled in this way. The remaining degrees of freedom, pitch and roll, are constrained during installation of the quad in the drift-tube housing.

Alignment system

The FMIT alignment system is shown in Fig. 3. Again, this is similar to the CERN concept except that it is carried through from the injector to the target. Alignment of each girder relative to the others is made with an alignment scope mounted on any of a number of

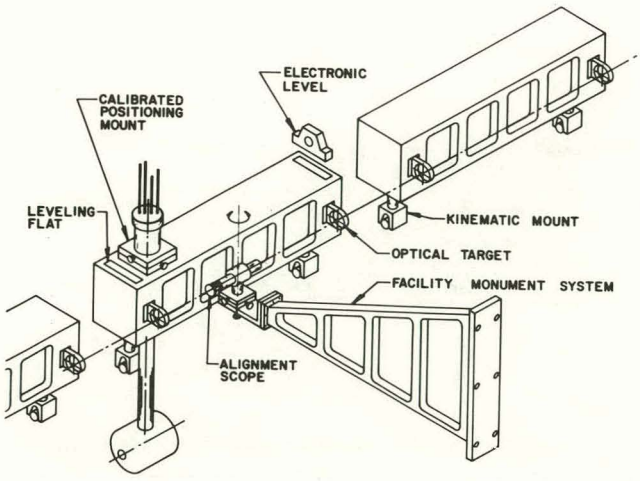


Fig. 3 The FMIT alignment system.

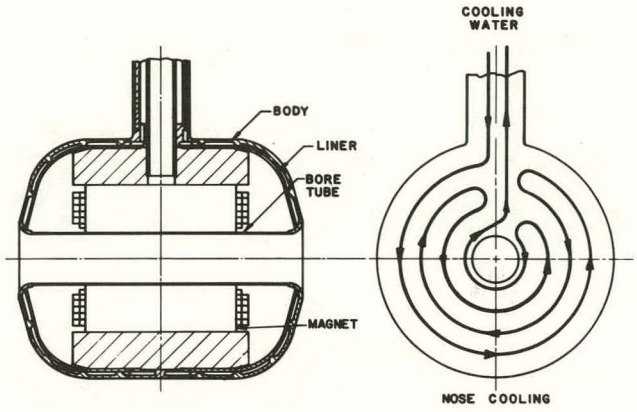


Fig. 4 Quad support and drift-tube shell cooling.

facility-surveyed monument fixtures sighting through transparent targets on each adjustable module. Theodolite stations are provided in the HEBT to turn the line of sight through precise angles. The system shown in Fig. 3 can deal with x, y, pitch, yaw, and roll errors. Roll is measured by an electronic level and z by digital tape. General alignment tolerances in FMIT are ±0.25 mm and ±1 mrad, although low-loss beam transport through the linac may require considerably tighter translational adjustments.

Drift tubes and quads

There are 72 free-standing drift tubes in FMIT and 4 captive in the end walls. All free-standing drift tubes are mounted on the 11 girders and the end-wall quads are all supported by separate, small girder fixtures. Each drift tube carries a quadrupole magnet. Each magnet is wound with a split winding that allows a dipole field component to be generated in the vertical plane by differential excitation of the field coils. This method of horizontal steering produces sextupole field distortion and can only be used in small amounts; another reason that calibrated positioning of the drift tubes has been adopted. Vertical steering at specific quads has been provided by trim coils.

The quads are mounted in cast stainless steel housings (Fig. 4). Castings are used because of the need for complex cooling courses and mechanical stiffness. Firm positioning and support for the quad is provided by the girth ring casting. The tapered drift tube shells are derived from SUPERFISH optimization studies and result in high rf power efficiency. Type 316L stainless steel was used because it is resistant to permeability changes during fabrication and because it has good weldability. After the shells are fabricated, they are copper plated before they are installed and aligned in the girders. The PARMILA beam dynamics studies have shown that a "constant-length, constant strength" concept can be used to reduce the number of quads and drift tubes that are required. Three quads and five shell models can be used to equip the FMIT girders. Those combinations are listed in Table I.

Essential linac peripherals

The peripheral attachments to the drift tube linac tanks include the post couplers, slug tuners, rf drive loops, intertank spacer, and energy dispersion cavity (Figs. 1 and 2). It will be noted that rf domes are absent; instead flat-plane rf windows were located at the 1/8 wavelength position from the loop (47 cm) so that the window will be exposed to high but not maximum fields during transients to better cope with multipactoring.

The intertank spacer provides a one-cell drift space for diagnostic purposes at the 20-MeV point. The quads in the drift space are supported by a yoke, which in turn is attached to an externally mounted small girder. This allows the modular external alignment system to be carried from Tank 1 to Tank 2 as well as to permit effective maintenance without tank disassembly and entry. The energy dispersion cavity (EDC) is attached to the downstream end of Tank 2. It exposes the 35-MeV beam to a sinusoidally varying voltage of ±500 kV at a beat frequency of a few megaHertz. This effectively disperses the energy of the micropulses by 1 MeV to ease the thermal stresses applied to the lithium target. In addition to its effect on beam dynamics, the EDC also provides the downstream pressure bulkhead for Tank 2.

Vacuum and cooling

Most vacuum seals on FMIT are conventional aluminum wire. The spanner hatch seals however are 7 m long and in addition they are exposed to thermal as well as rolling stresses caused by spanner deflection under vacuum. Preliminary

TABLE I

SUMMARY OF FMIT DRIFT TUBE AND QUADRUPOLE MAGNET PARAMETERS

Drift Tube						Quadrupole Magnet	
Drift Tube Number	Bore Diam (cm)	Outside Diam (cm)	Face Angle (degrees)	Length min/max (cm)	Type	Gradient (G/cm)	Approx. Power (kW)
1-15	5.0	42.0	4	14.24/20.77	A	2750	6.6
16-25	6.0	38.0	8	22.35/27.60	B	1885	7.7
26-37	6.0	38.0	12	28.48/34.53	B	1885	7.7
38-51	6.0	38.0	15	35.69/42.12	B	1885	7.7
53-73	8.0	38.0	15	44.72/53.46	C	990	9.4

model tests on all important seals, including the spanner hatch, have been completed and full scale testing of the spanner hatch seal is continuing.

The tanks and drift tubes are temperature controlled to dissipate about 5 kW/m^2 at 31^{o}±0.3^{o}C, by a servo-controlled cooling system that mixes 85% mainstream water from a heat exchanger with 15% water from heaters and chillers. This system has been simulated and it readily controls the major transient resulting from loss of 1.5 MW of rf in the copper. A time constant of about one minute results from thermal lag in the tanks and the response of the heat exchanger. The tanks are longitudinally channel cooled by counterflowing the coolant over channel lengths as great as 18 m in Tank 1. A 3^{o}C temperature rise in the channel is allowed with full rf power dissipation.

Radio-frequency tuning

The drift tube linac tanks must resonate at 80 MHz when fully loaded with the drift-tube clusters. The presence of the girder slots and the open vacuum ports lowers the resonant frequency by about 250 kHz. The post couplers and centered tuning slugs raise the frequency by about 25 kHz. It is essential that the tanks be fabricated low in frequency. A tuning bar area of 50-70 cm^2 is required to tune the tanks. These must be cut by trial and error with the tanks under partial vacuum. Once tuned, the resonance control system and slug tuners will only be able to control the frequency by ±6 kHz. The required fine balance of mechanical adjustments will be verified by the construction and test of reduced-scale rf models.

Conclusions

The FMIT drift tube linac is moving from conception into preliminary design. To solve the problems with maintenance of potentially activated components, as well as to provide for precision alignment, a modular design system has been adopted. Alignment can be checked externally because all components are mounted on girders or carriages outside the vacuum and rf envelopes. Calibrated positioning fixtures on the drift tube stems allow reproducible adjustments of individual drift tubes in response to beam dynamics measurements. In principle, it may be possible to steer a low-loss beam through FMIT without the use of steering magnets in the drift tube linac portion. This is a decided advantage, because packaging restrictions prevent the use of discrete steering elements and only allow minor steering, using trim coils or differential excitation of the quadrupole field windings with undesirable sextupole side effects. Unusual fabrication techniques are required in this accelerator because the design is being done by LASL for HEDL, fabrication is by U. S. industry, and installation will be by HEDL personnel at Richland, Washington.

References

1. E. L. Kemp, D. J. Liska and M. D. Machalek, "The Fusion Materials Irradiation Test (FMIT) Accelerator," proceedings of this conference.

2. G. P. Boicourt and R. A. Jameson, "A Statistical Approach to the Estimation of Beam Spill," proceedings of this conference.

3. M. V. Fazio, H. P. Johnson and D. M. Riggin, "Developments on the rf System for the Fusion Materials Irradiation Test Facility Accelerator," proceedings of this conference.

4. D. Liska, R. G. Schamaun, C. Potter, C. Fuller, D. Clark, D. Greenwood and J. A. Frank, "Design of the Accelerating Structures for FMIT," IEEE Trans. Nucl. Sci. NS-26, No. 3, 3052 (June 1979).

5. K. E. Melson , J. A. Farrell and D. J. Liska, "A High-Energy Beam Transport System for the Hanford FMIT Linear Accelerator," proceedings of this conference.

6. Kapchinskii, et al., "Linear Ion Accelerator with Spatially Homogeneous Strong Focusing," Nuclear Experimental Techniques, UDC 621.384.64.

Discussion

Grand, BNL: What is the maximum energy spread you expect to have with the energy dispersion cavity, and what does it do to the transport line?

Liska: We expect to swing the cavity plus or minus 750 kilovolts.

Grand: And you have to add to that the energy spread in the beam due to the linac. So you end up having 1 MeV spread. What does that do to the transport in the bends?

Liska: Yes, that's right. But the transport system is quite achromatic - it has been designed to handle this sort of a spread - actually 1.5 MeV spread has been designed into the HEBT. The spread of the beam is very important, as Jameson has shown. If it is not taken into account properly, then very strong bimodal shaping of the dispersion can take place, which can do more harm to the target than no dispersion. But if the linac energy spread is properly taken into account, then quite good flattening of that energy spread can be achieved.

Miller, SLAC: Do you anticipate wobbling individual quadrupole excitations in order to check the alignment of each quad with the beam?

Liska: Yes, I expect that one technique we will use to check alignment will be individual operation of the quads to check the steering effects that this might cause. I didn't point it out, but we do have on our girders what amounts to a panel in which all the utilities are delivered, including in effect, a huge Burndy connector on each quad, which would allow us to individually excite it to check this sort of thing.

MECHANICAL DESIGN CONSIDERATIONS IN FMIT RFQ DEVELOPMENT*

C. W. Fuller, S. W. Williams,† and J. M. Potter
Los Alamos Scientific Laboratory
Los Alamos, New Mexico 87545

Summary

The mechanical features of the several rf structures that have been made to test the theory of the radio-frequency quadrupole (RFQ), are briefly described. A 425-MHz structure, designed as a proof-of-principle (POP) test, is described in detail. Methods of coupling rf power into the structure, temperature control, tuning, and mode separation are discussed. The methods and setup of numerical control machinery used to generate the critical geometry surrounding the RFQ aperture are detailed fully.

Finally, the applicability of experience and methods gained from the high-frequency (425-MHz) RFQ development to the 80-MHz prototype and ultimate Fusion Materials Irradiation Test (FMIT) machine are mentioned.

Cold Test RFQ Structures

Recent experiments with RFQ structures by the Accelerator Technology Division, Los Alamos Scientific Laboratory (LASL), have focused on the four-vane geometry. One reason for this selection over other geometries is the four-vane's comparative ease of manufacture, considering the close mechanical tolerances that are required.

The first four-vane cavity was a length of aluminum pipe, 12-in diameter, 40-in long. Vanes were attached inside at 90° intervals. Their penetration into the cavity could be varied using spacers, and several different pole tips were machined and attached (Fig. 1).

This cavity was useful in determining which modes could be excited, how they overlapped, and in suggesting methods of tuning the cavity and separating and suppressing unwanted modes. The hardware was soon outgrown and a better cold model, made to closer mechanical tolerances, was needed.

For low-power testing a four-pipe, or cloverleaf model (Fig. 2), was designed around 4-in o.d. stock aluminum tubing and other readily available materials. Problems caused by wide manufacturing tolerances for such tubing (roundness, straightness, etc.) were avoided by machining reference surfaces along the length and at the ends of the tubes. The end plates were designed and machined to register the tubes and other parts accurately during welding of the

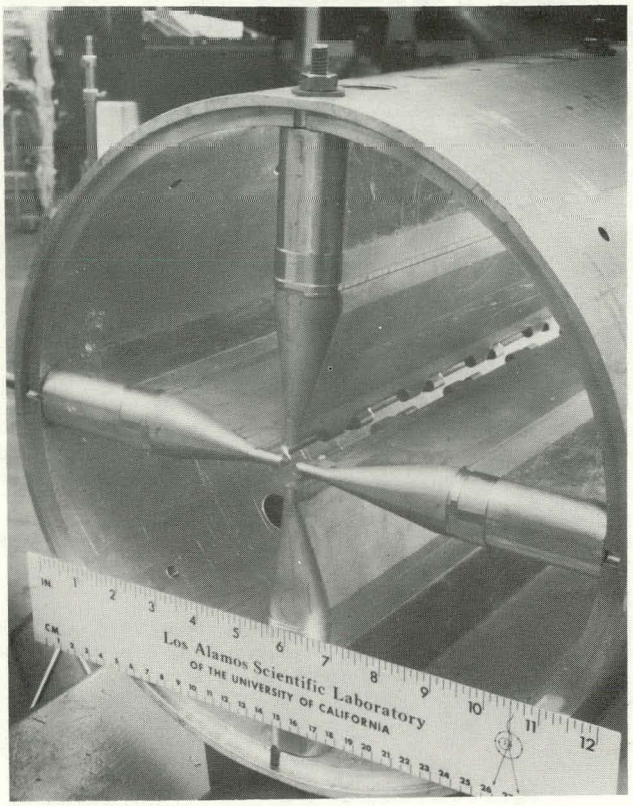


Fig. 1 Four-vane structure.

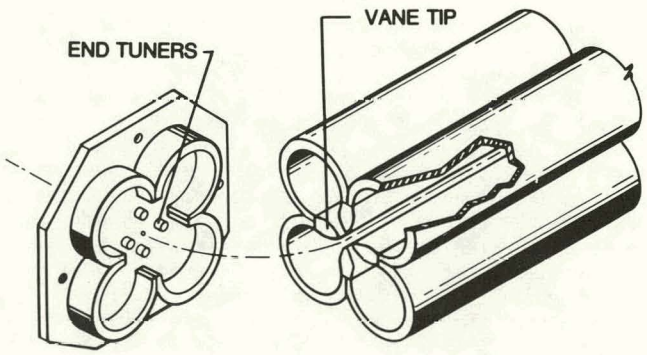


Fig. 2 Four-pipe structure.

*Work performed under the auspices of the U. S. Department of Energy.
†Westinghouse/Hanford Engineering Development Laboratory employee working at the Los Alamos Scientific Laboratory.

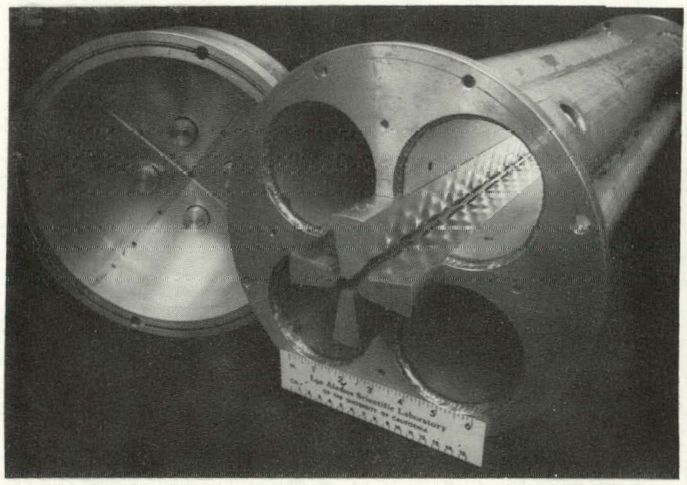


Fig. 3 Four-pipe cavity with vanes installed.

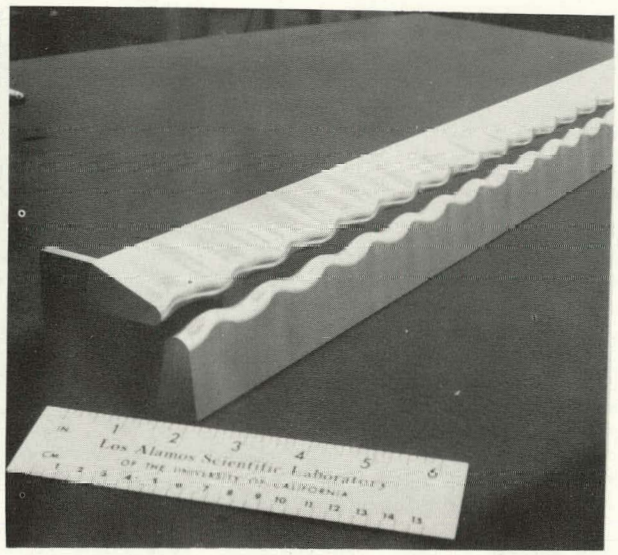


Fig. 4 Constant-$\beta\lambda$ modulated vanes.

assembly. Intermittent welds were used along the length to minimize distortion. A center hole was then bored through the axis of the cavity, forming straight, parallel, accurately machined surfaces on which to mount the electrodes. The concept of the center bore to form a machined seat for the vane tips continues to be important in designs of future RFQ structures.

A set of four constant-$\beta\lambda$, modulated vanes was made for this cavity (Figs. 3 and 4) using a numerically controlled three-axis milling machine. The test results were very encouraging and were reported by Potter and Williams.[1]

In these cold test models, cooling and vacuum were not factors because the experiments were at atmosphere and at low rf power. Further, at low power, the quality of rf surfaces and the contact between parts were not critical. Now, however, a POP test structure through which a beam will be accelerated is being designed. This is the next step in the development of an 80-MHz RFQ for the FMIT accelerator (a full-scale prototype will be constructed and installed at LASL).

RFQ Proof-of-Principle Cavity

Copper tubing, 6.125-in o.d. by 0.192-in wall, was chosen as the main structural element for the POP four-vane cavity (Fig. 5). Square ends are brazed to the tube, then accurately machined and faced to length. The ends form three mutually perpendicular planes; two are parallel to, and equidistant from, the cavity center line. In this form, the part is easily indexed and clamped in jig boring and other machine tools, where dowel pin and screw holes can be accurately located and drilled.

The vane bases are machined from solid OFHC copper. Slots are made to receive 0.25-in o.d. copper refrigerator tubing for cooling water. The bases, including water tubes, are located in the cavity with dowels and screws and the whole assembly is then furnace brazed.

Next, a 2.250-in diameter center hole is bored through the cavity on a horizontal mill (Fig. 6). This bore becomes a datum surface for subsequent machining operations. Dowel holes and screw holes for the vane tips are jig bored with their locations measured relative to the squared ends.

Next, rf coupling slots are machined into each of the cavity's four chambers at 45° to the axis. Finally, the square ends are rounded and the entire outside of the cavity cleaned up to 6.095-in diameter.

The RFQ is suspended inside another cylindrical rf cavity by means of two copper disks (Fig. 5). Contact fingers connect the inner surface of the outer cavity through the disks to the outer surface of the RFQ, forming a coaxial line terminated at each end by an electrical short circuit. The outer cavity, or manifold tank, is connected to vacuum and cooling water services.

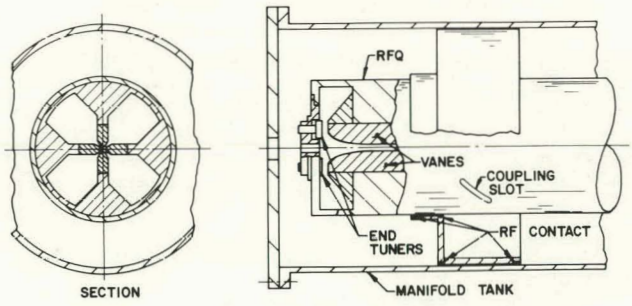


Fig. 5 The RFQ POP test cavity.

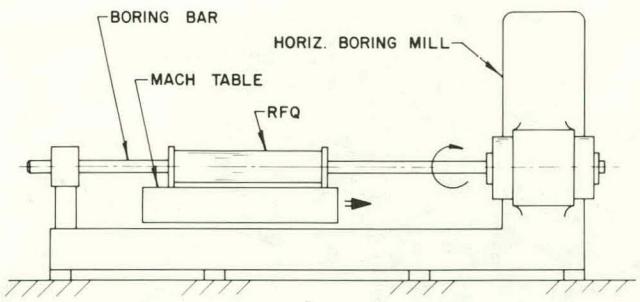


Fig. 6 Center-bore machining.

The rf power is fed through a waveguide to the manifold tank. The magnetic field couples through the angled slots in the RFQ side walls to magnetic fields inside the RFQ. Power is uniformly distributed to all four chambers of the RFQ.[2]

Each end of the cavity is closed by a disk assembly containing four small tuning slugs. The slugs vary the capacitance between the vane ends and the cavity and they are used to adjust the electrical field distribution along the axis of the RFQ.

Vane Tip Numerical Control Machining

With properly shaped vanes, the fields in the RFQ are perturbed to produce a longitudinal component of the electric field. This longitudinal component bunches and accelerates the beam in preparation for its injection into a drift-tube linac. The correct vane shape is necessary to obtain the proper field distribution for accelerating the beam with minimum losses. The shape is described by an equipotential surface in the electrostatic solution for the structure.[3]

Figure 7 illustrates sections from one of four vanes to be made for the POP test cavity. Each diagram represents 10 cells; there are 165 cells in the vane design. The first segment shown (Fig. 7a) is the radial-matching section. In this region, the beam is exposed to gradually increasing radial-focusing forces formed by the decreasing aperture radius. Near the center of the RFQ, the vanes have the appearance of those in Fig. 7b. The modulations are about 15% of their final value. In this region, the beam is bunched and is radially focused with little longitudinal acceleration. Figure 7c shows the vane near the exit of the RFQ. The modulation reaches its maximum amplitude and most of the beam acceleration occurs around this exit region.

Fabrication of the vanes incorporates an EX-CELL-O, three-axis, numerically controlled, vertical mill (Fig. 8). Normally, this machine reads its control data from a punched paper tape that has a capacity of about 800 data blocks. The vanes require approximately 20,000 data blocks for an adequate description. Equipment and software exist for converting the mill control system to use cassette magnetic tapes instead of paper tape. This scheme reduces the volume of the data set to a few cassette tapes and simplifies handling.

A spherical tool is used to cut the vanes. The path that the tool center follows is in the xy plane (Fig. 9) and is constrained to consist only of straight lines and circular arcs. As each cross section is cut, the machine table moves an increment Δz along the vane's longitudinal axis. The process is slow (Δz = 0.020 inches), moving 1-2 inches per hour in the z direction.

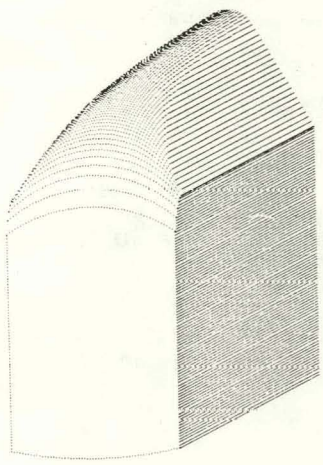


Fig. 7a Cells 1-10.

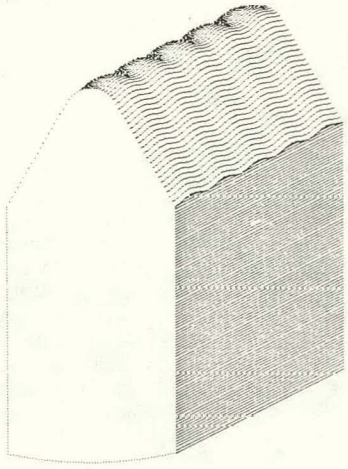


Fig. 7b Cells 101-110.

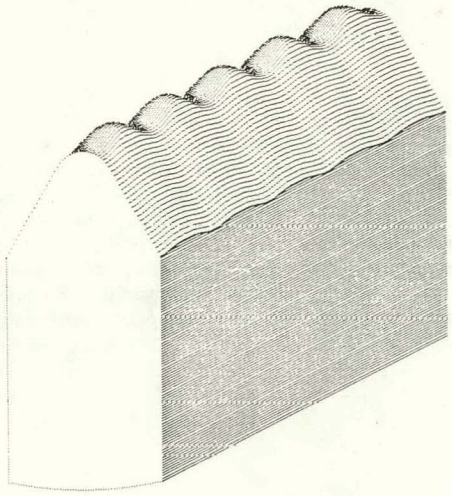


Fig. 7c Cells 151-160.

Fig. 7 Segments of POP vanes.

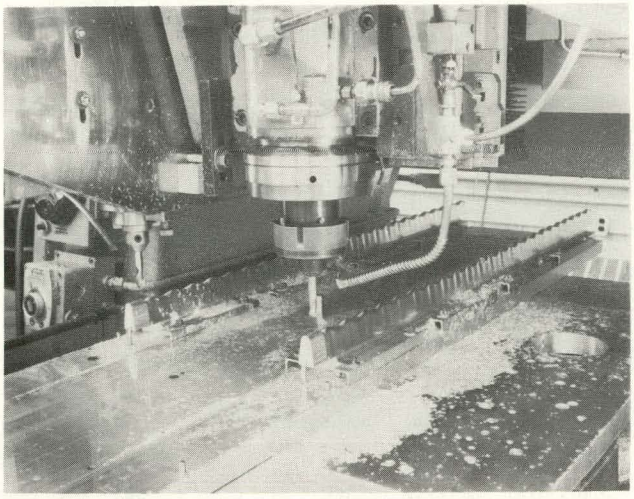


Fig. 8 Vane machining operation.

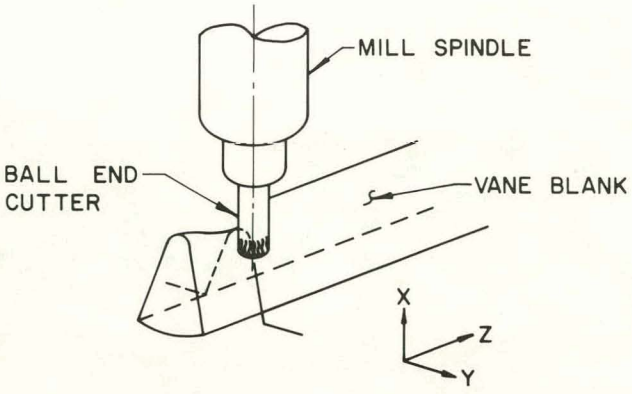


Fig. 9 Cutter path.

If the radius of the tool were zero, the tool path would be identical to the cross section of the vane. However, with a finite tool radius, the cutting path of the tool is not always in the same plane that the tool travels (Fig. 10). The deviation depends on both the cutter radius and the slope of the vane. The program that computes the machine instructions compensates for this error.

80-MHz RFQ

The 80-MHz RFQ is still evolving. It has nearly doubled in length from 3.5 m a year ago, to 6 m now, to keep transverse emittance growth small. Several methods of coupling rf power from another cavity into the RFQ have been studied. A very promising scheme uses a concentric outer coaxial tank operating in the TEM mode. Magnetic fields in the coaxial tank cross-couple to fields in the RFQ through angled slots, as in the POP test cavity.

At least one mechanical technique which was developed in the high-frequency RFQ work will be useful in building an 80-MHz system; that is, the precision machining of the vane electrodes. It is expected that tolerances in the critical aperture of the RFQ will scale with the frequency; i.e., larger structures should accommodate more generous machining tolerances. Computer studies are planned to determine the effect of machining tolerances on beam dynamics.

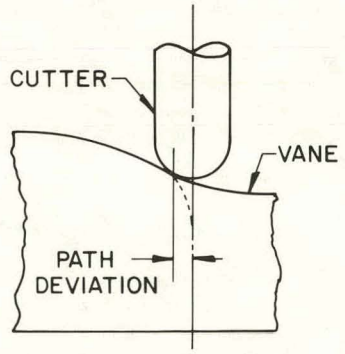


Fig. 10 Cutter-path error.

Acknowledgments

We thank E. Riggs, R. Larson, G. Anderson, O. Maier and others of the LASL Shops Department for their very important contributions.

References

1. J. M. Potter, S. W. Williams, F. J. Humphry and G. W. Rodenz, "Radio-Frequency Quadrupole Accelerating Structure Research at Los Alamos," IEEE Trans. Nucl. Sci. NS-26, No. 3, 3745 (June 1979).
2. J. M. Potter, "An RF Power Manifold for the RFQ Linear Accelerator," proceedings this conference.
3. R. H. Stokes, K. R. Crandall, J. E. Stovall, and D. A. Swenson, "RF Quadrupole Beam Dynamics," IEEE Trans. Nucl. Science NS-26, No. 3, 3469 (June 1979).

Discussion

Mittag, Karlsruhe: Do you expect any problems with the brazed rf joints?

Fuller: Probably not with this proof of principle test. I think the currents may not be so high that we would have trouble.

Meads, Brubeck: What is the ratio of your machining tolerance to the aperture of the P.O.P. structure?

Fuller: The milling machine has, of course, finite accuracy, around ± .0002. Other sources of machining errors are holding fixtures and the behavior of the vane material under tool pressure. I expect that we'll be able to hold to within 2 or 3 thousandths (± .002 or .003) of the desired dimensions in the aperture region. The aperture diameter at the smallest point is about 100 thousandths (.100) so that's about 3%.

THIS PAGE

WAS INTENTIONALLY

LEFT BLANK

Section VIII
Ion Sources and Preaccelerators

THIS PAGE

WAS INTENTIONALLY

LEFT BLANK

1979 LINEAR ACCELERATOR CONFERENCE

RECENT PROGRESS IN ION SOURCES AND PREACCELERATORS*

David J. Clark
Lawrence Berkeley Laboratory
Berkeley, California

Summary

Recent progress in ion sources is reviewed. The types of sources discussed include positive and negative proton and deuteron sources developed for conventional preaccelerators and for neutral beam applications. Positive heavy ion sources for conventional linacs and for induction linacs are included. Negative heavy ion sources are used for tandem electrostatic accelerators. Positive and negative polarized ion sources for protons and deuterons inject cyclotrons, tandems and linacs. Some recent preaccelerator designs are summarized.

Introduction

Ion source development of many different types of sources has been undertaken by groups throughout the world. Groups working on each type of source generally have good communication with each other, but it is also valuable to have interaction between research groups working on different source types. For example, the development of the multiaperture sources in the ion engine field and for neutral beams offers useful computer methods and extractor designs for high current injectors for particle physics and heavy ion fusion. The techniques developed in experimental plasma physics are also valuable for ion sources. The contact ionization sources developed in plasma studies and also for ion engines are useful for negative heavy ion sources and for high current induction linac injection. Also, the magnetic bucket confinement system for plasmas is finding applications in high current sources for neutral beam formation. So, a healthy interaction between various source people, with those in plasma science, is needed.

The listing and description of ion sources is such a large field that it would take a book to do it justice, such as the one by Valyi.[1] Recent reviews have been given by Osher[2] on many light and heavy ion sources, by Curtis[3] on duoplasmatrons for proton linacs, by Middleton[4] on negative heavy ion sources, by Clark[5] on heavy ion sources, by Clark and Seliger[6] on sources for heavy ion fusion, by Haeberli[7] and Glavish[8] on polarized ion sources, and by Kunkel[9] on neutral beams for fusion. The present review will concentrate on sources developed for particle accelerators and sources developed for other fields which may have useful applications in particle accelerators. In such a large field of development, only a few typical examples can be chosen to illustrate recent developments in each source area.

Positive Light Ion Sources

Positive sources for accelerators

Sources for conventional linacs, summarized by Curtis,[3] have traditionally been duoplasmatrons producing up to 0.5A of proton current, with a normalized emittance after the column of 0.5π cm-mrad, at a duty factor of 10^{-3}. Recently, duoplasmatrons have been developed for dc operation for several applications.

Los Alamos has tested an annular duoplasmatron[10] which produces a 250-mA dc beam of hydrogen ions at 125 keV, as a prototype for the Intense Neutron Source (INS) of tritium bombarding a deuterium gas jet. The annular design was chosen because it could produce a large area plasma, and could be easily cooled for long lifetime. The emittance was found to be large, perhaps due to the radial arc contribution to the transverse ion velocity. A Pierce column was used with a 6.4 cm diameter extraction iris. The authors suggest that a cusp-field source would satisfy the requirements of simplicity, uniform plasma and low emittance, and a modified Pierce column is preferred.

Chalk River has developed a dc duoplasmatron[11] for the Fast Intense Neutron Source (FINS) project, which will use a 25-mA, 300-keV deuterium beam on a rotating tritium-titanium target. The source uses a ceramic plasma expansion cup to reduce the emittance. Beam intensity is 44 mA of hydrogen ions at 74 kV, with 73% protons and a normalized emittance of 0.1π cm-mrad.

The duopigatron has also been developed for dc beams in the 100-mA range. J. Osher of the Lawrence Livermore Laboratory is developing a dc duopigatron source for 150 mA of 400-keV D^+ beams to bombard a rotating tritium target for the Rotating Target Neutron Source-II (RTNS-II).[12] The source is one of the MATS series, which is scaled down from a 1 A injector[13] for the Baseball fusion experiment, shown in Fig. 1. It uses a multi-aperture (round holes) extraction system. The 3-grid plate accel-decel arrangement blocks secondary electron flow and increases extraction voltage. The beam is analyzed by a 90^o magnet in the high voltage terminal to separate the D^+ from molecular species. A solenoid lens then matches the beam to a large aperture (10-cm diameter), low gradient (15-kV/cm) column. Complete space charge neutralization is assumed in the terminal and in the ground transport. The per-

*Work supported by U.S. Department of Energy.

formance has been consistent with design expectation. The source has produced 104 mA of D^+ at 22.5 keV and 87 mA of D^+ on target at 300 keV. Normalized emittance is 0.1 π cm-mrad.

A duopigatron is being developed by Chalk River[11] for a 50-keV 500-mA dc proton beam, as an injector for a 1-GeV, 300-mA fissile fuel breeder accelerator. It is based on an Oak Ridge design with accel-decel extraction electrodes using a multi-aperture array of circular holes. Up to 450-mA total hydrogen ion current has been extracted from the source.

The SIN group in Zurich is building a new injector for its ring cyclotron meson factory. The design[14] calls for a 40-keV, 30-mA dc proton source in a 860-kV terminal. The source, Fig. 2, is a scaled down version of a fusion research design built at Culham using magnetic bucket confinement and a 4 electrode extraction system. Figure 3 shows the terminal, with isolation of the source from the column as at Livermore.[12] This isolation provides separation of H^+ from molecular ions before the column, good vacuum in the column, beam matching and diagnostics in the terminal. Initial source tests show 35-mA total dc current at 40 keV.

At LASL, a dc source[15] is being designed for the Fusion Materials Irradiation Test Facility (FMIT). The requirement is 125 mA of D^+ at 100 keV, to accelerate 100 mA of B^+ to 35 MeV. The source is based on the single aperture duopigatron, SARA designed by Osher of Livermore, which will provide the necessary current with an excellent normalized emittance of 0.02π cm-mrad. A total ion current of 100 mA at 100 keV has been obtained. A cusp field is being tested, based on a Culham design.

High current sources for neutral beams

The use of multiampere neutral hydrogen beams has proven very successful in heating plasmas for magnetic fusion experiments.[9] A neutral beam injection line[9] is shown in Fig. 4. The first component in the system is a multiampere positive ion source. The development of sources for these systems has provided many useful ideas for accelerator sources.

Present Berkeley sources produce 65-A beam currents in an extraction area of 10 x 40 cm^2 at 120 keV, with 5-sec pulses. Filament and arc currents are each 1000 A. A recent Berkeley source[16] is shown in Figs. 5 and 6. It is cubical in shape, 24 cm on a side. It uses hot tungsten filaments to generate plasma, and line-cusp fields for confinement. Filaments are operated space charge limited for stable pulsed operation. Arc current is 500 A and plasma density is 400 mA/cm^2 at the extraction grid. The line-cusp version gives higher D^+ fraction of 75%, compared to 65% without cusps. Future requirements include longer pulses of up to 30 sec, where cathode life is a problem, so lanthanum hexaboride and oxide cathodes are being investigated.

At Oak Ridge a magnetic bucket confinement system is used in the plasma expansion section of their duopigatron source,[9] (Fig. 7). The buckets damp out plasma fluctuations, spread the plasma more uniformly over the extraction electrode and give high atomic ion fractions; up to 80%. This model produces 60 A at 40 kV for 300-ms pulses.

Extraction systems have been extensively developed for these high current sources. Accel-decel systems are used to block electrons and increase extraction voltage. Multiaperture arrays of either slots, or round holes, are used to produce the multiampere currents required. A Berkeley slotted extractor[9] is shown in Fig. 8. The calculation of beam trajectories through this extractor[9] for 120 keV is shown in Fig. 9. It uses a computer code which iterates the trajectory calculation in the presence of space charge to obtain electrode shapes giving minimum beam divergence. The first electrode has a Pierce shape for initial electrostatic focusing. A fourth electrode is added to a 3-electrode, 20-keV extractor, to give 120 keV.

Positive Heavy Ion Sources

Present sources

In present positive heavy ion accelerators such as linacs and cyclotrons, the principal source used is the Penning Ion Gauge (PIG) type. Since these sources have been reviewed previously,[5] only brief mention of them will be made here. They produce microamp to milliamp beams of all elements with charge states up to about Xe^{12+}, at duty factors up to 100%. Since they are still the best high intensity source of heavy ions, they will be used in several new heavy ion accelerators, such as the new SuperHILAC injector at Berkeley, the superconducting cyclotrons at Michigan State University and the GANIL cyclotrons in France. Active development programs are underway at these labs.

At the UNILAC in West Germany, extensive development has been done on the duoplasmatron[5] for heavy ions at high duty factors of 30-100%. Great improvements were made in its high charge state output, but it did not equal the PIG at the high charge states and for solid material feed reliability. The duoplasmatron has been tested at several other labs[5,6] for low duty factor operation with low charge states.

The Hughes Research Labs have developed a high brightness Penning source[17] for 30 mA of Xe^{1+} using a single extraction aperture, and 100 mA with multiapertures. It is shown in Fig. 10. It uses a diverging magnetic field of tens of Gauss and permanent magnets around the outside. The extractor has a Pierce geometry. It will be used with the Argonne National Lab 1.5-MV accelerating column for ion beam fusion injector development.[18] A calculation of beam trajectories in this column, including space charge, is shown in Fig. 11. This 3-gap configuration would accelerate 100 mA of Xe^{1+} to 1.5 MeV.

A source for 60 mA of Xe^{1+} was built at Berkeley.[19] It is shown in Fig. 12. It is based on the original Berkeley hot filament plasma generator of Ehlers[20] and the multiaperture extraction system of Osher[12] using a round hole array in an accel-decel geometry. A 30-mA beam at 22 keV was transported 1 meter with a magnetic quadrupole triplet, and the normalized emittance was 0.03π cm-mrad. The beam was almost completely space charge neutralized by residual gas. Currents up to 60 mA have been measured through a 500-kV accelerating column.

Advanced high charge state heavy ion sources

If a source could produce charge states twice as high as the PIG, the energy from a cyclotron would be four times higher, and linacs could be designed with half the present length for a given energy. Progress has been made toward this goal in the past few years.[5]

The Electron Cyclotron Resonance (ECR) source has shown great promise in this area. The most advanced version,[21] called SuperMAFIOS B, is shown in Fig. 13. It is a two stage plasma device. Plasma is created in the first stage at high pressure (10^{-3} Torr) by microwave power at the electron cyclotron resonance frequency. It diffuses to the second stage at better vacuum (10^{-7} Torr), where high charge states are created by a second microwave system. Mirror and sextupole magnetic fields confine the plasma in the second stage. Operating power is 3 MW. Charge states such as N^{7+}, Ar^{12+} and Xe^{26+} have been observed at 10^{12}-10^{10} per second intensities, much higher than those of a PIG. Much interest has developed in this type of source, particularly in Europe. A small version, MicroMAFIOS,[21] has just begun operation at Grenoble. It is shown in Fig. 14. It uses a simpler single microwave frequency system and a permanent magnet sextupole to save power. ECR sources are being built at cyclotrons in Louvain, Belgium,[22] and Karlsruhe, Germany.[23]

The Electron Beam Ion Source (EBIS) is another advanced high charge state source with promising results. This source was pioneered by Donets at Dubna[24] and later developed by other groups. The CRYEBIS[25] source at Orsay, France is shown schematically in Fig. 15. An electron gun injects beam into a series of drift tubes in a superconducting solenoid magnet, where it ionizes a pulse of gas. The ions are confined radially by the electron beam and axially by potential barriers at the end drift tubes. When the high charge states have been built up, a voltage ramp is put on the drift tubes to extract the ions. The Orsay electron gun is shown in Fig. 16. The electron beam is compressed electrostatically and magnetically. Charge states of up to Kr^{34+} and Xe^{44+} have been reported. The accumulation time of only 5 ms is much shorter than expected, likely due to reduced electron beam diameter from neutralization. This means that high repetition rates could be used and duty factors of about 50% could be obtained by storing and extracting for equal times. Average beam currents would be comparable to those of ECR sources, and higher for the heavier ions. The duty factor is ideally matched to a synchrotron. CRYEBIS will be installed on the Saturne II synchrotron in France. An EBIS has also been used on a synchrotron at Dubna.[24] The CRYEBIS will also be used to ionize a polarized atomic hydrogen beam entering through a hole in the cathode. It will be a very high efficiency ionizer compared to those mentioned in the later section on "Polarized Ion Sources."

Other methods of producing high charge state heavy ions, such as lasers and exploding wires, have very low duty factors. The use of a 300-500-keV proton beam, instead of an electron beam, in a modification of the EBIS called the PROBIS has been suggested.[26] The motivation is that the ionization cross-sections are higher. However, the radial electrostatic confinement disappears with protons, leaving only magnetic confinement.

Large area contact ionization source

One of the principal candidates for heavy ion fusion applications is a linear induction accelerator. This accelerator can accelerate large beam currents (amperes) of singly charged heavy ions starting at a few MeV. At Berkeley, a Cs^{1+} contact ionization source of 1 ampere has been developed[27] for this application. This type of source was chosen because of its high brightness (less transverse velocities than a plasma source), > 99% singly charged ions, and its high mass (uranium may be possible). The source and pulsed drift tube preaccelerator are shown in Fig. 17. Cesium vapor is sprayed onto the 30-cm diameter hot iridium anode. The space-charge limited beam is extracted by the pulsed anode voltage. The extracted current follows the predicted $V^{3/2}$ Childs' Law up to 1 ampere at 500 kV, with 4 μsec pulses. One drift tube is now operating to give 1 ampere at 1 MeV, and 3 drift tubes are expected to be in operation in late 1979.

Negative Light Ion Sources

There is a need for H^- sources for injection into synchrotrons by stripping, for injection into LAMPF, and for neutral beam magnetic fusion injectors at higher energies. Development has been done at Brookhaven, Fermilab and Los Alamos in the U.S., using designs from the Novosibirsk group in Russia.

Fermilab has developed a magnetron H^- source[28] from a design of Brookhaven. It is shown in Fig. 18. The H^- is formed by the E X B discharge in the thin annulus between cathode and anode. Cesium is added to increase the H^- production and the source is run at 350°C to prevent condensation. High ion current densities of several amperes/cm^2 are created at the extraction gap. The source, analyzing magnet and accelerating column are shown in Fig. 19. The 90° analyzing

magnet removes electrons and matches the beam to the column. The source has produced 50 mA of H^- from the 750-kV column, and is the principal injector at Fermilab.

At Los Alamos, a Penning source of the Novosibirsk type has been developed,[29] shown in Fig. 20. It has given 108 mA at 18kV through a 90^0 bending magnet.

Negative Heavy Ion Sources

Negative heavy ions are widely used in tandem electrostatic accelerators. They are produced[4] by direct extraction, charge exchange from a positive beam, head-on collision of a positive beam with a vapor, and by sputtering from a solid surface with a positive beam.

One of the most useful designs is that of Middleton,[4] shown in Fig. 21. A cesium beam from surface ionization is accelerated and focused to bombard a sputter cone of the desired material. Negative ions are sputtered out and accelerated into the downstream lens system. A desired ion can be quickly selected from an array of cones of different materials, making this a very versatile source.

A negative heavy ion source was recently developed at Wisconsin.[30] The source is shown schematically in Fig. 22. It uses the filament design from the Hill-Nelson source and a sputter cathode of the desired material like the Aarhus source; Cesium vapor is added. The negative ions from the cathode are focused toward the extraction aperture. The source produces beams of good intensity and brightness. Middleton is testing a similar source, but without the magnetic field.

Polarized Ion Sources

Polarized hydrogen or deuterium ions are produced[7] in an atomic beam source by separating spin components of the atomic beam in a multipole magnet and then ionizing the beam, and in the Lamb shift source, by selective quenching of the 2S metastable state and charge exchange in vapor or gas.

Recent improvements have been made in the atomic beam source by ANAC, Inc.[8] Figure 23 shows the new atomic beam system with the dissociator closer to the first sextupole, four independent short sextupoles instead of one or two long ones, and better pumping along the beam.

Improvements by ANAC[8] have also been made in the electron beam ionizer, as shown in Fig. 24. The solenoid is split into 6 parts to produce an optimum magnetic field, which normally is higher on the ends than in the center. Power supplies and mechanical rigidity have been improved to stabilize the operating point. The beam currents, resulting from these improvements in the atomic beam and ionizer, have increased from 10 μA to 60 μA dc and 100 μA pulsed.

Recent advances have been made in negative ion polarized beams from an atomic beam source. Haeberli's group at Wisconsin[7] has used a colliding beam method of fast Cs^0 with polarized thermal H^0, Fig. 25. The Cs^0 donates an electron to the H^0 by charge exchange. A current of 3-μA polarized H^- was obtained, larger than is available from present sources. Further improvement is expected.

An even more promising development for negative ions is the use of colliding beams of fast D^- with thermal polarized H^0, proposed by Haeberli. High intensity D^- beams are available and the cross-section is higher than for Cs^0. Figure 26 shows a possible arrangement for this scheme. The main problem is space-charge blow-up of the newly formed polarized H^- by the fast D^- beam. This can be controlled by using a strong solenoid magnet and by injecting a neutralizing positive beam as shown in Fig. 26, although neutralization would also be supplied by residual gas. A colliding beam experiment is underway at Argonne[7] using this reaction, (Fig. 27), which uses a small interaction region to reduce the space charge problem with a pulsed H^- beam of 1A or more.

Sources of other polarized ions[7] have also been built, such as ^3He, ^6Li, ^7Li and ^{23}Na, and some of these have been used on accelerators.

Acknowledgments

The author received valuable assistance in the preparation of this paper from K. Ehlers, W. Haeberli, R. Middleton and C. Kim.

References

1. L. Valyi, "Atom and Ion Sources," Wiley, New York, 1977.

2. J.E. Osher, IEEE Trans. Nucl. Sci. NS-22, 3, 1626 (1975).

3. C.D. Curtis, Proc. 1976 Proton Linear Accelerator Conf., 179, A.E.C.L. Canada (1976).

4. R. Middleton, Revue de Physique Appliquee 12, 10, 1435 (1977).

5. D. J. Clark, IEEE Trans. Nucl. Sci NS-24, 3, 1064 (1977).

6. D.J. Clark and R.L. Seliger, Proc. Heavy Ion Fusion Workshop, ANL-79-41, 127 (1978).

7. W. Haeberli, Proc. Conf. on High Energy Physics with Polarized Beams and Polarized Targets, AIP No. 51, 269 (1979).

8. H.F. Glavish, Proc. 5th Conf. on Applications of Small Accelerators, Denton, Texas (1978).

9. W. B. Kunkel, IEEE Trans. Nucl. Sci, NS-26,

3, 4166 (1979).

10. D.D. Armstrong, C.R. Emigh, J.C. Hyde, E.A. Meyer, and J.D. Schneider, IEEE Trans. Nucl. Sci. NS-26, 3, 3055 (1979).

11. M.R. Shubaly, IEEE Trans. Nucl. Sci. NS-26, 3, 3065 (1979).

12. J.C. Davis, D.W. Heikkinen, J.L. Held, C.M. Logan and J.E. Osher, IEEE Trans. Nucl. Sci. NS-26, 3, 3058 (1979).

13. J.E. Osher and G.W. Hamilton, Proc. 2nd Symp. on Ion Sources and Formation of Ion Beams, p. VI-7-1, Lawrence Berkeley Laboratory, LBL-3399 (1974).

14. M. Olivo, W. Joho and U. Schryber, IEEE Trans. Nucl. Sci. NS-26, 3, 3980 (1979).

15. D.D. Armstrong, E.A. Meyer, H.L. Rutkowski and J.D. Schneider, IEEE Trans. Nucl. Sci. NS-26, 3, 3009 (1979).

16. K.W. Ehlers and K.N. Leung, LBL-9107 (1979).

17. R.P. Vahrenkamp and R.L. Seliger, IEEE Trans. Nucl. Sci. NS-26, 3, 3101 (1979).

18. J.M. Watson, Proc. Heavy Ion Fusion Workshop, ANL-79-41, 17 (1978).

19. W. Chupp, D. Clark, R. Richter, J. Staples and E. Zajec, IEEE Trans. Nucl. Sci. NS-26, 3, 3036 (1979).

20. W.R. Baker, K.W. Ehlers, W.B. Kunkel and A.F. Lietzke, Proc. Symp. on Ion Sources and Formation of Ion Beams, BNL 50310, 145 (1971).

21. R. Geller, IEEE Trans. Nucl. Sci., NS-26, 2, 2120.

22. Y. Jongen, C. Pirart, G. Ryckewaert and J. Steyaert, IEEE Trans. Nucl. Sci. NS-26, 3, 3677 (1979).

23. V. Bechtold, H.P. Ehret, L. Friedrich, J. Mollenbeck and H. Schweickert, IEEE Trans. Nucl. Sci. NS-26, 3, 3680 (1979).

24. E.D. Donets, IEEE Trans. Nucl. Sci. NS-23, 2, 897 (1976).

25. J. Arianer, A. Cabrespine, Ch. Goldstein and G. Deschamps, IEEE Trans. Nucl. Sci. NS-26, 3, 3713 (1979).

26. A. Roy and R.H. Davis, IEEE Trans. Nucl. Sci., NS-26, 2, 2151 (1979).

27. S. Abbott, W. Chupp, A. Faltens, W. Herrmannsfeldt, E. Hoyer, D. Keefe, C. Kim, S. Rosenblum and J. Shiloh, IEEE Trans. Nucl. Sci. NS-26, 3, 3095 (1979).

28. C.W. Schmidt and C.D. Curtis, IEEE Trans. Nucl. Sci. NS-26, 3, 4120 (1979).

29. P.W. Allison, IEEE Trans. Nucl. Sci. NS-24, 3, 1594 (1977).

30. G. T. Caskey, R.A. Douglas, H.T. Richards and H.V. Smith, Jr., Nucl. Instr. Meth. 157, 1 (1978).

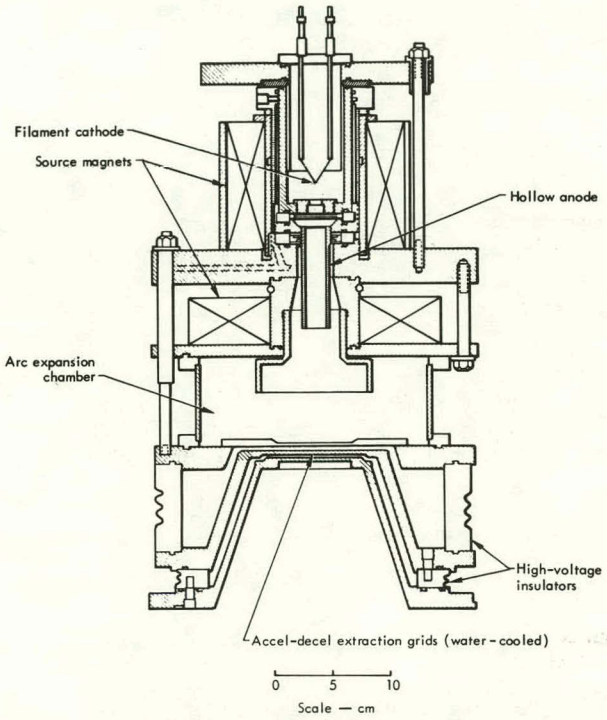


Fig. 1 Osher's MATS III source.

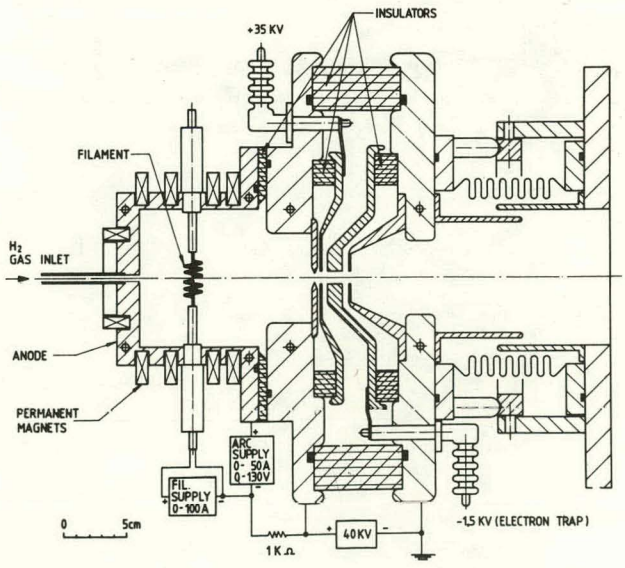


Fig. 2 Culham source built for new SIN injector.

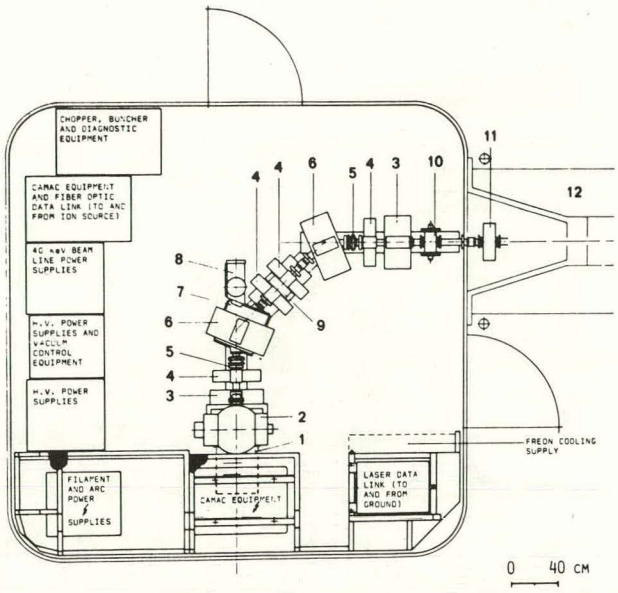


Fig. 3 860-kV terminal for new SIN injector. 1) ion source, 2) turbopump, 3) - 9) beam transport, 10) chopper, 11) buncher, 12) accelerating column.

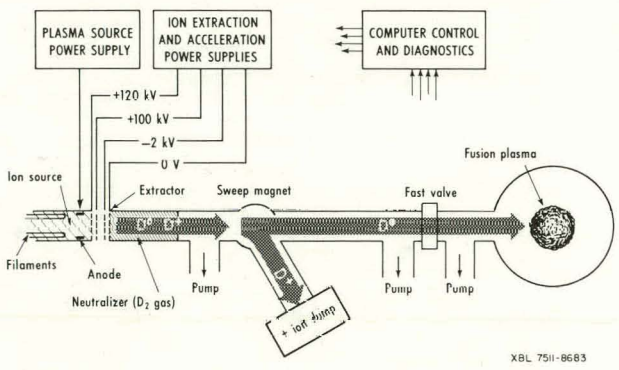


Fig. 4 Typical neutral beam line for magnetic fusion.

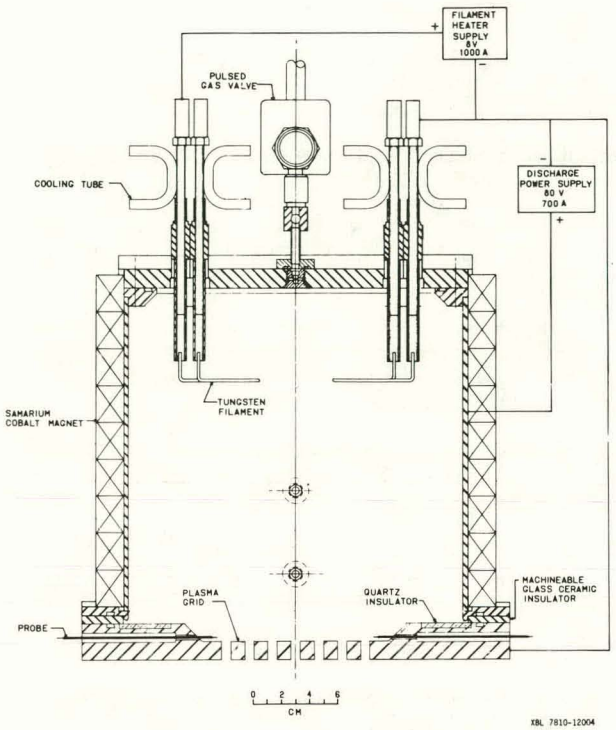


Fig. 5 Plasma region of new line cusp source for neutral beams at LBL.

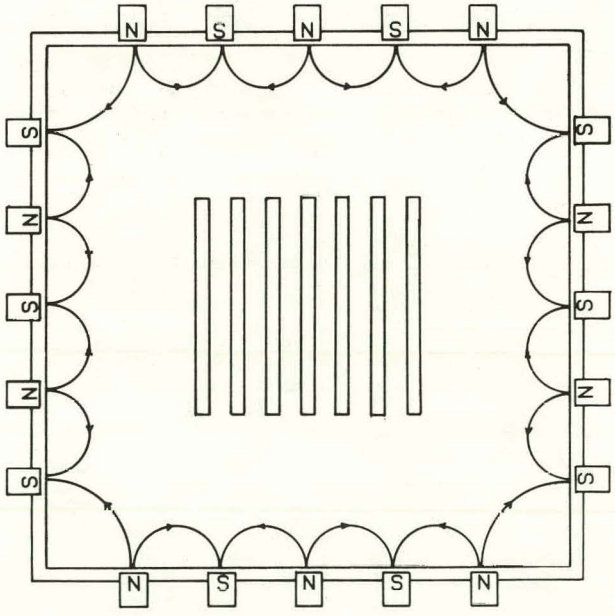


Fig. 6 Section of Fig. 5 showing line-cusp fields.

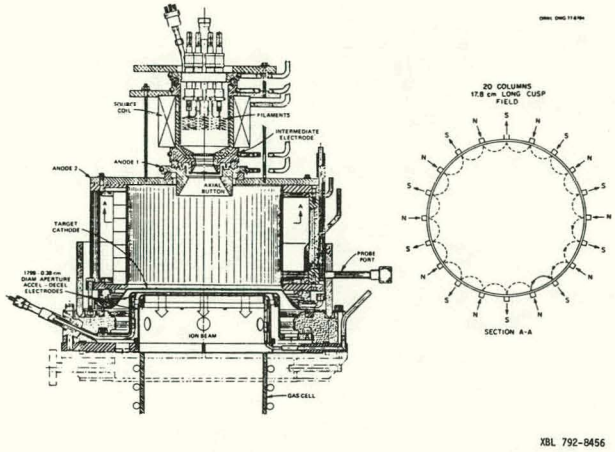


Fig. 7 ORNL 22-cm duopigatron with magnetic buckets.



Fig. 8 LBL 120-keV, 65A source, showing extraction slot plates.

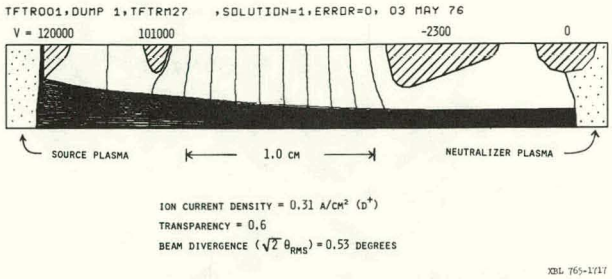


Fig. 9 Computer designed 4-electrode extractor system for 120 kV at LBL.

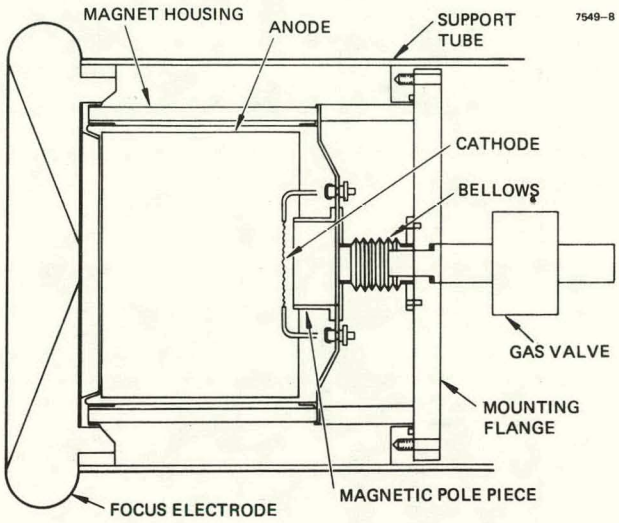
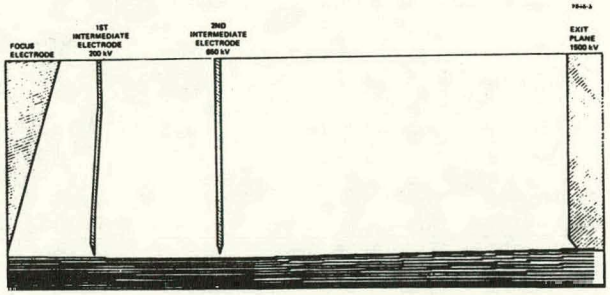


Fig. 10 Hughes Research Labs Penning Source for Xe^{1+}.



Ion trajectories for 100 mA of Xe^{+}

Fig 11. Argonne 1.5-MV accelerating column for heavy ion fusion.

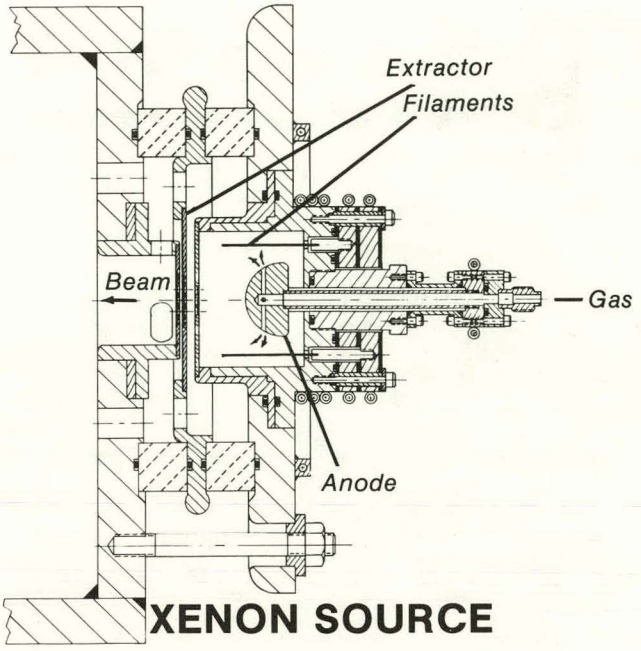


Fig. 12 LBL multiaperture Xe^{1+} source.

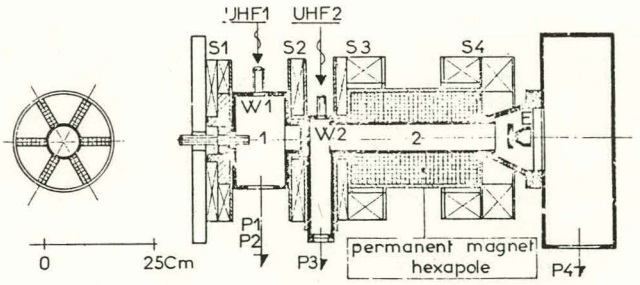


Fig. 14 MicroMAFIOS compact ECR source at Grenoble.

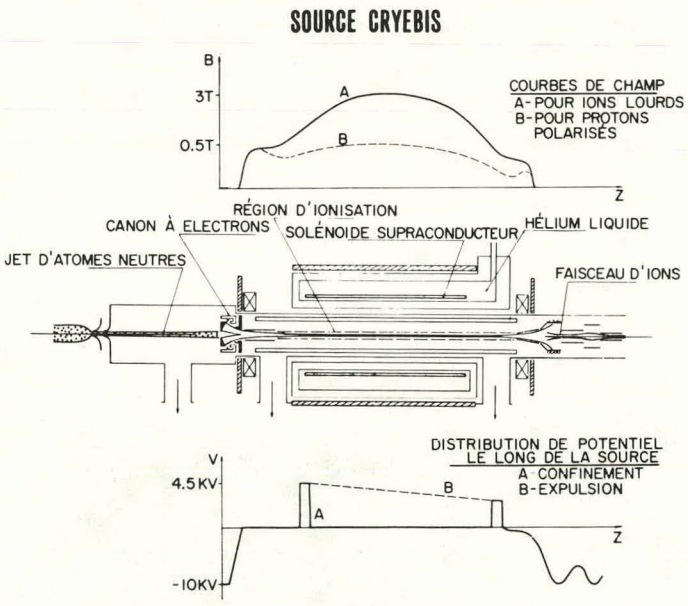


Fig. 15 Orsay CRYEBIS. Polarized atomic beam enters from left through hole in cathode. Ion beam is extracted on right.

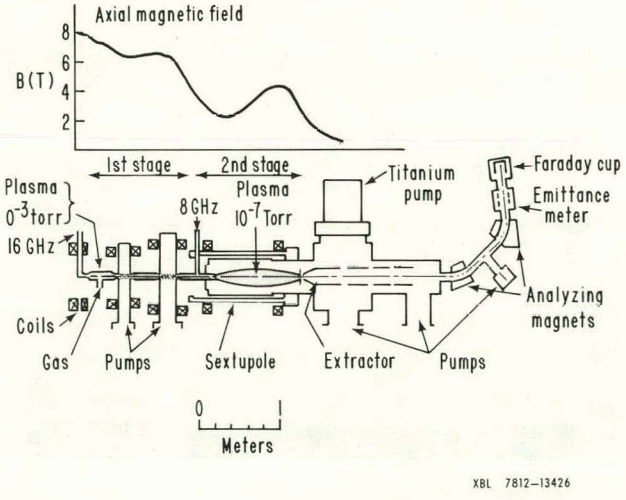


Fig. 13 Geller's SuperMAFIOS-B ECR source at Grenoble.

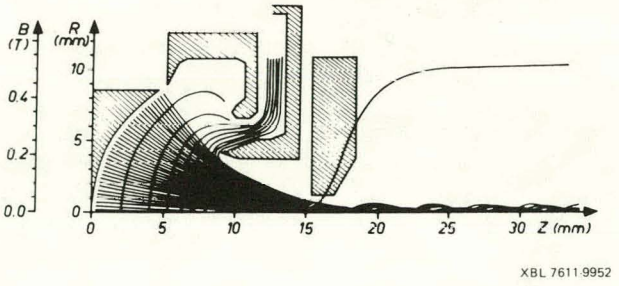


Fig. 16 Electron gun for Orsay EBIS.

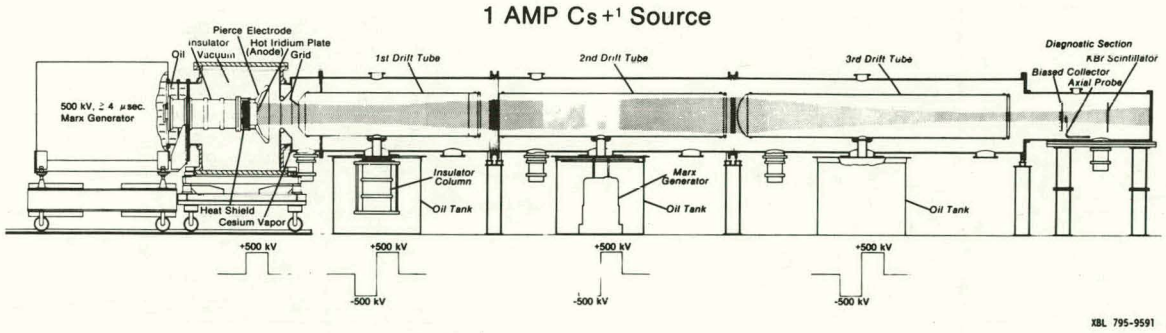


Fig. 17 LBL 1 A cesium contact ionization source and pulsed drift-tube linac.

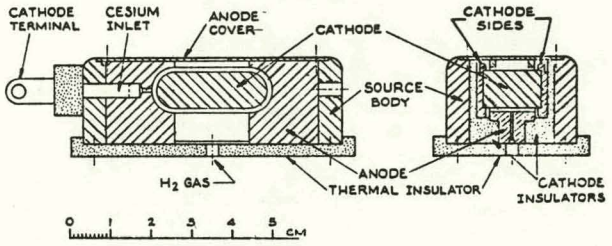


Fig. 18 Fermilab H⁻ magnetron source.

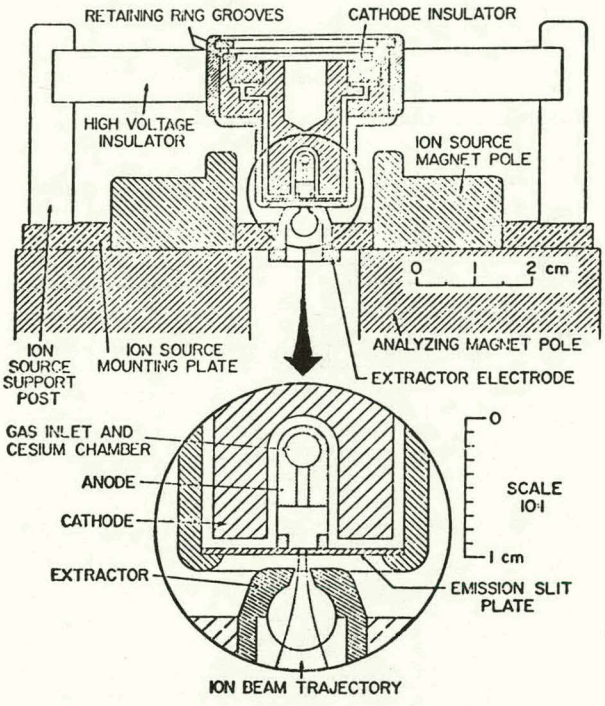


Fig. 20 Los Alamos Penning Source for H⁻.

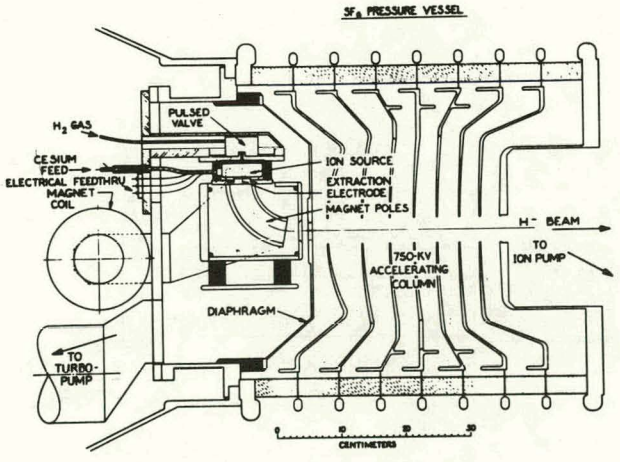


Fig. 19 Fermilab high voltage terminal with analyzing magnet for H⁻ source.

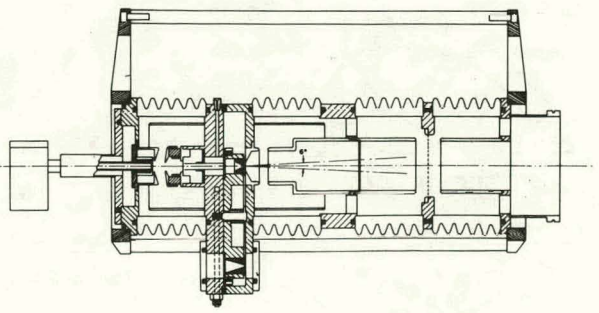


Fig. 21 Middleton sputter source for negative heavy ions. Cesium beam enters from left. Ion beam is extracted from right.

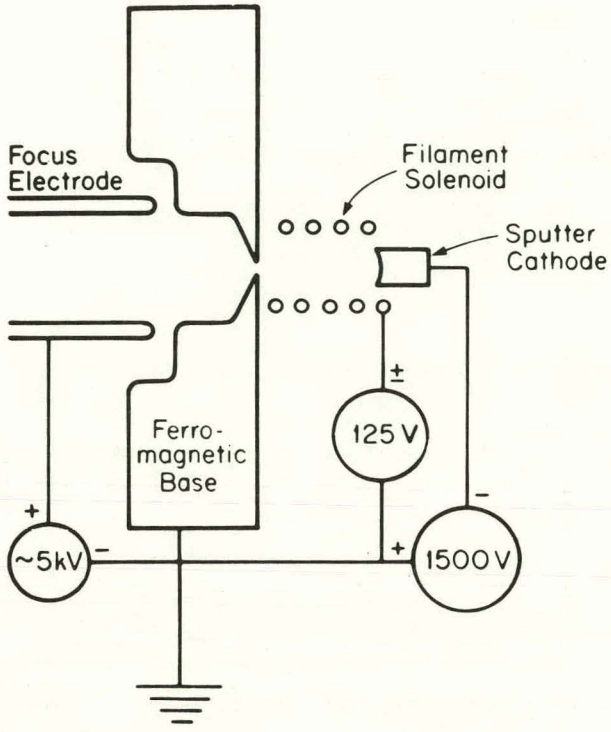


Fig. 22 Wisconsin axial plasma sputter source for negative heavy ions.

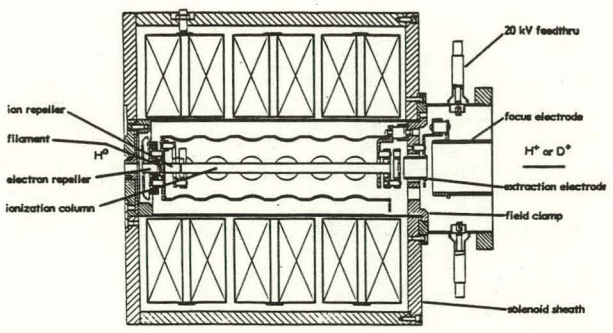


Fig. 24 ANAC improved ionizer for polarized atomic beam.

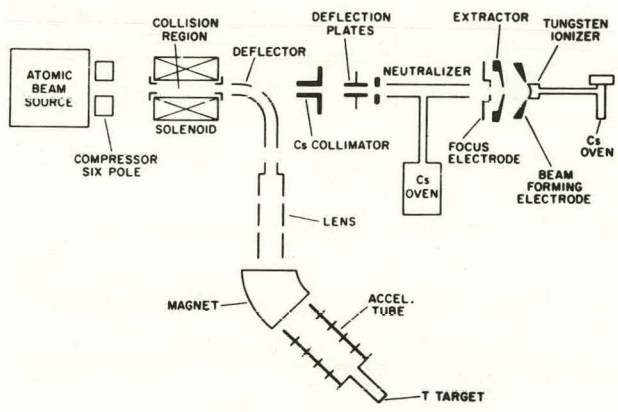


Fig. 25 Experiment at Wisconsin which produced 3 μA of H^- polarized beam by charge exchange with fast cesium beam.

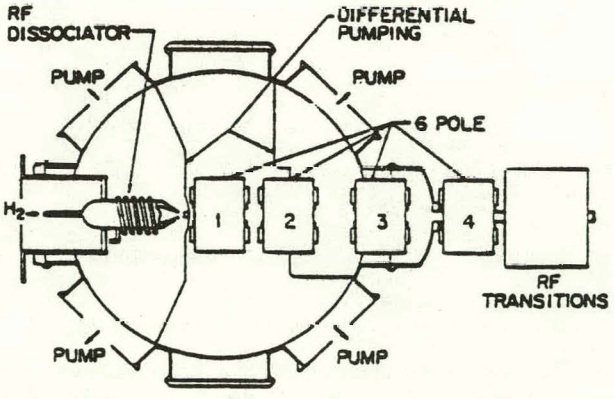


Fig. 23 ANAC new polarized atomic beam system.

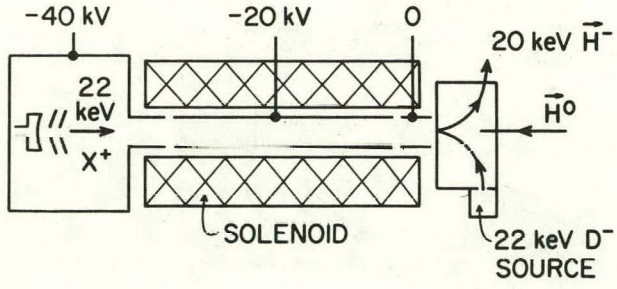


Fig. 26 Proposed system for producing high intensity polarized H^- beam by charge exchange with fast D^- beam.

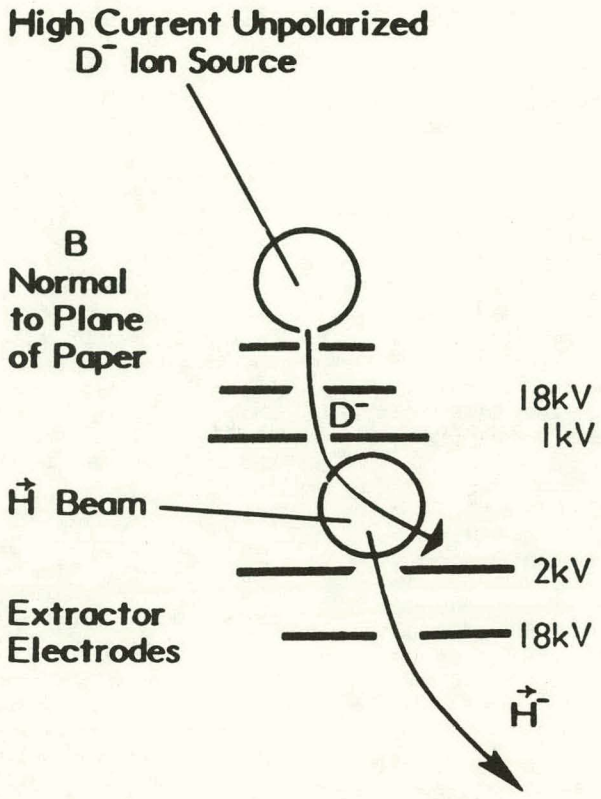


Fig. 27 Argonne system for producing high intensity polarized H⁻ beam by charge exchange with fast D⁻ beam.

Discussion

Hepburn, AECL: Does the Wolf computer code iterate the plasma surface shape?

Clark: I'm not positive about that.

Halbach, LBL: It does iterate on the meniscus - it finds the shape that gives a self-consistent solution.

Blewett, BNL: It was not clear to me in your pictures of polarized ion sources, where the polarization takes place. Most of the pictures seemed to show only components that are axially symmetrical.

Clark: The polarization takes place in the sextapole magnets, by separating the electron spins - they align either parallel to the field or perpendicular to the field - so in the sextupole one component is defocused and one component is focused due to the sextupole gradient. After that there is an rf transistion.

Blewett: I think the problem was that I didn't see them.

Clark: They were in the first viewgraphs. I may have not made that clear. These are the sextupoles here - "6 poles" - this is a standard component of the source. It is symmetric except for the "6 poles".

Blewett: This component appears by assumption in all of your other pictures.

Clark: Yes, this item, the sextapoles, are used in every atomic beam type of source and the colliding beams have that as a first stage.

Meads, Brobeck: Would you say something about reliability of some of these sources?

Clark: Well, that varies tremendously from one source to another. Some sources will run for weeks or months. The negative heavy ion sources can run for weeks. Some of the PIG sources run for 3 hours and then they have to be changed. Some of them run for a day: 8-12 hours. That's probably the complete range. At the 88 Inch, we sometimes change the source every 3 hours for difficult ions and run up to weeks with dueplasmatrons at low duty factor. But everybody wants to get better reliability.

TESTS WITH A MULTIDIPOLE ION SOURCE ON THE CERN 500-keV EXPERIMENTAL PRE-ACCELERATOR

J. Grando, H. Haseroth, C. Hill, M. Hone
CERN, Geneva, Switzerland

Summary

A pulsed, multidipole ion source (bucket ion source), similar to dc ones used in the fusion field for neutral injection, has been built and tested on an experimental pre-accelerator. Preliminary results are given and a comparison is made with the usual duoplasmatron ion source. Because of its very low noise, simple design, smaller number of variable parameters and lower power consumption, the eventual installation in the preinjector of the new CERN 50-MeV linac looks attractive.

Introduction

The CERN duoplasmatron[1] ion sources have proved to be reliable and efficient sources of protons for the CERN accelerator complex. However, the "grass", or noise inherent in the beam pulse when the source is being operated at high currents, is giving rise to concern. This noise can only be eliminated at the cost of inferior beam quality and is believed to arise inside the expansion cup.

A multipole confinement device[2] essentially has a quiet plasma contained in a region of practically zero magnetic field. Ion sources based on this principle have been built[3] generally as direct current or long pulse sources for use in nuclear fusion experiments.

For accelerator use, the multidipole source (or MDS) seemed worthy of investigation, in view of its reported low noise properties and apparent small emittance.[4] A short test on a dc source at Culham Laboratory,[4] indicated that it might be possible to operate with pulses as short as 100 μs with fast rise-times.

Description of the source

When deciding to build a prototype MDS source, the first limiting parameter was the space available inside the preinjector columns, especially as it was not intended to use a special extractor electrode. The inside diameter of the anode of the 750-keV column of the new linac; therefore, limited the maximum outside diameter of the source to 210 mm. Figure 1 shows the source as built in its water-cooled version. Figure 2 is a cross-section of the source also showing electrical connections. An air-cooled source had a welded stainless steel plasma chamber but the water-cooled source has an aluminum alloy body. Most of the data and results presented here refer to the air-cooled source.

The space limitation and available magnets led to the adoption of the full line cusp geometry proposed by Leung et al.,[5] and considered by them as the best one. The plasma vessel is 110 mm diameter by 100 mm deep and 1.3 mm thick, with a port in one end for the cathode. Twelve rows of rare earth-cobalt plastic magnets produce the multipole field and are continued radially over the backplate to the cathode hole. These magnets give a maximum field of about 1.5 kG at the walls and a region of about 50 mm diameter at the center with less than 10 G.

As there was no experience with bright thermionic emitters and as there were power supplies and components available, the standard oxide coated duoplasmatron cathode[6] was used in the source. At its working temperature, the cathode dissipates about 150 W and the magnets seem to stay below 100° C. It is doubtful if a bright thermionic emitter could be used in the air-cooled source.

The front plate of the source is an insulated stainless steel disc carrying a titanium (TA6V) alloy nose with a 14 mm extraction hole and Pierce angle geometry. Titanium was used to ensure that the high voltage performance of the preinjector would not be deteriorated. This front plate can be biased relative to the source body.

In view of the geometry of the source, the cathode can see down the high voltage column. After considerable problems with high voltage stability and radiation, a small floating shield of titanium was mounted in front of the cathode, and this seems to have given greater stability without apparent beam loss.

Arc characteristics

Before the source was mounted in the experimental preinjector, the arc characteristics were studied in a grounded test rig. A standard CERN arc power supply,[7] which consists of a thyristor discharged 10 Ω delay line pulser with about 5 Ω of series resistance, was used.

Initially the source was difficult to fire and high arc voltages were measured (≈150 V), but after some hours the arc voltage dropped to around a normal value of 80 V. It is not yet known if this phenomena is inherent in the source, but there are indications that these problems may have been due to the state of the cathode, or to surface phenomena in the arc chamber. These phenomena have not been seen in the water-cooled source.

The arc voltage and current were insensitive to the negative bias on the front plate down to about -40 V, corresponding to the potential of the plate if it was allowed to float. Grounding the front plate drastically increased the arc current rise-time. Normally the plate was held at -100 V.

Once the arc became normal, it was found to be very sensitive to cathode temperature. Acceptable operation could only be obtained in a temperature band of about 60° C around the nominal cathode temperature of about 800° C (i.e., approximately ±3 A on a filament current of 50 A). The cathode showed less sensitivity at higher arc currents. Figure 4 shows oscilloscope pictures of the arc voltage and current for the conditions of too cold, normal and too hot operation. Again, there are indications that these effects may be

due to the particular cathode used in these tests.

With high currents (∿100 A) and low gas flows (2-5 cc/min), the arc firing delay was observed to increase in the air-cooled stainless steel source; delays of several tens of milliseconds could be produced. This effect was not observed with the water-cooled aluminium source.

Measurements of the radial current density distributions obtained using standard Langmuir probe techniques in the water-cooled source are shown in Fig. 3. The uniformity of the current density across the back of the exit hole is quite apparent.

Tests in the experimental preinjector

It quickly became obvious during tests in the experimental preinjector, that the extracted current and beam quality were very dependent upon source position. By trial-and-error techniques, it was found that the best beam conditions, as defined by the cleanest pulse in the first current transformer and the best transmission through the first triplet, were obtained when the position of the hole in the nose relative to the preinjector anode roughly corresponded to that found in the past for the duoplasmatron. If the source was too far forward, little current was extracted, whereas if it was too far back, a large current could be obtained but with very poor transmission and poor voltage holding of the preinjector column.

With the source positioned as near as possible to the optimum, it was found that the beam pulse reflected certain characteristics of the arc voltage, which enabled the source filament current to be adjusted to its optimum value. Figure 4 shows the beam pulse as measured in the first current transformer for the conditions of too cold, normal and too hot cathode.

The almost complete absence of noise on the beam pulse during normal operating conditions (Fig. 4b) can be clearly seen and should be compared with a comparable beam from a duoplasmatron (Fig. 5).

Currents obtained from the MDS were roughly linear with respect to arc current. Typical values were 190 mA for 60 A arc, to 420 mA for 100 A arc current and 10 cc/minute of hydrogen. The source output saturated above about 110 A arc. Beam composition was not measured.

It was found that the source parameters for a given beam remained stable from day-to-day and could also be reproduced, with a short running in period, after a cold start.

Manual emittance measurements suggested that it would be worthwhile to perform a test run on the new linac.

Measurements on the new linac

After installation in the 750-keV preinjector of the new linac and proper source parameter set-up, the MDS again showed little noise and extremely good stability. Figure 6 shows a comparison of the MDS and duoplasmatron beam profile measurements in the LEBT, made with a movable slit and a beam transformer behind it. In the former, even several scans did not show any variations.

The emittance measured in EM2 (Fig. 7) did not seem very encouraging, but it is highly probable that there was considerable contamination from H_2^+, H_3^+ and perhaps N^+ or O^+, especially in view of the high losses in the beam transformer readings between IM4 and IM5. Typical values for 102 A arc and 10.2 cc/min hydrogen were:

IM2 (after column)	325 mA
IM4 (before buncher)	301 mA
IM5 (after buncher)	163 mA
IM6 (into Tank 1)	163 mA
IM9 (out of Tank 3)	140 mA

The emittance measured in EM3 (after the buncher) was much more reasonable (Fig. 8).

The maximum current obtained at 50 MeV was 140 mA compared to a maximum of 160 mA normally obtained with the standard duoplasmatron. Emittance measurements at 50 MeV indicate that the beam quality was certainly not worse, but was probably better than that obtained from the duoplasmatron source. There is still room for improvement in the linac settings, but this was not tried because of lack of time.

Conclusions

The object to build a pulsed MDS has been achieved and initial tests indicate that all its promises can be fulfilled.[8] However, further fundamental investigations are needed to understand some of the early problems and more operational experience will be needed before it can be envisaged using this source operationally for the CERN accelerator complex.

Acknowledgements

The authors would like to acknowledge the information obtained from and the very useful discussions with E. Thompson and A. Holmes of Culham Laboratory.

References

1) B. Vosicki, M. Buzic, A. Cheretakis, MPS/Int. LIN 66-1 (1966) and Linac Accelerator Conference, Los Alamos 1966.

2) R. Limpaecher, K. Mackenzie, Rev.Sci.Instr. 44, 726, 1973.

3) K. Leung, R. Collier, L. Marshall, T. Gallaher, W. Ingham, R. Kribel, G. Taylor, Rev.Sci.Instr. 49, 321, 1978.

4) E. Thompson, A. Holmes, Culham Laboratory UKAEA, private communication.

5) K. Leung, T. Samec, A. Lamm, Phys.Let. 51A, 490 (1975).

6) Technology note B18 - Meetings on Technology arising from high energy physics, CERN 74-9 (1974).

7) H. Haseroth, P. Têtu, CERN/PS/LIN 76-6 (1976), and 1976 Proton Linear Accelerator Conference, Chalk River, Canada.

8) M. Hone, CERN Internal Report - to be published.

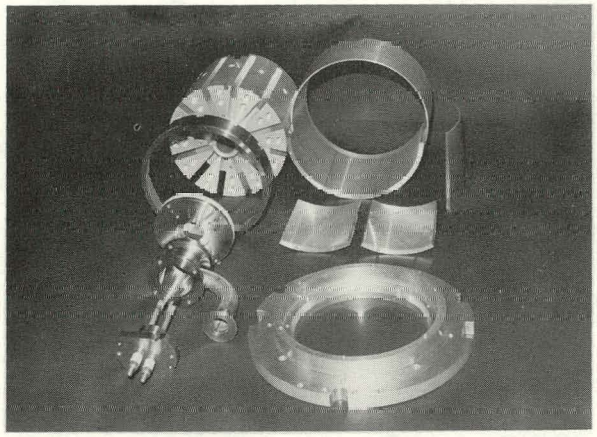


Fig. 1 Prototype MDS

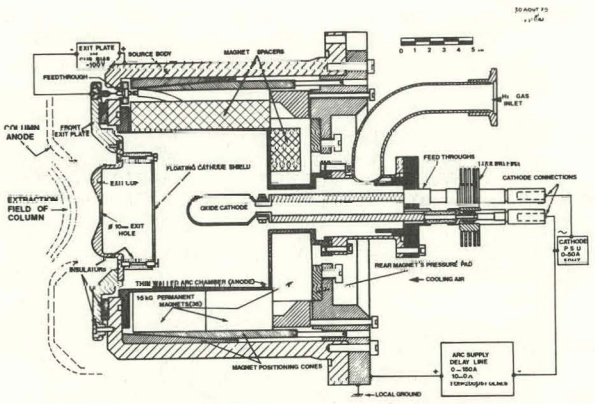


Fig. 2 MDS1 cross section and electrical schema

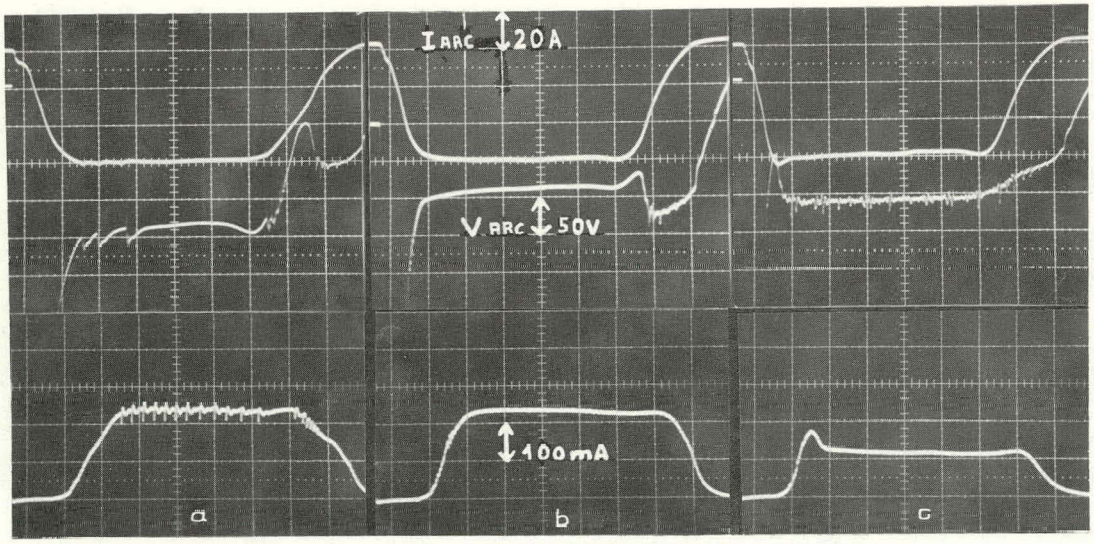


Fig. 4 Arc and beam characteristics for (a) too cold, (b) normal, (c) too hot cathode - upper-arc, lower-beam pulse

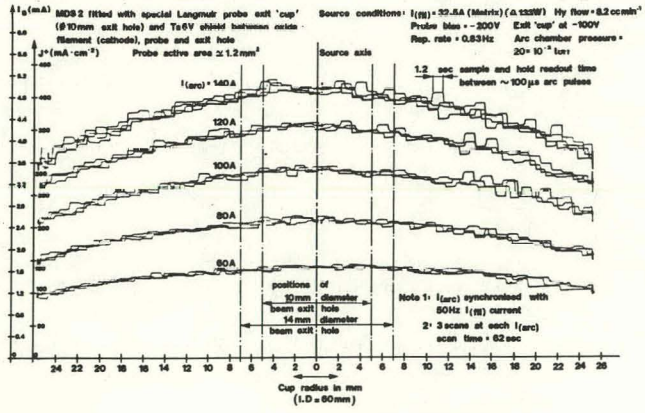


Fig. 3 Plasma + VE ion current $1_{(s)}$ and current density (J^+) variation across 'cup' with $1_{(arc)}$

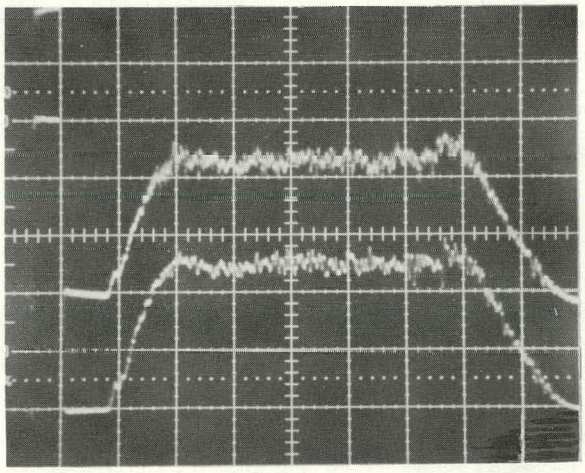
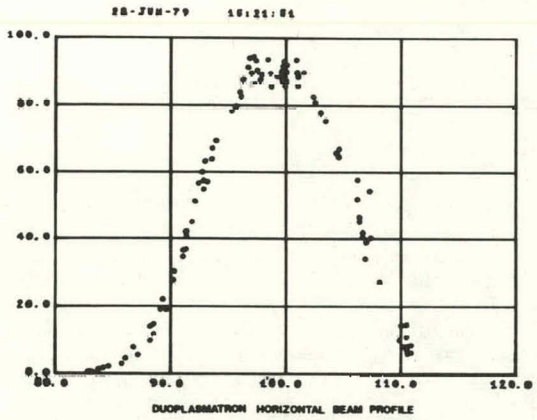


Fig. 5 Typical duoplasmatron output 100 mA/div.



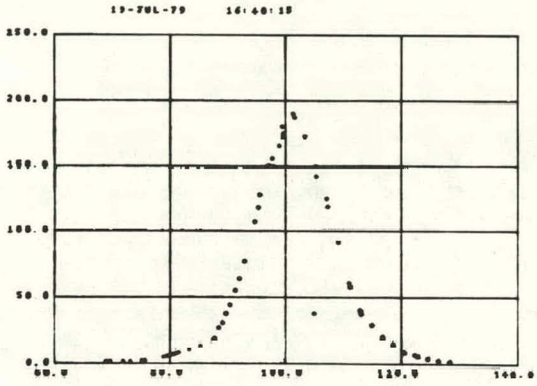


Fig. 6 Multidipole ion source horizontal beam profile

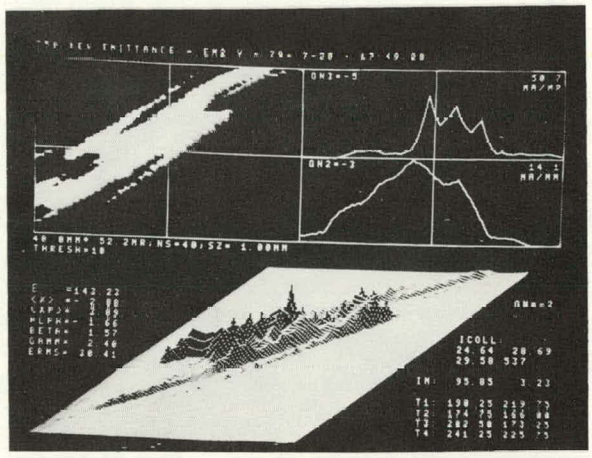


Fig. 7 Emittance in EM2

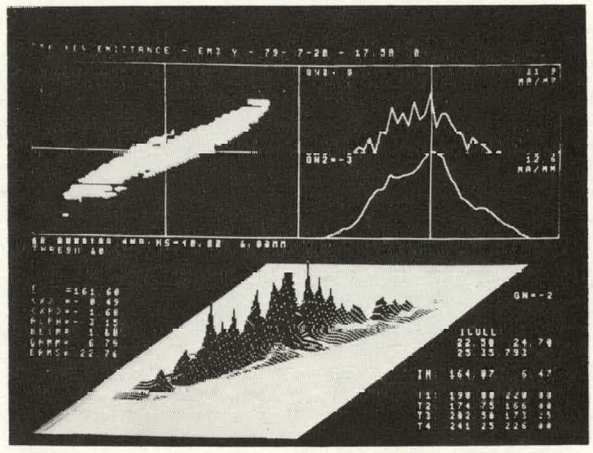


Fig. 8 Emittance in EM3

1979 LINEAR ACCELERATOR CONFERENCE

DEVELOPMENT OF A HIGH BRIGHTNESS ION SOURCE

A.J.T. Holmes and M. Inman
Culham Laboratory, Abingdon, Oxon. OX14 3DB, U.K.
(Euratom UKAEA Fusion Association)

SUMMARY

The brightness and emittance of an ion beam can depend on the ion temperature, aberrations and scattering, as well as other factors. However, it is the ion temperature which determines the irreducible minimum value of the emittance and hence brightness, as the other components can be eliminated by careful design.

In this paper an ion source design is presented which has attained this minimum value for the emittance; the dependence of the ion temperature on the plasma source parameters is discussed.

THE ION SOURCE

Figure 1 presents an illustration of the ion source, which comprises the plasma generator and ion acceleration structure. Both of these components have been developed at the Culham Laboratory as part of an ongoing program for the injection of intense neutral atom beams into magnetically confined plasmas, for controlled thermonuclear research.

The plasma source is of the magnetic multipole type[1,2] sometimes called a "bucket" source, which has the advantages of a very high electrical efficiency, a low gas operating pressure and the production of a large volume of quiescent plasma. All these advantages arise from the magnetic multipole method of plasma confinement, which creates a magnetic well on all sides except the beam extraction surface, where the magnetic field is virtually zero.

The electrical efficiency is such that each kilowatt of arc power produces typically 4 amps of ions (in hydrogen) over the entire extraction area of about 80 cm^2. The uniform plasma area is about 40 cm^2 and is large enough, as can be seen in Fig. 1, for a multi-aperture extraction system, which is capable of giving a beam current of about 1 ampere. In these experiments, however, only a single aperture is used.

The gas pressure for reliable source operation can be as low as 2 m Torr; the electric efficiency does decrease, however, at this pressure, which minimizes the effects of scattering collisions in the extraction system. Hence, these collisions do not influence the beam emittance.

The ion extraction system is of the tetrode type; an illustration is shown in Fig. 2. The tetrode structure reduces the effects of the anode hole effect, by decoupling the extraction from the post acceleration gap, which raises the beam to its final energy. It also adds an additional electrostatic lens to the system, which enables the beam to be extracted with negligible compression. The divergence of the extracted ion beam depends on the degree of space charge neutralization, which in turn, depends on the diameter of the extracted beam.[3] Thus tetrode extraction systems have a big advantage as there is little beam compression and large diameter apertures can be used, as the anode hole effect is weaker.

The extraction geometry developed at Culham, shown in Fig. 2, has 12-mm diameter apertures, which are suitable for beam energies up to 70-80 kV. The maximum beam current through a single aperture extracted so far is 230 mA of mixed species H-ions at 70 kV, or 150 mA He^+ at the same energy. The extraction geometry is designed with water cooling, so that it can operate continuously. The beam divergence angle is 0.5^o, which arises from the finite ion temperature and residual space charge. Figure 2 also shows the calculated ion trajectories, and as can be seen, there is little aberration with this extraction geometry because of the flat plasma boundary and the large aperture in the second electrode.

Hence, the only contribution to the beam emittance arises from the finite ion temperature in the plasma source. This is discussed later, where it is shown that the observed temperatures can be explained by purely classical processes. The field-free plasma and its quiescent uniform behavior, make it unlikely that any non-linear processes contribute to the emittance.

BEAM EMITTANCE AND ION TEMPERATURE

The normalized emittance and brightness for a cylindrical beam are defined as:

$$\varepsilon_n = \beta\gamma\, A(r,r')/\pi$$

$$B_n = 2I_b/\pi^2\varepsilon_n^2 \quad ,$$

where I_b is the beam current. The ion temperature gives rise to a Maxwellian velocity distribution; hence the emittance of a non-relativistic beam of this type at the 1/e intensity contour at the extraction aperture is:

$$\varepsilon_n = \frac{4a}{\pi} \cdot \left(\frac{2e\, T_i}{m_i\, c^2} \right)^{1/2} \quad , \qquad (1)$$

and the diagram is rectangular in shape. The brightness is, hence:

$$B^2 = I_b\, m_i c^2/16a^2\, eT_i$$
$$= \pi J_i m_i c^2/16\, eT_i \quad , \qquad (2)$$

where J_i is the current density at the plane of extraction. The value of J_i depends on the extraction voltage and inter-electrode gaps and is only limited by the voltage breakdown strength of the extraction geometry.[4]

The ion temperature has been derived from the measured emittance, using Eq. 1 over a range of extracted current densities for both hydrogen and helium, as shown in Fig. 3. In the hydrogen discharge, a considerable rise in the value of T_i with increasing values of j_i is observed. Such an increase is not seen in a helium discharge, which suggests that there is a correlation between the increasing ion temperature and the increasing proton yield (also shown in Fig. 3). This may arise since the protons are more energetic than the other ions, because of their dissociation energy.

An emittance diagram of the hydrogen beam is shown in Fig. 4 for a beam energy of 40 keV. The normalized emittance for H_2^+, the average ion mass, is 0.12 πmm-mrad, which leads to a temperature of 0.68 eV and a brightness of 5.10^{11} mA/cm^2/steradian. Also shown in Fig. 5, is the output from the diagnostic device, which shows that both the beam spatial and angular profiles are gaussian in shape. The helium beam emittance for the same extraction geometry is much lower, only 0.055 πmm-mrad, which corresponds to a temperature of 0.32 eV and a brightness of 1.4×10^{12} mA/cm^2/steradian.

DISCUSSION

The ion temperature is determined by the gas temperature in the source, the heating caused by classical ion-electron coulomb collisions, thermalization of the plasma potential energy, and the cooling effects caused by charge-exchanging collisions. In addition, in hydrogen discharges the dissociation energy released in the reaction:

$$H_2^+ + e \rightarrow H^+ + H + e$$

must also be considered. Non-classical ion heating processes, such as electron beam-plasma interactions, are not considered, as they do not generate the observed Maxwellian (or gaussian) velocity distributions.

From the work by Spitzer,[5] the rate-of-change of ion energy with time is:

$$\frac{dU_i}{dt} = C\, n_e / T_e^{\frac{1}{2}}\, m_i \quad \left[Js^{-1}\right] , \qquad (3)$$

in the limit where T_e is much greater than U_i. The constant C, for electron collisions is 2.17×10^{-57} in mks units. Ion-ion collisions transfer energy far more rapidly, in the ratio of m_i/m_e. Hence, all the ions in the plasma have virtually the same temperature, although small differences in beam profile have been observed between the various hydrogen ion species.[6]

Before Eq. 3 is integrated, the cooling effects of charge exchange must be considered, which convert energetic ions into cool ions, while the fast neutrals, so formed, escape. However, if the discharge is large enough, these fast neutrals undergo a second charge-exchanging collision and re-form the original hot ion. As the cross-section is the same in both cases, the energetic particle spends half the distance it travels in the form of an ion and the other half in the form of a fast neutral atom or molecule.

However, the distance an ion travels in the plasma source, S_i, is a function of the source geometry alone. In the case of a bucket source:

$$S_i = \frac{A_T\, d}{A_i} ,$$

where A_T is total surface area, A_i is the ion collection area and d is the plasma diameter. Hence, the effect of charge-exchange collisions is to reduce the distance during which ions can be heated, to $S_i/2$. This conclusion is in agreement with experiment, as no variation in T_i was observed by varying the source pressure.

It is now possible to evaluate U_i by integrating Eq. 3. The equation can be transformed to:

$$\frac{dU_i}{dt} = \frac{dU_i}{ds}\left(\frac{2U_i}{m_i}\right)^{1/2} = \frac{C\, n_e}{T_e^{1/2} m_i} .$$

$$\text{Hence, } \frac{2}{3}(U_i)^{3/2}\left(\frac{2}{m_i}\right)^{1/2} = \frac{C n_e S_i}{2 T_e^{1/2} m_i} + \text{constant} . \qquad (4)$$

The constant is defined by the initial temperature of the ions, which depends on the gas temperature, the proton fraction, and lastly, the plasma potential. The first and last of these are constant and do not depend on n_e; however, the proton fraction does depend on the ion current density, which is proportional to n_e. Hence, the initial energy, U_{io}, is:

$$U_{io} = 1/2\, m_i v_o^2 + \beta k T_e + fT = E_o + fT , \qquad (5)$$

where v_o is the gas temperature, β is a numerical factor, which is small compared to unity, f is the fractional proton yield and T is the dissociation energy. The term E_o, is virtually invariant to all changes in the discharge parameters.

Combining Eq. 4 and Eq. 5 gives:

$$U_i^{3/2} - (E_o + fT)^{3/2} = \frac{3C\, n_e\, S_i}{4(2m_i T_e)^{1/2}} = \frac{3C\, J_i\, S_i}{4(2k)^{1/2} e T_e}\ [J]^{3/2} , \qquad (6)$$

where U_i is the final ion temperature at extraction, assuming ions leave the plasma at the ion sound speed.

Equation 6 shows that the RHS is independent of the gas except for T_e, which is unlikely to vary greatly. For helium, there is no dissociation; hence, f is zero and Eq. 6 can be linearized when the RHS is small, to give:

$$U_i = E_o + \frac{2J_i}{3} \cdot \left(\frac{3\, C\, S_i}{4.(2k)^{1/2} e T_e\, E_o^{1/2}}\right) .$$

This expression can be tested against the helium data shown in Fig. 6. The slope gives a value of 5.4×10^{-23} Jm^2/A, which is in reasonable agreement with the equation above, which yields a value of 5.7×10^{-23} Jm^2/A.

The hydrogen discharge is more difficult to analyze, but the value of U_i for H and He can be compared at the same current density. Thus, as the RHS is mass independent, and the electron temperature is constant, then:

$$U_{iH}^{3/2} - U_{iHe}^{3/2} = (E_{oH} + fT)^{3/2} - E_{oHe}^{3/2} ,$$

or

$$(U_{iH}^{3/2} - U_{iHe}^{3/2} + E_{oHe}^{3/2})^{2/3} = E_{oH} + fT.$$

This is plotted in Fig.7 and a straight line is obtained. The slope of the line indicates that T is approximately 0.6 eV and E_{oH} is 0.22 eV, the same value as E_{oHe}.

The energy level diagram of H_2^+ shows that the full Frank-Condon energy between the $1S\sigma_g$ level (H_2^+) and the unstable $2P\sigma_u$ level ($H^+ + H^o$) depends very strongly on the vibrational level occupied by the H_2^+ ion. The small value of T suggests that H_2^+ ion is excited to a high vibration level in the $1S\sigma_g$ level before it is dissociated to the $2P\sigma_u$ level by electron impact. The Frank-Condon energy appears in the kinetic energy of the two daughter particles and hence this energy is 1.2 cV.

The value of E_o corresponds to 2500°K for both H and He discharges. An estimate for β, based on the ionization rate and the plasma size, is in the region of 0.04, which suggests that βkT_e forms the major contribution to the value of E_o. The gas temperature in this small source could be close to room temperature because of the high collision rate with the source walls.

CONCLUSION

Extraction of ions from a quiescent plasma source, using a specially designed tetrode extraction system with a single aperture, allows ion beams to be formed whose emittance and brightness are only limited by the ion temperature. This temperature is mainly determined by the H_2^+ dissociation energy in hydrogen discharges and by the ion-electron collision rate in helium discharges, where ion dissociation does not occur.

Such ion temperature dominated beams are presently being used for neutral injection experiments in controlled thermonuclear fusion, but could be used in other applications.

ACKNOWLEDGEMENTS

The author would like to thank Dr T.S. Green for his encouragement in this work.

REFERENCES

1 Limpaecher, R, and Mackenzie, K R, Rev. Sci. Inst. 44, 726 (1973).

2 Hemsworth, R S., Culham Report CPNI-CUL(77)8.

3 Holmes, A J T. Phys. Rev. A, 19, 389 (1979).

4 Green, T S. Rep. Prog. Phys. 37, 1257 (1974).

5 Spitzer, L. Physics of Fully Ionized Gases, Wiley, 1967, New York.

6 Holmes, A J T, Thompson, E. & Watters, F., to be published.

7 Massey, H S W.,"Electronic & Ionic Collision Phenomena", 2, 914, O.U.P., Oxford (1969).

FIG 1

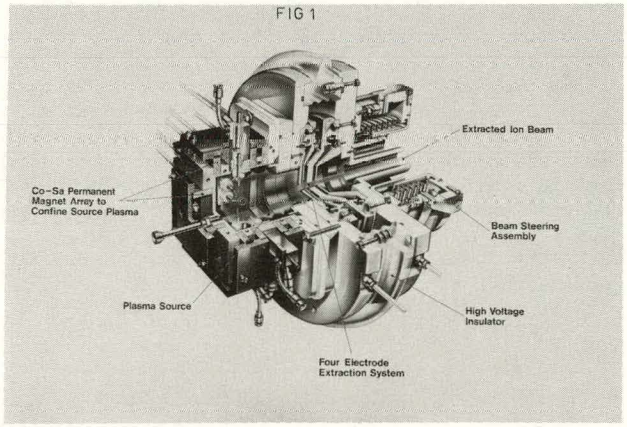


Fig.1 Cut-away view of ion source

FIG 2

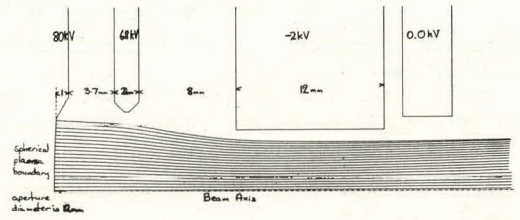


Fig.2 Numerical view of ion trajectories

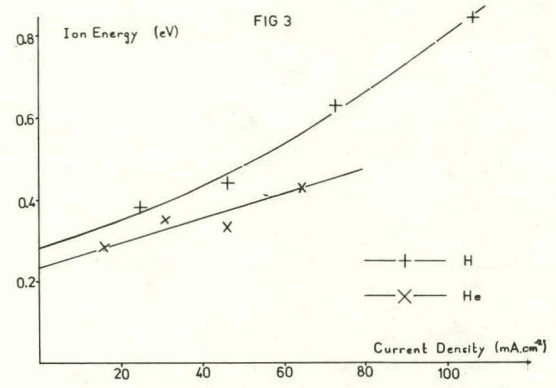


Fig.3 Measured ion temperature of ion derived from beam emittance in hydrogen and helium discharges as a function of ion current density

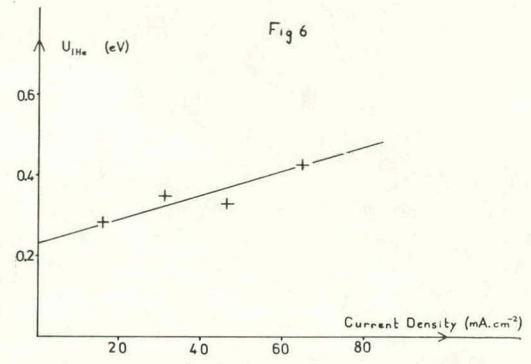


Fig.6 Scaling of the helium temperature with ion current density

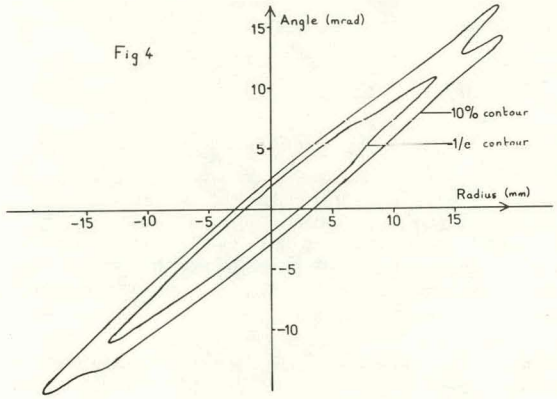


Fig.4 Typical emittance diagram

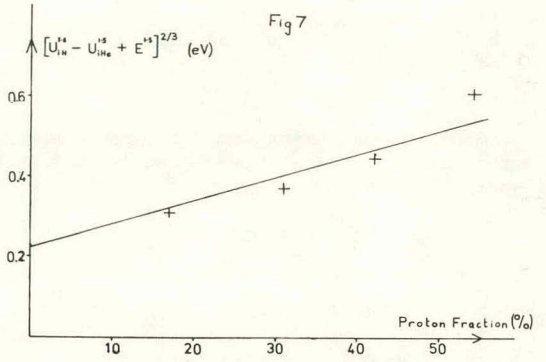


Fig.7 Scaling of hydrogen temperature with fractional proton density

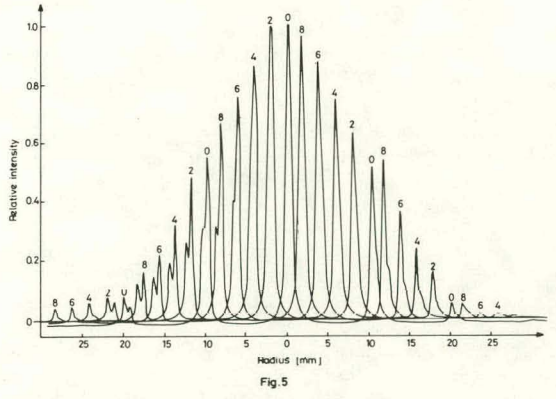


Fig.5 Raw data from emittance device showing the gaussian beam profile and the individual peaks

1979 LINEAR ACCELERATOR CONFERENCE

PROPERTIES OF H^- and D^- BEAMS FROM MAGNETRON AND PENNING SOURCES*

Th. Sluyters and V. Kovarik
Brookhaven National Laboratory
Upton, N. Y.

Summary

The quality of negative hydrogen isotope beams are evaluated after extraction from magnetron and Penning sources. The general conclusions of these measurements are: (A) the beam quality from these plasma sources are adequate for the transport of high current negative ion beams in bending magnets; (B) there is evidence of practically complete space-charge neutralization in the drift space beyond the extractor; (C) the beam performance from the Penning source appears to be better than that of the magnetron source, and (D) it is likely that the high electric field gradient and a concave ion emission boundary are responsible for a beam cross-over near the anode aperture, which causes beam divergence practically independent of the extraction geometry.

Introduction and Experimental Results

For the design of an H^- beam transport and acceleration system, it is necessary to know the beam quality, i.e. the current density distribution and the emittance in the (x, x') and (y, y') phase planes.

The density distribution and emittances were automatically measured and analyzed by an on-line mini-computer[1] and two emittance monitors: one for the horizontal (x, x') emittance and the other for the vertical (y, y') emittance. Each monitor head consists of a 0.004" sample slit and 30 Faraday cups (Fig. 1). The angle resolution is 25 mrad/cup. The monitors, located at 4 or 8 cm. from the source, move in steps of 0.016" to 0.040" per pulse. The computer graphics displays: (A) the emittance in two-dimensional phase-space, (B) the emittance values as a function of threshold level, (C) the density distribution, and (D) the emittance in a three-dimensional plot in which the third coordinate is the beam intensity.

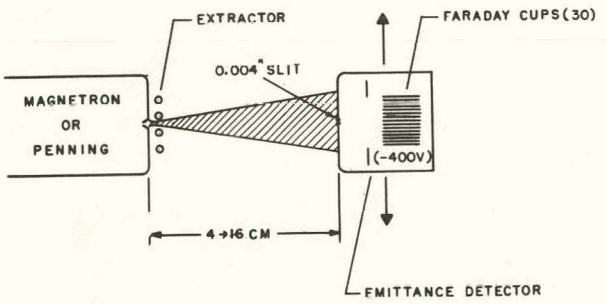


Fig. 1 Experimental arrangement

*Work done under the auspices of the U.S. Department of Energy

The studies were carried out with three types of source covers and a single extractor grid. Their configurations are sketched in Fig. 2.

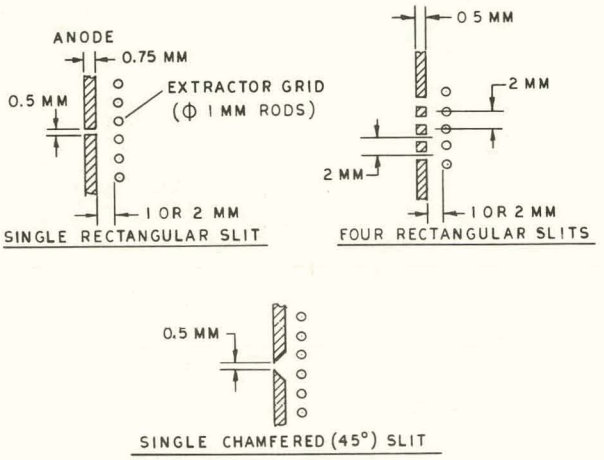


Fig. 2 Emission slit and extractor configurations

Some typical computer output displays are shown in Figs. 3, 4, 5, 6, and 7. Only the display in Fig. 5 was obtained with the monitor at 4 cm from the source. Table I summarizes parameters of several measurements for Penning and magnetron sources, for single slit and four slits. The slit configuration is either rectangular or chamfered.

Discussion

The emittance measurements for beam currents up to 0.35 A, show that the divergence of the negative ion beam perpendicular to the slits is between ±200 and 275 milliradian for energies up to 11 keV. The divergence in the direction of the slits is between ±75 and 125 milliradian.

Measurements also indicate that the angle of the beam envelope does not change in the drift space beyond 4 cm downstream of the source. Figure 5 is the emittance of a 0.2 A beam from a Penning source with four emission slits. All four beams are separated in phase-space. Tracing these beams back to the extractor slit without space charge, the width of each beamlet is very close to that of the aperture, which is 1 mm. These results suggest that for the measured current densities of up to about $1 A/cm^2$ and background pressure of about 10^{-4} Torr, space charge does not play an important role in the drift space beyond the extractor. The divergence of the beam is then determined: (A) by the optics of the extraction system, including the magnetic field and the space charge of the beam in and around the extraction region and (B) by the initial ion emitting surface. Figure 8 shows

TABLE I

Penning Source (Slit dimension 0.5 x 25 mm^2)

SCAN DIRECTION AND SLIT GEOMETRY	BEAM CURRENT [A]	EMISSION CURRENT DENSITY [A/cm]	LINEAR CURRENT DENSITY [A/cm]	ENERGY [keV]	H.V. GRADIENT [kV/cm]	EMITTANCE [cm.mrad]	MAX [mrad]	CATHODE POWER DENSITY [kW/cm]	CROSS OVER WIDTH [mm]	ARC I [A]	ARC V [V]
Hydrogen											
⊥Slit(1, rect.)	0.1	0.8	0.04	7.5	75	208 (82%)	260	8.0	5.0	100	160
⊥Slit(1, chamf.)	0.125	1.0	0.05	10.0	100	110 (80%)	200	6.4	3.6	80	160
⊥Slit(4, rect.)	0.3	0.6	0.12	10.5	52	353 (85%)	200	12.0	10.0	300	80
∥Slit(1, rect.)	0.1	0.8	0.04	8.5	85	600 (82%)	160	8.8	17.0	110	160
∥Slit(1, chamf.)	0.09	0.7	0.04	7.5	75	520 (75%)	80	7.2	26.0	60	240
∥Slits(4, rect.)	0.3	0.6	0.12	10.5	52	450 (85%)	100	11.0	26.0	220	100
Deuterium											
⊥Slit(1, chamf.)	0.11	0.88	0.04	11.3	66	227 (87%)	250	12.2	5.8	350	70
⊥Slit(4, rect.)	0.22	0.44	0.09	10.0	50	296 (85%)	210	10.0	9.0	200	100

Magnetron (slit dimension 0.5 x 43 mm^2)

SOURCE AND SLIT GEOMETRY	BEAM CURRENT [A]	EMISSION CURRENT DENSITY [A/cm]	LINEAR CURRENT DENSITY [A/cm]	ENERGY [keV]	H.V. GRADIENT [kV/cm]	EMITTANCE [cm.mrad]	MAX [mrad]	CATHODE POWER DENSITY [kW/cm]	CROSS-OVER WIDTH [mm]	ARC I [A]	ARC V [V]
Hydrogen											
⊥Slit(1, rect.)	0.2	0.9	0.05	8.5	85	250 (85%)	275	2.3	5.5	140	200
⊥Slit(1, chamf.)	0.2	1.0	0.05	11.0	110	290 (85%)	275	1.8	7.0	150	150
⊥Slit(4, rect.)	0.25	0.3	0.06	9.5	48	380 (85%)	210	2.5	7.7	140	220
∥Slit(1, rect.)	0.35	1.6	0.08	10.0	100	600 (75%)	75	2.6	4.3	160	200
∥Slit(4, rect.)	0.25	0.3	0.06	7.0	35	600 (80%)	90	2.3	4.3	140	200

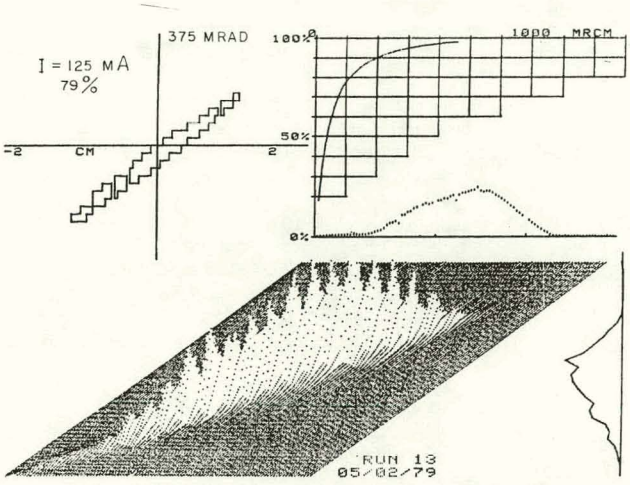


Fig. 3 Penning emittance perpendicular to single emission slit

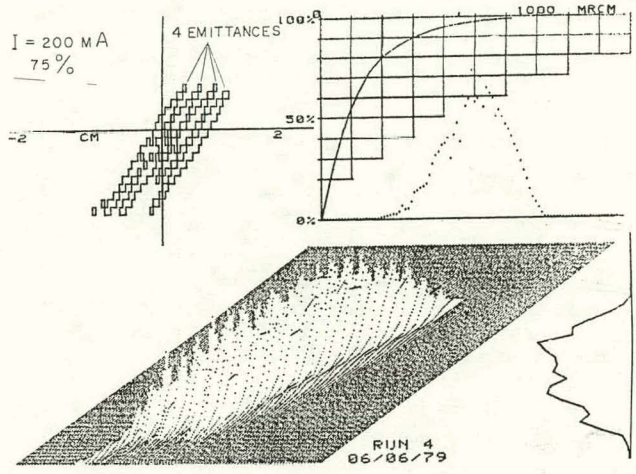


Fig. 5 Penning emittance perpendicular to 4 emission slits

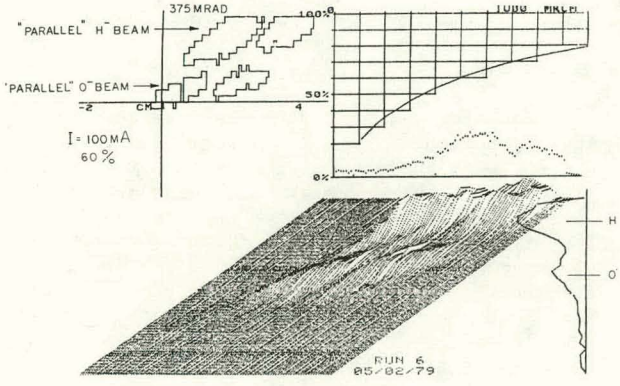


Fig. 4 Penning emittance parallel to single emission slit

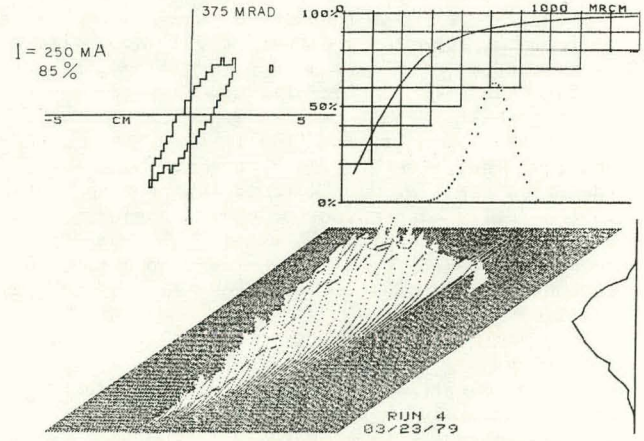


Fig. 6 Magnetron emittance perpendicular to 4 emission slits

the envelope of a negative ion beam with a density of 0.5 A/cm^2, calculated with the SLAC Electron Trajectory Program (SLAC 166) for a field gradient

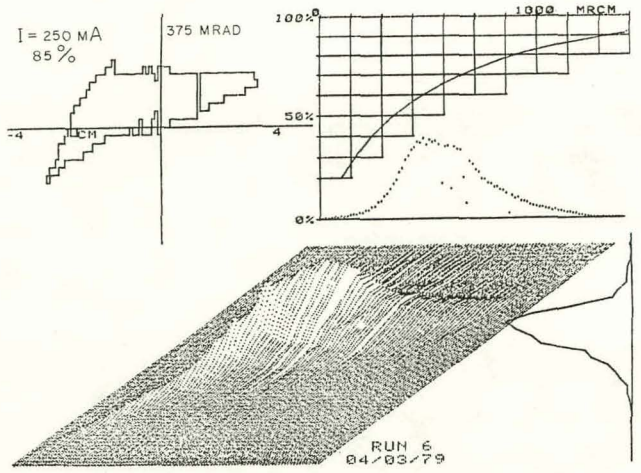


Fig. 7 Magnetron emittance parallel to 4 emission slits

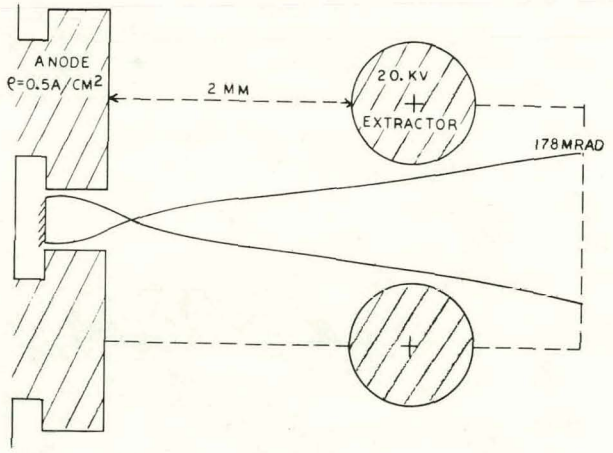


Fig. 8 Beam envelope for an ion beam of 0.5A/cm^2

of 50 kV/cm and taking into account space charge. This calculation suggests that even for a flat emission boundary at the inside plane of the anode, there is strong over-focusing of the beam. The particles are intercepted either at the anode slit or at the extractor electrode. Reduction of extraction voltage should, in principle, move the cross-over point downstream; however, lower extraction voltage also changes the trajectories in the slit region and the final beam divergence remains practically the same (see Fig. 9). Without taking into account what actually happens at the plasma boundary, it is clear that the beam optics should be a compromise between the need for high gradients to extract an intense beam and for low gradients to attain a more parallel beam.

Providing a 45° chamfer on the anode slit reduces the electrostatic shadowing, allowing the extraction field to penetrate deeper into the slit, alleviating some space-charge dilation and blockage. Figure 10 demonstrates the different beam trajectories expected with and without a 45° chamfered anode slit, assuming a flat plasma boundary.

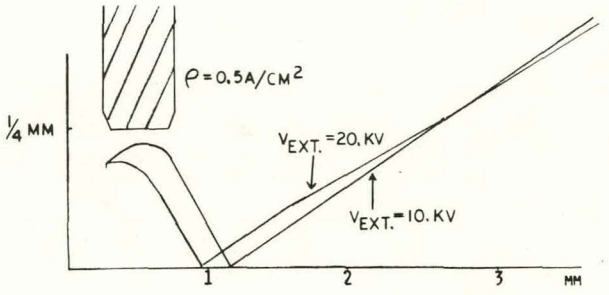


Fig. 9 Beam envelopes for 10 and 20 kV extraction with rectangular emission slit

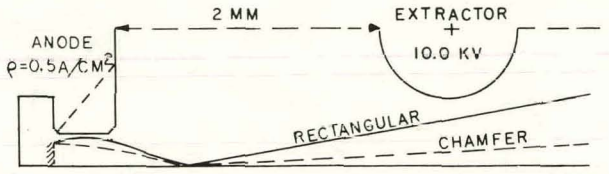


Fig. 10 Beam envelopes for rectangular and chamfered emission slits

For higher initial current densities, lower divergences can be expected (see Fig. 11).

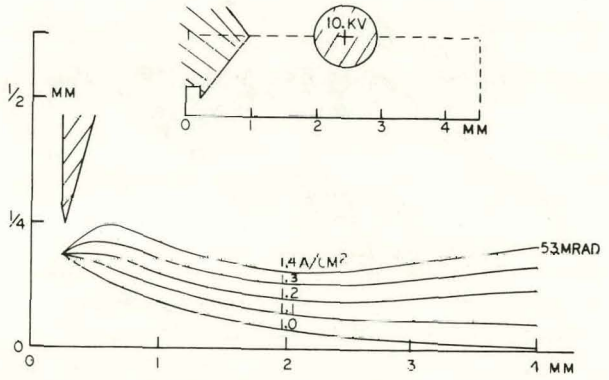


Fig. 11 Beam envelopes for various densities with chamfered emission slit and flat plasma boundary

In practice, only with the Penning source some reduction (∿75 mrad) in angle was observed, but not with the magnetron source. With the Penning source, there was also the tendency of smaller emittance for higher current densities. The different origins of the H$^-$ ions in these plasma sources may explain the difference in performance. For the magnetron, the H$^-$ ion originates from the cathode and may or may not transfer its electron to a slow hydrogen atom. The ion boundary is, therefore, mainly determined by the shape of the cathode and the divergence is not affected by the shape of the anode slit. A concave cathode in the magnetron may improve the optics of the extracted beam. For the Penning source, the H$^-$ ions are formed in the plasma and,

therefore, there is some kind of plasma boundary which will be shaped by the field gradient. Therefore, the flat boundary in Fig. 10 and Fig. 11 is in reality probably concave so that cross-over of the beam in the extraction gap can always be expected.

The beam performance of the Penning source is, in general, better than the magnetron. Its emittance is smaller, in particular for high emission current densities. As mentioned earlier, lower divergence can be obtained by chamfering the source emission slit. The density distribution along the slit is also more uniform than in the magnetron. This is observed both in the emittance measurements and by visual inspection. It should be noticed that the Penning mode of operation is obtained with high ($5kW/cm^2$) cathode power density.

The emittances in the direction parallel to the slit(s) (Fig. 4, and Fig. 7) show no important space-charge blow-up; the beam size increased only by a few millimeters across a drift of 8 cm. The split in the middle of the emittance in Fig. 4 is caused by a metal bar in the center of the emission slit. The split remained even after an 8 cm drift of the beam, confirming the negligible space-charge forces in that part of the beam. The aberrations of the emittances in the direction of the slits are probably caused by misalignment of the electrodes and the off-axis, non-uniform magnetic field. In general, emittances were cleaner with low magnetic field. With identical fields in the bending and source magnet, these aberrations can be expected to be reduced significantly.

The operation of the Penning source with low magnetic field (600 Gauss) and high magnetic field (1100 Gauss) allowed mass analysis of the emerging beam and separation of the emittance of the negative hydrogen ion from that of the heavy ion (O^- or OH^-), as demonstrated in Fig. 4. The proportion of heavy ions in the beam can be large in an unconditioned source. When the source is baked out properly, the heavy ion part of the beam practically disappears.

When hydrogen gas was replaced with deuterium gas, the same beam parameters (current densities and emittances) could be achieved. With deuterium, the source preferred to operate at higher magnetic field and higher ignition voltage, resulting in high arc currents.

With improved electrode alignments, higher extraction voltages, and with the source magnetic field the same as in the beam transport magnet, the matching of high current negative ion beams to the high voltage accelerator looks very promising.

Reference

1 Omnibyte Corporation.

THE EBIS AS AN INJECTOR FOR HEAVY-ION LINACS*

R. W. Hamm
Los Alamos Scientific Laboratory
Los Alamos, New Mexico 87545

Summary

The Electron Beam Ion Source (EBIS), because of its high-charge states and pulsed operation, is ideally suited as an injector for a heavy-ion linac operating at a low duty factor. Although presently in use with conventional linacs, the low emittance and the large yield of highly charged ions in each pulse make the EBIS even more interesting as an injector for the new linac accelerating structures, such as the alternating-phase-focusing (APF) structure, or the radio-frequency quadrupole (RFQ) structure. These new structures could be used with an EBIS to produce a small, efficient, low-duty-cycle accelerator. Coupled to a conventional linac, the resulting accelerator could be used for heavy-ion medical therapy, or nuclear physics, or, it could be used as an injector for a synchrotron or storage ring.

Introduction

The EBIS, Fig. 1, consists of a very dense, energetic electron beam, magnetically confined within a series of insulated cylindrical electrodes along the axis of a solenoid. The space charge of the dense electron beam creates a radial potential well that traps ions as they are created by ionization of atoms injected into the electron beam. A potential distribution, applied to the insulated electrodes, prevents the axial escape of the ions, so that they become highly ionized by successive electron impact ionizations. The ions are trapped within the electron beam until the production of a desired charge state has reached its optimum, and then the ions are extracted by lowering the axial potential on the output end of the source. The total positive charge in the ion source cannot exceed the negative charge in the electron beam. The ionization rate of the ions is dependent on the current density of the electron beam. Thus, the total ion current extracted from the source in each pulse is proportional to the electron beam current, while the confinement period to achieve a particular charge state is inversely proportional to the electron beam current density.

*Work performed under the auspices of the U. S. Department of Energy.

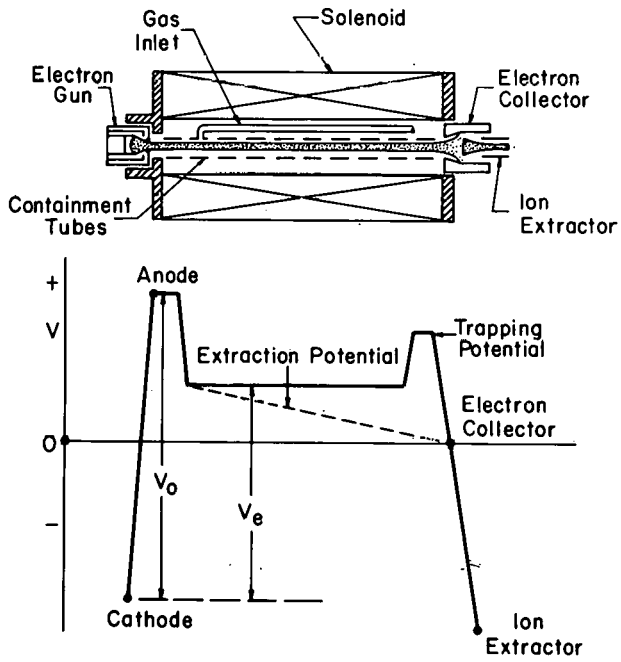


Fig. 1 Schematic of the EBIS.

The ion source configuration was introduced in Dubna[1] and it is currently being studied in Frankfurt, Giessen, Orsay, Cern, Kyushu University, and Texas A&M University.[2] Recent results on the latest version of the EBIS at Orsay[3] have shown spectra containing N^{+7}, Ne^{+10}, A^{+18}, and Kr^{+44} ions. With an electron beam of only 250 mA at 4.3 keV, this EBIS produced 3×10^9 particles/pulse of Ne^{+10} with a confinement time of only 7 ms. The normalized emittance of this source was measured to be 1.2π mm-mrad and the energy spread of the extracted ions was estimated to be 1.4 %/q, where q is the charge of the ions. Figure 2 gives the projected yields from this source operating at the design goal of a 2-A, 10-kV electron beam.[4] These results are for operation of the source with the maximum repetition rate possible and are misleading for low-duty-cycle operation, because of the vanishing duty cycle required for the high-charged, very heavy ions. The projected yields for each pulse of this ion source are given in Table I for several different, fully stripped ions.[5] The calculated confinement period to achieve these charge states is shown and the experimental confinement times given in recent data[3] are shown for N^{+7} and Ne^{+10}.

This EBIS, called CRYEBIS because of the superconducting solenoid and cryogenic pumping, will soon be mounted in a 375-kV high-voltage dome and will be used with a conventional 100-MHz linac to produce beams at 5 MeV/nucleon for injection into the Saturne II synchrotron.[5] Fully stripped ions (q/m = 0.5) up to Ne^{+10}, as well as polarized H^+ ions, will be injected

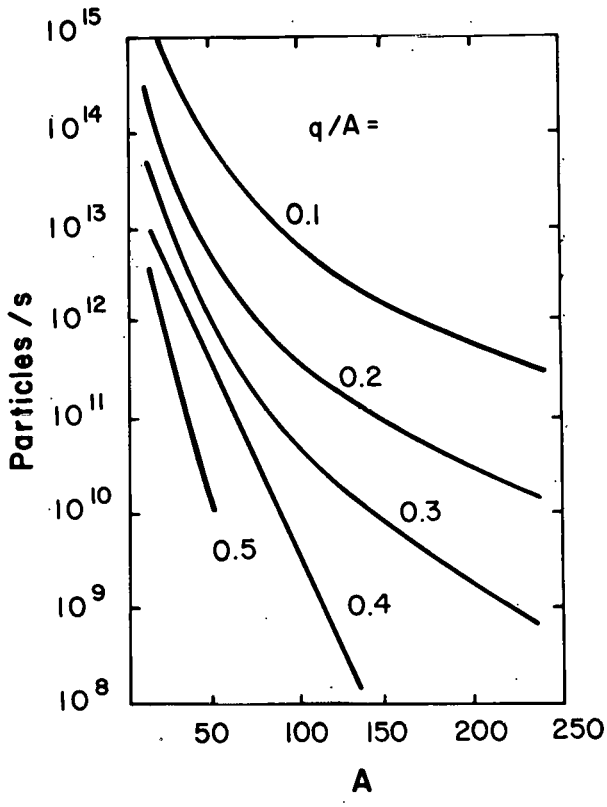


Fig. 2 Projected yields of CRYEBIS.

into the linac from the ion source with the use of a buncher system.

Two such cryogenic EBIS's have been built by Donets and his co-workers in Dubna. These sources have been used to study the time evolution of charge states in nitrogen, oxygen, neon, argon, and xenon.[6] For all ions except xenon, fully stripped nuclei were observed; and in the case of xenon, the highest charge state observed was Xe^{+37}, with the peak intensity being at Xe^{+33}. In addition, the first of these sources (KRION-I) was used with a conventional linac and a 600-kV injector, to inject carbon and oxygen nuclei at 10 MeV/nucleon into the Dubna synchrophasatron.[7] Carbon ions accelerated to 4.2 GeV/nucleon were used in high-energy heavy-ion experiments.

Proposed System

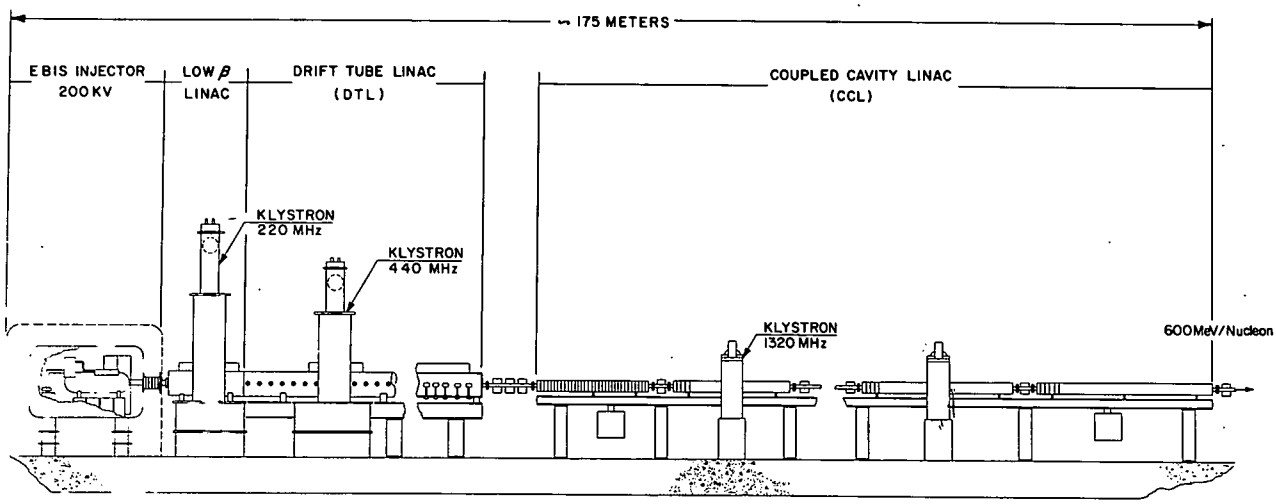
A conservative extension of the present experimental results from the EBIS, yields a very interesting heavy-ion accelerator system when combined with the new linac structures being studied by the Accelerator Technology Division of the Los Alamos Scientific Laboratory (LASL). Programs such as the Pion Generator for Medical Irradiation (PIGMI) Study[8] could have a significant impact on the cost and size of a low-duty-cycle linac for heavy ions, if these new technical innovations are put to use with an EBIS as the linac injector. Figure 3 shows an adaptation of the PIGMI technology to a low-duty linac for heavy ions. This system, designed specifically for injection of fully stripped ions up to calcium (q/m = 0.5), would only be 50 meters longer than the proposed 650-MeV proton linac, and would use the rf and control systems already developed for the proton machine. The low-beta section necessary to accelerate the ions to 1 MeV/nucleon for injection into the drift-tube linac could be either an APF or an RFQ.

TABLE I
YIELD PER PULSE FOR FULLY STRIPPED IONS

Ion	Confinement Time Calculated (ms)	Confinement Time Experimental (ms)	Particles per pulse (10^{10})
C^{+6}	5.6	--	2.6
N^{+7}	9.6	6.0	2.5
O^{+8}	16	--	1.8
Ne^{+10}	40	7.0	2.2
Ca^{+20}	500	--	1.1

The advantage of using an EBIS as the injector in such a system is clearly seen in the study of these low-beta structures. A comparison of a heavy-ion APF proposed by Swenson,[9] and the combination of an EBIS and an APF of approximately the same length and gradient is shown in Table II. An increase in the charge state by a factor of 4 reduces the injector voltage from 1 MV to the inexpensive, manageable, 250 kV presently being used in the PIGMI injector.[10] With the same input energy, gradient and cavity length, the number of cells in the APF are less, and the energy gain is four times greater. The heavy-ion beam would, however, have to be injected into the APF through a buncher system, such as the one used in the PIGMI system.

The alternate solution to the low-beta acceleration in this scheme is the RFQ, an accelerating structure first proposed by Kapchinskii and Teplyakov,[11] which is currently being studied at LASL. Preliminary calculations have shown this structure capable of very high capture efficiency, without the aid of a separate bunching system. The beam dynamics in this structure are described in more detail elsewhere in this conference.[12] The results of a beam dynamics calculation for a Ne^{+10} beam injected into a 200-MHz RFQ from a 200-kV injector are shown in Fig. 4. A modest yield of 10^{10} particles/pulse was assumed to be extracted from an EBIS during 50 μs. With a normalized emittance of 1.2π mm-mrad, 98% of the ions was captured and accelerated to 1 MeV/nucleon, within a 5.3-m structure. The parameters of this RFQ structure are given in Table III. At a repetition rate of 120 Hz, this combination of EBIS and RFQ could produce an accelerated beam of ~2 μA.



LINAC PARAMETERS

FREQUENCY	LOW β SECTION	220 MHz
	DTL SECTION	440 MHz
	CCL SECTION	1320 MHz
GRADIENT	DTL SECTION	6 MV/m
	CCL SECTION	8 MV/m
TRANSITION ENERGY	LOW β/DTL	1 MeV/Nucleon
	DTL/CCL	150 MeV/Nucleon

BEAM PARAMETERS

INJECTOR VOLTAGE	200 kV
INJECTION ENERGY	100 keV/Nucleon
FINAL ENERGY	600 MeV/Nucleon
PEAK BEAM CURRENT	600-800 μA
PULSE LENGTH	50 μs
REPETITION RATE	30-120 Hz
AVERAGE BEAM CURRENT	1-5 μA

Fig. 3 Heavy-ion linac utilizing EBIS and the PIGMI technology.

Applications

The combination of an EBIS and the PIGMI technology will produce a low-duty, low-cost heavy-ion linac that could find application in a number of areas. A machine, such as the one shown in Fig. 3, would provide the desired dose rate for the requirements in the medical program associated with heavy-ion therapy. In addition, such an accelerator could be used in heavy-ion physics and heavy-ion fusion research. If a storage ring is to be used as a source of high-energy heavy ions for physics or heavy-ion fusion research, such a high-gradient, compact linac appears to be an optimum method for filling the ring.

The beam produced by the low-energy section of such a machine (10 to 20 MeV/nucleon) could be used for low-energy heavy-ion physics, and it would also be ideally suited for injection into a synchrotron designed to produce relativistic heavy ions.

Finally, it is obvious from the present EBIS results that a heavy-ion linac for physics applications could be designed for a charge-to-mass ratio of 0.2 to 0.3, using the concepts described above, that would yield useful beams of all elements up to uranium.

Conclusion

The EBIS, as a new alternate source of heavy ions for linear accelerators, has obviously become more realistic with the recent experimental results from the new cryogenic versions. Combining the EBIS with the new innovations in linac technology discussed at this Conference, will yield an efficient, low-duty-cycle, heavy-ion linac useful in several areas. The new low-velocity linac structures, such as the APF and RFQ, make the use of an EBIS with a conventional drift-tube linac much easier, and much more interesting with regard to accelerated ion yields. This is particularly true with the RFQ, if the capture efficiency is near the calculated values.

Even at the present experimental yields from the EBIS, these new linac structures make a low-duty-cycle heavy-ion linac interesting, but the projected yields from the present EBIS and the projections for a future EBIS make such a linac even more interesting. Thus, because it is ideally suited to the operation of a pulsed linac, the use of the EBIS as an injector for future heavy-ion linacs should be pursued.

TABLE II

HEAVY-ION APF STRUCTURE

	APF w/Conventional Source[9]	APF + EBIS
Injected ion (Tin)	$^{124}Sn^{+9}$ (q/m = 0.072)	$^{124}Sn^{+36}$ (q/m = 0.29)
Injection voltage (MV)	1.0	0.25
Injection energy (MeV/nucleon)	0.072 (β = 0.0124)	0.072 (β = 0.0124)
Final energy (MeV/nucleon)	0.285 (β = 0.0247)	1.14 (β = 0.0494)
Total length (m)	1.0	~1.0
No. of cells	40	32
Axial gradient (MV/m)	3.7 to 7.2	3.7 to 7.2

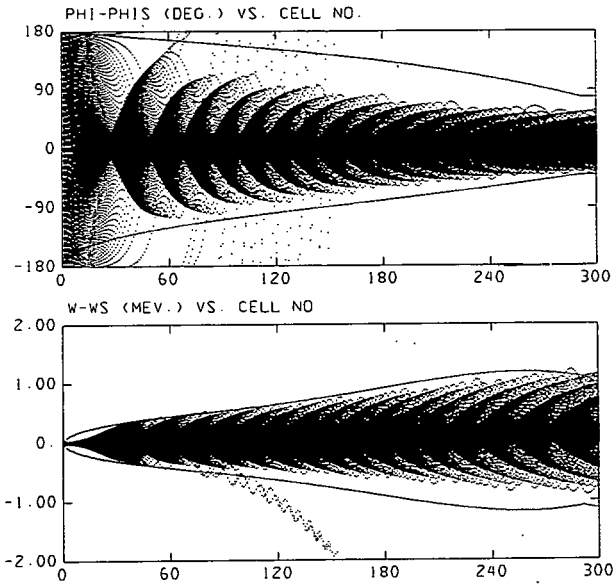


Fig. 4 The RFQ beam dynamics for Ne^{20}.

TABLE III

HEAVY-ION RFQ PARAMETERS

Injection voltage (V_i)	200 kV
Injection energy (W_i)	0.10 MeV/nucleon ($\beta\lambda$ = 2.18 cm)
Frequency (f)	200 MHz
Initial radius (a_i)	0.33 cm
Final energy (W_f)	1.0 MeV/nucleon ($\beta\lambda$ = 6.90 cm
Final radius (a_f)	0.21 cm
Structure length (ℓ)	5.3 m
Final synchronous phase (ϕ_s)	-39°
Peak voltage between electrodes	55 kV

Acknowledgments

The author is indebted to Donald Swenson for his encouragement and discussions during this work, and to R. H. Stokes, T. P. Wangler, and K. R. Crandall for the calculation of the RFQ beam dynamics.

References

1. E. D. Donets, V I. Ilyushchenko, V. A. Alpert, "Electron Beam Multicharged Ion Source," JINR P7-4124, Dubna (1968).
2. Workshop on EBIS and Related Topics, GSI P-3-77, Darmstadt (1977).
3. J. Arianer, A. Cabrespine, Ch. Goldstein, "CRYEBIS, A Multi-Purpose EBIS for the Synchrotron Saturne II," IEEE Trans. Nuc. Sci. NS-26, No. 3, 3713 (1979).
4. J. Arianer and Ch. Goldstein, "Summary of the CRYEBIS Results," IPNO-79-02, Orsay (1979).
5. J. Arianer, A. Cabrespine, G. Deschamps, and Ch. Goldstein, "EBIS Adaptations to Particle Accelerators," GSI P-3-77, Darmstadt, p. 85 (1977).
6. E. D. Donets and V. P. Ovsyannikov, "Production of Nitrogen, Oxygen, Neon, and Argon Nuclei in the KRION-2 Electron Beam Ion Source," JINR P7-10438, Dubna (1977).
7. V. P. Vadeev, E. D. Donets, V. D. Dudnikov, and A. I. Pikin, JINR P7-10823, Dubna (1977).
8. E. A. Knapp and D. A. Swenson, "The PIGMI Program at LASL," 1976 Proton Linear Accelerator Conf., AECL-5677, 230 (1976).
9. D. A. Swenson, "Alternating Phase Focused Linacs," Particle Accelerators, Vol. 7, 61 (1976).
10. R. W. Hamm, R. R. Stevens, Jr., D. W. Mueller, H. M. Lederer and J. N. Leavitt, "A Compact 250-kV Injector System for PIGMI," IEEE Trans. Nuc. Sci., NS-26, No. 1, 1493 (1979).
11. I. M. Kapchinskii and V. A. Teplyakov, "Linear Ion Accelerator with Spatially Homogeneous Strong Focusing," Prib. Tekh. Eksp., No. 2, 19 (1970).
12. K. R. Crandall, R. H. Stokes, and T. P. Wangler, "RF Quadrapole Beam Dynamics Design Studies," proceedings this conference.

DEVELOPMENT OF HIGH CURRENT HEAVY ION SOURCES AT GSI

R. Keller, N. Angert
GSI, Gesellschaft für Schwerionenforschung mbH
Darmstadt, Fed. Rep. of Germany

Summary

Reflex type sources and an ECR source are being investigated at GSI for the improvement of Unilac performance and new accelerator projects. In first runs with a reflex source, ion currents of up to 4 mA have been achieved for argon, krypton, xenon and mercury from 0.5 cm^2 extraction area. The beam brightness was in the range of 115 to 14 $A/(cm\ mr)^2$.

Introduction

At the present time, the ion sources used for Unilac operation are Penning-type. The development of this source has achieved such a level, that most experimental requirements can be satisfied. There are, however, several reasons for starting research activities on ion sources. The lifetime of the Penning-source is sometimes rather short when it is operated in discharge modes required for the production of highly charged heavy ions. In addition, beam current and emittance show a time dependence due to erosion of source and extractor electrodes. For a detailed description of source operation experience see Ref. 1. For isotopes with low natural abundance, ranging from few percent for light ions to about 20% for the heaviest ones, the output intensities of the Unilac are marginal, if natural materials are used in the source. In order to get a better performance in experiments with neutron rich medium mass isotopes, it would be necessary to raise intensities[1] by one or two orders of magnitude to get rid of the dependence on enriched materials. Plans for a synchrotron for relativistic heavy ions, with the Unilac as injector, are based on even higher peak intensity increases, but at a very low duty cycle of only 10^{-4} (100 µs, 1 Hz) compared to 0.25 (5 ms, 50 Hz) of the Unilac. The third aspect for new sources is the inertial confinement fusion with heavy ions. Beams of 50 - 100 mA of singly charged ions of a specific heavy element, are necessary for the rf linac concept to be investigated at GSI.

Source Concepts

For the application at the Unilac two different concepts are being considered. The first is a two stage ECR-type source.[2] In the first stage, a dense, low ionized plasma is produced by microwave heating in a magnetic field. It then drifts to a second stage, where ionization to higher charge states takes place, due to lower background pressure and intensified electron cyclotron resonance heating by microwaves in a magnetic mirror. There should be no lifetime problems, at least for gaseous elements, since this source needs no electrodes. In addition, the current densities in the extraction area will be low compared to a Penning-source, so that negligible erosion and a stable beam can be expected. The distinction between the GSI concept and others proposed for cyclotrons,[3,4] is that this source is for comparatively low charge-to-mass ratios and high current. The design aim is an electrical current of 100 µA of U^{10+} out of the source. The first stage of the ECR source has been constructed. Tests with 2.4 GHz, instead of 14.5 GHz, which is the design frequency, have been performed just recently.

As an alternative to the production of highly charged ions directly within the source, there exists the possibility to produce high current beams of singly or doubly charged ions and strip them to the wanted charge states after an appropriate preacceleration. However, this way is much more expensive than using a source for high charge states, and only justified if very high currents are needed.

In connection with inertial confinement fusion, sources have been developed which deliver 50 to 100 mA of singly charged heavy ions.[5,6] The fraction of doubly charged ions lies between 5 and 10%. This 2+-current would be already enough to increase the intensities from the Unilac as a synchrotron injector, by a factor of 1000. It would require a preaccelerator for 100 keV/u to get the appropriate charge states after stripping in gas. This means that such a source will satisfy both the goals of inertial confinement fusion and of the heavy ion synchrotron. However, the latter application claims a broad range of elements. Several high current source designs were investigated, including even the first stage of the ECR source. The source design which has proceeded furthest, is the so-called picket fence type,[7] which is to be described in the following section.

Ion Source

This approach to getting high currents is based on a source design for neutral injection systems developed at Culham.[8] A schematic of the source is shown in Fig. 1. A cathode disc heated by two filaments delivers the electrons to the plasma. A copper cylinder of 5-cm diameter serves as anode, which is lined with permanent magnets. The two reflector electrodes should reflect the primary ionizing electrons. The extraction is performed by a 7-hole accel-decel system.

The magnets on the anode are arranged to form a 12-pole line-cusp field. Figure 2 shows cross-sections of the source and the radial and axial dependence of the azimuthal field component. A schematic of the electrical supplies is shown in Fig. 3. The source is typically operated with a discharge voltage of 50 to 100 V, and about 40 to 80 A discharge current, at a pulse width of 2-ms and 50-Hz repetition rate. Figure 4 shows the oscillogram of voltage and current

for an argon discharge, indicating a very quiet plasma in the source compared to our earlier experiences with high current duoplasmatron sources. The choice of discharge parameters and pulse width was dominated by present limitations of the power supplies; a 300-A power supply is under construction. The disc cathode, developed earlier for GSI duoplasmatron sources,[9] proved to be quite adequate for the high duty cycle.

Experimental Setup

Extraction of ions is performed by a multi-aperture accel-decel system with 7 holes arranged within a circle of 14.4-mm diameter. Its design follows guide lines of the Culham group,[10] developed for single aperture systems. The first experiments used holes with a radius of 2.05 mm. Due to limitations of the extractor supply, the holes presently utilized have only a radius of 1.55 mm, adding up to an extraction area of 0.53 cm^2. With the smaller holes, the optimum extraction voltage lies in the range of 30 kV, with about - 1 kV for the

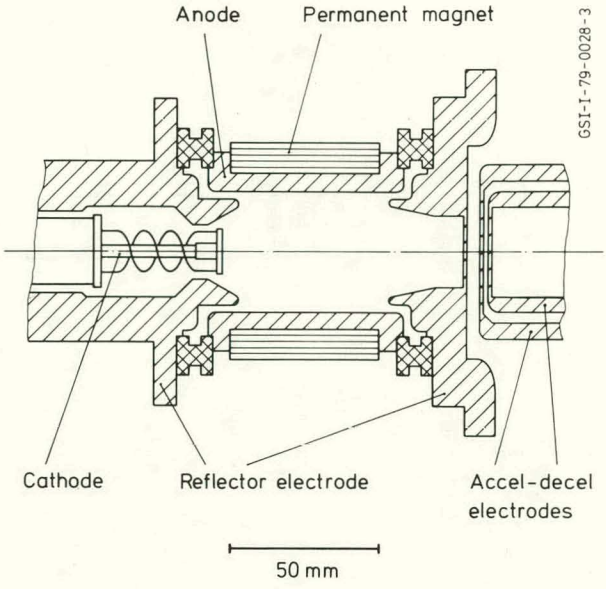


Fig. 1 Schematic of the ion source

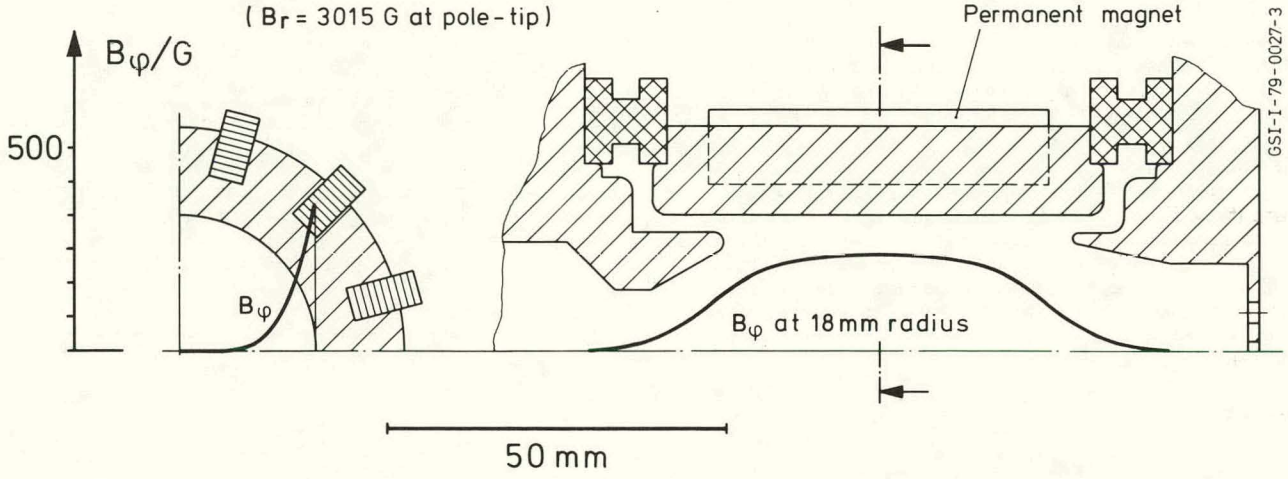


Fig. 2 Azimuthal component of the 12-pole line cusp-field

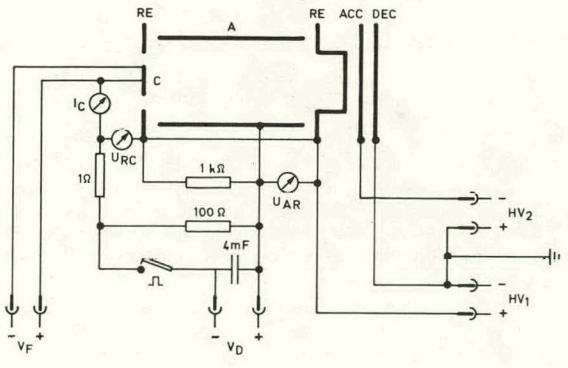


Fig. 3 Schematic of the electrical supplies of the ion source

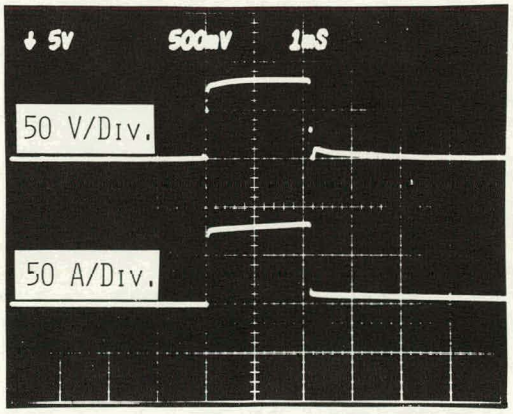


Fig. 4 Source pulse characteristic

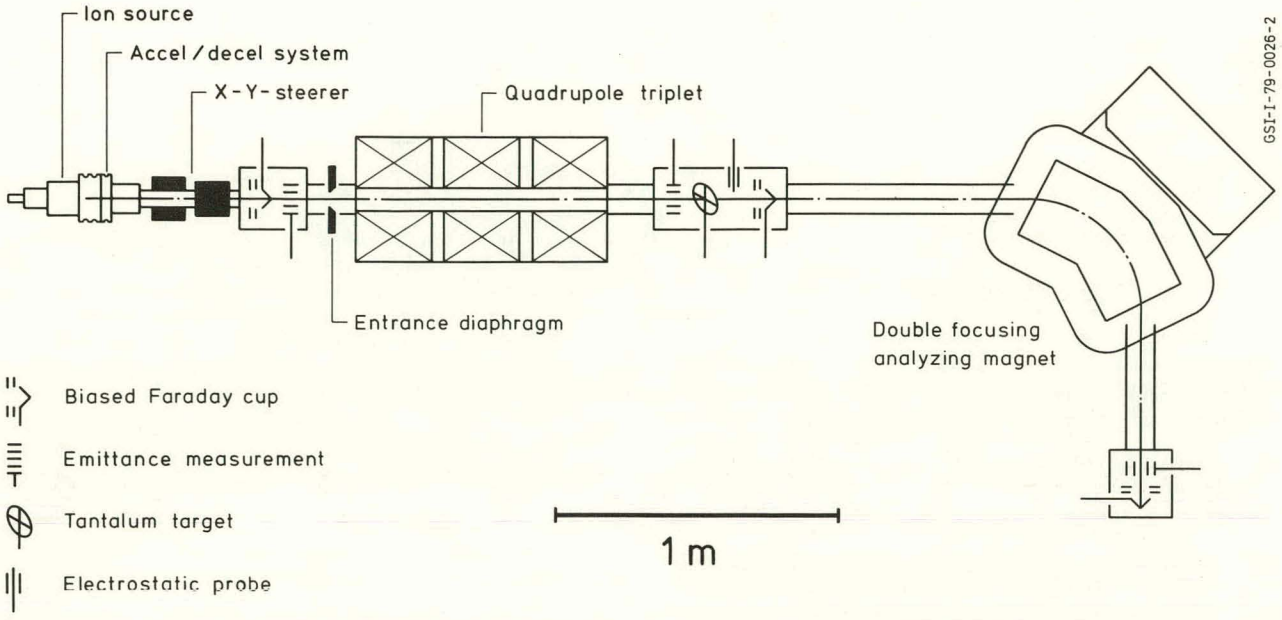


Fig. 5 Experimental Setup

accel electrode, at electrode spacings of 3.8 and 1.5 mm, respectively. Behind the extractor system (Fig. 5), a steering magnet is installed to enable correction of the beam position for the following beam diagnostic systems and for the straight through transport to the analyzing magnet. Biased Faraday cups with additional magnetic electron suppression, are used for current measurements. For the emittance measurement, a pepper pot device is presently used. An on-line emittance measurement device is going to be installed. The quadrupole triplet and the electrostatic probes are under construction. During operation of the source, the pressure in the beam line is about 5×10^{-5} Torr.

Experimental Results

The source was operated with argon, krypton, xenon and mercury. For the rare gases, the source runs in the magnet field as shown in Fig. 2. For mercury, a source with a slightly weaker magnetic multipole field was used, substituting for the copper anode cylinder, a slightly different stainless steel cylinder, to avoid build up of amalgam. The beam current was measured with two cups of different design: a short (FC1, 50 mm) and a long (FC2, 200 mm) one. The current-versus-bias characteristics of both cups are shown in Fig. 6. Table I gives the total pulse currents for the different elements, as measured with the short Faraday-cup at a distance of 300 mm from the source. Figure 7 shows a corresponding beam pulse for argon. The pulse is smooth up to 40 mA. One can increase the beam current above this value up to 55 mA, but then it starts showing strong oscillations of up to 20% of the pulse height.

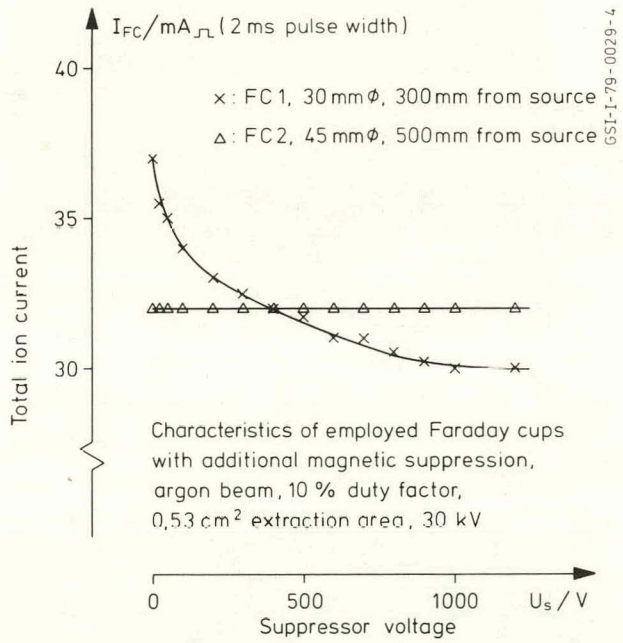


Fig. 6

Due to the high pressure in the beam line and because presently there is no quadrupole triplet available, only a fraction of about 20 % of the total extracted beam has been analyzed in 4.5 m distance from the source. The 2+-portion in Table I corrected for the corresponding emittance, but not for charge-exchange losses. Measurement of the beam emittances was done in a distance of 300 mm behind

Table I

Total beam currents measured 300 mm from the source in a 30-mm diameter Faraday-cup and charge state fractions measured behind the analyzing magnet (≤ 20% of the beam were analyzed). Extraction voltage 30 kV.

Element	Total Current mA (2ms)	Relat. Abundance %	
		1+	2+
Ar	40	97	3
Kr	31	94	6
Xe	26	87	13
Hg	18	93	7

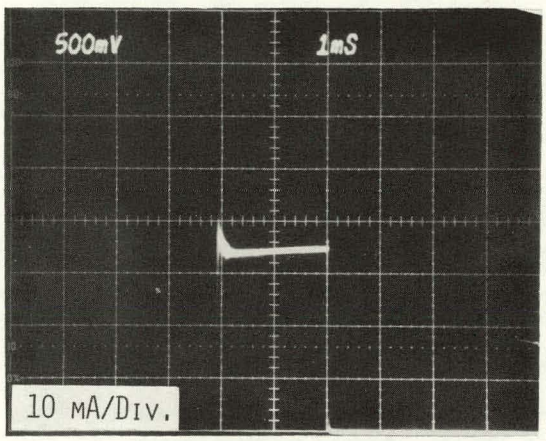


Fig. 7 Argon beam pulse signal measured 300 mm behind the source

the source. The evaluated normalized emittances ε_N, are in the range between 0.015 to 0.017 cm-mrad, thus resulting in brightnesses $B = I/\varepsilon_N^2$, of 115 A/(cm mr)^2 for xenon and 140 for argon.

The experiments with this source are in a very early state. The reflector electrodes could not yet operate biased negative with respect to the cathode, thus ensuring reflection of the primary electrons and reducing the discharge power. With the rare gases, the reflector electrode is biased about +20V with respect to the cathode during the discharge pulse. With mercury, the reflector potential was near to cathode potential, resulting in a reduction of the discharge power: 50%, compared to rare gases for about the same plasma density.

Acknowledgements

The authors acknowledge the assistance and information received from colleagues at LBL, in designing the multiaperture extraction system. The authors also thank F. Schäffer for his skillful assistance in the experiments, and our colleagues of the Ion Source Group for their collaboration and support in constructing and installing the test bench.

References

1. D. Böhne, "Status Report on the Unilac", proceedings of this conference.
2. R. Geller, Electron Cyclotron Resonance (ECR) Multiply Charged Ion Sources, IEEE Trans. Nucl. Sci., NS-26, No. 2, 2120, April 1979.
3. Y. Jangen et al., "Status of the ECR Heavy Ion Source and its Interfacing with Cyclone", IEEE Trans. Nucl. Sci., NS-26, No. 3, 3677, June 1979.
4. V. Bechtold, "An ECR-Type Light Ion Source for the Karlsruhe Isochronous Cyclotron", IEEE Trans. Nucl. Sci., NS-26, No. 3, 3680, June 1979.
5. W. Chupp et al., "Operation of High Current Xenon Source", IEEE Trans. Nucl. Sci., NS-26, No. 3, 3036, June 1979.
6. R.P. Vahrencamp et al., "A 100-mA Low-Emittance Ion Source for Ion-Beam Fusion", IEEE Trans. Nucl. Sci., NS-26, No. 3, 3101, June 1979.
7. L.D. Stewart et al., ORNL-5154 Ann. Rep., 118, (1976).
8. A. Goede et al., "Particle Balance in a Picket Fence Ion Source", 8th Europ. Conf. on Controlled Fusion and Plasma Physics, Prague, 1977.
9. R. Keller, Int. Conf. on Ion Implantation Equipment, Povo (Italy) 1978, to be published in Radiation Effects.
10. J.R. Coupland et al., Rev. Sci. Instr. 44, 1258 (1973).

1979 LINEAR ACCELERATOR CONFERENCE

NEW METHOD FOR POSITRON PRODUCTION AT SLAC*

B. Aune+ and R. H. Miller
Stanford Linear Accelerator Center
Stanford, California 94305

Summary

The focusing system for the positron beam at SLAC makes use of an adiabatically tapered solenoid, whose transverse acceptance remains high over a broad energy band. From the computed distribution in energy of the accepted positrons, one can estimate that approximately one-half of the total number of positrons lie within the energy band from 2 - 4 MeV. Due to the debunching effect over the drift space following the target, only the high energy part (from 4.5 MeV to 10 MeV, or more) of the accepted spectrum contributes to the useful current (within 1% energy bin). By decelerating the beam in a special short section very near the converter, it is possible to obtain a bunching of all the accepted positrons with energy above 2 MeV within approximately 5°, giving an improvement of a factor of two on the analyzed current.

Description

Focusing system

The focusing system for the positron beam[1] consists of a 7-meter long solenoid (up to an energy of 55 MeV) and of quadrupole triplets and doublets. The emittance matching between the plane of the target and the solenoid uses an adiabatically tapered solenoid. Recent computations made by M.B. James et al.,[2] showed that the transverse momentum accepted by the system remains high ($p_t \geq 0.6$ MeV/c) over a very broad energy band (2.5 MeV $\leq E \leq$ 30 MeV). In addition they computed the distribution in energy of the accepted positrons from which one can estimate that approximately one-half of the total number of accepted positrons lie within the energy band from 2 - 4 MeV. To maximize the current of positrons it is then necessary to accelerate the broadest energy band possible, starting from the lowest energy possible. The limitation in that process is the debunching effect in the drift space following the target and in the first few cm of the acceleration, leading to a broadening of the energy spectrum.

Rf system

The distance between the target and the first accelerating section had been set rather large (93 cm), mainly to provide space for collimators. It was decided last year to insert in that space a special short section (Fig. 1). This section is a 5λ-long (52.5 cm), constant impedance structure; the group velocity is $v_g/c = 0.0204$. The accelerating field is related to the input power by $E\,(\text{MeV/m}) = 3.55\sqrt{P}\,(\text{MW})$. The distance between the target and the first section is then reduced to 14.2 cm. The section is followed by a drift space of 26.5 cm, in which are located a collimator and a fast vacuum valve.

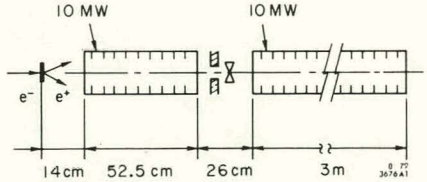


Fig. 1. Positron source accelerator structure.

Longitudinal Motion of Positrons

Debunching

In the drift space from the target to the section, the beam is debunched because of different energies, hence different velocities, and because of the spiralling path of positrons with different transverse momentum.

Let D be the length of the drift space. The phase slippage, with respect to a wave traveling at the velocity of light, is given by:

$$\Delta\phi = \frac{2\pi}{\lambda}\left(1 - \frac{1}{\beta_z}\right) D \quad , \tag{1}$$

where β_z is the axial velocity in units of c, and λ is the rf wavelength. The axial momentum is given by:

$$p_z^2 = \gamma^2 - 1 - p_t^2 \quad ,$$

where p_t is the transverse momentum in units of mc and $\gamma = E/mc^2$. The axial velocity is $\beta_z = p_z/\gamma$. In the tapered field region the transverse momentum varies as:[3]

$$p_t(z) = p_{to}\left(\frac{B(z)}{B_o}\right)^{\frac{1}{2}} \quad , \tag{2}$$

where p_{to} and B_o are the transverse momentum and the magnetic field on the target. The phase slippage is then:

$$\Delta\phi(\gamma_o \quad p_{to}) = \int_o^D \frac{2\pi}{\lambda}\left(1 - \frac{\gamma_o}{(\gamma_o^2 - 1 - p_t^2(z))^{\frac{1}{2}}}\right) dz \quad , \tag{3}$$

with $p_t(z)$ given by Eq. 2 , which can be approximated by:

$$\Delta\phi = -\frac{\pi}{\lambda}\frac{1}{\gamma_o^2} p_{to}^2 \frac{1}{B_o}\int_o^D B(z)dz - \frac{\pi}{\lambda}\frac{1}{\gamma_o^2} D + \ldots \quad .$$

The total longitudinal phase-space can be calculated for a distance D and a range of energy and transverse momentum, for a given law of magnetic field $B_{(z)}$. Figure 2

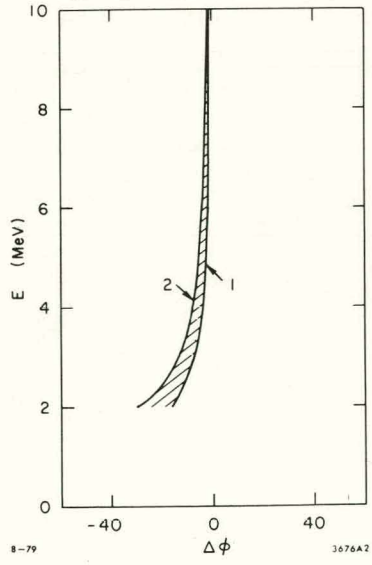


Fig. 2 Longitudinal phase-space after a 14.2 cm drift: Curve 1 for $p_{to} = 0$; Curve 2 for $p_{to} = 0.6$ MeV/c.

*Work supported by the Department of Energy under contract DE-AC03-76SF00515.
+On leave from Centre D'Etudes Nucléaires (Saclay) France.

shows the results in the case of D = 14.2 cm, for energies from 2 - 10 MeV and a maximum transverse momentum on the target of 0.6 MeV/c. The total bunch length is about 30°. The bunch length for energies from 4 - 10 MeV is only 8°. The contribution to the phase dispersion from the spiralling path is approximately equal to that of the velocity dependent effect for a given energy. Clearly, one needs a rebunching process to accelerate all the accepted positrons within a reasonable energy spectrum.

Principle of bunching

1.) Let us first consider the case of positrons moving on the axis ($p_{to} = 0$) and assume that the beam enters an accelerator which is long enough to consider the asymptotic behavior of the positrons. The motion of the positrons can be described by orbits, Fig. 3, in the

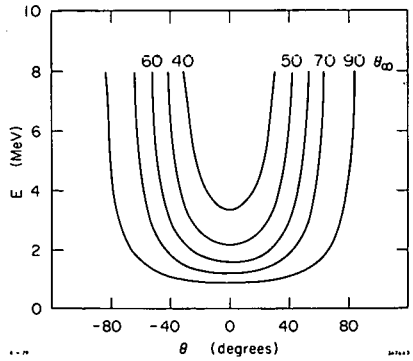


Fig. 3 Orbits in longitudinal phase for particles in a linac.

phase-space E, ϕ. The equation for the orbits[4] is:

$$\cos\phi - \cos\phi_\infty = \frac{2\pi}{\alpha}\left[\gamma - (\gamma^2 - 1)^{\frac{1}{2}}\right] \quad , \quad (4)$$

where $\alpha = eE'\lambda/mc^2$ is the energy gain per wavelength in the units of mc^2, and ϕ_∞ is the asymptotic phase. The reference of phase is such that the electric field is 0 for $\phi = 0$.

On the other hand, there exists a relation between phase and energy as the beam enters the accelerator, which can be written, using Eq. 1 :

$$\phi_o = \Phi_o + \frac{2\pi}{\lambda} D\left(1 - \frac{\gamma_o}{(\gamma_o^2 - 1)^{\frac{1}{2}}}\right) \quad , \quad (5)$$

Φ_o being a parameter which represents the input phase of the field for a $\beta = 1$ positron.

By using Eqs. 4 and 5 one can compute optimum values for the parameters α, D and Φ_o, in order to obtain a minimum dispersion in asymptotic phase for a given range of γ_o. The asymptotic phase ϕ_∞ must be chosen near -90° in order to obtain the maximum acceleration. The orbits (γ, ϕ) resulting from Eq. 4 are symmetric with respect to $\phi = 0$. Positive values of ϕ_o (decelerating field) give a positive slope $d\gamma_o/d\phi_o$. Equation 5 gives a positive slope $d\gamma_o/d\phi_o$. The best fit between relations 4 and 5 will then be obtained when the beam enters the accelerator in a decelerating field. The optimum value of Φ_o will be near 90° for $\phi_\infty = -90°$ This can be easily understood by looking at Fig. 2 and comparing it with the general shape of the phase-space orbits in Fig. 3.

As an illustration of this bunching process, Fig. 4 shows the phase space resulting from the drift space of 14.2 cm for energies from 2 MeV to 10 MeV (solid curve), together with the orbits $\phi_\infty = -85°$, -90° and -95°, for an accelerating field of 12 MeV/m (dotted curves) and $\Phi_o = 86°$ (decelerating field). It is seen that the

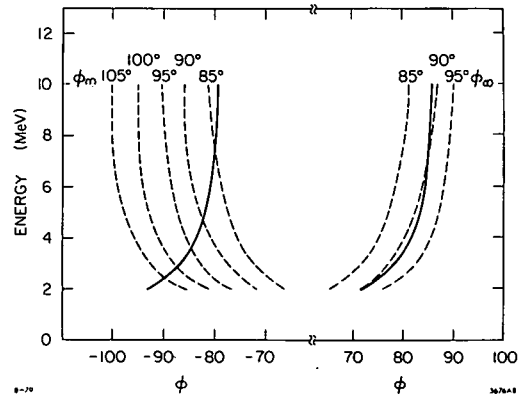


Fig. 4 Longitudinal phase space at entrance to acceleration section

fitting with the -90° orbit is achieved within less than ± 2° and one can expect a dispersion of asymptotic phase (i.e., a bunch length) of less than 4°. On the other hand, Fig. 4 also shows the same phase-space for the beam together with the orbits -75°, -80°, -90° and -100° in the case $\phi_o = -70°$ (accelerating field). It is evident that the dispersion in asymptotic phase will be greater than 25°. The integration of the equations of motion over a distance of 3 m gives a total bunch length of 31°; the output energy varies from 37 MeV to 44 MeV.

It appears that this bunching process is very efficient for an initially bunched beam, which contains particles within a large energy band extending down to a very low energy, and which has been debunched under the action of different velocities over a drift space.

2.) Positrons With Transverse Momentum - If it is assumed that there exists no other transverse force than the focusing effect of the dc magnetic field, then the transverse momentum remains constant in a constant focusing field, or varies according to Eq. 2 if the magnetic field varies slowly. The equations of longitudinal motion can be written in that case:

$$\begin{cases} d\gamma = -\alpha \sin\phi \, dz \\ d\phi = 2\pi\left(1 - \dfrac{\gamma}{(\gamma^2 - 1 - p_t^2(z))^{\frac{1}{2}}}\right) dz \end{cases} \quad (z \text{ in units of } \lambda)$$

For constant p_t, these equations can be combined and integrated, giving:

$$\cos\phi_o - \cos\phi_\infty = \frac{2\pi}{\alpha}\left[\gamma_o - (\gamma_o^2 - 1 - p_t^2)^{\frac{1}{2}}\right] \quad , \quad (6)$$

which defines new orbits in the phase space E, ϕ. Let us consider two positrons of the same energy γ_o, one moving on the axis and one leaving the target with a transverse momentum p_{to}. Let ϕ_{o1} be the entrance phase for first one and $\phi_1 = \phi_{o1} - \delta\phi$ the phase for the second one, where

$$\delta\phi = \Delta\phi\,(\gamma_o, 0) - \Delta\phi\,(\gamma_o, p_{to}),$$

where $\Delta\phi$ is given by Eq. 3. In the approximation of small angle of emission, one can write

$$\delta\phi = \frac{\pi}{\lambda}\frac{p_{to}^2}{\gamma_o^2}\frac{1}{B_o}\int_o^D B\,dz \quad ,$$

which can also be written

$$\delta\phi = \frac{\pi}{\lambda}\frac{p_t^2}{\gamma_o^2} \cdot K \quad ,$$

where p_t is the transverse momentum in the section and

$$K = \frac{1}{B_2} \int_o^D B_{(z)} dz$$

B_2 being the magnetic field in the section, which is supposed to be constant. Equation 6 can be approximated by:

$$\cos\phi_o - \cos\phi_\infty = \frac{2\pi}{\alpha} \left[\gamma_o - (\gamma_o^2 - 1)^{\frac{1}{2}} + \frac{1}{2} \frac{p_t^2}{(\gamma_o^2 - 1)^{\frac{1}{2}}}\right] \quad (6b)$$

Using Eqs. 4 and 6b together with the expression for $\delta\phi$, the dispersion in asymptotic phase is given by:

$$\delta\phi_\infty \sin\phi_\infty = \left[\frac{\pi}{\lambda} \frac{1}{\gamma_o^2} K \sin\phi_{o1} - \frac{\pi}{\alpha} \frac{1}{(\gamma_o^2 - 1)^{\frac{1}{2}}}\right] p_t^2 \quad (7)$$

It is seen that one can choose the accelerating field and input phase, for a given energy, to make the asymptotic phase independent of the transverse momentum.

It is evident from Eq. 7 that ϕ_{o1} must be positive, i.e., the beam must be decelerated. The accelerating field E' and input phase are simply related to the energy E_o by:

$$E' \sin\phi_{o1} \approx \frac{E_o}{K}$$

In the case of SLAC, K is of the order of 0.45 m. For E_o = 2 MeV, this gives $E' \sin\phi_{o1} \approx 4.4$ MeV/m. The equations of motion have been integrated over a distance of 3 m for E_o = 2 MeV, E' = 10 MeV/m, p_{to} = 0 to 0.6 MeV/c, and $\phi_{o1} = 25°$ (ϕ_o in Eq. (5) $\simeq 40°$). The resulting phase dispersion is less than 1°, for an input dispersion of 15°.

This bunching process could be very useful in the case of a high transverse acceptance over a narrow energy band centered on a low energy (use of a quarter wave transformer).

It is concluded that by first decelerating the positron beam, one can take advantage of using very low energy and high acceptance (in this case the angular acceptance at 2 MeV is 18°) together with large energy band, leading to a maximum current of positrons within a narrow energy spectrum. The limitation may be the initial energy dispersion in the case of a low final energy.

Results of Calculations in the Case of SLAC

The first section is a very short one, followed by a drift space (Fig. 1). With an accelerating field of the order of 10 MeV/m, it is evident that one cannot take full advantage of the bunching process described above, mainly because the minimum energy at the end of the first section must be high enough to avoid a debunching effect over the second drift space. The longitudinal motion was computed for several values of the parameter ϕ_o (see Eq. 5) and the accelerating field. Figure 5 shows the resulting phase space at the entrance of the second section in the cases ϕ_o = 70° and 30° (beam initially decelerated) and ϕ_o = -70° (beam accelerated), and a field of 10 MeV/m. For each case, the two solid curves with cross-hatching between them represent the phase space for positrons with initial transverse momenta between 0 and 0.6 MeV/c. The effect of the second drift space is clearly seen in the case ϕ_o = 70°: the minimum energy is about 1 MeV and the phase-space is completely distorted. In the case ϕ_o = 30° the minimum energy is 2.5 MeV and the distortion of the phase space is much less important. The orbits for ϕ_∞ = -40° and ϕ_∞ = -50° are shown on the same scale for an accelerating field of 10 MeV/m (the second section is long enough to consider at a first approximation the asymptotic behavior). The fitting between these orbits and the phase-space of the

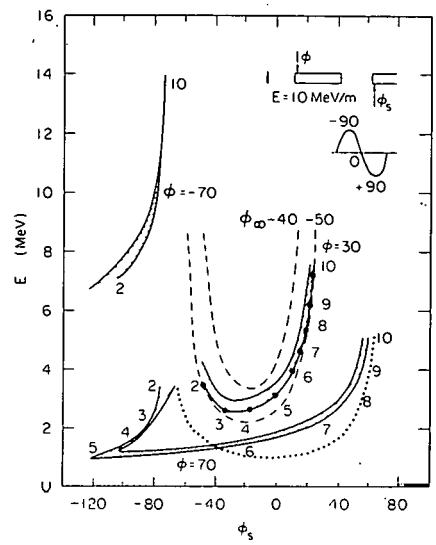


Fig. 5 Longitudinal phase-space at entrance to second section, for three phases entering short section: ϕ_o = 70°, ϕ_o = +70° and the optimum ϕ_o = +30°.

beam is reasonably good and one can expect a total bunch length of less than 10°. In addition, it can be seen that the bunching of low energy positrons with transverse momentum from 0 to 0.6 MeV/c has been achieved in the short section.

In the case ϕ_o = -70° (beam accelerated), no bunching effect has occurred; the total bunch length is 46° and no further bunching can occur in the second section. The phase space at the end of the second section has been computed for various values of the accelerating field, input phase and different phase space configurations resulting from the first section. Figure 6 shows, on the

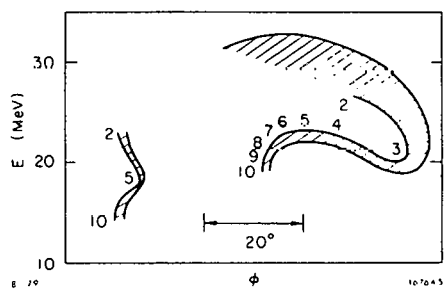


Fig. 6 Phase space at output of second section;
Left: New section in use.
Right: Without new section.

left, the result in the case of the phase-space shown in Fig. 5 for ϕ_o = 30°. The input phase for the second section is ϕ_o = 50° (phase of the field for a β = 1 particle). The average output phase is -45°, giving a total phase slippage for the beam of about 95°. The bunch length is 6° and the energy dispersion 10.5 MeV. Shorter bunches can be obtained at the expense of final energy and energy dispersion. The transition between the solenoid and the quadrupole must take place at an energy of at least 55 MeV in order to keep an admittance of 0.15 π MeV/c-cm]. With the phase-space of Fig. 6, adding a 3 m-long section with the same field gives an energy from 44 MeV to 54 MeV. Studies have been made of two

ways of increasing the energy without perturbing the bunching process, for the same accelerating field:

- Detuning of three cavities of the long section at 1.2 m from the rf input (giving a phase shift of 20° to 45°) increases the output energy by about 5 MeV, giving a bunch length of 7°.
- Lowering the temperature of the section by 4°C, to increase the phase velocity, gives approximately the same result.

These techniques are possible because the bunching process takes place mainly in the first meter of the structure, after which the phase of the field remains around -45°.

Remarks on the Calculations

1. It is known [5] that during the bunching of electrons, the space harmonics of the field can lead to a broadening of the bunch width. The equation of motion has been integrated, taking into account the space harmonics n = 1 and n = -1, whose amplitudes for a SLAC structure are $E_1 = -0.077$, $E_{-1} = 0.454$ for an amplitude of the fundamental $E_o = 1$. Even in the case of a strongly decelerated positron, the changes in phase and energy were found to be not significant within the accuracy needed.

2. Influence of the E_r and β_ϕ components of the field

(a) Transverse motion - During their motion with respect to the wave, in a region where $\partial E/\partial z < 0$, the positrons will experience a defocusing force due to the E_r and β_ϕ components of the field. The radial equation of motion can be written [6]

$$\frac{d}{dz}\left(\beta\gamma \frac{dr}{dz}\right) = r\left[\frac{\pi}{\lambda} \frac{E_o}{\beta^2\gamma^2} \cos\phi - \frac{B_{ext}^2}{4\beta\gamma}\right] , \quad (8)$$

where r = distance from the axis, E_o = accelerating field in units of 0.511 MeV/cm, and B_{ext} is the dc magnetic field in units of $mc^2/e/cm$ (= 1704 Gauss). The first term, which is due to the rf fields, can have a magnitude about 1/4 the magnitude of the second term for distances of a few centimeters, when a low energy positron passes through zero phase.

(b) Longitudinal Motion - When the bunching of positrons of the same energy and different transverse momentum was studied, the effect of the axial force resulting from the interaction of radial velocity and azimuthal magnetic field was neglected. The complete equation of motion can be written in the case of the fundamental alone [7]:

$$d\gamma = -\alpha\left[\sin\phi - \frac{2\pi}{\lambda} \frac{r\, p_r}{\beta\gamma} \cos\phi\right] dz \quad . \quad (9)$$

This equation has been integrated in the case mentioned before (E_o = 2 MeV, E' = 10 MeV/m, $\phi_o = 25°$, p_{to} = 0 to 0.6 MeV/c) for various values of the initial azimuth angle. It was found that the maximum output phase variation is about 2°.

Comparison with the Present Mode of Operation

In the present mode of operation, the short section is not used. The rf phases of the linac are not changed from electron to positron acceleration. The positron beam is then decelerated in the 3-m long section. The phase-space at the end of the section was computed for different values of the input phase and field which give a total phase slippage for the beam of about 180°. Figure 6 shows the resulting phase-space for a field of 10 MeV/m and an input phase of $\phi_o = 00°$. Positrons with energies from 4.5 MeV to 10 MeV are bunched within approximately 10°. Positrons from 2 to 4 MeV are far away in phase and will not contribute to the useful beam (within 1% energy bin).

Results of Experiment

The short section was used in June 1979 for an experiment with positron beams of final energy 1.8 GeV and 10 GeV. The analyzed current within 1% was increased in both cases by at least a factor of two with respect to the usual current. The optimum shift for the rf downstream of the target, versus electron operation, was found to be about 80°, giving a phase slippage for the beam of about 100°. These results are in good agreement with the calculated values. The short section will be put into normal operation next October, with 75° pulsed phase shifters for the kylstrons upstream the converter.

References

1. The Stanford Two-Mile Accelerator, R. B. Neal, ed. (W.A. Benjamin, New York, 1968).
2. M. B. James. R. H. Miller, B. M. Woo, "A Calculation of Positron Source Yields," Xth International Conference on High Energy Accelerators, Serpukhov, USSR, 1977.
3. R. H. Helm, "Adiabatic Approximation for Dynamics of a Particle in the Field of a Tapered Solenoid," Stanford Linear Accelerator Center Report SLAC-4 (1962).
4. R. H. Helm, R. Miller Linear Accelerators ed. by P. Lapostolle and A. Septier (North-Holland Publishing Company, Amsterdam, 1970).
5. J. Haimson, "Electron Bunching in Traveling Wave Linear Accelerators," Nucl. Instr. and Methods 39 13 (1965).
6. R. H. Helm, "Notes on Electromagnetic Forces in Linear Accelerators," Report SLAC-TN-62-107 (1963).
7. The Stanford Two-Mile Accelerator, R. B. Neal ed. 261 (1968).

THE COMPENSATION FOR BEAM LOADING ON THE PREINJECTOR OF THE NEW CERN 50 MeV LINAC

H. Haseroth, M. Hone and J.L. Vallet
CERN, Geneva, Switzerland

Summary

The original two-tube bouncer built by Haefely has been replaced by a single tube bouncer featuring a simpler and cheaper design, without compromising on the precision of the HV regulation. This paper describes the basic design and construction of the new system, putting special emphasis on reliability and ease of maintenance.

Introduction

The problem of HV beam loading compensation for pulsed beams is well known, but technical problems and solutions can be quite different. The first approach at CERN was a programmed compensation using a triggered spark gap. In 1970, a compensation with feedback and regulation with a series tube had been installed.[1] For the preinjector of the new linac, the HV compensation was built by Haefely. It had to cope with currents of up to 400 mA, a pulse length of up to 200 μs (the maximum charge being limited to 50 mC), and a repetition frequency of up to 2 Hz. The Haefely bouncer used a two-tube configuration and a 1 MHz carrier frequency to drive the grids. Its performance was within the specification (5×10^{-4}) but its reliability caused problems. Especially, the 1 MHz rectifying diodes caused several breakdowns and were difficult to replace. The main parts of this bouncer, i.e., the 100 kV supply, the two tubes, their filament transformers, the 1 MHz transformer and the rectifying diodes, were housed in a big oil-filled steel tank. Just to undo the bolts and lift the top cover with a crane took a very long time.

The new bouncer construction

It was decided to completely rebuild the bouncer, simplifying it and paying special attention to ease repairs. It was clear that only an open construction could satisfy the last condition, because only then would it be possible to have immediate access to a faulty component. It was also clear that two tubes (one only for reducing the 5 kHz ripple from the Cockroft-Walton generator) are not at all necessary, as we (like other people too) were already accepting an initial transient of some 10 μs. The value of the HV between beam pulses is completely unimportant; what matters is just the value during the beam time. This means that one single tube to "bounce up" the HV is completely sufficient. All one has to do after the beam has started, is just to wait until the HV drops down to a level, which is equal to or smaller than the minimum reached due to the presence of the ripple before the beam pulse. Only then the compensation should start and keep the HV constant.

As can be seen from Figs. 1 and 2, the large high-voltage, high-μ triode (ML 7668) sits in an air-cooled, oil-filled copper and glass reservoir. The design of the reservoir radiator is closely based on that of the earlier device used for many years on the old linac,[2] and which has the useful fail-safe characteristic of maintaining the oil temperature below the critical value in the event of a ventilator failure. For the new device, a 12 mm-thick lead glass (∿30% PbO content) cylinder serves as the insulation between the anode and cathode sides of the reservoir. This helps to reduce the X-radiation emitted by the triode, which can be a hazard for personnel working close to the device during testing and setting up. It was not possible to find a supplier of such a cylinder with a higher PbO content. Since the triode is mounted with the anode down, forced circulation of the oil is not necessary to remove the 365 Watts generated in the tube filament. The power dissipated during the beam pulse is, of course, negligible with a duty cycle of 10^{-4}. For the electrical connections on the tube, standard rf type finger contacts are used, inserted in special housings, to avoid any undue mechanical stresses on the glass envelope.

The whole assembly of triode, reservoir and electronics, plus anti-corona housing or dome, is mounted on three standard HV insulator legs of the kind used on some electricity transmission lines. These have proven reliability, great strength and low cost. The large alloy disc which serves as the anode connection to the triode and support, is screened from the cathode side of the reservoir by means of the large impregnated glass fiber insulation disc. The main storage capacitor of 80 nF, is of a dual dielectric plastic film double-paper type, capable of repeatedly accepting short-circuit conditions at the full voltage of 100 kV, without damage.

The 100 kV HV source being used is a home-built Cockroft-Walton generator also of open air construction for easy accessibility. The rectifier assemblies are made from 15 controlled avalanche-type diodes in series with alternate limiting resistors, each set being cast in araldite. The voltage rating of each set is >10 kV and they screw together easily to form assemblies of higher voltage ratings. These diode assemblies have proved very reliable in the past on other HV equipment.

All the HV resistors used, such as the 5 MΩ on the bouncer output, are constructed from chains of low inductance carbon resistors, selected for their reliability and stability. The soldered chains are enclosed in standard PVC tubing and wound on plexiglass support tubes. Although plexiglass is not the best material under high voltage arcing conditions, no problems have been found yet and are not expected, due to the "over dimensioning" of these components. The individual resistors in each chain are operating well below their rated voltage and current/power values.

The 5 MΩ resistor assembly, in parallel with the output of the bouncer serves as the high voltage side of a resistor-divider network for measuring the output voltage and I_K, the cut-off current of the triode.

After some months of operation, it has been noted that the ML 7668 shows an increase in leakage current, but according to the manufacturer, this is probably normal and should not exceed 1 mA eventually.[3]

Also across the output is a diode chain, identical to those used on the 100 kV generator, and a spark-gap. The spark gap and diode chain protect the triode, etc., from overvoltage during any HV flashovers on the 750 kV column. Extensive double screening is also employed at many points in the circuit for the same reasons. The 50 Hz/220V power for the electronics in the HV "dome" is provided by a 1:1 isolation transformer, rated at 1 kW. In the apparatus working at present and shown here, an epoxy-insulated, commercially supplied unit has been used with no problems to date. An alternative oil-insulated type, has also been purchased and will be tested on a second version of the compensation. A HV breakdown in the epoxy transformer would probably be impossible to repair, whereas an oil-filled type can be opened and rewound if necessary. It remains to be seen which type will prove to be the more reliable in the long run.

Electronics

Figure 3 shows the block diagram of the bouncer circuit. Except for the final stages in the power amplifier, all the other amplifiers are solid state but protected adequately against possible transients due to HV breakdowns of the column. A special feature is the signal transmission to the grid of the HV tube via a commercial current transformer, sitting in an oil bath. From this side there is no bandwidth limitation as given by the modulation of a 1 MHz carrier frequency. The first amplifier (high input impedance amplifier) has a built-in threshold, acting in the sense described above, to guarantee stable HV without suffering from the residual ripple. To avoid the 5 KHz ripple having too much influence on the amplifier chain, some attenuation of low frequencies is included. Nevertheless, the presence of the 5 KHz signal in this scheme is a limitation to the possible gain of the whole loop. If the gain is too large, too much current is drawn in parts of the electronics which are made for pulsed but not continuous operation. In order to achieve even larger gain and better HV compensation a gated amplifier has been built (Fig. 4), to replace the first amplifier in the chain. Tests are not yet completed, but it is already possible to beat the performance of the previous system. The basic principle is to open an analog gate when the HV voltage, due to the beam, drops below a certain level and to close the gate again with a trigger from the external timing system. Thus it is possible to use a higher gain without overloading the amplifiers with the continuous 5 KHz signal. Also the bandwidth of the system can then be adjusted more easily with a variable filter.

CONCLUSION

This bouncer has been in operation for about six months without any fault on the larger components, so there was no occasion to prove the ease of repairs. The stability is within the specification. Further improvement is expected from the use of the gated amplifier. The use of only one expensive HV tube will largely reduce the maintenance costs.

ACKNOWLEDGEMENTS

It is a pleasure to acknowledge the help of our workshop people, who worked willingly to produce unusual shapes without understanding always the exact reasons for them.

REFERENCES

1. F. Chiari, R. Dubois, "Preinjector experimental Hall Sud, Faisceau de protons à 500 keV de longue durée - 100µsec." MPS/LIN Note 70-6.

2. R. Dubois, "Compensating the drop in accelerating voltage caused by the beam by means of an electronic servo system", CERN/MPS/LIN 71-9, 1971.

3. Communication between M.D. Crepin, Commissariat à l'Energie Atomique, Dép. Saturne, Saclay, and the Machlett Laboratories, Inc. USA, Apr. 23, 1970.

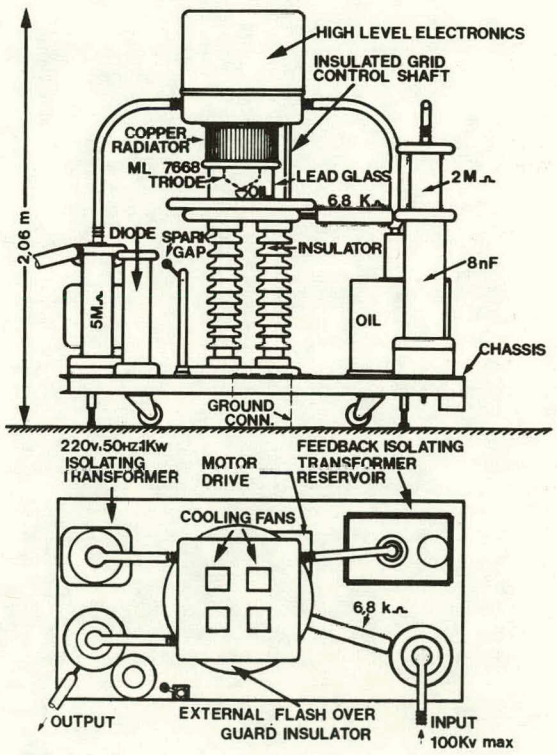


Fig. 1 Side and plan views of the bouncer

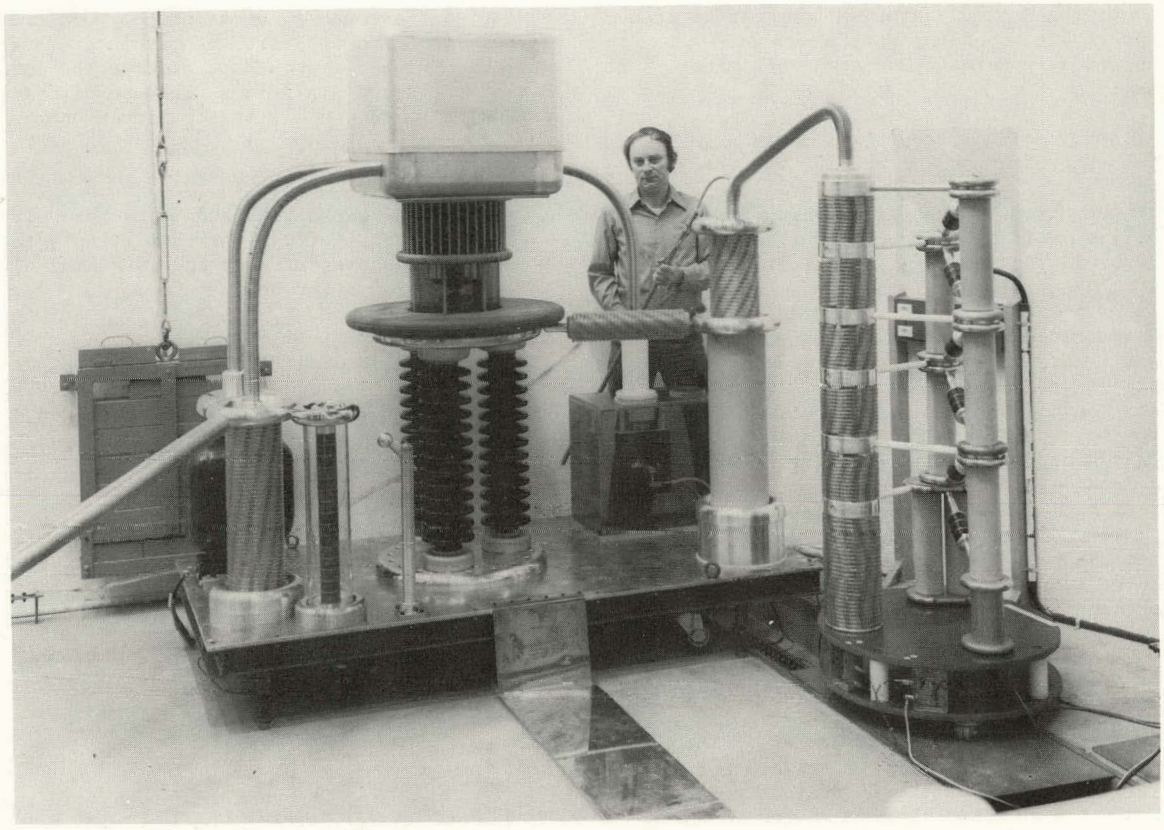


Fig. 2 Bouncer and 100-kV generator

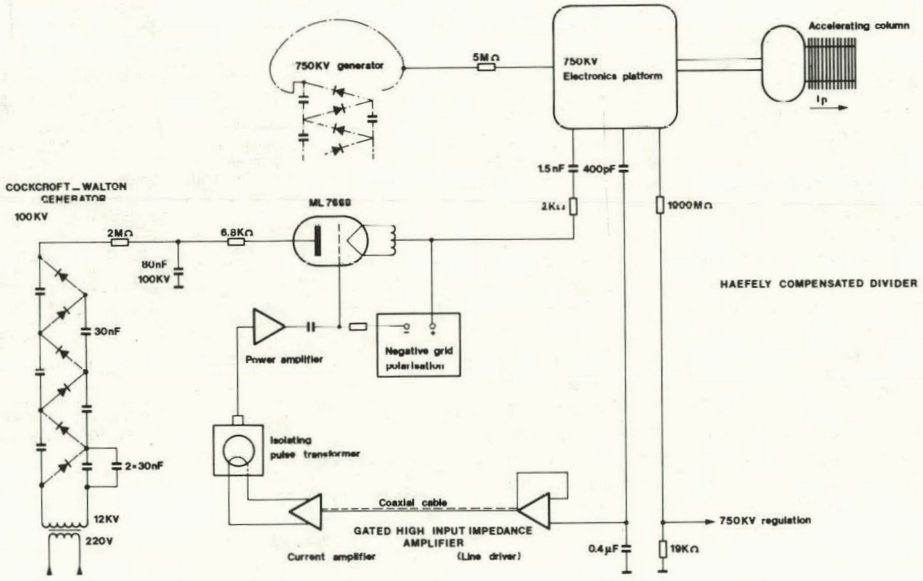


Fig. 3 Bouncer circuit (schema)

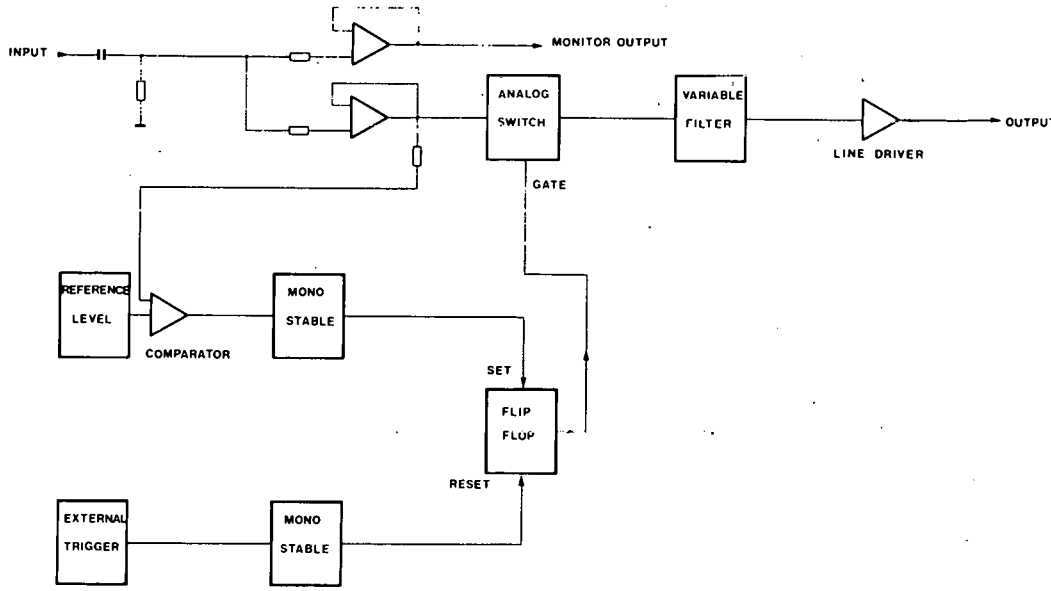


Fig. 4 Gated high impedance amplifier

DESIGN CRITERIA FOR HIGH VOLTAGE, HIGH CURRENT ACCELERATING COLUMNS

J.D. Hepburn, J. Ungrin, M.R. Shubaly and B.G. Chidley
Atomic Energy of Canada Limited, Research Company
Physics Division, Chalk River Nuclear Laboratories
Chalk River, Ontario, Canada K0J 1J0

Summary

A continuing development program has increased the reliability of two 100% duty factor single-stage accelerating columns at the Chalk River Nuclear Laboratories. Experiments on the two columns have included studies in gap voltage, accelerating gradient, extraction geometry, electrode materials and shape, column bleed current, insulator design, and the effect of backstreaming electrons. A set of design criteria for accelerating columns, based on these experiments, has been formulated. While the reliability of the existing single-stage columns has been improved, the criteria can best be satisfied by a two-stage accelerating system with ion species separation and beam shaping between a low voltage ion source and the main accelerating column.

Introduction

The Chalk River Nuclear Laboratory is investigating high-voltage, high-current accelerator technology to establish the feasibility of converting fertile materials to fissile nuclear fuel in an accelerator-based breeder.[1] Requirements are for a 1-GeV, 300-mA, 100%.duty factor proton beam with very high reliability,[2] but existing dc injector technology is as yet inadequate for this application.

Two accelerators have been available at the Chalk River Nuclear Laboratories for injector technology studies. One is the 750-keV, 100-mA dc, H^+ injector for the High Current Test Facility (HCTF).[3] The injector has operated at up to 50-mA total beam, with beam-induced high-voltage breakdowns being the predominant problem. The other accelerator is the 300-keV, 25-mA dc, D^+ accelerator for a 4×10^{12} n/s Fast Intense Neutron Source (FINS).[4] It has operated at 40-mA total hydrogen beam and 30-mA total deuteron beam, again with beam-induced high voltage breakdown problems. Some initial experiments on these machines have been previously described.[5,6]

Experiments aimed at improving the reliability of the two dc accelerators have led to a set of design criteria which could be used for accelerator breeder, neutron generator, and fusion research applications.

The Problem

An accelerating column will typically voltage-condition readily with no beam present, but will spark down when ion beams are being accelerated. Its performance can be improved by gradually increasing the accelerator current, i.e. the column will "current-condition". Interruptions in beam production are short but they may be intolerable to the overall facility.

Figure 1 schematically shows the number of runs observed as a function of the duration of each run for two kinds of problem: inter-electrode sparks and microdischarges, which give an exponential distribution, and surface breakdowns on the ceramics, which give a peaked distribution. Generally the effects are superimposed, although usually the HCTF results follow an exponential-like pattern, while FINS follows the peaked function or distribution. The average time in a series of runs decreases with higher current, accelerating voltage, and externally measured radiation.

Observations

Figures 2 and 3 show the latest, most successful versions of the HCTF and FINS columns. Some experiments and observations on these columns are now discussed.

It was found that electron beams of 10-50 μA, accelerated from a filament at the ground end of the FINS column with the ion source removed, gave the same external radiation level and produced the same breakdown rate as did typical ion beams.[5] The energetic electrons produce bremsstrahlung inside the column. The experimental configuration was varied and the breakdown effect was shown to be related primarily to the ceramic. It is postulated that electrons created on the ceramic surface by bremsstrahlung via the photo-electric effect charge the surface and provoke breakdowns. Ultraviolet light from the ion source or beam plasmas could do the same thing. Operation of a FINS column whose electrodes were 1.5-mm thick stainless steel was greatly improved by addition of 6-mm thick copper plates positioned to shield the ceramics from x-rays generated at the ion source. Operation was further improved with 12-mm thick copper electrodes.

The HCTF ceramics, and early versions of the FINS ceramics, are right circular cylinders with a notch at the ceramic-metal-vacuum interface (see Fig. 2). The HCTF ceramics have suffered only a few damaging tracks on the vacuum side. However, two early versions of the FINS column suffered extensive track damage whether or not the ceramic-metal-vacuum interface was shielded by electrodes. Convolutions on the inner surfaces of two later FINS columns (see Fig. 3 for geometry) have prevented any track damage from occurring, possibly because the bands of high and low electric field on the ceramic surface created by the convolutions tend to stabilize surface charges. The presence of ceramic in a complicated electrode configuration can greatly influence the equipotential distribution; the convolutions can be used to reduce electric fields on the adjacent electrodes. Electrostatic analysis of the latest FINS column (Fig. 3) using an electron gun code

from SLAC[7] (neglecting surface charge) shows the convoluted ceramic shape to be close to optimum.

All the FINS and HCTF columns have used $\geq$ 95% Al_2O_3 ceramic insulators bonded with either polyvinyl acetate or Torr-Seal epoxy (from Varian Associates). One FINS column glazed on both inner and outer surfaces has been operated. In all the columns, radiation damage has yellowed the ceramic material in places where x-ray bombardment is high. The color fades slowly (over months) if the ceramic is not in use or if it is heated. No difference in operation can be attributed to the insulator materials; however, the glaze makes cleaning the column much easier and prevents the adherence of metal if the column is rubbed accidentally.

The ceramic-to-metal vacuum interface in a column can emit electrons which start breakdowns. Dependence of column reliability on bond properties can be greatly reduced through use of metal electrodes to reduce electric fields in the bond region. This approach has worked well on FINS, with the convolutions on the ceramics assisting in the field shaping.

Given restraints such as available ceramic sizes and choice of accelerating gradient, the electrodes must be designed to minimize surface electric fields - particularly on the cathode surfaces. A useful guideline is the Kilpatrick criterion for vacuum sparking.[8] For ease of use in dc applications, substitution of $E = \alpha V$ eliminates the peak cathode surface electric field E. This leaves a universal equation relating the Kilpatrick sparking threshold voltage V to the voltage-independent, geometry-dependent parameter α. In practice, α is found analytically (for simple geometries) or by using the modified SLAC electron gun code[7] to solve for surface fields for given applied voltage. Then, the sparking threshold voltage is found from the universal curve of V vs α. At present, the FINS and HCTF columns operate with surface fields less than or equal to the Kilpatrick limit on anode surfaces and 0.7 times the limit on cathode surfaces. These columns voltage-condition readily without beam and operate better than columns with lower safety factors.

While long acknowledged as being an excellent material for high voltage electrodes, titanium (or Ti6Al4V alloy) appears to be unsuitable in the hydrogen atmosphere of a proton accelerator. Here, titanium hydride forms on electrode surfaces, leading to outgassing during beam spills and formation of titanium hydride microparticles that possibly loosen and cause voltage breakdown. Materials tests done on smaller experimental setups at CRNL showed molybdenum, stainless steel and copper to be superior with either ion beams or electron beams (equivalent to typical backstreaming electron currents in proton accelerators) present. Molybdenum is preferred because it has good thermal conductivity and does not sputter. The most recent HCTF column uses mainly stainless steel and TZM molybdenum alloy. FINS has operated well with copper electrodes provided that no abrasives were used in fabrication. (Abrasive-treated copper exhibits many microdischarges in the presence of ion beams.) This restriction on abrasives probably also applies, to a lesser degree, to the harder electrode materials.

Voltage and gradient effects have been studied. On the HCTF, a change from a column gradient of 3.1 MV/m (with Pierce geometry over the first 200 kV) to a uniform column gradient of 2.1 MV/m over 750 kV gave a modest improvement in reliability. Also, with fixed 50 kV per ceramic, a change from 100 kV to 200 kV between adjacent accelerating electrodes gave slightly improved reliability. Originally, FINS used a single 300 kV, 2.7 MV/m gap. A single 1.8 MV/m gap operated no better. It now has three 100 kV gaps and an average gradient of 2.5 MV/m.

Column bleed currents of 0.25, 0.5 and 2.25 mA gave the same reliability in the HCTF. A bleed current of 800 μA instead of 250 μA made the FINS column more tolerant of column problems, such as electrode microdischarges, but did not significantly improve reliability. Apparently, electrons and gases produced by beam spills cause breakdowns before electrode potentials are significantly perturbed.

The bad effects of beam spill on column reliability imply that knowledge and control of ion optics in a column must be good. However, computer codes now used for beam optics analysis have trouble modelling halo on beams from non-uniform plasma surfaces. Work on this problem continues at CRNL. In the meantime, beam optics in FINS is controlled by a passive shaped-focus plate replacing the original biased, Pierce extraction electrode. The HCTF column has a Pierce extractor for beam focusing, followed by a uniform gradient column.

Design Criteria

A set of design criteria for accelerating columns formulated from the foregoing experimental results is outlined in Table I.

Discussion

Figures 2 and 3 show the present configurations of the HCTF and FINS columns. The criteria of Table 1 have been incorporated into the HCTF as far as possible, subject to existing mechanical and operational constraints. The FINS column was subject to fewer constraints, and follows the criteria more closely.

The column criteria above can best be satisfied by a two-stage system in which the ion beam is first extracted from the ion source, focused, magnetically analyzed, and stripped of high emittance components and then in the second stage accelerated to the required total energy. The RTNS accelerators at Livermore,[9] and a recent FMIT injector proposal[10] (400 kV version) use two-stage designs.

Table I

Desirable Features of High Current, High Voltage Accelerating Columns

Feature	Remarks
A. Good Electrode Design	
- use accelerating gradient of $\leq$ 2.5 MV/m	
- choice of voltage per gap should be $\sim$ 100 to 200 kV, subject to ease of satisfying the remaining electrode design requirements	- this gives a column diameter to electrode gap ratio convenient for incorporating the required shielding from x-rays and allows convenient shielding of ceramic-to-metal joints
- use massive electrodes	- shields ceramic from x-rays and reduces ceramic charging
- minimize surface fields on electrodes using electrostatic analysis and a sparking criterion	- reduces sparks and microdischarges
- hide the ceramics from direct or reflected ultraviolet light from the ion source or beam plasmas	- reduces ceramic charging
- water-cool or heat-sink all electrodes	- reduces outgassing and effects of beam spill
- use electrodes to hide the ceramic-to-metal bond	- reduces electric fields where electrons may be produced
- select electrode material and finish to suit application (molybdenum seems best; no abrasive should be used)	- aids voltage stand-off with or without beam
B. Good Ceramic Design	
- use convoluted ceramics, designed using electrostatic analysis	- prevents track damage, stabilizes charge distributions, reduces fields on adjacent electrodes
- standard materials and bonding agents are suitable	
C. Minimize Electron Backstreaming and x-rays	
- effective electron trap required	- prevents downstream space-charge electrons from entering column
- use a very stiff electron trap power supply, or do not have trap electrode as one side of a high voltage gap	- reduces chance of losing electron trap during high voltage transients
- locate the first restrictive beam aperture downstream from electron trap	- avoids production of secondary electrons in the column
- reduce beam spill by making column bore as large as possible	- reduces column voltage perturbations, secondary electron production, and electrode heating and outgassing (but may harden bremsstrahlung spectrum)
- pump gas as efficiently as possible (use pumping slots and large bore)	- reduces electron and ultraviolet light production from ion-molecule collisions
D. Other Considerations	
- magnitude of bleed current not critical	- any beam spill creates electrons which cause breakdowns before voltages are significantly perturbed
- examine beam spill in the column over entire operating range (by computer analysis if possible)	- may show problems from space charge, mixed ion beam, high emittance components, or change of focusing with beam current
- avoid PIG discharge regions, and avoid crossed E and B fields	- prevents stable electron orbits
- minimize the area of electrodes at high voltage, put highest electric fields on-axis	- reduces sparking probability

The advantages of a two-stage system are many. Coupling between the ion source and main column is reduced, so that operation of one is not compromised by operation of the other. The gas loads can be differentially pumped to remove source gas and optimize space-charge neutralization in beam drift regions, yet allow very high vacuum (hence low electron production) in the main acceleration column. The system can be selectively opened to air without venting the whole system and losing high voltage and current conditioning of the remaining components. Backstreaming electrons passing through the main column can be intercepted by a low-Z shielded dump. Electrical power is saved by dumping the unwanted portions of the beam at low voltage. Beam spill in the main column is much reduced by the prior removal of unwanted ion species and high emittance components.

Conclusions

The design criteria described in this paper are the result of extensive experimental work on two accelerating columns with very different operating conditions. Application of the criteria has markedly improved operation of the columns.

Two-stage accelerators appear to have the best configuration for production of high voltage ion beams, but design criteria such as those presented here must be carefully applied to realize the potential of two-stage accelerators for reliable operation.

References

1. S.O. Schriber, J.S. Fraser and P.R. Tunnicliffe, "Future of High Intensity Accelerators in Nuclear Energy", Atomic Energy of Canada Limited, Report AECL-5903 (1977).
2. J.D. Hepburn and M.R. Shubaly, "Future Development of High Current dc Injectors for Accelerator-based Breeding Systems", Atomic Energy of Canada Limited, Report AECL-6537 (1979).
3. J.H. Ormrod, M.D. Snedden and J. Ungrin, "The High Current Test Facility", Atomic Energy of Canada Limited, Report AECL-4224 (1972).
4. J.D. Hepburn, J.H. Ormrod and B.G. Chidley, "Design of an Intense Fast Neutron Source", IEEE Trans. Nucl. Sci., NS-22, 1809 (1975); Atomic Energy of Canada Limited, Report AECL-5183 (1975).
5. J. Ungrin et al., "Chalk River Experience in the Operation of High Current 100% Duty Factor Accelerating Columns", Proc. of the 1976 Proton Linear Accelerator Conference, Atomic Energy of Canada Limited, Report AECL-5677 (1976).
6. M.R. Shubaly, "Chalk River Experience with High Voltage High Current dc Accelerators", in FMIT Injector Workshop Notes, Los Alamos Scientific Laboratories, Report LA-UR-78-3082 (1978).
7. W.D. Hermannsfeldt, "Electron Trajectory Program", Stanford Linear Accelerator Center, Report SLAC-166 (1973).
8. W.D. Kilpatrick, "Criterion for Vacuum Sparking Designed to Include both rf and dc", Rev. Sci. Instr. 28, 324 (1957).
9. R. Booth et al., "Rotating Target Neutron Generators", Report UCRL-78805 (1976).
10. R.A. Jameson, "High Intensity Deuteron Linear Accelerator (FMIT)", IEEE Trans. Nucl. Sci., NS-26, 2986 (1979).

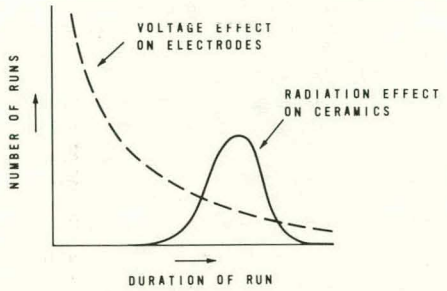


Fig. 1 Distribution of the number of runs as a function of the duration of each run.

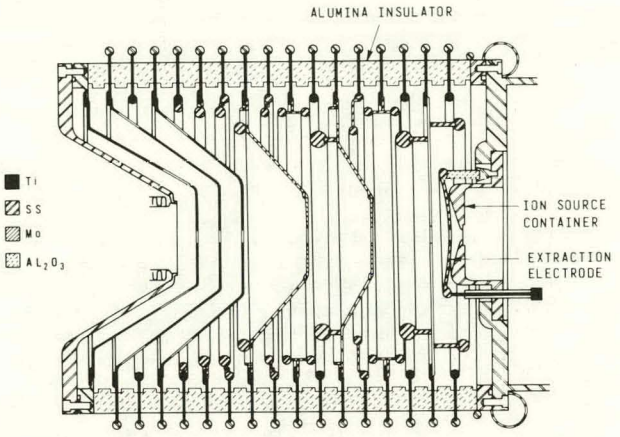


Fig. 2 Cross-sectional view of the HCTF injector column.

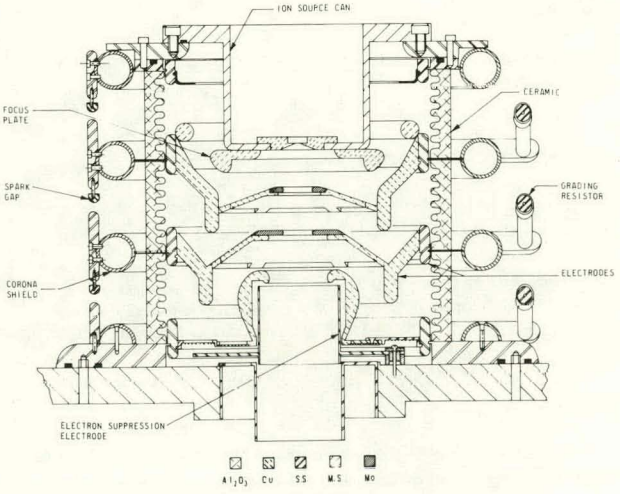


Fig. 3 Cross-sectional view of the FINS accelerating column.

Discussion

West, RHEL: To avoid breakdown problems, should we perhaps move towards lower gradients and incorporate permanent magnet quadrupoles inside the column accelerating structure?

Hepburn: I have seen designs which did that. They essentially had meters for acceleration with solenoids or whatever; it is a different approach. But with 300 milliamps and 1% duty factor, space charge is an enormous problem. Then, you try to get the ions going, you obviously accelerate them as quickly as possible.

West: Well, my point is that we've seen that permanent magnet quadrupoles are a reality and they are there to match to a particular beam space charge defocusing.

Hepburn: I do not know what they will do to the electrical design of the column if they are insulating or conducting. If they are conducting, it means that you cannot have thin electrodes - you have to have an electrode long enough to incorporate each magnet, which is a radical departure, that I would be interested to try.

Curtis, FNAL: Do I understand properly, that you have included all your design criteria in the last column figure which you showed? Have you attempted to put up to 100 mA through this column?

Hepburn: The answer to the first question is, not quite. We have no cooling on the electrodes, and I would prefer to be able to machine them out of molybdenum instead of copper. As for the improvement we have been able to make on FINS, the first column operated - it was very similar to a short section of say the high current test facility column, or Los Alamos' column. That operated for a few milliamps for a few minutes between spark downs. We've got that up to 40 milliamps for half an hour or an hour.

Curtis: You have not reached your 100 milliamp goal yet?

Hepburn: I'm sorry - you are confusing the two machines.

Curtis: Right, but have you tried for a higher current in that particular column?

Hepburn: No, I'm limited by target problems at the moment.

Curtis: Right.

Grand, BNL: I wonder if it would be relevant right now to ask anyone in the audience if they have any present knowledge of the status of John Osher's column, which is relevant to this talk?

Clark, LBL: Yes, it is a medium gradient column, with large aperture. He has had trouble with backstreaming from the gas - ionization of the column gas, but I don't know any other current information.

Unidentified voice in audience: They have increased the pumping in the dome substantially - theirs is a two stage system, and they have increased the pumping substantially and done much better. I think - this is a vague memory - about the order of 100 milliamps 100 kilovolts.

Grand: And what gradients do they have in the column?

Same unidentified voice in audience: That I don't know, but I do know they are seeing one thing we've seen on all our columns: a yellowing of the ceramic, which I assume is radiation damage. They are getting that and they are also getting the peak type of run distribution, where the run durations cluster around a mean value. I would recommend going to look at the ceramics and the shielding in the column for that one.

Bentley, NEN: What was the time scale on that graph of peaking of the runs?

Hepburn: On the first FINS column it was a few minutes average and on later ones it has gone up to an hour or two hours, so it is a function of how good your column design is.

Bentley: There was a paper on Osher's column at the Particle Accelerator Conference in San Francisco. They had increased pumping on the upstream end of the column and put in a trap at the high voltage end of the column to protect against slow ions going into the column, and I think everything was operating fine as of that point.

Hepburn: Again, beam spill. On the question of reliability: The 750 kv set has operated up to 50 milliamps with runs up to an hour. The problem there seems to be the arc transient during turn-on. It means the extractor is not matched during the first current pulse - that is, difficulty in turning on, not really reliability.

Dup

1979 LINEAR ACCELERATOR CONFERENCE

ION SOURCE AND TRANSPORT SYSTEM FOR BNL-HIF PRE-ACCELERATOR*

G.M. Gammel, E.F. Meier and R.M. Mobley
Brookhaven National Laboratory
Upton, N.Y.

SUMMARY

The operating characteristics of the ion source and an initial model of a transport system developed by the Heavy Ion Fusion group at BNL will be presented. The purpose of the assembly, was to transport a 30 mA beam of heavy ions a few feet inside a small, inexpensive Cockcroft-Walton, at the source voltage ($\leq$ 50 kV) to a single 3" diameter high voltage gap ($\leq$ 500 kV).[1] This isolation of the gap from the source prevented high voltage breakdown due to gas loading from the source. After the gap, the beam was to be matched into a 2 MHz electrostatic quadrupole linac, which would in turn, be the first stage of a heavy ion fusion accelerator.[2]

ION SOURCE

The ion source shown in Fig. 1 is a modified version of the original prototype of the LBL CTR sources developed by K. Ehlers and others.[3] At least three other small versions are described in the literature,[4,5,6] The arc chamber is fabricated using a copper-plumbing end cap for the barrel. The end is slotted radially to allow the filaments to protrude into the chamber. The filament plate is of stainless steel, with silver-brazed filament feedthroughs and gas inlet pipe. The anode consists of 3/4 inch copper-plumbing end caps. Four of these are connected together outside the vacuum region.

The arc is struck between the filament and the anode by pulsing the center-tap of the filament secondary ac-winding with ~-50 V. The whole arc chamber (including the vacuum flanges, filament plate, and beam hole cover) floats to a potential slightly below the arc potential, forming a sheath, to maintain plasma neutrality in the usual way.

The extraction electrode can be grounded in several ways. The source and power supplies are isolated at high voltage.

Favorable features of this source may be separated into two categories: 1) features in the original concept and 2) features in this modified version.

1) • The plasma density can be uniform to 5% over 90% of the beam cover plate.

• The filaments are inexpensive, run-of-the-mill, tungsten wire.

• The plasma is very quiet, due to the low magnetic fields, and to space charge shielding of the filaments from the anode potential. That is, the electrons are freely generated by thermionic emission and arc "spotting" can be avoided.

2) • Few vacuum seals (three as shown).

• The anodes are separate from any other parts, and the area of the anode surface can be easily varied.

• The gas inlet pipe, as well as the entire inner surface of the arc chamber, can run at elevated temperatures for Hg operation.

• The filament plate can be removed easily to replace the tungsten wires. Since modest arc densities exist, compared to CTR applications, no filament has yet worn out.

• The high voltage insulator is an inexpensive item. The 4" ID size shown here costs $60, including the end clamps (not shown).

The requirements for pellet ignition favor the heaviest possible ions for overall system economics. This means the use of heavy metal ions. This source can readily be run with Hg^+, and uranium sources are being investigated.

ION SOURCE OPERATION

For the Gabor lens transport system presented here, a Veeco piezoelectric gas valve was used to admit Xe into the arc chamber. The filaments were run cw with 6-9 Vac and 10-20 amps/filament. The source is at a dc potential of up to 50 kV, and the beam pulse is generated by the arc pulser. The arc pulser is a BNL duoplasmatron unit with the following features:

1) Arc voltage up to 300 V, arc current up to 40 Amperes.

2) Variable repetition rate from 1 pulse/10 sec to 10 pulses/sec. The arc-on time is synchronized with the ac line.

3) Light pipe controls for variable beam width to 1 msec, and variable beam delay.

4) HV spark overload protection as developed for the AGS Cockcroft-Waltons.

The source can be run in an ion gauge mode (Ehlers gauge) to allow tuning of the timing between gas-on and start of arc. This feature led to the observation that the main gas load was coming in a large burst some 40 msec after the chamber pressure was ideal for arc pulsing. This has not yet been corrected and is largely responsible for the low repetition rates attained

*Work performed under the auspices of the U.S. Department of Energy.

with the Gabor lens transport system. It would also cause unnecessary gas loading the Cockcroft-Walton accelerating gap.

ION SOURCE PERFORMANCE

Emittance measurements for this type of source made at BNL and elsewhere are shown in Table I. For acceleration of beams of high 6-D phase-space density, the major problem is to preserve this high brightness. Gabor lenses, as well as magnetic quadrupoles, allow neutral beam transport to the high gradient gap.

Extractor design is largely dictated by the Langmuir-Child formula:

$$K = \frac{4}{9} \epsilon_o \sqrt{\frac{2e}{m}} A V^{3/2}/d^2 \quad , \qquad (1)$$

in which

A = area

m = ion mass

d = extraction gap

ϵ_o = permittivity of free space

e = ion charge .

On inserting values for Xe^{+1}:

$$I = 4.76 \times 10^{-9} A V^{3/2}/d^2 \text{ Amperes.} \qquad (2)$$

The flux of ions J, within the arc and arriving at the extraction hole, must match the space-charge limit to maintain nearly planar geometry at the plasma meniscus.

Moreover, to keep the beam divergence reasonably low, the gap d, should be about twice the radius of the extraction hole. For a circular aperture and an extraction voltage of 50 kV, Eq. (2) then yields 45 mA, independent of the hole size. Considering extractor geometry only, one can substantially defeat this limit two ways: 1) use a slit extractor, in which case it has been measured that an aspect ratio of 3:1 yields $\epsilon_x = \epsilon_y$. 2) use a multiple aperture array, in which case the current increases linearly with the number of holes. The best solution is a combination of both ideas, that is, a multiple slit array.

The best result was obtained using an extractor shaped in a cross, with the slits measuring 1-1/8" x 3/16" for an extraction area of 7 cm^2. The gap d was .7".

Extraction voltage	44 kV
Filament voltage	7 volts
Filament current	145 Amps
Anode voltage	70 volts
Arc current	15 Amps
Plasma current density $\vec{J}$	15 mA/cm^2 (inferred)

Applying Eq. (2) yields 97 mA, and the 7 cm^2 extraction area provided 105 mA total current, in good agreement. Thus, about 85% of beam loss was in the transport system.

The beam purity was measured and the results obtained are shown in Fig. 2.

TABLE I

$$Xe^{+1} \text{ Emittance} = \frac{A(x,x')}{\pi} \beta\gamma$$

I(mA)	V(kV)	Emit. cm-mrad.	Extractor	Ref.
22.5	20	27×10^{-3}	13 holes	2
35	500	84×10^{-3}	13 holes	2
25	30	3.5×10^{-3}	0.2" x 1.25" slit	BNL (unpub)
10	44	11×10^{-3}	Crossed slits	This report
180	35	10×10^{-3}	(0.2 cm x 7 cm slits)	7

TRANSPORT SYSTEM

A pair of large aperture Gabor lenses[8] (see Fig. 3) was chosen for the transport system. These are electrostatic elements, which are superior to magnetic focusing for low velocity particles, such as heavy ions. The large aperture was needed because the beam was emerging from the source at a 15 to 20 degree half-angle, and the first lens could not be much closer to the source than 10 inches, otherwise gas from the source tended to initiate glow discharge breakdown in the lens. The first lens rendered the diverging beam from the source approximately parallel, and the second lens, which had to have about the same aperture, brought the beam to a waist of less than 3" diameter.

The magnetic fields in the two lenses were not measured precisely, but were around 200 Gauss, and were independently adjusted for best strength. Some interesting features about the lens operation are brought out in Fig. 4. First, it was observed that 25 ms were required after the magnetic field pulse started for the electron population in the lens to build up. At that time, high frequency pick-up was observed on the Faraday cup signal, indicating that the lens was "active". Second, if the magnetic field was left on too long, the noise would worsen and the lens would eventually break down into a glow discharge. This also happened if the repetition rate of the beam was too high. In this case, if a spark occurred, gas was released in the neighborhood of the lens and the lens

broke down with no chance to recover before the next pulse. The maximum safe rate was one pulse every five seconds, in which case the pressure always recovered to below a few times 10^{-6} Torr before the next pulse.

Best results for 3 and 5 foot transport are given in Table II. It should be noted that this transport system has the same focusing strength for any heavier ion at the same energy as for the test case of Xenon.

TABLE II

	3' Transport	5' Transport
Extractor voltage	26 kV	47 kV
Upstream lens		
voltage	4.3 kV	9 kV
radius	2.2"	2.5"
length	4"	3"
Downstream lens		
voltage	8.2 kV	9 kV
radius	2.65"	2.65"
length	2"	2"
From source to center of upstream lens	10.5"	14.5"
Lens separation	14.5"	33.5"
Xe current into 3" diameter (1' downstream of 2nd lens)	14 mA	11 mA

CONCLUSIONS

The lenses worked well, although the repetition rate had to be kept to less than one pulse per five seconds, in order to obtain smooth operation. The best current, of 14 mA, did not reach the desired 30 mA, but we feel that with further development--just putting more power into the source or adding yet another lens, more current could have been obtained. However, about a month before this conference, the Gabor lens transport system was abandoned in favor of a better idea.

A multiple beamlet transport and acceleration system (1 or 2 mA per beam) with electrostatic quadrupole focusing is now being investigated. In this scheme, rf acceleration begins directly from the source, and the bulky Cockcroft-Walton pre-accelerator is no longer needed. Single channel models for transport only have already been built and tested, and a current density 7.5 times greater than that obtained with the Gabor lens system has already been obtained at lower beam energy (15 keV). The transport system is not pulsed, and the beam repetition rate has been increased to 10 pulses per second. The progress of this work will appear in future reports.

1. J. Brodowski, et. al., IEEE Trans. Nucl. Sci., NS-26, #3, 3039 (June 1979).
2. BNL 50817, A.W. Maschke.
3. K.W. Ehlers et. al., Proc. 2nd Symposium on Ion Sources and the Formation of Ion Beams, Berkeley, 1974, pp. 1-5, UCRL Report.
4. W. Chupp et. al., IEEE Trans. Nuc. Sci. Vol. NS-26, No. 3, June 1979.
5. R.W. Bickes, Jr. et. al., Rev. Sci. Instrum., 49 1513, Nov. 1978.
6. G. Fisher et. al., J. Phys. E Sci. Instrum., 12, p 522, 1979.
7. R. Mobley, Proceedings of the Heavy Ion Fusion Workshop ANL-79-41, Sept. 1978 p. 265.
8. R. Mobley, et. al., IEEE Trans. Nucl. Sci., NS-26, #3, 3112 (June 1979); see also R. Booth and H. Lefevre, Nucl. Instr. and Meth., 151, 143 (1978).

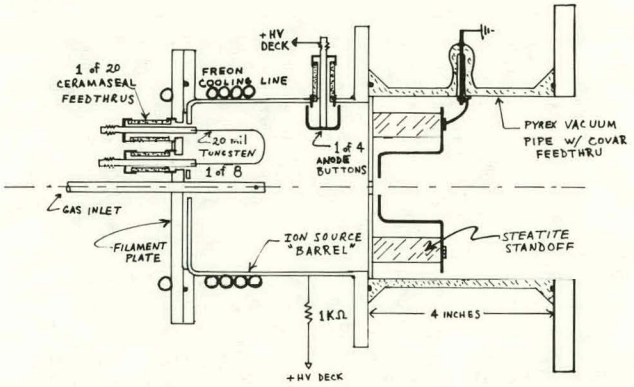


Fig. 1 Schematic of ion source.

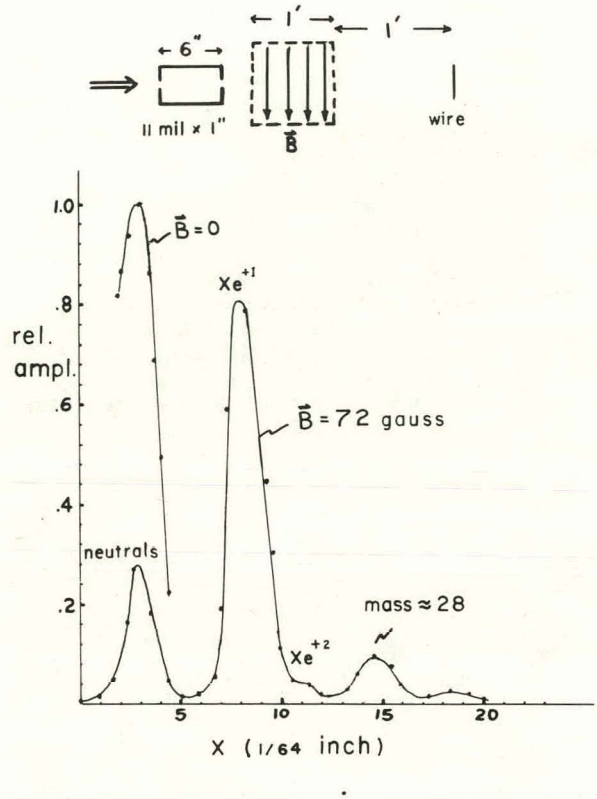


Fig. 2 Spectra of ions obtained with and without deflecting B field, showing ∿80% Xe^{+1} purity. Note that dip between neutral peak and deflected Xe^{+1} peak indicates that charge exchange losses occur near the source only.

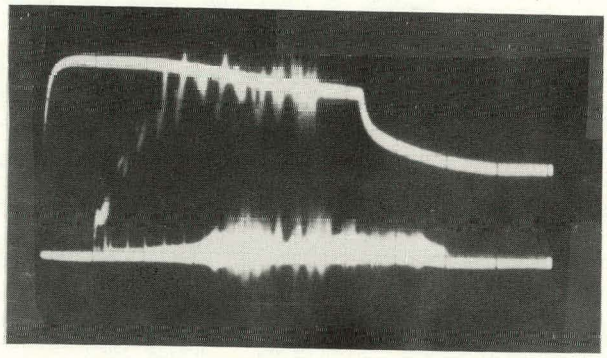


Fig. 4 Upper trace measures the magnetic field in the lens; (∿60 ms duration) lower trace is a multiple exposure of Faraday cup beam measurements at different times (beam is ∿ 1 ms wide).



Fig. 3 Pair of Gabor lenses used for beam transport from source. Ruler is 6" long. Each lens consists of an electrode sandwiched between grounded electrodes around which coils are wrapped in a Helmholtz configuration. For typical voltages, such as indicated in Table I, typical magnetic field strengths were ∿200 Gauss. Freon cooling tubes for dc operation of the coils are visible. The plate between these lenses was not used in the experiments described in this paper.

dup

1979 LINEAR ACCELERATOR CONFERENCE

DEVELOPMENT OF A HIGH-CURRENT DEUTERON INJECTOR FOR THE FMIT FACILITY*

J. D. Schneider, H. L. Rutkowski,† E. A. Meyer,
D. D. Armstrong, B. A. Sherwood and L. L. Catlin
Los Alamos Scientific Laboratory
Los Alamos, New Mexico 87545

Summary

The injector for the Fusion Materials Irradiation Test (FMIT) Facility has been designed to deliver a 100-keV, 125-mA dc deuteron beam (Fig. 1). A prototype injector has been built to run with a H_2^+ ion beam. Two ion sources are being tested--one with magnetic-cusp geometry. The injector transport consists of a single-stage modified Pierce-extractor, a double-focusing 90° analyzing magnet, a high-power emittance scanner, steering and quadrupole focusing magnets, a mechanical beam-current modulator and a deflection type beam pulser. The performance of the prototype injector is discussed.

Introduction

A preprototype test stand has been used to generate the design of a 100-keV, 125-mA dc deuteron beam injector for the FMIT facility. An ion source of Osher design and three of cusp-field geometry were fabricated. A single-aperture extraction system was designed using the beam extraction code SNOW.[1] Because no operational differences were predicted, single-gap extraction was chosen over the two-gap system that originally was considered. Magnetic beam analysis is used to select the desired ion species in the beam from the ion source-extractor system. The tests of these systems, as well as tests of the vacuum pumping and remote control systems, are discussed below.

Both calculation and tests have shown that very good quality beams can be achieved by sizing the aperture diameters such that operation is at 60% of the space-charge limit and by using electrode profiles based on the space-charge-limited "Pierce" geometry. A key factor in minimizing space-charge divergence of the beam was the installation of a negatively biased (-1 kV) electron trap only 0.15 cm downstream from the ground electrode. At a similar distance downstream from the electron trap, a hollow cylinder was used to re-establish ground potential and thus enhance, in a very short distance, space-charge neutralization of the drifting beam.

Ion Source

Initial tests were performed on a Los Alamos Scientific Laboratory (LASL) version of the Osher design reflex-arc source. This unit originally was built by the Lawrence Livermore Laboratory (LLL) for another program at LASL and was delivered as a multiaperture source. It was converted to a single-aperture source with improved extraction optics. Although it delivered the required current density easily, a plasma instability developed that would seriously affect linac operation.

Three versions of cusp-field ion sources have been built and tested. Mark 1 was a relatively large (18-cm dia. by 31-cm long) water-

*Work performed under the auspices of the U. S. Department of Energy.
†Westinghouse/Hanford Engineering Development Laboratory employee working at the Los Alamos Scientific Laboratory.

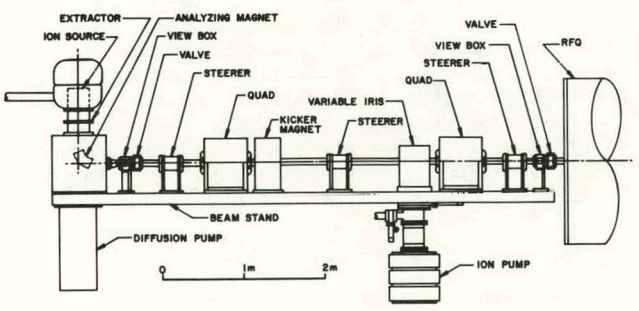


Fig. 1 Proposed FMIT injector system.

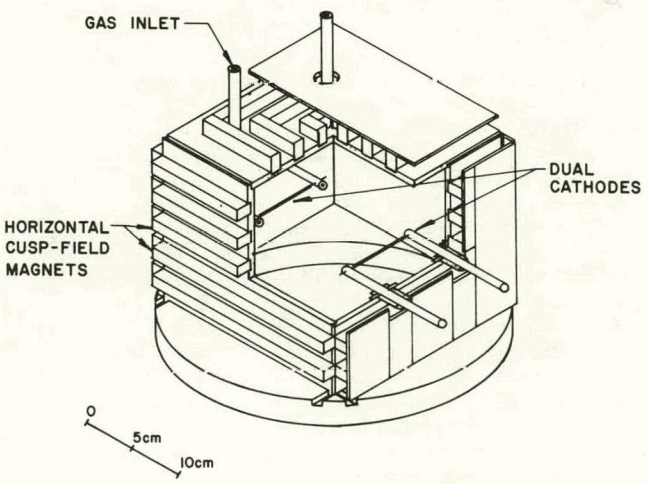


Fig. 2 Mark 2 cusp-field ion source.

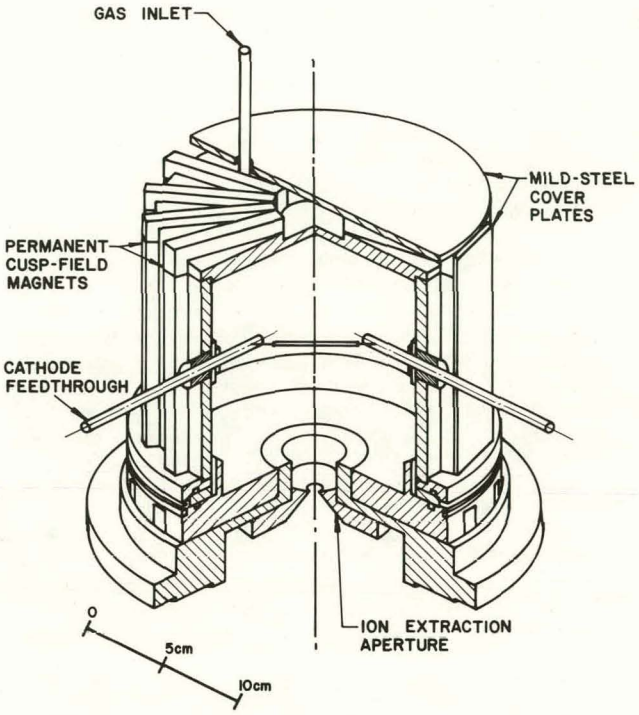


Fig. 3 Mark 3 cusp-field ion source.

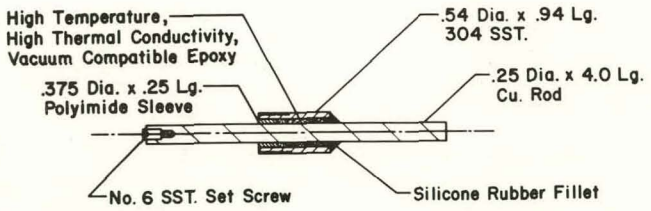


Fig. 4 Ion source cathode feedthrough.

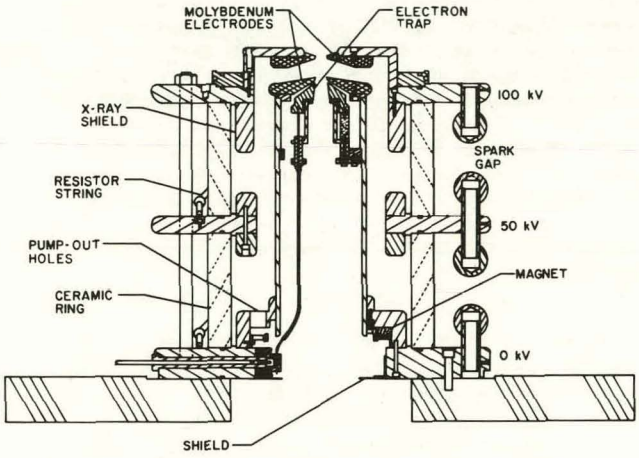


Fig. 5 The 100-kV extractor.

cooled cylindrical chamber. Thirty permanent magnets were installed, on the curved walls only. Operational stability was impressively good, but excessive ion losses to the noncusped end walls made it impossible to achieve an adequate ion density. The next version, Mark 2 (Fig. 2), featured simplicity and low cost, and reduced the ion loss area to one-quarter that of Mark 1. This was a nearly cubical chamber (18 cm per side) with five horizontal rows of magnets along the sides and three rows of magnets providing a cusped field on the top plate. Performance of Mark2 was approximately five times better than its predecessor and easily delivered the required current density. Gas efficiency was very high (>40%), but the ion-species ratio still needs some improvement.

In an attempt to reduce ion losses even further, Mark 3 (Fig. 3) has been constructed with cusp-field magnets on both top and bottom plates, as well as on the cylindrical side walls. Initial tests showed that performance was not as good as with the Mark 2 source. All results reported pertain to the Mark 2 source.

Two major problem areas with the cusp ion sources have been the directly heated cathodes and the cathode feedthroughs. Several years of good experience with flat nickel-gauze oxide-coated filaments in a duoplasmatron ion source provided the incentive to try a similar-type filament on the cusp source. However, under conditions of high-plasma density, it was impossible to achieve long lifetimes. A successful new cathode geometry consists of a 1.0-mm tantalum wire tightly wrapped with 0.1-mm nickel gauze and coated with a barium-strontium oxide. Spot welding the nickel gauze to the tantalum wire was found to improve lifetime somewhat.

Many designs of filament feedthroughs were tried before the present concept evolved. Commercially available vacuum-compatible high-current electrical feedthroughs utilizing ceramic insulators invariably failed with destructive arcs that originated on the vacuum surface of the ceramic. Organic insulators (nylon, epoxy, Kel-F) held up better in the arc environment, but could not withstand the high temperatures without the use of complicated cooling devices. The design currently in use (Fig. 4) employs four separate insulating materials. It has resulted in a high-current feedthrough that is a simple one-piece construction, low in cost, very compact, and that is reliable in the high-temperature arc environment.

100-kV Extractor

The 100-kV extractor is a single-gap accelerating column as shown in Fig. 5. Externally, it consists of two 20.3-cm-id by 12.7-cm-long

alumina insulating rings sealed with O-rings between three annular 38.1-cm od stainless steel plates. Voltage grading is provided by a 0.67-mA resistor; string and arc protection is furnished by atmospheric spark gaps. This initial design utilizes an aperture (1.13-cm dia.) of one-half the area anticipated for use in the FMIT extractor. Design current for this half-area aperture is 100 mA at 100 kV, which results in the same current density as required for the FMIT extractor.

Careful attention has been given in the design to minimize high-voltage breakdown across the insulators, caused mainly by photoelectric charging from x-ray impingement, that is normally a problem in high-voltage extractors of high-average current. The x-rays (bremsstrahlung) are caused by electrons, accelerated in the gap, striking the 100-kV surface. The electrons are produced by beam-induced ionization of the residual gas in and downstream of the accelerating gap. Specifications for the FMIT extractor require that voltage breakdown be limited to less than one per eight hours.

Design features to minimize breakdown are as follows:

1. The maximum gradient in the acceleration gap is 50 kV/cm.
2. Flashover across the ceramic insulating rings is inhibited by the use of long insulators divided into two sections to limit the voltage across each section to 50 kV.
3. Reentrant geometry is used at the inside corner of the insulating rings to keep the electric field low at these critical points.
4. The insulating rings are shielded from x rays by 2-cm-thick steel rings and by the molybdenum electrodes.
5. An electron trap biased at -1 kV is used to prevent entry into the gap of electrons formed downstream of the acceleration gap.
6. Low residual gas pressure in the acceleration gap is obtained by use of a 10,000-ℓ/s oil diffusion pump and sixteen 1.9-cm dia. pump-out holes in the extractor. Low pressure here is of critical importance because it is the only way to reduce the x-ray level caused by electrons formed in the gap because of beam-induced ionization.
7. An array of permanent magnets producing a transverse 500-G magnetic field at each pump-out hole prevents electron backstreaming through these holes into the high field region.

The grounded molybdenum electrode is attached to a 10.0-cm od tube that can be adjusted axially to obtain the required gap spacing. This tube and the x-ray shield ring are made of mild steel; they help to shield the extraction area from any stray magnetic fields.

The stainless steel electron trap is attached by insulators to the inside of the tube with the electrode surface 0.15 cm from the 0-kV molybdenum electrode. A grounded shield placed a similar distance below the electron trap electrode reduces field penetration into the region below. A coaxial lead is used to supply -1 kV to the trap so that the beam will be shielded from the field of this conductor. The beam-line region below the electron trap must be kept free of electric fields so that a high degree of space-charge neutralization of the beam will occur and reduce beam divergence.

The effectiveness of the electron trap and of these precautions is quite pronounced and is shown for a 95-mA beam at 100 kV in Figs. 6a and 6b. Figure 6a shows the diameter of the beam 1.0 m below the 0-kV electrode (analyzing magnet off) as a function of electron trap voltage. With -1 kV on the trap, the beam is 2.0-cm dia. as compared to the 1.13-cm dia. aperture in the molybdenum electrodes. With the trap off, the beam spreads out to >15-cm dia. Figure 6b shows the effectiveness of the electron trap in reducing the x-ray level measured 1.2 m from the ion source. With 0 kV on the trap, the x-ray level is 16 mR/h as compared to 1.6 mR/h with -1 kV on the trap.

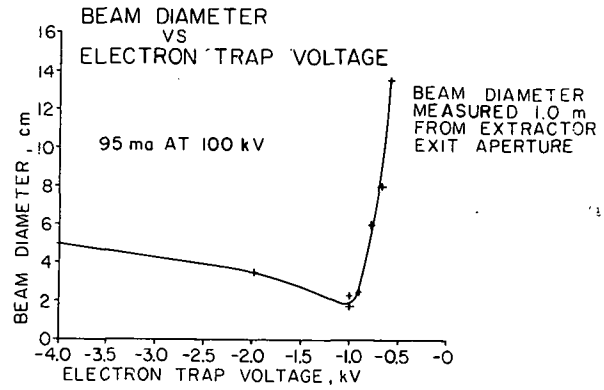


Fig. 6a Beam diameter vs electron trap voltage.

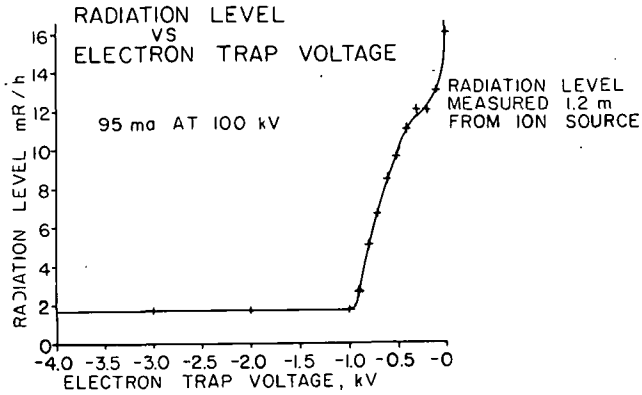


Fig. 6b Radiation level vs electron trap voltage.

Beam Transport

A double-focusing 90° analyzing magnet steers the beam into the horizontal beam line and eliminates unwanted ion species. Excitation coils, wound of hollow copper conductor and potted with a vacuum-compatible epoxy, are directly behind the pole faces. Water-cooled beam dumps protect the bottom and downstream side of the magnet box from the impingement of the unwanted species.

The analyzed beam will be tailored for acceptance by the rf quadrupole (RFQ) by two beam steerers and two magnetic quadrupole doublets. An eight-vane water-cooled variable iris structure will be used to adjust the beam current while maintaining a near-constant current density. A combination kicker magnet and beam dump will be used to provide H_2^+ ion beam pulses for tuning purposes.

Beam Diagnostics

Beam diagnostic equipment will include three multidimensional optical beam profile monitors and appropriate beam-current monitors. Two emittance measuring devices are being built. One is a two-meter-long drift tube terminated with a water-cooled pepperpot analyzer. The other is a more sophisticated double-scanning high-power density unit for measuring detailed structure of the beam. Observation of the extracted beam (including all ion species) in the one-meter-long drift space below the extractor, assuming that only emittance contributes to beam divergence, leads to an upper-limit estimate of normalized emittance $E_n < 0.04\pi$ cm-mrad.

Vacuum System

The injector vacuum system, utilizing a 10,000-ℓ/s oil-diffusion pump and beam-line ion pump, is described elsewhere.[2] Considerable attention has been given to minimizing oil contamination, which might coat the insulators and cause high-voltage breakdown in the extractor. Experience to date after 10 months of continuous operation has been very satisfactory. The system has remained clean and there is no trace of oil on the ion gauge walls. There have been no high-voltage breakdown problems in the 100-kV extractor.

Controls

Because the ion source and associated equipment dome must sit at a 100-kV potential, all controlling must be handled remotely. A microcomputer-based control and data-acquisition system utilizing fiber-optic links has been implemented. This system uses CAMAC hardware and is compatible with the facility control philosophy.

Acknowledgments

The authors wish to thank all the people who participated in setting up the injector test stand. Special thanks go to T. J. Zaugg for his work on the control system and to T. A. Stephens for much of the detailed design.

1. J. Boers, Sandia Laboratories, Albuquerque, Private Communication (1978).
2. M. D. Machalek, E. A. Meyer and L. S. Price, "The FMIT Accelerator Vacuum System," IEEE Trans. Nucl. Sci. NS-26, No. 3, 3015 (June 1979).

Discussion

West, RHEL: Do you intend to collimate the beam in the LEBT at only one longitudinal position?

Schneider: There is need to collimate it at only one position, I guess, right at the entrance of the RFQ.

West: Not if you want to maintain a constant current density, because, effectively, you are producing a beam that is not mismatched.

Schneider: Yes.

West: You have to collimate in phase space effectively.

Schneider: Right. I did not mention it but one thing that is being considered would be the use of solenoid focusing magnets here which would avoid the asymmetric focusing of the quadrupoles. By going through a circular symmetric variable iris we should be able to maintain a circular profile going into the RFQ.

West: I'm not sure I understand that.

Muller, GSI: How did you measure or estimate the degree of space charge compensation?

Schneider: That was done somewhat indirectly, using a code that has been developed and is in use at Los Alamos - one of them is a multiple species transport that Dale Armstrong has been working with. The estimate there, and we have verification of it from some other results, says that with 97% space charge neutralization, we would see the approximate beam profile that we do see. So it's indirect inference.

Curtis, FNAL: I suppose the collimator you are talking about using is for tune-up purposes only, or do you plan to continue collimating the beam when you are running full current deuterons? In which case, you will have to give some thought to the neutron yield.

Schneider: We have given some thought to that - we do have the capability of running - this entire thing will sit inside a vault behind thick concrete walls. We don't think the activation problem would be serious. It would be enough that personnel could not be inside but normally if we can run the entire accelerator at full beam current, this thing could be wide open.

Wadlinger, LASL: Why use an oil diffusion pump to pump the column?

Schneider: We have been asked that many times. I think the answer is that we have used it for some length of time and have had absolutely no problem with it. The alternative would be something like a turbo-molecular pump, which has its own problems - it is a mechanical device. This one has a lot of fast acting valves to protect it - the polythenol-ether fluid has not caused any contamination in about 2½ years of operation. It is heavily trapped - we have a freon refrigerated baffle above it, as well as the cold traps right in the trop of the pump and we get tremendous pumping by doing it. I did not mention it, but part of the motivation for that was to absolutely minimize the pressure in the high voltage region, which of course minimizes the production of x-rays.

Barton, BNL: What assumptions have been made about space charge effects in your LEBT design?

Schneider: We assumed that the beam is mostly space charge neutralized. Maybe I don't follow your question.

Barton: Well, I asked it because I understand from your vacuum system specifications you have quite different vacuum and could expect different behavior from several aspects as you go through that line.

Schneider: Oh, because the vacuum profile does change?

Barton: Not only that - just electron effects in varying magnitude.

Schneider: It is possible we'd have difficulties although we have a very substantial safety margin in that. I think there is 90% or less neutralization, the beam would still be able to be transported easily.

Pre-Accelerator for the NEN Linac

R. F. Bentley
New England Nuclear Corp.
N. Billerica, Mass. 01862

Summary

The design of the ion source, mass selector, accelerating column and transport system is described for a 780-keV proton beam of 8-mA average current. Departures from previous linac preaccelerator designs to achieve this current include a cusp field bucket ion source and a 90° analysis bend in the high voltage terminal prior to the second acceleration stage to 780 keV. The layout, beam optics and design philosophy are presented.

High Voltage Power Supply

In order to minimize the linac project staff, systems were to be designed and fabricated by vendors where this expertise was available. This system was ordered from Haefely, to an NEN performance specification, and includes the ion source terminal, and fast "bouncer" regulation to ±.1%. The design is similar to other models, but with higher stored energy to accomodate the increased beam current. Figure 1 shows the block schematic for this system which is presently assembled and operating in Haefely test facilities.

High Voltage Equipment Terminal

Power will be provided to the high voltage terminal for the ion source and other equipment by an isolation transformer stack. Five sections, each rated at 30 KVA of 208-V 3-ϕ, 8% impedance and insulated against 200 kV have been designed, tested, and delivered by Hipotronics. Figure 2 shows the equipment in the terminal. The ion source is pulled back from the accelerating column, to allow for momentum selection of the proton beam before acceleration to 780 keV. This also permits pumping of the gas load from the ion source before it enters the high gradient region in the accelerating column where it can contribute to x-ray and electron production. The field index of 0.5 on the 90° bending magnet and the solenoid magnet[1] provide focusing and allow flexibility in the beam optics through the accelerating column and into the low energy beam transport system at 780 keV. This concept has been used elsewhere on high current electrostatic accelerators.[2] The ion source[3] is of the cusp-field type, selected for its stability, low emittance and high average current capability. Extraction voltage will be 60 kV requiring ion source supplies to be in an isolated rack elevated to this potential within the equipment terminal. The extraction supply will provide 150-mA peak current at a 10% duty cycle (arc pulsed at 60 pps, 1.7 ms). This should yield 80-mA peak, 8-mA average of protons after momentum analysis.

Vacuum pumping is provided through the bore chamber of the 90° bend magnet by a 2000 l/sec turbomolecular pump. A Faraday cup and valve are provided so that the ion source and optics can be tested and serviced independent of column vacuum or high voltage. Control will be via a microprocessor at the 720 kV (terminal) potential and the 780 kV (ion source) potential, communicating over serial

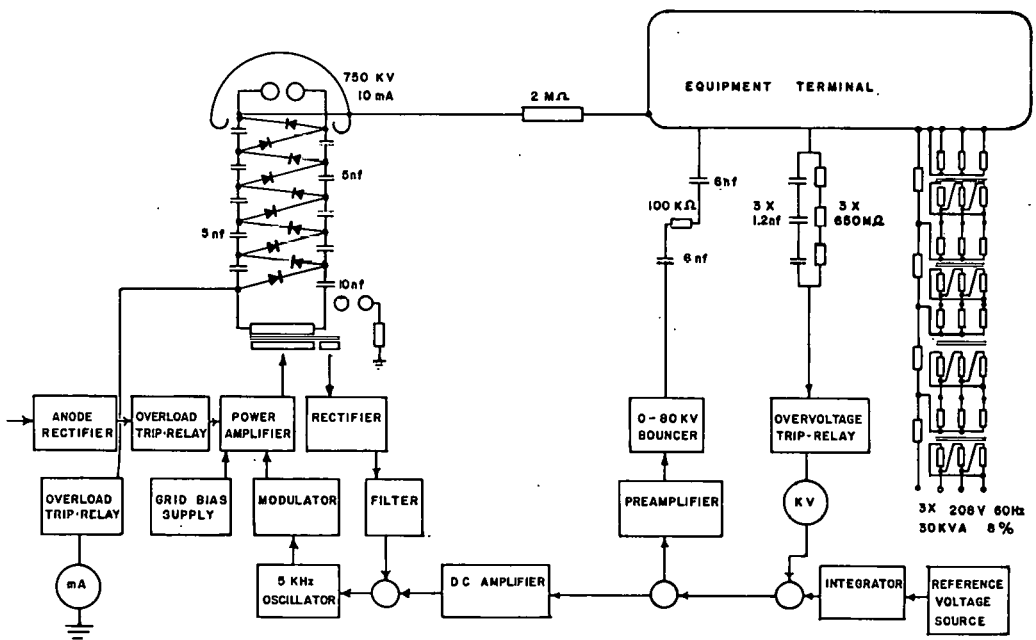


Figure 1
INJECTOR SCHEMATIC

fibre optic links with the control computer. All terminal equipment is duplicated in an ion source test stand to provide spares and development capability.

Accelerating Column

The accelerating column is a modified form of the LAMPF design, employing an intermediate SF_6 jacket, (Fig. 3). The spark gaps are inside the SF_6 on the circumference of the insulator stack to maximize energy transfer to these gaps in case of column arc-down. The stack itself, Fig. 4, is 3/4" glass rings 13" od separated by titanium discs and bonded with polyvinyl chloride.[4] The 19 electrodes will be identical, removable and nested to protect the insulator surfaces.[5] They will give a flat field of 2.1 kV/mm with a 100-mm beam aperture and have an overall length of 343 mm. The features of low gas flow through the column, good insulator protection and large beam aperture are expected to give adequate performance at 8-mA average current.

Beam Transport

The linac entrance is about 5.5 m from the column exit. Three quadrupole triplets transport the beam through 4 meters to the buncher cavities. The two large drift sections will be used for measurement of the beam parameters, an electrostatic chopper and apertures which, along with apertures in front of the buncher, will be used to define the beam envelope. The last triplet is a matched 90° phase advance unit cell in both x and y to facilitate this emittance definition. The buncher will be a copy of the CERN 200-MHz, 400-MHz buncher cavities chosen for its high capture performance and compact design. Table I and Fig. 5 show the beam optics[6] of the system source to buncher. This is a SPEAM run with 100% space charge neutralization except in the column. The quadrupoles are sized, however, for full space charge in case the neutralization proves troublesome.

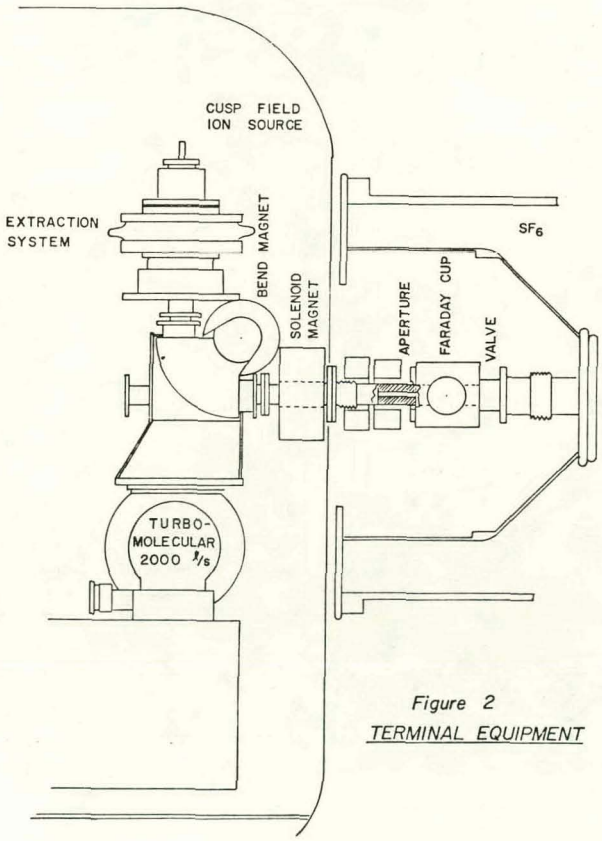


Figure 2
TERMINAL EQUIPMENT

Acknowledgements

Specific designs, vague ideas and stimulating conversations with colleagues from more than 12 laboratories in North America and England and Europe have lead to the design of this preaccelerator. I acknowledge all their contributions and hope to return their hospitality when this equipment is assembled. J. A. Farrell, R. R. Stevens and

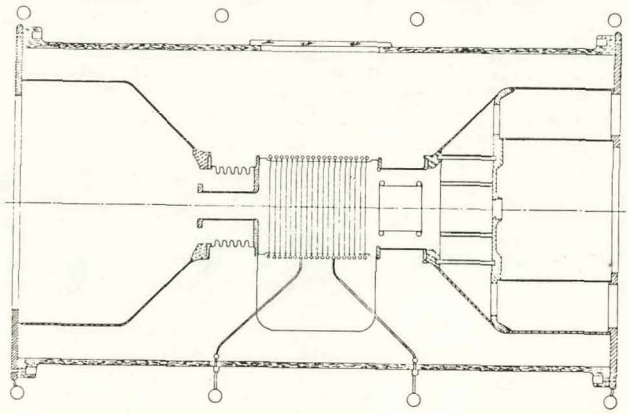


Figure 3
ACCELERATING COLUMN

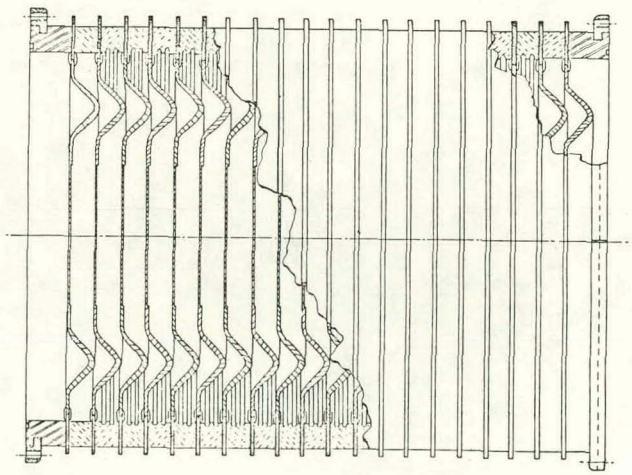


Figure 4

J. N. Leavitt of LASL have consulted on specific design problems. Finally, New England Nuclear Corporation has provided a very positive atmosphere for this effort, and every individual in the Linac Group has contributed in the pre-accelerator area.

References

1. Both designed by R. Holsinger, NEN.

2. Lawrence Livermore Laboratory, RTNS II project, J. Osher and J. C. Davis, also M. Olivo SIN and R. R. Stevens, LASL, Private Communication.

3. Source and extraction system supplied by A. Holmes, Culham Laboratory, proceedings--this conference.

4. Fabricated by Dowlish Development, Ilminster, England.

5. Cross-section of these electrodes is a modification of a shape used on the FINS column at Chalk River Nuclear Laboratories.

6. Extensive optics calculations have been carried out on the NEN VAX 11/780 computer system with the codes SPEAM (W. Joho, SIN), TRANSPORT (K. Brown, SLAC, et al.) and TRACE (K. Crandall, LASL).

Table 1

Element	Effective Length(m)	Aperture Radius(mm)	Field
ION SOURCE			
DRIFT	.15		
BEND	.28	25	.2 T
DRIFT	.15		
SOLENOID	.15	25	.23 T
DRIFT	.75		
COLUMN	.54	50	1.33 MV/M
DRIFT	.45		
QUADRUPOLE	.12	38	1.8 T/M
DRIFT	.10		
QUADRUPOLE	.24	38	1.8
DRIFT	.10		
QUADRUPOLE	.12	38	2.5
DRIFT	.87		
QUADRUPOLE	.10	25	7.2
DRIFT	.10		
QUADRUPOLE	.20	25	3.7
DRIFT	.10		
QUADRUPOLE	.10	25	3.0
DRIFT	.80		
QUADRUPOLE	.10	25	2.9
DRIFT	.10		
QUADRUPOLE	.20	25	2.6
DRIFT	.10		
QUADRUPOLE	.10	25	2.9
DRIFT	.40		
BUNCHER		9	

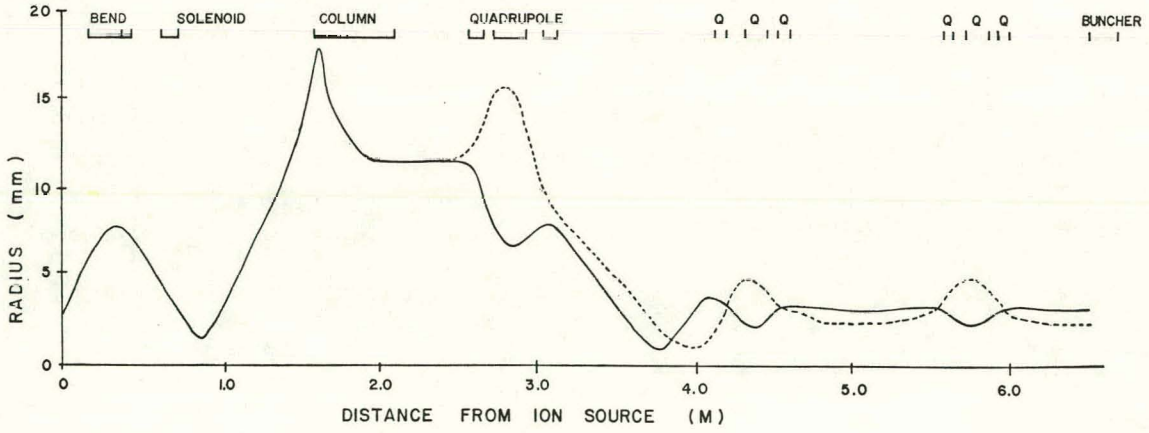


Figure 5 *BEAM PROFILE*

1979 LINEAR ACCELERATOR CONFERENCE

INJECTOR OPERATIONS AT LAMPF*

Ralph R. Stevens, Jr., John R. McConnell, E. P. Chamberlin, R. W. Hamm, and R. L. York
University of California
Los Alamos Scientific Laboratory
Los Alamos, New Mexico 87545

Summary

The injector complex at LAMPF consists of three on-line 750-kV injectors, which provide simultaneous H^+ and H^- beams for LAMPF production and an off-line 200-keV injector for ion source and beam diagnostic development studies. The present operation now entails a 500-μA_a H^+ beam accelerated simultaneously with either a 6-μA_a unpolarized or 10-nA_a polarized H^- beam. In order to obtain the low-beam spill required for the operation of the LAMPF accelerator, it has been necessary to increase the brightness of the high-intensity H^+ beam. The operating experience and development work that has been carried out on all of these injectors to improve the quality and intensity of these beams will be presented. The details of the construction of the test stand injector and the development program planned for this injector will also be outlined.

Introduction

The injector complex at LAMPF is now fully operational and consists of three 750-kV on-line injectors that provide high-intensity H^+ beams simultaneously with lower-intensity H^- beams, which may be either polarized or unpolarized. The utilization of H^- beams is now approximately equally split between polarized and unpolarized operation. At present, LAMPF is operating at a 7.5% duty factor with a 9% duty factor planned for the coming year. The overall operation of all the injectors at these duty factors continues to be relatively reliable and stable with most of the operating problems now being associated with changes incurred due to ion source development. In order to preclude these operating problems which result from on-line development of ion sources, a test stand injector is now being constructed which will provide off-line capability for developing new ion sources and beam diagnostic systems.

H^+ Beam Operation

After 1.6-mA_p (100-μA_a) beam current operation[1] was obtained in the LAMPF accelerator in 1976, it was found that the aperture limit in the accelerator was the transition region between the 201.25-MHz linac and the 805-MHz linac. Operation with the accelerator would then have been limited to currents less than 10 mA_p because of beam spill in the transition region. Studies of beam emittance growth in the linac indicated that there was little, if any, difference in the emittance growth in the 201.25-MHz linac between the low-brightness H^- beams and the higher-brightness H^+ beams then being used. It was, therefore, concluded that for the relatively low-peak currents required at LAMPF, it would be useful to increase the brightness of the H^+ beams being injected into the linac. Theoretical studies[2] of stationary distributions also indicated that a significant increase in beam brightness could be accommodated in the LAMPF accelerator. Thus, a program was initiated to increase the beam brightness for the H^+ beams.

During the past three years, a variety of approaches have been explored for increasing beam brightness. These range from optimization of ion source parameters and extraction geometry to exploration of different modes of beam transport and emittance tailoring on the low-energy beam transport lines. It was decided to retain the present ion source and optimize its operation for these relatively low-peak currents (20 to 30 mA_p). These efforts have resulted in an improvement in beam brightness by approximately a factor of four over the original beams and have permitted the desired operation of LAMPF at the 6.4-mA_p (500-μA_a) level. The present constraint for increasing H^+ beam current now is a power limitation in the pion production targets. A history of the beam emittances that have been run at LAMPF for the past three years is shown in Table I.

The major improvement in beam quality has occurred as a result of changes in the ion source and extraction system. The original LAMPF duoplasmatron was patterned closely after the BNL duoplasmatron and employed an extraction system with exact Pierce optics. This ion source has now been replaced with a different, empirically determined design employing a higher gradient extraction system. In this design, the Pierce anode has been replaced by a modified focus electrode having a much smaller aperture (6 mm instead of 14 mm) with a shape determined from calculations with the plasma simulation code SNOW. The extraction electrode has been moved closer to the ion source (1.27 instead of 2.5 cm) and now has a 6-mm aperture instead of a 14-mm aperture. This design entails higher-arc current (24 amperes instead of 8 amperes) and somewhat higher gas flow (1.5 std cc/min instead of 1.2 std cc/min). The beam profiles in the LAMPF column as calculated by the plasma simulation code SNOW are shown in Fig. 1 and a schematic diagram of the present LAMPF ion source extraction system is shown in Fig. 2.

A systematic survey of the effect of varying the ion source geometry and operating parameters has been carried out in order to arrive at this design. The basic approach has been to reduce the

*Work performed under the auspices of the U.S. Department of Energy.

TABLE I

HISTORY OF LAMPF BEAM EMITTANCES

	INJECTOR				TRANSITION REGION			
Date	Current (mA)	2% Threshold Emittance (cm-mrad)†	Brightness 2% Threshold (mA/cm^2-mrad^2)	RMS Emittance (cm-mrad)†	Current (mA)	2% Threshold Emittance (cm-mrad)†	Brightness 2% Threshold (mA/cm^2-mrad^2)	RMS Emittance (cm-mrad)†
Mar 1977	2.0 mA$_p$	V 1.46π		0.23π	1.6 mA$_p$	V 0.65π		0.07π
		H - - - - - - NO DATA - - - - - - - - -				H - - - - - NO DATA - - - - - - - - -		
July 1977	4.6 mA$_p$	V 1.34π	0.40π	0.21π	3.7 mA$_p$	V 0.51π	3.7π	0.05π
		H 1.51π		0.20π		H 0.40π		0.04π
Aug 1978	6.5 mA$_p$	V 1.50π	0.56π	0.25π	4.8 mA$_p$	V 0.44π	4.9π	0.05π
		H 1.57π		0.21π		H 0.45π		0.05π
Mar 1979	7.8 mA$_p$	V 1.00π	1.53π	0.13π	6.2 mA$_p$	V 0.36π	10.5π	0.04π
		H 1.03π		0.13π		H 0.28π		0.03π
Aug† 1979	8.0 mA$_p$	V 1.30π	0.96π	0.18π	6.4 mA$_p$	V 0.36π	10.2π	0.04π
		H 1.33π		0.19π		H 0.35π		0.04π

†The emittance values quoted are phase-space area/π and are un-normalized.

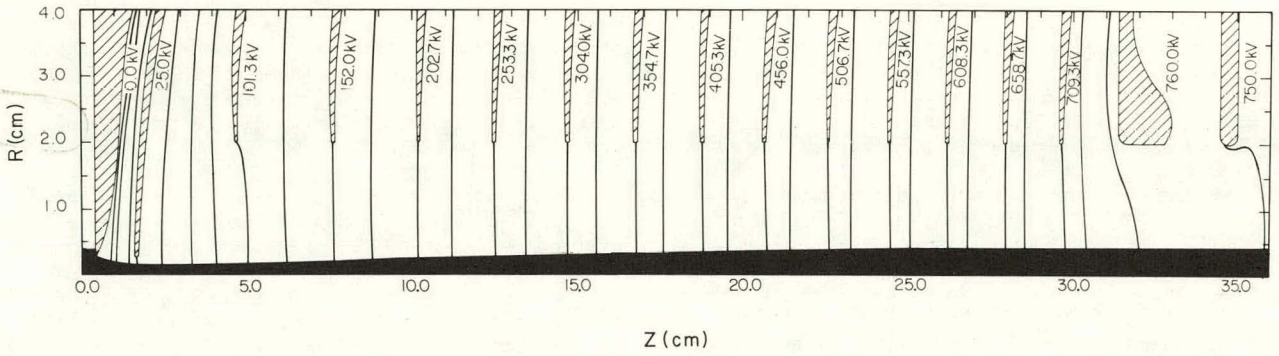


Fig. 1 Beam profiles in the H^+ accelerating column.

size of extracted beam and at the same time increase the extraction gradient so as to keep a constant extracted current. For each change in ion source geometry, optimum operating parameters were established to produce the smallest beam emittance. In general, it was found that arc current and arc-magnet current were the most critical parameters to be optimized for maximum beam current with the focus electrode potential being important for minimizing beam emittance.

The changes in operation of the ion source systems to obtain brighter beams have resulted in some on-line operating problems. Cathode failures are now much more frequent; lifetimes under best conditions are now only 500 hours instead of 3000 hours. Anode aperture units now require the use of molybdenum inserts to prevent premature melting.

A number of other ion source components have failed as these changes were made and better designs have had to be employed. The arcdown rate of the injector, however, has continued to decrease as beam brightness has been increased. The only serious high-voltage problems that occurred during these development periods resulted when spalling of the focus electrode led to ion exchange loading with the electron trap electrode. This problem was corrected by replacing the titanium focus electrode with one made of stainless steel.

Although the primary improvements have occurred from ion source changes, the details of beam transport to the linac are also important in providing high-quality beams. It is apparent, from tuning and matching exercises carried out during beam tuneup, that there can be significant emittance

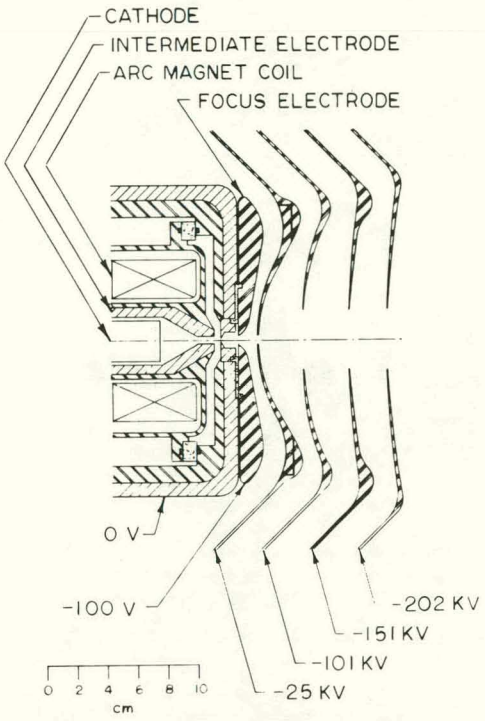


Fig. 2 Present LAMPF duoplasmatron extraction system.

distortion introduced in the low-energy beam transport system, particularly in the rf gaps of the bunchers, and that this distortion will be a limiting factor in obtaining still further improvement in the quality of beams injected into the linac. The dual-beam requirements of the linac also impose constraints on transport tunes. The original transport design of employing fixed aperture collimators to ensure axial transport into the 201-MHz linac had to be abandoned because dual-beam operation could not be effected with axial injection into the linac with the present linac misalignments.

H^- Beam Operation

There are two injectors available for providing H^- beams for LAMPF operation. One injector houses a duoplasmatron hydrogen-charge-exchange canal source while the other injector houses a Lamb-shift polarized ion source. Present operation with these injectors entails 10 μA_a of unpolarized H^- beam, which is limited by experimental area shielding, and 10-nA_a polarized H^- beam, which is limited by the ion source.

The unpolarized H^- beam is produced in the hydrogen charge-exchange canal from several molecular species of hydrogen ions. It has been necessary at LAMPF to analyze the various components of the H^- beam in the low-energy beam transport line and select that portion of the beam formed from a particular species; in this case the H^- ion formed from H_2^+ ions in the canal is used. Although the energy spread of the various components is only a few kilovolts and in itself not important, the multiple component beam has a transverse emittance distribution which is non-ellipsoidal and cannot be matched to the linac with the precision required for spill-free operation in a dual-beam operating mode. This energy analysis has resulted in a reduction of the available H^- current to only 250 μA_p, but this current is still adequate to provide the required 6-μA_a operation. Beam emittances from this injector are typically twice as large as those from the H^+ injector.

The polarized H^- beams are produced in a Lamb-shift polarized ion source, which is housed in an independent 750-kV injector. Beam currents on target of 10 nA_a are now routinely produced with 20-nA_a operation planned for the coming year. Beam polarization of 80 to 90% is produced by a spin filter system which permits on-line measurement of polarization by the quench-ratio method to better than 1%. Beam emittances are typically one-half to one-third those of the high-intensity H^+ beams and essentially 100% transmission of polarized beam captured in the linac can be obtained in spite of the poor matching obtained for H^- beams. No depolarization of polarization enhancement effects to the 1% level have been observed in the operation of the accelerator. A rapid spin-reversal capability which can flip orientation of the proton spin at a rate of up to 3 kHz has recently been put into operation for a parity violation experiment; the normal spin-reversal clocking system is generally run with a three-minute period. A spin precessor on the low-energy beam transport line permits production of beams with any desired polarization orientation in the experimental areas.

Test Stand Injector

A 200-kV test stand injector is now being constructed in the injector area to provide a means for developing new ion sources on an off-line basis. A diagram of the high voltage portion of the injector is shown in Fig. 3, and a photograph of the present construction is shown in Fig. 4.

The injector consists of a 200-kV high voltage power supply which floats an equipment rack and ion source at the desired potential. The ion source is mounted at one end of an accelerating column cantilevered from a grounded vacuum chamber. The accelerating tube consists of glass rings which have been bonded with torr seal epoxy to stainless steel washers and is mounted inside a Lucite jacket containing SF_6. Vacuum pumping is provided by two 1500 ℓ/s turbopumps mounted at ground potential; the base vacuum of the system is in the low 10^{-7} range. The ion beams are accelerated to ground potential, analyzed in a 45° bending magnet and transported to an emittance scanning station. A solenoid lens has been placed at the exit of the accelerating tube to focus these low-energy beams into the transport system.

A detailed study of the LAMPF duoplasmatron is planned as soon as construction of the injector is completed. It is anticipated that this effort will develop a duoplasmatron which will provide the

required 1-mA_a beams for the present operating mode with a single high-intensity beam. Further development of H^- ion sources required for new applications at LAMPF is then planned.

Acknowledgements

The authors wish to acknowledge the work of John Leavitt in carrying out the design work on the test stand and the work of Larry Dauelsberg and Harold Lederer in the construction of this injector.

1. John R. McConnell, Ralph R. Stevens, Jr., Paul W. Allison, and Earl A. Meyer, "Status of Injector Complex at LAMPF," Proc. of the 1976 Proton Linear Accel. Conf., Chalk River, October (1976)

2. W. P. Lysenko, "Equilibrium Phase-Space Distributions and Space Charge Limits in Linacs," Los Alamos Scientific Laboratory Report LA-7010-MS (October 1977).

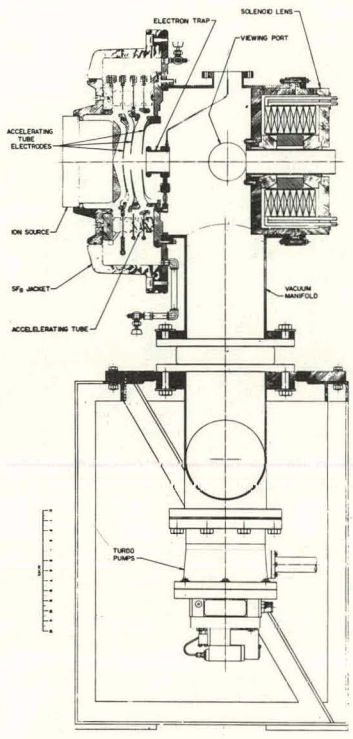


Fig. 3 The 200-kV accelerator for the ion source test stand.

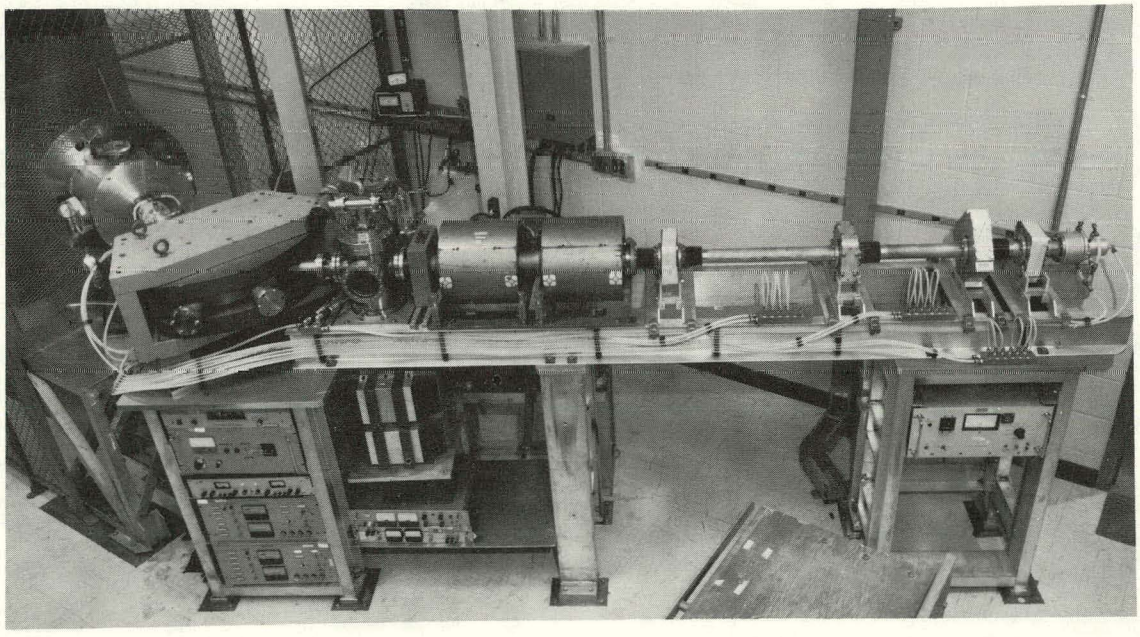


Fig. 4 Present construction of the ion source test stand.

Conference Participants

THIS PAGE

WAS INTENTIONALLY

LEFT BLANK

CONFERENCE PARTICIPANTS

Academy of Sciences of UKR.SSR
Physico-technical Institute
Kharkov, USSR

A. N. Dovbnya

Argonne National Laboratory
9700 South Cass Avenue
Argonne, Illinois 60439

R. Burke
T. Khoe
A. Moretti
E. Parker
K. W. Shepard

William F. Brobeck and Associates
1235 Tenth Street
Berkeley, California 94710

P. F. Meads

Brookhaven National Laboratory
Associated Universities, Inc.
Upton, New York 11973

D. Barton
K. Batchelor
J. P. Blewett
N. Fewell
P. Grand
E. Grove
R. E. Lockey
V. Lodestro
R. McKenzie-Wilson
S. Okumura
J. Sheehan
R. Witkover

California Institute of Technology
Low Temperature Physics
Sloan 63-37
Pasadena, California 91125

J. Dick

CERN
PS Division
1211 Geneva 23
Switzerland

E. Boltezar
D. Warner
M. Weiss

CGR MEV
Route de Guyancourt
BP No. 34
78530 BUC
France

D. T. Tran

Chalk River Nuclear Laboratories
Atomic Energy of Canada Limited, Physics Division
Chalk River, Ontario, K0J 1J0
Canada

B. G. Chidley
J. S. Fraser
L. W. Funk
J. D. Hepburn
G. E. McMichael
J. Ungrin

Daresbury Laboratory
Warrington WA4 4AD
England

E. Hughes

Department of Energy
Division of High Energy Physics
Washington, D.C. 20545

J. E. Leiss

Efremov Institute of Electro Physical Apparatus
Leningrad, USSR

A. V. Ryabtson

Fermi National Accelerator Laboratory
Post Office Box 500
Batavia, Illinois 60510

F. Cole
C. Curtis
R. Goodwin
R. Huson
P. V. Livdahl
S. Ohnuma
C. Owen
M. Palmer
C. Schmidt
M. Shea
L. Teng
D. Young

Gesellschaft fur Schwerionenforschung MBH
Postfach 110541
6100 Darmstadt 11
West Germany

N. Angert
D. Bohne
J. Klabunde
R. W. Müller
H. Trautman

J. W. Goethe University
Institute fur Angewandte Physik
Robert Maier Str. 2-4
D-6000 Frankfurt AM Main 1
West Germany

P. Junior
A. Schempp

Hanford Engineering Development Laboratory
Post Office Box 1970
Richland, Washington 99352

E. W. Pottmeyer
L. Trego

Institute of High Energy Physics - China
Post Office Box 918
Beijing, China

C. I. Chou
K. L. Li
Y. H. Lo
J. J. Zhuang

Institute of Physics and Chem. Research - Japan
Rikagaku Kenkyusho
Wako-shi, Saitama 351
Japan

T. Kambara

Institute of Theoret. - Expertl. Physics - USSR
117259 Moscow, USSR

N. V. Lazarev

Jaeri-Japan Atomic Energy Research Institute
Tokai Research Establishment
Tokai-mura, Naka-gun, Ibaraki-gen
Japan

K. Tsukada

Karlsruhe University
Institut fur Experimentelle Kernphysik
Postfach 3640, 7500 Karlsruhe 1
West Germany

A. Citron
K. Mittag
K. Zieher

Laboratoire National Saturne
CEN Saclay-LNS
BP No. 2, 91190 Gif-Sur-Yvette
France

B. Aune
J.-P. Auclair
J.-L. Lemaire

Lawrence Berkeley Laboratory
University of California
Berkeley, California 94720

D. Clark
J. Glatz
K. Halbach
D. Judd
J. Kalnins
D. Keefe
H. Lancaster
F. Selph
J. Staples

Lawrence Livermore Laboratory
University of California
Post Office Box 808
Livermore, California 94550

R. A. Alvarez

Los Alamos Scientific Laboratory
Division MS-817
Post Office Box 1663
Los Alamos, New Mexico 87545

K. Crandall
R. Hamm
L. Hansborough
F. Humphrey
S. Klosterbuer
W. Lysenko
J. M. Potter
G. W. Rodenz
S. O. Schriber
W. Stein
R. Stokes
J. Stovall
D. A. Swenson
A. Wadlinger
T. Wangler
L. Wilkerson

Los Alamos Scientific Laboratory
Division MS-821
Los Alamos, New Mexico 87545

D. D. Armstrong
G. P. Boicourt
D. D. Chamberlin
M. F. Fazio
J. Frank
C. Fuller
R. A. Jameson
J. A. Johnson
E. L. Kemp
E. A. Knapp
D. J. Liska
M. D. Machalek
H. Rutkowski
R. G. Schamaun
J. D. Schneider
A. R. Swanson

Los Alamos Scientific Laboratory
MP Division
Los Alamos, New Mexico 87545

D. Hagerman
V. Hart
R. E. Hill
O. Sander
R. R. Stevens
G. R. Swain
G. Wallace

Massachusetts Institute of Technology
Physics Department
Cambridge, Massachusetts 02139

P. T. Demos

Max Planck Institut fur Kernphysik
6900 Heidelberg
West Germany

E. Jaeschke
R. Repnow

Mexico - Instituto Politecuico Nacional
Escuela Superior de Fisicz y Matematicas
Zacatenco, Mexico 14 D.f.

V. Flores

National Bureau of Standards
United States Department of Commerce
Center for Radiation Research
Washington, D.C. 20234

I. J. Livant
D. L. Mohr
S. Penner
J. Rose
M. Wilson

National Laboratory for HEP (KEK) - Japan
Oho-machi, Tsukuba-gun, Ibaraki-ken
300-32 Japan

Y. Kojima
J. Tanaka

New England Nuclear Corporation
601 Treble Cove Road
Billerica, Massachusetts 01862

R. Bentley
D. Comastra
R. Damm
S. Dinaro
R. Holsinger
R. Lankshear
J. Liebau
H. Schneider

RCA Electro Optics and Devices
Solid State Division
Lancaster, Pennsylvania 17604

J. D. Stabley

Rutherford Laboratory
Chilton, Didcot
Oxfordshire OX11 OOX
England

B. G. Brady
A. D. Marshall
N. D. West

Stanford Linear Accelerator Center
Post Office Box 4349
Stanford, California 94305

M. A. Allen
Z. Farkas
H. A. Hogg
M. Jablonka
J. V. Lebacqz
R. H. Miller

State University of New York at Stony Brook
Department of Physics
Stony Brook, New York 11794

J. Brennan
C. Pancake

Systems Science and Software
Post Office Box 4083
Hayward, California 94540

S. Farrell

Temple University
College Liberal Arts
Sullivan Hall - 2nd Floor
Philadelphia, Pennsylvania 19122

G. W. Wheeler

University of Maryland
Office of the Chancellor
College Park, Maryland 20742

R. Gluckstern

University of Tokyo
Institute for Nuclear Study
Tanashi, Tokyo 188
Japan

S. Arai
E. Tojyo

Varian Associates
611 Hansen Way
Palo Alto, California 94303

J. Manca
E. Tanabe

Varian Associates, Eimac Division
301 Industrial Way
San Carlos, California 94070

J. R. Faulkner

THIS PAGE

WAS INTENTIONALLY

LEFT BLANK

AUTHOR INDEX

A

Aggus, J. - 384
Anami, S. - 8,94,319,367
Angert, N. - 17,436
Arai, S. - 184
Armstrong, D.D. - 457
Aron, J. - 104
Artyomov, V.I. - 118
Auclair, J.-P. - 37,43,364
Aune, B. - 440

B

Baba, H. - 94,367
Barton, D.S. - 47
Batchelor, K. - 13
Benaroya, B. - 104
Bentley, R.F. - 462
Besse, L.J. - 269
Bittner, J. - 13
Blasche, K. - 249
Blewett, J.P. - 1
Böhne, D. - 17,98,348,388
Boicourt, G.P. - 238
Bollinger, L.M. - 104
Boltezar, E. - 66,392
Brau, C.A. - 53
Brown, J.C. - 360
Bukharin, V.L. - 197
Burke, R.J. - 152
Bywater, J.A. - 152

C

Caspar, W. - 159
Catlin, L.L. - 457
Chamberlin, D.D. - 314
Chamberlin, E.P. - 465
Chamouard, P.-A. - 37,43,364
Chang, Y.-J. - 5
Chiba, Y. - 28
Chidley, B.G. - 360,448
Clark, D.C. - 396
Clark, D.J. - 409
Clifft, B.G. - 104
Cole, T. - 396
Comastra, D. - 32
Coops, W. - 396
Crandall, K.R. - 205
Creek, K. - 396
Cuperus, J. - 344

D

Dahl, L. - 291
Damm, R. - 384
Deitinghoff, H. - 217
Dickinson, T. - 13
Dovbnya, A.N. - 118

E

Emmerling, M. - 348
Enomoto, A. - 8

F

Fahmie, M.P. - 269
Farkas, Z.D. - 190
Farrell, J.A. - 25
Faulkner, J.R. - 336
Fazio, M.V. - 356
Fewell, N.M. - 83
Fouan, J.P. - 114
Fox, W. - 396
Franczak, B. - 249
Frank, J.A. - 396
Franzke, B. - 249
Fraser, J.S. - 180
Fukuda, S. - 8,319
Fukumoto, S. - 94,367
Fuller, C.W. - 401
Furuya, T. - 194

G

Gaiser, H. - 388
Gammel, G.M. - 453
Gasper, A. - 348
Gastebois, J. - 114
Giles, P. - 396
Glatz, J. - 269
Gluckstern, R.L. - 245
Goodwin, R.W. - 274
Grando, J. - 420
Greenberg, G. - 384
Greenwood, D. - 396

H

Hagerman, D.C. - 78,262
Hamm, R.W. - 432,465
Haseroth, H. - 66,286,420,444
Henning, W. - 104
Hepburn, J.D. - 448
Hill, C. - 420
Hill, R.E. - 283
Hochschild, G. - 114
Holmes, A.J.T. - 424
Holsinger, R.F. - 373
Hone, M. - 420,444
Hornung, A. - 114
Hosoyama, K. - 194
Huck, B. - 109
Humphry, F.J. - 144

I

Ingwersen, H. - 109
Inman, M. - 424
Ito, K. - 94,367

J

Jaeschke, E. - 109
James, F. - 344
Jameson, R.A. - 231,238,314
Johnson, H.P. - 356
Johnson, J.A. - 279
Johnson, K.W. - 104
Joly, P. - 114
Jorna, S. - 152
Judd, D.L. - 61
Junior, P. - 217

K

Kakuyama, T. - 94
Kalnins, J.G. - 223
Kambara, T. - 28
Kato, T. - 194
Keith, S.R. - 269
Keller, R. - 436
Kemp, E.L. - 21
Khoe, T.K. - 152
Klabunde, J. - 17,291,297
Klein, H. - 159,217
Kobayashi, K. - 118,184,319
Kojima, Y. - 194
Kolb, B. - 109
Konno, O. - 194
Kovalenko, N.A. - 118
Kovarik, V. - 428
Kubota, C. - 94,367

L

Lancaster, H.D. - 269
Lankshear, R.F. - 340
Lari, R.J. - 152
Lazarev, N.V. - 380
Lebacqz, J.V. - 327
Lemaire, J.-L. - 37,43,364
Liska, D.J. - 21,25,396
Lo, T.-H. - 5
Lo, Y.-H. - 5
LoDestro, V. - 83
Loree, T.R. - 53
Lotterbach, G. - 159

M

Machalek, M.D. - 21
Machen, D.R. - 279
Magyary, S.B. - 269
Malwitz, E. - 388
Markovich, P. - 104
Matsumoto, K. - 8,319
Meads, P. - 25
Meier, E.F. - 453
Melson, K.E. - 25
Meyer, E.A. - 457
Miller, R.H. - 440
Mills, R.S. - 231
Minerbo, G.N. - 314
Mittag, K. - 253
Mobley, R.M. - 453
Moenich, J.S. - 152
Moretti, A. - 152
Mori, Y. - 94,367
Müller, E. - 159
Müller, R.W. - 147

Mc

McConnell, J.R. - 465
McKeown, J. - 180
McMichael, G.E. - 180

N

Nakahara, K. - 8
Nikolaev, V.M. - 122
Nixon, J.M. - 104
Norman, H. - 396
Novozhilov, A.Y. - 197

O

Odera, M. - 28

P

Peng, H. - 257
Pirkl, W. - 66,344
Plass, G. - 66
Plink, O.V. - 197
Potter, C. - 396
Potter, J.M. - 138,144,176,401

R

Racaniello, V. - 13
Repnow, R. - 109
Riggin, D.M. - 356
Ritchie, A.L. - 269
Rjactsov, A.V. - 122
Rockwood, S.D. - 53
Rodenz, G.W. - 144
Rohrbach, W. - 159
Rutkowski, H.L. - 457

S

Sakaue, T. - 94,367
Sander, O.R. - 314
Sato, I. - 8,94,319
Schaa, V. - 291,297
Schaffner, E. - 297
Schamaun, R.G. - 396
Schempp, A. - 159
Schneider, J.D. - 457
Schriber, S.O. - 164,176
Selph, F.B. - 269
Severgin, Yu. P. - 122
Shea, M.F. - 274
Sheehan, J. - 13
Shepard, K.W. - 104
Sherwood, B.A. - 457
Sherwood, T. - 66
Shidara, T. - 8
Shilov, V.K. - 197
Shinohara, K. - 367
Shkolnikov, E.J. - 197
Shubaly, M.R. - 448
Skachkov, V.S. - 380
Sluyters, Th. - 428
Smirnov, V.L. - 122
Sobenin, N.P. - 197
Stein, W.E. - 53,57
Stepnov, V.V. - 197
Stevens, R.R., Jr. - 465
Stockley, R.J. - 152
Stokes, R.H. - 205
Stover, G.R. - 269
Strehl, P. - 291,297
Suyama, R.M. - 279
Svistunov, Yu. A. - 122
Swain, G.R. - 262
Swanson, A.R. - 283
Swenson, D.A. - 129

T

Tabata, Y. - 319
Tagawa, S. - 319
Takagi, A. - 94
Takano, S. - 94
Takenaka, T. - 94,367
Tallgren, U. - 66
Tanaka, J. - 8,94,319,367
Têtu, P. - 66,309
Tojyo, E. - 184
Trautmann, H. - 17

U

Ungrin, J. - 360,448

V

Vakhrushin, Yu.P. - 122
Vallet, J.L. - 444
Vilhjalmsson, H. - 297
Vineyard, G. - xvii
Vishnyakov, V.A. - 118

W

Wadlinger, E.A. - 242
Walcher, Th. - 109
Wang, S.-H. - 5
Wangler, T.P. - 205
Warner, D. - 66,304
Washio, M. - 319
Watson, J.M. - 152
Weiss, M. - 66,227
West, N.D. - 88
Wheeler, G.W. - xiii
Williams, S.W. - 144,401
Wilms, D. - 297
Witkover, R.L. - 47

Y

York, R.L. - 465
Yoshida, K. - 184

Z

Zhuang, J. - 257
Zieher, K.W. - 114

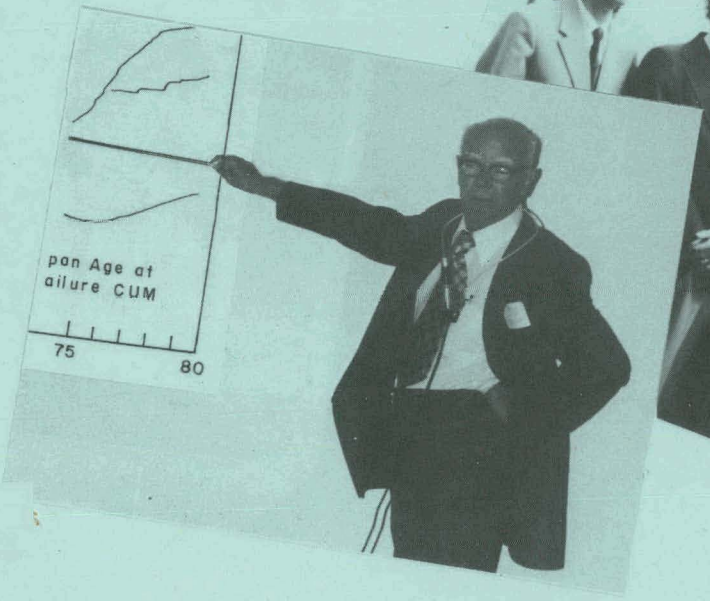
☆ U.S. GOVERNMENT PRINTING OFFICE: 1980— 44










pan Age at
ailure CUM
75
80